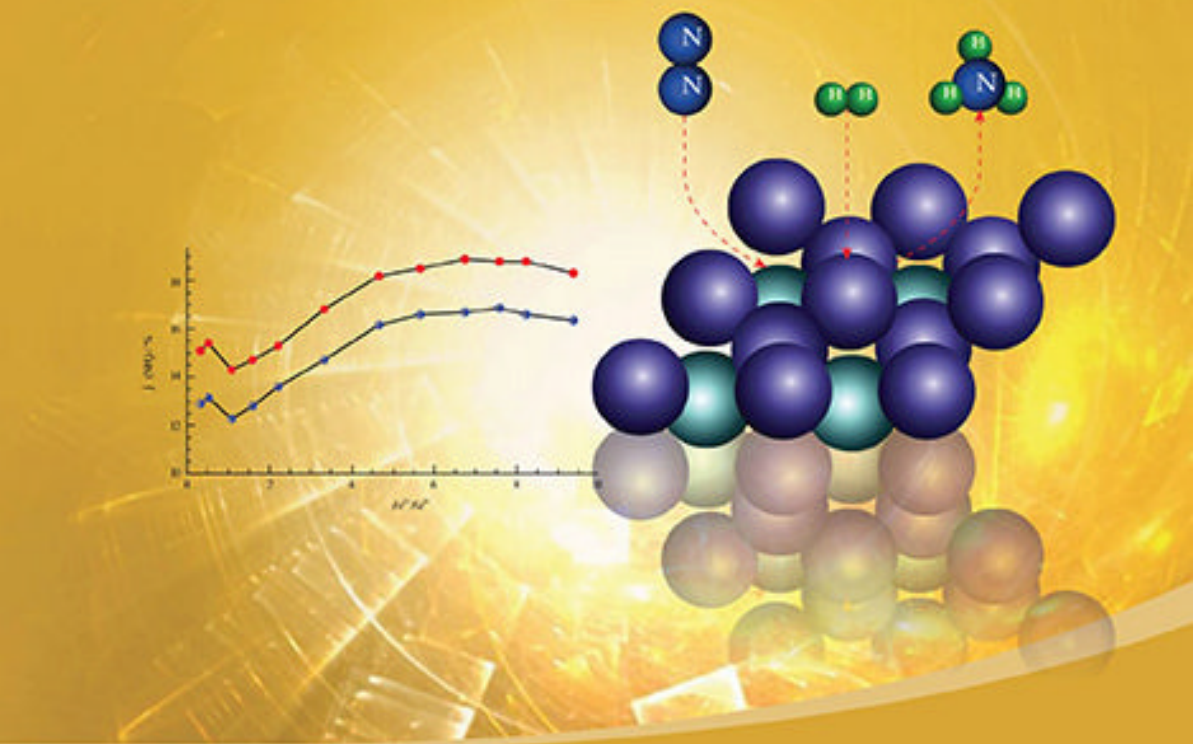
Ammonia Synthesis Catalysts

Innovation and Practice

Huazhang Liu



Chemical Industry Press

World Scientific

Ammonia Synthesis Catalysts

Innovation and Practice

This page intentionally left blank

Ammonia Synthesis Catalysts

Innovation and Practice

Huazhang Liu

Zhejiang University of Technology, China



Chemical Industry Press

World Scientific

NEW JERSEY • LONDON • SINGAPORE • BEIJING • SHANGHAI • HONG KONG • TAIPEI • CHENNAI

Published by

World Scientific Publishing Co. Pte. Ltd.

5 Toh Tuck Link, Singapore 596224

USA office: 27 Warren Street, Suite 401-402, Hackensack, NJ 07601

UK office: 57 Shelton Street, Covent Garden, London WC2H 9HE

and

Chemical Industry Press
No. 13 Qingnianhu South Street
Dongcheng District
Beijing 100011
P.R. China

British Library Cataloguing-in-Publication Data
A catalogue record for this book is available from the British Library.

This edition is jointly published by World Scientific Publishing Co. Pte. Ltd. and Chemical Industry Press, P. R. China.

AMMONIA SYNTHESIS CATALYSTS
Innovation and Practice

Copyright © 2013 by World Scientific Publishing Co. Pte. Ltd. and Chemical Industry Press

All rights reserved. This book, or parts thereof, may not be reproduced in any form or by any means, electronic or mechanical, including photocopying, recording or any information storage and retrieval system now known or to be invented, without written permission from the Publisher.

For photocopying of material in this volume, please pay a copying fee through the Copyright Clearance Center, Inc., 222 Rosewood Drive, Danvers, MA 01923, USA. In this case permission to photocopy is not required from the publisher.

ISBN 978-981-4355-77-3

Typeset by Stallion Press
Email: enquiries@stallionpress.com

Printed in Singapore.



Liu Huazhang

Professor, Director of Institute of Industrial Catalysis, Zhejiang University of Technology (ZJUT); Syndic and Vice Director of Chemical Fertilizer Committee of Chemical Industry and Engineering Society of China and Member of the Catalysis Committee of Chinese Chemistry Society.

Liu was born in Zhejiang in 1940. He received his bachelor degree in Chemical Engineering at the ZJUT in 1964 and has been working in ZJUT since then. As a visiting scholar, he was engaged in catalytic reaction engineering in National University of Yokohama of Japan in 1982 and in catalytic chemistry in Hokkaido University of Japan in 1996.

Since 1964, he has been engaged in the study of ammonia synthesis catalyst and Fischer–Tropsch synthesis catalyst and chemical engineering, including iron based- and ruthenium based-catalysts. He invented the first $Fe_{1-x}O$-based ammonia synthesis catalysts and their theoretic system in the world in 1986, and developed successfully the A110-2, A301, ZA-5 series industrial ammonia synthesis catalysts. He has over 270 scientific papers, 21 patents and books to his credit. As a first contributor, he has received many important national awards of science and technology, including the second and third prize of National Invention Award, the second prize of National Scientific & Technological Progress Award, and seven times for the first prize of Scientific & Technological Progress Award from Zhejiang province and the Ministry of Chemical Industry.

Professor Liu has won a series of prestigious honors, such as the National Outstanding Specialized Technical Talent, the National Young Experts in Science & Technology with Prominent Contribution, the National Overseas Returnees with Prominent Contribution, the National WUYI Labor Medal, the Achievement Award of HOU Debang Chemical Industry Science & Technology Award and the Honor Teacher and the Superfine Professor of Zhejiang province and so on.

Preface

The first high-pressure ammonia synthesis reactor in the world designed by C. Bosch in 1911 is still standing in a small garden in front of the building of BASF ammonia synthesis institute. It is a milestone in the history of catalytic ammonia synthesis process. On 9 September 1913, the first catalytic ammonia synthesis setup started its commission which could produce five tons of ammonia per day in the world. After that, the industry of ammonia synthesis has been developed rapidly. The catalytic ammonia synthesis technology has played a central role in the development of the chemical industry during the 20th century. Till the beginning of the 21st century, the ammonia synthesis plants with a capacity of 1,000 or 2,000 tons per day spread all over the world. This is an epoch-making achievement which proved that the ability of human could conquer the nature.

The tremendous success of synthetic ammonia industry not only meets the growing need for food due to the growth of population, but also leads the development of a series of basic theories. Ammonia synthesis industry itself contains a great number of creative scientific thoughts. All of the following theories promoted the development of the entire chemical industry and materials industries, including the application of chemical equilibrium and the law of mass action forward; high-pressure reaction technology realized by Haber, operating in a closed flow path, the concept of dynamic reaction rate and the concept of multi-promoters complex catalysts put forward by Mittasch etc. It is a precedent of the success that leads to the close cooperation of chemists, physicists, engineers, material scientists and various artisans. The tremendous success of ammonia synthesis industry and its catalytic process established a foundation for heterogeneous catalysis. Often new techniques, methods and theories of catalysis have initially been developed and applied in connection with studies of this system.

The fused iron catalyst is one of the most successful and most fully studied catalysts in the world. But the discussion on the inbeing of the ammonia synthesis reaction has not ended. There are a lot of questions still needing to be answered on the structure of the catalysts and the formation mechanism of ammonia molecules. Although the relative importance of research on catalytic ammonia synthesis has decreased and now it is not the focus of research on catalysis due to the development of the fields on petrochemistry, biochemistry, macromolecule and environmental catalysis etc, the development of ammonia synthesis industry and the progress of the catalytic technology will never stop.

The modern industrial iron catalyst is a nanostructured metastable substance, which is formed during the surprisingly complex synthesis of the oxide precursor.

Its metastability is the reason for its sensitivity towards thermal overstress during activation and oxidation of the activated material. The formation of the nanostructured system is related to alternative preparation routes i.e., the oxide precursor. It was commonly considered for about 100 years that the fused iron catalysts with Fe_3O_4 as precursor were the most active. Therefore the research for fused iron catalysts was limited to Fe_3O_4 and the effect of the oxide precursor on the performances of catalyst was neglected. The iron catalysts used in industry almost have no fundamental differences compared with the one that BASF Company developed 100 years ago. On the whole, this catalyst with Fe_3O_4 as precursor was considered well consolidated and no special improvement was expected. It will prompt people to seek a new technical breakthrough — a kind of discontinuously and leapfrog technical progress. The discovery of $Fe_{1-x}O$-based and ruthenium-based catalysts and Co–Mo bimetallic nitride catalyst is a proof of the idea.

The discovery of the $Fe_{1-x}O$ based catalyst with wüstite structure was a breakthrough of the classical theory on the oxide precursor and the activity is higher than the best magnetite-based catalysts in the world. This invention indicates an essential improvement on the research for ammonia synthesis catalysts since 1913. It is a chance for further progress of iron catalyst and aroused much attention of the scientists in the field. At present, the $Fe_{1-x}O$ based catalyst has been widely used in industry.

Ruthenium and Co–Mo bimetallic nitrides stand out in the group of the non-iron catalysts. Among single metal, ruthenium, osmium and iron are the most active catalysts for ammonia synthesis. Ruthenium-based catalysts have a much longer history of development and are applied successfully. However, these metals are very expensive and thus less commercially attractive compared to the third-best catalyst, Fe, and there is no significant advantage in terms of energy-saving. Therefore, in industry, it is still necessary to find a catalyst which is cheaper and more efficient than ruthenium catalysts.

Norskov proposed a more scientific and effective theory, i.e., interpolation in the periodic table, for designing bimetallic catalysts. According to this theory, a reasonable assumption is to combine the most active and less active elements for activation of nitrogen together to construct an active surface to achieve the best performance. The idea was proved by an efficient non-ruthenium catalyst on the basis of cobalt–molybdenum nitride, which can be regarded as the current climax of a systematically but empirically justified development based on the theoretical prediction of the ammonia synthesis catalyst research up to now.

At present, the whole world has paid more and more attention to the energy problems and the strict limit of CO_2 emission. This makes the ammonia synthesis industry face a great new challenge.

The new challenge on the theory is about the prediction of biomimetic ammonia-synthesis path at room temperature and atmospheric pressure. There are some reports on the study of photocatalytic, bio-catalytic and electrochemical ammonia synthesis catalysts. The latter should be achieved preferably by electrochemical processes with efficiency similar to the synthesis strategies that are available today.

There are also new challenges for new applications. In the 21st century, nitrogenous fertilizer is not only an agrochemical but also an industrial product which is responsible both for the increase of agricultural production and the bio-energy. Ammonia would make a convenient storage molecule for hydrogen for operation in

fuel cells. Synthesis and decomposition of ammonia can be well controlled and it is one of the preferred work-medium for effective solar energy conversion, transmission and storage. Ammonia synthesis plant is actually an energy conversion device; if a practical and safe transfer of the industrial logistic into an end-consumer field were to be obtained, then a powerful alternative for the generation of hydrogen could be at our disposal.

Nitrogen atoms are essential for the function of biological molecules and thus are important component of fertilizers and medicaments. Ammonia is also used in non-biological field, such as printing and dyeing, explosives and resins. Synthesis of these materials requires ammonia as an activated nitrogen building block. The nitrogen cycle is one of the most important cycles in nature that maintains life in the world. The catalytic ammonia synthesis is one of the key elements in the nitrogen cycle in nature, which is very important complementarity for activated nitrogen. At present, catalytic ammonia synthesis is still the only way to obtain activated nitrogen in industry.

There is no other practically relevant reaction that leads to such a close interconnection between theory, model catalysis and experiment as the high-pressure synthesis of ammonia. As well as being of high industrial relevance, the catalytic synthesis of ammonia is also a key reaction for creating new life and a prototypical model reaction that helps in gaining a fundamental understanding of catalysis in general and therefore of considerable scientific and cultural importance. It is mainly this reason that drives the ongoing research in ammonia synthesis, especially since evidence for a knowledge based improvement of a catalyst would have a strong signaling effect on other fields of catalysis research.

Fortunately, since 1960s, the author has discerned the development of ammonia synthesis industry in China, and has joined in the research of Fe_3O_4-based, Fe_3O_4-cobalt-based, $Fe_{1-x}O$-based and ruthenium-based catalysts. The author and his co-workers have first invented a novel generation of $Fe_{1-x}O$-based catalysts which is more active than the best magnetite-based catalysts in the world, and have developed successfully a series of new catalysts such as A110-2, A301 and ZA-5 etc that are widely used in industry.

These are outlines of the development of ammonia synthesis catalyst and also our experience of the research on catalyst for the past 46 years. This book is based on the new generation of $Fe_{1-x}O$-based catalysts, and focuses on the innovation, development and application of catalyst and is mainly based on our own practice. At the same time, this book draws a lot of achievements of research in the field, which makes this book unique with depth to explain basic concepts and the scientific basis, and combines catalyst with engineering, so it can help readers understand more about ammonia synthesis.

This book comprises 10 chapters which can be classified into four parts. The first part deals with the catalyst itself, including the development (Chapter 1), chemical components and physical structure (Chapter 3); preparation and reduction (Chapters 4 & 5) and the performance evaluation of the catalysts (Chapter 7). Those of ruthenium catalysts are solely put in Chapter 6. The second part is about the reaction mechanism and kinetics of ammonia synthesis (Chapter 2). The third part is a combination of the above two, namely, is centered on the relationship between the performance of catalysts and reaction, which includes reaction condition, reactor, process and application condition and its impact on the economic benefit of

catalytic process (Chapters 8 & 9). In the final part of this book, new exploration for catalyst and new technologies for ammonia synthesis including Co–Mo nitride catalyst, photo-catalysis, electrochemical catalysis, and biocatalysis, and new use of ammonia are introduced.

Here, I would like to thank all of my co-workers for their contribution and support during my over 46 years of catalytic study. I wish to extend my appreciation to all my friends and scholars, e.g., Prof. Chen Songying (Zhejiang University), Liang Changhai (Daliang University of Technology), Polock Yue (Hong Kong University of Science and Technology), Kong Yuhua (Hubei Research Academy of Chemistry), and Hu Weixiao, Chang Hai, Xiao Lihua, Wang Jianguo, Huo Cao, Shi Hongxian, Yao Nan, Li Ying, Hu Xiaojun, Zhou Chunhui, Han Wenfeng, Liu Zhongjian (Zhejiang University of Technology) *et al.*, and N. Pernicone (Universities of Milan and Venice in Italy) for their support, and also for the support from Chemical Industry Press in China, World Scientific Publishing Co. Ptc. Ltd. in Singapore and Zhejiang University of Technology. I thank Dr. Cen Yaqing for her assistance with preparation of this manuscript.

LIU Huazhang
18 December 2010

Foreword

Human beings live on grains and grain production is inseparable from fertilizers. In the past, human beings used to add animal excrements and rotten plants to soil as fertilizers. The use of chemical fertilizers has changed the history of grain production. According to Food and Agriculture Organization (FAO), the contribution of chemical fertilizers in grain production is about 40%. Without chemical fertilizers, more people would be under the threat of hunger and poverty. It would be impossible for China to feed the world's 22% population with only 7% arable land.

There are mainly three kinds of chemical fertilizers, i.e., nitrogen, phosphorus and potassium fertilizers. In order to increase the production and quality of grain, different kinds of chemical fertilizers should be used according to the nature of the soil and the crops. Among the three fertilizers, nitrogen fertilizer based on synthetic ammonia is the most widely used.

China is the largest producer of synthetic ammonia in the world. Ammonia production in 2007 reached 53 million tons in China, which greatly contributed to grain production. Producing synthetic ammonia is highly energy-consuming. The annual energy consumption for ammonia production is about 100 million tons of standard coal according to current energy consumption level, which is responsible for 3.4% of China's total energy consumption. Thus, reducing energy consumption in ammonia production is a great challenge for the industry. Practices show that reduction in energy consumption in chemical production mainly comes from technology advance in catalysts and process innovation. The catalytic ammonia synthesis process has been developed to a mature stage in the past century; therefore lower energy consumption will depend mainly on the technique development of catalysts and process improvement based on the new catalysts. Fortunately, the new generation of ammonia synthesis catalysts has been industrialized, which is expected to bring revolution to the ammonia synthesis industry. With the application of new catalysts, the synloop operating pressure will be further reduced. Through the use of $Fe_{1-x}O$-based fused iron catalysts and ruthenium catalysts, it is possible to realize the isotonic pressure ammonia synthesis for the process using partial oxidation of heavy oil at 8.7 MPa. If the pressure can be decreased to below 5 MPa, the isotonic pressure ammonia synthesis for the process using natural gas reforming can also be realized in the near future. With the innovation of new catalysts and related development of low pressure process, it is possible to skip out of the scope of high-pressure industry for ammonia synthesis, significantly saving energy. More than half of the output of ammonia in China is by small to medium scale equipments. Their energy consumption is 50% higher than that at the advanced level, thus with high potential in

energy-saving. The application of new energy-saving catalysts and the technology based on low-pressure process are effective in saving energy.

Ammonia synthesis catalyst is well known as a textbook catalyst, which is mentioned in most of the textbooks and publications on catalysis. However, the information and knowledge about ammonia synthesis is not complete and only mentioned in some chapters of those books. In this sense, this book is a rare one, presenting relatively thorough and systematic description of ammonia synthesis catalysts and their industrial application.

The author, Professor Huazhang Liu, has been working in catalysts and related engineering techniques of ammonia synthesis for more than 40 years. He contributed a lot to the research of the Fe_3O_4-based, $Fe_{1-x}O$-based, and ruthenium-based ammonia synthesis catalysts. He invented the novel $Fe_{1-x}O$-based ammonia synthesis catalysts. His research also covers the theory and methodology on catalysts preparation, reaction mechanism, catalytic reactor, chemical engineering and related fields.

This book puts more attention on the development and applications of the catalysts with a combination of the author's experience and updated research results. This book is useful due to a combination of practices and theory, including the research, development, application and reaction engineering of catalysts. It has practical value as well as theoretical depth. These features make the book more comprehensive, novel and practical.

This book is of important reference value to researchers, engineers and graduate students who undertake catalysis research and industrial applications. It is believed that the publication of this book will promote the development and industrial applications of ammonia synthesis catalysts and is beneficial for energy saving of the ammonia synthesis industry.

Academician of the Chinese Academy of Engineering
CAO Xianghong
16 December 2010



Cao Xianghong

Professoriate senior engineer, Vice President and Chief Engineer of Sinopec Group, Board Director and Senior Vice President of Sinopec Corp., President of Chemical Industry and Engineering Society of China, Vice President of Chinese Petroleum Society, Vice President of China Energy Research Society, Director of Refined Products and Lubricant Technical Committee of Chinese Standardization Administration, Member of National Energy Expert Committee, and Member and Director of Chemical, Metallurgical and Materials Engineering Division of CAE (Chinese Academy of Engineering). Since 2008, he is Senior Advisor of the Sinopec.

Mr. Cao was born in Jiangsu in 1945. Since 1970, he had been working in Yanshan Petrochemical for 30 years and in Sinopec since 2000, responsible for the company's development and management of technology and production. He has contributed enormously to the improvement of Sinopec's core competitiveness and the development of China's refining and petrochemical industry. He has received many important national awards of science and technology, including five National Science & Technology Advancement Awards (one special prize, one first prize, one second prize and two third prizes), and nine Provincial/Ministry-level Science & Technology Advancement Awards.

Contents

Preface **vi**

Foreword **x**

Chapter 1. Historical Evolution of Catalysts for Ammonia Synthesis **1**

1.1 Introduction of Catalysts for Ammonia Synthesis 2
1.1.1 Co–Mo hydrogenation catalysts 6
1.1.2 Zinc oxide desulfurizer 7
1.1.3 Hydrocarbon steam reforming catalysts 8
1.1.4 CO high-temperature shift catalysts 11
1.1.5 CO low-temperature shift catalysts 14
1.1.6 Methanation catalysts 15
1.1.7 Refine catalysts 16
1.2 Historical Retrospect of Catalysts for Ammonia Synthesis 21
1.2.1 Basic studies on physical chemistry of ammonia synthesis reaction 21
1.2.2 Realization of ammonia synthesis under high pressure 23
1.2.3 Development of fused iron catalysts for ammonia synthesis . . . 25
1.2.4 Development of ammonia synthesis catalysts in China 29
1.2.5 Development trend of ammonia synthesis catalysts 30
1.3 Development of Magnetite (Fe_3O_4) Based Fused Iron Catalysts 32
1.3.1 Magnetite (Fe_3O_4) based fused iron catalysts 32
1.3.2 Development of Fe_3O_4 based catalysts containing cobalt 32
1.4 Discovery of Wüstite Based Fused Iron Catalysts 33
1.4.1 Search for new breakthrough of the technique 33
1.4.2 Activity of wüstite ($Fe_{1-x}O$) based catalysts 39
1.4.3 Reduction of $Fe_{1-x}O$ based catalysts 42
1.4.4 Technical characteristics of wüstite-based catalysts 46
1.4.5 Significance of the $Fe_{1-x}O$-based catalysts in theory 49
1.4.6 Industrial application 50

1.5 Discovery of Ruthenium Based Catalysts 51
1.5.1 Properties of the elements in the activation of dinitrogen 51
1.5.2 Properties of the elements in ammonia synthesis 52
1.5.3 Alloying effect 55
1.5.4 Activated carbon supported ruthenium catalysts for ammonia synthesis 59
References 62

Chapter 2. Catalytic Reaction Mechanisms of Ammonia Synthesis 67

2.1 Introduction 67
2.1.1 The development of catalysis theory 68
2.1.2 The chemical essences of catalysis 70
2.1.3 The methodology of catalytic investigation 73
2.2 Adsorption and Heterogeneous Catalysis 76
2.2.1 Adsorption and heterogeneous catalysis 77
2.2.2 Non-uniformity of the surface of heterogeneous catalysts 80
2.2.3 Isotherms of chemisorptions 83
2.2.4 Rate of adsorption: Elovich equation 87
2.2.5 Chemisorption state 88
2.2.5.1 Chemisorption states of hydrogen 88
2.2.5.2 Adsorption states of nitrogen 89
2.2.5.3 Infrared spectroscopy study of nitrogen adsorption 94
2.2.5.4 The study of electronic energy spectroscopy for nitrogen adsorption 96
2.2.5.5 The study of adsorption of N_2 on non-iron metals 97
2.3 Mechanism of Catalytic Ammonia Synthesis Reaction 102
2.3.1 Elementary reactions 102
2.3.2 Catalytic reaction mechanisms for ammonia synthesis 104
2.3.2.1 The mechanisms of ammonia synthesis reaction . . . 105
2.3.2.2 The mechanisms of ammonia decomposition 109
2.3.2.3 Isotope exchanges of N_2 111
2.3.2.4 Distinguishing reaction mechanisms 112
2.3.3 Analysis of microreaction (intrinsic) kinetics of ammonia synthesis 117
2.3.3.1 Analysis of reactor 118
2.3.3.2 The conclusion of microkinetic analysis 123
2.4 Kinetics of Overall Reactions for Ammonia Synthesis 124
2.4.1 General relation between overall reaction and elementary steps 125
2.4.2 Two-step sequences 126
2.4.3 Fundamental hypothesis of Temkin theory 131
2.4.4 The reaction rate equation of Temkin–Pyzhev for ammonia synthesis 137

2.4.5 Consequence of Temkin's theory and search for best catalysts . . . 140
2.4.5.1 The riddling search for the optimal active site or the best catalyst . . . 140
2.4.5.2 Difference of catalytic activity on different active site (or catalyst) . . . 142
2.4.5.3 Interpretation of very large differences in catalytic activity . . . 144
2.4.5.4 Structure-sensitivity of ammonia synthesis reaction . . . 147
2.5 Apparent Reaction Kinetics . . . 153
2.5.1 External diffusion . . . 154
2.5.2 Internal diffusion . . . 156
2.5.3 Utilization ratio of internal surface . . . 158
2.5.4 Macrokinetic equation of catalytic reactions . . . 161
2.6 Design of Ammonia Synthesis Reactor . . . 163
2.6.1 Applied form of kinetic equation . . . 163
2.6.2 Mathematic model for design of reactor . . . 167
2.6.3 Distribution between various beds of multi-beds adiabatic reactors for ammonia synthesis . . . 169
2.6.4 Fundamental data for design of ammonia synthesis reactor . . . 173
2.6.5 An example of simulating design calculation . . . 176
References . . . 177

Chapter 3. Chemical Composition and Structure of Fused Iron Catalysts 185

3.1 Iron Oxides . . . 185
3.1.1 Fe_2O_3 . . . 185
3.1.2 Fe_3O_4 . . . 185
3.1.3 FeO . . . 188
3.1.3.1 Oxidative . . . 188
3.1.3.2 Non-stoichiometry . . . 189
3.1.3.3 Metastability-disproportionating reactions . . . 196
3.1.4 Relationship between various iron oxides . . . 201
3.1.5 Complex oxides and their solid solution of irons . . . 202
3.1.5.1 Compound-type complex oxides . . . 202
3.1.5.2 Sosoloid-type complex oxides . . . 205
3.1.6 Defect structures of iron oxides . . . 205
3.1.6.1 Classification of defects . . . 209
3.1.6.2 Intrinsic defects and impurity defects . . . 211
3.1.6.3 Irregularity of lattice and heterogeneous catalysis . . . 213
3.2 Iron Oxides and Catalytic Activity . . . 214
3.2.1 Classical volcano-type activity curve . . . 214
3.2.2 Hump-type activity curve . . . 216
3.2.3 Monophasical principle . . . 219

3.2.4 Activity pattern of reduced catalyst with iron oxides as precursor . . . 223
3.2.5 Iron oxides and reduction performance of catalysts . . . 224
3.2.6 Iron oxides and the surface textures of catalysts . . . 229
3.2.7 Iron oxides and the adsorption properties on catalyst . . . 235
3.3 Promoters of Fused Iron Catalyst . . . 238
3.3.1 Design of promoter . . . 240
3.3.2 Structural promoters . . . 245
3.3.3 Electronic promoters . . . 249
3.3.4 Enrichment phenomena of promoters partial to surface of catalysts . . . 255
3.3.5 Distribution of promoters in unreduced catalysts . . . 260
3.4 Structures of Unreduced Catalysts . . . 266
3.4.1 Structural images of the classical fused iron catalysts . . . 266
3.4.2 Structural images of $Fe_{1-x}O$ based fused iron catalysts . . . 268
3.5 Structure of Activated Iron Catalyst . . . 270
3.5.1 Pore structures . . . 270
3.5.2 Surface structure of activated iron catalyst . . . 272
3.5.3 The role of surface restructuring . . . 279
3.5.4 Nanometer effect . . . 281
3.5.5 Single-crystal structure of α-Fe and the active sites . . . 285
3.6 About $Fe_{1-x}O$ Based Catalysts and Their Highly Active Mechanism . . . 300
References . . . 304

Chapter 4. Preparation of Fused Iron Catalysts 311

4.1 Technology and Equipments for the Preparation of Fused Iron Catalysts . . . 311
4.1.1 Purification of raw materials . . . 312
4.1.2 Proportion and mixing of materials . . . 315
4.1.3 Melting of materials . . . 316
4.1.4 Discharging and cooling of molten material . . . 318
4.1.5 Crushing and sieving of molten materials . . . 319
4.1.6 Packing, storage and transportation . . . 319
4.2 Chemical Reaction During Preparation Process . . . 319
4.3 Phase Transformation and Phase Diagram Analysis During Preparation . . . 323
4.4 Segregation of Promoters During Solidification Processes . . . 327
4.5 Preparation of Prereduced Catalysts . . . 337
4.6 Preparation Technique of Spherical Catalysts . . . 345
4.6.1 Shaping technique of catalysts . . . 345
4.6.2 Preparation technique of spherical catalysts for ammonia synthesis . . . 349
4.6.2.1 Methods of mechanical impact dispersion and liquid spurt impact dispersion . . . 350
4.6.2.2 Continuous glomeration method . . . 351
4.6.2.3 Spraying glomeration method . . . 351

4.7 Recycling of Waste Catalyst for Ammonia Synthesis 354
References 356

Chapter 5. Reduction of Fused Iron Catalysts 359

5.1 Solid-State Reactions Involved in Reduction Process 361
5.1.1 General laws of solid state reaction 361
5.1.2 Solid state reaction kinetics 366
5.2 Kinetic model of solid state reaction 367
5.2.1 Kinetic model for gas–solid non-catalytic reaction 367
5.2.2 Kinetic model for reduction of fused iron catalyst 372
5.2.3 Crystal nucleus growing model 377
5.3 Reduction Process of Oxides 379
5.4 Reduction Thermodynamics for Iron Oxides 386
5.5 Reduction Reaction Kinetics of Iron Oxides 390
5.5.1 Reduction mechanism of oxides 390
5.5.2 Reduction of single particle catalyst 393
5.5.3 The relation between activity and physical properties with the reduction degree 400
5.6 Factors of Influence on Reduction Rate 403
5.6.1 Influence of temperature 403
5.6.2 Influence of pressure 404
5.6.3 Influence of space velocity 405
5.6.4 Influence of gas composition 406
5.6.5 Influence of oxide precursor 407
5.6.6 Influence of promoters to reduction rate 408
5.7 Reduction in Industrial Equipments 409
5.7.1 Reduction rate of catalyst in industrial reactor 410
5.7.2 Characteristic of reduction processes in catalyst bed 411
5.7.2.1 Characteristic of reduction processes by pure H_2 in catalyst bed 411
5.7.2.2 Characteristic of reduction processes by syngas in catalyst bed 415
5.7.3 The choice of reduction condition in industrial reactor 419
5.7.4 The reduction program in the industrial converter 421
References 422

Chapter 6. Ruthenium Based Ammonia Synthesis Catalysts 425

6.1 Chemical Compositions of Ruthenium Catalysts 426
6.1.1 Ruthenium precursor compound 426
6.1.2 Supports of ruthenium catalysts 428
6.1.2.1 Activated carbons 428
6.1.2.2 Oxides 435
6.1.2.3 Molecular sieve 439
6.1.2.4 Other supports 439
6.1.3 The promoter of ruthenium catalyst 441
6.1.4 Mechanism on the role of support and promoter 444
6.1.4.1 Hydrogenolysis of precursor of promoter 444
6.1.4.2 Electronic contribution of active site 447

6.2 Preparation of Ruthenium Catalyst 454
6.2.1 Outline 454
6.2.2 Pretreatment of supports 456
6.2.2.1 Graphitization of activated carbons 458
6.2.2.2 Acid treatment 462
6.2.2.3 The treatment in H_2 or inert atmosphere 464
6.2.2.4 Microwave treatment 465
6.2.3 Impregnation 466
6.2.3.1 Impregnation methods 466
6.2.3.2 The influencing factors during impregnation 467
6.2.4 Reduction of $RuCl_3 \cdot xH_2O$ and elimination of chlorine ions . . 472
6.2.4.1 The effect of chlorines on catalytic performances . . . 472
6.2.4.2 The elimination of chlorines in catalyst 474
6.2.4.3 Discussion on mechanism of chlorine poison on Ru catalyst 487
6.2.5 Drying 488
6.3 Performance Characteristic of Ruthenium Catalysts 492
6.3.1 Structural sensitivity 492
6.3.2 The activity of ruthenium catalyst 501
6.3.3 The strong inhibition of H_2 507
6.3.3.1 The phenomenon of strong H_2 inhibition 507
6.3.3.2 The possible reasons of hydrogen inhibition 510
6.3.3.3 Measures to reduce hydrogen inhibition 515
6.3.4 Methanation reaction of activated carbon 521
6.3.4.1 The stability of ruthenium catalyst 521
6.3.4.2 The effect of graphitization on methanation 522
6.3.4.3 Influence of physical and chemical property of activated carbon on methanation 524
6.3.4.4 The effect of compositions of catalyst on the methanation 527
6.3.4.5 Thermodynamics and mechanism of methanation reaction of carbon 534
References 537

Chapter 7. Performance Evaluation and Characterization of Catalysts 543

7.1 Performance Evaluation of Catalysts 544
7.1.1 Basic concepts 544
7.1.1.1 Activity 544
7.1.1.2 Selectivity 548
7.1.1.3 Stability 548
7.1.2 Performance evaluation of catalysts 550
7.1.2.1 The reactor for performance evaluation and dynamic test of catalyst 550
7.1.2.2 Experimental device 555
7.1.2.3 Evaluation of catalytic activity 557
7.2 Measurement of Physical Properties of Catalysts 561
7.2.1 Particle size and density 562

7.2.1.1 Particle size and particle shape factor (φ_s) 562
7.2.1.2 Density of catalyst 564
7.2.1.3 Voidage of catalyst bed (ε) 567
7.2.2 Surface area and pore structure 568
7.2.2.1 Specific surface area 568
7.2.2.2 Pore volume 570
7.2.2.3 Porosity 570
7.2.2.4 Average pore size 571
7.2.2.5 Twist-factor 572
7.2.2.6 Distribution of pore size 572
7.2.2.7 Lag-ring and pore structural model 575
7.3 Nature and Structure of Surface 577
7.3.1 Introduction 577
7.3.1.1 Intensity and quantity of chemisorption 579
7.3.1.2 Adsorbed state of gas on surface of catalysts 580
7.3.1.3 Chemisorption stoichiometry 582
7.3.2 Physical and chemical adsorption experiment on iron catalyst 583
7.3.3 Measuring the number of total surface metal atoms by chemisorption 585
7.3.4 Measuring surface area and acid-base of various component by chemisorption 586
7.3.5 Measurement of exposed fraction of surface metal atoms 588
7.3.6 Measurement of metal particle nanosize on the surface of catalyst 589
7.3.7 Turnover frequency and active site 591
7.3.8 Chemisorption: measure the rate and activation energy of adsorption 592
7.4 Temperature Programmed Analysis Technology (TPAT) 593
7.4.1 Temperature programmed desorption (TPD) 594
7.4.2 Temperature programmed reduction (TPR) 600
7.4.2.1 TPR dynamic equation 600
7.4.2.2 Impact factors of TPR dynamic equation 602
7.4.2.3 Measurement dispersion of metal catalyst by TPR 603
7.4.3 Temperature programmed oxidation (TPO) 604
7.4.4 Temperature programmed sulfuration (TPS) 604
7.4.5 Temperature programmed surface reaction (TPSR) 604
7.5 Application of Thermal Analysis Technology in Catalyst Research . . . 605
7.5.1 Derivatography analysis (DTA) and its application 606
7.5.2 Thermogravimetric analysis (TGA) and its application 607
7.6 Characterization of the Microstructure and Properties of Catalysts . . 608
7.6.1 Application of XRD in the study of catalysis 609
7.6.1.1 Quantitative analysis of phase composition 610
7.6.1.2 Determination of lattice constant 614
7.6.1.3 Determination of average nanoparticle size by line width method 615

7.6.1.4 Extended X-ray absorption fine structure (EXAFS) analysis . . . 615
7.6.1.5 Multicrystalline structure determination . . . 616
7.6.1.6 Structure analysis by Rietveld fitting . . . 617
7.6.2 Application of XRD in the research of ammonia synthesis catalysts . . . 624
7.6.2.1 Structure of precursor and active phase of Fe_3O_4-based ammonia catalyst . . . 625
7.6.2.2 Grain-growth kinetics and microstructure evolution of nanocrystalline iron . . . 636
7.6.3 Application of other modern physical methods in catalyst characterization . . . 639
References . . . 643

Chapter 8. Performance and Application of Catalysts 649

8.1 Activity of catalysts . . . 650
8.1.1 Reaction pressure . . . 650
8.1.2 Reaction temperature . . . 653
8.1.2.1 Active temperature of catalyst . . . 653
8.1.2.2 The optimum reaction temperature . . . 655
8.1.2.3 Realization of the optimum reaction temperature curve . . . 657
8.1.2.4 Control of temperature of catalyst beds . . . 660
8.1.3 Space velocity . . . 662
8.1.4 Gas compositions . . . 664
8.1.4.1 H_2/N_2 ratio . . . 664
8.1.4.2 Content of inert gas . . . 670
8.1.4.3 Content of ammonia in the inlet gas and temperature of ammonia refrigeration . . . 673
8.2 Particle Size of Catalysts . . . 674
8.2.1 Effect of particle size on catalytic activity and reaction rate of catalyst . . . 675
8.2.2 Effect of particle size on the utilization ratio of inner surface of catalyst . . . 676
8.2.3 Effect of particle size on the pressure drop of catalyst bed . . . 680
8.2.4 Choice of catalyst particle size for industrial applications . . . 684
8.3 Poison and Life of Catalyst . . . 686
8.3.1 Thermal sintering and changes of chemical composition of catalyst . . . 687
8.3.2 Poisons and the phenomenon of poisoning of catalyst . . . 690
8.3.2.1 Types of catalyst poisoning . . . 690
8.3.2.2 Poisons of catalyst . . . 691
8.3.2.3 Factors affecting toxicity . . . 692
8.3.2.4 Poisons and the poisoning phenomena for ammonia synthesis catalysts . . . 695
8.4 Mechanical Strength of Catalysts . . . 705

8.4.1 Theoretical research on the mechanical strength for the solid catalyst . . . 706
8.4.2 The basis of catalyst solid mechanics . . . 707
8.4.3 The measurement of mechanical strength for solid catalyst . . . 712
8.4.4 Effect of chemical composition of catalysts on its mechanical strength . . . 716
8.4.5 The requirement of mechanical strength of catalysts in industry . . . 718
8.5 Usage and Maintenance of Ammonia Synthesis Catalysts . . . 721
8.5.1 Selection of the type of catalyst to use . . . 721
8.5.1.1 Type of catalysts for ammonia synthesis . . . 722
8.5.1.2 Pre-reduced catalysts . . . 726
8.5.1.3 Spherical catalysts for ammonia synthesis . . . 726
8.5.2 Proper use of catalysts . . . 727
8.5.3 The transport and storage of catalysts . . . 728
References . . . 728

Chapter 9. Effect of Catalyst Performance on the Economic Benefits of Catalytic Process 733

9.1 Synthesis Processes and Catalysts . . . 734
9.1.1 Process with classical molten iron catalysts . . . 735
9.1.1.1 Kellogg process . . . 735
9.1.1.2 Topsøe process . . . 736
9.1.1.3 Braun process . . . 738
9.1.2 ICI–AMV process with Fe-Co catalyst . . . 739
9.1.3 Synthetic process flow with Ru catalysts . . . 741
9.1.3.1 The synthesis process with low ratio of H_2 to N_2 . . . 741
9.1.3.2 Synthetic process flow without circulation . . . 742
9.1.3.3 Process flow of using Fe catalyst combined with Ru catalyst . . . 744
9.1.4 Pressure of reaction and isopiestic process . . . 748
9.1.4.1 Pressure of reaction . . . 748
9.1.4.2 Process of synthesis at isotonic pressure . . . 750
9.1.4.3 The low-pressure renovation for the small-medium ammonia plant . . . 755
9.2 Ammonia Converter and Catalysts . . . 756
9.3 Performance of Catalyst and Recovery of Reaction Heat . . . 760
9.3.1 The theoretic energy consumption of synthesis ammonia . . . 760
9.3.2 The actual energy consumption of the ammonia production . . . 763
9.3.3 Catalyst activities and the use of the reaction heat . . . 767
9.4 Influence of Performance of Catalyst on the Economic Benefits of Catalytic Process . . . 771
9.4.1 Catalyst-consumed cost . . . 771
9.4.2 Economic factor of reduction for catalyst . . . 774

9.4.3 The economic benefits using the pre-reduced catalyst 775
9.4.4 Effect of catalyst performance on the economic benefits of process 776
9.4.5 Selectivity of catalyst 784
9.4.6 Life period and service time of ammonia catalyst 784
9.4.6.1 Economic appraisement of the service time of the catalyst 786
9.4.6.2 Economic appraisement on replacement of catalyst 788
9.5 Benefits of Operating Rate and Management of Enterprise 789
References 790

Chapter 10. Innovation and Speculation 793

10.1 New Exploration of Ammonia Synthesis Catalyst 793
10.1.1 Revelation of theory and practice of fusing-iron catalyst 794
10.1.2 Exploration of non-iron and alloy catalysts 798
10.1.3 Exploration of other non-iron catalyst for ammonia synthesis 803
10.1.4 Non-crystal catalyst 807
10.2 New Catalytic Technique for Ammonia Synthesis 809
10.2.1 Progress in ammonia synthesis at normal pressure and temperature 809
10.2.2 Photocatalysis for ammonia synthesis 813
10.2.2.1 Photocatalytic reaction and photocatalyst 813
10.2.2.2 Photocatalytic ammonia synthesis by water and dinitrogen 816
10.2.3 Electrocatalytic ammonia synthesis at normal pressure 817
10.2.3.1 Electrocatalytic reaction and electrocatalyst 817
10.2.3.2 The progress of electrochemical ammonia synthesis 820
10.2.4 Biocatalytic ammonia synthesis at normal temperature 831
10.2.5 Ammonia synthesis at supercritical condition 834
10.3 New Application of Ammonia 835
10.3.1 Ammonia synthesis device is a highly efficient device for energy transformation and hydrogen production 836
10.3.2 New application of ammonia 841
References 846

Index 851

Chapter 1

Historical Evolution of Catalysts for Ammonia Synthesis

Catalytic ammonia synthesis technology has played a central role in the development of the chemical industry during the 20th century. This industrial importance has been paralleled by a significant scientific interest in understanding and improving the ammonia synthesis catalyst. Often new techniques, methods, and theories of catalysis have initially been developed and applied in connection with studies of this system. Similarly, new discoveries in the field of ammonia synthesis have been extended to other areas of catalysis. The combined influence of refined characterization techniques, improved kinetic analysis, and new possibilities in theoretical modeling, has led to a detailed insight into the fundamentals of ammonia synthesis catalysts. Several recent reviews give a comprehensive account of the current understanding.

Ammonia is primarily used as nitrogenous fertilizer and as a raw material of inorganic compounds including nitric acid, ammonium salts, cyanide and organic compounds, such as amines, sulfanilamide and so on. In addition, ammonia is also an excellent refrigerant. Since ammonia is a key raw material for industry and agriculture, the process of ammonia synthesis has an extremely important position in any economy.

In the 19th century, ammonia was obtained from natural saltpeter or recovered from coal. In order to meet the increasing demand for nitrogenous fertilizers, a variety of methods were tried to fix nitrogen from air at the beginning of the 20th century. From 1902 to 1913, three nitrogen-fixing processes were created, i.e., the electric arc process, calcium cyanamide process and catalytic ammonia synthesis technology.[1]

The electric arc method (1902) which produces nitric oxide *via* reaction of nitrogen with oxygen at the high temperatures under the electric arc was inspired by the fulmination phenomena in nature. Then, nitric oxide is further oxidized by oxygen in air into nitrogen dioxide, followed by adsorbtion in water to form nitric acid. About 50–80 $\mathrm{kW \cdot h}$ of electric energy is required to convert one kg of nitrogen. High energy consumption limited the wide application of this process in industry.

The cyanamide process is based on the formation of calcium cyanamide ($CaC_2 + N_2 = Ca(CN)_2$) through the reaction of calcium carbide (CaC_2) with nitrogen. Calcium carbide is produced by the reaction of calcium oxide and carbon at high temperatures. Calcium cyanamide can be either directly used as nitrogenous fertilizers or as a raw material to produce cyanides and nitrogen-containing organic compounds. To fix one kg of nitrogen by this cyanamide process, the electrical energy consumption was about 16–18 $\mathrm{kW \cdot h}$, which is only a quarter of that consumed by the arc process. The cyanamide process was widely

applied in Europe and was the major method for nitrogen fixation before the First World War.

Catalytic ammonia synthesis from N_2 and H_2 was developed by Fritz Haber, and then Carl Bosch applied this process to industrial production successfully at the beginning of 20th century. The first ammonia plant was built for the production of 30 ton of ammonia per day in 1913 at Oppau, Germany. Up to 1934, this catalytic process became the dominant route for nitrogen fixation. Because of the extensive use of nitrogenous fertilizers, catalytic ammonia synthesis plays an important role in agriculture and other industries. The huge market demand drives larger production scale and complexity of the equipments and processes of production. Nowadays, because ammonia synthesis requires extensive capital investment and massive energy consumption and the price of products is low, the development of industrial ammonia synthesis process emergences in following features[2]:

(1) **Increasing in scale of unit equipment.** With the increasing demand for ammonia, the scale of unit equipment is continuously increased to decrease the investments and production costs. At present, the production capacity of single-stream equipment has reached 1,850 ton of ammonia per day.
(2) **Unceasing innovations in its process including catalysts.** Different types of catalysts are used in ammonia plant. The improvement of catalysts not only increases the efficiency of production, but also saves consumption of the power. For example, the pressures of ammonia synthesis were 20–30 MPa and even 100 MPa in the early years. Now the pressure has been decreased to 8–10 MPa over the new developed catalysts. Because these catalysts are sensitive to impurities in synthesis gas, innovation in purification technology of synthesis gas arises and develops.
(3) **Wide application of various energy-saving technologies.** Because the major raw material of synthesis ammonia is fuel, the price of ammonia largely depends on the price of energy resource, and the energy-saving technologies are becoming more and more important with the increase of the price of energy resource. To decrease the unit energy consumption, the pressure of syngas production was increased and the high-pressure steam produced by the reaction heat is recovered as power. With the development of ammonia synthesis technology, the energy consumption has been decreased to 27 GJ in advanced modern ammonia plants, which is very close to the theoretical value of 20 GJ.

1.1 Introduction of Catalysts for Ammonia Synthesis

Although a lot of technology progress has been achieved, the basic principles and process in modern ammonia plants are essentially the same as original ones developed by Haber and Bosch, a century ago. The major procedures can be outlined as follows[2]:

(1) **Production of synthesis gas.** Synthesis gas, containing hydrogen and carbon monoxide, is produced by the reaction of steam with solid fuels such as coals, cokes, heavy oil, light hydrocarbon or gaseous hydrocarbon such as natural gas at high temperatures. During this procedure, certain amount of air, oxygen-enriched air or oxygen are introduced, wherein oxygen is combusted with fuels

to provide heat for reactions and produce carbon monoxide. Following reactions, the residue nitrogen remains in the gas for ammonia synthesis. When pure oxygen is used, nitrogen has to be supplied from air separation unit. Carbon monoxide formed during these reactions is converted to hydrogen and carbon dioxide by the water-gas shift reaction.

(2) **Purification of synthesis gas.** The sulfur- and carbon-containing compounds in synthesis gas must be removed in order to avoid the poisoning of catalysts in the following processes. Sulfur and carbon containing compounds are absorbed by different solvents. The used solvents are regenerated by desorption and H_2S (or element S) and carbon dioxide are recovered. The trace amounts of carbon monoxide and carbon dioxide which remained in synthesis gas is removed *via* the reaction of methanation or other methods. After a series of purifications, the content of carbon monoxide and carbon dioxide in the synthesis gas are on the levels of ppm ($1\ \text{ppm} = 1\ \text{ml} \cdot \text{m}^{-3}$).

(3) **Compression of synthesis gas.** The synthesis gas composed by hydrogen and nitrogen is compressed to required pressures, usually 10–30 MPa, by piston-type or centrifugal compressors. During ammonia synthesis, single-pass conversion is only 10%–20%, and therefore, most of the synthesis gas must be recycled, compressed and returned to the synthesis loop again.

(4) **Synthesis and separation of ammonia.** After exchanging heat with the hot gas which comes from the reactor, synthesis gas is introduced into the reactor to form ammonia over the catalyst. Following the reaction, the gas containing ammonia reaches heat exchanger to generate steam under high-pressures, and then is cooled down by water and ammonia. Ammonia in syngas is condensed into liquid and separated from the syngas. The remaining syngas is recycled to the synthesis loop again. Figure 1.1 shows the typical schematic diagram for ammonia synthesis using different feedstock.

During ammonia synthesis, the major reactions of production and purification of synthesis gas and the synthesis of ammonia, all are carried out over different catalysts. At least eight kinds of catalysts are used in the whole process, where natural gas or naphtha is used as feedstock and steam reforming is used to produce synthesis gas. These catalysts are Co–Mo hydrogenation catalyst, zinc oxide desulfurizer, primary- and secondary-steam reforming catalysts, high- and low-temperature shift catalysts, methanation catalyst and ammonia synthesis catalyst etc (Table 1.1).

The eight kinds of catalysts may be roughly classified as "protective catalysts" and "economic catalysts". Co–Mo hydrogenation catalyst and zinc oxide desulfurizer are "the protective catalysts" for the primary steam reforming catalysts. The high-temperature shift catalyst protects the low-temperature shift catalyst, and the methanation catalyst are "the protective catalyst" for ammonia synthesis catalyst. The catalysts for primary- and secondary-steam reforming, low-temperature shift and ammonia synthesis are responsible for the conversions of raw materials and the yield of products, and have direct effect on economic benefits of the whole plant, and are thus called as "economic catalysts." The amount of catalysts used depends on the process and raw material. Table 1.2 represents the amount of the eight kinds of catalysts used in the different processes. The total volume of the catalysts is about $330\,\text{m}^3$ in every plant, while there are only two kinds of catalysts with the volume of about $100–140\,\text{m}^3$ when heavy oil or coal is used as raw material. Both shift

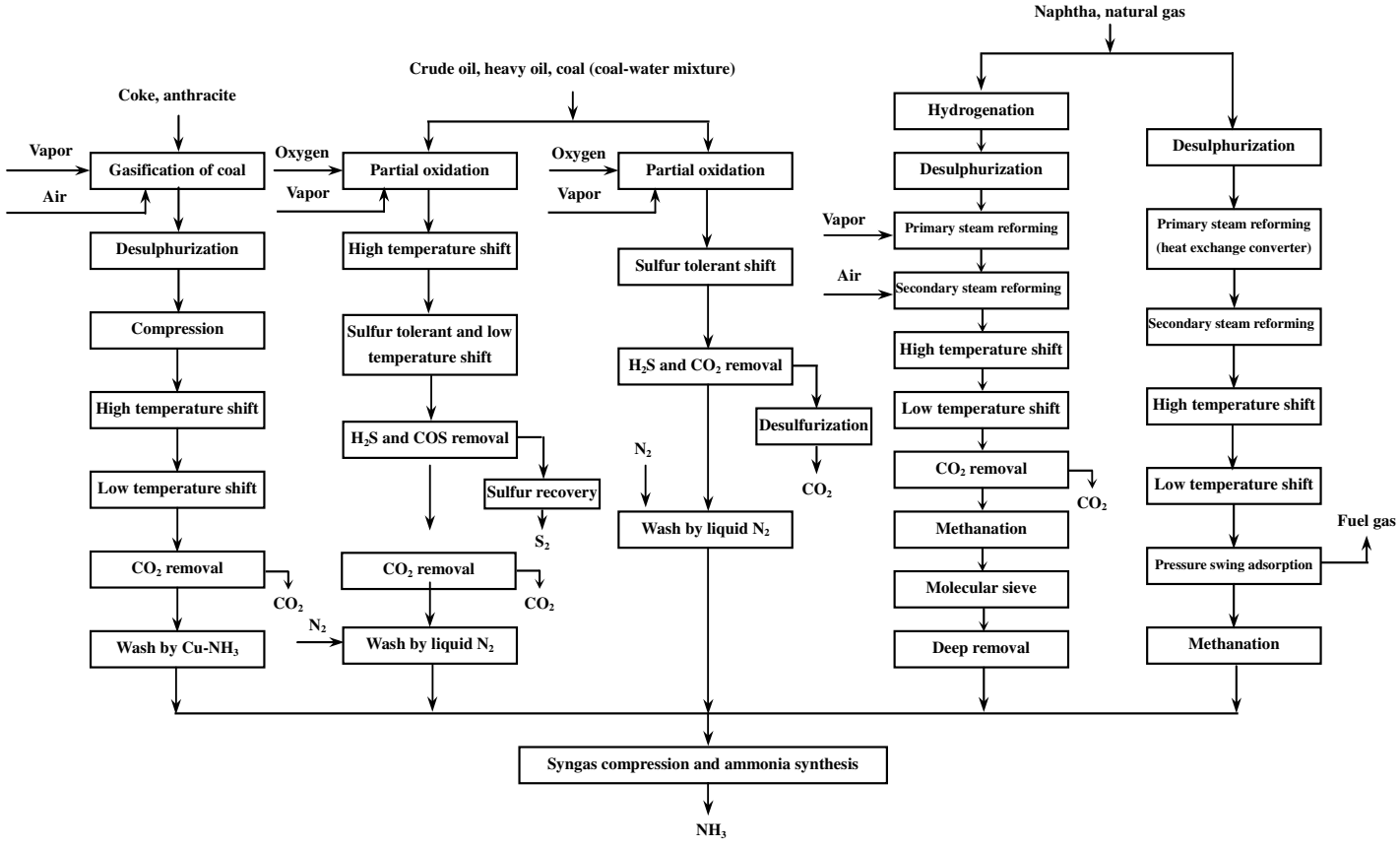


Fig. 1.1 Schematic diagram for ammonia synthesis processes from different feedstock

Table 1.1 Eight kinds of catalysts, catalytic reactions and operation conditions involved in modern ammonia plants

Reactor	Catalyst	Catalytic reaction	Operation conditions		Life/a
Hydrogenation	$Co/Mo/Al_2O_3$	$R_2S + 2H_2 \rightarrow 2RH + H_2S$	300–400°C	3 MPa	4–8
Desulphurization	ZnO	$H_2S + ZnO \rightarrow ZnS + H_2O$	300–400°C	3 MPa	2–4
Primary steam reforming	$Ni/CaO/Al_2O_3$	$CH_4 + H_2O \rightarrow CO + 3H_2$	500–850°C	3 MPa	22.5
		$C_nH_{2n+2} + nH_2O \rightarrow nCO + 2(2n-1)H_2$	380–790°C	3 MPa	
Secondary steam reforming	$Ni/CaO/Al_2O_3$	$CH_4 + 1/2O_2 \rightarrow CO + 2H_2$	900–1100°C	3 MPa	3–6
High-temperature shift	Fe_3O_4/Cr_2O_3	$CO + H_2O \rightarrow CO_2 + H_2$	350–500°C	3 MPa	2–4
Low-temperature shift	$Cu/ZnO/Al_2O_3$	$CO + H_2O \rightarrow CO_2 + H_2$	200–250°C	3 MPa	2–2.8
Methanation	Ni/Al_2O_3	$CO/CO_2 + H_2 \rightarrow CH_4 + H_2O$	250–350°C	3 MPa	5–6
Ammonia synthesis	$Fe/Al_2O_3/K_2O/CaO$ $Ru/Ba/K/AC$	$N_2 + 3H_2 \rightarrow 2NH_3$	400–500°C	10–30 MPa	6–10

Table 1.2. Dosage of the catalyst in different ammonia synthesis processes (m^3)

Raw material	Process	Total	Hydro-genation	ZnO desul-furization	Primary steam reforming	Secondary steam reforming	High temperature shift	Low temperature shift	Methanation	Ammonia synthesis
Natural gas	Kellogg	331.5	28.3	56.6	15.3	33.4	55.2	58.7	19.8	73.4
	TEC	327.8	27.8	58.2	16.2	28.2	54.0	62.6	24.7	53.7
	AMV	407.3	17.3	84.0	17.3	24.0	55.7	90.0	23.0	96.2
	Bruan	323.5	17.1	64.6	17.2	26.1	36.9	56.8	23.2	79.6
Light oil	Heurtey	281.2	14.3	36.6	24.9	26.4	58.0	68.8	20.5	29.1
	Kellogg	328.3	28.3	56.6	15.5	33.0	55.1	58.8	20.0	70.1
Dreg oil	High sulfur	114.1	—	—	—	—	87.0	—	—	27.1
	Low sulfur	130.5	—	—	—	—	100.0	—	—	30.5
	Low sulfur	116.7	—	—	—	—	90.0	—	—	26.7
Coal	Lurgi	96.4	—	—	—	—	65.8	—	—	30.0
Coal-water mixture	Texaco	140.3	—	—	—	—	87.0	—	—	53.3

catalyst and ammonia synthesis catalyst are indispensable in any process, and are key catalysts in the ammonia synthesis industry.

Seven of the above-mentioned catalysts except ammonia synthesis catalyst and their catalytic reactions and other related catalysts will be briefly introduced below in order to get some basic understanding for the overall ammonia synthesis process.

1.1.1 *Co–Mo hydrogenation catalysts*[3]

Gaseous and liquid hydrocarbons, such as natural gas, refinery gas, oil field gas, light gasoline and light cut fraction with boiling point range from 40°C to 180°C etc, always contain some sulfides. The metal catalysts, e.g., nickel-containing reforming and methanation catalysts, copper-containing low temperature shift and methanol synthesis catalysts, and iron-based ammonia synthesis catalysts etc, will be poisoned by sulfur. Desulphurization of the feedstock is an important process in ammonia synthesis processes.

(1) **Basic principle.** It is well known that inorganic sulfur compounds, i.e., H_2S, may be removed by absorption on desulfurizer (such as zinc oxide). However, this method is not applicable for removal of organic sulfur compounds, which are normally removed by catalytic hydrodesulphurization process.

Catalytic hydrodesulphurization is based on the reaction of organic sulfur compounds with hydrogen as catalysts. During reactions, the organic sulfur compounds are first converted to the inorganic sulfur compounds such as H_2S, and then removed by the absorption of zinc oxide. The reactions involved are summarized as follows.

$$CS_2 + 4H_2 = CH_4 + 2H_2S. \tag{1.1}$$

$$COS + 4H_2 = CH_4 + H_2O + H_2S. \tag{1.2}$$

$$C_2H_5SH + H_2 = C_2H_6 + H_2S. \tag{1.3}$$

$$C_4H_8S + 2H_2 = C_4H_{10} + H_2S. \tag{1.4}$$

$$C_6H_4SC_6H_4 + 3H_2 = 2C_6H_6 + H_2S. \tag{1.5}$$

$$C_6H_4SSC_6H_4 + 4H_2 = 2C_6H_6 + 2H_2S. \tag{1.6}$$

Although hydrogenolysis reaction is an exothermic reaction, the heat released by the above reactions is negligible due to the low content of sulfur in hydrocarbon cut fractions. The chemical equilibrium constants of the above-mentioned reactions are high enough to remove sulfur, which means that hydrogenation reactions are determined mainly by reaction kinetics, not the chemical equilibrium. The rates of hydrogenolysis of organic sulfur compounds depend on their structures and roughly follow the order of $RSH > RSSR' > RSR' >$ thiophene, indicating that the reactivity decreases with increasing of molecular weight. When several organic sulfur compounds are present, the hydrogenolysis rate is determined by the one with the lowest reactivity. Normally, the ramifications derived from thiophene have the lowest reactivity.

Some side reactions occur simultaneously during hydrogenolysis such as C–C bond rupturing and C=C bond hydrogenation. For ideal hydrogenation catalysts, the catalytic hydrogenation only breaks the C–S bonds to form hydrocarbons and H_2S.

(2) **Composition, structure and performance of Co–Mo catalysts.** Co–Mo hydrogenation catalysts consist of cobalt and molybdenum oxides supported on

high-surface-area alumina. Generally, the fresh catalysts contain Al_2O_3, $CoAl_2O_4$, CoO, MoO_3, $CoMoO_4$ and a Co–Mo composite oxide. Among them, Al_2O_3 and $CoAl_2O_4$ are inactive, CoO, MoO_3 and $CoMoO_4$ have mild activity, and Co–Mo composite oxides are the most active components. Prior to hydrodesulphurization, presulfurization of catalyst is necessary to transform Co–Mo oxides into sulfides. When hydrogen is used as carrier gas and H_2S is used as vulcanizing agent, following reactions take place:

$$MoO_3 + 2H_2S + H_2 = MoS_2 + 3H_2O. \tag{1.7}$$

$$9CoO + 8H_2S + H_2 = Co_9S_8 + 9H_2O. \tag{1.8}$$

In addition, methyl mercaptan and thiophene are also used as vulcanizing agent. However, research results indicate that H_2S is the most suitable vulcanizing agent. After presulfurization, the compositions of catalyst are Al_2O_3, $CoAl_2O_4$ (inactive), Co_9S_8, MoS_2 and a little of MoO_2. Actually, MoS_2 promoted by active Co^x functions as active site, and reaches the highest activity when the Co^x/Mo ratio is 0.18.

Although iron molybdate, nickel molybdate as well as cobalt molybdate, are active in hydrogenation of organic sulfur compounds, their activities are much lower than that of cobalt molybdate.

(3) **Preparation, usage, deactivation, and regeneration.** Three routes including dry-mixing, coprecipitation and impregnation are used to prepare Co–Mo hydrogenation catalysts. Among them, only impregnation method is widely adopted in industry.

In order to ensure high activity for hydrodesulphurization, the catalysts should be remained in sulfide state in reactor under normal operating conditions. If the sulfur content in the feedstock is lower than the limit value for a long time, the catalysts will release sulfur, resulting in lower activity.

The catalysts are usually regenerated *via* combustion in air. During regeneration, temperature control is essential and rapid ramp in temperature should be avoided.

1.1.2 *Zinc oxide desulfurizer*

The role of Co–Mo based hydrogenation catalysts is to convert organic sulfur compounds to H_2S. The catalyst itself has limited ability for the removal of produced H_2S, and only (1%3%) sulfur can be adsorbed by these catalysts even under equilibrium conditions. Thus, zinc oxide is used to remove H_2S after hydrogenation procedure in industry. Some organic sulfur compounds can also be removed simultaneously by zinc oxide.

(1) **Desulphurization reactions on zinc oxide.** The reaction of zinc oxide with H_2S is a non-catalytic chemical reaction in stoichiometry.

$$H_2S + ZnO = ZnS + H_2O. \tag{1.9}$$

Simultaneously, some organic sulfur compounds are also absorbed by zinc oxide.

$$COS + ZnO = CO_2 + ZnS. \tag{1.10}$$

$$CS_2 + 2ZnO = CO_2 + 2ZnS. \tag{1.11}$$

$$C_2H_5SH + ZnO = C_2H_5OH + ZnS. \tag{1.12}$$

$$C_2H_5SH + ZnO = C_2H_4 + H_2O + ZnS. \tag{1.13}$$

Thermodynamically, the above-mentioned reactions are irreversible at the temperature range of 200°C–400°C, and therefore sulfur can be removed completely.

Iron oxide is another important desulfurizer and its reaction mechanism is the same as that of zinc oxide. Because the reaction conditions, e.g., steam content, must be controlled strictly when iron oxide is used, Zinc oxide is widely used in industry although the price of iron oxide is lower.

(2) **Composition, structure, and preparation.** Zinc oxide desulfurizer is a reactive solid adsorbent. Zinc oxide deactivates at temperatures above 400°C because of the formation of coke. In order to reduce the desulphurization temperature, small amounts of CuO, MnO_2, and MgO are added to zinc oxide.[4]

Desulphurization is a typical gas–solid absorbing reaction on zinc oxide. Sulfur adsorption capacity with the mass fraction of sulfur absorbed per gram catalyst is about one percent if only surface zinc oxide is reactive. Therefore, the desulphurization performance of zinc oxide adsorbent not only depends on the content of zinc oxide, but also on the utilization ratio of zinc oxide (related to porous structure and surface area), and thereby preparation conditions. It is commonly proposed that the zinc oxide prepared from zinc carbonate possesses small crystal size, high surface areas and therefore good desulphurization performances.

(3) **Lifetime.** During desulphurization, zinc oxide transforms into zinc sulfide, loses absorption ability gradually, and at last, must be replaced by fresh ones. Therefore, zinc oxide desulfurizer belongs to reactive fine adsorbent, and is suitable in situation with low sulfur content for desulphurization. Generally, the sulfur content must be reduced to below 100 mg/m^3 in the feedstock *via* the wet desulphurization or other dry desulphurization before zinc oxide can be served as desulfurizer. The sulfur content in purgative gas might be below 0.3 mg/m^3 after desulphurization by zinc oxide. The lifetime of zinc oxide desulfurizer depends on the sulfur content in the feedstock gas and the operating conditions. The designed lifetime is about one to two years when the sulfur content in the feedstock gas is below 20 mg/m^3.

(4) **Fine desulfurizer at room temperature.** Since the end of 1980s, Imperial Chemical Industries Ltd (ICI) developed a fine desulphurization process on "Hydrolyzed Zinc Oxide" at room temperature. Yuhua Kong *et al.*[5] in Hubei Institute of Chemistry, China, developed T504 catalysts for COS hydrolysis and T101 activated carbon fine desulfurizer successfully, and achieved fine desulphurization at room temperature, with the sulfur content below 0.1 mg/m^3 in the gas after desulphurization. These desulfurizers are suitable to protect the catalysts for the methanation, ammonia synthesis and methanol synthesis.

1.1.3 *Hydrocarbon steam reforming catalysts*

Since 1930s, production of hydrogen-containing gases from the reaction of hydrocarbons with steam over catalysts has been a mature method. In 1936, the first steam reforming factory was set up under atmospheric pressure in ICI using hydrocarbons (from methane to butane) as feedstock. The feedstock was extended to hydrogenated gasoline in 1954, and further to naphtha. The first naphtha steam reforming factory was built in 1959. Now the naphtha steam reforming is widely

applied in the production of synthesis gas for ammonia manufacture, and is also extended to produce town gas.

Hydrocarbon steam reforming catalysts are classified into natural gas steam reforming catalysts and light-oil steam reforming catalysts according to the feedstock, and primary- and secondary- steam reforming catalysts according to the processes.

(1) **Steam reforming reactions.** The hydrocarbons after hydrodesulphurization react with a proportion of steam on primary steam reforming catalysts at high temperatures, and produce the mixed gases containing H_2, CO, CO_2 and small amounts of methane. The mixed gas has to be further catalytically converted in the secondary steam reformer at high temperatures in order to reduce methane content and meet the requirement as a feedstock of ammonia synthesis. A proper amount of air is added to raise the reaction temperature and to reduce methane content, as well as increase the nitrogen content to meet the requirement of ratio of H_2 to N_2 in ammonia synthesis.

(i) **Primary steam reforming reactions.** When gaseous hydrocarbons in which methane is a major component are adopted as feedstock in the primary reformer, the following steam reforming reactions occur.

$$CH_4 + H_2O = CO + 3H_2. \quad \Delta H_{298} = 206.3\,kJ \cdot mol^{-1} \tag{1.14}$$

$$CH_4 + 2H_2O = CO_2 + 4H_2. \quad \Delta H_{298} = 165.3\,kJ \cdot mol^{-1} \tag{1.15}$$

$$CO + H_2O = CO_2 + H_2. \quad \Delta H_{298} = -41.2\,kJ \cdot mol^{-1} \tag{1.16}$$

$$CO_2 + CH_4 = 2CO + 2H_2. \quad \Delta H_{298} = 247.3\,kJ \cdot mol^{-1} \tag{1.17}$$

Although the CO shift reaction, i.e., (1.16), is a moderate exothermic reaction, the reactions of (1.14), (1.15) and (1.17) are strongly endothermic. Therefore, methane steam reforming is a strongly endothermic reaction. Tube-type reactor with external heat-supplier is usually applied in industry.

It is known from the above reactions that low-pressures and high-temperatures are beneficial to methane steam reforming. Pressurized reactions are adopted in industry for the sake of economy.

With liquid-hydrocarbon such as naphtha as feedstock, the steam reforming reactions are very complicated, and the reactions can be summarized as follows:

$$C_nH_m + nH_2O = nCO + (n + m/2)H_2. \tag{1.18}$$

$$CO + 3H_2 = CH_4 + H_2O. \quad \Delta H_{298} = -206\,kJ \cdot mol^{-1} \tag{1.19}$$

Reaction (1.18) is strongly endothermic and its reaction heat is higher than the whole heat released from reactions (1.19) and (1.16). Therefore, the overall process is endothermic, and low-pressure and high-temperature are favorable. Reaction (1.18) is irreversible at normal temperatures. Other than CO, CO_2, H_2, and residual steam, there is no hydrocarbon in the outlet gases. The reaction equilibration is dependent on the reactions (1.19) and (1.16). The outlet gases equilibrium compositions are related to temperature, pressure and ratio of H_2O/C, as well as molar ratio of H/C in raw hydrocarbons. Excess of steam is beneficial to the conversion of naphtha.

(ii) Although the primary reactions are different if different feedstock (methane or naphtha) is used, the secondary steam reforming reactions are the same. Combustion reactions between the introduced air and the gases dominate the reactions from the primary reactor over the catalysts in the vertical kiln.

$$H_2 + 1/2O_2 = H_2O. \qquad \Delta H_{298} = -241\,kJ \cdot mol^{-1} \tag{1.20}$$

$$CO + 1/2O_2 = CO_2. \qquad \Delta H_{298} = -283.2\,kJ \cdot mol^{-1} \tag{1.21}$$

$$CH_4 + 1/2O_2 = CO + 2H_2. \quad \Delta H_{298} = -35.6\,kJ \cdot mol^{-1} \tag{1.22}$$

The combustion reaction rate of hydrogen and oxygen is $1 \times 10^3 - 1 \times 10^4$ times faster than those of other reactions. The combustion reaction takes place mainly on the top of the vertical kiln, producing steam and releasing a great deal of heat. Oxygen is consumed completely when the mixed gases arrive at the catalyst bed of the vertical kiln. Therefore, the reactions occurred in the catalyst bed mainly include methane steam reforming reactions (1.14), (1.15), and shift reaction (1.16).

The steam reforming section is the highest energy-consumption part in the ammonia synthesis process. The whole feedstock and the fuel are introduced from this section. The energy consumption at this stage accounts for 60% of the whole process. If the strongly endothermic reactions in the primary reactor are displaced to the secondary reactor to make the reaction autothermal, it can reduce the external heat supply and save energy. In the new energy-saving process,[6] the inlet temperature is raised to 650°C and outlet temperature is dropped to about 700°C in the primary reactor. Meantime, high content of residual methane in outlet gases of primary reactor is permitted, and sequentially the reaction conditions of the primary reactor became moderate. The superfluous load is shifted to the secondary reactor. The heat in the secondary reactor is supplied through the addition of excess of air, and superfluous nitrogen is removed in the purification process. These measures exhibit positive effect of energy saving. Development of catalysts for ammonia synthesis at low temperatures and with low ratios of H_2/N_2 provides guarantees for the energy-saving process.

(2) **Catalysts for steam reforming reactions**

(i) **Chemical compositions.** The catalysts are different for different hydrocarbons or for the same hydrocarbons on the primary or secondary reforming reactors. Hydrocarbon reforming catalysts are composed of active component, support and promoters. Nickel is an effectively active component, and its content ranges from 5% to 30%. Precursor of nickel catalyst is commonly in the state of NiO. Prior to using, NiO is reduced directly to metallic nickel in the reforming reactor. Up to now, nickel is still the active component in most catalysts, while supports and promoters, including Al_2O_3, MgO, CaO etc., are various. The support and promoter have important effects on the performance of the catalyst and its physical properties, e.g., strength, density and thermal stability. The support should remain stable under high temperatures and the presence of steam. Therefore, the support is usually refractory oxides, such as Al_2O_3, MgO, CaO, ZrO_2 and TiO_2 etc. Al_2O_3 is a good support, but should be prepared and calcined to ceramic framework. MgO alone cannot be used as a support because MgO and steam reacts at low temperatures. Also, CaO has the similar problem.

Promoters can suppress fusion and sintering, preventing particle growth and improving capability of resisting to carbon deposit or sulfur, resulting in the

extended lifetime of catalysts. The non-reducible and lowly volatile oxides such as Al_2O_3, MgO and CaO are usually used as promoters. In order to suppress carbon formation, the major deactivating reaction in the reforming process, alkali and alkaline-earth metals oxides (such K_2O, CaO and MgO) and rare earth oxides are added to decrease surface acidity of the catalysts. This is particularly important for the catalysts in liquid-hydrocarbon reforming reactions. Carbon formation is the prominent problem for nickel catalysts in the primary steam reforming process, while strength and thermal stability are the key problems in the secondary steam reforming.

Usually, the reforming catalysts are prepared *via* impregnation method.

(ii) **Physical structure.** The rate of reforming reaction is controlled by the internal diffusion in industrial units. The catalytic performance is related to porous structure, particle size and shape. It is generally considered that the change of catalyst shape is more effective than the changes of support and promoter for improving the apparent activity. In the past 20 years, the research about the designing of shapes of the catalysts is very active. The abnormity catalyst with high geometric surface is an important research direction for the steam reforming catalysts. The wheel-like, cellular and interlocking columnar catalysts, which were developed by Southwestern Institute of Chemical Engineering, China, have been used.

(iii) **Carbon deposition and poisoning.** Carbon formation or carbon deposit is a destructive side reaction in the steam reforming process. Although a lot of studies were carried out on the carbon formation mechanism, yet there are no widely accepted conclusions. Improving on catalytic selectivity is a basic route besides controlling appropriate reaction conditions. For example, addition of alkali as promoter can accelerate the rate of carbon eliminating. MgO is used as a support to keep basicity of the catalyst, and further to avoid deposition of carbon. Addition of rare earth oxides is also suggested to resist coking.

The steam reforming catalysts are very sensitive to some impurities in the feedstock such as sulfur, arsenic, halogens, phosphorous and lead etc., even with very low contents. Generally, sulfur content is required to be below $0.5\,\mathrm{ml}\cdot\mathrm{m}^{-3}$. Halogen such as chlorine, poisoning role is similar to sulfur, has the same limited content. Arsenic poisoning is permanent and irreversible. Thus, the restriction for arsenic is very strict. The steam reforming catalysts must be replaced when they are seriously poisoned by arsenic.

1.1.4 *CO high-temperature shift catalysts*

The concentrations of CO (10%–50%) are different in the synthesis gases produced from different feedstock. CO must be removed because it is a poison for ammonia synthesis catalysts. Generally, CO is converted *via* reaction with steam to form CO_2 and H_2 over a catalyst, and then CO_2 is removed. The reaction between CO and steam over a catalyst is called CO shift reaction as shown in Eq. (1.16).

In modern ammonia plant, it commonly adopts two-step shift processes, i.e., high-temperature shift and low-temperature shift. High-temperature shift reaction is run over Fe–Cr catalysts at 350°C–500°C, while low-temperature shift reaction is carried out over Cu–Zn catalysts at 200°C–280°C. The concentration of CO in the synthesis gas is reduced to 2%–3% over the high-temperature shift catalyst, and

0.5%–1.0% over the low-temperature shift catalyst. The residual 0.5%–1.0% CO is further reduced to trace level (below 10×10^{-6}) by methanation in the following procedure to meet the requirement for ammonia synthesis catalyst.

In the late 1960s, with the development of gasification technology which uses heavy oil and coal as raw materials, high sulfur content in synthesis gas led to the deactivation of Fe–Cr high-temperature shift catalyst. Thus, sulfur tolerant Co–Mo shift catalysts have been developed and applied widely since then. The catalysts are active in the temperature range of 160°C–500°C, and also are called wide temperature-range shift catalysts.

(1) **CO shift reaction.** CO shift reaction (1.16) is reversible and exothermic. The reaction heat and the equilibrium constant of the reaction decrease with temperature. The following factors have effects on chemical equilibrium of CO shift reaction.

(i) **Temperature.** Low temperature is beneficial to decrease the CO concentration.
(ii) **Ratio of steam to gas.** H_2 and CO_2 will be favored with increasing the ratio of steam to gas. Increasing ratio of steam to gas is often used to increase equilibrium conversion of CO in industry. However, it also brings some problems in process and economy.
(iii) **CO_2.** It is seen from Eq. (1.16) that the removal of CO_2 is beneficial for hydrogen formation. Accordingly, a system for CO_2 removal is built between two beds of catalyst in shift reactor to increase conversion of CO. The pressure has no apparent effect on the shift reaction equilibrium.

(2) **Fe–Cr catalysts**

(i) **Composition of iron-chromium catalyst.** Since the beginning of 1900s, hydrogen has been produced through CO shift reaction over Fe–Cr oxides in the ammonia plant. Up to now, Fe–Cr catalysts are still widely used in industry. The Fe–Cr catalysts contain mainly iron oxide, with 6%–12% Cr_2O_3 and small amounts of K_2O and some adhesives.

Fe_3O_4 is an active component of high-temperature shift catalysts. Iron oxides prepared by different methods have different compositions and crystal phase. Some results show that the catalysts derived from the precursors of γ — Fe_2O_3 and $Fe(OH)_3$ — are the most active ones.

Cr_2O_3 is considered as a structural promoter. It can prevent or postpone the crystal growth and surface area reduction at high temperatures, avoid excessive reduction of iron oxide, increase strength and prevent carbon formation. Oxide of chromium is commonly added in the state of Cr^{6+}.

Potassium is an effective promoter. The catalyst with about 0.5% K shows the highest activity, and when K content is high than 3% the activity of the catalyst decreases. In addition, potassium salts have a negative effect on the release of sulfur in the catalysts.

Fe–Cr catalysts are prepared *via* co-precipitation of $FeSO_4$ and CrO_3 to form hydroxides of Fe and Cr, and following drying and calcining.

(ii) **Structure and mechanical strength.** CO shift reaction is a typical gas–solid catalytic reaction. The changes in physical structure has an important effect

on reaction rate, conversion, pressure drop, lifetime, strength, resisting sulfur and thermal stability during the whole process at high temperatures. In fact, the replacing of CO shift catalysts in industry is not due to the loss of activity, but due to the large pressure drop. Strength is one of the key factors for evaluating the catalytic performance. For high-temperature shift catalyst, strength is even more important than activity. Surface structure and strength of the catalyst depend on the state of iron oxide precursor, Cr_2O_3 content, granule size and shaping pressure. The Fe–Cr catalysts can be manufactured with low density and high strength.

(iii) **Reduction of Fe–Cr catalysts.** Fe–Cr catalysts must be reduced from Fe_2O_3 to Fe_3O_4 *prior* to use. Generally, the reduction of Fe–Cr catalysts carries out in process gas containing CO, H_2, CO_2 and H_2O. The reaction during the reduction process is as follows:

$$3Fe_2O_3 + H_2 = 2Fe_3O_4 + H_2O. \quad \Delta H_{298} = -9.63 kJ \cdot mol^{-1} \tag{1.23}$$

$$3Fe_2O_3 + CO = 2Fe_3O_4 + CO_2. \quad \Delta H_{298} = -50.83 kJ \cdot mol^{-1} \tag{1.24}$$

Phase equilibrium between Fe_2O_3 and Fe_3O_4 is dependent on the ratios of H_2/H_2O and CO/CO_2. Under normal conditions, there is enough amount of H_2 and CO in process gas. The reactions (1.23) and (1.24) run along the forward directions, and Fe_3O_4 is a stable phase. The reduction of Fe_3O_4 to metallic iron should be avoided. Accurately, excessive H_2O can prevent the over-reduction.

The residual sulfates in precursor of catalyst react with hydrogen to produce H_2S, and it releases sulfur during the reduction. The produced H_2S may poison the low-temperature shift catalysts in the following step. Therefore, the process gases can be sent to the low-temperature shift reactor only after the release of sulfur is finished.

(iv) **Development of high-temperature shift catalysts.** Fe–Cr catalysts are well-known catalysts in high-temperature shift reaction. However, Cr_2O_3, as a structural promoter, is toxic and may be harmful to health during the manufacture and use of catalysts. Also, the used catalysts lead to the environment pollution. In the late 1970s, China began to develop chromium-free high-temperature shift catalysts. In 1995, the NBC-1 chromium-free iron-based high-temperature shift catalysts were developed successfully by Hengfang Jin[7] at Inner Mongolia University of Technology in China, and applied in industry. Moreover, decreasing sulfur content in Fe–Cr catalysts is another important issue.

(3) **Sulfur-tolerant Co–Mo shift catalysts.** Some metal oxides or their mixture in group VI and VIII of the periodic table supported on alumina are good sulfur tolerant shift catalysts. The catalysts used in industry are based on Co–Mo–Al_2O_3, and contain alkaline metals as promoters. Among alkaline metals, potassium is the most effective promoter, and the content is about 0.1%–0.6%. Co–Mo catalysts are prepared through impregnation method by using cobalt nitrate, ammonium molybdate and alkaline metal salts as source materials.

Co–Mo catalysts provided by manufacturer are usually in the form of oxides of Co and Mo, and must be converted to sulfides, which are considered as the active phases. The result of sulfuration process is good or not is a key step on activity. CS_2 is usually chosen as sulfurization agent. The sulfurization reactions in the process

gas are as follows,

$$CS_2 + 4H_2 = 2H_2S + CH_4. \quad \Delta H_{298} = -240.6\,kJ \cdot mol^{-1} \tag{1.25}$$

$$MoO_3 + 2H_2S + H_2 = MoS_2 + 3H_2O. \quad \Delta H_{298} = -48.1\,kJ \cdot mol^{-1} \tag{1.26}$$

$$CoO + H_2S = CoS + H_2O. \quad \Delta H_{298} = -13.4\,kJ \cdot mol^{-1} \tag{1.27}$$

The above-mentioned reactions are strongly exothermic. To avoid the rapid increase of temperature, the amount of CS_2 and temperature must be controlled during the sulfurization. This is one of the shortcomings of the Co–Mo catalysts.

Active components in Co–Mo catalysts are metal sulfides, which can resist 10 grams of sulfur per cubic meter which is much better than Fe–Cr catalysts and Cu–Zn catalysts. Therefore Co–Mo catalysts are particularly suitable for hydrogen production processes with high sulfur content, such as residue oil gasification, heavy oil partial oxidation and coal-produced gas. Co–Mo catalysts can be used as both high-temperature shift catalysts and low-temperature shift catalysts, due to its special properties such as high activity at low temperatures, wide applicable temperature range and high tolerance to sulfur.

In China, Co–Mo catalysts have been applied since 1980s. Shanghai Institute of Chemical Engineering successfully developed B301 Co–Mo catalysts prepared by mixed grinding method in 1985. Hubei Institute of Chemistry developed B302Q spherical sulfur tolerant shift catalyst prepared by impregnation method.[8] These catalysts have been widely applied. New processes such as series connection between high-temperature shift and low-temperature shift process, doubly low-temperature shift process and whole low-temperature shift process were brought up sequentially in industrial applications.

1.1.5 *CO low-temperature shift catalysts*

It is possible to use Cu-based CO shift catalysts since sulfur content in synthesis gas can be reduced to below $0.1\,ml \cdot m^{-3}$ with the changes of industrial feedstock for ammonia synthesis and development of gas purification technology. Low-temperature shift process was first commercialized in the United States in 1963. The same process was also industrialized in China in 1965.

After high-temperature shift reaction, CO content is about 3%–4% in the process gas, and can be reduced to about 0.2%–0.4% after low-temperature shift reaction. Both theoretical calculation and practical production have proved that the yield of hydrogen or ammonia can be increased by about 1.1%–1.6% if CO content is decreased by about 0.1% after low-temperature shift reaction. Therefore, low-temperature shift catalyst is one of key "economic catalysts" in the production processes of hydrogen and ammonia.

(1) **Chemical composition.** It was found that Cu is an effective catalyst for CO shift reaction, and can catalyze the reaction at low temperatures (200°C–250°*C*), where equilibrium conversion of CO may reach about 99%. However, metallic Cu catalysts are easy to sinter and to be poisoned. It is necessary to add appropriate structural promoter as an isolate between finely dispersed Cu crystallites. The promoters include oxides of non-reducible and refractory such as ZnO, Al_2O_3, Cr_2O_3, MgO and MnO_2 etc. Among those, ZnO, Al_2O_3 and Cr_2O_3 can prevent sintering of

Cu crystallites at operating temperatures, and are the best promoters. At present, Cu–ZnO–Al_2O_3, Cu–ZnO–Cr_2O_3, Cu–ZnO catalysts and Cu–ZnO–Al_2O_3 catalysts are widely applied.

(2) **Catalytic performance**

(i) **Reduction and oxidation.** CuO must be reduced to metallic Cu *prior* to use. The reduction reactions are as follows:

$$CuO + H_2 = Cu + H_2O. \quad \Delta H_{298} = -86.67\,kJ \cdot mol^{-1} \tag{1.28}$$

$$CuO + CO = Cu + CO_2. \quad \Delta H_{298} = -127.7\,kJ \cdot mol^{-1} \tag{1.29}$$

The reduction reactions release a great deal of heat, while the Cu catalysts are very sensitive to heat. Therefore, the shift catalysts are usually reduced by hydrogen at below 250°C although the reduction of CuO is easy either by H_2 or CO. The reduced catalysts will spontaneously combust when it is exposed to air because there are a lot of H_2 and CO adsorbed on the internal surface. Thus, the reduced catalysts must be carefully removed from the reactor when reduction process is finished.

(ii) **Poisoning and deactivation.** Poisoning, heat aging and steam condensation are main reasons leading to deactivation of Cu-based catalyst. It is very sensitive to poisons and heat. Sulfur-containing compounds are the main poisons, while chlorides are permanent poisons that damage the catalysts badly in which the toxicity is 5–10 times higher than that of sulfur-containing compounds. The chloride commonly comes from process steam or cooling water. When the reaction temperature is higher than 280°C, metallic Cu is easily heat-sintered. Meanwhile, steam condensation may cause the physical damages on catalysts. Therefore, the reaction temperature must be 20°C–30°C higher than the dew points of gases at the reaction conditions.

It is inevitable that Cu based catalysts are poisoned. Self-protection is usually adopted to assure CO conversion. The choice of catalysts and their replacement periods are directly based on the efficiency and economy of an ammonia plant. A little increase in CO conversion will compensate the fee of replacement of catalysts in short term.

1.1.6 *Methanation catalysts*

In the process of ammonia synthesis, trace oxygen or oxygen-containing compounds in the syngas can poison the catalysts. Generally, the shift-gas from the low-temperature shift system contains small quantities of CO and CO_2 (less than 1%), which should be removed or transformed into inert gases before coming into the ammonia synthesis system. In the past, copper–ammonia solution was employed to eliminate CO and CO_2 by washing and absorbing. But this method requires high-investment, complicated operation and consumed large amounts of copper. At present, a methanation process is widely used because it has many advantages, such as simple process, easy operation, small installation and low cost of catalysts.

(1) **Methanation reaction.** In the methanation process, H_2, CO and CO_2 in the syngas react *via* the following reactions on catalyst.

$$CO + 3H_2 = CH_4 + H_2O. \quad \Delta H_{298} = -206.2\,kJ \cdot mol^{-1} \tag{1.30}$$

$$CO_2 + 4H_2 = CH_4 + 2H_2O. \quad \Delta H_{298} = -165.0\,kJ \cdot mol^{-1} \tag{1.31}$$

Additionally, trace of O_2 in the syngas reacts with H_2 to form H_2O. These two reactions are strongly exothermic, and their equilibrium constants increase rapidly with the decrease of temperature. This requires a lower operating temperature as possible. To design a methanation reactor, the total concentration of carbon-containing compound (CO and CO_2) in outlet of methanation reactor must be lower than $5\,ml \cdot m^{-3}$ or $10\,ml \cdot m^{-3}$, which plays a decisive role on the lifetime of the ammonia catalyst. The methanation reaction conditions can be determined by calculating the concentration of CO and CO_2 desired and the equilibrium constants of the reactions. The methanation reaction is carried out far away from its chemical equilibrium. Therefore it is not limited by thermodynamical equilibrium.

(2) **Methanation catalysts**

(i) **Chemical composition.** The activities of the following elements for the methanation reaction follow the decreasing order, Ru, Fe, Ni, Co, Rh, Pd, Pt and Ir. Ni, Ru and Fe are the main components which attract attention. Ruthenium possesses a high activity but is extremely expensive and rare. Activity and selectivity of iron are not as high as nickel, but Ni easily forms high-hydrocarbons and possibly leads to CO boudouard reaction, which could result in the deposit of carbon on iron-based catalysts. Nickel-based catalysts exhibit high activity, selectivity, low carbon deposit and low probability of formation of hydrocarbons. Almost all methanation catalysts used in industry adopt nickel as the active component. Generally, Nickel is supported on the heat-resistant oxides, such as Al_2O_3, SiO_2, MgO, CaO, Cr_2O_3 and rare earth oxides etc., which favor the dispersion and stabilization of the active component.

The methanation catalysts are commonly prepared by impregnation and precipitation methods. Precursor of Nickel is NiO, which must be reduced to metallic Ni before use. The reduction process uses the processed gases after removal of CO_2 as reducing reagent, where the total concentration of CO and CO_2 is controlled strictly to below 1% in the process gases.

(ii) **Deactivation.** The methanation catalyst can be used for about 3–5 years or even longer at industry. Poisoning and sintering are the two main factors leading to deactivation. Even a trace amounts of As, S or halogens can poison the catalyst and reduce its activity dramatically. Moreover, the poisoning caused by S is irreversible and the damage is accumulated. In order to prevent the catalyst poisoning by As, S and Cl, and simultaneously to ensure the low concentration of CO and CO_2 to less than 10 $ml \cdot m^{-3}$, the loading volume of the catalysts generally preponderate over 2–3 times of requirement by the reaction kinetics.

1.1.7 *Refine catalysts*

Beside the above-mentioned catalysts used for the production processes of ammonia, hydrogen, urea and other important inorganic chemicals, some other catalysts might be used during some accessorial processes. They are N_2 production catalysts, CO selective oxidation catalysts, sulfur recovery catalysts, CO_2 dehydrogenation catalysts, molecular sieve desiccants and de-poison catalysts such as desulfurization, dechlorination, and dearsenization, etc.

(1) **N_2 production catalysts.** During the chemical processes, N_2-rich gas or pure N_2 as inert carrier gas is frequently used for replacement or purging equipments and piping and protecting the catalyst.

N_2 can be generated *via* ammonia combustion. The combustion of ammonia in air over catalyst produces N_2 and H_2O. The above generated N_2 along with the original N_2 in air is used as an inert gas, while the generated H_2O is removed by cooling. The reactions of combustion and decomposition of ammonia in the primary burning furnace filled with N_2 production catalysts are as follows:

$$4NH_3 + 3O_2 = 2N_2 + 6H_2O. \quad \Delta H_{298} = -1269\,\text{kJ}\cdot\text{mol}^{-1} \tag{1.32}$$

$$2NH_3 = N_2 + 3H_2. \quad \Delta H_{298} = 92\,\text{kJ}\cdot\text{mol}^{-1} \tag{1.33}$$

A series of side reactions may occur. However, the final products have only N_2 and H_2O under the designed temperatures and ratios of air to NH_3. The ammonia combustion method has high production capacity, low investment, low energy consumption, simple operation and high purity of N_2 in comparison with air separation method.

The industrial catalysts for nitrogen production include platinum-based catalysts, copper-based and nickel-based catalysts. Due to their low loadings, high activity, high thermal stability, high poison resistance and long lifetime, the platinum-based catalysts are widely used in industry. D101Q and D201Q are two main type catalysts in China.[3]

(2) **Selective CO oxidation catalysts in hydrogen stream.** There is still 0.3%–0.5% CO, which needs to be removed, in the synthesis gas from the low-temperature shift stream during production processes of ammonia and hydrogen. The methanation reaction needs to consume three times more H_2 than CO, and whereas the selective oxidation method oxidizes CO to CO_2 selectively, by introducing a fixed amount of O_2. Thus it decreases the consumption of H_2 and amount of vent gas. 4 mol of H_2 can be reclaimed after every mol of CO is oxidized selectively. That is, removal of 0.1% CO results in more 1.3% of ammonia production. Generally, yields of ammonia and CO_2 can be increased by 3%–5% and 1.0%–2.5%, respectively, by using CO selective oxidation method for the same amount of syngas. Therefore, the selective oxidation technology has been widely used.

With the presence of H_2, the selective oxidation of CO to CO_2 competes with the oxidation reaction of H_2 to H_2O. Both reactions possess high equilibrium constants, which can reach up to 10^{24}–10^{25} below 200°C. This side reaction cannot be ignored because of the high H_2 content in the low-temperature shift gas, even if the equilibrium constant of selective oxidation of CO is much higher than the oxidation reaction of H_2 under relatively low temperatures. Therefore, the CO selective oxidation reaction demands not only a low temperature but also a catalyst with high selectivity. It was reported that Y101-type platinum catalyst patented in China for CO selective oxidation achieves conversion and selectivity higher than 90%.[3]

(3) **Sulfur recovery catalysts.** Sulfur reclaim is to transform the acidic gas containing H_2S produced during processes into sulfate, and then sulfate is recycled. The sulfur recovery has many methods, such as iron oxide process, ADA process, G-V process, hypermanganate process, dichromate process, catalytic combustion process and Claus method etc. Herein, the Claus method will be introduced briefly.

The Claus method is based on reaction that H_2S is combusted into SO_2 with a mole ratio (H_2S/SO_2) of 2:1 in the presence of limited amount of air. The resulted gas mixture is then transformed into elemental sulfur on Al_2O_3 catalyst. Meanwhile, the organic sulfur compounds are hydrolyzed on the Claus catalyst. The basic reactions are as follows:

$$\text{Combustion reaction} \quad H_2S + 1.5O_2 = SO_2 + H_2O. \tag{1.34}$$

$$\text{Claus reaction} \quad 2H_2S + SO_2 = 3S + 2H_2O.$$

$$\Delta H_{298} = -146.54\,\text{kJ} \cdot \text{mol}^{-1} \tag{1.35}$$

$$\text{Hydrolysis reactions} \quad COS + H_2O = H_2S + CO_2. \tag{1.36}$$

$$CS_2 + 2H_2O = 2H_2S + CO_2. \tag{1.37}$$

The combustion reaction is realized in the firebox of the waste heat boiler within the Claus unit, while the Claus reaction and hydrolysis reactions take place in the Claus reactor filled with a catalyst. This process requires two or three Claus reactors. The sulfur recovery is 90%–96% in the first two reactors and is 95%–98% in the third reactors. Recently, super-Claus process has emerged. In the super-Claus process, the sulfur recovery can reach up to 99% and 99.5%, respectively, after adding a selective oxidation step or a hydrogenation reactor followed by a selective oxidation reactor on the basis of Claus. For the purpose of meeting the atmospheric emission standard, acidic gas in the outlet of reactor should be combusted at 1,200°C to transform the remaining H_2S into SO_2.

The sulfur recovery catalysts are mainly used at refineries, petrochemical companies and ammonia plants with drege oil or coal as raw materials. Except for a few companies where bauxite is used, most plants adopt Al_2O_3-catalysts. LS822, LS821, CT6-2 and CT6-3 are the catalysts made in China for sulfur recovery.

(4) **Dehydrogenation catalysts in CO_2 stream.** The small quantities of H_2 and O_2 existed in the high pressure syringe or in the tail gas absorber at urea plant may lead to explosion occasionally. Oxidation combustion method has been employed to eliminate H_2 contained in CO_2 stream since 1970s. The dehydrogenation catalysts from CO_2 stream is a noble metal catalyst supported on γ — Al_2O_3, such as CN-101 catalyst manufactured by Engelhard Industrial Corp., composed of 0.3% Pt/γ — Al_2O_3, has a two-dimension structure with a Φ 3 mm × 3 mm sheet and DH-2 is a Pd/γ — Al_2O_3 catalyst with thin shells developed by China.

The principle of catalytic dehydrogenation is developed based on the idea that trace of H_2 in CO_2 stream can react with O_2 to form H_2O on Pt/γ-Al_2O_3 catalysts. The trace amounts of CO remaining in CO_2 stream will also be oxidized into CO_2. If the H_2 concentration in the gas after CO_2 dehydrogenation is about 0.2%, the explosion reaction will not occur according to the mass balance in the urea production of steam stripping process. However, the actual concentration of H_2 is only $200\,\text{ml} \cdot \text{m}^{-3}$ after dehydrogenation. According to their reaction heat, the complete oxidation of 1% H_2 brings about a temperature rise of 48°C. The working temperature must be strictly controlled to be above the dew point in order to avoid the vapor condensation on the catalyst, which may reduce the activity and corrosion of the equipment.

(5) **Molecular sieve desiccants.** Molecular sieve, a kind of natural or synthesized zeolite, is a silica aluminate with tetrahedron as structural units. Molecular sieve is a highly efficient and high selective adsorbent due to its huge inner

Table 1.3 Characteristics of several molecular sieves

Type	Si/Al molar ratio	Pore size/nm	Water adsorption capacity/%		Main applications
			Theoretical	Experimental	
3A	2.0	0.3	25	≥18	Drying of cracking gas, coking gas, oil field gas
4A	2.0	0.4	27.5	≥21	Drying, desulphurization, removal of CO_2, Argon purification
5A	2.0	0.5	27	≥21	Drying and purification of air, oxygen production by pressure swing adsorption
10X	2.5	0.8–0.9	39.5	≥23	Removal of aromatic hydrocarbon and organic sulfur compounds, adsorption separation of hydrocarbons
13X	2.5	0.9–1.0	35.5	≥23	Drying and purification of air, supports
Y	4.5–5.0	0.9–1.0	35.2	≥23	Catalysts or supports

space, high surface area, uniformly distributed micropores. Moreover, it is capable of adsorption and separation of different molecules.

Difference between various molecular sieves lies in their chemical composition. Various molecular sieves form with different metal ions (Na, K, Ca, Mg, etc.) and different mole ratios of SiO_2:Al_2O_3. A-type, X-type and Y-type molecular sieves are often used as desiccants. Their main properties, water adsorption capacities and main applications are listed in Table 1.3.

Molecular sieves have strong affinity toward H_2O, and thus are usually used to dry and purify gases. For instance, it has been used in air separator to dry and remove CO_2 and C_2H_2, to remove sulfur in the feedstock and to recover H_2 from vent gas in ammonia synthesis loop, to remove SO_2 or NO_x in H_2SO_4 or HNO_3 tail gas, and to dry H_2 and rare gases. There are some characteristics of molecular sieves for drying: (i) High drying extent. Molecular sieves could dry air to about −90°C–60°C on its dew point, which is effective to eliminate trace H_2O out of air. (ii) Molecular sieves are the sole effective adsorbents at high temperatures. However, molecular sieves can only retain certain adsorbing activity above 200°C. (iii) Drying and purifying realized simultaneously to eliminate impurities and H_2O. (iv) Selective adsorption with different pore sizes. For example, when olefin hydrocarbon is dried using 3A-type molecular sieve only H_2O is adsorbed.

(6) **De-poison catalysts.** Although the catalysts used in inorganic chemical production always own high activity and selectivity, they are also extremely sensitive to poisons. In order to ensure long lifetime and economical production, some impurities in the raw materials, processed water and air must be strictly purified. The most common and harmful poisons are sulfides, chlorides and some organic metallic compounds.

(i) **Antichlor.** Cu-based catalysts are very sensitive to chlorides, which will combine with active metals in the catalysts to form low melting-point compounds. This leads to lower activity and rapid aging of the catalysts due to sintering of the active phase. At the same time, chlorine ions have high migration coefficient and move along with gas stream, which will threaten the downstream catalysts and the safety of equipments and pipes due to heavy corrosion. Generally, the concentration of chlorine ions should not be higher than 5×10^{-9}.

Chlorides derive commonly from process water, accessorial air and hydrocarbon when they are used as raw materials. In particular, when river water is used, it should be paid much attention because it might have residual pesticides containing organic chlorides. The light oil contains at most 15×10^{-6} of chloroalkanes, which are seldom found in the natural gas.

Removing these chlorides from raw materials is very difficult. Although deionized water can eliminate inorganic chlorides effectively, it cannot remove the organic ones. The power plants always adopt the reverse osmotic treatment to remove organic chlorides. However, it is uneconomical to those ammonia plants because of the large quantities of water needed.

The principle of dechlorination by antichlor is that hydrogenolysis of organic chlorides on Co–Mo or Ni–Mo catalysts generating HCl. Then HCl reacts with metallic oxides and alkaline which has a rather strong affinity, generating stable metal chlorides, and is thus fixed.

T402, T403 and modified Zn–Ca antichlors[8] are commonly used in China. Normally, the antichlors should be placed ahead of desulfurizer.

(ii) **Dearsenic agents.** Arsenide-containing compounds are toxic for the catalysts in various chemical productions. Generally, arsenide exists in the form of AsH_3, whose concentration reaches up to about $0.2\,ml \cdot m^{-3}$ in the light oil. The concentration of Arsenic is $1\,ml \cdot m^{-3}$ in the tail gas of adsorption converter in fluid catalytic cracking in petroleum refining industry, $0.5\,ml \cdot m^{-3}$ in the high-concentrated ethylene of petrochemical industry, $0.15\,ml \cdot m^{-3}$ in the refined propylene, and $0.06\,ml \cdot m^{-3}$ in the mixture of ethylene-propylene, respectively.

The industrial dearsenic agents include four types, Cu-based, Pb-based, Mn-based and Ni-based dearsenic agents. Among these four types, Cu-based dearsenic agent is most widely used. Moreover, Cu-based dearsenic agent can be classified as metallic copper, $CuO \cdot Al_2O_3$, activated carbon supported $CuO \cdot Al_2O_3$, aluminum silicate supported $CuSO_4$, $CuO \cdot ZnO \cdot Al_2O_3$, $CuO \cdot SnO_2$, activated carbon supported $CuO \cdot Cr_2O_3$ and BaO promoted $CuO \cdot Cr_2O_3$ etc. The Pb-based dearsenic agent is mainly based on $PbO \cdot Al_2O_3$. The Mn-based dearsenic agent mainly consists of MnO_2 and the Ni-based dearsenic agent can be derived directly from the $NiO \cdot MoO_3/Al_2O_3$ hydrodesulphurization catalyst or aluminum silicate supported NiO and Ni catalyst.

Using Cu based dearsenic agent as example, AsH_3 is adsorbed by the active CuO followed by reactions such as 1.38 and 1.39.

$$3CuO + 2AsH_3 = Cu_3As + As + 3H_2O. \tag{1.38}$$

$$3CuO + 2AsH_3 = 3Cu + 2As + 3H_2O. \tag{1.39}$$

AsH_3 can also undergo decomposition reactions: $AsH_3 = 1.5H_2 + As$. Cu_3As and As deposit on the surface of dearsenic agent. These agents are recovered by oxidation with air or oxygen containing vapor.

The Cu based dearsenic agent has a high capacity for the removal of As. The dearsenic agent can function under low-temperatures and low-pressures, even under room temperature and atmospheric pressure. However, acetylene in the feedstock is not allowed, otherwise, it will form copper acetylide leading to explosion. Pb-based dearsenic agent is suitable for the alkynes-containing circumstance and is able to deal with alkenes. But its As-capacity is inferior to that of the Cu-based dearsenic agent. The Mn-based dearsenic agent is cheap and may be regenerated, and is often used for the removal of the arsenic in liquefied petroleum gas. The Ni-based dearsenic agent is not only to remove arsenic but also to remove organic sulfur. Thus it is appropriate to eliminate trace of arsenic in naphtha and to protect the catalysts of methanol synthesis and low-temperature shift for the synthesis ammonia process.

1.2 Historical Retrospect of Catalysts for Ammonia Synthesis

Catalysts for ammonia synthesis are very important among the thousands of catalysts. The first ammonia synthesis catalyst was discovered in 1909, applied successfully to the first catalytic process under elevated pressures in industrially. This is a milestone in the history of catalytic process. It marks the beginning of a new age in industrial catalysis. Only a few years later, catalytic methanol synthesis succeeded and high pressure technology became a basic practice in organic chemistry field. For the whole 20th century, ammonia synthesis catalyst is the starting point for many basic researches on fundamental theories and concepts in the field of heterogeneous catalysis. The tremendous success in ammonia synthesis industry and its catalytic process established a foundation for heterogeneous catalysis. Once a new theory and idea related to catalysis is formed, ammonia synthesis is commonly used as touchstone probe reaction. Development history of ammonia synthesis catalysts is considered as an epitome of development history for catalysis science. So far, it still attracts much attention from many researchers. At present, the catalysts are still being developed, and a lot of new ideas can be obtained. The setup of ammonia process itself contains high creativeness and brilliant scientific ideas. Therefore, detailed retrospect of development course for ammonia synthesis catalysts is helpful.

1.2.1 *Basic studies on physical chemistry of ammonia synthesis reaction*

In 1754, Briestly first obtained ammonia from heating ammonium chloride with lime. In 1787, Berthollet reported that ammonia is composed of both elements of nitrogen and hydrogen. Accordingly, contemporary chemists attempted to synthesize ammonia from elements of nitrogen and hydrogen. However, they encountered insurmountable difficulties, because chemical laws about mass balance and chemical equilibrium had not been built up at that time. Some outstanding chemists, including Nernst, Ostwald and Haber, had devoted themselves to solve these problems, although they had controversy in equilibrium constants.

The reaction for the formation of ammonia from nitrogen and hydrogen is,

$$N_2 + 3H_2 \leftrightarrow 2NH_3 + 46.1\,\mathrm{kJ \cdot mol^{-1}}. \tag{1.40}$$

This is an exothermic and volume reduction reaction. The higher pressure, the lower temperature, the higher concentration of ammonia can be achieved under equilibrium conditions. However, no detailed studies were carried out at that time.

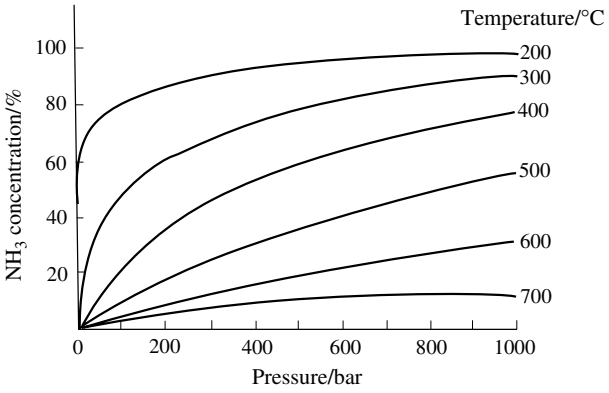


Fig. 1.2 Equilibrium concentration of ammonia as a function of temperature for various pressures (1 bar = 10^5 Pa)

Haber *et al.* obtained the equilibrium concentration of ammonia on pure iron catalyst at 1,000°C and 101 kPa (Fig. 1.2). They obtained 0.012% ammonia at 1,020°C and 101 kPa. This result indicated that ammonia could be synthesized even at pressure of 101 kPa.

At the same time, Nernst, who was doing the same research in the University of Berlin, found that the amount of ammonia generated in Haber's experiment was significantly higher than that obtained from the thermodynamic calculation. They thought that the difference was from experimental error due to low concentration of ammonia. To get the accurate equilibrium concentration, Nernst *et al.* conducted experiments on iron catalyst at elevated pressures. The results showed that equilibrium concentration of ammonia was 0.003% at 1,024°C and at 101 kPa, which was well consistent with the theoretical prediction. Nernst *et al.* successfully obtained about 1% ammonia at 50 atm (1 atm = 101.325 kPa) and 685°C in their experiments. This is also an important experiment in history. It indicated the synthesis of ammonia in industrial scale is possible if a good catalyst was found and used at high pressures.

Haber *et al.* also carried out their experiments in detail again, and found that their previous results were not correct. Then, they carried out the same high-pressure experiments as Nernst *et al.* did and obtained almost the same result.

It was soon confirmed that the high-pressure and low-temperature were more favorable for the synthesis of ammonia. It is Haber who claimed that ammonia synthesis would be realized industrially under high-pressures. If ammonia needs to be formed at atmospheric pressure, the temperature must be lower than 300°C, and its concentration is only several percent. In addition, at that time, no catalyst was available to accelerate this reaction under these conditions. On the other hand, the yield of ammonia rapidly decreased due to its decomposition at 75 bars and above 600°C. Many scientists thought that there was an insurmountable obstacle to synthesize ammonia from its elements. At the critical moment, Haber (Fig. 1.3) made an unprecedented progress in ammonia synthesis. He found that ammonia synthesis from hydrogen and nitrogen must be conducted at much higher pressures than the previous ones, and this idea constructed the base for the continuous production of ammonia.



Fig. 1.3 Fritz Haber (1868–1934)
German chemist, contributes to physical chemistry and electrochemistry. He studied at the University of Berlin under the supervision of Hoffmann and then at the University of Heidelberg under the supervision of Robert Bunzen. In 1906, he became a full time professor at the Fridericiana Technische Hochschule in Karlsruhe. F. Haber engaged in organic chemistry study initially and then thermodynamics and electrochemistry. Since then he studied the thermodynamics in gas-phase reaction, and then moved on to the field of chemical equilibrium and ammonia synthesis from nitrogen and hydrogen. In 1919, he was awarded Nobel Prize in chemistry for his contribution in ammonia synthesis from its elements on the high-pressure recycling reaction equipments. Since 1911, he was appointed as director of Keiser Wilhelm Institute für physicalisce chemie (Max Plank Institute) at Dahlem.

1.2.2 *Realization of ammonia synthesis under high pressure*

The amount of ammonia formed in a single-pass is too little so that it is impossible to achieve the production in commercial scale. Therefore, Haber proposed to place the reactor in a closed system and circulate the gas mixture after flowing through the catalyst. This great idea provides foundation for industrial ammonia synthesis and numerous other synthesis reactions at high pressures in organic chemistry area.

In 1908, Haber *et al.* was awarded a patent on ammonia synthesis from its elements by using high pressure circulating method, in which ammonia was condensed and separated continuously and N_2–H_2 mixture was recycled under high pressures, as shown in Fig. 1.4.

Badische Anilin und Soda Fabrik (BASF) in Germany was interested in Haber's studies on ammonia synthesis. In February 1908, BASF and Haber signed an agreement about the use of Haber's idea at BASF and industrialization of chemical synthesis of ammonia. BASF appointed chemist Carl Bosch (Fig. 1.5) to take the mission of industrial development. Bosch immediately recognized that he had to solve three problems: Developing a cheap process to produce hydrogen and nitrogen, finding an efficient and stable catalyst and designing applicable apparatuses for ammonia synthesis under high pressures. Therewith, the development of ammonia synthesis process in commercial scale was officially started.

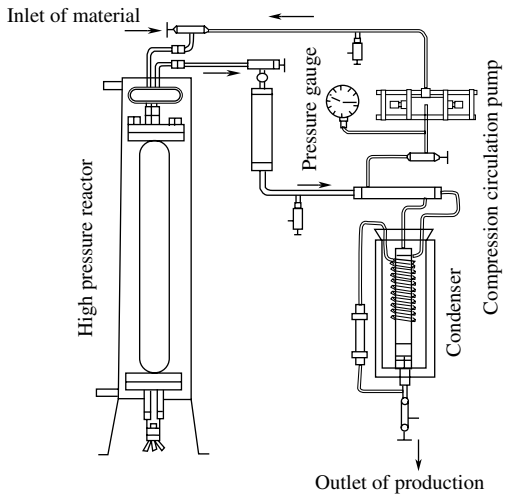


Fig. 1.4 Circulation equipment for ammonia synthesis under high pressure used by Haber *et al*.

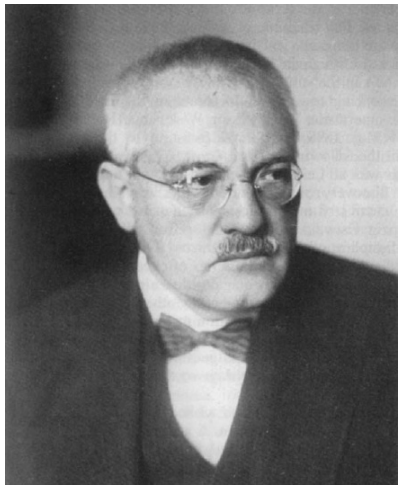


Fig. 1.5 Carl Bosch (1874–1940)

Graduated from Berlin Technische Universität, obtained his doctorate degree in the field of organic chemistry at Leipzig (1898), and joined BASF in 1899. Bosch carried out simulating experiment in BASF for Ostward's findings from which ammonia was obtained on iron catalyst; however, he could not repeat Ostward's results and argued with Ostward. Finally, Bosch knew the reason, that Ostward's iron catalyst contained some impurities (is also possible iron nitrides). Since then, Bosch as an assistant to Haber, realized successfully industrial ammonia synthesis process under high-pressure. He shared Nobel Prize in chemistry with Friedrich Bergius in 1932 for his contributions and established the foundation of industrial synthesis of ammonia.

Although iron catalysts were already used in ammonia synthesis at that time, excellent industrial catalysts had not been found yet. Haber energetically screened about 20,000 catalysts. In the March of 1909, he found that osmium exhibits excellent activity in ammonia synthesis. He obtained 8% ammonia concentration on

osmium powders at 150 atm and about 550°C and patented his discovery immediately. In response, BASF attempted to buy all osmium stock, totally about 100 kg, from all over the world. It reflected the scientists' enthusiasm at that time.

On 2 July 1909, Haber successfully obtained about 90 g of ammonia per hour over Os catalyst at 600°C and 175 atm with the high-pressure circulating flow equipment by using nitrogen and hydrogen as the raw materials. Since 1784 Berthollet revealed that ammonia is consisted of nitrogen and hydrogen, after about 125 years, Haber finally prepared ammonia from hydrogen and nitrogen for the first time in practice.

However, osmium is a very rare resource and osmium oxide volatilize easily. Therefore, it was necessary to develop cheaper catalysts with excellent performances for ammonia synthesis. Since then, Haber identified that uranium is active for ammonia synthesis. However, in 1912, he was appointed as the director of Institute of Physical Chemistry and Electrochemistry in the Kaiser Wilhelm Institute, indicating the end of the research activity of Haber in the field of ammonia synthesis. Since then, Bosch and Mittasch became the principal researchers in BASF to continue the industrialization process for the ammonia synthesis. Bosch was the leader of the whole research group, and Mittasch became the main investigator for the exploration of catalysts.

Haber's idea on closed process and gas mixture circulation means that previously static approach was replaced by dynamic method in chemistry. In corresponding to thermodynamic equilibrium, he introduced an important concept, reaction rate. He emphasized on space-time yield instead of reaction yield. Thus, it was apparent that the key problem was to find a suitable catalyst.

1.2.3 *Development of fused iron catalysts for ammonia synthesis*

Like other researchers, Mittasch (Fig. 1.6) first explored many metal nitrides and expected to fix nitrogen from air. He provided valuable information on the catalytic properties of almost all metal elements in the periodic table, although his studies on ammonia synthesis were not successful. Mittasch hypothesized that although some metals did not have catalytic activities or have very low activities themselves, some additives could significantly enhance the catalytic activities. In spite of no experimental confirmation, he thought that the hypothesis was so important that he recorded the accurate date i.e., 24 February 1909, in his experimental log, and gave the following instructions to his group:

(1) Looking for suitable catalysts. They should explore a considerable number of elements and a large number of additives.
(2) Catalytic materials should be conducted under the same conditions as Haber's experiments at high-pressures and high-temperatures.
(3) Series of tests had to be conducted.

A variety of model reactors were manufactured by BASF for the series of tests. Every reactor was filled with a few grams of catalyst, and continuously run from 24 h to 48 h repeatedly. At that time the experimental scale could be seen from the following data: About 6,500 times of tests were carried out and about 2,500 of catalysts was studied in about one and half years till the beginning of 1912.



Fig. 1.6 Alwin Mittasch (1869–1953)

German chemist in catalysis. He obtained a doctorate in chemical philosophy at Leipzig University under the supervision of Bodenstein after twists and turns. In 1904, he joined BASF and studied on ammonia synthesis as an assistant of Bosch. He noticed in study of iron nitrides that trace components changed catalytic performance dramatically and conducted studies of multi-component catalysts. He is a genius who found the doubly promoted iron catalysts only in more year. Haber and Bosch were awarded Nobel Prize for their contribution to the technology of ammonia synthesis. It should be noted that the contribution of Mittasch was no less than those of them.

Mittasch as central one developed ZnO/Cr_2O_3 catalysts for methanol synthesis and Cobalt catalyst for Fischer-Tropsch synthesis.

Up to 1919, tests had been undertaken for more than 10,000 times and about 4,000 catalysts had been studied. Such research approach consisting of a large numbers of experiments reflected a completely new way of research in chemistry. Anyway, the combination system of various materials was found, which laid the foreground of industrial catalysts for ammonia synthesis in the relatively short time. From this point of view, the research approach was successful.

In 1905, it was already known that iron is an effective catalyst for ammonia synthesis. However, the experimental results were often contradictory and difficult to reproduce. In BASF, the initial results of these experiments were also disappointing. After the experimental device was modified, experiments were performed more easily. At this time, Wolf, an assistant of Mittasch, unconsciously used the magnetite from Gallivare in Sweden, which stood in the laboratory shelf for many years, as catalyst to conduct activity test for ammonia synthesis. Under the experimental conditions, ammonia concentration in the outlet gas was 3% and remained same for a long time, which is much higher than the best result previously reported (less than 1%). On the basis of this surprising result, a variety of iron ores were tested, but many of them showed almost no activity. Initially, the formation process and structure of magnetite were considered to play an important role in their activities. However, it was soon recognized that small amounts of other elements i.e., impurities in the natural magnetite were the predominant factor influencing its activity. The ores were strictly and carefully analyzed in order to detect their components, even for trace elements. In order to exclude effects of these external

impurities, Mittasch decided to use pure iron to prepare the synthetic magnetite with the same composition as Gallivare magnetite. It was composed of Fe_3O_4 (20), CaO (0.2), Al_2O_3 (0.4), MgO (0.1), Cr_2O_3 (0.1). Many synthetic magnetites were tested as catalysts for ammonia synthesis. In the end of 1909, finally they obtained a new discovery. The synthetic magnetite was successfully prepared by melting the mixture of pure iron, several percent of alumina, a little amount of potassium salt and lime. The best catalyst was proved to be a multi-component mixture, whose composition was similar to Gallivare magnetite from Swedish. However, the proportion of impurities was different from Swedish magnetite. The multi-component catalyst was so effective that the catalysts for ammonia synthesis are still based on this theory all over the world up to now. The small differences between the catalysts provided by various manufacturers lie only in the amount or type of the additives. The characteristics of these catalysts are their stabilities, that is, no deactivation will be observed in that way as the single-flow under layer of catalyst bed in converter, if no poison is introduced (Fig. 1.7).

In a congratulation letter to Mittasch for the discovery of the new catalysts, Haber wrote "The role of the promoters is enigmatical. Ostwald first studied the Fe catalysts, and we have also tested them several hundreds times. However, all of us worked with the pure iron, no experiments were conducted on the iron with impurities."

In 1910, an effective catalyst was finally obtained. The next task was to collect the data for the construction of industrial production equipments. The suitable materials had to be developed to manufacture machines and for controlling equipments. These materials have to resist high temperatures and at least 200 bar of pressure. It must be solved no matter how difficult it was. Those study results were proved to be helpful not only for chemical industry but also for related areas.

During whole development of catalytic ammonia synthesis technology, Haber completed the research foundation of the theory and the technology for ammonia synthesis, and Bosch made it applicable for industrialization. As a result, the process is called "Haber–Bosch process." In 1911, first ammonia plant commenced to be built. In 9 September 1913, the plant with reactor of 285 mm diameter and 90 L of catalyst was switched on at 200 bar (Fig. 1.8). Initially, ammonia production was about 3–5 tons per day. But the production scale was rapidly expanded. In 1917, the ammonia produced from Haber–Bosch process exceeded 60,000 tons per

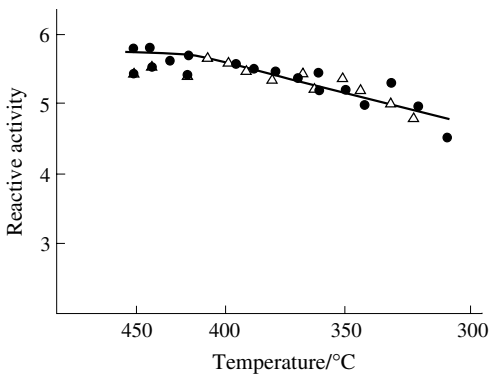


Fig. 1.7 Activity of iron catalyst with double promoters for ammonia synthesis. • Fresh catalyst, □ Catalyst after using 14 years

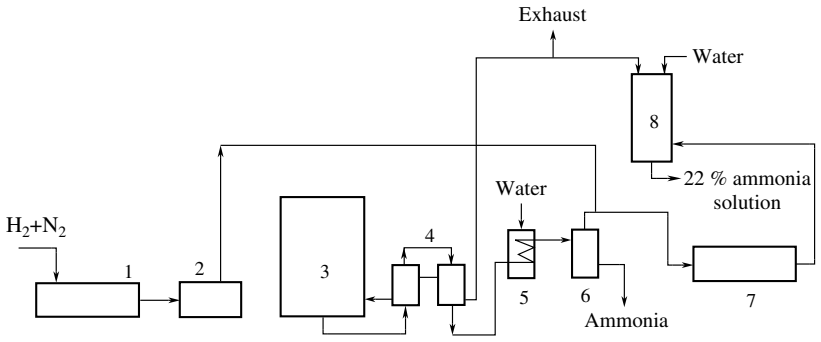


Fig. 1.8 Process flow diagram of the first set of ammonia synthesis equipment in the world

1-Compressor, 2-Filter, 3-Converter, 4-Heat exchanger, 5-Condenser, 6-Separator, 7-Recycle compressor, 8-Absorber.

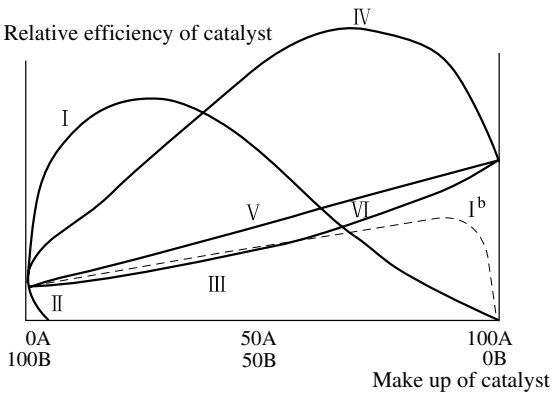


Fig. 1.9 Heterogeneous catalyst

I-Simple promoter (as Fe–Al_2O_3), I ^{b}-Support effect (as Fe–SiO_2), II-Poisoning (as Fe–S); III, V-Additive effect; IV-Cooperative effect (as Fe–Mo); VI-Deactivation.

annum. For the purpose of commercial production, BASF set up an ammonia plant at Oppau in 1911. In the following several years, the plant was developed into a huge industrial company. According to modern standards, it was incredible to develop a new technology in such a short time. However, it took 159 years to produce ammonia commercially since the first time when ammonia was obtained in the laboratory.

In 1920s, the studies on the catalysts for ammonia synthesis were performed sporadically in BASF, instead, the company mainly focused on the organic synthesis under high pressures and the new fields in heterogeneous catalysis. During the development of ammonia synthesis catalysts, researchers provided valuable information about the durability, thermal stability, sensitivity to poisons, and in particular to the concept of promoter. Mittasch[10] summarized the roles of various additives as shown in Fig. 1.9. The hypothesis of "successful catalyst is multi-component system" proposed by Mittasch was confirmed to be very successful. Iron-chromium catalysts[11] for water gas shift reaction, zinc–chromium catalyst[12] for methanol synthesis, bismuth–iron catalysts[13] for ammonia oxidation and iron/zinc/alkali catalysts[14] for coal hydrogenation were successively developed in BASF laboratories.

The catalyst for ammonia synthesis is the most intensively investigated one in the world. Although there were mass researchers who have been focused on this, the exploration of nature of ammonia synthesis is never ending. Lots of questions on the structures of ammonia catalysts as well as the mechanisms for the formation of ammonia molecule are not clarified completely.

At present, the production cost of ammonia has been decreased stupendously due to the adoption of large-capacity plants, change of raw materials and application of some other catalysts in this process. The total energy consumption per ton ammonia is $(28 - 30) \times 10^9$ J in modern ammonia plant, which is close to theoretical value $(22 \times 10^9$ J). It should be recognized that the energy utilization can be maximized only through these catalytic reactions. Clearly, any basic improvements at efficiency of ammonia catalyst will help to narrow this gap.

Catalytic ammonia synthesis technology is one of the greatest discoveries for human in the 20th century. The fused iron catalyst is one of the most important catalysts in the world. The studies to the currently used ammonia synthesis catalysts have been much deeper than that of any other catalyst. All these work has been reviewed by different researchers at different stages, such as Emmett in 1955,[15] Nielsen in 1968,[16,17] Slack in 1979,[18] Boudart in 1981,[19] Jennings in 1991,[20] and Somorjai *et al.* in 1994.[21]

1.2.4 *Development of ammonia synthesis catalysts in China*

In 1951, A102 catalyst, the first ammonia synthesis catalyst in China, was developed and manufactured by Nanjing Chemical Industry Corporation. A106 and A109 catalysts were developed in 1956 and 1967, respectively, and were widely used in industry, but their activity were low and running temperatures were high.

In the late of 1960s, ammonia plants from chemical fertilizer industry in China emerged like bamboo shoots after a spring rain. It was significant in technology and economy to develop new ammonia synthesis catalysts. In the beginning of 1970s, a project entitled "Chemical Simulation of Biological Nitrogen Fixation" was studied by Lu Jiaxi, Tang Aoqing, Cai Qirui and other famous chemists from Chinese Academy of Sciences and universities, including Zhejiang University of Technology, Fuzhou University, Zhengzhou University and Hubei Institute of Chemistry.[22]

In 1979, Zhejiang University of Technology developed successfully,[23] A110-2 low temperature ammonia synthesis catalysts by adjusting interaction between electronic promoters and structural promoters. This catalyst was the pioneer of Chinese A110 series catalysts. Later, Nanjing Research Institute of Chemical Industry, Fuzhou University, Linqu catalyst plant, Zhengzhou University and Hubei Institute of Chemistry developed A110-1, A110-3, A110-4, A110-5Q (spherical) and A110-6 ammonia synthesis catalysts, which forms the A110 series catalysts and have been most widely used in China since 1980s.[24]

In 1978, ICI patented a Fe–Co catalyst for ammonia synthesis. In 1985, Fuzhou University successfully developed cobalt-containing A201 catalysts.[25] In addition, Nanjing Research Institute of Chemical Industry and Zhengzhou University also developed Fe–Co catalysts for ammonia synthesis. Later, Fuzhou University reduced the cobalt content in A201 catalyst and added CeO_2 to improve its catalytic property. In 1995, A202 catalyst containing cobalt was introduced.

In 1986, Zhejiang University of Technology made an important breakthrough on iron catalyst, invented a novel $Fe_{1-x}O$ based catalyst system.[26−28] In 1992, the first $Fe_{1-x}O$ based catalyst (A301) at low temperatures and pressures was successfully developed, which was superior to the best magnetite-based catalysts in the world. In 1998, they further developed ZA-5 catalyst, and the running temperature was further decreased, which established the technical foundation for low pressure ammonia synthesis process.

The annual production of ammonia is about 1.8×10^8 tons (from FAO), while the annual demand of the catalyst is about $(18-23)\times10^3$ tons in the world.[29] In China, the capacity of ammonia synthesis catalysts is about 7,000 tons, the production is about 5,000–6,000 tons recently. Among these catalysts, about 4,500–5,000 tons are supplied to domestic market and the rest, about 1,000 tons, are exported.

1.2.5 *Development trend of ammonia synthesis catalysts*

It is well known that the conversion of hydrogen and nitrogen per pass is only 20%–30% for the present catalytic ammonia synthesis technology (Table 1.4). Most synthesis gases need to be returned to the reaction system, which increases power consumption. In order to increase conversion per pass, it must increase the outlet ammonia concentration of reactor. Accordingly, it can be seen from Table 1.4 that it is necessary to increase reaction pressure for small and medium scale ammonia plants and Topsøe process, or to reduce the content of inert gas in synthesis gas for Topsøe and Braun processes, or to reduce ammonia concentration in the inlet of converter for small and medium scale ammonia plants and Kellogg process. But all of these operations will add the power consumption or unit gas consumption.

Production scale is continuously expanded in modern ammonia plants. In China, there are a number of small and medium scale ammonia plants, where multiple series of apparatus are used and the operating conditions are high pressures (30 MPa), high space velocity (20,000–30,000 h^{-1}) and high content of inert gas (20%–30%). Although the production capacity of ammonia is increased, production efficiency is low and energy consumption is very high. The high space velocity make reaction far from its equilibrium, but it also has some shortcomings, for example, increasing circulating gas flow and pressure drop, increasing the power consumption of cycling compressor and refrigeration compressor, and reducing the recovery efficiency of reaction heat. Therefore, the operation under high space velocity is not recommended. It will make a breakthrough if ammonia synthesis catalysts are obtained

Table 1.4 Synthetic coefficient of ammonia at present industrial processes

Processes	Small and medium scale ammonia plants	Kellogg	Topsøe	Braun	ICI–AMV
Pressure/MPa	31.38	14.7	26.5	15	10.3
Space velocity/h^{-1}	20,000	10,000	12,000	7,600	4,000
Inlet content of inert gas/%	18	13.6	2	1–2	8.8
Inlet ammonia concentration/%	2	2.17	3.63	4	4.18
Outlet ammonia concentration/%	10–12	12.03	16.0	21	17.18
Net value of ammonia/%	8–10	9.86	12.37	17	13
Synthetic coefficient of ammonia/%	18.2–22.3	20.9	22.4	29.6	25.5

Table 1.5 Catalytic efficiency (φ_{ex}/φ_e) of ZA-5 catalyst at 15 MPa

Temperature/°C	500	475	450	425	400	375	350	325	300
Equilibrium ammonia (φ_e)/%	14.86	18.23	22.31	27.17	32.83	39.20	46.19	53.56	60.84
SV = $3 \times 10^4\,h^{-1}$:									
Outlet ammonia (φ_{ex})/%	14.79	17.36	19.15	18.51	16.68	13.75	10.13	5.92	1.20
Catalytic efficiency (φ_{ex}/φ_e)/%	99.53	95.28	85.84	68.13	50.81	35.01	21.93	11.05	1.97
SV = $1 \times 10^4\,h^{-1}$:									
Outlet ammonia (φ_{ex})/%	—	18.15	21.87	22.50	23.26	20.14	—	—	—
Catalytic efficiency (φ_{ex}/φ_e)/%	—	99.56	98.03	82.81	70.85	51.38	—	—	—

with high activity under high space velocity to enhance synthetic quotient per pass and reduce energy consumption.

For the improvement of synthetic quotient per pass, it is also an effective approach to increase volume of catalyst in order to reduce space velocity such as ICI–AMV and Braun processes.

Nevertheless, either increasing the outlet ammonia concentration or reducing space velocity is confined by the equilibrium ammonia concentration. Where, the catalyst efficiency (φ_{ex}/φ_e) is defined as the ratio of outlet ammonia concentration (φ_{ex}) to equilibrium ammonia concentration (φ_e) under same conditions, which indicates the degree of the reaction close to the equilibrium. The efficiency of the present catalysts used in industry is about 90% at higher temperatures, as shown in Table 1.5. For example, the efficiency of ZA-5 catalyst is about 95% at about 475°C at the space velocity of $3 \times 10^4\,h^{-1}$ and pressure of 15 MPa, which is very close to the equilibrium concentration of ammonia. With low space velocities, the operating temperature can be decreased as the outlet ammonia concentration is close to equilibrium concentration. As shown above, the efficiency of ZA-5 is about 98% at above 450°C and at the space velocity of $1 \times 10^4\,h^{-1}$. Thus, it is impossible to further increase the outlet ammonia concentration under these conditions. As a result, the activity at low temperatures must be increased, since equilibrium ammonia concentration is higher at low temperatures. The outlet ammonia concentration is 16.68% on ZA-5 catalyst at 400°C and with the space velocity of $3 \times 10^4\,h^{-1}$ and pressure of 15 MPa, the equilibrium concentration is 32.83%, and therefore the catalyst efficiency is only 50.8%. If the catalytic efficiency can be increased to more than 95% at 400°C by increasing the catalyst's activity at this temperature, the synthetic quotient per pass could be about 50%.

Obviously, the most effective approach for increasing the synthetic quotient per pass is increasing the catalyst's activity at low temperatures. It is necessary for ammonia synthesis industry to develop the catalysts with higher activities at lower temperatures and pressures. Correspondingly, new process and reactors should be developed based on these novel catalysts.[30]

Since 1980s, ruthenium based catalysts discovered by British Petroleum of UK[31–33] and $Fe_{1-x}O$ based catalyst developed by China had made new progresses on ammonia synthesis catalysts. Three technical routes were developed including the magnetite based (Fe_3O_4) route, $Fe_{1-x}O$ catalysts and Ru catalysts, and have achieved significant progresses, respectively.

1.3 Development of Magnetite (Fe_3O_4) Based Fused Iron Catalysts

1.3.1 *Magnetite (Fe_3O_4) based fused iron catalysts*

Fe_3O_4 is the main component in the magnetite based fused iron catalyst. Its content is about 90 wt % before reduction. The promoters mainly include metal oxides of Al, K, Ca and Mg etc. Magnetite is usually used as the raw material to manufacture the catalyst by fusion method.

Due to the cheapness of raw materials, the simple preparation techniques, the high mechanical strength, the high poison resistance and thermal stability, the fused iron catalysts modified by some special components to increase their activity for ammonia synthesis have been used for nearly a century. Especially, efforts have been centered on changing the kind and amount of the promoters, such as Li, Na, K, Cs, Mg, Ca, Sr, Ba, Ti, Zr, V, Cr, Mo, W, Mn, Ru, Th, Cd, B, Al, Si, La, Ce and rare earth oxides. The studies are carried out much more carefully than for any other catalysts but significant progresses have not been achieved yet. Fused iron catalysts become one of the well-investigated catalysts in the world. Hereinto, the progress has as the following: (1) Adding rare earth oxides into fused iron catalysts[34] mainly cerium oxide, as well as lanthanum oxide, neodymium oxide, and yttrium oxide. (2) Adding cobalt oxide.

Non-fused iron catalysts have been studied earlier. The famous Uhde catalyst was KAl ($Fe(CN)_6$), which was used, to be applied in industry. It was abandoned because of its poor stability, and up to now there are still reports about its modifications. Intermetallic compound and alloy catalysts, such as $LaNi_x$, FeTi, Fe_2Ce and FeZr etc., were also expected to be prospective, but until now they have not been put into practice. In 1970s, the well-known electron donor-acceptor (EDA) catalysts, e.g., phthalocyanine iron-alkali metal, molysite — graphite — potassium and ferrocene-activated carbon-potassium catalyst systems, were found to have the ability to synthesize ammonia under mild conditions in the laboratory. Unfortunately, their activities declined rapidly in the experiments of scale-up. The application of EDA catalysts in industry turned to be a visionary. Therefore, replacement of fused iron catalyst is not an easy thing for a very long time.

1.3.2 *Development of Fe_3O_4 based catalysts containing cobalt*

Fe_3O_4 based catalysts containing cobalt is one of the main progresses for magnetite based fused iron catalysts.

Cobalt is one of the single metal catalysts for ammonia synthesis investigated in the early years. Mittasch reported that 10 metals including Fe, Co, Ni, Ru, Os, Mn, Mo, U, and Ce are active for ammonia synthesis. The activities of metals follow the order of Fe, Os, U, Mo, Ru, Mn and Ce. Ni has the lowest activity, followed by Co. It means that the activity on pure metal cobalt was very poor. In 1967, Artyukh *et al.*[35] investigated doubly promoted fused iron catalysts based on Fe–Co and Fe, and found that the activity of the catalyst containing 15% cobalt is three times higher than that of the catalyst without cobalt, below 400°C. Since then, adding cobalt to fused iron catalysts has attracted considerable attention. In the early 1970s, Zhejiang

College of Chemical Engineering investigated fused iron catalysts containing cobalt oxide and found that the activity increased significantly. Work of ICI in UK was noticeable for cobalt containing catalysts, and patented the Fe–Co catalysts.

Assuming that the activity of catalyst without cobalt is 100, the activities of Fe–Co catalysts at 40 bars at different temperatures would be as follows: 134 at 450°C, 144 at 400°C, and 160 at 350°C, respectively.

ICI 74-1 catalyst which contains cobalt has been successfully developed, and applied in the low pressure ICI–AMV process by ICI.[36] The catalyst used in this process is ICI 74-1. The diameter of the converter is 2.9 m, with the height of 24 m. The volume of the catalysts is 96 m^3 (250 tons in weight) in total, which is separated into three catalyst beds. The operation conditions are: Pressure of 10 MPa, temperature of 450°C, space velocity of 5,00 h^{-1}, net value of ammonia (10%–11%) and pressure drop of 0.4 MPa. The content of inert gases such as methane is limited to about 7%. The reduction temperature at which water is produced is 370°C. The highest reduction temperature is about 480°C. In Hainan Fudao Fertilizer Plant of China, the volume of the catalyst of the converter is increased to 122.4 m^3 in Ude–ICI–AMV process.

UCI in USA introduced 73-03-2 spherical catalyst containing cobalt. The catalyst is prepared *via* powder sintering method. The process technology and devices was complex, and it was hard to produce catalysts with small particles. The particles of the catalysts are so large that the advantages of small particles which have high activities are completely lost.

In 1985, Fuzhou University[37] in China successfully developed A201 Fe–Co catalyst for ammonia synthesis. Compared with A110-3 without cobalt, A201 increases net ammonia concentration by about 0.5%–1% under the same conditions. In 1995, they added rare earth oxide and reduced cobalt content, which is called as A202 catalyst. Moreover, the Research Institute of Nanjing Chemical Industry Company and Zhengzhou University developed Fe–Co catalysts, and applied in industry.

Cobalt oxide can be reduced to metallic cobalt by hydrogen, but the activity of cobalt self is poor for ammonia synthesis. Cobalt oxide forms solid solution with Fe_3O_4 in the Fe_3O_4-based catalysts with the form of $CoFe_2O_4$.[38] Cobalt distributes uniformly in the catalysts, simultaneously, $CoFe_2O_4$ is reduced readily. All the above factors lead to changes in the macroscopic geometry structure of the catalyst, especially the crystal size is small after reduction.[39] As a result, the activity of the catalyst is increased at low-temperatures and low-pressures, but mechanical strength of the catalysts decreases a little bit.[40]

At present, most manufacturers can provide A110-2 catalysts. A110-1, A110-2, A202, A301 and ZA-5 catalysts are most widely applied in China.

1.4 Discovery of Wüstite Based Fused Iron Catalysts

1.4.1 *Search for new breakthrough of the technique*

In the past century, it was commonly believed that a catalyst has the best activity when its chemical composition and crystal structure of the precursor are most similar to those of magnetite. The relationship between the activity and the ratio

(Fe^{2+}/Fe^{3+}) is as a volcano type curve, which seems to be an unquestioned classical conclusion. For several decades researchers have developed new catalysts, while rigidly adhered to this conclusion, and never changed the precursor composition (Fe_3O_4), except the promoter components and their amounts. Thus almost all elements in the periodic table which might be used as promoter have been investigated widely, while the effect of iron precursor was neglected. Also, only minor improvement has been achieved during this period. During 1970s and 1980s, Strel'tsov *et al.* and Artyukh *et al.*[41,42] studied the effect of the Fe (II) content in precursor on the performances of catalysts. They found that the activity of the catalyst with 3.5%wt of $A1_2O_3$ as the only promoter increased, with increasing of FeO content from 52.8% to 73.4%, and the catalysts showed a slight decrease in their activity from 41.8% to 52.8%. However, no further research was reported.

Till 1960s and 1970s, classical fused iron catalyst was basically the finalized design. The industrial catalyst presently used is not basically different from that developed about a century ago.[43] Table 1.6 represents the development history and status of ammonia synthesis catalysts. From Table 1.6, it can be seen that all the catalyst precursors are Fe_3O_4 without exception from the first iron catalyst in 1913 to A202 catalyst in 1994. From A106 in 1950s to A202 in 1990s, the activity was increased only by 2%–3% for more than 40 years. It was found very difficult to enhance the activity by modifying the classical fused iron catalyst. Therefore, it is necessary to seek new technique breakthrough.

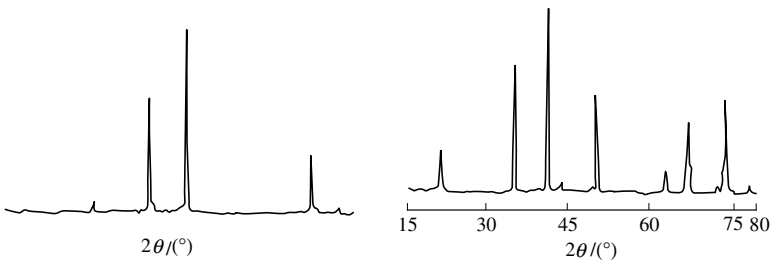
Since this catalyst was considered well consolidated and no special improvement was still expected, researchers began to search for non-iron and noble metal catalyst. Ruthenium catalyst was discovered under such background.[44–46] Although Ru/C catalyst prepared by supporting ruthenium carbonyl compounds on graphitized carbon shows rather high activity, the manufacturing cost of the catalyst is too high, to compare with the fused iron catalysts. Although it has been more than 10 years since 1992 when the catalyst was developed successfully; there are only 10 industrial plants using the Ru catalyst in all over the world. Further researches need to be done for wide application of the Ru catalyst in industry.

In 1986, Liu *et al.* found that the iron catalyst with wüstite as the precursor has extremely high ammonia synthesis activity and rapid reduction rate, which led to the invention of wüstite ($Fe_{1-x}O$) based catalyst for ammonia synthesis.[47] The relationship between the activity and the iron oxides (Fe_3O_4, FeO and Fe_2O_3) and their mixtures in the precursor were studied systematically, and a hump type curve was found between the activity and the ratio (Fe^{2+}/Fe^{3+}). It was speculated that the monophase of iron oxide phase in the precursor is an essential condition for high activity of the catalyst and a uniform distribution of iron oxide phase and promoters is a key to make a better performance of catalyst. The "hump type" curve was interpreted by the ratio of phase compositions in the precursor, that is, the activity change of the fused iron catalyst depends essentially on the molecule ratio of different iron oxides but not on the atomic ratio of Fe^{2+} and Fe^{3+}, or Fe^{2+}/Fe^{3+}, in the precursor under certain promoters. Thus we found that $Fe_{1-x}O$ based catalyst with wüstite phase structure ($Fe_{1-x}O$, $0.04 < x < 0.10$) for ammonia synthesis has the highest activity among all the fused iron catalysts for ammonia synthesis.

Table 1.6 History and development of ammonia synthesis catalysts

			Chemical component/%wt		Activity[a]/%NH_3			
Country	Date	Type	Precursor	Promoters	400°C	425°C	450°C	475°C
Fe_3O_4 based catalyst								
Germany	1913	BASF	Fe_3O_4	$Al_2O_3 + K_2O$	—	—	—	—
China	1958	A106	Fe_3O_4	$Al_2O_3 + K_2O + CaO$	11.46	13.46	15.59	15.76
USA	1960s	C73-1	Fe_3O_4	$Al_2O_3 + K_2O + CaO$	11.86	14.39	15.73	15.76
Danmark	1964	KM-I(II)	Fe_3O_4	$Al_2O_3 + K_2O + CaO$	12.21	14.84	16.12	15.89
UK	1966	ICI35-4	Fe_3O_4	$Al_2O_3 + K_2O + CaO + MgO$	—	—	—	—
Danmark	1966	KM-VII	Fe_3O_4	$Al_2O_3 + K_2O + CaO + MgO$	—	—	—	—
China	1969	A109	Fe_3O_4	$Al_2O_3 + K_2O + CaO + MgO$	11.75	14.39	16.39	16.00
China	1979	A110-2	Fe_3O_4	$Al_2O_3 + K_2O + CaO$	12.80	15.34	16.45	16.09
UK	1979	ICI74-1	Fe_3O_4	$Al_2O_3 + K_2O + CaO + CoO$	13.73	16.06	16.99	16.31
China	1984	A201	Fe_3O_4	$Al_2O_3 + K_2O + CaO + CoO$	12.77	14.67	15.69	—
China	1994	A202	Fe_3O_4	$Al_2O_3 + K_2O + CaO + CoO + Ce_2O_3$	13.60	15.14	16.4	—
$Fe_{1-x}O$ based catalyst								
China	1992	A301	$Fe_{1-x}O$	$Al_2O_3 + K_2O + CaO + \cdots$	15.20	17.59	18.12	16.97
China	1998	ZA-5	$Fe_{1-x}O$	$Al_2O_3 + K_2O + CaO + \cdots$	16.68	18.50	19.15	17.36
Ru based catalyst								
UK/Japan	1992	KAAP	Ru/AC	Ba–K				

[a]Activity testing under pressure of 15 MPa and space velocity of $3 \times 10^4\,h^{-1}$ with 75% H_2 and 25% N_2.



(a) Wüstite catalyst (b) Traditional Fe_3O_4 catalyst

Fig. 1.10 XRD pattern of unreduced catalyst

This invention broke through the conventional theory that fused iron catalyst with Fe_3O_4 as precursor has the best activity, and found a new way to increase the activity of the fused iron catalyst. It was a sign of major breakthrough for the development of fused iron catalysts in the past 80 years, and initiated a new development stage. Meanwhile, the activity of ammonia synthesis catalyst achieved a solid progress, and this breakthrough provided a new chance for the development of low-temperature ammonia synthesis catalyst. The discovery inspired new speciation and chances for the development of the fused iron catalysts. This result attracted extensive concerns and great interests of researchers in this area.[48−50]

X-ray diffraction analysis of the $Fe_{1-x}O$ catalyst before reduction shows that only wüstite is present in the XRD spectrum which shows only three $Fe_{l-x}O$ peaks ($I/I_0 = 36$, 100 and 38, $2\theta = 42.18°$, 49.10°, and 71.90°, respectively) as illustrated in Fig. 1.10(a), while the Fe_3O_4 phase disappears completely, though it is expected to exists according to chemistry when $Fe^{2+}/Fe^{3+} < \infty$. It is due to the fact that Fe^{3+} in the samples does not compose an independent magnetite phase, but dissolves into the wüstite phase non-stoichiometrically. This indicates that, when Fe^{2+}/Fe^{3+} is higher than about 3.5, iron oxides transfer to the non-stoichiometric ones with iron cation defects, namely wüstite phase expressed as $Fe_{1-x}O$, where x is the defect concentrations of the Fe^{2+} iron cations. From a solid-chemistry viewpoint, $Fe_{l-x}O$ is a solid solution of Fe_2O_3 and FeO, therefore x value may be calculated by chemical analysis.

The results mentioned above are in agreement with the Mössbauer spectroscopy of these samples shown in Fig. 1.11(a). The Mössbauer spectroscopy of magnetite based catalyst consists of two typical hexa-finger peaks of Fe_30_4 as in Fig. 1.11(b), and that of $Fe_{1-x}O$ catalyst consists of one typical dissymmetrical double peak of $Fe_{l-x}O$ as Fig. 1.11(a) presents.

Although the precursor of wüstite based and magnetite based catalyst are different, their active states are the same i.e., α-Fe as shown in Fig. 1.12.

The chemical composition, crystal phases and some structure parameters of $Fe_{1-x}O$ catalyst and magnetite based catalyst are listed in Tables 1.7–1.9.

Table 1.10 shows a comparison between the wüstite based and the magnetite based catalyst. It is shown that the wüstite ($Fe_{1-x}O$) based catalyst is a new generation of ammonia synthesis catalyst that is completely different from the magnetite (Fe_3O_4) based catalyst (including Fe–Co catalyst) in the chemical composition, crystal structure, physical–chemical property, and producing principle etc.

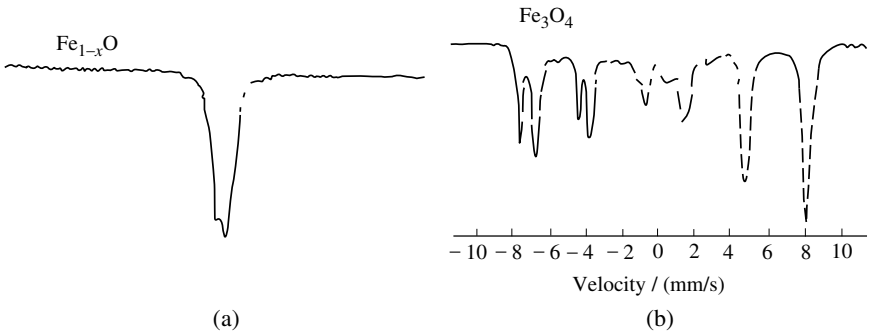


Fig. 1.11 Mössbauer spectrum of unreduced catalyst

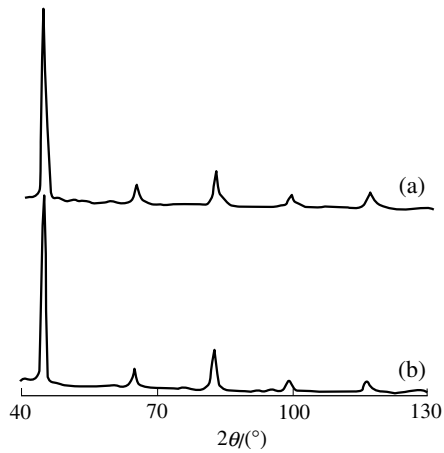


Fig. 1.12 XRD pattern of reduced catalyst. (a) FeO-based; (b) Fe_3O_4-based

Table 1.7 Chemical composition of catalysts for ammonia synthesis

Catalysts	FeO/%	Fe_2O_3/%	Fe^{2+}/Fe^{3+}	Total Fe/%
A301 ($Fe_{1-x}O$ based)	74.4–84.6	10.4–20.6	4–9	71–73
A110-2 (Fe_3O_4 based)	29.5–33.5	61.7–65.5	0.5–0.7	67–69

Therefore, it is not correct to say that the $Fe_{1-x}O$ based catalyst is the catalyst with high ratio of Fe^{2+}/Fe^{3+}, or the catalyst is only prepared from different raw material. $Fe_{1-x}O$ based catalyst is specifically defined as a new kind of catalyst, in which there is only one iron oxide — $Fe_{1-x}O$, and only one crystal structure — wüstite in the precursor. Liu Huazhang *et al.*[51] pointed out that high activity can only be obtained when only the wüstite phase is present in the catalyst, while, when wüstite and magnetite are present together, the catalyst always shows a low activity. Lendzion-Bieluñ *et al.*[49] obtained different results by using the catalyst with the high ratio of Fe^{2+}/Fe^{3+} as mixed FeO with Fe_3O_4, and mistook it as the $Fe_{1-x}O$

Table 1.8 Crystal structure of catalysts for ammonia synthesis

Catalyst	Crystal phase		Cell constant/nm		Particle size[a]/nm	
	Unreduced	Reduced	Unreduced	Reduced	Unreduced	Reduced
A301 ($Fe_{1-x}O$ based)	$Fe_{1-x}O$	α-Fe	0.4312	0.2865	99.5 ± 25.2	20.4
A110-2 (Fe_3O_4 based)	$Fe_3O_4 + FeO$ (a few)	α-Fe	0.8396	0.2867	72.1 ± 4.2	20.1

[a]According to Scherrer equation

Table 1.9 Texture parameters of prereduced catalyst

Catalyst	Density/g·cm^{-3}			Surface area $m^2 \cdot g^{-1}$	Pore structure			
	Packing density[a]	Pellet density	True density		Pore volume/ $cm^3 \cdot g^{-1}$	Porosity	Average pore size/nm	Void ratio[a]
A301R ($Fe_{1-x}O$ based)	2.34–2.38	4.32	6.85	13.34	0.0855	0.3693	12.85	0.4530
A110-2R (Fe_3O_4 based)	2.15–2.25	3.60	7.40	13.31	0.1089	0.4642	16.36	0.4537

[a]Particle size of 2.2–6.7 mm.

Table 1.10 Comparison of wüstite based and magnetite based catalyst

Item	Magnetite based catalyst		Wüstite based catalyst
	A110 type	Fe–Co type	(A301, ZA-5 type)
Chemical component			
Molecular formula	Fe_3O_4		FeO
Structure	Fe_3O_4		$Fe_{1-x}O$
Theoretic oxygen content/%	27.6		About 22.3
Fe^{2+}/Fe^{3+} ratio	0.5–0.6		3–20
Promoters	Al_2O_3, K_2O, CaO, ...	Al_2O_3, K_2O, CaO, CoO, ...	Al_2O_3, K_2O, CaO, ...
Crystal structure			
Crystal phase	Magnetite		Wüstite
Crystal lattice	Spinel (cubic)		Halite (cubic)
Crystal lattice constant/nm	0.8396		0.4313
Physical properties			
Magnetism	Ferromagnetism		Non-ferromagnetism
Melting point/°C	1597 (Fe_3O_4)		1377 (FeO)
Density/g/ml	5.14 (Fe_3O_4)		5.7 (FeO)
Fusing heat/KJ/mol	139600 (Fe_3O_4)		30930 (FeO)
Preparation			
Production principle	Physical fusion		Chemical reaction
Production method	Fusion		Fusion
Production cost	Low	Special high	Low
Catalytic properties			
Reduction performance	Easy	Easier	Easiest
Reduction temperature (fast)/°C	530°C	516°C	480°C
Reduction temperature (final)/°C	619°C	569°C	516°C
Reduction rate (relative)	1.0	1.6	4.3
Active temperature/°C	470 ± 5	460 ± 5	440 ± 5
Use temperature range/°C	360–520	350–500	300–500
Activity/NH_3% (relative)	15 (100)	16 (106.7)	18.5 (123.3)
Resisting heat	Good	Good	Good
Ability of Anti-poisoning	Good	—	Good
Mechanical strength	High (abrasion 1.5%)	Lower	Higher (abrasion 0.5 %)

based catalyst. Furthermore, in fact, the main raw material for the preparation of $Fe_{1-x}O$ based catalyst is still magnetite. The presence of the only wüstite is the precondition of the $Fe_{1-x}O$ based catalyst with high activity.

1.4.2 *Activity of wüstite ($Fe_{1-x}O$) based catalysts*

The effects of temperature, pressure and space velocity on the activity of $Fe_{1-x}O$ based catalyst and magnetite based catalyst are shown in Figs. 1.13–1.15.

From Fig. 1.13, it can be seen that the activity of $Fe_{1-x}O$ based catalyst is much higher than those of the magnetite based catalysts. For example, ammonia concentration reached about 19.15% over the $Fe_{1-x}O$ based catalyst under 15 MPa,

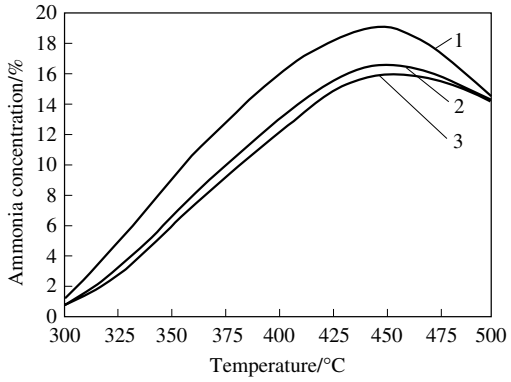


Fig. 1.13 Effect of temperature on activity

1-$Fe_{1-x}O$ based catalysts; 2-Fe_3O_4-CoO based catalysts; 3-Fe_3O_4 based catalysts ($p = 15$ MPa; $S_v = 3 \times 10^4\,h^{-1}$).

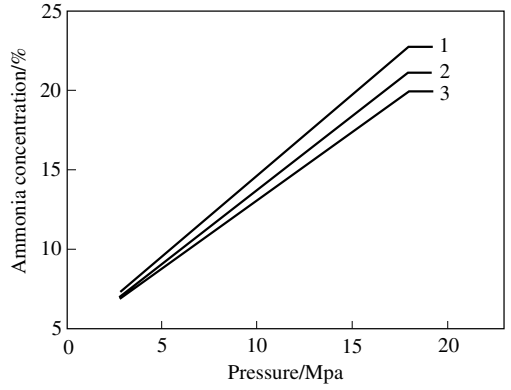


Fig. 1.14 Effect of pressure on activity

1-$Fe_{1-x}O$ based catalysts; 2-Fe_3O_4-CoO based catalysts; 3-Fe_3O_4 based catalysts ($t = 425°C$; $S_v = 2 \times 10^4\,h^{-1}$).

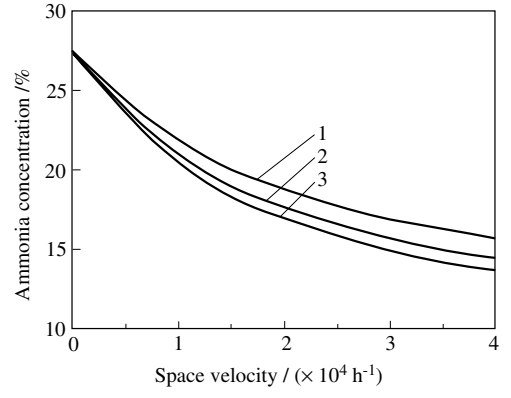


Fig. 1.15 Effect of space velocity on activity ($p = 15$ MPa, $T = 425°C$)

1-$Fe_{1-x}O$ based catalysts; 2-Fe_3O_4-CoO based catalysts; 3-Fe_3O_4 based catalysts

Table 1.11 Kinetics parameters of different catalysts

Temperature/ °C	$k_T/(\mathrm{MPa}^{0.5}\cdot\mathrm{s}^{-1})$			$K_0\times10^{-13}/(\mathrm{MPa}^{0.5}\cdot\mathrm{s}^{-1})$			$E_r/(\mathrm{kJ}\cdot\mathrm{mol}^{-1})$		
	ZA-5	ICI74-1	A110-2	ZA-5	ICI74-1	A110-2	ZA-5	ICI74-1	A110-2
475	50.58	41.27	37.19						
450	22.98	17.21	14.72						
425	8.73	6.340	5.643						
				0.4973	2.588	5.923	159.03	168.38	173.85
400	3.06	2.202	1.838						
375	0.9518	0.6207	0.4790						
350	0.2182	0.1262	0.0893						

Note: Temkin–Pyzhev equation: $r = k_1 f_{N2}(f_{H2}^{1.5}/f_{NH3})^{1-\alpha} - k_2(f_{NH3}/f_{H2}^{1.5})^{\alpha}(\alpha = 0.5)$, $k_T = k_0 e^{-Er/RT}$.

Table 1.12 Activity of $Fe_{1-x}O$ based catalyst at low pressure ($H_2/N_2 = 3$)

Pressure/ MPa	Temperature/°C	Space velocity/h^{-1}	Activity/ $\%NH_3$	Catalytic efficiency[a]/%
3.0	375	3,000	8.87	65.7
	375	10,000	6.70	49.6
	400	3,000	8.81	87.1
	400	6,000	7.94	78.5
	400	10,000	7.20	71.1
5.0	375	4,000	12.65	63.9
	400	4,000	13.08	85.1
	425	5,000	11.67	98.4
7.0	400	10,000	17.60	88.9
	425	5,000	15.09	96.7
8.5	425	5,000	17.38	96.0
10.0	425	5,000	19.23	94.1

[a]Catalytic efficiency equals to the ratio of the concentration in outlet of reactor and equilibrium concentration of ammonia at the same conditions.

$3\times10^4\,h^{-1}$ and 425°C, while only 15.47% over the magnetite based catalyst under the same conditions. This means that the outlet ammonia concentration of $Fe_{1-x}O$ based catalyst is about higher by 4%, and the relative activity is 24.2% higher than those of the magnetite based catalysts at the same temperature. The reaction rate calculated by these data is 1.55 times as high as those of the magnetite based catalysts at 425°C as shown in Table 1.11. This difference increases with the decrease of temperature, for example, the reaction rate is 2.4 times as high as those of the magnetite based catalysts at 350°C.

In the temperature range of 400°C–460°C, typical of a modern low-pressure ammonia synthesis unit, the reaction rate of $Fe_{1-x}O$ based catalyst is, on the average, 70% higher than that of the magnetite-based catalyst.[48]

Table 1.12 lists the activity of $Fe_{1-x}O$ based catalyst at low pressures. It is seen from Table 1.12 that $Fe_{1-x}O$ based catalyst has very high activity at low-pressures and low-temperatures. For example, the ammonia concentration is 8.87% at pressure of 3 MPa and temperature of 375°C.

In addition, it is seen from Fig.1.13 that the activity of $Fe_{1-x}O$ based catalyst at 400°C equals to the highest activity of magnetite based catalyst at 455°C, i.e.,

the active temperature of $Fe_{1-x}O$ based catalyst is 55°C lower than those of the magnetite based catalysts under the same pressure, same space velocity and same outlet ammonia concentration. Therefore, $Fe_{1-x}O$ based catalyst is an excellent low-temperature and low-pressure catalyst for ammonia synthesis.

The activity of $Fe_{1-x}O$ based catalyst at different pressures is shown in Fig. 1.14. It can be seen that the activity of $Fe_{1-x}O$ based catalyst is the highest at both high and low pressures. This kind of catalyst could be used in a wide range of operating pressures. The reaction pressure may be decreased by more than 3.5 MPa as compared to the magnetite based catalyst with the same ammonia yield.

Effect of space velocity on the activity of the $Fe_{1-x}O$ based catalyst is shown in Fig. 1.15. With the increase of space velocity, the ammonia concentration decreased gradually on both the $Fe_{1-x}O$ based catalyst and the magnetite based catalyst. However, the ammonia concentration of the $Fe_{1-x}O$ based catalyst is higher than that of the magnetite based catalyst under the same space velocities. When the ammonia concentration is 18%, the space velocity of magnetite based catalyst needed is $1.75 \times 10^4\,h^{-1}$, while the space velocity of $Fe_{1-x}O$ based catalyst is $3.25 \times 10^4\,h^{-1}$, which is 85% higher than that of the former. This is advantageous for ammonia synthesis producer to increase the productivity.

The above results showed that the $Fe_{1-x}O$ based catalyst is an ideal low-temperature and low-pressure catalyst that has the highest activity among all the fused iron catalysts for ammonia synthesis in the world.

1.4.3 *Reduction of $Fe_{1-x}O$ based catalysts*

The reduction reaction of $Fe_{1-x}O$ based catalyst is shown as follows:

$$Fe_{1-x}O + H_2 = (1 - x)Fe + H_2O. \tag{1.41}$$

The reduction reactions of magnetite based catalyst are:

$$Fe_3O_4 + 4H_2 = 3Fe{+}4H_2O. \tag{1.42}$$

$$FeO + H_2 = Fe + H_2O. \tag{1.43}$$

The theoretical weight (oxygen) loss during the reduction from iron oxides to metallic iron, namely mass fraction, could be calculated by the Eqs. (1.41)–(1.43) based on the content of iron oxides in the catalyst precursor. The actual weight (oxygen) loss of the sample could be obtained from thermogravimetry (TG-DTG) as shown in Fig. 1.16 under the reduction conditions. The reduction degree R is defined as the ratio of the actual weight (oxygen) loss to the theoretical weight (oxygen) loss. TG-DTG curves of $Fe_{1-x}O$ based catalyst and magnetite based catalyst during reduction by H_2 are shown in Fig. 1.16. Isothermal reduction curve at 450°C and reduction curve in reaction equipment are shown in Figs. 1.17 and 1.18, respectively. Some characteristic values are listed in Table 1.13.

TPR patterns of the $Fe_{1-x}O$ based catalyst and the magnetite based catalyst are shown in Fig. 1.19.[48] It can be seen that the reduction peak of wüstite catalyst is shifted towards lower temperatures, thus confirming the advantage of this catalyst as to shorter reduction period in the industrial reactor. This result is in agreement with the better reducibility of wüstite with respect to magnetite.[52]

From Figs. 1.16–1.18 and Table 1.13, the following characteristics might be obtained:

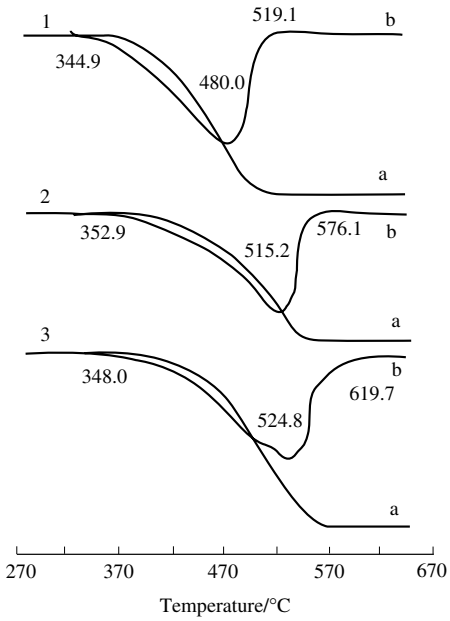


Fig. 1.16 TG(a)–DTG(b) curves of catalysts

1-$Fe_{1-x}O$-based catalyst; 2-Fe_3O_4-CoO-based catalyst, 3-Conventional Fe_3O_4-based catalyst (Instrument: TGA-41; catalyst particle sizes: 0.034–0.044 mm; H_2 flow rate: 175.

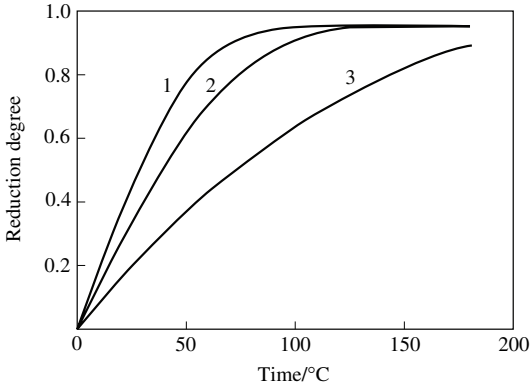


Fig. 1.17 Isothermal reduction curves in 450°C (experimental conditions as Fig. 1.16)

1-$Fe_{1-x}O$-based catalyst; 2-Fe_3O_4-CoO-based catalyst; 3-Conventional Fe_3O_4-based catalyst.

(1) The initial reduction temperatures of the $Fe_{1-x}O$-based and magnetite based catalysts are almost same, and 344.9°C and 348°C, respectively.
(2) The terminal reduction temperature of $Fe_{1-x}O$-based catalyst is 490°C, which is 147°C lower than 637°C of the magnetite based catalyst, indicating that $Fe_{1-x}O$-based catalyst has a much lower reduction temperature. The reduction degrees of $Fe_{1-x}O$ based catalyst and the magnetite based catalyst are 98.89%

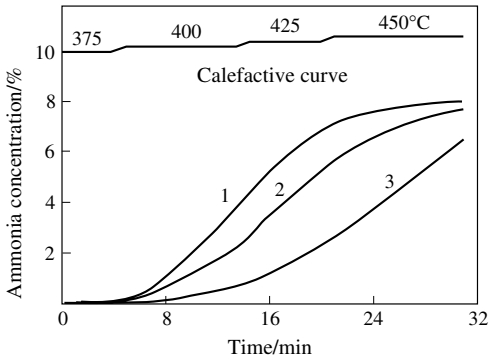


Fig. 1.18 Reduction curve of the catalysts in the reaction equipment
1-$Fe_{1-x}O$-based catalyst; 2-Fe_3O_4-CoO-based catalyst; 3-Conventional Fe_3O_4-based catalyst (Experimental conditions, 5 MPa, 30,000 h^{-1})

Table 1.13 Characteristic values of catalysts by TG-DTG thermo gravimetric analysis

Catalysts	T_{in}/ °C	T_f/ °C	T_m/ °C	D_f/ %	$D_{85\%}$/ min	WL (O_2)/ %	W(H_2O)/ (kg/t)
$Fe_{1-x}O$-based catalyst	330.0	490.0	434.0	98.89	34	20.55	231.2
Fe_3O_4–CoO-based catalyst	352.9	576.1	515.2	97.88	69	25.33	285.0
Fe_3O_4–based catalyst	366.0	637.0	534.6	95.48	153	26.03	292.8

T_{in} = initial temperature; T_f = final temperature; T_m = temperature with the highest reduction rate; D_f = final reduction degree; $D_{85\%}$ = required time reached 85% reduction degree; WL (O_2) = weight loss of samples; W (H_2O) = formed H_2O.

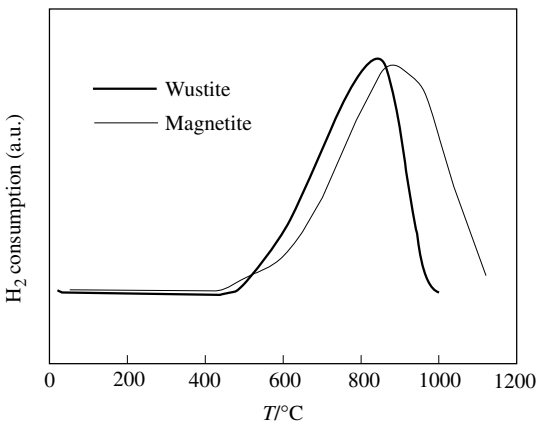


Fig. 1.19 TPR patterns of wüstite- and magnetite-based catalysts

and 95.48%, respectively, at their terminal reduction temperatures, further indicating that the $Fe_{1-x}O$-based catalyst is much easier to be reduced than the magnetite based catalyst.

(3) The temperature, at which the fastest reduction rate is obtained, for $Fe_{1-x}O$-based catalyst is 434°C, which is about 100°C lower than that of the magnetite based catalyst.

(4) The reduction rate of the $Fe_{1-x}O$-based catalyst is 4.5 times higher than that of the magnetite based catalyst.

(5) The reduction process of the magnetite based catalyst has a long induction period (as shown in Figs. 1.18 and 1.19), before reaching a stable stage. The reduction process of the $Fe_{1-x}O$-based catalyst did not have such a distinct induction period, and reached the stable stage quickly. Considering such features, the reduction process of the $Fe_{1-x}O$-based catalyst may step directly into the stable stage, without the need of the initial period as the magnetite based catalyst usually needs during the industrial reduction process.

In summary, the $Fe_{1-x}O$-based catalyst is novel and easily reduced catalyst that exhibits faster reduction rate, lower reduction temperature and easier to be reduced thoroughly as compared to the magnetite based catalyst. The reasons may be due to the high concentration of defects of iron ions in the wüstite structure. Meanwhile, the oxygen content of $Fe_{1-x}O$ (if $x = 0.05$, the oxygen content is 23.17 wt%) accounts to only 83.8% of the amount contained in the Fe_3O_4 (27.64%). In other words, Fe_3O_4 needs to remove additional 19.3% oxygen compared to $Fe_{1-x}O$ ($x = 0.05$).

Figure 1.20 compares the thermal-stability of three catalysts. It is found that the activity of $Fe_{1-x}O$-based catalyst almost remains the same following operation at 500°C for 20 h, indicating that the $Fe_{1-x}O$-based catalyst exhibits similar thermal stability as the magnetite based catalysts.

As for the resistance to deactivation, after the standard sintering treatment (16 h at 600°C in synthesis gas), the percentages of the original reaction rate at 430°C retained by the two catalysts are as follows: A301 catalyst is 78%, magnetite-based

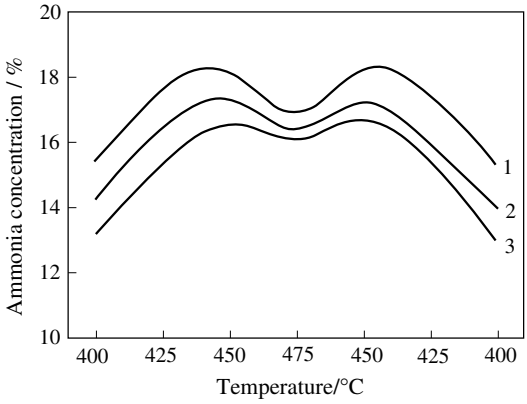


Fig. 1.20 Comparison of thermal stability of three catalysts (at 500°C for 20 h)

1. $Fe_{1-x}O$-based catalyst; 2. Fe_3O_4-CoO-based catalysts; 3. Conventional Fe_3O_4-based catalyst.

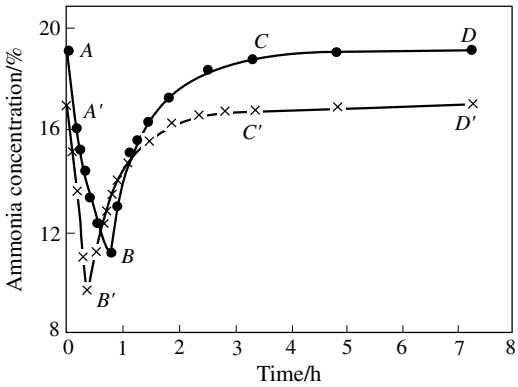


Fig. 1.21 Comparison of poisoning-resistant capability of catalysts. • $Fe_{1-x}O$-based catalyst (ZA-5), × conventional Fe_3O_4-based catalyst (A110-2)

Measurement conditions: 15 MPa; 450°C; 30,000 h^{-1}; Concentration of poison (CO): 500 $ml \cdot m^{-3}$.

catalyst is 80%. Therefore, the two catalysts do not differ appreciably for the resistance to deactivation.[48]

The effect of carbon monoxide on the activities of wüstite and magnetite-based catalyst is shown in Fig. 1.21. When carbon monoxide is introduced into reaction system, the drop of activity for wüstite catalyst is less than that of magnetite-based catalyst (Fig. 1.21, AB section). Once carbon monoxide is removed from reaction system, wüstite catalyst recovers its activity more quickly than that of magnetite-based catalyst (Fig. 1.21, BC section). It can be concluded that the sensitivity of wüstite-based catalyst to CO poisoning is lower than magnetite-based catalyst.

Another characteristic of the $Fe_{1-x}O$-based catalyst is its higher mechanical strength. The crushing strength of ammonia synthesis catalysts is not usually measured, as it is always high enough for the current requirement. The abrasion resistance must be as high as possible, in order to avoid dust formation during reactor loading. Under the same conditions, the abrasion loss of the magnetite based catalyst is about 1.5%, while $Fe_{1-x}O$-based catalyst is only 0.5%. It was reported[48] that the abrasion loss was measured for both catalysts, using the ASTM standard method D4058-96. The following values of fine particles formed during the standard abrasion treatment were found: Catalyst A301 is 0.7%, magnetite catalyst is 1.0%. So, catalyst A301 shows a higher abrasion resistance.

1.4.4 *Technical characteristics of wüstite-based catalysts*

The basic technical characteristics of the wüstite-based catalyst (A301 and ZA-5) for ammonia synthesis are high activity at low-temperature, and easy reduction. The following results could be obtained by comparison with the magnetite-based catalyst under the same conditions.

(1) **Easy reduction.** Its intrinsic reduction rate is 4.5 times that of the magnetite-based catalyst. Reduction temperature of wüstite-based catalyst is lower by about 80°C–100°C than that of the magnetite-based catalyst, and the terminative

reduction temperature is about 475°C–480°C. In the reduction process, the water is formed quickly accompanied by large quantities of ammonia formation. It is necessary to control its reduction rate and prevent its disproportionation reaction in application at present ammonia synthesis unit.

(2) **Low temperature.** Under the same conditions, the active temperature of the $Fe_{1-x}O$-based catalyst is 15°C–30°C lower than that of the magnetite-based catalyst. The initial active temperature is about 225°C–250°C. The operating temperature range is about 300°C–500°C.

(3) **High activity.** The wüstite-based catalyst has the highest activity among all the fused iron catalysts for ammonia synthesis, and is competitive with Ru/C catalysts. Ammonia concentration of the outlet of reactor reaches up to 19.15% at space velocity of $3 \times 10^4\,h^{-1}$, pressure of 15 MPa and temperature of 425°C, which is 3%–4% higher, and relative activity is about 36% higher, and in the temperature range of 400°C–460°C, typical of a modern low-pressure ammonia synthesis unit, the reaction rate of wüstite-based catalyst is, on the average, 70%–90% higher than that of the magnetite-based catalyst.

Table 1.14 presents comparison of the activity between wüstite-based catalyst (A301) and Ru-based catalyst. It is seen from Table 1.14, that ammonia concentrations in the outlet of reactor of A301 catalyst are the same as Ru-based catalyst under same pressures, temperatures and similar space velocities.

Figure 1.22 illustrates comparison of the activity of catalyst A301 and the best Ru/AC catalyst.[48] It can be seen from Fig. 1.22 that they are virtually identical, except for activities at high space velocities, where the lower sensitivity of Ru to ammonia plays an important role in this difference. However, it should be pointed out that, to achieve the highest activity, the Ru/AC catalyst requires a H_2/N_2 feeding ratio of 1.0–1.5.[54] Moreover, under ammonia synthesis conditions, support degradation *via* Ru-catalyzed methanation sometimes accompanies Ru/AC catalyst, if the carbon support is not properly designed. So, catalyst A301 appears to be competitive with Ru/AC, and the related choice should be made on the basis of the specific plant characteristics and operation conditions.

Table 1.14 Comparison of the activity of wüstite-based and Ru-based catalyst

Catalyst	Pressure/MPa	Temperature/°C	Space velocity/h^{-1}	$\Phi_{NH3,\,out}$/%
Ba–La–K–Ru/AC[53]	5.0	420	3,000	12.5
	6.8	420	6,000	14.6
K–Ba–Ru/AC	5.0	400	30,000	8.03
	7.0	400	20,620	15.49
	10.0	400	11,700	23.70
	15.0	425	30,000	23.31
A301 (Wüstite)	5.0	400	4,000	13.08
	7.0	425	20,000	11.98
	10.0	425	5,000	19.23
	15.0	425	10,000	23.42

$\Phi_{NH3,\,out}$ — The ammonia concentration in outlet of reactor

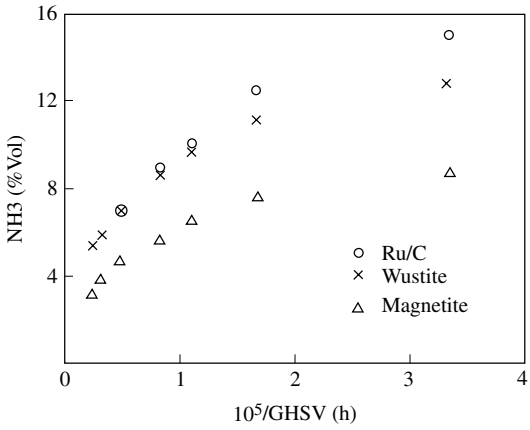


Fig. 1.22 Conversion curves of wüstite-, magnetite- and Ru/C-based catalysts (100 bar, 430°C, H_2/N_2 is three for the two Fe catalysts, but 1.5 for Ru/C)

(4) **High heat-resistant, high poisoning-resistant and high mechanical strength.** The character in industrial use is that the operating temperature fluctuates a little after the catalyst is poisoned temporarily by poisons containing oxygen but the activity recovers rapidly. The abrasion resistance of wüstite-based catalyst measured using the ASTM standard method D4058-96 is the highest among all fused iron catalysts.

(5) **Without noble metals in the composition of the catalyst.** The production cost of wüstite catalyst is much lower than that of cobalt-containing magnetite-based catalyst and Ru/AC catalysts.

In addition, the energy consumption is low for the production and reduction of the $Fe_{1-x}O$-based catalyst. With comparison of the magnetite-based catalyst, since melting point and melt heat of FeO is lower than those of Fe_3O_4, the electric power consumption can be reduced by 25%–30% for the production of catalyst. The heat required for reduction reaction (endothermic) is reduced by 53%, and hydrogen consumption and amount of formed water is decreased by 19.3% and 19.7%, respectively (Table 1.15).

Thus it can be concluded that $Fe_{1-x}O$-based catalyst is currently the most active and advanced catalyst with low cost in the world, and its discovery has significant industrial value.

Table 1.15 Characteristic parameters of wüstite- and magnetite-based catalysts during preparation and reduction

	Preparation process		Reduction process		
Catalyst	Melting point/°C	Melting heat/(MJ/t)	Reaction heat/(MJ/t)	Hydrogen consumption/ (m^3 H_2/t)	Formed water/(kg/t)
Fe_3O_4	1,597	602.88	785.1	387.0	292.5
FeO	1,377	430.48	513.1	324.4	244.3
Ratio/%	—	−28.6	−53.0	−19.3	−19.7

1.4.5 *Significance of the* $Fe_{1-x}O$*-based catalysts in theory*

Ammonia synthesis catalyst with Fe_3O_4 as precursor has been studied widely and deeply in the past one century.[55–57] These results have greatly promoted the development of heterogeneous catalysis and surface science. Ammonia synthesis reaction is a green chemical reaction without side reaction and with molecular efficiency and selectivity of 100%. It is used as the ideal model reaction in heterogeneous catalysis, and all general concepts of catalysis were developed and formulated in relation to ammonia synthesis. So ammonia synthesis catalyst is also called "textbook catalyst."

Liu Huazhang *et al.* have studied the relationship between the activity and the iron oxides and their mixtures systematically. The hump-shaped activity curve was obtained, which modified the classical volcano-shaped activity curve. We found that the wüstite-based $Fe_{1-x}O$ catalyst has the highest activity among all the fused iron catalysts, breaking through the classic conclusion that "the Fe_3O_4-based catalyst has the highest activity." On these basis, we put forward the concept of molecular ratio of iron oxide and the principle of single-phase, that is, high activity can be obtained only when the wüstite phase is present alone in the catalyst, while, when wüstite and magnetite are present together, the catalysts always show a low activity. Wüstite or magnetite is present alone in the catalyst is an indispensable condition to achieve high activity, which establish the theoretical foundation for the preparation of the fused iron catalyst.

The modern industrial iron catalysts are nanostructured metastable substances, which is formed during the surprisingly complex synthesis of the oxide precursor. Alternative preparation routes for the nanostructured system are possible. The new invention of the wüstite-based catalyst provided a surprising example for the classical ammonia synthesis catalyst. It has been confirmed that a much higher activity can be obtained if the Fe surface is formed from wüstite rather than magnetite. The nanostructure of metal surface can be drastically changed simply by using different precursors (oxides, for instance). The results show that the high activity of $Fe_{1-x}O$ catalysts mainly comes from the change of preparation routes, the growth of active phase and the development of internal lattice defects. It is a challenge to the so-called textbook catalyst which has been studied for more than a century. Therefore, following the discovery of wüstite-based catalyst, many researchers in different countries such as Poland,[58] Italy[59] and France[60] have investigated the wüstite-based catalysts.

In addition, the high activity of the wüstite-based catalyst is partly originated from its high bulk density and Fe content. However, this high activity should be mainly attributed to the high efficiency of Fe surface sites for the activation of dinitrogen. The authors proposed some preliminary understandings on the high activity of the wüstite-based catalyst from the point of view of chemical and physical properties of $Fe_{1-x}O$. Substituting of Fe_3O_4 by $Fe_{1-x}O$ as catalyst precursor has several effect, including the easy reduction and quantity of water formed during reduction. It changes the type and distribution of promoters, and thus influences the surface properties of catalyst after reduction, such as the coverage degree of surface acid and base and their ratios. The synergy effect between acid and base sites and promoted surface reconstruction may also contribute the decrease of desorption activation energy of nitrogen[61] and weaken the strong chemical adsorption of H_2 which might be related to the catalyst surface

acid-base.[62] All these changes might increase the activity, and these changes are caused by chemical and physical properties of $Fe_{1-x}O$.

It is known that the presence of some nanoclusters of Fe atoms with specific geometrical structure is responsible for the activation of dinitrogen molecules. The similar active sites are also probably present on the Fe surface derived from wüstite with much higher efficiency for the dissociation of dinitrogen. In fact, the kinetic data show that both the activation energy and the pre-exponential factor of wüstite-based catalyst are lower than other catalysts. Although the structural and surface properties of the wüstite-based catalyst need to be investigated more deeply, it should be pointed out that wüstite is much more capable of dissolving Ca^{2+} ions within its structure than magnetite. The best proof of such an interaction is represented by the very unusual stabilization of the wüstite structure even at room temperature. Following reduction, CaO particles in nanosize are present on the surface of catalyst. In addition to the well-known role of potassium, these CaO particles also contribute to the activation of dinitrogen due to their basic nature. It is expected that a careful investigation of size and distribution of CaO nanoparticles can further explain the notable distinction between wüstite- and magnetite-based catalysts.

It is clear that these new insights and the potential science — hint behind the discovery of the wüstite-based catalyst — have a strong impact on the consolidated scientific knowledge of ammonia catalysts and moreover opens a way for industrial application. It is suggested that a reconsideration of the present consolidated knowledge on Fe-based ammonia synthesis catalyst might be convenient. It is possible that an extensive and deeper investigation of the new catalyst will bring to some revision of the present consolidated knowledge on ammonia synthesis.

1.4.6 *Industrial application*

Since 1992, the wüstite-based catalysts including A301and ZA-5 have been widely applied in the world. Up to 2008, more than 20,000 tons of catalysts have been used by thousands of ammonia plants in China and all over the world. These catalysts can be used in plants with different capacity (from 25,000 tons per year to 450 thousands tons per year) and diameters of converters from ϕ600 mm to ϕ3,000 mm (Table 1.16).

Table 1.16 Production and application scales of the wüstite-based catalysts

			Capacity of ammonia plants	
Type	Catalyst Co. Ltd	Total sales volume/t	Capacity/ (tons $\times 10^3$/ year)	Diameter of converter/mm
A301	Shangyu catalyst Co. Ltd Catalyst factory of Zhejiang University of Technology	12,000	25–450	600–3,000
ZA-5	Shangyu catalyst Co. Ltd Catalyst factory of Zhejiang University of Technology BASF(Nanjing) catalyst Co. Ltd	11,000	25–450	600–3,000

According to survey data from ammonia plants, compared with other catalysts, the industrial application of the wüstite-based catalyst reduces the reduction time, decreases the operation temperature and pressure, increases the net ammonia concentration and production capacity, reduce the energy consumption. Compared with the Ru/C catalyst, the wüstite-based catalyst has the advantages of cheap raw material, low cost of production and comparative high activity at low temperatures. Thus, it is promising for Further development and application.

1.5 Discovery of Ruthenium Based Catalysts

1.5.1 *Properties of the elements in the activation of dinitrogen*

In order to seek for non-iron catalysts to replace iron catalysts, many researchers, as Mittasch did in the past, have studied metal nitrides extensively. They expected to get some valuable information on catalytic properties of metal elements in the periodic table by this indirect way.

The ammonia synthesis reaction from nitrogen and hydrogen includes several steps: (1) dissociation of the N≡N bond; (2) dissociation of the H–H bond and (3) formation of a N–H bond. Generally, the first step is the most difficult (the rate determining step), since the bond energy of N≡N is the highest among the diatomic molecules ($942\,\mathrm{kJ \cdot mol^{-1}}$). One important role of the catalyst is to break N≡N bond, and to form dissociative adsorption or surface nitrides. It is still unclear that whether the hydrogenation of nitrogen or disconnection of N≡N triple bond is the first step on the surface of metal catalyst? Therefore, it is necessary to study the nature of dissociative adsorption of N_2 and its relationship with the reaction of H_2, which has the close relation with the reaction mechanism of ammonia synthesis. Most elements form one or several nitrides. Elements in IA and IIA groups form ionic compounds. Elements in IA group react with N_2 to form stable nitrides, but the alkaline-earth metals with large atomic weights do not react directly with N_2. Group IIIA elements react with N_2 to form the stable covalent nitrides. The elements in IVB–VIII groups react with N_2 to form nitrides with defect lattice interstitial. The elements in IVA group have a great affinity for N_2, but the affinity reduces gradually from IVA to VIII group, where only, Fe, Co and Ni form the nitrides. Both Fe_2N and Fe_4N are formed by reaction of Fe with NH_3 at 673 K–773 K. Although Mo_2N could be formed by the direct reaction with N_2, the formation relies on the presence of H_2.[63,64] Elements of IB and IIB groups are not active toward N_2, so their nitrides can only be formed by the indirect route and are unstable. The elements in IIIB group react with N_2 to form stable covalent nitrides.

The active elements that can be served as catalysts for ammonia synthesis are found in IVB to VIII groups, which form interstitial nitrides. Metal lattices are expanded due to the fact that nitrogen atom occupies the lattice defect positions. Because the interstitial nitrides are similar to metals, they are called metallic nitrides.

Chemisorptions of N_2 are easier than nitride formation, because the surface atoms are more active than the bulk metal atoms. If N_2 is a gaseous deposition film, the chemisorptions may occur on some metals at room temperature. Those

metals include IIA (Ca, Sr, Ba), IVB (Ti, Zr, Hf), VB (V, Nb, Ta), VIB (Cr, Mo, W), VIIB (Re) and VIII (Fe).[65,66] It is interesting to note that metals in IIA group chemically adsorb N_2 and metal nitrides are quite effective catalysts for the isotopic equilibrium of N_2. However, they are inactive for ammonia synthesis because they react with hydrogen forming hydrides in an N_2–H_2 mixture.[67–69]

Other metals also have the abilities of adsorption of N_2 without forming nitride. However, their capacity of chemisorption for nitrogen is so low that N_2 cannot be activated. Copper has poor activity for N_2, but copper surface can also chemisorbs N_2 when the copper surface is activated by ion bombardment. In addition, Cu_3N is unstable. Reduced cobalt oxide as well as some noble metals (Ru, Rh, Os and Ir) can chemisorb nitrogen at room temperature in the presence of alkali oxides as promoters.[70–72]

Another reason of low activity for N_2 chemisorption is that the bond energy of metal–nitrogen is not high enough. Chemisorption heat usually decreases with the increase of surface coverage.[73] The initial chemisorption heat on the vapor deposition film is larger than those on powders or supported metal, but it decreases quickly, probably because of a larger degree of disorder in crystallinity. Table 1.17 lists the initial adsorption heat and the desorption energy.

The initial chemisorption heat of N_2 could be evaluated by a semi-empirical approach,[74] which is developed by Sacher and Reijen *et al.*[75] from the interrelation of the initial chemisorption heat and formation heat of hydrides, nitrides, oxides.[76–78] The calculated results and the measured results are shown in Table 1.17. Negative values of formation heat of nitrides listed in Table 1.17 are smaller than the corresponding chemisorption heat, but their values are parallel. It is notable that the initial chemisorption heat of N_2 is $293\,kJ \cdot mol^{-1}$ on iron, while the formation heat of Fe_4N is just $12.5\,kJ \cdot mol^{-1}$, indicating that the chemisorption evolves a large amount of excess energy due to the bonding ability of surface available bonds.

The results from adsorption on the single crystal surfaces show that there can be several binding states of adsorbed species on a certain surface and the difference of chemisorption heat may be as high as $80\,kJ \cdot mol^{-1}$. Thus, it is impossible to give a definite value of chemisorption heat for a metal, unless for a known adsorption state or for a metal with only one definite adsorption state.[79]

It is notable that the heats of N_2 chemisorption on noble metals are negative (see Table 1.17). The negative values are caused by the large value of D_{N2} (bond energy) as compared with the metal-nitrogen bond energy. Thus, the adsorption state of nitrogen atoms on noble metals should be unstable if the chemisorption heat of N_2 is really negative. The results of Mimeault and Hansan demonstrated that nitrogen atoms (desorbed from a tungsten wire at 2,000 K) can be adsorbed on an iridium and rhodium filament at 300 K. Since the iridium wire was not polluted by tungsten vapor, the nitrogen atoms must be held by the surface of iridium. It seems that nitrogen atom stays on the surface because of a very slow rate of the second order desorption at lower temperatures (with its high activation energy). Active elements for N_2 activation are summarized in Fig. 1.23 in the form of the periodic table.

1.5.2 *Properties of the elements in ammonia synthesis*

Systematic studies about the catalytic activities of various single metals for ammonia synthesis were first made by Haber, including easily and not easily reduced

Table 1.17 Heats of dissociative adsorption of N_2 from observed and calculated[74]

Metals	Heat of adsorption/(kJ · mol^{-1})		−2 × (Heat of nitride formation)[e]/ (kJ · (N-atom)$^{-1}$)
	Calculated[64]	Observed	
IVB			
Ti	481	—	−610
Zr	657	—	−686
Hf	816	—	−652
VB			
V	469	—	−344
Nb	582	>502[a]	−494
Ta	732	590[b]	−486
VIB			
Cr	410	439[b]	−242
Mo	335	263[a], 289[a], 259[a]	−142
W	536	397[b], 385[a], 314[a], 389[a], 334–372[a]	−142
VIIB			
Mn	465	—	−234
Tc	126	—	—
Re	167	284–313[a]	—
VIII			
Fe	205	293[b]	−24
Co	134	—	—
Ni	138	—	0
Ru	−117	92–167[f]	—
Rh	−146	—	—
Pd	−209	−159[d]	—
Os	−67	—	—
Ir	−109	242[e]	—
Pt	−142	25[a], 92[c]	—

[a]Initial heat of adsorption on film at room temperature.
[b]Initial heat of adsorption on filament at room temperature.
[c]Desorption energy on filament.
[d]Estimation from the heat of dissociative adsorption of NO and O_2.
[e]From Table 1.18.
[f]Ru or Ru/Al_2O_3 with K.

metals for ammonia synthesis reaction. These early results are shown in Fig. 1.24. In addition to the metals shown, Re,[80] Cr,[81] V,[82] Rh,[83] Ir,[83] and Tc,[84] can act as catalysts for ammonia synthesis. Platinum was also tested, but its activity is poor. Among these elements, some metals, such as Mo, V, and U are transformed into nitrides during the reaction. The activity of these elements in the form of film was investigated for ammonia decomposition (Fig. 1.24).

In 1970s, a catalyst system promoted by metallic potassium was investigated in detail.[86,90] Figure 1.24 shows the rates of ammonia synthesis and decomposition over various metal catalysts.[83,85,86] The rate of isotopic equilibration of dinitrogen ($^{28}N_2 + {}^{30}N_2 = 2\,{}^{29}N_2$) over various metal catalysts at 588 K and a pressure of 20 kPa (150 Torr) are shown in Fig. 1.25.[78,87–89] In these cases, ruthenium is the most active metal. It is generally believed that Fe, Ru and Os are the most active elements in ammonia synthesis, ammonia decomposition and isotope equilibration of nitrogen. These elements have medium metal-nitrogen bond energy. Radioactive

Table 1.18 Reactivity of the elements with N_2 and properties of their nitrides[63]

Element		Reactivity with N_2 [a]	Nitride	Standard heat of formation/ (kJ · (N-atom)$^{-1}$, 25°C)	Decomposition temperature/°C
IA	Li	++	Li_3N	−197	(S)
	Na	−	Na_3N	−155	150
	K	−	K_3N	+84	L
	Rb	−	Rb_3N	+180	L
	Cs	−	Cs_3N	+314	L
IIA	Be	+	Be_3N_2	−285	>220
	Mg	+	Mg_3N_2	−230	700
	Ca	++	Ca_3N_2	−213	H
	Sr	++	Sr_3N_2	−197	H
	Ba	++	Ba_3N_2	−184	H
IIIB	Sc	+	ScN	−285	H
	Y	+	YN	−301	H
	La	+	LaN	−301	H
IVB	Ti	+	TiN	−305	H
	Zr	+	ZrN	−343	>3,000
	Hf	+	HfN	−326	H
VB	V	+	VN	−172	>2,300
	Nb	+	NbN	−247	>2,300
	Ta	+	TaN	−243	>3,000
VIB	Cr	+	CrN	−121	H
	Mo	+	Mo_2N	−71	H
	W	+	WN	−71	H
	U	+	UN	−335	H
VIIB	Mn	+	Mn_5N_2	−117	>1,200
	Tc		TcN		
	Re		Re_2N		
VIII	Fe	−	Fe_4N	−12	440
	Co		Co_3N		
	Ni	−	Ni_3N	+0	
	Ru	− −			
	Rh	− −			
	Pd	− −			
	Os	− −			
	Ir	− −			
	Pt	− −			
IB	Cu	−	Cu_3N	+75	450
	Ag	−	Ag_3N	+285	Ex
	Au	−	Au_3N		Ex
IIB	Zn	−	Zn_3N_2	−12	H
	Cd	−	Cd_3N_2	+79	
	Hg	−	Hg_3N_2	+8	
IIIA	B	+	BN	−134	>3,000
	Al	+	AlN	−243	2,000
	Ga	−	GaN	−105	H
	In	−	InN	−21	H
	Tl	−	Ti_3N	+84	

(*Continued*)

Table 1.18 (*Continued*)

Element		Reactivity with N_2 [a]	Nitride	Standard heat of formation/ (kJ/N atom, 25°C)	Decomposition temperature/°C[b]
IVA	C	+	$(CN)_2$	+155	
	Si	+	Si_3N_4	−188	H
	Ge	−	Ge_3N_4	−17	450
	Sn	−	Sn_3N_4		<360
	Pb	− −			
VA	P	+	PN	−84	750
	As	− −			
	Sb	− −			
	Bi	−	BiN		
VIA	O	+	NO	+92	
	S	−	S_4N_4	+134	178 Ex
	Se	−	Se_4N_4	+176	U
	Te	−	Te_3N_4		
VIIA	F	−	NF_3	−109	S
	Cl	−	NCl_3	+230	Ex
	Br	−	NBr_3	+335	U
	I	−	NI_3	+272	Ex

[a] + +: Reacts with N_2 directly below 300°C, +: Reacts with N_2 directly about 300°C, −: Made from nitrogen compounds, − −: Nitride unknown.
[b] L: Low temperature, H: High temperature, S: Stable, U: Unstable, Ex: Explosive.

element, technetium (Tc, fission product of U), was also proved to be one of the most active ammonia catalysts. The activities in unit weight of Tc powders, 5.9% $Tc/BaTiO_3$ and 5.3% Tc−4.1% $BaO/\gamma - Al_2O_3$ were comparable with that of Fe-K_2O-Al_2O_3-CaO-SiO_2.[91] The supported Tc catalyst was prepared by impregnation with NH_4TcO_4, followed by the reduction by a N_2–H_2 mixture at 593 K to 773 K for 5 h. Under the reaction conditions, Tc was reduced almost completely to the metal with only 0.01% oxides of the technetium remaining. Its catalytic activity is stable for several months. A constant radiation from ^{99}Tc (E_{max} = 0.29 MeV (1 MeV = 1.60×10^{-13} J), half-life of 2.12×10^5 year) emits counts of (4–8) $\times 10^3$ rad/day. The radiation is thought to create a defect on the support which may stabilize the technetium metal clusters or create an active center on technetium which activates dinitrogen.[91]

It is obvious that osmium and iron are the most effective elements under the conditions studied by Haber. On the other hand, ruthenium is the most active metal in ammonia decomposition. Since the two reactions are forward and backward steps of the same reaction, the most active metals should be the same, at least near equilibrium. The difference disclosed above is probably caused by some discrepancy in the reaction conditions. The ratio of H_2/NH_3 in the ammonia synthesis is much higher than that in the ammonia decomposition. Adsorbed N_2 and H_2 usually become inhibiting species, which depend on the ratio of H_2/NH_3 ratio.

1.5.3 *Alloying effect*

The reaction rate of ammonia synthesis depends on the rate of nitrogen chemisorption, the amount of adsorbed nitrogen (retardation), and the amount of adsorbed

IIA	IIIB		VIB	VIIB	VIII		
				Mn	Fe	Co	Ni
Sr			Mo	Tc	Ru	Rh	
Ba	Ce		W	Re	Os	Ir	
	U						

Fig. 1.23 Active elements for N_2 activation in the period table

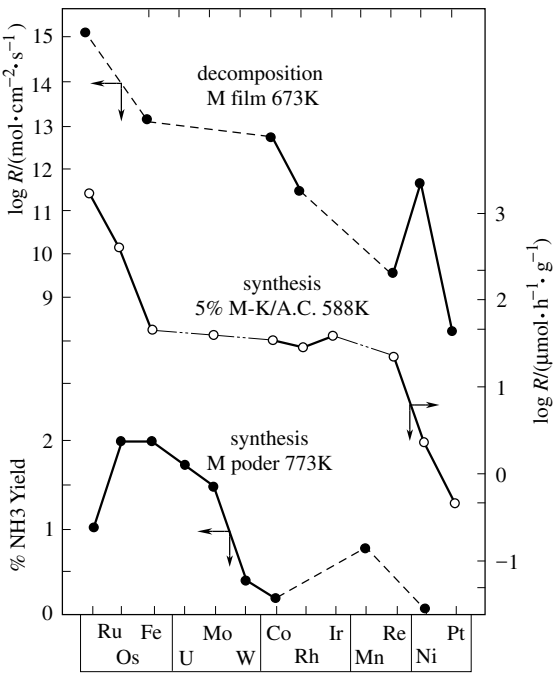


Fig. 1.24 Rates of ammonia synthesis and decomposition over various metal catalysts: Decomposition at 0.2 kPa–0.8 kPa, synthesis on 5% M–K/AC at 80 kPa and on M powder at 5 MPa (M-transition metals)

hydrogen (retardation). These factors in turn depend on the nature of elements and the reaction conditions (temperature, pressure, flow rate). Therefore, we might change the reaction rate or kinetics on a new active center which is composed of two elements (ensemble effect). If an alloy is used as an initial material and the two elements are separated and transformed into an active metal and an inert metal oxide, which is classified as a support effect.

A number of bimetallic catalysts have been studied for their activity in ammonia synthesis. A Fe–Mo (1:1) catalyst exhibits a high activity, although it decreased remarkably for a prolonged run when the content of molybdenum is lower than 80%.[89] This catalyst is prepared by calcining the mixtures of metal nitrate and

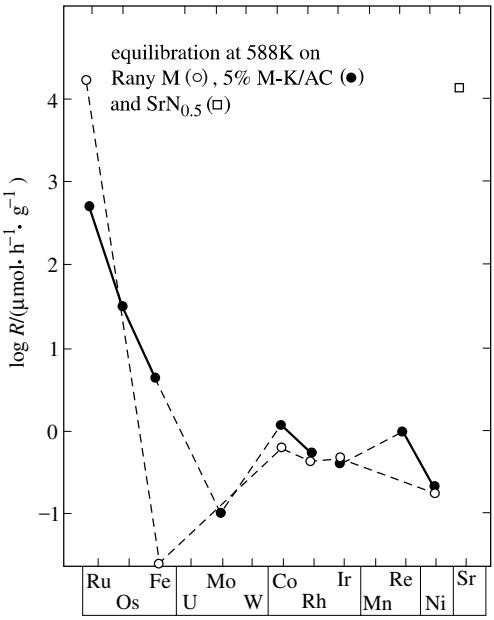


Fig. 1.25 Rate of isotopic equilibration of dinitrogen ($^{28}N_2 + {}^{30}N_2 = 2\,{}^{29}N_2$) over various metal catalysts at 588 K and a pressure of 20 kPa (150 Torr) (M-transition metals)

ammonium molybdate, followed by reduction in a mixture of N_2–H_2.[89] The adsorption of nitrogen on the catalysts increase with the increase of the content of molybdenum, but the absorbed nitrogen can gradually desorb during the reaction, resulting in the decrease of the activity. X-ray diffraction analysis of the catalysts indicates that desorption of N_2 is accompanied by the formation of mixed crystals of molybdenum. It seemed that the real active component is Mo in this system. The activity of Fe and Mo seemed to be lost with the formation of the mixed crystals. As regarding the other metals mixed with molybdenum, Cu behaved as a simple diluent effect, and Mn displayed positive effect while Cr and W showed the negative effect on the activity of Mo.

Mo and W have a higher affinity to nitrogen and higher melting point than that of iron. Adding Mo and W into iron catalyst, nitrogen can be adsorbed on Mo and W with the strong chemical bonds, the hydrogenation of chemisorbed nitrogen becomes more difficult. However, metal-nitrogen bond energy is reduced with the addition of alkali metal (potassium). When a certain proportion of Mo and W are introduced, their bond energy can be achieved to the best value for the two steps of chemisorption of nitrogen and hydrogenation of adsorbed nitrogen with the comparable speeds. So their activities, stabilities and heat-resistances are increased. However, the preparation method is a key factor. The catalysts, prepared by adding promoters from acidic to basic in turn, the addition of calcium salt, molybdenum oxide and tungsten oxide at same time, exhibit the best activity.[92]

The activity of the magnetite based catalyst is decreased by adding Ni,[93,94] and enhanced by adding Co. The catalyst is prepared by burning a Fe–Co alloy in oxygen followed by adding the promoters.[95] The alloy effect of Fe–Co and Fe–Ni has

Table 1.19 Rate of ammonia synthesis reaction on rare earth metal inter-metallic compounds[101]

Catalyst[a]	Surface area (m^2/g)	Rate at 588 K (mmol $NH_3/(g \cdot h)$)[c]	Activation energy (kcal/mol)
$Fe–Al_2O_3–K_2O$[b]	5.21	3.50	20.5
$CeFe_2$	0.45	0.41	13.2
Ce_2Fe_{17}	—	1.01	8.0
$TbFe_{17}$	—	0.04	23.0
$DyFe_3$	—	0.10	7.4
$HoFe_3$	—	0.02	18.6
$ErFe_3$	—	1.24	(4.3)
$ThFe_3$	0.60	0.36	10.6
$CeRu_2$	0.33	1.41	10.3
$Ce_{24}Co_{11}$	—	1.06	5.6
$CeCo_2$	0.61	1.45	9.2
$CeCo_3$	0.12	1.33	8.7
$CeCo_7$	0.11	0.30	13.6
$CeCo_5$	0.21	0.73	9.3
$PrCo_2$	0.38	0.13	14.4
$PrCo_3$	0.12	0.17	11.9
$PrCo_5$	0.20	0.51	11.9

[a]Catalyst weight *ca.* 3.3 g, volume *ca.* 1 cm^3.
[b]Catalyst 416 (Fe – 0.97% Al_2O_3 – 0.65% K_2O).
[c]$N_2 + 3H_2 = 5$ MPa, space velocity of 1,20,000 h^{-1}.

been studied in detail.[96] The iron catalyst has the high activity and heat resistance which is composed of RuO_2 of 3%–7%, cobalt ferrite (Co of 25%–35%), magnesium ferrite (Mg of 20%–25%), K_2O (0.5%–2%) and iron oxide.[97]

Transition metals can be activated by alloying with positive charges. Raney Ru prepared by the Al–Ru alloy has the higher activity than that of pure Ru in terms of the activity per unit area. The activity is even higher with the addition of K. The catalyst has activity even at 373 K.[98] Raney Ru is also very active when $CsNO_3$ acts as a promoter.[99,100]

The activity of rare earth-transition metal inter-metallic compounds such as $CeCo_3$, $CeCo_5$, $CeRu_2$ and $CoFe_2$ is more active than that of doubly promoted iron catalyst on a unit (BET) area basis for ammonia synthesis under 5 MPa and 873 K, although the actual activity is very low because of the relatively small surface areas of the inter-metallic compounds. The recalculated reaction rates at total pressure of 5 MPa, at 588 K are shown in Table 1.19. Cerium intermetallic compounds with Fe, Co and Ru were active, and praseodymium inter-metallic compounds with Co and $ErFe_3$ were also active. $GdFe_3$, Gd_2Fe_{17}, Th_2Fe_{17}, Er_2Fe_{17}, $HoFe_2$, $TbMn_2$, $HoMn_2$, $CeCu_5$, $LaCu_5$, Y_6Mn_{23}, Tb_6Mn_{23}, CeNi, $CeNi_5$, $CeCo_2$, CeIn, $CeOs_2$, $CeRe_2$, $HoCo_2$ and $DyCo_3$ had lower activities than those shown in Table 1.19.

The inter-metallic compounds are decomposed into high dispersed transition metals and cerium nitrate during the reaction.[101,102] The observed high specific activity suggested that the rare earth elements donate electrons to transition metals.[101] The results from *in situ* powder X-ray diffraction technique analysis showed that inter-metallic compounds such as $CeRu_2$, $CeCo_2$, and $CeFe_2$ are converted to cerium hydride (CeH_{2+x}) and transition metals under the synthesis

reaction conditions (N_2+H_2 = 50 bar, 450°C–550°C). These phases are considered to be the active components, which are sensitive to oxygenous compounds (CO, air, H_2O) and easily form an inactive transition metal and CeO_2 phase.

Ti–Fe alloy with the surface species of Fe, TiN, and TiO_x are active catalyst for ammonia synthesis. But Ti–Ru alloy has no activity because the surface of TiRu and Ru bulk phase is covered by TiN and TiO_2[103] $Fe_{91}Zr_9$ is also an active catalyst, Fe–ZrO_x. So it can be seen that alloying do not seem to have a significantly positive effect for the increase of the activity.

The above examples indicate that it is possible to develop the non-iron catalysts. For example, some non-iron catalysts that is not commercialized, such as the catalysts with ruthenium or rhodium as the active components, have the high activities, and may be developed to become the second-generation catalysts for ammonia synthesis. In 1913, Haber and Bosch developed doubly-promoted iron catalyst (Fe–Al_2O_3–K_2O) for synthesis ammonia, and also investigated other metal catalysts besides iron. They found that osmium has a high activity in ammonia synthesis at 550°C and 19 MPa, and the outlet concentration of ammonia could be maintained at 8% for a long time. In July, 1909, the process with osmium as catalyst was developed.[104] However, it could not be used to the large scale production because osmium is extremely expensive. Uranium is also very active, but it is easy to be poisoned by traces of water or O_2. Among series exploration, ruthenium is the only successful example.

1.5.4 *Activated carbon supported ruthenium catalysts for ammonia synthesis*

The first ruthenium catalyst for ammonia synthesis was reported in 1917, and Mittasch *et al.* found that the activity of ruthenium catalyst is not as good as iron catalyst during ammonia synthesis. No further work was reported for a long time since then. Up to 1968, Tamaru proposed an electron donor-acceptor (EDA) transition metal catalyst system for ammonia synthesis. In this system, alkali metals including potassium and sodium acted as electron donors, transition metals including iron, ruthenium, osmium and cobalt acted as electron acceptors, while some materials with electron transfer capability, such as phthalocyanin, poly-quinone, graphite and graphited activated carbon, were chosen as the supports.[105] It was found that these catalysts have higher activity for ammonia synthesis under mild conditions. From then on, researchers in China, Japan, Soviet Russia, Britain, America and Italy, made great efforts to develop ruthenium catalysts, aiming at replacing the conventional iron catalysts. Therein, British Petrochemical Corporation (BP) made with the most contribution.

As early as the middle of 1960s, BP successfully developed a kind of oleophylic graphite with excellent adsorption ability, and then a kind of graphited carbon in 1974, which could be used as supports for various catalysts. From 1978 to 1984, BP claimed a series of patents on ruthenium catalysts for ammonia synthesis. In 1979,[106] a novel catalyst for ammonia synthesis was prepared by loading carbonyl compound of ruthenium on carbon containing graphite in laboratory. This kind of catalyst, with graphited carbon as support and $Ru_3(CO)_{12}$ as the precursor, possessed some special features that may be summarized as follows:

(1) Promoted ruthenium on proprietary support.
(2) High activity (more than 10–20 times than magnetite) and at high ammonia concentrations: Outlet ammonia of reactor may be 20%–21.7% at 91.4 Kg.cm^2; and over a wide range of H/N ratios.
(3) Low temperature initiation, low pressure performance.
(4) Expected catalyst life is the same as for magnetite, and is determined by loss of carbon support.
(5) Poisons are the same as for magnetite and to approximately the same degree. Catalyst recovers after temporary poisons (H_2O, O_2, CO, CO_2) are removed.[107]

Like iron catalyst, dissociative adsorption of N_2 is also the rate determining step on ruthenium catalyst. The difference is that the absorption of H_2 strongly inhibits the adsorption of N_2, while the inhibition effect for the production of NH_3 is not apparent on ruthenium catalyst.[108−110] The latter is an advantage of ruthenium catalyst, so that the ruthenium catalyst can be placed behind iron catalyst in synthesis ammonia process, e.g., KAAP process.[107] The former effect is still a problem that needs to be solved for the ruthenium catalysts.

Inhibition effect of H_2 also exists on the fused iron catalyst, but the effect is less important than that on ruthenium catalysts. There is no consistent point of view on the mechanism of the H_2 inhibition effect so far. The author thought that this may relate to the surface basicity of the catalysts.[111] When the $H_2/N_2 = 3$, ruthenium catalyst exhibits the higher activity than the iron catalyst at high temperatures, while the activity is reversed at low temperatures. In addition, the situation is the opposite with the decease of the H_2/N_2 ratio. Thus, ruthenium catalyst is suitable for use at low H_2/N_2 ratios.

For the ruthenium catalyst supported on activation carbon, the methanation reaction of the carbon support can also be catalyzed by ruthenium. This is another shortcoming of ruthenium catalyst which results in the loss of carbon support and impact on the catalyst lifetime. However, researchers have found that methanation reaction occurs at higher temperatures than ammonia synthesis reaction, so that the loss of carbon *via* methanation might be avoided when the reaction is performed at relatively low temperatures.

Since ruthenium catalyst is expensive, highly active and readily inhibited by H_2, the process for the ammonia synthesis must be modified to fit these features. In 1980, BP and Kellogg Corporation cooperated to develop a novel ammonia synthesis system, in which BP was to develop a new ammonia synthesis catalyst with high activity at low temperatures and low pressures, while Kellogg was responsible for the development of the matching technology for the process of ammonia synthesis. After a joint effort for 10 years, a process called Kellogg Advanced Ammonia Process (KAAP) was developed successfully (Fig. 1.26).

KAAP synloop's operating pressure is 1,300 psig (91.4 kgf $\cdot$ cm^{-2}, 1 kgf $\cdot$ cm^{-2} = 98.0665 kPa). The value was chosen because, it matched well with a single-case syngas compressor while KAAP remains very active, even at this lower pressure. There are savings in compression equipment and synthesis loop piping and equipment at 91.4 kgf $\cdot$ cm^{-2}. With these savings, the synthesis loop costs less which can compensate the additional cost of Ru catalyst.[112] The key part of the KAAP system is the converter. This converter possesses the following characteristics:

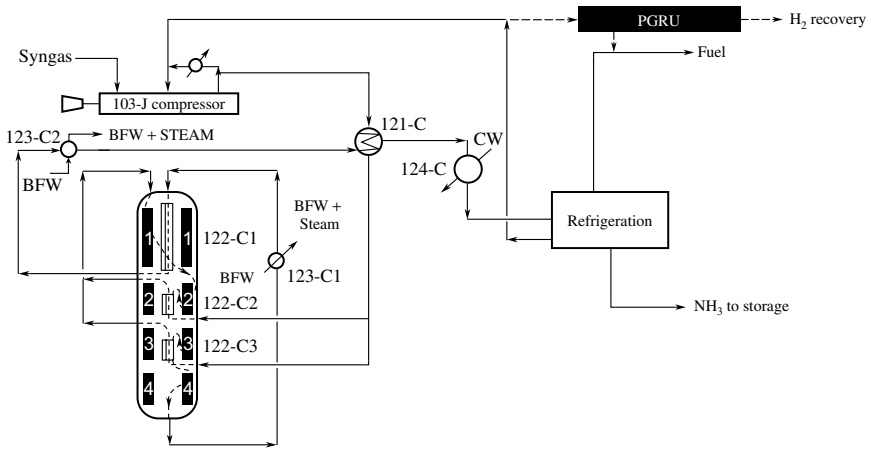


Fig. 1.26 KAAP grassroots synthesis loop flowsheet

Table 1.20 Designed and running parameters of the KAAP converter

Items	Design	Actual
Production capacity/(t/d)	1,850	1,918
Temperature-rising of converter (ΔT)/°C	262	286
Ammonia concentration at the outlet (mole)/%	20	21.7

(1) Hot-wall reactor was used for the first time.
(2) Converter is a four-bed, intercooled, radial-flow. The first four-bed intercooled ammonia converter is contained in one shell.
(3) The first bed contains iron catalyst, which accounts for about half of the total catalyst volume, and the remaining three beds contain KAAP catalyst.

The operation parameters of KAAP-converter are presented in Table 1.20. The ammonia concentration of outlet in the converter reaches 21.7%.

KAAP is operated under a pressure of 91.4 kgf $\cdot$ cm^{-2}, in order to match a single case synthesis gas compressor. Therefore, the whole investment was decreased by about 10%, in which the investment for the synthesis loops decreased by about 20%. In addition, the energy consumption decreased to about 0.28 Gcal/t (1.17 GJ/t). The saved costs in pipelines and equipments were greater than the increased cost in catalyst.

In 1990, the Pacific ammonia synthesis project was initiated. At the same year, Engelhard Corporation obtained the production license of the catalyst. In 1991, Kellogg obtained the catalyst technology from BP Company. In November 1992, Kellogg announced that the first KAAP started up successfully based on ruthenium ammonia synthesis catalysts at Pacific Ammonia.[107]

In 1995, Kellogg developed the first grass roots KAAP plant. In 1998, two new 1,850 t/d grassroots ammonia plants using Kellogg Brown & Root (KBR) Advanced

Table 1.21 Commercial Experience of the KAAP process (www.kbr.com/technology)

Client	Location	Capacity. (t/d)	Type	Start-up
Pacific Ammonia	Kitimat, BC, Canada	771	Retrofit	1992
Triad Nitrogen	Donaldsonville, LA, USA	1,633	Retrofit	1996
Incitec	Brisbane, Australia	726	Retrofit	1997
FMCL	Pt Lisas, Trinidad	1,850	Grassroot	1998
PCS Nitrogen	Pt Lisas, Trinidad	1,850	Grassroot	1998
Carribean Nitrogen Co	Trinidad	1,850		2002
Nitrogen 2000	Trinidad	1,850		2004
EBIC	Egypt	2,000		2008
MHTL	Trinidad	1,850		2009
Pequiven	Venezuela	1,800		2010

Ammonia Process (KAAP) technology were started up in Point Lisas and Trinidad. These plants, Farmland Miss Chem. Ltd. (FMCL) and PCS Nitrogen Train 4 (PCL), represent the new generation of Kellogg Brown & Root ammonia plants. This is the first time that the KBR Advanced Ammonia Process (KAAP) and KAAP catalyst have been used in a grassroots ammonia plant. Not only are these the first grassroots plants to use KAAP technology, but they also have the largest nameplate capacity among all ammonia plants ever built (Table 1.21).

Researchers in Zhejiang University of Technology, Fuzhou University, Xiamen University and Dalian Institute of Chemical Physics in China also developed ruthenium catalysts for ammonia synthesis.[113–116] Although large numbers of catalysts were proposed, only the catalyst prepared with activated carbon as support and $Ru_3(CO)_{12}$ as precursor of Ru was industrialized. The improvement of ruthenium catalyst is inhibited by the complicated factors which affect the performance of catalyst significantly. In addition, the cost is much higher for the ruthenium catalyst than the fused iron catalyst. The ruthenium catalyst has been used in 10 ammonia plants all over the world since it was successfully developed in 1992. There is still a great deal of work need to be done before it can be widely used in industry.

The detailed discussion on ruthenium catalyst will be presented in Chapter 6 of this book.

References

1. Shen J. (ed.). *Synthesis Ammonia*, in Series of Fertilizer Engineering, Beijing: Chemical Industrial Press, 2001.
2. Editorial committee for Encyclopedia of Chemical Technology, *Encyclopedia of Chemical Technology,* Vol. 6, Beijing: Chemical Industrial Press, 1994, 821.
3. Xiang DH, Liu HY. *Practical Handbook of Fertilizer Catalysts*, Beijing: Chemical Industrial Press, 1992, 45.
4. Yu ZX, *et al. Practical Technologies of Fertilizer Catalysts*, Beijing: Chemical Industrial Press, 1998.
5. Kong YH, Wang GX, *et al.* Chinese Patents CN92104524.7, CN92105197.2. 1992.
6. Yu ZH, Zhu BC, Shen CD, *et al. Analysis of Process of Large-scale Plants for Ammonia Synthesis*, Beijing: China Petroleum Press, 1993.
7. Diao LT, Jin HF, Zhang XN, *et al. Chin. J. Catal.* **19**(2): 103–106, 1998.

8. Kong YH, *et al.* Chinese Patent CN87107892.9, 1989.
9. Timm B. In: Dechema (ed.) *Ammonia Synthesis and Heterogeneous Catalysts*. Proc. 8th Intern. Congr. Catal., Weinheim: Verlag Chemie, 1984.
10. Mittasch A. *Ber. Deut. Chem. Ges. Abt. B.* **59**: 13, 1926.
11. Bosch C, Wild W. USP 1.113096; Bosch C, Mittasch A, Beck Ch. USP 1.330772.
12. Mittasch A, Schneider Ch. USP 1.201850, 1913; Pier M, Winkler K. USP 1.558559, USP 1.569775, 1923.
13. Bosch C, Mittasch A, Beck Ch. USP 1.207707, 1.207708, 1.211394, 1914.
14. Mittasch A, Schneider Ch. USP 1.201850, 1913.
15. Frankenburg WG. *Catalysis*, Emmett PH (ed.), New York: Reinhold Pub. Corp., Vol. III, 1955.
16. Nielsen A. *An Investigation on Promoted Iron Catalysts for the Synthesis of Ammonia*, 3rd ed. Copenhagen: Jul. Gjellerups Forlag, 1968.
17. Nielsen A. *Catal. Rev.-SCI. Eng.* **23**(1&2): 17–51, 1981.
18. Slack AV, James GR. (ed.) *Ammonia*, Part I–IV, New York: Marcel Dekker, (1973, 1974, 1977, 1979).
19. Boudart M. *Catal. Rev.-SCI. Eng.* **23**(1&2): 1–15, 1981.
20. Schögl R. In: Jennings JR (ed.) *Catalytic Ammonia Synthesis, Fundamentals and Practice*, New York: Plenum Press, 1991.
21. Somorjai GA, Materer N. *Top Catal.* **1**(3&4): 215, 1994.
22. Fixed nitrogen group in Department of chemistry of Jilin University. *Progress on Chemical Stimulation of Biological Fixation Nitrogen*, Beijing: Science Press, 1973.
23. Zhejiang College of Chemical Engineering, *Fertilizer and Catalysis*, **1**: 1–13, 1979.
24. Xiang DH, Liu HY. *Practical Handbook of Fertilizer Catalysts*, Beijing: Chemical Industrial Press, 1992, 226.
25. Wei KM, Wang R, Chen ZY, *et al. Chemical Fertilizer Industry*, **3**: 10–14, 1985.
26. Liu HZ, Xu RY, Jiang ZR. Chinese Patent CN86108528.0, 1986.
27. Liu HZ, Hu ZN, Li XN, *et al. J Chem. Ind. & Eng.* **45**(4): 222, 385–392, 1994.
28. Liu HZ, Li XN, Hu ZN. *Appl. Catal. A*: General, **142**(2): 202, 1996.
29. Zhao X. *Nitrogenous Fertilizer Progress*, **3**: 1–26, 1994.
30. Huang SG. *J Chem. Ind.& Eng.* **19**(2): 24–27, 1998.
31. Tennison SR. In: Jennings JR (ed.) *Catalytic Ammonia Synthesis*. Chapter 9, New York: Plenum Press, 1991.
32. Forni L, Molinari D, Rossetti I, *et al. Appl. Catal. A*: General, **185**(2): 269, 1999.
33. Rossetti I, Pernicone N, Forni L. *Appl. Catal. A*: General, **208**: 271, 2001.
34. Lin WM, Huang CR, Gan SF, *et al. Guangdong Chemical Industry*, (2): 6, 1984.
35. Artyukh YN, Rusov MT, Boldyreva NA. Kinetika i Kataliz (in Russian), **8**(6): 1319–1324, 1967.
36. Zardi V, Autonini A. *Nitrogen*: 122, 1979.
37. Wei KM, Wang R, Chen ZY, *et al. Chemical Fertilizer Industry*, **3**: 10–14, 1985.
38. Wei KM, Yu XW, Wang R, *et al. Industrial Catalysis*, **3**: 14–20, 1995.
39. ICI/CFDC Technical symposium, Shanghai, April 1989.
40. Ryszard J Kalenczuk. *International Journal of Inorganic Materials*, **2**(2&3): 233–239, 2000.
41. Strel′tsov OA, Dvornik OS, Lytkin VP. *Iz v V yssh Uchebn Zaved: Khim Khim Tekhnol* (Russia), **20**(11): 1662, 1977.
42. Artyukh YN, Fedun OS, Zyuzya LA. *Katal Katal* (Russia), **18**: 20, 1980.
43. Tamaru K. In: Jennings JR (ed.) *Catalytic Ammonia Synthesis*. Chapter 1, New York: Plenum Press, 1991.
44. Forni L, Molinari D, Rossetti I, *et al. Appl. Catal. A*: General, **185**(2): 269, 1999.
45. Rossetti I, Pernicone N, Forni L. *Appl. Catal. A*: General, **208**(1&2): 271, 2001.
46. Rossetti I, Pernicone N, Forni L. *Appl. Catal. A*. **208**: 271, 2001.

47. Liu HZ, Li XN. *Science in China* (Series B), **38**(5): 529, 1995.
48. Pernicone N, Ferrero F, Rossetti I, *et al. Appl. Catal. A*: General, **251**(1): 121–129, 2003.
49. Lendzion BZ, Arabczyk W, Figurski M. *Appl. Catal. A*: General, **227**(1&2): 255–263, 2002.
50. Pernicone N. *Cattech*, **7**(6): 196–204, 2003.
51. Liu HZ, Li XN. In: *Studies in Surface and Catalysis* (Part C). 12th International Congress on Catalysis, Granada, Spain: 2000. Elsevier, 2000, 2207–2212.
52. Pinna F, Fantinel T, Strukul G, *et al. Appl. Catal. A*: General, **149**(2): 341, 1997.
53. Xing L. *Translation in Chemical Fertilizer Industry*, (1): 13–21, 1990.
54. Forni L, Molinari D, Rossetti I, Pernicone N. *Appl. Catal. A*. **185**: 269, 1999.
55. Boudart M. *Topics in Catalysis*, **1**(3&4): 405–414, 1994.
56. Somorjai GA, Materer N. *Topics in Catalysis*, **1**(3&4): 215–232, 1994.
57. Nielsen A. *Catal. Rev.–SCI. Eng.* **23**(1&2): 17–51, 1981.
58. Lendzion BZ, Arabczyk W, Figurski M. *Appl. Catal. A*: General, **227**(1&2): 255–263, 2002.
59. Pernicone N, Ferrero F, Rossetti I, *et al. Appl. Catal. A*: General, **251**(1): 121–129, 2003.
60. Pattek Janczyk A,Grenier JC, Miczko B. *Solid State Ionics*, **117**: 95–103, 1999.
61. Guan S, Liu HZ. *Ind. Eng. Chem. Res.* **39**(8): 2891–2895, 2000.
62. Liu HZ, Liu CB, Li XN, *et al. Ind. Eng. Chem. Res.* **42**(7): 1347–1349, 2003.
63. Aika K, Tamaru K. *Ammonia Synthesis over Non Iron Catalysts and Related Phenomena*. In: Nielsen A (ed.) Ammonia Catalysis and Manufacture. Chapter 3, Heidelberg: Springer, 1995, 104–143.
64. Ailka K, Ozaki A. *Bull. Chem. Soc. Jpn.* **41**: 2818, 1968.
65. Trapnell BMW. *Proc. Roy. Soc. A* **218**: 566, 1953.
66. Bond GC. *Catalysis by Metals*. London, New York: Academic Press, 1962.
67. Ertl G. In: Anderson JR, Boudart M (eds.) *Catalysis, Science and Technology*. Chapter 4, Berlin: Springer Verlag. 1983, 209.
68. Panov GI, Boreskov GK, Kharitonov AS, *et al. React. Kinet. Catal. Lett.* **16**: 247, 1981.
69. Panov GI, Boreskov GK, Kharitonov AS. *Kinet. Ketal.* **23**: 438, 1982.
70. Toyoshima I, Takezawa N, Suzuki H. *J. Chem. Soc. Chem. Commun.*: 270, 1973.
71. Toyoshima I, Takezawa N, Suzuki H. In: Bond GC *et al.* (eds.) *Proc. 6th Intern. Congr. Catal. Chem. Soc.* London: 1977, 708.
72. Ko SM, Schmidt LD. *Surf. Sci.* **42**(2): 508, 1974.
73. Scholten JJF, Zwietering P. *Trans. Farad. Soc.* **53**: 1363, 1957.
74. Miyazaki E, Yasumori I. *Surf. Sci.* **55**(2): 747, 1976.
75. Sachtler WMH, Van Reijen LL. *J. Res. Inst. Catal. Hokkaido Univ.* **10**: 87, 1962.
76. Brenann D, Hayward DO, Trapnell BMW. *Proc. Roy. Soc.* **A256**: 81, 1960.
77. Roberts MW. *Nature*, **188**: 1020, 1960.
78. Tanaka K, Tamaru K. *J. Catal.* **2**(5): 366, 1963.
79. Toyoshima I, Somorjai GA. *Catal. Rev. Sci. Eng.* **19**(1): 105, 1979.
80. Stathism E.*Oster Chemiker Ztg.* **40**: 80, 1937.
81. Mittasch A, Keunecke EZ. *Phys. Chem.*, 574, 1931.
82. King DA, Sebba F. *J. Catal.* **4**(2): 253, 1965.
83. Aika K, Yamaguchi J, Ozaki A. *Chem. Lett.* **2**: 161, 1973.
84. Spitsyn VI, Mikhailenko IE, Pokrovskaya OV. *Dokl. Akad. Nauk SSSR* **263**: 656, 1982.
85. Logan SR, Kemball C. *Trans. Farad. Soc.* **56**: 144, 1960.
86. Ozaki A, Aika K, Hori H. *Bull. Chem. Soc. Jpn.* **44**: 3216, 1971.
87. Urabe K, Oh yA, Ozaki A. *J. Catal.* **54**(3): 436, 1978.

88. Ogata Y, Aika K, Onishi T. *Bull. Chem. Soc. Jpn.* **62**: 642, 1989.
89. Keunecke EZ. *Elektochem.* **36**: 690, 1930.
90. Aika K, Hori H, Ozaki A. *J. Catal.* **27**(3): 424, 1972.
91. Parry AA, Pryde JA. *Br J. Appl. Phys.* **18**: 329, 1967.
92. Блескин О И. Хим. Пром, **10**: 29–31, 1986.
93. Brill R, Osumi Y. *Bull. Chem. Soc. Jpn.* **39**: 1678, 1966.
94. Zabuga VY, Markova GP. Katalizi Katalizatory, *Akad. Nauk. Ukr SSR*, *Resp Mezhved sb.* 110 (CA64: 4312d), 1965.
95. Artyukh YN, Rusov MT, Boldyreva NA. *Kinet. Katal.* **8**: 1319, 1967.
96. Smith PJ, Taylor DW, Dowden DA, *et al. Appl. Catal.* **3**(4): 303, 1982.
97. Komarov VS, Efros MD, Rabina PD, *et al.* SU 988327. (CA98: 114516b), 1983.
98. Urabe K, Yoshioka T, Ozaki A. *J. Catal.* **54**(1): 52, 1978.
99. Hikita T, Aika K, Onishi T. *Catal. Lett.* **4**(3): 157, 1990.
100. Hikita T, Kadowaki Y, Aika K. *J. Phys. Chem.* **95**(23): 9396, 1991.
101. Takeshita T, Wallace WE, Craig RS. *J. Catal.* **44**(2): 236,1976.
102. Wallace WE, France J, Shamsi A. In: Mccarthy GJ, Rhyne JJ, Siber HB (eds.) *Rare Earth Mod. Sci. Technol.* Vol. 3. New York: Plenum Press, 1982, 561.
103. Kirch G, Schwab E, Wicke E, *et al.* In: Dechema (ed.) *Proc. 8th Intern. Congr. Catal.* Weinheim: Verlag Chemie. **4**: 209, 1984.
104. Mittasch A. *Geschichte der Ammoniak Synthesis.* Weinheim: Verlag Chemie. 1951.
105. Aika K, Horti H, Ozaki A. *J. Catal.* **27**: 424, 1972.
106. US Patent 4 163 775, 1979.
107. Kellogg, Engelhard. In: *Ammonia Technology Seminar Organized by the Ministry of Chemical Industry.* Beijing: 1997.
108. Hikita T, Aika K. *J. Phys. Chem.* **95**(23): 9396–9402, 1991.
109. Niwa Y, Aika K. *Chem. Lett.* **25**(1): 3–4, 1996.
110. Siporin SE, Davis RJ. *J. Catal.* **222**: 315–322, 2004.
111. Liu HZ. *Chin. J. Catal.* **26**(1): 79–86, 2005.
112. Rich S. *Nitrogen & Methanol*, **238**: 37–43, 1999.
113. Liang CH,Wei ZB, Xin Q, *et al. Appl. Catal. A*: General, **208**(1&2): 193–201, 2001.
114. Wang LH, Lin YJ, Jiang J, *et al. J. Xiamen University* (Natural Science), **38**(1): 148–151, 1999.
115. Liu GZ, Zheng XL, Xu WX, *et al. Ind. Catal.* **12**(6): 44–47, 2004.
116. Wang X, Zhu H, Xia W, Liu H, *Chin. J. Catal.* **21**(3): 276–278, 2000.

This page intentionally left blank

Chapter 2

Catalytic Reaction Mechanisms of Ammonia Synthesis

2.1 Introduction

Ammonia synthesis is a typical heterogeneously catalytic reaction and it has been widely and deeply investigated. The history of ammonia synthesis and its catalysts is just like a miniature of the development of heterogeneous catalysis. During the past century (it has been a century since the discovery of ammonia synthesis catalyst), much fundamental research in the field of heterogeneous catalysis was initiated by the study on ammonia catalyst. Ammonia synthesis catalyst is always as a touchstone when a new theory about catalysis is proposed. It is safe to say that the research achievements in catalysts, kinetics and mechanism of ammonia synthesis laid the foundation of science on heterogeneous catalysis, such as the development of the well-known equation by Brunauer, Emmett and Teller (BET equation), the catalytic theory about metal clusters, the concept about structure sensitivity of catalytic reactions which are based on the study of selective chemisorptions on iron catalysts, the concept of chemical stoichiometric number that was first proposed for the reaction mechanism determination of ammonia synthesis, Temkin theory and the well-known kinetic equation for ammonia synthesis on heterogeneous surface of catalyst which is still used for the design of ammonia synthesis reactor up to now. Therefore, this chapter discusses the reaction mechanism of ammonia synthesis and the achievements about it, as well as the theory and concept of heterogeneous catalysis concerned.

Catalysis is one of chemical phenomena in nature. However, the development of theory on catalysis shows that it is a field of multi-disciplines with concentrated knowledge and technology. The achievements in catalytic science and technology can serve many scientific branches and industrial branches.

The subjects of catalytic science include catalysis (catalytic phenomena and principle); catalyst (composition, structure, performance and manufacturing method and principle); catalytic reaction kinetics (chemical kinetics and mechanism) as well as catalytic reaction engineering (apparent kinetics inclucing transport process and reaction process and reactor design) etc. The main tasks of catalytic science are to elucidate the nature of catalytic active sites, the function of catalyst and reaction mechanism; to explore the main factors influencing activity, selectivity and stability of catalyst; to accumulate acknowledge for the exploitation and development of chemical catalysis and to open up its relatively new disciplines — bionic catalysis, photo catalysis, electro catalysis and photoelectric catalysis — to indicate

the direction for the improvement of current catalysts and the development of new catalysts and catalytic reactions; to develop catalytic reaction engineering, and to increase step by step our ability to select and design catalyst and to study them even at molecular level.

It is necessary to get much information from other disciplines, especially organic metallic chemistry, surface sciences, solid-state chemistry, material sciences, biochemistry and bionic chemistry, chemical reaction engineering, chemical kinetics and dynamicology's because of the complexity of catalyst and catalytic phenomena.

2.1.1 *The development of catalysis theory*

Up to now, the universal catalysis theory has not been developed yet. Catalysis is understood gradually with the progress of modern science and technology as well as the fast development in the industrial fields. The large progresses in the fields of coordination chemistry (complex), quantum chemistry, solid physics and surface science etc. provide the theoretic basis for the development of catalysis theory. During the long developing period, some theories or concepts have been proposed which had profound effect on the development of catalytic science. For example, the adsorption theory proposed by Langmuir in 1918 is the mainstay of catalytic reaction kinetics; and the concept of active sites put forward by Taylor in 1925 suggests that there exist active sites on catalyst surface being non-uniform. The multiple-sites theories proposed by Balahbuh in 1929 and active site group theories by Kobogeb in 1936 explain the structure and property of active sites. At the early stage of development of modern catalytic theory, a further understanding of active site concept was based on the intermediate compound theory from homogeneous reactions and the study for adsorption and catalytic reaction kinetics. The catalytic theory at initial stage is "chemical" in nature and the concept of active sites is commonly accepted. Since Volkenstein proposed the electronic theory based on the energy band theory in solid physics, the main objects of theoretical research on catalysis were solid catalysts. The homogenous complex catalyst has not attracted much attention, and enzyme catalysis is the only research topic of biology chemist which is disconnected with catalysis research. The electronic theory using solid energy band model suggests that the nature of catalyst is controlled by energy band effect. The valence electrons in the valence band can be excited to conduction band, and the electrons in conduction band can move to the surface of the solid and then reduce adsorbed species (n-type semiconductor). In reverse, the cavity in the conduction band tends to move to the surface and accept electron from adsorbed species and oxidize them if the adsorbed species lack electron (p-type conductor). In other words, this model believes that the interaction between molecules in chemical reaction i.e., electron exchange process, equals to electron transfer process which determines the electronic property of the semiconductor, and the activity of a catalyst can be ascribed to the concentration of electrons or cavities in solid and the magnitude of electron transfer potential is usually expressed by Femi energy level. Obviously, the "long range" action in interaction between molecules is mainly accounted for in this model. However, the "localized" interaction between reactant and surface has been neglected in the model. Neither the geometric factors, such as exposed crystal face and ratio of edge/face of surface atoms, nor the chemical natures of surface molecules, such as surface hydroxyl group in oxide catalyst, are

considered. So, it seems that the electron theory is only a "physical" model and the localization is rather large. Furthermore, many practical catalysts are not semiconductors or metals. Therefore, catalytic scientists gradually placed the electron theory on aside in the middle of 60s' last century.[1]

The catalytic theory has achieved new progress due to the great achievements in homogeneous coordination catalysis and enzyme catalysis. In the research of homogeneous coordination catalysis, the catalysts used are simple complex molecules with definite chemical composition and geometric configuration, and the activated intermediates formed from complex molecules and reactant molecules during reaction can be separated and detected. Based on the achievements obtained from complex and metallic organic chemistry, the catalytic scientists could make the study on the series of basic subjects of catalysis such as the nature of active sites and reaction mechanism and so on. At the same time, much progress has been made on the research of bioenzyme catalysis. Up to now, there has been some explanation for the enzyme catalysis phenomena at molecular level. It is well known that the enzyme has the features of both homogeneous and heterogeneous catalysts. The stereo configuration, coordination and reaction mechanism of enzyme catalyst have the similar characters and contents with homogeneous coordination catalyst. On the other hand, there is essential difference in heterogeneous catalysis features between enzyme and solid catalysts, which can make a reference for finding new catalytic theory for heterogeneous.[1]

The effect of the achievements of homogeneous coordination and enzyme catalysis on heterogeneous catalysis has been proved to be significant. For example, the commonly accepted "surface molecular model" is derived directly from the above achievements. The interaction of adsorbed molecules and atoms on catalyst surface, according to the model, is assumed to be limited to stringently local interaction, and any effect of energy bands or effect involving energy bands is fully neglected. In other words, the interaction of electrons in catalytic reaction is "short range." Based on the model, the active sites at surface can be considered as the unsaturated coordination ions (for oxides) or atoms (for metals), and the reactants act as ligands that can complete or partially complete the coordination bonds with the unsaturated species on surface, which are equivalent to the function of homogeneous coordination catalysts. That makes the model to be endowed with the nature of "chemical model." At present, the investigation of multiphase homogeneous catalysts actually is simulating the ability of enzyme active sites.[1]

In summary, at present, the investigation on heterogeneous catalytic theory is significantly different from that in 50s' of last century, and is in the important revolution stage from "physical model" coming back to "chemical model." The main characteristic is, through the permeation of heterogeneous, homogeneous and bioenzyme catalysis to each other, to fully understand the relation between molecule complex, enzyme and catalyst, and establish correct catalytic model to reach the goal for the scientific selection of catalyst, then to develop the new methods and scientific bases for catalyst synthesis and to accomplish the task of simulation of bioenzyme.

These theories and concepts combine the following factors of catalysis from a microscopic point of view:

(1) The space factors in catalysis, such as geometric correspondence principle in Balandin's multi-sites theory.

(2) The electronic or energetic factors in catalysis, such as electronic theory that is mainly used for studying solid physics, including finding a link between catalysis and the bottom energy level, conductivity, work function and d-electron character etc, and considering the difficulty of formation of ionic state species from reactant molecules on the surface of a solid.
(3) The chemical factors in catalysis, especially the chemical essences of catalytic processes.

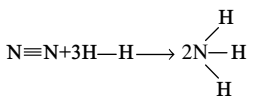
2.1.2 *The chemical essences of catalysis*

At the initial phase of the development of chemical industry, all large chemical industries were based on the non-catalytic reactions, such as ceramic and metallurgic industries at high temperatures as well as ammonium carbonate and electrochemical industry which are produced through reactions between ions in solution etc. Most of them belong to: (1) the reactions purely between ions; (2) the reactions related to free radicals; (3) the coordination reactions with large polarity; (4) the reactions at high temperatures. However, the occurrence of reactions is not easy for stable compounds especially organic compounds because it is difficult to form active particles, such as ions, free radical and complex with large polarity. So, the catalytic reactions were introduced such as the oxidation of SO_2 for manufacturing sulphuric acid and ammonia synthesis etc. Hereafter, in neoteric chemical industries, there are very rare important chemical industries which do not use catalysts.[1]

It is not so easy to crack or dissociate chemical bonds in most compounds to form new bonds, because of the requirement of energy i.e., activation energy. However, the reactions mentioned above by ions, free radical and forming complex compound, can take place without catalysts because only smaller energy is required to dissociate chemical bonds partially or wholly. While in reaction systems that require higher energy to dissociate chemical bonds, it is necessary to add other substances to help the rearrangement of their chemical bonds. In other words, the reaction processes, i.e., the realization of ionization, radicalization and coordination of reactant molecules, can only be accomplished by these substances' medi-acting, and thus probably the reaction could take place faster. This is the chemical essence of catalysis.

The role of catalyst in catalytic reactions is just to reduce the reaction activation energy that is necessary for cracking chemical bonds and forming new bonds during chemical reactions.

Taking ammonia synthesis reaction as an example:



The cleavage of one tri-bond N≡N and three H–H bonds and formation of six N–H bonds lead to the change of energy being $6 \times 385.4 - 941 - 3 \times 430.5 \approx 80\,\mathrm{kJ{\cdot}mol^{-1}}$, which is similar as the observed reaction heat of $92\,\mathrm{kJ{\cdot}mol^{-1}}$. The Gibbs free energy, $\Delta_r G^{\theta}_{298} = -33.4\,\mathrm{kJ{\cdot}mol^{-1}}$, the absolute value is high enough for ammonia synthesis reaction.

Therefore ammonia synthesis reaction from N_2 and H_2 is a spontaneous reaction in thermodynamics at room temperature and atmospheric pressure. However, there is no any detectable reaction between N_2 and H_2 in a stoichiometric mixture even for several years. The reason is that when two molecules form new bond *via* electron clouds redistribution, i.e., in order to make two frontal orbitals in molecules overlapping each other for pairing electrons to form a new bond, the best energy saving way is that there is only one electron in a frontal orbital of every molecule. For N_2 and H_2, this means that an electron in a frontal orbital of ground state molecules in N_2 or H_2 needs to excite to an anti-bonding orbital from bonding orbital, leading to the cleavage of an H–H bond or a triple N≡N bond. The cleavage of an H–H bond requires energy of $430\,kJ{\cdot}mol^{-1}$. Another better way is that the frontal orbital of one of molecules is full and another is empty, so they overlap each other to form new bond. But this is not easy to realize because of asymmetry of orbital. The attempt to compensate the energy required for bond cleavage from the energy released by bonding through a four atoms reaction $\begin{matrix} N\cdots H \\ \| \quad | \\ N\cdots H \end{matrix}$, is prohibited because of limit of symmetry.

The role of a catalyst is, first, to form a complex molecule with reactant molecule coordination through its appropriate frontal orbital and thus fully weaken the H–H bond and triple N≡N bond. For example, H–H changes to two coordinated hydrogens and then may easily form new bond with the activated reaction intermediates. In other words, catalyst can participate in the reaction and form unstable intermediate complexes with reactants and form products at last. The activation energies required for every step are much lower than that for the reaction without catalyst, and therefore the reaction rate is accelerated. Consequently, the reaction pathway is changed by catalysts. For the case of ammonia synthesis reaction on Fe (111), Ertl,[2] a winner of the Nobel chemistry prize in 2007, proposed a thermochemical kinetic profile, as shown in Fig. 2.1.

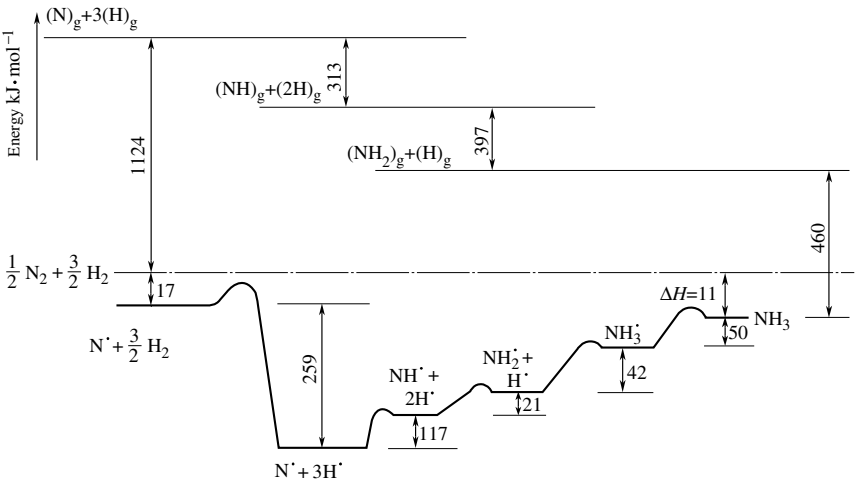


Fig. 2.1 Thermo chemical kinetic profile of ammonia synthesis on Fe (111)

It can be seen that the energy requirement for the transformation of N_2 and H_2 to N and H is very high.

The reaction mechanism for ammonia synthesis on industrial iron catalyst is still uncertain. Maybe it can be said that the reaction mechanism for ammonia synthesis are well understood when the remaining uncertainties in Fig. 2.1 are resovled.[3]



Gerhard Ertl
Nobel Prize 2007

Energy profile for a catalytic cycle is highly significant for the understanding of its reaction mechanism. If one really wants to understand the reaction mechanism of a catalytic reaction as done for ammonia synthesis, a thermochemical kinetic profile as shown in Fig. 2.1 must be provided. Theorists are currently trying to calculate many of the missing values of energy involved in the elementary steps of the catalytic cycles.[4,5]

For a catalytic reaction,

$$A + B \xrightarrow{C} AB,$$

the profile of potential energy versus reaction coordinate is given in Fig. 2.2. Curve 1 is for non-catalytic reaction that must pass a notable energy rampart, i.e., reaction activation energy E. Curve 2 for catalytic reaction on an excellent catalyst C that can lead to the formation of an unstable intermediate A···C with reactant *A*:

$$A + C \rightarrow (A \cdots C)^* \rightarrow A \cdots C.$$

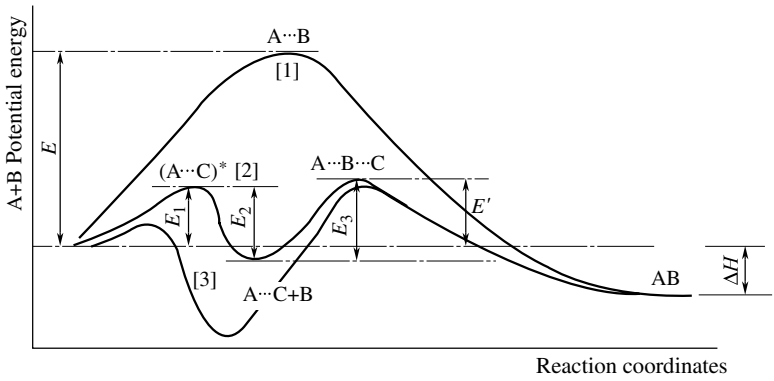


Fig. 2.2 Potential energy versus reaction coordinates

The activation energy is E_1 which is much lower than E. Then the formation of AB *via* the reaction A$\cdots$C with B whose activation energy E_3 is also much lower than E, and meanwhile the catalyst is regenerated:

$$A\cdots C + B \rightarrow (A\cdots B\cdots C)^* \rightarrow AB + C.$$

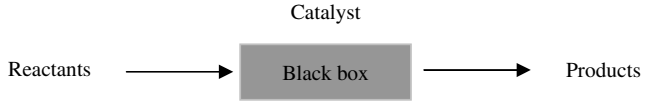
It can be known from Fig. 2.2 that the activation energy required for catalytic pathway is lower, thus leading to a high reaction rate. Of course, the reaction pathway and activation energy are different for various catalysts, which determines catalytic performance is good or not.

If reaction pathway follows curve 3, the intermediate formed is so stable that considerable activation energy is needed to make further reaction although the activation energy of intermediate formation is low. So, for a good catalyst, in order to make the total energy minimum, the match of activation energies of different steps is important. A good catalyst can form a relatively stable intermediate i.e., its stability is neither too strong nor too weak. This is the "golden rule" of catalysis proposed by Sabatier. The catalysis by chlorine atoms in ozone decomposition, which takes place in the stratosphere, is a perfect example illustrating Sabatier principle.

An energy diagram of the form of Fig. 2.2 can be used for a quantitative understanding of a catalytic cycle.

2.1.3 *The methodology of catalytic investigation*

The goal of theoretical study is not only to know the nature, but also more important to use and change the nature. For a long time, the selection and preparation of a catalyst mainly depend on experience and experimental screening, so the development of catalyst is considered as art rather than science. The investigation of microkinetics and reaction mechanism for the synthesis of ammonia is still a research topic up to now, although there is nearly 100 years of history for the study of ammonia synthesis. The application of Ziegler–Natta catalyst for olefin polymerization and NO–Bi–O catalyst for allyl oxidation has had several decades, and the study on its mechanism is still going on. Therefore, catalyst is iconically considered as a "black box":



Generally, we only know what enters into and comes out of the black box, but we do not know what happens in "black box" for long time. The reactivity of some well-known simple molecules is far from well understood. The reactivity relates to kinetic parameter. It should not be confused that the thermodynamic quantity deterring "how far" goes on the reaction from reactive potential at equilibrium conditions and the kinetic parameter deterring "how fast" the reaction takes place. The latter can only be understood *via* studying the motion of molecule. The study on kinetics in catalytic fields can only provide, but incomplete, an explanation for reaction pathway or partial mechanism at some extent, because there is no consideration at all for the change of catalyst itself and no information about the interactional nature between reactants and catalysts can be provided. Therefore, this empirical screening method is only an eigent method.

With the progress of modern theory and accumulation of data obtained from exact observation and tests, some rules appear and scientific design of catalyst is gradually established and some design concepts are clearer and clearer. Now we know more for the design of macro-physical structure of catalysts, but less for that of chemical composition and micro-configuration of catalysts. Although it is far from perfect, it can provide us assistance for drawing up a rational plan and decreasing amount of testing work.

An important progress in investigation methods of solid catalysts was the establishment of the method of measuring surface area by Brunauer, Emmett and Teller (BET) in 30's of last century. After that, many new physical and physico-chemical methods on the research of catalysis and adsorption showed up, such as electromagnetic, tracing atom, HRTEM and SEM, as well as molecular beam and energy spectrum. The goals are to make observation at approaching micro-scope, to know the nature of materials and to characterize exactly catalysts and catalytic reaction systems.

Since 40's of last century, catalytic scientists have combined the results obtained on catalysts from the study of reaction kinetics with the characterization or measurement at static state conditions by XRD, adsorption, thermal analysis, and IR etc. Although now the correlations have not been limited to bulk catalysts, and moreover can be extended to their surface features, this phenomenological method can only provide partial information about reaction mechanism.

Catalytic study and characteristic methods developed with the development of physics. In the past, we do not know what happens in "black box" and only can speculate on the reactive mechanism from apparent behaviors of kinetics. At present, there are means to observe the interior of black box. Reactive intermediate species, surface structure and adsorbed state etc. during catalytic reaction can be observed by many neoteric techniques. The progresses of electronic, vacuum and computer technique supply favorable conditions for exact measurement. Now many catalytic scientists are engaging in experimental study minutely at different area of catalytic science.

There are many techniques for the experimental observation in catalytic investigation, such as BET and chemisorptions, XRD (*in situ*), EPR, SEM, VPR, TEM, TPD, TPR (*in situ*), EMPA, TG, AES, GC, LEED, EELS, EXAFS (*in situ*), XPS (ESCA), Mössbauer (*in situ*), IR (FTIR) (*in situ*), RAM and so on. Many of these techniques require extra-high vacuum conditions and can only investigate crystal faces of solids or model catalysts, which have a large difference with practical catalytic systems and catalysts.

In order to understand the interaction mode between catalyst surfaces and reactive substances, as well as the changes of structure and the catalytic cycles during reaction process, i.e., research on real catalytic mechanism, it is necessary to conduct experimental studies at dynamic conditions or working state, including *in situ* measurement of kinetics and characterization of catalysts. Only by this, the direct observation could be carried out for the micro-mechanism steps and the structure information about various intermediate species during the conversion processes of molecules.

The features of catalytic sites on the surfaces of solid catalysts at working state should be different from those on cleaning surface. Under the real reaction conditions, molecules of reactants, products and intermediate species as well as other

species can often be adsorbed on the surfaces of catalysts and will affect the surface properties, leading to the changes in adsorption heat and the electronic properties for dotation-acceptment which depends on different nature and amount of adsorption species. In some cases, for example, the surface composition of an alloy catalyst is not only different from its bulk composition, but also can change because of chemisorptions occurred. The surface properties of catalyst would be changed with the transformation of adsorbed species. For example, the reaction between H_2 and O_2 taking place on the surfaces of copper catalyst can carry out through the repeated oxidation and reduction of copper. Therefore, there are copper oxides and hydroxide or chemisorbed oxygen and oxide which partially cover the surfaces of metal copper, leading to the distinct difference from the clean copper surface. In such a case, work function of clean copper surface measured at ultra-high vacuum has nothing to do with the understanding of catalytic reaction mechanism.

Adsorption extent on the surfaces of catalyst during real reactions cannot be evaluated from the measurement of individual reactant and product. The nature and extent of adsorption depend not only on the interactions between adsorbed species but also on the location of rate determining step which mainly decides the chemical potential of reaction intermediates. If the removal rate of chemically adsorbed species by reaction is higher than the desorption rate, the establishment of adsorption equilibrium is not possible. For example, for the decomposition of ammonia over transient metal catalysts at 400°C, if the rate determining step is the desorption of nitrogen, the chemical potential of adsorbed nitrogen at reaction conditions will correspond to nitrogen pressure of 5×10^{16} MPa, while the real pressure of nitrogen and hydrogen is only 1.33×10^{-3} Pa and 1.33×10^{-5} Pa, respectively. Thus, it is meaningless to extend the results from clean surface to working conditions. The presence of some adsorbed species, including the most abundant adsorption species, could not guarantee that it must be as a reaction intermediate in overall reaction. The behaviors of every adsorbed species, especially for the measurement of their concentrations at reaction conditions, should be related to the reaction mechanism.

Obviously, when the dynamic properties of catalyst are studied at its working state, it is only possible that the explanation of real reaction mechanism based on reaction pathway, and the correlation between the rate of each elementary step consisting of overall reaction pathway or single step and the properties of catalytic active sites at working state could be conducted. The results obtained by this way are true foundation for discussing the relation of catalyst activity and the properties of active sites, and the designing catalysts.

At present, some effective instrument for phenomenological investigation, such as IR, XRD, TG-DTA, TPD-IR (temperature programmed desorption — infrared) etc. can be extended to do dynamic research of catalyst properties at working conditions (*in situ*) by refit or re-combination. In addition, some new instruments and physical techniques, such as LEED, UPS, XPS, AES etc. (see chapter 7) provide wide channels for receiving dynamic information about catalyst surfaces. Many systems have achieved the goal that the dynamic behavior is studied by dynamic mode. For instance, Somorjai *et al.* designed a combined instrument that can be used for the measurement of surface structures of catalysts and the structures of adsorbed reactants. Then this instrument was used for the evaluation of catalyst activity and selectivity and the identification of surface adsorbed species after reaction.

Their results showed that the catalytic activity for Fe (111) crystal face is 430 times higher than that of Fe (110) crystal face and 13 times higher than that of Fe (100) crystal face for ammonia synthesis. The exposed crystal face for industrial iron catalysts for ammonia synthesis mainly is Fe (111). Their results also showed that the catalytic activity is much higher over the flat hexagonal crystal face than over tetragonal crystal face of platinum for the reaction of normal heptane dehydrogen and cyclization to form toluene. These results confirm that the concept of structure suitability and sensitivity are valid. It is believed that once the dynamic study methods are widely used, it is not far for the explanation of catalytic reaction mechanism based on the results obtained from dynamic techniques.

The new experimental methods with high sensitivity and high resolving power (i.e., atom resolving power), including *in situ* one, are introduced and developed continually for the characterization of catalysts and catalytic reaction, the interactions among catalyst–reactant, reaction intermediates and surface adsorbed species, the compositions and structures of catalysts, as well as the relations between structures and functions or performances of the catalysts and catalytic processes including the existing, potential and interesting processes to industrial community.

On the other hand, the theoretical research provides a framework for recognizing the relations between the compositions, structures and performances of catalysts, and becomes more and more important, although the experimental study is still the key. The development of super-computer makes it possible to simulate larger catalytic systems, even to predict the catalyst properties in some cases. The images with high resolving power made by super-computer are useful especially for visualizing of a complex calculation results and for recognition of space relations between catalysts and reactants at molecular level.

The consciousness of molecule design in catalyst developments will continuously increase based on the masterstroke for the study of the relations between the structures and performances of catalysts. A very active direction in catalytic fundamental investigation is the study and development of new catalytic systems for important processes, the thorough research of catalytic reaction mechanisms from the view of molecular catalysis and the scientific basis for the design and development of molecular catalysts and solid catalysts with high performance. Although a deep study of reaction mechanisms falls always behind the industrial practice for several years, this theoretical investigation in a special field will contribute to the establishment of perfect catalytic theory and the development of new industrial catalytic processes, as well as raise continuously our recognition level for catalytic theory. In these studies more attention should be paid to the development of related disciplines and the new useful concepts and methods should be absorbed.

In summary, the study on catalytic science are starting a leap from macro- to micro-, bulk to surface and steady-static to dynamic state, and entering a new stage, i.e., finding a catalyst mainly from experience rules to observing catalytic phenomena at molecular and atomic level.

2.2 Adsorption and Heterogeneous Catalysis

A reaction can be accelerated greatly by a catalyst, mainly due to the decrease of its activation energy. In general, the reduction of activation energy is achieved by

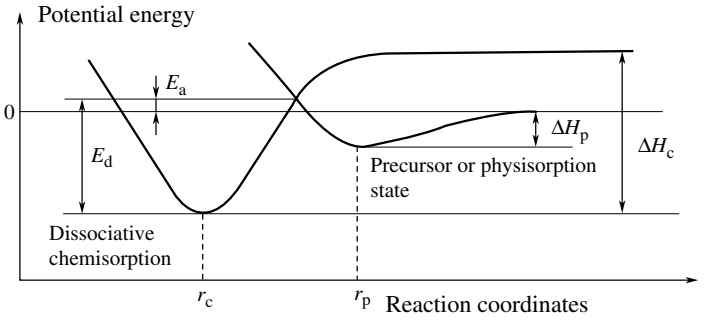


Fig. 2.3 Lennard–Jones pattern of adsorption

the chemisorption of reactant molecules on catalyst surfaces that can lead to the deformation or dissociation of reactant molecules. So, chemisorption plays a very important role in heterogeneous catalysis. The essence of catalysis is determined by the behavior of reactant molecules in adsorption phase.

2.2.1 *Adsorption and heterogeneous catalysis*

Chemisorption essentially is a chemical reaction, and the relationship between adsorption heat and adsorption activation energy should be similar to the relationship between reaction heat and reaction activation energy. Adsorption processes can usually be expressed by Lennard–Jones diagram shown in Fig. 2.3, which gives the potential energy of a system as a function of the distance between reactant and the surface of catalysts. The potential energy is zero for molecules in gas phase, and the physical and chemical adsorption states lies low and deep potential wells, respectively. It is necessary to overcome an energy well E_a as the formation of a chemical adsorption state from a physical adsorption state, but the E_a may be zero. Physical adsorption occurs first when gas molecules are approaching catalyst surfaces which can cause a reduction of activation energy to a lower level E_a and the adsorbed molecules take up easily the place of chemisorptions or dissociation.

It can be seen from potential curve in Fig. 2.3:

$$q = E_d - E_a, \tag{2.1}$$

where q is the adsorption heat, E_d and E_a are the activation energies of desorption and adsorption respectively.

The magnitude of adsorption heat corresponds to the strength of adsorption bond, and so there should also be some relationship between adsorption and catalytic activity. The catalytic activity is reversely proportional to adsorption strength when the surface coverage of reaction molecule reaches certain level, as indicated by Sabatier's theory of intermediate complex and experience. On the other hand, if adsorption is too weak, it is difficult to activate adsorbed molecules. The best activity can be obtained only in the case with suitable adsorption strength. This relationship is usually called as a "volcano" type curve, as shown in Fig. 2.4.

Taking the combination between nitrogen and hydrogen to form ammonia as an example, if the strength of adsorption bond between nitrogen atoms and the surfaces of metal is too strong, it will become impossible to react with hydrogen. However,

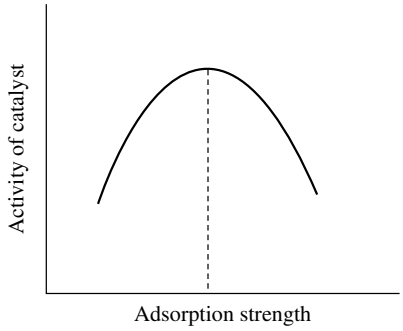


Fig. 2.4 A volcano relation between catalytic activity and adsorption strength

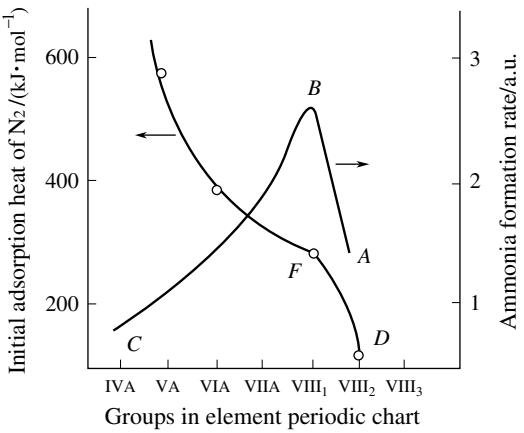


Fig. 2.5 Relationship between the rate of ammonia synthesis and adsorption strength of N_2 and groups of elements in periodic chart

if adsorption of nitrogen is so weak then the reaction rate of ammonia synthesis will be very low. This means that the topgallant rate for ammonia synthesis can only be obtained at moderate strength of nitrogen adsorption, and in this case the majority of surfaces of catalyst are covered by adsorbed nitrogen atoms and they can easily react with adsorbed hydrogen to form ammonia. This view is supported by the experimental results given in Fig. 2.5 which shows the relation between ammonia synthesis rate and nitrogen adsorption strength on different groups in element periodic table.

It can be seen that from VA to VIII groups, the initial adsorption heat of nitrogen decreases and ammonia synthesis rate reaches a maximum value, and after that the rate goes down due to the reduction of surface coverage of adsorbed nitrogen.

The close relationship between adsorption heat and catalytic activity is supported further by the relation between group number in the periodic table and catalytic activity. Therefore, the magnitude order of catalytic activity can be arrayed approximately according to the size of adsorption heat, which is of reference values for selecting active components of a catalyst or estimating catalytic performance of

elements. For catalyst research and development, it can also be used as a forward step.

It is not practical for catalyst development to look for the correlation of adsorption heats and catalytic activities from adsorption heat measurements. First, the measurement of adsorption heat is more difficult and more complicated than the evaluation of catalyst activity in general. Second the adsorption heat varies with surface coverage. Although it is known that catalytic activity does not depend on initial adsorption heat, it is still used for correlating catalytic activities of ammonia synthesis and ethylene hydrogenation because of the lack of experiment data. Therefore, there is a certain limit for the study of catalyst and catalytic reaction using adsorption heat.

Taking ammonia synthesis as an example again, it is usually believed that N_2 and H_2 adsorb chemically on the surfaces of iron catalysts and dissociate to form adsorbed intermediate states N^* and H^*. Then the two species undertake a series of reactions on the surfaces, until the formation of product ammonia. This pathway can be expressed in general as follows:

$$A_2 + 2* \rightarrow 2A*$$
$$B_2 + 2* \rightarrow 2B*$$
$$A* + B* \rightarrow AB*$$
$$\vdots$$
$$\cdots \rightarrow C*$$
$$C* \rightarrow C + *$$

Where, * denotes active site. The mechanism of reaction between two adsorbed species on the surface is called as Langmuir–Hinshelword or L–H mechanism which is widely accepted for ammonia synthesis from N_2 and H_2.

Another type of reaction mechanism is for catalytic oxidation of CO on MnO_2 catalyst. The product CO_2 is formed from the reaction between adsorbed oxygen on the surface and CO in gas phase. This mechanism can be represented as:

$$A + * \rightarrow A*$$
$$A* + B \rightarrow AB*$$
$$AB* \rightarrow AB + *$$

This is called as Rideal–Eley or R–E mechanism: Reaction between a surface species and a gas molecule.

The two reaction mechanisms mentioned above basically outline all mechanistic models in heterogeneous catalysis. It should be noted that for any mechanism, one of reactants must be adsorbed on the surfaces of solid catalysts. Therefore, the prior condition for catalytic reaction to take place is chemisorption of at least one reactant. In some cases, the rate of catalytic reaction is directly related to that of reactant chemisorption. So, two regulations can be generalized for the relation between chemisorption and heterogeneous catalysis:

(1) The requirement for a solid having catalytic activity is that at least one of the reactants can undergo chemisorption on the solid surface. In other words, a solid has catalytic activity only when it has the ability to undergo chemisorption of at least one of the reactants. This concept was developed by Taylor in 1931.

(2) The adsorption of molecule on the surface of solid is neither too strong nor too weak, which is so-called Sabatier's principle. Relatively stable intermediate species can be formed by chemisorption of reactant and from those which can easily convert to products by reactions or/and decomposition. Obviously, if adsorption of reactant is too weak, the adsorbed molecules cannot be activated thoroughly and the reaction rate is low. On the contrary, over-stable intermediates can be formed on surface if adsorption of one or more reactants is too strong, which then inhibit forward reaction like a poisonous coverage over the active surface. Therefore, the requirement for solid surface having excellent catalytic activity is that the catalyst contains as many chemisorptions sites as possible and appropriate chemisorption strength. This rule can be expressed as: If a reaction can be catalyzed by various solid materials, then their reaction rate per unit area is reversely proportional to the adsorption strength of reactants at the same surface coverage.

The close relationship between chemisorptions and heterogeneous catalysis can be described by two regulations mentioned above. The chemisorption study is very important for the explanation of catalysis principles and the understanding of catalytic activity and selectivity. The theory of chemisorption is one of the most important components in heterogeneous catalytic theory. Concerning with practical application, the active component for given reaction can be generally selected based on the regulations mentioned above and the known experimental data about chemisorption.

2.2.2 *Non-uniformity of the surface of heterogeneous catalysts*

Even for very smooth surface, it is still very rough on an atomic scale. A popular model of single crystal surface evolved from investigation on the crystal growth can trace back to the early work of Stranski[6,7] and KosseI,[8] further developed by Hirth and Pound.[9]

A single crystal surface exhibits terraces (T) with low Miller index crystal faces and high surface density. They are separated by ledges (L) which may have kinks (K). A terrace between two ledges is a step. Defects on terraces consist of vacancies or adsorbed atoms. Thus the smooth surface may indeed be rough on an atomic scale. This model is called as TLK model (Fig. 2.6). The systematic

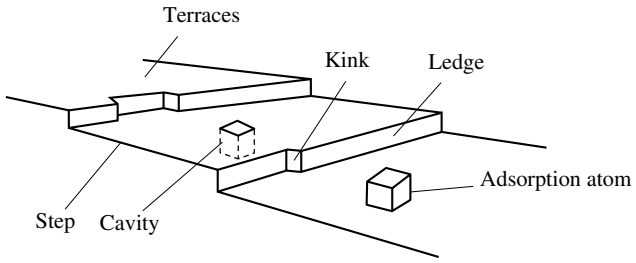


Fig. 2.6 TLK model of single crystal surface

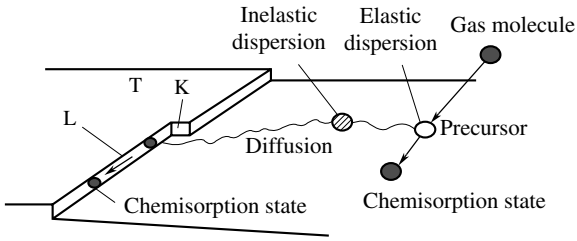


Fig. 2.7 Adsorption of molecule on single crystal surface

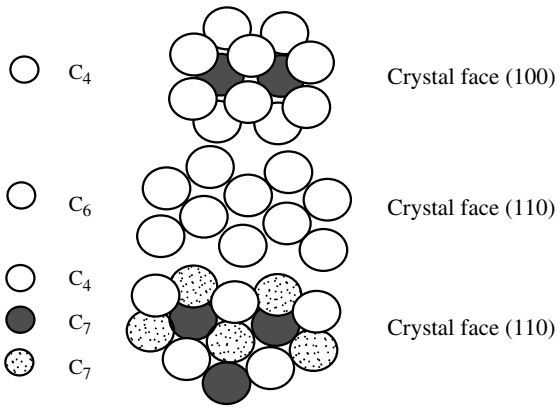


Fig. 2.8 Coordinating atoms C_i on surface with low Miller index faces of body-centered cubic lattice

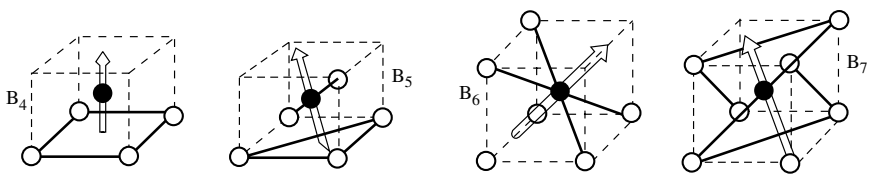


Fig. 2.9 Surface active sites B_j on faces of body-centered cubic lattice

use of stepped single crystals with regularly spaced ledges has been popularized by Somorjai.[10] These surfaces are effective crystal faces with high Miller index. The adsorption process and state of a molecule on TLK surface are given in Fig. 2.7.

For very small metallic particles, or clusters, crystal faces have no meaning. It is better to define surface structure with the notation introduced by Van Hardeveld and Hartog.[11] They consider the coordination number i of a surface atom and the coordination number j of a surface active site, which was called as coordination model. Surface atom is denoted by C_i when it has i nearest neighbors. The active site is denoted by B_j when it has j nearest neighbors. Examples of C_4, C_6 and C_7 atoms are shown in Fig. 2.8. Several active sites, B_4, B_5, B_6 and B_7 are shown in Fig. 2.9.

Large single crystals are ideal model systems and the data obtained from them are now recognized as standards. One of the reasons is that catalysis researchers always hope to avoid the surface contamination. Impurities that come from within or from the outside of system can accumulate at the surface. The lower the dispersion of the metal, the more chances of surface contamination comes from inside. For single crystals, the chance of contamination coming from outside is also very high. Indeed, if every collision of contaminant molecules with surface once at 10^{-6} torr (1 torr = 133.332 Pa) sticks to the surface upon, a monolayer can be built up in one second. Exposure, the product of pressure and time (i.e. 10^{-6} torr during one second) is called as one Langmuir (exposure). One Langmuir of exposure is enough to contaminate a surface completely if every molecule sticks to it by collission.

Recently, a major development in heterogeneous catalysis is the accumulation of data on the kinetics of elementary steps on well-defined surfaces of large single crystals that are atomically clean and smooth faces. Cleanliness is achieved by high-temperature evacuation, treatment with reactive gases, and/or ion bombardment. The structure of the surface is established by low-energy electron diffraction. Its composition is checked and monitored by Auger electron spectroscopy. All observations are made on the sample in an ultrahigh vacuum chamber with a background pressure of 10^{-8} to 10^{-10} Pa. Residual gas composition is monitored by mass spectroscopy. Very pure gases are leaked into the sample chamber with the pressure of 10^{-4} to 10^{-7} Pa.

At least there exist two kinds of surface heterogenicity: (1) different active sites come from surfaces with different structures; (2) the interaction of adsorbed molecules. In the first case, because of the existence of surface atoms with different coordinations, for instance, the surface atoms in TLK model, there exist types of active sites before adsorption; and for the second case, because the interaction between adsorbed molecules makes kinetic parameters depend on the surface coverage, the active sites seem non-uniform. In essential, it is more difficult to treat as a general form and get an analytical form of rate expression for the second one. As so far, the treatment of surface non-uniformity is mainly limited in the non-uniformity of surface atoms or sites in literature.

The heterogenicity of catalyst surfaces makes problems complicated. If the kinetic data were obtained in a narrow range of experimental conditions, only Langmuir kinetics could be applied. If using the wide range of experimental conditions, micro-kinetic model may involve non-Langmuir effect of surface coverage state.

The non-uniformity of surface sites can be defined as a function of affinity A, $\Phi(A)$, that can characterize the properties of surface sites. The affinity can be expressed as an absolute value that is the adsorption heat (or the change of Gibbs free energy) divided by RT of probe molecules related. For example, for ammonia synthesis reaction over iron catalysts, the affinity is defined as the adsorption heat of nitrogen molecules because it is rate-determining step in ammonia synthesis catalytic reactions. Correspondingly, the active sites with stronger adsorption for nitrogen molecules are defined to have higher affinity.

The function $\Phi(A)$ defines a probability of affinity A for any sites and can be summation of finite sites with different affinity. $\Phi(A)$ is expressed by a continuous function, usually power function or linear function in references. Non-uniformity is a collection of small surface areas which are uniform with affinity A.

Because the behavior of different sites is independent of each other, the contribution of different sites can be obtained *via* the rate expression based on uniform surfaces varying with affinity. For ammonia synthesis, the reasonable assumption is that the activation energies of the elementary steps involving nitrogen adsorption changes linearly with affinity and other steps are independent of affinity. For rate expressions $r(A)$ of uniform surface with special affinity, the overall rate of non-uniform surface characterized by a non-uniformity function of active sites $\Phi(A)$ can be calculated by the an integration $\int \Phi(A)\ \mathrm{d}A$, and its lower limit is A_1 that is for weakest sites (θ value closes to 1) and upper one A_0 for strongest sites (θ value closes to 0). If the integration $\Phi(A)$ is not normalized, the value of the integration must be divided by $\int \Phi\ (A)\ \mathrm{d}A$.

The adsorption isotherms on non-uniform surface can be obtained as follow. First, it can be given that the expression for the variation of surface coverage with pressure on uniform surface can be characterized by a given affinity $\theta\ (P,\ A)$. Then an integration $\int \theta(P, A)\Phi(A)dA/\int \Phi(A)dA$ can be done which is the isotherms on non-uniform surface characterized by a function $\Phi(A)$ of non-uniformity of active sites. The upper and lower limits of the integration, which is a range of non-uniformity of active sites, vary in a wide range from A_0 to A_1. An important result obtained by the treatment above is that the active sites with weakest affinity A_1 is hardly occupied by adsorbed species and has very low catalytic activity, while that with the strongest affinity A_0 is saturated and the activity is also very lowbecause desorption rate of adsorbed species from the sites is very low, and therefore utilization of these sites is also very low. Therefore the maximum catalytic activity takes place at the active sites with moderate affinity, and these sites with moderate affinity make major contribution to the activity of catalysts.

Fortunately, the micro-kinetics analysis can be applied to the study of catalysis without the detailed knowledge about the effect of surface non-uniformity. For the deduction of reaction mechanism from steady state kinetics, the effect of surface non-uniformity should be involved in rate expressions. However, in order to describe, with a unified mode, the kinetic behavior in wide range and the results (data) from spectroscopic measurement and theoretical study, some minor effect of surface non-uniformity can be neglected. Correspondingly, the effective values of thermodynamic and kinetic parameters applied in the analysis represent the catalytic surface and its coverage state for the collection of experimental data under reaction conditions, and the effect of surface coverage on kinetic parameters is necessarily considered only when the range of experimental conditions is wide enough leading to a change of whole surface coverage states of catalyst.

2.2.3 *Isotherms of chemisorptions*

Langmuir investigated adsorption phenomena systematically in the early 20th century and proposed the famous monolayer adsorption theory in 1918. Langmuir's theory is the foundation of the kinetics of surface catalytic reaction. Other adsorption theories basically are the amendment or supplement to Langmuir's adsorption theory.

According to the collision theory, if θ is the surface coverage occupied by adsorbed molecules, the rate expressions for adsorption and desorption are v_a and

v_d as follows:

$$v_a = \frac{P}{\sqrt{2\pi mKT}} f(\theta) S^* \exp\left(\frac{-E_a}{RT}\right), \tag{2.2}$$

$$\nu_a = k_a P(1-\theta), \tag{2.3}$$

$$k_a = \frac{S^*}{\sqrt{2\pi mKT}} \exp\left(\frac{-E_a}{RT}\right) = k_{a,0} \exp\left(\frac{-E_a}{RT}\right), \tag{2.4}$$

$$\nu_d = k_d \cdot f^{'}(\theta) = k_{d,0} \exp(-E_d/RT) \cdot f^{'}(\theta), \tag{2.5}$$

$$\nu_d = k_d \theta, \tag{2.6}$$

$$k_d = k_{d,0} \exp(-E_d/RT), \tag{2.7}$$

where p is equilibrium pressure of adsorbate in gas phase; S^* is sticking coefficient; E_a, E_d are activation energy for adsorption and desorption, respectively; $f\ (\theta)$, $f'(\theta)$ are functions for surface adsorption sites of empty and occupied by adsorbed molecules, respectively; k_a,k_d are rate constants for adsorption and desorption, respectively.

The net adsorption rate is:

$$v_a - v_d = \frac{P}{\sqrt{2\pi mKT}} f(\theta) S^* \exp\left(\frac{-E_a}{RT}\right) - k_{d,0} \exp\left(\frac{-E_d}{RT}\right) f'(\theta). \tag{2.8}$$

Equation (2.8) is the common rate equation of adsorption and desorption, and the detailed forms depend on the function relation between S^*, $f(\theta)$, $f'(\theta)$, E_a, E_d and θ.

To apply the monolayer model to the adsorption process, Langmuir suggested four basic assumptions: (1) the energy or heat of each adsorption site on surface of solid is identical (2) only monolayer adsorption is possible; (3) there is no interaction between adsorbed molecules; (4) adsorption and desorption processes are in kinetic equilibrium.

Langmuir surface is actually an ideal surface. Therefore, S^*, $f(\theta)$, $f'(\theta)$, E_a and E_d are independent of θ. Since adsorption is in equilibrium, the following equation is obtained from Eq. (2.8):

$$\theta = \frac{k_a p}{k_d + k_a p} = \frac{Kp}{1+Kp}, \tag{2.9}$$

where K is adsorption equilibrium constant.

$$K = \frac{k_a}{k_d} = K_0 e^{q/RT},$$

where q is adsorption heat. Equation (2.9) is so-called Langmuir isotherm, which represents the change of adsorption amount with pressure at a given temperature.

The study on adsorption discovered that the relation between adsorption amount and adsorbate pressure can be approximately classified as five types, as shown in Fig. 2.10.

Langmuir's monolayer adsorption model can only describe the first type of adsorption isotherms which happen frequently in micro-pore adsorbents (pore size

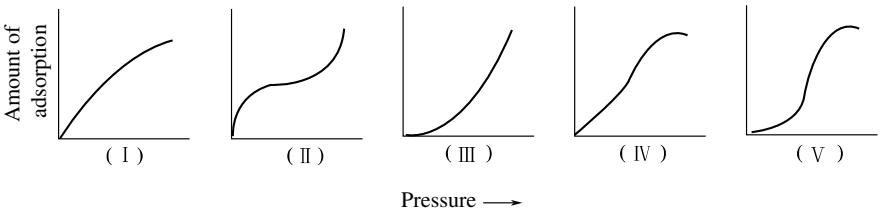


Fig. 2.10 Types of adsorptive isotherms

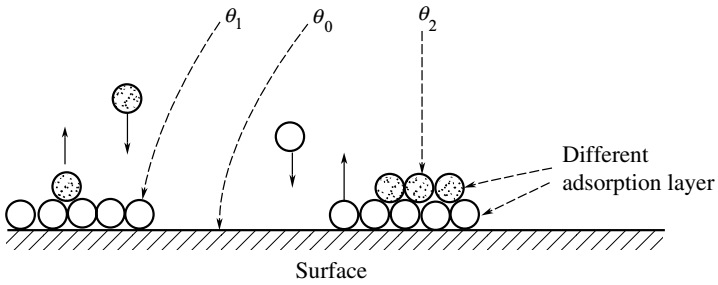


Fig. 2.11 Multilayer adsorptive model of BET

<2.5 nm). The adsorption amount almost does not change at high pressures, indicating that saturation of adsorption is reached.

The second type of isotherms are S-shape curves, which happen frequently in experimental measurements, corresponding to the adsorption on mesoporous (pore size $>$20 nm) solid materials. The first bend in the isotherm should correspond to the monolayer saturation, but no horizontally stable level appears which means that adsorption can be multilayer rather than monolayer. The section of the curve at high pressures goes up very fast due to the occurrence of capillary condensation in small pores. Other types of isotherms also predict the occurrence of multilayer adsorption. So, the assumption of monolayer absorption proposed by Langmuir has to be modified, and thereafter BET, Temkin's and Freudlich's adsorptive theory were developed.

The multilayer adsorption model, as shown in Fig. 2.11, was proposed by Brunauer, Emmet and Teller (BET) in 1938 to modify Langmuir's monolayer one. BET theory developed from the multilayer model can be applied to explain all types of isotherms. Based on the BET theory, a standard method for determining the specific surface area of solid catalysts was developed, which brought catalysis study into a new stage.

The assumptions and main points of multilayer adsorption model are as follows:

(1) The same assumption as Langmuir's monolayer model was made, namely the surface of solid is uniform and there is no interaction between adsorbed molecules and no effect of adsorbed molecules on the adsorption probability on vacancy sites.

(2) Multilayer adsorption is formed by Van de Warr force between adsorbed molecules and molecules in gas. Layer number could be infinite in theoretical. The adsorption on second or more layers can take place simultaneously before the first layer is saturated, and for adsorptions over second layer, they are all similar to condensation of adsorbate vapor as liquid.
(3) The adsorption rate of each layer is proportional to the vapor pressure and vacant sites, while the desorption rate is proportional to the number of qualified desorbed molecules of that layer.

Assuming that the adsorption heat from second layer to nth layer ($n = 2 \rightarrow \infty$) is equal to liquefaction heat of adsorbate vapor, BET equation with two parameters was obtained:

$$\frac{p}{V(p_0 - p)} = \frac{1}{V_m C} + \frac{(C-1)}{V_m C} \times \frac{p}{p_0}, \tag{2.10}$$

where p_0 is saturation vapor pressure of adsorbate at adsorption temperature; C is constant; V_m is monolayer adsorption capacity.

The Langmuir's and BET's two-parameter equations are the extreme cases at $n = 1$ and $n = \infty$, respectively. If adsorption happens on definite space, such as pores with limited sizes, rather than free space, the layers of adsorption would be limited. In this case, three-parameter BET equation should be used:

$$\frac{V}{V_m} = \frac{Cx[1 - x^n(n+1) + nx^{n+1}]}{(1+x)[1 + x(C-1) - Cx^{n+1}]}, \tag{2.11}$$

where $x = P/P_0$. When $n = 1$ in Eq. (2.11) it can be reduced to Langmuir equation, and for $n = \infty$ it changes into two-parameter BET equation. Based on the magnitude of C value, the adsorption behavior of a solid can be speculated as I or II types.

Temkin and Freundlich *et al.* proposed a major modification for uniform surface assumption made in Langmuir theory, because the energy and adsorption heat released are different from various adsorption sites on solid surface, i.e., solid surface is non-uniform.

Temkin considered that adsorption is stronger at initial stage than that at later and the adsorption heat released decreases linearly with coverage on actual non-uniform surfaces:

$$q = q_0(1 - \alpha\theta), \tag{2.12}$$

where q_0 is adsorption heat at coverage $\theta = 0$; α is constant.

Substituting Eq. (2.12) into Eq. (2.9), we get Temkin isotherm with moderate coverage:

$$\theta = \frac{1}{f} \ln A_0 P \tag{2.13}$$

f and A_0 are constants, depending on temperature and the properties of adsorption system.

Freundlich supposed that adsorption heat decreases exponentially rather than linearly with coverage:

$$q = q_0(1 - \alpha' \ln\theta), \tag{2.14}$$

Substituting it into Eq. (2.9), Freundlich isotherm can be obtained:

$$V = C_0 p^{1/n}. \tag{2.15}$$

Constant C_0 depends on temperature and the properties of adsorption system, and another constant $n > 1$, relates to temperature. Freundlich isotherm initially was obtained based on experimental data and is more suitable for the fitting and interpolating of experimental data. It is frequently applied in the adsorption in solution, and seldom applied in physical adsorption of gases.

2.2.4 *Rate of adsorption: Elovich equation*

For non-uniform surface, various adsorption sites are of different energy. The adsorption heat and activation energy depend on the coverage. Figure 2.12 shows that there is a linear relation among adsorption heat, activation energy and coverage at moderate coverage, for N_2 adsorption on Fe catalyst. The linear relation between activation energy and coverage is also followed by H_2 chemisorptions on Fe.

Supposing that the adsorption activation energy (E_a) increases and the desorption activation energy (E_d) decreases linearly with coverage θ, then we have,

$$E_a = E_a^0 + \gamma\theta, \tag{2.16}$$

$$E_d = E_d^0 - \eta\theta, \tag{2.17}$$

where $E_{\mathrm{a}}^0, E_{\mathrm{d}}^0$ are activation energy at coverage of $\theta = 0$ for adsorption and desorption, respectively; γ, η are constants.

Substituting Eqs. (2.16) and (2.17) respectively into Eqs. (2.2), (2.5) and (2.8), and setting $f(\theta) = 1 - \theta$, $\mathrm{f}'(\theta) = \theta$, after simplifying we get:

$$\nu_a = k_a P e^{-g\theta}, \tag{2.18}$$

$$\nu_d = k_d e^{h\theta}, \tag{2.19}$$

$$\nu = k_a P e^{-g\theta} - k_d e^{h\theta}, \tag{2.20}$$

Where $g = \gamma/RT$, $h = \eta/RT$.

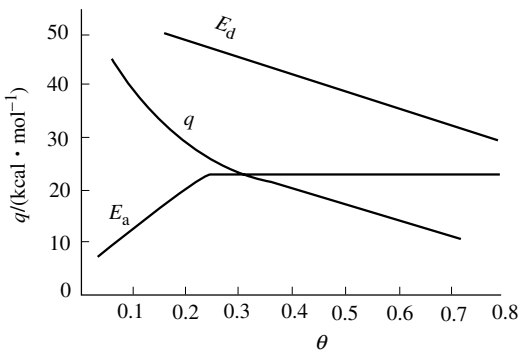


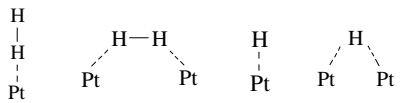
Fig. 2.12 Relationship between adsorption heat and activation energy with coverage of N_2 on Fe catalyst. ($1\,\mathrm{kcal \cdot mol^{-1}} = 4.184\,\mathrm{kJ \cdot mol^{-1}}$, below the same)

Equations (2.18), (2.19) and (2.20) are the expressions of Elovich's adsorption rate equations,[12,13] which have been widely applied in describing chemisorptions rates. It can be seen form Eq. (2.18) that adsorption rate drops exponentially with increasing of coverage. Langmuir also proposed a similar equation for the explanation of the phenomenon that adsorption rate decreases with increasing of coverage. The example for Elovich's and Langmuir's equations is N_2 adsorption on iron catalyst[14] and N_2 desorption from molybdite catalyst.[15]

2.2.5 *Chemisorption state*

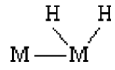
2.2.5.1 *Chemisorption states of hydrogen*

The adsorption–desorption processes of hydrogen on platinum electrode, $Pt+H_3O+e = PtH + H_2O$, were studied by circulating volt-ampere method and found that there were four chemisorptions states shown as follows:

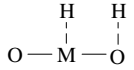


The former two forms belong to molecule adsorptions and the later two forms are atom adsorptions. Among the four adsorption states, the dominant adsorption state is variable with reaction conditions. In catalytic reactions, dissociated adsorption, i.e., atom state, plays a main role. A programmed-temperature desorption spectroscopy of hydrogen on single crystal tungsten (110) face is given in Fig. 2.13, which indicats that there exist four adsorption states, although the adsorption states of effluent cannot be determined.

The dissociated adsorption of hydrogen can be classified as homolysis and heterolysis. The dissociated adsorption of hydrogen on metals belongs to homolysis:

$$M - M + H_2 \rightarrow$$  or 

The dissociated adsorption of hydrogen on metal oxides belongs to heterolysis.

It was found from the $O-M-O+H_2 \longrightarrow$  experimental data that all metals that can chemisorb hydrogen can catalyze hydrogen–deuterium exchange reaction. The results provide a powerful evidence for dissociation adsorption of hydrogen.

$$H_2 + D_2 \rightarrow 2HD.$$

Based on experimental observation of hydrogen adsorption on the surface of activated iron catalyst, it was found[16] that the adsorption state of hydrogen on iron catalyst relates with the precursors of catalyst. The adsorption state of hydrogen changes place when the catalyst precursor is changed from Fe_3O_4 to $Fe_{1-x}O$. It is found that there is a strong chemisorption state which has no activity for ammonia synthesis. Because the strong chemisorption state of hydrogen occupies active sites

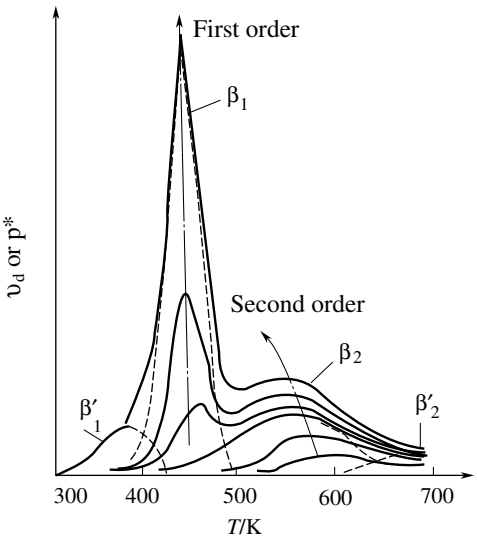


Fig. 2.13 Programmed-temperature desorption spectroscopy of hydrogen on single crystal (110) face of tungsten.

of catalyst surface with no activity for ammonia synthesis, it restrains chemisorption of N_2. A critical attention has been paid to ruthenium-based ammonia synthesis catalysts for the strong choke effect of strong chemisorption of hydrogen on N_2 chemisorption.[17–19] The strong inhibition by H_2 adsorption over catalysts will be further discussed in Chapter 3, Sec. 3.2.7.

2.2.5.2 *Adsorption states of nitrogen*

The study on the pattern of nitrogen chemisorption is very important for the understanding of reaction mechanism of ammonia synthesis. But the chemisorption of nitrogen on the surface of transient metals is very complex. Taking chemisorption on iron catalyst for ammonia synthesis as an example, it was found that the formation rate of ammonia depends on pre-adsorption temperature if the adsorption of nitrogen was preceded first on the surface of activated catalyst, and then hydrogen was passed on surface of pre-adsorbed nitrogen. It is considered that there exist two adsorption patterns: The first one is of L-type which appeared at 200°C of pre-adsorption temperature, in which the formation rate of ammonia was proportional to $p_{H_2}^{1.35}$; the second one is of H-type which appeared at 400°C–440°C of pre-adsorption temperature, in which the formation rate of ammonia was proportional to $p_{H_2}^{0.96}$.

There is very different behavior for the two-type adsorption states. For instance, H-type nitrogen has no effect on CO adsorption, while L-type nitrogen inhibits CO adsorption. L-type is more active for ammonia synthesis than H-type. If iron nitride was hydrogenated to ammonia, the formation rate of ammonia was also proportional to $P_{H_2}^{1.35}$, indicating that the H-type adsorption state of nitrogen is similar to that on iron nitride, i.e., one nitrogen atom is coordinated with several iron atoms,

and attributes dissociated adsorption of N_2. The form (structure) of L-type is not clear yet.

However, there still is no common sense about that the nitrogen adsorption on iron catalyst for ammonia synthesis is dissociation or not.

(1) The dissociation adsorption of N_2 is supported by many experimental results: (i) Only NH and N were detected after N_2 and H_2 were adsorbed on dual-promoter iron catalyst at reaction temperature and 101.3 kPa and vacuumed at 200°C; (ii) N_2^* adsorption state has never been found by XPS detection. Heat desorption data provided by Toyashima and Xiamen University showed that N_2^* is not the main adsorption species under the conditions of ammonia synthesis at 400°C–450°C; (iii) Ertl[20] provides a powerful support for the dissociation adsorption of N_2 by the following results from energy spectroscopy:

Based on molecule adsorption of N_2, the reaction mechanism is as follows,

$$H_2 \overset{K_1}{\longleftrightarrow} 2H^*,$$

$$N_2 \overset{K_2}{\longleftrightarrow} N_2^*,$$

$$6H^* + N_2^* \longleftrightarrow 2NH_3.$$

Based on dissociation adsorption of N_2,

$$N_2^* \overset{k_3}{\longleftrightarrow} 2N^*,$$

$$N^* + 3H^* \overset{k}{\longleftrightarrow} NH_3.$$

By using steady-state approach,

$$\frac{d[N^*]}{dt} = k_3[N_2^*] - k[N^*][H^*]^y = k_3K_2P_{N_2} - kK_1^{y/2}[N^*]P_{H_2}^y = 0,$$

$$[N^*] = k'\frac{P_{N_2}}{P_{H_2}}.$$

The relation between [N*] determined by Aüger energy spectroscopy and p_{H_2} illustrates that the adsorption of N_2 on the surface of ammonia synthesis catalyst was dissociated. If its adsorption was in molecular state, N* should be independent of p_{H_2} and was constant, as it plays no role in kinetics.

N_2 adsorption on Fe catalyst was investigated with molecule beam experiment by Rettner and Stein.[21] They found that the dissociation coefficient S_0 of N_2 was about 10^{-6} at low incident kinetic energy, up to 10^{-2} at 1 eV (1 eV = 1.60×10^{-19} J) of incident kinetic energy and 0.1 which was the saturation value at 1.5 eV. For Ru,[22] W,[23] Re[24] etc., similar results were obtained, as shown in Fig. 2.14.

The fact that the dissociation coefficient of N_2 increases with incident kinetic energy indicated that activation energy was required for the dissociation of N_2. If the energy possessed by N_2 molecule exceeds the activation energy required for the dissociation of N_2 molecule, it would dissociate directly into atoms. The effect of temperature on metal surface on dissociation coefficient is much smaller than that of incident kinetic energy. However, dissociation coefficient decreases with temperature on iron surface at the same incident kinetic energy, which is so-called negative temperature effect. But for metal Re, the effect of temperature is positive. The explanation given by Katz *et al.*[25] is that they are different in atom weight. After the collision between Fe and N_2 molecules, Fe atoms migrate along

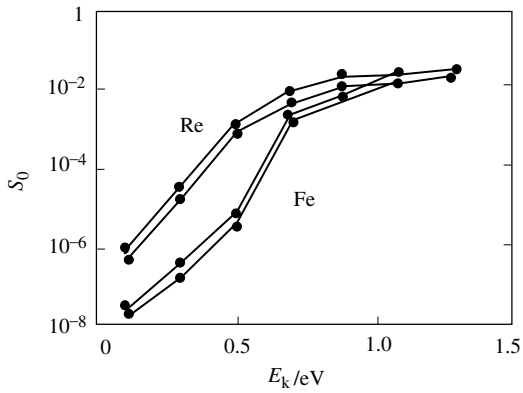


Fig. 2.14 Relation between the dissociation coefficient of N_2 and incident kinetic energy obtained by molecule beam experiments for Fe and Ru

surface because atom weight of Fe is smaller, leading to the decrease of the energy obtained by N_2 molecule for dissociation. Liu *et al.*[26] studied the behavior of N_2 adsorption–desorption on fused iron catalysts with various precursors and found that the magnitudes of activation energy of N_2 desorption (E_d) and reaction activation energy of ammonia synthesis (E_r) are very close and their order are the same, as shown in Chapter 3, Table 3.20. This fact indicates that the dissociation adsorption of N_2 is the rate-determining step of ammonia synthesis reaction. Futhermore, the peak temperature of nitrogen desorption is 842 K over activated $Fe_{1-x}O$ catalyst. The results obtained by Vandervell *et al.*[27] show that there are two forms of adsorbed nitrogen: The desorption peak temperature at 120 K is assigned to the desorption of adsorbed nitrogen N_2(ad), and that at 800 K–820 K assigned to the desorption of N(ad), which is in agreement with the results given by Liu *et al.*[26] This agreement implies that the desorption peak of nitrogen comes from desorption of the dissociatedly adsorbed N (ad) on Fe (111) face. Usually, the adsorption of N_2 mainly takes place over Fe (111) crystal face.

(2) The dinitrogen adsorption is also supported by many experimental results: (i) N_2^+ over iron catalyst without K_2O promoter was detected by field emission mass spectroscopy; (ii) the experimental results from isotope exchange obtained by Morikawa and Ozaki showed that there still exists dinitrogen adsorption state until 380; (iii) the spectroscopic lines of adsorbed N_2H_x were detected by infrared experiments of Birll; (iv) the kinetic data given by Ertl demonstrated that the rates on single crystal iron are at least two orders faster for dinitrogen adsorption than for nitrogen dissociation adsorption.

A lot of surface science investigations on N_2 adsorption processes over Fe (111) crystal face have been carried out by Ertl *et al.*[28,29] and Fig. 2.15 is one of their achievements. There are two weak molecular adsorption states γ and α, whose desorption temperature were 98 K and 160 K, respectively. The sticking coefficients were $\sigma_\gamma \geq 0.7$ for γ state, indicating that it comes from physical adsorption, and $\sigma_\alpha = 10^{-2\pm0.5}$ for α state. Obviously, under certain conditions, γ state could transform to α state, even to dissociation state β. Ertl *et al.* measured the sticking coefficient σ_β of β state at a temperature range of 214 K to 423 K and found that

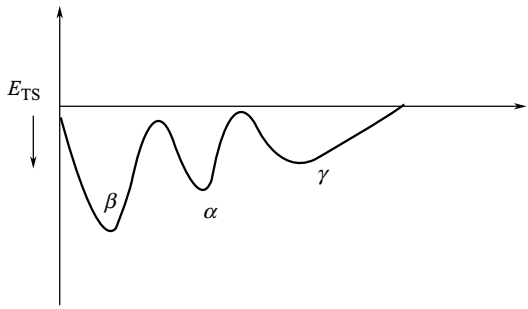


Fig. 2.15 Potential profile of N_2 adsorption and dissociation potential on Fe (111) face obtained by surface science experiments

its value decreases slightly with temperature.

$$\sigma_\beta = V_\sigma \exp\left(\frac{-E_{TS}}{RT}\right), \tag{2.21}$$

where $V_\sigma = 2.2 \times 10^{-6}$, $E_{TS} = -0.034\,\text{eV}$. Negative E_{TS} values indicate that the maximum energy required for the transformation from α to β adsorption states is lower than that of gas molecule.

The coverage of nitrogen atoms over iron surface was measured on XPS by Alstrup *et al.*[30] The initial sticking coefficients were determined on Fe (111) face by exposing N_2 and by changing temperature and pressure of N_2. They found that initial sticking coefficients in the range of 393 K–578 K and pressure of 1.33×10^{-2} Pa–6.65×10^4 Pa is independent of gas temperature, which showed that the dissociation of N_2 is conducted through an intermediate state whose temperature is that of metal surface rather than gas temperature. At high temperatures and high pressures, an adsorptive state with 5×5 structure can form on iron surface.

The energy pathway for adsorption of N_2 on Fe (111) face was estimated with density function theory (DFT) by Mortensen.[31] It was found from their results that there exist five adsorption states on Fe (111) face, and four of them are in molecular form and aother one in atomic form. The scheme is given in Fig. 2.16.

It can be seen from Fig. 2.16 that there are two adsorption states orthogonalized with the iron surface. The combination between iron atoms and adsorbed N_2 on top of its first layer is the closest, corresponding to physical adsorption state γ. N_2 adsorbed on top of second iron layer is not so closely linked and is called as δ adsorption state; its energy is higher than that of 0.14 eV. In addition, there exist two adsorption states parallelized with iron surface: α state with asymmetrical structure and α' one with symmetrical structure. There are two ways for the transformation of molecular nitrogen adsorption states to atomic nitrogen adsorption one is $\gamma \rightarrow \delta \rightarrow \alpha \rightarrow \alpha' \rightarrow \beta$ which has no enthalpy change but has much entropy change; others form α' state directly and then dissociates into β state with large energy change. Mortensen thought that the first way was dominent. α' state only exists in calculation and not in experiment, probably due to its short lifetime.

The reaction investigation of ammonia synthesis on iron catalysts by laser Raman and *in situ* FT–IR spectroscopy showed that[32,33] the main chemisorbed species were molecular state N_2(ad) rather than atomic one N (ad). The analysis with AES by Spencer *et al.*[34] showed that N (ad) was of very high coverage on

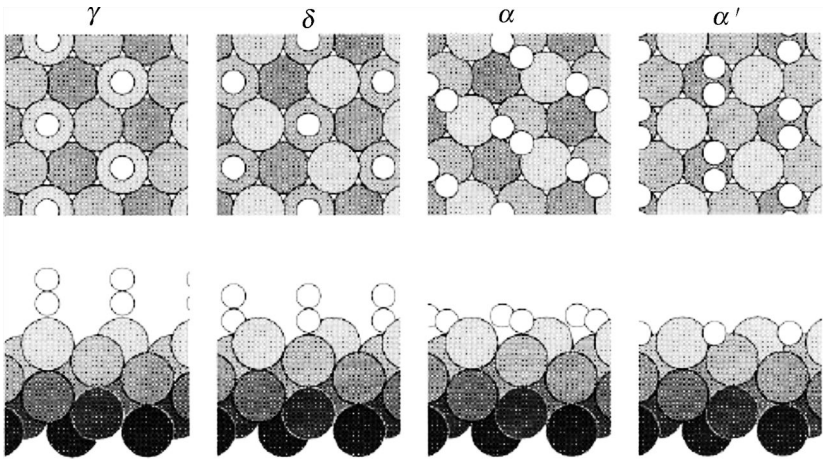


Fig. 2.16 Schematic drawing of N_2 adsorbed on Fe (111) face (upper: Vertical view, lower: Side view)

the surface of iron catalysts at high pressures, implying that nitrogen dissociation was not a rate determining step. Liao *et al.* indicated that[35] it was possible that chemisorbed N_2(ad) molecules on the surface of iron catalysts underwent reorientation to dissociation under reaction conditions. However, the process cannot be completed because there exist many chemisorbed hydrogen which can lead to the occurrence of symmetrical and asymmetrical hydrogenation and hydrogenolysis reactions to form ammonia for activated adsorbed N_2(ad) rather than dissociated atomic nitrogen. At local active sites that was in lack of chemisorbed hydrogen, minor N_2(ad) can be dissociated and then hydrogenated to form ammonia. Cai *et al.*[36] also indicated that the reaction mechanism for ammonia synthesis could be a combined mechanism in which the addition reaction between chemisorbed nitrogen and chemisorbed hydrogen was considered as a rate determining step, which was a main reaction pathway while a competition reaction pathway proceeded according to dissociation mechanism.

Recently, the various mechanisms mentioned above were summarized.[37] The key point was placed on the specific energy way and reaction conditions. In addition, N_2 adsorption was compared with the dissociation adsorption of O_2 on the surface of Ag. The results showed that nitrogen was dissociated under the conditions of industrial ammonia synthesis and not dissociated but was activated under some experimental conditions.

To synthesize the molecular orbit theory and complex coordination valence bond theory, the explanation for the catalysis of iron is as follows: The electronic assignment in the most outer layer of Fe atom is $3d^6 4s^2$ and there are empty orbits 4p and four half-filled d orbits. The multi-symmetry existent is possible for d orbits as it can take multi-orientation in space. There exists s, p disturbance in the molecular orbits of N_2 and the configuration of its molecular valent electron is $(1\sigma_g)^2(1\sigma_u)^2(1\pi_u)^4\ (2\sigma_g)^2(1\pi_g)^0$, in which $(1\sigma_g)^2$ and$(1\sigma_u)^2$ are weak bonding orbit and weak anti-bonding one, respectively, and there is a symmetrical match and close energy between the empty anti-bonding orbits $(1\pi_g)^0$ and d_{xz} orbits of Fe atoms. The d electron in Fe atoms can back-feed to empty anti-bonding orbits

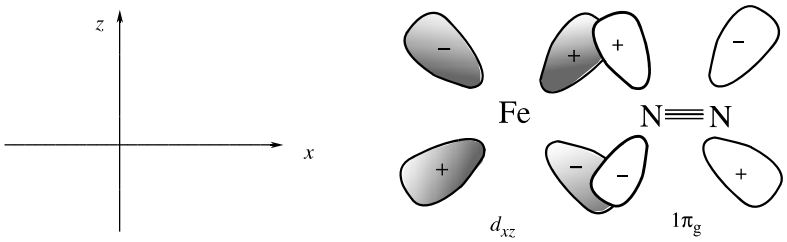


Fig. 2.17 Feedback π bond formed from Fe and N_2

$(1\pi_g)^0$ of N_2 to form so-called "feedback π bond" when N_2 molecules approach the surface of catalysts. At this moment, a transient state with Fe–N–N structure is formed from Fe and N_2 molecules, which weakens the strong bonding interaction between $(1\sigma g)^2$ and $(1\pi u)^4$ and activates N_2 molecules. Meanwhile, it can keep off a lot of accumulation of negative charge on metal atoms which can lead to unstable states. This abridged generai view is shown in Fig. 2.17.

2.2.5.3 *Infrared spectroscopy study of nitrogen adsorption*

The nitrogen adsorption states were studied by various instruments and spectroscopy techniques. Table 2.1 lists some infrared spectroscopy data of nitrogen adsorption.[38] The adsorbed species observed at room temperature could be desorbed at high temperatures, which is short-lifetime intermediate species in ammonia synthesis. As mentioned above, if nitrogen must be dissociated before reaction with hydrogen, in reaction mechanism, the main adsorbed species N (a) is more important than the species N_2 (a). However, N_2 (a) also can give important information, i.e., how N_2 is activated and converted to dissociated adsorbed species N (a).

Ni is used to be considered inert for N_2 chemisorptions. However, the activated adsorbed nitrogen molecules on Ni/SiO_2 were found by IR and disappeared at vacuum and 303 K. The experiments of isotope exchange for adsorption state by IR tracking (2,195 cm^{-1}, 2,160 cm^{-1} and 2,123 cm^{-1} for ^{28}N, ^{29}N and ^{30}N, respectively) demonstrated that adsorption is in molecular form and belongs to $Ni–N{\equiv}N^+$.[39] Later, it was found that these species can only be detected by IR on 1.5 nm–7.0 nm of Ni particle supported SiO_2. The effect of particle size can be interpreted as follows: When the range of particle sizes is in 1.5 nm–7.0 nm, the concentration of B5 active sites (upside down square pyramid) is the maximum.[40] The similar activated species were also observed by IR on other metals. These adsorption bands are also demonstrated to be attributed to diatoms[41] by isotope displacement[39,42,43] and first order desorption kinetics. Comparing to CO adsorption, these bands are of high delustering coefficient, indicating the adsorption on terminal group rather than side group.[44]

The formation of weak adsorption was interpreted as the interaction of electric field.[39] But later discovery reveals the chemical nature of adsorption: (i) the initial adsorption heat on Ni surface is considerably high (50 kJ mol^{-1}); (ii) the change of IR wave number is quite large; (iii) the effect of hydrogen leads to shift of the wavenumber towards high direction.[39–42] The wavenumber for the deviation of adsorption band is 2,123 cm^{-1} and the adsorption degree of gas dinitrogen can be

Table 2.1 Infrared spectroscopy data of nitrogen adsorbed on metal

Metal	Support	Wavelength/ cm^{-1}	Difference from dinitrogen gas/cm^{-1}	Adsorption heat/ $kJ \cdot mol^{-1}$
Fe	Al_2O_3	2,200	131	—
	MgO	2,200	131	—
	MgO	2,050	281	—
Co	Al_2O_3	2,214	117	—
Ni	SiO_2	2,202	129	50
	SiO_2	2,202	129	—
	SiO_2	2,195	136	—
	SiO_2	2,202–2,220	129–111	—
	evaporation	2,202	129	—
Ru	K-Al_2O_3	2,020	311	—
	—	1,935	396	—
	SiO_2	2,240	111	—
	Al_2O_3	2,214	117	—
	MgO	2,168	163	—
	CsOH/MgO	1,910	421	—
Rh	SiO_2	2,236	95	—
		2,255	76	—
	Al_2O_3	2,257	74	9
		2,252	79	—
	TiO_2	2,254	77	49
Pd	Al_2O_3	2,260	71	—
Ir		2,185	146	17
Pt	SiO_2	2,230	101	—
	SiO_2	2,230	101	15
	Similar to Pt black	—	—	18
ZnO	—	2,337	–6	19
Na-A-Zeolite	—	2,339	–8	
$\eta-$ Al_2O_3	—	2,360	–29	46
TiO_2	—	2,337	–6	11
	—	2,348, 2,340	–17, –9	25
ZrO_2	—	2,341	–10	—
SiO_2	—	2,329	2	—
BeO	—	2,350, 2,337	–19, –6	—
SiO_2- Al_2O_3	—	2,357	–26	31
H-mordenite	—	2,356, 2,335	–25, –4	—

used for the strength measure of M–N bond on metal surfaces. On the other hand, the very weak interaction between metal and nitrogen has no effect on the strength of N–N on metal oxides in which the wavenumber of IR absorption peak is higher than common N≡N bond. The examples are ZnO, zeolites, TiO_2 and ZrO_2.

Although iron is a well-known metal for the activation of nitrogen molecules, only at high temperatures and on iron surface treated by ammonia or a mixture of N_2–H_2, the similar species can be observed by IR. It can be seen from the deviation of gaseous dinitrogen adsorption band 2,123 cm^{-1} that the adsorption strength on Co/Al_2O_3 was affected by hydrogen co-adsorption,[45] on Ru/Al_2O_3 by the position of oxidation state ruthenium and on Pt/SiO_2 by other elements such as Ag.

A stably activated dinitrogen molecular species at 2,020 cm^{-1} is found by IR on $Ru–K/Al_2O_3$ at 473 K after N_2 treatment and can be converted to ammonia in the

co-existence of hydrogen.[46] If $^{15}N_2$ is used, IR wavenumber shifts to 1,997 cm^{-1}. The above adsorbed species could be a new K–N_2 complex and might be a by-product rather than intermediates beacuse an infrared absorption is observed at 2,020 cm^{-1} when ammonia is decomposed over Al_2O_3–K (no ruthenium) at 623 K. Recently, a spectrum related to the intermediate species was observed on activated ruthenium. The shift of isotope exchange demonstrated that these species were terminal group adsorption (Ru–N ≡ N), and the wavenumbers are 1,910 cm^{-1} for Ru–CsOH/MgO, 2,214 cm^{-1} for Ru/Al_2O_3 and 2,240 cm^{-1} for Ru/SiO_2, comparing with the adsorption of gaseous dinitrogen, shifts are 421 cm^{-1}, 136 cm^{-1}, 117 cm^{-1} and 111 cm^{-1}, respectively. These data can be used for the measurement of N_2 activation, N≡N bond loosing, donating electron degree and interaction between ruthenium and supports or promoters.

2.2.5.4 *The study of electronic energy spectroscopy for nitrogen adsorption*

The investigation on adsorbed species by electronic spectroscopy has advanced rapidly in recent years. The electronic states of the most outer atoms of solid surface can be measured by AES and XPS. Therefore, they can be used for the study of adsorbed species. A single adsorption peak was observed at 385 K when dinitrogen molecules adsorbed on Mo at 83 K or on Fe at 373 K (prospective adsorption as molecule state). But if the adsorption happened at 373 K on Mo or 673 K on Fe, three peaks were observed. Mo has three similar adsorption peaks, so the species observed at high temperatures belongs to the atomic nitrogen.[47]

The similar Auger spectrum was detected for the N_2 adsorption on W (110) at 100 K. The amount of adsorbed dinitrogen can be estimated from the height of Auger spectroscopy peak such as 390 eV peak for W (Ref. 48) and 380 eV peak for Fe.

At a temperature of 100 K or less there are two adsorption peaks — 400 eV and 406 eV — on W, Ni and Fe, and they are assigned to: (i) N_2(ad)-W for 406 eV and to N(ad)-W for 397 eV, as the former disappears but the latter still exists at 300 K; (ii) two types of N_2(ad), i.e., terminal group and bridge form; and (iii) two terminal group adsorption of atomic nitrogen, i.e., W ≡ N ≡ N and W ≡ N.

It is commonly accepted that the atomic adsorption nitrogen could form peaks at about 400 eV. For example, the adsorbed N on W at 300 K has two peaks at 397.2 eV and 398.0 eV, one peak at 397.2 eV on Fe at 290 K, and one peak at 397.5 eV on Fe with promoter at 673 K. The surface reconstruction caused by nitrogen adsorption was observed for many metals.

It is still uncertain whether the nitrogen adsorption on iron surface is dissociated or not. Most researchers agree that the adsorption is dissociated as the activation of tri-bond of N ≡ N structure is more difficult, and the molecule adsorption cannot work for synthesis of ammonia. A great deal of experiments showed that the adsorption of dinitrogen and the formation of ammonia are all intimately related to (111) crystal face of α-Fe, which is one of low Miller index faces with the sparsest configuration of atom. The highly selective adsorption of dinitrogen on various crystal faces of Fe implies that the active sites for adsorption of N_2 are multi-core, not single-core. The nature of dinitrogen adsorption is still a very important subject in the study of ammonia synthesis reaction.

2.2.5.5 *The study of adsorption of N_2 on non-iron metals*

(1) Ru, Os — The detailed investigation on N_2 adsorption and the hydrogenation of adsorbed nitrogen on Ru metal powder has been carried out.[49] The activity of 1 g Ru powder ($0.1 m^2 \cdot g^{-1}$) for ammonia synthesis is 0.011 mmol $NH_3 \cdot h^{-1} \cdot g^{-1}$ for N_2+3H_2 reaction at 573 K and 101 kPa. If inhibition of ammonia is ruled out, the activity of 1 g Fe powder ($0.1\ m^2\ g^{-1}$) will be 0.040 mmol $NH_3 \cdot h^{-1} \cdot g^{-1}$ under same conditions. Therefore, reaction activity of Ru seems lower than that of iron, as the reaction rates of Ru is inhibited by hydrogen adsorption. When the ratio of H_2/N_2 decreases, the activity of Ru is higher than Fe because the adsorption rate of nitrogen jumps due to the decrease of hydrogen inhibition. The adsorption rate of nitrogen on Ru was estimated to be 40 mmol$\cdot h^{-1} \cdot g^{-1}$ at zero coverage of N_2 and $[N_2] = 2.7$ kPa at 573 K in the absence of hydrogen. Therefore, the intrinsic activity for N_2 activation on Ru is 10^3 times higher than that of Fe, if there is no hydrogen. The hydrogenation rate of adsorbed nitrogen on Ru at above 413 K is so fast that the rate is controlled completely by the flow rate of H_2 and equilibrium pressure of ammonia and the actual rate of hydrogenation of adsorbed nitrogen only can be conducted at low temperatures (203 K–298 K). The rates of N_2 adsorption and hydrogenation of adsorbed nitrogen on Ru catalyst are faster than that of Fe. However, because of effect of hydrogen adsorption, their reaction rates are comparable.[49] The ammonia synthesis with the presence of only N_2 or H_2 confirmed this view.[50,51]

The rate expression for ammonia synthesis on 1g of Os powder catalyst (7.5 mmol sites per gram) is as follows[52]:

$$V_s = k_s \frac{[N_2]}{[H_2](1 + K[NH_3])^2}. \tag{2.22}$$

It indicates that the rate is inhibited by both H_2 adsorption and NH_3 and is relatively less insignificant than Ru. If N_2 adsorption is the rate determining step, hydrogenation rate of adsorbed nitrogen is also very fast at 473 K, which is very similar to Ru catalyst. The ammonia synthesis rate, i.e., N_2 adsorption rate, at one bare site of Os is 100 times faster than that of Fe and 100 times slower than Ru at 473 K. But the ammonia synthesis rate of Os is 100 times slower than Fe powder at the conditions of 101 kPa, 673 K and mixture gas with chemical stoichiometric ratio.[52]

The isotope exchange rates over Ru catalysts (Ru–K,Ru–K/Al_2O_3,Ru–K/AC (Ref. 53) and Raney Ru–$CsNO_3$(Ref. 54)) are inhibited by hydrogen, which is related to the inhibition of hydrogen for adsorption of nitrogen on Ru powder[49] or the negative power for hydrogen pressure in reaction rate equation of ammonia synthesis. For Raney Ru promoted with $CsNO_3$ (one of ammonia synthesis catalysts with the highest activity), the isotope exchange rates are proportional to $(1+b\ [H_2]^{0.5})^{-2}$ (Ref. 54). The isotope exchange rates of nitrogen on Ru go up with the increase of temperature. For example, for Ru–K/Al_2O_3 catalyst, it increases from 0.26 to 0.45 when the temperature increases from 553 K to 593 K and from 0.44 to 0.79 if temperature increases from 593 K to 653 K on Ru–K catalyst. In addition, ammonia synthesis over Ru/Al_2O_3 catalyst at 653 K–713 K is first order reaction.[53] The kinetic equations for Ru–K and Ru–Al_2O_3 catalysts could be derived from Langmuir's dissociation adsorption mechanism as follows:

$$V = k \frac{[N_2]}{(1 + K^{0.5}[NH_3]^{0.5})^2}. \tag{2.23}$$

The N_2 chemisorption heat on Ru–K estimated from the equilibrium constant by the above equation is 167 kJ·mol^{-1}. But, it is worth noting that the isotope exchange and chemisorption of nitrogen over iron catalysts with K promoter are strengthened by hydrogen adsorption,[55] and none of this kind of effect was observed on pure iron catalyst.[56,57] But the phenomena are also found over Ru catalyst with rare earth promoters.[58] The reasons of the phenomena is not clear yet, but it seems to depend on the kinds of supports and promoters for Ru catalysts, which is of important guiding meaning for the study of Ru catalysts at high pressures.

It is worth noting that the effective adsorption of nitrogen is impossible at high temperatures for very clean single crystal Ru (0001), and the sticking coefficient of dissociated nitrogen adsorption is very small. No nitrogen desorption peaks could be observed at 400 K–760 K after exposing Ru crystal to 10 L of N_2.[59,60] However, for molecular adsorbed species there is very high sticking coefficient (about 0.4) for Ru (001) at 78 K. Two structures of adsorbed species could be assumed based on the correlation between special coverage and sticking coefficient at 78 K.[61,62]

(2) The desorption rate of adsorbed nitrogen on the films of W or Mo does not change with temperature although TPD or heat desorption spectroscopy could give their (W, Fe, Mo, Re) adsorption states. Three desorption peaks (α, β, γ) of adsorbed nitrogen on W, listed in Table 2.2, were observed in TPD spectra and characterized their forms and features of adsorbed species. It can be learned from γ and α states that their first-order desorption kinetics depends on the nitrogen coverage and activation energy is lower, indicating that the adsorption is single molecule or diatoms. This was confirmed by isotope experiments of N_2 adsorption in which no isotope was detected in desorption N_2 after preadsorption of $^{28}N_2$ and $^{30}N_2$.[63,64] On other hand, it is considered that β state following second desorption kinetics was dissociated adsorption, has higher activation energy and the isotopes were detected during adsorption/desorption experiments.[65–69]

Table 2.2 lists the TPD data obtained on the surface of single crystal W. From weaker interaction between adsorbed nitrogen and surface W atoms, it can be concluded that γ state occurs for all three W faces (100),[68] (110)[70,71] and (111)[72] and α only for (111), confirmed by FEM[68] and pore-probe emission spectroscopy.[72] There is also much difference in values of N_2 sticking coefficients: 0.3–0.6(Refs. 73–75) for (100) face, 0.01–0.005 for (110) and 0.08 for (111), confirming that β adsorption

Table 2.2 Adsorption states of nitrogen on W (Ref. 55)

Parameters	γ-state	α-state	β-state
Desorption temperature/K	About 150	About 300	About 1,000
Desorption energy/kJ·mol^{-1}	8–40	80	300–320
Desorption kinetics	First order	First order	Second order
N_2 isotope mixture	No	No	Yes
Supposed states	Molecular state	Molecular state	Atomic state
(110) crystal face selectivity	Configuration	No	A little
Desorption energy/kJ·mol^{-1}	< 38	—	330
(111) crystal face selectivity	Configuration	Configuration	A little
Desorption energy/kJ·mol^{-1}	38	67	314
(100) crystal face selectivity	Configuration	No	Configuration
Desorption energy/kJ·mol^{-1}	38–44	—	314–334

Table 2.3 Sticking probability at zero converge (s_0) at 300 K of nitrogen on vatious W planes[55]

Crystal face	s_0	Crystal face	s_0
(110)	$< 10^{-3}$	(411)	0.31
(211)	$< 10^{-2}$	(210)	0.25
(321)	$< 10^{-2}$	(311)	0.29
(111)	Ca.10^{-2}	(100)	0.4
(310)	0.28	—	—

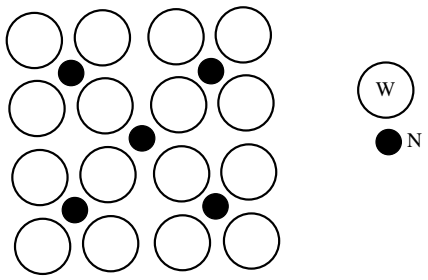


Fig. 2.18 Surface structure of W (100) with nitrogen atoms

state is mainly on W (100) face (see Table 2.3). The desorption activation energies are also included in Table 2.2.[76] Adams and Germer demonstrated by LEED that β nitrogen atoms on (100) mainly located at the interstitial position surrounded by four tungsten atoms, as shown in Fig. 2.18.[73,77]

The sticking probability (s) (adsorption rates obtained by separating collision flux) and coverage (θ) on W single crystal face were studied. The initial values of s obtained on bare surface with four layer symmetry positions as (100) face were as high as 0.3–0.4 (Table 2.3 and Fig. 2.18). Its location was in opposite of single crystal iron. The molecular beam experiments showed that the priority of dissociation occurred for adsorbed species in empty location on W (100) faces.[75,78] A convex curve appeared for $s \sim \theta$ curve on polycrystal slice in which s value decreases with θ at low coverage and then increases fast with θ. If s is independent of θ and keeps constant, indicating that the life time of precursors is so long that it can be transformed to chemisorption state before being desorbed. Concerning with chemisorbed nitrogen on W (100) face, its adsorption heat is 43 kJ·mol^{-1} (Table 2.2), but it is difficult to determine the precursor of γ state. s is a function of θ i.e., $s = \alpha Z/[1 + k_d/Kf(\theta)]$, showing the process as follows:

$$N_2(g) \underset{k_d}{\overset{\alpha z}{\rightleftharpoons}} N_2(a) \underset{}{\overset{kf(\theta)}{\rightleftharpoons}} 2N(a),$$

where α is a concentrated coefficient, Z is collision flux, k_d is desorption rate and k is conversion rate constant. The experimental value of s was about 0.4 and the activation energy of k about 39 kJ·mol^{-1}(Ref. 79) at the temperature range of 190 K–600 K. For N_2 on W (111), s decreases linearly with θ, showing that it is chemisorbed directly with molecules (α state) and there exists no precursors [78]. The adsorption and decomposition of ammonia on clean W (100) face were studied

by XPS and UPS and a comparison was made between the results and those came from that of c (2×2)-N on W (100).[80]

Although the affinity between clean W surface and N_2 is very strong, its catalytic activity is not high in ammonia synthesis. Part of W surface is converted to tungsten nitride (WN) under the conditions for ammonia synthesis, so the reaction rate depends on the dynamic equilibrium between the formation of nitride and its hydrogenation.

The states of similarly adsorbed nitrogen were studied by thermal desorption technique on the surface of Mo–W[81–84] and Re–W.[85] The desorption heat of adsorbed nitrogen measured were $41\,kJ{\cdot}mol^{-1}$ for γ states on Mo (100), $364\,kJ{\cdot}mol^{-1}$ (Ref. 82) for β states on Mo (100), and $364\,kJ{\cdot}mol^{-1}$ for β state on Mo (110). The β state on Re single crystal was considered to be an intermediate for ammonia synthesis.

For Mo single crystal, Mo (111) can be transformed to Mo (433) at 850 K, and the coverage of adsorbed nitrogen atoms on it can be up to 0.35 and sticking coefficient of 0.05 which is less than that on Mo (100). The fact that coverage is independent of sticking coefficient can be interpreted by the formation of superstructure with island-shape on the surface.[86] The rate of N_2 isotope exchange over KMo_2N ($5\,m^2/g$) at 725 K–774 K was measured to be 0.85×10^{11} mol N_2 $(cm^2{\cdot}s)^{-1}$ at 748 K and 21 Torr of p_{N2}, and the rate of ammonia synthesis was estimated to be $0.68 \times 10^{11}\,mol\,N_2$ $(cm^2{\cdot}s)^{-1}$ assuming that there was the same intermediates of adsorbed nitrogen. The very good agreement between this rate data and experimental value of $(0.75 \times 10^{12}\,mol\,N_2$ $(cm^2{\cdot}s)^{-1})$ at 748 K, 760 Torr and $N_2{+}3H_2$ implies that the rate determining step is dissociated adsorption and desorption of nitrogen.[87]

The sticking coefficient is about 0.9 for N_2 adsorption on Re (0001) and Re (1120) faces at low temperatures (∼80 K).[88] The bond between adsorbed nitrogen and the catalyst surface was considered to be vertical to the molecular axis.[89] The probability of dissociation process is between 10^{-2}–10^{-6} at high temperatures (∼218 K) and depends on the concentration of surface defects. Two molecular forms (β and γ) were considered as precursors for dissociation.[90]

Metal nitrides, in particular V and Mo nitrides, seem to accelerate the rate of nitrogen chemisorption and slow hydrogenation rate of adsorbed nitrogen. In fact, N_2 chemisorption rate is very fast on pure Mo even at 580 K, but it deceases rapidly with the increase of adsorption nitrogen or nitrides. Therefore, this rate is much less on Mo_2N than Mo. Even for Fe, it was reported that ammonia decomposition rate was two orders smaller on iron nitride (Fe_4N) than pure iron.[91]

Kinetic study showed that N_2 chemisorptions were rate determining step for nitride formation, and this was confirmed by the observation that there was no isotope mixture of N_2 on Mo_2N.[92] In this experiment, the content of ^{15}N in product ammonia collected in trap is always lower than that in N_2, showing that, exchange reactions take place between the nitrogen in Mo_2N bulk and adsorbed nitrogen or nitrogen in ammonia. Furthermore, reaction rate of ammonia formation is as low as the predicted value.[92] Assuming that there are the same rate determining step for ammonia synthesis and isotope exchange, the ammonia synthesis rate can be estimated from isotope exchange rate and the values estimated are in very good agreement with observed values on Mo_2N.[87]

(3) Ni, Pt, Rh, Pd, Ir and Cu – The rate determining steps for ammonia synthesis and decomposition on Ni powders were studied at 743 K by trace isotope method (isotope amount was measured), and the slowest step is always the dissociated adsorption and desorption.[93] The N_2 adsorption amount on Ni powder is small at 523 K–573 K. Therefore, it can be inferred that adsorbed nitrogen on Ni is in atomic state.[94] There are two heat desorption peaks at 470 K (low temperature peak) and 800 K (high one), indicating that the adsorption of nitrogen is dissociated on Ni (110) face. Nitrogen desorbed at 591 K gives an Auger peak at 380 eV and its sticking coefficient is very low.[95]

The study on dissociation adsorption of nitrogen on Pt, Rh, Pd and Ir is limited. The sticking coefficient for dissociation adsorption of nitrogen on belt polycrystal platinum is about 10^{-2}. Desorption of dissociatedly adsorbed nitrogen is second-order kinetics at 650 K and its apparent activation energy is 80 $kJ \cdot mol^{-1}$.[96] There are no other reports for nitrogen dissociation adsorption on Pt. N_2 on Pt,[97,98] Pd[99] and Cu[98] can be activated by high frequency emission and heat tungsten filament. N_2 on Rh activated by field emission is dissociated in addition to the molecular form. The adsorbed nitrogen in an atomic form can be produced by electron bombardment[99–101] and NO reduction on Pd.[102,103] On Ir, only at low temperatures (<300 K), adsorbed nitrogen in a molecular form (γ state) can be observed and dissociated form (β state) only can be obtained by electron beam method.[90] Dissociated adsorption nitrogen can also be observed on Raney Ru, Ir and Pt in addition to Raney Fe, Co and Ni.

(4) Alkali metal, alkali earth metal, scandium, lanthanum N_2 isotope exchanges on alkali metal and earth alkali metal nitrides and rare earth metal,[104–107] are summarized in Table 2.4, along with the results studied on kinetic effect of U, Fe and Mo. The migration of nitrogen atoms is a feature of many nitrides. The nitrogen atoms in various layers of many elements in IIA or IIIA groups can take part in isotope exchange of N_2, and even at 573 K the nitrogen in solid phase bulk can also take part in isotope exchange.[107] However, it is worthy to indicate that there is no direct relation between this migration and exchange activity, and the activity seems only to relate to the energy of surface bond M–N i.e., adsorption energy. Isotope exchange reaction is usually accompanied with dissociation adsorption and desorption, and the activation energy is equal to adsorption energy at low coverage levels and to desorption activation energy at high coverage levels. Concerning with nitrides, because its coverage is very high, comparing with adsorption heat, the activation energies in Table 2.4 are more representative of desorption activation energies. The nitrides with low activation energy (or low adsorption heat) are of isotope exchange activity.

It should be pointed out that the activity for nitrides of Sr and Ba is considerably high. Their activity per area is highest in all elements reported. However, the estimated activity per mass of $SrN_{0.5}$ is lower than that of Raney ruthenium and higher than that of 5% Ru–K/AC. The high activity for barium nitride is considered as various nitrides exist on its surface (Ba_2N, BaN and Ba_3N_2) which can lead to elongation of bond to make dissociation easy.[104]

The ammonia synthesis rates over various nitrides were measured.[105] The experimental values of the rates are lower than the values that were estimated from isotope exchange rates after neglecting hydrogen effect. If the nitrides of Ba, Sr, Ca and Li are replaced by their hydrides, the activity will decrease. In the presence

Table 2.4 Isotope equilibration of N_2 on nitrides or metals[55]

Nitrides or metals[a]	Exchangeable N(a) (monolayer)	Reaction order	Activation energy (kJ·mol)	log υ^b (mol/(cm^2/s))	Surface area (m^2/g)	υ^c (μmol/(h·g))
$BaN_{0.62}$	50	0.7	50	12.4	0.1	550
$SrN_{0.5}$	60	0.8	55	12.5	1.1	12500
$UN_{1.70}$	Bulk phase	0.5	105	10.7	—	—
Ru	—	0.7	125	8.6	—	—
Fe	—	0.5	130	10.1	5	82
$CaN_{0.5}$	0.7	0.7	130	9.0	2.2	7.5
CeN	3	0.5	130	8.8	0.9	0.74
Mo_2N	Bulk phase	0.5	155	7.0	5	0.075
Li_3N	Bulk phase	0.4	175	7.5	—	—
α–U_2N_3	Bulk phase	0.5	226	5.1	0.6	0.00021

[a]activity of LaN, PrN and ErN is very low, $MgN_{0.6}$ is inactive.
[b]the rate at $p_{N_2} = 1.3$ kPa, 537 K.
[c]estimated rate at $p_{N_2} = 20$ kPa (150 Torr), 588 K.

of hydrogen, the most active element Sr would become inactive and Ba is also not active. Barium nitrides formed only at the absence of hydrogen have hydrogenation activity. The isotope exchange rate for $UN_{1.70}$ is –0.2 orders with respect to hydrogen.[107] The rate of ammonia synthesis reaction estimated from the data is close to the experimental values of synthesis rates.[105,107] For CeN, hydrogen has no effect on the rate of nitrogen isotope exchange.

It is speculated that N_2 dissociated adsorption occurs over dysprosium at 115 K. XPS results showed two peaks at 396.2 eV and 398.2 eV in N_{1s} range, which can be assigned to nitride and chemisorbed species [N (a)], respectively. Another peak (400.2 eV) corresponding to the molecularly adsorbed species was not detected. N (a) was converted to nitride and covered only 10% of total surface area after heating at 300 K.

2.3 Mechanism of Catalytic Ammonia Synthesis Reaction

2.3.1 *Elementary reactions*

The elementary reactions with elimination of the internal and external diffusion refer to the elementary steps taking place on catalyst surface, generally including adsorption of reactant molecules, surface reactions of adsorbed species and desorption of adsorbed product molecules. There are many surface reaction mechanisms proposed by scientists for catalytic ammonia synthesis reaction. A sequence of elementary steps and microkinetic model were structured and the values of rate constants, pre-exponential factors and activation energies were estimated by means of the collision theory of gas and transient state theory by Stoltz and Norskov,[108−111] and Bowker and his colleagues.[112,113] Initialy, they adjusted microkinetic model with experimental data and then examined their ability to predict the performance of industrial reactors. The rate constants of adsorption and desorption in the mechanism were estimated by Stoltze and Norskov who used the results obtained on single crystal iron at extra-high vacuum by Ertl *et al.*,[114] while the values

Table 2.5 Reaction mechanism and rate expression for ammonia synthesis[115].

Rates of positive reactions	Model I	Rates of reverse reactions
$2\times10^{1}P_{N_2}\theta^*$	$N_2+^*\leftarrow1\rightarrow N_2^*$	$2\times10^{14}e^{-43/RT}\theta^*_{N2}$
$4\times10^{9}e^{-29/RT}\theta^*_{H2}\theta^*$	$N_2^*+^*\leftarrow2\rightarrow2N^*$	$1\times10^{9}e^{-155/RT}(\theta^*_N)^2$
$2\times10^{9}e^{-81/RT}\theta^*_H\theta^*_N$	$H^*+N^*\leftarrow3\rightarrow NH^*+^*$	$1\times10^{7}e^{-23/RT}\theta^*_{NH}\theta^*$
$1\times10^{13}e^{-36/RT}\theta^*_{NH}\theta^*_H$	$NH^*+H*\leftarrow4\rightarrow NH_2^*+^*$	$1\times10^{12}\theta^*_{NH_2}\theta^*$
$4\times10^{13}e^{-39/RT}\theta^*_{NH_2}\theta^*_H$	$NH_2^*+H^*\leftarrow5\rightarrow NH_3^*+^*$	$2\times10^{13}\theta^*_{NH3}\theta^*$
$4\times10^{12}e^{-39/RT}\theta^*_{NH3}$	$NH_3^*\leftarrow6\rightarrow NH_3+^*$	$2\times10^{3}P_{NH3}\theta^*$
$7\times10^{1}P_{H2}(\theta^*)^2$	$H_2+2^*\leftarrow7\rightarrow2H^*$	$3\times10^{13}e^{-94/RT}(\theta^*_H)^2$
Rates of positive reactions	Model II	Rates of reverse reactions
$3\times10^{1}P_{N_2}\theta^*$	$N_2+^*\leftarrow1\rightarrow N_2^*$	$2\times10^{10}e^{-46/RT}\theta^*_{N_2}$
$3\times10^{6}e^{-31/RT}\theta^*_{N_2}\theta^*$	$N_2^*+^*\leftarrow2\rightarrow2N^*$	$3\times10^{12}e^{-199/RT}(\theta^*_N)^2$
$1\times10^{12}e^{-65/RT}\theta^*_H\theta^*_N$	$H^*+N^*\leftarrow3\rightarrow NH^*+^*$	$2\times10^{12}e^{-19/RT}\theta^*_{NH}\theta^*$
$8\times10^{11}e^{-65/RT}\theta^*_{NH}\theta^*_H$	$NH^*+H^*\leftarrow4\rightarrow NH_2^*+^*$	$2\times10^{12}e^{-19/RT}\theta^*_{NH2}\theta^*$
$7\times10^{12}e^{-65/RT}\theta^*_{NH2}\theta^*_H$	$NH_2^*+H^*\leftarrow5\rightarrow NH_3^*+^*$	$2\times10^{12}e^{-19/RT}\theta^*_{NH3}\theta^*$
$1\times10^{13}e^{-53/RT}\theta^*_{NH3}$	$NH_3^*\leftarrow6\rightarrow NH_3+^*$	$2\times10^{2}P_{NH3}\theta^*$
$3\times10^{3}P_{H2}\theta^*$	$H_2+^*\leftarrow8\rightarrow H_2^*$	$2\times10^{13}\theta^*_{H2}$
$3\times10^{12}\theta^*_{H2}\theta^*$	$H_2^*+^*\leftarrow9\rightarrow2H^*$	$3\times10^{12}e^{-92/RT}(\theta^*_H)^2$
Rates of positive reactions	Model III	Rates of reverse reactions
$3\times10^{1}P_{N_2}\theta^*$	$N_2+^*\leftarrow1\rightarrow N_2^*$	$2\times10^{10}e^{-46/RT}\theta^*_{N_2}$
$2\times10^{9}e^{-31/RT}\theta^*_{N_2}\theta^*$	$N_2^*+^*\leftarrow2\rightarrow2N^*$	$2\times10^{9}e^{-144/RT}(\theta^*_N)^2$
$1\times10^{11}e^{-54/RT}\theta^*_H\theta^*_N$	$H^*+N^*\leftarrow3\rightarrow NH^*+^*$	$2\times10^{12}e^{-17/RT}\theta^*_{NH}\theta^*$
$8\times10^{10}e^{-54/RT}\theta^*_{NH}\theta^*_H$	$NH^*+H^*\leftarrow4\rightarrow NH_2^*+^*$	$2\times10^{12}e^{-17/RT}\theta^*_{NH2}\theta^*$
$7\times10^{11}e^{-54/RT}\theta^*_{NH2}\theta^*_H$	$NH_2^*+H^*\leftarrow5\rightarrow NH_3^*+^*$	$2\times10^{12}e^{-17/RT}\theta^*_{NH3}\theta^*$
$1\times10^{13}e^{-53/RT}\theta^*_{NH3}$	$NH_3^*\leftarrow6\rightarrow NH_3+^*$	$2\times10^{2}P_{NH3}\theta^*$
$3\times10^{3}P_{H2}\theta^*$	$H_2+^*\leftarrow8\rightarrow H_2^*$	$2\times10^{13}\theta^*_{H2}$
$3\times10^{12}P_{H2}\theta^*$	$H_2^*+^*\leftarrow9\rightarrow2H^*$	$3\times10^{12}e^{-92/RT}(\theta^*_H)^2$

Note: Unit of rate: molecular numbers · (active site)$^{-1}$ · s^{-1}, Pressure: Pa, activation energy: kJ·mol^{-1}, θ^*: coverage of active sites, θ_i: coverage of active sites occupied by i species.

for surface hydrogenation reaction were approximated qualitatively by estimating relative stability of various surface species NH_x. A series of kinetic parameters were estimated by Bowker *et al.* using the same procedure and using the kinetic data from industrial ammonia synthesis reactor to produce modified kinetic parameters. The kinetic parameters of all elementary steps cannot be determined accurately from reaction mechanism that was in general known incompletely. So, their strategy must be to utilize an applicable reaction mechanism with known key surface chemistry and to estimate the kinetic parameters of the important steps involved in this mechanism. The elementary reactions and rate expressions proposed and their estimation values for analysis of microkinetics are listed in Table 2.5.[115]

The only difference between the similar mechanisms of model I which is proposed by Stolze and Norskov and model II and III by Bowker is the dissociation adsorption of hydrogen from a precursor indicated by reactions 8, 9 and 7, respectively.

Three microkinetic models cannot be distinguished by the kinetic data we have, but the information that could be applied to make better distinguishing of these

microkinetic models comes from the ability of the description and explanation of nitrogen adsorption and desorption kinetics on single crystal iron under extra-high vacuum.

Ertl[114] reported that the sticking coefficients of dissociated nitrogen adsorption obtained on Fe (111) at 430 K were in the range of 5×10^{-6} for clean surface to 4×10^{-4} for optimum surface promoted by K. The values estimated by the analysis of micro-kinetics are 1.4×10^{-5}, 1.2×10^{-4} and 1.2×10^{-2} for model I, II and III, respectively. Obviously, the sticking coefficients predicted by model III is too high.

Ertl *et al.* also reported that the apparent activation energy of the dissociated nitrogen adsorption obtained on Fe (111) promoted by K at near 400 K is –12 kJ·mol^{-1}. The values predicted by these micro-kinetic models are –13 kJ·mol^{-1}, –13 kJ·mol^{-1} and –0.5 kJ·mol^{-1}, respectively for the rate constants of steps 1 and 2 in the mechanism. Thus, the prediction by microkinetic model III is not successful.

Boszo[116] reported the temperature programmed desorption spectroscopy, indicating that the temperature of maximum desorption rate on Fe (111) is at the range of 850 K–890 K. The prediction temperatures by analysis of three microkinetic models are 820 K–870 K, 790 K–830 K and 760 K–820 K, respectively. The value predicted by model III seems too low, but close to the temperatures with maximum desorption rate in the nitrogen temperature programmed desorption experiments carried out by authors[117] on Fe obtained after reduction of $Fe_{1-x}O$-basis catalyst. Possibly, it relates to the catalytic activity.

The results mentioned above show that the kinetic parameters provided by Stolze and Norskov and first set of Bowker, apparently, can successfully describe and explain the surface chemistry in whole range of conditions studied. On the contrary, the second set parameters of Bowker cannot fit data obtained on iron single crystal at extra-high vacuum.

2.3.2 *Catalytic reaction mechanisms for ammonia synthesis*

Catalytic reaction mechanisms represent the elementary steps at molecular level, but the expression in detail at molecular level is difficult for the catalytic reactions on solid surfaces. So, the usual strategy is to propose applicable reaction mechanisms for key chemical processes occurring on catalyst surface, based on a series of assumptions that must be in agreement with experimental data and could be modified indispensably.

A workable reaction mechanism must embrace all reactants, products and reaction intermediates produced and consumed in a catalytic reaction. In gas-phase reactions, two-molecule reaction is popular and three-molecule reaction is very less. For catalyst surfaces, multi-molecule steps become important as the concentration of chemical species is higher than that of gas-phase, and even in this case the reaction between more than three molecules is in general not common.

The availability of the elementary steps in a reaction sequence is usually estimated by the number of chemical bonds broken and formed, and it is not reality that a step involves a change of several chemical bonds. The formation of a reaction mechanism according to the molecular processes taking place on catalyst surface should be based on the kinetic parameters for expression of reaction mechanism which needs trading-off the experimental measurements or theoretical predictions.

The trade-off between detail levels of reaction mechanism and the estimations of kinetic parameter plays an important role in the analysis of microkinetics.

2.3.2.1 *The mechanisms of ammonia synthesis reaction*

Based on the principle of equilibrium state approximation, only one elementary step is the determining step for the three kinetic models listed in Table 2.5. The overall rate of a reaction is determined by the rate of the rate determining step (RDS) with slowest rate, while other steps are approximately in chemical or adsorption equilibrium. There are three opinions or possibilities for the rate determining step of ammonia synthesis reaction on fused iron catalyst: (i) RDS is the dissociation of adsorbed dinitrogen[118]: $N_2(ad) \rightarrow 2N$ (ad); (ii) the surface reaction of adsorbed species[119]: N (ad) + H (ad) → NH (ad); (iii) the desorption of adsorbed ammonia[120]: $NH_3(ad) \rightarrow NH_3(g)$.

Now, it is generally accepted that the dissociated adsorption of N_2 is the rate determining step, because it has been confirmed by many results from surface science experiments.[121] The contradictions about the pathway of nitrogen dissociation adsorption still remains, as different conclusions were obtained from different experimental measures. Meanwhile, there are also different results for different metals and crystal faces under various experimental conditions. Some experiments showed that N_2 was dissociated directly to nitrogen atoms on Fe surface,[122–124] and others found that N_2 were dissociated to nitrogen atoms by intermediates,[124–126] based on fact that the formation of ammonia is through the reaction between atomic nitrogen and hydrogen,[127,128] or between partially activated molecular nitrogen and hydrogen.[129,130] In 1943, Emmett and Brunauer discovered that the chemisorptions of N_2 on iron surface proceeded very slowly and the macro-rate of ammonia synthesis is about the same as the rate of chemisorptions during the reactions of ammonia synthesis.

Scholten measured the BET surface areas and CO chemisorption amount on an activated iron catalysts containing 0.85% Al_2O_3 at adsorption temperature range of 297 K–485 K and desorption temperature of 718 K–480 K, being $5.6\,m^2{\cdot}g^{-1}$ and $33.2\,\mu mol{\cdot}g^{-1}$, respectively. The N_2 chemisorption amount was $16.0\,\mu mol{\cdot}g^{-1}$. So, he proposed that the route of N_2 adsorption on the surface of this iron catalyst is dissociation, and the activation energy of N_2 adsorption was $E_{ads} = 22.0 + 324\theta_N\,kJ{\cdot}mol^{-1}$ ($\theta_N \leq 0.22$), $E_{ads} = 93.28\,kJ{\cdot}mol^{-1}$ ($\theta_N > 0.22$) and that of desorption $E_{des} = 230 - 122\theta_N\,kJ{\cdot}mol^{-1}$.

Napolskikh also considered that the dissociation adsorption of nitrogen was RDS. He found that the following reactions proceeded very slowly:

$$^{14}N^{14}N + {}^{15}N^{15}N = 2{}^{14}N^{15}N$$

$$^{14}NH_3 + {}^{15}N^{15}N = {}^{15}NH_3 + {}^{14}N^{15}N$$

$$2NH_3 = N_2 + 3H_2$$

But the reaction $NH_3 + D = NH_2D + HD$ was relatively fast.

It was observed by labeled atoms ^{15}N that NH_3 and $N{-}^* + 1.5\ H_2$ was in equilibrium, and N_2 and $2\ N{-}^*$ were not equilibrated during ammonia synthesis. The rate of ammonia formation is much faster for $2N{-}^* + 3\,H_2$ than for $N_2{+}3\ H_2$.

Zwietering *et al.* measured the amount of N−* at the conditions of ammonia synthesis by weight analysis and it was 1% of equilibrium adsorption amount over iron catalyst containing 0.85% Al_2O_3 at 0.52–0.69 of surface N−* coverage and 568 K of temperature. Aika and Ozaki further verified that H−* was not a factor in the RDS, by the determination of label atom experiments.

These results clearly indicate that step 2 in the ammonia synthesis procedure is relatively slow and the other elementary steps are in rapid equilibrium.

Temkin and Pyzhev[131] took N_2 adsorption rate as rate determining step of ammonia synthesis (step 1), while the H_2 adsorption (step 2) and nitrogen hydrogenation (step 3) reached equilibrium rapidly.

$$N_2 + {}^* \rightarrow 2N(a) \quad \text{(step 1)}$$

$$H_2^* + {}^* \leftrightarrow 2H(a) \quad \text{(step 2)}$$

$$N(a) + 3H(a) \leftrightarrow NH_3 \quad \text{(step 3)}$$

The rate of N_2 adsorption can be expressed as:

$$V_s = k[N_2]\exp(-g\theta_N), \tag{2.24}$$

where N_2 is partial pressure of N_2; θ_N is coverage of adsorbed nitrogen; k, g are constants.

Assuming that θ_N is a function of partial pressure $[N_2^*]$ of N_2 which was equilibrated with H_2 and NH_3:

$$\theta_N = \frac{1}{f}\ln(A[N_2]^*) = \frac{1}{f}\ln\left(AK\frac{[NH_3]^2}{[H_2]^3}\right), \tag{2.25}$$

where A is a constant and K is the equilibrium constant of ammonia decomposition. Then the reaction rate of ammonia synthesis is:

$$V_s = k[N_2]\left(AK\frac{[NH_3]^2}{[H_2]^3}\right)^{-g/f} = k_s[N_2]\left(\frac{[H_2]^3}{[NH_3]^2}\right)^{g/f}. \tag{2.26}$$

If the rate of N_2 desorption is the rate determining step for ammonia decomposition, similarly the rate of ammonia decomposition is:

$$V_d = k_d\left(\frac{[NH_3]^2}{[H_2]^3}\right)^{1-g/f}. \tag{2.27}$$

Temkin–Pyzhev equations mentioned above was in agreement with a number of kinetic measurement made on various catalysts such as Mo, W, Tc, Ru, Os and promoted Fe. One characteristic feature of ammonia synthesis rate is the retardation by the product ammonia, and reasonably explained by the Temkin theory. The assumption of rate determining step is also supported by the chemisorption of nitrogen.

Although Eq. (2.24) can well interpret experimental data, the experimental value of g/f is not completely constant and is in the range of 0.5–0.8 based on the different temperatures. The reason is that Eq. (2.24) is only valid at moderate nitrogen coverage ($\theta_n = 0.2 - 0.8$). So, the g/h value becomes larger or smaller when the content of ammonia in gas mixture is higher or lower.[132,133] The rate constants of

Temkin equations depend on the ratio of H_2/N_2 or total pressure even at moderate coverage.[134–137] The g/f value obtained from reaction rate is an average value at experimental conditions, rather than an intrinsic constant from theory formulation. However, these equations are applied widely in industrial apparatus for ammonia synthesis over iron catalyst at high-pressures.

If the adsorption of nitrogen is described by Langmuir equation $V = K[\mathrm{N_2}](1-\theta_\mathrm{n})^2$, the rate equation for ammonia synthesis is as follows:

$$V_s = k_s \frac{[N_2]}{(1 + K[NH_3]/[H_2]^{1.5})^2}. \tag{2.28}$$

It can also be applied at low-pressures. If catalysts are tested at atmosphere pressure, their activity or ammonia pressure is very low. Under such conditions, the Langmuir equation can be used.

NH (a) is the main inhibiting species in Eq. (2.28) based on steps (1–3). If NH (a) is the main inhibiting species, then the rate equation of ammonia synthesis can be also written as:

$$V_s = k_s \frac{[N_2]}{(1 + K[NH_3]/[H_2])^2}. \tag{2.29}$$

The rate equation derived from Temkin equation can also be written in a similar form:

$$V_s = k[N_2] \left(\frac{[H_2]^2}{[NH_3]^2} \right)^{g/f}. \tag{2.30}$$

Actually, a power-rate equation can be given very easily in the case of very complicated reaction mechanism.

When the reaction conditions for ammonia synthesis are far from equilibrium, such as at very high space velocities or low temperatures, in which case reverse reaction can be neglected, the overall reaction rates are equal to the rates of nitrogen chemisorption (V_n) or hydrogenation rate of adsorbed nitrogen at steady-state, i.e., that of third step. If

$$V_n = k_n[N_2](1-\theta_N)^2 = k_n[N_2](1-2\theta_N), \quad V_h = k_h[H_2]\theta_N \tag{2.31}$$

and $V_s = V_n = V_h$, eliminating θ_N, we get V_s:

$$V_s = k_n k_h \frac{[N_2][H_2]}{2k_n[N_2] + k_h[H_2]} = k'[N_2]^m[H_2]^n, \tag{2.32}$$

where m and n are apparent reaction orders and $m < 1$, $n < 1$, and $m + n = 1$. Temkin *et al.* found that $m = n = 0.5$ (Ref. 138) of Eq. (2.32) at the conditions far from equilibrium i.e., very high space velocities (about 10^6 $\mathrm{h^{-1}}$) and 627 K–723 K of temperatures. All rates for every elementary step can be well expounded by kinetic method, and the rates measured may be a function of adsorption amount in catalytic processes. It was observed that the rates of hydrogenation were lower than that of nitrogen chemisorption over two-promoter iron catalysts at the conditions of very low-pressure of H_2 and very high reaction temperature.[139]

For ruthenium catalyst, same as iron, it was in general considered that dissociated adsorption of nitrogen was also rate determining step, but the reaction

Table 2.6 Kinetic parameters in ammonia synthesis on various ruthenium catalysts[55]

Form of catalysts	Temperature/K	Pressure/kPa	n	m	a
Ru powder	598	80	0.96	−0.72	−0.15
	553–581	101	1	−1	0[a]
Ru/SiO_2	825–1009	101	1	1.25	−1
	574–671	101			−0.56
Ru/Celite	619–683	80	1	0	0
Ru/Al_2O_3	610–691	101	—	—	−1.0
	638	80	1.1	0.3	−0.74
	500–725	150	1	0.6	—
Ru/MgO	593	80	1	0.66	−0.78
	500–725	150	0.9	0.2	—
$Ru–Cs^+/Al_2O_3$	595	80	1	−0.55	0
$Ru–K^+/Al_2O_3$	500–725	150	1	−0.3	—
$Ru–Cs^+/MgO$	548	80	1	−0.43	−0.12
$Ru–K^+/MgO$	500–725	150	1	−0.5	—
Ru powder–Cs^+	598	80	0.95	−0.9	−0.07
$Ru–K/Al_2O_3$	500–725	150	0.9	−1.1	—
Ru–K/MgO	500–725	150	1.2	−0.5	—

[a]At high flow rates (100 ml–1,000 ml/min).

mechanisms still need to be studied. Aika *et al.* used power function to express the reaction rates of ammonia synthesis over ruthenium catalyst:

$$V_s = k[N_2]^n[H_2]^m[NH_3]^a, \tag{2.33}$$

where n, m and a are reaction orders of hydrogen, nitrogen and ammonia, respectively. The kinetic parameters obtained over ruthenium catalyst by various researchers are listed in Table 2.6. The kinetic parameters of ruthenium catalysts can be classified into three types: (i) catalyst without supporter, (ii) supported catalysts without promoter, (iii) supported catalysts containing alkali metal promoter. The reaction orders of nitrogen are close to one for all three types of catalysts. For catalyst (ii) the orders of hydrogen are positive and negative for ammonia; for type (i) and (iii), the orders of hydrogen are negative and close to zero for ammonia. Activated carbon supported ruthenium catalysts show the similar phenomena. It indicates that the adsorption of hydrogen has strong inhibition, and the reaction rates are decreased with increases of hydrogen pressure. However, the inhibition of ammonia is very weak. On the other hand, the inhibition is very strong by ammonia and very weak by hydrogen for iron catalysts,[140,141] and the degree of inhibition by ammonia depends on promoter type.[142−144] The strong inhibition by H_2 adsorption over ruthenium catalysts will be further discussed in Chapter 6, Sec. 6.3.3.

Under conditions having inhibition effect of hydrogen adsorption, N (a), NH (a) and H (a) can all inhibit the reaction

$$V_s = k[N_2](1 - \theta_N - \theta_H) = k\frac{[N_2]}{(1 + K_1[NH_3]/[H_2]^{1.5} + K_2[H_2]^{0.5})^2}. \tag{2.34}$$

For the convenience of analysis, the equation can be converted into

$$V_s = k\frac{[N_2]}{(K_1[NH_3]/[H_2]^{1.5})^{2y}(K_2[H_2]^{0.5})^{2Z}} = k_s\frac{[N_2]}{[H_2]^{-3y+Z}[NH_3]^{2y}}. \tag{2.35}$$

Table 2.7 Kinetic parameters of NH_3 decomposition according to the equation $V = k(P_{NH3})^m/(P_{H2})^n$ (Ref. 55)

Metals	Temperature/K	Pressure/kPa	m	n	n/m	E_{act}/ kJ·mol^{-1}
VB : V	673–753	Ca.100 (low P_{H2})	0.5	0	0	138
	673–753	High P_{H2}	1.0	1.5	1.5	138
VIB : Mo	1,027–1,273	13.3	0	+	–	134–180
W	548–873	2–20	0–1	–	–	205
	903–1,023	4.7–20	0	–	–	146
	953–1,153	0.1	0	0	–	176
	904–1,214	7–26	0	0	–	163
	1,073–1,523	2–35	0	+	–	146–197
	950–1,150	1–5	0	0	–	113–130
	1,073	10^{-9}–10^{-6}	0.8	–	–	–
VIIB : Re	653–713	ca. 100	0.53	0.89	1.68	134
	728–843	1.3–7	0.7	1.4	2.0	205
VIII : Fe	608–743	1–4.4	0.5	0.7	1.4	163
	653–773	1.3–10.6	0.9–1.0	1.4–1.5	1.5	176–209
	765–797	ca. 100	0.9	1.5	1.67	226
Fe(Al_2O_3-K_2O)	608–703	100	0.6	0.85	1.42	192
	693	13	0.48	0.72	1.5	
	752	13	0.75	0.38	0.5	
Co	643–753	1.3–7	0.85	1.42	1.67	188
Ni	573	0.2–5.3	1.0	1.5	1.5	
	663–773	1.3–7	0.96	1.53	1.59	18
	623–723	4×10^{-3}–0.17	1	–	–	–
Ru	543–738	1.3–7	1.2	2.0	1.67	188
	623–673	80–106	0.6	0.9	1.5	130
	825–1,009	–	1.0	1.75	1.75	247
Rh	693–773	1.3–7	1.35	2.45	1.81	239
Pt	763–833	0.001	1.5–2.0	2.2–3.0	1.5	205
	793–883	1.3–7	0.96	1.63	1.7	247
	978	10^{-5}	0.63–0.84	0.25	0.34	17
	1,045–1,131	Low P_{H2}	1	1	1	167
	1,045–1,131	High P_{H2}	1	0	0	167
	1,100–1,485	0.03–0.5	1	1	1	14
	1,100–1,485	1.3–39	1.4	2.3	1.64	419
	1,206–1,488	13–26	1	1	1	586
	1,173–1,623	ca. 10^{-3}	1	0	0	21
IB : Cu	768–893	5–67	1	1	1	192
	993–1,183	100	1	1.5	1.5	243–259

2.3.2.2 *The mechanisms of ammonia decomposition*

Based on Temkin–Pyzhev mechanisms (steps 1–3), the rates for ammonia decomposition can be expressed by Eq. (2.27), and its kinetic parameters calculated from equation $V = k\,(P_{NH_3})^m/(P_{H_2})^n$ are given in Table 2.7. The value of parameter n/m in Table 2.7 is about 3/2, demonstrating that the Temkin–Pyzhev mechanisms can be used for most metal catalysts, such as Re, Fe, Co, Ni, Ru and Rh, at the common conditions of ammonia decomposition.

However, reaction order of hydrogen is zero for tungsten and platinum catalysts, which should be elucidated by different reaction mechanisms.[145] The ammonia

decomposition over clean tungsten surface was studied directly or indirectly at temperatures of 773 K–1,473 K and ammonia pressure of 10^{-6}–10^{-3} Pa.[146] The reaction orders expressed with pressure of ammonia in rate expression change with temperature, from 1 at 1,473 K to 2/3 at 773 K. There is no hydrogen adsorption above 973 K, and the increase of hydrogen partial pressure has no effect on reaction rates and adsorption amount of nitrogen (θ_N) during reaction process.

The rate of nitrogen desorption from surface increases with θ_N:

$$V_d = k_d \exp(h\theta_N) \tag{2.36}$$

The rate of nitrogen adsorption decreases with θ_N, and increases with the P_{NH3}

$$V_a = k_a P_{NH_3} \exp(-g\theta_N) \tag{2.37}$$

The conclusion obtained from these data is as follows: the overall reaction rate (V_s) comes from dynamic reaction equilibrium between two continuous rate determining steps, $2NH_3 \rightarrow 2N(a) + 3H_2(V_a)$ and $2N(a) \rightarrow N_2(V_d)$:

$$V_s = V_a = V_d = k_d(KP_{NH_3})^{h/(h+g)}. \tag{2.38}$$

It can rationally interpret the reaction orders without hydrogen[146,147] and is in agreement with the observation of isotope effect of NH_3/ND_3 exchange.[148] If the hydrogenation rate of N(a) [$2N(a)+3H_2 = 2NH_3$; V_h] is lower than that of V_d and thus can be neglected, the mechanism(W-Type) is obtained, which was observed over W, Pt, and even Fe catalysts at high-temperatures and low–pressures.[149,150]

The rate of ammonia decomposition over platinum net at 1.3 Pa is in agreement with that of ammonia desorption (rate determining step) at 1,273 K and with that of N_2 desorption at 773 K.[151,152] The kinetics of ammonia decomposition over polycrystal platinum filament was investigated in detail by disturbing steady state method in continuous flow micro-reactor.[149,150,153] The dissociation of first N–H bond during surface reaction determines the rates of ammonia decomposition ($V_h \ll V_d$, W-Type mechanism) at high-temperatures and low-pressures such as 550–1,200 K, 10^{-3} Torr or 550 K–1,400 K, 10^{-6} Torr. The activation energy is 17.6 kJ·mol^{-1} and the decomposition rate are affected by isotope effect. At low-temperatures and high-pressures such as 480 K–550 K, 10^{-3} Torr or 550 K–800 K, 0.5 Torr, the surface is almost saturated by nitrogen and the desorption of adsorbed nitrogen determines overall rates ($V_h \gg V_d$).

Therefore, the rate of ammonia decomposition is independent of P_{NH3} and apparent activation energy of 92 kJ·mol^{-1} is equal to that of nitrogen desorption. The activation energies for adsorption E_a and desorption E_d of elementary steps as well as those in other steps on Pt are as follows[153]:

$$NH_3(g) \Leftrightarrow NH_3(a) \quad \Delta H = -E_d = -50\,\text{kJ·mol}^{-1} \tag{2.39}$$

$$NH_3(a) \rightarrow NH_2(a) + H(a) \quad E_a = 67\,\text{kJ·mol}^{-1} \tag{2.40}$$

$$ND_3 \rightarrow ND_2(a) + D(a) \quad E_a = 72\,\text{kJ·mol}^{-1} \tag{2.41}$$

$$2N(a) \rightarrow N_2(g) \quad E_a = 92\,\text{kJ·mol}^{-1} \tag{2.42}$$

$$N_2 \rightarrow 2N(a) \quad E_a = 67\,\text{kJ·mol}^{-1} \tag{2.43}$$

$$2H(a) \Leftrightarrow H_2(g) \quad E_d = 79.5\,\text{kJ·mol}^{-1} \tag{2.44}$$

These data can be used for the construction of one dimension potential pattern of the reaction, assuming that the adsorption of ammonia is *via* individual adhesive probability.[153]

W-type mechanism is suitable for terrace sites of Ru $(1, 1, 10)$ surface, and Temkin–Pyzhev mechanism applies to its step-sites at similar conditions.[147] Sebb *et al.* studied the ammonia decomposition mechanism on metal nitrides such as TiN, VN and Cr_3N_2 and found that VN was very active.[154] If VN catalyst is contaminated by oxygen, the kinetics of ammonia synthesis[155] and decomposition[156] on it at about 773 K follows Temkin–Pyzhev mechanism. The zero order reaction was found for ammonia decomposition over VN at low hydrogen pressures, indicating that it follows W-Type mechanism.[156] The kinetics also keeps with Temkin–Pyzhev mechanism of ammonia synthesis on uranium nitride of U_2N_3-UN_2 at 648 K–823 K and 3 MPa[157] as well as on molybdenum nitride Mo_2N at 720 K–828 K.[158]

2.3.2.3 *Isotope exchanges of N_2*

If the chemisorption or dissociated adsorption of N_2 is rate determining step mentioned above, isotope exchanges of N_2 must be a slow process:

$$^{15}N_2 + {}^{14}N_2 \Leftrightarrow {}^{15}N^{14}N \tag{2.45}$$

The rate of ammonia synthesis and isotope exchange reactions are not the same completely, because the surface on which isotope exchange reactions occurred were covered completely by N species, while partial surface was covered by hydrogen for ammonia synthesis reaction. Kummer and Emmett demonstrated that the rates of isotope exchange and N_2 desorption are similar over the same iron catalyst at 773 K.[159] The effective catalysts for isotope exchanges are also effective for ammonia synthesis, such as the well-known active catalysts Fe,[160–162] Os,[163] Co,[164] Raney Ni[164] and other metal catalysts.[165] The reaction rates on Os catalysts are very fast at 573 K, and they still have activity of isotope exchange reactions even at temperature as low as 473 K.[163] For Re,[166] W[167,168] and Mo[161–171] catalysts, they require higher reaction temperatures.

The specific activities of ammonia synthesis and N_2 isotope exchange reactions over the catalysts of transient metal supported on activated carbon and promoted with potassium are parallel. In general, the activities are higher for ammonia synthesis than that for isotope exchange, and the reasons could be: (i) adsorption step is dynamic for ammonia synthesis while quasi-steady states for isotope exchanges; (ii) the reduction of catalysts may be incomplete for isotope exchange reactions. The activities of nitrogen exchange reactions are not high for Raney metals except ruthenium, and the reason may be the second one mentioned above. However, the reaction rates were not in parallel with the desorption energy of atomic nitrogen. The adsorption states on Raney metal studied by TPD show that the atomically adsorbed nitrogen related to isotope exchange was activated intermediates for ammonia synthesis.[165]

The rate of nitrogen isotope exchange corresponds to the forward and backward rate of the first step. If the rate determining step is the first step, the rate of isotope exchange (reverse reaction) should be zero at ammonia synthesis conditions. This method can be used for the determination of reaction rate determining step for Ru–K/AC(Ref. 172) and Mo_2N.[173]

2.3.2.4 *Distinguishing reaction mechanisms*

The same rate expression can be derived from various reaction mechanisms, so the reaction mechanism cannot be decided exclusively by fitting kinetic data with different kinetic equations despite that the kinetic data have no experimental errors. Therefore, the reflection between rate expression and mechanism is one-way, namely the rate expression can be derived from the reaction mechanism, while the mechanism cannot be confirmed by the rate expression. This one-way situation makes the study of chemical kinetics incomplete, only focusing on measurement of the reaction rate. It also needs to deal with the collection of spectroscopy and other data to obtain information about the nature of adsorption intermediates and important elementary steps in reaction mechanisms. That is to say, other experimental evidences are demanded in order to obtain a reaction mechanism.

The methods for distinguishing reaction mechanisms derived from rate expression include pressure test, transient-response, equivalent two-step principles and stoichiometric number and so on. The detail of the former three methods can be seen in the literature.[174] Here we only introduce stoichiometric number method that is very effective for deciding which step is rate determining step. In particular, it played a very important role in the kinetic study of ammonia synthesis reactions.

Stoichiometric number, σ, is the number of times an elementary step may repeat, after an overall reaction in the series of elementary reactions sequence.

For a reversible reaction, it is difficult to obtain the rate equation of reverse reaction from that of forward reaction according to thermodynamic conditions, if the reaction mechanism is unknown. It is known from chemical equilibrium that:

$$K = \vec{k}/\overleftarrow{k} = F_{-1}/F_1. \tag{2.46}$$

The rate expressions for forward and reverse reactions are $\vec{v} = \vec{k}F_1$, $\overleftarrow{\nu} = \overleftarrow{k}F_{-1}$, respectively. Then, $\overleftarrow{k}$ may be calculated if $\vec{k}$ and K are known, and vice versa. However, many equilibrium expressions can be written if different stoichiometric numbers were selected. For instance, reactions of ammonia synthesis could be expressed as the following two forms:

$$N_2 + 3H_2 \overset{A}{\longleftrightarrow} 2NH_3. \tag{2.47}$$

$$\frac{1}{2}N_2 + \frac{3}{2}H_2 \overset{A}{\longleftrightarrow} NH_3. \tag{2.48}$$

Corresponding equilibrium constants are:

$$K_A = \frac{[NH_3]^2}{[N_2][H_2]^3}. \tag{2.49}$$

$$K_B = \frac{[NH_3]}{[N_2]^{1/2}[H_2]^{3/2}}. \tag{2.50}$$

For the same reaction, equilibrium expressions (2.49) and (2.50) are equivalent, but the equilibrium constant and the reaction heat are different. The same situation falls across for the ascertaining of activation energy from the heat effect of reaction $Q = E_1 - f$.

$$K_A = K_B^2 \quad Q_{\mathrm{A}} = 2Q_{\mathrm{B}}$$

Thus, it is difficult to inquire the rate constants of reverse reaction from that of forward reaction and thermodynamic equilibrium constants because we do not know which K is correct.

It can be seen that ascertain of rate equation of reverse reaction is impossible for a complex multi-step catalytic reactions by only relying on mass interaction law which is only true for elementary step. In addition, the exact K and Q values are necessary.

In order to obtain the rate equation of reverse reaction from that of forward reaction, it is required to introduce a concept of stoichiometric number. Stoichiometric number, σ, reprensents the number of times an elementary step may repeat, after an overall reaction.

A complex reaction is accomplished by many continuous elementary steps. The reaction intermediates formed in anterior steps must be consumed in latter steps because they are not involved in products.

For ammonia synthesis reaction

$$N_2 + 3H_2 = 2NH_3$$

It might involve five elementary steps as follows:

	Stoichiometric number σ
① $N_2 + 2^* \longrightarrow 2N^*$	1
② $H_2 + 2^* \longrightarrow 2H^*$	3
③ $N^* + H^* \longrightarrow NH^* + ^*$	2
④ $NH^* + H^* \longrightarrow NH_2^* + ^*$	2
⑤ $NH_2^* + H^* \longrightarrow NH_3 + 2^*$	2

Obviously, in order to consume the intermediates formed in former steps, some steps must be carried out more than once. The stoichiometric numbers of every elementary step for ammonia synthesis reactions, as shown above, are 1, 3, 2, 2 and 2, respectively. If there is only one rate determining step and different stoichiometric number σ for each elementary step, it is possible to use stoichiometric number to decide which step are RDS. Once the stoichiometric number of RDS in reactions is known, the rate equation of reverse reaction can be calculated from forward reaction rate and thermodynamic equilibrium relationships.

Considering a common reaction:

$$A + B = C + D$$

Assuming the accomplishment of the reaction is *via* the steps as follows:

$$\text{① } A + ^* \rightarrow A^*$$
$$\text{② } B + ^* \rightarrow B^*$$
$$\text{③ } A^* + B^* \rightarrow C^* + D^*$$
$$\text{④ } C + ^* \rightarrow C^*$$
$$\text{⑤ } D + ^* \rightarrow D^*$$

The affinity of overall reaction, i.e., the change of the value of Gibbs free energy from thermodynamics:

$$A = A_0 + RT \ln \frac{[C][D]}{[A][B]}, \tag{2.51}$$

where A_0 is the standard affinity, and $A_0 = -RT \ln K$.

If step ③is RDS, the change of its affinity is,

$$A_{\mathrm{rds}} = -RT\ln K_{\mathrm{rds}} + RT\ln\frac{[C^*][D^*]}{[A^*][B^*]}. \tag{2.52}$$

Since RDS is an elementary step, Eq. (2.53) can be applied directly,

$$K_{\mathrm{rds}} = \frac{k_1^{\mathrm{rds}}}{k_{-1}^{\mathrm{rds}}}. \tag{2.53}$$

Then,

$$A_{\mathrm{rds}} = RT\ln\frac{k_{-1}^{\mathrm{rds}}}{k_1^{\mathrm{rds}}} + RT\ln\frac{[C^*][D^*]}{[A^*][B^*]} == RT\ln\frac{k_{-1}^{\mathrm{rds}}[C^*][D^*]}{k_1^{\mathrm{rds}}[A^*][B^*]}. \tag{2.54}$$

Obviously, the numerator and denominator in the right of the equation are the rates of reverse $\vec{v}_{\mathrm{rds}}$ and forward reactions $\overleftarrow{v}_{\mathrm{rds}}$ in rate determining step, respectively. Therefore, we get,

$$A_{\mathrm{rds}} = RT\ln\frac{\overleftarrow{v}_{\mathrm{rds}}}{\vec{v}_{\mathrm{rds}}} \tag{2.55}$$

The rate of overall reaction is determined by that of RDS,

$$\frac{\overleftarrow{v}_{\mathrm{rds}}}{\vec{v}_{\mathrm{rds}}} = \frac{\overleftarrow{v}}{\vec{v}}. \tag{2.56}$$

$$A_{\mathrm{rds}} = RT\ln\frac{\overleftarrow{v}_{\mathrm{rds}}}{\vec{v}_{\mathrm{rds}}} = -RT\ln\frac{\overleftarrow{v}}{\vec{v}}. \tag{2.57}$$

Therefore, the overall reaction proceeds once, rate determining step needs to proceed σ_{rds} times, then

$$A = \sigma_{\mathrm{rds}}A_{\mathrm{rds}}$$

Or

$$-RT\ln K\frac{[A][B]}{[C][D]} = -\sigma_{\mathrm{rds}}RT\ln\frac{\vec{v}}{\overleftarrow{v}}. \tag{2.58}$$

After rearrangement,

$$\frac{\vec{v}}{\overleftarrow{v}} = K^{1/\sigma_{\mathrm{rds}}}\left(\frac{[A][B]}{[C][D]}\right)^{1/\sigma_{\mathrm{rds}}} = \frac{\vec{k}}{\overleftarrow{k}}\frac{F_1}{F_{-1}}. \tag{2.59}$$

At constant temperature, the right of the equation involves a constant term of $\vec{k}/\overleftarrow{k}$ and a variable factor term of F_1/F_{-1}. Its left side also contains the same type constant term $K^{1/\sigma_{\mathrm{rds}}}$ and variable factor term $\left(\frac{[A][B]}{[C][D]}\right)^{1/\sigma_{\mathrm{rds}}}$. Then, the equation can be separated leading to the Horiuti formulation,

$$\vec{k}/\overleftarrow{k} = K^{1/\sigma_{\mathrm{rds}}}. \tag{2.60}$$

Equation (2.60) is a very common relation between reaction rate constant and chemical equilibrium constant. In addition, the exponential of K represents special physical meaning.

$$\frac{F_1}{F_{-1}} = \left(\frac{[A][B]}{[C][D]}\right)^{1/\sigma_{\mathrm{rds}}}. \tag{2.61}$$

Equation (2.61) is also applicable under equilibrium conditions. Then,

$$\frac{F_1}{F_{-1}} = \left(\frac{1}{K}\right)^{1/\sigma_{\mathrm{rds}}} \quad \text{or} \quad F_{-1} = K^{1/\sigma_{\mathrm{rds}}}F_1. \tag{2.62}$$

The rate equation for reverse reaction can be calculated from that of the forward reaction.

It is known from the Eq. (2-60) that,

$$\frac{\vec{k}_0}{\overleftarrow{k}_0} e^{(\overleftarrow{E}-\vec{E})/RT} = K_0^{1/\sigma_{\text{rds}}} e^{Q/RT}. \tag{2.63}$$

$$\overleftarrow{E} - \vec{E} = Q/\sigma_{\text{rds}}. \tag{2.64}$$

At the same time, the activation energy for reverse reaction $\overleftarrow{E}$ can be calculated from the thermodynamic data Q and activation energy of forward reaction $\vec{E}$. The key step is the measurement of σ_{rds}.

If there exists a rate determining step, an isotope tracer method can be used for the determination of $\bar{\sigma}$ or σ_{rds} at equilibrium or near equilibrium conditions. Its basic principle has been expounded systematically by Horiuti,[175] Temkin[176] and Happel.[177] If the exchange rate or rate at equilibrium v^0 defined by Wangner[178] is introduced, when the reaction approaches equilibrium, A is close to zero for any elementary step. Consequently, Horiuti–Temkin relation can be deduced:

$$\nu = \nu^0 \frac{A}{\overline{\sigma} RT}. \tag{2.65}$$

It gives the rate of overall reaction expressed by exchange rate and affinity at near equilibrium. If v and v^0 is determined, $\bar{\sigma}$ can be obtained.

The initial method for the measurement of $\bar{\sigma}$ was to determine the rate at approaching equilibrium.[179] Taking ammonia synthesis over iron catalyst as an example,[180–182] tracer is ^{15}N. Assuming elementary step sequence of the reaction as follows:

				σ_i
①	$N_2 + 2^*$	$\rightleftharpoons$	$2N^*$	1
②	$N^* + H^*$	$\rightleftharpoons$	$NH^* + ^*$	2
③	$NH^* + H^*$	$\rightleftharpoons$	$NH_2^* + ^*$	2
④	$NN_2^* + H^*$	$\rightleftharpoons$	$NH_3^* + 2^*$	2
⑤	$H_2 + 2^*$	$\rightleftharpoons$	$2H^*$	3
	$N_2 + 3H_2$	$\rightleftharpoons$	$2NH_3$	

The tracer goes through all steps except the last one, which is considered to be in quasi-equilibrium. For steps 1–4, we assume that equilibrium is not reached ($\nu_i \neq \nu_{-i}$). The overall reaction is:

$$^{15}NN + 3H_2 = {}^{15}NH_3 + NH_3, \tag{2.66}$$

where the tracer ^{15}N is transferred from the reactant N_2 to the product NH_3 in a net rate ρ:

$$\rho = \vec{\rho} - \overleftarrow{\rho} \tag{2.67}$$

and

$$\nu = \vec{\nu} - \overleftarrow{\nu}. \tag{2.68}$$

But ^{15}N does not go through all steps. Two sets of steps must be defined: One set involving ^{15}N (set j), the other one without ^{15}N.

For j = 1, 2, 3, 4 the general Temkin relation is valid:

$$\frac{\vec{\nu}^{(j)}}{\overleftarrow{\nu}^{(j)}} = \frac{\prod_{i}^{j} \nu_i}{\prod_{i}^{j} \nu_{-i}}. \tag{2.69}$$

The average stoichiometric number is:

$$\bar{\sigma}^{(j)} = \frac{\sum_{i-1}^{j} \sigma_i A_i}{\sum_{i-1}^{j} A_i} = \frac{A}{\sum_{i-1}^{j} A_i}. \tag{2.70}$$

According to equations:

$$\frac{\overleftarrow{v}}{\vec{v}} = \exp \frac{-A}{\bar{\sigma} RT}. \tag{2.71}$$

$$\frac{\vec{\nu}^{(j)}}{\overleftarrow{\nu}^{(j)}} = \exp \frac{A}{\bar{\sigma}^{(j)} RT}. \tag{2.72}$$

If x_{A} and x_{B} are the molar fractions of the tracer atom in the reactant N_2 and the product NH_3, the exchange rate of the tracer is:

$$\vec{\rho} = \mu x_A \vec{\nu}^{(j)} \quad \overleftarrow{\rho} = \mu x_A \overleftarrow{\nu}^{(j)}, \tag{2.73}$$

where, μ is the number of equivalent atoms that can be labeled.

From Eqs. (2.67), (2.68) and (2.73), we get:

$$\vec{\nu}^{(j)} = \frac{\rho - \mu x_B \nu}{\mu(x_A - x_B)}. \tag{2.74}$$

$$\overleftarrow{\nu}^{(j)} = \frac{\rho - \mu x_A \nu}{\mu(x_A - x_B)}. \tag{2.75}$$

Dividing the two equations side by side, we get:

$$\frac{\vec{\nu}^{(j)}}{\overleftarrow{\nu}^{(j)}} = \frac{\rho - \mu x_B \nu}{\rho - \mu x_A \nu} = \exp \frac{A}{\bar{\sigma}^{(j)} RT}. \tag{2.76}$$

Hence,

$$\bar{\sigma}^{(j)} = \frac{A}{RT} \ln \frac{\rho - \mu x_A \nu}{\rho - \mu x_B \nu}. \tag{2.77}$$

Thus, $\bar{\sigma}^{(j)}$ can be determined from the overall net rate v and the net rate of tracer transfer ρ. If the steps through which the tracer does not pass are equilibrious, as in the example considered:

$$\bar{\sigma}^{(j)} = \bar{\sigma}$$

and if there exists a rate determining step, then,

$$\bar{\sigma} = \sigma_{\mathrm{rds}} = \bar{\sigma}^{(j)}. \tag{2.78}$$

In other words, the stoichiometric number determined from the transfer of a tracer is also equal to that of the overall reaction and of the rate determining step. In the example of ammonia synthesis on iron catalyst, σ_{rds} can be equal to one or two. Experimental studies have reported both values. Horiuti *et al.*[183,184] found $\sigma_{\mathrm{rds}} = 2$ for an iron catalyst at near equilibrium. Tanaka[185]

found $\sigma_{rds} = 2$ for synthesis and $\sigma_{rds} = 1$ for decomposition of ammonia at far from equilibrium. The value $\sigma_{rds} = 2$ is compatible with step 2 being rate determining. But most of the evidence indicates that adsorption of dinitrogen is the rate determining step, which means $\sigma_{rds} = 1$.[186] Still, it cannot be said whether adsorption of N_2 is dissociated or not. Indeed, the following reaction sequence can be envisaged:

				σ_i
①	$N_2 + 2^*$	$\rightleftharpoons$	N_2^*	1
②	$N_2^* + H_2^*$	$\rightleftharpoons$	$N_2H_2{}^*$	1
③	$N_2H_2{}^* + H_2$	$\rightleftharpoons$	$N_2H_4{}^*$	1
④	$N_2H_4{}^* + H_2$	$\rightleftharpoons$	$2NH_3 + ^*$	1
	$N_2 + 3H_2$	$\rightleftharpoons$	$2NH_3$	

The first two steps are considered to be the steps *via* which the nitrogenase fixes nitrogen. If so, σ_{rds} would still be equal to one. Nevertheless, the evidence for dissociated chemisorption of dinitrogen on iron is now overwhelming. The two sequences, dissociated adsorption on iron and associated one on nitrogenase might be their respective characteristics of industrial catalysis at high-temperatures and enzymatic catalysis at low-temperatures. To essentially improve the activity of present iron catalysts for ammonia synthesis, it might be necessary to fundamentally modify the nature of every step in the reaction sequence on iron catalysts.

2.3.3 *Analysis of microreaction (intrinsic) kinetics of ammonia synthesis*

Ammonia synthesis is one of the heterogeneous catalytic reactions which are investigated most widely. Although the reaction is favorable in energy and there are no side reactions, solid catalyst and high temperature are necessary conditions to get ideal kinetics as its limitation. The requirement of high-temperature is not favorable for reaction thermodynamics because ammonia synthesis is an exothermal reaction. The number of molecules decreases for ammonia synthesis reaction, and thus increasing the pressure can compensate for the negative effect of equilibrium conversion caused by high-temperature. Based on these facts, ammonia synthesis reactions are generally carried out at high-pressures (about 10 MPa–30 MPa).

It can be seen from the above analysis that the general features of reaction mechanisms of ammonia synthesis on metal iron are related to the dissociation of nitrogen and hydrogen molecules on the surfaces of iron, then hydrogenation to form adsorbed surface species NH_x step by step and desorption of NH_3 from the surface of catalysts. The dissociation rate of dinitrogen is considered as one of rate determining steps in kinetics and mechanisms. The first hydrogenation step of adsorbed nitrogen atoms to form adsorbed species NH is also slow. The important thing is that the synthesis reaction is inhibited by product ammonia, indicating that the adsorbed species NH_x(x = 0–2) are surface abundant reaction intermediates under reaction conditions.

The fundamental principles of chemical kinetics, rate constant estimation and chemical reactor design are the basis of the analysis and study of microkinetics.

The basic tasks for the analysis of microkinetics are to obtain the kinetic parameters in rate expressions, to give unambiguous physical meaning for these parameters, and to obtain the parameters which can be proof-tested by theory and experiments. If the parameters such as sticking coefficient, pre-exponent factor, adsorption entropy, geometric factor, surface cluster size of active centers, surface bond energy, activation energy and density of active sites etc. can be estimated reasonably, it would be possible to give which steps in given mechanism are of importance in kinetics and which surface species are the most abundant. This information is of very importance for predicting how each step in the mechanisms has effect on catalytic performance of catalysts.

The microkinetics analysis, as a useful and powerful tool to interpret, harmonize and consolidate the study of catalytic phenomena, can describe various results obtained at wide experimental conditions. For ammonia synthesis reaction discussed in this section, the microkinetic models are evaluated from the experimental data such as the sticking coefficient of dissociated nitrogen adsorption, the spectrum of programmed-temperature desorption of adsorbed nitrogen as well as the kinetics of ammonia synthesis at industrial conditions and at laboratory conditions are far from equilibrium.

Dumesic *et al.*,[115] by the analysis of microkinetics, probed into the extension ability of the pressure for microkinetics of ammonia synthesis on iron catalysts, and their results indicated that it could extrapolate 11 orders from adsorption and desorption on single crystal iron at extra-vacuum to industrial reaction conditions (for example, 700 K and 10 MPa).

2.3.3.1 *Analysis of reactor*

The purpose of Stoltze *et al.* was to interpret the experimental results obtained in high pressure reactors for ammonia synthesis reported by Nielsen *et al.*,[187] by extension of kinetic data obtained on a single crystal iron. In order to carry out proof-test, Bowker *et al.* selected a special experimental point, the reactor used is plug-flow reactor, volume of 5 cm^3, packed catalyst 2.5 cm^3 (other space was filled by solid thinner), reactor pressure 10.7 MPa, H_2/N_2 ratio 3:1, space velocity 16,000 h^{-1}, the density of catalyst bed 2.5 $g \cdot cm^{-3}$, the concentration of active sites on the surface of iron catalyst 6×10^{-5} $mol \cdot g^{-1}$.

Dumesic *et al.*[115] generalized these methods proposed by Stolze and Norskov as well as Bowker *et al.* so that the same analytical strategy could be applied to evaluate any set of kinetic data obtained. In the analysis of microkinetics, an industrial plug-flow reactor could be simulated by using a succession of well-mixed units and in each unit the steady-state equations could be solved,[188] which involve all surface intermediates, equilibrium of active sites at catalyst surface and mass equilibrium of species at surface and in gas, without beforehand assumptions about possible rate determining steps or the most abundant reaction intermediates. The results of microkinetics analysis are given in Fig. 2.19 in which the percentage of formed ammonia is a function of the position in reactor. Compared with the only experimental value at outlet of reactor, the predicted concentrations at outlet of reactor by all three microkinetics models are close to the experimental value of 13.2%. Hence, at the stage of microkinetics analysis, the surface science data obtained on single crystal iron could be extended

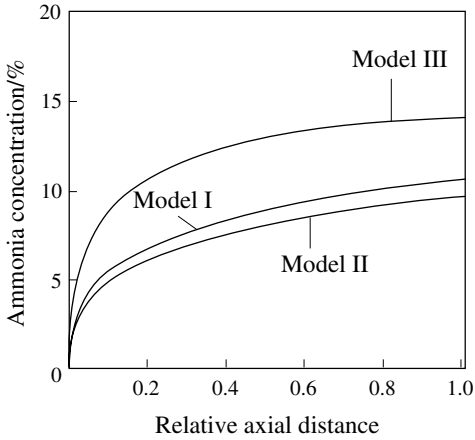


Fig. 2.19 Ammonia concentration calculated as function of relative position in reactor

effectively to predict formation rate of ammonia at industrial reactor reported by Neilsen.

Two of three microkinetic models could give these data obtained at the range of 11 orders pressure i.e., from ultrahigh vacuum to 10 MPa, and the third model could represent reasonably the kinetic data obtained at industrial reaction conditions and cannot be extended to describe suitably these data obtained at ultrahigh vacuum conditions. Hence, analysis of microkinetics could provide a frame for quantitative comparison of kinetic information obtained at wide experimental conditions, and this comparison could distinguish the ensembles of kinetic parameters, which seem to be equivalent, obtained in more narrow range of conditions.

It is surprising that the study of adsorption and desorption on the surface of single crystal iron could be used for predicting of the operating performance of ammonia synthesis reactor, because it is very difficult for the precise determination of rate constants for seven or eight elementary steps in the reaction mechanism. Why is there such a success for reactor analysis of microkinetics? The dissociation of adsorbed dinitrogen (step 2 in model) is the slowest step in mechanism at operationg conditions that are for experimental measurements, whose characteristics could be seen in Fig. 2.20 in which equilibrium deviation (forward rate - reverse rate)/forward rate) is plotted as the axial position in plug-flow reactor. Figures 2.21–2.23 show the change of coverage fraction along with relative axial distance, calculated by the three models. It can be seen from these figures that for all cases, adsorbed nitrogen atoms are the most abundant reaction intermediates. In particular, the predictions from microkinetics analysis have been approved by Nwalors' experiments.[189] Obviously, the rate constants of steps 3–8 are raletively less important in kinetics. In order to achieve the purpose of predicting the turnover number of ammonia synthesis, the prediction of kinetics and thermodynamics of nitrogen adsorption (steps 1 and 2) is enough. Fortunately, these steps can be studied facilely by programmed-temperature desorption over single crystal face under ultrahigh vacuum conditions. Therefore, as long as any microkinetics model can reasonably describe step 1 and 2, and is in accordance with thermodynamic

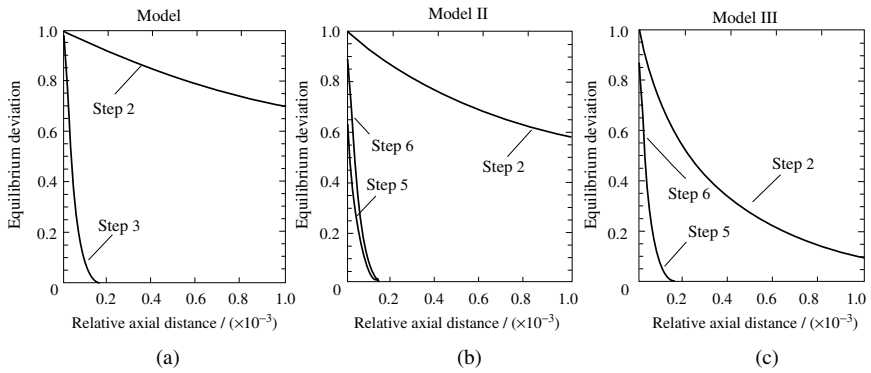


Fig. 2.20 Plots of equilibrium deviation calculated as function of axial distance in plug-flow reactor for the slowest step

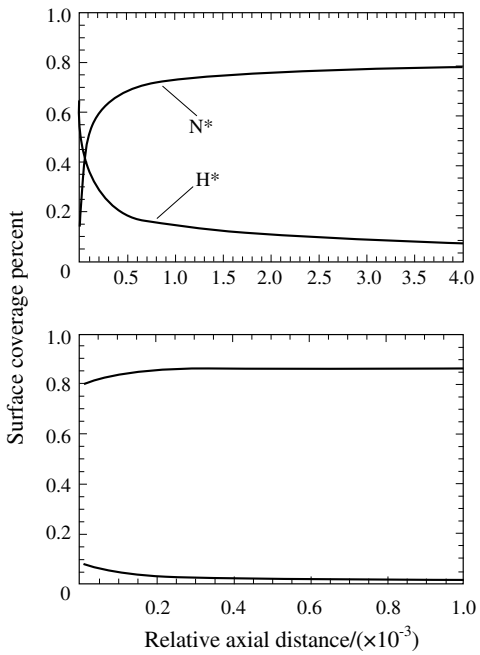


Fig. 2.21 Change of coverage calculated with relative axial distance (Model I)

nature of ammonia synthesis (defined as a suitable product of equilibrium constants of elementary step), the kinetics of ammonia synthesis can be described effectively.

The rate constants used in all the three models reflect a feature that the surface of catalyst is almost covered by nitrogen atoms. The crucial point is that there is also this case in programmed-temperature desorption experiments over the surface of single crystal iron. Therefore, by the microkinetics analysis, the reason that the relation between experimental results obtained at ultrahigh vacuum conditions and at high pressure reactor could be established is because the important kinetic steps

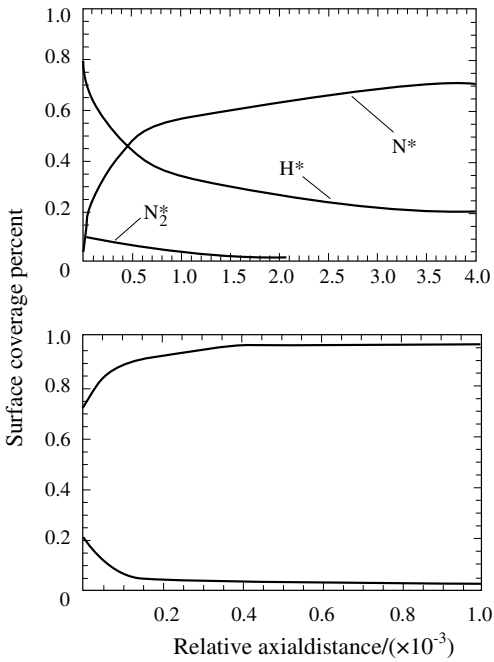


Fig. 2.22 Change of coverage calculated with relative axial distance (Model II)

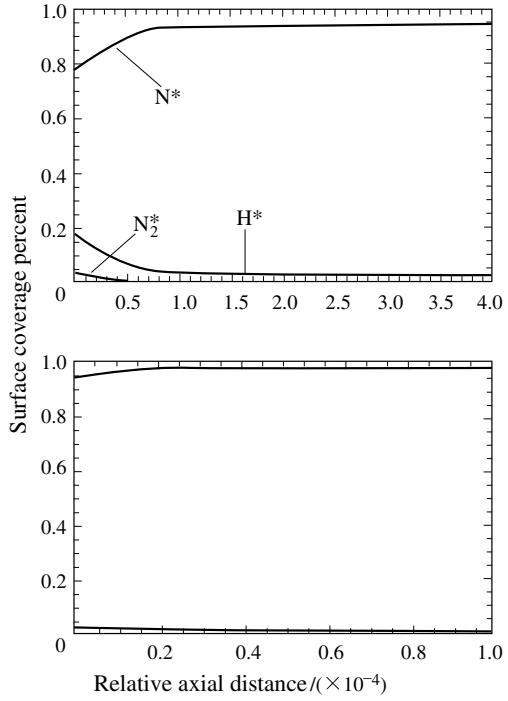


Fig. 2.23 Change of coverage calculated with relative axial distance (model III)

have been considered by these experiments carried out at ultrahigh vacuum with the surface covered by species in a typical industrial process.

This conclusion is very important, because it cannot be expected for those surfaces with a wide range of surface coverage to obey usual Langmuir's kinetics. For instance, the interaction strength between adsorbed species usually depends on surface coverage, and the sticking coefficient during adsorption process must not be expressed as a simple power function of empty active sites. A more detailed discussion about the non-Langmuir effect has been done on ethylene hydrogenation on platinum.[115] Hence, the kinetic analysis for ammonia synthesis, which is the feature of high surface coverage of nitrogen atoms, would not be so successful at the conditions of low surface coverage of nitrogen or that adsorbed nitrogen is not the most abundant reaction intermediates.

The microkinetic model that is in accordance with overall thermodynamics of ammonia synthesis could be used for the reasonable prediction of operating performance near equilibrium point, as appeared in Fig. 2.19, but not for the cases far from equilibrium. So, the effectiveness of microkinetic model was further tested by the evaluation of its ability for the prediction at whole range of reaction conditions used for experimental measurements.

For example, Dumesic *et al.*[190] measured the conversion at atmospheric pressure and the turnover number of ammonia synthesis under conditions far from equilibrium over various iron catalysts supported on magnesium oxide. The number of active sites on the surface of these catalysts was determined by chemical titration of CO adsorption. Ammonia yield under experimental conditions is predicted by these microkinetic models, and the results calculated were four times higher at most. If it is taken into account that these catalysts without potassium promoter and exorbitant estimation for the number of active sites measured by CO chemisorption, this result could be considered as in fair agreement with experimental one.

Spencer *et al.*[191] measured the turnover number on Fe (111) face at ammonia concentration less than 1.5% of equilibrium value and at 2.0 MPa of total pressure and 748 K. These data were a very good proof-test for microkinetic models under conditions far from equilibrium, and the models could be considered successful if the difference between the values predicted by models and obtained from experiments is in the range of about three times.

Topsøe *et al.*[192] determined active sites on iron catalysts for ammonia synthesis by nitrogen titration and point-time yields of ammonia (the ammonia molecules produced per second per active site in reactor) at 15% of conversion of equilibrium value at atmospheric pressure and 673 K and stoichiometric mixture. The difference between the values predicted by the models and obtained by experiments was less than three folds.

Stolze *et al.* analyzed the investigating results for ammonia synthesis kinetics at wide experimental conditions which are described by all three microkinetic models, and indicated that all models were established on, in fact, the same chemical reaction mechanisms. The difference between them is only that the estimated values of kinetic parameters used are different for each elementary step. In the special example above, the precise kinetic data on iron single crystal were provided only for adsorption step and for other steps the data were estimated indirectly. Accordingly, the extension of data from single crystal to industrial reactions is valid only for the case that adsorption step is rate determining step and the most abundant surface reaction

intermediates dominate surface coverage. In other cases, the extension is only of qualitative worth.

2.3.3.2 *The conclusion of microkinetic analysis*

Microkinetic analysis made a very good prediction for the rate of ammonia synthesis reaction at 678 K–748 K of temperature, at 0.1–10.7 MPa of pressure and in the range of approaching equilibrium (1.5%–78%). Furthermore, two of microkinetic models could reasonably describe the sticking coefficient of dinitrogen dissociated adsorption and the programmed-temperature desorption spectroscopy of nitrogen from the surface of Fe (111). It is markedly that these simple microkinetic models (models I and II) could suitably predict the behavior of adsorption and desorption of dinitrogen and ammonia synthesis at the conditions in the range from ultrahigh vacuum to 10.7 MPa. Of course, the prediction by them would not be so successful at very small coverage of nitrogen or for the case that adsorbed nitrogen is not the most abundant surface reaction intermediates, because at this moment there is large deviation from basic conditions for the adsorption and desorption experiments on single crystal at ultrahigh vacuum.

Nevertheless, these microkinetic models still contain no information about the effect of catalysts on the parameters in rate equations for elementary steps. In addition, there is no verification for important kinetic steps 1 and 2, but they were checked in other cases of elementary reaction steps.

However, microkinetic analysis provides the important basis for designing new experimental and theoretical information. For example, when a new generation of ammonia synthesis catalyst is developed by a great deal of catalyst preparations and catalytic performance tests, the behavior about dinitrogen dissociated adsorption coefficient and the desorption of adsorbed nitrogen on new catalysts could be more characterized. The correlation between the research results about adsorption–desorption of nitrogen and the structure and composition of the catalysts could be done so that there is possibility to find a catalyst with high sticking coefficient of dissociation adsorption. At this point, theoretical study plays a useful role in proposing a suggestion for surface morphology and electron configuration in favor of dissociation of nitrogen molecules. Then, microkinetics analysis could be used for the determination if there is an actual relation between different catalytic performance of various catalysts and the change of the kinetics of adsorption–desorption of dinitrogen, and if it changes the nature of basic mechanism and important steps of kinetics of ammonia synthesis on these catalysts. On the other hand, a new catalyst could be found from a comparison between microkinetics of different catalysts which could have different operating mechanism or important steps of kinetics involved.

For the important and industrial iron catalyst, a good picture of its structure and its activity as an accelerator for the dissociation of dinitrogen, which is the kinetics determining step, can be drawn. Results from pioneering experiments on iron crystals[193] at lower pressures, were quantitatively corroborated by high-pressure experiments. This apparent lack of a pressure gap allowed the theoretical description of the nitrogen activation and therefore the quantitative extrapolation of the kinetics from ultra-high vacuum conditions to industrial conditions.[194] Furthermore, studies on single crystals showed that the lack of a pressure gap only occurred at low nitrogen coverages, whereas at high nitrogen coverages, a considerable deviation

from the theoretical adsorption behavior is caused by the formation of a subnitride surface phase. Although other researchers have also successfully extended the data collected at ultra-high vacuum on single crystal to the kinetics on supported or industrial catalysts observed at much higher pressures.[195,196] At present, there are no other practically relevant reactions that lead to such a close interconnection between theory, model catalysis, and experiment[197] as the high-pressure synthesis of ammonia. This statement is not only valid for the iron system but also for the ruthenium system and, in foreseeable future, for the Co–Mo–N alloy system. Despite the catalyst is getting more complex both chemically and structurally, the time frame for the acquirement of knowledge is truly remarkable. It took decades for the case of the iron system but just 10 years for the ruthenium system, and it will take only a few years for the case of the alloy system. It is because there was a great deal accumulation of experimental data and theoretical knowledge obtained in long term study for reaction mechanism of ammonia synthesis. As well as being of high industrial relevance, the catalytic synthesis of ammonia is also a key reaction for creating new life and a prototypical model reaction[198] that helps in gaining a fundamental understanding of catalysis in general and therefore of considerable scientific and cultural importance. It is mainly this reason that drives the research in ammonia synthesis forward, especially since evidence for a knowledge based improvement of a catalyst would have a strong signaling effect on other fields of catalysis research. In addition to itself still needing to be developed, catalytic ammonia synthesis is still an ideal model system in the theoretical fields of heterogeneous catalysis

2.4 Kinetics of Overall Reactions for Ammonia Synthesis

Traditionally, exponential law equations are used to approximately express kinetics of chemical reactions. In the form of rate expressions, apparent rate constants include the effect of temperature and the relationship of rate and concentration is expressed by power function, namely the concentration of reactants and products is in accordance with the square of their reaction orders. Its advantages are simple and valid in a very wide range of operating conditions for some reactions, and can also be an approximation of more complicated rate expressions. The reaction order and apparent activation energy is a function of the reaction conditions if it is used as an approximation expression, i.e., exponential law is valid only in a narrow range of temperature and concentrations. In general, any rate expression can be simplified to a rate form of exponential law in a range of limited conditions. The power function expression is simple and convenient to use for design of reactors and at least can be as the first approximation.

In the chemical engineering of non-catalytic gas reactions, power function is a perfect expression of reaction rate. However, it is improper for a wide operating range of catalytic reactions. For example, the most catalytic reactions have saturation or suppression effects that lead to, with concentration increases of some special species, a zero or negative reaction order. Therefore, the more desirable rate expressions for heterogeneous catalysis are Langmuir–Hinshellwood and Hougen–Watson expressions that are very useful for expression of kinetic data of many heterogeneous catalytic reactions.

It is assumed that catalytic reaction kinetics is obtained on perfect and uniform surfaces (Langmuir surface), in which all active sites are of the same nature of

thermodynamics and kinetics. The investigation shows that the two step mechanisms can be used in most cases and the assumption of rate determining step and the most abundant reaction intermediate are usually valid. Therefore, a surface of real catalysts i.e., non-uniform surface, such as iron catalysts for ammonia synthesis, can be expressed by a series of ensembles. For the active sites in every ensemble, there are the same natures in thermodynamics and kinetics, if the reaction mechanism can be treated or simplified as a two-step mechanism. The kinetics obtained by this way can also be used for optimization and selection of catalysts.

2.4.1 *General relation between overall reaction and elementary steps*

Supposing that a reaction includes with n elementary steps, and each one with a stoichiometric number σ_i, following Temkin method (1971), we can write:

$$\begin{aligned}&(\nu_1-\nu_{-1})\nu_2\nu_3\cdots\nu_n+\nu_{-1}(\nu_2-\nu_{-2})\nu_3\cdots\nu_n+\nu_{-1}\nu_{-2}\\&\quad\times(\nu_3-\nu_{-3})\nu_4\cdots\nu_n+\nu_{-1}\nu_{-2}\cdots\nu_n-(n-1)(\nu_n-\nu_{-n})\\&=\nu_1\nu_2\nu_3\cdots\nu_n-\nu_{-1}\nu_{-2}\nu_{-3}\cdots\nu_{-n}\end{aligned}\tag{2.79}$$

With the quasi-stationary approximation, the net rate v of the overall relation is equal to the difference between forward and reverse rates of each step with the suitable weighing of the stoichiometric number of that step:

$$\sigma_i\nu=\nu_i-\nu_{-i}.\tag{2.80}$$

Substituting Eq. (2.80) into (2.79) gives a general relation of Temkin:

$$\nu=\frac{\prod_{i=1}^{n}\nu_i-\prod_{i=1}^{n}\nu_{-i_i}}{\sigma_1\nu_2\cdots\nu_n+\nu_{-1}\sigma_2\nu_3\cdots\nu_n+\cdots+\nu_{-1}\nu_{-2}\cdots\nu_{-(n-1)}\sigma_n}.\tag{2.81}$$

But the net rate of overall reaction can be expressed as the difference between a forward and a reverse rate:

$$\nu=\vec{\nu}-\overleftarrow{\nu}.\tag{2.82}$$

Substitute Eq. (2.81) and separate it:

$$\vec{\nu}=\prod_{i=1}^{n}\nu_i/D\quad\overleftarrow{\nu}=\prod_{i=1}^{n}\nu_{-i}/D,\tag{2.83}$$

where D is the denominator in Eq. (2.81). The result is:

$$\frac{\vec{\nu}}{\overleftarrow{\nu}}=\frac{\prod_{i=1}^{n}\nu_i}{\prod_{i=1}^{n}\nu_{-i}}.\tag{2.84}$$

The affinity of the elementary step i.e., negative value of its Gibbs free energy is:

$$\frac{\nu_i}{\nu_{-i}}=\exp\frac{A_i}{RT},\tag{2.85}$$

where

$$A_i=A_i^0-RT\ln\frac{[C][D]}{[A][B]}=RT\ln\frac{\nu_i}{\nu_{-i}}\tag{2.86}$$

$A_i^0 = RT \ln K$is the standard affinity. The equation is correlated to the ratio of forward–reverse rates and the affinity of the reaction.

The affinity of the overall reaction is:

$$A = \sum_i \sigma_i A_i. \tag{2.87}$$

Then, Eq. (2.85) gives:

$$A = RT \sum \ln \left(\frac{\nu_i}{\nu_{-i}} \right)^{\sigma_i}. \tag{2.88}$$

If there exists a rate determining step (rds), all other steps being equilibrated or quasi-equilibrated, i.e., $A_i = 0$, $v_i = v_{-i}$ except for $i = d$, the (2.88) becomes:

$$A = \sigma_d A_d = RT \sum \ln \left(\frac{\nu_d}{\nu_{-d}} \right)^{\sigma_d}. \tag{2.89}$$

Then,

$$\sigma_d = \frac{A}{RT} \ln \frac{\overleftarrow{\nu}}{\vec{\nu}}. \tag{2.90}$$

Since A can be obtained from thermodynamic data, and σ_d can be determined if $\vec{\nu}$ and $\overleftarrow{\nu}$ are known. σ_d plays a very important role in verifying reaction mechanism. If there is no rate determining step in a catalytic reaction, the concept of average chemical stoichiometric number can be introduced. The kinetics of reverse reaction can be determined from that of forward-reaction kinetics by σ_d or $\bar{\sigma}$.[199]

2.4.2 *Two-step sequences*

For an overall reaction involving multi-elementary steps, Temkin formula can be used for the calculation of kinetics although it is very complicated. If a rate determining step is existed, the kinetic equations could be derived simply by a two-step mechanism. Two-step sequence is a simple method and can be used to obtain a better kinetic expression even though the understanding for reaction mechanism is not complete.

The so-called two-step sequence method is that the derivation of reaction rate expression only requires to consider two key steps for a reaction involving multi-elementary steps. Only the rate constants or equilibrium constants of the two key steps appear in rate expression, which are of clear physical meaning. In order to determine the key steps, a concept of most abundant reaction intermediate (Mari) must be introduced. Mari is an intermediate of maximum concentration among all reactive intermediates invovled in the reaction, and the concentration of other intermediates can be ignored. Based on the concepts of both rate determining step and most abundant reaction intermediate, the mechanisms of many catalytic reactions can be simplified to two-step sequences for the derivation of kinetic equations. In order to explain the rules for the treatment of heterogeneous catalytic reaction kinetics by simplest two-step sequences method, two examples are given as follows:

$$\begin{aligned} &\mathrm{S_1 + A_1} \underset{\mathrm{k_{-1}}}{\overset{\mathrm{k_1}}{\rightleftharpoons}} \mathrm{B_1 + S_2} \\ &\mathrm{S_2 + A_2} \underset{\mathrm{k_{-2}}}{\overset{\mathrm{k_2}}{\rightleftharpoons}} \mathrm{B_2 + S_1} \\ &\hline \\ &\mathrm{A_1 + A_2} \rightleftharpoons \mathrm{B_1 + B_2} \end{aligned}$$

S_1 and S_2 denote empty and occupied active sites, respectively,

$$[L] = [S_1] + [S_2]. \tag{2.91}$$

To simplify the writing, the following notation will be adopted:

$$\begin{aligned} a_1 = k_1[A_1] \quad a_2 = k_2[A_2], \\ a_{-1} = k_{-1}[B_{-1}] \quad a_{-2} = k_{-2}[B_{-2}], \end{aligned} \tag{2.92}$$

where, a_i may be considered as pseudo-first-order rate constants or the reciprocal of the mean lifetime of the Bodenstein active intermediates at the case of S_1 and S_2.

Combining with Temkin (Eq. 2.81) it leads to the overall rate:

$$\nu = \frac{\nu_1\nu_2 - \nu_{-1}\nu_{-2}}{\nu_{-1} + \nu_2} = \frac{[S_1](a_1a_2 - a_{-1}a_{-2})}{a_{-1} + a_2}. \tag{2.93}$$

Since the order of steps in Temkin's relation does not matter, we also have:

$$\nu = \frac{[S_2](a_1a_2 - a_{-1}a_{-2})}{a_1 + a_{-2}}. \tag{2.94}$$

Dividing the two preceding equations side by side leads to the ratio u of the concentration of empty and occupied sites:

$$u = \frac{[S_1]}{[S_2]} = \frac{a_{-1} + a_2}{a_1 + a_{-2}}. \tag{2.95}$$

This ratio is readily obtained from the quasi-stationary state approximation, noting that $v = v_1 = v_2$. The use of Temkin relation illustrates how the unknowns can be eliminated by alternation of the indices. Thus the rate can always be obtained, at least in principle, although it can be difficult when the rates of elementary steps are not linear with the concentration of active intermediates, e.g., for dissociated adsorption.[200] The turnover rate is then:

$$\nu_1 = \frac{\nu}{[L]} = \frac{[S_1](a_1a_2 - a_{-1}a_{-2})}{([S_1] + [S_2])(a_2 + a_{-1})}. \tag{2.96}$$

Or finally:

$$\nu_1 = \frac{\nu}{[L]} = \frac{a_1a_2 - a_{-1}a_{-2}}{a_1 + a_{-1} + a_2 + a_{-2}}. \tag{2.97}$$

Equation (2.97) can be generalized to a sequence with i steps: The numerator will still be of the form of the mass action law while the denominator is a polynomial of i^2 terms. In practice, the least number of parameters is best and simplifications that correspond to various experimental situations will be discussed below.

For the case of a saturated surface, $[S_2] \gg [S_1]$, substituting the values of a_i into Eq. (2.96) and it simplifies to:

$$\nu_1 = \frac{k_1k_2[A_1][A_2] - k_{-1}k_{-2}[B_1][B_2]}{k_1[A_1] + k_{-2}[B_2]}. \tag{2.98}$$

If step (1) is irreversible, $k_{-1} = 0$, we get an equation which starts to resemble those of Langmuir, and popularized by Hinshelwood:

$$\nu_1 = \frac{k_2[A_2]}{1 + \frac{k_{-2}[B_2]}{k_1[A_1]}}. \tag{2.99}$$

For case of a rate determining step (2) and irreversible, a_2, $a_{-2} \ll a_1$, a_{-1}, v_1 becomes in the absence of $[B_1] = 1$:

$$\nu_1 = \frac{k_2 K_1 [A_2][A_1]}{1 + K_1[A_1]}, \tag{2.100}$$

where, $K_1 = k_1/k_{-1}$. There is the classic equation of Michaelis–Menten equation in enzyme catalysis, Langmuir–Hinshelwood equation in physical chemistry, and Hougen–Watson equation in chemical engineering.

So far, it has been supposed, with Langmuir type surface, that all catalytic active sites are uniform and do not interact with each other. This formula has its limitation, but it is very useful. The equations obtained can be compared to empirical power rate laws:

$$\nu = k[A_1]^{\alpha_1}[A_2]^{\alpha_2} \cdots, \tag{2.101}$$

where k is an apparent rate constant and α_1, α_2 are apparent reaction orders with respect to reactants and products. But the orders of reactants and products are often fractional. Now let us take decomposition and synthesis of ammonia as examples.

[**Example 1**]: Decomposition of ammonia on a platinum filament.[201]

The overall reaction is:

$$2NH_3 = N_2 + 3H_2.$$

The reaction can be interpreted by a sequence:

$$NH_3 + * \rightarrow NH_3^*,$$
$$NH_3* \xrightarrow{\Lambda} \cdots.$$

The quasi-stationary state approximation leads to a rate expression:

$$\nu = [L]k_2 \frac{K_1[NH_3]}{1 + K_1[NH_3]}. \tag{2.102}$$

Although NH_3^* is the Mari, it is weakly adsorbed on Pt compared to the other dissociated fragments such as N^*, NH^* which would be more abundant than NH_3^*, especially at high temperatures.

Only two key steps are required for two-step sequence method:

$$NH_3 + 2* \xrightarrow{k_1} NH_2 * + H*$$
$$\cdots$$
$$\cdots$$
$$2N* \xrightarrow{k_2} N_2 + 2*.$$

With N^* being the Mari, applying the quasi-stationary state approximation, we get:

$$\nu = \nu_1 - \nu_2 = k_1[NH_3][*]^2[L]^{-1} - k_2[N*]^2[L]^{-1} \tag{2.103}$$

Thus after elimination [L],

$$\frac{[N*]}{[*]} = \left(\frac{k_1}{k_2}[NH_3]\right)^{1/2} \tag{2.104}$$

and

$$[L] = [*] + [N*] = [N*]\left(1 + \frac{[*]}{[N*]}\right) \tag{2.105}$$

Hence:

$$[N*] = [L]\frac{(k_1/k_2[NH_3])^{1/2}}{1+(k_1/k_2[NH_3])^{1/2}}. \tag{2.106}$$

The overall reaction rate is then:

$$\nu = k_2[L]\left[\frac{(k_1/k_2[NH_3])^{1/2}}{1+(k_1/k_2[NH_3])^{1/2}}\right]^2. \tag{2.107}$$

Just from fitting the kinetic data, it is not possible to discriminate between Eqs. (2.102) and (2.107) as they are so similar.

The mechanism described above, with irreversible adsorption of reactants and irreversible desorption of the Mari explained very satisfactorily all the experimental data of Tamaru *et al.*[202] and Boudart *et al.*[203] for the decomposition rate of ammonia at high temperatures and low pressures on tungsten and molybdenum respectively with simultaneous measurement of the surface concentration of N^* by Auger electron spectroscopy. Disturbing the stationary state by flashing desorption of the metal catalysts, the rate of returning to steady state of the two postulated irreversible steps of adsorption and desorption could be evaluated separately.

[**Example 2**]: Synthesis of ammonia.

The overall reaction:

$$N_2 + 3H_2 = 2NH_3.$$

Its reaction mechanism:

$$\begin{aligned} N_2 + 2^* &\rightarrow 2N^* \\ N^* + H^* &\rightarrow NH^* + ^* \\ NH^* + H^* &\rightarrow NH_2^* + ^* \\ NH_2^* + H^* &\rightarrow NH_3^* + ^* \\ NH_3^* &\rightarrow NH_3 + ^* \\ H_2 + 2^* &\rightarrow 2H^* \end{aligned}$$

For the sake of simplicity, the reaction will be assumed to preceed far from equilibrium so that the reverse rate can be neglected. According to general equilibrium method, it must find out the expression of all reaction intermediates, and then the expression of reaction rate can be derived. Obviously, the processes are very complicated. If assuming that there both exist rate determining step and the most abundant reaction intermediate, reaction sequence can be reduced to two-step sequence. There are three cases as follows:

(1) Dissociated adsorption of dinitrogen is the rds that produces the Mari N^*. Because of this assumption, all the other equilibrated steps may be summed up into an overall equilibrated reaction. So, the two-step sequences are:

$$\begin{aligned} &① \ N_2 + 2^* \xrightarrow{k_1} 2N^* \\ &② \ N^* + \frac{3}{2}H_2 \xrightarrow{k_2} NH_3 + ^* \end{aligned}$$

It must be noted that step (2) is not an elementary step, as it contains a non-mechanistic stoichiometric coefficient of 3/2.

The overall rate is then:

$$\nu = k_1[N_2][*]^2[L]^{-1}. \tag{2.108}$$

But as usual:

$$[L] = [*] + [N*]$$

and

$$K_2 = \frac{[N*][H_2]^{3/2}}{[NH_3][*]} \tag{2.109}$$

Thus we get:

$$[*] = \frac{[L]}{1 + \{K_2[NH_3]/[H_2]^{3/2}\}}. \tag{2.110}$$

Hence,

$$\nu = [L].\frac{K_1[N_2]}{[1 + \{K_2[NH_3]/[H_2]^{3/2}\}]^2}. \tag{2.111}$$

This result is the same as that derived by common method.

(2) Associative adsorption of dinitrogen is the rds that produces the Mari of N_2^*. In this case we write:

$$N_2 + * \xrightarrow{\Lambda} N_2*$$
$$N_2^* + 3H_2 \rightarrow 2NH_3 + ^* .$$

The rate expression obtained from the derivation as the same in case (1):

$$V = [L]\frac{k_1[N_2]}{1 + (K_2[NH_3]^2/[H_2]^3)}. \tag{2.112}$$

It would be very difficult to discriminate between Eqs. (2.112) and (2.111) on the basis of fitting degree of kinetic data. To decide whether the adsorption of dinitrogen is dissociated or not, other experiments are needed.

(3) Dissociated adsorption of N_2 is the rds with NH^* as the most abundant reaction intermediate. The sequence considered is:

$$\text{(i)} \quad N_2 + 2* \xrightarrow{k_1} 2N*$$
$$\text{(ii)} \quad H_2 + 2* \leftrightarrow 2H*$$
$$\text{(iii)} \quad N* + H* \rightarrow NH* + *$$
$$\text{(iv)} \quad H_2 + NH* \xleftrightarrow{K_4} NH_3 + *$$

Steps (i) and (iii) are irreversible. Thus neither of them can be considered as rds. The fourth reaction is not an elementary step but a sum of equilibrated steps. We write the three usual equations:

$$\nu = \nu_1 = k_1[*]^2[N_2][L]^{-1}. \tag{2.113}$$
$$[L] = [*] + [N*]. \tag{2.114}$$
$$K_4 = \frac{[N*][H_2]}{[NH_3][*]}. \tag{2.115}$$

As before, K_4 is written in the direction of adsorption. We obtain:

$$[*] = \frac{[L]}{1 + (K_4[NH_3]/[H_2])} \tag{2.116}$$

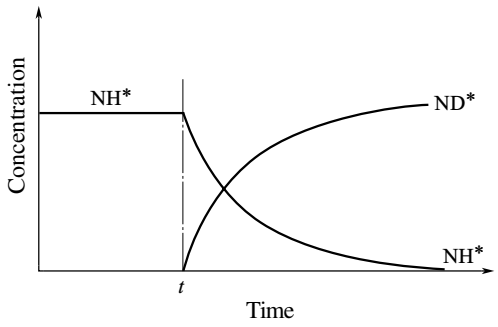


Fig. 2.24 Isotope jump technique following the method of Tamaru[204]

and finally,

$$\nu = [L]\frac{k_1[N_2]}{\{1 + (K_2[NH_3]/[H_2])\}^2}. \tag{2.117}$$

The last expression is quite close to a former one (2.111). To decide whether NH^* is the Mari or not, one might use the isotope jump technique of Tamaru.[204] At the steady state, one would replace at time $t = 0$ the normal feed N_2+$3H_2$ by N_2+$3D_2$. Spectroscopy observation of the surface by infrared could detect the relaxation of NH^* to ND^*, as shown in Fig. 2.24.

In conclusion, the above two examples allow us to generalize the treatment of single-path reactions as follows. Two major simplifications are introduced as a result of the assumption of a most abundant reaction intermediate, Mari, if possible, of a rate determining step, rds. Three rules can then be formulated.

First, in a reaction sequence, if the rds produces or destroys the Mari, then the sequence can be reduced to two steps i.e., adsorption equilibrium and the rds, and all other steps have no kinetic significance.

Second, if all steps are practically irreversible and there exists a Mari, then only two steps need to be taken into account i.e., the adsorption step and the reaction (or desorption) step of the Mari. All other steps have no kinetic significance. In fact, they may be reversible, in part or in whole.

Third, all equilibrated steps following the rds which produces the Mari may be summed up in an overall equilibrium reaction. Similarly, all equilibrated steps that precede the rds that consumes the Mari may be represented by a single overall equilibrium reaction.

Two general procedures can be used. First, if the rds consumes the Mari, the concentration of the latter is obtained from the known equilibrium relation and that of active sites. Second, if the steps of the two-step sequence are practically irreversible, the quasi-stationary state approximation leads to the solution.

2.4.3 *Fundamental hypothesis of Temkin theory*

The model of the non-uniform surface is that of a collection of micro-area, ensembles E_j of catalytic active sites with identical thermodynamic and kinetic properties in each ensemble, as shown in Fig. 2.25. Each ensemble has uniform surface and contains dS'_j sites per cm^2. The distribution of active sites on catalyst surface is

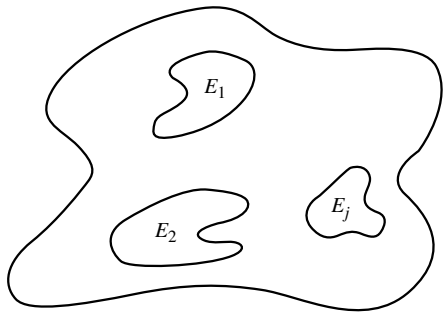


Fig. 2.25 Non-uniform distribution of active sites on surface of catalysts

continuous as mentioned in Sec. 2.2.2.[205] So, the total site density [L] is obtained by integral over all ensembles:

$$\int \mathrm{dS'_j} = [\mathrm{L}] \tag{2.118}$$

The total reaction rate is the sum of the partial reaction rates on each ensemble, with the assumption of a continuous distribution of the reaction rate. We write:

$$\nu = \int \nu_{\mathrm{t,j}} \mathrm{dS'_j}, \tag{2.119}$$

where $v_{t,j}$ is the turnover rate on sites of ensemble E_j, calculated for a uniform surface.

For each ensemble, we can write the value of $v_{t,j}$ for a two-step catalytic reaction sequence:

$$\begin{gathered}
\mathrm{S_1 + A_1} \underset{\mathrm{k_{-1}}}{\overset{\mathrm{k_1}}{\rightleftharpoons}} \mathrm{B_1 + S_2} \\
\mathrm{S_2 + A_2} \underset{\mathrm{k_{-2}}}{\overset{\mathrm{k_2}}{\rightleftharpoons}} \mathrm{B_2 + S_1} \\
\hline
\mathrm{A_1 + A_2 = B_1 + B_2}
\end{gathered}$$

Equation (2.120) can be obtained directly by means of the quasi-steady state approximation:

$$\nu_{\mathrm{t,j}} = \frac{\nu_{\mathrm{j}}}{[\mathrm{L_j}]} = \frac{\mathrm{k_1 k_2 [A_1][A_2] - k_{-1} k_{-2} [B_1][B_2]}}{\mathrm{k_1[A_1] + k_{-2}[B_2] + k_2[A_2] + k_{-1}[B_1]}}. \tag{2.120}$$

For each ensemble, the active site balance is:

$$[\mathrm{L}_j] = [\mathrm{S_1}] + [\mathrm{S_2}], \tag{2.121}$$

where, $\mathrm{S_1}$ and $\mathrm{S_2}$ are empty and occupied sites, respectively. The ratio of the concentrations of these sites is Eq. (2.95):

$$\mathrm{u} = \frac{\mathrm{S_1}}{\mathrm{S_2}} = \frac{\mathrm{k_{-1}[B_1] + k_2[A_2]}}{\mathrm{k_1[A_1] + k_{-2}[B_2]}}. \tag{2.122}$$

(1) The first hypothesis of Temkin theory. The first hypothesis of Temkin theory is that active sites on catalyst surface exist a continuous distribution function in the following form,

$$dS' = a \exp\left(\frac{-\gamma A^0}{RT}\right) d\left(\frac{A^0}{RT}\right), \tag{2.123}$$

where γ is a parameter characterizing the distribution of active site and dS' is the number of sites per cm^2 with a standard affinity for adsorption between A^0 and A^0+dA^0 in the ensemble E_j. The constant α is determined by means of the integration (2.118). It should be emphasized that the character of active site distribution γ is a special concept and basis of Temkin theory, from which the expressions of isotherm and rate of adsorption can be derived,[199] showing the universal applicability of Temkin theory.

(2) The second hypothesis of Temkin. The second hypothesis of Temkin theory is that the relation between rate constants k_i and equilibrium constants $K_i = k_i/k_{-i}$ obeys a Bronsted-type relation:

$$k_i = \text{constant} \times K_i^{\alpha}, \tag{2.124}$$

where α is so-called transfer coefficient and its value is between zero and unity, frequently in the vicinity of 0.5. Relation (2.124) is very general in chemical kinetics, e.g., also so-called the relation of Polanyi and Semenov in acid-base catalysis.[206]

The Polanyi relation can be understood qualitatively for a family of exothermic elementary reactions with increasing values of the enthalpy of reaction $|\Delta H|$. To an increase $\Delta|\Delta H|$, corresponds a decrease $|\Delta E_a|$ in the activation barrier (see Fig. 2.26) so that:

$$|\Delta E_a| = \alpha \Delta |\Delta H|,$$

or more simply:

$$E_a = E^0 + \alpha \Delta H, \tag{2.125}$$

where ΔH is negative for exothermic reaction and $0 < \alpha < 1$ and E^0 is another constant for the particular family of reactions.

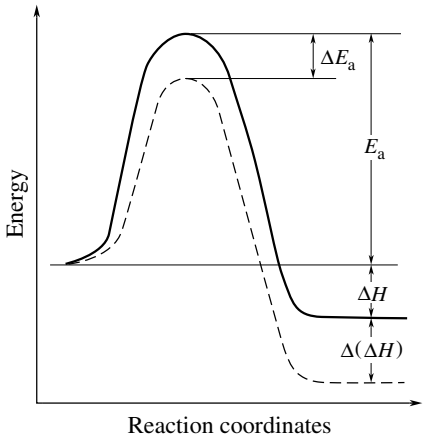


Fig. 2.26 Relation of Polanyi. E_a: activation barrier; ΔH: Enthalpy of reaction

The Bronsted relation obtained from Polanyi relation:

$$\frac{E_a}{RT} = \text{constant} + \alpha\frac{\Delta \text{H}}{RT}$$

$$\exp\left(-\frac{E_a}{RT}\right) = \text{constant}' \times \exp\left(\frac{-\alpha\Delta \text{H}}{RT}\right) \tag{2.126}$$

If we assume that the entropy of activation and the entropy of reaction do not change from one reaction to another among the family considered, then Eq. (2.124) becomes:

$$k = \text{constant} \times K^{\alpha} \tag{2.127}$$

Similar relations are also used in physical organic chemistry under the name of linear free-energy relationships.

(3) The third assumption of Temkin. From the preceding relations, we can now relate the four rate constants in the rate equation (2.120) to the standard affinity of adsorption. So, the third assumption proposed by Temkin is that Bornsted transfer coefficient is the same for the two chemically similar steps (e.g., adsorption and desorption):

$$k_1 = \text{constant}_1 \times \text{K}_1^{\alpha} = \text{constant}_1 \times \exp(\alpha \text{A}_1^0/\text{RT}) \tag{2.128}$$

$$k_{-1} = k_1/K_{-1} = \text{constant}_1 \times \text{K}_1^{\alpha-1} = \text{constant}_1 \times \exp[(\alpha-1)\text{A}_1^0/\text{RT}] \tag{2.129}$$

$$k_2 = \text{constant}_2 \times \text{K}_2^{\alpha-1} = \text{constant}_2 \times \exp[(\alpha-1)\text{A}_2^0/\text{RT}] \tag{2.130}$$

$$k_{-2} = \text{constant}_2 \times \text{K}_2^{\alpha} = \text{constant}_2 \times \exp(\alpha \text{A}_2^0/\text{RT}). \tag{2.131}$$

The standard affinities A_1^0 and A_2^0 are defined as positive in the direction of adsorption, i.e., from left to right for the first step, and even reverse for the second step. They are related to each other:

$$A_1^0 - A_2^0 = A_{\text{Overal}}^0$$

where A_{overall}^0 is the standard affinity of overall reaction, which is a constant in certain sense as it is independent of nature of the sites. Hence, only one affinity, A_1^0, needs to be considered in the above equations.

Let,

$$t = A_1^0/RT, \tag{2.132}$$

where t is a dimensionless affinity, the variation of which, through the distribution function (2.123) defines the non-uniformity of the catalyst surface. It is assumed that t has upper value t_0 and a lower value t_1, so that the width f of the distribution is:

$$f = t_0 - t_1 \tag{2.133}$$

The rate constants (2.128) to (2.131) can be written in a form that leads to an easy integration of Eq. (2.119). Thus,

$$k_1 = \text{constant}_1 \times \exp(\alpha \text{t}).$$

But when $t = t_0$, $k_1 = k_1^0$ so that:

$$\text{Constant}_1 = k_1^0 \times \exp(-\alpha \text{t}_0)$$

or

$$k_1 = k_1^0 \exp(t - t_0) \tag{2.134}$$

Similarly,

$$k_{-1} = k_{-1}^0 \exp[(\alpha - 1)(t - t_0)] \tag{2.135}$$

$$k_{-2} = k_{-2}^0 \exp \alpha(t - t_0) \tag{2.136}$$

$$k_2 = k_2^0 \exp[(\alpha - 1)(t - t_0)] \tag{2.137}$$

In the expressions (2.134)–(2.137) of rate constants, the pre-exponential factors represent the rate constants values at the maximum value of the affinity. Now the constant α in Eq. (2.123) can be evaluated:

$$\int \text{dS}' = \int_{\text{t}_1}^{\text{t}_0} a \exp(-\gamma t)\text{dt} = [\text{L}]$$

$$\frac{[\text{L}]}{a} = \left[-\frac{1}{\text{r}} \exp(-\gamma t)\right]_{\text{t}_1}^{\text{t}_0} \tag{2.138}$$

and

$$a = \frac{[\text{L}]\gamma \exp(\gamma t_0)}{[\exp(\gamma f)] - 1} \tag{2.139}$$

Substitute Eq. (2.139) into (2.123), we get:

$$\text{dS} = \text{dS'}/[\text{L}]$$

$$\text{dS} = \frac{\gamma \exp(\gamma t_0)}{[\exp(\gamma f)] - 1} \times \exp(-\gamma t)\text{dt}, \tag{2.140}$$

where dS is the fraction of active sites with affinity between t and $t + dt$.

To integrate Eq. (2.119), let us introduce the auxiliary variable u (Eq. (2.122)) instead of t:

$$u = u_0 \exp(t_0 - t), \tag{2.141}$$

with

$$\text{u}_0 = \frac{\text{k}_{-1}^0[\text{B}_1] + \text{k}_2^0[\text{A}_2]}{\text{k}_1^0[\text{A}_1] + \text{k}_{-2}^0[\text{B}_2]}. \tag{2.142}$$

Clearly, u_0 is the value of u for $t = t_0$.

The overall rate on the collection of sites can be written as:

$$\nu = \int \nu_{t,j} dS'_j = \int \frac{k_1 k_2 [A_1][A_2] - k_{-1} k_{-2} [B_1][B_2]}{k_1 [A_1] + k_{-1} [B_1] + k_2 [A_2] + k_{-2} [B_2]} dS'_j. \tag{2.143}$$

By introducing the expression for the k_i and dS'_j and regrouping the terms, we get,

$$\nu = \int_{t_1}^{t_0} \frac{k_1^0 k_2^0 [A_1][A_2] - k_{-1}^0 k_{-2}^0 [B_1][B_2] \exp a(t - t_0)}{(k_{-1}^0 [B_1] + k_2^0 [A_2]) + (k_1^0 [A_1] + k_{-2}^0 [B_2]) \exp(t - t_0)}$$

$$\times \frac{[L]\gamma}{[\exp(\gamma f)] - 1} \times \exp -\gamma(t - t_0) dt \tag{2.144}$$

Further let $m = \alpha - \gamma$, since $dt = -du/u$:

$$\nu = -\int_{u_1}^{u_0} \frac{[L]\gamma}{[\exp(\gamma f) - 1]} \times \frac{(k_1^0 k_2^0 [A_1][A_2] - k_{-1}^0 k_{-2}^0 [B_1][B_2]) u_o^m}{(k_{-1}^0 [B_1] + k_2^0 [A_2]) u + (k_1^0 [A_1] + k_{-2}^0 [B_2]) u_0} \times u^{-m} du, \tag{2.145}$$

where u_1 is the value of u for $t = t_1$. Replacing the value of u_0 by its expression (2.142) gives:

$$\nu = -\frac{[L]\gamma}{[\exp(\gamma f) - 1]} \times \frac{k_1^0 k_2^0 [A_1][A_2] - k_{-1}^0 k_{-2}^0 [B_1][B_2]}{(k_1^0 [A_1] + k_{-2}^0 [B_2])^m (k_{-1}^0 [B_1] + k_2^0 [A_2])^{1-m}}$$

$$\times \int_{u_1}^{u_0} \frac{u^{-m}}{1 + u} du \tag{2.146}$$

(4) The fourth hypothesis of Temkin. To evaluate the integral in (2.146), Temkin put forward the fourth hypothesis that the concept of the moderate coverage, and also that of concerning the limits u_0 and u_1. The moderate coverage refers to that almost sites are occupied for the most active adsorption area, but the most inactive adsorption area is almost completely empty on a non-uniform surface. It is assumed that for the upperior limit of t, all active sites are occupied. This means:

$$u_0 = [S_1]/[S_2] \to 0.$$

On the other hand, for the inferior limit of t, assuming that all sites are empty:

$$u_1 \to \infty.$$

From the definition integral table, we obtain:

$$\int_0^\infty \frac{u^{-m}}{1 + u} du \approx \frac{\pi}{\sin(\pi m)}. \tag{2.147}$$

Hence the final expression of the rate on a non-uniform surface following the formula of Temkin becomes:

$$\nu_t = \frac{\nu}{[L]} = \tau \frac{k_1^0 k_2^0 [A_1][A_2] - k_{-1}^0 k_{-2}^0 [B_1][B_2]}{(k_1^0 [A_1] + k_{-2}^0 [B_2])^m (k_{-1}^0 [B_1] + k_2^0 [A_2])^{1-m}} \tag{2.148}$$

$$\tau = \frac{\pi}{\sin(\pi m)} \times \frac{\gamma}{[\exp(\gamma f)] - 1} \tag{2.149}$$

It is noteworthy that there exists the similarity in form between Eq. (2.148) on non-uniform surface and (2.120) on uniform surface. For both expressions, the numerators are identical, while the denominators contain the same terms, although grouped in different ways.

2.4.4 *The reaction rate equation of Temkin–Pyzhev for ammonia synthesis*

The first application of Temkin theory in history was on catalytic reaction for ammonia synthesis on iron catalyst. The famous reation rate equation of Temkin–Pyzhev was obtained, corresponding to the overall reaction:

$$\mathrm{N_2} + 3\mathrm{H_2} = 2NH_3.$$

The two-step mechanism without dissociation of dinitrogen can be written as:

$$① \ N_2 + * \underset{k_1}{\overset{k_{-1}}{\rightleftharpoons}} N_2^*.$$

$$② \ N_2^* + 3H_2 \overset{K_2}{\longleftrightarrow} 2NH_3 + *,$$

where $\mathrm{K_2} = k_{-2}/k_2$, $\mathrm{N_2^*}$ as the most abundant reaction intermediate, and step (1) is the rate determining step. By hypothesis of the latter, it can be written as:

$$k_2^0, k_{-2}^0 \gg k_1^0, k_{-1}^0.$$

Applying Temkin Eq. (2.148), and if

$$[A_1] \equiv [N_2], \ [A_2] \equiv [H_2], \ [B_2] \equiv [NH_3] \quad \text{and} \quad [B_1] \equiv 1,$$

we get,

$$\nu_{\mathrm{t}} = \tau \frac{\mathrm{k_1^0 k_2^0 [N_2][H_2]^3 - k_{-1}^0 k_{-2}^0 [NH_3]^2}}{(\mathrm{k_1^0[N_2] + k_{-2}^0[NH_3]^2})^{\mathrm{m}} (\mathrm{k_2^0[H_2]^3 + k_{-1}^0})^{\mathrm{1-m}}}.$$

With the above inequalities, we obtain:

$$\nu_{\mathrm{t}} = \tau \left\{ \mathrm{[N_2] k_1^0} \left[\frac{\mathrm{k_2^0}}{\mathrm{k_{-2}^0}} \frac{\mathrm{[H_2]^3}}{\mathrm{[NH_3]^2}} \right]^{\mathrm{m}} - \mathrm{k_{-1}^0} \left[\frac{\mathrm{k_{-2}^0}}{\mathrm{k_2^0}} \frac{\mathrm{[NH_3]^2}}{\mathrm{[H_2]^3}} \right]^{\mathrm{1-m}} \right\} \tag{2.150}$$

or

$$\nu_{\mathrm{t}} = \vec{\mathrm{k}}\mathrm{[N_2]} \left[\frac{\mathrm{[H_2]^3}}{\mathrm{[NH_3]^2}} \right]^{\mathrm{m}} - \overleftarrow{k} \left[\frac{\mathrm{[NH_3]^2}}{\mathrm{[H_2]^3}} \right]^{\mathrm{1-m}}. \tag{2.151}$$

Replacing by partial pressure,

$$\nu_t = k_1 P_{N_2} \left(\frac{P_{H_2}^3}{P_{NH_3}^2} \right)^m - k_2 \left(\frac{P_{NH_3}^2}{P_{H_2}^3} \right)^{1-m}, \tag{2.152}$$

where

$$k_1 = \vec{k} = \tau k_1^0 \left(\frac{\mathrm{k_2^0}}{\mathrm{k_{-2}^0}} \right)^{\mathrm{m}} = \tau k_1^0 (K_2^0)^{-m}. \tag{2.153}$$

$$k_2 = \overleftarrow{k} = \tau k_{-1}^0 \left(\frac{\mathrm{k_{-2}^0}}{\mathrm{k_2^0}} \right)^{\mathrm{m}} = \tau k_{-1}^0 (K_2^0)^{1-m}. \tag{2.154}$$

Thus the overall rate constants can be expressed in terms of validity for sites with the highest affinity. It is noted that the second step is not the elementary step, but it appears in the rate equation (2.151) only through its equilibrium constant K_2^0 and not through its rate constants k_2^0, k_{-2}^0.

Equation (2.151) was first obtained by Temkin and Pyzhev in 1940.[207] Up to now, it is still used, in this form or in a very similar form, in the design of ammonia converters built all over the world.

During 60's of last century, Temkin *et al.* proposed that the reaction could be divided into two steps: The first step is an activated adsorption of dinitrogen:

$$\text{(i) } N_2 \xrightarrow{Activesurface} (N_2).$$

The second step is the hydrogenation of nitrogen:

$$\text{(ii a) } (N_2) + H_2 \rightarrow (N_2H_2).$$

With an equilibrium step

$$\text{(ii b) } (N_2H_2) + 2H_2 \rightarrow 2NH_3.$$

The overall reaction rate depends on the rates of step ① and step ② a. A new generalized rate equation was derived based on the two-step mechanism:

$$r_{NH_3} = \frac{k^* p_{n_2}^{1-m}\left(1 - \frac{p_{NH_3}^2}{K_p^2 p_{N_2} p_{H_2}^3}\right)}{\left(\frac{l}{p_{H_2}} + \frac{p_{NH_3}^2}{K_p^2 p_{N_2} p_{H_2}^3}\right)^m \left(\frac{l}{p_{H_2}} + 1\right)^{1-m}}, \tag{2.155}$$

where the l/P_{H2} is ratio of desorption rate and hydrogenation rate of adsorbed nitrogen. Later, it was pointed out by many scholars that the rate constants from reaction rate calculated with partial pressure are related to the pressure. So, Temkin suggested in 1950 that the Eq. (2.151) should be multiplied by a correct factor and replacing partial pressure by fugacity at high pressures, thus Eq. (2.151) becomes:

$$r_{NH_3} = \left\{k_1 f_{N_2}\left(\frac{f_{H_2}^3}{f_{NH_3}^2}\right)^m - k_1\left(\frac{f_{NH_3}^3}{f_{H_2}^2}\right)^{1-m}\right\} \exp\left[-\frac{(V_a - V_S a)p}{RT}\right], \tag{2.156}$$

where V_a and V_s are the partial molar volumes of activated complex and adsorbed ammonia, respectively.

For the simplicity of calculation, Dasen and Shimen proposed that the fugacity, under the pressure of 15 MPa–30 MPa, could be used to replace directly partial pressure in Eq. (2.151) and no correct factor was needed. In addition, there are other rate equations:

$$\text{Kapeili} \quad r_{NH_3} = \frac{k_1 f_{N_2}^{0.5}[1 - f_{NH_3}/(f_{H_2}^{1.5} f_{N_2}^{0.5} K_f)]}{1 + K_1 f_{NH_3}/f_{H_2}^{1.5} + K_2 f_{NH_3}/f_{H_2} + K_3 f_{NH_3}} \tag{2.157}$$

$$\text{Feralis} \quad r_{NH_3} = \frac{k_1[f_{N_2} f_{H_2}^2 - f_{NH_3}^2/(f_{H_2} K_f^2)]}{K_1 f_{N_2}^2 + K_2 f_{NH_3}^2/f_{H_2} + K_3 f_{H_2} f_{NH_3}} \tag{2.158}$$

$$\text{Nilson} \quad r_{NH_3} = \frac{k_2(f_{N_2} K_f^2 - f_{NH_3}^2/f_{H_2}^3)}{(1 + K_3 f_{NH_3}/f_{H_2}^{\omega})^{2\alpha}} \tag{2.159}$$

The kinetic equation (2.151) came from a theoretical derivation of experimental results. The relation between the reaction rates of various elementary steps still needs to make verification by new experimental data. With the formation and development of chemical reaction engineering, one takes care not only for the micro-mechanism of catalytic reactions, but also for what kinetic model and its parameters can more properly fit, correlate and predict the dynamic behavior of a catalyst in industrial reactor. Therefore, a new research method by macro-simulation-mathematics modeling is developed to fulfill the requirement of reaction engineering.

An attempt was made by Ozaki *et al.*[208] to verify the mechanism, on which the Temkin–Pyzhev equation was derived, by comparing the rate of the following two reactions obtained on the same catalyst:

$$\mathrm{N_2} + 3H_2 \underset{\longleftarrow}{\overset{k_H}{\longrightarrow}} 2\mathrm{NH_3}. \tag{2.160}$$

$$\mathrm{N_2} + 3D_2 \underset{\longleftarrow}{\overset{k_D}{\longrightarrow}} 2\mathrm{ND_3}. \tag{2.161}$$

According to Eq. (2.152), the ratio of overall rate constant in the forward direction of synthesis with H_2 or D_2 should be:

$$\frac{\vec{\mathrm{k}}_{\mathrm{H}}}{\vec{k}_{\mathrm{D}}} = \frac{\mathrm{k}^0_{1,\mathrm{H}}}{\mathrm{k}^0_{1,\mathrm{D}}} \left(\frac{\mathrm{K}^0_{2,\mathrm{H}}}{\mathrm{K}^0_{2,\mathrm{D}}} \right)^{-\mathrm{m}}. \tag{2.162}$$

But since hydrogen does not participate in the rds, we should have:

$$\mathrm{k}^0_{1,\mathrm{H}} = \mathrm{k}^0_{1,\mathrm{D}}. \tag{2.163}$$

Moreover, the ratio $k^0_{2\mathrm{H}}/k^0_{2\mathrm{D}}$ corresponds to the ratio of the equilibrium constant of following two reactions:

$$\mathrm{N}^*_2 + 3\mathrm{H}_2 = 2NH_3 + {}^*.$$

$$\mathrm{N}^*_2 + 3\mathrm{D}_2 = 2\mathrm{ND}_3 + {}^*.$$

Namely:

$$\frac{\mathrm{K}^0_{2,\mathrm{D}}}{\mathrm{K}^0_{2,\mathrm{H}}} = \frac{[\mathrm{NH_3}]^3[\mathrm{D_2}]^3}{[\mathrm{ND_3}]^3[\mathrm{H_2}]^3}. \tag{2.164}$$

This equation does not contain $[\mathrm{N}^*_2]$ or $[^*]$. The ratio on the left side is actually that of the overall equilibrium constants. Thus:

$$\left(\frac{\mathrm{K}^0_{2,\mathrm{H}}}{\mathrm{K}^0_{2,\mathrm{D}}} \right)^{-\mathrm{m}} = \left(\frac{\mathrm{K_H}}{\mathrm{K_D}} \right)^{\mathrm{m}}. \tag{2.165}$$

Hence the equation of Temkin–pyzhev predicts that:

$$\left(\frac{\mathrm{k_D}}{\mathrm{k_H}} \right) = \left(\frac{\mathrm{K_H}}{\mathrm{K_D}} \right)^{\mathrm{m}}. \tag{2.166}$$

The result can be verified readily, which has been done thereafter by Shapatina *et al.*[209] on an iron catalyst with m being found to be 0.5. Thus m was not an

Table 2.8 Validation of Temkin–Pyzhev mechanism for ammonia synthesis.

Temperature/K	$\vec{K}_D/\vec{K}_H$ calculated	$\vec{K}_D/\vec{K}_H$ experimental
673	2.87	3.13
723	2.60	2.89
753	2.52	2.61

adjusted parameter, and the comparison of calculated and experimental values without an adjustable parameter is shown in Table 2.8. The agreement between theory and experiment is exceptionally good, in view of the total absence of approximations necessary for the calculation.

2.4.5 *Consequence of Temkin's theory and search for best catalysts*

A concept of distribution function γ of active sites was introduced in the deduction of Temkin theory, from which well-known expressions for adsorption isotherms, such as Freundlich's and Frumkin–Temkin's isotherms and others, and for rate laws of adsorption such as Elovich's one were obtained. Analytical forms of isotherms depend on the forms of adsorptive energy distribution function, because the physical meaning of these distribution function is based on the inherent non-uniform of catalyst surfaces and the interaction between adsorbed species. Therefore, this formulation accounts for two physical effects caused by non-ideality of adsorptive phase.

It can be seen from the above-mentioned discussion that the Temkin's theory of catalytic reaction kinetics on heterogeneous surfaces is confirmed not only by overall reaction kinetic data of ammonia synthesis, isotherms and adsorptive rates of nitrogen on iron catalysts, more importantly, perhaps, but also some very useful generalization results derived from this theory. For instance, Temkin's equation is obtained based on two steps or simplified two steps mechanism. So, it can apply to any kind of catalytic reactions. The problem is: Are some simplifications required by reasonable formation of two step mechanism, and can the assumption of rate determining step be made for non-uniform surface? The answer of Temkin's theory is positive, and especially Temkin's theory of catalytic reaction kinetics on non-uniform plays an important role in solving the selection and improvement of catalysts.

2.4.5.1 *The riddling search for the optimal active site or the best catalyst*

On a non-uniform surface, which are the sites with the highest turnover frequency? Consider once more a two-step reaction. The turnover frequency on a given site among a collection of non-uniform sites, or on a given catalyst among a collection of catalysts, is given by:

$$\nu_t = \frac{k_1 k_2 [A_1][A_2] - k_{-1} k_{-2} [B_1][B_2]}{k_1 [A_1] + k_{-1} [B_1] + k_2 [A_2] + k_{-2} [B_2]}. \tag{2.167}$$

To simplify matters, let us write $\alpha = 1/2$ for the Bronsted exponent, then substitute it into the $k_{\pm j}$ from Eq. (2.134) to Eq. (2.137) yields:

$$\nu_t = \frac{k_1^0 k_2^0 [\mathrm{A}_1][\mathrm{A}_2] - k_{-1}^0 k_{-2}^0 [\mathrm{B}_1][\mathrm{B}_2]}{\mathrm{E}_1 \exp \frac{1}{2}(t - t_0) + \mathrm{E}_2 \exp \frac{1}{2}(t_0 - t)}, \tag{2.168}$$

where E_1 and E_2 are defined as:

$$\mathrm{E}_1 = k_1^0 [\mathrm{A}_1] + k_{-2}^0 [\mathrm{B}_2]. \tag{2.169}$$

$$\mathrm{E}_2 = k_2^0 [\mathrm{A}_2] + k_{-1}^0 [\mathrm{B}_1]. \tag{2.170}$$

For the highest activity and the highest turnover frequency or the best catalyst:

$$\frac{d\nu_t}{dt} = 0.$$

Since the numerator of Eq. (2.168) only relates to t_0 and not to t, so we can write $\mathrm{d}\nu_\mathrm{t}/\mathrm{dt}$ as:

$$\frac{dD}{dt} = 0,$$

where, D is the denominator of the same equation. It follows that,

$$\frac{d}{dt}\left[\left(\mathrm{E}_1 \exp \frac{1}{2}(t_{\max} - t_0) + \mathrm{E}_2 \exp \frac{1}{2}(t_0 - t_{\max})\right)\right] = 0, \tag{2.171}$$

where, $t_{\max}$ is the value of t for the highest turnover frequency $v_{t,\max}$. The condition is:

$$E_2/E_1 = \exp(t_{\max} - t_0). \tag{2.172}$$

Hence,

$$\mathrm{D}_{\nu_{\mathrm{t,max}}} = 2(\mathrm{E}_1\mathrm{E}_2)^{1/2}. \tag{2.173}$$

But the ratio E_2/E_1 is equal to u_0 (see Eq. (2.142)). Since also, according to Eq. (2.141):

$$u_{t_{\max}} = u_0 \exp(t_0 - t_{\max}).$$

It follows that:

$$\frac{E_1}{E_2} = \frac{1}{\exp(t_0 - t_{\max})} = \frac{u_0}{\mathrm{u}_{t_{\max}}} = u_0 \tag{2.174}$$

and

$$u_{t_{\max}} = 1 \tag{2.175}$$

If we remember that $u = [\mathrm{S}_1]/[\mathrm{S}_2]$ (Eq. (2.122)), then the result of Eq. (2.174) simply and legibly tells us that the optimum active site or catalyst ought to have:

$$[\mathrm{S}_1] = [\mathrm{S}_2].$$

That is to say, the fractional surface coverage is equal to 1/2. Since surface coverage is the highest on sites with the largest affinity, and vice versa, the conclusion is that the optimum site or catalyst is one with a moderate value of the affinity. As will be seen below, it corresponds to the center of the distribution of surface energy i.e., for $t = f/2$ where $f = t_0 - t_1$.

The above conclusion, based on a simplified model, must be considered in the light of the experimental results, according to the above conclusion that an iron catalyst for ammonia synthesis is about half-covered with nitrogen during the steady state reaction. Another way to look at these results is to consider them as expressions of the principle of Sabatier, who considered that the optimum catalyst was capable of adsorbing an intermediate compound sufficiently, but not to stably.

In practice, to optimize a catalyst, what must be done is to change the value of the affinity t. This can be done with metallic catalysts in three different ways. First, the surface structure can be changed by changing the exposed crystal faces or by changing the particle size. In both cases, this consists of modification of the relative surface distribution of atoms with different coordination numbers. Second, the metals can be modified by alloy formation (e.g., Cu into Ni) or addition of a surface impurity, such as sulfur, carbon, oxygen and nitrogen. Third, the search for the optimum catalyst may consist in changing the nature of the metal by going over the periodic table. For the comparison to be meaningful, it is assumed that the reaction mechanism does not change. If it does, this may be favorable or not, but that is another matter.

By optimization, here only means the optimum turnover rate or activity. We do not discuss other essential performances of an optimum catalyst such as selectivity, porosity, mechanical intensity, and stability against sintering or poisons.

Frequently, soon after introduction of a new catalyst, its activity can be improved. After a while, further improvement in activity becomes marginal until a plateau is reached. To overpass the plateau, it seems that a different sequence of chemical steps or a different reaction mechanism must be discovered.

2.4.5.2 *Difference of catalytic activity on different active site (or catalyst)*

It is quite instructive on how v_{t} changes between the upper and lower values of t, on both sides of its maximum value $t_{\max}$ for values of t equal to $t_{\max} \pm t_i$. Thus, replacing t in Eq. (2.168) by $(t_{\max} - t_i)$, we obtain:

$$\nu_t = \frac{k_1^0 k_2^0 [\mathrm{A}_1][\mathrm{A}_2] - k_{-1}^0 k_{-2}^0 [\mathrm{B}_1][\mathrm{B}_2]0}{E_1 \exp \frac{1}{2}(t_{\max} - t_i - t_0) + E_2 \exp \frac{1}{2}(t_0 - t_{\max} - t_i)}. \tag{2.176}$$

Now, Eq. (2.172) can be rewritten as:

$$E_1^{1/2} = E_2^{1/2} \exp \frac{1}{2}(t_0 - t_{\max}). \tag{2.177}$$

The denominator D of the expression for ν_t can be written in the form:

$$D_{t_i} = (E_1 E_2)^{1/2} [\exp(-t_i/2) + \exp(t_i/2)] \tag{2.178}$$

But this also leads to the result if we replace t by $(t_{\max} + t_i)$. Thus v_t changes symmetrically with t_i on the both sides of $v_{\mathrm{t,max}}$ (Fig. 2.27)

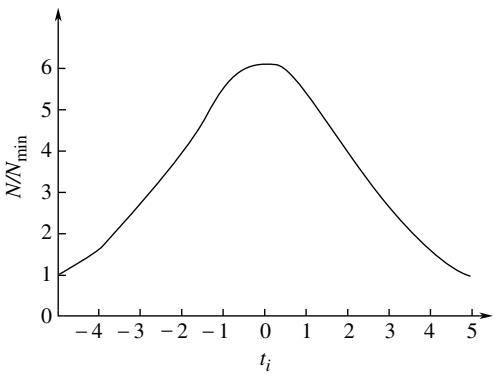


Fig. 2.27 Variation of v_t in the range of values of t defined by $f = 10$: a typical volcano curve.

In particular, $v_{t,\max}$ lies at the center of $t_0 - t_\mathrm{i} = f$ and the values of $v_{\mathrm{t},\max}$ on both sides are the same. They correspond to values of:

$$t_i = \frac{t_0 - t_1}{2} = \frac{f}{2}.$$

The denominator becomes for these values:

$$D_{\nu_t,\min} = (E_1 E_2)^{\frac{1}{2}} \left[\exp\left(\frac{f}{4}\right) + \exp\left(-\frac{f}{4}\right) \right] \tag{2.179}$$

To make the above ideas clearly, let $f = 10$, a reasonable value:

$$f = t_0 - t_1 = \frac{(\mathrm{A}_0^0 - \mathrm{A}_1^0)}{\mathrm{RT}}$$

Indeed, at 750 K, this would correspond to a variation of $\Delta\ \mathrm{A}^0$ equal to $63\,\mathrm{kJ{\cdot}mol^{-1}}$, a moderate spectrum of values for different sites or catalysts. Then, the term $\exp(-f/4)$ in Eq. (2.179) can be neglected and:

$$D_{\nu_t,\min} = (E_1 E_2)^{\frac{1}{2}} \exp\left(\frac{f}{4}\right). \tag{2.180}$$

This result must be compared to that for $D_{\nu_t,\max} = 2(E_1 E_2)^{\frac{1}{2}}$ (Eq. (2.173)), and the ratio between maximum and minimum turnover is:

$$\frac{D_{\nu_t,\max}}{D_{\nu_t,\min}} = \frac{1}{2} \exp(f/4) \tag{2.181}$$

The activity of a collection of sites or catalysts changes because of three factors. The first factor is thermodynamic and defined $K = \exp(t)$ for the higher and lower values of t so that:

$$\frac{K_{t_0}}{K_{t_1}} = \exp(t_0 - t_1) = \exp(f) \tag{2.182}$$

The second factor is kinetic and defined by the Bronsted relation for the rate constants. If $\alpha = 1/2$ for simplicity, the values of rate constant change by the amount:

$$\frac{k_{t_0}}{k_{t_1}} = \exp\left(\frac{f}{2}\right) \tag{2.183}$$

The third factor is the one of interesting for the catalytic reaction: It is expressed by Eq. (2.181) and shows that the ratio of maximum and minimum values of the turnover rates is only 1/2 exp $(f/4)$. This is due to compensation effect caused by k and K change in the same direction, i.e., the active sites become better, but there are much less of them available for reaction.

Another result is interesting. It is a ratio between $v_{\mathrm{t,max}}$ and v_{nu}. The v_{nu} calculated for a non-uniform distribution with $\gamma = 0$, corresponding to a surface where there is the same number of sites with each value of t between t_0 and t_1. For $v_{\mathrm{t,max}}$:

$$\nu_{\mathrm{t,max}} = \frac{k_1^0 k_2^0 [\mathrm{A_1}][\mathrm{A_2}] - k_{-1}^0 k_{-2}^0 [\mathrm{B_1}][\mathrm{B_2}]}{2(E_1 E_2)^{1/2}}. \tag{2.184}$$

In both cases, we assume $\alpha = 1/2$. Then from the general Eq. (2.148) and $m = \alpha - \gamma = 1/2$ and:

$$\lim_{r \to 0} \frac{r}{[\exp(rf) - 1]} = \frac{1}{f}.$$

We get:

$$\nu_{\mathrm{t,nu,r=0;\alpha=1/2}} = \frac{\pi}{f} \frac{k_1^0 k_2^0 [\mathrm{A_1}][\mathrm{A_2}] - k_{-1}^0 k_{-2}^0 [\mathrm{B_1}][\mathrm{B_2}]}{(E_1 E_2)^{1/2}}. \tag{2.185}$$

Thus, the ratio we want is:

$$\frac{\nu_{t,\mathrm{max}}}{\nu_{t,nu}} = \frac{f}{2\pi}. \tag{2.186}$$

This result is rather striking: The activity of the best site or catalyst is only $f/2\pi$ times higher than that of a non-uniform catalyst with a collection of sites, each ensemble of the collection having the same number of sites with t between t_0 and t_1 with $f = t_0 - t_1$.[210]

In conclusion, it appears that a non-uniform surface behaves catalytically much more like a uniform surface than suspected from a knowledge of its thermodynamic behavior. Rate equations are similar for a given mechanism on a uniform or non-uniform surface. This result justifies the common practice of neglecting non-uniformity of catalytic surfaces in kinetic studies.

Yet, there are cases where different catalysts exhibit very large differences in activity.

2.4.5.3 *Interpretation of very large differences in catalytic activity*

Such large differences are not readily accessible to experimental verification for sites on a given surface. But they are found when certain reactions are studied on different catalysts. How can they be explained?

In the point of view of Boudart,[211] if the reactant involved in the rate determining step requires several adjacent surface atoms, i.e., a multiple sites (ensemble, cluster), a broad spectrum of activities is expected, and the larger the size of the cluster, the broader distribution the is. This is easily seen with a simple two-step sequence:

$$\begin{aligned} A + n^* &\xrightarrow{k} An^* \\ &\vdots \\ \mathrm{B}* &\underset{\longleftarrow}{\xrightarrow{k}} * + \mathrm{B}. \end{aligned}$$

The overall reaction is A = B with the species B* being the most abundant reaction intermediate, and A requires n adjacent surface atoms in the rate-determining adsorption step. The rate is then:

$$\nu = k[A][*]\left\{\frac{[*]}{[L]}\frac{Z}{2}\right\}^{n-1}, \tag{2.187}$$

where the last term to the $(n-1)$ the power are the probability of finding $(n-1)$ free atoms that are adjacent to the first one, Z being the coordination number of nearest neighbors to a given atom.[199] As ever:

$$[L] = [*] + [B*].$$

With

$$K = \frac{[B*]}{[*][B]}.$$

Elimination of [B*] and [*] yields:

$$v = k\left(\frac{Z}{2}\right)^{n-1}[A][*]^n[L]^{-(n-1)} = \frac{k'[A]}{(1+K[B])^n}$$

$$k' = k(Z/2)^{n-1}[L]. \tag{2.188}$$

The Bronsted relation with $\alpha = 0.5$ relates the equilibrium constant to the rate constant:

$$k' = \mathrm{C}K^{1/2}, \tag{2.189}$$

where, C is a constant. Substitution gives:

$$\nu = \frac{\mathrm{C}K^{1/2}[A]}{(1+K[B])^n}. \tag{2.190}$$

Suppose that the affinity of adsorption changes as a result of a change in structure, addition of a modifier or change in the nature of the metal. The catalysts with most active or maximum reaction rate should be obtained in the presence of

maximum K_0. When

$$\frac{d\nu}{d\mathrm{K}} = 0. \tag{2.191}$$

$$K_0 = \frac{1}{[\mathrm{B}](2n-1)}. \tag{2.192}$$

The maximum rate v_0 will be obtained for an optimum value K_0 of K,

$$\frac{\nu}{\nu_0} = \left(\frac{K}{K_0}\right)^{\frac{1}{2}} \left\{\frac{1+K_0[B]}{1+K[B]}\right\}^n \tag{2.193}$$

Let us write:

$$\frac{K}{K_0} = \zeta \tag{2.194}$$

The ratio of rates becomes, with the help of Eq. (2.192)

$$\frac{\nu}{\nu_0} = \zeta^{\frac{1}{2}} \left\{\frac{1+[1/(2n-1)]}{1+[\zeta/(2-1)]}\right\}^n. \tag{2.195}$$

Values of v_0/v are collected in Table 2.9 for sets of values of ζ and n.

For a single adsorption site, $n = 1$, when K changes one hundred folds on both sides of K_0, from $\zeta = 10^{-1}$ to $\zeta = 10$, the rate varies by a factor of less than two. Here the compensation effect plays a very important role. But for multiple adsorption site, when multiplicity n of the sites goes up, e.g., $n = 6$, a hundred folds change in K on the both sides on K_0 modifies the rate by a factor of 10^9 folds. It is easy to prove, since $K = \exp(A^0/RT)$, that a variation in ζ by 10^{n} is due to a change in the standard affinity by an amount of $2n\,\mathrm{kcal\,mol^{-1}}$ at temperature of 453 K. This cases is familiar for catalytic study in practice.

Since Langmuir proposed the adsorption theory with multiple sites, the idea of multiple active sites has been stressed many times. For example, Kobozev[212] proposed that supported cluster compounds could be called as ensembles. Balandin[213] used the concept of multiplets to emphasize the geometry of sites; Ponec, Sachtler[214] and Dowden[215] proposed that use ensembles again to denote atomic group of the same nature at the surface of an alloy; and Muetterties[216] used clusters to define metal–metal bonded entities in homogeneous or heterogeneous catalysis.

Table 2.9 Ratios of reaction rates (Eq. 2.195)[211]

Ratio of equilibrium constants for adsorption:	Number n of atoms in the multiple chemisorption sites					
$\zeta = \mathrm{K/K_0}$	1	2	3	4	5	6
10	1.7	3.3	4.9	6.4	7.8	9.1
10^2	5.0	66.3	5.4×10^2	3.2×10^3	1.5×10^4	6.3×10^4
10^3	15.8	2.0×10^2	1.5×10^5	7.9×10^6	3.3×10^8	1.1×10^{10}
10^4	50.0	6.2×10^4	4.6×10^7	2.4×10^{10}	1.0×10^{13}	3.4×10^{15}
10^5	1.6×10^2	2.0×10^6	1.5×10^{10}	7.7×10^{13}	3.2×10^{17}	1.1×10^{21}
10^6	5.0×10^2	6.2×10^7	4.6×10^{12}	2.4×10^{17}	1.0×10^{22}	3.4×10^{26}

In the present context, these multiple sites explain large differences in catalytic activity. They will be essential for structure-sensitive reactions in heterogeneous catalysis.

2.4.5.4 *Structure-sensitivity of ammonia synthesis reaction*

Whether on iron catalysts or ruthenium catalysts, ammonia synthesis reaction has been proved to be a structure-sensitive reaction, and has been discussed in literature. Ertl[217] and Spencer[218] made tremendous contributions to the final determination of reaction mechanism and structure-sensitivity.

Consider a series of catalyst samples on an inert support, with each one consisting of metal particles of size d, with d values varying from 1 nm to 10 nm from sample to sample. As d increases, the relative concentrations of surface atoms C_i and sites B_j change, as i and j increase from low to high values. This means that the surface structure changes. If the turnover frequency for a reaction varies with d as shown in Fig. 2.28 the reaction is said to be structure-sensitive.[219] If the turnover frequency is independent of the size of metal particles and crystal faces, it is said to be a structure-insensitive reaction. Of course, it must be shown that the variation in turnover frequency is not caused by other factors, for instance, due to an effect of support. Because of such complication, a safer test of structure-sensitivity is the one performed on large single crystals exposing well-defined crystal faces of varying Miller indices, as shown in Table 2.10. In both cases, variations of rate equation should be attributed, and if possible, to variations in kinetic (E, A) and

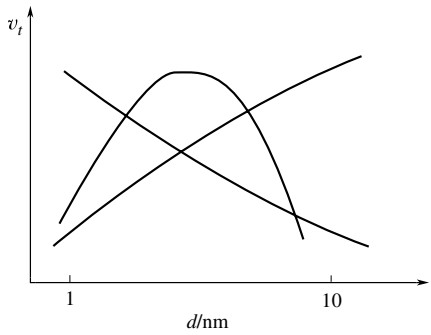


Fig. 2.28 Changes of turnover frequency with particle size for a structure-sensitive reaction

Table 2.10 Change of a real rate with crystal-lograpic orientation for a structure-sensitive reaction (ammonia synthesis on iron single crystal)[218]

Crystal face	Reaction rate/ (mol $NH_3 \cdot cm^{-2} \cdot s^{-1}$)	Crystal face	Reaction rate/ (mol $NH_3 \cdot cm^{-2} \cdot s^{-1}$)
(111)	46.00	(100) disordered	4.50
(100) ordered	2.80	(110) disordered	0.97
(110) ordered	0.11	—	—

Note: Conditions: T = 798 K, p = 2.03 MPa, stoichiometric N_2–H_2 mixture.

Table 2.11 Coverage (θ) of nitrogen on iron surface

T/K	θ_{syn}	θ_{chem}	θ_{isot}	$(N_2)_v$/Pa	T/K	θ_{syn}	θ_{chem}	θ_{isot}	$(N_2)_v$/Pa
483	0.44	0.45	0.27	0.89	549	0.51	0.53	0.47	83.8
522	0.45	0.46	0.40	5.32	568	0.54	0.52	0.55	199.5

Note: θ_{syn}, θ_{chem} and θ_{isot} correspond respectively to synthesis, chemisorption and the adsorption isotherm of Frumkin–Temkin.

thermodynamic (ΔS_{ads}, ΔH_{ads}) parameters in the rate equation. Ultimately, the question is: What is the cause of structure-sensitivity?

(1) The kinetic result. There are many facts in support of the two step mechanism with N^* as the most abundant reaction intermediate:

$$N_2 + 2* \xrightarrow{\Lambda} 2N*$$

$$N^* + \frac{3}{2}H_2 \xrightarrow{k_2} NH_3 + *$$

If the reaction is conducted under conditions far from equilibrium, the dissociated chemisorption of dinitrogen (step 1) is practically irreversible and constitutes the rate determining step. The overall equilibrium (step 2) may be treated formally like an elementary step since it carries no kinetic meaning. Rate expressions found experimentally can be obtained from above mechanism. It was also shown earlier that, at lower temperatures, the most abundant reaction intermediate may contain hydrogen, e.g., as in NH^*. Then, the rate equation is not very different from the one obtained with N^* as Mari. More direct kinetic evidence in favor of step (1) being the rate determining step was obtained from the isotope effect on rates with H_2 and D_2 as well as by determination of the average stoichiometric number σ of the reaction. There was another kinetic and thermodynamic study in favor of the above mechanism, and the underlying idea of this work is: If step (1) is the rate determining step, the rate of N_2 adsorption must be equal to the ammonia synthesis rate under well-defined conditions. Since the adsorption rate is known to obey the Elovich equation:

$$v_{ads} \propto \exp(-\text{const.} \times \theta) \tag{2.196}$$

In any comparison with v_{ads}, it is thus necessary to specify the value of the surface coverage θ for which the comparison is made. The θ value can be determined by vacuum microbalance in which an iron catalyst was placed in bucket in a steam of either dinitrogen or a stoichiometric mixture of N_2 and H_2. Weight changes are attributed to adsorbed nitrogen atoms, and hydrogen is being neglected because of its small mass. Thus, θ can be monitored at any moment during chemisorption or ammonia synthesis.

Columns 2 and 3 in Table 2.11 show the values of θ, at equal rates of ammonia synthesis and chemisorption, respectively. The extreme agreement at various temperatures confirms the view that chemisorption of dinitrogen is the rate determining step.

A third measure of θ confirms this view, with θ_{isot} being calculated from a separately measured adsorption isotherm following Frumkin–Temkin.

$$\theta = \frac{1}{f}\ln[K_1^o](N_2)_e, \tag{2.197}$$

where, by definition of an equilibrium isotherm, $(N_2)_e$ corresponds to the pressure of dinitrogen at equilibrium with the surface of the catalyst. However, at the kinetic steady state, H_2 and NH_3 in the gas-phase are equilibrated with N^*, the Mari, but the latter is not in equilibrium with gaseous N_2. Thus, to calculate θ_{isot} it is the fictitious pressure, i.e., called virtual pressure, and not the equilibrium pressure that must be substituted in the Frumkin–Temkin isotherm. The columns 4 and 5 of Table 2.11 show the corresponding values of the virtual pressure P $(N_2)_v$ and θ_{isot} at various temperatures. Except the case at the lowest temperature, in spite of the large change in virtual pressure, the value of θ varies little, which is close to those of columns 2 and 3 and is in the vicinity of 0.5. These observations are explained respectively by the logarithmic form of the isotherm, the self-consistency of the assumed mechanism, and the behavior of a non-uniform surface equation (2.175) with the optimum catalyst corresponding to a value of θ equal to 0.5.

The concept of fictitious equilibrium pressure (virtual pressure) was introduced by Temkin and Pyzhev and further developed by Kemball. It is well illustrated by the formation of iron nitride Fe_4N at 673 K. At this temperature, direct reaction between iron and dinitrogen leads to nitride only if the pressure is higher than 100 MPa, namely above the decomposition pressure of the nitride. If, however, N_2 is replaced by NH_3, even at only 100 kPa, the nitride is formed as if a virtual pressure of N_2 exceeding 100 MPa is used. The virtual pressure of N_2 can indeed be kept very high, as the equilibrium constant of the reaction of ammonia decomposition is equal to about 6,000 atm at 673 K. Thus if the partial pressure is of the order of 1 atm, the virtual pressure of dinitrogen can be of the order of 100 MPa, and goes up as the partial pressure of H_2 goes down.

In the catalytic synthesis or decomposition of ammonia, adsorbed N^* is, by assumption, in equilibrium with gaseous NH_3 and H_2. By contrast, gaseous N_2 is not in equilibrium with N*. The virtual pressure of N_2 can be understood from Fig. 2.29.

The dashed arrows represent virtual equilibrium (case (b)). Since both systems (b) and (c) are equivalent, the equilibrium constant for case (c) can be used to define the virtual pressure of N_2:

$$K = \frac{[NH_3]_e^2}{[N_2]_e[H_2]_e^3} = \frac{[NH_3]^2}{[N_2]_v[H_2]^3}, \tag{2.198}$$

subscripts e and v refer respectively to concentrations in an equilibrium mixture and in a mixture with a virtual concentrations of N_2 that would be in equilibrium with N^* and with concentrations of NH_3 and H_2, without subscript, actually present

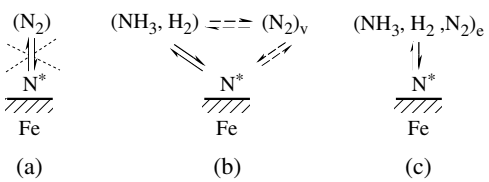


Fig. 2.29 Mechanism diagrams of the catalytic synthesis and decomposition of ammonia

during ammonia synthesis or decomposition. From Eq. (2.198), $[N_2]_v$ is obtained:

$$[N_2]_v = \frac{1}{K}\frac{[NH_3]^2}{[H_2]^3}, \tag{2.199}$$

$$[N_2]_v = [N_2]_e\frac{[NH_3]^2}{[H_2]^3}\frac{[H_2]_e^3}{[NH_3]_e^2}, \tag{2.200}$$

where $[NH_3]/[NH_3]_e$ is by definition the efficiency η of the synthesis reaction. It is convenient to use η, as the rate depends on the concentration of ammonia. Values of equilibrium conversion can be found in the literature. At 673 K, considering a reacting stoichiometric mixture that has reached $\eta = 0.1$, the total pressure is equal to 1 atm. The degree of conversion is so small that, to an excellent approximation:

$$[N_2] \approx [N_2]_e,\ [H_2] \approx [H_2]_e$$

Hence,

$$[N_2]_v = \eta^2[N_2]. \tag{2.201}$$

From this relation, it is easy to calculate the virtual pressure of N_2 during ammonia synthesis (Table 2.13).

(2) Effect of particle size on turnover rate for ammonia synthesis. Small particles of metallic iron supported on magnesia were prepared by Boudart *et al.*[220] The iron particle size could be changed between 1.5 nm and 30 nm and determined, in part, by electron microscopy, X-ray diffraction, magnetic susceptibility and Mossbauer spectroscopy. Agreement was satisfactory with particle size values obtained by selective chemisorption of carbon monoxide (if 2 Fe for 1 CO). Two results are noteworthy. (i) The turnover rate for ammonia synthesis increases by a factor of 35 as the iron particle size increases (Table 2.12). (ii) A pretreatment of the iron catalyst with ammonia increases the turnover rate by only 10% for the larger particles, but quite appreciable for iron clusters (Table 2.13).

One possible interpretation of the change in rate with particle size is a metal-support interaction that becomes more important as the size of the clusters becomes smaller. This interaction could modify the electronic structure of the metal accounting for the change in catalytic activity. This explanation can be rejected because

Table 2.12 Turnover rate (v_t)

Catalysts	Particle size/nm	$v_t/(\times 10^{-3}s^{-1})$
1 % Fe/MgO	1.5	1.0
5 % Fe/MgO	4.0	9.0
40 % Fe/MgO	30.0	35.0

Note: $T = 678$ K, $p = 101$ kPa, $\eta = 0.15$, stoichiometric mixture.

Table 2.13 Relation between turnover rate (v_t) and the pretreatment conditions

Pretreatment, in turn	$v_t/10^{-3}s^{-1}$	Pretreatment, in turn	$v_t/10^{-3}s^{-1}$
Reduction by H_2- deoxy	9.0	H_2-deoxy (20 h)	9.0
NH_3 (1 h)	13.0	Pure H_2 (20 h)	7.0

Note: $T = 678$ K, $p = 101$ kPa, $\eta = 0.15$, stoichiometric mixture, catalyst of 5% Fe/MgO.

the Mossbauer spectral parameters of metallic iron are identical within experimental error, for all of the supported samples and for bulk iron. Hence, it was concluded that ammonia synthesis on iron catalysts is a structure-sensitive reaction.

Besides, it is possible, for the first time, to propose what type of surface structure was responsible for the enhanced rate of reaction. Clearly, the surface atoms or active sites involved become more abundant as the cluster size grows. Since we deal with clusters, with ill-defined crystal faces, it is better to describe the surface structure in terms of the number of surface atoms C_i with coordination number equal to i, rather than in terms of Miller indices used for large crystals. Dumesic *et al.*[221] showed the parallel between enhanced values of turnover rates of ammonia synthesis and the following three phenomena.

The first phenomenon is ammonia pretreatment which reconstructs the surface with formation of iron nitride because of the very high virtual pressure of nitrogen.[222] It must be noted that the bulk nitride disappears when the particles are contacted with synthesis gas and that the surface reconstruction is reversibly erased by prolonged reduction in deoxo-H_2 without nitrogen or palladium diffused H_2, the latter being rigorously devoid of nitrogen. The second phenomenon is a decrease of CO chemisorption which can be attributed to less accessiblity of the atoms below surface layer. Such atoms do not chemisorb CO. On iron surface, C_7 atoms are of this type. The third phenomenon is ammonia pretreatment which brings about a decrease in the surface magnetic anisotropy of the metallic cluster predicted early and observed by means of a decrease in the area of the hyperfine split lines in the Mossbauer spectrum of Fe with a simultaneous increase in the area of the peaks ascribed to super paramagnetic iron.[222] Thus, catalysts with smaller particles exhibit an increase in super paramagnetic iron by only 3% following ammonia treatment, while this increase reaches 20% for large particles. These observations can be explained by an increase in the surface concentration of C_7 atoms which exhibit a lower energy barrier to magnetic anisotropy. Moreover, since the surface concentration of C_7 atoms increases with cluster size, all phenomena linked with ammonia pretreatment, along with the effect of particle size on turnover rate, lead to the conclusion that sites associated with C_7 atoms have a higher activity in ammonia synthesis. This conclusion is in harmony with early results.[223]

When single crystal iron is exposed to nitrogen at 673 K, Fe (111) faces grow on it. The (111) face is the face with a high concentration of C_7 atoms as shown in Fig. 2.30. In another related study, an increase in the rate of ammonia synthesis is observed when an iron catalyst is reduced in a stoichiometric mixture of N_2 and H_2, with the intent to expose more (111) faces that can be achieved by reduction in H_2 alone. Other related study show that the real rate of decomposition of NH_3 is 10 times larger on (111) faces of tungsten than that on (100) or (110) faces.[224] Also, the rate of chemisorptions of N_2 at 673 K is 200 or 60 times higher on Fe (111) than on Fe (100) or Fe (110), respectively.[218] Finally, at 2 MPa and 798 K the relative real rate of ammonia synthesis on the (111), (100) and (110) faces of iron are 418, 25 and 1, respectively.[219,225] The conclusion of Dumesic *et al.* is thus supported by a considerable amount of work. For example, there is a work which reaffirmed the increase in turnover rate for ammonia synthesis on iron particles of increasing size, but this was found to be true when the sites are counted by selective chemisorption of either H_2 or CO. By contrast, when sites are counted

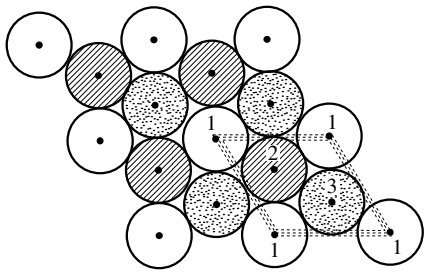


Fig. 2.30 (111) crystal face of body centered cubic lattice

by means of high temperature chemisorption of N_2, the turnover rate remains the same for Fe/MgO with iron particles of various sizes, as well as for unsupported promoted iron catalysts with smaller or larger particles than those of supported samples.

Thus, it appears that high temperature chemisorption of N_2 counts correctly, not the iron surface atoms, but the sites required for chemisorption of N_2, the rate of which is the rate determining step in ammonia synthesis reaction. It would be wrong to conclude that the reaction is structure-insensitive because the turnover rate is independent of particle size when the sites are counted with chemisorption of N_2. On the contrary, all the combined results confirm the view that a site for ammonia synthesis comprises a certain number of atoms, including C_7 atoms, forming a multiple, or ensemble, or cluster. Perhaps these consist of the six atoms as shown in Fig. 2.30.[226]

It was considered early that the differences of roughness and opening wide lead to the different activities for various crystal faces on iron catalysts. Fe (111) face is a type of opening structure, and has low surface coordination, high surface energy and strongly driving force of thermodynamics which are in favor for the occurrence of adsorption and catalysis. On the other hand, Fe (110) and Fe (100) face which is of tightness accumulation and low surface energy is of lowest roughness and lower catalytic activity for ammonia synthesis. However, Strongin[227] indicated that the reaction activity of Fe (211) and Fe (111) faces are about the same, but the roughness and opening wide of Fe (111) is larger. Therefore, the difference in activity for various faces of iron catalysts is due to the change in amount of seven Fe atomic clusters involving C_7 atoms which can effectively activate adsorbed dinitrogen rather than the surface roughness. Furthermore, Fe (210) faces are of very high opening wide and roughness and three atom layers exposed, but involve no C_7 atoms, and experimental results showed that its catalytic activity is less than those of Fe (111) and Fe (211) faces. The model of N_2 activation by the sites with C_7 atoms (Fe (111) which is a type of body-center atoms is of seven nearest neighbor Fe atoms) is given in Fig. 2.31.

In summary, it seems that the structure-sensitivity and the surface reconstruction induced by nitrogen are due to the availability or to the creation of more active sites that induce C_7 atoms. The authors found that the activity increase of wüstite-based catalyst, after reduction, also showed that there are more active sites including C_7 atom.[228,229]

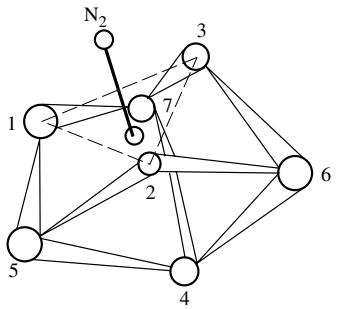


Fig. 2.31 Activation model of N_2 by iron atomic cluster

2.5 Apparent Reaction Kinetics

In general, a gas-solid catalytic reaction involves seven processes on porous catalysts as follows:

(1) Diffusion of reactant molecules from bulk gas stream to external surface of catalyst.
(2) Diffusion of reactant molecules in pore of catalyst.
(3) Adsorption of reactant molecules on surface of catalyst.
(4) Surface reaction of adsorbed species.
(5) Desorption of product molecules from catalyst surface.
(6) Diffusion of product molecules from internal pore to external surface of catalyst.
(7) Diffusion of product molecules from external surface to bulk gas stream.

Among these, (1) and (7) are called as external diffusion, (2) and (6) internal diffusion, and both of them are physical processes; the others are chemical kinetic processes.

The mechanism or sequence about gas-solid catalytic reactions can be roughly shown in Fig. 2.32. There must be mass transfer processes between gas-solid and in pores of solid for the whole process of gas-solid catalytic reaction.

Reaction heat and temperature difference between gas stream and catalyst leads to the heat transfer processes between gas and solid. The mass and heat transfer coefficients depend on Reynold and Prandtl numbers of fluid flow, i.e., state and physical properties of fluid flow. Mass and heat transfer processes in solid catalyst and catalytic reaction process on internal surface of catalysts take place simultaneously, which relate to the diffusion coefficients of reactants and products as well as the heat conductivity coefficient of catalysts. Therefore, the overall rate of a catalytic reaction depends not only on the rate of chemical reaction, but also on several physical processes such as flowing state, mass and heat transfer. The kinetics involving physical process effect is usually called as apparent or macrokinetics, while that having no physical processes is called intrinsic or microkinetics.

So, the physical transportation and adsorption–desorption should be involved in the interpretation of heterogeneous catalytic processes compared with that of homogeneous ones. It should be considered to understand the regularity of each step, to compare the effect of each step on total reaction rate and to find the slowest step that is called as rate determining step.

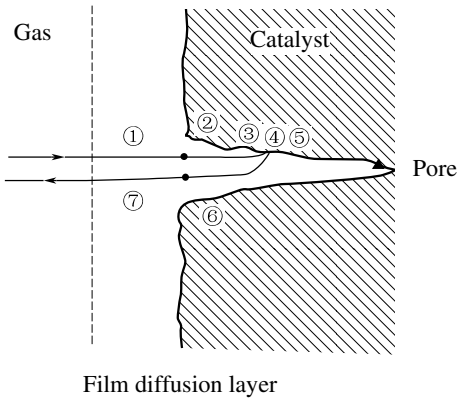


Fig. 2.32 Schematic of heterogeneous catalytic reaction mechanism

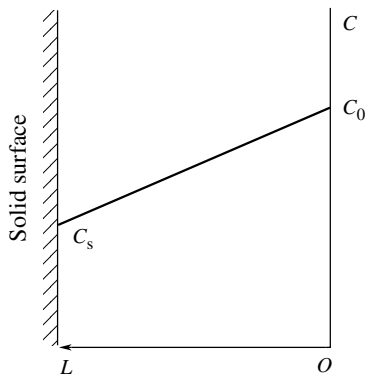


Fig. 2.33 Concentration gradient of exterior diffusion process

2.5.1 *External diffusion*

If the diffusion of reactants and products from fluid stream to the external surface of catalysts is the slowest step in the whole process, the concentration of reactants at the interface of fluid–solid must be less than that of gas bulk. Similarly, the concentrations of products are higher than that of the bulk phase. There exists a border-layer L and concentration gradient $\mathrm{d}C/\mathrm{d}L$ on the surface of catalyst. Figure 2.33 is a sketch of reactant concentration gradients, where $\mathrm{C_0}$ and $\mathrm{C_s}$ are the concentration in gas bulk and external surface of catalysts.

The diffusion rate v_D at border-layer, based on Fick's diffusion first law, is as follows:

$$v_D = -D{\cdot}S{\cdot}\frac{dc}{dL} = D{\cdot}S{\cdot}\frac{C_0 - C_s}{L}, \tag{2.202}$$

where S is the interface area and D is the diffusion coefficient.

The chemical reaction rate v is proportional to reactant concentration C_s for simple first order reaction:

$$v = k_s S C_s, \tag{2.203}$$

where, k_s is the reaction rate constant per area of external surface. If reaction is controlled by external diffusion and at steady state, we have $v_D = v$ and get from Eqs. (2.202) and (2.203) the following,

$$v = k_s S \frac{C_0}{\left(1 + \frac{k_s L}{D}\right)} = k_s S C_0 \eta, \tag{2.204}$$

where $\eta = \frac{1}{\left(1+\frac{k_s L}{D}\right)}$.

Comparing with the case without external diffusion effect, the difference in rates is η fold. η is called as external diffusion factor if rate is only limited by external diffusion. Smaller η means that the reaction is majorly dominated by diffusion. Otherwise, surface reaction is overwhelming. η approaches 1 when $\frac{k_s L}{D} \ll 1$ i.e., $k_s \ll \frac{D}{L}$, indicating that the diffusion effect can be neglected. In order to eliminate the effect of external-film diffusion, it is necessary to reduce values of k_s and L, or to increase value of D.

Based on the discussion above, there are two ways to estimate and eliminate the external diffusion effect. The first is to decrease the thickness L of gas film in interface-layer. The effect of reactant flow velocity (flow system) and stirring rate (batch system) on reaction rates should be measured at the same conditions. If the reaction rates change, there exists the limit of external diffusion influence, and the increase of flow velocity or stirring rate can reduce the thickness of interface layer until the reaction rate does not increase indicating that the effect of exterior diffusion has been eliminated. Figure 2.34 shows the relation between reaction rate and linear velocity. In order to avoid or eliminate the effect of external diffusion on kinetic experiments, the linear velocity of reactant through catalyst bed must be higher than v_0.

It should be noted that the space velocity should be kept unchanged, i.e., to keep the constant value of V_0/V_{cat} when eliminating the effect of external diffusion by increasing linear velocity of fluid. Otherwise, the contact time between reactant and catalyst drops with the increase of space velocity, which can lead to the decrease of conversion. So, during experiments, the increase of reactant flux should be realized by increasing the catalyst volume and keeping the contact time or space velocity constant, only by which correct results can be obtained.

The second way is to measure the change of reaction rate with temperature under the same experimental conditions, as the dependence of k_s (reaction rate

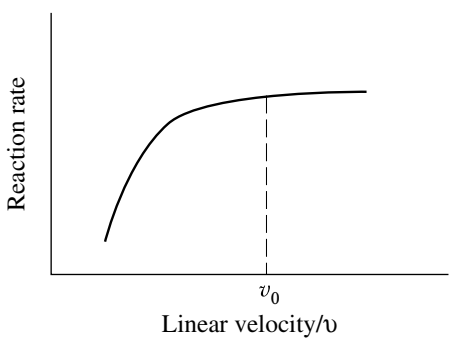


Fig. 2.34 Schematic of reaction rate and linear velocity

constant) and D (diffusion coefficient) on temperature is different: $k_s \propto -e^{E/RT}$, $D \propto T^{3/2}$. If the change of reaction rate observed is not so obvious, and activation energy is also less than $20\,kJ{\cdot}mol^{-1}$, it is possible that the catalytic reaction carries out at the region of external diffusion. In order to reach η close 1, i.e., $k_s \ll D/L$ or reaction rate is not limited by external diffusion, the reaction temperature should be further decreased and thus rate constant can decrease faster.

2.5.2 *Internal diffusion*

A part of reactants have been involved in reactions before they enter into the pores of catalysts from the external surface through the orifice of solid. Therefore, diffusion and reaction of reactant molecules take place simultaneously in pores. If the reaction rate of a reactant on the surface of catalyst is higher than diffusion rate, the reactant will be used up before it reaches to the deep sides of pores, indicating that only part of catalyst is utilized. In other words, the using ratio of catalyst internal surface is lower if there exists internal diffusion effect. The lower the diffusion rate and the bigger the catalyst particle, the lower the usage ratio of internal surface is. The concentration distribution of a reactant in a pore of catalyst is shown in Fig. 2.35.

The diffusion processes in a catalyst can be classified as molecular diffusion, Knudsen diffusion and surface diffusion etc.

(1) **Molecular diffusion**. The diffusion is molecular diffusion if the radius of pore in porous solids is larger than the mean free path of gas molecular motion, i.e., the probability of collision between molecules is larger than that between molecules and wall of pore. In this case, the resistance of transfer process mainly comes from the collision between molecules and is independent of the radius of pore. The main contribution is molecular diffusion for the systems with larger pore diameter ($>10^{-4}$ cm, comparing with mean free path 10^{-6} cm at 101.3 kPa) and with higher pressures.

The diffusion coefficient of molecular diffusion D_{Am} is:

$$D_{\mathrm{Am}} = \frac{1}{3}\tilde{\nu}\lambda, \tag{2.205}$$

where $\tilde{\nu}$ is the average velocity of molecules; λ is the mean free path of molecules.

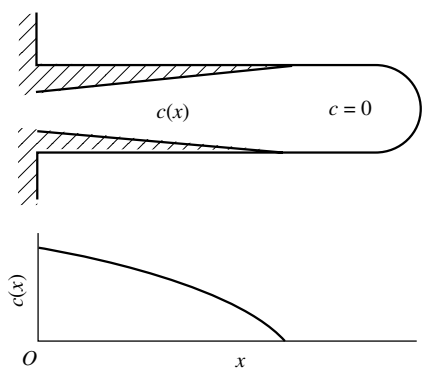


Fig. 2.35 Variation of reactant concentration in pore

It is known from theory of ideal gas molecular motion:

$$\tilde{\nu} = \sqrt{\frac{8RT}{\pi M}}.$$

$$\lambda = \frac{kT}{\sqrt{2}\pi d^2 p}.$$

Instituting them into Eq. (2.205), we get:

$$D_{\mathrm{Am}} \propto \frac{T^{3/2}}{p}.$$

The expression above shows that D_{Am} is proportional to $T^{3/2}$, inversely proportional to total pressure of gas and independent of the radius of pore.

(2) **Knudsen diffusion**. If the radius of pore is smaller than the mean free path of gas molecular motion or gas molecules collide with the wall of pore rather than other molecules, the diffusion is called as Knudsen diffusion. The main contribution comes from Knudsen diffusion for the system with smaller radius of pore and with low gas pressures.

In a small cylindrical pore, Knudsen diffusion coefficient $D_{\mathrm{AK}}(\mathrm{m^2\ s^{-1}})$ for component A can be calculated by expression as follows:

$$D_{AK} = 9700r\sqrt{\frac{T}{M_A}}, \tag{2.206}$$

where r is the average radius of pore in catalysts, cm; M_{A} is the relative molecular weight of component A; T is Kelvin temperature, K.

It can be noted from Eq. (2.206) that D_{AK} is independent of total pressure of gas and proportional to radiu r of pore and $T^{1/2}$.

There are many factors influencing internal diffusion, such as the size of particles and pore of catalysts, molecular diffusion coefficient, temperature, pressure and other parameters in reaction kinetics etc. Among these factors, the size of catalyst particles and reaction temperature are the most important and easily adjustable parameters. The estimation and elimination of internal diffusion effect can usually use the ways as follows:

The first method is to decrease the size of catalyst particles i.e., shortening length of micro-pore in catalyst particles, while keeping constant for other conditions. Because the usage ratio of internal surface is enhanced, conversion level will be higher. Figure 2.36 gives the relation curve of reaction rate or conversion with the

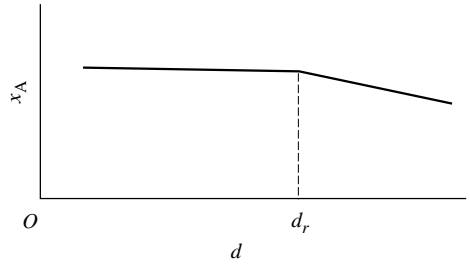


Fig. 2.36 Checkout of internal diffusion effect

diameter of catalysts at constant linear velocity. It can be seen from Fig. 2.36 that x decreases with increase of d_r when d is larger than d_r, indicating that there exists the internal diffusion effect. With further decrease of catalyst particle size to less than d_r, the conversion does not change with catalyst particle size as shown at the left side of d_r, indicating that the internal diffusion effect has been eliminated. Thus, the diameter of catalyst particles applied for kinetic experiments should be less than d_r, and for fused iron catalyst for ammonia synthesis when its size is less than 0.4 mm–0.5 mm, the internal diffusion effect has been eliminated.

The second way is that, as mentioned above, the dependence of k and D on temperature is different. The decrease of k is much faster than that of D, and so the change of temperature can be used for the elimination of internal diffusion effect.

The relative magnitude of mean free path λ of molecule motion and radius r of catalyst pore can be used for estimating if molecular or Knudsen diffusion is overwhelming. When r is less than λ, the process rate is controlled by Knudsen diffusion. On the other hand, molecular diffusion is predominated. If their values are similar, process carries out in transitional region, in which molecular (D_{Am}) and Knudsen (D_{Ak}) diffusion coefficients must be combined as a synthesized diffusion coefficient D_{Ae}. According to diffused flux series-wound principle, for equal molar reverse diffusion in a pore in multicomponent system, we have:

$$\frac{1}{D_{Ae}} = \frac{1}{D_{Am}} + \frac{1}{D_{Ak}}. \tag{2.207}$$

For an actual catalyst, pore system is very complex, because the sizes and shapes of pores are different from each other and intercross with each other. In addition, their walls may not be smooth.These factors can influence the diffusion and hydrodynamics of gas, and a tortuosity factor, expressed by δ, which is introduced to account for or check their effects. The value of δ is determined experimentally. The effective diffusion coefficient of component A is defined as:

$$D_{eff,A} = \frac{\theta}{\delta} D_{Ae}. \tag{2.208}$$

The value of tortuosity factor depends on the composition and preparation methods of catalysts. The values measured for $Fe_{1-x}O$-based A301 ammonia synthesis catalyst are: Porosity $\theta = 0.36$, average radius of pore is 16 nm, and tortuosity factor is 3.28.[230]

2.5.3 *Utilization ratio of internal surface*

Ammonia synthesis reaction is a complex multi-component and reversible reaction, and the kinetic equation can be expressed by power function. For simplification, the multi-component diffusion model is usually simply treated in engineering as a single-component diffusion model of key component, and the utilization ratio of internal surface is obtained by an approximate method from a simplified first-order reaction model.

The characters of single-component model are as follow.[231]: (1) a key component is selected to be used for the establishment of mass balance for diffusions and reaction processes in catalyst particle, and the variation of molecular fraction for other reaction components is used for finding the relation with key component according to stoichiometric equations;

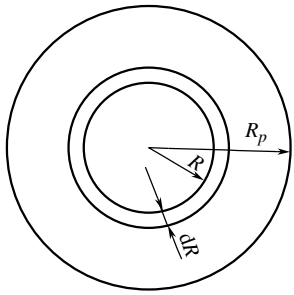


Fig. 2.37 Micro-volume element in a spherical catalyst particle

(2) Neglecting the effect of gas composition on molecular diffusion. Coefficients of key component in gas mixtures is estimated based on gas composition at external surface of catalyst, and its Knudsen diffusion coefficient and effective diffusion coefficient are calculated based on average pore radius.

For ammonia synthesis, ammonia is selected as key component because of its relative large molecular weight and the smallest molecular diffusion coefficient. So, the mass balance in catalyst particle for ammonia synthesis reaction can be expressed by the following differential equation (see Fig. 2.37):

$$D_{\text{eff}} = \left(\frac{d^2C_{NH_3}}{dR^2} + \frac{2}{R}\frac{dC_{NH_3}}{dR}\right) = \left(\frac{s_s}{1-\varepsilon}\right) r_{NH_3},$$

where S_s is internal surface area of catalysts per unit volume of bed, m^2/m^3.

Substituting $x = R/R_\text{P}$, $C_\text{NH3} = py_\text{NH3}/ZRT$, we get:

$$\frac{d^2y_{NH_3}}{dx^2} + \frac{2}{x}\frac{dy_{NH_3}}{dx} = -\left(\frac{ZRT}{P}\right)\left(\frac{s_s}{1-\varepsilon}\right)\frac{R_P^2}{D_{eff}} r_{NH_3}, \tag{2.209}$$

where p is the total pressure of the system; Z is the compressuring factor.

According to Temkin–Pezhev's equation,

$$r_{NH_3} = \frac{dN_{NH_3}}{ds} = k_1\frac{p_{N_2}p_{H_2}^{1.5}}{p_{NH_3}} - k_2\frac{p_{NH_3}}{p_{H_2}^{1.5}} = k_1P^{1.5}\frac{y_{N_2}y_{H_2}^{1.5}}{y_{NH_3}} - k_2P^{-0.5}\frac{y_{NH_3}}{y_{H_2}^{1.5}}.$$

Substituting it into Eq. (2.209) and rearranging, we have:

$$\frac{d^2y_{NH_3}}{dx^2} + \frac{2}{x}\frac{dy_{NH_3}}{dx} = -M\phi(y_{NH_3}), \tag{2.210}$$

where

$$M = \frac{ZRTk_2s_iR_P^2}{P^{1.5}(1-\varepsilon)D_{eff}} = \frac{ZRTkR_P^2(3/4)^{1.5}}{22.4P^{1.5}(1-\varepsilon)D_{eff}},$$

$$\phi(y_{NH_3}) = \frac{K_P^2p^2y_{N_2}y_{H_2}^{1.5}}{y_{NH_3}} - \frac{y_{NH_3}}{y_{H_2}^{1.5}}.$$

Both M and $\varphi(\text{y}_\text{NH3})$ are dimensionless parameters.

One of an approximative solution for Eq. (2.210)[232] is to expand $\varphi(y_{NH3})$ by Taylor series in the y_{NH3} on external surface of particle, i.e.,

$$①\phi(y_{NH_3}) = \phi(y_{NH_3,s}) + \phi'(y_{NH_3,s})(y_{NH_3} - y_{NH_3,s}) + \phi''(y_{NH_3,s}) \times (y_{NH_3} - y_{NH_3,s})^2/2! + \cdots$$

Neglecting the terms higher than second order and simplifying,

$$②\phi(y_{NH_3}) = \phi(y_{NH_3,s}) + \phi'(y_{NH_3,s})(y_{NH_3} - y_{NH_3,s})$$

Only one order is contained in equation above. For first order reaction, let us take:

$$\mu = y_{NH_3,s} - y_{NH_3} - \phi(y_{NH_3,s})/\phi'(y_{NH_3,s})$$

Then

$$\frac{d\mu}{dx} = -\frac{dy_{NH_3}}{dx},$$

$$\frac{d^2\mu}{dx^2} = -\frac{d^2y_{NH_3}}{dx^2},$$

and

$$-\mu\cdot\phi'(y_{NH_3,s}) = \phi(y_{NH_3,s}) + (y_{NH_3} - y_{NH_3,s})\phi'(y_{NH_3,s}) = \phi(y_{NH_3}).$$

Hence, we get,

$$\frac{d^2\mu}{dx^2} + \frac{2}{x}\frac{d\mu}{dx} = -M\phi'(y_{NH_3,s})\mu. \tag{2.211}$$

The equation above is a differential equation for first order and irreversible reaction at constant temperature carried out in spherical catalyst particles.

Let

$$\psi_s = \frac{1}{3}\sqrt{-M\phi'(y_{NH_3,s})}. \tag{2.212}$$

Then, Eq. (2.211) becomes,

$$\frac{d^2\mu}{dx^2} + \frac{2}{x}\frac{d\mu}{dx} = 9\psi_s^2\mu.$$

The solution of the equation above can be obtained and then the utilization ratio of internal surface is[233]:

$$\zeta = \frac{1}{\psi_s}\left[\frac{1}{th(3\psi_s)} - \frac{1}{3\psi_s}\right], \tag{2.213}$$

where ψ_s is Thiele modulus; th is hyperbolic tangent function.

Using the kinetic equation and reaction rate constant for ammonia synthesis, it is not so difficult to calculate the internal surface utilization ratio under reaction conditions.

Obviously, system pressure has serious influence on internal diffusion resistance. Firstly, molecular diffusion coefficient decreases proportionally with the increase of pressure. Secondly, high pressure leads to the enhancement of productivity of catalysts which would lead to the increase of internal diffusion resistance.

The internal utilization ratio of ammonia synthesis catalysts depends on particle size and radius of micro-pore of catalyst, reaction rate constant, operation temperature and pressure as well as the difference between the concentration of reaction components in gas bulk and equilibrium concentration etc., among which the most

prominent factors is the particle size of catalyst.[234−238] The experimental results will be further discussed in chapter 8, Sec. 8.9.

2.5.4 *Macrokinetic equation of catalytic reactions*

At steady state, for a gas–solid catalytic process, the amount of reactive components diffusing from bulk gas to external surface of catalyst actually equals to the amount consumed within particle of catalyst:

$$(r_A)_g = k_g S_g (C_{Ag} - C_{As}) = k_s S_s f(C_{As})\zeta, \tag{2.214}$$

where $(r_\mathrm{A})_\mathrm{g}$ is the apparent reaction rate of component A; S_g is the external surface area of particles per volume of catalyst bed; S_s is the internal surface area of particles per volume of catalyst bed; $f\ (C_\mathrm{As})$ is the concentration function calculated from concentration of reactive component based on external surface of particles.

Equation (2.214) is a macrokinetic equation involving the effects of transfer processes.

If first order reversible reactions are assumed, the concentration function in kinetic equation can be expressed as:

$$f(C_A) = C_A - C_A^*.$$

Then the equation can be rewritten in following form:

$$(r_A)_g = \frac{C_\mathrm{Ag} - C_\mathrm{A}^*}{\frac{1}{k_g S_g} + \frac{1}{k_s S_s \zeta}}. \tag{2.215}$$

It can be seen from Eq. (2.214) or (2.215) that the processes are in various controlling regions by chemical kinetics, internal diffusion or external diffusion for various values of k_g, S_g, k_s, S_s and ζ.

(1) **Chemical kinetics controlling**: If $\frac{1}{k_g S_g} \ll \frac{1}{k_s S_s \zeta}$, and the utilization ratio of internal surface is close to one, the effect of external and internal diffusion can be neglected, Eq. (2.215) becomes:

$$(r_\mathrm{A})_\mathrm{g} = k_s S_s (C_\mathrm{Ag} - C_\mathrm{A}^*) = k_\mathrm{s} S_\mathrm{s} (C_\mathrm{As} - C_\mathrm{A}^*). \tag{2.216}$$

The concentration distribution is,

$$C_\mathrm{Ag} \approx C_\mathrm{As} \approx C_\mathrm{Ac} \quad \text{and} \quad C_\mathrm{Ac} \gg C_\mathrm{A}^*,$$

C_Ac is the concentration of reactant A at the center of particles.

This case happens if the coefficient of external mass transfer k_g is considerably large and the catalyst particles are smaller i.e., the effects of internal and external diffusion have been eliminated.

(2) **Serious internal diffusion effect**: If $\frac{1}{k_g S_g} \ll \frac{1}{k_s S_s \zeta}$, and $\zeta \ll 1$, inhibition effect of external diffusion can be neglected. Then, $C_\mathrm{Ag} \approx C_\mathrm{As}$ and there is high effect of internal diffusion on rate of reaction, Eq. (2.215) becomes,

$$(r_A)_g = k_s S_s (C_{Ag} - C_A^*)\zeta. \tag{2.217}$$

The concentration distribution,

$$C_\mathrm{Ag} \approx C_\mathrm{As} \gg C_\mathrm{Ac} \quad \text{and} \quad C_\mathrm{As} \gg C_\mathrm{A}^*.$$

This case happens if catalyst particles and external mass transfer coefficient are considerably large.

(3) **Controlling by external diffusion**: If $\frac{1}{k_g S_g} \gg \frac{1}{k_s S_s \zeta}$, the main part of the resistance is possessed by external diffusion, Eq. (2.215) becomes,

$$(r_A)_g = k_g S_g (C_{Ag} - C_{As}) = k_g S_g (C_{Ag} - C_A^*). \tag{2.218}$$

The concentration distribution,

$$\mathrm{C_{Ag}} \gg \mathrm{C_{As}} \quad \text{and} \quad \mathrm{C_{As}} \approx \mathrm{C_{Ac}} \approx .\mathrm{C_A^*}.$$

This case occurs rarely. It usually happens at the cases of considerably small catalyst particles, less external mass transfer coefficient and relative large reaction rate constant. This will happen when the porousless netlike materials are used for catalyst as platinum-net for ammonia oxidation, or thin layer distribution of active component at external surface of catalysts. Besides, it is commonly considered that Fischer–Tropsch synthesis reaction to produce hydrocarbons is also controlled by external diffusion on iron catalysts.

If the process is controlled by external diffusion, the reaction order will change from n-order to first order, and the effect of temperature on reaction rate constant will follow the rule of external diffusion effect with temperature, and will decrease more rapidly than the effect of temperature including the activation energy.

The catalysts for ammonia synthesis are porous particles with weenie and interlaced micro-pores. The active sites playing the role of surface catalysis are distributed on the internal surfaces formed by these micro-pores. The internal surface area of ammonia synthesis after reduction is about $10\,\mathrm{m^2 \cdot g^{-1}}$–$15\,\mathrm{m^2 \cdot g^{-1}}$, and the external surface area is only $0.1\,\mathrm{m^2 \cdot g^{-1}}$. So, the surface area playing the role of surface catalysis mainly is internal surface. The equivalent diameter of catalyst particles used in industrial ammonia reactor is between 1.5 mm and 13 mm, and the inhibition effect of diffusion should be considered in real ammonia synthesis rates. When designing industrial reactor, the resistance of external diffusion can be neglected by increasing contact between gas flow and external surface of catalysts. The catalytic reaction processes for ammonia synthesis pertain to considerable internal diffusion process in most cases.

The basis for calculation of catalyst amount in an industrial reactor is the intrinsic kinetic equation and the relationship between reaction rate constant and temperature, which are obtained and collected from catalytic activity data measured with small particles of catalyst at laboratory conditions.

However, there is large difference between the conditions in industrial and in laboratory reactor. In addition to the size of catalyst particles for which the surface utilization ratio can be adjusted by Eq. (2.214), the catalyst amount used is much more for industrial reactor than laboratory one; the reduction conditions and two-dimension distributions of gas flow and temperature caused by reactor structure are also different, as well as there is catalyst deactivation etc. Therefore, intrinsic rate constant k derived from activity data measured at laboratory cannot be used directly for the design calculation of industrial reactor. In order to simplify calculation, a concept of "active coefficient" is introduced, since it is too complicated to consider the process factors such as pore diffusion in large catalyst particles, industrial reduction and deactivation and two streams of gas flow and temperature distributions in industrial reactor etc, for which direct engineering applications are more difficult. That means that the intrinsic rate constant k obtained in laboratory or Eq. (2.214) is produced by the "active coefficient." The magnitude of the active

coefficient depends not only on the utilization ratio of catalyst internal surface, but also on the decrease of activity caused by reduction processes of large particles and non-perfect reduction operation, the non-uniform distributions of fluid stream and temperature as well as deactivation, declining and poisoning etc., during operating. The relation between active coefficient and these factors above can be expressed by the following equation:

$$Cor = C_p C_R C_b C_d \tag{2.219}$$

where Cor is the active coefficient, its value is in general less one; C_p is the coefficient for reduction of large particle catalyst; C_R is the correction factor for various reduction conditions; C_b is the correction factor for non-uniform distributions of gas flow and temperature caused by structural factors of reactor; C_d is the correction factor for the declining and poisoning.

Thus, macrokinetic equation used practically in engineering can be expressed as:

$$r_s = Cor \cdot \zeta \cdot r_e, \tag{2.220}$$

where r_e is the rate calculated from activity data measured at bench scale, or a rate equation obtained from a correlation between experimental data under laboratory conditions and intrinsic kinetic equation. The active coefficient of catalysts at different positions in reactors of various types can be calculated and simulated by Eq. (2.251) (see Sec. 2.6.2) from operating data of reactors under the conditions of industrial production.

The method for adjustment of active coefficients is a simplified treatment for real complex kinetic reactions and of a very simple form. However, it cannot reveal the nature of the process. The decrease of apparent activation energy due to diffusion effect cannot be reflected by the equation that intrinsic kinetic equation is produced by active coefficients including various factors.

2.6 Design of Ammonia Synthesis Reactor

2.6.1 *Applied form of kinetic equation*

At present, Temkin–Pyzhev equation expressed by fugacity is still applied frequently for the design of industrial reactors with iron-based ammonia synthesis catalysts:

$$r_{NH_3} = k_1 f_{N_2} \left(\frac{f_{H_2}^3}{f_{NH_3}^2} \right)^{\alpha} - k_2 \left(\frac{f_{NH_3}^2}{f_{H_2}^3} \right)^{1-\alpha} \tag{2.221}$$

or its generalized Temkin equation is:

$$r_{NH_3} = \frac{k^* f_{N_2}^{1-\alpha} \left(1 - \frac{f_{NH_3}^2}{K_f^2 f_{N_2} f_{H_2}^3}\right)}{\left(\frac{l}{f_{H_2}} + \frac{f_{NH_3}^2}{K_f^2 f_{N_2} f_{H_2}^3} \right)^{\alpha} \left(\frac{l}{f_{H_2}} + 1 \right)^{1-\alpha}}, \tag{2.222}$$

where r_{NH3} is the instantaneous reaction rate and can be defined as the amount of ammonia formed on unit surface area of catalyst, and expressed as, for example, kmol/(m^2·h),

$$r_{NH_3} = \frac{dn_{NH_3}}{dS}, \tag{2.223}$$

where n_{NH3} is the molar number formed by ammonia per time, kmol/h; S is the effective surface area, m^2.

Since

$$n_{NH3} = N y_{NH3}.$$

In order to have the same basis for all materials, molar flux N_0(kmol/h) and volume flux $V_0[m^3(STP)/h]$ are used, both based on ammonia decomposition, then,

$$n_{NH3} = N y_{NH3} = \frac{N_0 y_{NH3}}{1 + y_{NH3}} = \frac{V_0 y_{NH3}}{22.4(1 + y_{NH3})}. \tag{2.224}$$

The differential of Eq. (2.224) is:

$$dn_{NH3} = \frac{V_0 dy_{NH3}}{22.4(1 + y_{NH3})^2}. \tag{2.225}$$

As the surface area of catalyst $S = \sigma V_K$(σ — specific surface area, m^2/m^3; V_K — the compacted packing volume of catalyst, m^3), its differential is:

$$dS = \sigma dV_K. \tag{2.226}$$

Then we get from Eqs. (2.223), (2.225) and (2.226):

$$r_{NH3} = \frac{dn_{NH_3}}{dS} = \frac{V_0}{22.4 \cdot \sigma (1 + y_{NH_3})^2} \cdot \frac{dy_{NH_3}}{dV_K}$$

$$= \frac{1}{22.4 \cdot \sigma (1 + y_{NH_3})^2} \cdot \frac{dy_{NH_3}}{d\tau_0}. \tag{2.227}$$

Equations (2.221) and (2.227) can be combined and integrated, to get:

$$\frac{dy_{NH_3}}{d\tau_0} = k_T (1 + y_{NH_3})^2 F_A, \tag{2.228}$$

where

$$k_T = 22.4\sigma k_2 = V_{0s} \int \frac{1}{(1 + y_{NH3})^2 F_A} dy_{NH3} \tag{2.229}$$

$$F_A = K_f^2 f_{N_2} \left(\frac{f_{H_2}^3}{f_{NH_3}^2} \right)^{\alpha} - \left(\frac{f_{NH_3}^2}{f_{H_2}^3} \right)^{1-\alpha}. \tag{2.230}$$

Also we can obtain from Eqs. (2.222) and (2.227), that

$$k_T^{'} = 22.4\sigma k^* = V_{0s} \int \frac{1}{(1 + y_{NH3})^2 F_A^{'}} dy_{NH3}, \tag{2.231}$$

where $F_A^{'}$ is the remaining term in Eq. (2.222) except $k^* : k^* = k_2 (K_f^2)^{1-\alpha}$. In order to make a comparison with the results calculated from Eq. (2.229), the results calculated from Eq. (2.231) should be divided by a factor $(K_f^2)^{1-\alpha}$ because these results are of the same meaning.

In the formula mentioned above, k_T is reaction rate constant, $MPa^{1-\alpha}h^{-1}$; τ_0 is virtual contacting time ($1/V_{0s}$), h; V_{0s} is space velocity (V_0/V_k), h^{-1}; and K_f is equilibrium constant expressed by fugacity, i.e., $(k_1/k_2)^{0.5}$.

Equation (2.228) is an applied rate equation for design of industrial reactor. Take the gas based on the decomposition of ammonia as basis, which are mixture gases including hydrogen, nitrogen, ammonia, methane and argon. Their molar

fractions are expressed by $y_{H2,0}$, $y_{N2,0}$, $y_{NH3,0}$, $y_{CH4,0}$ and $y_{Ar,0}$, respectively. After reaction, if the instantaneous molar fraction and flux of ammonia are y_{NH3} and N_{NH3} respectively, the instantaneous molar flux of its mixture gases is N_i. Based on mass balance, the molar fractions of hydrogen, nitrogen, methane and argon in mixture gases are, respectively:

$$y_{H_2} = y_{H_2,0}(1 + y_{NH_3}) - 1.5y_{NH_3}, \tag{2.232}$$

$$y_{N_2} = y_{N_2,0}(1 + y_{NH_3}) - 0.5y_{NH_3}, \tag{2.233}$$

$$y_{CH_4} = y_{CH_4,0}(1 + y_{NH_3}), \tag{2.234}$$

$$y_{Ar} = y_{Ar,0}(1 + y_{NH_3}). \tag{2.235}$$

Partial pressure and fugacity of any components can be expressed as:

$$P_{NH3} = P_t y_{NH3}, \tag{2.236}$$

$$P_{H2} = P_t y_{H2}, \tag{2.237}$$

$$P_{N2} = P_t y_{N2}, \tag{2.238}$$

$$f_{NH3} = P_t \gamma_{NH3} y_{NH3}, \tag{2.239}$$

$$f_{N2} = P_t \gamma_{N2} \left(\frac{a}{3r}\right)(1 - b_2 y_{NH3}), \tag{2.240}$$

$$f_{H2} = P_t \gamma_{H2} a(1 - b_1 y_{NH3}), \tag{2.241}$$

where p_t is the total pressure of mixture gases, p_i is the partial pressure of i component in mixture gases, y_i is the molar fraction of i component in mixture gases, γ_i is the fugacity coefficient of i component in mixture gases;

where,

$$a = \left(\frac{3r}{1 + 3r}\right)(1 - y_{CH4+Ar}), \tag{2.242}$$

$$b_1 = \frac{y_{CH4+Ar} + 0.5 + 0.5/r}{1 - y_{CH4+Ar}}, \tag{2.243}$$

$$b_2 = \frac{y_{CH4+Ar} + 0.5 + 1.5r}{1 - y_{CH4+Ar}}, \tag{2.244}$$

where y_{CH4+Ar} is the molar fraction of inert gases in mixture gases, $3r$ is the proportion of hydrogen and nitrogen for NH_3 complete decomposition.

The equilibrium constant of ammonia synthesis reaction, expressed by the fugacity of various components, is:

$$K_f = \frac{f_{NH_3}}{f_{N_2}^{0.5} \cdot f_{H_2}^{1.5}}. \tag{2.245}$$

It can be calculated by using the formula of Gillespie and Beattie,

$$\lg K_f = -2.69112 \lg T - 5.51926 \times 10^{-5} T + 1.84886$$

$$\times 10^{-7} T^2 + \frac{2001.6}{T} + 2.6899, \tag{2.246}$$

where K_f is the equilibrium constant, T is the temperature, K.

Table 2.14 The value of A_{0i}, B_{0i}, C_{0i} for various component

Gas	A_{0i}	B_{0i}	C_{0i}
H_2	0.1975	0.02096	0.0504×10^4
N_2	1.3445	0.05046	4.2×10^4
NH_3	2.3930	0.03415	476.87×10^4
CH_4	2.2769	0.0	0.0
Ar	1.2907	0.0	0.0

In order to calculate the fugacity of various components of ammonia synthesis reactions $f = P_t \cdot y_i \cdot \gamma_i$, it is required to calculate the fugacity coefficients of various components γ_i, in addition to know the total pressure of mixture gases and their molar fractions y_i.

These coefficients γ_i can be estimated by using Bettie–Bridgeman state equation:

$$RT \ln \gamma_i = (B_{0i} - A_{0i}/RT - C_{0i}/T^3) \cdot P + \frac{P}{RT}(A_{0i}^{0.5} - Sum)^2, \tag{2.247}$$

where Sum $= \sum y_i^* \cdot A_{0i}^{0.5}$; $R = 0.08206$, (atm·m^3)/(kmol·K); P is pressure, atm; A_{0i}, B_{0i}, C_{0i} are constants for various components as shown in Table 2.14; y_i^* is the equilibrium composition.

The calculation of γ_i values for various components from Eq. (2.247) is possible only if the equilibrium compositions are known beforehand, which depends also on equilibrium constants at this conditions.Therefore, the solutions are obtained only by iterative method, i.e., in order to obtain $y_{NH_3}^*$ and corresponding fugacity coefficients of various components, Eq. (2.248) needs to be solved by iterative method using Eqs. (2.245) and (2.246):

$$F(y_i) = K_f - \frac{f_{NH_3}}{f_{H_2}^{1.5} f_{N2}^{0.5}} = 0. \tag{2.248}$$

The integration terms in Eqs. (2.229) or (2.231) and corresponding reaction rate constants k_T are calculated by using Simpson's integration method with variable step length after obtaining the above parameters.

According to Arrhenius equation:

$$k_T = k_0 \exp\left(-\frac{E_a}{RT}\right) \tag{2.249}$$

or

$$\ln k_T = \ln k_0 - \frac{E_a}{R \cdot T}, \tag{2.250}$$

where $R = 8.314$J/(mol.K).

By the application of linear regression program, pre-exponent factor k_0 and apparent activation energy E_a can be obtained, and then k_{cal} and y_{cal} can be calculated. At last, the feasibility and reliability of the equation is evaluated by the targets such as correlation coefficient, standard deviation of ammonia content etc.

Based on the method mentioned above, the authors carried out the kinetic measurement for 110-2 and ZA-5 ammonia synthesis catalysts that were developed lately, at medium and low temperature, and the results obtained by treating these data are given in Table 2.15.

Table 2.15 Front-exponent factor (k_0) and activation energy (E) of reaction rate constant ($k_T=k_0e^{-E/RT}$.)

Catalysts	Items Range of temperature/°C	Equation (2.221) 375°C–475°C	Equation (2.222) 325°C–475°C
ZA-5	α in kinetic equation	0.5	0.35
	Activation energies of reverse reactions E/kJ·mol^{-1}	159.033	151.559
	Pre-exponent factor k_0/MPa$^{0.5}$s^{-1}	0.4973×10^{13}	0.4898×10^{13}
	Standard error of reaction rate constants	0.99927	2.02423
	Average standard error of ammonia concentrations	0.00214	0.00149
	Correlation coefficients	0.99955	0.99993
A110-2	α in kinetic equation	0.5	0.5
	Activation energies of reverse reactions E/kJ·mol^{-1}	171.581	171.028
	Pre-exponent factor k_0/MPa$^{0.5}$s^{-1}	2.7837×10^{13}	2.5742×10^{13}
	Standard error of reaction rate constants	0.43974	0.47376
	Average standard error of ammonia concentrations	0.00161	0.00151
	Correlation coefficients	0.99979	0.99991

2.6.2 *Mathematic model for design of reactor*

The ways to take out reaction heat from catalyst bed have only two routes: Heat exchange within the bed and no heat exchange, no matter what the structures of reactors and the size of their diameters are. The former is called as a continuous heat exchange in fixed bed, and has only a catalyst bed with cooling tubes. Reaction and heat exchange process take place simultaneously in this kind of reactor. The latter is called as an adiabatic fixed bed and is made up of several catalyst beds, and the heat exchange process is carried out between these beds. In this kind of reactor, the reactions are carried out in the beds and heat exchange process occurs between the beds, namely two processes take place separately. The so-called multi-beds are the reactors with reactions and heat exchanges progressing alternately. The ways of heat exchanges can be classified into direct heat exchange between beds and indirect heat exchange between beds as well as their combination. For multi-bed reactors with direct heat exchange the cold gas is added directly to the stream from the outlet of neighboring bed to reduce the temperature of gas enteringthe next bed. So it is called quench-cooling type.

Thus, the mathematic models for reactor design are also classified into continuous heat exchange bed and adiabatic one. Usually, the design of reactor adopts one-dimension quasi-homogeneous model which considers that when reactive gas passes the catalyst bed like a plug-flow, there exist no radial and axial return mixture, and microkinetics can be treated in intrinsic kinetics multiplied by an effective factor that involves the effects of transfer processes, and by an active coefficient that involves the effects of reduction, poisoning and declining etc. Macrokinetics can be

obtained from intrinsic kinetics regulated by the result of catalyst correction of coefficient and internal diffusion efficiency factor.

Consider a micro-volume segment in catalyst bed, the area for fluid flow (height dL) in axial bed is,

$$F = \pi(r_{\text{out}}^2 - r_{\text{in}}^2)$$

For radial bed, there are two directions for fluid flow: From the center to the wall of reactor (from inside to outside) and from the wall to the center of reactor (from outside to inside). Usually, gas flows from the wall to the center of reactor, and other parameters can be obtained as axial bed except area:

$$F = 2\pi rL,$$

where r is the radius of catalyst bed, m; L is the height of catalyst bed, m.

With the mass balance in this micro-volume segment and considering active coefficient and effective factor for internal diffusion, we get:

$$\frac{dy_{NH_3}}{dL} = \zeta \cdot Cor \cdot \frac{F}{22.4N_{T0}} \cdot \frac{dy_{NH3}}{d\tau_0}, \tag{2.251}$$

where y_{NH3} is the molar fraction of NH_3 in mixture gases; ζ is the effective coefficient for catalyst internal diffusion; Cor is the correction coefficient for catalyst activity; N_{T0} is the flux of gases in bed, kmol·h^{-1}; $\frac{dy_{NH3}}{d\tau_0}$ is the reaction rate determined by Eq. (2.228).

From heat balance in this micro-volume segment, we get:

For adiabatic bed,

$$\frac{dT}{dL} = -\Delta H_R \cdot \frac{dy_{NH_3}}{dL} \cdot \frac{1}{(1 + y_{NH_3}) \cdot C_p}. \tag{2.252}$$

For continuously heat exchange at inner of bed,

$$\frac{dT}{dL} = -\Delta H_R \cdot \frac{dy_{NH_3}}{dL} \cdot \frac{1}{(1 + y_{NH_3}) \cdot C_{pb}} - K_{ba} \cdot \frac{(1 + y_{NH_3}) \cdot (T_b - T_a) \cdot m_t \cdot \pi \cdot d_{T_0}}{N_{T_a} \cdot C_{pb}} - 1.5 \tag{2.253}$$

$$\frac{dT_a}{dL}/ = K_{ba} \cdot \frac{m_t \cdot \pi \cdot d_{T_0}}{N_{T_b} \cdot C_{pa}} (T_b - T_a), \tag{2.254}$$

where T is the temperature of gas, K; T_{a} is the temperature of gas in cooling tubes, K; T_{b} is the temperature of gas in bed, K; H_{R} is the reaction heat, kJ·k^{-1} mol; C_{p} is the constant-pressure specific heat of gas; C_{pa}, C_{pb} are the constant-pressure specific heat of gas in cooling tubes and bed, respectively; K_{ba} is the total heat transfer coefficient of cooling tubes, W·K^{-1}·m^{-2}; N_{Ta} is the gas flux in cooling tubes, kmol·h^{-1}; N_{Tb} is the gas flux in bed, kmol·h^{-1}; m_{t} is the number of cooling tubes in heat exchange bed; d_{T0} is the external diameter of cooling tubes, m.

Pressure drop of gas mixture through fixed bed can be calculated according to Eugen formula, expressed by differential equations as:

$$\frac{dP}{dL} = -\frac{f_m \cdot G^2 \cdot (1-\varepsilon)}{\rho \cdot d_s \cdot \varepsilon^3},$$
$$f_m = 1.75 + \frac{150}{\mathrm{Re}_m},$$
$$\mathrm{Re}_m = -\frac{d_s \cdot G}{\mu \cdot (1-\varepsilon)}, \tag{2.255}$$

where p is the pressure of gas, MPa; f_m is the modified friction coefficient; R_em is the Reynold Number of gas; G is the mass flux of gas, $\mathrm{kg \cdot h^{-1} \cdot m^{-2}}$; μ is the viscosity of gas, $\mathrm{Pa \cdot s^{-1}}$; ε is the porosity of catalyst bed; d_s is the diameter of catalyst particles, m; ρ is the density of mixture gases, $\mathrm{kg \cdot m^{-3}}$.

The one-dimension quasi-homogeneous model consists of first order differential equations group including Eqs. (2.251), (2.252) and (2.255) for adiabatic catalyst beds and Eqs. (2.251), (2.253), (2.254) and (2.255) for heat exchange beds. The solutions of the equation groups can be obtained by numerical integration method of Lange–Gutta with fixed step length, giving operating conditions at the outlet of various beds as well as the distributions of temperature, concentrations of various components and pressure along with the height of catalyst beds.

Boundary conditions are:

$$y_{NH_3} = y_{NH_3,0},\ T = T_0,\ P = P_0. \quad \text{at} \quad L = 0 \tag{2.256}$$

2.6.3 *Distribution between various beds of multi-beds adiabatic reactors for ammonia synthesis*

There are two types of heat exchange for a multi-beds adiabatic reactor: Indirect and direct heat exchange. If the amount and composition of entering gas, ultimate content of ammonia and number of beds have been fixed, the remaining problem is how to determine the temperature and gas composition (or conversion) at the inlet and outlet of various beds, i.e., optimum distributions between beds. As an example, the optimum distributions for multi-bed reactors with indirect heat exchange are discussed as follows[240]:

Usually, selecting the minimum value of total catalyst amount (sum of catalyst amount required by each bed) V_RT as a goal function, i.e., the distributions of temperatures and gas compositions at inlet and outlet of each bed should insure optimum distributions of this catalyst:

$$V_{RT} = \sum_{i=1}^{n} V_{Ri} = \sum_{i=1}^{n} V_{0,i}\tau_{0,i}. \tag{2.257}$$

If all standard molar fluxes of reactant gas based on ammonia decomposition for various beds are equal, the goal function above can be rewritten as:

$$V_{RT} = V_0 \sum_{i=1}^{n} \tau_{0,i}. \tag{2.258}$$

The dosage of catalysts is only the function of the temperatures and gas compositions (or conversion) at the inlet and outlet of each bed with given amount and composition of gas entering reactor. For multi-bed and indirect heat exchange reactor, it can be written as:

$$V_{RT} = f(y_{NH_{3,1}}, y_{NH_{3,2}} \ldots y_{NH_{3,1}}, y_{NH_{3,1}} \ldots T_1, T_2 \ldots T_1^{'}, T_2^{'} \ldots), \quad (2.259)$$

where $y_{\mathrm{NH3,i}}$, T_i and T_i' are ammonia molar fraction and temperatures at inlet and outlet in i bed of catalyst, respectively. Now the problem comes down to calculate the extremum of this goal function.

For a reactor with n beds, there are four variables for each bed: The temperatures and ammonia contents at its inlet and outlet of bed which must follow the expression of adiabatic temperature rise, and the temperature and ammonia content at its outlet are the same as those at inlet of next stage; and ammonia contents are the given values for the inlet of first bed and outlet of n bed. So, there are only $2n$-1 independent variables. Now we take ammonia contents at outlet from 1 to n-1 beds (n-1 variables) and temperatures at inlets (n variables) as independent variables. The necessary conditions having minimum value of the goal function V_{RT} can be obtained from Eq. (2.258) as follows:

$$\left(\frac{\partial V_{RT}}{\partial y'_{NH_3,i}}\right)_{T_i, y_{NH_3}, j(j\neq i)} = \frac{\partial \tau_{0,i}}{\partial y'_{NH_3,i}} + \frac{\partial \tau_{0,i+1}}{\partial y'_{NH_3,i+1}} = 0, \quad (2.260)$$

$$\left(\frac{\partial V_{RT}}{\partial T_i}\right)_{y_{NH_3}, T_j(j\neq i)} = \frac{\partial \tau_{0,i}}{\partial T_i} = 0, \quad (2.261)$$

where $y'_{NH_3,i}$ is the ammonia content at the outlet of i bed. T_{i} is the inlet temperature of i bed, °C.

The physical meaning of the Eq. (2.260) is that the reciprocal of reaction rate of outlet in i bed is equal to the reciprocal absolute value of reaction rate of inlet in $i+1$ bed. $\frac{\partial \tau_{0,i}}{\partial y'_{NH_3,i}}$ is positive because $\tau_{0,i}$ increases with increase of $y'_{\mathrm{NH3,i}}$, but $\frac{\partial \tau_{0,i+1}}{\partial y'_{NH_3,i+1}}$ is negative because $\tau_{0,i+1}$ decreases with increase of $y'_{\mathrm{NH3,i+1}}$. It is the first condition for minimum catalyst volume and can confirm the heat exchange processes in reactor.

The second condition Eq. (2.261) is used for determination of optimum temperatures of gases entering into each bed.

Substituting $\tau_{0,i} = \int_{y_{NH_3,i}}^{y'_{NH_3,i}} \frac{d\tau_0}{dy_{NH_3}} dy_{NH_3}$ into second condition, we get:

$$\frac{\partial \tau_{0,i}}{\partial T_i} = \int_{y_{NH_3,i}}^{y'_{NH_3,i}} \frac{\partial \left(\frac{d\tau_0}{dy_{NH_3}}\right)}{\partial T_i} dy_{NH_3} = 0, \quad (2.262)$$

where $y_{\mathrm{NH3,i}}$ is the entering ammonia content of i bed.

Equation (2.262) shows that the value i.e., integral of reciprocal of reaction rate with respect to entering temperature along with the adiabatic reaction process is zero, and this is a criterion for distinguishing optimum condition for entering temperature of each bed.

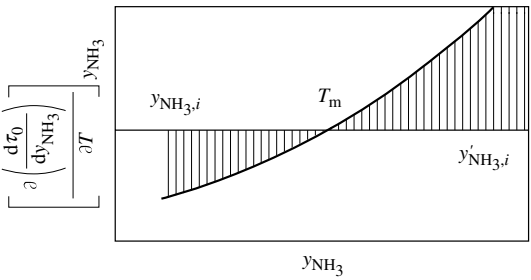


Fig. 2.38 Relationship between $\frac{\partial(d\tau_0/dy_{NH_3})}{\partial T} < 0$ and y_{NH3}

The condition satisfying the derivative of reciprocal of reaction rate with respect to temperature is zero at optimum temperature T_m, while $T < T_{\mathrm{m}}$, $\frac{\partial(d\tau_0/dy_{NH_3})}{\partial T} < 0$; and $T > T_{\mathrm{m}} \frac{\partial(d\tau_0/dy_{NH_3})}{\partial T} > 0$. So it can be seen that at the optimum entering temperature the operating line of adiabatic beds must lie above optimum temperature point T_{m}, which can make the value of integral along with reaction process (Eq. (2.262)) to zero, as shown in Fig. 2.38.

The steps of calculation for disjunctive intervals of a multi-bed indirect exchange reactor based on conditions of Eqs. (2.260) and (2.262) are as follows: At first, inlet temperature T_1 in first bed is given and outlet ammonia content $y_{\mathrm{NH3},1}$ at first bed are determined from second condition (2.262); then inlet temperature T_2 and outlet ammonia concentration $y_{\mathrm{NH3},2}$ at the second bed are calculated based on first condition (2.260); calculations are repeated until the inlet temperature T_{n} and outlet ammonia content $y_{\mathrm{NH3,n}}$ at the nth bed are obtained. If the $y_{\mathrm{NH3,n}}$ obtained is not in agreement with design value given, an adjustment is required until agreement is approached.

The discussion about optimum design parameters does not consider the temperature limit for industrial catalysts. It is actually possible that the outlet temperature at first bed determined by the method mentioned above will excess the functionable temperature of the catalyst, especially for some new catalysts that can operate at low temperatures and low pressures such as A301 and ZA-5. In practice, this case happens frequently.[241] It is a problem that the optimum interval distribution is restricted by the limit of heat-resistant temperature.[242]

When the outlet temperature of i bed is limited by $T_{\max}$, the correlation of adiabatic temperature rise is:

$$T_i = T_{\max} + \Lambda_i(y'_{NH_3,i} - y_{NH_3,i}), \tag{2.263}$$

where T_i is the inlet temperature of i bed; Λ_i is the coefficient for adiabatic temperature rise for i bed.

Equation (2.263) shows that there is a correlation between inlet temperature T_{i} and outlet ammonia content y_{NH3}, thus only a variable is independent. So, the necessary condition for minimizing goal function V_{RT} can be expressed by,

$$\left(\frac{\partial V_{RT}}{\partial y'_{NH_3,i}}\right)_{y_{NH_3,j(j\neq i)}} = \frac{\partial V_{R,i}}{\partial y'_{NH_3,i}} + \frac{\partial V_{R,i+1}}{\partial y'_{NH_3,i}} + \frac{\partial V_{R,i}}{\partial T_i}\frac{\partial T_i}{\partial y'_{NH_3,i}} = 0. \tag{2.264}$$

Substituting $\frac{\partial T_i}{\partial y'_{NH_3,i}} = -\Lambda_i$obtained from Eq. (2.263) into Eq. (2.264), we get the condition of optimum outlet temperature restricted by a limit $T_{\max}$:

$$\frac{\partial V_{R,i}}{\partial y'_{NH_3,i}} + \frac{\partial V_{R,i+1}}{\partial y'_{NH_3,i}} - \Lambda_i \frac{\partial V_{R,i}}{\partial T_i} = 0. \tag{2.265}$$

All volume fluxes at standard state (no ammonia) $V_{0,\mathrm{i}}$ are equal for heat exchange reactor, and the Eq. 2.265 can be written as:

$$\frac{\partial \tau_{0,i}}{\partial y'_{NH_3,i}} + \frac{\partial \tau_{0,i+1}}{\partial y'_{NH_3,i}} - \Lambda_i \frac{\partial \tau_{0,i}}{\partial T_i} = 0. \tag{2.266}$$

It can be seen from the comparison between Eqs. (2.260) and (2.266) that the outlet ammonia content $y'_{NH_3,i}$ cannot be varied independently at restricted outlet temperature. Increasing outlet ammonia content $y'_{NH_3,i}$ will lead to a decrease of inlet temperature T_{i}, as the temperature rise has been limited. So, it is necessary to calculate the effect of decrease in inlet temperature on catalyst amount of i bed $(-\Lambda_i \frac{\partial \tau_{0,i}}{\partial T_i})$.

If all beds except the first bed is not limited by heat-resistant temperature in a multi-beds reactor, the calculation method will be: At first, selecting the inlet temperature and given ammonia content of the first bed, and the outlet states of this bed have been determined as limiting temperature that depends on the heat-resistant temperature of catalyst; the inlet states of the second bed are calculated by Eq. (2.266), as its outlet temperature is not restricted, and the state points are selected according to Eq. (2.262); the inlet states of the third bed are determined by (2.260), and an analogy can be done for other beds until the ammonia content in last bed is obtained. If the last content is not in agreement with given value, an adjustment is required until agreement is approached.

For multi-bed sharp-cooling type reactors, the optimum distribution between beds is different from that mentioned above, as sharp-cooling gas is added continually, which changes the gas flux of each bed $V_{0,\mathrm{i}}$. Assuming that the proportion of gas flux distribution for various beds is δ_1, δ_2, $\delta_3 \cdots \delta_{n-1}$, and there are $2n$-1 independent variables for sharp-cooling catalyst beds with n beds. If the temperature at inlet of first bed has been given, the independent variables becomes $2n$-2 by selecting δ_1, δ_2, $\delta_3 \ldots \delta_{n-1}$ and the ammonia contents at outlets of 1 to n-1 beds $y'_{NH_3,1}$, $y'_{NH_3,2}, \ldots, y'_{NH_3,n-1}$ as variables and thereby the system will be determined. Also, the necessary conditions for minimizing goal function V_{RT} can be written:

$$\left(\frac{\partial V_{RT}}{\partial y'_{NH_3,i}}\right)_{\delta_1, y'_{NH_3,j(j\neq i)}} = 0,$$

$$\left(\frac{\partial V_{RT}}{\partial \delta_i}\right)_{y'_{NH_3,i}, \delta_j (j\neq i)} = 0. \tag{2.267}$$

The results calculated for the first and second condition equations mentioned above are respectively:

$$\left(\frac{\partial \tau_{0,i}}{\partial y'_{NH_3,i}}\right) + \frac{(1+y'_{NH_3,i})^2}{(1+y_{NH_3,i+1})^2}\left(\frac{\partial \tau_{0,i+1}}{\partial y'_{NH_3,i}}\right) = 0. \tag{2.268}$$

$$-\frac{\partial \tau_{0,i+1}}{\partial y_{NH_3,i+1}} = \frac{C_1}{C_2}\frac{\partial \tau_{0,i+1}}{\partial T_{i+1}}. \tag{2.269}$$

Table 2.16 Comparison of optimum design conditions between sharp–cooling and heat-exchange for multi-beds reactor

items	Heat exchange between beds	Sharp-cooling between beds
First condition	$\frac{\partial \tau_{0,i}}{\partial y'_{NH_3,i}} + \frac{\partial \tau_{0,i+1}}{\partial y_{NH_3,i+1}} = 0$	$\left(\frac{\partial \tau_{0,i}}{\partial y'_{NH_3,i}}\right) + \frac{(1+y'_{NH_3,i})^2}{(1+y_{NH_3,i+1})^2} \left(\frac{\partial \tau_{0,i+1}}{\partial y'_{NH_3,i}}\right) = 0$
Second condition	$\frac{\partial \tau_{0,i}}{\partial T_i} = 0$	$\frac{\partial \tau_{0,i}}{\partial T_i} = -\frac{C_2}{C_1} \frac{\partial \tau_{0,i}}{\partial y_{NH_3,i}}$

The optimum conditions for multi-beds reactors with sharp-cooling are that the rate at outlet of i bed is $\frac{(1+y_{NH_3,i+1})^2}{(1+y'_{NH_3,i})^2}$ fold lower than the rate at inlet of $i+1$ bed. Partial derivate of virtual resident time required with respect to inlet temperature for each bed equals to C_2/C_1 fold of the rate at inlet of this bed.

A comparison between optimum equations for multi-beds sharp-cooling reactors and heat exchange reactors between beds is given in Table 2.16.

The value of $\partial \tau_{0i}/\partial T_i$ is positive for the catalyst beds with multi-beds sharp-cooling, so, the extent that the adiabatic operating lines exceed optimum temperature is higher for catalyst beds with sharp-cooling than that with heat exchange between intervals.

2.6.4 *Fundamental data for design of ammonia synthesis reactor*

(1) Reaction heat for ammonia synthesis. Ammonia synthesis reaction can be expressed:

$$\frac{1}{2}N_2 + \frac{3}{2}H_2 = NH_3 - \Delta H_R \tag{2.270}$$

It is carried out at high pressures in industry, and all gases cannot be treated as ideal gases. Therefore, the reaction heat is a function of temperature, pressure and initial gas composition, and a modification for reaction heat obtained at ideal state is needed. The formation and heat of mixing of the system that pure $3H_2 + N_2$ form 17.6% NH_3 + 20.6% N_2 + 61.8% H_2 have been calculated and the reaction heat obtained from this are given in Table 2.17.

Table 2.17 Reaction heat of system that pure $3H_2 + N_2$ form 17.6 %NH_3

p/MPa	150°C	200°C	300°C	400°C	500°C
0.101	−48417.25	−49731.02	−51095.01	−52634.72	−53952.68
10.3	−50986.12	−51475.75	−52571.96	−53513.26	−54559.36
20.3	−50492.51	−51308.39	−52831.39	−54086.27	−55153.49
30.4	−50605.48	−51237.26	−52392.05	−53994.52	−55266.46
40.5	−51333.50	−51592.91	−52078.25	−53764.40	−54576.10

The equations for the calculation of reaction heat in Table 2.17 obtained by regression with least square method, respectively[243]

$$30.4\ \text{Mpa}: \ -\Delta H_R = 48427 + 13.465t, \tag{2.271}$$

$$20.3\ \text{MPa}: \ -\Delta H_R = 48631 + 13.364t, \tag{2.272}$$

$$10.3\ \text{MPa}: \ -\Delta H_R = 49458 + 10.203t, \tag{2.273}$$

where, unit of t is °C.

(2) Constant-pressure specific heat: Specific heat at constant pressure of a mixture gas at high pressure is:

$$C_p = \sum y_i C_{p,i}(P_i, T). \tag{2.274}$$

The relationships between specific heats at constant pressure $C_{\text{p,i}}$ [kJ/(kmol·K)] and temperature T(K), partial pressure of various components p_i (MPa) for each component are, respectively:

$$\begin{aligned} C_{p,N_2} = {} & (7.371 - 0.145 \times 10^{-2}T + 0.144 \times 10^{-5}T^2 \\ & + 0.00661P_{N2} - 0.755 \times 10^{-5}TP_{N2}) \times 4.184 \end{aligned} \tag{2.275}$$

$$\begin{aligned} C_{p,CH_4} = {} & (4.750 + 1.200 \times 10^{-2}T + 0.3030 \times 10^{-5}T^2 \\ & - 2.630 \times 10^{-9}T^3 + 0.26 \times 10^{-2}P_{CH_4}) \times 4.184 \end{aligned} \tag{2.276}$$

$$\begin{aligned} C_{p,Ar} = {} & (4.975 - 0.205 \times 10^{-4}T - 0.305 \times 10^{-5}TP_{Ar} \\ & + 0.946 \times 10^{-8}T^2 + 0.0046P_{Ar}) \times 4.184 \end{aligned} \tag{2.277}$$

When $T > 500\,\text{K}$,

$$\begin{aligned} C_{p,NH_3} = {} & (9.330 - 0.299 \times 10^{-2}T + 0.876 \times 10^{-5}T^2 + 0.0945P_{NH_3} \\ & + 0.119 \times 10^{-3}TP_{NH_3}) \times 4.184. \end{aligned} \tag{2.278}$$

When $T < 500\text{K}$,

$$\begin{aligned} C_{p,NH_3} = {} & (56.853 - 0.2646T + 0.3565 \times 10^{-3}T^2 + 0.988P_{NH_3} + 0.117 \\ & \times 10^{-2}P_{NH_3}^2 - 0.2168 \times 10^{-2}TP_{NH_3}) \times 4.184. \end{aligned} \tag{2.279}$$

(3) Viscosity of mixture gas: Viscosity of mixture gas containing ammonia can be estimated by the following equation:

$$\mu_m = \frac{\sum y_i C_i \mu_i \sqrt{M_i}}{\sum y_i \sqrt{M_i}}, \tag{2.280}$$

where μ_i is the viscosity of component i in mixture gas at total pressure p (MPa) and temperature t (°C), Pa·s; y_{i} is the molar fraction of component i in mixture gas, dimensionless; M_{i} is the molecular weight of component i in mixture gas, dimensionless; C_{i} is the correct coefficient of component i in mixture gas, dimensionless.

The relations between viscosities μ_i and total pressures p (MPa) and temperatures t (°C) for hydrogen, nitrogen, ammonia, argon and methane are as follows,

respectively:

$$\mu_{H_2} = (856.94 + 1.8906T - 0.36221 \times 10^{-3}T^2 - 0.37343 \times 10^{-3}T{\cdot}P + 0.53485 \times 10^{-3}P^2) \times 10^{-8}. \quad (2.281)$$

$$\mu_{N_2} = (1846 + 3.3715T + 0.3416 \times 10^{-2}TP + 0.6044 \times 10^{-2}P^2) \times 10^{-8}. \quad (2.282)$$

$$\mu_{NH_3} = (43569 - 0.84605 \times 10^4 \ln T - 0.25907 \times 10^5 T^{-1} + 0.10883 \times 10T^2 - 0.11781 \times 10^{-3}T^3 - 0.01807TP + 0.02574P^2) \times 10^{-8}. \quad (2.283)$$

$$\mu_{CH_4} = (1343.9 + 0.84653 \times 10^{-2}T^2 - 0.77685 \times 10^{-5}T^3 - 0.60536 \times 10^{-2}TP + 0.01014P^2) \times 10^{-8}. \quad (2.284)$$

$$\mu_{Ar} = (2495.6 + 4.4133T - 0.68328 \times 10^{-2}TP + 0.010686 \times 10^{-2}P^2) \times 10^{-8}. \quad (2.285)$$

The relations between correct coefficients and total pressures p (MPa) and temperatures t (°C) for hydrogen, nitrogen ammonia, argon and methane are as follows, respectively:

$$C_{H_2} = 1.0 \quad (2.286)$$

$$C_{N_2} = 0.90011 + 0.71278 \times 10^{-2} \ln T + 0.23144 \times 10^{-3}T + 0.3905 \times 10^{-6}TP - 0.12008 \times 10^{-5}P^2 \quad (2.287)$$

$$C_{NH_3} = -0.19825 + 0.26392T^{-1} + 0.79454 \times 10^{-2}T - 0.74743 \times 10^{-5}T^2 - 0.47034 \times 10^{-5}TP + 0.25252P^2 \quad (2.288)$$

$$C_{CH_4} = 0.20845 + 0.16188 \ln T + 0.49762T^{-1} + 0.19363 \times 10^{-3}T - 0.14746 \times 10^{-5}P^2 \quad (2.289)$$

$$C_{AR} = 1.0 \quad (2.290)$$

(4) Heat conductivity of mixture gas: Heat conductivity of mixture gas at high pressure λ_{m}[kJ/(m·h·°), total pressure p (MPa) and temperature t (°) can be estimated by following equations:

$$\lambda_m = \lambda_R \lambda_{cm} \times 360 \times 4.184 \quad (2.291)$$

$$\lambda_R = 0.86778 + 0.014399T_R^2 - 0.3705 \times 10^{-3}T_R^3 - 0.32481 \times 10^{-2}T_R P_R + 0.052976P_R \quad (2.292)$$

$$\lambda_{cm} = \sum y_i \lambda_{ci} \quad (2.293)$$

$$P_R = \frac{P}{\sum y_i P_{ci}} \quad (2.294)$$

$$T_R = \frac{T}{\sum y_i T_{ci}} \quad (2.295)$$

Table 2.18 Correctional critical parameters for various gas

Parameters	N_2	H_2	NH_3	CH_4	Ar
P_{ci}/kPa	33.5	15.68	178.0	229.0	48.0
T_{ci}/K	126.2	33.3	405.5	239.0	151.2

The correctional critical parameters for various components are given in Table 2.18.

$$\lambda_{cN_2} = 8.55, \tag{2.296}$$

$$\lambda_{cAr} = 7.10, \tag{2.297}$$

$$\lambda_{cH_2} = \frac{1}{0.039465 + 1.0558/(t + 273.15)}, \tag{2.298}$$

$$\lambda_{cNH_3} = 20.0703 + t^{0.14018}, \tag{2.299}$$

$$\lambda_{cCH_4} = 29.7527 + 0.03309t + 0.17490 \times 10^{-3}t^2 - 0.25908 \times 10^{-6}t^3 + 0.16707 \times 10^{-9}t^4. \tag{2.300}$$

2.6.5 *An example of simulating design calculation*

The structural parameters for S-200 type radial flow ammonia synthesis reactor with two beds of indirect heat exchange between beds and capacity of 1,000 t/d are as follows : For the first catalyst bed the internal diameter, outer diameter and height are, 1.17 m, 2.946 m and 3.425 m, respectively with the volume of prereducted catalyst V_{R1} of 19.6 m^3; for the second bed the corresponding values are, 0.650 m, 2.946 m and 7.925 m, respectively with the volume of unreduced catalyst V_{R2} of 51.4 m^3. The particle sizes of the catalysts are 1.5 mm–3.0 mm. The direction of gas flow is from outer to center.

The calculation is based on the mathematic model and fundamental data mentioned above and kinetic parameters listed in Table 2.18 and the restrictive condition is that the outlet temperature of first bed is not higher than 480°C and 500°C for ZA-5 and A110-2 catalyst, respectively. The results obtained by simulating calculation are listed in Table 2.19.

The considerable agreement is reached between the results of simulation design calculation and their actual operating parameters. It can be seen from Table 2.19 that under the same conditions the output of ammonia can increase up to 1,158.6 tons per day, if A110 is replaced by ZA-5 catalyst. The temperature of the whole reactor decreases, but that of outlet of the reactor rises. Thereinto, (1) the inlet temperature of the first bed decreases from 359°C to 325°C; (2) temperature at the outlet of the reactor rises to 34.5°C which is still in the range of design values permitted; (3) net ammonia value increases by 2.3%, and output of ammonia increases up to 1,158.6 t/d, or raises by 15.8%.

The result of simulation design calculation shows that it is feasible to replace A110 by ZA-5 with high activity in the synthesis reactors used originally for A110 catalyst.[244,245] However, it should be noted that ZA-5 is a new wüstite-based catalyst operating at low-temperatures. Its superiority can be better if it is used at low-temperatures. Therefore, it is not necessary to use it at high-temperatures at

Table 2.19 Results obtained by simulating design calculation

Item		A110-2	ZA-5
Pressure/MPa		12.64	12.64
Gas flux at inlet of reactor/kmol·h^{-1}		22,000	22,000
Composition of gases at inlet of reactor/%	H_2	65.1	65.1
	N_2	21.7	21.7
	CH_4	8.0	8.0
	Ar	4.0	4.0
	NH_3	1.2	1.2
Temperature of gases at inlet of first bed/°C		359	325
Temperature of gases at outlet of first bed/°C		489.6	479.3
Temperature of gases at inlet of second bed/°C		384	360
Temperature of gases at outlet of second bed/°C		446	429.5
Ammonia concentration at outlet of reactor/%		13.89	16.19
Pressure drop of the bed/MPa		0.02	0.02
Temperature of gases at inlet of reactor/°C		141	140
Temperature of gases at outlet of reactor/°C		306.5	341.0
Output of liquid ammonia/t·d^{-1}		1,000.65	1,158.63

which the efficiency catalyst is not high. If the temperature at the outlet of the first bed reaches to 489.6°C or higher, which is required by A110-2 catalyst, ammonia output will be lower. Therefore, no matter for design or normal operation, the outlet temperature of first bed should be less 480°C only in the late operating stage, at which catalytic activity decreases, can the temperature be gradually raised up to 500°C–520°C. This is one of difference between wüstite-based (ZA-5) and magnetite-based (A110) catalysts.

References

1. Wu Y. *Catalytic Chemistry*. Beijing: Science Press, 1999, 725.
2. Ertl G. *Catal. Rev. Sci. Eng.* **21**: 201, 1980. In: Boudart M, Djega-Mariadassou G. *Kinetics of Heterogeneous Catalytic Reactions* (Chinese), Translated by Gao C, Zheng S, Li C, Liu D, Shanghai: Fudan University Press, 1988.
3. Boudart M, Djega-Mariadassou G. *Kinetics of Heterogeneous Catalytic Reactions*, Princeton, NJ: Princeton University Press, 1984.
4. Rappi AK, Goddard WA. In: Truhlar DJ (ed.) *Potential Energy Surfaces and Dynamics Calculations*. New York: Plenum Press, 1981, 661.
5. Benson SW. *Thermochemical Kinetics,* New York: Wiley Interscience, 1976.
6. Stranski IN. *Z. Phys. Chem.* **136**: 259, 1928.
7. Stranski IN. *Z. Phys. Chem.* **11**: Abstract D, 342, 1931.
8. Kossel W. Nach. Ges. Wiss. Gottingen: 135, 1957.
9. Hirth JP, Pound GM. *Codensation and Evaporation, Nucleation and Growth Kinetics*, Oxford: Pergamon, 1963.
10. Somorjai GA. *Chemistry in Two Dimensions Surfaces*, Ithaca and London: Cornell University Press, 1981.
11. Van Hardeveld R, Harfog F. *Surface Sci.* **15**: 189, 1969.
12. Low MJD. *Chem. Rev.* **60**: 267, 1960.
13. Aharoni C, Tompkins FC. *Advan. Catal. Relat. Sub.* **21**: 1, 1970.
14. Scholten JJE, Zwietering P, Konvalinka JA, *et al. Trans. Faraday Soc.* **55**: 2166, 1959.

15. Boudart M, Egawa S, Oyama ST, *et al. J. Chim. Phys.* **78**: 987, 1981.
16. Liu HZ, Liu CB, Li XN, *et al. Ind. Eng. Chem. Res.* **42**(7): 1347, 2003.
17. Urabe K, Aika K, Ozaki A. *J. Catal.* **42**: 197, 1976.
18. Rambeau G, Amariglio H. *J. Catal.* **72**: 1, 1981.
19. Siporin SE, Davis RJ. *J. Catal.* **225**(2): 359, 2004.
20. Ertl G. *Catalysis.* Lee SB, Weiss M. *Surface Science.* **114**(2&3): 527, 1982.
21. Rettner CT, Stein H. *Phys. Rev. Lett.* **59**: 2768, 1987.
22. Urphy MJ, Samson P, Skelly JF, *et al.* http: www.sci.liv.ac.uk/∼dynamics/MolBeams.pdf.
23. Pfnur HE, Rettner CT, Lee J, *et al. J. Chem. Phys.* **85**: 7452, 1986.
24. Por E, Haase G, Citri O, *et al. Chem. Phys. Lett.* **188**(5&6): 553, 1991.
25. Katz G, Kosloff R. *J. Chem. Phys.* **103**(21): 9475, 1995.
26. Guan S, Liu HZ. *Ind. Eng. Chem. Res.* **39**(8): 2891, 2000.
27. Vandervell HD, Vaugh KC. *Chem. Phys. Lett.* **171**(5&6): 462, 1990.
28. Ertl G., *Catal. Rev. Sci. Eng.* **21**(2): 201, 1980.
29. Grunze M, Strasser G, Golze M, *et al. Appl. Phys. A.* **44**: 19, 1987.
30. Alstrup I, Chorkendorff I, Ullmann S. *J. Catal.* **168**: 217, 1997.
31. Mortensen JJ, Hansen LB, Hammer B, *et al. J. Catal.* **182**: 479, 1999.
32. Shen HB, Liao YY, Zhang HB, *et al. Chin. Chem. Lett.* **4**(5): 457, 1993.
33. Zhang HB, Schrader GL. *J. Catal.* **99**: 461–471, 1986.
34. Spencer MS. *Catal. Lett.* **13**: 45–49, 1992.
35. Liao DW. *J. Mol. Struc.* **121**: 101–107, 1985.
36. Tsai KR. In: 7th ICC. Nitrogen Fixation, Tokyo: 1980.
37. Bowker W. *Top Catal.* **1**(3&4): 265, 1994.
38. Aika K, Tamaru K. In: Nielsen A ed. Ammonia Catalysis and Manufacture. Chapter 3. Heidelberg: Springer, 1995. 104–143.
39. Eischens RP, Jacknow J. In: WHM *et al.* eds. Proc. 3rd Intern. Congr. Catal., Sachtler Amsterdam: 1965. North Holland Pub, 1965, 627.
40. Hardeveld RV, Montfoort AV. *Surf Sci.* **4**(4): 396, 1966.
41. Egerton TA, Sheppard N. *J. Chem. Soc. Farad. Trans.* **170**: 1357, 1974.
42. Hardeveld RV, Montfoort AV. *Surf Sci.* **17**(1): 90, 1969.
43. Borodko YG, Lyutov VS. *Kinet. Katal.* **12**: 238, 1971.
44. Eischens RP. *Acc. Chem. Res.* **5**: 74, 1972.
45. Kinoshita K, Kido K, Domen K, *et al. J. Chem. Soc. Farad. Trans.* **182**: 2269, 1986.
46. Ohkita M, Aika K, Urabe K, *et al. J. Catal.* **44**: 460, 1976.
47. Mahnig M, Schmidt LD. *Z. Phys. Chem.* (N F). **80**: 71, 1972.
48. Joyner RW, Rickman J, Roberts MW. *J. Chem. Soc. Farad. Trans.* **170**: 1825, 1974.
49. Rambeau G, Amariglio H. *J. Catal.* **72**: 1, 1981.
50. Rambeau G, Amariglio H. *Appl. Catal.* **1**: 291, 1981.
51. Rambeau G, Jorti A, Amariglio H. *Appl. Catal.* **3**: 273, 1982.
52. Rambeau G, Jorti A, Amariglio H. *J. Catal.* **74**: 110, 1982.
53. Urabe K, Aika K, Ozaki A. *J. Catal.* **42**: 197, 1976.
54. Hikita T, Kadowaki Y, Aika K. *J. Phys. Chem.* **95**(23): 9396, 1991.
55. Aika K, Tamaru K. In: Nielsen A (ed.) Ammonia Catalysis and Manufacture, Chapter 3. Heidelberg: Springer, 1995, 104–143.
56. Morikawa Y, Ozaki A. *J. Catal.* **12**: 145, 1968.
57. Schulz G, Schaefer H. *Z. Phys. Chem.* **64**: 333, 1969.
58. Kadowaki Y, Murata S, Aika K. New Frontiers in Catalysis, In: Guczi L *et al.* (eds.) Proc 10th Intern Congr Catal Budapest. Elsevier, 1993, 2055.
59. Danielson LR, Dresser MJ, Donaldson EE, *et al. Surf Sci.* **71**: 599, 1978.
60. Danielson LR, Dresser MJ, Donaldson EE, *et al. Surf Sci.* **71**: 615, 1978.
61. Feulner P, Menzel D. *Phys. Rev.* **B25**: 4295, 1982.

62. Menzel D, Pfnur H, Feulner P. *Surf Sci.* **126**: 374, 1983.
63. Rigby LJ. *Can. J. Phys.* **43**: 532, 1965.
64. Tates JT Jr, Madey TE. *J. Chem. Phys.* **43**: 1055, 1965.
65. Oguri T. *J. Phys. Soc. Jpn.* **18**: 1280, 1963.
66. Madey TE, Yates JT Jr. *J. Chem. Phys.* **44**: 1675, 1966.
67. Joyner RW, Rickman J, Roberts MW. *J. Chem. Soc. Farad. Trans.* **170**: 1825, 1974.
68. Delchar TA, Ehrlich G. *J. Chem. Phys.* **42**: 2686, 1965.
69. Goymour CG, King DA. *J. Chem. Soc. Farad. Trans.* **169**: 749, 1973.
70. Yates JT Jr, Klein R, Madey TE. *Surf Sci.* **58**: 469, 1976.
71. Fuggle Jc, Menzel D. *Vak. Tech.* **27**: 130, 1978.
72. Wilf M, Folman M. *Surf Sci.* **52**: 10, 1975.
73. Adams DL, Germer LH. *Surf Sci.* **26**: 109, 1971.
74. King DA, Wells MG. *Proc. Roy. Soc. Ser. A.* **339**: 245, 1974.
75. Singh Boparai SP, Bowker M, King DA. *Surf Sci.* **53**: 55, 1975.
76. Toyoshima I, Somorjai GA. *Catal. Rev. Sci. Eng.* **19**: 105, 1979.
77. Adams DL, Germer LH. *Surf Sci.* **22**: 365, 1971.
78. Aika K, Hori H, Ozaki A. *J. Catal.* **27**: 424, 1972.
79. Clavenna LR, Schmidt LD. *Surf Sci.* **22**: 365, 1970.
80. Egawa C, Natio S, Tamaru K. *Surf Sci.* **131**: 49, 1983.
81. Gasser RPH, Hale A, Marsay C. *J. Trans. Farad. Soc.* **62**: 1789, 1967.
82. Han HR, Schmidt LD. *J. Phys. Chem.* **75**: 227, 1971.
83. Pasternak RA, Endow N, Bergsnov HB. *J. Phys. Chem.* **70**: 1304, 1966.
84. Kunimori K, Kawai T, Kondow T, *et al. Surf Sci.* **54**: 525, 1976.
85. Yates JT Jr, Madey TE. *J. Chem. Phys.* **51**: 334, 1969.
86. Egawa C, Naito S, Tamaru K. *Surf Sci.* **125**: 605, 1983.
87. Boreskov GK, Kolchnova VM, Rachkovskii EE, *et al. Kinet. Katal.* **16**: 1218, 1975.
88. Haase G, Asscher M. *Surf Sci.* **191**: 75, 1987.
89. Grunze M, Golze M, Fuhler J, *et al.* In: Dechema (ed.) Proc 8th Intern Congr Catal. Weinheim: Verlag Chemie. 1984. 4, 133
90. Haase G, Asscher M. *Chem. Phys. Lett.* **142**: 241, 1987.
91. Khrizman IA, Korneyyiuchuk G. *Acta. Physico Chim.* (URSS). **18**: 420, 1943.
92. Aika K, Ozaki A. *J. Catal.* **14**: 311, 1969.
93. Kazusaka A. *J. Res. Inst. Catal. Hokkaido Univ.* **19**: 42, 1971.
94. Kokes RJ, Emmett PH. *J. Am. Chem. Soc.* **80**: 2082, 1958.
95. Grunze M, Driscoll RK, Burland GN, *et al. Surf Sci.* **89**: 381, 1979.
96. Wilf M, Dawson PT. *Surf Sci.* **60**: 561, 1976.
97. Schwaha K, Bechtold E. *Surf Sci.* **66**: 383, 1977.
98. Kiss J, Berko A, Solymosi F. *Magy Kem Foly.* **87**: 566, 1981.
99. Kunimori K, Kawai T, Kondow T, *et al. Surf Sci.* **59**: 302, 1976.
100. Davies PW, Lambert RM. *Surf Sci.* **110**: 227, 1981.
101. Kuwahara Y, Fujisawa M, Jo M, *et al. Surf Sci.* **180**: 421, 1987; *ibid* **188**: 490, 1987.
102. Obuchi A, Naito S, Onishi T, *et al. Surf Sci.* **122**: 235, 1982.
103. Matsuo I, Nakamura J, Hirano H, *et al. J. Phys. Chem.* **93**: 7747, 1989.
104. Panov GI, Boreskov GK, Kharitonov AS, *et al. React Kinet. Catal. Lett.* **16**: 247, 1981.
105. Panov GI, Kharitonov AS. In: Dechema (ed.) Proc 9th Intern Congr Catal Verlag Chemie. Veinheim: 1984. 3, 371.
106. Kharitonov AS, Boreskov GK, Panov GI, *et al. React Kinet. Catal. Lett.* **22**: 309, 1983.
107. Panov GI, Boreskov GK, Kharitonov AS, *et al. Kinet. Catal.* **25**: 123, 1984.
108. Stoltze P, Norskov JK. *Phys. Rev. Lett.* **55**: 2502, 1985.
109. Stoltze P, Norskov JK. *Surf Sci Lett.* **197**: 1230, 1988.

110. Stoltze P, Norskov JK. *J. Catal.* **110**: 1, 1988.
111. Stoltze P. *Phys. Scr.* **36**: 824, 1987.
112. Bowker M, Parker I, Waugh KC. *Appl. Catal.* **14**: 101, 1985.
113. Bowker M, Parker I, Waugh KC. *Surf Sci. Lett.* **197**: 1223, 1988.
114. Ertl G, Lee SB, Weiss M. *Surf Sci.* **114**: 527, 1982.
115. Dumesic JA, Rudd DF, Aparicio LM, *et al.* The Microkinetics of Heterogeneous Catalysis, Translated by Sheng Jiayi, Beijing: National Defence Industry Press, 1998.
116. Boszo E, Ertl G, Weiss M. *J. Catal.* **50**: 519, 1977.
117. Guan S, Liu HZ. *Ind. Eng. Chem. Res.* **39**(8): 2891–2895, 2000.
118. Stoltze P, Norskov JK. *Phys. Rev. Lett.* **55**: 2502, 1985.
119. Ertl G. *Catal. Rev. Sci. Eng.* **21**(2): 201, 1980.
120. Spencer MS. *Catal. Lett.* **13**: 45, 1992.
121. Vandervell HD, Vaugh KC. *Chem. Phys. Lett.* **171**: 462, 1990.
122. Ettner CT, Stein H. *Phys. Rev. Lett.* **59**: 2768, 1987.
123. Asscher M, Becker OM, Haase G, *et al. Surf Sci.* **206**: L880, 1988.
124. Scholten JJF, Zweitering P, Konvalinka JA *et al. Trans. Farad. Soc.* **55**: 2166, 1959.
125. Spencer ND, Schoonmaker RC, Somorjai GA. *J. Catal.* **74**: 129, 1982.
126. Alstrup I, Chorkendorff I, Ullmann S. *Z. Phys. Chem.* **198**: 123, 1997.
127. Liu HZ, *Chin. J. Catal.* **22**(3): 304, 2001.
128. Bowker W. *Top Catal.* **1**: 265, 1994.
129. Liao DH, Lin ZY and Cha QR. J. Xiamen Univ. (Nature Science). **35**(5): 734, 1996.
130. Zhang HB, Schrader GL. *J. Catal.* **99**: 461, 1986.
131. Temkin MI, Pyzhev VM. *Acta. Physicochim (USSR).* **12**: 327, 1940.
132. Ozaki A, Taylor HS, Boudar M. *Proc. Roy. Soc.* **258**: 47, 1960.
133. Brill R, Tauster S. *J. Chem. Phys.* **36**: 2100, 1962.
134. Nielsen A. An Investigation on Promoted Iron Catalysts for the Synthesis of Ammonia, Jul Giellerups Forlag, Copenhagen, 1968.
135. Peters C, Krabetz R. *Z. Elektrochem.* **60**: 859, 1956.
136. Emmett PH, Kummer JT. *Ind. End. Chem.* **35**: 677, 1943.
137. Bokhoven C, van Raayen W. *J. Phys. Chem.* **58**: 471, 1954.
138. Temkin MI, Morozov NM, Shapatina EN. *Kinet. Katal.* **4**: 260, 1963.
139. Tamaru K. Proc 3rd Intern Congr Catal, Sachtler WHM *et al.* (ed) Amsterdam, North Holland Pub, 1965, 664.
140. Kadowaki Y, Murata S, Aika K. New Frontiers in Catalysis, Proc, 10th Intern Congr Catal Budapest, Guczi L., *et al.* eds, Elsevier, 1993. 2055.
141. Aika K, Kumasaka M, Oma T, *et al. Appl. Catal.* **28**: 57, 1986.
142. Shiflett WK, Dumesic JA. *J. Catal.* **77**: 57, 1982.
143. Holzman PR, Shiflett WK, Dumesic JA. *J. Catal.* **62**: 167, 1980.
144. Shiflett WK, Dumesic JA. *Ind. End. Chem. Fundam.* **20**: 246, 1981.
145. Tamaru K. *Acc. Chem. Res.* **21**: 88, 1988.
146. Shindl H, Egawa C, Onishi T, *et al. J. Chem. Soc. Faraday Trans.* **76**: 280, 1980.
147. Egawa C, Nishida T, Natio S, *et al. J. Chem. Soc. Faraday Trans.* **80**: 1595, 1984.
148. Shindo H, Egawa C, Onish T, *et al. Z. Naturforsch.* **34a**: 96, 1979.
149. Loeffler DG, Schmidt LD. *J. Catal.* **44**: 244, 1976.
150. Loeffler DG, Schmidt LD. *J. Catal.* **41**: 440, 1976.
151. Apel'baum LO, Temkin MI. *Zh. Fiz. Khim.* **33**: 2697, 1959.
152. Robertson AJB, Willhoft EMA. *Trans. Farad. Soc.* **63**: 476, 1967.
153. Vajo JJ, Tsai W, Weinberg WH. *J. Phys. Chem.* **89**: 3243, 1985.
154. McCarroll JJ, Tennison SR, Wilkinson NP. US 4600571. 1986.
155. King DA, Sebba F. *J. Catal.* **4**: 253, 1965.
156. McGill WJ, Sebba F. *J. Catal.* **2**: 104, 1963.
157. Segal N, Sebba F. *J. Catal.* **8**: 105, 1967.

158. Kiperman S, Temkin MI. *Acta Physicochim* (USSR). **21**: 267, 1946.
159. Kummer JT, Emmett PH. *J. Chem. Phys.* **19**: 289, 1951.
160. 160 Morikawa Y, Ozaki A. *J. Catal.* **12**: 145, 1968.
161. 161 Schulz G, Schaefer H. *Z. Phys. Chem.* (N F). **64**: 333, 1969.
162. Schulz-Ekloff G. *Ber. Bunsenges Phys. Chem.* **75**: 110, 1971.
163. Guyer WRF, Joris GG, Taylor HS. *J. Chem. Phys.* **9**: 287, 1941.
164. Gorbunov AI, Boreskov GK. *Prolemy Kinet. Katal. Akad. Nauk* (USSR). **10**: 192, 1960.
165. Ogata Y, Aika K, Onishi T. *Bull. Chem. Soc. Jpn.* **62**: 642, 1989.
166. McGeer JP, Taylor HS. *J. Am. Chem. Soc.* **73**: 2743, 1951.
167. Joris GG, Taylor HS. *J. Chem. Phys.* **7**: 893, 1939.
168. Gasser RPH, Lowrence CP, Newman DG. *Trans. Farad. Soc.* **61**: 1771, 1965.
169. Gasser RPH, Hale A, Marsay CJ. *Trans. Farad. Soc.* **62**: 1789, 1967.
170. Boreskov GK, Kolchnova VM, Rachkovskii EE, *et al. Kinet. Katal.* **16**: 1218, 1975.
171. Moore GE, Unterwald FC. *J. Chem. Phys.* **48**: 5393, 1968.
172. Urabe K, Aika K, Ozaki A. *J. Catal.* **42**: 197, 1976.
173. Aika K, Ozaki A. *J. Catal.* **14**: 311, 1969.
174. Deng JF. *Introduction of Catalysis.*, Chanchun: Jilin Science and Technology Press, 1984.
175. Horiuti J. *J. Res. Inst. Catal. Hokkaido Univ.* **2**: 87, 1957.
176. Temkin MI. Ann NY. *Acad. Sci.* **213**: 79, 1973.
177. Happel J. *Catal. Rev.* **6**: 221, 1972.
178. Wangner C. *Advan. Catal. Relat. Subj.* **21**: 233, 1970.
179. Horiuti J, Nakamura T. *Advan. Catal. Relat. Subj.* **17**: 1, 1967.
180. Boudart, M. *Kinetics of Chemical Processes*, New York: Prentice-Hall, Englewood Cliffs, 1968. 350.
181. Temkin MI. *Inst. Chem. Eng.* **11**: 709, 1971.
182. Happel J. *Catal. Rev.* **6**: 221, 1972.
183. Horiuti J, *et al. J. Res. Inst. Catal.* (Hokkaido Univ.). **2**: 87, 1953.
184. Horiuti J, *et al. J. Res. Inst. Catal.* (Hokkaido Univ.). **3**: 185, 1954.
185. Tanaka K. *J. Res. Inst. Catal.* (Hokkaido Univ.). **13**: 119, 1965.
186. Boer JH de (ed.). *The Mechanism of Heterogeneous Catalysis*, Amsterdam: Elsevier, 1960.
187. Nielsen A. *An Investigation of Promoted Iron Catalysts for the Synthesis of Ammonia*, Copenhagen: Gjellerup, 1968.
188. Dumesic JA, Trevino AA. *J. Catal.* **116**: 119, 1989.
189. Nwalor JU, Goodwin JG, Biloen P. *J. Catal.* **117**: 121, 1989.
190. Dumesic JA, Topsoe H, Khammouna H, *et al. J. Catal.* **37**: 503, 1975.
191. Spencer ND, Schoonmarker RC, Somorjai GA. *J. Catal.* **74**: 129, 1982.
192. Topsoe H, Topsoe N, Bohlbro H, *et al.* In: *Proc. 7th Intl. Congr. Catal.* New York: Elsevier, 1980, 247.
193. Ertl G, *Vac. J. Sci. Technol. A.* **1**: 1247–1253, 1983.
194. Alstrup I, Chorkendorff I, Ullmann S. *J. Catal.* **168**: 217–234, 1997.
195. Oh SH, Fisher GB, Carpenter JE, *et al. J. Catal.* **100**: 360, 1986.
196. Waletzko N, Schmidt LD. *AICHE J.* **34**: 1146, 1988.
197. Schlögl R. *Angew. Chem. Int. Ed.* **42**: 2004–2008, 2003.
198. Boudart M. *Top Catal.* **13**: 147–149, 2000.
199. Boudart M, Djega MG. *Kinetics of Heterogeneous Catalytic Reactions.* Princeton: Priceton University Press, 1984.
200. Boudart M. *Kinetics of Chemical Processes.* New York: Prentice Hall, Englewood Cliffs, 1968. 350.
201. Löffler DG, Schmidt LD. *J. Catal.* **41**: 440, 1976.

202. Tamaru K, Shindo H, Egawa C, *et al. J C S Faraday I.* **2**: 280, 1980.
203. Boudart M, Egawa S, Oyama ST, *et al. J. Chim. Phys.* **78**: 987, 1981.
204. Tamaru K. *Dynamic Heterogeneous Catalysis.* London: Academic Press, 1978.
205. Schmid TLD. *Catal. Rev. Sci. Eng.* **9**: 115, 1974.
206. Boudart M. *Kinetics of Chemical Processes.* New Jersey: Prentice Hall, Englewood Cliffs, 1968, 167.
207. Temkin MI, Pyzhev V. *Acta. Physicochim.* (URSS) **12**: 327, 1940.
208. Ozaki A, Taylor H, Boudart M. In: Bond GC, Wells PB, Tompkins FC (eds.) *Proc. 5th Intl. Congr. Catal.* New York: American Elsevier, 1960, 645.
209. Shapatina EI, Kuchaev VL, Temkin MI. *Kinet. Katal.* **12**: 1476, 1971.
210. Kiperman SL. *Introduction to the Kinetics of Heterogeneous Reaction.* Moscow: 1964.
211. Boudart M. In: Bond GC, Wells PB, Tompkins FC (eds.) *Proc. 6th Intl. Congr. Catal.* London: 1976. The Chemical Society, 1977.
212. Kobozev NJ. *Acta. Physicochim.* URSS, **9**: 805, 1938.
213. Balandin AA. *2 physik. Chem.* **B2**: 289, 1929.
214. Ponec V, Sachtler WMH. In: Bond GC, Wells PB, Tompkins FC (eds.) *Proc. 5th Intl. Congr. Catalysis*, New York: American Elservier, 1972, 645.
215. Dowden DA. In: Bond GC, Wells PB, Tompkins FC eds. *Proc. 5th Intl. Congr. Catal.* New York: American Elservier, 1972, 621.
216. Muetterties EL. *Bull. Soc. Chim. Belge.* **34**: 959, 1975.
217. Ertl G. In: Sci yama T, Tanabe K (eds.) *Proc. 7th Intl. Congr. Catal.* Tokyo: Kodansha, 1981, p21.
218. Spencer ND, Schoonmaker RC, Somorjai GA. *J. Catal.* **74**(1): 129, 1982.
219. Boudart M. *Advan. Catal. Relat. Subj.* **20**: 153, 1969.
220. Boudart M, Delbouille A, Dumesic JA, *et al. J. Catal.* **37**: 486, 1975.
221. Dumesic JA, Topsoe H, Boudart M. *Proc. Nat. Acad. Sci. of USA.* **74**: 806–810, 1977.
222. Dumesic JA, Topsoe H, Boudart M. *J. Catal.* **37**: 513, 1975.
223. Brill R, Richter EL, *Ruch E. Angew. Chem. Int. Ed. Engl.* **6**: 882, 1967.
224. Mcallister J, Hansen RS. *J. Chem. Phys.* **59**: 414, 1973.
225. Somorjai GA. *Introduction to Surface Chemistry and Catalysis*, New York: Wiley, 1994.
226. Huang. In: Sci yama T, Tanabe K (eds.) *Proc. 7th Intl. Cong. Catal.* Tokyo: Kodansha, 1981, 554.
227. Strongin DR, Carrazza J, Bare SR, Somorjai GA. *Journal of Catalysis*, **103**: 213, 1987.
228. Liu HZ, Li XN, Shzyki S, Ohnishi R and Ichikawa M. *CIESC J.* **51**(4): 462–467, 2000.
229. Guan S, Liu HZ. *Ind. Eng. Chem. Res.* **39** (8): 2891–2895, 2000.
230. Li T, Zhu Y, Li SS, Zhu JC and Zhu BC. *J. East China Univ. Techology,* **26**(3): 256–259, 2000.
231. Zu B. *Journal of East College of Chemical Industry and Engineering*, **1**: 59, 1983.
232. Kjaer J. *Measurement and Calculation of Temperature and Conversion in Fixed-Bed Catalytic Reactions.* Chapter 2, Giellerup, 1958.
233. Zu B. editor in chief, *Inorganic Chemical Reaction and Engineering*, Beijing: Chemical Industry Press, 1981, 35.
234. Русов МТ. иДР Т О Х Т. ТОМ 5. **3**: 382–387, 1971.
235. БесквБ С. иДР Т О Х Т. ТОМ 5. **4**: 537–541, 1971.
236. Kazарноъская Д. Б. иДР. Жур. Физ. Хим, **47**: 1445, 1973.
237. Liu HZ, Li XN, Hu ZN, Cheng YQ and Fu GP. *CIESC J.* **52**(11): 1030–1034, 2001.
238. Yu ZH, Zhu BC, Shen CD, *et al. Analysis of Processes and Technology for Large-Scale Ammonia Synthesis Factory*, Beijing: China Petrochemical Press, 1993.
239. Liu HZ, Li XN, Hu ZN, Jiang ZR, Lin WZ. *Chemical Fertilizer Industry,* **26**(4): 17–21, 1999.

240. Li S, Zu B. *Kinetics in Inorganic Chemical Reaction Industrial Process*, Beijing: Chemical Industry Press, 1966.
241. Liu HZ, Li XN, Hu ZN, Jiang ZR, Lin WZ. *Chemical Fertilizer Industry*, **26**(5): 20–24, 1999.
242. Keisa KK. *Chemical Engineering*, **21**: 780, 1957.
243. Ting LJ. *Calculation Method in Numerical Value*. Beijing: Beijing University of Technology Press, 1997.
244. Liu HY, Liu HZ. *Chemical Fertilizer Industry*. **29**(2): 28–32, 2002.
245. Dai XH, Liu HZ. *Chemical Fertilizer Industry*. **33**(3): 12–16, 2006.

This page intentionally left blank

Chapter 3

Chemical Composition and Structure of Fused Iron Catalysts

3.1 Iron Oxides

Iron which shows +2 and +3 chemical valences reacts with O_2 to form three kinds of oxides chemically: Fe_2O_3, Fe_3O_4 and FeO. These oxides are called as hematite, magnetite and wüstite in crystallography, respectively. Table 3.1 gives the characteristics of various iron oxides. Figure 3.1 illustrates the crystal structure of Fe_2O_3, Fe_3O_4 and FeO.

3.1.1 Fe_2O_3

Fe_2O_3, known as ferric oxide or hematite, possesses rhombohedral crystal lattice structure, which includes two of Fe_2O_3 molecule, namely contains four of Fe^{3+} ions and six of O^{2-} ions in the corundum unit cell. Hematite exists in wide temperature ranges, while it begins to decompose as the temperature reaches up to 1,100°C as for its decomposing pressure in closing to the partial pressure of oxygen in atmosphere. It decomposes completely at melting point of iron for 1,597°C.

Many crystal compounds have heteromorphism. This phenomenon means there are diverse crystal changes for one single chemical substance. Fe_2O_3 has three kinds of isomeric crystal forms: α, β and γ, where the stability of each isomeric crystal form at an appointed temperature is related to its free energy. α-Fe_2O_3 is a stable iron oxide thermodynamically, while it also changes to β-Fe_2O_3 and γ-Fe_2O_3 under certain conditions. α-Fe_2O_3 (hematite) is a non-ferromagnetic material, which shows trigon crystal lattice, with lattice constant $a = 0.5427\,\text{nm}$, and such kind of characteristic is distinguished from other iron oxides.

Under certain conditions, magnetic hematite of γ-Fe_2O_3($a = 0.8322$–$0.8340\,\text{nm}$) can be obtained, that has ferromagnetic properties the same as magnetite.

The third crystal form of Fe_2O_3 is β-Fe_2O_3; however, its features are not studied sufficiently yet.

3.1.2 Fe_3O_4

Fe_3O_4 is magnetic iron oxide crystallographically. It has the crystal lattice with spinel-type cubic crystal system, unit crystal cell including eight of Fe_3O_4 molecules. Magnetic iron oxide is an independent phase, not a simple molecular mixture of FeO and Fe_2O_3. Each of Fe^{2+} iron cation should be spelled with two of Fe^{3+} iron cations,

Table 3.1 Characteristics and structure of iron oxides

Material	Relative molecular (atomic) weight	Density	Crystal type	Lattice constant/nm	Molar volume	
					Iron atom	Oxygen atom
Fe	55.85	7.86	NaCl	0.286	1	—
Fe_3O_4	231.55	5.1	Spinel	0.837	2.10	0.93
α-Fe_2O_3	159.70	5.26–5.355	Rhombus	0.542, $\alpha = 55°17'$	2.09–2.13	0.82–0.83
γ-Fe_2O_3	159.70	4.4	Spinel	0.833	2.55	1.00
FeO	71.85		Aberrant rhombus	—	—	—
$Fe_{0.95}O$	69.05	5.73	NaCl	0.4301	1.78	1.00
α-FeO	71.85	—	NaCl	0.4282	—	—
γ-FeO	71.85	—	Spinel	0.837	—	—

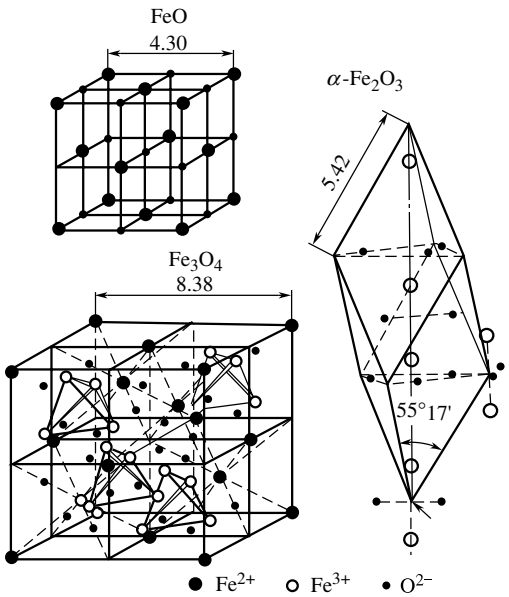


Fig. 3.1 Crystal structure of iron oxides

each other in a correct crystal order in crystal lattice of magnetic iron oxide. This kind of oxide is ferromagnetically different from other oxides (besides γ-Fe_2O_3). Magnetic iron oxide is chemically stable in whole temperature range from room temperature to the melting point of iron (1,597°C). Fe_3O_4 has nearly pure electron conductivity, and the reason is due to the strict order of Fe^{3+}-Fe^{2+}-Fe^{3+} in its crystal structure which ensures the electron transfers easily from one cation node to another accompanying with the valent changes of iron ions.

Magnetic iron oxide can change to α-Fe_2O_3 in two steps when it is heated at oxidative ambience. First, the Fe_3O_4 changes to transitional structure of γ-Fe_2O_3 at temperatures reaching up to 220°C, during which only the component of Fe_3O_4

changes to that of Fe_2O_3, namely there occurs the reaction with oxygen. As a consequence, bivalent iron cation shifts to trivalent cation ($2Fe_3O_4 + [O] \rightarrow 3Fe_2O_3$), while the crystal structure remains unchanged and even retains the ferromagnetism of Fe_3O_4. It is proved experimentally that the oxidation of magnetic iron oxide and its conversion to γ-Fe_2O_3 are as follows: Some of bivalent iron cations are away from the lattice and leave over the unfilled nodes-cavities, and the rest of Fe^{2+} cations are oxidated to trivalent Fe^{3+}. At last, it loses the magnetism and forms the stable structure of α-Fe_2O_3 lattice when it is heated sequentially up to 400–500°C.

It is seen from above description that γ-Fe_2O_3 has the pseudocrystal structure which converts from Fe_3O_4 to α-Fe_2O_3.

Magnetite has the lattice of spinel crystal structure, lattice constant in the range of 0.8378–0.8397 nm. Spinel is structured of oxygen ions in the most close cumulate cube, including 32 oxygen ions in its unit cell, which structures 64 interspaces of tetrahedron and 32 interspaces of octahedron. Metal ions can be embedded into these interspaces, and 32 oxygen ions correspond to 24 metal ions in the unit cell. If it is an ideal crystal lattice, there should be eight metal ions that are assigned to the interspaces of tetrahedron (or *A* nodes), and 16 metal ions are assigned to the interspaces of octahedron (or *B* nodes).

There may be two cases when the metal ions fill in apexes of octahedron and tetrahedron. The first case has normal cation arrangement as character, where all the bivalent ions are located in *A* nodes, e.g. $ZnFe_2O_4$ belongs to this type. In the second case, the apexes of the octahedron are occupied with different valence ions. Magnetite has a so-called metamorphic spinel structure, and also there is a complex cation replaced spinel structure (Table 3.2).

Two types of spinels, namely normal and metamorphic structure, may convert each other in spinel sosoloid. Besides, some of pure spinels are made up of both a normal and a reverse spinel sosoloids that have the same chemical composition, e.g., magnesioferrite $(Fe^{3+}_{1-x}Mg^{2+}_{x})[Fe^{3+}_{1+x}Mg^{2+}_{1-x})]O_4$. The similar sosolids could be disordered into normal and metamorphic spinels if they do not deviate from boundary structure.

There may be other disordered states, such as some of lattice points are occupied but which should be idle, and in another case it is reversed in an ideal crystal.

Table 3.2 Cation assignment of spinel structure and oxygen constant of ferrite

Ferrite	a/nm	μ^a	λ^b	Cation assignment[c]
Fe_3O_4	0.8390	0.379	1.00	$(Fe^{3+})[Fe^{2+}Fe^{3+}]O_4$
$MgFe_2O_4$	0.8380	0.381	0.90	$(Mg^{2+}_{0.1}Fe^{3+}_{0.9})[Mg^{2+}_{0.9}Fe^{3+}_{1.1}]O_4$
$MnFe_2O_4$	0.8507	0.385	0.20	$(Mn^{2+}_{0.8}Fe^{3+}_{0.2})[Mn^{2+}_{0.2}Fe^{3+}_{1.8}]O_4$
$FeAl_2O_4$	0.8096	0.389	0.25	$(Fe^{2+}_{0.75}Al^{3+}_{0.25})[Fe^{2+}_{0.25}Al^{3+}_{1.75}]O_4$
$ZnFe_2O_4$	0.8440	0.381	0	$(Zn^{2+})[Fe^{3+}_{2}]O_4$

[a] μ is oxygen constant, $\mu_i = 0.375$ for ideal spinel lattice.
[b] λ is extent of lattice conversion, which is equal to the ratio of high valence ions in A node.
[c] Parenthesis expresses A node, square brackets expresses B node.

The functions of both disordered states on the diffusion of iron ions in magnetite are important.

Ion exchanges between bivalent and trivalent iron cations located in the apexes of octahedron are easily carried out, which is the reason for the higher conductivity of oxides. Magnetite is hardly dissolved in α-Fe_2O_3, but the utmost solubility increases with temperature, and the formed sosoloid can be regarded as submerged sosoloid.

It is obtained from the investigation results of the magnetic hematite (γ-Fe_2O_3) that lattice distortion deviated from the stoichiometry magnetite. The ferromagnetic hematite has the same structure as magnetite but the $2 \times \frac{2}{3}$ apexes of octahedron, possessed by iron ions, are not filled in every cell with 32 oxygen ions. It is a typical structure for the magnetite which can take on residual oxygen numbers. Magnetite has ferromagnetism and its Curie point is 627°C. When magnetite is oxidized, a variety of oxide phases can be obtained while its chemical compositions are identical to Fe_2O_3. Figure 3.2 gives the stable regions of iron oxides thermodynamically.

3.1.3 *FeO*

FeO has three chemical characteristics, i.e., oxidative, non-stoichiometry and meta-stability. They must be taken seriously during the manufacture, reduction and application of $Fe_{1-x}O$ based ammonia synthesis catalyst. As shown in the researches on iron catalyst during the past century, the iron oxides precursor of the catalysts is Fe_3O_4 all along, so it has been studied intensively, while that of FeO is not. Hence, here is a detailed introduction to FeO.

3.1.3.1 *Oxidative*

FeO, which is a low valence iron oxide, can be transferred to high valence ones. There may be reactions during preparation at the high temperatures and atmospheric

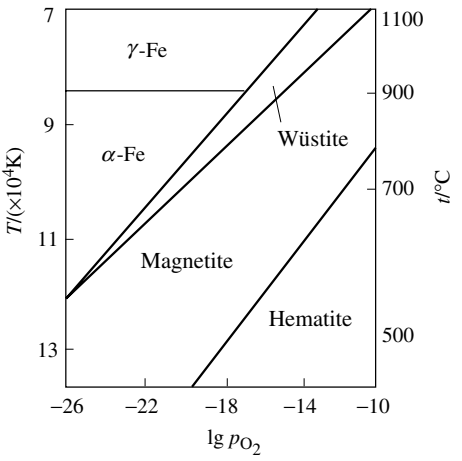


Fig. 3.2 Thermodynamical stable regions of iron oxides

pressure as follows:

$$FeO + 1/6O_2 = 1/3Fe_3O_4. \quad \Delta G^{\theta}_{298} = -86.94\,kJ \cdot mol^{-1} \tag{3.1}$$

$$FeO + 1/4O_2 = 1/2Fe_2O_3. \quad \Delta G^{\theta}_{298} = -120.26\,kJ \cdot mol^{-1} \tag{3.2}$$

As a result of these reactions, ratio of Fe^{2+}/Fe^{3+} lowers and original crystal structure of catalyst (product) would be destroyed. The oxidation reaction could be controlled effectively if there are reduction agents (such as Fe) with a little excessive amount:

$$Fe + 1/2O_2 = FeO. \quad \Delta G^{\theta}_{298} = -251.60\,kJ \cdot mol^{-1} \tag{3.3}$$

It was confirmed by experiments that the oxidation reaction rate is rather slow under atmosphere and normal temperature.

3.1.3.2 *Non-stoichiometry*

(1) About law of constant composition and stoichiometric compounds. Both concepts about definite composition or stoichiometry by Dalton are the criterion and standard for confirming a compound, and many properties of compounds are explained by the infrangible theory of constant composition. Problems concerning the molecular crystals in organic chemistry were explained well by this theory according to the principle of constant valence, while it was found out to be not always proper to the case of atomic or ionic crystal compounds. In fact, Berthollet pointed out early based on the experimental results that crystal compounds would not always follow the law of constant composition. The compositions of an identical compound could be changed in a certain ranges.

In 1930, it was pointed out that the changes of the composition in ionic or molecular compounds are existent widely by Schenck and Dingmann during their studies about Fe–O systems and by Biltz and Jusa in their studies about decomposition equilibrium pressure of binary compounds. For example, studies about phases of wüstite indicated that its composition should be $Fe_{1-x}O$, $0.09 < x < 0.19$ (900), and moreover that of iron pyrite should be FeS_{1+x}.

At the same time, Wagner and Schottky pointed out from the studies in statistical thermodynamics on the actual crystal and lattice defects that, at any temperature above 0 K, every solid compound only owns a single phase, although its composition changes under certain conditions. There is no thermodynamic status that the compounds which either compose strictly in accordance with the ideal chemical stoichiometry, or deduce single phase from rules of valence bond.

From the modern point of view in theory of crystal structures and experimental studies, both the stoichiometrical and non-stoichiometrical compounds are existent universally. Even more exactly, the existent of non-stoichiometrical compounds is more prevalent phenomena.

It can be divided into two aspects for the specifications of non-stoichiometrical or that deviated from the stoichiometrical solid substances:

(i) The first case is that such of non-stoichiometrical compounds prescribed by the pure chemical definition, which is a uniform phase that compositional deviation from the stoichiometry can be determined by the means of such as chemical

analysis, X ray diffraction and the measurement of equilibrium vapor pressure etc., such as transitional metal compounds as $Fe_{1-x}O$, FeS_{1+x}, P_dH_x etc.

(ii) From the point of view for lattice structure, it is a compound with deviation of concentration of lattice defects from stoichiometry and although its deviation amplitude of lattice defects is too small to be detected by the means of chemical analysis or X ray diffraction, whereas it can be detected by the nature of optics, electricity and magnetism of them. Those compounds that show low deviations from stoichiometry have great technical properties that should be the target of central discussion in solid chemistry.

Non-stoichiometry of pure solid compounds without exotic impurities, is caused by a variety of intrinsic defects existed in their phases, such as vacancy defect, interstitial atoms, dislocation etc.

FeO is an oxygen excessive (defect of Fe ions) non-stoichiometrical oxide, usually expressed as $Fe_{1-x}O$, and commonly known as wüstite in crystallography. Wüstite ($Fe_{1-x}O$) contains 23.1%–25.6% of oxygen, which indicates that it cannot reach the theoretical ratio of Fe: O = 1 that is corresponding to 22.3% of oxygen. Wüstite is a non-ferromagnetic substance as same as hematite.

(2) Crystal structure of wüstite. FeO cell consists of four FeO molecules, and makes up eight of tetrahedral interspaces and four of octahedral interspaces in the NaCl type cubic lattice with the most close cumulate of O^{2-} anion (Fig. 3.3). It constitutes the ideal lattice of FeO with NaCl type structure, if all of Fe^{2+} cations enter the interspace of octahedron and that of tetrahedron is empty. Nevertheless, for the reason of Fe^{2+} ions defect, there still exists small amounts of Fe^{3+} ions in the structure of wüstite in order to maintain its charge-neutrality. These Fe^{3+} cations occupy frequently the original empty interspace of tetrahedron.[1] At the same time, if they form one defect of Fe^{2+} cation in the lattice, there must be two Fe^{2+} cations which would be transfered to two of Fe^{3+} in order to maintain the charge-neutrality and one of which would enter the tetrahedral interspace and leave a vacancy in octahedral interspace, while another Fe^{3+} stays in octahedral interspace. The positive charges of the residual iron cations may move along in the lattice between bivalent and trivalent irons. These charges are called as defective electrons, and are electron carriers and also is the reason that wüstite has the

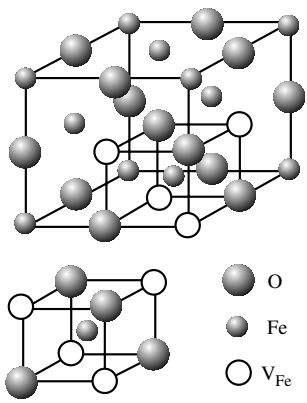


Fig. 3.3 Cell structure of wüstite

electron conductivity. Due to the defects of iron ions, there is a possibility for the iron ions moving along with the lattice and as a result, the defects of iron ions themselves move along with the reverse direction. There is a following relationship between the self-diffusion coefficient of iron ($D*_{\mathrm{Fe}}$) and diffusion coefficient of defect (D_{V}) in wüstite structure:

$$yD_{\vee} = (1-y)D^{*}_{\mathrm{Fe}}. \tag{3.4}$$

The self-diffusion coefficient of iron is a direct proportion to the partial pressure of oxygen $\left(P_{O_2}^{0.4}\right)$.[4] The defect diffusion coefficient is basically not related with the concentration of defect (y). It can be calculated by the following equation proposed by Богданди and Энгель:

$$D_{\vee} = D^{0}_{\vee} \exp(-27800/RT). \tag{3.5}$$

$$D^{0}_{\vee} = 4.5 \times 10^{-2}\,\mathrm{cm}^2 \cdot \mathrm{s}^{-1}. \tag{3.6}$$

Due to the known vacant concentration causing the shortages of iron, it should be considered that there would be certain amount of iron ions leaving their own nodes and transferring to ion states between the nodes in wüstite which is supposed to be chemically stoichiometrical.

It can be considered that the experimental value of diffusion coefficient is a direct proportion with defect concentration in wüstite (Fig. 3.4). There are certain amount of Fe^{3+} cations in the structure of wüstite, which not only ensured the electrical neutrality in lattice, but also offered the favorable conditions for Fe^{3+} cation to move along with the cavity and for electrons to transfer ($Fe^{2+} \rightarrow O \rightarrow Fe^{3+}$). As a consequence, the activation energy for diffusion of Fe in FeO is the lowest, only as small as $96\,\mathrm{kJ} \cdot \mathrm{mol}^{-1}$ (Table 3.3), compared with that of other metal oxides. This is the structural factor for $Fe_{1-x}O$ to be reduced easily by H_2.

Researches show, the magnitude of lattice constant for wüstite is related to the content of oxygen in it, as shown in Fig. 3.5.[5] It is seen from Fig. 3.5 that the lattice constant becomes small with the increasing content of oxygen. The probable reason is that the amount of Fe^{2+} defects increase with the increasing content of oxygen, and cause the decreasing of lattice constant. Table 3.4 gives the compositions and parameters of wüstite, which indicates that the lattice constant of wüstite shows nearly direct proportion to the defect concentration. If the oxygen content (X_O) of a wüstite sample is given, the approximate lattice constant of that could be deduced according to Fig. 3.5, and contrarily, the oxygen content of a given sample can also be concluded from the lattice constant.

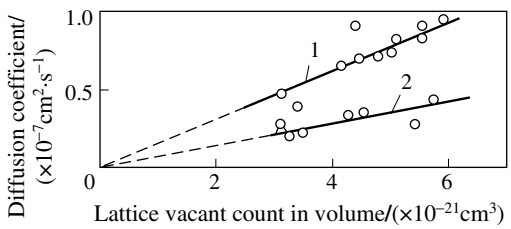


Fig. 3.4 Relationship between diffusion coefficient and defect concentration for iron in wüstite. 1–983°C; 2–897°C

Table 3.3 Activation energy for diffusion of metals in their own oxides

Diffusion systems	Activation energy $Q/(kJ \cdot mol^{-1})$	Diffusion systems	Activation energy $Q/(kJ \cdot mol^{-1})$
Fe in FeO	96	Mg in MgO	347
Na in NaCl	172	Ca in CaO	322
U in UO_2	318	Cr in $NiCrO_4$	318
Co in CoO	105	Ni in $NiCrO_4$	272
Fe in Fe_2O_3	201	O in $niCrO_4$	226

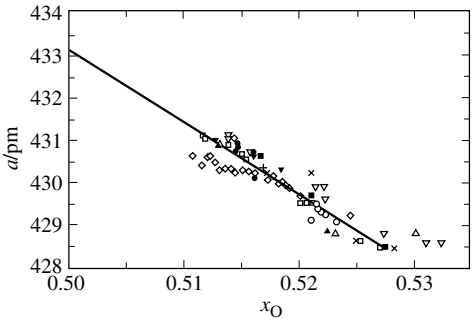


Fig. 3.5 Lattice constant of wüstite

Table 3.4 Composition and structural parameters of wüstite

Compositions	Iron content (atoms)/%	Lattice constant/nm	Density/$(g \cdot cm^{-3})$
$Fe_{0.91}O$	47.68	0.4282	5.613
$Fe_{0.92}O$	47.85	0.4285	5.624
$Fe_{0.93}O$	48.23	0.4292	5.658
$Fe_{0.945}O$	48.65	0.4301	5.728

(3) Model of defect structure of wüstite.[6] The defect structures of wüstite were well studied by many researchers[7−12] and it is commonly considered that the basic unit of that is as shown in Fig. 3.6, and the defect cluster structure of that is as shown in Fig. 3.7. It will be seen from Fig. 3.7(a) that one of Fe^{3+} cation located in the interspace of tetrahedron is surrounded by four Fe^{2+} located in interstitial of octahedron. This structure is called as 4:1 defect clusters, 4 indicates the defect amount of cations and 1 indicates the interstitial amount of tetrahedron. The defect unit possesses five units with negative charges. It was proved for the existence of the mentioned defect structures by theoretical calculation in the works of Catlow,[13] Grimes[14] and Press.[15]

Single crystal and polycrystals of wüstite have been studied by many researchers using variety of experimental technologies such as X-ray diffraction (XRD), Neutron diffraction, Electron diffraction, Mössbauer spectroscopy etc. It is found that besides the 4:1 defect clusters, there are also other types of defect clusters which are formed by way of common face, common side and common angle based on

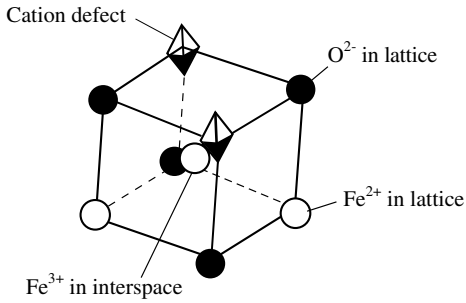


Fig. 3.6 Interspace ion-defect cluster in $Fe_{1-x}O$

those 4:1 defect clusters to be the base units in the crystal phases of wüstite. These structures of defect clusters were detailly summarized by Schweika[16] as shown in Fig. 3.7.

Catlow *et al.*[13] researched on the relative stability of defect cluster in wüstite by HADES (Harwell Automatic Defect Evaluation System) and they proved first by theory that the crystal structure tends to be more stable if it is formed *via* isolated 4:1 defect clusters. The 6:2 and 8:3 defect clusters that are formed by common faces with those 4:1 defect clusters to be base units are the most stable ones. Catlow and Fender found by calculation that the stability of other types of defect clusters are far lower than that of 6:2 and 8:3 defect clusters. Therefore, they suggested that the 6:2 and 8:3 defect clusters are formed by common faces based on 4:1 defect cluster in wustite, and it is not possible for other types of defect clusters to be formed by common angles or common side. This has a discrepancy with the former results of experiments.

Greenwood *et al.*[6] proposed a connection between the quadrupole splitting of Fe^{2+} of Mössbauer spectra and defect structure for a water-quenched sample at 1,520 K. By the result of a calculation based on the structure of cluster that confirmed by diffraction experiment, the smallest cluster in high temperature region which is replaced by neutron diffraction is $\{^{t}Fe^{3+}(\square_{+})_4\}5^{-}$: One of Fe^{3+} cation located in tetrahedron is surrounded by four interstitial of iron cations[17] and the biggest cluster is $\{^{t}Fe_4^{3+}(\square_{+})_{13}\}^{14-}$, as same with the phase of $Fe_{0.88-0.90}O$.[8]

The two clusters are shown diagrammatically in Fig. 3.8. The proportion of Fe^{2+} ions which have 0–9 defects (taken as Fe^{3+} or vacant cation sites) at any of the 18 surrounding cation positions in the lattice is shown in Fig. 3.8, for the two cluster sizes with the compositions of $Fe_{0.918}O$ and $Fe_{0.947}O$. The cation positions which have most influence on the quadrupole splitting are the 12 nearest neighbor cation sites plus the six next nearest neighbor cation sites on the far side of the six oxygen ions which octahedrally coordinate the Fe^{2+}. It has been assumed that the clusters are evenly distributed throughout the lattice and the Fe^{3+} ions which are not on tetrahedral sites only occupy those sites which have a lower electrostatic potential due to the presence of vacancies at any of the 18 neighboring positions. Such a Fe^{3+} ions distribution which enables the charge carriers to move preferentially along paths of low-potential cation site is suggested by conductivity studies.[18] The single cluster comprising 36 such sites peripheral to the cluster of four vacancies, is filled by five

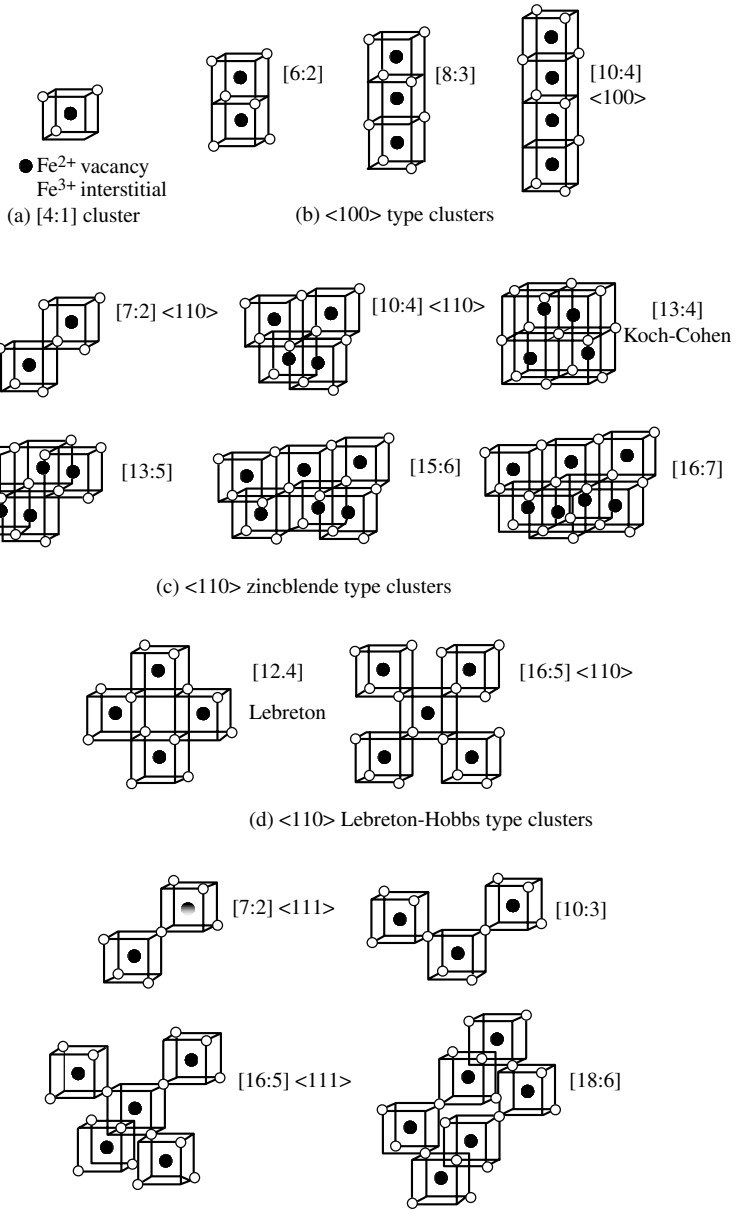


Fig. 3.7 Defect clusters in wüstite[13]

Fe^{3+} (thus balancing the five-fold negative charge on the cluster) and 31 Fe^{3+}. Each of the 31 peripheral Fe^{2+} has either one or three neighboring vacant sites and 4, 7 or 9 neighboring peripheral sites, the occupancy of which was calculated as the probability of $0, 1, \ldots 9$ Fe^{3+} ions, where $5/36$ was the probability that any one of the sites would be occupied by Fe^{3+}. The remaining non-peripheral Fe^{2+} (approximately

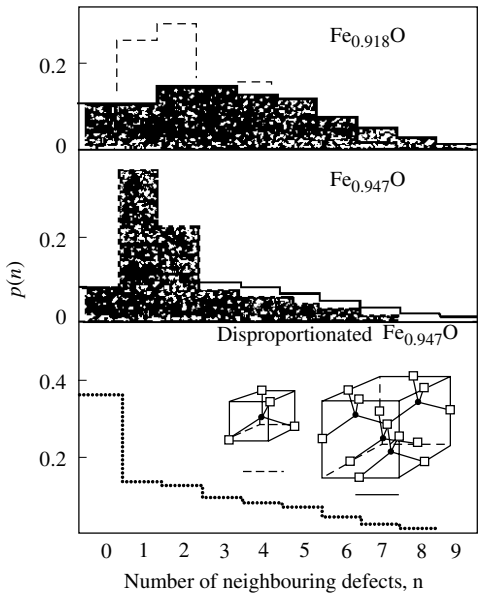


Fig. 3.8 Histograms showing the proportion, p(n), of Fe^{2+} ions having 0–n neighboring detects (Fe^{3+} or cation vacancies) calculated for single-cluster model (dashed line) and the four-fold-cluster-cluster model (full line) for two typical compositions. The effect of disproportionation on defect distribution is shown by the bottom line in the bottom histogram

Table 3.5 Binding energy of defect clusters in $Fe_{1-x}O$

Clusters	Binding energy of each vacancy/eV	Clusters	Binding energy of each vacancy/eV
4:1	1.98	Koch–Cohen	2.1
6:2	2.42	16:5	2.38
8:3	2.52		

16 per cluster in the case of $Fe_{0.947}O$) have only neighboring Fe^{3+} ions, the number of which was again calculated from the above probability. The histograms shown in Fig. 3.8 were obtained after summing over all Fe^{2+} ions in the lattice. For the four-fold cluster, 14 Fe^{3+} and 40 Fe^{2+} were randomized over the 54 peripheral sites around each cluster, and the results are also shown in Fig. 3.8. Table 3.5 shows the binding energy of clusters in $Fe_{1-x}O$.[13] Corresponding distribution of defects are shown in Fig. 3.8 in black section. The transferring of single-fold cluster of $Fe_{0.947}O$ to four-fold cluster of $Fe_{0.918}O$ leads to the increase of Fe^{2+} with more than two of near neighbor defects.

It can be anticipated that the Mössbauer parameter which is sensitive to the distribution of local defect can better reflect the early changes in aggregated defects than X-ray spectra and electron microscopy. The Mössbauer spectra of quenched sample is, therefore, very dependent on cooling conditions.

(4) Measurement of lattice defects.[19] As the defect has little influence on the lattice sizes and crystal density, its measurement needs a rather high accuracy. If the defect concentration changes obviously with temperature, it is comparatively easy to distinguish the effect caused by defects and that by crystal itself. At higher temperatures, if the crystal sizes increase outstandingly, one can consider that it is the result of a formation of Frenkel defect. There will be excess amounts of interstitial metallic ions in lattice by measurement of the lattice constant accurately. According to comparison of the true density of a crystal with that of calculated by lattice constant obtained by XRD, it cannot only determine the defect concentration, but also can classify the types of defects.

Defect concentrations of Fe in $Fe_{1-x}O$ are usually measured by chemical analysis. It is impossible to determine the compositions of non-stoichiometric compounds, because the error of an ordinary quantitative analysis is about $\pm 10^{-3}$, while the deviation of a crystal with intrinsic defect from its stoichiometric composition is about $\leq 10^{-3}$. Nevertheless, it is possible for chemical analysis to determine if the metal atoms in non-stoichiometric compounds are excessive or less. Because a non-stoichiometric compound, in common, is a multi-component solid solution in which the different components have different valences, e.g., $Fe_{1-x}O$ can be viewed as a solid solution which consists of $Fe^{2+}O$ and $Fe_2^{3+}O_3$. Deviation of those types of compounds can directly be determined by measuring of the concentration of an atom that shows an abnormal valence in it. For example, it forms the solutions containing large amounts of Fe^{2+} ion and less amounts of Fe^{3+} ion, when $Fe_{1-x}O$ (catalyst) is solved by hydrochloric acid solution under conditions with the absence of air or oxygen. Among these ions, the contents of both Fe^{3+} and Fe^{2+} can be determined by a titration of EDTA, but the Fe^{2+} needs to be oxidated to Fe^{3+} by ammonium persulfate prior to titration. The volume ratio of EDTA solutions that are consumed by Fe^{2+} and Fe^{3+} ions respectively is the ratio of Fe^{2+} and Fe^{3+} in sample, namely defect concentration of Fe, i.e., $x = 1/(3 + 2Fe^{2+}/Fe^{3+})$. There is also Kulun titration or polarographic analysis except for oxidation–reduction titration which can be used for such measurement of an ion with abnormal valence in the solution of a solid sample.

3.1.3.3 *Metastability-disproportionating reactions*

Figure 3.9 indicates that FeO is a metastable phase substance in thermodynamics. FeO is stable only at temperatures above 570°C and oxygen partial pressure of $-26 < \lg p_{O2} < -6$ (p_{O2} in bar), below this temperature FeO cannot form in thermodynamics.[20] When it is cooled down from high temperatures, FeO will undergo disproportionating reaction to form the stable products, Fe and Fe_3O_4, that is,

$$4FeO = Fe + Fe_3O_4. \quad \Delta G^{\theta}_{298} = -9.53\,kJ \cdot mol^{-1} \tag{3.7}$$

Castelliz *et al.*[21] found that an iron rich wüstite phase would occur during the disproportionating process, namely near stoichiometric FeO. According to the studies of Fischer *et al.*,[22] disproportionating of wüstite divides into two steps: First it changes to iron rich wüstite phase accompanied by the formation of Fe_3O_4; second, this iron rich wüstite disproportionates to Fe_3O_4 and Fe. Chemical equations of the

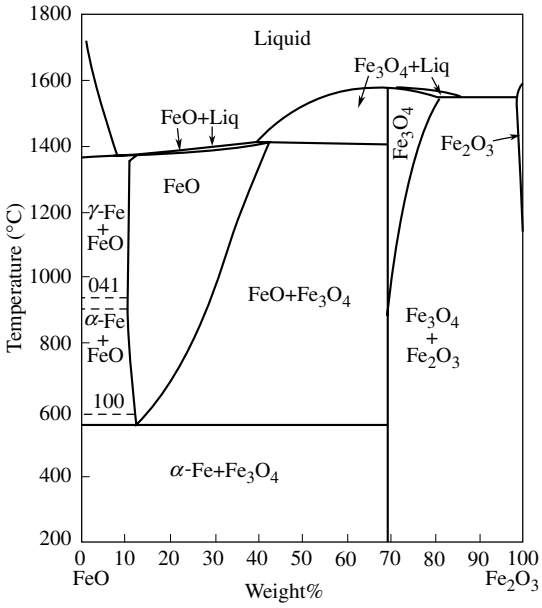


Fig. 3.9 Equilibrium diagram of iron-oxygen systems

two reactions are as follows:

$$Fe_{1-x}O = [(4x-1)/(4y-1)]Fe_{1-y}O + [(y-x)/(4y-1)]Fe_3O_4. \tag{3.8}$$

$$Fe_{1-y}O = [(1-4y)/4]Fe + 1/4Fe_3O_4, \tag{3.9}$$

where, $x > y$. Stolen *et al.*[5] studied the disproportionation of wüstite in greater detail and found that disproportionation of it is so slow that it could not be observed under low temperatures and short reaction times. With increase of the reaction temperature and reaction times, the iron rich wüstite and Fe_3O_4 can be observed first, followed by elementary iron. Stolen gave the comparative diagram for Gibbs formation free energy of different phases, as shown in Fig. 3.10.

Greenwood *et al.*[23] studied the disproportionation behavior of $Fe_{1-x}O$ at temperature range of 27°C–427°C by Mössbauer techniques and proposed that the disproportionation of $Fe_{1-x}O$ is related with temperature. At temperature below 227°C, the disproportionating reaction is in progress with Eqs. (3.8) and (3.9); at above this temperature, $Fe_{1-x}O$ disproportionates to Fe_3O_4 and Fe because the reaction (3.8) is so fast that it could not be observed. Stolen[5] observed by experiment that the reaction (3.8) occurs at a temperature of about 197°C and that is consistent with the result of Greenwood.

Pattek-Janczyki[24] studied the phase changes of wüstite before or after the annealing by microscope and microprobe, and proposed a possible model of the formation process of active sites of catalyst during the initial activation stage. The model assumed: (i) The reaction (3.8) is regarded as a transform reaction from elementary state to intermediate state, then intermediate state transforms to

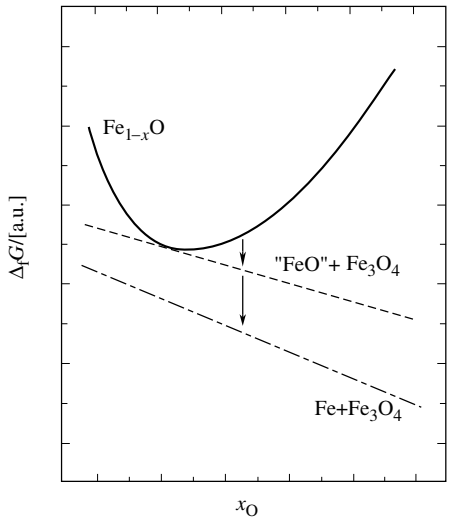


Fig. 3.10 Gibbs free energies of phases during the disproportionation of wüstite

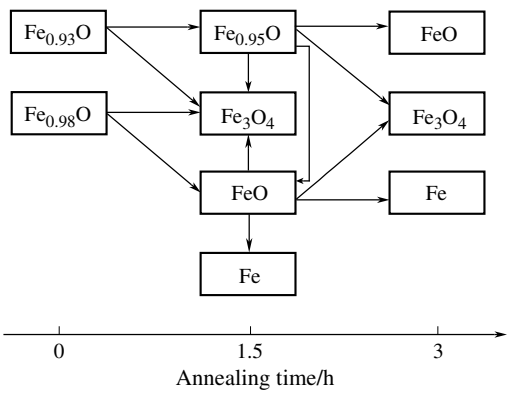


Fig. 3.11 Nucleation model of catalyst (Solid line represents disproportionating reaction, and the initial magnetite is not in)

the product; (ii) The reaction (3.9) occurs only at $y = 0$. Model of the catalyst produced by slow cooling (in which half amount of wüstite is in near stoichiometric composition and another half can be expressed by $Fe_{0.93}O$) is given in Fig. 3.11.

Therefore, the total reaction pathways in wüstite $Fe_{1-x}O$ can be illustrated as follows:

$$\mathbf{Fe_{1-x}O} \longrightarrow \mathbf{Fe_{1-x1}O} \longrightarrow \mathbf{Fe_{1-x2}O} \longrightarrow \ldots \longrightarrow \mathbf{FeO} \begin{matrix} \nearrow \mathbf{Fe_3O_4} \\ \searrow \mathbf{Fe} \end{matrix}$$

where, $x > x_1 > x_2 > \cdots > \mathrm{x_n}$. If iron content in the final product is very small, the content of magnetite in that would then be extremely high.

Adulterating other oxides in wüstite can influence its disproportionating behavior. We investigated disproportionating behaviors of a series of $Fe_{1-x}O$ ($x = 0.055 - 0.060$) that is adulterated with such oxides as CaO, MgO, BaO, MnO and ZrO_2, chemical compositions of which is shown in Table 3.6.

Table 3.6 Crystal phase and chemical compositions of samples

Sample	Dopant	Doping number (atomic ratio)	Fe^{2+}/Fe^{3+}	Crystal phase	Defect concentration (x) of Fe^{2+} in $Fe_{1-x}O$
Y_0	—	—	7.55	$Fe_{1-x}O$	0.055
Y_{Ca}	CaO	0.05	6.91	$Fe_{1-x}O$	0.059
Y_{Mg}	MgO	0.05	7.26	$Fe_{1-x}O$	0.057
Y_{Zr}	ZrO_2	0.05	6.82	$Fe_{1-x}O$	0.060
Y_{Ba}	BaO	0.05	7.12	$Fe_{1-x}O$	0.058
Y_{Mn}	MnO	0.05	6.91	$Fe_{1-x}O$	0.059

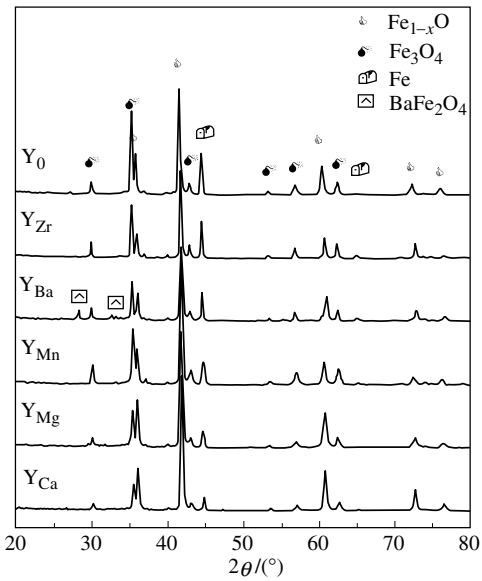


Fig. 3.12 XRD pattern of samples doped with different oxides after heat treating

The samples were treated at 400°C or 60 h at vacuum conditions and the quantitative analysis of phase was conducted with XRD. The XRD spectra of samples are shown in Fig. 3.12. The disproportionating ratio of wüstite is calculated with the following equation:

$$\alpha = \frac{3n_{Fe_3O_4} + n_{Fe}}{(1-y)n_{Fe_{1-y}O} + 3n_{Fe_3O_4} + n_{Fe}} \times 100\%, \tag{3.10}$$

where, n is molar numbers of $Fe_{1-x}O$, Fe and Fe_3O_4. For the samples before disproportionation, it is single phase of wüstite. Defect concentration (x) in $Fe_{1-x}O$ can be obtained from Fe^{2+}/Fe^{3+} value, while y is close to zero as mentioned above.

Table 3.7 Influence of temperature on disproportionation ratio of $Fe_{1-x}O$ doped with different oxides

Samples	Disproportionation ratio/%			
	350°C	400°C	450°C	500°C
Y_0	43.06	45.93	49.97	68.85
Y_{Ca}	11.38	15.84	22.46	25.09
Y_{Mg}	14.97	19.02	30.70	35.39
Y_{Zr}	35.40	39.97	41.08	54.72
Y_{Ba}	28.88	35.41	41.54	52.05
Y_{Mn}	28.32	34.63	40.68	44.83

Notes: Treated for 60 h under vacuum at different temperature.

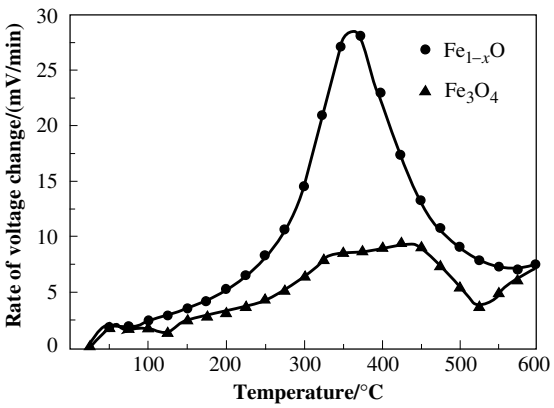


Fig. 3.13 DSC spectra of tri-promoted $Fe_{1-x}O$ and Fe_3O_4 based catalysts (Weight of sample: 27.1 mg, heating rate: 10 $K \cdot min^{-1}$, N_2 flow of 50 $ml \cdot min^{-1}$)

Disproportionation ratios of wüstite doped with oxides calculated from Fig. 3.12 are listed in Table 3.7. It will be seen from Table 3.7 that the disproportionating ratio of sample y_0 without doped oxides is the highest, reaching 45.93%, while all that of other samples doped with oxides are much lower, in which the samples doped with CaO and MgO are the most marked ones. The reason is, after doping with oxides, especially with CaO, large amounts of metal ion enters the lattice of $Fe_{1-x}O$ and inhibits the disproportionation of $Fe_{1-x}O$ effectively. The inhibition of studied oxides on disproportionation is ordered as: CaO > MgO > MnO > BaO > ZrO_2,[25] and the disproportionating ratios increase obviously with increasing temperature.

Figure 3.13 shows the DSC spectra of $Fe_{1-x}O$ and Fe_3O_4 catalysts containing three kinds of promoters at N_2 atmosphere. It indicates that there are appreciable phase changes for wüstite at about 370°C, which means the disproportionating reactions. Table 3.8 is the result of the experiments at constant temperature and under vacuum. The disproportionating ratio is only 2% at temperature of 500°C for 24 h, while disproportion is not observed below this temperature. It is obvious that the synergy of doping the various oxides can more effectively inhibit the disproportionation of $Fe_{1-x}O$. Therefore, though FeO is unstable thermodynamically, its rate of disproportionating reaction is rather slow in dynamics.[26] It can be found from

Table 3.8 Disproportionation ratio of wüstite added with Al_2O_3, K_2O, CaO

Treatment method	Fe^{2+}/Fe^{3+}	Disproportionation ratio/%
None	7.38	—
Vacuum treated at 350°C for 24 h	7.14	—
Vacuum treated at 400°C for 24 h	7.36	—
Vacuum treated at 500°C for 24 h	6.85	1.96

Fig. 3.9 that wüstite phase with ratio of Fe^{2+}/Fe^{3+} ranging in 1.9–11 is chemically stable below its melting point. Metastable wüstite $Fe_{1-x}O$ can be obtained when it is cooled rapidly from high temperatures to room temperature (fast crystallization). Fe^{2+}/Fe^{3+} ratios of all of wüstite catalysts are consistent with those ranges.[27]

3.1.4 *Relationship between various iron oxides*

Iron oxides with different crystal types show rather different structures. FeO belongs to NaCl-type cubic structure, α-Fe_2O_3 shows a corundum-type hexagonal structure, while Fe_3O_4, γ-Fe_2O_3 show spinel-type cubic structures. However, it is seen from the point of view of crystallography that various iron oxides are correlated intimately in their structures, and the differences lie in relative ratio of bivalent iron ions (Fe^{2+}) and trivalent iron ions (Fe^{3+}) in the structures which are closely packed by O^{2-} anions. FeO and α-Fe_2O_3 represent two of extremity components, but with continuous component between the two of them. Only when the ratio of Fe^{2+} to Fe^{3+} is equal to 1:2, they could form the most stable structure of Fe_3O_4. For example, FeO with NaCl type structure could be expressed as:

$$(\Delta_{2.00})_t[M_{1.00}\square_{0.00}]_oO,$$

where, $(\ )_t$ - tetrahedron, Δ-tetrahedral interspace, $[\ ]_o$- octahedron, [□]-octahedral interspace, M-metal cation, O-oxygen anion.

But this structure is unstable and usually accompanied with the defects of metal ions. As a consequence, there would be certain amounts of Fe^{3+} cations to maintain the charge-neutrality. These Fe^{3+} cations often enter into the original unoccupied tetrahedral interspaces. For example, when the defect concentration of metal ions is x, the wüstite could be expressed as $Fe_{1-x}O$, where $x < 1$. And if $x = 0.1$, according to the principle of charge-neutrality, then:

$$(Fe^{3+}_{0.1}\Delta_{1.90})_t[Fe^{2+}_{0.70}Fe^{3+}_{0.10}\square_{0.20}]_oO.$$

If Fe^{2+} cations are replaced with appropriate amounts of Fe^{3+}, the rest of that is equal to 1/4:

$$(Fe^{3+}_{0.25}\Delta_{1.75})_t[Fe^{2+}_{0.25}Fe^{3+}_{0.25}\square_{0.50}]_oO.$$

This is $Fe_{0.75}O$, i.e., Fe_3O_4 and Fe^{3+} ($Fe^{2+}Fe^{3+}$) O_4, which is the formula of ions distribution in inverse spinel of magnetite.

If the whole Fe^{2+} cations are replaced with Fe^{3+}, then:

$$(Fe^{3+}_{0.25}\Delta_{1.75})_t[Fe^{3+}_{0.42}\square_{0.58}]_oO.$$

It is the formula of ions distribution in spinel of γ-Fe_2O_3 with cation defects, i.e., $Fe_{0.67}O \rightarrow Fe_2O_3$.

Therefore, iron oxides with different crystal types could transform to each other under certain conditions and they may be expressed as $Fe_{1-x}O$ or Fe_yO; their chemical compositions can be written as $(a\text{FeO}) \cdot (b\text{Fe}_2\text{O}_3)$, while crystal phase compositions can be written as $c\text{Fe}_2\text{O}_3$ $(\text{FeO}) \cdot d\text{Fe}_3\text{O}_4$. However, their crystal structures or phases only have three kinds, hematite (Fe_2O_3), magnetite (Fe_3O_4) and wüstite ($Fe_{1-x}O$) in crystalography, in which, each of x, y, a, b, c, d could be expressed by the molar ratio ($Fe^{2+}/Fe^{3+} = R$) of bivalent (Fe^{2+}) iron ions and trivalent (Fe^{3+}) iron ions or the atom molar ratio (O/Fe) of oxygen atom to iron atom (Table 3.9).

It is seen from Table 3.9 that any iron oxides could be expressed as $a\text{FeO} + b\text{Fe}_2\text{O}_3$ in chemistry, while as Fe_2O_3, Fe_3O_4, FeO or $Fe_{1-x}O$ in crystal structure, respectively.

3.1.5 *Complex oxides and their solid solution of irons*

For fused iron catalyst with iron oxides as precursor and high melting metal oxides as promoters, researchers are much interested in the metal oxides added into it and the ordinary principles associated with the formation of complex compounds. Table 3.10 lists the iron oxides and other metal oxides usually used as promoters, which show a similarity of crystal structures above-mentioned. The enthalpy of each oxygen atom that could form the metal oxides with high or low valent is different.[28] It can be concluded that the catalytic activity is related to how easily the oxygen atom can be removed from the surface of catalysts. Under the circumstances, equilibrium pressure of oxygen which is being released from hot oxides under high vacuum, is the index to express how easily the oxygen can be removed. Another method for measuring the reactivity of oxygen may be carried out by quantifying the difficulty for oxygen to be exchanged with its isotope. Iron oxides and metal oxides as promoters may be either a co-crystal mixture or a complex solid solution. Solid solution of oxides is very important both in theory and practice for heat resisting capability and stability of catalysts. Because only with such solid solution of oxides, the promoter oxides in catalyst could be well distributed, and increases the heat resisting ability and stability of α-Fe after the iron oxide is reduced.

Iron oxides with metal oxides as promoters can form two kinds of complex oxides:

(i) Compound-type complex oxides such as $m\text{FeO} \cdot n\text{MeO}$ or $m\text{MeO} \cdot n\text{Fe}_2\text{O}_3$, whose character is that a quantitive ratio between one kind of metal oxide and another one would be affirmatory completely.
(ii) Sosoloid type complex oxides that contain one kind of oxide (MeO) solved in another one (FeO), whose quantitive ratio between components (FeO and MeO) is not affirmatory.

3.1.5.1 *Compound-type complex oxides*

The most representative compound type oxides are those complex ones that are constituted from iron oxide of Fe_3O_4 as base. It is known that this oxide has two of different cation nodes (Fe^{3+} and Fe^{2+}). Due to either of bivalent iron ion or trivalent one in this oxide is only replaced by the other metal ions, so it could form two kinds

Table 3.9 Relationship amongst Fe^{2+}/Fe^{3+}, O/Fe, chemical and phase compositions of FeO system

Fe^{2+}/Fe^{3+} atom ratio	Fe_yO or $Fe_{1-x}O$	O/Fe atom ratio	Chemical composition ($aFeO \cdot bFe_2O_3$)	Phase composition [$cFe_2O_3(FeO) \cdot dFe_3O_4$]	Structure formula[a]
R	$y = 1-x$ $x = 1/(3+2R)$	O/Fe = 1/y	$a = 2R/(1+2R)$ $b = 1/(1+2R)$	$c = 1-1/(2R)$ $d = 1/(2R)$	$(Fe^{3+}{}_m\Delta_n)[Fe_o^{2+}Fe^{3+}{}_p\square_r]O$
0	$Fe_{0.667}O$	1.500	Fe_2O_3	**Fe_2O_3**	$(Fe^{3+}{}_{0.25}\Delta_{1.75})$ $[Fe^{3+}{}_{0.42}\square_{0.58}]O$
0.25	$Fe_{0.714}O$	1.400	$FeO \cdot 2Fe_2O_3$	$Fe_2O_3 \cdot Fe_3O_4$	$(Fe^{3+}{}_{0.286}\Delta_{1.714})$ $[Fe^{2+}_{0.143}\ Fe^{3+}{}_{0.286}\square_{0.572}]O$
0.33	$Fe_{0.727}O$	1.375	$2FeO \cdot 3Fe_2O_3$	$Fe_2O_3 \cdot 2Fe_3O_4$	$(Fe^{3+}{}_{0.273}\Delta_{1.727})$ $[Fe^{2+}_{0.182}Fe^{3+}{}_{0.273}\square_{0.545}]O$
0.50	$Fe_{0.750}O$	1.333	$FeO \cdot Fe_2O_3$	**Fe_3O_4**	$(Fe^{3+}{}_{0.25}\Delta_{1.75})$ $[Fe^{2+}_{0.25}\ Fe^{3+}{}_{0.25}\square_{0.50}]O$
0.75	$Fe_{0.778}O$	1.286	$3FeO \cdot 2Fe_2O_3$	$FeO \cdot 2Fe_3O_4$	
1.00	$Fe_{0.800}O$	1.250	$2FeO \cdot Fe_2O_3$	$FeO \cdot Fe_3O_4$	$(Fe^{3+}{}_{0.20}\Delta_{1.80})$ $[Fe^{2+}_{0.40}\ Fe^{3+}{}_{0.20}\square_{0.40}]O$
2.00	$Fe_{0.857}O$	1.161	$4FeO \cdot Fe_2O_3$	$3FeO \cdot Fe_3O_4$	$Fe^{3+}_{0.143}\Delta_{1.857})$ $[Fe^{2+}{}_{0.571}$ $Fe^{3+}{}_{0.143}\square_{0.286}]O$
3.00	$Fe_{0.889}O$	1.125	$6FeO \cdot Fe_2O_3$	$5FeO \cdot Fe_3O_4$	
3.50	$Fe_{0.900}O$	1.111	$7FeO \cdot Fe_2O_3$	$Fe_{0.900}O$ $(6FeO \cdot Fe_3O_4)$	$(Fe^{3+}{}_{0.10}\Delta_{1.90})$ $[Fe^{2+}{}_{0.70}Fe^{3+}_{0.10}\square_{0.20}]O$
4.00	$Fe_{0.909}O$	1.100	$8FeO \cdot Fe_2O_3$	$Fe_{0.909}O$ $(7FeO \cdot Fe_3O_4)$	
4.50	$Fe_{0.917}O$	1.091	$9FeO \cdot Fe_2O_3$	$Fe_{0.917}O$ $(8FeO \cdot Fe_3O_4)$	$(Fe^{3+}{}_{0.08}\Delta_{1.92})$ $[Fe^{2+}{}_{0.75}Fe^{3+}{}_{0.08}\square_{0.17}]O$
5.00	$Fe_{0.923}O$	1.083	$10FeO \cdot Fe_2O_3$	$Fe_{0.923}O$ $(9FeO \cdot Fe_3O_4)$	
5.50	$Fe_{0.929}O$	1.077	$11FeO \cdot Fe_2O_3$	$Fe_{0.929}O$ $(10FeO \cdot Fe_3O_4)$	$(Fe^{3+}{}_{0.071}\Delta_{1.929})$ $[Fe^{2+}{}_{0.786}Fe^{3+}_{0.071}\square_{0.143}]O$
6.00	$Fe_{0.933}O$	1.070	$12FeO \cdot Fe_2O_3$	$Fe_{0.933}O$ $(11FeO \cdot Fe_3O_4)$	
6.50	$Fe_{0.938}O$	1.067	$13FeO \cdot Fe_2O_3$	$Fe_{0.938}O$ $(12FeO \cdot Fe_3O_4)$	
7.00	$Fe_{0.941}O$	1.060	$14FeO \cdot Fe_2O_3$	$Fe_{0.941}O$ $(13FeO \cdot Fe_3O_4)$	$(Fe^{3+}{}_{0.059}\Delta_{1.941})$ $[Fe^{2+}{}_{0.824}Fe^{3+}{}_{0.059}\square\Delta_{0.117}]O$
7.50	$Fe_{0.944}O$	1.059	$15FeO \cdot Fe_2O_3$	$Fe_{0.944}O$ $(14FeO \cdot Fe_3O_4)$	
8.00	$Fe_{0.947}O$	1.056	$16FeO \cdot Fe_2O_3$	$Fe_{0.947}O$ $(15FeO \cdot Fe_3O_4)$	
9.00	$Fe_{0.952}O$	1.050	$18FeO \cdot Fe_2O_3$	$Fe_{0.952}O$ $(17FeO \cdot Fe_3O_4)$	
10.00	$Fe_{0.957}O$	1.045	$20FeO \cdot Fe_2O_3$	$Fe_{0.957}O$ $(19FeO \cdot Fe_3O_4)$	$(Fe^{3+}{}_{0.043}\Delta_{1.957})$ $[Fe^{2+}{}_{0.870}Fe^{3+}_{0.043}\square_{0.087}]O$
∞	FeO	1.000	FeO	**FeO**	$(Fe^{3+}{}_{0.00}\Delta_{2.00})$ $[Fe^{2+}_{1.00}\square_{0.00}]O$

[a]Parentheses-( ) represent A-node, square brackets-[ ] represent B-node; □ represents tetrahedral interstitial; □ represents octahedral interstitial.

Table 3.10 Crystal lattice types of several metal oxides

Crystal lattice types	Metals							
	Fe	Al	Ti	V	Cr	Mn	Co	Ni
Rock salt (cubic crystal system)	FeO	—	TiO	VO	—	MnO	CoO	NiO
Spinel (cubic crystal system)	Fe_3O_4	—	—	—	—	Mn_3O_4	Co_3O_4	—
Spinel (cubic crystal system)	γ-Fe_2O_3	γ-Al_2O_3	—	—	γ-Cr_2O_3	—	—	—
Corundum (rhombic hexahedral system)	α-Fe_2O_3	α-Al_2O_3	Ti_2O_3	V_2O_3	α-Cr_2O_3	—	—	—

Table 3.11 Spinel type complex oxides of iron

Fe_2O_3 based		FeO based	
Phases	Crystal lattice constant/nm	Phases	Crystal lattice constant/nm
$MnO \cdot Fe_2O_3$	0.857	$FeO \cdot Cr_2O_3$	0.835
$TiO \cdot Fe_2O_3$	0.854	$FeO \cdot Al_2O_3$	0.810
$CuO \cdot Fe_2O_3$	0.844	$FeO \cdot V_2O_3$	0.840
$CoO \cdot Fe_2O_3$	0.837	$FeO \cdot Fe_2O_3$	0.838
$NiO \cdot Fe_2O_3$	0.834	—	—

of complex oxides that show spinel type crystal structure: Fe^{2+} is replaced with Me^{2+} to form $MeO \cdot Fe_2O_3$ and Fe^{3+} is replaced with Me^{3+} to form $FeO \cdot Me_2O_3$. Table 3.11 gives the examples for those spinel type complex oxides. According to the principle of isomorphous miscibility, spinel type complex oxides show the same crystal types with Fe_3O_4, and can make a solid solution with the latter and distribute homogeneously into it. For example, both Fe_3O_4 and $FeO \cdot Al_2O_3$ or $FeAl_2O_4$ which are made up from FeO and Al_2O_3 show same spinel type structures and react with each other to form a new solid solution of $(FeO \cdot Al_2O_3) \cdot (Fe_3O_4)$. As a result, it enables Al_2O_3 to be distributed homogeneously in the precursor (Fe_3O_4) of catalyst and take an effect of skeleton or compartment in reduced catalyst. Therefore, Al_2O_3 is a main structural promoter for typical fused iron catalyst. The complex oxides listed in Table 3.11 could be the effective promoters for Fe_3O_4 based catalyst, except CuO, NiO due to their poison for ammonia synthesis reaction.

However, it is not the same in the case of $Fe_{1-x}O$ based catalyst with FeO as precursor. $Fe_{1-x}O$ with the above-mentioned spinel type of complex oxides could not constitute a solid solution because of the different crystal types of them and would bring group by group crystallization during the procedure due to different melting points and crystal types of them. As a result, Al_2O_3 is commonly not the best structural promoter for $Fe_{1-x}O$ based catalyst. However, Al_2O_3 still is a necessary structural promoter for $Fe_{1-x}O$ based catalyst because it can increase the surface area of catalyst. Rock-salt type metal oxides given in Table 3.12 are of the same crystal type with FeO and could make a solid solution with the latter. Among

Table 3.12 Rock-salt type metal oxides

Oxides	FeO	CoO	NiO	CaO	MgO	SrO	BaO	CdO	MnO	TiO
Lattice constant/nm	4.29	4.26	4.20	4.81	4.21	6.01	5.53	4.70	4.44	4.25

those oxides, MgO and MnO with FeO could make a complete solid solution and distribute uniformly into $Fe_{1-x}O$ precursor.[1]

3.1.5.2 *Sosoloid-type complex oxides*

Solid solution of oxides could either be a replaced type (in which case, part of iron ions in the lattice are replaced by other metal ions) or an interstitial type (in which case, the other metal ions are located between the nodes of ion lattices of base oxides). Those oxides that consisted of part of iron ions being replaced by other metal ions with the same valent have been well studied. Examples for these kinds of solid solution type complex oxides include: FeO–NiO, FeO–CoO, FeO–MnO, FeO–MgO, FeO–BaO, FeO–CaO, FeO–SrO, Fe_2O_3–Cr_2O_3 and the others that are more complicated oxides. Characteristic of those oxides is that the bigger cation is embedded on the cation sites of iron and then the ion lattice is stretched slightly. In reverse, small cation embedded on the cation sites of iron would result in the shrinking of the lattice. It should be pointed out that, however, the oxide (FeO) would be characterized by the excess oxygen (compared with the one that is calculated stoichiometricaly) and insufficiency of the cations on its lattice nodes and can be viewed as a solid solution consisting of those blank points ("cavity") in the oxide. In the XRD spectra of this kind of solid solution, there is no spectrum line that is super-organized. This proved that the secondary component (or "cavity") are disorderly distributed in the oxides, in other words, these particular cation nodes are out-of-order distributed statistically. Figures 3.14–3.22 show the binary phase diagrams[29] of FeO or Fe_2O_3 and those oxides that are used commonly as promoters like FeO–Al_2O_3, FeO–MgO, FeO–ZrO_2, FeO–MnO, FeO–SiO_2, FeO–TiO_2, Fe_2O_3–La_2O_3, Fe_2O_3–Al_2O_3 and Al_2O_3–Cr_2O_3. It can be seen from the figures that the oxides, except for those like FeO–MgO, Cr_2O_3–Al_2O_3 and FeO–MnO (different data from different authors) could form the complete solid solution in full scale, can only form the partial ones with FeO or Fe_2O_3. These are worth to be referenced for the selection of promoters and determination of their content.

In the catalytic researches, it would be expected that the oxides usually used as promoters such as Al_2O_3, CaO, MgO, BaO, ZrO_2, TiO_2, La_2O_3 etc., could form solid solution with FeO or Fe_3O_4, so that the homogeneous distribution effect would be achieved. The contents of them are, consequently, limited in the ranges of that of local solid solution.

3.1.6 *Defect structures of iron oxides*

Many properties of solid, in greater extent, are correlated with the weeny differences between the crystal structure of it and that of the ideal one. An ideal crystal means the lattice of which shows order entirely. Atoms in such crystal lattice are inactive and the electrons in it are arranged according to the minimum energy state.

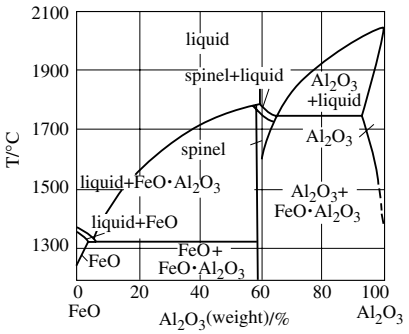


Fig. 3.14 Binary phase diagram of $FeO–Al_2O_3$

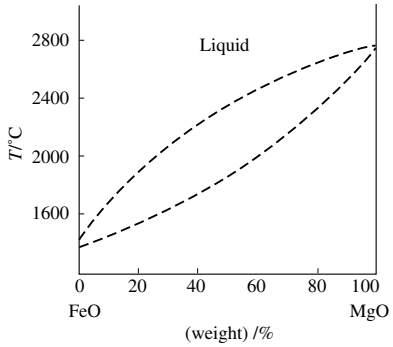


Fig. 3.15 Binary phase diagram of FeO–MgO

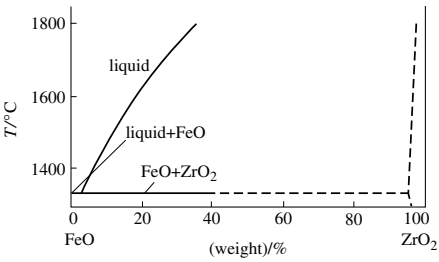


Fig. 3.16 Binary phase diagram of $FeO–ZrO_2$

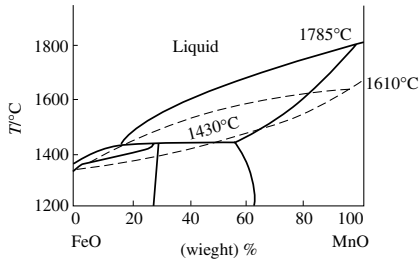


Fig. 3.17 Binary phase diagram of FeO–MnO

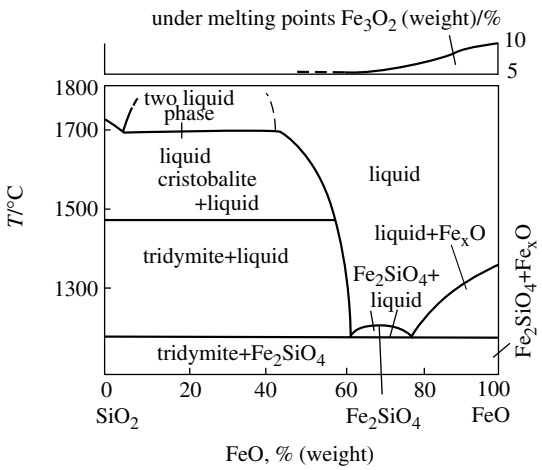


Fig. 3.18 Binary phase diagram of $FeO–SiO_2$

Practical crystals may have several kinds of defects and one kind of which would be caused by the increasing of atomic amplitude and the others by variable electron arrangements in accordance with the possible energy levels. Combination of a series of atomic defects may also forms the linear incompleteness i.e., displacement.

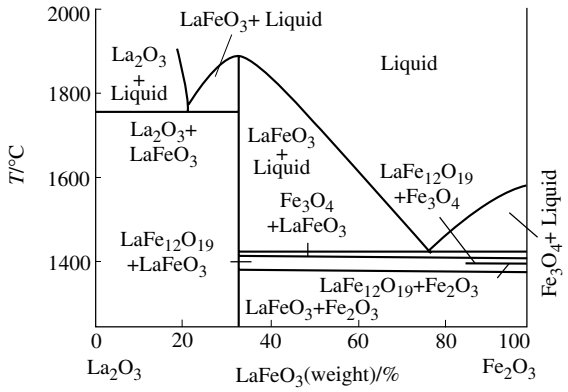


Fig. 3.19 Binary phase diagram of Fe_2O_3–La_2O_3

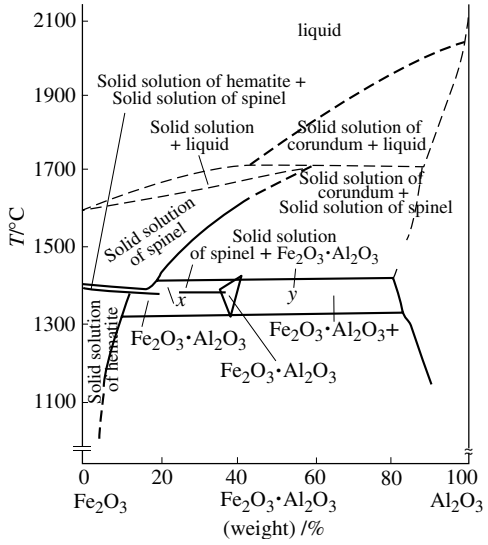


Fig. 3.20 Binary phase diagram of Fe_2O_3–Al_2O_3

Defect structures of oxides are the most interested regions in the study of solids. The reasons are that first, the various defects, as discussed in the following context, could be observed from the oxides, which offer wide base of substances for discussion theoretically. Second, oxides are the basic substances of a variety of matters and are important components of catalyst. To study the oxide catalysts or metal catalysts with oxides as precursors in depth and defect structure of oxide itself has, ever since, been the important theoretical foundations for the discussion of relation between the structure and catalytic performances of catalysts. Yue Wu[30] considered that compared with ordinary defect structures, the followings have particular meanings for catalysis studies:

(i) Most of oxides as catalyst, are transitional metal oxides, in which all of metal ions show a reduction–oxidation properties, e.g., Fe^{2+} is oxidized conveniently

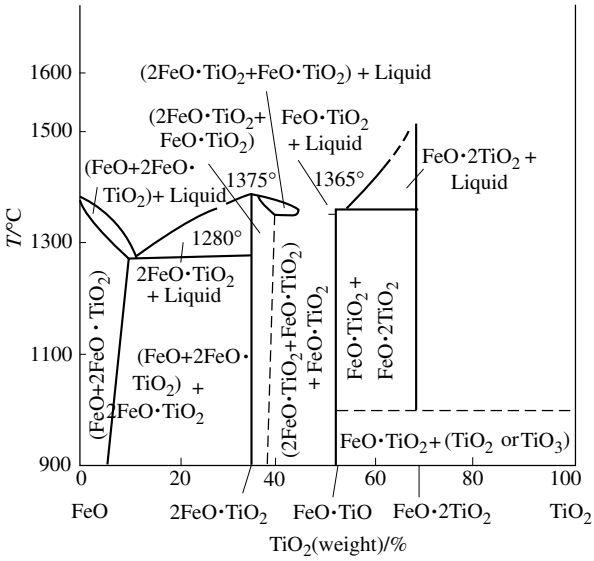


Fig. 3.21 Binary phase diagram of FeO–TiO_2

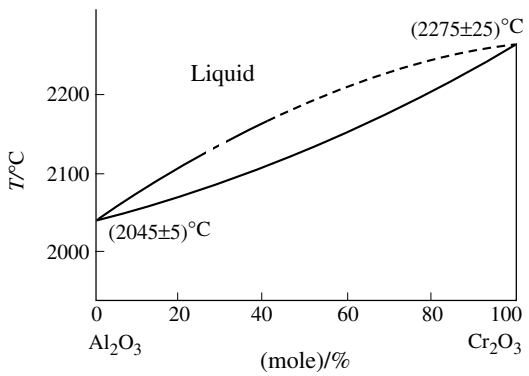


Fig. 3.22 Binary phase diagram of Al_2O_3–Cr_2O_3

to Fe^{3+}, while Ce^{4+} is reduced easily to Ce^{3+}, by which it offers a base for the formation of electron defect in oxides.

(ii) Most of transitional metal oxides are nonstoichiometric, which could either be oxygen defective (anions) or metal ion defective (cations). Those defects take an important effect in catalytic reactions.

(iii) According to the modern defect theory, many oxide catalysts easily form the extended defects during use, with the most representative one of MoO_3 and its complex oxides.

(iv) Oxide catalysts are usually exposed into oxygen atmospheres, in which case the defect will be different from the above-mentioned intrinsic ones and need to take into consideration the effect of gaseous oxygen on defect structure itself.

Physical and chemical properties of transitional metal oxides are related mainly with the departure stoichiometricity of themselves, while the latter would be determined on two important parameters: Temperature and equilibrium partial pressure of oxygen. It has been understood that when the change of temperature or oxygen partial pressure plays the rate controlling role in formation of defect structure, those species with slower migration could either be metals (such as U in UO_2) or oxygen (such as in TiO_2). This kind of process, commonly, is subordinated to the home diffusion dynamics, but with a possible exception. Faster migration species with different transmission mechanisms, e.g., diffusion, evaporating, coacervation through surface or crystal boundary, etc. could also be diffusion rate controlled.

3.1.6.1 *Classification of defects*

Defects in solid include micro defects at atomic or electronic level and microscopic defects could be divided into the following kinds according to defect sizes.

(1) **Point defect or zero-dimensional defect.** This kind of defects include both the possible existence of vacancies and substituted impurity atoms on their sites of crystal lattice structure and include misplaced parts of atoms with each other in solid compound of AB, namely, A atom occupies the B atomic site, while inversely B atom occupies A, or to say there are misplaced atoms or variable valence ions on the sublattice sites. The interstitial atoms sited in the interstitials of lattice structure are also parts of those point defects. It can further be divided into Schottky defects and Frenkel defect. The former means a metal atomic defect and the original metal atoms are transformed to the metal surface and the latter is composed of an atomic defect and an interstitial atom, as presented in Fig. 3.23. It could be imagined that the existence of inner defects would bring the distortions of lattice, as shown in Fig. 3.24. The issue of point defect is the major subject and key problem for the studies of solid chemistry.

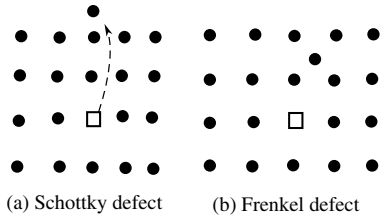


Fig. 3.23 Point defect of crystal lattice

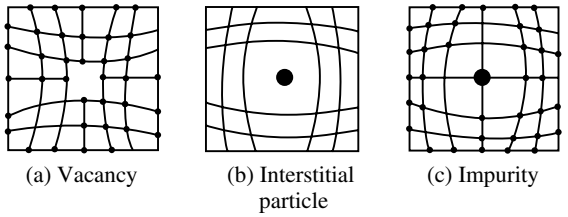


Fig. 3.24 Distortion of lattice caused by three kinds of point defects

(2) **Line defect or one-dimensional defect.** It is defined as any deviation of atomic arrangement along with a certain line in lattice from an ideal lattice structure, e.g., dislocation is one of line defects. For more instances, discontinuity of one of crystal face during its growth process results in parts of shortages of crystal face between the two neighboring crystal faces or the case of insertion of an incomplete crystal face into the two neighboring crystal faces and as a consequent, part of the atoms in lattice would be extruded, while the other parts are elongated. This kind of defect is called as edge dislocation. Another kind of dislocation is formed by the aslant spiralling of a crystal face around a axis, which is up to one of a crystal face every one of spiralling, though the crystal face grows without discontinuity. This kind of defect is called as screw dislocation. It is also possible that some of impurity atoms assemble in the dislocation sites. Dislocation theory was a postulation that was originally attempted to interpret the plasticic deformation of metals and proved by experiments at late 1950s, e.g., it could be observed directly that the existence of dislocation in alloy films by transmission electronic microscopy. Dislocation in metal materials is the essential factor of determining the mechanical properties of metals.

(3) **Face defect or two-dimensional defects.** It can be seen that metal surface is composed of many of little grains from the observations of metal surface after polished and eroded by metallographic microscope. Every grain is a single crystal and the solid composed of many of those single crystal grains are called as polycrystal. The interface between the grains with different orientations in polycrystal is called as grain-boundaries, which occurr when many of crystal nucleus form the grain aggregate (Fig. 3.25). The atomic arrangements about the grain-boundaries are rather in chaos and so is the formation of the face defect. As there atoms are not sufficient at the interface to make up the complete lattice order and perfect valent bonds, therefore, there would be dangling bonds. Consequently, these crisscrosses in grain boundaries and above-mentioned dislocations are the active sites of catalytic reactions. Though the atoms in solid are closest packed, if there occurs a disorder of stacking order of the atomic planes when they are closely arranged and stacked with layer by layer, e.g., the occurrence of the case such as ABCABCA → ABCBCA with absence of A plane, which formed stacking faults are also one kind of face defect, as shown in Fig. 3.26.

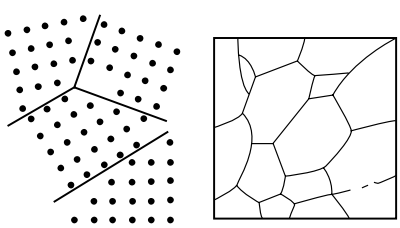


Fig. 3.25 Grain boundaries

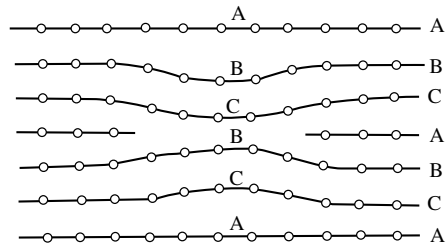


Fig. 3.26 Stacking faults defect

(4) **Body defect or three-dimensional defects.** It means that there are larger defects in three-dimensional orientation, such as impurities, settlings and hollow spaces included in solids. This defect is not a part of the same phase with the fiducial crystal, but a heterogeneous defect.

In an ideal and perfect crystal, all of the electrons would sit on the lowest energy level and energy levels in valence band are completely occupied and conduction bands include no electrons, namely be empty hole. However, in a practical crystal, due to the existence of point defects, which result in the electron current carriers in conduction bands and hole current carriers in valence bands, of which the former is expressed by e' and the latter by h^*. These electrons and holes are also one kind of defects, called as electronic defects.

3.1.6.2 *Intrinsic defects and impurity defects*

Point defect is the major subject and key problem for the studies of solid chemistry. It is also the most interesting subject in catalytic researches. In solid chemistry, we would discuss mainly the formation and equilibrium of point defect, the changes of current carriers (electron and cavity) and the influences of it on solid properties caused by the existence of point defect and how to control the types and concentrations of it in solid. Point defects can be divided into intrinsic defects and impurity defects.

(1) **Intrinsic defects.** Crystals with intrinsic defect are those that show incomplete structures and are without impurities. The faultiness of this kind of crystal structures are displayed as follow: (i) Deviation of crystal composition from chemical stoichiometry; (ii) Absences of certain atoms on lattice sites; (iii) Existent of interstitial atoms in the interstitials of lattice; (iv) Some kind of atoms occupy the lattice sites that are expected to be occupied by another kind. So, there would appear correspondingly the vacation defects, interstitial atomic defects and dislocation defects and so on.

Wüstite is the first compound to be found with a nonstoichiometric structure. Subject to heating, wüstite may lose parts of its cations, releasing two electrons at the same time and then form a positive vacant defect $V_{Fe}^{\cdot\cdot}$ in the original cationic lattice site. For example, excessive Zn atoms can be dissolved into ZnO and enter the interstice of lattice, make up an interstitial ion defect $Zn_i^{\cdot\cdot}$ and at the same time, take two electrons tied flabbily surrounding it, while the two electrons are excitated easily to the conduction bands. The defect can be expressed as $(Zn_i^{\cdot\cdot} + 2e^{\cdot})$ or $Zn_i^{\times}$. In Fe_3O_4 lattice, all of Fe^{2+} and 1/2 of Fe^{3+} distribute statistically in the interstitials of octahedron that is composed of the closely packed O^{2-} ions, while the rest 1/2 of Fe^{3+} locates in the interstitials of tetrahedral. This is the case of different valent ions being located on the lattice sites of the sublattice, which is also one kind of intrinsic point defect. Because the electrons can move along between $Fe^{2+} - Fe^{3+} - Fe^{2+} - Fe^{3+} \ldots$, so Fe_3O_4 is a native semiconduct material.

When the temperature of a perfect crystal is above 0 K, the atoms in the crystal would take a thermal motion around the equilibrium sites. With the increasing temperature, the average kinetic energy and the vibration scopes of atoms increases. Energy distributions between the atoms will follow the Maxwell distribution law. When the energies of some atoms, which are of energies larger than average one, come to large enough then they will leave the equilibrium sites and pile into the interstitials of lattice to become the interstitial atoms, while the original lattice sites become vacant. This kind of interstitial atom and a vacancy are also in motion, which either recombine or move to other sites. A pair of interstitial atom and a vacancy is formed simultaneously in crystal and is also an intrinsic defect, or called as Frenkel defect, as shown in Fig. 3.23(b).

Concentration C_F of Frenkel defect in crystal can be expressed as:

$$C_F = \frac{n_F}{(N \cdot N_i)^{1/2}} = \exp\left(-\frac{\varepsilon_F}{2 \cdot k \cdot T}\right), \tag{3.11}$$

where, n_F is the number of Frenkel defect; N is the number of lattice sites; N_i is the number of interstices; ε_F is the energy needed for forming a pair of a vacancy and an interstitial atom.

Another vacancy defect is called as Schottky defect, as shown in Fig. 3.23(a). It is composed of a pair vacancy of positive ion and negative ion with equal number. The existence of vacant defect could be detected directly by Field ion microscope.

Concentrations of Schottky defect can be measured with experiment of thermal expansion of metals, namely the determination of thermal expansion coefficient of both the whole crystal and lattice parameters, respectively. The thermal expansion coefficient of the whole crystal includes not only the thermal expansion of crystal lattice itself, but the formation of Schottky defect. Therefore, the difference of two results can reflect both the existence and concentration of Schottky defect. For instance, at conditions near to the melting point, the concentration of Schottky vacant for alumina is about 1×10^{-3}, and formation energy of its vacant is about 0.6 eV (1 eV = 1.60×10^{-19} J); while that of NaCl is 10^{-3}–10^{-4} and formation energy is 2 eV, respectively.

The concentration of Schottky vacant defect increases exponentially with temperature as expressed:

$$C_S = \frac{n_S}{N} = \exp\left(-\frac{\varepsilon_S}{2 \cdot k \cdot T}\right), \tag{3.12}$$

where, ε_S is the formation energy of vacancy. Because the formation energy of a vacancy in crystal is so close to the latent heat of gasification of solid, the concentration of vacant in solid could be estimated from the concentration of the saturated vapor at circumambience of solid, at the same temperature. For the atoms in metals are ordered by close packing, escaping of parts of atoms from it and to form a vacant defect would be rather easy compared to those insertion of atoms into it and making up of an interstitial defects. Namely, the formation energies of vacant defect are lower than that of interstitial defect.

(2) **Impurity defects.**[31] The possibility that one kind of impure atom could or could not enter into a crystal of some substances and substitute some atoms are decided by whether the energy effect of substitution is favourable or not. The effect of energy includes electrostatic acting energy, binding energy and the corresponding volume effect etc. between ions. In ionic crystals, the differences of electronegativity between cations and anions are very large; and therefore the energies of doping process are the decisive factor. Impure atoms ought to enter the corresponding ionic sites with close electronegativity and in other words, metal impurity ions occupy the original metal ionic sites, while the nonmetallic impurities do the original ones.

When the electronegativity of composition elements in crystal compounds are close to each other and that of impure atoms lie between that of two composition elements, geometric factors like atomic sizes etc. are the main factor if the doping process proceeds. For example, in various intermetallic compounds or covalent ones, those atoms with close radius (differences no more than 15%) could substitute each other to form substituted impurity defects.

Usually, those impure atoms would not change the original structure of the basic crystal when they replace the atoms in lattice sites or enter the interstitial locations. Therefore, for the interstitial atoms or extraneous impurity atoms, whether they can or cannot enter the interstitial spaces of crystal would be decided by the volume effect. It is limited only to those atoms or ions with small radius that could be the interstitial impurity defects.

The extraneous impure atoms could exist either in an atomic state or an ionic state, i.e., it would exist as a state of losing or binding of electrons, which contributes to increase local area energy levels in the forbidden bands of crystals.

If the valent state of impure ions are different from those of replaced ions in original crystal, added charges would be obtained by the crystal, which must be compensated by the other impure defects that are of the corresponding opposite charges, so as to maintain the charge neutrality of the whole crystal, and assure the doping reactions being continued. For instance, if small amounts of Fe^{2+} in $Fe_{1-x}O$ be replaced with Al^{3+}, there must be corresponding amounts of Fe^{3+} reduced to Fe^{2+}, of which the compositions of product would be $Al^{3+}_{\delta}Fe^{2+}_{1-x}Fe^{3+}_{x-\delta}O$. This kind of substance is an N-type semiconductor.

On the basis of the above-mentioned doping process and according to electron neutrality principle, the substances with a given concentration of current carrier could be produced.

All diversified point defects mentioned above, including intrinsic, impurity and electron defects, can be regarded as quasi-chemical species like atoms or ions, which would exist or participate in chemical reactions as a composition of substance.

3.1.6.3 *Irregularity of lattice and heterogeneous catalysis*

As various irregularities of crystals lattice are discussed above, it is now necessary to analyze their effect and importance in heterogeneous catalysis. There are at least two facts confirming the relation of crystal irregularity with the catalytic active center on catalyst surface. One of them is on those sites where the dislocations and surface point defects occur, and the atomic arrangements would differ from the others sites in catalyst surface, while surface atomic space and the properties of stereochemistry would remain the important factors to decide the catalytic activity.

Those sites of dislocations of edge and screw are beneficial to the catalytic reactions. The other is that the electronic factors on those sites of crystal lattice irregularity enhance the high catalytic activities, because the surface points correlated with the dislocations and defects can modify the electrical properties of solids.

(1) **Dislocation and compensation effect.** During the early 40's, the effect of surface lattice irregularity on the catalytic activity of metal catalysts was suggested. From the catalytic decomposition of formic acid on metal nickel catalyst treated with cold rolling, it was found that the decomposition rates increased accompanying with the increase of reaction activation energy because the treating of the catalyst with cold rolling increased its dislocation. In 1960s, the effect of dislocation on catalytic activity was further studied. It was found that activity of ethylene hydrogenation over Ni and Pt catalysts were increased by the ionic bombardment of its clear surface with regular structure. The reason of that was originated from the comprehensive effect of both dislocation and defect. At the same time, it was better interpreted for the common phenomena of compensation effect in heterogeneous catalysis. After the bombardment of high purity single crystal silver with positive argon ion, the rate equations of decomposition of formic acid on three of crystal surface i.e., silver [111], [100] and [110] crystal face, respectively, show that the pre-exponential factor of A increases always accompanied by the increase of activation energy E. This is just the compensation effect. Because the surface area of single crystal silver should not increase with the ionic bombardment, the increase of dislocation effect and the concentrated point defect function as the surface active sites. This is consistent with the results of the metal catalyst treated with cooling as described above.

(2) **Point defect and "super activity" of metals.** The catalytic activity of metal wire catalyst at high temperatures is markedly different before and after the occurrence of rapid flash vaporization. Before the rapid flash vaporization, the catalysts have normal activities. After the rapid flash vaporization at high temperatures, the activities of the metal wire catalysts such as Cu, Ni etc. increase approximately by 10^5 times, which are called as "super activities." This is because of the formation of highly nonequilibrium concentrations of point defects after the high temperature flash vaporization, which is much important to produce the "super activity" of catalysts. It disappeares rapidly when it is treated with cooling due to the diffusion of vacancies and rapid displacement of surface atoms in it.

3.2 Iron Oxides and Catalytic Activity

3.2.1 *Classical volcano-type activity curve*

During their initial studies about the ammonia synthesis catalysts, Bosch *et al.*[33] found that the catalysts obtained from the reduction of natural magnetite are better than the catalysts from other iron compounds. Almquist *et al.*[34] studied the relation between the activity of iron catalyst and the oxidization degree before its reduction and found that those catalysts, of which the ratio of Fe^{2+}/Fe^{3+} is closer to be 0.5 and compositions closer to magnetite, has the highest activity. Bridger *et al.*[35] further studied the fused iron catalysts promoted with binary promoters Al_2O_3–K_2O,

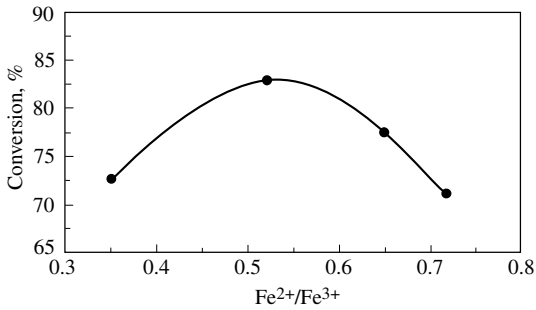


Fig. 3.27 Classical volcano type activity curve.[35] Promoters: Al_2O_3; K_2O; temperature: 450°C; space velocity: 10,000 h^{-1}; pressure: 100 atm

Table 3.13 Influence of Fe^{2+}/Fe^{3+} on activity for Fe_3O_4-based ammonia synthesis catalyst[36]

Fe^{2+}/Fe^{3+}	Activity before heat-resistant /NH_3%	Activity after heat-resistant /NH_3%	Fe^{2+}/Fe^{3+}	Activity before heat-resistant /NH_3%	Activity after heat-resistant /NH_3%
0.45	15.7	15.6	0.66	20.1	19.9
0.51	18.9	18.8	0.70	20.0	20.0
0.55	20.0	20.1	0.73	18.4	17.8
0.60	20.1	20.2	0.80	16.8	16.1

Notes: Testing conditions for activity: space velocity of 30,000 h^{-1}, pressure of 30 MPa, H_2:N_2 of 3:1, temperature of 475°C; for heat-resistant: temperature is 525°C for 24 h.

under the conditions of 10.13 MPa, 450°C, space velocity of 1×10^4 h^{-1} and found the catalysts, of which the ratio of Fe^{2+}/Fe^{3+} is closer to be 0.5 has the highest conversion (the ratio of ammonia concentration at reactor output to the equilibrium concentration of that under the same conditions) (Fig. 3.27). For several decades it was commonly believed that there is a close relationship between the performances of fused iron catalysts and the atomic ratio of Fe^{2+}/Fe^{3+} and of which the most optimum ratio was considered to be 0.5, and the most suitable precursor to be magnetite. Figure 3.27 has consequently been a classical conclusion over several decades. However, it has not given the proper interpretations in theory. All of the industrial ammonia synthesis iron catalysts in the world, without an exception, have the chemical composition as Fe_3O_4 before reduction. The conventional fused iron catalyst is made with melting magnetite as a main component and additives such as $A1_2O_3$, K_2O, CaO, CoO and etc., as promoters. The ratio of Fe^{2+} and Fe^{3+} is in the range of 0.4 to 0.8 (Table 3.13).

Although research and improvement on the conventional fused iron catalyst has been in progress for more than 80 years, there has been no essential breakthrough in improving the catalyst based on magnetite (Fe_3O_4). The ammonia synthesis catalyst in industry is still the iron catalyst based on magnetite. It was commonly believed that the catalyst had the best activity when its chemical composition and crystal structure of the precursor are most similar to those of magnetite. The volcano type curve between the activity and the Fe^{2+}/Fe^{3+} ratio are shown in Fig. 3.27.[35] That

seems to be an unquestioned classical conclusion. For several decades, researchers have developed new catalysts, while rigidly adhered to this conclusion and never changed the precursor composition (Fe_3O_4), only with the modifications of the promoter components and their amounts. Thus, almost all elements in the periodic table which might be used as promoters have been investigated widely. However, the activity of the catalyst was only improved slightly.

3.2.2 *Hump-type activity curve*

During the long period of research and developments, researchers have noticed the effect of the oxidization degree of iron or contents of Fe (II) on the catalytic properties. During 1970s and 1980s, Strel'tsov, Artyukh *et al.* studied the effect of the Fe (II) content in precursor on the performances of catalyst. They found that "the activity of the catalyst with 3.5%wt $A1_2O_3$ as the only promoter decreases with the increase of FeO content from 41.8% to 52.8% before it increases again with FeO content from 52.8% to 73.4%."[37,38] Wenxiang Wang *et al.*[39] found that the appearances of many FeO phases in water quenched spherical catalyst resulting in the variations of reducibility, activity and heat resisting ability of the catalyst. They believed that the ratio of Fe^{2+}/Fe^{3+} in spherical catalyst could be a little higher than that of non-spherical ones, but it would not exceed a certain degree. However, with the ratio of Fe^{2+}/Fe^{3+} in the studied catalysts not exceeding 1 or 3, more importantly, the insights into the changes caused by the increasing Fe (II) contents or Fe^{2+}/Fe^{3+} ratio were not taken into notes.

We have noticed the inherent correlations of three of iron oxides (Fe_3O_4, FeO, Fe_2O_3). It will be seen from the Table 3.9 that the catalyst precursor should be the magnetite phase (Fe_3O_4) when the ratio of Fe^{2+}/Fe^{3+} is 0.5 and the mixtures of Fe_3O_4 with FeO when the ratio of Fe^{2+}/Fe^{3+} changes from 0.5 to about 3.5, while it becomes to be a wüstite phase ($Fe_{1-x}O$) as the ratio being larger than 3.5. Therefore, the changes of Fe^{2+}/Fe^{3+} ratio means not only the increase of Fe (II) contents, but more importantly are the changes of phase compositions or crystal structure in the catalyst precursor.

Therefore, we systematically studied the relationship between the activity and the phase compositions of the precursor in a wider range of Fe^{2+}/Fe^{3+} ratio and found a hump type curve between the activity and the ratio (Fe^{2+}/Fe^{3+}) as shown in Fig. 3.28.[40] It can be seen from the Fig. 3.28 that the catalytic activity shows "hump type" (binary peaks) along with the changing of Fe^{2+}/Fe^{3+}; namely with the increase of Fe^{2+}/Fe^{3+}, there arises two high activity peaks. The first peak present to the Fe^{2+}/Fe^{3+} is equal to approx 0.5 (namely the traditional catalyst) and then the activity decreases with the increasing of Fe^{2+}/Fe^{3+} ratio, until Fe^{2+}/Fe^{3+} ratio equals to about one. After that, it rises up again with the continually increasing of Fe^{2+}/Fe^{3+} and shows the second peak and reaches its maximum value as Fe^{2+}/Fe^{3+} varying between five to eight, it at last drops slowly with the further increase of Fe^{2+}/Fe^{3+}.

The above-mentioned experimental results indicated that, in the ranges of $Fe^{2+}/Fe^{3+} < 1$ i.e., the first peak, the relation between catalytic activity and the Fe^{2+}/Fe^{3+} ratio is consistent with those results of traditional catalysts, in which the precursor is magnetite phases (Fig. 3.27). The facts of the decreasing activity with increasing of Fe^{2+}/Fe^{3+} ratio from 0.5 to 1, also coincides well with the results

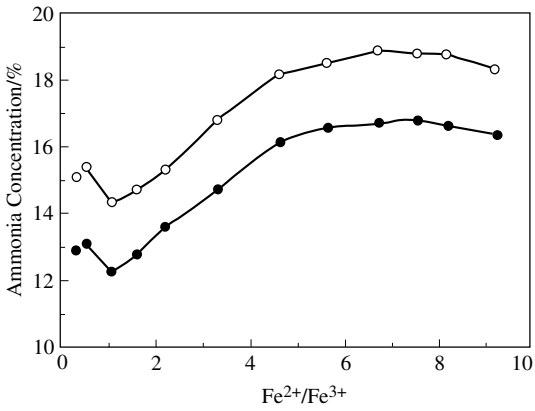


Fig. 3.28 Hump type activity curve for iron catalyst

Experimental conditions: pressure: 15.0 MPa; temperature: 425°C (□), 400°C (●); Space velocity: $3 \times 10^4\ h^{-1}$; promoters: Al_2O_3, K_2O, CaO

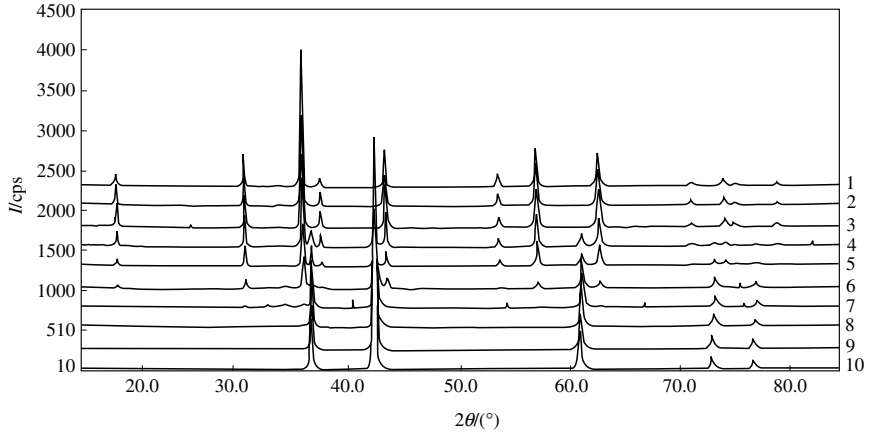


Fig. 3.29 XRD pattern of of unreduced catalysts with iron oxides and their mixtures as precursor

Fe^{2+}/Fe^{3+}: 1-0.313; 2-0.476; 3-0.500; 4-0.891; 5-1.110; 6-2.164; 7-3.148; 8-4.617; 9-6.547; 10-7.559.
Fe_3O_4 characteristic peaks (2θ): 18.27, 30.06, 35.43, 43.09, 53.58, 56.95, 62.57, 73.97,
FeO characteristic peaks (2θ): 36.23, 42.05, 60.90, 72.84, 76.61

obtained by Artyukh *et al.* that the activity of the catalyst with 3.5 wt% $A1_2O_3$ as the only promoter decreases with increasing of FeO content from 41.8% to 52.8% (namely Fe^{2+}/Fe^{3+} would be 0.8–1.2), then increases with increasing of FeO content from 52.8% to 73.4% (namely Fe^{2+}/Fe^{3+} would be 1.2–3.3). However, the case with Fe^{2+}/Fe^{3+} ratio higher than 3.3 was not studied by them.

Figure 3.29 is the XRD spectra of the catalyst with iron oxides and their mixtures as precursor. It is indicated from the Fig. 3.29 that there is only Fe_3O_4 phase when $Fe^{2+}/Fe^{3+} \leq 0.5$ without the Fe_2O_3 phase, which is expected to appear according to chemistry (see Table 3.9). The reason for this is that, during the fusion process, part of Fe_2O_3 undergoes the decomposition reaction to form Fe_3O_4 and

oxygen, while the rest of α-Fe_2O_3 which is too late to decompose, either transfers to γ-Fe_2O_3 isomorphous and then to Fe_3O_4, or dissolves in Fe_3O_4 to form the non-stoichiometric magnetite phase as $Fe_{3-y}O_4$. When the ratio of Fe^{2+}/Fe^{3+} is in the range of 0.5–3.15, it is a binary phase regions with Fe_3O_4 and FeO co-existing, where each of them presents independently. The content of Fe_3O_4 reduces with increase of Fe^{2+}/Fe^{3+}, while that of FeO does inversely. Among them, when $Fe^{2+}/Fe^{3+} = 1.0$, i.e., the molar ratio of FeO and Fe_3O_4 phase is equal to one, the two phases coexist equimolarly. When Fe^{2+}/Fe^{3+} is higher than 3.15, there is only FeO phase while the Fe_3O_4 phase disappears completely, though it is expected to exist according to chemistry. It is due to the Fe^{3+} in the samples that does not compose an independent magnetite phase, but dissolves into the wüstite phase non-stoichiometrically. This indicates that, when Fe^{2+}/Fe^{3+} is higher than 3.15, iron oxides transfer to the non-stoichiometric oxides with iron cation defects, namely wüstite phase expressed as $Fe_{1-x}O$, where X is the defect concentrations of the Fe^{2+} iron cations, value of which can be calculated by the Fe^{2+}/Fe^{3+} ratio and the Eq. (3.13). Crystal structure of iron oxide and their mixtures and activity of them after reduction are listed in Table 3.14.

$$x = \frac{1}{3 + 2(Fe^{2+}/Fe^{3+})}. \tag{3.13}$$

The precise lattice constants of the samples are given in Table 3.14. Initially, the lattice constants of Fe_3O_4 with spinel type cubic crystals become larger with increase of Fe^{2+}/Fe^{3+}, but decrease when the Fe^{2+}/Fe^{3+} is higher than 0.5, which is consistent with the experimental results of traditional Fe_3O_4 based catalysts. The decreasing lattice constants of the samples No. 1 and 2 with Fe^{2+}/Fe^{3+} smaller than 0.5, may be caused by the fact that the crystal itself at the moment shows a γ-Fe_2O_3 spinel structure with the Fe^{3+} ion defect. Because the samples No. 4, 5 and 6 with Fe^{2+}/Fe^{3+} larger than 0.5 are those with Fe_3O_4 and FeO presence independently, the lattice constants of the two phases are able to be detected, respectively. Their values become smaller along with the increasing Fe^{2+}/Fe^{3+} ratio. Obviously, this is the result of the influences of the two crystals mutually. It is worth noticing that the lattice constants of $Fe_{1-x}O$ with Fe^{2+} defect rock-salt type crystals increase with the

Table 3.14 Crystal structure of iron oxide and their mixtures and activity of them after reduction

Sample No.	Fe^{2+}/Fe^{3+} ratios	Crystal phase (XRD)	X values in $Fe_{1-x}O$	Lattice constant/nm		Reaction rate [a]/ ($mmol \cdot g^{-1} \cdot h^{-1}$)
				Fe_3O_4	FeO	
1	0.313	Fe_3O_4	—	0.8391	—	81.33
2	0.476	Fe_3O_4	—	0.8390	—	84.97
3	0.500	Fe_3O_4	—	0.8396	—	85.82
4	0.891	Fe_3O_4·FeO	—	0.8392	0.4299	76.04
5	1.110	FeO·Fe_3O_4	—	0.8391	0.4290	78.12
6	2.164	FeO·Fe_3O_4	—	0.8387	0.4268	81.60
7	3.148	FeO	0.108	—	0.4289	87.61
8	4.617	FeO	0.082	—	0.4301	96.50
9	6.547	FeO	0.062	—	0.4313	96.16
10	7.559	FeO	0.055	—	0.4313	95.78

[a]Experimental conditions: Pressure of 15 MPa, temperature of 698 K, space velocity of 30,000 h^{-1}, $H_2/N_2 = 3$.

increasing of Fe^{2+}/Fe^{3+} ratio, beginning from sample No. 6, and until levels off in about 0.4313 nm of samples No. 9 and 10. This is due to the metal ions such as Al^{3+}, K^{+}, Ca^{2+} etc. contained in the promoters entering into the defect lattice of $Fe_{1-x}O$, or forming a solid solution. It was found from the room temperature Mossbauer spectra of $Fe_{1-x}O$ that there are Ca^{2+} ions in the lattice, as well as little amounts of $FeO \cdot Al_2O_3$ solid solutions.[41] As the radius of Ca^{2+} ions is larger than Fe^{2+} ions, replacing of Fe^{2+} ions by the former makes the lattice constants become larger, and it will inevitably result in the distortions of the lattice. This is also responsible for the high activity of $Fe_{1-x}O$ based catalysts. However, the amounts of Al^{3+} and Ca^{2+} entering the defects are in the inverse proportion to the defect concentrations (x value) from the point of view of lattice constant. This probably relates with the regularities and chemical surroundings of the crystallization of $Fe_{1-x}O$ crystals.

In other words, the activity of fused iron catalysts with iron oxides as a precusor relates to not only the content of FeO, but also, more importantly, to its crystal structure of wüstite. When the Fe^{2+}/Fe^{3+} ratio is smaller than one, although the content of FeO increases the activity decreases, because the crystal structure of wüstite is not yet formed. When the Fe^{2+}/Fe^{3+} ratio is smaller than 3.15 where the catalyst precursor begins to come to an incomplete structure of wüstite, the activity increases and surpasses strikingly that of the traditional catalyst with Fe^{2+}/Fe^{3+} at about 0.5. After the Fe^{2+}/Fe^{3+} reaches five, catalyst precursor forms a complete wüstite structure, while the fused iron catalysts shows its highest activities. Both the activity and reduction behavior are enhanced significantly compared to that of the traditional catalysts.

Thereout, it is found that the catalyst has the highest activity among all the fused iron catalysts for ammonia synthesis when its chemical composition and crystal structure of the precursor are those of wüstite ($Fe_{1-x}O$). It is called $Fe_{1-x}O$ or wüstite based ammonia synthesis catalysts, where the defect concentration x of iron ion is: $0.04 \leq x \leq 0.10$. These experimental results break through the classical conclusion that lasted for more than 80 years, namely the catalyst has the best activity when its chemical composition and crystal structure of the precursor are most close to those of magnetite. It also provides a new approach for a novelcatalytic system — wüstite $Fe_{1-x}O$ system for improving the performances of the fused iron catalysts.

3.2.3 *Monophasical principle*

(1) Concept of molecular ratio of iron oxides. Why does the activity show hump-type curve (binary peak) with the ratio of Fe^{2+}/Fe^{3+}? At first, someone suggested that it is possible the result of the increasing contents of iron in the catalysts. However, it is seen from Fig. 3.28 that the activity displays the hump-type curve along with the increasing Fe^{2+}/Fe^{3+} and this kind of difference of activity is not caused by the changing contents of the iron. Because the contents of the iron increase monotonically with the increasing Fe^{2+}/Fe^{3+}, while the activity does not.

First, Fe^{2+}/Fe^{3+} ratio reflect only the chemical compositions of iron oxides, but not the crystal structures of them. It is clearly seen from Fig. 3.28 that the

Table 3.15 Relationship between crystal structure and chemical compositions of iron oxides

Fe^{2+}/Fe^{3+} (R)	Chemical compositions	Phase compositions	f in Eq. (3.14)	Crystal type
0	Fe_2O_3	Fe_2O_3	1	Fe_2O_3
0.25	$0.5FeO + Fe_2O_3$	$Fe_2O_3 + Fe_3O_4$	0.5	$Fe_{3-y}O_4$
0.5	$FeO + Fe_2O_3$	Fe_3O_4	1	Fe_3O_4
1	$2\ FeO + Fe_2O_3$	$FeO + Fe_3O_4$	0.5	$FeO + Fe_3O_4$
3	$6\ FeO + Fe_2O_3$	$5\ FeO + Fe_3O_4$	0.83	$5\ FeO + Fe_3O_4$
7.0	$14\ FeO + Fe_2O_3$	$13\ FeO + Fe_3O_4$	0.93 (1.0)[a]	$Fe_{1-x}O$
9.0	$18\ FeO + Fe_2O_3$	$17\ FeO + Fe_3O_4$	0.94 (1.0)[a]	$Fe_{1-x}O$
∞	FeO	FeO	1	FeO

[a]See in the text.

activity of catalyst correlates not only with the chemical compositions, but also the crystal structure of them. The relationship between the chemical compositions and the crystal structure of iron oxides are given in Table 3.15.

Table 3.15 indicates that the iron oxide with ratio of Fe^{2+}/Fe^{3+} (R) of three, is composed of six of FeO and one of Fe_2O_3 in a view of chemical compositions and five of FeO and one of Fe_3O_4 in crystal structure.

If both of FeO and Fe_3O_4 are present independently, then the molecular ratio of the main phase of FeO with minor phases of Fe_3O_4 will be 5:1, and the phase fraction will be $5/(5+1) = 0.83$. This ratio is called as the molecular ratio or phase fraction (f) of iron oxides in catalysts respectively, which is attempted to replace the classical concept of atomic ratio (R) of Fe^{2+} to Fe^{3+} and to express the monism of the phase composition of iron oxides in precursor[40]:

$$f = \frac{n_m}{n_m + n_s}, \tag{3.14}$$

where, n_m and n_s denote the mole numbers of major phases and minor phases, respectively in the precursor. As $f = 1$, it means $n_s = 0$ and that the precursor is composed of a single iron oxide (Fe_2O_3, Fe_3O_4 or $Fe_{1-x}O$), just as those cases of the $R = 0$, 0.5 and ∞ or more than seven listed in Table 3.15; as $f \neq 1$, it indicates there are at least two of iron oxide phases in the precursor, especially as $f = 0.5$, it indicates the simultaneous existing of the two of iron oxide phases in equimolar with the different crystal structures, just as those of the $R = 0.25$ and 1 listed in Table 3.15. Consequently, the physical meaning of the f is the molecular ratio or phase composition fraction of the different iron oxides (Fe_2O_3, Fe_3O_4 and $Fe_{1-x}O$) in the precursors of fused iron catalysts, which reflects the crystal structure of them. While $Fe^{2+}/Fe^{3+} = R$ is the atomic ratio of Fe^{2+} and Fe^{3+}, which reflects only the chemical compositions of iron oxides.

(2) Monophasic principle. There is the following relationship between f and R in the different regions of phase diagram of FeO system as shown in Fig. 3.30.

When $0 \leq R \leq 0.25$ (phase region of Fe_2O_3 (m)-Fe_3O_4 (s)),

$$f_1 = \frac{[Fe_2O_3]}{[Fe_2O_3] + [Fe_3O_4]} = 1 - 2R. \tag{3.15}$$

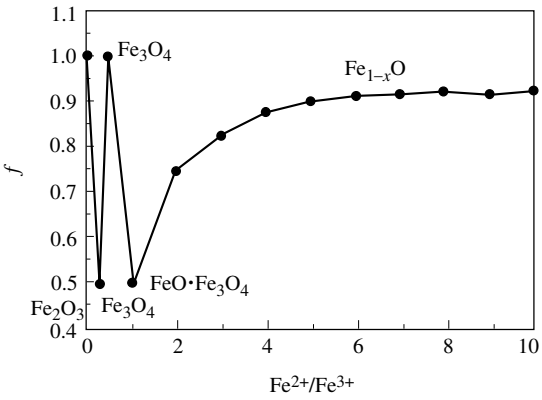


Fig. 3.30 Relationship between molecular ratio (f) and Fe^{2+}/Fe^{3+} ratio of iron oxides

When $0.25 \leq R \leq 0.5$ (phase region of Fe_3O_4 (m)-Fe_2O_3 (s)),

$$f_2 = \frac{[Fe_3O_4]}{[Fe_3O_4] + [Fe_2O_3]} = 2R. \tag{3.16}$$

When $0.5 \leq \mathrm{R} \leq 1$ (phase region of Fe_3O_4 (m)-FeO (s)),

$$f_3 = \frac{[Fe_3O_4]}{[Fe_3O_4] + [FeO]} = \frac{1}{2R}. \tag{3.17}$$

When $1 \leq \mathrm{R} \leq 8.2$ (phase region of FeO (m)-Fe_3O_4 (s)),

$$f_4 = \frac{[FeO]}{[FeO] + [Fe_3O_4]} = 1 - \frac{1}{2R}. \tag{3.18}$$

When $\mathrm{R} \geq 8.2$ (phase region of FeO (m)-α-*Fe* (s)),

$$f_5 = \frac{[FeO]}{[FeO] + [a - Fe]}. \tag{3.19}$$

The theoretic value of f in the different phase regions can be calculated in accordance with the Fe^{2+}/Fe^{3+} ratio (R) which is obtained by chemical analysis and the relation curve between f and Fe^{2+}/Fe^{3+} is shown in Fig. 3.30. It is clearly seen from the comparison of Figs. 3.28 and 3.30 that the relation curve of f-Fe^{2+}/Fe^{3+} is extremely similar to that of the activity $-Fe^{2+}/Fe^{3+}$. In the range of $Fe^{2+}/Fe^{3+} < 1$, the slope of both curves is large; while in the range of $Fe^{2+}/Fe^{3+} > 1$, both the curves are of the small slopes. However, there is difference between the calculated molecular ratios (f value) based on the data from chemical analysis and the measurement by XRD. For example, when $Fe^{2+}/Fe^{3+} = 7.0$, it is a solid solution composed of 13 of FeO and one of Fe_3O_4 from the Table 3.15, of which the f is 0.93 calculated with Eq. (3.18). Whereas, only the wüstite $Fe_{1-x}O$ phase was detected by the XRD spectra, indicating the f should be one. This is due to the Fe^{3+} ion in sample was not making an independent magnetite phase, but dissolving into the wüstite non-stoichiometrically, namely the minor phase of Fe_3O_4 in it was not present, and value of f should be equal to one. The $f(f_5)$ decreases again due to the formation of α-Fe phase (Eq. 3.19) when $Fe^{2+}/Fe^{3+} > 8.2$.

It will be seen from above discussion that the activity of ammonia synthesis catalyst correlates not only with the chemical compositions, but also the crystal types and crystal structure of iron oxides. The relationships between the activity and the Fe^{2+}/Fe^{3+} ratio can be interpreted perfectly by the molecular ratio f of the iron oxides, which have the different crystal structures in their precursors. At the same time, it also gives the theoretical explanation for those results of the classical catalysts (Fig. 3.27). For example, for the classical volcano-type activity curve, when $Fe^{2+}/Fe^{3+} = 0.5$, then $f = 1$ (Eqs. 3.16 and 3.17), so the catalyst has the good activity; both sides at $Fe^{2+}/Fe^{3+} = 0.5$, due to $f < 1$, so the activity of the catalyst decreases.

Therefore, the change of the activity for ammonia synthesis iron catalyst is essentially not decided by the atomic ratio (Fe^{2+}/Fe^{3+}) of the iron which has different valence in the precursor oxides, but the molecular ratio (f value) of iron oxides (Fe_2O_3, Fe_3O_4 and $Fe_{1-x}O$) with different crystal structures.

According to this, the author put forward the monophasic principle as follows.[42–47]

(i) The precursor of fused-iron catalyst with the highest activity should be only composed of one kind of iron oxide ($f = 1$) and one kind of crystal structure.
(ii) Mixing (doping) of any two iron oxides or two kinds of crystal structures in precursor will result in the decrease of catalytic activity of fused-iron catalyst. The high the mixing extents, the low the activity is. When the two iron oxides coexist equimolarly i.e., the molecular ratio of f is 0.5 (coexisting of two of iron oxides with two crystal structures), the activity decreases down to the lowest value. From this can be expected that, both of another maximum and the minimum of activity would occur possibly when $Fe^{2+}/Fe^{3+} = 0$ (pure Fe_2O_3, $f = 1$) and $Fe^{2+}/Fe^{3+} = 0.25$ (Fe_2O_3:Fe_3O_4 = 1:1, $f = 0.5$) respectively, but the catalysts with such Fe^{2+}/Fe^{3+} cannot be obtained by melting method.
(iii) Only one iron oxide phase in precursor leads to the uniform distribution of promoters, and then the high activity of fused iron catalyst can be obtained. Single iron oxide phase in precursor is the precondition of uniform distribution of promoters.

It was commonly believed that the uniform distributions of promoters into the catalyst are crucial for the high activity. When the precursor is composed of a single iron oxide with the single crystal structure, which is beneficial for promoters to be well-distributed. When the precursor is composed of two kind of iron oxides with different crystal structures, due to the different phases having individual features in both physical–chemistry and crystal structure, e.g., the melting point of Fe_3O_4 is 1,597°C while that of $Fe_{1-x}O$ is 1,377°C, at which a crystallization takes place stage-by-stage or a peritectic crystal phenomenon occurs in the step of the cooling and solidification during preparation. This results in the non-uniform distribution of promoters in precursor. Futhermore, the distribution of the promoters in different iron oxides are different due to the difference of their crystal structures and their properties such as the valance state and solubility of metal ions, resulting in the non-uniform distribution of the promoters in it. Therefore, in the case of coexistence (or hybrid) of two kind of iron oxides in the precursor, it occurs in the non-uniform distribution of the precursor itself, and intensifies the non-uniform distribution of promoters as well. Of course, the low activity of fused-iron catalyst

is mainly attributed to the coexistence of two iron oxides in precursor. Hence, it can be believed that the uniform distributions of the iron oxides in precursor are also crucial for preparing the catalysts with high performances. However, only when the precursor is the single iron oxide and the single crystal structure, it may be possible to obtain the uniform distribution of promoters, that is, the former is the premise conditions of the latter. As a consequence, the above-mentioned monophasic principle found the theoretical foundations for preparing the fused iron catalysts.

3.2.4 *Activity pattern of reduced catalyst with iron oxides as precursor*

Research on fused iron catalysts were, in the past, confined with those catalysts based on one kind of iron oxide of magnetite as precursors. In fact, iron oxide includes Fe_2O_3, FeO, Fe_3O_4 and their mixtures which have the activity for ammonia synthesis reaction. It was pointed out by Trimm *et al.*[48] that, in common, it is possible to find out an activity pattern for one type of solid (such as iron oxides) which catalyses one type of reaction (such as ammonia synthesis reaction). The activity is the most useful guide for the same type of reactions. Figure 3.31 shows the ammonia synthetic activity pattern of the fused iron catalysts prepared by different iron oxides and their mixtures. The differences in the activities of the various samples reflect the influences of various iron oxides on the performances of the reduced catalysts, because the types and contents of promoters are identical to each of samples in the experiments. It is seen from the Fig. 3.31[43,44] that the order of activity for ammonia synthesis is as follows: $Fe_{1-x}O > Fe_3O_4 > Fe_2O_3 >$ mixture of any two iron oxides. Among all iron-melting catalysts with iron oxides as precursor, the catalyst prepared from non-stoichiometric ferrous oxide with Wustite structure (expressed as $Fe_{1-x}O$) has the highest activity.

The aim of putting forward the above activity pattern is to design and develop highly active catalysts. To obtain high activity is the criterion to prove this model. The validity of above pattern has been proved positively by the successful development and wide application in industry of A301 and ZA-5 type $Fe_{1-x}O$ based

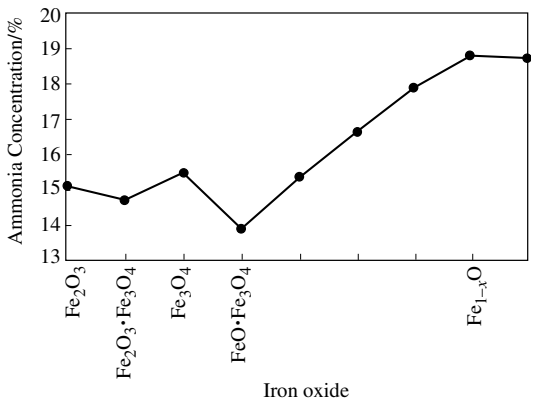


Fig. 3.31 Activity pattern for ammonia synthesis of reduced catalyst with iron oxides as precursor

catalysts which have the highest activity in the fields of fused iron catalysts.[49,50] As is known, a good catalyst is not only decided by the chemical essence of its active phase, but also related with the composition of promoters and the preparing conditions of them.

All of the results including the establishments of activity pattern, the discovery of the monophasic principle and their mathematical models are the great achievements in the theoretical studies ever since the findings of fused iron catalysts at the early periods in 20th century. Just as pointed out by Pernicone[51] that, the metal surface nanostructure can be drastically changed simply by using different precursors, a striking example concerns the classical ammonia synthesis catalyst. It has been confirmed that a much higher activity can be obtained if the catalytic Fe surface is formed from wüstite rather than from magnetite, thus suggesting that a reconsideration of the present consolidated knowledge on Fe ammonia synthesis catalyst and questioning a century of research and speculations of so-called textbook catalyst.

3.2.5 *Iron oxides and reduction performance of catalysts*

The simple overall reduction reaction is a gas–solid interface reaction.

$$Fe_3O_4 + 4H_2 = 4H_2O + 3Fe. \tag{3.20}$$

The product iron is much more dense as the educt magnetite. The metal forms after the initial reduction of a layer around the core of oxide and rapidly blocks the gas exchange from the outer gas–solid interface with the bulk. For this reason the mechanism cannot be based upon the removal of oxide ions from the lattice but requires the iron to move to a reaction interface at the gas–solid boundary.

The mechanism is considered to involve diffusion of ions and electrons and to contain two types of sites. One type allows the oxidation of oxide ions and the other type generates diffusion of iron ions and their reduction. The overall processes are:

$$Fe_3O_4 + Fe^{2+} + 2\text{electrons} \rightarrow 4FeO \tag{3.21}$$

$$FeO \rightarrow Fe^{2+} + O^{2-} \tag{3.22}$$

$$O^{2-} + H_2 \rightarrow H_2O + 2\text{electrons} \tag{3.23}$$

$$Fe^{2+} + 2\text{electrons} \rightarrow Fe \tag{3.24}$$

$$Fe_3O_4 + Fe + 4H_2 \rightarrow 4Fe + 4H_2O \tag{3.25}$$

Here, two conclusions are important from this mechanism derived from metallurgical samples of magnetite/wüstite synthetic mixtures.[52] First, the elemental iron is essential to reduce magnetite with hydrogen gas at low temperature. This elemental iron is produced from thermal decomposition of the wüstite mixture in the precursor. Stability and bulk distribution of the wüstite determine the abundance of reaction interfaces in the polycrystalline solid. The grain structure and porosity of the final catalyst is mainly predetermined by the disposition of these reaction centers representing the nuclei of the iron metal crystallines. Second, the reaction involves movement of all iron ions and allows a complete bulk restructuring of the solid at low temperature. The topochemistry of the reduction process will determine

the texture of the resulting ion. The grain structure of the precursor oxides which is essential for a finite reactivity of the bulk oxide mixture is only one of the factors controlling the reduction kinetics.

The reduction of a pure Fe_3O_4, obviously, cannot be explained by this mechanism. But the traditional fused iron catalysts, in common, always contain small amounts of FeO. As for $Fe_{1-x}O$ based catalysts, the forward reaction of Eq. (3.21) will be inhibited by the large amount of FeO and it will proceed along with the Eqs. (3.22)–(3.24) in turn. As for the Fe_3O_4 based catalysts containing small amounts of FeO, the reactions also proceed first *via* Eqs. (3.22)–(3.24) and then the reaction of (3.21) will be accelerated by the elemental irons generated by Eq. (3.24). Therefore, for the catalyst which is composed of two phase, such as FeO and Fe_3O_4, the reduction processes are first *via* Eqs. (3.22)–(3.24) and then along with Eqs. (3.21)–(3.24) in turn.

The experimental results for catalysts with various iron oxides as precursors shown in Figs. 3.32–3.35 indicate that, when the catalyst precursor is composed of two of the different phases, temperature t_m at the fastest reduction speed shows two of maximum values (Table 3.16) under the pure H_2 atmosphere. They represent the reduction behaviors of FeO and Fe_3O_4, respectively according to the XRD measurements. Note that especially in Fig. 3.34 there are two t_m values when the Fe^{2+}/Fe^{3+} ratios of samples are 0.89, 1.10 and 2.16, respectively. This is because the precursors of the three samples are composed of two phases, e.g., FeO and Fe_3O_4 and both exist in independent phases. The reduction process is divided into several steps according to phases in order of FeO and then Fe_3O_4; i.e., FeO is reduced first

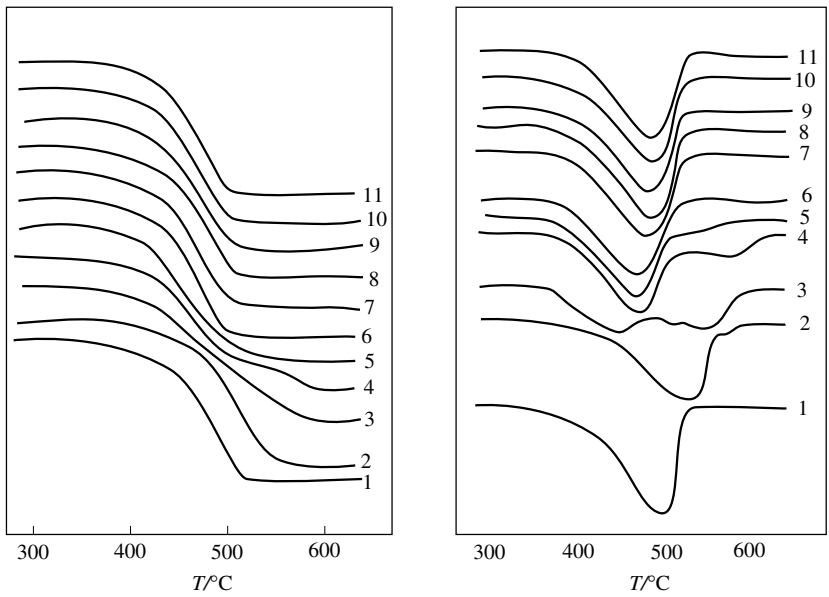


Fig. 3.32 TGA and DTG spectra of catalysts with iron oxides and their mixtures as precursor

Fe^{2+}/Fe^{3+}: 1-0.32; 2-0.52; 3-1.09; 4-1.60; 5-2.22; 6-3.33; 7-4.65; 8-5.66; 9-7.56; 10-8.22; 11-8.97

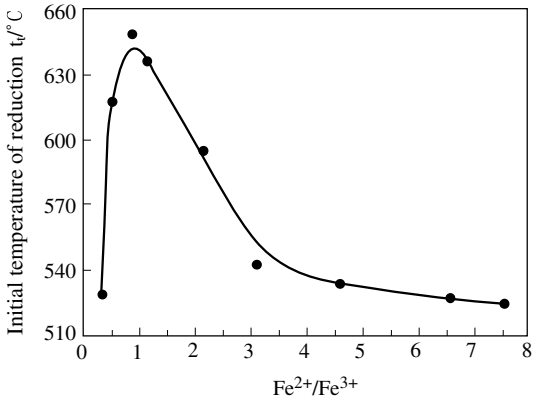


Fig. 3.33 Relation curves between terminal reduction temperature and Fe^{2+}/Fe^{3+} of catalysts

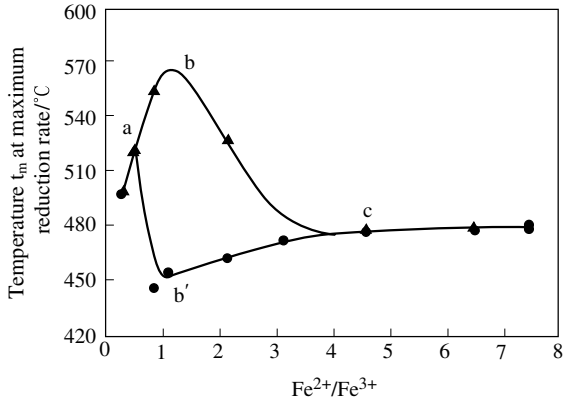


Fig. 3.34 Relation curves between temperature of the fastest reduction rate and Fe^{2+}/Fe^{3+} of catalysts

and after the reduction is nearly finished, reduction of Fe_3O_4 begins, which obeys the competitive mechanism. FeO and Fe_3O_4 are both reduced to α-Fe directly. This is proved by the experimental result shown in Fig. 3.35. It is seen from Fig. 3.35 that after the end of first stage reduction, there are only α-Fe and Fe_3O_4 peaks and the FeO peaks disappears in the XRD spectra. This indicates that FeO had been reduced fully in the first stage and the unreduced part is Fe_3O_4. This is also proved by the fact that the second peaks (Fe_3O_4 reduction peaks) become smaller with the decrease of the Fe_3O_4 content in Fig. 3.32. This is in agreement with the conclusion obtained by Clausen studying a commercial catalysts reduction with Mossbauer.[53] As the result of the reduction of dispart stages in phase, the reduction speed will decrease and the temperature will increase and also the activity of the catalysts after reduction will decrease.

The average reduction rate of the samples can be calculated by the total weight loss of each sample divided by the reduction time. The relationship between the average reduction rate and Fe^{2+}/Fe^{3+} is shown in Fig. 3.36. Comparing Fig. 3.36

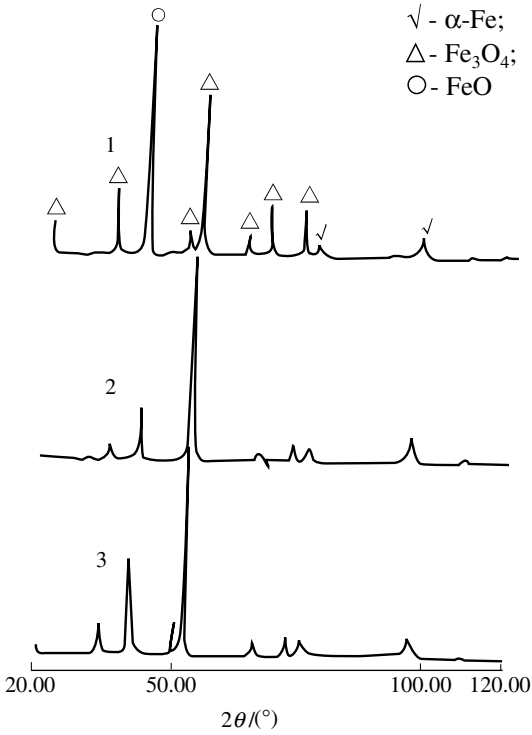


Fig. 3.35 XRD spectra of catalysts after the reduction at first stage

1. $Fe^{2+}/Fe^{3+} = 0.89$; the temperature stopped reduction = 450°C; cooling time = 1 min;
2. $Fe^{2+}/Fe^{3+} = 1.10$; the temperature stopped reduction = 510°C; cooling time = 1 min;
3. $Fe^{2+}/Fe^{3+} = 2.16$; the temperature stopped reduction = 500°C; cooling time = 1 min.

Table 3.16 Characteristic parameter of reduction for catalysts with different precursor

Samples	Fe^{2+}/Fe^{3+} (R)	t_b/°C	t_t/°C	t_m/°C	θ/%
1	0.313	290.0	529.3	500.0	94.35
2	0.476	347.6	618.3	524.0	95.67
3	0.500	348.0	619.0	526.0	95.51
4	0.891	352.4	648.9	447.6/556.0	95.19
5	1.100	356.5	636.9	456.2/577.3	93.00
6	2.164	358.6	594.6	463.8/530.1	94.70
7	3.148	362.4	542.3	473.7	98.50
8	4.617	358.7	533.5	480.0	96.69
9	6.547	353.5	526.9	480.6	97.29
10	7.559	352.1	524.6	480.6	96.63

Notes: 1. Experimental conditions: Heating rate 3°C min^{-1}; H_2 flow rate 175 ml · min^{-1}; Instrument: Shimadzu TGA-41.
2. t_b, t_t and t_m are the reduction temperature of begining, terminal and with maximum rate respectively; θ is the reduction degree.

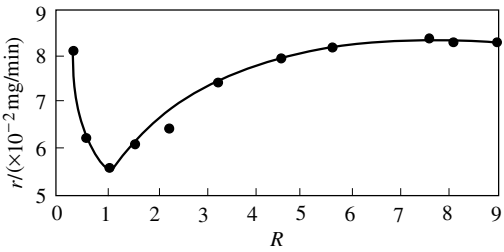


Fig. 3.36 Relation curve between reduction rate (r) and R (Fe^{2+}/ Fe^{3+}) of catalysts

and Fig. 3.33, we found that the shape of the curve between the reduction rate and Fe^{2+}/Fe^{3+} is just opposite to that of the curve of t_t and Fe^{2+}/Fe^{3+}. The reduction rate of the sample requiring a high reduction temperature is slow and the reduction rate of the sample requiring a low reduction temperature is fast. The shape of the curve between the reduction rate and Fe^{2+}/Fe^{3+} is similar to that of the curve between f (for definition, see above) and Fe^{2+}/Fe^{3+} shown in Fig. 3.30. With certain promoters and same manufacturing method, the reduction rate is determined by phase composition ratio f in precursor. When the precursor consists two phases of FeO and Fe_3O_4, the reduction rate will be reduced; and the larger the mixing extent of two phases (f value is reduced), the lower would be the rate of the reduction. Besides this, by comparing Figs. 3.28 and 3.36, we found that the activity of catalyst is consistent with its reduction rate. The more easily the catalyst is reduced, the higher is the activity.

It is noted that nonstoichiometric $Fe_{3-y}O_4$ (as sample 1) and $Fe_{1-x}O$ (such as sample 10) have similar reduction properties and faster reduction rates and lower reduction temperatures than those of a stoichiometric oxide (such as sample 2) are observed. So, we suggest that the reduction rate and reduction temperature of the catalyst are related with not only its precursor oxide but also the defect concentration of the iron ion in the iron oxides. The $Fe_{1-x}O$ and $Fe_{3-y}O_4$ with iron ion defects have faster reduction rates and lower reduction temperatures.

Among all catalysts with the iron oxides and their mixtures as precursor studied, $Fe_{1-x}O$ based catalyst with nonstoichiometric and wüstite structure has the fastest reduction rate and lowest reduction temperature. In a wüstite structure, large amounts of defects are iron ions, which enable the diffusion of Fe in oxide lattices, and will be preferable to electron transferences. This is the structural factor for the easy reduction of $Fe_{1-x}O$ based catalysts.

The activity decrease in two phase regions is caused by not only the non-uniform of both the precursor iron oxide and promoters, but also the stage reduction of catalyst precursor according to phase. As is well known, reduction reaction under hydrogen gas is a reversible one. In the case of stage reduction according to phase, the product α-Fe produced in the first stage (FeO) can be reoxidized by the water vapor produced in the second stage reduction (Fe_3O_4). This kind of repeated redox reaction makes the α-Fe crystallite grow up and causes the activity decreasing. However, in $Fe_{1-x}O$ based catalysts, which only contain the single iron oxide ($Fe_{1-x}O$), it is not the stage reduction behavior and the contents of the oxygen in it is about 20% lower than that in Fe_3O_4 catalysts, namely the water amount produced from the reduction of it is lowered by about 20%. Consequently, the influences of the

crystallite growth of α-Fe caused by those redox reactions are weakened strikingly. This is one of the reasons for the higher activity of $Fe_{1-x}O$ based catalysts, which are the results of the chemical properties and physical structures of themselves.

At the same time, $Fe_{1-x}O$ shows the marked vacant type crystal defects due to the some of its inborn reasons and there also is an obvious crystal defect during the growth of both the intermediate phase and α-Fe crystallites, where both carry through the continuously structural adjustment in order to compensate their defects. Both the boundary and defect between the intermediate phase and α-Fe may be with an appropriate matching. The interactions between them may repair the defects from the higher active crystal faces of (111), (211) so as to achieve more growth and stability and offer relevant adjustment to the lower active crystal faces of (100) and (110) as well. As a result, the numbers and intensities of active sites can be increased.

3.2.6 *Iron oxides and the surface textures of catalysts*

In heterogeneous catalysis, physical adsorption is one of the important methods for the measurement of surface textures of catalysts. On the other hand, much helpful information can be obtained *via* the measurements of the surface area of metal components in a multicomponent catalyst and the supported ones by the selective chemisorption.[52,54] It was first proposed by Emmett *et al.*,[55] where the techniques of CO, CO_2 chemisorption was utilized to measure the surface area of active iron and K_2O, Al_2O_3 in ammonia synthesis iron catalysts and the beneficial enlightenments were gained: The promoters, in spite of their low contents, cover the most surface of catalyst, which indicates that the promoters are likely to occupy the surface of catalysts. Since then the chemisorption method has progressively been used by many researcher[56–58] to investigate the role of various components in the traditional Fe_3O_4 based catalysts, as well as the relations between the changing tendency of them and the changes of the activity during the industrial operation processes. Streltsov *et al.*[59] also studied the effect of FeO contents on the surface area of Fe_3O_4 based catalysts and found that the iron surface area decreased by 3/5, basisc surface area decreased by 3/4 as the FeO contents increased from 21% to 64%.

In order to reveal the intrinsic relation between the surface properties and textures with the hump-type activity curve, the specific surface area of both the ammonia synthesis fused iron catalyst with different iron oxides as precursors and their active components were measured by the means of low temperature physical adsorption of N_2 and selective chemisorptions of CO, CO_2 as shown in Table 3.17.

(1) Iron oxides and the total specific surface area (S_T). When the type and amount of promoters is the same, the surface area of the highly active catalysts derived from $Fe_{1-x}O$ (samples with Fe^{2+}/Fe^{3+} 4.61–7.54) is $13\,m^2 \cdot g^{-1}$–$14\,m^2 \cdot g^{-1}$; while that of low active ones (samples with Fe^{2+}/Fe^{3+} to be 0.89–3.15) derived from the mixture of FeO and Fe_3O_4 is 11–$13\,m^2 \cdot g^{-1}$; and surface area of iron catalysts derived from Fe_3O_4 which shows medium activity is 13–$17\,m^2 \cdot g^{-1}$. These results indicate that the catalytic activity is not strictly related with its total surface area, because the specific surface area of the highest active catalyst is in the middle level.

Table 3.17 Data of physisorption and chemisorption of CO, CO_2 and N_2

No.	Fe^{2+}/Fe^{3+}	Uptake /(cm^3/g)			Total surface area, S_T/ ($m^2 \cdot g^{-1}$)	Surface area of Fe, S_{Fe}/ ($m^2 \cdot g^{-1}$)	(S_{Fe}/ S_T)/%	Surface area of alkali, S_K/ ($m^2 \cdot g^{-1}$)	(S_K/ S_T)/%	Surface area ofacid, S_A/ ($m^2 \cdot g^{-1}$)	(S_A/ S_T)/%
		N_2	CO	CO_2							
1	0.313	3.0575	2.3455	1.2772	13.309	4.092	30.75	4.868	36.58	4.349	32.68
2	0.476	3.9268	2.6792	1.7024	17.093	4.674	27.34	6.489	37.96	5.930	34.69
3	0.500	2.9276	2.3926	1.3519	12.744	4.174	32.75	5.153	40.43	3.417	26.81
4	0.891	3.0229	2.3394	1.5858	13.160	4.081	31.01	6.044	45.93	3.035	23.06
5	1.100	2.6246	2.0322	1.1538	11.425	3.545	31.03	4.398	38.49	3.482	30.48
6	2.164	2.4995	1.9904	0.9816	10.880	3.472	31.91	3.741	34.38	3.667	33.70
7	3.148	2.9761	2.0276	1.1780	12.956	3.537	27.30	4.490	34.66	4.929	38.04
8	4.617	2.8939	2.0307	1.1181	12.597	3.543	28.13	4.262	33.83	4.792	38.04
9	6.547	3.1972	2.2670	1.2059	13.917	3.955	28.42	4.596	33.02	5.366	38.56
10	7.559	3.2165	2.2650	1.2568	14.001	3.952	28.23	4.790	34.21	5.259	37.56

Notes: (i) The content and type of promoters (Al_2O_3, K_2O, CaO etc.) is the same in all samples. (ii) S_T is the total surface area measured by N_2 physisorption at 77.4 K (BET); S_{Fe} is the surface area of active α-Fe measured by chemisorption of CO at 77.4 K; S_k is the surface area of alkali measured by chemisorption of CO_2 at 194.8 K according to calculation of the content of K_2O; Surface area of acid is defined as $S_A = S_T - S_{Fe} - S_K$.

Therefore, although the variations of precursor oxides of fused iron catalyst will result in certain changes of the specific surface area, more importantly, they would cause changes in the surface properties. When the precursor oxide changes from Fe_3O_4 to $Fe_{1-x}O$, with the same promoters, their surface area is basically unchanged, while the activity increases obviously. This means the number or intensity of the active sites per unit surface area is increased. The surface area will be lowered when the precursor composed of the mixtures of FeO and Fe_3O_4 (especially with equimolar). As a consequence, the catalytic activity will be improved effectively by only increasing the surface area and the simultaneous increase of the number or intensity of active sites per unit surface area by changing the composition of iron oxide precursor or accession of valid promoters.

(2) Iron oxides and the iron surface area (S_{Fe}). Along with the changes of compositions of precursor oxides, the surface area of the active α-Fe, which were measured by the selective CO chemisorptions are not changed that obviously, which is usually in the range of approx. 3.5–4.0 $m^2 \cdot g^{-1}$ (except for the sample No. 2). The relation between the ratio of various active surface areas to the total areas and the Fe^{2+}/Fe^{3+} value are shown in Fig. 3.37. The Fig. 3.37 indicates that the surface area of the iron is only 27.3%–32.75% of the total area. But, the mass of the iron occupies 91%–92% of the total mass of catalyst, while those irreducible oxides of promoters or impurities account for 8%–9% in the reduced catalysts. It is suggested that the great mass of iron is covered with small amounts of promoters, which is in good agreement with the results of Emmett *et al.*[55] It is also clear from the Fig. 3.37 that the surface coverage (31%–32%) of the iron in lower active catalysts is higher than that of the higher active ones (27%–28%). This reveals again that to the factor deciding the catalytic activity is not the number of exposed iron surface, but the structures and electrical features.

(3) Iron oxides and the alkali surface area (S_K). Alkali metal and alkali earth metal oxides such as K_2O, CaO, MgO etc. are common electron-type promoters for fused iron catalysts. The surface area measured by the selective chemisorption of CO_2 at 194.8 K can be considered to be the total surface area of the basic oxides in

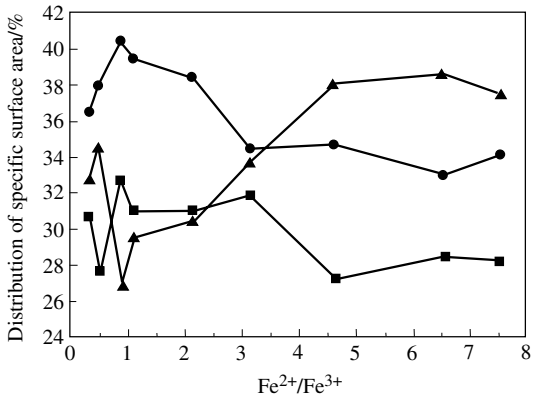


Fig. 3.37 Relationship between the ratio of various surface areas to the total surface area and Fe^{2+}/Fe^{3+}
■: S_{Fe}/S_T; ●: S_K/S_T: ▲: S_A/S_T.

the samples. Here, S_K was calculated according to the amount of CO_2 chemisorption and the nominal content of K_2O in Table 3.17. It can be seen from Table 3.17 that with the variations of iron oxides in precursor, the volume of CO_2 adsorption is 1.0–1.7 ml $\cdot g^{-1}$, and S_K is 3.7–6.5 $m^2 \cdot g^{-1}$, and the surface coverage of the alkali is 33.0%–46.0%. Clearly, they correlate with the iron oxides in precursor. It is seen from Fig. 3.37 that the alkali surface coverage of higher active $Fe_{1-x}O$ based catalysts are 33%–35%, and that of Fe_3O_4 based catalysts with medium activity are 36.6%–38% and less active catalysts of mixture oxides of FeO and Fe_3O_4 are 38%–46%. In this case, although the contents of alkali promoters is the same, the change of precursor oxides changes the surface coverage of alkali on catalyst surface and results in the variation of catalytic activity. In another case of precursor iron oxides with different features and compositions, the catalytic activity shows the inverse proportion to the coverage of alkali on catalyst surface. The activity decreases when the alkali surface coverage is too high. This conclusion is not consistent with previous results[60] of traditional Fe_3O_4 based catalysts. Someone considered that the increase of the surface coverage of alkali is beneficial to improve the catalytic activity for traditional catalysts. Almquist *et al.*[61,62] noticed that the comprehensive utilizations of both alkali and acid oxides are more effective, where the influence of proportion of the two oxides is a matter of preparation method. Krabetz[63,64] found that there is a certain relation between the catalytic activity and the surface basicity and the activity does not relate with the absolute contents of K_2O, although K is advantageous to the activity improvement while the K contents must be suitable.

(4) Iron oxides and the acidic surface area (S_A). Such acidic or amphoteric metal oxides as Al_2O_3, V_2O_5, Cr_2O_3, SiO_2 (impurity) etc. are the main structural promoters for the fused iron catalysts. In the total surface area of reduced catalysts, besides the surface area of metallic iron and basic oxides, the rest should be that of the acidic or amphoteric oxides, which is called as acidic surface area (S_A), and the value are taken from the difference of the surface area of iron and alkali subtracted from the total one. As is known from Table 3.17 and Fig. 3.37, the S_A of the higher active $Fe_{1-x}O$ based catalyst is 4.8–5.4 $m^2 \cdot g^{-1}$, acidic coverage of that is 37.6%–38.6%; the both value of medium active Fe_3O_4 based catalyst are 4.6–5.9 $m^2 \cdot g^{-1}$ and 32.7%–34.7%; while that of lower active catalysts derived from mixtures of FeO and Fe_3O_4 are 3.0–3.5 $m^2 \cdot g^{-1}$ and 23%–33%, respectively. These data reveal that, along with the variations of properties and compositions of precursor iron oxides, the acidic surface area changes regularly: As the precursor iron oxide transfers from Fe_3O_4 to mixtures of FeO and Fe_3O_4, acidic surface coverage decreases, while as it changes to be $Fe_{1-x}O$, the coverage increases. This kind of changing regularity of surface coverage is contrary to that of alkali ones. At the same time, the alkali coverages are in direct proportion to the contents of alkali metal elements, while the acidic coverage are of no such direct relations with the contents of acidic or amphoteric metal oxides on surface. Though the forming mechanism of acidic surface still needs to be explored in depth, from these it can be concluded that $Fe_{1-x}O$ as catalyst precursor is advantageous for the formation of acidic surface. There is an intrinsic relation between the catalytic activity and acidic coverage and in a given range, the activity increases with the increasing acidic coverages.

(5) Acid-base cooperative effect. Figure 3.38 shows the relationship between the ratio (S_A/S_K) of acidic surface area (S_A) to the basic surface area (S_K) and the

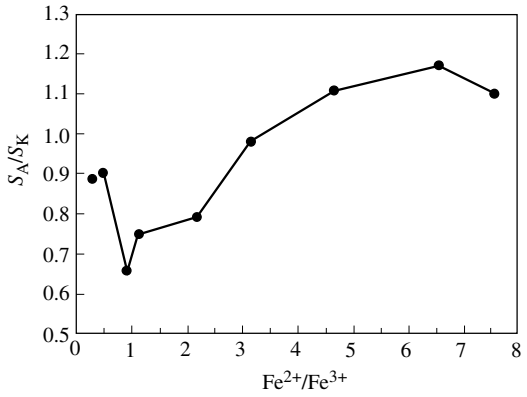


Fig. 3.38 Relationship between the ratio of surface coverage rate of acid to base and Fe^{2+}/Fe^{3+}

compositions (Fe^{2+}/Fe^{3+}) of iron oxides in the precursor before reduction. It can be seen from Fig. 3.38 that with the variations of the Fe^{2+}/Fe^{3+} of iron oxides in precursor, the S_A/S_K value of surface on reduced catalyst changes regularly along with the Fe^{2+}/Fe^{3+}, though the atomic ratios of the acidic or amphoteric metal elements to basic ones as promoters are all 0.87 (molecular ratio is 0.57) in the all samples.

It is clearly seen from Fig. 3.38 that the ratio (S_A/S_K) of surface coverage of acid and base also shows two peaks along with change of Fe^{2+}/Fe^{3+}, which is well consistent with the hump-type activity curve (Fig. 3.28). The activity increases first followed by decrease and then increase again with the increasing S_A/S_K value, reaches the maximum when S_A/S_K is in the range of 1.1–1.2, and is very low when $S_A/S_K < 0.9$. Therefore, the high activity of $Fe_{1-x}O$ based catalyst is related with their surface acid-base cooperative effect.

One of the roles of K_2O as promoter is its basicity being beneficial to desorption of product NH_3. But it is noticed that the rate determining step of the ammonia synthesis reaction is N_2 adsorption. Although the N_2 adsorption sites are those active iron atoms, the influences of structural and chemical circumstance around active iron atoms should not be neglected. Offering a sound circumstance for N_2 adsorption is one of the functions of promoters. There are lone-pair electrons in the molecular structure of N_2, which belongs to Lewis base. Acidic circumstance is obviously advantageous to N_2 adsorption on the Fe atoms. The acidic surface on a catalyst should be beneficial to N_2 adsorption, as well as to NH_3 desorption. Hence, there must be some synergistic effect between the acidic and basic centre. Plotting the activity *vs.* the ratio (S_A/S_K) of surface acid to base coverage as a function is shown in Fig. 3.39. It can be found from Fig. 3.39 that the catalytic activity increases with the increase of the S_A/S_K. Figure 3.39 reflects the synergistic effect of surface acidic and basic centres.

This kind of acid-base synergistic effect relates with the precursor of catalysts (to be expressed by Fe^{2+}/Fe^{3+}), but not directly with the absolute amounts of acidic ad basic oxides. It can be seen from Fig. 3.39 that the ratio of acid and base surface area of the highest active catalyst is about 1.1 and the catalyst precursor phase is

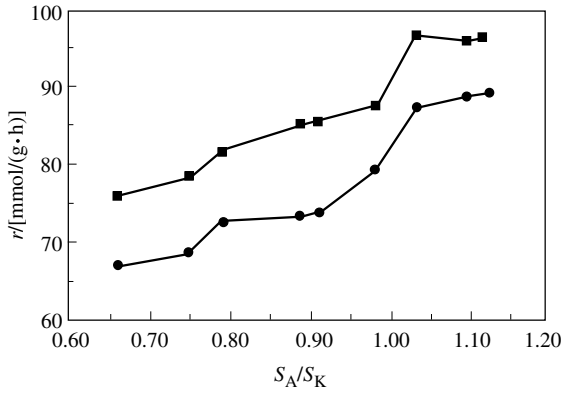


Fig. 3.39 Cooperative effect of surface of acid and base. Conditions for activity testing: Pressure of 15 MPa, Temperature of 698 K (●) and 673 K (○), Space velocity of 10,000 h^{-1}

$Fe_{1-x}O$. The ratio of 1.1 also reflects the adsorpion of N_2 being more important than desorption of NH_3. For this reason, it is considered that the acid-base cooperative effect of catalyst surface is one of the important reasons for $Fe_{1-x}O$ based catalysts to have the higher activity. It is quite a common phenomenon in catalysts such as acid, base and oxide ones, but it is not noticed as fully as possible in the case of metal catalyst such as iron catalyst. At the same time, it is found that the phenomena of acid and base coverage and their ratio relates with the properties and compositions of precursor iron oxide are derived from the severe enrichments as well as the excess coverage of alkali on the surface and resulting in the decreasing of the activity.

(6) Pore structure. Density, specific surface area, pore volume, pore diameter and its distribution, as well as macroscopical structures of catalysts reflect chemical mechanism and physical molding factors in catalyst preparation procedure. These parameters and structures influence not only the catalytic activity itself, but also the mass and heat transferences, flow states and hydromechanics and much more, influence the catalyst life during the industrial processes. Therefore, the following parameters are extremely important for the studies of the new type A301 catalyst, for characterization of the concerned properties in the process of catalyst preparation, for the studies of catalytic fundamental theory of new type catalyst (such as higher activity mechanism). Especially, it supplies the necessary parameters for engineering applications and the design of industrial reactors.

The average pore radius (r) and its distribution is shown in Fig. 3.40 for the catalyst with different iron oxides as precursors before reduction. All of the samples in Fig. 3.40 contain the same promoters. It can be seen from Fig. 3.40 that the pore radius and its distribution move towards the direction of large pore radius to small pore radius with the increase of Fe^{2+}/Fe^{3} before reduction, namely the pore radius of reduced catalyst with $Fe_{1-x}O$ as precursor is smaller than that of reduced Fe_3O_4 catalyst, in which the average porediameter and the most probability one of the former are 12.85 nm and 5–10 nm, while that of the latter are 16.36 nm and 10–20 nm, respectively. The pore volume and porosity change in the similar regularity (Table 3.18). It is the reason that the amount of removed oxygen (21.78%)

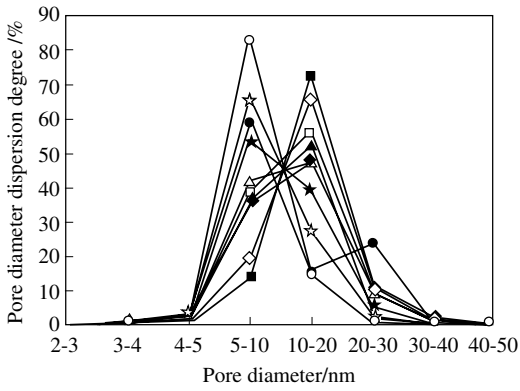


Fig. 3.40 pore radius and its distributions of reduced catalysts. Fe^{2+}/Fe^{3+} before reduction: ■-0.48; □-0.50; ▲-0.89; Δ-1.11; ♦-2.16; ◇-3.15; ★-4.61; ⋆-6.21; ●-6.52; ○-7.54

Table 3.18 Parameters for pore structure of catalyst

Catalyst procursor	Pore volume/ (cm^3/g)	Porosity/ %	Average pore radius/nm	Pore radius (nm) distribution/%				
				3–4	4–5	5–10	10–20	20–30
$Fe_{1-x}O$	0.0855	36.93	12.85	0.53	3.44	65.81	28.73	1.53
Fe_3O_4	0.1089	46.42	16.36	0.28	1.75	31.54	66.16	0.28

for $Fe_{1-x}O$ catalyst is less by approximately 17% than that (26.26%) of Fe_3O_4 catalyst during reduction.[58]

3.2.7 *Iron oxides and the adsorption properties on catalyst*

It is found from the results of H_2-TPD spectra[65] that the adsorption species of H_2 on the reduced catalyst surface changes as the catalyst precursor transfers from Fe_3O_4 to $Fe_{1-x}O$. Figure 3.41 illustrates the H_2 TPD spectra on the catalysts with different iron oxides as precursor and Table 3.19 gives the H_2 adsorption species and their desorption temperatures (t), and activation energy (E_d) resulted from TPD measurements. It can be seen clearly from samples of 1–6 in Fig. 3.41 that there are three adsorption species β_1, β_2 and β_3 of H_2 on the surface of traditional Fe_3O_4 based catalysts, among which β_1, β_2 are the dissociative adsorption species of H_2 (the activation energies of which are $78.5\,kJ\cdot mol^{-1}$ and $96.9\,kJ\cdot mol^{-1}$ respectively). They can be eliminated by reaction with N_2, indicating that they have the activity forming ammonia with N_2. While, β_3 is a strong chemisorption species of H_2 (the activation energy of desorption is $177.1\,kJ\cdot mol^{-1}$), which is not able to be eliminated by reaction with N_2, indicating that they are incapable of forming ammonia with N_2. However, there are only two H_2 adsorption species of β_1 and β_2 on the reduced $Fe_{1-x}O$ based catalysts, among which β_1 is non-activated adsorption (or physisorption) species of H_2 (the desorption activation energy of them is only $21.9\,kJ\cdot mol^{-1}$) and β_2 is the dissociative chemisorption species of H_2 (the desorption activation energy of them is $72.0\,kJ\cdot mol^{-1}$), which is close to β_1 but less than

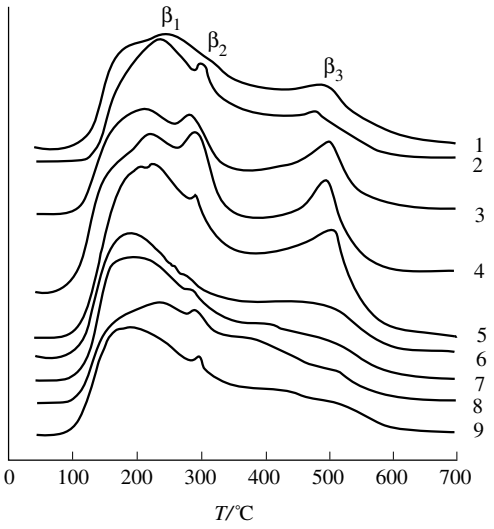


Fig. 3.41 H_2-TPD spectra of reduced catalysts with different precursors

Fe^{2+}/Fe^{3+}: 1-0.32; 2-0.52; 3-1.09; 4-1.60; 5-2.22; 6-3.33; 7-4.65; 8-5.66; 9-7.56.

Table 3.19 Adsorption species of H_2 on reduced catalysts derived from different iron oxides as precursor

Precursor oxide	β_1 t/°C	β_1 $E_d/(kJ \cdot mol^{-1})$	β_2 t/°C	β_2 $E_d/(kJ \cdot mol^{-1})$	β_3 t/°C	β_3 $E_d/(kJ \cdot mol^{-1})$
Fe_3O_4	240	78.5	321	96.9	560	177.1
$Fe_{1-x}O$	176	21.9	310	72	—	—

Notes: Heating rate is 30°C min. t is temperature of desorption peak-top, and E_d is desorption activation energy.

the β_2 species of Fe_3O_4 based catalysts. The strong chemisorption species of β_3 does not appear for $Fe_{1-x}O$ based catalysts. Probably it is one of the important reasons that $Fe_{1-x}O$ based catalysts have high activity. Although the strong chemisorption species of H_2 does not have activity for ammonia synthesis reaction, it is able to occupy the surface active sites to inhibit the chemisorption of N_2.

The phenomena of the inhibition effect of strong chemisorption of H_2 on adsorption of N_2 have aroused the attention for the studies of ruthenium ammonia synthesis catalysts.[66–68] Hikita *et al.*[69] pointed out that there are competitive adsorption of H_2 and N_2 on ruthenium catalyst surface, because the adsorption heats of H_2 is larger than that of N_2. The strongly chemisorbed H_2 occupies the active sites of ruthenium catalyst and possibly makes the sublayer hydrogen-bridged compounds. In particular, in the case of alkali metal hydroxides as promoters, strong adsorption of H_2 is common feature of ruthenium based ammonia synthesis catalysts. Niwa *et al.*[70] found that the strong adsorption of H_2 can be effectively inhibited by the addition of the rare earth compounds. Siporin *et al.*[71] suggested that the stronger the basicity of supports, the larger would be the adsorption enthalpy of hydrogen (with larger coverage), and the reaction order of hydrogen would be negative. This

is possibly the result of the changes of reaction order caused by different geometric configuration of H_2 bindings with the different supports. Every kind of catalyst has at least two kinds of active sites and the addition of basic promoters result in the one kind of active sites with high activity. Zhonglai Li *et al.*[72] found that desorption of nitrogen is the rate controlling step of ammonia decomposition reaction on ruthenium catalyst. Its desorption rate relates with the concentration of hydrogen on surface, while there is the spill-over phenomena of H_2 on the surface. The co-adsorption of hydrogen on surface inhibits desorption of nitrogen. Barium as promoter has the role of hindering the migrations of hydrogen. Hence, the phenomenon of strong chemisorption of H_2 is considered to be correlated probably with the coverage of acid and base on catalyst surface. Activated carbon (or MgO) supported ruthenium catalysts are usually with alkali metals or/and alkali earth metal oxides as promoters, where the surface is completely basic, and the inhibition effect of strong H_2 chemisorption is the most serious one; on the surface of classical Fe_3O_4 based catalyst, the basicity of it is stronger than its acidity (Fig. 3.38), where there is also strong chemisorption of H_2 present; while on the surface of $Fe_{1-x}O$ based catalyst, the basicity is weaker than acidity and consequently it is without the strong chemisorption of H_2 (without the species of β_3 of H_2). This indicates that the stronger the basicity, the stronger would be the chemisorption of H_2 on the catalyst surface. But inversely, there is not yet the experimental evidence which shows the stronger the acidity, the weaker the chemisorption of H_2. The reason for this is, as mentioned above, that there is a certain kind of synergistic effect between acid and base. Therefore, an introduction of a proper acidic promoter into ruthenium catalysts may possibly inhibit the strong chemisorptions of H_2.

Figure 3.42 is the TPD results of N_2 on catalysts with different precursors. Table 3.20 gives the activation energy of both desorption (E_d) measured by TPD and reaction of N_2 by activity testing. The activation energy and temperature of N_2 desorption on a variety of catalysts were investigated,[73] and the relationship of the desorptive activation energy of N_2 with the changes of types and compositions of precursor iron oxides was found to be similar to the hump-type activity curve of fused iron catalyst. The order of desorption activation energies E_d of N_2 which were measured through TPD is as follows: Two phase region (Fe_3O_4+ FeO) > Fe_3O_4 > $Fe_{1-x}O$. This is just the opposite to the order of the catalytic activity. In other words, the order of the desorption activation energy of N_2 is in accordance with the reaction activation energy E_r of the ammonia synthesis. This phenomenon shows that the dissociation adsorption of dinitrogen is the rate determining step for ammonia synthesis reaction. Desorption temperature has also the same changing tendency. N_2 desorption peak on the catalyst reduced from $Fe_{1-x}O$ occurs approximately at 569°C at 30°C min), which is in good agreement with the results by Boszo,[74] in which the desorption peak of N_2 appeared at about 587°C on iron single crystal (111) face used the flash desorption method. It is probably generated by desorption of N-* which is dissociatively adsorbed on the Fe (111) crystal face. It will be seen from this that the main active center on surface is probably similar to structure of the Fe (111) crystal face, where the main adsorption species of N_2 is generated. This result provides the important information that the precursor of catalysts has obvious influence on the adsorption behavior of N_2. The high activity of A301 catalyst originates mainly from the changes of precursor oxides, which enables more of Fe (111) crystal faces to be exposed. By the investigations of the surface

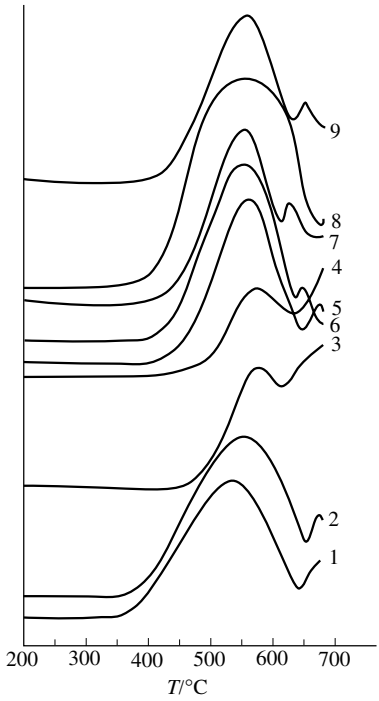


Fig. 3.42 N_2-TPD spectra of reduced catalysts with different precursors (β = 20°C/min)

Fe^{2+}/Fe^{3+} before reduction: 1-0.32; 2-0.52; 3-1.09; 4-1.60; 5-2.22; 6-3.33; 7-4.65; 8-5.66; 9-7.56

Table 3.20 Activation energy of desorption of N_2 and ammonia synthesis reaction on the reduced catalysts derived from different precursors

Precursor oxides	Desorption activation energy $E_d/(kJ \cdot mol^{-1})$	Reaction activation energy $E_r/(kJ \cdot mol^{-1})$
$Fe_{1-x}O$	163.2	159.0
Fe_3O_4	170.3	171.5
Fe_3O_4+FeO	222.3	—

active sites and reaction rates on a series of ammonia synthesis catalysts derived from different iron oxides, there is no obvious difference of density (the number of Fe atoms exposed per unit surface) of surface active site between the $Fe_{1-x}O$ and Fe_3O_4 based catalyst, while the intensity (TOF) of active sites of the former is 56% higher than the latter. The increasing active site intensity indicates that more of Fe (111) crystal faces are exposed on the surface.[75,76]

3.3 Promoters of Fused Iron Catalyst

The ammonia synthesis catalyst used in modern industry is composed of the iron oxides with a given ratio of Fe^{2+}/Fe^{3+} and small amounts of promoters. The α-Fe

obtained from the reduction of iron oxides is the active phase for ammonia synthesis reaction. However, the catalyst reduced from pure iron oxides deactivates rapidly during the ammonia synthesis processes. Taken as promoters, the high melting metal oxides such as Al_2O_3, K_2O, CaO, MgO and SiO_2 etc. are unreducible and provide no catalytic activity. The roles of them are to improve the catalytic activity of α-Fe, to increase the heat resisting and antitoxic performances, as well as to prolong the catalyst life. The influences of the above-mentioned metal oxides on catalytic activity, heat resistances, antitoxicity and the surface area are shown in Figs. 3.43–3.46.[77]

The promoters are commonly divided into two types of structural and electronic promoter according to their main roles. There is a relationship between the two kinds of promoters and under an identical preparing condition, there would have an optimum combination (proportion) between them, which is decided mainly by a feat such as "cooking." In the investigation of A110-2 catalyst, it was obtained with

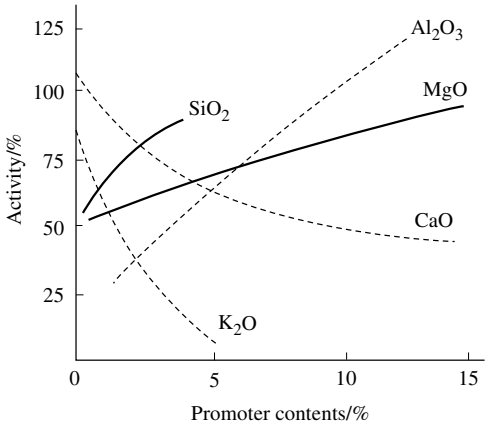


Fig. 3.43 Influence of promoter contents on activity of catalyst

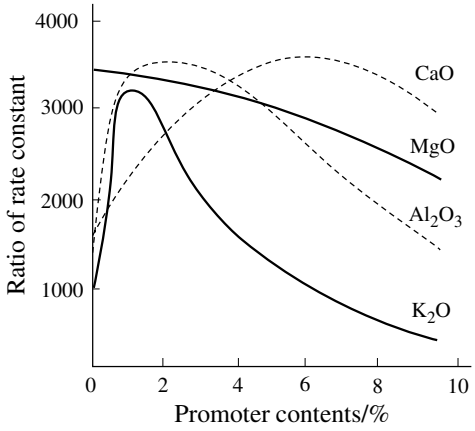


Fig. 3.44 Influence of promoter contents on the activity of catalyst after overheating

(Expressed by the ratio of rate constant before and after overheating)

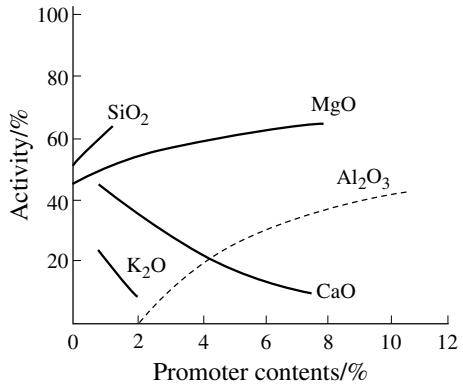


Fig. 3.45 Influence of promoter contents on activity of catalysts after poisoning

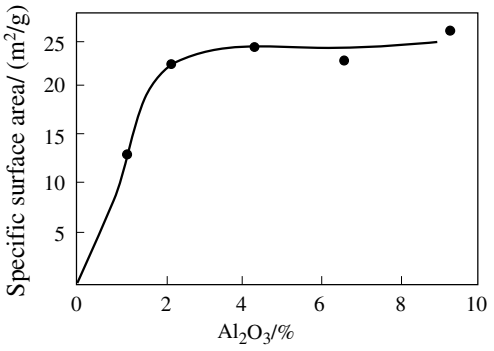


Fig. 3.46 Relation of the surface area with the contents of Al_2O_3 in Fe-Al_2O_3 catalyst

an ideal proportion of tripromoted (Al_2O_3, K_2O and CaO) fused iron catalyst by experiments and formulating of recipe according to orthogonal design in statistics. It has been proved by wide application in industry for more than 30 years that A110-2 type catalyst has not only high activity at low temperatures, easy reduction ability, but also a high heat-resisting and antitoxic ability. Thus, the selection and the optimization of the promoter is one of the crucial aspect of the catalyst investigations, as well as the core secret of the commercial catalysts.

3.3.1 *Design of promoter*

During the early stages in the development of ammonia synthesis catalysts, German chemists investigated over 20,000 catalyst formula proportions and spent amazing efforts into it. Over the century, the compositions, properties, reaction mechanism and kinetics of the catalysts have been extensively studied in the world and we have accumulated large number of data and information. Now, it is possible to design the ammonia synthesis catalysts on those bases.

Presently, catalysis science is developing towards the aspect of "molecular levels," while at the same time, many research workers are trying to design new type

of catalysts in a molecular level based on the present theories and references. The objective is to achieve the catalysts as early as possible, as they are needed urgently in areas such as environmental protection, resource utilization, energy exploitation and other new catalytic reactions. However, the dream of "molecular level" design of catalyst is not yet realized, because there is not an ideal catalytic theory until now. The design of catalyst at present is *via* the reasonable uses of available data and selecting an appropriate catalyst for a given reaction.

In 1968, catalytic scientist D. A. Dowden in England suggested the concept of "catalyst design" in the world, where the procedure included: Chemical stoichiometric analysis, thermodynamic analysis, hypothetic molecular mechanism, hypothetic surface mechanism, discerns of reaction route, definition of the properties requiring the catalyst, seeking the suitable catalytic materials and hypothetic catalysts and so on. There are, two shortcomings in this kind of method: The first is the selection of surface reaction mechanism; and the second is the proposing of the chemical reaction equations and the calculation of the thermodynamics which are required for the analysis of chemical stoichiometry and thermodynamics. Since 1968, many scholars have reported the catalyst designs. These various designing programs, from the view of the designing thinking, can be divided into several small issues, so that the problems will be resolved one by one and a majority of the issues are similar or closer, even though they are advanced in the different ways.

The molecular designing processes of catalysts are illustrated in Fig. 3.47.[78,79] The close combination between the commercial demands for the new products, processes, recent process and concepts of technical materials provided the new knowledge for the catalyst design.

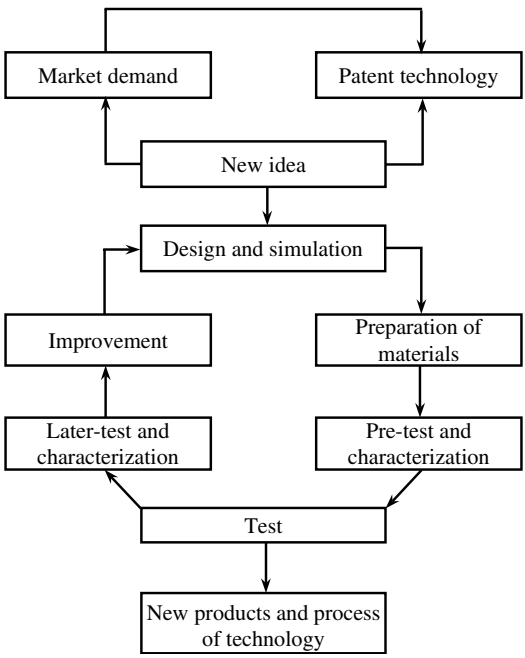


Fig. 3.47 Molecular design for catalyst

Catalyst molecular design in theory and application rely mainly on the following developments: Theoretical chemistry and simulations, analytical instruments, surface chemistry and physics, organometallic chemistry, molecular sieve sciences and reaction engineering.

In order to design a new catalyst, the molecular design is carried out mainly with the aid of the method and technology in following fields: Preparative chemistry, surface sciences, structural sciences, coordination chemistry, organometallic chemistry and quantum chemistry etc. The catalyst molecular design has special characteristics, but the design has not yet been completed owing to following reasons:

(1) **Weak progress in theories.** The molecular design requires a ripe guidance in theory, while the most of the concerning theories about it presently are based on experiences. The modern catalytic theories cannot handle the tasks in the molecular design until an occurrence of a great breakthrough. There is a need to develop more research in this area, in order to improve the success and reliability of the molecular design.

(2) **Complexity of the catalytic process itself.** The catalytic processes are very complicated. One of the factors that influences catalyst properties includesnonlinearity of surface catalytic reactions which is rarely taken into considerations. The catalyst surface has a feature of fractional-dimension structures where the distributions of the active center on surface show multi-fractional-dimension characteristics. At the same time, there is a non-equilibrium phase change and space-time ordered structures such as the chemical oscillation and chaos during a certain process.

A summarization and discussion about the scientific designing method and its theoretical foundation for some catalysts were suggested by Trimm in the book of "design of an industrial catalyst."[80] While on the other hand, those methods are still under development.

Design of a catalyst includes both of the main component (active phase) and the minor ones. The minor ones mean the promoters, additives and supports etc. in catalysts.

The active components for ammonia synthesis catalyst are presently iron and ruthenium in industry. Precursors of iron catalyst include iron oxides which are limited to magnetite of Fe_3O_4 for a long time. In fact, oxides of iron include Fe_2O_3, FeO, Fe_3O_4 and their mixtures. As mentioned above, the sequences of the activity for ammonia synthesis reaction on reduced catalysts derived from following the precursor iron oxides are $Fe_{1-x}O > Fe_3O_4 > (Fe_2O_3) >$ mixtures ($Fe_2O_3 + Fe_3O_4$ or $Fe_3O_4 +$ FeO). These facts provide the foundation for the design of main component or precursors of iron catalysts.

The design of fused iron catalysts are mainly for those promoters or the minor components. In fact, investigations of fused iron catalyst over a century were focused almost on the design of the promoters. The reason from this is that the main components (iron) has been determined while some of their properties may not be ideal on some aspects (e.g., the rapid deactivation).

There are two methods to be adopted for the designs of promoters. The first is the application of present scientific knowledge to resolve the lying crux to the question. This method is frequently more effective and useful, though it is the only practical method. The design of promoters in iron catalyst is generally carried out by this method. There are at least following several "scientific general knowledge" must be taken into account on the design of promoters by this method:

(i) **The chemical valances and ionic radius of metal ions in promoters.** The metal ions of promoters should be able to enter into or replace the lattice of precursor iron oxides to form the substituted or replaced type solid solution, which will settle out at the outer sites of α-Fe lattice to compose a central layer on the boundary among the iron crystallites contacting each other. The central layer will be taken as barriers (or called as skeleton) to inhibit as well as delay the recrystallization and aging.

(ii) **Melting point of promoter.** Its Hutting temperature ($\approx 1/3$ of melting point) should be far higher than the operation temperature of catalytic reactions.

(iii) **Electronegativity.** Electronegativity of ions should be advantageous to offer electrons for iron, so that it will be able to lower the effusion work of the surface electrons.

(iv) **Influencing the distribution and surface enrichments.** The mobility of ions, surface tension, sublimation heats etc. will influence the distribution and surface enrichments of promoters and relate to the catalytic activity, mechanical intensity and the stability.

(v) **Acidity and basicity.** For oxide catalysts, taken as the common regularity, the alkali stabilizes the high-valent oxides, while the acid does the low ones. Alkali is beneficial to offer electrons for iron or to transfer electrons, as well as to the dissociative adsorption of N_2 or desorption of NH_3.

The second approach is based on the intensive studies of the reaction mechanism, which with the ultimate modifications for the catalyst will be done after the clear understanding. More considerations are needed for this kind of approach, so the results could be scientific and effective. However, the application is in a given range, where the occasion is greatly influential and is worthy to deliberate and results in huge benefit once being modified. Therefore, this kind of research approache is usually used only in universal catalysts where considerable improvements are possible. Few reports about similar approaches can be found in the studies of fused iron catalysts.

Thus far, essentially all heterogeneous catalysts of industrial importance have been developed by trial-and-error experimentation. The classic example of this approach is the discovery of the iron-based ammonia synthesis catalyst by Mittasch *et al.*, who tested more than 2,500 different catalysts in 6,500 times of experiments. Parallel testing methods, which can speed up screening of catalyst obviously, have recently been introduced, but a better scientific basis could make catalyst development substantially more efficient. Nørskov *et al.*[81] suggested a kind of catalyst design by interpolation in the periodic table. This kind of catalyst designing strategy is obtained by the simple physical principles, and use the ammonia synthesis reaction to illustrate the approach, but the general principles should be broadly applicable.

Along with the development and deepening of the theoretical knowledge and regularities of catalytic science and the accumulation of the large number of data and experiences, the experts provide a possibility for the design of catalyst at "molecular level." Particularly along with the developments of computer techniques, many expert systems to assist the catalyst design are developed one after another. Banares-Alcantara *et al.*[82,83] developed the classical expert system with

CO hydrogenations as example, namely the Design Expert for Catalysts Development (DECADE). Koerting *et al.*[84] developed the Expert System for Catalyst Design (ESYCAD) based on the works of CO hydrogenation and paraffin dehydrogenation, who, at the same time, accomplished the selection and designs of the catalysts and the optimizations of the operating parameters for catalysts. Speck *et al.*[85] gave a discussion of the selection and design for both the single and multicomponent catalysts, which was carried out by the analysis of the selections of reaction parameters, design of the catalyst preparing method and the optimizations of catalysts, finally developed the Expert System for the Selection and Optimization of Catalysts (ESSOC). Zunnan Huang *et al.*[86−88] reported the Expert System of Molecular Design of Catalyst (ESMDC) and used it to design and optimize the catalysts for methane oxidative coupling. However, for the reason that the expert design requires an enormous database for catalytic knowledge to be established, the information such as dynamics for catalytic reactions, preparing methods of catalyst, thermodynamics and the mechanisms of catalytic reactions has to be accumulated. Therefore, the operation of that is extremely difficult, consuming both time and powers. Furthermore, the applications of the expert system are not so universal.

Jie Sun *et al.*[89] developed the software (developed in Visual Basic 6.0) for the catalyst design of heterogeneous catalysis (HGMDS1.0). This software is based on the theoretical method of UBI-QEP and adopts the modularized design, the functions of which includes: A database which can be utilized to inquirements, additions and modifications of the bond energy of gaseous dissociative bond and the adsorption heats of the small groups on the transitional metal surfaces; the second one is the calculating modular of the chemisorption heats, which can be used to calculations of various adsorption heats with different types by allocating the data from the database; the third is the calculating modular of the activation energy of the elementary reactions, which can be used to carry out the energetic calculations of the elementary reactions, so as to analyze at what extent the reaction exceeds easily and the reaction courses. This system can also be used to discuss the optimizations of the catalysts and mechanisms for heterogeneous catalysis.

Artificial Neural Network (ANN) is another assistant method for the catalyst design, which is used more often presently. Compared with the expert system, ANN is under the case of a rather obscure catalytic mechanism based on the experimental data, and is able to establish the reflecting relationship between the catalyst compositions, preparing conditions and catalytic properties (including selectivity and conversion) and then obtain such parameters as the proportions through with the optimizations. This kind of method is simple and universally applicable, and is especially suitable for the design of the multi-component catalysts.

Currently, there are examples realizing successful design and optimizations of catalysts by the use the Back Propagation Networks (BPN). Kito *et al.*[90,91] obtained a considerable result for the fittings and optimizations of the surface acidity of the mixed oxide catalysts by the help of the BP network. Hou *et al.*[92] found a fine catalyst of VSbWSn (P, K, Cr, Mo)/SiO_2-Al_2O_3, which improved the yield of acrylonitrile up to 55% *via* the design and optimization of the catalysts for propane ammoxidation using the BPN. Liquan Han[93] used the combination of BPN with Genetic Algorithm (GA) to optimize the proportion of the catalyst for aliphatic alcohol and resulted in the better effect. Furthermore, the BPN was used to assist the design and optimization of the catalysts for methane oxidative coupling by

Huang *et al.*,[94,95] and Yan Liu *et al.*[96] also used the BPN to design the CO_2 hydrogenation catalysts and Corma *et al.*[97] utilized the combination of BPN and Genetic Algorithm to optimize the paraffin epoxidation catalysts. All of them achieved satisfied results. On the other hand, there are still such shortcomings for BPN such as [98,99] slower convergences, tendency to go into localized optimizations, hardly adjusting of extensive capability, which influence the design and optimization of catalysts.

The main role of the ANN in the catalyst design and optimization is to establish an accurate pattern of relationship between the catalytic activity and the influencing factors for it, so as to forecast the experimental results. Based on the pattern of the establishments by ANN, the design and optimization of catalysts have to seek the optimization method, e.g., Sequential Search, Genetic Algorithm and Ant Colony Algorithms[100] etc.

3.3.2 *Structural promoters*

High melting point oxides such as Al_2O_3, Cr_2O_3, MgO, ZrO_2, TiO_2 and SiO_2 are commonly structural promoters. These promoters can increase the heat-resisting and antitoxic abilities, and also play a role in increasing surface area, stabilizing the structure, decreasing the specific activity per unit total surface area and reduction rates. This kind of effect relates closely with that of magnetite and wüstite, which is able to absorb the other ions with closer ionic radius into the lattices of them, or to form solid solutions with other spinels or compounds, so as to the well-dispersion of promoters.

Al_2O_3 is the most typical structural promoter. If alumina is omitted, dramatic sintering of iron occurs, making the catalyst completely useless. This key role of alumina comes from the cationic substitution of Fe^{3+} with Al^{3+} ions, as roughly shown in Fig. 3.48. Al_2O_3 is able to be dispersed uniformly into the catalyst because it can compose two types of solid solution with magnetite, i.e., the substituted sosoloid such as the spinel type of $Fe_{3-x}Al_xO_4$ and the compound type sosoloid such as $FeAl_2O_4$, and also form solid solution which can further form a complex sosoloid with the host magnetite. This is because the two types of solid solutions belong to the spinel lattice which show the same crystal type as the host magnetite Fe_3O_4. According to the principle of isomorphous miscible, these two type solid solutions are able to make a complex solid solution with Fe_3O_4.[101] For example, both $FeO \cdot Al_2O_3$ and Fe_3O_4 react with each other to form a new complex solid solution $(FeO \cdot Al_2O_3) \cdot (Fe_3O_4)$, during which Al_2O_3 is well-dispersed into the catalyst

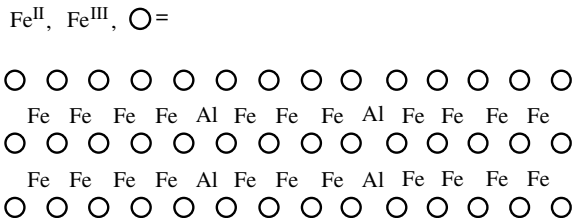


Fig. 3.48 Simplified scheme showing Fe^{3+}-Al^{3+} cationic substitution in magnetite[51]

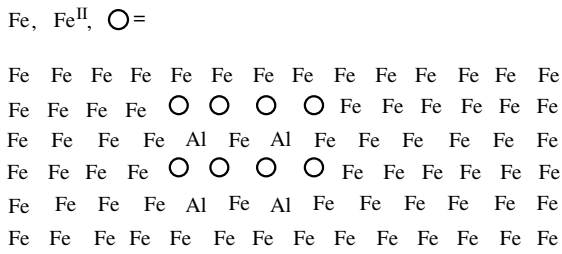

Fe, Fe^{II}, O=
Fe Fe Fe Fe Fe Fe Fe Fe Fe Fe Fe Fe Fe Fe
Fe Fe Fe Fe O O O O Fe Fe Fe Fe Fe Fe
Fe Fe Fe Fe Al Fe Al Fe Fe Fe Fe Fe Fe
Fe Fe Fe Fe O O O O Fe Fe Fe Fe Fe Fe
Fe Fe Fe Fe Al Fe Al Fe Fe Fe Fe Fe Fe
Fe Fe Fe Fe Fe Fe Fe Fe Fe Fe Fe Fe Fe

Fig. 3.49 Formation of Fe aluminate nanoensembles embedded in metallic iron upon reduction of ammonia synthesis catalyst[51]

precursor (Fe_3O_4). For this reason, about 3% of Al_2O_3 can solve into Fe_3O_4. In recent years, the solid solution between Fe_3O_4 and $FeAl_2O_4$ was again investigated, and it was found that there is a limit of interfusion when the temperature is below 850°C, for e.g., no more than 7.5% of $FeAl_2O_4$ can be bound into the mixed crystal of magnetite at 500°C. Therefore, when more Al_2O_3 is added, two phases will occur, among which only the part resolved in magnetite is important for the catalyst properties.

When oxygen anions are withdrawn by hydrogen during catalyst reduction, except for those linked to aluminum, several iron aluminate nanoregions, roughly shown in Fig. 3.49, remain embedded in the structure of α-iron, causing a stiffening of the latter with consequent decrease of the sintering rate. The solved alumina or magnesia will be deposited out, and will be accumulated between the iron grains, thereby expanding the stabilizers. These stabilizers can exist as the types of components between the grain boundaries of magnetite. There has been the experimental evidence of electron microscopic detection for this kind of pattern.[102] The ultimate forms of the solved alumina depend on the reduction conditions.[103–106] They exist obviously as the form of $FeAl_2O_4$. Under the violent reduction conditions (reduced in hydrogen for 23 h at 700 K, 101.325 kPa),[106] all of $FeAl_2O_4$ transform to iron and alumina, while under the conditions that are rather mild (e.g., 670 K, in nitrogen/hydrogen synthesis gas),[103–105] there still remains part of $FeAl_2O_4$ (not the whole). These kinds of phenomena may be seen from the adsorption dada[107] and the broadening of the XRD peaks. Those alumina derived from the reduction of $FeAl_2O_4$ exist in α-Fe particles as the small parts of foreign impurities. In these studies [3% of alumina (mass percent)], in α-Fe particles sized with approx. 25 nm the sizes of the foreign impurities are about 3 nm, existence of which should easily be detected by the help of transmission electron microscopy. It can be predicted that the strain resulting from the foreign impurities of alumina will result in the sizes of α-Fe crystal shifting toward small ones. In fact, because of the reduction temperature lower than 500°C, nano regions of iron aluminates (with estimated radius of 2 nm–3 nm) have no sufficient energy to recompose them to form the larger crystal grains, which can only be composed during the changing procedure of α- $\rightarrow$ γ-iron at the extremely high temperature (950°C. Al_2O_3 in the rich-Al_2O_3 phase during reduction will be deposited out at outside of α-Fe crystal lattice to form central layers. They exist on the interface between iron crystallites contacted each other, and act as barriers (called also as skeleton) to inhibit the further closing of α-Fe crystallites to merge and growth, because the smaller α-Fe crystallites, the higher

the dispersion degrees are, and the larger the outer surface area of iron provided by per unit mass, and also the higher the surface free energies are. During the following long period's predictions and utilizations, these oxides inhibit as well as prolong the recrystallization and aging of catalysts.

If the usage of Al_2O_3 is in order to improve the thermo-stability, and their contents are >1% (molar fractions), then in practice they may be solved incompletely,[108] where a part would still exist as a form of separate phases. There is an evidence of electron probe studies[109] for their existence. Thereafter, the maximum content is below 4%, with appropriate value to be about 2% (see Fig. 3.46). To further increase thermal stability, it may be possible to introduce such oxides as MgO, ZrO_2 and SiO_2.

Al_2O_3 is able to increase the surface area of catalysts because it can be well-dispersed into the catalyst during the catalyst preparation. Al_2O_3 in the reduced catalysts shows molecular state, being dispersed mainly in the surface layer of α-Fe crystallites. Both the average radius of micropore and average size of iron crystallites of catalyst are all going to be decreased. Hence, the total surface areas increase with increasing the Al_2O_3 contents after reduction.

Arabczyk *et al.*[110] proposed a double layer structure model of the surface of a fused iron catalyst for ammonia synthesis. It is assumed that the iron surface is covered with a double layer due to wetting by promoter oxides. The first sublayer in the direct vicinity of the iron atoms is filled with oxygen atoms and the free adsorption sites are present in this sublayer. The second sublayer located over the first one is filled with promoter atoms. The number of oxygen atoms and free adsorption sites are determined by the nature of the promoter. Every atom of alkali metal needs one oxygen atom to stablize on the iron surface under ammonia synthesis conditions; and one atom of alkali earth element needs two oxygen atoms; one atom of aluminum needs three. The number of the free adsorption sites is directly related to the number of oxygen atoms on the surface. When there are more oxygen atoms on the iron surface, there would be lesser number of free adsorption sites for dinitrogen adsorption. The surface area of the iron catalyst is also dependent on the number of oxygen atoms on the surface. Therefore, elements such as Ca and Al, which need a high concentration of oxygen on the surface, lead to the formation of the catalyst exhibiting the highest surface area, in which the maximum specific surface area can approach $20\,m^2 \cdot g^{-1}$.[38] Between the surface, the iron bulk, and the spacers located between the iron crystallites, the thermodynamic equilibrium is maintained. From this, we can attribute reasons as to why those promoters like potassium and the other alkali earth metals affect the catalyst surface area negatively. Because alkali metals need less amount of oxygen in order to be stabilized on the iron surfaces, the small amount of Fe–O bonds and the higher energies of the rest of the surface result in the decrease of surface area. These conclusions are in good agreement with many experimental results.[111]

Other structural promoters such as MgO and TiO_2 show certain extents of dissolvability in magnetite, which are the same as for CaO, Li_2O and Na_2O. Mg^{2+} is also able to replace Fe^{2+} and enter into the lattices of Fe_3O_4 or FeO, while Ca^{2+} is not due to its larger structure. However, during preparation of catalysts, it commonly uses $CaCO_3$ as raw material. It is decomposed to CaO, which are well-dispersed into the melt fusion under high temperatures (1,600°C–3,000°C), and after cooling it shows highly dispersed states.

Table 3.21 Room temperature mössbauer parameters of $Fe_{1-x}O$ and Fe_3O_4 based catalysts

Catalyst	Phase	IS/ ($mm \cdot s^{-1}$)	QS/ ($mm \cdot s^{-1}$)	MF/ ($kA \cdot m^{-1}$)	Iron content/wt%
$Fe_{1-x}O$	$Fe_{1-x}O$	0.908	0.950	—	53.80
	(containing Ca^{2+})	0.953	0.411	—	43.43
	$FeAl_2O_4$	0.919	—	—	2.77
Fe_3O_4	Fe_3O_4 (A)	0.390	0.111	38,789	26.82
	Fe_3O_4 (B)	0.778	0.060	36,459	43.92
	FeO	1.036	1.020	—	5.68
	—	0.923	0.449	—	2.77
	$KFe_{11}O_{17}$	0.745	0.240	35,189	9.48

SiO_2 and ZrO_2 are usually the impurity in magnetite are not added deliberately. They do not seem dissolve in magnetite, and when they act as a stabilizer, they can be found in the barrier layers between grain boundaries of magnetite. Nevertheless, silica oxides have an inhibiting effect in the dissolution of basic oxides into magnetite (due to form compounds), and the existence of which would make the alkali or alkali earth oxides as chemical promoters even more difficult to be well distributed.[112] The catalysts containing higher contents of SiO_2 and ZrO_2 possess stronger resisting ability for water vapor, while their low temperature activities are rather poor.

The same characteristic applies to the traditional Fe_3O_4 based fused iron catalysts, Al_2O_3, K_2O, CaO etc. are still the main promoters for $Fe_{1-x}O$ based catalysts, while their roles differ slightly. The variation in the ionic properties and crystal structures of $Fe_{1-x}O$ and Fe_3O_4 result in the difference of the combining patterns of promoters with them.[113]

For Fe_3O_4-based iron catalysts, Al^{3+} acts as above-mentioned. Table 3.21 shows the room temperature Mössbauer parameters listed for $Fe_{1-x}O$ and Fe_3O_4 based catalysts. It is clearly seen from the table that the B sites of Fe_3O_4 lattice in magnetite catalysts contain the effect of Al^{3+}, indicating Al^{3+} entered into lattice of Fe_3O_4. Consequently, Al_2O_3 is the main structural promoter for the traditional fused iron catalysts.

One of the differences between $Fe_{1-x}O$-based and Fe_3O_4-based catalysts is that in $Fe_{1-x}O$-based catalyst, the solid solution containing alumina such as $FeAl_2O_4$ is not able to form a new complex solid solution with the host $Fe_{1-x}O$. In $Fe_{1-x}O$-based catalysts, although there are small amounts of Fe^{3+}, and the cation substitution of Fe^{3+} with Al^{3+} ions is possible, the amounts of the cation substitution are far less than Fe_3O_4-based catalysts.[114] Even though FeO and Al_2O_3 can form the compound type solid solution, such as $FeAl_2O_4$ ($FeO \cdot Al_2O_3$) (see in Table 3.21), the former belongs to NaCl type lattice, while the latter is spinel lattice. These two types of crystals are immiscible with each other due to the differences in their crystal structure, and so cannot make a complex solid solution with the host $Fe_{1-x}O$. For this reason, the distribution of Al_2O_3 in $Fe_{1-x}O$ based catalysts is not so uniform compared to that in Fe_3O_4 based ones. Therefore, Al_2O_3 is probably not the main structural promoter for $Fe_{1-x}O$ based catalysts.

A clear difference between wustite and magnetite precursors is the higher ability of dissolving Ca^{2+} ions for wustite.[115] After reduction, well dispersed CaO should be present on the surface of the wustite-based catalyst and could contribute, due to

its basic nature, to activate dinitrogen dissociation on the geometrically suitable Fe sites. Our experimental data are in full agreement with this tentative explanation. In this respect it should be stressed that Fe^{2+} substitution with Ca^{2+} is favored by the presence of Fe^{3+} ions in the wüstite lattice. In fact, it has been found by authors that there is a flat maximum of the catalytic activity for a Fe^{2+}/Fe^{3+} ratio of about seven. This maximum could be due to the opposite effect of increasing magnetite content and increasing $Fe^{2+} - Ca^{2+}$ substitution when the Fe^{2+}/Fe^{3+} ratio decreases. CaO is able to make substituted solid solution with FeO, so it exists in both lattices of two precursors of $Fe_{1-x}O$ and Fe_3O_4. While its solubility in the lattice of magnetite is restricted due to the cross-linked structure of $CaFe_2O_4$, its contents in $Fe_{1-x}O$ based catalysts are obviously larger than that in the lattice of Fe_3O_4. While in the magnetite-based catalyst the resistance to sintering is mainly due to the presence of very well dispersed Al oxide and/or Fe aluminate, Al^{3+} ions are likely to be much less dispersed in wüstite, so that an additional similar effect of CaO in wüstite seems to be reasonable. As previously discussed, a further key role of Ca^{2+} ions is to give stability to the wüstite phase at low temperatures as well as to inhibit, in given extent, the disproportionation of $Fe_{1-x}O$.[55,116] Therefore, CaO is the main structural promoter for $Fe_{1-x}O$ based catalysts.[117]

The second difference between wüstite and magnetite precursors is the roles of MgO. In $Fe_{1-x}O$ based catalysts, it is not only the cationic substitution of Fe^{2+} with Mg^{2+} ions, but also the fact that MgO can form a complete solid solution with FeO in the ranges of 0%–100%, and be well-dispersed into the catalyst precursor ($Fe_{1-x}O$). This, to a certain extent, compensates the roles of Al_2O_3.

3.3.3 *Electronic promoters*

The roles of alkali, alkali earth and rare earth metal oxides seem different from the structural promoters. These oxides are able to increase the specific activity per unit surface area, while decrease the heat-resisting and anti-toxic ability. Thus, they are called as electronic promoters. Because the diameter of K^+ ions is quite large, it is not possibly for K to enter into the lattice of magnetite. After reduction, K_2O diffuses to the surface of crystallite. The surface potassium is able to accumulate with various forms during reduction and operations, to accelerate the recrystallization effect, but due to the electron, negative alkali metals decrease the effusion work of iron atoms, and accelerate the adsorption of dinitrogen or desorption of ammonia and finally are able to increase the specific activity per unit surface area.

K_2O is the most important electronic promoter. It is, although in small amounts (usually added approximately by 1%), able to be enriched on the surface of the α-Fe crystallites during reduction. It was indicated by the studies of the chemisorption of CO_2, that the major parts of the surface of α-Fe crystallites were covered by K_2O or KOH. Small amounts of K_2O are able to increase the intrinsic activity of catalyst up to 10 times after reduction.

It is seen from Table 3.22 that potassium as a promoter is able to decrease the effusion works of electron.[118] When N_2 is adsorbed on the iron surface, where K_2O promoters are present, there will be formation of the dipoles. The electrons of iron will then incline to N_2 molecules, and weaken the bonds between nitrogen atoms, making ammonia molecules to be more easily produced. The surface of iron coverd by alkali impels easier desorption of the formed NH_3.

Table 3.22 Promoted iron catalyst and effusion work of electrons[a]

No.	Promoters (mass fraction)%[b] Al_2O_3	K_2O	CaO	SiO_2	Space velocity/ h^{-1}	Outlet NH_3/%	Total surface area/ $m^2 \cdot g^{-1}$	Surface area without promoter/ $(m^2 \cdot g^{-1})$	Rate constant $K_s = k_T$ Total surface area	Rate constant $K_s = k_T$ Iron surface area	Change of effusion work $\Delta\varphi$/eV
1	0.2[c]	—	—	—	14,500	0.25	0.5	0.33	2.8×10^{-1}	4.3×10^{-1}	−0.18
2	10.2	—	—	—	14,800	3.6	17.0	3.9	1.8	7.95	0
3	0.3[c]	2.0	—	—	15,000	3.5	0.7	0.35	4.3×10	8.6×10	−0.79
4	4.8	2.3	0.3	0.15	30,000	11.0	11.0	2.2	5.5×10	2.7×10^2	−1.18
5	3.2	0.9	4.0	0.9	29,600	6.4	13.0	1.04	1.1×10^2	1.3×10^3	−1.31
6	3.1	0.7	2.0	—	30,000	17.8	12.0	1.44	1.3×10^2	1.1×10^3	−1.80

[a]Sheet metal iron without promoter, the surface area of which is 1 $m^2 \cdot g^{-1}$, is without activity at 550°C and 30 MPa, which is used as sample in order to measure the highest electron effusion work.
[b]Content of MgO, MnO_2, P_2O_5, SiO_2, Cr_2O_3 and the other oxides is 0.5%.
[c]Present as impurities in samples.

It has been widely investigated on the role of potassium.[119] The most important issue is the chemical states of potassium on iron surface. It was reported that the existence of metallic potassium on catalyst surface is impossible under the reaction conditions of ammonia synthesis.[120] AES studies found that the desorption energy of potassium from iron surface is 480 K.[121] According to the studies of TPD, even if there are oxygen atoms present at 900 K (oxygen atoms are able to increase the thermostability of potassium)[121,122] the potassium is present on the different iron crystal faces [Fe(111), Fe(110), Fe(100)[123,124] and Fe (multiple)]. Based on the conclusion above-mentioned, one of the indefinite structures (K + O) is suggested to act as the active surface of iron catalysts.[122,125] The catalyst surfaces are completely and uniformly covered by the potassium–oxygen layer. Postulating the ratio of K/O as 1:1, with the potassium atoms being present on the outer layer, and iron surfaces without other adsorption sites being occupied, then 50%–57% of adsorption sites on iron surface will be occupied by oxygen atoms. The free adsorption sites would be present to be exposed to vacuum due to the oxygen atoms located underside of the potassium atoms. Nitrogen molecule should be able to reach the free adsorption sites throughout between the potassium atoms.

The double-layer model by Arabczyk *et al.*[110] suggested that 0.48% (mass fraction) of K_2O is sufficient to cover iron surface by monolayer potassium. Industrial catalysts commonly contain 0.5%–1% (mass fraction) of K_2O, with remanent potassium forming a tousy compound with alumina, silica or calcium in catalysts. Because at least 10% of potassium in the compounds is unchangeable, the content of 0.55% (mass fraction) is sufficient. This conclusion is obtained from the experimental results by Kowalczyk.[126] It was found in their experiment that in the double-promoted catalysts, those with content of potassium in the range of 0.5%–0.7% (mass fraction) resulted in highest activity.

Somorjai *et al.*[76,127] investigated the effect of potassium on the ammonia synthesis reaction over iron single crystal face. The potassium entered into the iron crystal face (111) containing C_7 site and therefore the decomposition probability is increased by eight times. On the iron (100) face, adsorption probability of N_2 increased by 280 times, while on the iron (110) face, that was turned to be increased by further multiples.[119,122,123] The iron faces of both (100) and (110) are without C_7 sites, which indicate that potassium has built its own active sites on iron surfaces for the dissociation of N_2. These active sites seem independent of the structure of metal surfaces and of C_7 sites (at least on the faces of iron (100) and (110)), because the C_7 sites are considered as the reason for the dissociation of N_2 on the clean surfaces.

However, there is no connection between the increase of catalytic activity and dissociation probabilities of N_2 on various crystal faces due to the presence of potassium. As shown in Fig. 3.50, after the potassium addition, reaction rates on both faces of iron (111) and (100) were increased by eight times, while the dissociation probabilities of N_2 on them were enhanced by two times and 280 times, respectively.[127] Therefore, they considered that the main role of potassium was to influence the binding form of NH_3. TPD studies indicated that when the coadsorption of NH_3 and potassium occurred, the adsorption heat of ammonia decreases by 2.4 kcal (1 kcal = 4.184 kJ, same as follows). Figure 3.51 indicates the TPD peaks and their displacement on iron (111) face when the co-adsorption of NH_3

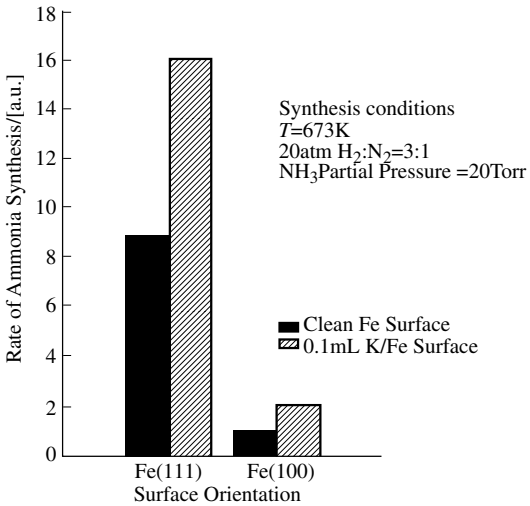


Fig. 3.50 The effect of potassium on the rate of ammonia synthesis on an iron single crystal face[127]

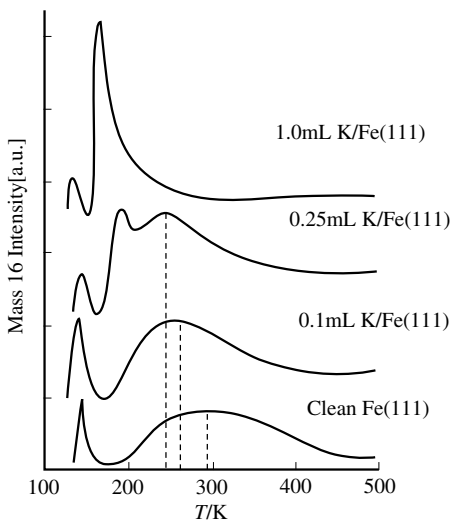


Fig. 3.51 Ammonia temperature-programmed desorption from the iron (111) face with and without co-adsorbed potassium[127]

and potassium occurs.[127] The main influences of the displacement of peaks caused by the coadsorption between NH_3 and potassium (because all of these two are electron-donating molecules) are aroused during periods when the reaction inclined higher equilibrium partial pressure of NH_3. Figure 3.51 shows the case of effects of potassium on the partial pressure of NH_3 in ammonia synthesis reaction. It can be found from Fig. 3.52 that in spite of potassium being present or not, all the scopes are negative, indicating that the existence of potassium enables the reaction shift toward the easier formation of NH_3 under the higher partial pressures of NH_3. The

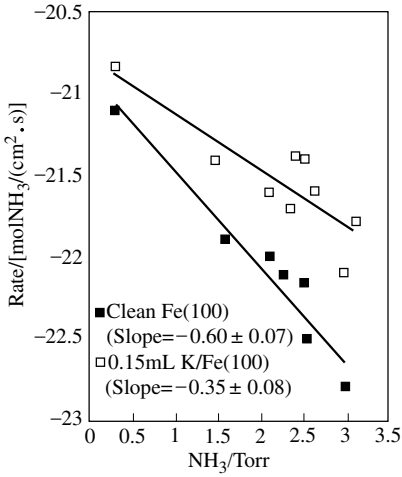


Fig. 3.52 The effect of potassium on the ammonia pressure dependence of ammonia synthesis[127]

coadsorption of potassium and NH_3 results in the equilibrium of the adsorption state of NH_3 shifting toward gaseous phases,[127] namely, the lower the adsorption heats of NH_3, the lower is the concentration of NH_3 on surface and then it makes the reaction moves toward gaseous phase. The active sites may be occupied by adsorbed NH_3, while the decrease of the adsorption heat makes the surface more active and produces more NH_3. The activation energy of the ammonia synthesis reaction is not changed when there is potassium in catalyst,[127] as shown in Fig. 3.53. With the existence of potassium, the increase of the reaction rate is marked, indicating that the rate determining steps are not affected by the addition of potassium on iron surfaces. Without oxygen bond with potassium on iron surfaces, the influence of potassium can be neglected. The reason for oxygen to stabilize potassium on iron surface lies in the capability of the oxygen to decrease the desorption rates of potassium. The existence of oxygen does not yet change the influence of potassium for the dissociation probability of N_2. In addition, oxygen also restructures iron surfaces.[128,129] It is probably because parts of potassium and oxygen bond together to form the new active sites. In order to build the new active sites for the dissociation of N_2, oxygen bonded with potassium assists to restructure the iron surface. Although these active sites differ from those C_7 sites on the iron crystal face of (111) and (211), it plays an extremely important role in the formation of NH_3 (especially under high partial pressure of NH_3). Figure 3.54 shows the restructuring and higher activity when iron crystal face of (110) is heated with oxygen for. Thus, oxygen connected with potassium is possible to enable the iron single crystal face to be restructured and to build a new active site. This is in consistent with the point of view by Arabczyk.[110]

The addition of potassium enables the catalytic activity to increase by 10 times, while the surface area of catalyst to decrease by $11\,m^2 \cdot g^{-1}$.[126] This is a matter of the enthalpy of the bond of promoter-oxygen because potassium is able to replace alumina atoms on iron surfaces (Fig. 3.55). The higher the enthalpy, the more advantageous the formation is. Therefore, potassium can be removed with alumina

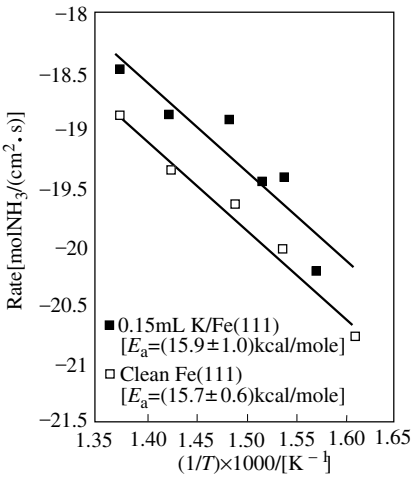


Fig. 3.53 The effect of potassium on the activation energy of ammonia synthesis between 623 and 723 K[127]

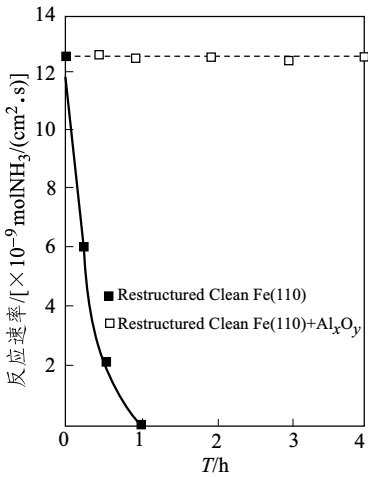


Fig. 3.54 The deactivation of the oxygen restructureed (110) iron surface along with the restructured (110) iron surface with alumina added[128]

and its corresponding oxygen atoms together from the surface and decrease the amounts of surface oxygen atoms and Fe–O bonds. It also increases the remanent surface energy, thereby resulting in the decrease of surface areas. While on the other hand, it enables iron surfaces with more of free adsorption sites to be utilized to the adsorption of dinitrogen, so increases the catalytic activity.

Rubidium and Cesium can obviously change the electron properties of iron surfaces. The surface area of the catalyst promoted with rubidium and cesium are less than that of those with potassium by 20%. The influences of potassium, rubidium and cesium on activities have controversy in references. Some reported that the orders of catalytic activity were potassium < rubidium < cesium[130]; while the

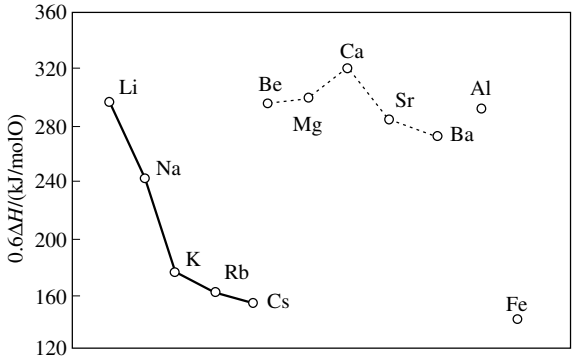


Fig. 3.55 Strength of the bonds in promoter oxides. The total value of the enthalpies of formation of oxides are divided by the number of oxygen bonds in the respective oxide

others considered that the activities of those promoted with rubidium and cesium were less than those with potassium by 20%.[131] In this case, the application of potassium is even more proper, which results in the higher activity.

If the roles of electronic promoters are donating electrons, and the migrations of electric charges, then they are the driving powers to decide the surface activity. Thus, the influences of sodium and barium for catalyst properties should be similar, because the nuclear/mass ratio of them are very closer, all to be 0.9. The influences caused by them on catalyst properties are completely different especially on the activity and surface area. This is because these two elements belong to the two distinct types of promoters. Sodium is regarded as the promoter for affecting the catalytic activity, while barium as a structural promoter. The difference between them is obvious. Sodium is advantageous to form the free adsorption sites, but barium is not. Barium requires more oxygen atoms to be stabilized (every barium atom requires two oxygen atoms), and results in the higher surface area, while decreases simultaneously the amount of the free adsorption sites.

3.3.4 *Enrichment phenomena of promoters partial to surface of catalysts*

Large numbers of researches indicated that the compositions of promoters on the noumenon and surface of the catalyst are different. This phenomenon is commonly called as surface enrichment. Surface enrichment of the promoters is commonly present, which plays specific roles on catalysts.

Heterogeneous catalysis is, in essence, a kind of surface process, while the properties of catalyst surfaces are mainly decided by its chemical compositions. Hence, in catalyst investigations, it is very important to make sense of the compositions of the catalyst surface. Several centuries ago, Gibbs proposed that the surface compositions may be different from the bulk ones and some components can enrich on the surface. However, there has not been the experimental evidence by an effective technique. Along with the rapid development of modern techniques of surface measurements, it has been possible both by quantitive and qualitative measurements in

the ranges of several atomic layers on surfaces, with considerable higher sensitivity. Gibbs consequently obtained the real information of surface compositions.

Surface enrichment is one of the major reasons resulting in the lower activity, poor selectivity or declining of activity of catalysts. Therefore, in the catalyst investigations, the phenomena of enrichment on the surfaces are extremely important and have been widely studied. Many researchers like Overbary,[132] Ponec[133] and Sachtler[134,135] gave the detailed description for the alloy catalysts and did the theoretical discussion. Menon[136] also gave a commendatory for the metal oxides and the supported metal catalysts.

Thermodynamic theories proved that the formation of surfaces need the energies and tend to go with the simultaneous changes of positive free energies. In order to reduce the positive free energies, the components with the lowest surface free energy will incline to migrate towards the surface. As a result, it is different between the composition of surface and that of bulk. It also results in the enrichment of the component with the lowest surface free energy on the surface.

In the multi-component substances, the following cases tend to occur on the surface enrichments.

(1) The components with small surface tension can segregate on surface. The larger surface tension in the systems, the more significant the enrichment effect is, e.g. the enrichment effect of alloy systems are more obvious than that of solution systems.
(2) Those components with small sublimation heats can segregate on surfaces because the surface tensions of metals are connected with its sublimation heats. There are no such connections between the surface tension and the sublimation heats on the surface of oxides.
(3) In the alloy of AB type, when A − B bonds on surfaces are stronger than that in bulk, B will be segregated on the surface of the alloy.
(4) Lattice tensions-stress caused by the mismatching of the atomic sizes will impel the formation of enrichment. For ionic solids, in spite of the large formation heats, they are unfavorable for the enrichment, but the existence of stresses results in the ions to be enriched on the surface. For the semiconductor oxides, the composition of the surface has striking inclination of non-stoichiometry at high temperatures. Besides this, there are some of abnormal oxides which are worthy of noting. For instance, there are abundant Ti^{3+} ions on the surface of TiO_2, which are due to the presence of large amounts of defects. Many Al^{+} and Al^{2+} ions presented on the surface of Al_2O_3 are also due to the same reasons. This kind of oxidative state is only stable on the surface and hence they have particular chemical performances.
(5) The phenomenon of enrichment connects with the temperature. The extent of enrichments is high when the temperature is low and the enrichment declines to zero at high temperatures.

In certain circumstances, surface enrichment is a factor of producing catalytic activity, while in many other cases, it represents loss of catalytic activity. The surface enrichments of one or multi-components in catalysts are produced in the following processes: (i) preparation process of catalysts; (ii) pretreatment, including the sintering, reduction, oxidation and regeneration; (iii) running process in industry.

During preparation of catalysts, as the result of surface segregation or enrichment, the composition on catalyst surface may be different from those in the bulk, and the chemical composition will continue to change during such pretreatments of catalysts as calcinations, reduction and oxidation as well as during the catalytic reactions. By this way, the main component measured on the surface for fresh catalysts which are not contaminated are possibly different from the active species under the reaction conditions. Therefore, the investigations of the working catalyst rather than the fresh ones are more important and even more likely to reveal the reasons that why the activated catalyst has activity as well as deactivation. Hence, an understanding of the change process of the surface composition as a function of time on streams under the practical reaction conditions is the first and foremost step for preparing the catalyst, which are more active and stable and improving the effect of them on an industrial application. The macroenrichments during catalyst preparation will be discussed in Chapter 4.

High temperatures are the necessary conditions for producing surface enrichments during the process of catalyst pretreatments and the reactions. The reason is that the enrichments need certain amounts of energies, in common, for the component to overcome the potential barrier of the activation energy in order to migrate to surface from the inner of solids. It is regarded by experiential regularities that under the Tamman temperature (approximately half of the melting point), the atoms or ions in bulk have sufficient migration abilities to approach the surface from bulk, while the Hutting temperature (approximately 1/3 of the melting point) is enough to make the surface species to be centralized or sintered, even though the operating temperature of the catalytic reactions are lower than the Hutting temperature of the component in solid catalysts. The real temperature of catalyst surface may increase further in the case of exothermic reactions. In several instances, many oxides using as the active species or supports of catalysts are of rather poor thermal conductivity, so then the heat released by the exothermic reaction cannot be removed as rapidly as possible, which result in hot spots on catalyst particles. Though such reactors as the highly efficient heat interchanging reactor or the fluidized bed reactor have been developed industrially, often there is local overheating on catalyst surfaces, which enables the melting of tube with catalyst in reactors or the distortions of high pressure reactors. At the same time, the high temperature makes certain components in catalysts generate the surface enrichments or loss, so that results in the decrease of catalytic activities and selectivities.

Another reason of the surface enrichments or loss is the formation of volatile compounds of a certain component of catalysts with reactants. For example, nickel can react with carbon monoxide in reactants to form the volatile and thermally unstable nickel carbonyl, which escapes gradually from the catalyst surface. The activated carbon supported ruthenium-based catalysts also loses obviously part of itself due to the volatilization of ruthenium oxides or the occurrence of methanation reactions of the activated carbon.

When gases or vapors occur during chemisorptions on the surface of heterogeneous catalysts, it can induce the surface enrichment due to the reason that the adsorption heat of every components of catalyst is different. The components which can form the strong chemical bonds with the adsorbent will be drawn out from the inner atomic layers and be congregated on the surface.

During a considerable long period, the gaseous chemisorption method is the sole one to probe the surface species of solid catalysts. Some of the modern techniques for surface measuring are: Measurements of effusion works, Auger electron spectroscopy (AES), Electron spectroscopy of chemical analysis (ESCA), X-ray photoelectron spectroscopy (XPS), Electron probe microanalysis (EPMA), Ion probe microanalysis (IPM), Ion scattering spectroscopy (ISS), Second ion mass spectroscopy (SIMS), Low energy electron diffraction (LEED), Vibration spectrum and Mössbauer spectroscopy etc. All these techniques provide favorable conditions for the surface research indepth.

However, the most experimental techniques are only used under the conditions of vacuum or super high vacuum, which are far away from the practical conditions in industry. In order to make a connection between the catalytic fundamental researches and an industrial catalytic process, Dwyer suggested one kind of equipment, putting the catalysts in a small room that can be pressurized and vacuamized in super high vacuum systems. Such *in situ* measurements of catalyst surface before as well as after the reactions can be carried out by means of Auger electron spectrum. Although the surface area of catalyst sample usually is only $1\,cm^2$, the reaction rates and product compositions can be completely determined by the help of the high sensitivity chromatographic detector. Baker *et al.* discussed about the application of the controlled atmospheric electron microscopy (CAEM) to investigate the interactions between various gas–solid phases. Besides the qualititive information about the structural details can be obtained where it can measure quantitively the kinetic parameters such as migration rates so as to postulate the reaction mechanisms. It can also be utilized to investigate the aggradation of reactants, gasification of materials, poisoning of metal particles as support and can induce motions of a certain species and so on.

High temperature/high pressure scanning tunneling microscope (STM) has emerged as a major new tool for studying surface structure and perhaps extending its use to study surfaces under catalytic reaction conditions. Somorjai *et al.*[137] have built up such equipment in their laboratory. The STM is surrouded by a furnace where the sample can be heated at high pressures while the STM tip scans the surface.[138] Early studies using platinum (110) single crystal show that the surface restructured dramatically when heated in atmospheric pressure of hydrogen, oxygen and carbon monoxide.[139] Their hope is to investigate the structural changes occurring on iron single-crystal surfaces, especially on the (111) and (211) iron surfaces during the ammonia synthesis, using such a high temperature/high pressure STM apparatus.

One of the earliest studies about the surface compositions of ammonia synthesis catalysts is the classical works conducted by means of chemisorption method by Emmett *et al.*[140] The results are as follows: Under the reaction atmosphere, molecular state carbon dioxide is chemisorbed particularly on those potassium atoms or ions on surfaces, while the atomic state hydrogen and nitrogen, molecular state CO and ionic state oxygen can be used to probe the iron atoms on surfaces. According to the interactions between the chemisorption of CO and CO_2, it can be inferred that the promoters enrich on catalyst surfaces and disperse effectively, so as to make the most of iron atoms being closer to promoter atoms. It was found

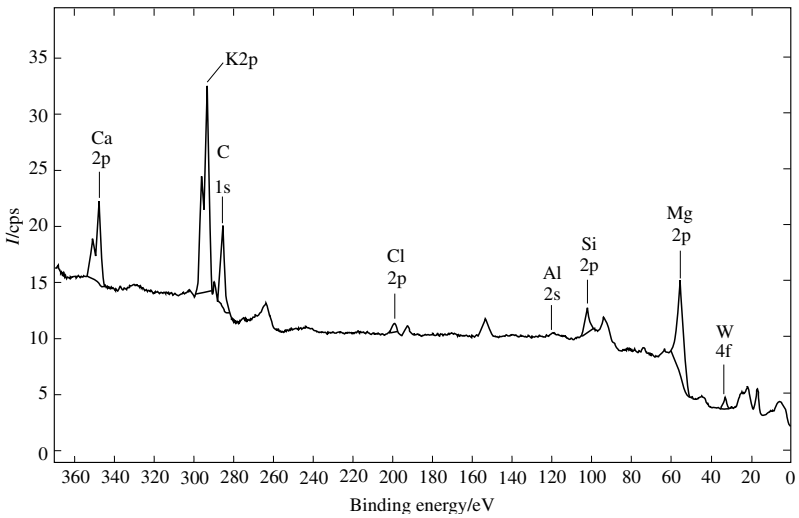


Fig. 3.56 X-ray photo electron spectrum

according to the measurement of the iron catalyst promoted with 1.3% Al_2O_3 and 1.6% K_2O that there was no dissociative Al_2O_3 on the surface, which was used to suggest that the pair of promoters had formed the compound of $KAlO_2$. While in the case of catalysts promoted with higher content of Al_2O_3, the most of the surface components are Al_2O_3, which shows chemisorptions neither for CO nor for CO_2. The catalyst promoted with higher ratio of K_2O/Al_2O_3 loses the basicity during usage. The studied results of Emmett indicated that the abundance of information about the chemical features of catalyst surface can be obtained by chemisorption method, which is, up to now the important approach of surface studies. Ertl *et al.* used X-ray photo electron spectroscopy (XPS) with probing depth of 5–20 Å measured ammonia synthesis iron catalysts and revealed that unreduced catalyst surface contains only several percent of iron, while the potassium and alumina as promoters in oxide state enriched strongly on the surface (Fig. 3.56). For instances, when the bulk concentrations of the potassium are lower than 0.5%, the surface concentration is actually 20%. This result is in good agreement with the above-mentioned results of Emmett *et al.*

Table 3.23 gives the surface compositions of A110 catalyst before and after the reduction as well as after the heat-resisting tests, which were obtained by the electron energy spectra (AES) and XPS (probing depth of 2×10^{-9} m). Before reduction, the number of iron atoms on the surface is only 5.4%, while the atomic compositions of the promoters are less than 10% in the bulk. However, on surface, the concentrations of promoters are above 50% no matter before or after reduction, or after the heat-resisting tests. It is clearly indicated that the phenomenon of surface segregation or surface enrichment of the promoters is commonly present and comparatively serious for fused-iron catalysts of ammonia synthesis. The surface states of catalysts are not only decided by their chemical composition and preparation method, but also connected with the reduction and use conditions.

Table 3.23 Surface compositions of A110 catalyst/%

Element	Fe	O	Al	Ca	K	Si	S
Before reduction	5.4	38.9	19.4	9.9	21.6	3.8	
After reduction	16.2	31	16.3	16.5	13.6	3.4	1.5
After heat-resisting test	21.1	31.7	13	14.7	11.3	4.7	2.5

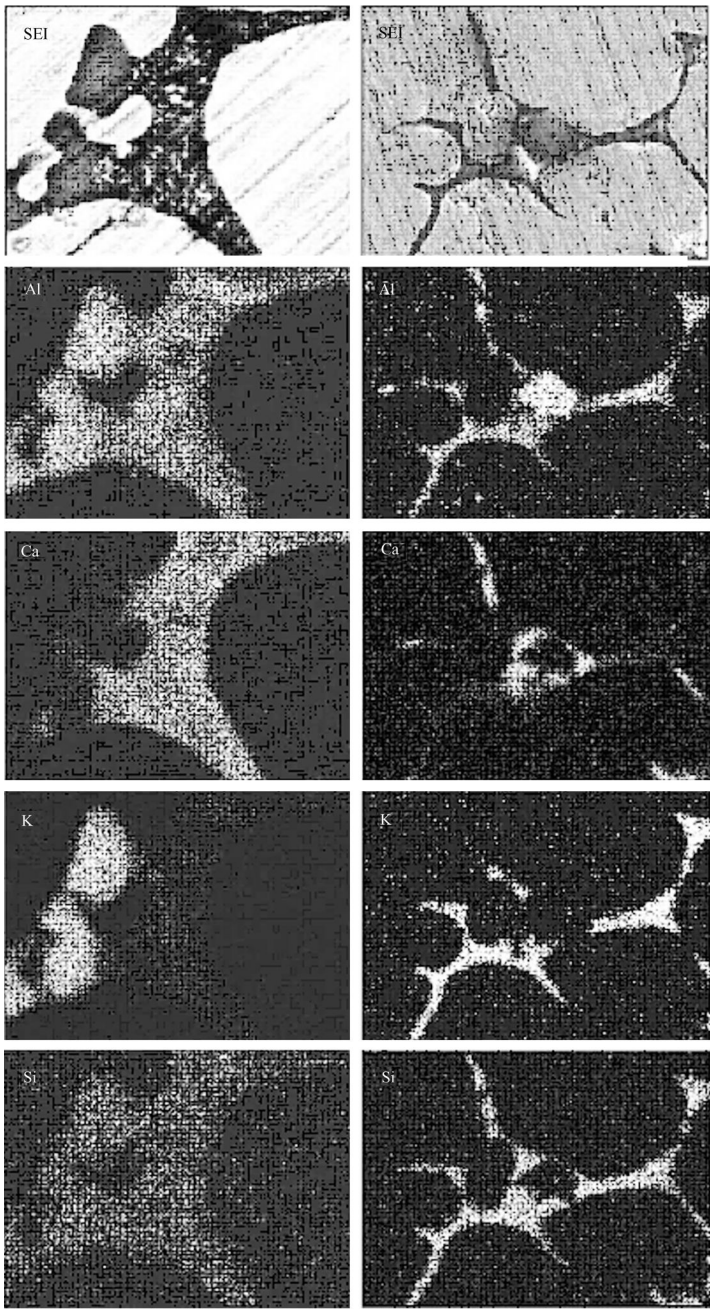
3.3.5 *Distribution of promoters in unreduced catalysts*

The uniform distribution of promoters in catalyst is the key and essential requirement for preparation of catalyst with high activity and stability. Promoters are present in the catalyst by following four states. The first one is congregated on the grain boundaries (such as K_2O). These kinds of promoters are extremely easy to be dissolved in the hydrochloric acid. The second one is that it can form a solid solution with the host iron oxides (such as $FeO \cdot Al_2O_3$). These kinds of promoters are dissolved along with the dissolution of iron oxides, which is somewhat slower compared to the first one. The third one is to be distributed uniformly into the catalysts (such as MgO toward FeO). The promoters with the solubility larger than that of iron oxides will be dissolved out *prior* to the latter. The fourth one is those promoters which are unable to be dissolved in the hydrochloric acid, such as certain metasilicates etc.

Therefore, the distribution status of promoters in catalysts may be measured by etching method of hydrochloric acid.[27] Figure 3.57 gives SEM and EDS spectra of catalyst K0 and K3 respectively. In both catalysts, the Fe^{2+}/Fe^{3+} ratios are all 4.5, the contents of Al_2O_3, K_2O, CaO, MgO is 3.3, 2.7; 0.66, 0.66; 2.9, 0.34; 0.57, 1.4% (mass fractions), respectively. It can be found from the spectrum of K0 in left side of Fig. 3.57 that the promoters occurred in the interstitial of grains are mainly composed of $Al_2O_3 \cdot nK_2O$, $Al_2O_3 \cdot nCaO$, pure CaO or small amounts of mixture with silica. The mixture of alumina and calcium oxide is intensively dissolved in HCl acid.

In catalyst K3, there is a highly visible grain of Al_2O_3, indicated with number "1" on the right-hand SEM image, which is not in the form of compound with any other promoter. The results of pointwise analysis indicate,[27] that aluminium oxide is at least partially bound with iron oxide. The form of aluminium-iron oxide compound obtained from these results is $Al_2O_3 \cdot FeO$ + pure Al_2O_3 (in molar proportions). Some amount of magnesium oxide is present in solid solution with the above compound, so that these species may constitute the non-HCl-soluble form of aluminium oxide found with selective etching.

In catalyst K3, there still are the compounds of alumina, ash and the residue calcium oxides. This phenomenon has been observed in the result of the selective etching approaches. Magnesia together with small amounts of alumina and silicon dioxides are dissolved in the wüstite. The content of alumina dissolved in wüstite obtained by point-by-point analysis is 1.0% (mass fractions). This is unlike the one obtained from selective etching approach, the value of which is 0.3% (mass fractions). The possible reason for this is, the promoters in glass phases undertake transformation during mechanical treatments in order to prepare the sample for EDS analysis and seem to be transformed into the wüstite phases. The selective



(a) K0 (b) K3

Fig. 3.57 SEM images and EDS mappings of the wüstite catalyst K0 (left-hand) and the Mg doped wüstite catalyst K3 (right-hand)

etching method gave the average result and the promoters sited in the interstitial grains are etched at the beginning. Hence the results that the content of Al_2O_3 in wüstite is 0.3% (mass fractions) obtained from this kind of method are reliable.

It can be seen from the results by Z. Lendzion-Bieluñ *et al.*[115] that, when the etchment degree of iron is quite small, along with the change of iron etching degree, the section of promoter etching degree with the fastest changes is corresponding to the etching of promoters on the grain boundaries in precursors, while the sections of slower etching change and show direct proportions to the iron etching degree, correspond to that of promoters which form the solid solutions with iron. M J. Figurski *et al.*[27] investigated by the method of hydrochloric acid etching the distribution of magnesium and aluminium oxides in the wüstite catalyst precursors and its influence on the surface properties of the resulting catalysts as well as clarified the distribution status of promoters in the precursor of wüstite catalysts with different ratios of Fe^{2+}/Fe^{3+} (R), namely, whether the promoters were enriched in wüstite phases or in magnetite phases.[141] The chemical composition of the investigated catalysts is presented in Table 3.24. The contents of potassium oxide and silica in these catalysts were 0.66 ± 0.04 and 0.45 ± 0.03 wt.%, respectively. Only the reflections from wüstite phase are present on the XRD patterns for the samples K0–K4, which is consistent with results of reference.[142] This is because the Fe^{3+} ions present in the sample does not form a separate magnetite phase, but are dissolved in the highly non-stoichiometric wüstite phase. From the Fe–O phase system we find, that the wüstite phase is stable at the melting temperature for R ranging from 1.9 to 11. The R of all of the obtained wüstite catalysts fits in this range. In the way of fast cooling the samples to the room temperature (rapid crystallisation), the metastable wüstite phase was obtained.

Table 3.24 Chemical composition, oxidation degree and phase concentration of catalyst precursor (mass fraction)

Catalyst	R	MgO (C_{total} and C_{ss})/%	CaO/%		
			C_{total}	C_{ss}	C_{total}
Industrial	0.63	0.53	2.9	1.0	3.3
K0	4.5	0.57	2.9	0.73	3.3
K1	3.7	4.0	0.43	0.12	0.45
K2	3.9	2.3	0.69	0.35	1.6
K3	4.5	1.4	0.34	0.13	2.7
K4	7.3	0.37	0.28	0.12	5.1

Catalyst	Al_2O_3/%			Total content C_{ss}/%	surface area/ $(m^2 \cdot g^{-1})$	
	C_{ss}	C_{i-sol}	C_{i-non}		Standard reduction	High-temp. reduction
Industrial	2.7	0.58	—	4.3	22.0	12.3
K0	0.35	2.5	0.45	1.6	10.7	5.4
K1	0.30	0.15	—	4.4	8.7	2.7
K2	0.34	0.96	0.30	3.0	21.1	11.4
K3	0.32	1.0	1.4	1.8	16.7	7.2
K4	0.33	1.0	3.8	0.82	15.0	7.1

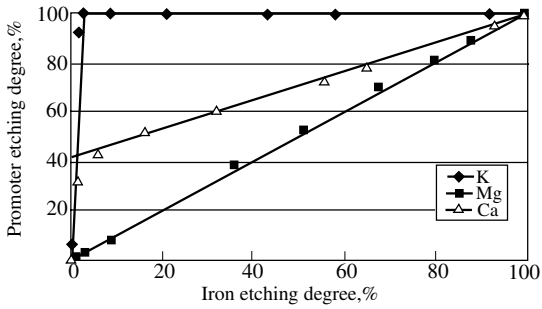


Fig. 3.58 Relationship of etching degree of potassium, magnesium and calcium to the etching degree of iron

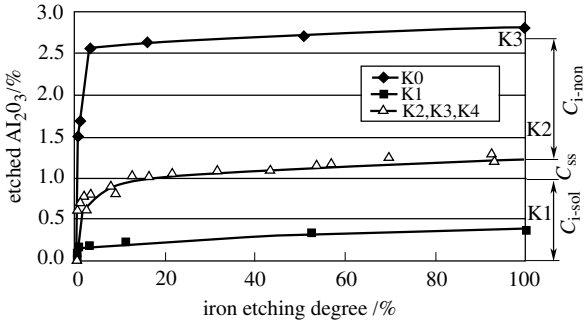


Fig. 3.59 Relationship of weight percent of aluminium oxide etched from the precursor (related to the mass of the precursor before etching) to the etching degree of iron. Total contents of Al_2O_3 in the precursors are marked on the right side of the chart area. For the catalysts K0 and K4 the total content of Al_2O_3 (see Table 3.26) exceeds the scale of y-axis

The relationship of etching degree of potassium, magnesium and calcium with the etching degree of iron is shown on Fig. 3.58 for all wüstite catalysts. When the etching degree of iron is below 3%, the etching degree of potassium reaches 100%. This result demonstrates that potassium is located in the gap of grains (glass phase) and is consistent with the results of other investigators.[141,143] Contrarily, the etching degree of magnesium rises proportionally to the etching degree of iron, which means that magnesium with wustite forms solid solution. About 40% of calcium oxide is located in the gap of grains, while the rest forms a solid solution with wüstite.

The promoter which is in the HCl-insoluble form is alumina. Figure 3.59 shows the relationship of mass percent of alumina etched from the precursor (related to the mass of the precursor before etching) to the etching degree of iron. The linear segments of etching curves for above 10% etching degree of iron are parallel to one another. This is an indication that the content of alumina in solid solution with wüstite (c_{ss}) is equal for all wüstite samples and amounts around 0.3 wt%, despite the different total content of alumina (c_{total}) and other promoters. Also the content of alumina etched at 100% of etching degree of iron, i.e., HCl-soluble, is nearly the same for the catalysts K2, K3 and K4. c_{total} and c_{ss}, as well as the contents of

Table 3.25 Tendencies of metal ions to occupy *A* site and *B* site

Item	Weak ← tended to occupy *B* site → strong Strong ← tended to occupy *A* site → weak										
Ions	Zn^{2+}	Cd^{2+}	Ga^{3+}	In^{3+}	Ge^{4+}	Mn^{2+}	Fe^{3+}	V^{3+}	Cu^{+}	Fe^{2+}	Mg^{2}
Ion radius/nm	0.082	0.103	0.062	0.092	0.044	0.091	0.067	0.065	0.096	0.083	0.078
Ions	Li^{+}	Al^{3+}	Cu^{2+}	Co^{2+}	Mn^{3+}	Ti^{4+}	Sn^{4+}	Zr^{4+}	Ni^{4+}	Cr^{3+}	
Ion radius/nm	0.078	0.058	0.078	0.082	0.070	0.064	0.074	0.087	0.078	0.064	

HCl-soluble ($c_{\text{i-sol}}$) and non-soluble ($c_{\text{i-non}}$) alumina in the intergranular spaces, are shown in Table 3.25. The way in which the values of c_{ss}, $c_{\text{i-non}}$ and $c_{\text{i-sol}}$ have been read from Fig. 3.57 is shown as an example for catalyst K3 on the right side of that figure.

It has been found that[27] the Al_2O_3 occurs in three forms in the wüstite catalyst precursor: One form is the solution in the wüstite phase; the other two are located in the intergranular spaces of the wüstite. The content of Al_2O_3 in the solid solution with wüstite phase amounts to about 0.3 wt% (from selective etching) and does not depend on the quantity of Al_2O_3 added or on the addition of other promoters. Content of HCl-soluble Al_2O_3 in the intergranular spaces depends on the addition of CaO. When only traces of CaO are present, the HCl-soluble Al_2O_3 exists at 1 wt% in the wustite catalysts, generally in the form of $K_2O \cdot SiO_2 \cdot 1/2\ Al_2O_3$ and $Al_2O_3 \cdot FeO$. The remaining pure Al_2O_3 and spinel comprise the non-HCl-soluble form of alumina. The surface area of the catalyst promoted with Al_2O_3 is about twice as that of the catalyst promoted with MgO. The high surface areas of catalysts containing both promoters may result from either the synergistic effect of MgO and Al_2O_3, or quite low optimal Al_2O_3 content for wüstite catalysts. Presuming that only the HCl-soluble Al_2O_3 is capable of surface area development, its optimal content for wüstite catalysts without containing calcium oxide should be around 1.3 wt%.

Another approach would be to focus solely on the alumina content, as it is the "strongest" structural promoter. We find that increasing the fraction of Al_2O_3 has led to the decrease of specific surface area. It is already known that the larger amounts of structural promoters tend to decrease the surface area of magnetite catalysts. This means that the amount of alumina above 2 wt% are too much for wüstite catalysts and the optimal amount of alumina for the development of surface area of wüstite catalyst lies in the vicinity of 1.6 wt%. For the magnetite catalysts, however, the addition of Al_2O_3 with amount up to 12 wt% results in an increase of the surface area.

It is possible that only the HCl-soluble form of Al_2O_3 is capable of development of surface area. Meanwhile, the excess alumina causes its decrease. The catalyst contains the smallest amount of insoluble Al_2O_3 possesses the highest surface area of all the aluminium-oxide-promoted catalysts. Based on the results of the distribution of Al_2O_3 from Table 3.26, we find that the optimal amount of alumina for the development of surface area of wüstite catalyst should be about 1.3 wt%, which comprises 0.3 wt% dissolved in wüstite phase plus about 1 wt% of HCl-soluble form of Al_2O_3.

Table 3.26 Relations of surface area, average pore size and reduction degree[a] of fused iron catalyst

Reduction degree/%	Total surface area/$m^2 \cdot g^{-1}$[b]	CO uptake/ $dm^3 \cdot kg^{-1}$	Average pore size[c]/nm
0	0	0	0
20	2.1	0.16	34.3
40	4.2	0.29	33.3
60	6.3	0.43	33.0
80	8.4	0.57	33.8
100	10.1	1.00	35.2

[a]Reduced with hydrogen at 720 K. [b]Calculated by unreduced catalyst per gram. [c]Estimated by surface area and pore volume.

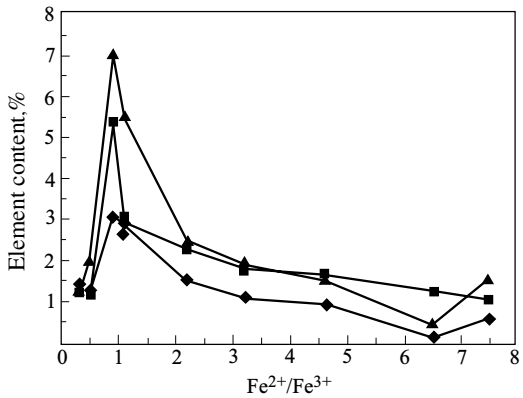


Fig. 3.60 Influence of iron oxide precursors on distribution of promoters measured by ESCA (♦: Al; ■: K; ▲: Ca)

The contents of the mixed structural promoters in iron oxides can determine the surface features, while the iron oxide precursors can influence the catalyst surface area, in order to perform the catalytic activity. From this point of view, the most optimum compositions of the structural promoters for wüstite catalysts are not identical to that of those magnetite catalysts.

The distribution of promoters on the reduced catalyst surface is related to the iron oxides precursor. Figure 3.60 shows the surface elemental compositions of the reduced catalysts derived from the different iron oxides precursors (expressed by Fe^{2+}/Fe^{3+}) measured by the Electron spectroscopy of chemical analysis (ESCA). It is seen clearly from the Fig. 3.60 that, in the two phase regions (Fe^{2+}/Fe^{3+} is in range from 0.5 to approx. 3.3), the promoter contents on the surface are obviously higher than that in monophase regions and it is especially obvious when the precursor made up of two iron oxides equimolarly i.e., Fe^{2+}/Fe^{3+} is about one, of which the surface concentrations of Al, K, Ca are respectively 2.87, 10.92 and 5.55 times higher than that in the bulks, so that made the surface concentrations of iron (not marked in Fig. 3.60) decrease from 75.7% to 22.6%. Without doubt, the over coverage of promoters on the surface decreased the activities in the two phase regions. It is because the different iron oxide precursors have different physical

chemical properties and the crystal structures, as well as by the appearance of the crystallization in batches or peritectic phenomena during the catalyst preparing process. In the meanwhile, it is also related with the reduction behaviors of the catalysts in the two phase regions, which occurs in turn according to the phases which belonging to competitive reduction mechanism.

3.4 Structures of Unreduced Catalysts

3.4.1 *Structural images of the classical fused iron catalysts*

The iron oxide of the precursor in classical fused iron catalysts is Fe_3O_4, which belongs to the inverse spinel-type crystal structure (Fig. 3.61). Every cell is composed with eight molecules of Fe_3O_4. The size of oxygen ions are larger than that of iron ions, and the oxygen ions are closely packed in a cube with a side length of 0.8396 nm, while the metal ions fill in the interspace of the cube (Fig. 3.62).

There are two types of interspace present amongst the cube: Octahedral interspace (B site) and tetrahedral interspace (A site), as shown in Fig. 3.62. The 32 of oxygen ions constitute the interspace of both 64 tetrahedrons and 32 octahedrons. In a crystal of Fe_3O_4, eight Fe^{2+} and eight Fe^{3+} ions occupy the octahedral interspace, while the another eight Fe^{3+} ions occupy the tetrahedral interspace, namely, Fe^{3+} (Fe^{2+} Fe^{3+}) O_4.

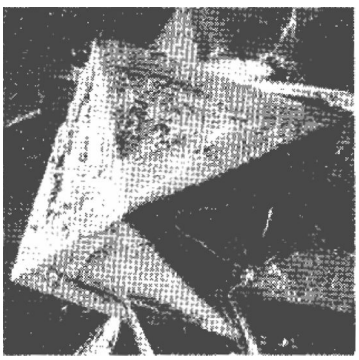
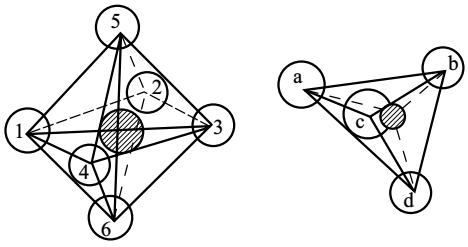


Fig. 3.61 Spinel structure of unreduced catalyst (230X)



(a)-site of octahedron (b)-site of tetrahedron

Fig. 3.62 Interspace of tetrahedron and octahedron



(a) (b) (c)

Fig. 3.63 SEM images of the ammonia synthesis catalysts before reduction

There still remain 72 vacant interspaces to, which is to be decided by such factors as the equilibrium effect of interionic chemical valences. This kind of vacant interspace is easily filled or replaced by the other metal ions, which provides the beneficial structural conditions for Fe_3O_4 to be doped as well as modified with the promoters. The whole structural images of the ammonia synthesis catalysts before reduction are composed of the filling, replacement of the metal ions with various promoters such as Al_2O_3, K_2O, CaO, MgO, SiO_2 in the crystal structure of Fe_3O_4, or forming solid solution of those promoters with Fe_3O_4.[144,145] Figure 3.63 is SEM images of the ammonia synthesis catalysts before reduction.

What kind of metal ions can fill into the vacant interspace or replace Fe^{2+}, Fe^{3+} ions? According to the principles of crystallography, the total amount of the chemical valences of several metal ions is equal to eight which makes the equilibrium of total chemical valences with four of oxygen ions. Various kinds of the metal ions can occupy A site or B site, respectively. The ionic distributions of which can be expressed by the following formulas:

$$(Me_\delta{}^{3+}Fe_{1-\delta}{}^{3+})[Fe_{1-x}{}^{2+}Me_x{}^{2+}Fe^{3+}]O_4.$$

A site B site

Next, the sizes of metal ionic radius and other factors such as the electronegativity of ions and temperatures etc. should be taken into consideration. According to the nearest packing principle, the largest metal ions radius that can be admitted for A and B sites are $r_A = 0.046\,\text{nm}$, $r_B = 0.054\,\text{nm}$, respectively, hence $r_A < r_B$. Hence, those metal ions with larger ionic radius, higher valences and with strong electronegativities are intended to occupy B sites; inversely, that are intended to do A sites. The radius of the various metal ions and their degree of tendencies to occupy A, B sites are shown in Table 3.25.

It is seen from the Table 3.25 that the metal ions such as electronic promoters as K_2O, CaO, due to the larger ionic radius are impossible to enter into the oxygen ionic interspace and also hardly replace the iron ions. These promoters are only present in the crystal boundaries of Fe_3O_4, or arise, under the high temperature during proparation, a complicated chemical reactions with iron oxides to form various solid solutions such as $K_2O \cdot Al_2O_3$, $K_2O \cdot FeO$, $Al_2O_3 \cdot FeO$, $CaO \cdot FeO$, $CaO \cdot Fe_2O_3$, $MgO \cdot FeO$, all of which are dissolved into Fe_3O_4 or FeO, or deposited on their surfaces. For the catalysts containing three promoters of Al_2O_3, K_2O, CaO, there are four kinds of mineral phases which can be distinguished by the X-ray crystal analysis i.e., magnetite, hematite, treble-ferrite and potassium ferrite (including the whole potassium). After reduction, in the four of fundamental phases, both the

relative contents of Al and Ca are kept constant, while the K distributes into all of the phases. The K_2O derived from the reduction of potassium ferrite $K_2O \cdot FeO$ diffuses toward the crystallite surfaces and reacts with compounds contained in Al and Si. Thereafter, it is well-distributed into the iron phases. The non-bonded K_2O is either transferred to KOH by H_2O from reductions, or to K by H_2. Therefore, potassium is able to be gathered on the surface of reduced catalysts t the various forms such as aluminates, silicates, solid solutions, KOH and the metallic potassium.

The structure of ammonia synthesis catalyst used in industry comprises promoters that are uniformly distributed into the inner or on the surface of iron oxide precursor. The crystallites are very small so the reduced catalysts show the stable structures and the largest surface areas.

3.4.2 *Structural images of $Fe_{1-x}O$ based fused iron catalysts*

As previously described, FeO is an oxygen excessive (Fe defect) non-stoichiometric iron oxide ($Fe_{1-x}O$), which shows the rock-salt type face center cubic structure (fcc). The unit cell of $Fe_{1-x}O$ are constituted from four $Fe_{1-x}O$ molecules, where there are eight tetrahedral interspaces (A site) and four octahedral interspaces (B sites) with O^{2-} closely packing onto NaCl-type cubic lattices.

Nevertheless, in the structure of wüstite, for the reason of Fe^{2+} cations being defective, there still exist given amount of Fe^{3+} cations besides Fe^{2+} cations in order to preserve electric charge neutrality. These Fe^{3+} cations enter generally into the original empty interspace of tetrahedron. At the same time, if one of the vacancies of Fe^{2+} is formed in the lattice, then in order to maintain the electric charge neutrality, there must be two of Fe^{2+} transferring to be two of Fe^{3+}, one of which will enter into the tetrahedron interspace and leave behind an empty space in the octahedral interspace, while the another Fe^{3+} stays in octahedral interspace. For example, when $x = 0.10$ in $Fe_{1-x}O$, then the structural formula can be written as:

$$({Fe^{3+}}_{0.10}\Delta_{1.90})[{Fe^{2+}}_{0.70}{Fe^{3+}}_{0.10}\square_{0.20}]O,$$

where, $\square$ represents octahedral interspace, $Fe^{2+}/Fe^{3+} = 3.50$. The unceasing process such as Fe^{2+} is removed and replaced by the proper amount of Fe^{3+}, and as a result, $Fe_{1-x}O$ with various x values can be obtained, which includes both Fe_3O_4 ($Fe_{0.75}O$) and Fe_2O_3 ($Fe_{0.67}O$) (Table 3.8). The vacant structure of the lattice of $Fe_{0.90}O$ can be illustrated as in Fig. 3.64.

The existence of the corresponding amounts of Fe^{3+} in wüstite structures not only ensures the electric charge neutrality in the lattice, but also provides the extremely favorable conditions for the migrations of Fe^{3+} along the cavity, as well as for the transferences of the electrons ($Fe^{2+} \rightarrow O \rightarrow Fe^{3+}$). This is the structural factor for the extremely easy reduction of $Fe_{1-x}O$ by H_2 and for $Fe_{1-x}O$ to be doped and modified with the promoters.

There is a linear relationship between x and the sizes of unit cells in $Fe_{1-x}O$ (see Fig. 3.65). In the defective structures of $Fe_{1-x}O$ lattices, the Fe^{2+}, Fe^{3+} and cavity's may be replaced by the metal ions of promoters. If the metal ions such as Al^{3+}, K^+, Ca^{2+} either entered into the cavity lattices of $Fe_{1-x}O$ or constituted solid solutions with them, then the lattice constants can become large. Especially in the case of Ca^{2+}, of which the radius is large than that of Fe^{2+}, if it replaces the latter, it makes the lattice constant obviously to become large. For example, the measured size of

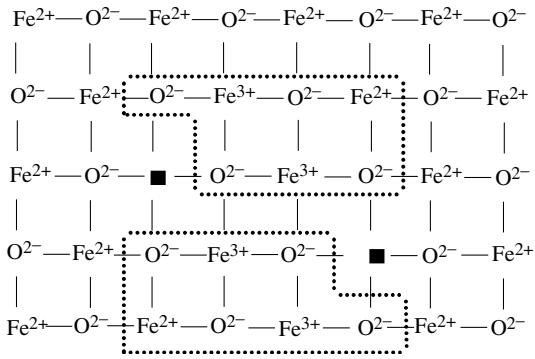


Fig. 3.64 Lattice defect structure of $Fe_{0.90}O$

There are 18 of Fe cations, 20 of O anions in 20 of $Fe_{0.90}O$ molecule, which constitute 12 of FeO molecule, 2 of Fe_3O_4 molecule (dashed box) and 2 of vacancy (■), where are 14 of Fe^{2+} cations, 4 of Fe^{3+} cations, and then $Fe^{2+}/Fe^{3+} = 3.5$.

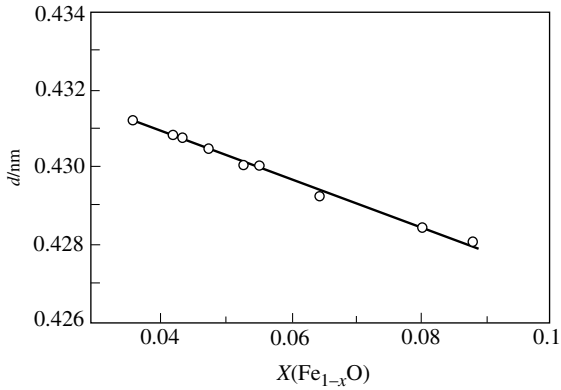


Fig. 3.65 Relationship between X in $Fe_{1-x}O$ and cell size of wüstite[147]

the unit cells of wüstite in A301 catalyst is 0.4310 nm. Obviously, the increases ini A301 catalyst lattices can be regarded as the result of Ca^{2+} replacements.[146,147] On the contrary, it can be revealed from XRD spectra that the wüstite in A301 catalyst is stable even as the temperature is lowered down to the room temperature. The reasonable interpretation for this phenomenon is that the wüstite is, to a certain extent, able to be stabilized by the replacements of such as Ca^{2+} for Fe^{2+}. The postulations of such cationic replacements have already been proposed.[115,148] The increases of lattice constants enable inevitably the lattice to be distorted, which is the one of important reasons for the improvements of catalytic activities of $Fe_{1-x}O$ based catalysts. However, the number of Al^{3+}, Ca^{2+} cations entered into the vacancies, from the point of view on lattice constants, is in the inverse proportions to the defect concentrations (X value). This may be related with the regularities of $Fe_{1-x}O$ lattices, as well as the chemical conditions for the crystallizations of them.

3.5 Structure of Activated Iron Catalyst

3.5.1 *Pore structures*[101]

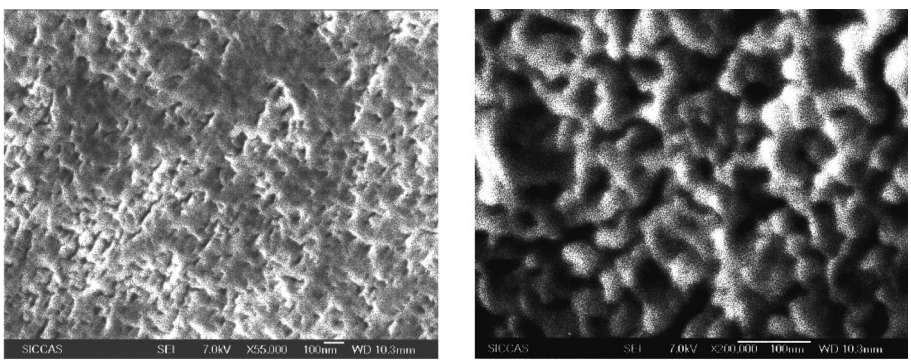
Pore structures of the fused iron catalysts are formed during the process of reduction. The unreduced catalysts are compacted solid without the pores. After reduction, the oxygen atoms in both magnetite Fe_3O_4 and wüstite $Fe_{1-x}O$ are removed, and the resultant α-Fe crystallites with body center cubic (bcc) structure will be formed. The shape in geometry of catalyst particles is not changed, and the new formed α-Fe crystallites connect each other by partly crystal faces to compose a porous skeleton. Due to the removal of oxygen, there arises a lot of interconnected pores among the inner of the particles. The various promoters are still present as oxide states and dispersed as well as distributed amongst the crystallites. K_2O is then enriched on the surface of α-Fe.

Figure 3.66 shows the scanning electron microscopic images of the surfaces of the reduced A301 catalysts. The porous skeleton structures and the morphology of the catalysts after reductions can be viewed vividly (see Fig. 3.66). The pore skeleton structures of the particles are commonly expressed by three kinds of parameters: Porosity, pore volume and pore diameters. Both the pore volume and porosity of iron catalyst after reduction are calculated by the lattice constants measured by XRD before and after the reduction, as seen in Chapter 7.

Due to the pore structure of the fused iron, catalysts are generated by the removed oxygen during the reduction process, so all of the pore structure parameters of $Fe_{1-x}O$ based catalyst are smaller than that of Fe_3O_4 based catalyst because the oxygen content of the former is lower than that the latter.

Since the pores in the real catalyst are very complex, there are two obvious differences from the hypothesis for the calculation of average diameter.

(1) **The actual shape of the pore is different.** It is not only the columniform pore, but all kinds of it may be straight or twist like a maze. The shape of the pore will affect the gas diffusion and hydrodynamics. The macroscopical nature of solid catalysts is usually characterized with twist-factor or maze-factor. For example, the average value of the tortuosity factor of A301 catalyst is 3.28.[149]



(a) (b)

Fig. 3.66 SEM image of reduced A301 catalyst

(2) **The actual pore has different sizes and distributions.** Sometimes catalysts with near average pore have different activities because they have different pore distributions. As a result, another important parameter of solid catalysts is the data of pore distribution and the most probable pore radius.

The sizes of the α-Fe crystallites are generally in the range of 20–50 nm. The sizes of the α-Fe crystallites for A110-2 and A301 catalysts are 25.2 nm and 25.3 nm, respectively. The iron crystallites will result in the growth in a given extent, when the fused iron catalysts are used in Fische–Tropsch synthesis reaction. The sizes of the α-Fe crystallites obtained by reduction of nature magnetite are extremely large. It indicates that the alumina and silica oxides in the nature magnetite are presumably present as the forms of larger grains/or foreign impurities. Therefore, the fusion is absolutely necessary for those oxides to be distributed throughout the whole magnetite.

The size of α-Fe crystallite is related with the reduction conditions. The iron surfaces of the reduced catalysts most likely (but not the unique one) expose prior-lyits (111) crystal face.[150,151] The higher the reduction temperature, especially the higher the vapor concentration during the reduction, the larger the α-Fe crystallites will be. The surface of both the metals (e.g., measured by the chemisorption of carbon monoxide) will increase progressively with the reduction degree. This phenomenon was proved by the data in the Table 3.26 that was given by Hall *et al.*,[152] in whose experiments the iron catalysts were prepared by the fusion method and containing 6.4% (mass fractions) of alumina and 0.8% (mass fractions) of potassium oxides (with the reduced catalysts as benchmark). It can be seen from Table 3.26 that the average pore diameter is nearly constant, but the total surface area increases linearly with the increasing reduction degree, while the effective surface area for the adsorptions of carbon monoxide is increased very slowly in the steps where the reduction degree are under 80%. However, this surface area increases quite rapidly as the reductions near to its end. This is presumably due to the chemisorbed oxygen and the inhibition of water vapor during the adsorption of carbon monoxide. In the evening (of reduction procedure), they are removed from the iron surface, increasing the surface of iron.

As the reduction temperature increases, the surface area decreases and the average pore size increases after reduction. For example, if the catalysts are reduced at 820 K, but not at 720 K as listed in the Table 3.26, then in the case of reduction degree by 100%, the total surface area decreases by about 60%, while the average pore size increases by 1.5 times. At the same time, such increase in reduction temperature can cause fractions of surface area which can adsorb the carbon monoxide in the total surface area declines by about 8%. It is possible due to the results of the conglomeration of iron crystallites in a given extents.

The sizes of α-Fe crystallites are related with the temperature of its use. The higher the temperature, the larger the α-Fe crystallite is. Figure 3.67 shows the α-Fe crystallite size of ZA-5 catalyst with the changing temperature.[153] In the figure, the increase of the α-Fe crystallite size should include the influences from the twofold factors: Thermal expansion of crystal and the conglomeration of the crystallite caused by the temperature.

To sum up, the reduction process of catalysts are of the decisive meaning for the formations of pore structure and the size of α-Fe crystallite. It must be fully

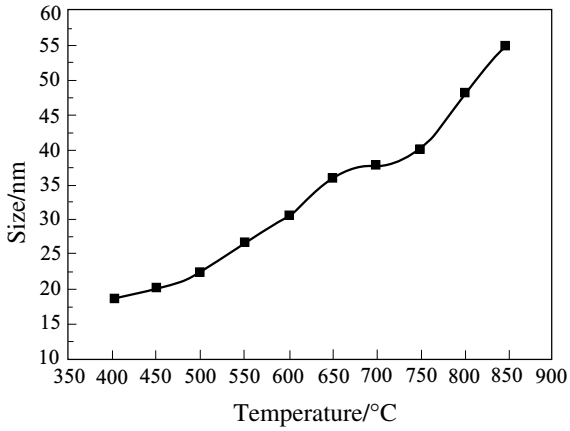


Fig. 3.67 Changes of grain size in ZA-5 catalyst with temperature (*in situ* XRD)

attached with the importance to the reduction process in an industrial application of catalysts.

3.5.2 *Surface structure of activated iron catalyst*

The surface structure of the ammonia synthesis catalysts continues to be investigated. The network structure composed of α-Fe crystallites shows a very large internal surface. Due to the nonuniform practical catalyst surfaces, there are many terraces on the surface. These terraces are also composed of the different steps in the highest ranges of 0.5–10 nm and to be cascaded step-by-step, which are called as ledges.

In these terraces, there are also a lot of defects present. Therefore, there are the various types of surface sites present on the catalyst surfaces, which are illustrated in Fig. 3.68. Those surface sites include the kink, step, point defect and the surface atom such as the bonding part of atoms adsorbed and vacancies etc. All these surface sites are very active, even though the equilibrium concentrations at the melting points are far less than 1% of the mono-molecular layer. They play an important role in the migration of atoms on the surface. The physical and chemical features of these surface sites are active. The rates of redox and chemical reactions

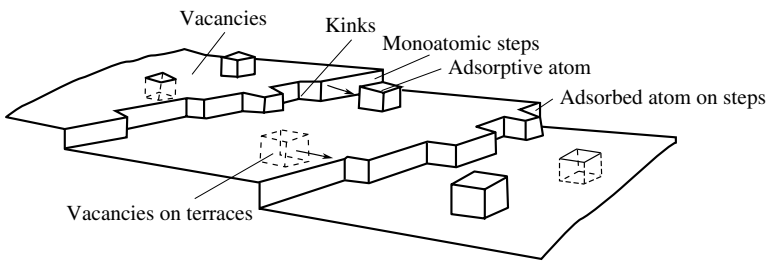


Fig. 3.68 Non-uniform solid surface (terraces and kinks in different surface site)

by themselves are rather fast, which, at point of view from the catalysis, are just the highly active sites. There are experimental evidences proving that various types of surface sites possess different chemical properties (for which there is a world of differences of adsorption heats for a specified molecule), as well as the different abilities to break the chemical bonds with large bonding energies (such bonds as H−H, N−O, N≡N, C=O etc.). This is due to the different charge densities localized on the different surfaces (caused by the splitting of the crystal fields) and the large surface dipole property by the redistribution of the charge densities.

Therefore, the chemical reaction rates and product distribution are only the average values in any experiment, because it is the sum of the effect of the various surface sites, for which such kind of concepts are very important for the interpretations of reaction mechanisms. For instances, if the density of surface kink site is rather high and the reaction rate is far more than the other surface site, then the experimental results are mainly contributed by the kink. In practice, it is difficult to clarify the related elementary chemical procedures of the each of surface sites.

The kink is an important surface site. For example, the growth of crystal requires necessarily the introduction of foreign atoms. While according to some of the modern theories of crystal growth, the new atoms introduced can only enter into the kink site, but not the other sites. The reason is simple. There are only three coordinate bonds on the surface kink site, where the energies needed for removing an atom and introducing an atom is equal. But the other sites are not the same, e.g., an atom in a crystal phase shows six coordinate bonds, which are required to break off six bonds when the atom is removed out. A foreign atom cannot be directly introduced into the crystal, but can only be added on the surface. Hence, adsorption on the kink site is in accordance ith the thermodynamic principles.[154] Recent studies have found that the most active regions for the nitrogen molecules occur frequently on those sites with the largest stress and defect density.[155]

In order to interpret the active surface structures of iron catalysts, numerous models for catalyst morphology have been postulated.[76,156] Schlögl suggested that there are iron lumps in the catalyst meshes, which are isolated by the oxide promoters. An individual piece of iron crystallites are accumulated loosely in the iron lumps and are commonly viewed as the iron (111) face.

Pennock *et al.* investigated the catalysts before and after reduction by *in situ* TEM reduction techniques. They observed iron cyrstals and the pore structure of approximately 20 nm–30 nm and indicated that the pores in magnetite grow along with (111) face. The same morphological trends of all of iron crystals are found in certain fields, namely, the crystal (100) face of both iron and magnetite are paralleled, while that (010) face, (001) face of iron are paralleled with (011) face, $(0\bar{1}1)$ face of magnetite.

The morphology and microstructure of catalysts in a wide range can be investigated by optical microscopy and transmission electron microscopy, so it is rather well understood that the procedures in the formation of porous iron promoted magnetite during reduction. To specify the structure of the active surface of the iron catalyst, many models have been proposed.

Arabczyk[121] postulated a simple model. Potassium atoms are adsorbed on iron surfaces, while in the free sites, adsorbed non-metals are present under the potassium atomic layers. Under the ammonia synthesis conditions, those free sites are partly occupied by oxygen atom in order to stabilize the potassium. The existence

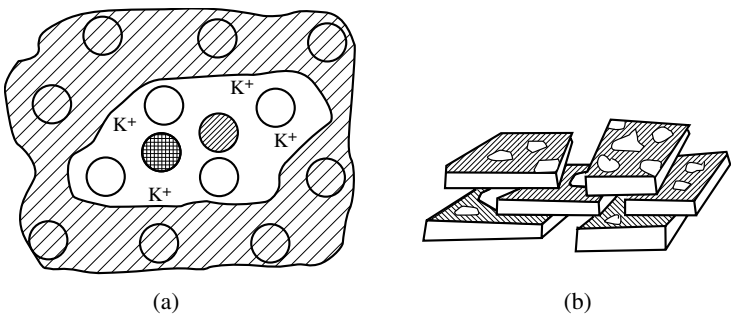


Fig. 3.69 A model of the active site in ammonia synthesis proposed by Bowker[158]

of hydrogen is not taken into consideration, because the hydrogen atoms are too small and their adsorption rates are not affected by potassium.[157] From a geometric point of view, there are the sufficient spaces for hydrogen atom. Nitrogen adsorption occupies possibly the place under the atomic layers of potassium.

Except for these, there are at least two other types of surface models for iron catalysts in literature.[76,156] The first one considered that the existence of alumina on the iron surface results in the restructuring of the surface and forms the atomic aluminium on the surface. After being exposed to the reaction mixture, iron will grow along with the orientations of (111) and (211) to iron-aluminium. The second one considered that the promoters are present on the surface by a thickness smaller than one nanometer and with an approximate diameter of two nanometers, which are seperated by the pure irons. However, none of the models can explain every experimental observation.

Figure 3.69 is a surface active site model for ammonia synthesis catalyst proposed by Bowker.[158] The model brings togther a variety of findings in the literature. In Fig. 3.69(a) a C7 site is shown as the active center as proposed by Ertl[124] and Somorrjai[76] from their work in this field. These are particular sites on a Fe (111) surface which is shown in the figure. The site is surrounded by areas of alumina and alkali (hatched region), with alumina acting as a skeletal support and as a medium for maintaining the active (111) plane. Potassium atoms at the edge of this region may play at least two roles. First, they enhance the activity of the surface for ammonia synthesis by enhancing nitrogen dissociation (largely due to electrostatic field gradients at the surface which perturb the orbital energies in incoming nitrogen molecules); second, they may weaken sites which strongly bind ammonia or intermediate species and result in poor activity of a singly promoted catalyst due to the blockage of the active site as shown. Figure 3.69(b) shows a somewhat more macroscopic view of the surface, illustrating slabs of active Fe (which have been described by Schlögl[52]) with the active site ensembles being shown on the surface of these slabs. It is well known from the earliest studies of this substance that most of the surface is covered by inactive compounds such as aluminates.

Børge *et al.*[159,160] further divided iron thick disk structures of the reduced magnetite crystallites into four kinds of configurations as followings: Normal structures (a, b, c), plain structures (d, e, f), finger structures (g, h, i), and flake structures (j, k, l), see Fig. 3.70. In reduced magnetite grains four different pore morphologies with characteristic crystallographic orientations exist. These structures are several

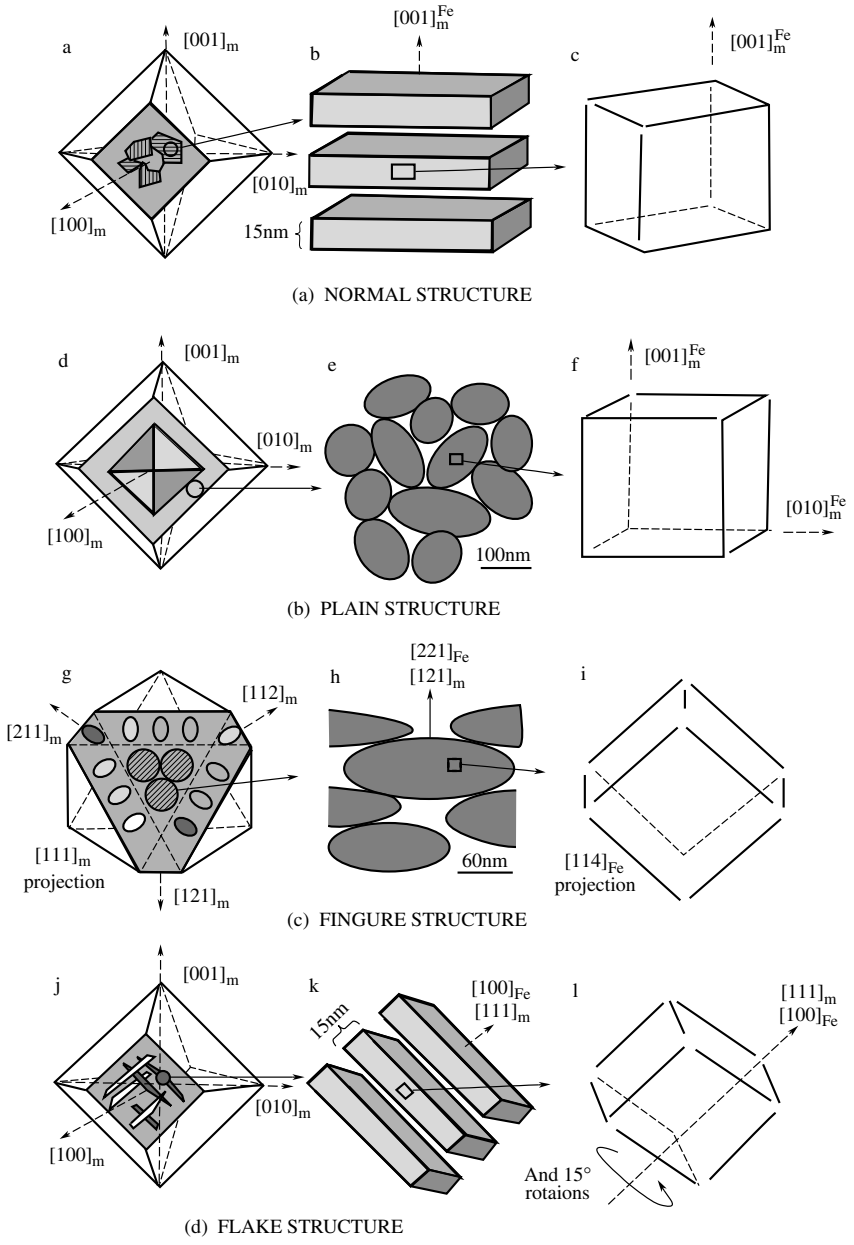


Fig. 3.70 Summary of the four structures found within reduced magnetite grains. The left column shows magnetite grains shaped like regular octahedra which have been ground and polished like a metallographic sample to reveal the various structures in the grey-shaded polishing plane. The middle column contains schematic drawings of the local pore structure from the selected regions shown by arrows from the left column. The body centered unit cells of α-Fe in the right hand column show the crystallographic orientation of iron in regions with the given pore structure.

micrometers in size and may be described as porous single crystals of bcc-iron. The dominant structure (roughly 80% of the catalyst volume) contains nearly random network of pores and the crystallographic orientation of the porous iron is the same as that of the original magnetite. Another structure (*ca.* 5% by volume) has sheets of iron along the three (100) planes of the former magnetite and a (100) axis of iron normal to the sheets. A third structure (*ca.* 3%) with weak sheet-like pores along the twelve (112) planes of the original magnetite has a (221) direction of iron to the pores. The most complex structure (very rare in the industrial catalyst) displays strong sheet-like pores along the four (111) planes of magnetite and has a (100) axis of iron to the sheets. The particular orientation relations between the original magnetite and the resulting iron suggest that epitaxy plays an important role in reduction. Alumina, which is added as a promoter, reduces the lattice parameter of magnetite. The local Al^{3+} concentration in the magnetite may influence the structure by changing the likelihood of the possible epitaxy relations. Differences in activity among the various structures may exist. However, activity measurements are not a part of this structural study of the porous iron ammonia synthesis catalyst.

Arabczyk *et al.*[110] suggested a double-layer model of the fused iron catalyst for ammonia Synthesis. This model is constructed on base in the following assumptions.

(1) The previously described model can be applied not only for potassium but also for other promoters. Promoter and nonmetal atoms are located in two separate layers. The layer in the direct vicinity of iron atoms is "reserved" for oxygen and other nonmetal atoms. The free sites for nitrogen adsorption are located in this layer. The promoter atoms are located "on top" of the oxygen atoms forming topmost layer (Fig. 3.71).

Iron surfaces are covered by the double-layer of promoter oxides. The first one of sublayers close to iron atoms is filled with oxygen atoms and shows the free adsorption sites; the second sublayer is present on the top of the first sublayer, and is filled with the promoter atoms. The amount of oxygen atoms and the free adsorption sites are decided by the properties of promoters (Fig. 3.71), of which the former is in a fixed proportion to that of promoter atoms. Under the ammonia synthesis conditions, the ratio of the number of oxygen atoms to the number of promoter atoms located on the iron surface is constant and equal to the valence of the promoter (for alkali metals, 1:1[121,122,125,161,162]; for alkali earth elements, 2:1[121]; for aluminum, 3:1). Thereby, the number of oxygen atoms on the iron surface is determined by the nature of the promoter.

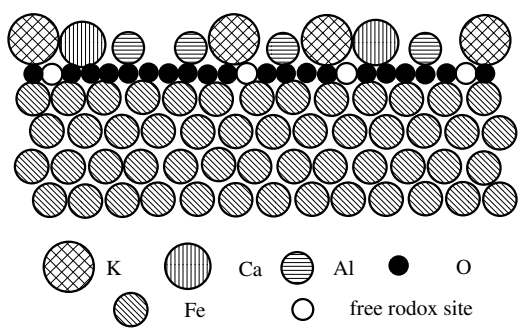


Fig. 3.71 Double-layer model of the surface of iron catalyst

The numbers of free adsorption sites connect directly connect to surface oxygen atoms. As the oxygen atoms increase on iron surfaces, lesser would be the free adsorption sites for dinitrogen tetroxides. The surface area of iron catalysts rely on the amounts of surface oxygen atoms. Therefore, the element of both Ca and Al requiring high concentrations of oxgygen is beneficial to the formation of catalysts with highest area. There is a thermal dynamic equilibrium among the interval points of surface area, volume of iron and crystal of iron [Fig. 3.70(b)]. The postulation is able to interpret the phenomena of an industrial catalyst, which is, even with its porous structures and the severe reaction conditions (high temperature and high pressure), able to maintain its structure and to be utilized for a long time on stream.

(2) The iron surface is "wetted" by promoter oxides. The potassium atoms can migrate to the iron surface under ammonia synthesis conditions to adsorb on the free iron atoms or cover the layer of the other promoter oxides present there earlier. A recent paper[163] demonstrates that under ammonia synthesis conditions a clean iron surface which is in direct contact with the multiply promoted iron catalyst is covered with a potassium oxygen layer. This result indicates that despite the presence of other promoters (Al, Ca) in the catalyst it is potassium that covers the iron surface. Even prolonged maintenance of such a sample under ammonia synthesis conditions (700 K, 10 MPa) does not change the composition of its surface.

(3) The equilibrium between the bulk, the surface, and the spacers placed between the iron crystallites is retained (Fig. 3.72) and the total surface area is determined by the number of oxygen atoms on that surface. This assumption is based on many observations of the behavior of the industrial catalysts. The iron catalyst for ammonia synthesis is very stable and possesses a long catalyst life. Despite the high porosity and severe work conditions (high temperature and high pressure), the structure of this catalyst remains almost unchanged for years. A slow sintering observed during catalyst use seems to be caused mainly by a local overheating. A system which is far from equilibrium would tend to reach this state as fast as possible, which is not observed in the case of the iron catalyst for ammonia synthesis. However, a change in the chemical composition of the catalyst, for example, potassium addition to the Al-promoted catalyst causes an immediate change of its surface area.[164]

(4) The clean iron surface exhibits a tendency to minimize an excess of the surface energy by reduction of the surface area. It is assumed in the model that the surface is covered by an oxygen layer (there are promoters on top). In this case the surface energy is compensated by Fe–O bonds. The greater the oxygen

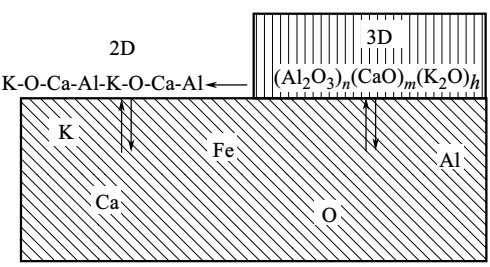


Fig. 3.72 Scheme of the equilibrium between the surface, the iron bulk, and the three-dimensional structures in iron catalyst

concentration, the higher the amount of Fe–O bonds and the greater the surface area should be. The catalyst containing the elements which need more oxygen atoms (Ca, Al) to be stable on the iron surface at a high temperature exhibits the highest BET area, reaching about $20\,m^2/g$.[38]

According to the model, it can be calculated for the quantitative relationships between the atoms of iron, oxygen and promoters on the surface of a model catalyst. Therefore, knowledge of the number of adsorbed oxygen atoms on the iron surface is necessary. The iron faces Fe (100) and Fe (111) are considered in the subsequent calculations. The surface structure formed by oxygen atoms on the Fe (100) face is described as Fe (100) p $(1\times1)-O$, and the number of oxygen atoms in the monolayer is $12 \times 10^{18}\,m^2$.[165,166] For the Fe (111) surface an appropriate reconstruction is Fe (111) $(2\sqrt{3} \times 2\sqrt{3})$ R30°$-$O and the number of oxygen atoms in the monolayer is $14 \times 10^{18}\,m^{-2}$.[156] During studies of coadsorption of different nonmetals on the iron surface, the equation $O_S + O_{N2} + O_{C2} + O_{O2} = 1$ was derived. Taking into account this equation and reconstruction structures the numbers 14×10^{18} and $12 \times 10^{18}\,m^{-2}$ are considered as the maximal numbers of free adsorption sites on the Fe (111) and Fe (100) surfaces, respectively.[167] The number of potassium atoms capable of being adsorbed on the iron surface should also be known. On the Fe (111) surface precovered with oxygen ($\Theta = 1$) the number of potassium atoms is about $6 \times 10^{18}\,m^{-2}$.[121]

Figure 3.73 shows the vertical views of Fe (100) face covered by potassium and oxygen in the double-layer model. The surface of the catalyst is fully and homogeneously covered with a potassium-oxygen layer. Due to the assumed K/O ratio being 1:1 and the location of potassium atoms on the outer layer, no other adsorption sites on the iron surface are occupied. According to this model, the oxygen atoms occupy from 50% to 57% of the adsorption sites on the iron surface,[168] but since they are located under the potassium atoms, the free adsorption sites exist and are exposed to vacuum (Fig. 3.73). Nitrogen molecules can find their way to these sites between potassium atoms.

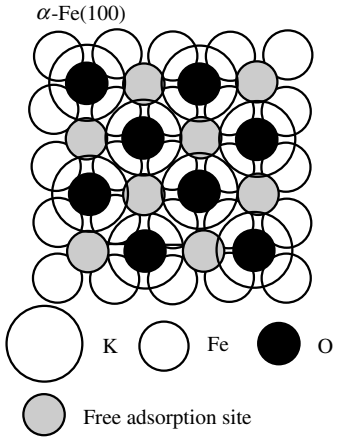


Fig. 3.73 Top view on the Fe (100) face covered with potassium and oxygen as proposed in double-layer model

The presented image has a lot in common with the real catalysts. TPD,[169] SEM/EDX and EXAFS[170] studies of the multiply promoted industrial catalysts show that their surfaces are completely covered with a K + O layer. The other studies carried out by means of electron spectroscopy indicate that the concentration of iron atoms on the catalyst surface is in the range of 4%–15%.[156,171,172] Former studies which exploit the methods with a lower surface resolution give a similar view as the model. The latter methods have better surface resolution, but it is difficult to distinguish a signal originating from the surface atoms and a signal coming from atoms located underneath.

According to the model, about 50%–60% of the adsorption sites are occupied by oxygen atoms. This means that there are 40%–50% of the free adsorption sites which may be occupied by adsorbing nitrogen and where the ammonia synthesis reaction might take place. Therefore, this number refers to the active surface of the catalyst. This property of the catalyst is usually examined by CO chemisorption and different values may be found,[173] and about 40% is widely accepted to be an appropriate value.[174]

The model structure of the surface of the iron catalyst may be used to explain the influence of different elements on the catalyst properties. The atoms of aluminium are able to be present on iron surfaces because it requires for a high concentration oxygen atoms, while potassium requires less of oxygen atoms in order to be stabilized on iron surfaces. Hence, alumina increases catalyst surface area, while alkali results in the declines of surface area.[111] The model states that 0.48 wt% K_2O is enough to cover the iron surface with a monolayer of potassium. Industrial catalysts contain usually from 0.5 wt% to 1 wt% K_2O. An excess is required to form some bulk compounds with alumina, silicon, or calcium found in the catalyst. Because at least 10% of the potassium is permanently bound in these compounds, 0.55 wt% is considered to be a sufficient concentration. This conclusion is supported by the experimental results of Kowalczyk.[126] It is found that the potassium concentration in doubly promoted catalysts leads to the highest activity in the range of 0.5–0.7 wt%.

3.5.3 *The role of surface restructuring*

The particles on solid surface, under the propelling of certain forces will be rearranged to form a new surface structure known as the surface restructuring. Ever since the 1980s, the phenomena of surface structure became a popular subject in the surface scientific field with the application low-energy Electron Diffractions (LEED), Auger Electron Spectrum (AES). For example, the structural role of alumina has been explored[175] on various iron single-crystal surfaces. Experimental results (Fig. 3.74) show that even the least active (110) face of iron becomes as active as the (111) iron crystal face, after the addition of alumina and subsequently annealed in oxygen and water vapor. Furthermore, electron microscopy, thermal desorption and other studies indicate that during ammonia synthesis all iron surfaces restructure in the presence of Al_2O_3. A proposed mechanism, supported by X-ray photoelectron spectroscopy (XPS), temperature programmed desorption (TPD) and electron microscopy studies, for this restructuring is shown in Fig. 3.75.[128] Alumina first forms a $FeAl_2O_4$ iron aluminate on the surface. This new surface then serves as a template on which iron grows with (111) or (211) orientation upon exposure to

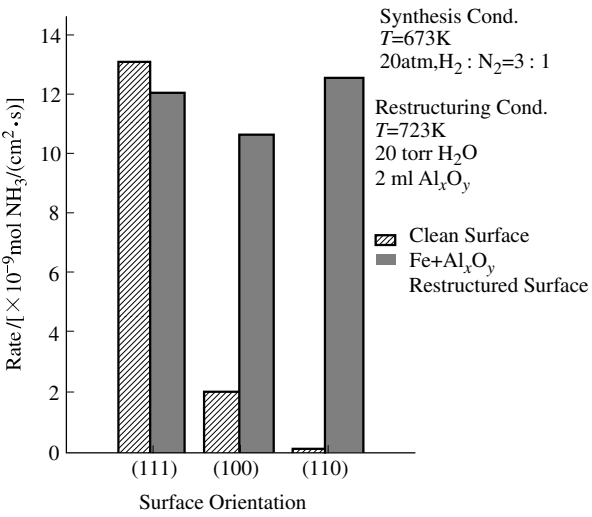


Fig. 3.74 The rate of ammonia synthesis of different iron surfaces showing that the addition of alumina and annealing in water and oxygen produce an active surface on the least active (110) face of iron[175]

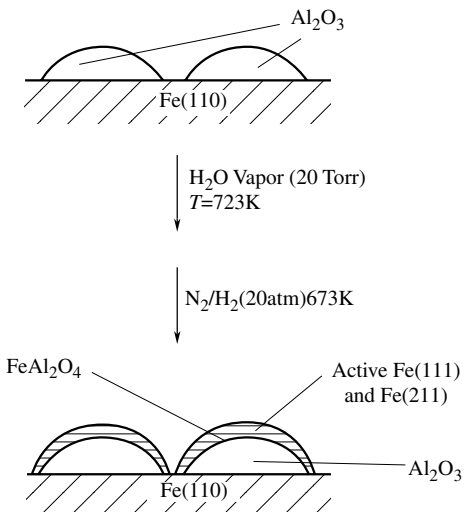


Fig. 3.75 A schematic depicting the mechanism of restructuring of iron induced by water vapor in the Presence of aluminum oxide[175]

the reaction mixture during ammonia synthesis. There is evidence that after heating in water vapor the iron growth orientation on the iron aluminate becomes (111) during ammonia synthesis.[176] The structural stability of the iron surface in the presence of ammonia is another question. Upon heating in ammonia, all iron surfaces most likely restructure to (211) crystal faces, with or without the presence of alumina.[177]

The reason for the occurrence of surface restructuring can be related to both catalyst and reactant (foreign atoms). From the point of catalyst itself, the surface enrichment mentioned above is one of the reasons. When a certain surface atom nanosize is quite large, in order to decrease the surface energy, the atom is compelled to migrate along with the surface toward a new location to form a new surface structure. The surface lattice atoms have the possibility to change after the foreign atoms (reactants) are adsorbed on solid surface and then form a new surface structure differing from the structure before adsorption. However, there are two common characteristics after any surface restructure: (i) As the surface structure changes from one to another, the body structure of them remains identical on the whole; (ii) As the difference of energy between the two surface structures is not great, the atoms can migrate on the surface only to overcome the small energy.

It is seen from the surface restructuring phenomena that, the molecules of reactants and products and catalysts are necessarily considered as one whole system in the studies concerning the active centers of catalyst and note the influences of reaction conditions. The active center structure is frequently a certain surface active species derived from the chemisorption of reactant molecules. Studies of the catalyst structure adsorbed by the foreign gases provide better understanding of the origins of the activity. This is also the reason why the various *in situ* investigations methods come in for great attentions and develop rapidly.

3.5.4 *Nanometer effect*

(1) **Nano materials.** The addition of the "nano" prefix to many technical terms is a quite recent practice that began with the introduction of the nanometer as a microscopic length unit in place of the Angstrom. Though nanoscience was formally born with that event, it is nevertheless clear that nanosize materials were being studied much earlier, especially in the area of catalysis. In fact, industrial catalysis has involved nanoparticles since its beginning at the dawn of the 20th century. For example, nanoparticles are typically present in supported metal catalysts. Here, metal particles with a size usually in the range of 1–10 nm are deposited on the external surface and/or in the porous texture of inert substances. Hence, the nanoscience concepts have been applied in industrial catalysis since its beginning, even if nobody was aware of that. In fact, the technique for obtaining metal particles with the required nanosize (metal dispersion) and for putting such nanoparticles in the right place throughout the porous structure of the carrier (metal distribution) are nothing other than nanotechnology. However nanoscience in catalysis is not restricted to supported metals. Both unsupported metal and mixed oxide catalysts can show situations where nanosize regions have some specific features that are key factors in the catalytic performances. In such circumstances, nanotechnology plays a crucial role in catalyst R&D.[178]

Currently, the applications of the regularities of nanoscience in the catalyst structure are the nanoclusters composed of either atoms or ions, which play an important role in improving the catalyst properties. The developments and conservations of such kind of nanoclusters require the deep backgrounds of solid state chemistry, which is the main target for any of catalyst producers.

The modern industrial iron catalyst is a nanostructured metastable substance, which is formed during the surprisingly complex synthesis of the oxide precursor.

This differs significantly from pure iron especially in the mesoscopic area despite the similarities in the local structure. Its metastability is the reason for its sensitivity towards thermal overstress during activation and oxidation of the activated material. Alternative preparation routes for the nanostructured system are possible and confirm the complex structure of this seemingly very simple ammonia iron. A quantitative analysis has shown[45] that only 1% of the geometric iron surface participates in the activation of nitrogen on an industrial catalyst. The remaining adsorption sites are filled from these centers by surface diffusion. Thus, the duality of plates and blocks has a functional equivalent as nitrogen activation and storage regions, which coincides quantitatively with theoretical and experimental findings. There is a striking example concerning the classical ammonia synthesis catalyst. The precursor oxides of catalysts for ammonia synthesis are changed simply by using wüstite rather than magnetite, which can drastically change the metal surface nanostructure of the cayalysts. It has been confirmed that a much higher activity can be obtained if the catalytic iron surface is formed from wüstite rather than from magnetite, thus questioning a century of research and speculations on what can be called a textbook catalyst. It is expected that a careful optimization of both size and distribution of such CaO nanoparticles can further increase the already considerable gap between wustite and magnetite catalysts. It is a good challenge for nanotechnology[178]!

Though the nanoscience concepts have been applied in industrial catalysis since its beginning, the catalyst research workers should be clear-headed and recognize that, the attentions of many in the past, was mainly focused on the size effect of materials, while, there are even more of interests in the nanosciences in addition to the size effect, that the surface effect and the quantum effect and from which the produced particularly excellent properties such as mechanics, optics, magnetism and calorifics.

(2) **Size effect and surface effect.** Metal particle size is a very important property of supported metal catalysts. The control of metal particle nanosize is of utmost importance for the performance of any industrial catalyst based on supported metals.

The surface effect refers to the consumedly increase of the ratios between surface atoms and total atoms, the surface energies and surface tensions of the particles with the decrease of the sizes of nanoparticles, which then result in the changes of the nature of nanoparticles. The crystal field and binding energy of the surface atoms in nanoparticles are somewhat different from that of the inner atoms, where in the former case, numerous dangling bonds are present and with the unsaturations these surface atoms are extremely easy to bond with other atoms in order to stabilize. Hence, the surface atoms have the very high chemical activities.

The surface area of spherical particle is in proportion to the square of its diameter, while its volume is in direct proportion to the cube of the diameter. Hence, the specific surface area (surface area/volume) is in inverse proportion to the diameter, namely, the specific surface area increases strikingly as the particle diameter becomes smaller, as shown in Table 3.27.

The surface activity of nanoparticles are very high, with the properties of which, the metallic nanoparticles are in accessible to be highly efficient catalysts and materials of hydrogen storage. However, the freshly prepared nanometallic particles, if

Table 3.27 Diameter and surface area of particles

Diameter of particle (d)	Volume of particle ($1/6\ \pi d^3$)	Number of particle in $\pi/6$ ml	Total surface area ($\pi d^2 \times$ numbers of particle)
1	$1/6\pi\ (1)^3$	1	3.14
0.1	$1/6\pi\ (1/10)^3$	1×10^3	31.42
0.05	$1/6\pi\ (5/100)^3$	8×10^3	62.83
0.01	$1/6\pi\ (1/100)^3$	1×10^6	314.16
0.005	$1/6\pi\ (5/1000)^3$	8×10^6	628.32
0.002	$1/6\pi\ (2/1000)^3$	120×10^6	1570.8
0.001	$1/6\pi\ (1/1000)^3$	1×10^9	3141.6
0.0005	$1/6\pi\ (5/10000)^3$	8×10^9	6283.2
0.0002	$1/6\pi\ (2/10000)^3$	125×10^9	15708
0.0001	$1/6\pi\ (1/10000)^3$	1×10^{12}	31416
0.00005	$1/6\pi\ (5/100000)^3$	8×10^{12}	62832
0.00002	$1/6\pi\ (2/100000)^3$	125×10^{12}	157080
0.00001	$1/6\pi\ (1/100000)^3$	1×10^{15}	314160
0.000005	$1/6\pi\ (5/1000000)^3$	8×10^{15}	628320
0.000001	$1/6\pi\ (1/1000000)^3$	1×10^{18}	3141600

once not treated by passivation, can rapidly self-ignite, but become inactive after passivation.

The surface adsorptibility of nanoparticles has also attracted great interest, especially preparing processes, such as the method of hydrogen-arc plasma, which are at the atmosphere of hydrogen present during preparations of nanoparticles. The experiments have indicated[179] that the nano transition metals have the ability to store hydrogen. The hydrogen in the nanocrystallites of transition metals can be divided into two types. First type is the hydrogen adsorbed on the surface, and the second one is the body-hydrogen as a form of solid solution integrated the hydrogen with the transition metal atoms. The behaviors of hydrogen in nanocrystal transition metals have established the experimental foundations for the application of functions of those nanocrystal metals. With the increasing contents of hydrogen, the specific surface area or the amount of active sites of nanometallic particles increase greatly.

(3) **Amounts of metal surface atoms.** Since the last century, nanoscience principles have always applied in industrial catalysis. In particular, supported metal catalysts are typical examples of nanomaterials. Accurate and reliable measurements of the size of metal particle and the ratio exposured on its surface are indispensable for the research on such materials in theory and industry.

Assuming the atomic space is about 0.3 nm, and the surface is only occupied by mono-layer atoms, then the ratio (percentage) between amounts of surface atom and total atom of particle can roughly be calculated, as shown in Table 3.28. It is clear seen from Table 3.28 that the surface effect can be neglected for those particles with diameter larger than 100 nm. The amount of atom on surface increases sharply and the sum of the surface area can approach about $100\,m^2 \cdot g^{-1}$ when the diameter of particle is smaller than 10 nm. In the absence of precise definition, it may occur that objects larger than 100 nm are defined as nanomaterials, though they have more to do with the micron rather than with the nanometer. Hence, someone considered that the maximum size for a nanomaterial should not appreciably exceed 10 nm.[179] However, solids including in their structures or at their surface nanometric bodies of

Table 3.28 Relationship between particle size and surface atomic numbers

Diametr/nm	Total atom number (N)	Percentage of surface atoms/%
1	30	100
5	4,000	40
10	30,000	20
100	30,00,000	2

Table 3.29 Relationship between particle size and dispersion (D)

Particle size/nm	D/%
1.4	78
2.8	49
5.0	30

relevant importance for their performances should be considered nanomaterials too. For some other cases, for instance, should solids with nanosize porosity be defined as nanomaterials? They should include zeolites and active carbons. In conclusion, there is an urgent need for the international agreement of "nanodefinitions."

The sizes of nanoparticles can be measured directly by the means such as HRTEM (High Resolution Transmission Electron Microscopy), SAXS (Small Angle X-ray Scattering). The traditional methods for measuring the amount of surface metal atoms are built on the foundations of chemisorptions (see the details in Chapter 7). Total amount of surface metal atoms measured by this method is related to the amount of gas molecules adsorbed on it. This value is not always equal to total amounts of catalytic active sites for some reactions.

The dispersion of metals is defined as,

$$D(\text{dispersion}) = \frac{\text{Surface atomic number of particle } M_S}{\text{Total atomic number of particle } M_T} \times 100\%.$$

When $D = 1$, all of the atoms are exposed on surface. As the crystal particle size increases, the amount of atoms (M_S) and dispersion (D) disperse on their surface decrease. The value of D for Pt reforming catalyst can approach 50% (Table 3.29).

"Exposure percentage" is more right than "dispersion" according to IUPAC. From the point of view in catalysis, exposure percentage is a most direct and most right measurement. If part of metal surface is poisoned, exposure percentage may directly relate to catalytic activity. Table 3.30 shows the exposure percentages of both Fe and K on the surface in the catalysts derived from different precursors, measured by the selective chemisorptions of CO and CO_2.

When the percentages of the exposed Fe atoms (D_{Fe}) are calculated from the quantities of CO chemisorption, the stoichiometry of chemisorption is taken as one, namely, it is postulated to be linear adsorptions. It can be seen from Table 3.30 that, with D_{Fe} in the ranges of 0.54%–0.73%, there is not an obvious and regular change with the changing of the iron oxide precursors.

The percentages of the exposed K atoms (D_K), which is calculated from the quantities of CO_2 chemisorption and the contents of K_2O, with the stoichiometry of

Table 3.30 Exposure percent of both Fe and K atoms on the surface of catalysts

Fe^{2+}/Fe^{3+} of unreduced catalysts	Exposed percentage/%		Active site density $A \times 10^6$	Active site number $N \times 10^4$	TOF/s^{-1}	
	D_{Fe}	D_k			425°C	400°C
0.31	0.64	89.12	7.849	1.045	0.226	0.195
0.48	0.73	118.79[a]	7.344	1.255	0.190	0.164
0.50	0.65	94.33	7.800	0.944	0.212	0.187
0.89	0.64	110.65[a]	7.953	1.045	0.207	0.182
1.10	0.55	80.51	7.883	0.901	0.252	0.224
2.16	0.54	68.49	8.134	0.885	0.275	0.248
3.15	0.55	82.20	6.960	0.902	0.297	0.268
4.62	0.55	78.02	7.162	0.902	0.294	0.272
6.55	0.61	84.15	7.190	1.000	0.267	0.247
7.56	0.62	87.70	7.149	1.001	0.264	0.249

Notes: D_{Fe} is the percentage of Fe atoms exposed on surface measured by chemisorption of CO; D_K is the percentage of K atoms exposed on surface measured by chemisorption of CO_2; $A = Fe\% \cdot D_{Fe}/55.85\,S_T$, active site density, $mol \cdot m^{-2}$; $N = AS_T$, active site number, $mol \cdot g^{-1}$; $TOF = r/(3600N) \times 10^{-3}$, turn-over frequency, s^{-1}; S_T is the BET total surface area.
[a]See in the text.

chemisorption to be two, are in the range of 68.49%–94.33%, except samples No. 2, 4. There are promoters such as CaO in addition to K_2O as alkali promoters in catalysts. For this, the chemisorption quantities of CO_2 should include the adsorbance of it on the other kinds of basic oxides. In other words, D_K should represent the percentages of the exposed total atoms of basic metal oxides. Consequently, the value of D_K calculated by the contents of K_2O alone may exceed one, which occurred for the results of samples No. 2 and 4. Beside that, the chemisorption stoichiometry of CO_2 is not necessarily the strict two. However, we can certitude from the Table 3.30 that the most parts of the basic oxides are undoubtedly exposed on the surfaces of catalysts.

The above-mentioned results indicate that, in the reduced fused iron catalysts with the total Fe contents of 91%–92%, there are only 0.54%–0.73% of Fe atoms exposed on the catalyst surface, while the ones that are larger than 99% still need to be imbeded in the inner of body catalysts or covered by promoters. Therefore, absolute great parts of Fe atoms in fused iron catalysts cannot bring into playing role in the catalytic reaction and in fact only play a role as carrier for transfer electron. If more of Fe atoms are exposed on the catalyst surface, then there are possibly the further improvements of the activities of fused iron catalysts.

3.5.5 *Single-crystal structure of α-Fe and the active sites*

It has been extensively studied indicating that all of the surfaces of α-Fe are actually not of the same activity and only those surface sites called as "active center" are able to show the high activity. So-called active center means those certain sites with the specific atomic structure, arrangement, charge density, geometric morphology on the surface.

After the fused iron catalysts with Fe_3O_4 or $Fe_{1-x}O$ as precursor are reduced, in which the oxygen anions are removed out and the iron cations form the α-Fe crystallites with body centered cubic lattice structures as shown in Fig. 3.76. Both

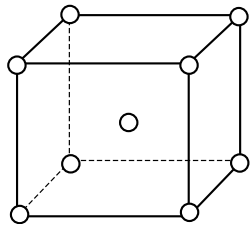


Fig. 3.76 Body centered cubic lattice of α-Fe

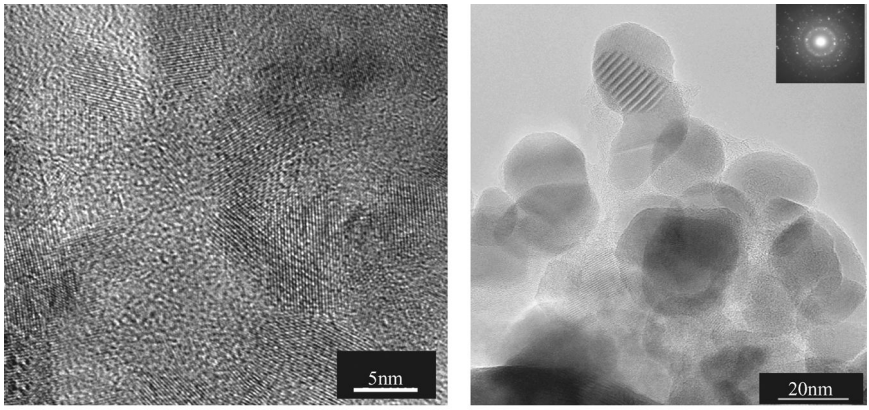


Fig. 3.77 HRTEM image of reduced A301 catalyst

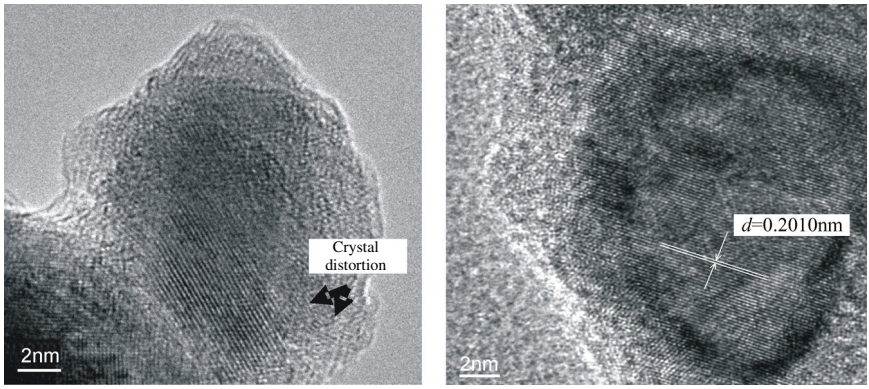


Fig. 3.78 HRTEM image of lattice distortion and ring structural map of reduced A301 catalyst

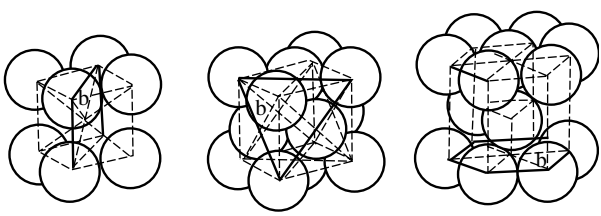
Figs. 3.77 and 3.78 illustrate the high resolution transmission electron microscopic images of A301 $Fe_{1-x}O$ based catalysts after reduction and prepared in our laboratory. Figure 3.77 is the image of the whole morphology, where the α-Fe crystallites are mainly elliptical shaped, with macroaxis direction of spheric ellipse being along with iron (110) face. This is consistent with the fact that the crystal size is the

largest when oriented with (110) directions by XRD calculations. Figure 3.78 shows the case of both the distance and dislocations of crystal lattice stripes. The space between iron crystal face (d) is about 0.2010 nm. By the statistical counting in different regions, the particles sizes is in the range of 8 nm–25 nm, of which the major part centralized in range of 15 nm–17 nm. This is also consistent with the distribution ranges of particles sizes from XRD measurements, especially close to the results calculated by the method of Warren-Averbach. It is worth of notice that during the observations of HRTEM images, the crystals with zone or core-shell structures are usually visible, of which the nucleus and the peripherals lattice texture are of dislocations or the different of crystallization direction, even some of which are ring structures composed of several convolutions, see in Fig. 3.78. The reasons for composing those structures indicate that the growth processes of the active α-Fe crystals are staggered step-by-step.

According to the observations of the integrality of growth of core-shell structural crystals, it can often be found that the crystallization of kernel are more integrity, from which it is able to be deduced that the crystal growth condition of the kernel are more superior and with slow growth rates, as well as with more of possibilities to growth at later periods. Therefore, the growth of active sites is possibly their own particular growth pattern.

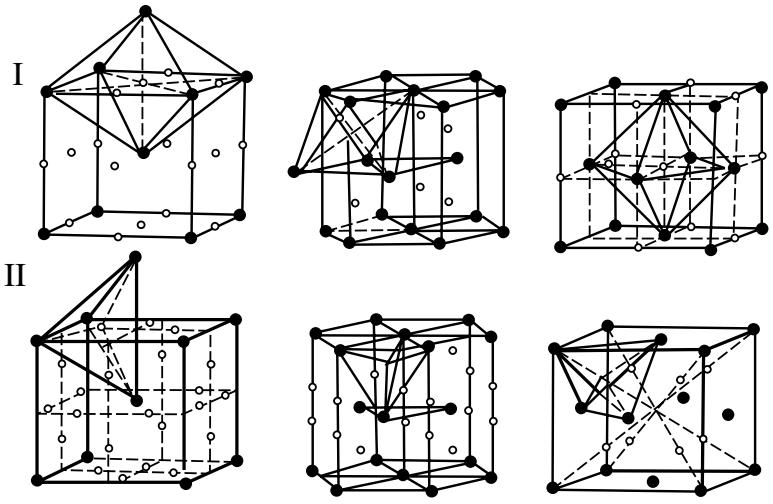
(1) Crystal structures and the surface geometric structures of metals. XRD studies proved that all of the metals, beside a few exceptions, belong to three kinds of crystal structures, namely, face centered cubic (F. C. C.), body centered cubic (B. C. C.) and hexagonal close packed structure (H. C. P.) as shown in Figs. 3.79, 3.80 and part of structural parameters are listed in Table 3.31.

The crystal lattices can be regarded as the different crystal faces, which are denoted by three of simple integers in crystallography.[32] For instance, metallic iron shows body centered cubic lattice (Fig. 3.76), where three kinds of simple crystal faces are (100), (110) and (111). The numbers in the brackets represent the reciprocal ratio of intercept of crystal face with each of three crystal axes, respectively; see Fig. 3.81(a). The geometric arrangements of metallic atoms as well as the atomic spacing on the different crystal faces are not the same. Figure 3.81(b) illustrates this kind of distributions. Ⓐ represents Fe atoms on the first layer of the surface, Ⓑ represents those on second layer and C represents those on the third



(a) Body-centered cubic lattice; (b) Face-centered cubic lattice; (c) Hexagonal close-packed lattice

Fig. 3.79 Lattice structures of three kinds of crystal of metal (1) (b in graph is dense surface)



(a) Body-centered cubic lattice; (B.C.C.) (b) Hexagonal close-packed lattice; (H.C.P.) (c) Face-centered cubic lattice (F.C.C.)

Fig. 3.80 Lattice structures of three kinds of crystal of metal (2).

I-Location of octahedron in lattice; II-Location of tetrahedron in lattice

Table 3.31 Structural parameters for F. C. C, B. C. C, H. C. P lattices

Parameters	FCC	BCC	HCP
Atomic numbers of cell	4	2	2
Size of cell	$a = b = c = \sqrt{2}d$	$a = b = c = 2\sqrt{3}d$	$a = b = c = d$, $h = \sqrt{2}d/\sqrt{3}$
Nearest coordination number	12	8	12
Hypo- neighboring coordination number	6	6	8
Hypo- neighboring distance	$d\sqrt{2}$	$2\sqrt{3}$	$d\sqrt{2}$
Largest percentage for occupying space of node/%	74	68	74

layer. (110) face is the closest arrangement of the first layer, where only Ⓐ is exposed, while the other Fe atoms are just hidden under Ⓐ. This kind of arrangement is of the lowest energy as well as the highest stability; whereas, those of (111) face is a precisely in inverse, where Ⓐ arrangement is the most laxation and with the highest energy as well as the lowest stability. Some studies indicated that those face (111) with the highest surface energy has the highest catalytic activity for the ammonia synthesis reaction. When the catalyst sinteres, the (111) face transfers to that of (110) and loses the catalytic activity consequently.

Crystals always tend to decrease the surface energy during their growth. Those crystal faces with low surface energy are quite easily exposed on the surface. The

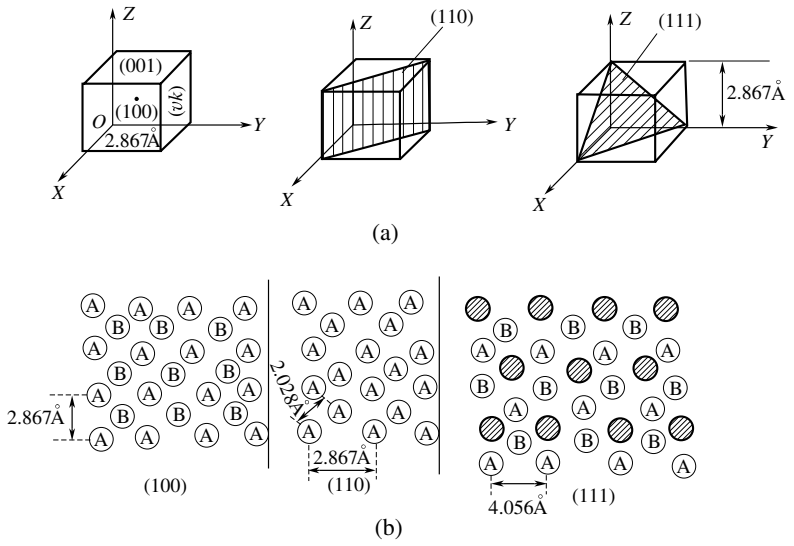


Fig. 3.81 Arrangement of Fe atoms on different crystal face in α-Fe crystal

metal atoms exposed on the surface are still closely packed on the most favorable crystal face which may form the face with low Miller Index in thermodynamics. Generally speaking, crystal face with low miller index has large particle density and coordination extent, so the surface energy is low. Hence, those crystal faces are often exposed on the surface. For example, the surface cell of many clean metal surfaces is (1×1) faces with low miller indexes. Such surfaces are stable thermodynamically, and the probability of change is small because the atomic arrangements on the surface are similar to that on the bulk, and also with the approximately same atomic spacing. On the catalytic studies, the catalytic effect of those crystal faces with low miller index is commonly taken into consideration precedence.

It is called as understratum structure, and denoted as - (1×1) when the atomic arrangements of the surface are same with the bulk unit cells. For example, the understratum structures of iron atoms on Fe (111) face are denoted as Fe (111)-(1×1). If the atomic arrangements on the surface are different from the underlayer, they are called as surface network or surface structure and also called as surface restructuring, e.g., unit network (2×2). The surface layer usually does not limit the first layer on the surface, but sometimes includes the several layers on surface. It is common that the structures of 1, 2 and 3 layers on surface are quite close.

The metal surfaces exposed to gaseous atmosphere can always produce the adsorption phenomena. Under most experimental conditions, the surfaces are always covered by the adsorbents closer to molecular layers. If the gaseous molecules are adsorbed on the surface atoms by one-to-one, then the arrangement of adsorbents is identical to the underlayer structures, which are denoted as (1×1)-G, where G represents adsorbed gases. For instance, Fe (111)-(1×1)-O_2 indicates that O_2 is adsorbed on the Fe (111) faces, where the arrangement of oxygen is same as underlayer structure. If the arrangements of unit cell of the adsorbed oxygen are twofold

of the underlayer structure, then it is denoted as Fe (111)-(2 × 2)-O_2. When the surface structure is rotated for one angle as for body unit cells, here unit cell size on underlayer structure is not an integer multiple proportion to the size of surface network, which can be denoted as $(\sqrt{2} \times \sqrt{2})$-$R45°$, namely the cell size of surface structure is $(\sqrt{2}a \times \sqrt{2}b)$, rotated clockwise for 45°, where R represents rotation. Other more complicated surface structure can adopt the Wood's or matrix mark symbol.

(2) Structure of active center. Ammonia synthesis is one of the most structure sensitive catalytic reactions. At the beginning of 1980s in 20th century, Somorjai *et al.* studied the ammonia synthetic reactions over single crystal using field ion microscope (FIM),[180,181] indicating that the open (111) and (211) crystal faces of iron are the most active ones, while the closely packed iron (110) crystal face is almost inactive. That is probably responsible for the surface structure sensitivity of the reaction discovered earlier. The dissociation probability of N_2 was found to be small,[119,122,123] even on the active iron (111) surface (of the order of 10^{-5}) and was found to decrease by orders of magnitude for other iron crystal surfaces. The catalytic reaction rates were measured on different crystal faces of iron using high/low pressure reactor in laboratory and it was further found that these reaction rates vary by order of magnitudes (with the (111) and (211) crystal faces of iron being the most active by far). The results of these studies are shown in Fig. 3.82. It was found that the relative ratio of the activities of Fe (111), Fe (100) and Fe (110) crystal faces is 418 : 25 : 1 at pressure of 2.0 MPa.[182] The activity of Fe (111) crystal face is 418 times higher than that of Fe (110) face, where the difference is amazing.

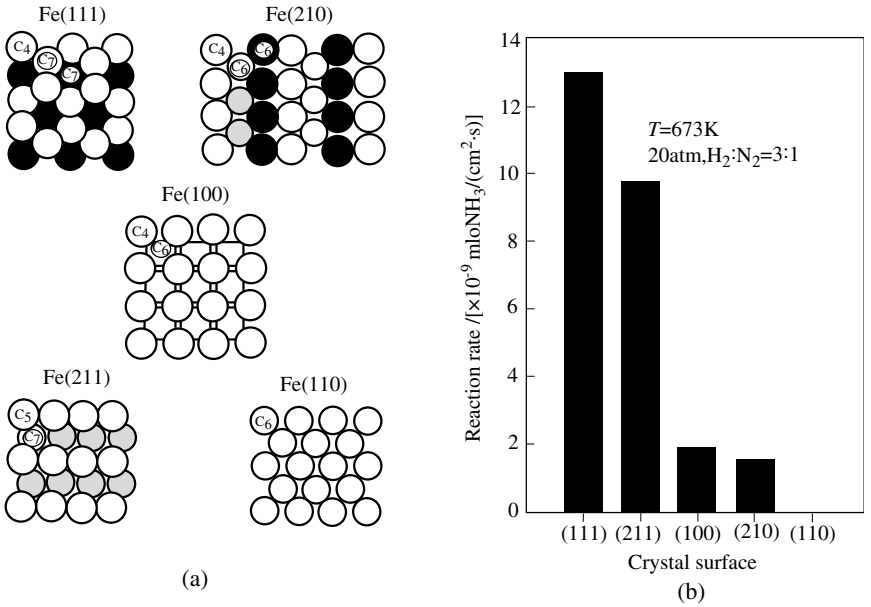


Fig. 3.82 Ammonia synthetic rate and displayed structural sensitivity on five of iron crystal faces

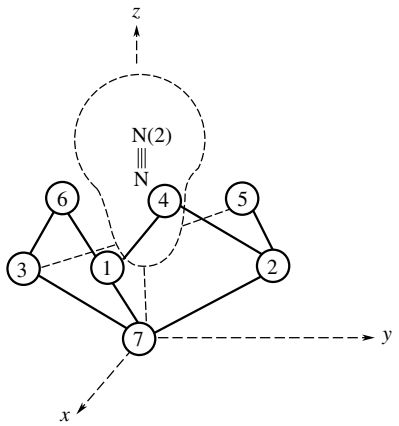


Fig. 3.83 Simplified model for seven nuclear active centers

Table 3.32 Activation of iron atoms and iron atomic cluster for ammonia molecules

Structure	Overlaped collective number of N–N bond		qN_1/e	qN_2/e
	σ/e	π/e		
N_2	0.795	0.845	—	—
Fe ... N≡N (end)	0.738	0.666	−0.170	−0.340
Fe ... N≡N (side)	0.850	0.547	−0.242	−0.243
$Fe_4N_2{}^*$	0.825	0.324	−0.146	−0.675
$Fe_4N_2{}^{**}$	0.786	0.492	−0.018	−0.504
Fe_5N_2	0.792	0.421	−0.045	−0.565
Fe_6N_2	0.797	0.260	−0.196	−0.897
Fe_7N_2	0.804	0.200	−0.207	−0.999

Somorjai's studies indicated that seven (C_7) and eight (C_8) metal atoms coordinated surface sites, which are available only on active surfaces, are very active for the dissociation of dinitrogen. In most experiments, the step of N_2 dissociation is the rate controlling step. According to these, Strongin *et al.*[127,183−185] suggested the so-called "seven atomic cluster active center model," namely there are more "sites" or "centers" of seven atoms surrounding only on the Fe (111) crystal faces, which can adsorb preferably the N_2 molecules. Figure 3.83 is one kind of simplified structural model of the active centers.[185]

Xinquan *et al.*[186] calculated the activation effect for the postulated seven iron atomic clusters and the structures which are absent of 1–3 iron atoms on molecular nitrogens, by the extended Hückel Method. The results indicated that the N–Nπ bonds are weakened by great extent, with the order as followings (Table 3.32):

$$Fe_7N_2 > Fe_6N_2 > Fe_4N_2{}^* > Fe_5N_2 > Fe_4N_2{}^{**} > FeN_2 \text{ (side)} > FeN_2$$

Here, the seven iron atom clusters are most active to activate nitrogen and the second one is six iron atom clusters. The polarizations of two nitrogen atoms are in consistence with the decreasing order of the π bond.

The activation of Fe_4N_2* on N_2 molecules is more favorable than the Fe_5N_2 and Fe_4N_2**, indicating that the activation of the iron atoms on the first layer on N_2 contribute than more the three Fe atoms on the second layer. The activation effect of active sites on N_2 is mainly weakening π bonds, while with little effect on σ bonds.

Somorjai *et al.*[76] discussed about three important questions related to the roles of iron surface structures in ammonia synthesis: (i) How strong is the evidence for the C_7 site as the most active site for N_2 dissociation? (ii) How do the catalytic reactions occur with strongly chemisorbed nitrogen atoms blocking the C_7 sites? (iii) How does potassium promote ammonia synthesis? They believe that there are evidences, for a second active site for N_2 dissociation involving potassium and oxygen (K-O-Fe).

Low energy electron diffraction (LEED)-surface crystallography studies clearly indicate that the surfaces of most clean metals relax inward.[187,188] The rougher the surface (the more open the surface structure), the greater is the relaxation. The (111) and (211) iron surface structures as determined by LEED-surface crystallography are shown in Fig. 3.84.[189,190]

There is a large inward relaxation in the topmost layer of both surfaces, bringing the exposed C_7 sites closer to the surface. The LEED results show no surface restructuring in the x-y surface planes. Figure 3.85 shows the percent contraction in iron single crystal surface as a function of surface roughness, which is defined as one-over-the packing density.[191] The most active (111) and (211) iron crystal faces show large contractions, but not as large as the roughest or most open (210) iron surface that is much less active in producing ammonia. Thus, there is no direct correlation between surface roughness and the corresponding lattice contraction and catalytic activity in ammonia synthesis.

Figure 3.86[128,176] shows the variational orders of the ammonia synthesis activity, the work function and the surface roughness on different iron crystal face. The work

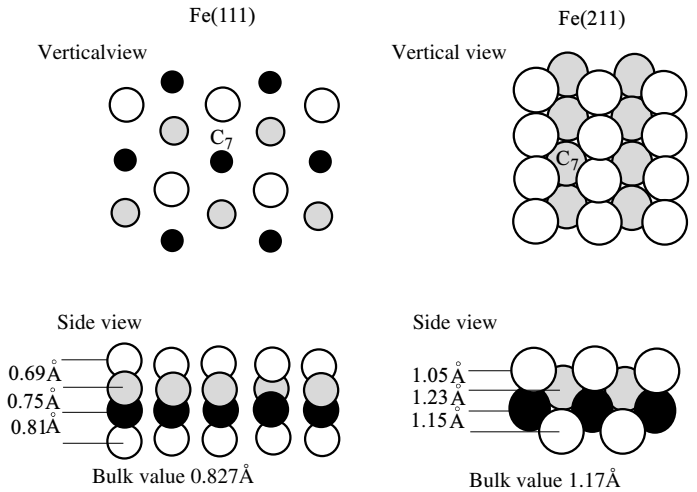


Fig. 3.84 Surface structure of iron (111) and (211) faces measured by LEED-surface crystallographic techniques

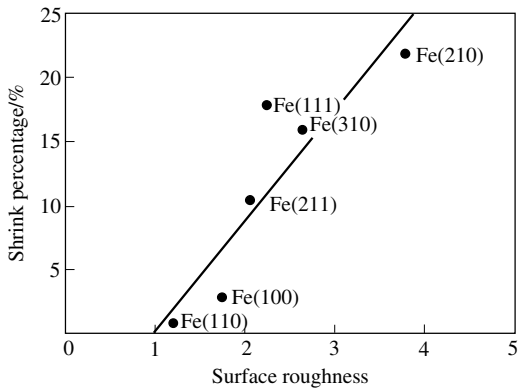


Fig. 3.85 Coordinate chart of shrink percentage of first layer and surface roughness on different iron single crystal face

Ammonia synthesis activity

$$(111) > (211) > (100) > (210) > (110)$$

Work function

$$(210) < (111) < (211) < (100) < (110)$$

Surface roughness

$$(210) > (111) > (211) > (100) > (110)$$

Fig. 3.86 Variational orders of the ammonia synthesis activity, the work function and the surface roughness on different iron crystal face

function change and surface roughness are correlated; the more open the surface, the lower is the work function. However, ammonia synthesis activity does not correlate with either one of these physical parameters of the iron system. The most active surfaces, the (111) and (211) faces of iron, have intermediate work function and surface roughness values. This implies special sites on the most active (111) and (211) iron surfaces must be responsible for the highest catalytic activity in ammonia synthesis. The C_7 sites are present only on these two iron surfaces. This behavior is unlike that of platinum where the catalytic activity for bond breaking of carbon–carbon or carbon–hydrogen correlates with surface roughness. Lack of this type of correlation with surface roughness is perhaps the best evidence that C_7 sites play unique roles in ammonia synthesis.

Unfortunately, there is no LEED-crystallography data on nitrogen chemisorbed on these most active (111) and (211) crystal surfaces of iron. There is data on atomic nitrogen chemisorbed on the iron (100) surface.[192] In this study it was found that nitrogen is adsorbed in a four-fold hollow site and its height above the surface and bond distances to the metal atoms have been determined. Thus chemisorption of nitrogen atoms in high coordination sites is expected. As long as there is no LEED-crystallography data available, based on this scant evidence one could propose that atomic nitrogen is likely to occupy the C_7 sites on both the (111) and (211) iron surfaces. It is hoped that LEED-crystallography of the nitrogen

chemisorption system on (111) and (211) iron surfaces will be studied in the near future.

There are no studies of hydrogen chemisorption on (111) and (211) iron surfaces by LEED crystallography method. However, there are two hydrogen structures reported on the catalytically inactive (110) closely packed iron surface. Hydrogen is believed to occupy a three-fold site on this surface.[193] It will be important to study hydrogen chemisorption and the order of hydrogen on the most catalytically active iron crystal surfaces. We hope that coadsorption of nitrogen and hydrogen will reveal the way nitrogen located on metal surface is changed as it becomes successively hydrogenated to NH, NH_2 and then to ammonia.

It is a pity that open surface of α-Fe single crystal is possibly obtained only under rigorously controlled laboratory conditions. In industrial production, we are ignorant of how the (111) surface of iron exposed fully on the surface of α-Fe crystallites during the manufacture and reduction of catalysts and also how the stability of the (111) surface is retained in the reactor. According to the studies of chemisorptions of CO and CO_2, more than 50% of α-Fe surface is covered by K_2O or KOH. Studies by Ertl *et al.*[119,194] indicated that when there are K_2O or KOH present on the α-Fe surface, the chemisorptions of dinitrogen can be increased by more than one order of magnitude. In the case of Al_2O_3 as promoter, the formation of Fe (111) faces can be induced. While the coverage of KOH or K_2O on α-Fe surface is not practically the fixed one, which can move freely on iron surfaces. Sidorov[195] considered that both adsorbed atoms of nitrogen and hydrogen can transfer toward the undersurface covered with K_2O, hence, covered iron surface is not fully unuseful one.

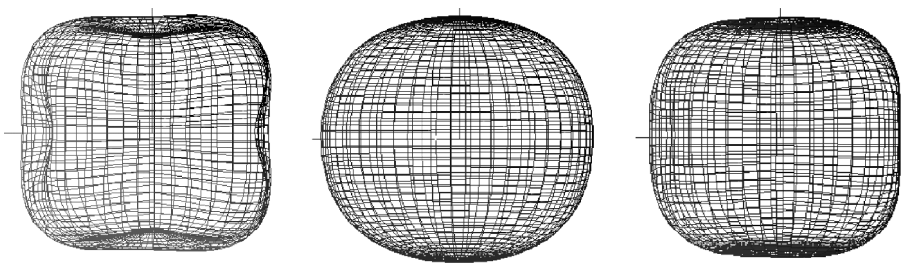
We[153] studied the growth of iron crystal face on different reduced catalysts by *in situ* XRD. It is known that the activity of α-Fe crystal faces are in the order of (111) > (211) > (110). But due to the symmetrical principles of crystals, the most active (111) crystal faces do not appear in XRD. Therefore, we selected faces of (211) and (110) which can be detected by XRD and they represent the high and low activity ones, respectively. Calculation of the ratio of grain size $D_{(211)}/D_{(110)}$ was conducted, which represents the relative extent of growth of two crystal faces, which relates directly to the amount of active sites. The smaller the ratio, the more active sites are. The average ratios of $D_{(211)}/D_{(110)}$ of four catalysts derived from different precursors are showm in Table 3.33.

It is seen from the Table 3.33 that the order of the $D_{(211)}/D_{(110)}$ ratio is as follows: A110 > ICI74-1 > A301 > ZA-5. According to the rule that grain size is contrary to the growth of crystal face, the order of the growth of crystal faces are ZA-5 > A301 > ICI74-1 > A110. This order is consistent with that of the catalytic activity of these catalysts. The $D_{(211)}/D_{(110)}$ ratio of the grain sizes of (211) and (110) crystal faces, which represent the high and low active crystal faces respectively,

Table 3.33 Average ratio of $D_{(211)}/D_{(110)}$ for four catalysts derived from different precursor

Parameter	ICI 74-1	A110-2	A301	ZA-5
$D_{(211)}/D_{(110)}$	0.7342	0.7497	0.7152	0.7072

Notes: A110-2 is Fe_3O_4-based traditionary catalyst, ICI74-1 is cobalt-contained Fe_3O_4-based traditionary catalyst, and A301 and ZA-5 are a novel $Fe_{1-x}O$-based catalyst.



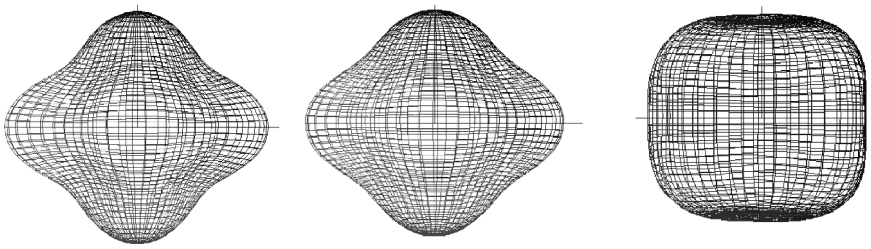
(a) A110 (b) A301 (c) ZA-5

Fig. 3.87 Simulation images of crystal shape of α-Fe derived from three catalysts

are A110 > ICI74-1 > A301 > ZA-5. The order of the crystal face growth, namely the amount of active sites is perfectly consistent with the catalytic activities for four catalysts. These results further proved that the catalytic activity of the active site originates from the growth of highly active crystal face or from the increase of active site numbers.

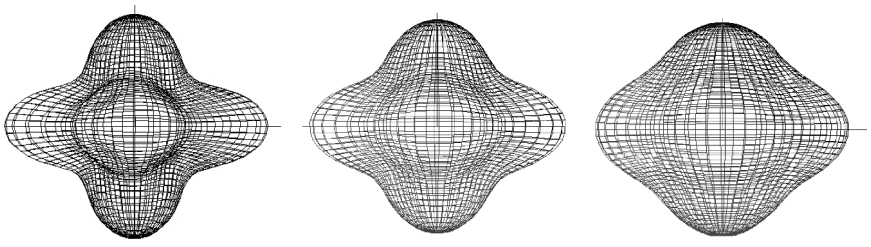
By simulating three dimensional growth morphology for the anisotropic broadening of crystal by Popa patterns,[196,197] the crystal morphological images of the three catalysts are obtained as shown in Fig. 3.87. It is seen from Fig. 3.87 that the crystal forms of α-Fe derived from A110 catalyst are the cubes with cupped crystal faces, among which the growth of (110) crystal face is better, while that of (111) and (211) faces are relatively hypogenesis. The crystal forms of α-Fe crystallite derived from A301 catalyst show a complex types from the spheric and cubic, in which the growth of (111) and (211) crystal faces are obviously better than that of A110 catalyst. The crystal form of α-Fe crystallite derived from ZA-5 catalyst shows a complex type of cubic and spheric. The difference is that ZA-5 shows a cubic as the main, while A301 with spheric. The growth extent of the crystal faces of (111) and (211) of iron on the ZA-5 catalyst is between A110 and A301 catalysts. Hence, the extent of the crystal face growth of (111) and (211) of iron on these catalysts are in the order of A301 > ZA-5 > A110. This is basically consistent with the order of crystal face growth of the catalysts ZA-5 > A301 > A110, which are determined by the help of grain size ratios $D_{(211)}/D_{(110)}$ in Table 3.35. However, the order of ZA-5 and A301 catalysts are of a little variety. This result further proved that the highly active crystal faces of α-Fe crystallite derived from $Fe_{1-x}O$-based catalysts are the more upgrowth than that from Fe_3O_4-based catalysts.

In order to investigate the dynamic evolution of crystal form of α-Fe crystallite on reduced iron catalysts, the fine XRD spectra of the two intermediate states formed respectively at 325°C and 355°C during the reduction of ZA-5 catalyst have been collected and their crystal forms were simulated by Popa pattern as shown in Fig. 3.88. It is seen from Fig. 3.88 that the crystal forms of α-Fe crystallite at both 325°C and 355°C show mainly the octahedrons and especially at 355°C, it shows the rather perfect octahedron and where the crystal face of (111) is the most full-growth. While the crystal forms of α-Fe crystallite turnarounds toward the cube with the increasing temperature or degree of reduction, where the extents of the growth of (111) crystal face decreased inversely.



(a) 325 °C (b) 355 °C (c) 400 °C

Fig. 3.88 Evolutional image of crystal shape of α–Fe derived from ZA-5 catalyst



(a) original (b) 325 °C (c) 355 °C

Fig. 3.89 Evolutional image of crystal shape of precursor during reduction for ZA-5 catalyst

The results studied with high resolution electron microscope and micropolariscope by Borge *et al.* indicated[198−200] that the structure of Fe_3O_4 precursor and the α-Fe crystallite after *in situ* reduction has a certain correlation in the crystallization directions of them, namely, the formation of α-Fe crystallites should be along some direction of magnetite precursors to extend with the nucleations during the reductions, so the direction of the crystallization of them need matching. In order to explore the inherent reason of the formation of octahedral crystal forms of α-Fe crystallite derived from ZA-5 catalyst during the reductions, it was simulated that the crystal forms evolution of α-Fe crystallite derived from $Fe_{1-x}O$ precursor with the progress of reductions as shown in Fig. 3.89. It is seen from the Fig. 3.89 that the crystal form of $Fe_{1-x}O$ precursor during reduction are mainly octahedrons and show a rather consistent synergy with the coexisting α-Fe crystallites. Especially at 355°C, the crystal forms of them are extremely kindred, which is probably one of the reasons why the $Fe_{1-x}O$-based catalysts are reduced easily.

(3) Characterization of active sites. In more fundamental studies, the reaction rateshould not refer to the mass of catalyst or metal, but to the active site. The detection of active sites, including the density (A) and the intensity of active site is a central subject of heterogeneous catalysis. The turnover number or turnover frequency (TOF) on per unit active site per unit time under the given conditions can be calculated according to active site determined. At present, TOF is a basis to obtain the intrinsic activity of metals as well as determine the reaction mechanisms. Due to the dimension of TOF is the reciprocal of second, the comparisons of the

results derived from different researchers or same kind catalysts with different composition should be more believable.

Although the concept, where the active sites are seven irons atomic cluster containing C_7 atom has been accepted commonly,[52,158,201,202], there have ever been various active sites model, including three iron atomic pattern,[203] six iron atomic pattern etc.[185] Hence, how many iron atoms are being accumulated actually on an active site is still out of the definite conclusion. Besides, irrespective of whether there are different active sites or not, and whether the adsorption forms and reaction rates of ammonia formation on various active sites are the same or not, these also are yet out of the unanimous conclusions.

As the total number of the active sites is unknown, it is common practice, to substitute it with the total number of surface metal atoms. The reaction rate expressed as the number of reacting molecules transformed per surface metal atom per second is often called turnover frequency (TOF) and is expressed as $\sec^{-1}$. TOF is currently used to draw fundamental conclusions about the intrinsic activity of metals and the mechanism of the reaction. If defining the amount of iron atoms exposed on the per unit surface as the characterization of active site density (A), then:

$$A = \frac{f_m D_{Fe}}{55.85 S_T}, \quad \mathrm{mol \cdot m^{-2}}, \tag{3.24}$$

$$TOF = \frac{r_m}{3600N} = \frac{55.85}{3600}\left(\frac{r_m}{f_m D_{Fe}}\right), \tag{3.25}$$

where f_m is mass fraction of iron in reduced catalyst; D_{Fe} is the percent of iron atom exposed on surface of the catalyst or the dispersion of metal; S_T is the total specific surface area of the catalyst, $\mathrm{r_m}$ is mass reaction rate, $\mathrm{mol \cdot g^{-1} \cdot h^{-1}}$. Therefore, active site numbers N is $N = AS_T$, $\mathrm{mol \cdot g^{-1}}$.

When promoters are the same, the surface active site densities of fused iron catalysts derived from the different iron oxides are not with the obvious differences, but all about $(7\text{–}\sim 8) \times 10^{-6}$ $\mathrm{mol \cdot m^{-2}}$, while the active site number approx. $(0.9 - 1.2) \times 10^{-4}\,\mathrm{mol \cdot g^{-1}}$, which is in the direct proportion to its specific surface area. It is seen from Table 3.32 that along with the variation of the precursor iron oxides, especially with the increasing content of FeO, the surface active site numbers are not increasing, but seem to be in decreasing tendency. It can be deduced from this that the reason why the $Fe_{1-x}O$ based catalysts show a higher activity than Fe_3O_4 based one is not the fact that the surface active site number of the former is higher than that of the latter.

For example, the ZA-5 $Fe_{1-x}O$ based catalyst contains 92% Fe after reduction, and the concentration of ammonia from outlet of the reactor is 18.94%. Reaction rate is calculated to be 96.50×10^{-3} $\mathrm{mol \cdot g^{-1} \cdot h^{-1}}$ at pressure of 15 MPa, space velocity of $30{,}000\,\mathrm{h^{-1}}$ and temperature of 425°C. The exposure fraction of Fe atoms on surface $\mathrm{D_{Fe}}$ is 0.55% and the number (active sites) of Fe atoms on the surface is 0.902×10^{-4} $\mathrm{mol \cdot g^{-1}}$ according to the CO chemisorption. Therefore, for this catalyst, the TOF of catalytic synthesis ammonia is $0.297\mathrm{s^{-1}}$.

The results mentioned, of course, are obtained under the postulation that the active sites are being composed by the same amount of iron atoms for different catalysts. If the active sites of the different catalysts are composed of the various amounts of iron atoms, then different results may occur. In spite of the active

sites composed of number of iron atoms, the results calculated will only be in multiple with the iron atom numbers of active site, for example, C_7 site containing seven iron atoms, and then the TOF for ZA-5 catalyst under above conditions is about $2s^{-1}$, that is, two ammonia molecules are produced on each active site in per second.

It is rather obvious that the number of active sites will always be lower than that of surface metal atoms, because the latter ones are not energetically equal under the reaction conditions or the active sites consist of nanoensembles of metal atoms (this point should be taken into account for any comparison with homogeneous or enzymatic catalysis). So it is convenient to introduce the concept of real turnover frequency, given by,

$$TOF_R = \frac{TOF}{f_{AS}}, \tag{3.26}$$

where, f_{AS} is the fraction of surface atoms working as active sites.

In fact, the reaction rate r expressed by the molar numbers of reactant that are converted on the per grams of catalyst per second is related with the TOF in the following function[178]

$$r = \frac{5C_m f_m f_{AS} TOF_R}{N_A d_m \phi_{av}}, \tag{3.27}$$

where, N_A is Avogadro's number; Φ_{av} is the average nanosize of metal particles; C_m is the surface concentration of metal atoms; d_m is the true density of metals. Therefore, when the reaction rate *vs* reciprocal Φ_{av} is plotted, for structure insensitive reaction a straight line is obtained, from whose slope the product $f_{AS} \times TOF_R$ can be calculated. Unfortunately there is presently no way to separate the two factors. The situation is more complex for structure-sensitive reactions. In one case, f_{AS} is higher for smaller nanoparticles, for example 0.5–2 nm (Fig. 3.90), giving a rate *vs* $1/\Phi_{av}$ plot, not very different from that of structure-insensitive reactions (Fig. 3.91). In the other cases, the formation of active sites requires large nanoparticles, for example for more than 3 nm size (Fig. 3.92), giving a very typical rate *vs* $1/\Phi_{av}$ plot (Fig. 3.93). As a concluding remark, in the author's opinion, extensive experimentation on the dependence of the reaction rate on metal particle nanosize could

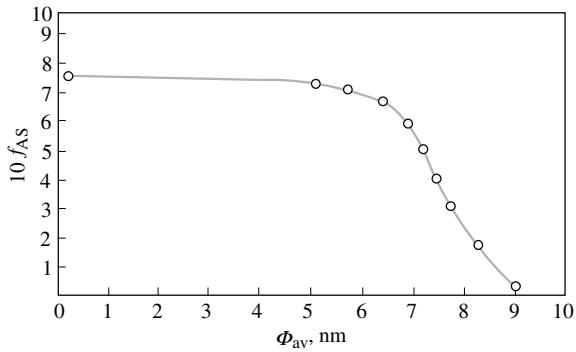


Fig. 3.90 Possible dependence of the fraction of surface atoms working as active sites on metal particle nanosize[178]

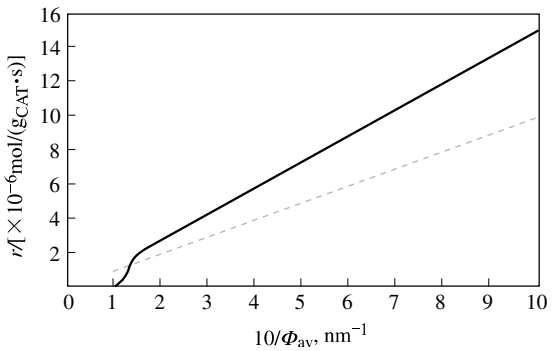


Fig. 3.91 Reaction rate *vs* reciprocal metal particle nanosize.
Dotted orange line[178]: No dependence of the fraction of surface atoms working as active sites on metal particle nanosize (structure-insensitive reactions). Full dark blue line: Dependence of the fraction of surface atoms working as active sites on metal particle nanosize as in Fig. 3.90 (structure-sensitive reactions)

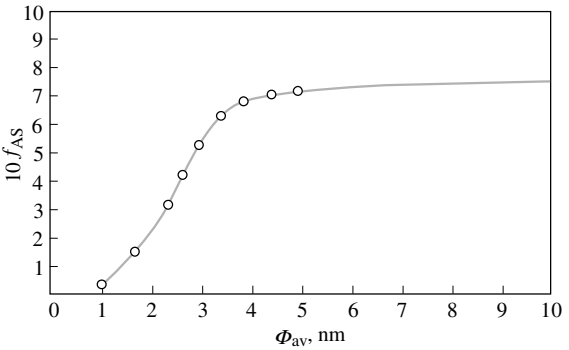


Fig. 3.92 Another possible dependence of the fraction of surface atoms working as active sites on metal particle nanosize[178]

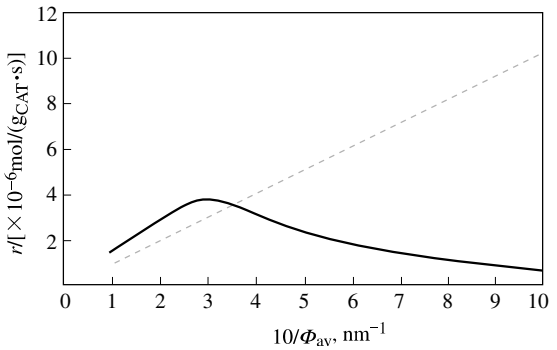


Fig. 3.93 Reaction rate *vs* reciprocal metal particle nanosize.
Dotted orange line: No dependence of the fraction of surface atoms working as active sites on metal particle nanosize (structure-insensitive reactions). Full dark blue line: Dependence of the fraction of surface atoms working as active sites on metal particle nanosize as in Fig. 3.92 (structure-sensitive reactions)

bring some advancement towards the quantitative evaluation of the Holy Grail of catalysis, the active site. Needless to say, such experimentation absolutely depends on the availability of accurate and reliable methods for the measurement of metal particle nanosize.

3.6 About $Fe_{1-x}O$ Based Catalysts and Their Highly Active Mechanism

$Fe_{1-x}O$ based ammonia synthesis catalysts such as A301, ZA-5 show the following excellent characteristics: Extremely easy reduction, very high activity at low reaction temperature and low pressure, high mechanical strength and being applicable at wide range of H_2/N_2 ratio.[51,204,205] Pernicone *et al.*[51] confirmed that catalyst A301, consisting of wustite phase, is much more active than the best magnetite-based catalysts which is used extensively in the world. It can be seen from comparision of activity of catalyst A301 with their best Ru/AC catalyst that they are practically equal, except for very high conversion, where the lower sensitivity of ruthenium to ammonia plays a decisive role. However, it should be stressed that, to give the highest activity, the Ru/AC catalyst requires a H_2/N_2 feeding ratio of 1.0–1.5. Moreover, support degradation by Ru-catalyzed methanation under ammonia synthesis conditions, sometimes accompanied by additional adverse effects due to water traces, can occur, if the carbon support is not properly designed. So, catalyst A301 appears to be competitive with Ru/AC and the related choice should be made on the basis of the specific plant characteristics and working conditions. At the same time, Ru-based catalyst is very expensive and thus less commercially attractive compared to the iron based catalyst. In addition, Ru catalyst does not exhibit obvious advantages for saving energy. Therefore, Ru-based catalyst only has theoretical meaning greater than applied meaning. Therefore, from an industrial point of view, the wustite-based catalyst has also the advantage of being more easily reducible, while thermoresistancy and mechanical strength are fully satisfactory. For this reason, the finding of such kind of new catalyst is an amazing example concerning the classical ammonia synthesis catalyst, as well as a material breakthrough of the studies concerning the ammonia iron catalysts. It is clear that such a discovery has a strong impact on the consolidated scientific knowledge of ammonia catalysts and moreover opens the way to interindustrial application, and thus it questions a century of research and speculations on what can be called a textbook catalyst. It is possible that an extensive and deeper investigation of the new catalyst will bring some revision of the present consolidated knowledge on ammonia synthesis.

Whereas, no matter what kind of iron oxide acts as precursor, the active phase after reduction is all of α-Fe. Why is the catalytic activity able to be improved markedly when the precursor changes from Fe_3O_4 to $Fe_{1-x}O$? Why does the catalytic activity cause the hump-type activity curve along with the variation of iron oxide precursor? How such different types of activities are aroused? All of these new subjects and the hidden scientific hints derived from the discovery of wüstite based catalysts need an extensive and deeper investigation further.

The reason that catalytic activity is improved markedly when the precursor changes from Fe_3O_4 to $Fe_{1-x}O$ is first considered that it is possible for activity to be derived from the increasing iron content. However, based on the experimental

result that the changes of catalytic activity show the hump-like curve, the difference is not mainly caused by the varying iron content. Because the iron content increases monotonically with the increasing Fe^{2+}/Fe^{3+} ratio, while the activity does not. In the second, the iron content of pure $Fe_{1-x}O$ ($x = 0.05$) is only 6.18% higher than that of pure Fe_3O_4, while the activity is increased by 70%.[51] It was regarded that the high activity of catalysts derived from wüstite is due partially to the larger density of itself, but due most importantly to the higher efficiency when the active sites on iron surfaces activate the nitrogen molecules. Hence, some understanding is proposed from two aspects of the precursor composition and surface properties of catalysts. Some understandings from the point of view of chemical–physical properties of $Fe_{1-x}O$ have been given.[206]

First, it must be pointed out emphatically that the fused-iron catalyst with the highest activity should be composed of one iron oxide and one type of crystal structure; the mixture of any two iron oxides or two types of crystal structures in precursor will result in the decrease of catalytic activity of fused-iron catalyst and the larger the mixture degree is, the lower the catalytic activity is. When the two iron oxides were mixed in the equimolar, the catalytic activity will reach the lowest value (as called a single-phase theory). Therefore, high activity can be obtained only when the wüstite phase is present alone in the catalyst, while, when wüstite and magnetite are present together, the catalysts always show a low activity.

Therefore, $Fe_{1-x}O$ catalyst is a novel catalyst for ammonia synthesis which is completely different from the conventional catalyst in chemical composition and crystal structure of the precursor. It is not correct to say that the $Fe_{1-x}O$ based catalyst is the catalyst with high ratio of Fe^{2+}/Fe^{3+}, or the catalyst is only prepared from the different raw material. Therefore, it should be noticed that the $Fe_{1-x}O$ based catalysts as a new generation of fused-iron catalyst have specifically meanings, i.e., it is composed of only one iron oxide — $Fe_{1-x}O$, and only one crystal structure — wüstite in its precursor. It has Fe^{2+}/Fe^{3+} ratio in the range of 4–12 and the high ratio of Fe^{2+}/Fe^{3+} is not an essential character of it. It is a mistake that someone [43] regarded the catalyst with the high ratio of Fe^{2+}/Fe^{3+}, derived from a mix of wüstite and magnetite phases as the $Fe_{1-x}O$ based catalyst. Furthermore, in fact, the main raw material for the preparation of $Fe_{1-x}O$ based catalyst is still magnetite. Therefore, it cannot be garbled that the $Fe_{1-x}O$ based catalyst is the catalyst with high ratio of Fe^{2+}/Fe^{3+}. The presence of wüstite as the only crystal phase in the catalyst precursor is indispensable precondition of the $Fe_{1-x}O$ based catalyst with high activity.

Second, the modern industrial iron catalyst is a nanostructured metastable substance, which is formed during the surprisingly complex synthesis of the oxide precursor. Alternative preparation routes for the nanostructured system are possible and it confirms the complex structure of this seemingly very simple ammonia iron. The fact that $Fe_{1-x}O$ based catalyst has the high activity confirms that the metal surface nanostructure can be drastically changed simply by using different precursors (oxides, for instance). The results show that the high activity of $Fe_{1-x}O$ catalysts mainly comes from the change of preparation routes and the growth of active phase and the development of internal lattice defects, which is the high-activity nature of $Fe_{1-x}O$ catalysts.[207]

With the same promoters, the differences in catalytic activity mainly resulted from the variations in the surface special features, surface structures and the

dispersions of promoters on surface of α-Fe active sites. The excess-coverage of promoters on the surface, obviously, decreases the activity of catalysts. While the excess-coverage and the ununiform distribution of promoters on surface are mainly caused by the crystallization, step-by-step or peritectics in the steps of the cooling and solidification during preparation because different precursor iron oxides have different physical–chemical properties and crystal structures.[208] At the same time, it connects with the reduction mechanism of catalysts in two phase regions in which the reduction of catalyst composed of two iron oxides occurs in turn according to the phases which belong to competitive reduction mechanism.

It can be indicated from the fact that the markedly improved activity of $Fe_{1-x}O$ based catalysts, the active centers and their surrounding microstructures of α-Fe after reduction are in the connection with the chemical characteristics and physical structures of $Fe_{1-x}O$ before reduction. FeO is an oxygen-excessive (Fe vacant) non-stoichiometric oxide and there is the corresponding amount of Fe^{3+} present in the structure of wüstite, which not only ensures the charge neutrality in the lattice, but also offers the extremely advantageous conditions for the migration of Fe^{3+} along with the cavities and the transportation of electron ($Fe^{2+} \rightarrow O \rightarrow Fe^{3+}$). This is the structural reason why $Fe_{1-x}O$ can be reduced easily with H_2. On the other hand, wüstite is non-stoichiometric chemically and the lattice defects and the interspace in the tetrahedrons and octahedrons of them are conveniently filled and replaced by other metal ions. All of these can provide the structural conditions for the adulterating and modifying of $Fe_{1-x}O$ with promoters. The evolution of microstructures of intermediate phases induces possibly the growth of α-Fe crystallite, especially of the (111) crystal face and to improve activity of the (100), (110) crystal faces.

The characteristics of the original microstructures of precursor, e.g., lattice defects, crystal morphology can affect the microstress and the crystal morphology of the active phase of product, namely, there is a certain relationship between them during reduction of catalysts with different structural precursor.[209–212] The results have indicated that the most active regions for nitrogen molecules are frequently in the sites with the largest microstress and the largest defect density.[155] Through the observation of the evolution of microstructure parameters in the active phases such as the analysis of crystal grains distribution and microstress during the reduction of precursors, the differences of the microstructure of the different precursors can be found, relating with activity of them to discuss the relationship between the activity and the microstructures of catalyst.

In order to discuss the influences of different precursors on the microstructures of the reduced catalysts and to simulate the characteristics and regularity of the growth of iron crystal face, by means of structural analysis of XRD peak shape and Rietveld whole spectra fittings to analyze the fine spectra gathered from the *in situ* XRD, the effect of crystallites and stress which caused by the broadenings of diffraction peaks of active phases are accurately separated, and the differences of microstresses in inner of active phases are also inspected. Table 3.34 gives the results of the average size and distribution range of grains and the results calculated by Scherrer equation for Fe (110) crystal face during the reduction of ZA-5 catalyst at 325°C–400°C Table 3.35 is the comparison of the general parameters of microstress of the A110 and ZA-5 catalysts.

Table 3.34 Distribution of crystal size and microstress of iron (110) crystal face on activated ZA-5 catalyst

Temperature/°C	Warren Averbach calculation model: Distribution of crystal size/nm	Warren Averbach calculation model: Average crystal size/nm	Calculated value by Scherrer equation/ nm	Difference of two kind of calculation/ nm	Microstress
325	8.5–20.0	14.3	18.94	4.64	0.0026
350	7.2–21.2	14.2	18.18	3.98	0.0024
375	7.7–22.5	15.0	18.46	3.46	0.0023
400	7.7–22.5	15.0	18.37	3.37	0.0020

Table 3.35 Comparison of general parameters of microstress on two kinds of catalysts

	A110 (Fe_3O_4)		ZA-5 ($Fe_{1-x}O$)	
Temperature/°C	Difference of two kind of calculation method	Microstress	Difference of two kind of calculation method	Microstress
325	—	—	4.64	0.0026
350	3.60	0.0020	3.98	0.0024
375	2.54	0.0021	3.46	0.0023
400	2.91	0.0017	3.37	0.0020
450	1.99	0.0016	—	—
Average	2.76	0.00185	3.86	0.00233

It is seen from Tables 3.34 and 3.35 that the order of the differences of average grain size (influential value of microstress) calculated by two methods is ZA-5 > A110, while the order of the microstress value is ZA-5 > A110.

Both the differences of average grain size and the microstress value are the main parameters for characterizing the presence of lattice defect in activated iron crystals. The order of these two parameters together illustrates that the lattice defect of active sites of catalysts derived from wüstite as precursor are larger than that of the catalysts derived from Fe_3O_4 as precursor.

Due to the growth degree of highly active iron (211) crystal face, values of microstress and influencing value of microstress on grain size of ZA-5 are larger than that of A110, where the order of the three microstructural factors are all in the perfect consistency. So it proved that the growth of iron crystal face and the microstress derived from $Fe_{1-x}O$ based ammonia synthesis catalyst are larger than that of the traditional Fe_3O_4 based one. This also indicates that the highly active mechanism of the former originates mainly from both growth of active phases and the inner lattice defects.

In the structure of catalysts with $Fe_{1-x}O$ as precursor, iron ionic defects result in substantial microstress present in its crystal. During reduction, because of this kind of relative structural instability, it can lead to the decrease of reduction temperature on the one hand, while on the other hand it can affect the reduction products which are of the conjugated growth with itself, making it possess the inherent and rather larger lattice stress in the active phases. The larger the lattice distortion which is delegated by the lattice stress, the higher the activity is.

Simply because the iron oxide precursor of catalyst changes from Fe_3O_4 to $Fe_{1-x}O$, it raises the intrinsic variations of the microstructures of α-Fe active phases after reduction such as the growth of the active sites and the inner lattice defects. It results subsequently in a series of benefits mentioned previously, which include easy reduction and the low temperature; fastened reduction rate and the declined amounts of water produced and redox during reduction (see Sec. 3.2.5); changes of the promoter kinds and their distributions in catalysts (see Sec. 3.3). Consequently, they change the surface characteristics of the reduced catalysts, including the acid and base coverage and their relative ratios on the surfaces, occurrence of the acid and base synergy on the surface (see Sec. 3.2.6), accelerating surface reconstruction (see Sec. 3.5.3), decreasing the adsorption activation energy of nitrogen, weakening the strong chemisorption of hydrogen (see Sec. 3.2.7). As a result of all of these changes, it increases the catalytic activity. While all these changes result from the chemical and physical performances of $Fe_{1-x}O$, the catalysts are highly active only when wüstite is present along in them.

Therefore, the results show that the high activity of $Fe_{1-x}O$ catalysts mainly comes from the change of preparation routes of the oxide precursor from Fe_3O_4 to $Fe_{1-x}O$ and that forms a metastable nanostructure which has high activity derived from the growth of active phase and the development of inner lattice defects.

References

1. Qian YT. *Chemistry of Crystal*. Hefei: University of Science and Technology of China Press, 1988, 327–328.
2. Zhou ZG, *et al. Ferrite Magnetic Materials*. Beijing: Science Press, 1981.
3. Юсфин, Ю С, *et al. Theory of Metallization Process for Iron Ore Raw Materials*, Translated by Hou XL. Beijing: Metallurgical Industry Press, 1991, 78–81.
4. Першеев Д И, Юсфин Ю С, ВегманЕ Ф. и др Изв Вуз Черная Металллугия. **5**: 31–32, 1976.
5. Stolen S, Glockner R, Gronvold F. Thermodynamic and Kinetic Aspects. *Thermochim. Acta*. **256**(1): 91–106, 1995.
6. Greenwood NN and Howe AM. Mössbauer Studies of $Fe_{1-x}O$. *J. Chem. Soc. Dalto Trans.* **1**: 110–116, 1972.
7. Roth WL. *Acta Crystallogr.* **13**: 140–149, 1960.
8. Koch F. and Cohen JB. *Acta Crystallogr.* **B25**: 275–287, 1969.
9. Andersson B and Sletnes JO. *Acta Crystallogr.* **A33**: 268–276, 1977.
10. Garstein E and Cohen JB. *J Solid State Chem.* **33**: 271–272, 1980.
11. Yamamoto A. *Acta Crystallogr.* **B38**: 1451–1456, 1982.
12. Catlow CRA, Stoneham AM. *J. Am. Ceram. Soc.* **64**: 234–239, 1981.
13. Catlow CRA, Fender BEF. *J. Phys.* **C8**: 3267–3274, 1975.
14. Grimes RW, Anderson AB, Heuer AH. *J. Am. Ceram. Soc.* **69**: 619–714, 1986.
15. Press MR, Elli DE. *Phys. Rev. B.* **35**: 9–16, 1987.
16. Schweika W, Hoser A, Carlsson AE. *Phys. Rev. B.* **51**: 771–788, 1995.
17. Cheettham AK, Fender BEF, Taylor RI. *Solid State Phys.* **4**: 2160, 1971.
18. Bransky I, Tannhauser DS. *Physica.* **37**: 547, 1967.
19. Su MZ. *Introduction to Solid State Chemistry*, Beijing: Beijing University Press, 1987, 150–151.
20. Darken LS, Gurry RW. *J. Am. Chem. Soc.* **67**: 1398–1403, 1945.
21. Castelliz L, Sutter W, Halla F. *Monatsh Chem.* **85**: 487–492, 1954.

22. Fischer WA, Hoffmann A, Shimada R. *Arch Eisenhtittenwes.* **27**: 521, 1956.
23. Greenwood NN, Howe A. *J. Chem. Soc. Dalto Trans.* **1**: 116–121, 1972.
24. Pattek Janczyk I A. *Appl. Catal. A: General.* **124**: 267–280, 1995.
25. Li XF. Microstructure, Structural Staibility and Macro Properties of Elementarily Dopped Wüstite, Dissertation, Hangzhou: Zhejiang University of Science and Technology, 2006.
26. Liu HZ, Li XN. *Chinese Journal of Chemistry and Engineering*, **49**(5): 534–541, 1998.
27. Figurski MJ, Arabczyk W, Lendzion, Bielún Z, *et al. Appl. Catal. A: General.* **247**: 9–15, 2003.
28. Trimm DL. *Design of Industrial Catalysts*, translated by Jing shenyong, Cao Meizao, Beijing: Chemical Industry Press, 1984.
29. Chen JX. *Steelmaking Common Chart and Data Handbook*, Beijing: Metallurgical Publishing House, 121–130, 1984.
30. Wu Y. *Catalytic Chemistry.* Beijing: Science Press, 1999, 725.
31. Su MZ. *Introduction to Solid State Chemistry.* Beijing: Beijing University Press, 1987, 100–109.
32. Huang ZT. *Industrial Catalysis.* Beijing: Chemical Industry Press, 1994, 51–58.
33. Timm B. In: Dechema (ed.) *Ammonia Synthesis and Heterogeneous Catalysts,* Proc. 8th Int. Congr. Catal. Weinheim: Verlag Chemie, 1984, 7.
34. Almquist JA, Criffenden ED. *Ind. Eng. Chem.* **18**: 1307–1309, 1926.
35. Bridger GL, Pole GR, Beinlch AW, *et al. Chem. Eng. Progr.* **43**(6): 291, 1947.
36. Xiang DH, Liu HY. *Practical Handbook of Chemical Fertilizer Catalysts*, Beijing: Chemical Industry Press, 1992, 264.
37. Strel'tsov OA, Dvornik OS, Lytkon VP. Izv Vyssh Uchebn Zavedcnii: Khimi Khim Teknol, **20**(11): 1622–1626, 1977.
38. Artyukh YN, Fedun OS, Zyuzya LA. *Katal. Katal.* **18**: 20–23, 1980.
39. Li LM, Wang WX. *J. College Chemistry*, **4**(6): 763–768, 1983.
40. Liu HZ, Li XN. *Science in China* (Series B). **38**(5): 529, 1995.
41. Liu HZ, Ning WS, Fu GP, *et al. J. Chem. Ind. Eng.* **50**(5): 671–677, 1999.
42. Liu HZ, Hu ZN, Li XN, *et al. J. Chem. Ind. Eng.* **45**(4): 385–392, 1994.
43. Liu HZ, Li XN. *Science in China* (Series B), **25**(1): 1–6, 1995.
44. Liu HZ, Li XN, Hu ZN. *Appl. Catal. A: General*, **142**: 209–222, 1996.
45. Liu HZ, Li XN, Suzuki S, *et al. J. Chem. Ind. Eng.* **51**(4): 462–467, 2000.
46. Liu HZ, Li XN. in *Studies in Surface and Catalysis* (Part C). 12th International Congress on Catalysis, Elsevier, 2000, 2207–2212.
47. Liu HZ. *Chinese Journal of Catalysis*, **22**(3): 304–16, 2001.
48. Trimm DL. In: Delmon B, Jacobs PA, PoceletG (eds.) *Preparation of Catalysts* II-*Scientific Bases for Preparation of Heterogeneous Catalysts*, translated by Wan Ren, Beijing: Chemical Industry Press, 1985, 6–8.
49. Liu HZ, Li XN. *Journal of Chemical Industry and Engineering* (China), **48**(3): 354–362, 1997.
50. Liu HZ, Hu ZN, Li XN, *et al. Journal of Chemical Industry and Engineering* (China) **52**(12): 1063–1067, 2001.
51. Pernicone N, Ferrero F, Rossetti I, *et al. Appl. Catal. A: General*, **251**: 121–129, 2003.
52. Schütze J, Mahdi W, Herzog B, Schlögl R. *Topics in Catalysis.* **1**: 195–214, 1994.
53. Clausen BS, Morup S, Topsoe H. *Phys. Collog.* **37**: 6–245, 1976.
54. Muller J. *Rev. Pure Appl. Chem.* **19**: 151, 1969.
55. Emmett PH, Brunauer S. *J. Am. Chem. Soc.* **59**: 1553–1564, 1937.
56. Nielsen A, Bohlbor H. *J. Am. Chem. Soc.* **74**: 963–966, 1952.
57. Emmett PH, Takezawa N. *J. Res. Inst. Catalysis Hokkaido Univ.* **26**(1): 37–52, 1978.
58. Nielsen A. *Catal. Rev.-Sci. Eng.* **23**(1&2): 17–51, 1981.

59. Streltsov OA, Dvornik OS, Lytkin VP. *Bulletin of the Institute of Higher Education Chemistry and Chemical Engineering*, **20**(110): 1662–1666, 1977.
60. Xiang D, Liu H. *Fertilizer Catalyst Practical Manual*, Beijing: Chemical Industry Press, 1992, 265.
61. Almquist J, Crittenden E. *Ind. Eng. Chem.* **18** CTP: 130, 1926.
62. Blasiak E. *Technolgia Zwiazkow Azomo WYCH*, Toml, Amoniak Syntetgczny, Warszawa, 464–466, 1995.
63. Slack AV, James GR. *Ammonia. Part* , New York: Marcel Dekker Inc, 1987, 85–93.
64. Kradetz R, Peters C. *Angew Chem. Int. Ed.*, **4**: 341, 1965.
65. Liu HZ, Liu CB, Li XN, Cen YQ. *Ind. Eng. Chem. Res.* **42**(7): 1347, 2003.
66. Urabe K, Aika K, Ozaki A. *J. Catal.* **42**: 197, 1976.
67. Rambeau G, Amariglio H. *J. Catal.* **72**: 1, 1981.
68. Siporin SE, Davis RJ. *J. Catal.* **225**: 359, 2004.
69. Hikita T, Aika K. *J. Phys. Chem.* **95**: 9396, 1991.
70. Niwa Y, Aika K. *Chem. Lett.* **25**(1): 3, 1996.
71. Siporin SE, Davis RJ. *J. Catal.* **222**: 315, 2004.
72. Li ZL. TAP Studies for Ammonia Synthesis and Dissociation on Carbon Nano Fiber Supported Catalysts, Disseratation, Dalian: Dalian Institute of Chemical Physics, Chinese Academy of Sciences, 2004.
73. Guan S, Liu HZ. *Ind. Eng. Chem. Res.* **39**(8): 2891, 2000.
74. Bozso F, Ertl G, Grunze M, Weiss M. *J. Catal.* **49**: 18, 1977.
75. Spencer ND, Schoonmaker RC, Somorjai GA. *J. Catal.* **74**: 129, 1982.
76. Somorjai GA, Materer N. *Topics in Catalysis.* **1**(3&4): 215–231, 1994.
77. Chen GR, *et al. Encyclopedia of Chemical Industry* VI, Editorial Board of Encyclopedia of Chemical Industry, Beijing: Chemical Industry Press, 1994.
78. Zhao JH, Song CY, Wang LC. *Structure and Molecular Design of Catalysts.* Beijing: Worker Press, 1998.
79. Xu Y. *Technology for Catalyst Design and Preparation.* Beijing: Chemical Industry Press, 2003.
80. Trim DL. *Design for Industrial Catalyst*, Translated by Jin XY, Cao MZ, Beijing: Chemical Industry Press, 1984.
81. Jacobsen CJH, Dahl S, Clausen BS, *et al. J. Am. Chem. Soc.* **123**: 8404–8405, 2001.
82. Banares AR, Westerberg AW, Ko EI, *et al. Computers & Chemical Engineering*, **11**(3): 265, 1987.
83. Banares AR, Ko EI, A Westerberg W, *et al. Computers & Chemical Engineering*, **12**(9&10): 923, 1988.
84. Koertintg E, Baerns M. *Comput. Aided Innovation* — New Mater 2. Amsterdam: Netherland, 1992, 1101.
85. Speck H, Hoelderich W. *Decheme Monogr.* **116**: 43, 1989.
86. Huang ZN, Liao DW, Lin YZ, *et al. Journal of Xiamen University* (Natural Science Edition), **35**(3): 389, 1996.
87. Huang ZN, Liao DW, Lin YZ, *et al. Journal of Xiamen University* (Natural Science Edition), **35**(5): 739, 1996.
88. Huang ZN, Liao DW, Zhang HB, *et al. Computer and Applied Chemistry*, **13**(3): 167, 1996.
89. Sun J, Xu M, Liao DW. *Computer and Applied Chemistry*, **21**(2): 245–248, 2004.
90. Kito S, Hamada H, Kintaichi Y, *et al. Catal. Today*, **10**: 223, 1991.
91. Kito S, Hattori T, Murakami Y. *Ind. Eng. Chem. Res.* **31**: 979, 1992.
92. Hou ZY, Dai QL, Wu XQ, *et al. Appl. Catal.* **161**: 183, 1997.
93. Han LQ. *Chemical Journal.* **50**(4): 500, 1999.
94. Huang K, Chen F, Lu D. *Appl. Catal.* **219**: 61, 2001.
95. Huang K, Zhan X, Chen F, *et al. Chemical Engineering Science*, **58**: 81, 2003.

96. Liu Y, Liu Y, Liu DZ, *et al. Computers & Chemical Engineering*, **25**: 1711, 2001.
97. Corma A, Serra JM, Serna PS, *et al. J. Catal.* **229**: 513, 2005.
98. Lu T, Chen DZ. *Computer Engineering and Applications*, **4**: 60, 2005.
99. Chai J, Jiang QY, Cao ZK. *Pattern Recognition and Artificial Intelligence*, **15(**3): 310, 2002.
100. Dorigo M, Maniezzo V, Colorni. Ant System: An Autocatalytic Optimizing Process. Technical Report, 1991, 91.
101. Anderson JR. *Structure of Metal Catalyst*. Beijing: Chemical Industry Press, 1985, 256–261.
102. Schafer KZ. *Electrochem.* **64**: 1190, 1194, 1996.
103. Hosemann R, Preisinger A, Vogel W. *Ber Brnsenges*, **70**: 796, 1966.
104. Hosemann R, Lemm K, Schionfeld A, Wilke W. *Kolloid Z.* 216–217: 103, 1967.
105. Hosemann R. *Chem. Ing. Tech.* **42**: 1252, 1325, 1970.
106. Topsoc H, Dumesic JA, Boudart M. *J. Catal.* **28**: 477, 1973.
107. Solbakken V, Solbakken A, Emmett PH. *J. Catal.* **15**: 90, 1969.
108. Maxwell LR, Smart JS, Brunauer SF. *Chem. Phys.* **19**: 303, 1951.
109. Chen HC, Anderson RB. *J. Coll. and Interface Sci.* **38**: 535, 1972.
110. Arabczyk W, Narkiewicz U, Moszynski D. *Langmuir.* **15**: 5785–5789, 1999.
111. Schlögl R. *Catalytic Ammonia Synthesis, Fundamental and Practice*. New York: Plenum Press, 1991, 19.
112. Dry ME, Ferreira LC. *J. Catal.* **7**: 198, 1967.
113. Li XN, Liu HZ, Chen SY. *Chinese Journal of Catalysis*, **19**(3): 201–205, 1998.
114. Li LM, Wang WX. *Chemical Journal of Chinese Universities.* **4**(6): 763, 1983.
115. Lendzion BZ, Arabczyk W. *Appl. Catal. A: General*, **207**(1&2): 37, 2001.
116. Almquist JA, Crittenden ED. *Ind. Eng. Chem.* **18**: 866, 1926.
117. Nielsen A. *Catal. Rev.* **4**(1): 1, 1970.
118. Jiang SJ, *et al. Ammonia Synthesis Engineering*, Part III. Beijing: Petrochemical Press, 1977, 224.
119. Ertl G, Weiss M, Lee SB. *Chem. Phys. Lett.* **60**: 391, 1979.
120. Van Ommen JG, Bolink WJ, Prasad J, *et al. J. Catal.* **30**: 120, 1975.
121. Arabczyk W, Narkiewicz U, Kalucki K. *Vacuum*, **45**(2&3): 267–269, 1994.
122. Paal Z, Ertl G, Lee SB. *Appl. Surf Sci.* **8**: 231, 1981.
123. Ertl G, Lee SB, Weiss M. *Surf Sci.* **114**: 527, 1982.
124. Lee SB, Weiss M, Ertl G. *Surf Sci.* **108**: 357, 1981.
125. Ertl G. In: Jennings JR (ed.) *Catalytic Ammonia Synthesis, Fundamental and Practice*. New York: Plenum Press, 1991, 109.
126. Kowalczyk Z. *Catal. Lett.* **37**: 173, 1996.
127. Strongin DR, Somorjai GA. *J. Catal.* **109**: 51, 1988.
128. Somorjai GA, Materer N. *Topics in Catalysis*, **1**: 227, 1994.
129. Garfunkel EL, Somorjai GA. In: Bonzel HP, Bradshaw AM, Ertl G (eds.) *Physics and Chemistry of Alkali Metal Adsorption*, Amsterdam: Elsevier, 1989.
130. Sintez A, Kuznetsov LD (eds.) Moscow: Chimia, 1982, 105.
131. Spencer MS. *Catal. Lett.* **13**: 45, 1992.
132. Overbury SH, *et al. Chem. Rev.* **75**: 547, 1975.
133. Ponec V. *Catal. Rev. Sci. Eng.* **11**: 41, 1975.
134. Sachtler WMH. *Catal. Rev. Sci. Eng.* **14**: 193, 1976.
135. Sachtler WMH, *et al. Adv. Catal.* **26**: 69, 1977.
136. Menon PG, *et al. Catal. Rev.* **20**: 97, 1979.
137. Somorjai GA, Materer N. *Topics in Catalysis*, **1**: 228, 1994.
138. McIntyre B, Somorjai GA, Salmeron M. *Rev. Sci. Instr.* **64**: 687, 1993.
139. McIntyre B, Salmeron M, Somorjai GA. *Catal. Lett.* **14**: 263, 1992.
140. Emmett PH, *et al. J. Am. Chem. Soc.* **59**: 310, 1932.

141. Lendzion-Bielu'n Z, Arabczyk W, Figurski M. *Appl. Catal. A.* **227**: 255, 2002.
142. Liu HZ, Li XN. *Ind. Eng. Chem. Res.* **36**(2): 335–341, 1997.
143. Dry ME, Ferreira LC. *J. Catal.* **7**: 352, 1967.
144. Winkler HGF. *Structure and Nature of Crystal.* Beijing: Science Press, 1960, 64.
145. Kearby KK. In: Emmett PH (ed.) *Catalysis.* Vol □. New York: Rheinhold, 1955, 469.
146. Flick, *et al.* USP 5846507. 1996.
147. Pernicone N, Traina F. In: Leach B (ed.) *Applied Industrial Catalysis*, Vol. 3, Chapter 1, London: Academic Press, 1984.
148. Li XN, Liu HZ. In: Proceedings of the 17th NACS Meeting, Toronto, Canada: 2001, 227.
149. Li T, Zhu Y, Li SS, *et al. Journal of East China University of Technology*, **26**(3): 256–259, 2002.
150. Bokhoven C, van Heerden C, Westrik, *et al.* In: Emmett PH (ed.) *Catalysis*, Vol. 3, New York: Reinhold, 1995, 265.
151. Westrik R, Zwietering P. *Proc. Konin Nederlandse Akad.* **B56**: 492, 1953.
152. Zwietering P, Koks HLT. *Nature.* **173**: 683, 1954.
153. Zheng YF, Liu HZ, Liu ZJ, Li XN. *Journal of Solid State Chemistry*, doi: 10. 1016/j. jssc. 2009. 06. **030**: 1–7, 2009.
154. Wu QH. *Surface Chemistry and Heterogeneous Catalysis.* Beijing: Chemica Industry Press, 1991, 30.
155. Homann K, Kuhlenbeck H, Freund HJ. *Surf Sci.* **327**(3): 216–224, 1995.
156. Silverman, DC, Boudart M. *J. Catal.* **77**: 208, 1982.
157. Ertl G, Lee SB, Weiss M. *Surf Sci.* **111**: L711, 1981.
158. N∉rskov JK. *Topics in Catalysis*, **1**: 385–403, 1994.
159. Børge H, Johan T. *J. Catal.* **152**: 243–251, 1995.
160. Børge H. *J. Catal.* **167**: 12–24, 1997.
161. Papageorgopoulos CA, Chen JM. *Surf Sci.* **52**: 40, 1975.
162. Arabczyk W, Narkiewicz U, Moszynski D. *Appl. Catal. A.* **182**: 379, 1999.
163. Connel G, Dumesic JA. *J. Catal.* **92**: 17, 1985.
164. Altenburg K, Bosch H, van Ommen JG, *et al. J. Catal.* **66**: 326, 1980.
165. Horiguchi T, Nakanishi S. *Jpn. J. Appl. Phys. Suppl.* **2**: 2, 1974.
166. Legg KO, Jona F, Jepsen DW, *et al. Phys. Rev. B.* **16**: 5271, 1977.
167. Arabczyk W, Dissertation B, Tech. Univ. Dresden, 1986.
168. Fastrup B. *J. Catal.* **150**: 345, 1994.
169. Muhler M, Rosowski F, Ertl G. *Catal. Lett.* **24**: 317, 1994.
170. Weinberg G, Beran B, Muhler M, *et al. Appl. Catal. A: General*, **163**: 83, 1997.
171. Ertl G, Prigge D, Schlogl R, *et al. J. Catal.* **79**: 359, 1983.
172. Ertl G, Thiele N. *Appl. Surf Sci.* **3**: 99, 1979.
173. Aika K, Christiansen L. *Ammonia Catalysis and Manufacture*, Berlin: Springer Verlag, 1995.
174. Brill R. *J. Catal.* **19**: 236, 1970.
175. Bare SR, Strongin DR, Somorjai GA. *J. Phys. Chem.* **90**: 4726, 1986.
176. Strongin DR, Carrazza J, Bare SR, Somorjai GA. *J. Catal.* **108**: 289, 1987.
177. Strongin DR, Somorjai GA. *J. Catal.* **118**: 99, 1989.
178. Pernicone N. *Cattech.* **7**(6): 196–204, 2003.
179. Zhang ZK, Cui ZL, Chen KZ. *J. Mater. Sci. Technol.* **12**: 75–77, 1996.
180. Brill R, *Bunsenges Ber. Phys. Chem.* **15**: 455, 1971.
181. Brill R, Richter EL, Ruch E. *Angew Chem.* **6**: 882, 1967.
182. Spencer ND, Schoonmaker RC, Somorjai GA. *J. Catal.* **74**: 129–135, 1982.
183. Dumesic JA, Tops EH, Boudart M. *J. Catal.* **37**: 513, 1975.
184. Somorjai GA, Castner DG, Blacksdar RL. *J. Catal.* **66**: 257, 1980.

185. Huang KH. In: Seigama T, Tanabe K (ed.) *Proc. 7th Intern. Congr. Cataltsis*, Tokyo: Kodansha Tok, 1981, 554.
186. Xin XQ, Zhu LG, Meng QJ, *et al. J. Chemistry*, **35**(3&4): 141, 1977.
187. Watson PR, Van Hove MA, Hermann K. *NIST Surface Database* (SSD). NIST Standard Reference Data Program, Gaithersburg, MD, 1993.
188. Starke U, Van Hove MA, Somorjai GA. *Progr. Surf Sci.* **46**: 305, 1994.
189. Somorjai GA, Materer N. *Topic in Catalysis*, **3&4**, 218, 1994.
190. Sokolov J, Shih HD, Bardi U, *et al. J. Phys. C.* **17**: 371, 1984.
191. Sokolov J, Jona F, Marcus PM. *J. Solid State Commun.* **49**: 307, 1984.
192. Imbihl R, Behm RJ, Ertl G, *et al. Surf Sci.* **123**: 129, 1982.
193. Moritz W, Imbihl R, Behm RJ, *et al. J. Chem. Phys.* **83**: 1959, 1985.
194. Ertl G, *et al. Appl. Surf Sci.* **8**: 23, 1981.
195. Sidorov LP, Istomina KE. *CA.* **54**(5&7): 6049, 1960.
196. Popa NC. *J. Appl. Crystallogr.* **31**(2): 176–180, 1998.
197. Popa NC. *J. Appl. Crystallogr.* **25**: 611–616, 1992.
198. Holme B, Tafto J. *J. Catal.* **152**: 243–251, 1995.
199. Pennock GM, Flower HM, Andrew SPS. *J. Catal.* **103**(1): 1–19, 1987.
200. Taftoe J, Kristiansen LA, Fuglerud T. *Philos. Mag. Lett.* **64**(2): 105–109, 1991.
201. Budart M, Djéga-Mariadassou G. *Kinetics of Heterogeneous Catalysis*, Translated by Gao Z, Zhen SA, Li CR, *et al.* Shanghai: Fudan University Press, 1988, 148.
202. Lu JX. *Chinese Science Bulletin.* **20**(12): 540–543, 1975.
203. Kobozev NJ. *Acta Physicochim* (USSR), **9**: 805, 1938.
204. Liu HZ, Xu RY, Jiang ZhR, *et al.* Europea Patent 0763379. 1994.
205. Liu HZ, Li XN, Hu ZN, *et al. Fertilizer Industry.* **26**(4): 17, 1999.
206. Liu HZ, Li XN. *Chinese Journal of Catalysis*, **26**(1): 79–86, 2005.
207. Schlögl R. *Angew Chem. Int. Ed.* **42**, 2004–2008, 2003.
208. Liu HZ, Li XN, Hu ZN, *et al. Chemical Journal of Chinese Universities*, **23**(1): 87–91, 2002.
209. Wang YH. *Fundamental X-ray Diffracting Techniques*, Beijing: Atomic Energy Press, 1985, 258–262.
210. Gubicza J, Szepvolgyi J, Mohai I, *et al. Materials Science and Engineering*, **A280**(2): 263–269, 2000.
211. Vives S, Gaffet E, Meunier C. *Materials Science and Engineering*, **A366**(2): 229–238, 2004.
212. Ortiz AL, Shaw L. *Acta Materialia.* **52**(8): 2185–2197, 2004.

This page intentionally left blank

Chapter 4

Preparation of Fused Iron Catalysts

4.1 Technology and Equipments for the Preparation of Fused Iron Catalysts

Although molten method is used extensively in modern industry as the standard method for the manufacture of catalysts of ammonia synthesis, other methods were also used such as the Farbenfabriken Bayer method.[1,2] In this method, cyanide iron compounds such as potassium ferrocyanide, and potassium aluminum ferrocyanide or calcium ferrocyanide were used as raw materials, which thermally decomposed into intermediates, ferric carbides and iron nitrides after they were heated in H_2 atmosphere and finally transformed into α-Fe by the usual activation method. This technology can only be used under certain conditions. Precipitation is another method. For example, the iron hydroxide and aluminum hydroxide are co-precipitated by flowing ammonia gas into aqueous solution containing ferric nitrate and aluminum nitrate. After other promoters are added, they are calcined into oxides. The application of this method is also limited, although it is the only method for the preparation of Fe_2O_3-based catalysts.[3] The main non-molten technology is the sintering process, which is used for the production of shaped catalysts.[4−10]

The molten method was the initial method for the preparation of iron catalyst. The conventional oxygen melting technology is that the pure iron (for e.g., iron or the horseshoe nail made from carbon in Sweden) is burned in the oxygen flow to produce Fe_3O_4. Actually, this technology has been replaced by the molten method, in which natural or synthetic magnetite and promoters were melted in an electric furnace. The character of molten method is that the magnetite is a stable iron oxide even when the temperature is higher than 1,000°C in air. The magnetite has solvent effect on the promoters such as Al_2O_3 and MgO, and then it can transform into the ultra-active crystal phase of α-Fe. In addition, the high electric conductivity of magnetite makes it possible to adopt the economic electric furnace technology. Generally, the magnetite is the optimal iron oxide to be used for molten method.

Presently, the Fe-based ammonia synthesis catalysts used in industry are produced by traditional molten method, and are also known as fused iron catalysts. The advantages of molten method include simple processes, easy operation, low cost and excellent performance of product. Even though there are some differences in the chemical composition and catalytic performance of various types of fused iron catalysts, their manufacture process is mainly the same as follow.[11,12]

1. Purification of raw materials.
2. Proportion and mixing of materials.

3. Melting of materials.
4. Discharging and cooling.
5. Crushing and sieving.
6. Reduction (for preparation of prereduced catalysts).

The preparation process flow-sheet of fused iron catalysts by molten technology is shown in Fig. 4.1. In general, the process is carried out as follows: First, the impurities of SiO_2, S and P etc. are removed from magnetite (natural, synthetic or a mixture) by a variety of magnetic separation methods. Second, the various promoters (Al_2O_3, KNO_3, $CaCO_3$ etc) of desired amount are added into the purified magnetite. Third, the magnetite and promoters are mixed in the mixer, and then the mixture is melted at about 1,600–3,000°C in the electric furnace (the melting point of Fe_3O_4 is 1,597°C) for several hours. The fused slurry is released and flows into the cooling trough with water jacket. After cooling, the solid is crushed and sieved into particles with different sizes. Finally, the catalyst products are packaged in an airtight metallic pail. Particles with the size less than 1.5 mm are returned to the electric furnace to remelt. In Fig. 4.1 the schematic diagram of preparing fused iron catalysts by molten technology is shown, in which the particles of size larger than the standard are returned to the crusher. The catalysts which need to be prereduced are sent to the reduction section, where they are reduced by N_2–H_2 mixture. Figures 4.2 and 4.3 are the sketch maps of the electric resistance furnace equipment for melting and the scene photo of the fused slurry flowing into the cooling trough, respectively. In the case of electric arc furnace, the process is similar as that in Fig. 4.1. Because of the high-temperature of the electric arc furnace (the arc flame temperature can be as high as 4,000–5,000°C) and the low-feed loading, the melting time is much shorter. The fused slurry flows into a turn plate-type cooler or a pedrail-type cooler and is cooled by fan or free air.

The preparation conditions of each step significantly influence the physical properties and catalytic performance of the catalyst. The key steps for production of ammonia synthesis catalysts by melting method are the purification of raw materials, controlling of Fe^{2+}/Fe^{3+} ratio, and the cooling speed during the solidification process.

4.1.1 *Purification of raw materials*

The production of fused iron catalyst is actually a "one boiler type" process. Therefore, all the raw materials remain in the ultimate product except for the volatile gases. Hence, the purity of raw materials is very important to insure the quality of the catalyst. The raw materials for the fused iron catalyst are mainly natural magnetite, promoters such as potassium nitrate (KNO_3) or potassium carbonate (K_2CO_3), alumina (Al_2O_3), calcium carbonate ($CaCO_3$), magnesium oxide (MgO), and other oxides or nitrates such as cerium nitrate ($Ce(NO_3)_3$) etc. as well as pure iron, which is used to control Fe^{2+}/Fe^{3+} ratio. Except refined magnetite, other materials are all commercial products (CP grade), in which the amount of chlorine, sulfur and phosphorus as well as the heavy metals such as Pb, Cd and As must be strictly controlled. In general, the amount of chlorine, sulfur and phosphorus should be less than 0.01%.

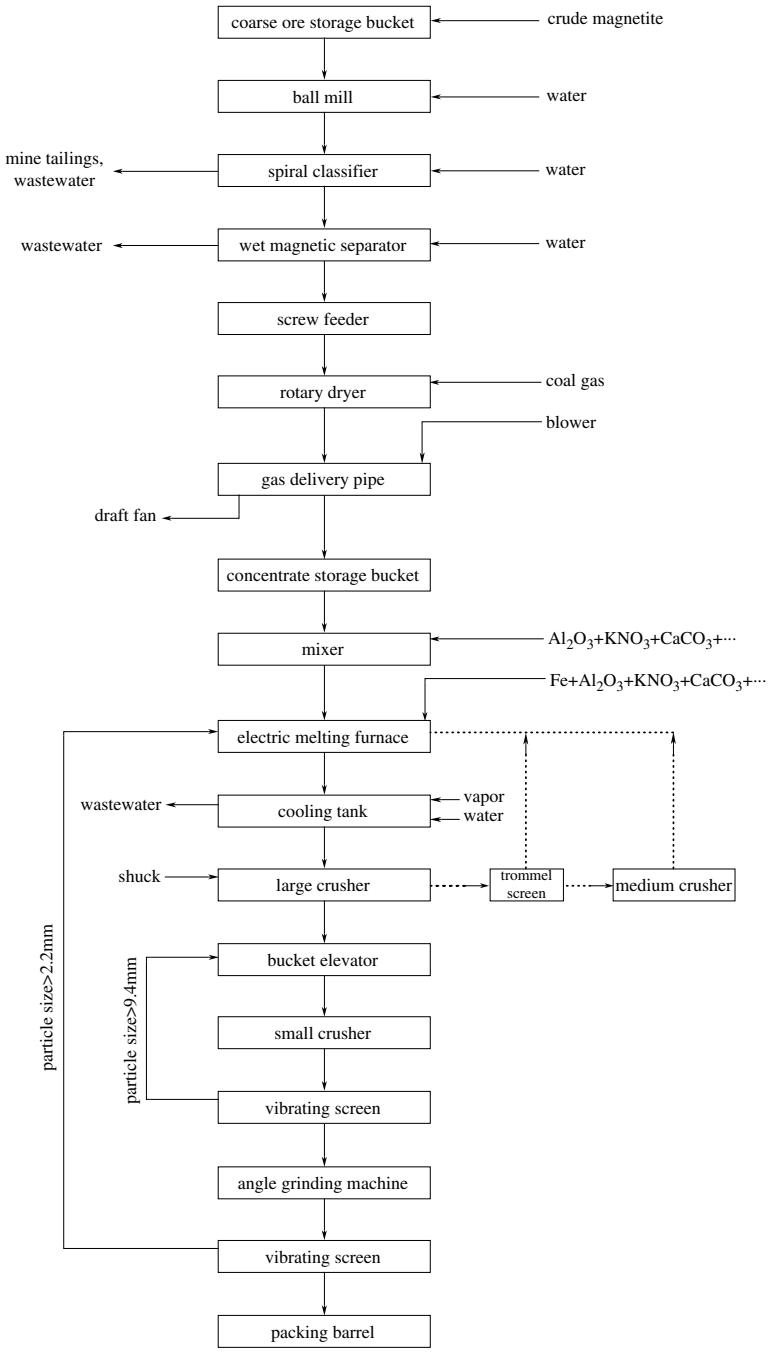


Fig. 4.1 Schematic diagram of preparing fused iron catalysts by molten technology

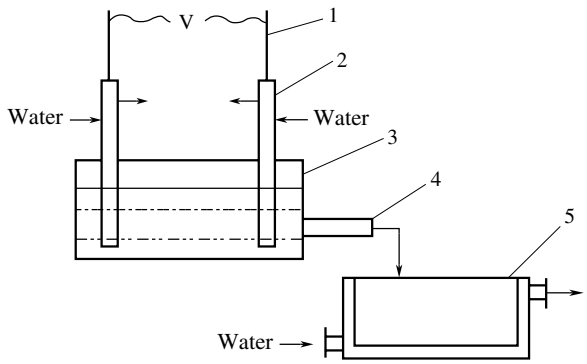


Fig. 4.2 Schematic diagram of electric resistance melting furnace devices
1, Electric cable; 2, Electrode with water jacket; 3, Steel furnace body; 4, Discharge port; 5, Cooling trough with water jacket.

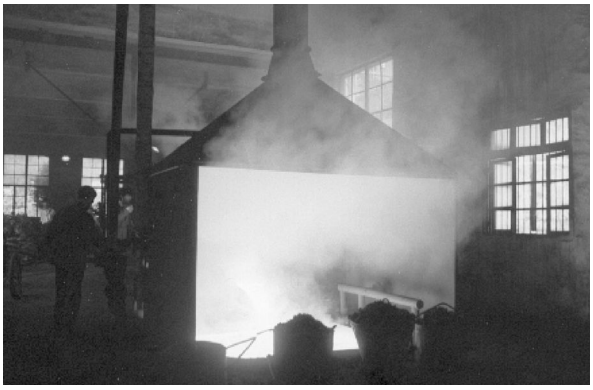


Fig. 4.3 Situation of fused slurry flowing into the cooling trough during preparation of fused iron catalyst

Among all the materials involved in the preparation of the catalysts, the content of the refined magnetite is between 70% and 95%, which is also the major source of the silicon dioxide and harmful impurities such as sulfur. Therefore, the quality of magnetite must be strictly controlled. The chemical composition of natural magnetite is listed in Table 4.1.

It is found that the natural magnetite is superior to the synthetic one. Very pure natural magnetite, such as Kiruna ore of Sweden, can be directly used to prepare the catalyst without refining. Natural magnetite such as Shandong ore of China usually needs to be refined *via* magnetic separation.

Natural magnetite is usually refined by the magnetic separation system including ball mill, classifier, magnetic separator and dryer. After refining, the content of SiO_2 can drop to below 0.4%. However, SiO_2 is also a structural promoter. For example, the content of SiO_2 in KM catalyst from Topsøe is higher than 0.5%. However, the nature of SiO_2 in the natural magnetite is different from that in KM catalyst. In natural magnetite, SiO_2 is often symbiotic with sulfur (especially for the symbiotic

Table 4.1 Composition of natural magnetite (wt in %)

Area	Total iron	Fe^{2+}/Fe^{3+}	FeO	SiO_2	Al_2O_3	CaO	MgO	K_2O	Na_2O	S	P_2O_5	TiO_2
Shandong	71.16	0.40	26.09	0.33	—	—	—	—	0.005	0.006	0.011	0.31
Huoshan	70.95	0.44	28.00	0.36	—	—	—	—	0.21	0.001	0.025	2.02
Jinjiang	71.23	0.40	25.60	0.23	—	—	—	—	0.004	0.004	0.02	0.20
Yingshan	71.90	0.44	—	0.19	—	—	—	—	—	0.003	0.003	0.20
Sweden[a]	—	—	29.31	0.38	0.49	0.04	0.32	0.053	—	0.011	0.01	0.38
Sweden[a]	—	—	29.17	0.41	0.35	0.04	0.26	0.013	—	0.009	0.015	0.25
Sweden[a]	—	—	29.0	0.34	0.34	0.06	—	0.22	—	0.027	0.01	0.22

[a]The standard sample of Kiruna ore, from AV Slark, ≪ Ammonia Synthesis *III* ≫ p. 98.

minerals), so that high content of SiO_2 means high content of sulfur. One of the purposes of the removal of SiO_2 is to remove the sulfur.

For China's natural magnetite, the sulfur content is not very high. After magnetic separation, the content of sulfur can be further reduced and other impurities such as pyrrhotite can be removed. Generally, the smaller the particles of magnetite used as raw materials, the easier would be the removal of impurities. The water used in magnetic separation process usually contains only traces of sulfur, phosphorus and chlorine. The strict controlling of the trace amounts of alkali metal or alkaline earth metal ions contained in water is unnecessary. After magnetic separation, the fined magnetite must meet the following requirements: $Fe^{2+}/Fe^{3+} > 0.4$, total iron content $> 70\%$, $SiO_2 < 0.4\%$, $S < 0.01\%$, $P < 0.04\%$.

During the manufacture of the catalyst, small amounts of impurities such as silicon, titanium, sulfur, phosphorus and chlorine can be inevitably introduced into the system. These impurities are catalyst poisons. Hence, the total content of impurities in catalysts should be limited in an allowable range, e.g. the content of sulfur must be less than 0.01%, phosphorus less than 0.04%, and chlorine less than $(5-10)\times10^{-6}$ in the ammonia synthesis catalyst according to Chinese standard.

4.1.2 *Proportion and mixing of materials*

The preparation of fused iron catalyst, either using electric resistance furnace, induction furnace or electric arc furnace, are performed by using intermittent batch operations. It is seen from Fig. 4.1 that the materials added into the furnace consist of three parts: (1) fresh material i.e., a mixture of refined magnetite and promoters; (2) Recycled catalysts during sieving whose particle sizes are too small (generally less than 1.5 mm) to meet the product requirements; (3) The slag and the skin materials that has not been spilled out and hence remain as residuals in the furnace (including the molten and semi-molten material). Therefore, the proportioning of materials contains two meanings: One is the ratio of the refined magnetite to the promoter in the fresh material, and another is the ratio of the fresh material and the returned materiel as well as the residue.

During a stable state of manufacture, the amount of fresh materials should be equivalent to that of the products. Therefore, the proportion of the fresh material, returned material and the residue is commonly unchanged. However, if the production process fluctuates or has accident, the balance of material will be broken. As a result, the change in the proportion occurs, which affects the quality of the product.

The proportion between the refined magnetite and the promoters in fresh materials should be strictly prepared according to the proportion in formula ratio of products. In addition, two factors must be considered: (1) The formula ratio should be able to complement the loss of the promoters during the melting process (especially potassium and other volatile components), so that the final catalyst can maintain the required components. (2) In the calculation of formula ratio of promoters, the contents of some promoter oxides in the refined magnetite should be taken into account. For some specific catalyst varieties, a definite magnetite was designated as raw material, and the content of promoter oxide in the magnetite has been included in the formula.

Fresh materials are mixed in the mixer as completely as possible. The resistance furnace is a long strip stove of 4–5 m. It is very difficult for the materials to diffuse from one side to another one if the mixture is inadequate. This results in non-uniform distribution of the promoter in the furnace.

The mixing efficiency of materials is related to the particle size of raw material and difference in density. Mixing is easier when the size of particles is uniform and difference of density is small. The density of the material cannot be chosen, but the uniform particle size can be adjusted. Therefore, the raw materials (especially KNO_3) should be crushed and sieved before mixing to obtain various raw materials with the same particle size.

4.1.3 *Melting of materials*

In order to achieve the best quality of catalyst, we must adjust the melting conditions, especially the melting temperature and duration to meet three requirements as follow: (1) the appropriate oxidation degree of iron, which makes the proportion of FeO to Fe_2O_3 approaching to the magnetite (for conventional fused iron catalysts) or makes the reaction complete between iron and magnetite to generate $Fe_{1-x}O$ (for $Fe_{1-x}O$-based catalyst). (2) The promoter is distributed as uniformly as possible in the melt. (3) Reducing the concentration of volatile poisons. Stoichiometric Fe_3O_4 melts at 1,597°C, while the oxidation degree is determined by temperature, partial pressure of oxygen, oxidation rate and the duration of melting. It also slightly depends on the chemical valence and concentration of the promoters.

It is favorable to promote the uniform distribution of melting materials and removal of poisons in the case of melting temperatures above 1,600°C. Higher the melting temperature, the smaller is the slurry viscosity, therefore more favorable is the diffusion and reaction velocity among the various components of catalyst. In addition, those promoters which cannot easily diffuse in solid solutions can be dispersed to a maximum degree and the ratio of Fe^{2+}/Fe^{3+} can be easily adjusted by melting under high-temperatures. Also, the fused materials must be maintained for a long enough time under the melting temperatures. It is noted that the melting conditions also relate with melting method and the type of furnace to some extent.

Different types of furnaces can be used for melting, among which electric resistance furnace is the most commonly used one in industry. Electrical resistance furnace is several meters long with open roof and its inner space is loaded with a layer of catalyst powder. Two iron electrodes are inserted into the both ends of the furnace. The raw materials are put into the furnace and the two electrodes are connected by an iron bar. After that, the material is heated to the operating

temperature. Once the material starts to melt, the resistance of the bed decreases chaperonage by the increasing current and the decreasing voltage. After the materials are fully melted and maintained for some time, the fused slurry is released into the cooler.

The main advantages of resistance furnace are that the structure is very simple while the consumption of electrode is not important from the economic point of view. In addition, the catalyst powder has a high electrical and thermal resistance, and the lining of the furnace is not needed. Therefore, it avoids additional impurities from lining into the material. The disadvantages of resistance furnace are that it needs more labor and the non-productive time is long. The space-time yield of resistance furnace is comparatively lower than electric arc furnace. The reason is that the original cold powder bed of resistance furnace has high-resistance, which does not allow a high-current, so that it requires several hours for each batch. The operating voltage must be lower than 80 V, so that the distance between the electrodes is only 4 m–5 m and the capacity of each furnace is about one ton. Another drawback of resistance furnace is that its highest temperature is low (about 1,600°C), which is not propitious to escape the volatile poisons. The basic principle of melting in resistance furnace is that the materials are melted at the temperature generated *via* the resistance of materials themselves under the strong current. In order to protect the body of steel furnace, it is prohibited to completely melt the materials in the furnace. Therefore, the melting temperature in the resistance furnace normally does not exceed the melting point of the material.

For the conventional Fe_3O_4-based catalysts, the melting temperature is generally 1,550°C–1,600°C (melting point of magnetite is 1,597°). Also for the $Fe_{1-x}O$-based catalysts, at the initial stage of magnetite powder melting, the melting temperature is 1,550°C–1,600°C and then with the formation of FeO, it will gradually decrease and stabilize at the melting point of FeO, around 1,377°C. That is, the melting temperature for the preparation of $Fe_{1-x}O$-based catalyst is about 200°C lower than that of Fe_3O_4-based catalyst. The results lead to energy consumption by about 25% than that of the former. Due to the lower melting temperature, the melting procedure in resistance furnace will take about 4 h–6 h for each batch, which is propitious to escape the volatile poisons and makes the various components of a catalyst to diffuse adequately and mix evenly.

Induction furnace is a refractory crucible, in which copper tube cooled by water is used as the primary coiler and the molten material as a secondary coiler. There is no iron core in the magnetic circuit and the magnetic flux is completely emanative, which leads to a waste of current. To overcome this weakness, capacitors and primary coilers are parallel connected. Intermediate frequency (500 Hz–1,000 Hz) is used in large-capacity induction furnace. Stoves are usually diagonal, and therefore the molten material can easily be poured out. It is also operated in batches as the resistance furnace.

Induction furnace has many advantages compared with the resistance furnace. Since the current can be very large, the temperature can reach above 2,000°C and is easy to be controlled. As a result, the melting time can be shortened. It also means that the oxidation degree of Fe^{2+}/Fe^{3+} can be accurately adjusted. In addition, the magnetic field formed by the primary coiler can maintain a continuous rotation of the melt, and the powerful magnetic line can play the role of automatic mix round, which helps the diffusion and distribution of promoters. This leads to the

uniform mixing of the materials in spite of the short time of melting. If a promoter oxide such as MgO is used as the crucible wall, the adverse effect of dissolved crucible material or erosion on the composition of the catalyst can be reduced. The disadvantages of induction furnace include high cost of the investment, low efficiency as a result of wasted current, and the erosion of lining. In addition, it is difficult to start cold stoves, while it usually can be overcome by adding a molten catalyst into the furnace. Nevertheless, it is impossible to completely avoid melting of lining materials like MgO, Al_2O_3, SiO_2 and so on into the catalyst, so that induction furnace is scarcely used for industrial manufacturing.

In the electric arc furnace method, the raw material is melted by a three-phase arc in a container lined with MgO or Al_2O_3 (available SiO_2). The "wiring voltage" between two electrodes (electrodes introduced vertically into the container and almost touching the material) is generally 75 V–180 V. To maintain a constant current, the distance between the electrodes and molten material must be adjusted automatically.

In the case of melting in electric arc furnace, the melting temperature is determined by the arc flame temperature, which can achieve as high as 4,000°C–5,000°C. Therefore, the melting in electric arc furnace has the advantages of short melting time, large production capacity, uniform distribution of the promoter, and that the volatile poisons such as sulfur and phosphorus can be released under the high-temperatures. Due to the quick and continuous melting of materials, the non-productive time is short and less labor is needed. For example, for a stove with the loading capacity of only 100 kg, its production capacity can still be higher than a resistance furnace with the loading capacity of one ton. However, due to the complexity of the equipment, the cost of investment is higher than the resistance furnace. The quick burning of carbon electrode will increase the operating cost even though the erosion of lining maintains low by using appropriate catalyst powder as the lining. Also, in the case of high-temperature, the loss of oxygen is higher due to the generation of CO in the electrode, and the ratio of Fe^{2+}/Fe^{3+} is not easy to control.

It is difficult to compare the preponderance of the three methods mentioned. The reasons are the difference of ratio between the investment cost and running cost because their relative income changes with the production capacity. Undoubtedly, the induction method is the preferred way to secure the best quality of catalyst, especially when the promoters are dispersed as molecular in the melt magnetite and the oxidation degree is close to the stoichiometric magnetite.

4.1.4 *Discharging and cooling of molten material*

The molten materials are usually poured into a cooling trough with a water jacket or a pedrail-type and planar turn plate-type cooler. The cooling rate is determined by the cooler type and the thickness of the molten material in the cooler, which indirectly affects the mechanical properties and the catalytic performance. The crisp metal oxides form during rapid quenching, which in turn form small patches with sharp-angles after crushing. This will produce more dust in the loading and operating process in the ammonia reactor, and will further plug the pipe or reduce the productivity. On the other hand, thicker melt would lead to a slow cooling rate resulting in non-uniform distribution of promoters, difficulties during crushing and finally, would form cubic patches after crushing.

4.1.5 *Crushing and sieving of molten materials*

The cooled molten material is usually crushed by the jaw crusher. The shape of particles and yield of product are affected by the shape and spacing of the jaw plate, its mode of motion as well as the crush speed. The particles of product are sieved into different sizes by the multistage vibrating screen. The edges and corners of particles are abraded by the angle-abrader. Small particles (for example, of size less than 1.5 mm or 2.2 mm) must be returned for remelting. In any case, there are large amounts of small particles. The product efficiency of fused iron catalyst is predominantly determined by the efficiency of crush process. The particle size and its size range should be selected according to the requirement of different converter type and the needs of the customer.

4.1.6 *Packing, storage and transportation*

The product of ammonia synthesis catalyst is generally packaged in an airtight iron barrel. During the transportation, collision and rolling of the barrel should be avoided in order to prevent the catalyst from comminuting, the barrel cover from loosening and gas from leaking. The moisture and pollution should be avoided in the storage of the catalyst, and the storage time is preferably not more than six months. Upon exposure to the air for long time, the ammonia synthesis catalyst will absorb moisture and white potassium salts will be dispersed. The ammonia synthesis catalyst which has been moistened had better not be used.

After passivation, the surface of the prereduced catalyst is covered with a layer of oxide film, which cuts off the internal active α-Fe from the air. The prereduced catalyst after passivation will still slowly react with oxygen in the air at room temperature. During transportation, the oxide film will flake off locally as the result of particle collisions and friction, while they can be reoxidized in air to form a new oxide film.

The catalyst should be stored in the dry storeroom. Prereduced catalyst cannot be contacted with water, because water molecules will go through the oxide film and react with the active α-Fe, and release H_2 as in the reaction, $Fe + H_2O = FeO + H_2$.

4.2 Chemical Reaction During Preparation Process

(1) **Preparation of conventional Fe_3O_4-based catalyst.** At high temperatures (1,500°C and above) and under the melting conditions, the Fe_2O_3 in magnetite reacts with the reductant as in the following equations:

$$Fe_2O_3 + \text{reductant} \rightarrow Fe_3O_4, \tag{4.1}$$

where, the reductant is usually pure iron such as iron bar or iron powder, or may also be a carbon material such as graphite, activated carbon and carbon electrode in electric arc furnace etc.

Equation (4.1) is the main reaction in the preparation of conventional Fe_3O_4-based catalysts. Due to the very low content of Fe_2O_3 in magnetite, the preparation of conventional Fe_3O_4-based catalysts is mainly a physical melting process. In refined natural magnetite, the Fe^{2+}/Fe^{3+} ratio is less than 0.5, while the generally

Fe^{2+}/Fe^{3+} ratio of conventional Fe_3O_4-based catalysts is in the range of 0.5–0.7. Also, Fe^{2+} can easily be oxidized into Fe^{3+} in the air, further decreasing the ratio of Fe^{2+}/Fe^{3+} during the preparation:

$$2Fe_3O_4 + 1/2O_2 \xrightarrow{\text{heat}} 3Fe_2O_3 \tag{4.2}$$

Therefore, during the melting process, the reductant must be added into the furnace to adjust the ratio of Fe^{2+}/Fe^{3+}:

$$4Fe_2O_3 + Fe \xrightarrow{\text{heat}} 3Fe_3O_4 \tag{4.3}$$

$$Fe_2O_3 + Fe \xrightarrow{\text{heat}} 3FeO \tag{4.4}$$

$$6Fe_2O_3 + C \xrightarrow{\text{heat}} 4Fe_3O_4 + CO_2\uparrow \tag{4.5}$$

$$2Fe_2O_3 + C \xrightarrow{\text{heat}} 4FeO + CO_2\uparrow \tag{4.6}$$

The ratio of Fe^{2+}/Fe^{3+} (or called oxidation degree) is the main controlled parameter during the preparation process, and should be measured at a certain period of time.

(2) **Preparation of $Fe_{1-x}O$-based catalysts.** For the preparation of novel $Fe_{1-x}O$-based catalyst, natural magnetite can also be used as main raw material and can be melted directly in the resistance furnace or electric arc furnace. However, during its preparation process, the chemical reaction between magnetite and iron occurs to form FeO as shown in Eq. (4.7) and (4.8) in addition to the process of physical melting.

$$Fe_2O_3 + \text{reductant} \rightarrow Fe_3O_4 \tag{4.7}$$

$$Fe_3O_4 + \text{reductant} \rightarrow 4FeO \tag{4.8}$$

This is essentially different from the preparation of Fe_3O_4-based catalyst, in which iron is only used to adjust the ratio of Fe^{2+}/Fe^{3+}, while iron is one of the necessary reactants in preparation of $Fe_{1-x}O$-based catalyst although the chemical composition is also controlled *via* adjusting the ratio of magnetite and iron. That is, the preparation of $Fe_{1-x}O$-based catalyst must be adopted by combining processes by the physical melting and chemical reaction.

The standard Gibbs free energy ΔG° $(kJ{\cdot}mol^{-1})$[13] for the formation of wüstite from the equivalent mixture of magnetite and iron is:

$$\Delta_r G^\Theta = 48.4 - 5.8 \times 10^{-2}\,T$$

The wüstite formation reaction will go to the right direction when $\Delta_r G^\Theta < 0$, i.e. $T > 833\,K$. In other words, if the magnetite is reduced by iron at temperatures higher than 833 K, wüstite forms.

When magnetite is used as the raw material and metal iron as reductant to prepare $Fe_{1-x}O$-based catalysts, the amount of iron cannot be calculated according to the stoichiometric of Eq. (4.8) because the composition of natural magnetite is not a pure Fe_3O_4 (see Table 4.1) and the dosage of iron theoretically is related to the composition of the magnetite such R_0 (Fe^{2+}/Fe^{3+}). The dosage of iron should be determined using the following equation:

$$Fe = \frac{0.35W(R - R_0)}{(1 + 0.9R_0)(1.5 + R)}, \tag{4.9}$$

where, Fe is the dosage of iron theoretically, kg; W is the weight of magnetite, kg; R_0 and R are the ratio of Fe^{2+}/Fe^{3+} in magnetite and in the product of designed catalyst, respectively. The Eq. (4.9) is applicable both to preparation of Fe_3O_4 based and $Fe_{1-x}O$ based-catalysts.

The Fe_2O_3 in the magnetite ore will be decomposed at temperatures above 1,000°C.

$$Fe_2O_3 = 2/3Fe_3O_4 + 1/6O_2\uparrow \tag{4.10}$$

The FeO formed according to Eq. (4.8) is the low-valence iron oxide, which can be transformed into high-valence oxides. The following reactions will occur in air at high temperatures:

$$FeO + 1/6O_2 = 1/3Fe_3O_4 \tag{4.11}$$

$$FeO + 1/4O_2 = 1/2Fe_2O_3 \tag{4.12}$$

If the reductant (such as iron) is slightly excessive in the reactant, the oxidation reaction of FeO can be effectively inhibited. The experimental results show that the oxidation of FeO is very slow at room temperature.

Also, oxygen will be released by the decomposition of the KNO_3 as promoter at high temperatures, which consumes a small amount of reducing agent. Therefore, the ratio of reductant (Fe) to magnetite (W) should be higher than the calculated value from Eq. (4.9). A variety of fused iron catalysts with different ratio of Fe^{2+}/Fe^{3+} can be prepared by adjusting the ratio (Fe/W) of reductant to magnetite, as listed in Table 4.2.

FeO is a metastable phase thermodynamically and it cannot be formed below 570°C. When FeO is cooled down from high temperatures, disproportionation

Table 4.2 Relation of chemical composition and phase with raw material proportioning

Sample No.	Ratio of Fe to magnetite[a]	Fe^{2+}/Fe^{3+} of products	Chemical composition(wt)/%		Phase(XRD)	X value in $Fe_{1-x}O$	Lattice constant/nm	
			FeO	Fe_2O_3			Fe_3O_4	FeO
1	Magnetite + Fe_2O_3	0.32	20.95	72.75	$Fe_{3-y}O_4$	—	0.8391	—
2	0.027	0.52	29.68	64.02	$Fe_3O_4 + FeO$	—	0.8390	—
3	0.085	1.09	46.40	47.30	$Fe_3O_4 + FeO$	—	0.8391	0.4299
4	0.126	1.60	55.30	38.40	$FeO + Fe_3O_4$	—	0.8392	0.4290
5	0.171	2.22	62.45	31.25	$FeO + Fe_3O_4$	—	0.8387	0.4268
6	0.196	3.33	70.27	23.44	FeO ($Fe_{1-x}O$)	0.104	—	0.4289
7	0.232	4.65	75.63	18.08	FeO ($Fe_{1-x}O$)	0.081	—	0.4301
8	0.270	5.66	78.32	15.38	FeO ($Fe_{1-x}O$)	0.070	—	—
9	0.286	6.74	80.44	13.26	FeO ($Fe_{1-x}O$)	0.061	—	0.4313
10	0.301	7.58	81.72	11.98	FeO ($Fe_{1-x}O$)	0.055	—	0.4313
11	0.315	8.22	82.54	11.16	FeO ($Fe_{1-x}O$)	0.051	—	—
12	0.350	8.97	83.37	10.33	FeO ($Fe_{1-x}O$)	0.048	—	—
13	0.404	9.36	83.76	9.94	FeO ($Fe_{1-x}O$)	0.046	—	—

[a]Fe/magnetite ratio is the experimental value and it is higher than the stoichiometric ratio in Eq. (4.8) or (4.9).

reactions will occur and FeO transforms to Fe and Fe_3O_4 as:

$$4FeO = Fe + Fe_3O_4 \tag{4.13}$$

It is indicated that the ideal FeO with Fe/O ratio of one can only be obtained at 3,600 MPa and 1,043 K, so that it is actually non-existent. Therefore, FeO obtained from (4.8) is a non-stoichiometric iron oxide of $Fe_{1-x}O$.

Our experimental results[14] show that the disproportionation reaction [Eq. (4.13)] of FeO was slow at room temperature, and some promoter such as CaO in catalyst can inhibit the reaction. Dynamically, the stable wüstite can be obtained by choosing a suitable preparation process (See Chapter 3).

In addition, the promoters such as KNO_3 and $CaCO_3$ etc will be decomposed at high temperatures and the released [O] will further oxidize Fe or FeO as:

$$2KNO_3 = K_2O + NO + NO_2 + O_2\uparrow \tag{4.14}$$

$$CaCO_3 = CaO + CO_2\uparrow \tag{4.15}$$

$$2Ce(NO_3)_3 = 2CeO_2 + 6NO_2 + O_2\uparrow \tag{4.16}$$

A variety of complex oxides are formed by the reactions among K_2O, CaO, Al_2O_3 etc. and iron oxides.

$$FeO + Al_2O_3 = FeAl_2O_4(FeO \cdot Al_2O_3) \tag{4.17}$$

$$Fe_2O_3 + K_2O = 2KFeO_2(Fe_2O_3 \cdot K_2O) \tag{4.18}$$

$$Al_2O_3 + K_2O = 2KAlO_2(K_2O \cdot Al_2O_3) \tag{4.19}$$

$$Fe_2O_3 + CaO = CaFe_2O_4(CaO \cdot Fe_2O_3) \tag{4.20}$$

The Gibbs' free energies given in Table 4.3 can be used to evaluate solid-phase reaction based on thermodynamics. In Table 4.3, some values are different from

Table 4.3 Standard Gibbs energy changes (ΔG°) of solid state reactions related iron oxides[15]

Number	Reactions	$\Delta G = A + BT$ A	$\Delta G = A + BT$ B × 10^3	Error kJ·mol^{-1}	Temperature range/K
1	$Fe_2O_3 + FeO \rightarrow Fe_3O_4$	−16.86	−11.55	1.2	1,100–1,700
2	$Fe_2O_3 + MgO \rightarrow MgFe_2O_4$	−24.06	1.34	1.7	1,100–1,700
3	$Fe_2O_3 + 1.07\ MgO \rightarrow (MgO)_{0.07}MgFe_2O_4$	−44.10	14.48	1.2	1,173–1,373
4	$Fe_2O_3 + MnO \rightarrow MnFe_2O_4$	−40.6	1.05	1.7	1,273–1,473
5	$6Fe_2O_3 + BaO \rightarrow BaFe_{12}O_{19}$	1.39	−89.2	0.3	935–1,187
6	$Fe_2O_3 + CaO \rightarrow CaFe_2O_4$	−29.71	−4.81	0.29	1,100–1,300
7	$Fe_2O_3 + 2CaO \rightarrow Ca_2Fe_2O_5$	−31.55	−23.01	0.67	1,100–1,300
8	$Fe_2O_3 + CoO \rightarrow CoFe_2O_4$	−22.6	−13.4	4.2	900–1,200
9	$Fe_2O_3 + NiO \rightarrow NiFe_2O_4$	−19.75	−4.18	1.2	1,173–1,473
10	$2\ FeO + SiO_2 \rightarrow Fe_2SiO_4$	−27.91	6.7	0.6	1,123–1,423
		−51.21	20.5	—	298–1,692
11	$FeO + Cr_2O_3 \rightarrow Fe_2Cr_2O_4$	−66.32	10.88	0.8	1,573–1,773
		−57.53	16.44	0.8	1,000–1,500
12	$Fe_{0.95}O + 0.05\ Fe + TiO_2 \rightarrow FeTiO_3$	−26.36	5.40	0.08	1,173–1,373
		−30.63	9.12	0.3	1,250–1,500
13	$Fe_{0.95}O + 0.05\ Fe + Al_2O_3 \rightarrow FeAl_2O_4$	−45.2	17.07	0.2	—
14	$Fe_{0.95}O + 0.05\ Fe + Cr_2O_3 \rightarrow FeCr_2O_4$	−64.18	18.07	0.3	—
15	$Fe + 1/2\ O_2 + TiO_2 \rightarrow FeTiO_3$	−301.67	79.41	—	—
16	$Fe + 1/2\ O_2 + FeTiO_3 \rightarrow Fe_2TiO_4$	−268.26	62.01	—	—

the gas-phase (or liquid) reactions. That is, the value of ΔS is small, which is undoubtedly related with the lattice reformation because it is commonly believed that $\Delta S = 0$ for the solid-state reaction. However, under the real conditions, the range of ΔS is -20 J–20 J·mol^1·K^{-1}. Usually, the value of ΔS relates with the products which has extremely disordered lattice caused by their own or impurities. From the examples listed above, wüstite has a high entropy (58 J·mol^{-1}·K^{-1}), which is due to the lattice disorder and to a certain extent, the course of this disorder is related to the non-stoichiometric reactions.

Here ΔH of solid-state reactions are in the range of -418.5 kJ·mol^{-1} -125 kJ·mol^{-1}, but the negative value of ΔH is larger only for the reaction with alkalis or alkaline earth's oxide as reactants. Due to $\Delta S = 0$ for most of the solid-state reactions, the value of ΔG approaches to that of ΔH.

4.3 Phase Transformation and Phase Diagram Analysis During Preparation

Fe–O equilibrium phase diagram is the thermodynamic basis for the preparation of fused iron catalyst. Figure 4.4 shows the Fe–O equilibrium phase diagram with the oxygen content in the range of 0%–30%, in which the temperature and oxygen content of each node are also given in Table 4.4. Customarily, the ratio of Fe^{2+}/Fe^{3+} is used to control the composition of iron oxide during the preparation, so we correlated the oxygen content (a) to Fe^{2+}/Fe^{3+}(R) in Fe–O system. In the FeO–Fe_2O_3 region, $R = (0.3 - a)/(0.9a - 0.2)$, and the values are listed in Table 4.4. Figure 4.4 can be divided into the following phase regions for discussion.

(1) Fe_2O_3+Fe_3O_4 phase region with the oxygen content in the range of 27.64%–30% and above. In both sides of Y-Z line, Fe_2O_3 will be decomposed to Fe_3O_4 when temperature is higher than 1,455°C, while it is a mixture of Fe_2O_3 and Fe_3O_4 at temperature lower than 1,455°C. When the catalyst is prepared by using the melting method in this region, the ratio of O/Fe decreases from 1.4 to 1.38 and R increases from 0.25 to 0.31 (the No. 1 sample in Table 4.2) after melting for the ratio of O/Fe of 1.4 in materials (O/Fe ratio is 1.5 for Fe_2O_3). It is shown that part of the Fe_2O_3 was decomposed [see Eq. (4.10)] during the melting process. Nevertheless, the molar ratio of Fe_2O_3/Fe_3O_4 in the mixture is still 0.597:1.0 according to Table 4.2, i.e., the molar fraction of Fe_2O_3 accounts for 37.5%, but without the Fe_2O_3 peaks that appeared in the XRD spectra as shown in Fig. 4.5 (sample No. 1). A similar result can be found in sample 2. This shows that the undecomposed α-Fe_2O_3 in the raw materials is transformed into γ-Fe_2O_3 which is isomorphism with Fe_3O_4 or reacts with Fe_3O_4 to generate a non-stoichiometric magnetite phase as $Fe_{3-y}O_4$ during the melting process at high temperatures.[16] This leads to the spinel-type Fe_3O_4 peak which appears in the XRD patterns. This explanation can also be confirmed by the fact that the lattice parameters of samples of No. 1 and No. 2 are slightly smaller than that of pure Fe_3O_4 (sample No. 3) from Table 4.2. We attempt to prepare the samples with O/Fe ratio of 1.4 and R of 0.25 by increasing the proportion of Fe_2O_3 in the raw materials, whereas the ratio of O/Fe was reduced to 1.37–1.38 and R was increased to 0.31–0.33 in all cases. Therefore, Fe_2O_3-based catalysts have to be prepared by other methods, for example, the precipitation method.[17]

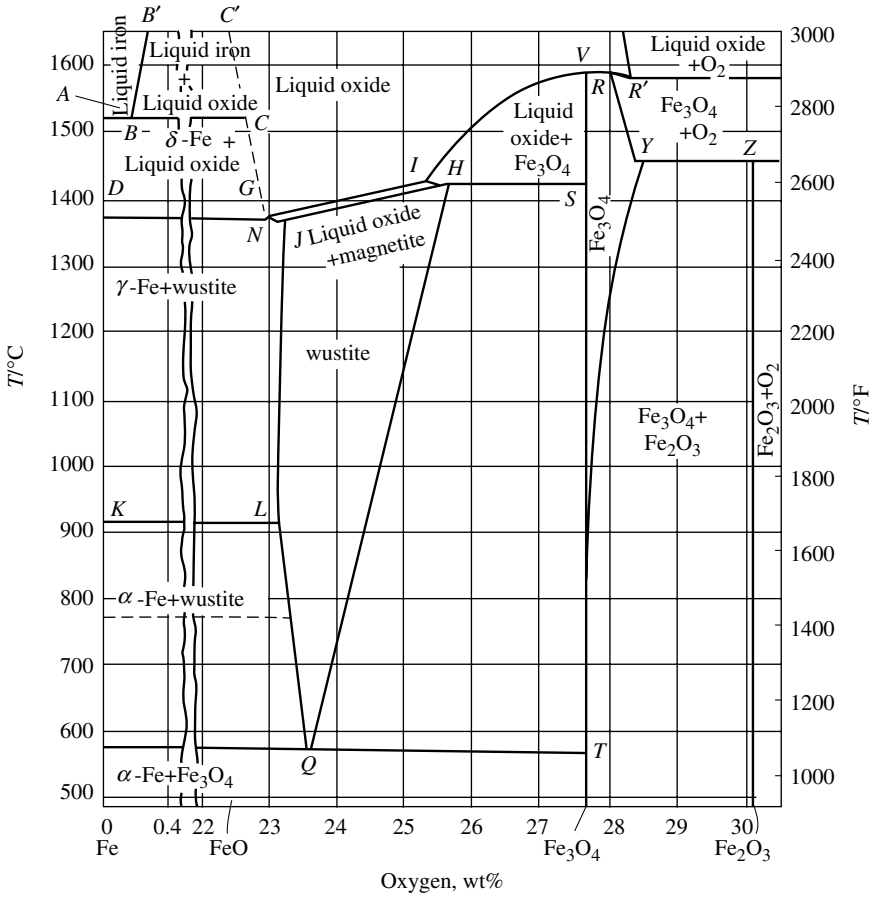


Fig. 4.4 Equilibrium phase diagram for Fe–O system

Table 4.4 Temperature (T), oxygen content (a) and the ratio of Fe^{2+}/Fe^{3+} (R) in Fig. 4.4

Node	T/°C	Oxygen content (*a*)/%	Fe^{2+}/Fe^{3+} (*R*)	Node	T/°C	Oxygen content (*a*)/%	Fe^{2+}/Fe^{3+} (*R*)
A	1535	0	—	N	1371	22.92	11.27
B	1534	0.16	—	Q	570	23.57	5.30
C	1524	22.63	20.08	R	1583	28.30	0.31
D	1400	0	—	R'	1583	28.08	0.36
F	770	0	—	S	1423	27.64	0.50
H	1423	25.60	1.45	U	570	27.64	0.50
I	1423	25.26	1.73	V	1597	27.64	0.50
J	1311	23.15	8.20	Y	1455	28.36	0.30
K	910	0	—	Z	1455	30.04	0
L	910	23.15	8.20				

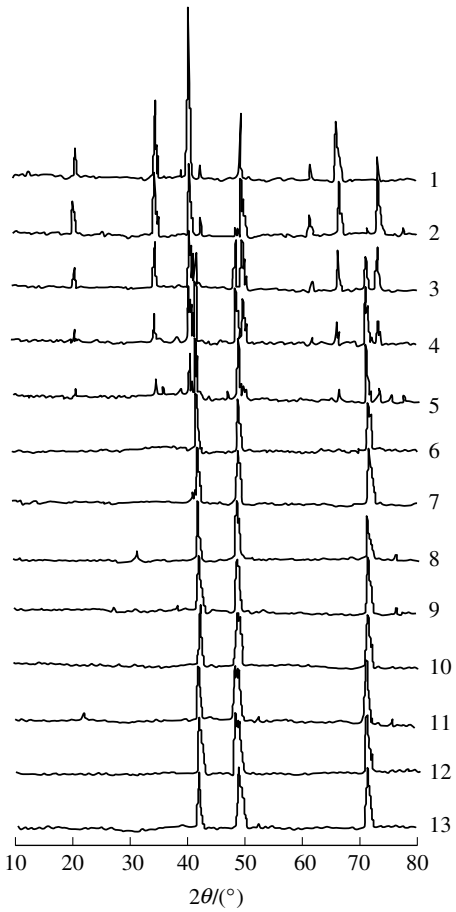


Fig. 4.5 The XRD patterns for Fe_3O_4 and FeO (Number of samples at right see Table 4.2)

Characteristic peaks of Fe_3O_4 (2θ): 18.27°, 30.06°, 35.43°, 43.09°, 53.58°, 56.95°, 62.57°, 73.97°; Characteristic peaks of FeO (2θ): 36.23°, 42.05°, 60.90°, 72.84°, 76.61°.

(2) VRYU, the small triangle region marked with VRYU is Fe_3O_4 phase. Conventional Fe_3O_4-based catalysts can be prepared in this region.

(3) The region marked with H (V)UQ is a two-phase region of FeO and Fe_3O_4. In the case of the temperature (570°C) below UQ line, the FeO will disproportionate to Fe and Fe_3O_4 and the final products are Fe and Fe_3O_4. When the FeO is cooled down rapidly from above 570°C, a mixture of FeO and Fe_3O_4 can be obtained. For example, in Table 4.2, the R value for samples No. 4, 5 and 6 is 0.89, 1.11 and 2.16, respectively. In their XRD patterns, both FeO and Fe_3O_4 peaks can be found, as shown in Fig. 4.5. It is observed that the intensity of characteristic peaks of Fe_3O_4 decreases with increasing R, indicating that the concentration of Fe_3O_4 decreases. By contrast, the intensity of peaks of FeO increases and its content increases with increasing R. The results show that Fe_3O_4 and FeO coexist independently in the range of $0.5 < R < 3.5$.

(4) The triangle region marked by JHQ is wüstite phase region. According to Fig. 4.4, the wüstite phase cannot be formed below 570°C (Q node). When FeO is cooled from a high-temperature, the disproportionation reaction occurs as in Eq. (4.13) and forms Fe and Fe_3O_4. Therefore, in order to obtain pure wüstite phase, the molten liquid oxides should be cooled down rapidly. In Fig. 4.5, only the peaks attributed to FeO phase appear and the peaks related to the Fe_3O_4 phase completely disappear in the case of $R > 3.33$. In this case, the molar ratio of Fe_3O_4 to FeO is approximately 1:5.29. If Fe_3O_4 phase exists independently in this region, it should be detected exactly by the MXP X-ray diffraction instrument. Therefore, when the molar ratio of FeO to Fe_3O_4 is higher than 5.29:1, Fe^{3+} ions are not located at an independent magnetite phase, rather they are dissolved in the wüstite phase non-stoichiometricly. This leads to the formation of non-stoichiometric ferrous oxide with iron ion defect or wüstite of $Fe_{1-x}O$.[18] The "x" represents the defect concentration of iron ion in $Fe_{1-x}O$. The relationship between x and R is expressed as Eq. (4.21), and x values are listed in Table 4.2.

$$x = \frac{1}{3 + 2(R)} \tag{4.21}$$

From the lattice parameters of samples listed in Table 4.2, it is seen that the lattice parameters decrease with the increase of x in the $Fe_{1-x}O$. The reason may be that the oxygen parameter reduces with the increase of iron ion defect in the rock salt cubic lattice by the dense accumulation of O^{2-} ions of $Fe_{1-x}O$ crystals. The R values of all wüstite catalyst are consistent with this scope. When Fe–O system is rapidly cooled down to room temperature (rapid crystallization) metastable wüstite can be obtained.

From the discussion above:

When $a \geq 30\%$ ($R = 0$), there is only Fe_2O_3 phase in the Fe–O system.

When $27.64\% < a < 30\%$ ($0 < R < 0.50$), there exists both Fe_2O_3 phase and Fe_3O_4 phase and the mixed oxide, i.e., two-phase coexists independently.

When $a = 27.64\%$ ($R = 0.5$), there is only Fe_3O_4 phase in the Fe–O system.

When $24.2\% < a < 27.64\%$ ($0.50 < R < 3.33$), there are two phases of Fe_3O_4 and FeO in the Fe–O system independently, in which when $R = 1.0$, Fe_3O_4 and FeO coexists in equal mole independently.

When $22.92\% < a < 24.2\%$($3.33 < R < 11$), the wüstite phase with lattice defect can be obtained by rapid cooling.

In Chapter 3, the authors proposed the single-phase principle of the preparation of fused iron catalyst. It is clearly pointed out that high catalytic activity can be achieved when wüstite or magnetite phase exists separately in the catalyst. When wüstite and magnetite coexist in the catalyst, the catalytic activity is always low. In the FeO phase region, the activity of the catalyst decreases due to the formation of a new phase α-Fe in the case of $R > 11$.

As a result, Fe_3O_4, non-stoichiometric ferrous oxide and its mixture-based fused iron catalyst can be prepared by using magnetite and reducing agents as raw materials under high-temperature melting conditions, while Fe_2O_3-based catalyst cannot be prepared. The oxidation and disproportionation reaction of FeO must be avoided during the preparation process for homogeneous phase $Fe_{1-x}O$-based catalyst. It is seen from the Fe–O system with R value of 3.33–11 that wüstite phase is stable below the melting temperature.

4.4 Segregation of Promoters During Solidification Processes

It is well known that the cooling rate of melt during preparation of catalyst has significant effects on the activity of the activated catalyst. For the A106 and A104 catalysts developed by Nanjing Chemical Industrial Institute in 1950s, in spite of the same chemical compositions, the activity of A106 catalyst prepared by fast-cooling is much higher than that of A104 catalyst by slow-cooling. They believed that the high activity of catalyst with fast-cooling originated from the small crystal grains and a higher surface area after reduction. Our results show that the cooling rate mainly affects the crystal structure and the distribution of the promoters in the catalysts as well as it also influences the crystal grain size. In other words, serious macrosegregation will occur in the samples prepared by slow-cooling.

During the preparation process of the fused iron catalyst, the most important factor influencing the quality of catalyst is the rate of solidification and cooling. The main purpose of high-temperature melting is to achieve uniform distribution of the promoters and to obtain the required iron oxide. The latter is easy to achieve by adjusting the ratio of Fe^{2+}/Fe^{3+} as the temperature reaches the melting point of iron oxide, while the former is determined by the solidification and cooling rates.

During the melting process, the molten material is liquid state, and iron oxides, Al_2O_3, K_2O as well as CaO etc. exist as ionic state in the liquid melt. They should be homogeneously distributed in the liquid melt theoretically. In the earlier discussion about the melting temperature, melting time[19] and other factors only influence the distribution of the promoters in liquid state melt. Once the liquid state melt is solidified, the distribution state of the promoter in the catalyst has been fixated (it may be changed slightly during the reduction process). During the solidification process, the solutes will redistribute and segregate resulting in non-uniform distribution of the promoters in final products.

Here, iron oxides (Fe_3O_4 or $Fe_{1-x}O$) are considered as "solvent," while promoter oxide such as Al_2O_3, K_2O, and CaO etc. as "solute." The melting points and the structure of different iron oxides (Fe_3O_4 or $Fe_{1-x}O$) and Al_2O_3, K_2O, CaO, as well as the possibly formed solid-solutions (such as $FeAl_2O_4$, $CaFe_2O_4$, $MgFe_2O_4$, $KFeO_2$ etc.) vary, such that the multi-promoters fused iron catalyst is a complex system composed of multi-phase and polycrystalline. Its internal structure is not a uniform and continuous material. Here, the shape and size of crystal grains are different and there are some impurities and gas holes both inside and at the boundaries of grains. Figure 4.6 shows the typical microstructure of such multi-phase and polycrystalline system. The shape and size of grains in iron oxides and the typical structure of the boundary between grains are shown in Fig. 4.7. It is observed that the number and the shape of the grain boundaries per grain are varying. When the surface energies of the grains in all directions are roughly equal, the grain boundaries consisting of three grains intersect at one point with 120° angle (Fig. 4.7, No. 3). The hexagonal grain boundary has linear contact with three interfaces intersected at 120°, whose form is relatively stable (Fig. 4.7, No. 6). In order to keep the intersection of grain boundaries at 120°, the interface of grains with more than six sides should slightly bend to the inside, and the interface of grains with less than six sides should slightly bend to the outside. When the system is sintered or solidified, the interface moves along the arrow shown in Fig. 4.7 to reduce the interface energy and to transform into a stable state.[20]

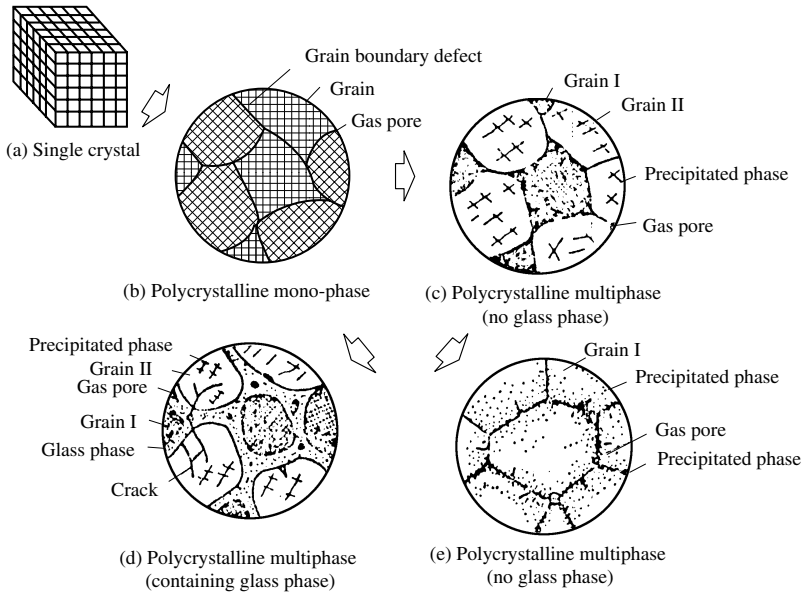


Fig. 4.6 Microstructures of single crystal and multiple crystal materials

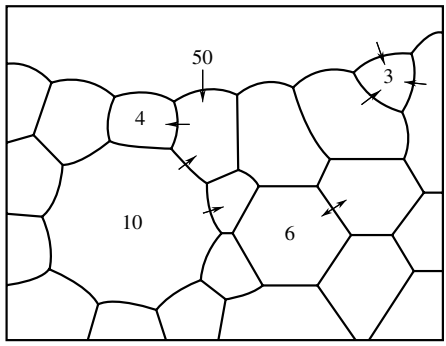


Fig. 4.7 Grain shape of iron oxide

(The numbers represent the amount of grain boundary, and the arrow represents the moving direction of the grain boundary).

Figure 4.8 shows the scanning electron microscope photographs of the fused iron catalyst before reduction and its surface elements distribution. The shape, size and boundaries of grains in the iron catalyst can be clearly observed from Fig. 4.8. It is clearly seen that the distribution of the promoter such as Al_2O_3, K_2O and CaO is uneven and especially their accumulation and segregation at grains inside or at the grain boundaries in the iron oxide are much obvious. Table 4.5 lists the EDS results of the element distribution on the surface, inside and boundaries of the grain. It is seen that there is serious aggregation of Al, K, Ca and Ti (impurities) on the grain boundaries and their aggregation degree (the ratio of elements located at grain boundaries to those in the grain) is 12.5, 43.1, 14.5 and 6.4, respectively. However, Mg and V do not significantly aggregate and segregate at grain boundaries.

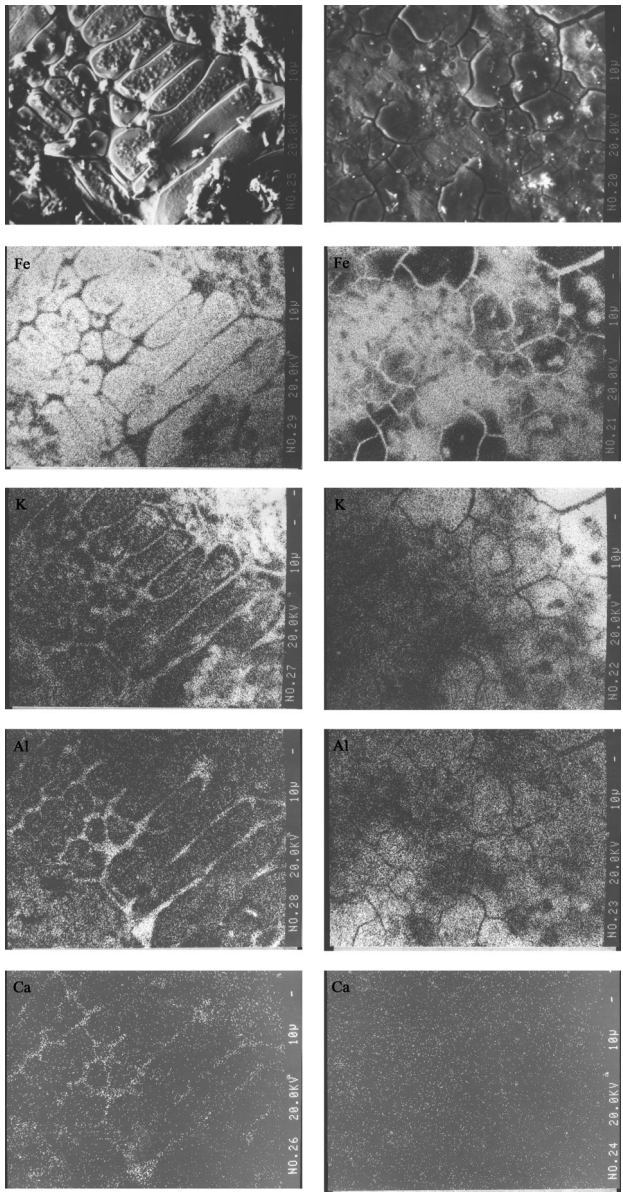


Fig. 4.8 SEM photographs of fused iron catalyst before reduction
(The left column is the cross section of the melt; the right column is the plane of the melt. From top to bottom: the shape, the distribution of the element of Fe, K, Al and Ca, respectively).

It is unavoidable that the solute redistribution occurs during the solidification process, while the accumulation and segregation of solute at the grain boundary are the results of solute redistribution.[21,22] The segregation includes macrosegregation and microsegregation. The former is also called long-range segregation, which refers to the chemical composition difference between the inside and outside or that between the upper and the lower parts of the melt dollop. Macrosegregation is

Table 4.5 Element distribution in the surface, grain and grain boundary of promoters/wt% (EDS)

Element	Al	K	Ca	Mg	Ti	V
Surface	3.56	0.76	1.81	1.80	0.39	0.49
Grain body	1.40	0.14	0.92	1.32	0.30	0.54
Grain boundary	17.50	6.03	13.30	0.50	1.91	0.74

mainly caused by the flow of the liquid during solidification, which is difficult to be eliminated and can only be reduced. Microsegregation is also called as short-range segregation, which has different forms such as cystiform segregation, dendritic segregation and grain boundary segregation etc. In the normal solidification process, microsegregation refers to the composition difference between the center of dendrite bole (or cystiform bole) and interdendrite (or intercellular crystal). The degree of segregation can be represented by SR, i.e., SR represents the ratio of the maximum concentration of the solute of interdendrite to the minimum concentration of the solute of dendrite bole. The SR value can be measured and calculated by electron microscopy. Table 4.6 lists the characteristics of macrosegregation and microsegregation.

Table 4.6 Characteristics of segregation

Segregation type	Characteristics of segregation
Macrosegregation	
1. Proportional segregation	1. Occur at the initial stage of solidification and originated from different densities
2. Positive segregation	2. High concentration at the beginning of solidification and low concentration at the last.
3. Reverse segregation	3. Contrary to the solute distribution of positive segregation, the originations of shrinkage that the high concentration liquid of solute in the center is squeezed to the surface when they are transmitted through the channel of the dendrite.
4. Channel segregation	4. The channel segregation is caused by the fact that flow of the liquid phase has more solutes with low melting point among the dendrite due to the contraction and density difference.
5. Zonal segregation	5. The composition changes in a zonary area parallel to the solid–liquid boundary, which is caused by the change in the growth rates.
Microsegregation	
1. Grain boundary segregation	1. The grain boundary segregation occurs when the solute concentration in the interface between two planar crystals or at the intersection of two planar crystals is higher than that of the center in the molten material.
2. Cystiform segregation	2. The cystiform segregation originates from the component difference between the interface and the heart of cystiform crystal.
3. Dendrite segregation	3. The dendrite segregation derives from the component difference of inside, the interdendrite and the dendrite bole of the usual equiaxed crystals or columnar crystals.

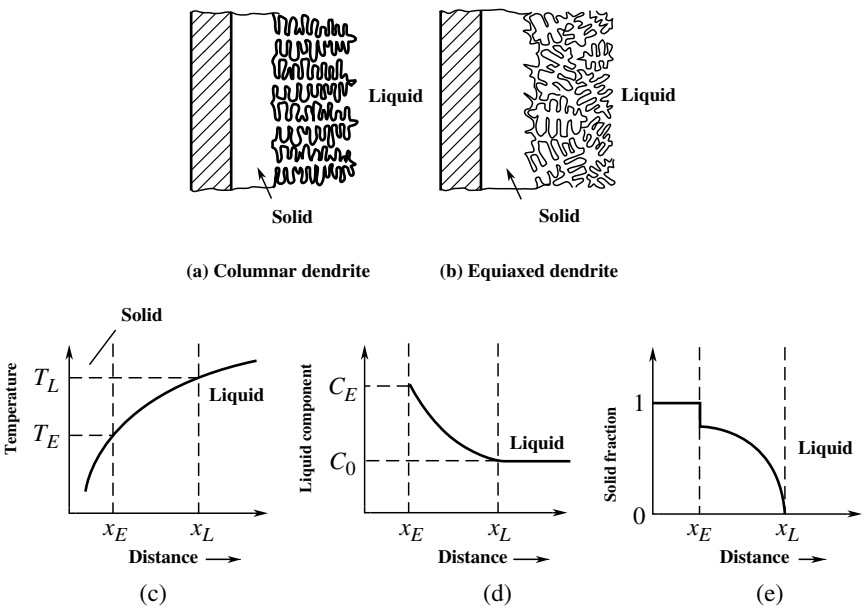


Fig. 4.9 Model of solid–liquid interface[21]

Figure 4.9 is the model of solidification in the area of liquid and solid, in which (a) and (b) show the segregation state appeared in the columnar dendrite and equiaxed grains, respectively. The factors influencing the dendrite segregation are as follows: The more rapid the cooling rate, the more serious the segregation is. Larger the horizontal distance between the solid-phase line and liquid-phase line in the equilibrium phase diagram, the more serious the segregation is. The smaller the diffusion coefficient of the element in the solid-phase, the greater the segregation is. To summarize, the third element which makes the solute equilibrium distribution coefficient K_0 of certain elements becomes smaller (when $K_0 < 1$) causes significant segregation. The harm of microsegregations on the performance of catalysts is evident, for example, the non-uniformity of components can cause differences in structure. Microsegregation can be eliminated or mitigated by diffusion annealing for a long time, but it is not feasible for fused iron catalyst.

During the solidification and crystallization process, the fused iron catalyst usually grows as dendritic crystal. A significant discrepancy exists in the ingredients of the liquid phase within the whole porridge-like zone at liquid–solid during the solidification process of dendrite crystals (Fig. 4.9). The flow of liquid enriched solute (promoter) becomes an important source of macrosegregation. It is the phase with high degree segregations that existed in the porridge-like zone, whose movement leads to the macrosegregation during the solidification process. At the early stage of solidification, the equiaxed grains are formed, which are not connected with other grains and can float up or sink. As a result, one of the moving forms of sedimentation phase is the precipitates floating up or sinking down. Also, due to thermal shrinkage, solidification shrinkage and the density difference among the interdendritic liquids occurs in the liquid–solid-phase regions. This motion of liquids has been regarded as an important source for the formation of segregation.

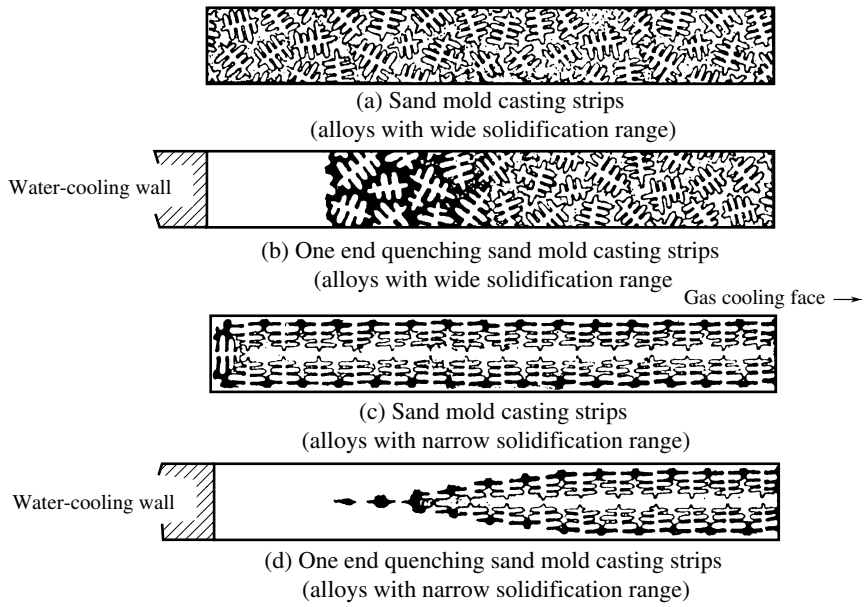

(a) Sand mold casting strips
(alloys with wide solidification range)
Water-cooling wall
(b) One end quenching sand mold casting strips
(alloys with wide solidification range
Gas cooling face
(c) Sand mold casting strips
(alloys with narrow solidification range)
Water-cooling wall
(d) One end quenching sand mold casting strips
(alloys with narrow solidification range)

Fig. 4.10 Section diagram of sand mold solidification casting strips (The dendrite was exaggerated)[21]

The cooling and solidification process of fused iron catalyst is similar to those produced in the sand mold solidification casting with quench wall as shown in Fig. 4.10. The quench wall is equivalent to the cooling face of water in the cooler, and the cap-side mouth is equivalent to the cooling face of gas. It is seen from Fig. 4.10 that the promoters are non-uniformly distributed in the center and surface in the melting body and between the dendrite crystals, which is consistent with the results obtained from scanning electron microscope as shown in Fig. 4.8. The results obtained by optical microscope on the spherical catalyst show [23] that a small amount of promoters are located at the quenched surface of the ball while a large amount of promoters exist in the center of the ball where the cooling rate is slow. Such macrosegregation was also confirmed by the SEM micro-area analysis performed on the quenched and slow cooling faces. On the contrary, when the cooling rate is fast, the solidification process is rapidly completed. All components are suddenly "frozen" so that the distribution of promoters in catalyst is uniform as the case near the quenching wall shown in Fig. 4.10. In addition, during the slow cooling, each component and solid solution with different melting points has varied freezing points, which leads to the solidification group by group, the transformation of crystal or phase. As a result, the homogeneous crystal structure cannot be obtained. The results obtained by Müssbaur studies on the spherical catalyst[24,25]show that there is a large amount of wüstite ($Fe_{1-x}O$) phase in the water-cooled samples (quenched samples). The reason is that under quenching conditions, FeO was frozen quickly and therefore the decomposition of FeO ($4FeO \rightarrow Fe + Fe_3O_4$) could not occur in time, leading to the retention of the remaining large amount of FeO.

In summary, if the direction of flow in the liquid which originated from the shrinkage of solidification were opposite to the crystal growth direction, it would

be favorable to form the dendritic segregation. If the flow direction were consistent with the crystal growth direction, such as a certain degree of agitation or centrifugal force field and the electromagnetic force field given during solidification process, the segregation of columnar crystal would decrease in the case where the flow speed is faster than the solidification rate, and *vice versa*. During the solidification process of fused iron catalyst, although there is solidification shrinkage force which leads to the flow in the internal liquid, the flow rate is lower than the solidification rate. Furthermore, because there is no mixing round and the effect of force mentioned on the flow of molten liquid is negligible, the material is basically in a static state. Therefore, larger dendritic segregation is inevitable for fused iron catalyst. High flow speed is required to ensure smaller dendritic segregation. The above discussion describes the common solidification of the melt with smaller cooling rates ($10^{-6}\,\mathrm{K{\cdot}s^{-1}}$–$10\,\mathrm{K{\cdot}s^{-1}}$). Under the fast- or ultra-fast cooling rate conditions with cooling rate of $10^{3}\,\mathrm{K{\cdot}s^{-1}}$–$10^{9}\,\mathrm{K{\cdot}s^{-1}}$ produced by powder atomization, liquid stamping, spray coating and electron beam or laser glazing film, the situation will be completely different.

At very high growth rates, the temperature at the end in the dendrite can reach that of solidest phase line and plane interface and its growth will happen (not dendritic growth). The concentration of components in the solid-phase is homogeneous and there is no segregation.

Under low overheat degree and high solidification rate conditions, it often appears as a solid–liquid two-phase region. In this situation, the macrosegregation may come from two ways that the solid-phase formed in early stage of the solidification or the floating/falling of the non-metallic inclusions, and flowing of liquid in dendrite gap of the two-phase region, which is driven by the solidification shrinkage and the density differences of the interdendritic liquids due to concentration difference.

The technological measures to reduce macrosegregation are as follows:

(1) To maintain the uniform composition of catalyst to minimize the density differences of the liquids during the solidification process which is the cause of the fluid flowing.
(2) To control appropriate height of melting material because the higher hydrostatic head of liquid leads to the more rapid flowing.
(3) To join a gestation agent into the molten material to fine grind the dendritic structure, so that the flow resistance is increased and the flow velocity is decreased.
(4) To accelerate the liquid convection at the initial stage of solidification to fine grind the grains, however, this process should be avoided during the solidification process. In the case of large speed of the natural convection in the liquid, magnetic field should be joined in addition to forcing the natural convection to stop. In this case, the macrosegregation in the centrifugal melting material is great.
(5) To accelerate cooling speed and shorten the solidification time of the solid–liquid two-phase region. The cooling of melting material will be slowed down, and the macrosegregation also becomes severer in the case of too high column temperature and too fast column speed of the system.

In order to obtain high activity of catalyst with satisfactory crystal structure, grain size, and uniform distribution of the promoter, it is significant to accelerate

the solidification and cooling speed during the preparation of fused catalyst. It is most effective to accelerate the cooling speed by heat transmission. Besides that, the following methods can also be considered: (1) To accelerate the solidification rate and fine the grains by adding a suitable amount of nucleating agents if the agents do not damage the catalytic activity. (2) To bring a disturbance or vibration on the liquid melt, such as mechanical vibration, sound waves, ultrasonic or electromagnetic vibration etc. (3) Heat treatment for the solid catalyst after solidification to reduce or eliminate macrosegregation.

Presently, the process with rapid rate of solidification and cooling is adopted for the preparation of fused iron catalyst. The rapid cooling rates can in turn rapidly solidify the involved components with different melting points without separation, thereby preventing the step-by-step crystallization and the occurrence of great internal stress. Consequently, the products with small crystal size of magnetite and uniform distribution of promoters can be obtained. In addition, decrease of Fe^{2+}/Fe^{3+} is avoided in the rapid cooling process. Rapid cooling process includes the indirect cooling method by water jacket and the direct cooling by solution (such as method used in spherical catalyst preparation) and others.

The solidification and cooling process during the preparation of fused iron catalyst is a natural cooling process, which is performed in a cooling trough with water jacket or pedrail-type cooler. The cooling rate is determined primarily by the thickness of the molten material layer. Figures 4.11 and 4.12 show the cooling curves and the cooling speed curves of samples with different thickness, respectively. It is observed that the solidification process could not be detected for the thin sample of 8 mm thickness, whose cooling rate after solidification is much faster than the sample with thickness of 41 mm. However, in the cooling process of thick samples with thickness of 41 mm, there is a solidification process with the duration from several to ten minutes, which is related to the thickness of the sample. The results of XRD show that the phase of both the thick and the thin samples is FeO, as given in Table 4.7.

It is indicated that the disproportionating reaction of FeO can be inhibited and $Fe_{1-x}O$ phase with lattice defect of iron ions is obtained when the average cooling

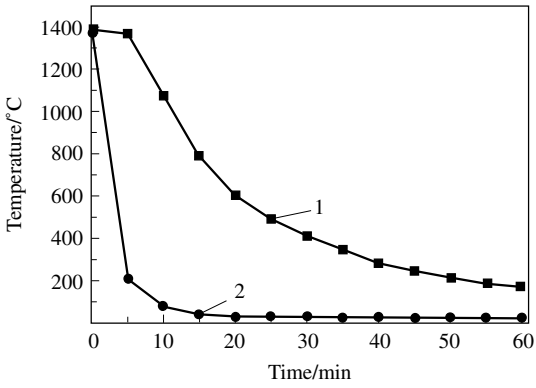


Fig. 4.11 Solidification and cooling curves

(Thickness of the sample: 1–41 mm; 2–8 mm).

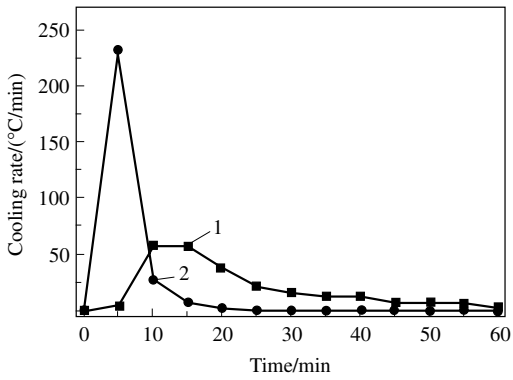


Fig. 4.12 Cooling rate curves

(Thickness of the sample: 1–41 mm; 2–8 mm).

Table 4.7 Influences of solidification rate on the distribution of surface element

		Surface element distribution/wt% (EDS)			
Thickness/mm	Phase (XRD)	Fe	Al_2O_3	K_2O	CaO
41	FeO	81.47	14.95	1.78	1.79
8	FeO	92.43	4.20	0.811	1.69

rate reaches $20°C \cdot C\,min^{-1}$ and above. However, for the thick samples, when the solidification process undergoes for several to 10 minutes, there appears serious macrosegregation of the promoters, influencing the grain size and distribution of promoter in the catalyst. Table 4.7 lists the results of EDS semi-quantitative analysis on the surface elements of the catalyst. It is seen that in the samples with thickness of 41 mm, the surface content of Al_2O_3 is 6.2 times higher than the bulk, while that of Al_2O_3 is only 1.7 times higher in the samples with thickness of 8 mm. This can be clearly seen from Fig. 4.13 (the SEM-EDS surface element distribution image). In the fast-cooling (thin samples) case, all components are suddenly "frozen" due to the rapid solidification, and the promoters can be homogeneously distributed [Fig. 4.13 (left tier)]. In the case of slow cooling rates (thick samples), the solidification in batches, crystal transformation or phase transformation occur because the components or solid solutions with different melting points have different freezing points. As a result, the obtained crystal structure is not homogeneous and the promoters gather or segregate in the grain boundaries, leading to the uneven distribution of promoters [Fig. 4.13 (right tier)]. The SEM backscattered electron images display that the grain size in the samples with slow cooling rate is larger than that of the samples with fast cooling rate.

The rapid solidification methods such as the single-roll method, twin-roll method and atomization method were adopted by the patent (CN1099353A), in which the cooling rate is more than $100\,K{\cdot}s^{-1}$ for the rapid solidification. That is, both structure of crystal and surface of iron oxide are changed, and the crystallite size in α-Fe phase decreases while the amount of high active crystal face increases. Quenching

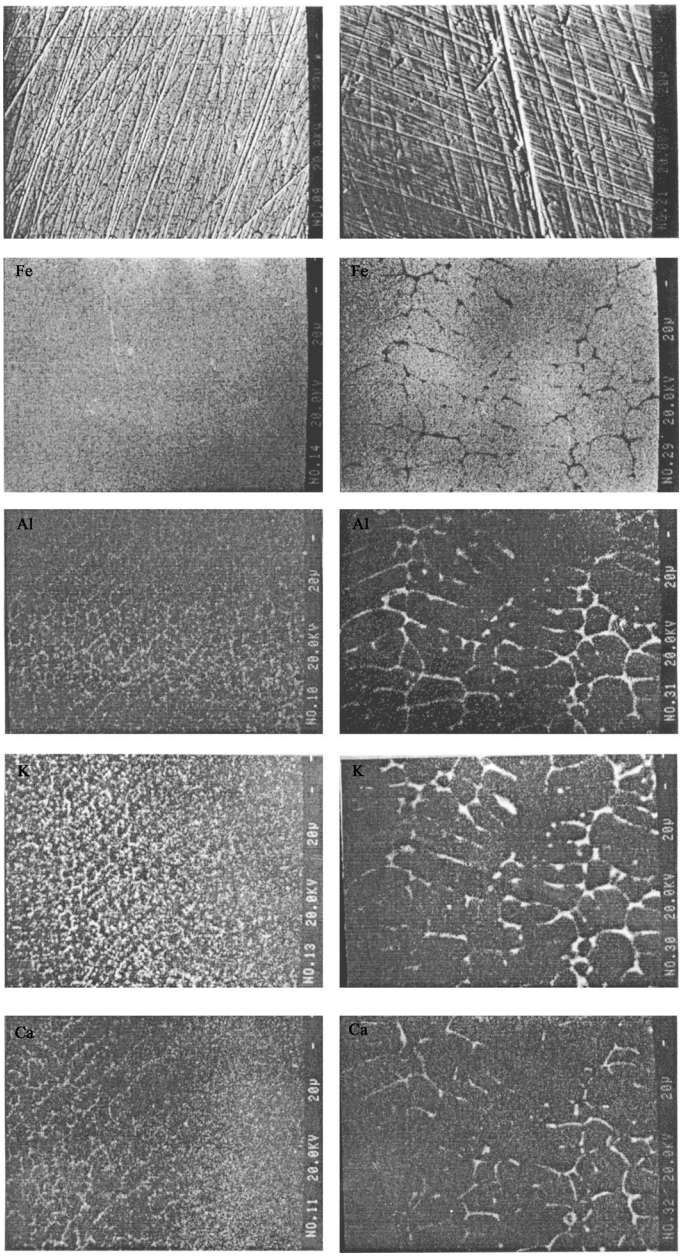


Fig. 4.13 SEM-EDS of surface element distribution (left column: 8 mm; right column: 41 mm)

also results in the formation of the pore structure, which is favorable for the diffusion of the reactants as well as the products after reduction. Due to the rapid cooling of the melt, it is too fast for the promoter to segregate, and so the promoters are evenly distributed. This prevents the crystallites from growing and sintering, leading to greater activity of the catalyst than the present ammonia synthesis catalyst.

4.5 Preparation of Prereduced Catalysts

Usually, fused iron catalyst is directly reduced in the converter of ammonia plant, while this reduction approach has some shortcomings.[26–28]

(1) It is difficult to ensure the quality of the reduced catalyst because the converter and its loop system are designed according to the best conditions of reaction for ammonia synthesis from N_2–H_2, and not to meet the optimum conditions for the reduction of catalyst even though the reducing requirements are also taken into account in some cases. However, some requirements of reducing reaction and ammonia synthesis reaction are contradictory, so that the former is usually considered as a secondary factor. In order to avoid the repeated redox of the catalyst by water vapor, the reducing reaction is better performed under the conditions of high-space velocity, low-pressure and low-concentrations of the vapor. It is difficult to meet the requirements of high-space velocity and low-pressure because the load of heater for start-up and the compressor's ability are limited in ammonia synthesis plant. It is also difficult to ensure that the temperature at high points do not exceed the normal operating temperature and at the same time, to enhance the reduction temperature as high as possible. Therefore, the intrinsic activity of the catalyst reduced directly in the ammonia plant is lower than that reduced at laboratory or in a separate equipment system.

(2) Reduction in the converter takes a long time and influences the productivity. To overcome this problem, the maximum water vapor concentration during the reduction period is allowed to about $3\,g{\cdot}m^{-3}$ or higher in a large-scale ammonia synthesis plant. However, even under these conditions, there is not only partial loss in the activity of catalyst, but for an ammonia plant with capacity of 1,000 tons per day, the reduction will be performed at least for four to seven days or longer. During this period, a large amount of raw materials and energy are consumed and thousands of tons of products are lost.

(3) For reduction in the ammonia plant, it is another trouble to treat with the large amounts of diluted ammonia liquor.[26] The pressure of reduction is usually in the range of 5–10 MPa. Under these conditions, once a small amount of the catalyst is reduced to the active α-Fe, the reaction of ammonia synthesis commences immediately. The reaction heat of ammonia synthesis can supplement the shortage of the heat supplied from outside and permits a much higher space velocity. Furthermore, a small amount of ammonia can prevent the generated water from condensing in the circulation loop, which reduces the temperature of ammonia to cool down to $-10°C$ to $-5°C$. It is easy for water to be fully condensed and separated, so that the content of water vapor of the inlet converter is decreased. These are beneficial for the reduction of catalyst. However, during the reduction period, the amount of formed ammonia is small while that of generated water is significant. That is, it will generate large amounts of diluted ammonia liquid, which has low concentration of ammonia and low merit in industrial application, and also cannot discharge it to environment directly. As a result, it is difficult to treat with the large amounts of diluted ammonia liquid.

In order to overcome these difficulties, a small amount of prereduced catalyst such as the KMR type catalyst appeared on the market and was used in a few ammonia plants at the end of the 1950s. In the mid-1990s, the prereduced catalysts

dominated the market sales volume of about 30% of the total amount of ammonia catalyst. Some plants used whole prereduced catalysts.[29]

The prereduced catalyst is reduced under ideal conditions and it is then passivated during the manufacture of the catalyst. After the prereduced catalyst is loaded into the converter, only a simple reduction is needed before functioning.

The preparation process of prereduction catalyst is divided into three steps:

(1) The preparation of catalyst in oxidation state:

$$Fe_2O_3 + Fe \rightarrow Fe_3O_4 \tag{4.22}$$

$$Fe_3O_4 + Fe \rightarrow 4FeO \tag{4.23}$$

(2) The reduction of catalyst:

$$Fe_3O_4 + 4H_2(3H_2 + N_2) \rightarrow 3Fe + 4H_2O \tag{4.24}$$

$$Fe_{1-x}O + H_2(3H_2 + N_2) \rightarrow (1 - x)Fe + H_2O \tag{4.25}$$

(3) The passivation of the reduced catalyst:

$$Fe + 1/2O_2 \rightarrow FeO \text{ (oxide film)} \tag{4.26}$$

The first step is the same as the process mentioned in Sec. 4.1. The second step is performed in a special device for the prereduction of the catalyst, in which the feed gas comes from the decomposition of ammonia or a pure fresh synthesis gas from an ammonia plant.

Figure 4.14 shows the prereduction process flow-sheet of ammonia synthesis catalyst. The reduction furnace and the process flow are designed to satisfy the optimum reducing conditions to improve the intrinsic activities of the reduced catalyst as high as possible. For example, the pressure of reduction is usually in the range from atmosphere to 1.0 MPa, and the high-power heater and cycle-compressor with large capacity of gases are chosen. Under these conditions, the catalyst is reduced

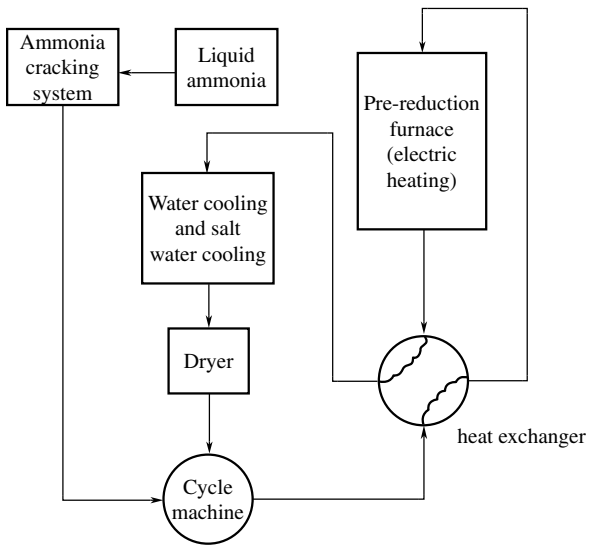


Fig. 4.14 Prereduction process flow-sheet of ammonia synthesis catalyst

at high-space velocity and appropriate temperature, and the content of water vapor is less than $1\,g{\cdot}m^{-3}$ (STP) or even as low as $0.5\,g{\cdot}m^{-3}$ in the gas from the outlet of reduction furnace. After water vapor has been separated, it is dehydrated by molecular sieves. The content of water vapor in the cycle gas can be reduced to $5\,mg{\cdot}m^{-3}$ when the gas enters into the reduction furnace. In the entire reduction process, the concentration of water vapor should be strictly controlled. To meet this requirement, the "four-high" conditions, i.e., high electric power, high space velocity, the appropriate high-pressure and high hydrogen concentration, and "four-low" conditions, i.e., low water vapor concentration, low temperature difference on the same plane, more water generated at low temperatures, low CO and CO_2 contents, are adopted in the initial stage of reduction. In order to shorten the initial reduction time and raise the furnace temperature to the same temperature range (as constant temperature) of catalysts in whole reactor the catalysts in the whole furnace can be reduced evenly and completely. It is difficult to achieve the "reduction layer by layer" of the catalyst in the ammonia plant, while this reduction can be easily realized in the catalyst manufacturing factory.

The third step is the passivation of the reduced catalyst, which is realized *in situ* in the prereduction device after the reduction. This is a key step in the preparation of prereduced catalyst because the reduced catalyst is extremely active iron with very high activity. When they contact with air, the intense oxidation and combustion will occur immediately. Thus, the reduced catalyst must be passivated. In passivation treatment process, the reduced catalyst is cooled down to slightly above room temperature, and then it is cycled in the system in which the inert gas (nitrogen or hydrogen–nitrogen mixture) containing a small amount of air is added. To form a layer of oxide film on the surface of α-Fe crystallites, the content of O_2 should be strictly controlled and gradually increased from 0.01% to 21%. Before the passivation, the reduced catalyst should be nitridized to improve its prereducing performance. The nitrification has a buffer effect on the passivation process, in which the active α-Fe is transformed to an unstable iron nitride in the presence of ammonia and then the nitrogen will be replaced by oxygen to form oxide during the passivation process. This reaction is much tender than that of direct oxidation of α-Fe, so that the loss of activity and mechanical strength of catalyst is less.

In China, Nanjing Research Institute of the Chemical Company and Catalyst Plant[30] investigated the passivation of the reduced catalyst and they suggested the appropriate passivation conditions as: The temperature range is from room temperature to–100°C, the gas is the nitrogen containing air, and space velocity of $1{,}000\,h^{-1}$–$5{,}000\,h^{-1}$. The passivation is divided into five stages, and the oxygen content in the system at various stages is listed in Table 4.8.

Table 4.8 Content of oxygen in N_2 gas at various stages during passivation

Stage	Content of oxygen/%	Stage	Content of oxygen/%
1	0.05	4	4
2	0.1	5	21 (100% air)
3	1.0	—	—

Purity of N_2: 99.9%, pressure: 0.6 MPa–0.7 MPa, time: 70 h–80 h.

The controlling of content of oxygen and the duration time at various passivation stages are critical factors for the success of passivation, which are usually evaluated and realized by adjusting the temperature of the catalyst bed. It is not appropriate to have a very high temperature or increase the temperature too quickly.

The oxide film on the surface of the reduced catalyst generated in passivation process isolates the active α-Fe from the air, which is favorable for package, store, transportation and loading of the catalyst. Therefore, the passivation treatment also can be adopted to prevent the catalyst from spontaneous combustion during the break of production and maintenance of equipments. The loading of the prereduction catalyst should be carried out under the protection of pure nitrogen gas.

The degree of oxidation or passivation is defined as the ratio of the oxygen content in the oxide film formed in passivation process to the total oxygen content of the oxidation catalyst (Fe_3O_4 or $Fe_{1-x}O$), and it can be calculated as follows:

$$\text{Passivation degree} = \frac{b \times (1-a)}{(1-b) \times a} \times 100\% \tag{4.27}$$

where "a" is the mass fraction of the reducible oxygen in catalyst before reduction and "b" is that of oxygen in prereduced catalyst. The value of a and b can be obtained from the thermogravimetric analysis (TGA).

For example, it is seen from Figs. 4.15 and 4.16 that the weight losses (oxygen content) from the TG curves of the oxidation state and prereduced state for ZA-5 catalyst are 20.64% and 5.43%, respectively. Thus, the passivation degree of ZA-5H is 22.05%.[31,32]

Generally, the passivation degree should be lower than about 15%. Very low passivation degrees indicate very thin oxide film and insufficient passivation. The catalyst will be reoxidized when it contacts with air during the package, transportation and loading. The oxidation generates heat, which further promotes the oxidation, i.e., the so-called "auto-ignition." Too high passivation degree and too thick oxide film indicates an excessive passivation. In this case, the catalyst needs a relatively deep reduction in the ammonia plant, so that the iron in the catalyst surface undergoes oxidation and reduction repeatedly, i.e., the reduction-oxidation-reduction process. In that case, the α-Fe crystallites grow up and the activity of catalyst is damaged, which ultimately affects the performance of catalyst in the

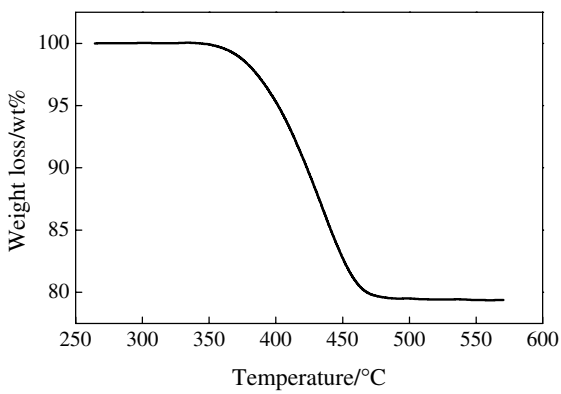


Fig. 4.15 TG curves of unreduced ZA-5 catalyst

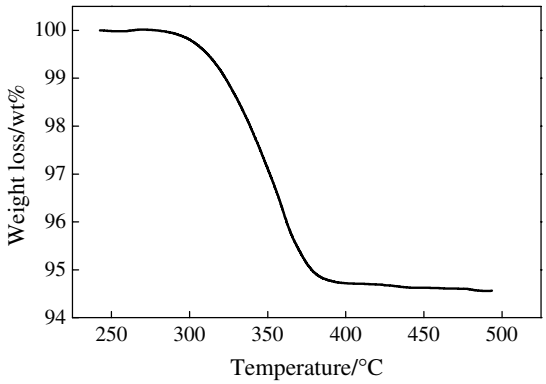


Fig. 4.16 TG curves of pre-reduced ZA-5H catalyst

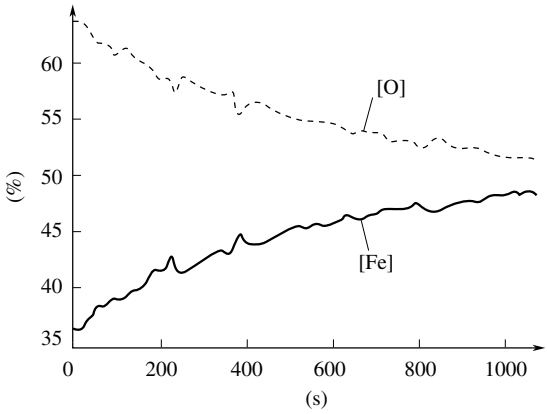


Fig. 4.17 PHI spectra of pre-reduced A110-1H catalyst

whole converter. Therefore, it is a key point to obtain appropriate thickness of protection layer of oxide film for the prereduction.

The passivation of prereduced catalysts is realized by controlling the maximum temperature of the oxidation process. Helin *et al.*[33] measured the change of the content of Fe,O in the catalyst with the sputtering depth by using the PHI-550 electronic energy spectrometer, as shown in Figs. 4.17 and 4.18.

It is seen that there is an obvious oxide protective layer in A110-1H with the thickness of about 20×10^{-10} m, while the protective film of ZA-5H is thin and its boundary is not so obvious. Ammonia synthesis catalyst contains potassium as the electronic promoter. In the humid atmosphere, the surface migration of potassium will be promoted, which affects the simultaneous ignition temperature of the catalyst. In the dry atmosphere, the simultaneous ignition temperature of the two prereduced catalysts, A110-1H and ZA-5H, is 72°C–75°C and 50°C–52°C, respectively. The A110-1 and ZA-5 catalysts show different performance after reduction i.e., ZA-5H is more active than that of A110-1H, so that its self-ignition temperature is lower than that of A110-1H. The effect of moisture on the autogenously ignition temperature of these two catalysts is not significant.

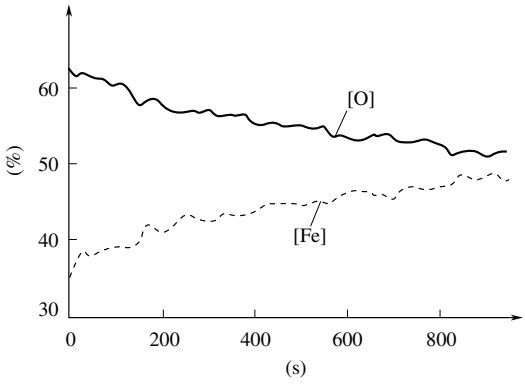


Fig. 4.18 PHI spectra of pre-reduced ZA-5H catalyst

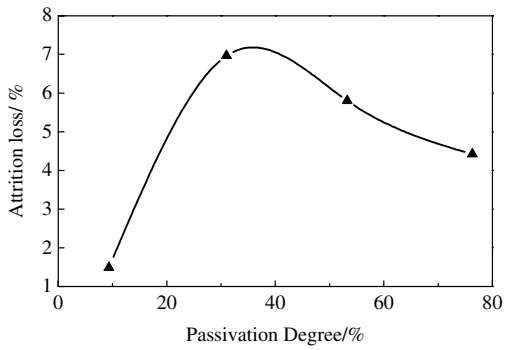


Fig. 4.19 Influence of passivation degree on the attrition loss of pre-reduced ZA-5H catalyst

Some believe [33]that the large-scale ammonia plant which has more abundant loading catalyst, the efficiency of the converter would not be affected by sacrificing the partial activity of catalyst to a certain extent and appropriately increasing the thickness of the protective oxide film in order to improve the security of the prereduced catalyst. It was reported that the KMIR-type prereduction catalyst produced by Topsøe Company at Denmark has a thicker protective oxide film than that of A110-1H catalyst, whose simultaneous ignition temperature is 100°C or above with sufficient security.

It is worth noticing that the mechanical strength (abrasion) of prereduced catalyst is closely related to the thickness of the oxide film. The thicker the oxide film, the greater the attrition loss, and the lower the mechanical (abrasion) strength. Figure 4.19 shows the influence of passivation degrees on the abrasion loss of prereduced ZA-5 catalyst. It is seen from Fig. 4.19 that with the increase of passivation degrees, the abrasion loss first rises and then slowly decreases. The abrasion loss approaches a maximum of 6.96% when the passivation degree reaches about 31%. With the passivation degree further increasing, the abrasion loss decreases while it is still much higher than 1.49% in the case of the passivation degree of 9.35%. This effect of passivation degree can be explained by the formation of the surface oxide film on the catalyst.

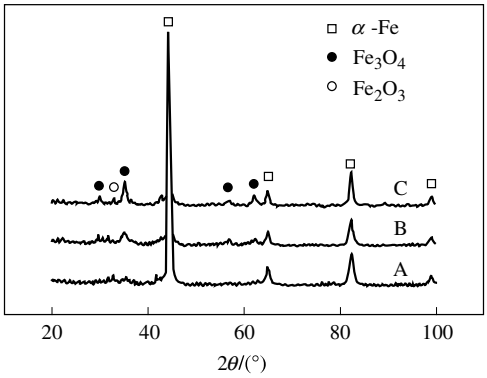


Fig. 4.20 XRD patterns of the surface layer of pre-reduced ZA-5H catalyst with various passivation degrees

(The passivation degrees of A, B, C is 9.35%, 22.05% and 31.01 %, respectively).

Figure 4.20 shows the XRD spectra of the surface layer on the prereduced ZA-5H catalysts with different passivation degrees. The protective oxide layer was rubbed away from the surface of the prereduced ZA-5H catalyst by using the abrasion tester, so that the powder of oxide protective layer was obtained as the sample of XRD measurements. In addition, the XRD spectra of the surface layer powder have some discrepancy because the powder will reacts with air during its cracking process. Some useful information can be obtained from Fig. 4.20. It is found that with the increase of passivation degrees, the Fe_3O_4 phase is gradually increased. Specially, sample C with passivation degree of 31.01% appears in Fe_2O_3 phase. In fact, the violent reactions can occur once when α-Fe contacts with O_2 as follows:

$$2\alpha - \mathrm{Fe} + \mathrm{O_2} = 2\mathrm{FeO} + \mathrm{Q} \tag{4.28}$$

$$3\alpha - \mathrm{Fe} + 2\mathrm{O_2} = \mathrm{Fe_3O_4} + \mathrm{Q} \tag{4.29}$$

$$4\alpha - \mathrm{Fe} + 3\mathrm{O_2} = 2\mathrm{Fe_2O_3} + \mathrm{Q} \tag{4.30}$$

where, Q is reaction heat. The oxygen anion O^{2-} in the oxide film can obtain energy from the reaction heat. When O^{2-} gets enough energy, it begins to move to the internal catalyst. With the temperature increasing, the energy of O^{2-} for the diffusion to the internal catalyst becomes higher, so that the diffusion speed becomes faster. In this case, the oxide film in the catalyst surface gradually grows thicker from outside to inside with the temperature during the passivation process. Due to the very rapid speed of the reaction of O_2 with α-Fe, the whole passivation process is controlled by the diffusion process. In the migration process of O^{2-} to the inner catalyst, it is more difficult for O^{2-} to diffuse and the energy required is higher with the diffusion depth, so that the oxygen content is lower in the inner of the oxide film. As a result, three oxide films of Fe_2O_3, Fe_3O_4 and FeO are formed from the outside to the inner,[32] while there are no clear boundaries between the oxide films, and the thickness of the films is different. Because the abrasion strength of the prereduced catalyst depends on the thickness of the oxide film, it is the key to control the thickness of the oxide film, i.e., the passivation degree, to prepare the high-strength prereduced catalyst.

However, in the industrial applications, the prereduced catalyst will again be reduced to eliminate the oxide film formed during passivation process. The above-mentioned abrasion strength which mainly depends on the oxide film thickness and the combining capacity with the matrix metals cannot truly represent that of the prereduced catalyst in the industrial reactors.

The prereduction catalyst is prepared under the ideal conditions, and its intrinsic activity before passivation should be higher than that of the catalyst reduced directly in ammonia plant. However, during the passivation process, the catalyst is again reoxidized, while oxygen is a poison for iron catalyst. Therefore, the passivation process is essentially a poisoning process, which damages the catalyst activity. In the industrial use, the catalyst will be re-reduced again, and this repeated oxidation–reduction process causes α-Fe crystals to grow up, irreversibly decreasing the activity of catalyst. Therefore, the high activity obtained in the second step has been partly or wholly offset by passivation process. That is, the activity of the prereduced catalyst is usually lower than that of the catalyst reduced directly in the ammonia plant.

At room temperature, the prereduced catalyst can still react slowly with the oxygen in air, but this can only be obviously perceived after several months. In the transportation process, the mutual friction and collision among the particles leads to the local shell-off of the oxide film, but a new oxide film will be formed by the reoxidation in air.

The prereduced catalyst must be stored in a dry storeroom. The catalyst is prohibited to contact water because water molecules can drill through the oxide film to react with the active α-Fe and H_2 is released following Eq. 4.31.

$$Fe + H_2O = FeO + H_2 \tag{4.31}$$

One should be very careful during the loading of the prereduced catalyst into the converter in plant. In order to achieve the solid filling of catalyst and insure a homogeneous distribution of gas flow, the loading of catalyst usually uses mechanical oscillator in large-scale converter. In this process, the oscillation should not be too strong; otherwise the oxide film of the particles will be worn away. In the case that small amounts of α-Fe are exposed in air, it will react with oxygen consuming the oxygen in the converter room. The staff in the converter room will be faced with the risk of suffocation without oxygen supply. Therefore, workers in the converter room must take adequate protection measures. For example, they should wear mask for oxygen supply. Another risk in the filling lies in the violent oscillation, which leads to the destruction of a large amount of oxide film. After that, oxidation reaction of iron will rapidly happen and result in a rapid increase in temperature of catalyst bed because the reaction as in Eq. (4.26) is a strong exothermic reaction. The rising of temperature in turn speeds up the oxidation of Fe, forming a vicious recycle and eventually leading to high temperature of 1,000°C or above. This leads the catalyst to sinter and lose the activity, and the high-pressure cylinder of converter will be jeopardized. Such serious incidents occasionally occur, and hence we must keep high caution. Therefore, during loading of the prereduction catalyst, the temperature of catalyst bed should be closely monitored and it is necessary to supply inert gases (such as N_2) at hand. Once it shows a trend of rapid increase of temperature of catalyst bed, the staff should immediately leave the converter and flush N_2 into the converter. When the temperature drops to a normal value, the loading can be resumed.

4.6 Preparation Technique of Spherical Catalysts

4.6.1 *Shaping technique of catalysts*

A successful solid catalyst must meet the requirements such as that it not only selectively catalyzes the target reaction but also has good mechanical strength and appropriate shape. The latter can avoid the large pressure drop or non-uniform distribution of liquid when it flows through the catalyst bed.[34] Moreover, the catalyst must keep its activity and mechanical properties during the long-term run (including the start and shut down of the converter). For that purpose, the catalyst must meet three basic conditions such as high-activity, reasonable fluid flow property and long lifespan, and also some structural properties of catalyst must be confined as shown in Fig. 4.21. In order to get high-activity, the catalyst must have high-surface area and appropriate porous structure, so that the reactant can enter into the inner surface of the catalyst particles by diffusion. Ideally, for the catalyst controlled by the strong internal diffusion, when the porosity is about 50% under the operating conditions, the catalyst has the highest activity per unit volume (for the metal catalyst, its activity is that of before reduction). Usually, for the catalyst particles with enough mechanical strength, it is difficult to achieve such a high-porosity. Part of the catalyst preparation technology is focused on dealing with these conflicting demands. The preparation of catalyst with high-strength and stability critically depends on the formation of a kind of structure in which all components are firmly felted together. This structure will not undergo significant decomposition or changes due to sintering during operation. For a successful industrial catalyst product, another demand is the reproducibility in performance and relatively cheap price of the catalyst.

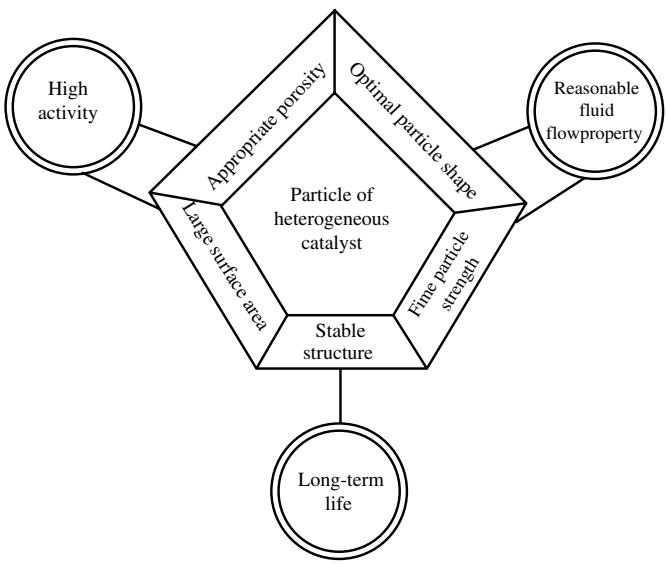


Fig. 4.21 Requirement of ideal catalyst

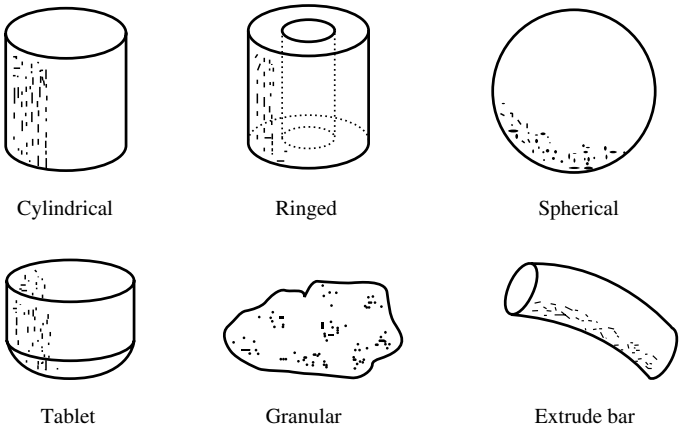


Fig. 4.22 Common particle shapes of industrial catalysts

Therefore, the prepared catalyst should possess the given chemical composition and physical structure and shape, which can meet the requirements of engineering. The geometrical shape and particle size of catalyst are determined by the requirements in industrial process, including the type of the reactor, the operation pressure, flow velocity, permitted pressure drop of the bed, the reaction kinetics, the physicochemical properties of the catalyst, shaping properties and economic factors.

The shape of particles in the catalyst commonly used in industries includes cylindrical, spherical, flake, mesh, powder-like, irregular-shaped and strip and so on (Fig. 4.22). During the recent years, there are also many special shapes of catalysts, such as the bowl, three leaf-like, the wheel-shaped, honeycomb and membranous etc.

One of the most common shaping methods for the catalyst is tabletting method by pelletizer. The advantage of this method is that the derived catalyst has cylinder or ring structures with very regular, smooth surface, which can easily roll and can be filled uniformly in the catalyst bed. A uniform free spatial distribution, uniform fluid flow property and good fluid distribution can be achieved. Pelletizer can produce hard troche that can withstand large impact load arising from the filling of catalysts. However, only when the punching nail and die of the pelletizer is of precise size, the feeding particles would have reasonable size. Also, the density of the troche should be appropriately adjusted. Under these conditions, the troche has these required properties. In addition, enough amount of (not too much) die wall lubricants must be added into the feed materials to reduce wall friction, which can deliver the pressure more evenly which is generated from the up-punching and down-punching the whole troche, resulting in uniform (not different) compacting stress. Otherwise, the troches are fractured when the compression load is removed and the stress is relaxed. The typical fragments are "unbonnet" (i.e., end-scale off) and "waist breaking" (that is, middle fracture) of troches. Graphite and calcium stearic acid are commonly used as die wall lubricants. Excessive lubricants in the catalyst will weaken the structure.

Theoretically, all solids can be squashed in three directions under large enough external force. In fact, it is performed on pelletizer which is made up of steel nails and dies. Therefore, the pressure must be lower than the limits that can cause the

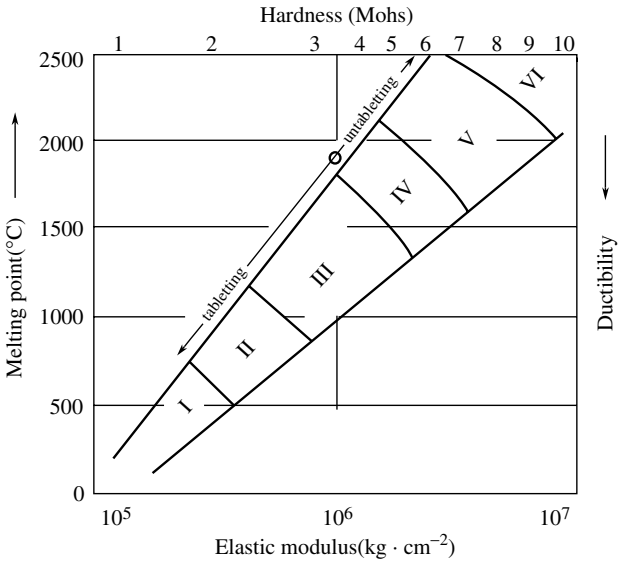


Fig. 4.23 Relation between the elastic module of inorganic solid and their melting points[34]

I, Halides, II, Sulphate and nitrate, III, Hydroxide, carbonate and sulfide, IV, Hard metal, V, Refractory oxide, VI, Diamond.

permanent deformation of punching nail and die. Thus, the major component of the compression material must be softer than the steel, and its plastic deformation must occur before the plastic deformation of the steel. In this respect, there is a rough correlation between the strength as well as hardness and their melting points of the inorganic solid (Fig. 4.23). The solid with low-melting point has a low hardness and strength, while that with high-melting point has a high hardness and strength. The general sequence from low to high hardness and strength is: Halide, sulfate-nitrate, hydroxide-carbonate-sulfide, hard metal, and high-temperature resistant oxide. In the usual pelletizer, only three softest types of materials with Mohs hardness not more than four can be pressed satisfactorily. For example, if the feed powder is only composed of Al_2O_3 and graphite, it cannot be squashed. In order to squashing the mixture, the third component should be added into the mixture according to the criteria of compression.

The integrated structure of the ammonia synthesis catalyst is formed in the final stage of catalyst preparation, i.e., the final reduction process in the reactor. Ammonia synthesis catalyst of oxidized state is composed of large crystalline magnetite aggregates, which contains the solid solution of alumina. Other promoters are introduced into the catalyst besides the major non-sintering component of alumina. The reduction reaction carries out from the outside to the inside of the catalyst particles, and alumina is preserved in the large magnetite particles along the mesh-like skeleton of crystal planes. Each magnetite crystal is reduced into large amounts of iron crystallites, and they are loosely located at the mesh-like skeleton of alumina. The total volume of solid-phase iron is clearly smaller than that of the magnetite. Electron microscopy photograph shows that the arrangement of crystalline iron is

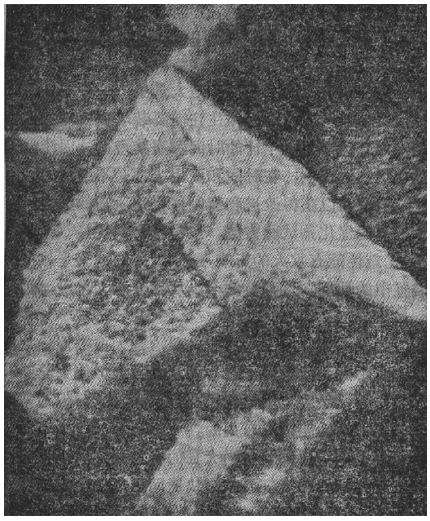


Fig. 4.24 Electron microscope photograph of the reduced catalyst for ammonia synthesis

just like stacks of eggs in a basket, in which the highly dispersed alumina and empty ditches are distributed between the iron crystals (Fig. 4.24).

The catalyst can be shaped by granulator and extruder besides the pelletizer. Various binders are often used in these two shaping processes in order to obtain the catalyst with sufficient mechanical strength. Each shaping process has its special technology. Therefore, the components which are appropriate for tabletting are generally not appropriate for the granulation and extrusion, and vice versa. As previously emphasized, it is necessary to take into consideration many conflicting demands for manufacturing an industrial catalyst. The general principles are easy to understand, while their detailed application and realization would need to combine the theories of catalysis, inorganic structural chemistry, colloid chemistry, materials technology, rheology and chemical engineering.

The shaped catalyst should have sufficient strength to resist the four types of stress without breaking. First, it must have sufficient strength to resist the wear caused by rolling and falling in packaging barrel during transit. Second, it must withstand the actual impact load originated from the falling from a few meters high to present material pile when the catalyst is loaded in reactor. Third, it must have sufficient cohesion especially for the prepared troche and it should not break due to the various chemical changes during operation (such as the reduction or oxidation of certain components in the troches). Fourth, the reduced particles must withstand the load caused by the pressure drop, the weight of the upper particles and the relative movement due to the expansion and shrinkage of the bed or reactor. The composition and structure of the catalyst remain unchanged after shaping and before the reduction in the reactor, so that the capability of withstanding the first and second kinds of load is directly related to the former operation. However, some shaped catalysts will be subject to further processing such as impregnation, calcination or cement condensation, and their final strength has little direct relationship to the former operations.

The impact force during the loading of catalyst is much larger than that during the transportation of catalyst. Under this kind of load, the particle strength can be expressed by the minimum loading height for causing a rupture. Of course, the loading surface property of the catalyst must be provided. The ideal case is that the loading surface has the same hardness as the catalyst, or it can be slightly harder than the catalyst, while it must not be softer than the catalyst. For example, the minimum loading height in the case of the troche breaking is related to the ratio of diameter to height and the ultimate tensile strength (UTS). A rough approximation of the relationship is expressed as follows:

$$\text{The loading height causing breakdown (m)} = 0.075\ (\text{UTS})\ \text{d/L, UTS: kg·cm}^{-2}$$

It is seen from the equation that the strength of gracile troches is smaller than that of the podgy troches. The most common ratio is $\text{d/L} = 1$, and the smallest landing height is designed for 3 m or UTS for $40\,\text{kg·cm}^{-2}$.

The strength requirement of troches is correlated with the porosity and ductility of troche described in Fig. 4.23. For many diffusion-controlled catalysts, the porosity of 0.4 to 0.6 is ideal, and to match this value, the UTS should be about $40\,\text{kg·cm}^{-2}$. The upper limit of hardness depends on the structure of the pelletizer, and therefore the production scope of satisfied troches is determined.

The strength of spherical catalysts are usually characterized by the crush strength of single grain (Chapter 8) or by the minimum loading height.

4.6.2 *Preparation technique of spherical catalysts for ammonia synthesis*

The shape of ammonia synthesis catalyst is usually irregular. However, the regularized shape is more favorable to the general requirements of ammonia synthesis catalyst. In order to maintain low pressure drop, the grinding angle technology was used in the preparation of United States UCIC73-1 and C73-RS catalyst. The shape of the KMRC catalyst produced by Topsøe Company at Denmark is dual-gibbosity cylinder of $\phi 6\,\text{mm} \times 6\,\text{mm}$ or ringed cylinder of $\phi 13/6\,\text{mm} \times 3\,\text{mm}$.

The shaping (spherical or other regular shapes) technology of ammonia synthesis catalyst has been extensively studied.[35–39] The processing routes can be roughly divided into two categories.

(1) The pressing and sintering technology, in which the processes usually include melting, solidification, cooling, crashing, compression molding, and then sintering at high-temperatures. This technology was adopted by Topsøe Company, Denmark, Casale Company, Sweden, and Empire Chemical Companies (ICI), Britain. In addition, the technology where the spheres were formed by disk granulator in the Soviet Union and then were sintered in helium at 1,350°C is included in the pressing and sintering technology. This technology is a complex process, and its energy consumption and cost of production are high, while the activity and mechanical strength of the catalyst are lower than those of the irregular-shaped catalyst made by direct solidification of the melt. Therefore, it is difficult to realize the application in industry.

(2) One-step shaping method was originally proposed in China, in which the melting material is directly dispersed into balls before the solidification and then

cooled and screened to obtain spherical catalyst. This technology is a relatively simple process, and it can improve the production efficiency compared with the sintering method. The preparation technology of spherical catalyst was developed successfully by Zhengzhou University[40,41] and Zhejiang University of Technology[42] in 1970's. A series of spherical catalysts of ZA-1 Q, A110-5 Q, A202 Q, and A310 Q have been widely used in ammonia plants.

The "liquid melt directly conglobating" process can produce the spherical catalysts in a variety of grain sizes. We have developed the mechanical impact dispersion method, the liquid spurting impact dispersion method, the continuous conglobating method and straight falling conglobating by a fixed nozzle or centrifugal spraying conglobating by a rotating nozzle.[43]

4.6.2.1 *Methods of mechanical impact dispersion and liquid spurt impact dispersion*

The two methods: Mechanical impact dispersion and liquid spurt impact dispersion are both batch production methods. The principle is that the liquid melt is dispersed into droplets by mechanical impact [Fig. 4.25(a)] or high-speed fluid impact [Fig. 4.25(b)]. The melt droplets shrink into a spherical or near spherical particles due to their own surface tension. The detailed technology is as follows: The feed magnetite and various promoters are mixed evenly and are then melted in electric furnace at position 1. When the melting is completed, the rear part of the electric furnace is stepped up and the liquid melt is discharged slowly from the outlet 2, and falls into the rotating roller 3, or impacts with the high-speed water stream from the nozzle 5, and it is dispersed into droplets due to the impact of the roller or high-speed water stream. The droplets of the liquid melt and then freely fall into the cooling pond 4 containing water or solutions and are cooled rapidly. The ball and the solution are separated through a segregator with a mesh in the inner of cooling pond 4. After heat treatment at 500°C–800°C, the irregular particles are removed by screening, so that the spherical catalyst with a variety of particle sizes is obtained.[44] This method is simpler compared to high-temperature sintering method, but the particle sizes of the catalyst are non-uniform and the shape factor is small due to the dispersion from impact. Non-spherical fragments and fine powders (microspheres, not used for industry) are more, so that the yield of the product is not high (30%–50%). In addition, the particles must be selected manually, which consumes much time and labor. The cost and energy consumption of products are

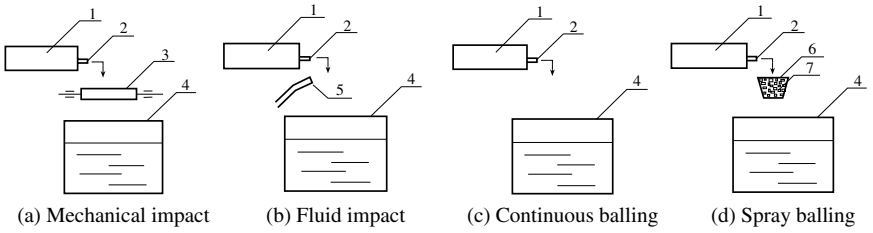


Fig. 4.25 Process diagram for one-step glomeration method

1, Electric molten furnace; 2, Exit; 3, Roller; 4, Cooling pond; 5, Nozzle of liquid; 6, Rotary nozzle; 7, hole of nozzle.

also high. Moreover, in this process, it is very easy to have a strong splash and burst as large amounts of liquid melt with high-temperature (1,550°C or so) dashes into the water or solution, which endangers the safety of the worker and the equipments. The spherical catalysts such as the A110-5Q and A310Q produced by this method have been used in industry for more than 20 years.[45–48]

4.6.2.2 *Continuous glomeration method*

The main difference between the continuous method[49] and the mechanical impact or the high-speed water impact method is that the former is a continuous production process (Fig. 4.25(c)). In the continuous process, the three-phase electric furnace is used, which allows the liquid to melt continuously. Then, the liquid melt is dispersed into the ball under a certain disturbance. The ZA-1Q spherical catalyst produced by this method has been used in China.[49]

4.6.2.3 *Spraying glomeration method*

The spraying balling method[50] is also a continuous production method (Fig. 4.25(d)). The difference between the spraying balling method and the continuous balling method mentioned above is that the continuous melt flow from the outlet 2 first goes through a specially designed and fixed nozzle or rotary nozzle 6. The nozzle 6 is a cone with the conical angle of 4°–16°, and the diameter of the nozzle hole 7 is 0.002 m–0.012 m and the rotation speed is 200 r· min^{-1}–500 r· min^{-1}. The distance between sprayer 6 and the discharge outlet 2 as well as that between sprayer 6 and the liquid plane of cooling trough 4 is less than 2 m. The liquid melt through the nozzle hole 7 is separated uniformly into many shares of trickles. Under the rotation and gravity, trickle fluids quickly break into droplets, and then shrink into spheres due to their own surface tension. In the granulation tower, the spherical particles are suspended under the reverse air flow with certain velocity (speed of less than suspension velocity) and fall in spiral trajectory. At the same time, they are cooled by the air flow. Then, they are transported into the grading sieve or directly fall into the cooling pond 4, which contains water or other solution for rapid cooling. The spherical particles and the solution are separated through the separation equipments. After heat treatment, the particles are sent to the grading screen and the products of spherical catalysts with different size of particle are obtained.

A single flow of liquid melt in which flow volume and flow rate from the electric furnace outlet are changed is transformed into many trickle flows with the same flow volume and flow rate and is uniformly sprayed into spheres when they go through the nozzle of fixed or rotary sprayer. Thus, the derived products have homogeneous particle size and the yield of products is especially high, in which the percentage of particles with diameter bigger than 0.002 m as high as for 90% when the hole diameter of nozzle is 4 mm (Table 4.9). The energy consumption and cost of production of catalyst are reduced greatly. Compared with the present balling technology, the energy consumption can be reduced by more than 30% and the production capacity can be increased by about 50% in the spray balling method. It is easy to prepare catalysts with different particle sizes according to the requirements by changing the

Table 4.9 Yield of the spherical catalyst prepared by spraying method

Glomeration method	Hole diameter of nozzle/mm	Yield (particle diameter of product $\geq$ 2 mm)/%
Spurt by fixed nozzle	4	84.1
(100kg of industrial test)	5	83.0
Spurt by rotary nozzle	4	93.9
	4	93.5
	4.7	97.0
	4.7	95.1

diameter of hole in the nozzle. This process is not only suitable for the aforementioned wet cooling (falling into the water or solution), but also applicable to dry cooling (cooling in the gas flow in granulation tower). That is, the spherical particles emitted from the nozzle and falling in spiral trajectory will be cooled by the reverse gas flow in the granulation tower, and therefore the heat treatment process can be omitted. In this way, the spherical particles have intact forms without gaps, and the shape coefficient of the particles is close to one. Furthermore, high mechanical strength (Table 4.10) and therefore low resistance of liquid flow can be achieved. The spray balling process effectively avoids the shape coefficient and mechanical strength decreasing caused by the mechanical dispersion and fluid impact method. In the latter two processes, when the surface of particles has solidified and the inside is un-solidified, the particles fall into the water or solution, forming the gaps under the impact of the water surface. Thereby it decreases the shape coefficient and mechanical strength of the catalyst. At the same time, for the spray balling process, the occurrence of high-temperature explosive and splash is avoided, so that the heat treatment and ball picking processes is not needed. This is preferred to simplify the process and achieve the safe and high efficiency production. The continuous balling technology has the characteristics of high granulation ratio, high mechanical strength and safe operation. The yield, spherical coefficient and mechanical strength of products are listed in Tables 4.9 and 4.10,[50] respectively.

As the spherical catalyst is prepared by quencher in water or aqueous solution, there are some differences between the spherical catalyst and the irregular catalyst cooled indirectly (such as air-cooled or water jacket cooled catalyst) as follows:[51]

(1) The internal structure of the spherical catalyst is closely stacked by different sizes of pebble-shaped grain, whose diameter and pore of grain are smaller than those of irregular-shape catalysts.
(2) More potassium is separated out, and the coverage of alkali after reduction (465°C–470°C for 60 h) in the spherical catalyst is higher than that of the irregular-shaped particles.
(3) The shape coefficient Φ_S of particle (for particle size of 2.2 mm–9.4 mm) achieves 0.75–0.97 and it is larger than that of the irregular-shaped particle Φ_S (0.3–0.5).
(4) More alumina enters into the Fe_3O_4 lattice, and they are homogeneously distributed in the Fe_3O_4 lattice.
(5) When the Fe^{2+}/Fe^{3+} ratio is the same, the spherical catalyst contains more wüstite phase, and so has faster reduction rate.

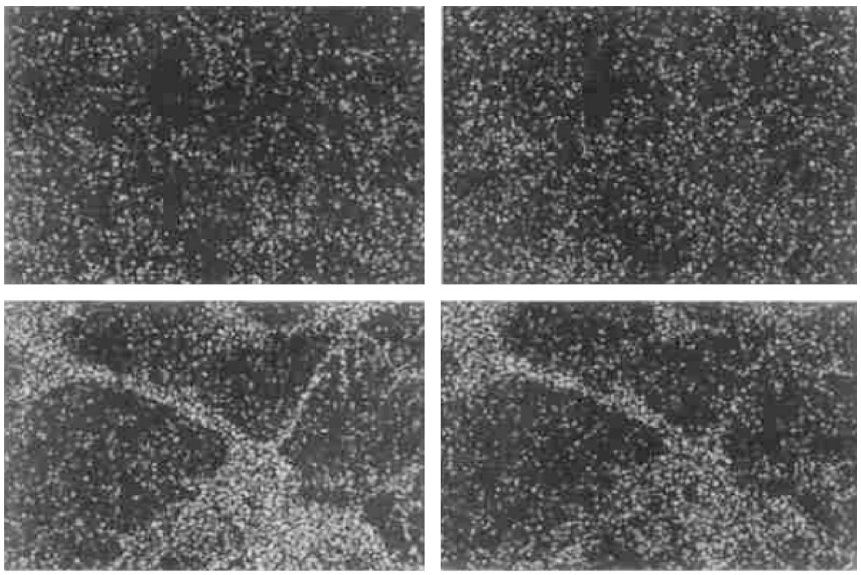
Table 4.10 Mechanical strength and spherical coefficient of the spherical catalyst prepared by spraying method

Sample No.	1	2	3	4	5	6
Particle diameter/mm	6.05	4.52	5.30	3.10	4.15	5.02
Spherical coefficient/Φs	0.98	0.95	1.00	1.00	1.00	1.00
Mechanical strength/(N/per grain)	192	404	372	198	251	87

Sample No.	7	8	9	10	11	12
Particle diameter/mm	6.1	3.82	3.55	3.05	4.15	4.47
Spherical coefficient/Φs	0.98	0.99	1.00	1.00	0.98	0.97
Mechanical strength/(N/per grain)	229	294	148	303	301	223

Note: $\Phi_S = (ac/(b^2))^{1/3}$, where a, b, c represent the size of pellet in three directions, respectively, and in which, b is most size.

Figure 4.26 is the surface element distribution[52] of the promoters in the water-cooled and gas flow-cooled catalysts. The EDS data are listed in Tables 4.11 and 4.12. It is seen that the distribution of promoters is more uniform in the water-cooled catalyst, which originates from the almost disappearance of promoter segregation due to the rapid cooling of the melting materials. In the contrary, for gas flow-cooled catalyst, it is difficult for Al^{3+} to enter into the $Fe_{1-x}O$ lattice, and it is easy for the promoters to segregate from the major phase of the catalyst due to the slow cooling rate. As can be seen from the surface distribution photographs, the



(a) Distribution of Al (b) Distribution of K

Fig. 4.26 Distribution of promoter in catalysts by the water cooled and gas flow cooled methods

Table 4.11 Distribution of element of promoter in the irregular catalyst cooled by gas flow (wt%)

Location	O	Al	Si	K	Ca	Mn	V	Fe
1	1.35	0.89	0.12	1.04	0.31	—	0.27	96.02
2	15.09	2.57	—	0.76	0.67	—	0.43	80.47
3	19.92	1.65	—	0.23	0.71	—	0.33	77.17
4	23.36	2.74	—	0.68	0.69	—	0.41	72.11
5	25.87	7.39	0.33	27.53	4.48	0.50	2.68	31.22
6	24.17	8.81	0.16	24.83	8.29	0.87	0.58	32.26
Maximum	25.87	8.81	0.33	27.53	8.29	0.87	2.68	96.02
Minimum	1.35	0.89	0.12	0.23	0.31	0.50	0.27	31.22

Table 4.12 Distribution of element of promoter in the spherical catalyst cooled by water (wt %)

Location	O	Al	K	Ca	V	Mn	Fe
2	26.69	2.52	—	0.74	0.28	—	69.75
3	18.91	1.73	0.21	0.73	0.34	—	78.28
4	20.28	2.42	0.22	0.40	0.31	—	76.37
5	14.83	1.84	0.34	0.66	0.31	—	82.02
6	21.91	2.29	0.22	0.55	0.31	0.25	74.46
7	21.64	1.61	1.04	0.68	0.34	0.19	75.04
8	16.28	1.87	0.37	0.72	0.34	—	80.42
9	15.14	2.57	1.33	0.74	0.24	0.27	79.71
10	24.01	6.86	2.17	0.72	0.23	—	66.00
Maximum	26.69	6.86	2.17	0.74	0.34	0.27	82.02
Minimum	14.83	1.61	0.21	0.40	0.23	0.19	66.00

promoter distribution of flow-cooled catalyst is apparently uneven. The promoters are enriched around the iron crystal. The distributions of Al and K are similar which indicates that the little acidic Al_2O_3 and alkaline K_2O amalgamate.

4.7 Recycling of Waste Catalyst for Ammonia Synthesis

The spent and discharged catalyst from converter in ammonia plant is called as waste catalyst. The waste catalyst is mainly composed of 65%–80% of metallic iron, 10%–20% of iron oxide and 8%–10% of promoter oxides such as Al_2O_3, K_2O, CaO, CoO etc. At present, they are generally abandoned or are interred in the scrapheap. This is not only a waste of resources, but also leads to environmental pollution, especially for the catalyst containing precious metals such as cobalt which has great recycling value. Example, the content of CoO and promoters in Fe-Co catalysts is illustrated in Table 4.13.

Table 4.13 Composition (%) of iron-cobalt catalyst before reduction

CoO	CaO	K_2O	Al_2O_3	MgO	SiO_2	Iron oxide
1–5	1.9	0.8	2.5	0.2	0.5	Residual

Every recovery of one ton of the waste catalyst is equivalent to the recovery of about 50 kg of CoO or 54 kg of Co_3O_4, 35 kg of $CaCO_3$, 17 kg of KNO_3, 25 kg of Al_2O_3 and 900 kg of magnetite etc. The consumption of ammonia synthesis catalyst is about 5,000–6,000 tons per year in China, in which catalyst containing cobalt is about 1,000 tons and the recoverable amount is 54 tons of Co_3O_4 where the recovery value is very great. Besides, for 5,000 tons of the waste catalyst, there are recoverable 175 tons of $CaCO_3$, 85 tons of KNO_3, 125 tons of Al_2O_3 and 4,500 tons of magnetite etc.

Technically, it is difficult to recover a single component in the waste catalyst and the total amount of waste catalyst is limited. It may not be rational in an economic sense. Probably, it is the best way to recycle the catalyst as a whole and then use the recycled catalysts for production of a fresh catalyst, so that all the components of waste catalyst can be used effectively. However, it is not an easy thing to transform the waste catalyst to new catalyst because the main component of the waste catalyst is metallic iron (Fe) with the content of more than 70% while the iron in the new catalyst should be iron oxide. Therefore, the metallic iron should be first transformed into iron oxide. The method for the transformation is varied according to the required state of iron oxide in the fresh catalyst.

(1) In the conventional fused iron catalyst, the iron oxide must be magnetite (Fe_3O_4) within the ratio of Fe^{2+}/Fe^{3+} in the scope of 0.4–0.8. Oxidation by air or oxygen is the only way to transform the metallic iron into Fe_3O_4:

$$\text{Waste catalyst (Fe)} + O_2 \rightarrow Fe_3O_4 \tag{4.32}$$

The recycling of waste catalyst has been studied.[53,54] Using the oxidation method, the metallic iron in waste catalyst was first transformed into magnetite (Fe_3O_4) and then was placed in an electrical furnace for remelting, or was directly loaded into the melting furnace for the oxidation by oxygen during melting. The precursor of the catalyst obtained by this method is still Fe_3O_4, and the catalytic activity is similar to that of the catalyst made from natural magnetite. In fact, most amount of waste catalysts have not been recycled because the recycling and manufacturing method described above is complicated and the cost is high compared with the process using cheap natural magnetite. Moreover, recycling by direct remelting is discouraged by the consideration that the Fe^{2+}/Fe^{3+} ratio must be in the scope of 0.4–0.8 for Fe_3O_4 precursor. That is, it is impossible to prepare the conventional fused iron catalyst using Fe_3O_4 as precursor and only the mixture containing metallic irons is obtained. Thereby, the ideas of recycling the waste catalyst were abandoned.

(2) The iron oxide in the novel $Fe_{1-x}O$-based catalyst is $Fe_{1-x}O$. In order to transform the metallic iron in the waste catalyst into $Fe_{1-x}O$, the following chemical reaction can be adopted:

$$\text{Waste catalyst (Fe)} + \text{Magnetite}(Fe_3O_4) \rightarrow Fe_{1-x}O \tag{4.33}$$

That is, the 70%–80% of metallic iron of the waste catalyst can be used as a reducing agent for the reduction of magnetite to FeO, and $Fe_{1-x}O$-based catalysts can be obtained. At the same time, all the promoters such as Al_2O_3, K_2O, CaO, CoO, etc in the waste catalyst enter into the fresh catalyst (the amount of promoters in fresh catalyst should include that from the waste catalyst), so that all of the components of the waste catalyst are utilized effectively. Based on this idea, the

waste catalysts which can be utilized include Fe_3O_4-based, Fe_3O_4–CoO-based and $Fe_{1-x}O$-based ammonia synthesis catalyst. The derived fresh catalysts are also same as mentioned above, only the ratio of waste catalyst (Fe) to magnetite is different for different type catalysts as shown in Eq. (4.9). For example, in the preparation of the conventional Fe_3O_4-based catalyst, a small amount of metallic iron is generally added into the system to regulate the ratio of Fe^{2+}/Fe^{3+} in the range of 0.4–0.8. Therefore, the waste catalyst can also be used instead of the metallic iron to regulate the Fe^{2+}/Fe^{3+} ratio, but it has little significance because the required amount of waste catalyst is small (less than 8%). For $Fe_{1-x}O$-based catalysts, 300 kg–400 kg of waste catalyst is required for production of one ton of $Fe_{1-x}O$-based catalysts. Therefore, the discovery of $Fe_{1-x}O$-based catalysts opened up a new route for the recycling of waste catalyst,[55] and completely solved the recovery and reuse of waste ammonia synthesis catalyst.

It is worth noticing that the waste ammonia synthesis catalyst recovered from the factory (especially the catalyst at the top of the converter) usually contains certain amounts of sulfur (the content varies with different factories), and some impurities such as dust may be mixed into the waste catalyst. The former can be determined by chemical analysis, and the part of waste catalyst which has excess content of sulfur is discarded. Dust can be removed by manual sorting or magnetic separation (waste catalyst has a strong magnetic). Modern ammonia plants have high degree of gas purification technology, and therefore the sulfur content in the waste catalyst usually is exceptionally low. Thus, the recycling of the waste catalyst is safe, credible and convenient.

References

1. Ullmanns Enzyclopädie der technischen Chemie, Urban u. Schwarzenberg, München-Berlin III, 525, 1953.
2. Slark AV, James GR. *Ammonia Synthesis* (Part III), Translated by Staff Room of Inorganic Chemical Engineering, Dianlian Institute of Technology, Beijing: Chemical Industry Press, 1980, 88.
3. Liu HZ, Li XN, Hu ZN, *et al. Chem. J. Chin. Univ.* **23**(1): 87–91, 2002.
4. Jennings JR. (Imperial Chemical Industries PLC). USP 4668658, 1987.
5. Morgan C. Sze (The Lummus Company). USP 3951862, 1976.
6. Nielsen A. (Bagsvaerd, Denmark). USP 3243386, 1966.
7. Giles WA. Midland, Mich (The Dow Chemical Company). USP 2276679, 1942.
8. Nicola PN (Fertimont S.p.A.,Milan). USP 4789657, 1988.
9. Khader, Mahmoud M, Albany C., *et al.* (Trustees of Boston University). USP 4703030, 1987.
10. Jennings JR. USP4668658, 1987.
11. Shen J, Zhu SY, Feng XT. *Ammonia Synthesis*, in Fertilizer Engineering Science Series, Editorial Board. Beijing: Chemical Industry Press, 2001, 852.
12. Wang SD, Sun JQ. *Catalyst Engineering Introduction*, Beijing: Chemical Industry Press, 2001, 60–82.
13. Yusfin YC. *Theory Mettallization Iron-ore Raw Material*. Moscow: Metallurgic, 30, 1982.
14. Liu HZ, Ning WS, Fu GP, *et al. J. Chem. Ind. Eng.* **50**(5): 671–677, 1999.
15. Yusfin YC. *Theory Mettallization Iron-ore Raw Material*. Moscow: Metallurgic, 32, 1982 (in Russian).

16. Yusfin Y.C. *Theory Mettallization Iron-ore Raw Material*. Moscow: Metallurgic, 85, 1982 (in Russian).
17. James RJ. (Imperial Chemical Industries PLC). USP, 4668658, 1987.
18. EL-Rahaiby SK, Rao YK. *Metallurgical Transactions* B. **10B**: 257–268, 1979.
19. Chemistry Department of Xiamen University, Nanjing Catalyst Factory. *Ammonia Synthesis Catalysts*, Beijing: Chemical Industry Press, 1980, 25–27.
20. Zhou ZG, *et al. Ferrite Magnetic Material*, Beijing: Science Press, 1981.
21. Flenmings MC. *Solidification Process*. Beijing: Metallurgical Industry Press, 1981.
22. Hu HQ. *Metallic Solidification*, Beijing: Metallurgical Industry Press, 1985, 307.
23. Wang QC, Li GQ. *Large Scale Nitrogenous Fertilizer Industry*, **5**(1), 1984.
24. Li LM, Wang WX. *Chem. J. Chin. Univ.* **4**(6): 763, 1983.
25. Wang WX, Li F, Guo XJ, *et al. J. Chem. Ind. Eng.* **5**: 583, 1990.
26. Shen J, Zhu SY, Feng XT. *Fertilizer Engineering Science Series*, Editorial Board. *Ammonia Synthesis*, Chemical Industry Press, Beijing, 2001, 864.
27. Slark AV, James GR. *Ammonia Synthesis* (Part III), Translated by Staff Room of Inorganic Chemical Engineering, Dianlian Institute of Technology, Chemical Industry Press, Beijing, 1980, 101.
28. Yu ZX, *et al. Application Techniques of Fertilizer Catalyst*, Chemical Industry Press, Beijing, 1988, 377.
29. Huang CR, Huang BY. *Chemical Fertilizer Industry*, **25**(2): 30–32, 2000.
30. Wang XJ, Ding JH. *J. Chem. Ind. Eng.* **15**(2): 21–24, 1994.
31. Lin J, Hu ZN, Liu HZ. *Industrial Catalysis*, **13**(3): 6–9, 2005.
32. Lin J. *Studies on the Mechanical Properties of Fused Iron Ammonia Synthesis Catalysts*: Degree Thesis. Hangzhou: Zhejiang University of Technology, 2005.
33. He L. *Chemical Fertilizer Industry*, **27**(6): 44–46, 2000.
34. *A Handbook of Ammonia Synthesis Catalysts*, translated by Nanjing Chemical Engineering Institute. China Petrochemical Industry Press, Beijing, 1977.
35. CA, 1964; 60: 1157g; 1963; 59: 5822a; 1960; 54: 3790c; 1964; 60: 15195a.
36. CA,1965; 63: 4986f.
37. Менътов ВН. и др Хим. Пром. **1**: 32–34, 1980.
38. Саркисян АА. и др Хим-сть. **8**: 25–27, 1979.
39. *Japan Powder Industry Society*, Granule Making Enchiridion. Ohmu Press, 1975, 256–262.
40. Wang WX, Feng DH, Zhai JK, *et al.* China Patent, CN 85101604B, 1985.
41. Zhengzhou University, China Patent, CN 85101606B, 1985.
42. Liu HZ, Hu ZN, Jiang ZR, *et al.* China Patent, ZL 88108727, 1988.
43. Chen SG. *Chem. Eng. Design Comm.* **29**(4): 14–16, 2003.
44. Wang WX, Li F, Guo XJ, *et al. J. Chem. Ind. Eng.* **41**(5): 583–589, 1990.
45. Lu RF, Hu JH. *Chemical Fertilizer Industry*, **21**(6): 35–37, 1994.
46. Wang WX, Li F. *Industrial Catalysis*, **1**(2): 42–47 , 1993.
47. Ren YW, Lin SR. *Appl. Chem. Ind.* **3**: 50–53, 1991.
48. Tian SR. *Chemical Fertilizer Industry*, **17**(6): 10, 18–19, 1990.
49. Jin YM, Chang JQ, Jiang ZR, *et al. J. Zhejiang Univ. Techn.* **4**: 41–51, 1984.
50. Liu HZ, Jiang ZR, Hu ZN, *et al. Indus. Catal.* **1**: 31–35, 1995.
51. Li F, Wang WX. *Fertilizer & Catal.* **1**: 12, 42–44, 1989.
52. Li LM, Gao GY, Wang LK. *J. Zhengzhou Univ.* (Natural Science Edition). **37**(1): 52–55, 2005.
53. Високов Г, Год Висш ХимТехнол ИНСТ. СофиЯ. **29**(11): 186–189, 1983.
54. Саркиагн А А, Кузнезов Л Д, Рабина П Д Хим. Пром. **8**: 25–27, 1979.
55. Liu HZ, Xu RY, Jiang ZR. China Patent, CN 86108528.0, 1986.

This page intentionally left blank

Chapter 5

Reduction of Fused Iron Catalysts

It is crucial for ammonia plant to choose ammonia synthesis catalyst with excellent capability to increase productivity and decrease energy consumption.

Fused iron catalysts are composed of iron oxides (Fe_3O_4, FeO) and a small amount of promoters which are usually metal oxides with high melting points such as Al_2O_3, K_2O, CaO, MgO and SiO_2 etc. The iron oxides must be reduced to metal state to have catalytic activity, but other oxides which act as promoters cannot be reduced. The activity and durability of catalysts are dependent upon the chemical composition, preparation method, reduction procedure and conditions. Thus the reduction is a crucial step in the manufacture and application of catalysts, and the performance and kinetics of reduction are important aspects in the study of catalysts.

Macroscopically, the fused iron catalyst is a non-porous solid before reduction. Due to the existence of structural promoters (Al_2O_3 etc.), the contraction of the catalyst pellet does not take place during reduction. After oxygen anions are removed by hydrogen during catalyst reduction, it forms a porous structure. The surface area increases greatly and the catalyst exhibits high activity. Nevertheless, the microstructure has big differences such as the surface area, pore size and their distribution for different types of catalysts.

The same type of fused iron catalyst may exhibit different structures and activities after reduction under different conditions (e.g., temperature, pressure, space velocity and gas composition etc.). Reduction condition is the external factor which affects the physical–chemical properties of catalysts. Thus, different reduction conditions are required for catalysts with different types, particle sizes or different types and content of promoters. The selection of the optimized reduction condition is very important to obtain a high performance for ammonia synthesis catalysts. It is the main reason to study the reductive performance and related kinetics of catalysts.

The reduction process of the fused iron catalyst in mixture of H_2 and N_2 is a complex physical–chemical process as displayed in Fig. 5.1.[1] Reduction includes several processes as follows:

(1) Chemical reaction. The main component of wüstite-based catalyst such as A301, ZA-5 etc. is $Fe_{1-x}O$. The reduction reaction is as follows:

$$Fe_{1-x}O + H_2 = (1 - x)\ Fe + H_2O - 37.3\,kJ \cdot mol^{-1}, \tag{5.1}$$

where x is the defect concentration of iron ions in the crystal lattice of $Fe_{1-x}O$.

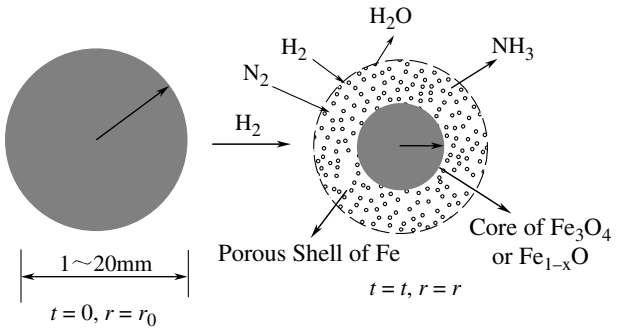


Fig. 5.1 Schematic diagram of reduction process in ($N_2 + 3H_2$) for ammonia synthesis catalyst

The component of the catalysts such as A110 and A201 is magnetite (Fe_3O_4). The reduction reaction is as follows:

$$Fe_3O_4 + 4H_2 = 3Fe + 4H_2O - 181.7\,kJ \cdot mol^{-1}. \tag{5.2}$$

As a chemical reaction, it is necessary that the effect of temperature, pressure and gas component on reaction is considered from the viewpoint of kinetics and thermodynamics of chemical reaction.

(2) Non-catalytic gas–solid reaction process. Reactions (5.1) and (5.2) are not common chemical reactions; these are non-catalytic gas–solid reaction processes. It is necessary to consider the heat and mass transfer process of reactants and products, and the reaction between gases and solid and between solids. The process follows the general rule of non-catalytic gas–solid reaction process.

In laboratory, thermogravimetric analysis (TGA) can be used to investigate this process quantitatively.

The amount of the catalyst used in industrial reactor is large and the particle size is big. The reduction process of the catalysts becomes very complex. For every pellet of catalyst in bed, the reduction in industrial reactor is carried out from outside to inside of the pellet step-by-step. For a whole bed of catalyst, the reduction is carried out from top (inlet of gas) to bottom layer (outlet of gas) of the bed step by step. It is considered that the reduction of catalyst is a gradual process step-by-step, when designing the reduction process in industry,

(3) The formation of α-Fe crystallite during reduction is a crystal growth process and it involves the theory and rule of crystallography. The basic requirement of this process is the formation of small α-Fe crystals without growth or conglutination of α-Fe crystals into big particles. This requirement is related with reaction rate, especially, temperature and the concentration of produced H_2O. Iterative redox of α-Fe by H_2O should be avoided. Thus, the low-temperature, high-space velocity and low-concentration of H_2O are preferred.

(4) The reduction process is accompanied with the formation of ammonia because the reduction of catalyst is usually carried out *in situ* in industrial reactor with feed gas (N_2+3H_2).

$$Fe_{1-x}O + H_2 \rightarrow (1 - x)[Fe] + H_2O - Q_1 \tag{5.3}$$

$$N_2 + H_2 + [Fe] \rightarrow NH_3 + Q_2 \tag{5.4}$$

Once the active [Fe] formed, the reaction (5.4) commences immediately. The effect of this process on the reduction reaction is both positive and negative as a double-edged sword. It is necessary to follow the principle of both using and controlling this process. Ammonia synthesis reaction is a strongly exothermal reaction. The reaction should be inhibited at the early stage of reduction to avoid the hot spot-temperature (HST, i.e., the highest temperature in bed) in the bed moving downwards too early, which will cause that the top layer catalyst in the bed cannot be reduced completely. At the middle and later stages of the reduction, it is important to use the heat produced by reaction (5.4) and raise the space velocity to decrease the concentration of H_2O and increase the reduction rate.

Furthermore, the following solid–solid reactions may occur during the preparation of fused iron catalysts.

$$Fe_2O_3(s) + Fe(s) \rightarrow Fe_3O_4(s) \tag{5.5}$$

$$Fe_3O_4(s) + Fe(s) \rightarrow FeO(s) \tag{5.6}$$

It can be seen that the preparation and reduction of catalyst is related to chemical reaction, solid state reaction, non-catalytic gas–solid reaction and crystal growth process. The solid state reaction, non-catalytic gas–solid reaction and crystal growth will be first discussed in the following sections.

5.1 Solid-State Reactions Involved in Reduction Process

Solid state reactions discussed here refer to the reactions which have at least one solid as reactants or products.[2] Both the preparation and reduction of fused iron catalyst are solid state reaction processes, but the role of solid reaction has never been studied thoroughly yet, although there are few reports in literature and textbooks on the preparation and reduction of fused iron catalyst. There is no doubt that the basic reactions during preparation and reduction of fused iron catalysts belong to orderliness of solid state reactions. The reduction and oxidation of solid oxide, the decomposition of carbonates and hydrates, and the oxidation of sulfides etc belongs to solid state reaction. The solid state reaction follows its unique law, and it must be considered in the analysis and interpretation of preparation and reduction of fused iron catalyst. Therefore, it should be understood on the basic law of solid state chemical reactions.

5.1.1 *General laws of solid state reaction*

The most common character of chemical reaction is the quantitative changes of substance at unit volume and time.

$$\upsilon = \pm\frac{1}{V} \cdot \frac{dN}{d\tau}. \tag{5.7}$$

Here, υ is the instantaneous rate of chemical reaction, N is the molar number of substance, V is the volume, τ is the time.

Because $\mathrm{N/V} = c$ is molar concentration of substance, when the reaction volume is a constant, the reaction rate can be expressed as:

$$\upsilon = \pm\frac{dc}{d\tau} \tag{5.8}$$

According to mass action law of the chemical kinetics, the reaction rate of $y_1A + y_2B + y_3D \rightarrow$ product is expressed as:

$$\upsilon = -\frac{dc_A}{d\tau} = kc_A^p c_B^q c_D^r, \tag{5.9}$$

where k is the reaction rate constant; $n = p + q + r$ of power index of concentration is the order of reaction kinetics.

Solid state chemical reaction involves local reactions. As at least one of the reactant and product is solid, the reaction does not occur in the bulk of substance, but on the interface of phase boundary. Therefore the above expression as chemical reaction rate cannot be used for local reactions. In local reactions, the reaction rate should be interpreted as changes of the conversion of substance with time.

$$\alpha = \frac{N_0 - N}{N_0}, \tag{5.10}$$

where α is conversion of substance, N_0 and N are the mass of substance before reaction and unreacted respectively. The reaction rate is decided by Eq. (5.11)

$$\upsilon = \frac{d\alpha}{d\tau}. \tag{5.11}$$

In the case of concentration C_A of gas A is a constant, for the unreacted solid

$$A(g) + B(s) \rightarrow \tag{5.12}$$

The reaction order is defined as:

$$-\upsilon_{\mathrm{B}} = -\frac{d(1 - X_{\mathrm{B}})}{d\tau} = k(1 - X_{\mathrm{B}})^{\mathrm{m}} \tag{5.13}$$

Where X_B is conversion of B, m is the reaction order, and so

(1) For shrinking core model and reaction-controlled process, $m = 2/3$.
(2) For shrinking core model and ash layer–diffusion–controlled process, m changes from $m = \propto$ when $X_B = 0$ to $m = 1/3$ when $X_B = 1$.
(3) For shrinking core model and gas-film diffusion-controlled process, $m = 0$.
(4) For other model, $m \neq$ constant, it changes with X_B and other parameters of system.

In a homogeneous reaction, the reaction order is associated with molecular interaction mechanism and has its specific mean of theory. For the process of catalysts deactivation, the index of activity loss is a convenient and simple tool that can be used to integrate and simplify the mathematical treatment and design. However,

for the conversion of solid, the reaction order is not a simple concept, and it is not understood very well. Therefore, it is better to avoid using it.

The direction of solid reaction can be determined by Gibbs' free energy.

$$\Delta G = \Delta H - T\Delta S, \tag{5.14}$$

where, ΔH is enthalpy change, ΔS is the entropy change of process; and T is temperature.

Thermodynamic data are necessary for judging the feasibility and direction of reaction. Some of the data are given in Table 5.1.[3]

For example, to calculate the starting temperature of magnetite reacting with iron to form the equivalent single state wüstite:

$$Fe_3O_4 + Fe = 4FeO. \tag{5.15}$$

If the variation of the standard Gibbs' free energies in the following reactions is known:

$$3FeO + 1/2O_2 = Fe_3O_4 \quad \Delta_r G^{\ominus} = -312 + 12.3 \times 10^{-2}\ T. \tag{5.16}$$

$$Fe + 1/2O_2 = FeO \quad \Delta_r G^{\ominus} = -263.6 + 6.5 \times 10^{-2}\ T. \tag{5.17}$$

Subtracting (5.16) from Eq. (5.17) leads to the $\Delta G^{\ominus}$ of Eq. (5.15):

$$\Delta_r G^{\ominus} = 48.4 - 5.8 \times 10^{-2}\ T.$$

If $\Delta_r G^{\ominus} < 0$ is used to give a rough estimation of whether the reaction goes to the right direction, and when Fe_3O_4 are reduced, only when the $\Delta_r G^{\ominus} < 0$ i.e., $T > 833\,K$, can the formation of wüstite and the mutual solubility of the metallic iron occur? Wüstite can be obtained if the reaction temperature is higher than 833 K when the magnetite is reduced by metallic iron.

The Gibbs' free energies given in Table 5.1 can be used to evaluate solid state reaction based on thermodynamics. In Table 5.1, a lot of data are different from that of a reaction involving gas or liquid reactants and products, that is, the value of ΔS is small (it is commonly believed that $\Delta S \approx 0$ for solid state reaction). This is undoubtedly related with the lattice reformation. However, under the conditions in reality, the range of ΔS is $20\,J/(mol{\cdot}K) > \Delta S > -20\,J/(mol{\cdot}K)$. Usually, the largest positive value of ΔS corresponds to products which have the crystal lattice being extremely disordered and this disorder may be caused by its own properties or existence of impurities. From the examples listed above, wüstite has a high entropy [58 J/(mol·K)], which is due to the existence of crystal lattice disorder. To some extent, this disorder is related with non-stoichiometric reactions.

Here ΔH of solid state reactions are in the range of $(-418.5{-}125)\ kJ{\cdot}mol^{-1}$, however the large negative value of ΔH is negative only for the reaction with alkalis or alkaline earths oxides as reactants and $\Delta S \approx 0$ for most of solid state reactions, and the value of $\Delta_r G^{\ominus}$ and ΔH are very close.

Table 5.1 Gibbs' free energies of some solid state reaction related with iron oxides

No.	Reaction	$\Delta G = A + BT$		Error/kJ · mol^{-1}	Temperature/K
		A	B × 10^3		
1	$Al_2O_3 + Fe_{0.95}O + 0.05Fe \rightarrow FeAl_2O_4$	−45.2	17.07	0.2	—
2	$Al_2O_3 + MnO \rightarrow MnAl_2O_4$	−51.00	9.62	2.9	1,273 − 1,973
3	$BaO + 6Fe_2O_3 \rightarrow BaFe_{12}O_{19}$	11.39	−89.2	0.3	935 − 1,187
4	$CaO + Fe_2O_3 \rightarrow CaFe_2O_4$	−29.71	−4.81	0.29	1,100 − 1,300
5	$2CaO + Fe_2O_3 \rightarrow Ca_2Fe_2O_5$	−31.55	−23.01	0.67	1,100 − 1,300
6	$CoO + Fe_2O_3 \rightarrow CoFe_2O_4$	−22.6	−13.4	4.2	900 − 1,200
7	$Cr_2O_3 + FeO \rightarrow FeCr_2O_4$	−66.32	10.88	0.8	1,573 − 1,773
8	$Cr_2O_3 + Fe_{0.95}O + 0.05Fe \rightarrow FeCr_2O_4$	−64.18	18.07	0.3	—
9	$FeO + Fe_2O_3 \rightarrow Fe_3O_4$	−16.86	−11.55	0.2	1,100 − 1,700
10	$Fe_2O_3 + MgO \rightarrow MgFe_2O_4$	−24.06	1.34	1.7	1,100 − 1,700
11	$Fe_2O_3 + 1.07MgO \rightarrow MgFe_2O_4$	−44.10	14.48	1.2	1,173 − 1,373
12	$Fe_2O_3 + MnO \rightarrow MnFe_2O_4$	−40.6	1.05	1.7	1,273 − 1,473
13	$Fe_2O_3 + NiO \rightarrow NiFe_2O_4$	−19.75	−4.18	1.2	1,173 − 1,473
14	$2FeO + SiO_2 \rightarrow Fe_2SiO_4$	−51.21	20.5	—	1,298 − 1,692
15	$Fe_{0.95}O + 0.05Fe + TiO_2 \rightarrow FeTiO_3$	−30.63	9.12	0.3	1,250 − 1,500
16	$Fe + 1/2O_2 + TiO_2 \rightarrow FeTiO_3$	−301.67	79.41	—	—
17	$Fe + FeTiO_3 + 1/2O_2 \rightarrow FeTiO_4$	−268.257	62.01	—	—

On interaction mechanism of solid–solid,[2] Лэнгмюр suggested that the solid–solid reaction only occurred on the phase boundary. Макдональд and Гиншельвуд suggested that the topochemical reactions proceed by forming and growing of the crystal nucleus of products. Therefore, it is related to increase of the surface of phase boundary at the first stage and the rate of process. Frenkel and Гец considered that this process started at a certain point (radical) on surface. This change is related to the crystal lattice defects (e.g., vacancy, distribution of ions between nodes and displacement on surface etc.). With the increasing of the surface of crystal nucleus, the reaction rate is increased, and then it is decreased when the crystal nucleus is converged. However, the above depiction will be complicated if the crystal forms cracks due to the density difference between the original and newly produced materials or others.

Thus, the basic contents of the theory on solid–state topochemical reaction occurring on the phase boundary are as follows:

① Reaction rate is dependent upon the diffusion rate of the ions getting across layer of the products.
② The product layers are dense and compact, and the mobility of non-equilibrium defects (defect of particle boundary, and displacement on surface etc.) in this layer on these ions is not critical.
③ The reaction on the phase boundary is more rapid than the diffusion process getting across layers of the products, and thermodynamic equilibriums of top chemical reactions are established on the phase boundary.
④ Electric neutral rule is followed on any cross section in products because some ions move independently in any reaction layer.

Calculations show that the number of products of solid–state reaction is not associated with the quality of ions which get across layers of the products and controlling migration of mass, but in accordance with the parabola growth law.

In new type of $Fe_{1-x}O$ based ammonia catalyst, $Fe_{1-x}O$ is a non-stoichiometric compound. The effect of the defect in non-stoichiometric structure on solid–state reaction has the three following aspects.

① If the formation of reaction products has resulted from cationic anti-diffusion, the rate constant is proportional to the diffusion coefficient of the cation which is not too active. If the diffusion occurs according to the defect mechanism, the cation which is not too active would be directly in proportion with the concentration of cation defects. It is obvious that the diffusion of the cation proceeds at a faster rate, and with a stronger response in the non-stoichiometric phase that is in defect of metal ion, and has a high concentration of cation defects than that in stoichiometric phase.
② If the formation of products is derived from the unilateral diffusion of anion and cation, the effect of non-stoichiometry is related to the proportions of D_0 and D_A. When $D_A > D_0$ and non-stoichiometric phase is in defect of metal ion, the reaction rate is faster than that in stoichiometric phase. If $D_A < D_0$ and reaction is throughout the transition in defect of oxygen, it may speed up access to the same effect.

③ If the reaction product relies on the same type of cation, electronic unilateral diffusion and migration of oxygen through the gaseous phase generated at the same time, then, the increased shortage of the metal in the products should accelerate the reaction process.

5.1.2 *Solid state reaction kinetics*

The research of reaction kinetics includes two stages:

① The reaction rate is measured under reaction conditions experimentally, and is given in a form of mathematic expression.
② Kinetic parameters are evaluated based on the rate expression, and then the explanation of these parameters is interpreted according to the nature of reaction.

The majority of solid state reaction is based on several basic unit stages, and the influences of the reaction conditions on the ratio of the reaction rate for the various stages are different. Overall rate of the process is determined by one stage while the other stages are carried through under conditions in equilibrium or in quasi-equilibrium.

As mentioned above, the numeric characteristic of solid state process is conversion. The concept of conversion is completely different from that of concentration. If the pressure and temperature are constant, the concentration is the only characteristic for the system. Even in a state of fixed parameter value, the conversion is not the single-value characteristic of multi state system. In various systems with same components, it is possible to achieve the same conversion. The difference between these systems is the structure of the reaction region, and in this region, the products are generated first, followed by aggregation of products.

Figure 5.2 shows the kinetic curve $\alpha = f(\tau)$ and $d\alpha/d\tau = f'(\alpha)$ for many solid state reactions. The initial reaction rate is initially low, which corresponds to the so-called induction period, and then follows a sharp increase (rate increase stage), before a maximum value is achieved. After that, it decreases to zero gradually. In this case, the curve of $\alpha = f(\tau)$ is S-shaped or Σ-shaped. Of course, the shape of kinetic curve is related to the nature of process. The character of the induction stage is the contact between the various components and an increase in the magnitude of reaction region. The stage of rapid growth is related to the generation and growth of crystal nucleus in reaction region. However, at this time, mutual dissolution of each component and further consumption of solid solution and the products are formed because of the disintegration of crystal bud.

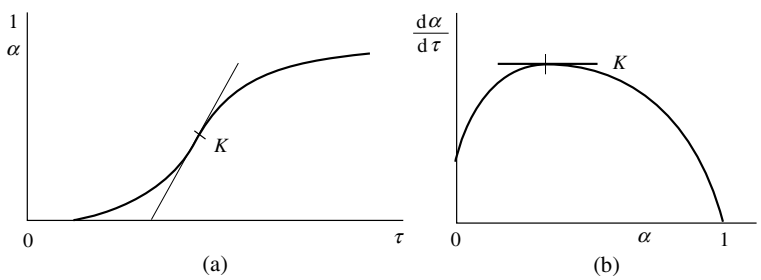


Fig. 5.2 Kinetic relationship of conversion ratio (a) and conversion rate (b)

5.2 Kinetic model of solid state reaction

5.2.1 *Kinetic model for gas–solid non-catalytic reaction*

According to the studies on reduction of fused iron catalysts following three premises can be established primarily.[4]

① The external shape and volume of particle do not change when the particle is reduced, and the pore structures are generated by removal of oxygen ions.
② The reduction is rapidly proceeded on the neighbor of the previously reduced place, but not completely. The reduction proceeds from Fe_3O_4 to Fe or $Fe_{1-x}O$ to Fe directly, which follows the thermodynamic rules.
③ Macroscopically, the reduction proceeds from the surface to the center of catalyst, and the process can be described by shrinking core model with diameter being unchanged. The interface between Fe and Fe_3O_4 or Fe and FeO moves smoothly inward.

Therefore, the simplest non-catalytic gas–solid reaction model with unchanged diameter is introduced here, i.e., the shrinking core model (SCM).[3,5,6] Figure 5.3 is the schematic diagram of SCM. It is commonly considered that SCM reasonably describes real particle behavior during reaction process and gives a simple conversion expression.

For reaction $A(g) + bB(s) \rightarrow R(g) + S(s)$, there are three type of resistances in turn as follows (See Figs. 5.4–5.6).

Diffusion through gas film surrounding pellet is:

$$-\frac{1}{4\pi R^2}\frac{dN_A}{dt} = bk_g(C_{Ag} - C_{As}) \tag{5.18}$$

Diffusion of reactant A passing through ash layer is:

$$-\frac{dN_A}{dt} = 4\pi r^2 D_{\text{eff}}\frac{dC_A}{dr} \tag{5.19}$$

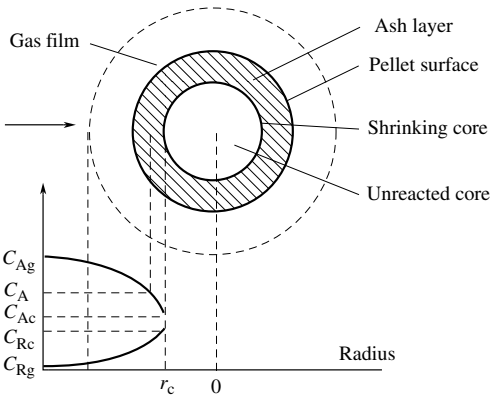


Fig. 5.3 Concentration distribution of reactants on shrink core model with obvious interface for gas–solid non-catalytic reaction[4]

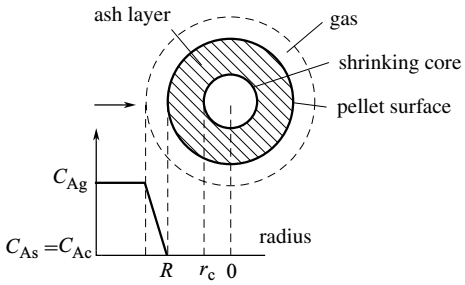


Fig. 5.4 Schematic diagram of gas-film diffusion controlling

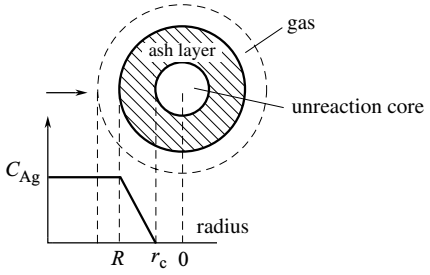


Fig. 5.5 Schematic diagram of ash-layer diffusion controlling

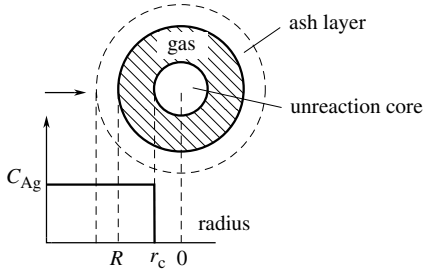


Fig. 5.6 Schematic diagram of surface reaction controlling

Reaction on the interface of unreacted core is:

$$-\frac{1}{4\pi r_c^2}\frac{dN_A}{dt} = bk_s C_{AC} \tag{5.20}$$

Here, k_g, $\mathrm{m{\cdot}s^{-1}}$; D_{eff}, $m^2{\cdot}s^{-1}$; k_s, $m{\cdot}s^{-1}$

For gas–solid reactions, the expression of reaction rate is fully different from other systems. Therefore, the kinetic parameters are denoted as τ (time for particle being fully converted).

If a reaction is controlled by one of three types of resistance respectively, then three kinds of expressions of rates can be obtained.

Gas-film diffusion-controlled expression of rate is:

$$\frac{\mathrm{t}}{\tau} = x_{\mathrm{B}} = 1 - \left(\frac{r_{\mathrm{c}}}{R}\right)^3 \tag{5.21}$$

$$\tau = \frac{\rho_{\mathrm{B}} R}{3bk_{\mathrm{g}} C_{\mathrm{Ag}}}, \tag{5.22}$$

where t is the time required for conversion of x_B; τ is the time required for complete conversion; ρ_B is density of B in particle; k_g is the mass transfer coefficient in gas film. For example, for a single particle it can be:

$$\frac{k_{\mathrm{g}} d\rho}{D} = 2 + 0.6(R_{\mathrm{e}})^{1/2}\, \mathrm{g}(S_{\mathrm{C}})^{1/3} \tag{5.23}$$

Ash layer diffusion-controlled expression of rate is:

$$\frac{\mathrm{t}}{\tau} = 1 - 3(1 - x_{\mathrm{B}})^{2/3} + 2(1 - x_{\mathrm{B}}) = 1 - 3\left(\frac{r_{\mathrm{C}}}{R}\right)^2 + 2\left(\frac{r_{\mathrm{C}}}{R}\right)^3 \tag{5.24}$$

$$\tau = \frac{\rho_{\mathrm{B}} R^2}{6bD_{\mathrm{eff}}\, C_{\mathrm{Ag}}}, \tag{5.25}$$

where D_{eff} is effective diffusion coefficient through the ash layer.

Reaction-controlled expression of rate is:

$$k_p(C_{\mathrm{Ag}} - C_0)\mathrm{t} = \rho_{\mathrm{B}} R[1 - (1 - x_{\mathrm{B}})^{1/3}]$$

$$\frac{\mathrm{t}}{\tau} = 1 - (1 - x_{\mathrm{B}})^{1/3} = 1 - \left(\frac{r_{\mathrm{C}}}{R}\right) \tag{5.26}$$

$$\tau = \frac{\rho_{\mathrm{B}} R}{bk_{\mathrm{s}} C_{\mathrm{Ag}}} \tag{5.27}$$

where $k_s C_{\mathrm{Ag}}$ express a first order reaction for gas A.

The above expressions of conversion with time are shown in Fig. 5.7.

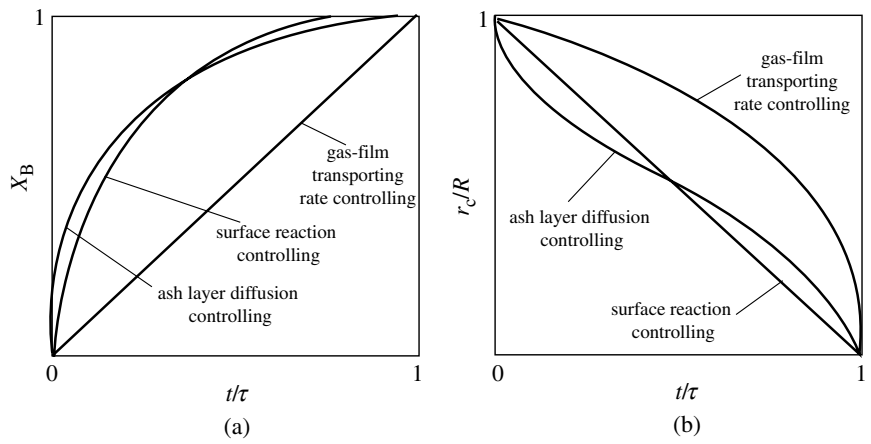


Fig. 5.7 Change diagram of reactive plane for single pellet reaction

In general, the resistances that affect conversion are more than one, and therefore, three equations of film, ash layer and reaction should be combined, and by eliminating the intermediate concentration C_{As} and C_{Ac}, the instantaneous reaction rate can be obtained:

$$-\frac{1}{4\pi R^2}\frac{dN_{\mathrm{A}}}{dt} = \left[b/\left(\frac{1}{k_{\mathrm{g}}} + \frac{R(R-r_{\mathrm{C}})}{r_{\mathrm{C}}\mathrm{D}} + \frac{R^2}{r_{\mathrm{C}}{}^2 k_{\mathrm{s}}}\right)\right] C_{\mathrm{Ag}} \tag{5.28}$$

When $X_{\mathrm{B}} = 1 - \left(\frac{r_{\mathrm{C}}}{R}\right)^3$, the time needed for any given conversion (X_B) is as follows:

$$t = t_{\mathrm{film}} + t_{\mathrm{ash}} + t_{\mathrm{reaction.}} \tag{5.29}$$

Here, t is time considering overall resistance, and $t_{\mathrm{film}}, t_{\mathrm{ash}}, t_{\mathrm{reaction}}$ are the time needed when conversion reaches X_B for the gas film, ash layer and reaction controlled, respectively. When the particle is transformed completely ($X_B = 1$), the overall times is:

$$\tau_{\mathrm{overall}} = \tau_{\mathrm{film}} + \tau_{\mathrm{ash}} + \tau_{\mathrm{reaction}} \tag{5.30}$$

Putting the corresponding t into the equation of the conversion, the relationship for the change of conversion with time can be got for resistance at all range. Thus

$$\begin{aligned}\frac{t_{\mathrm{overall}}}{\tau_{\mathrm{overall}}} &= x_B\frac{\tau_{\mathrm{film}}}{\tau_{\mathrm{overall}}} + [1-3(1-x_B)^{2/3} + 2(1-x_B)]\frac{\tau_{\mathrm{ash}}}{\tau_{\mathrm{overall}}} \\ &\quad + [1-(1-x_B)^{1/3}]\frac{\tau_{\mathrm{react}}}{\tau_{\mathrm{overall}}}\end{aligned} \tag{5.31}$$

or

$$t_{\mathrm{overall}} = \frac{\rho_m R}{6bC_{\mathrm{Ag}}}\left\{\frac{2}{k_{\mathrm{g}}}\left[1-\left(\frac{r}{R}\right)^3\right] + \frac{R}{D_{\mathrm{eff}}}\left[1-3\left(\frac{r}{R}\right)^2 + 2\left(\frac{r}{R}\right)^3\right] + \frac{6}{k_{\mathrm{s}}}\left(1-\frac{r}{R_B}\right)\right\}, \tag{5.32}$$

where $t_{\mathrm{overall}}, \tau_{\mathrm{overall}}$ is the overall time and overall resistance, respectively.

The relationship between conversion and time according to SCM for non-spherical solid particle with different shape and constant size are given in Table 5.2.

The relationship between particle size, τ and the form of equation as well as the clue to seek mechanism are the same with spherical particles. For second-order reaction, when reactant A is gas, it can simply be used:

$$\tau_{\mathrm{react}} = \frac{\rho_B \mathrm{R}}{\mathrm{bk}_s\,\mathrm{C}_{\mathrm{Ag}}^2}, \tag{5.33}$$

where k_s is the rate constant, $\mathrm{m}^4/(\mathrm{mol{\cdot}s})$.

Similar amendments are used for other orders of reactions.

In the three mechanisms mentioned above, the resistance of diffusion of ash layer is usually greater than that of the diffusion of gas film, and thus, the diffusion

Table 5.2 SCM of non-spherical solids particle with different shape and constant diameter

Shape	Gas-film diffusion controlling	Ash-layer diffusion controlling	Surface reaction controlling
Disk $X_B = 1 - \frac{1}{L}$	$\frac{t}{\tau} = X_B$, $\tau = \frac{\rho_B L}{bk_g C_{Ag}}$	$\frac{t}{\tau} = X_B^2$, $\tau = \frac{\rho_B L^2}{2bD_{eff} C_{Ag}}$	$\frac{t}{\tau} = X_B$, $\tau = \frac{\rho_B L}{2bk_s C_{Ag}}$
Cylinder $X_B = 1 - \left(\frac{r_c}{R}\right)^2$	$\frac{t}{\tau} = X_B$, $\tau = \frac{\rho_B R}{abk_g C_{Ag}}$	$\frac{t}{\tau} = X_B + (1 - X_B) \times \ln(1 - X_B)$, $\tau = \frac{\rho_B R^2}{4bD_{eff} C_{Ag}}$	$\frac{t}{\tau} = 1 - (1 - X_B)^{1/2}$, $\tau = \frac{\rho_B R}{bk_s C_{Ag}}$
Spherical $X_B = 1 - \left(\frac{r_c}{R}\right)^3$	$\frac{t}{\tau} = X_B$, $\tau = \frac{\rho_B R}{3bk_g C_{Ag}}$	$\frac{t}{\tau} = X_B + 3(1 - X_B)^{2/3} + 2(1 - X_B)$, $\tau = \frac{\rho_B R^2}{6bD_{eff} C_{Ag}}$	$\frac{t}{\tau} = 1 - (1 - X_B)^{1/3}$, $\tau = \frac{\rho_B R}{bk_s C_{Ag}}$

resistance of gas film can be neglected as long as the ash layer exists. It is the main control stage which can be judged by calculating τ and linear fitting according to (5.30) ash layer diffusion and reaction control. Because X_B and t curves between ash layer diffusion and reaction control are similar, the judgment by this method is unreliable.[3]

Usually, the sensitivity of reaction steps on temperature is higher than diffusion steps. If the solid structure changes due to sintering, the resistance to diffusion will be changed obviously.

In case of reaction control or ash layer diffusion-control, SCM is a single parameter model, and τ_{reaction} or τ_{ash} as characteristic time. The above equations show that, to achieve any conversion of X_B, for the diffusion of gas film, $\tau \propto R^{1.5-2.0}$, when R increases, the index decreases, and for ash diffusion control, $\tau \propto R^2$; and for reaction-control, $\tau \propto R$. For the latter two cases, the data obtained from different particle sizes of solid are a shortcut to determine the kind of mechanism.

These relations show that when the particle size R increases, the reaction rate of ash layer diffusion-controlled decreases faster than that of reaction-controlled. Therefore, if reaction is the control-step for given R, it is possible to find a corresponding point of the ash layer control for particle with large size. Therefore, it is unsafe when the reaction control is extrapolated to larger particles, while it is safe for small particles. In contrast, it is safe when ash layer is extrapolated to larger particles, and it is unsafe to smaller particles.

The mechanism of reaction-control can transform into ash layer-control, but the reverse does not occur during the conversion. This is because there is no ash layer and therefore no ash layer resistance at the beginning of reaction. Generally, if the ash layer diffusion exists when the conversion is low, it means that the reaction

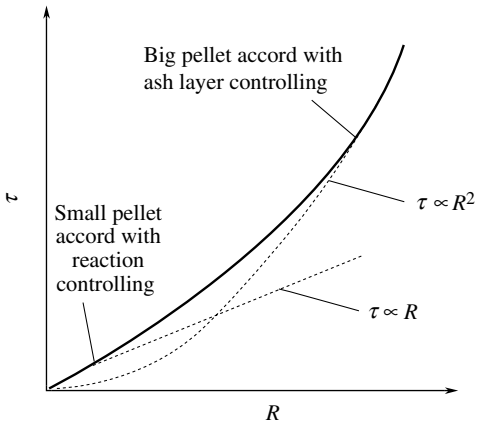


Fig. 5.8 Controlling mechanism of different particles

is controlled by some other kind of resistance. Different mechanisms for different particle sizes are given in Fig. 5.8.

SCM is a phenomenological model, and therefore, the characteristics of the model can be observed for many types of solids and possible mechanisms e.g., for porous and non-porous solids, solid reactions with gas or otherwise, etc. *S*-shaped characteristic curve of conversion *vs.* time cannot be produced for SCM. According to the SCM prediction, the solid will be transformed completely in proper time, or the time needed for 100% conversion is doubled than that needed for 87% conversion. It cannot be used to explain this status, i.e., when conversion is less than 100%, the conversion seems to tend to approach a certain equilibrium value.

Kinetics models of gas–solid non-catalytic reaction include uniform conversion model (UCN), multiple fine particle model (GPM), crack core model (CCM), phase-change model (PCM), change void model (CVM), thermal decomposition model (TDM), shrinking core model with multi-step reactions, and multi-step reaction model of formation porous structure in reaction etc.[7] Among these models, the shrinking core model (SCM) is the most important and most widely used. For conversion of solid it is also the most simple and practical model. Commonly it is suitable for experimental data. However, it can only be used in some reactions of many solid reactions. A more complex model must be used in other cases.

5.2.2 *Kinetic model for reduction of fused iron catalyst*

Large amounts of research show that the reduction reaction of fused iron catalysts fits the SCM model with unchanged particle diameter. The reduction mechanism may be divided into three stages. The first stage is controlled by reaction on the phase boundary, and once iron layer is formed, in the second stage the diffusion of gas transit ash layer (iron) becomes controlling factor. In the third stage the reduction rate is obviously decreased due to the increasing of gases passage resistance of iron layer.

The experimental reduction results of iron oxides show that the reduction rate is controlled by combined mechanisms of boundary reaction and gas diffusion. It is in consequence that the mechanism is simply attributed to controlling of one factor. This conclusion can be obtained by the following analysis.[4]

For spherical pellets, if the initial radius is R and density is ρ_0, r_c is the radius of the unreduced oxide at any time t, gas concentration is C_{Ag} at R, C_{As} and r_c, equilibrium concentration is C_0, then the reaction rate at boundary is:

$$u_s = 4\pi r_c^2 k_s (C_{\mathrm{As}} - C_0). \tag{5.34}$$

The diffusion rate is:

$$u_g = 4\pi r_x^2 \kappa_{\mathrm{g}} \frac{C_{\mathrm{Ag}} - C_{\mathrm{As}}}{R - r_C}, \tag{5.35}$$

where $r_x^2 = R r_c$.

In a steady state the diffusion rate of the gas should be equal to the surface reaction rate, that is, $u_s = u_g$, the following equation can be obtained:

$$C_{\mathrm{As}} = \frac{C_{\mathrm{Ag}} + (R - r_C)(r_C/R)(k_s/\kappa_{\mathrm{g}})C_0}{1 + (R - r_C)(r_C/R)(k_s/\kappa_{\mathrm{g}})} \tag{5.36}$$

When combined with (5.34), we get:

$$u = \frac{dw}{dt} = \frac{4\pi r_C^2 k_s (C_{Ag} - C_0)}{1 + (R - r_C)(r_C/R)(k_s/\kappa_{\mathrm{g}})}, \tag{5.37}$$

where w is the mass reacted. If f is the fraction of thickness of product layer

$$\mathrm{f} = \frac{\mathrm{R} - \mathrm{r_C}}{\mathrm{R}},\ r_c = R(1 - f),$$

and
$$\mathrm{w} = \frac{4}{3}\pi\rho_B(R^3 - \mathrm{r_C^3}) = \frac{4}{3}\pi\rho_B \mathrm{R}^3[1 - (1 - \mathrm{f})^3]$$

So
$$\frac{\mathrm{dw}}{\mathrm{dt}} = 4\pi\rho_B \mathrm{R}^3(1 - \mathrm{f})^2 \frac{\mathrm{df}}{\mathrm{dt}} \tag{5.38}$$

Let Eq. (5.37) = (5.38) by integration, Eq. (5.39) is obtained

$$\begin{aligned}
\frac{4\pi \mathrm{r_C^2} k_s(\mathrm{C_{Ag}} - \mathrm{C_0})}{1 - \frac{\mathrm{r_C}}{R}(R - \mathrm{r_C})k_s/\kappa_{\mathrm{g}}} &= 4\pi\rho_B \mathrm{R}^3(1 - \mathrm{f})^2 \frac{\mathrm{df}}{\mathrm{dt}} \\
\frac{\mathrm{R}^2(1 - \mathrm{f})^2 k_s(\mathrm{C_{As}} - \mathrm{C_0})}{1 + R\mathrm{f}(1 - \mathrm{f})k_s/\kappa_{\mathrm{g}}} &= \rho_B \mathrm{R}^3(1 - \mathrm{f})^2 \frac{\mathrm{df}}{\mathrm{dt}} \\
\frac{k_s\kappa_{\mathrm{g}}(\mathrm{C_{Ag}} - \mathrm{C_0})}{\rho_B R}\mathrm{t} &= \kappa_{\mathrm{g}}\mathrm{f} + Rk_s \int \mathrm{f}(1 - \mathrm{f})\mathrm{df} \\
&= \kappa_{\mathrm{g}}\mathrm{f} + Rk_s \left(\frac{\mathrm{f}^2}{2} - \frac{\mathrm{f}^3}{3}\right).
\end{aligned} \tag{5.39}$$

The reduction degree of ammonia synthesis catalysts can be defined as

$$x_B = \frac{\text{Amount of the oxygen removed from particle}}{\text{Amount of the oxygen can be removed in particle}}$$

The relationship between the mass of reacted and initial mass of particle can be expressed as x_B,

$$x_{\mathrm{B}} = \frac{\mathrm{w}}{\mathrm{w}_0},$$

where w_0 and w are the mass of substance before reaction and reacted, respectively. Therefore, the reduction degree is:

$$x_{\mathrm{B}} = \frac{\frac{4}{3}\pi\rho_B R^3[1-(1-\mathrm{f})^3]}{\frac{4}{3}\pi\rho_B R^3} = 1-(1-\mathrm{f})^3.$$

Therefore,

$$\mathrm{f} = 1-(1-x_B)^{1/3} \tag{5.40}$$

Then, by substituting Eq. (5.40) in Eq. (5.39), get

$$\frac{k_s\kappa_{\mathrm{g}}(C_{\mathrm{Ag}}-C_0)}{\rho_B R}\mathrm{t} = \kappa_{\mathrm{g}}[1-(1-x_B)^{1/3}] + Rk_s\left(\frac{[1-(1-x_B)^{1/3}]^2}{2} - \frac{[1-(1-x_B)^{1/3}]^3}{3}\right)$$

Predigest,

$$\frac{k_s}{\rho_B R}(\mathrm{C_{Ag}}-C_0)\mathrm{t} = [1-(1-x_B)^{1/3}] - \frac{\mathrm{R}k_s}{\kappa_{\mathrm{g}}}\left[\frac{1}{2}-\frac{x_B}{3}-\frac{(1-x_B)^{2/3}}{2}\right] \tag{5.41}$$

Equation (5.41) can be rewritten as:

$$\alpha\mathrm{t} = \beta[1-(1-x_B)^{1/3}] + \left[\frac{1}{2}-\frac{x_B}{3}-\frac{(1-x_B)^{2/3}}{2}\right].$$

Here, $\alpha = \frac{\kappa_{\mathrm{g}}}{\mathrm{R}^2\rho_{\mathrm{B}}}(\mathrm{C_{As}}-\mathrm{C}_0)$, $\beta = \frac{\kappa_{\mathrm{g}}}{k_s R}$, and when rewritten as linear equation, it is:

$$\frac{\mathrm{t}}{1-(1-x_B)^{1/3}} = \frac{\beta}{\alpha} + \frac{1}{6\alpha}\left[\frac{3-2x_B-3(1-x_B)^{2/3}}{1-(1-x_B)^{1/3}}\right]. \tag{5.42}$$

When $\frac{t}{1-(1-x_B)^{1/3}}$ *vs.* $\frac{1}{6}\left[\frac{3-2x_B-3(1-x_B)^{2/3}}{1-(1-x_B)^{1/3}}\right]$ plots, get a linear, the slope is $1/\alpha$, intercept is β/α, *and* k_s and k_g is calculated according to α and β.

Two special conditions can be acheived from Eq. (5.41):

① If reduction is controlled by interface reaction, then:

$$\frac{k_s}{k_g} \approx 0.$$

So

$$\frac{k_s}{\rho_{\mathrm{B}}R}(\mathrm{C_{Ag}}-\mathrm{C}_0)\mathrm{t} = [1-(1-x_B)^{1/3}]$$

$$\mathrm{t} = \frac{\mathrm{R}\rho_{\mathrm{B}}}{k_s(\mathrm{C_{Ag}}-\mathrm{C}_0)}[1-(1-x_B)^{1/3}]. \tag{5.43}$$

It can be seen that if the reaction rate is fully controlled by the interface area, then time t required for particles with the same density reached up to a certain reduction degree under the same conditions should be changed directly with the particle radius, and the slope in $lgt_x - lgR$ should be 1.

② If reduction is controlled by gas transfer, then:

$$\frac{k_g}{k_s} \approx 0$$

So

$$\frac{\kappa_{\mathrm{g}}}{R\rho_B}(C_{\mathrm{Ag}} - C_0)t = R\left[\frac{1}{2} - \frac{x_B}{3} - \frac{(1-x_B)^{1/3}}{2}\right]$$

$$\mathrm{t} = \frac{\rho_{\mathrm{B}}\mathrm{R}^2}{\kappa_{\mathrm{g}}(\mathrm{C_{Ag}} - \mathrm{C}_0)}\left[\frac{1}{2} - \frac{x_B}{3} - \frac{(1-x_B)^{2/3}}{2}\right]. \qquad (5.44)$$

It is seen that if reduction rate is controlled by gas transfer, the time for achieving x_B should be changed with R^2 at same condition and same density of particle, and the slope in $\log t_x$ *vs.* $\log R$ plot should be 2.

Therefore, controlling step of reduction rate is possibly confirmed according to the slope in $\log t_R$ *vs.* $\log R$ plot.

It is known from Fig. 5.9 that the overall slope during reduction is not constant. For example, when $x_B = 10\%$ and 85%, the slope = 1.33 and 1.88, respectively.

It can be seen from the relationship between the particle size and time required when reduction reaches to a certain degree that the reduction process is not completely interfacial reaction controlled, nor is the diffusion controlled, but it is a combination of both.

For each situation, the reduction rate is a function of x_B. At beginning of reduction, the slope is close to one, that is, the reduction rate is mainly controlled by area of interface. With the process of reduction, the slope increases equally indicating that the diffusion of gas is more and more important. This is because the degree of reduction being higher, the iron layer becomes thicker and the resistance of gas diffusion increases, which makes the diffusion of gas difficult. For example, when $x_B = 85\%$, due to the increasing and sintering of iron layer, the porosity is reduced which makes diffusion of gas more difficult. Here the reduction rate is controlled by diffusion of gas, and the slope = 1.88 in $\log t_x$ *vs.* $\log R$ plot (see Fig. 5.9).

The author studied the reduction kinetics of A301, ZA-5 wüstite-based catalysts.[8,9] A large number of experimental data confirm the applicability of SCM and its expressions. The following five experiments have been done in our lab.

① **The intrinsic kinetics of reduction.** The reduction rate was measured by thermogravimetric analysis (TGA) under conditions of particle sizes of 0.034 mm–0.054 mm, H_2 flow of 175 ml·min^{-1}, temperatures at 350°C, 375°C, 400°C, 475°C, and 500°C, respectively. The effect of diffusion has been eliminated at such particle size range. If the shape of catalyst is taken as spheroid, reduction of fused iron catalysts can be described by SCM. The intrinsic kinetics of reduction is expressed as in Eq. (5.45).

$$\frac{dx_B}{dt} = k_0 \exp\left(\frac{-E}{RT}\right) P_{H_2}^n (1-x_B)^{2/3}, \qquad (5.45)$$

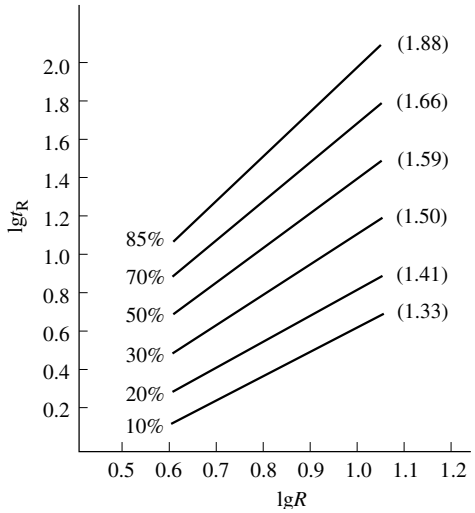


Fig. 5.9 log t_R vs log R plots

where x_B is the degree of reduction, t is time, k_0 is pre-exponential factor, and E is the activation energy (kJ·mol^{-1}).

In the case of pure H_2, P_{H2} is constant; the following Eq. (5.46) *via* fitting experimental data is obtained:

$$\frac{dx_B}{dt} = k_x(1-x_B)^{2/3} = 4248\exp\left(\frac{-71680}{RT}\right)(1-x_B)^{2/3} \tag{5.46}$$

② **The effect of gas composition of reductant on the reduction degree.** Under the same conditions as mentioned above, the influence of concentration of H_2 on reduction kinetics of ZA-5 catalyst was studied at 500°C. The concentrations of H_2 are 100%, 87.55%, 83%, 75% and 50% in the mixture with N_2 balance, respectively. The results show the average reaction order of H_2 is about 1.5. The intrinsic kinetic equation on the ZA-5 catalyst is expressed as Eq. (5.47).

$$\frac{dx_B}{dt} = k_x P_{H_2}^{1.5}(1-x_B)^{2/3} = 4248\exp\left(\frac{-71680}{RT}\right)P_{H_2}^{1.5}(1-x_B)^{2/3} \tag{5.47}$$

③ **Influence of particle size on reduction degree.** The reduction of singe-particle catalysts was studied by temperature-program reduction (TPR) method. The particle sizes of catalyst are 1.8 mm, 2.8 mm, 4.0 mm and 5.7 mm, respectively, and flow rate of H_2 is 175 ml·min^{-1}, with temperature-program from 200°C to 500°C with heating rate of 0.1°C·min^{-1}. The results show the temperature and reduction time increase with increasing particle size. At the same time (same temperature at 450°C),the degrees of reduction with particle size of 1.8 mm, 2.0 mm, 4.0 mm and 5.7 mm are 96%, 90%, 51%, and 39%, respectively. If the effect of particle size on the reduction property is semi-quantitatively expressed by the ratio of reduction degree of big particles to powders under the same conditions, then the particle effect of the four above particles is 0.96, 0.90, 0.51, and 0.39, respectively.

④ **The reduction of catalyst with industrial particle size.** The reduction of singe-particle industrial catalysts was studied under isothermal condition. The particle size is 2.2 mm, and H_2 flow rate is 175 ml·min^{-1} with temperatures of 380°C, 400°C, 420°C, 440°C and 460°C respectively. The results show that time needed for degree of reduction higher than 95% is 34.27 h, 23.12 h, 17.37 h, 13.32 h and 8.20 h, respectively. Reduction of single-particle industrial catalysts may be described by SCM and the kinetic equation (5.48) is as follows:

$$\frac{dx_B}{dt} = 644 \exp\left(\frac{-87260}{RT}\right)(1 - x_B)^{2/3}. \tag{5.48}$$

Compared with intrinsic kinetic equation (5.47), the pre-exponential factor of kinetic equation is reduced obviously, which indicates the reaction surface area of catalyst particle decreases with increasing particle size, but activation energy increases obviously.

⑤ **Comparison of reduction properties of three industrial catalysts.** The reduction performances of three series of catalysts (Fe_3O_4(A110-2), Fe_3O_4–CoO (ICI74-1) and $Fe_{1-x}O$ (ZA-5)) were studied under the same conditions with the particle size of 0.054 mm, H_2 flow of 175 ml·min^{-1} by programmed-temperature reduction method using a constant heating rate and constant temperature methods. It is found that the temperature of reduction of ZA-5 catalyst is 50°C lower than A110-2 and 30°C lower than ICI74-1 catalyst. A110-2 and ICI74-1 have obvious induction periods while it is very short for ZA-5 catalyst. It results from the defect crystal lattice in non-stoichiometric wüstite of ZA-5 catalyst.

5.2.3 *Crystal nucleus growing model*

The formation of reduction product α-Fe of ammonia synthesis catalyst is a crystal growth process, which follows the principle and law of crystallography. The basic requirement for this process is that it should form the small α-Fe crystal without growth or conglutination. This requirement is related with the reaction rate, particularly temperature and the concentration of another product H_2O, in particular reoxidation of α-Fe should be avoided. Thus, reduction conditions with low-temperatures, high-space velocities and low-water vapor concentrations are required in actual operation.

The solid state reaction kinetic model mentioned above is based on such an assumption that the rate determined step in chemical interaction between solid states is the formation and growth of crystal nucleus of products on the active sites. The active site can be the defects of surface and point or the outcrop moved to the crystal surface. As the volume of the original material and products varies, the generation process of crystal nuclei will be accompanied by the lattice deformation, that is, the speed of the process depends not only on chemical factor but also depends on the nucleation chemistry.

There are several solid state kinetic models related to nucleation and growth processes. One of the most commonly used is the equation proposed by Колмогоров-Ерофеев.[10]

$$\alpha = 1 - \exp(-k\tau^n). \tag{5.49}$$

Kolmogorov proposed two equations after he studied the crystallization process.

Table 5.3 n value for various boundary conditions

Boundary condition	n value
Polycrystalline change, nucleus grow up by controlling of boundary	
Rising rate of nucleation	> 4.0
Constant rate of nucleation	4.0
Rate decreasing of nucleation	3.0−4.0
Nucleation on edge after saturation	1.0
Diffusion controlling nucleus grow up	
From original small nucleus growth to arbitrary crystal shape	
Nucleus formation rate in continues rising	> 2.5
Nucleus formation rate in constant	2.5
Nucleus formation rate in decreasing	1.5−2.5
Nucleus formation rate down to zero	1.5
Crystal nucleus with arbitrary from obvious growth	< 1.5
Crystal nucleus of small needles or slices	1.0
Thickness increasing of columns holding constant longth	1.0
Thickness increasing of large slices holding constant surface	0.5

① The equation for spherical crystal nucleus growth with a constant rate, considering the coverage conditions of crystal nucleus:

$$\alpha = 1 - \exp\left(-\frac{4}{3}\pi n_0 k_p^3 \tau^3\right). \tag{5.50}$$

② The number of crystal nucleus increases with a constant rate in (5.50), then (5.51) is obtained, (the coverage of crystal nucleus was also considered).

$$\alpha = 1 - \exp\left(-\frac{1}{3}\pi n_0 k_p^3 \tau^4\right), \tag{5.51}$$

where n_0 is the number of crystal buds that can grow up to crystal nuclei, k_p is the rate constant for radial growth of nucleation.

The value of n in the Eq. (5.49) is related with reaction mechanism, the rate of nucleation, and the size of crystal buds. The n values are given in Table 5.3.[11]

Equation 5.49 is often used to express a variety of local-chemical processes. Transformation constants k and n values can express all kinds of relationships. However, the weakness of this equation is obvious, because the equation during the application for the choice of the experimental data does not give a certain physical sense for conclusion. Graphic method can be used to test the applicability of Eq. (5.49). The graphical method involves double logarithm calculations, which further increase the uncertainty of the equation. However, the deviation of experimental from the theoretical relations can be minimized.

In fact, all isothermal kinetic equation can be expressed as the following equation,[12]

$$\frac{d\alpha}{d\tau^Z} = k(1 - \beta\alpha)^m, \tag{5.52}$$

where k is the constant; β- is the dimensionless parameter; Z is the parameter related to interaction mechanism; and m depends on mechanism and pellet shape.

Table 5.4 Explanation of parameters in Eq. (5.52)

	Parameters		
Physical models	Z	β	m
Reaction controlled *via* boundary process			
Reactants like spheres	1	1	2/3
Reactants like needles	1	1	1/2
Reactants like very thin sheet of round	1	1	0
Diffusion models	1/2	1	0
	1/2	1	0.29
	1/2	1	2/3
	1/2	1	0.43
Nucleation mechanism	> 1	1	1

The m value is similar to the reaction order, which is called as the reaction index. Table 5.4 lists the parameters in Eq. (5.52), which corresponds to a variety of dynamic models.[13]

5.3 Reduction Process of Oxides

The precursors of most metal catalysts are metal oxides, which should be reduced to metal state to get catalytic activity. When H_2 is used as the reductant, the beginning temperature of reduction can be determined by comparing the affinity of O_2 to metal oxide and H_2 (the affinity is determined by the change of Gibbs' free energy in the chemical reaction, ΔG). Studies show that the reduction temperature of metal oxides may be judged by the strength of chemical bond between metal and oxygen. The strength of M–O bond can be judged by the heat of formation of metal oxides. The larger the heat of formation, the stronger the M–O bond, the more difficult is the reduction of materials, and the higher is the reduction temperature. The relationship between the heat of formation and beginning reduction temperature of metal oxide by using of H_2 is shown in Fig. 5.10.[14] The beginning reduction temperatures given in Fig. 5.10 are only for pure metal oxides, but the temperature can be affected by preparation conditions, doping and other factors. The reduction temperature increases when the catalysts contain hard-to-be reduced materials. The temperature decreases when the catalysts contain easy-to-be reduced materials because they (catalysts) will be reduced first and induce the reduction of other materials leading to the decrease of reduction temperature; but if the interaction between different components is strong, for example, the formation of spinel complex oxide, or solid solution etc., it will increase the reduction temperature. According to Fig. 5.10, the initial reduction temperatures of CuO, NiO, CoO, ZnO and Fe_2O_3 are 140°C, 290°C, 230°C, 560°C, and 320°C, respectively. After complex solid solutions such as $CuFe_2O_4$, $NiFe_2O_4$, $CoFe_2O_4$ and $ZnFe_2O_4$ are formed, the initial reduction temperatures change to 212°C, 215°C, 301°C, 318°C according to H_2–TGA curves, respectively. For oxides with low-reduction temperature such as CuO, CoO, the initial reduction temperature increases after formation of spinel complex oxides and decreases for oxides with high-initial reduction temperature such as NiO, ZnO.

The reduction temperature can be decreased for the sample containing a certain amount of amorphous phase. Such a result gives the preparation of catalysts a good

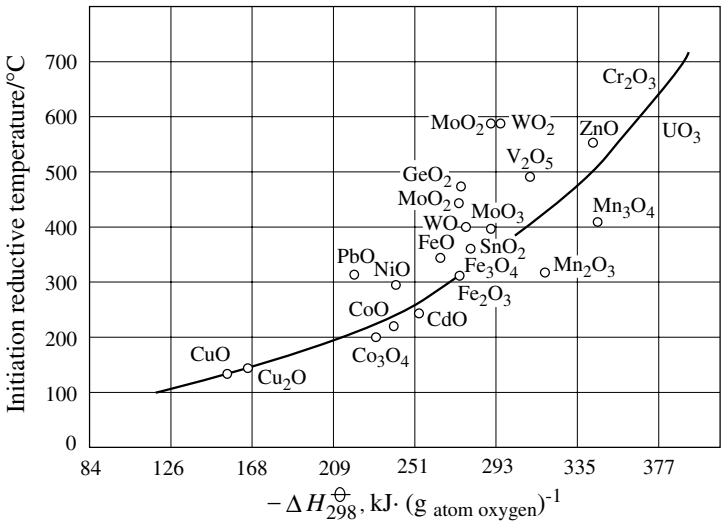


Fig. 5.10 Relationship between formation heat of metallic oxides and initation reductive temperature

Table 5.5 Elements formed stable oxides at reduction conditions

IA	IIA	III B	IV B	VB	VIB	VII B	VIII	IB	IIB	III A	IV A	VA	VI A	VII A
Li	Be									B	C	N	O	F
Na	Mg									Al	Si	P	S	Cl
K	Ca	Sc	Ti	V	Cr	Mn	Fe	Co	Ni	Cu	Zn	Ga	Ge	As	Se	Br
Rb	Sr	Y	Zr	Nb	Mo	Tc	Ru	Rh	Pd	Ag	Cd	In	Sn	Sb	Te	I
Cs	Ba	La	Hf	Ta	W	Re	Os	Ir	Pt	Au	Hg	Tl	Pb	Bi	Po	At
Fr	Ra	Ac	Rf	Ha	U											
		Rare Earths														

inspiration, i.e., catalysts with very small grains can be used at very low-reduction temperatures. To obtain the ferrite with oxygen defect structure, the initial reduction temperature can be increased a little with hydrogen as reductant. Table 5.5 gives the elements that can form very stable oxides under reducing conditions.

It is impossible to evaluate and analyze processes occurred during reduction of the fused iron catalyst without studying the nature and the state of the fused iron catalyst or the main compounds produced during reduction.

(1) Crystal Structure.[15] The fused iron catalyst is not a single crystal phase, but a mixture, which is made up of two or more crystal phases and amorphous phases. In addition, the pores should be taken as a separate phase. The crystal compounds are the basic components of fused iron catalyst.

The basic force that leads to the formation of stable molecular is electrostatic gravitation between the opposite charged ions (ionic bond), as well as the stability of the structure of electron shells. In this case, the electrons belong to two atoms (covalent bond), or it belongs to mixed bonds. The additional type of bond is the weak electrostatic force between the atoms and molecules and this forces changes with the dipole moment of electrons and moment place (van der Waals force).

The force between atoms of solid is similar to the bond mentioned above. The atoms in the crystals of the solid should be configured periodically so that the electrostatic repulsive force is the smallest and forms the most favorable angle and the bond in lattice distance corresponding with minimum energy. To determine the type of energy and bond, the main characteristic is electronic distribution between atom and molecule. In short, the solid can be divided into several types with crystal lattices with the ionic bond, covalent bond, molecular bond, metal bond and hydrogen bond.

The compounds composed of metal and oxygen basically have the nature of ionic compounds. Electrovalent bond has low conductivity at low-temperatures and high conductivity at high-temperatures. With the increase of charge, the strength of electrovalent bond also increases. Representative nature of the metal is its high-conductivity. Metal contains a large number of charge carriers — the electrons.

Crystal is composed of atoms or molecules configured orderly and periodically. The most stable crystal structure is the crystals with the most closely atomic arrange to suffice the following requirements: It has a certain number of bonds in every atom, atomic size and the direction of bond, etc. To simplify, atoms can be taken as spheres arranged in various ways. As we all know, there are 14 kinds of lattice spaces, which are divided into seven crystal systems according to the growth of the order of symmetry: Three-wedged, single-wedged, triangular, hexagonal, diamond, and square and cubic. In ionic crystals, the lattice structure of the crystal is associated with the chemical radius of the ions as shown in Table 5.6.

In general, the cation size is smaller than anion size. The lattices of ionic compounds may be formed by the small cation distributed in the vacancies between anions, so that negative and positive ions are able to accommodate in the lattice, and the gravitational force can be the largest and the repulsive force is the smallest. For example, the iron ions in ferrous oxide (FeO) are surrounded by six oxygen ions

Table 5.6 Structural-chemical radiuses of ions in ionic crystals

Ion	Crystal chemical radius of ions/nm	Ion	Crystal chemical radius of ions/nm
O^{2-}	0.140	Mn^{2+}	0.080
Mg^{2+}	0.065	Fe^{2+}	0.075
Al^{3+}	0.050	Cr^{3+}	0.064
Si^{4+}	0.041	Mn^{3+}	0.062
Ca^{2+}	0.099	Fe^{3+}	0.060

(in the coordination of six). Coordinating valence of anion distributed around the cations depends on the geometry, i.e., the cation must contact with every anion, that is to say the distance between anion and cation is equivalent to the lowest energy.

Many crystal compounds have polymorphs, that is, crystal with the same chemical substance may have a variety of crystal forms. For example, hematite (Fe_2O_3) has three kinds of polymorphs i.e., α, β and γ. At the specific temperature, the stability of various polymorphs is related to the free energy. The most stable hematite in thermodynamics is α-Fe_2O_3, but β-Fe_2O_3 and γ-Fe_2O_3 also can form under certain conditions.

(2) Lattice defects. To a large extent, many characters of solid are related with the small differences between the solid lattice structure and the ideal solid lattice structure. Ideal crystal lattice is fully ordered. Atoms in this lattice are inactive, and electronics are distributed based on the lowest energy state. However, there are some defects in real crystals. One of these defects represents an increase of the oscillation amplitude of atoms. The other defects are caused by the electronic distribution due to the possible changes in energy levels. There are a series of atomic defects (with other atoms replacing the atoms in lattice or putting the atoms to the middle of the lattice crunodes or to configure to the defects and the lattice crunodes which is not occupied by atoms), and may also form an incomplete linear displacement.

In many types of aberrancy from the regular occurrence of the atom, it often happens that other atoms come into the basic lattice of crystal (the replacement of solid solution). For example, magnesium oxide crystal often contains a lot of iron, nickel or other elements. The lattice in wüstite may contain calcium, magnesium, manganese and other ions. A similar series of solid solution can be seen in Fe_2O_3–Al_2O_3 and many spinels. The following factors can be used to judge the replacement of the basic ions by other ions.[16]

① If the difference between two ions size does not exceed about 15%, it will promote the formation of replacement solid solution. This factor is most important for ionic crystal. It will limit the formation of solid solution when the other ions introduced have different valences with the basic ion.

② Higher the possibility of a chemical reaction, higher will be the restriction of the possibility for replacement of basic ion to other ions. The same type of lattices easily promote the generation of solid solution.

③ In general, the formation of replaced solid solution induces the generation of defect because the lattice must be an electric charge neutral. For example, the introduction of trivalent iron ions to wüstite leads to the generation of cationic vacancy. If the other atoms are smaller, they can enter the crunode between lattice sites (called immersion solid solution).

④ Formation of defects in crystals is not caused by entering of other ions. If a defect is composed by same amounts of vacancies and atoms between nodes, then it is called as a Frenkel defect. Such default can be formed in priority at high temperatures in the thermodynamic sense. According to Fraenkel's report, the concentration n_v of vacancies and n_i of atoms between crunodes is

$$n_i = n_V = n_l \frac{-E}{RT}, \tag{5.53}$$

where n_l is the concentration of normal crunodes, E is the atomic potential energy difference between the normal crunodes and inside of crunodes, k is Boltzmann constant.

⑤ The ratio between ion number of normal crunodes and inside crunodes is fixed at a certain temperature. At room temperature, the equilibrium concentration of defects is very low, but is high at high temperatures. However, for the pure crystal without impurities, when the amounts of atoms in crunodes and in vacancies are the same, the defect only exists in crystals in stoichiometric form. This situation is very rare for oxides.

⑥ Other possible types of defects for ionic crystal is the generation of a vacancy of cation and anion with the equilibrium concentration at the same time, i.e., Schottky defect. Existence of vacancy results in a high lattice energy of crystal. The equation for calculation concentration of vacancy is similar to Eq. (5.53) for the NaCl type of crystal.

⑦ In addition to the vacancy and ions, the stoichiometric of the cation and anion between crunodes can be damaged. That is generation of a non-stoichiometric compound, and the typical example is wüstite. The character of non-stoichiometric oxide is a function of their composition; the common nature is their composition and can be changed by the surrounding gas atmosphere and temperature.

(3) Interface and boundary. The interface and the boundary between each phase are of great significance in the study of the reduction process of the catalysts. Usually the surface tension and surface energy can be used to express the state of the surface. For liquids, these values are equal, while for solids, they are different. Surface crystals with a variety of crystal orientations have various values of surface energy. The surfaces with the closest arrangement coincide with the surface atoms that has the smallest surface energy, and hence it is the most stable one.

Many phenomena related to the interface and the boundary between the phases which affect the process of reaction is constrained by the following status, that is, the existence of the surface energy leads to pressure differences in the environment above the distortion surface. At this point, the pressure of vapor increases on large curvature:

$$\ln \frac{P}{P_0} = \frac{M\gamma}{\rho RT}\left(\frac{1}{r_1} + \frac{1}{r_2}\right), \tag{5.54}$$

where p is the vapor pressure above the distortion surface, p_0 is the vapor pressure above the smooth surface, M is the relative molecular weight, γ is the surface energy, T is the temperature, ρ is the density, R is the universal gas constant, r_1, r_2 is the main radius of curvature of the surface.

The simplest type of interface is the interface between the particles of same catalysts. If the crystals are tilted with one another, certain incompatible spaces can be produced on boundary. This is equivalent to the introduction of the edge displacement between the crystals. The quantity and boundary energy of the latter is increased with the increase of angle of inclination of crystal. If the crystals cause rotation among each other, a network of screw displacement will appear. The combination of tilt and rotation will form a complex system of spiral and edge displacement.

Phases in fused iron catalyst have different thermal expansion coefficients. Therefore stress can be produced on boundary which causes crack and damages the integrity of the particles during cooling process. This phenomenon can be observed at the single-phase system, and the coefficients of thermal expansion in these systems are different in all directions. Here the particle size plays an important role. The bigger the particle size, higher would be the stress.

Because the interface between the various phases has higher energy than the internal, the interface tends to have relative position with the lowest energy. Therefore, the dissolved substances that can lower the surface energy will be concentrated on the interface. When the oxide crystals are destroyed, the interface will become more active in chemistry. Here, under the atmosphere, the interface of oxide crystal immediately adsorbs oxygen atoms to reduce the surface energy.

(4) Displacement of atoms within solid phase. The atoms or ions must move for chemical reaction or structural changes of solids. This phenomenon may have a variety of mechanisms. One mechanism among them is that an atom moves from normal lattice sites to ordered vacancies. As mentioned above, at all temperatures except for the absolute zero degrees, there are always all kinds of vacancies in each crystal. In such cases, the diffusion speed of atoms is related with the concentration of the vacancy and the difficulty in the movement of atoms. Atom movement in a random direction is equivalent to the opposite movement of the vacancy. Therefore, in similar status, it can be considered as diffusion of vacancy.

Another possible mechanism is the movement of atoms along the crunodes. Frenkel vacancies are said to occur when the atoms move easily along with crystal from the normal crunodes to the crunodes in lattices. A program of this process is the so-called "relay" mechanism, the atom located between crunodes transfers to the normal crunodes, where the original atom is pushed out to a new crunodes.

In this system, mechanism of the process can be calculated from the relative energy value which is the necessary energy to drive the process. Commonly, the rate of reaction is determined by the process of diffusion at a large extent.

In quantitative sense, the diffusion can be expressed by the Fick's law:

$$J = -D\frac{\partial c}{\partial x}, \tag{5.55}$$

where J is the diffusion flux (the amount of substances passed per unit surface area in unit time), c is the concentration of substances in the unit volume, x is the distance on the diffusion direction, D is the diffusion coefficient, cm^2/s.

If D does not depend on C, then,

$$\frac{\partial c}{\partial \tau} = D\frac{\partial^2 c}{\partial x^2}, \tag{5.56}$$

where τ denotes time.

According to Nernst–Einstein equation,

$$D_{\mathrm{i}} = B_{\mathrm{i}}RT, \tag{5.57}$$

where B_i is the mobility of atom (velocity under unit force).

This equation is convenient to study the activity of charged particles and the relationship between diffusion coefficient and conductivity.

When atoms displace from one state to another one in lattice, which has to pass the mediacy of high energy, the necessary energy is called as activation energy of the process. The temperature relationship of the diffusion coefficient can be expressed as the following equation:

$$D = D_0 \exp \frac{-E}{RT}, \tag{5.58}$$

where E is apparent activation energy of diffusion.

The diffusion coefficient and the change of it with temperature first relate with the concentration of the lattice vacancies and relates with the activation energy of displacement of defect along lattice too.

In general, there are two stages in the relationship curve between the temperature and diffusion coefficient, i.e., low-temperature part (the impurities diffusion region determined by the impurities) and the high-temperature part (the diffusion region). The relationship between diffusion coefficient of iron and the concentration of vacancies in wüstite is shown in Fig.3.4 of Chapter 3. It is seen from Fig.3.4 that the experimental value for the diffusion coefficient is directly in proportion to the vacancy concentration in wüstite.

For non-stoichiometric oxides, the concentration of lattice vacancy is higher than Frenkel and Schottky vacancy (the stoichiometric oxides), or higher than that of the oxide containing impurities. When the composition of wüstite is fixed, the activation energy of cation diffusion is equivalent to that of the vacancy moving along cation crunodes, i.e., 125 kJ/mol–150 kJ/mol.

The diffusion along with the boundary of particles makes the ordering of the latter become worse. Such diffusion is faster than that in the crystals. Similarly, the activities of the atoms on surface are higher than internal ones. This means that the diffusion at low-temperatures should be along the particle surface and the border; while at high-temperature the diffusion should be in the internal volume of the crystals.

Wüstite $Fe_{1-x}O$ (x = 0.04–0.15) contains 23.0%–25.2% of oxygen. The stoichiometric FeO(Fe/O = 1) containing 22.3% of oxygen is impossible in reality. Wüstite has a face center of cubic lattice as NaCl type. If all lattice sites of oxygen ions are occupied, then in the lattice sites of iron, ions should have vacancies. Therefore, there should be equivalent amounts of ferric ions in lattice of wüstite; otherwise the neutral electronics condition cannot be fulfilled.

The remaining positive charge of iron ions can move along the lattice between the divalent iron and trivalent iron ions. These charges are called as defect electrons, which are electric carriers that are also the reasons that wüstite has conductivity. Because of the existence of vacancies, iron ions can move along the lattice, and the vacancies move in an opposite direction roundabout.

Due to the existence of iron vacancies, there should be a certain amount of iron ions leaving from its own lattice site, and transfer to the status of ions between lattice sites in assumed stoichiometric wüstite.

Magnetite has a spinel-type lattice. The lattice constant is in the range of 0.8378 nm–0.8397 nm. In $Me_xFe_{3-x}O_4$ -type compounds, if the iron ion has been replaced by other elements, the lattice constant can be changed to the range of 0.8 nm–0.89 nm. The character of spinel is a cubic crystal made up of oxygen ions with the most closely arrangement in lattice. Basic cell in spinel has 32 ions of

oxygen. The latter includes 64 tetrahedral interspaces and 32 octahedral interspaces. The metal ions can insert into these interspaces. In the unit cell, 32 oxygen ions are corresponding to 24 metal ions. For the ideal lattice, there are eight metal ions distributed into the tetrahedral interspaces (A node) and 16 metal ions distributed into the octahedron crunodes (B node).

When metal ions fill in the vertex of tetrahedral and octahedral, there may be two cases of boundary. One is the normal feature of the cation distribution. At this case, all the divalent ions are located at A site, for example, $ZnFe_2O_4$. The second situation is that ions with various valences occupy octahedral vertex. Magnetite has an abnormal spinel-type structure, and also has mixed cation configuration.

In the spinel type solid solution, one is the normal type of spinel, while the others are abnormal spinel type. In addition, the transition from one type to another type is possible. Some pure spinels make up of a normal spinel and an opposite formation of solid solution with the same chemical composition such as $Fe^{3+}_{1-x}Mg^{2+}_{x}(Fe^{3+}_{1+x}Mg^{2+}_{1-x})O_4$. A similar solid solution, especially without deviating from one of the interface structure, can be a disorder of normal spinel and abnormal spinel.

There may be other types of disorder such as in the ideal crystal, in which some top of the crystal should be free, but occupied, or they are occupied, but not filled.

Both types of disorders play an important role in diffusion of iron ions in magnetite. Usually, compared with the diffusion coefficient of iron, the diffusion of oxygen is limited in the lower range when the lattice has higher levels of oxygen.

The ion exchange between divalent and trivalent iron ions located at the top of the octahedral lattice is easy, which is the reason why the oxide has high conductivity.

Upon heating, the magnetite is able to accept residual amount of trivalent iron oxide. Considering magnetic hematite (γ-Fe_2O_3), the information of lattice distortion related to magnetite on the deviation from the stoichiometric composition can be obtained. Magnetic hematite has the same structure with magnetite. However, in each basic cell with 32 oxygen ions, $2 \times 2/3$ octahedral tops occupied by the iron ions are not filled. The experiment proves that such a structure of the magnetite for accepting the remaining oxygen is also typical. According to the reports, self-diffusion coefficient $D_{Fe}{}^{*}$of iron is in proportion to the partial pressure of oxygen ${P_{O2}}^{0.4}$.

5.4 Reduction Thermodynamics for Iron Oxides

There are several different views about the reduction process of iron oxides and their mixtures. According to the principle so-called transportation stage-by-stage, the reduction of iron oxides is from the oxide of high valence to low valences in turn as follows:

$$Fe_2O_3 \rightarrow Fe_3O_4 \rightarrow FeO \rightarrow Fe \text{ (above } 570^{\circ}C)$$

or

$$Fe_2O_3 \rightarrow Fe_3O_4 \rightarrow Fe \text{ (below } 570^{\circ}C)$$

According to Fe–O state diagram (see Fig. 4.4 in Chapter 4), not only metal and oxide with low valance but also the solid solution can be generated in the system.

The thermodynamic region of the stable iron oxide has been shown in Fig. 3.2 in Chapter 3.

For the reduction of fused iron catalysts, the reduction temperature is lower than 570°C, regardless of iron oxide in catalysts is Fe_3O_4, FeO or their mixtures (of the $Fe^{2+}/Fe^{3+} \geq 0.5$, Fe_2O_3 does not exist in this system), therefore they can be directly reduced to Fe.[17]

In general, when H_2 and CO are used as reductants, the possible reduction reaction of iron oxides is as follows:

$$3Fe_2O_3 + H_2 = 2Fe_3O_4 + H_2O - 4.2\,\text{MJ} \tag{5.59a}$$

$$3Fe_2O_3 + CO = 2Fe_3O_4 + CO_2 + 37.25\,\text{MJ} \tag{5.59b}$$

$$Fe_3O_4 + H_2 = 3FeO + H_2O - 62.41\,\text{MJ} \tag{5.60a}$$

$$Fe_3O_4 + CO = 3FeO + CO_2 - 20.96\,\text{MJ} \tag{5.60b}$$

$$FeO + H_2 = Fe + H_2O - 27.80\,\text{MJ} \tag{5.61a}$$

$$FeO + CO = Fe + CO_2 + 13.65\,\text{MJ} \tag{5.61b}$$

Either H_2 or CO and their mixtures can be used as reductant for F–T synthesis iron catalysts, while only H_2 can be used as reductant for ammonia synthesis iron catalysts. It is the reason that the active phase for the former is iron carbide and the latter is metal iron after reduction.

Each reaction process has three components and three phases, i.e., the number of degree of freedom of the system is two. Therefore, there are only two values that can be changed among four of them (total pressure, temperature, partial pressure of reducing agent and products), the other two values are their functions, and the equilibrium of the system has nothing to do with total pressure, that is:

$$K_p = f(T) = \frac{p_{H_2O(CO_2)}}{p_{H_2(CO)}}. \tag{5.62}$$

Therefore, the system can be taken as a single variable parameter.

The relationship of equilibrium constant with temperature for Eqs. (5.59)–(5.61) is as follows in turn[18]:

$$\lg K_p = \lg \frac{p_{H_20}}{p_{H_2}} = -\frac{160}{T} + 4.48 \tag{5.63a}$$

$$\lg K_p = \lg \frac{p_{CO_2}}{p_{CO}} = \frac{1720}{T} + 2.81 \tag{5.63b}$$

$$\lg K_p = -\frac{3440}{T} + 3.67 \tag{5.64a}$$

$$\lg K_p = -\frac{1560}{T} + 2.00 \tag{5.64b}$$

$$\lg K_p = -\frac{690}{T} + 0.405 \tag{5.65a}$$

$$\lg K_p = \frac{1190}{T} - 1.26. \tag{5.65b}$$

Table 5.7 Equilibrium constant of reduction reaction for $1/4\ Fe_3O_4 + H_2 = 3/4Fe + H_2O$

T/°C	200	300	400	500	550
K_p	0.013	0.044	0.107	0.214	0.283

However, because of the non-stoichiometric of wüstite in the Eq. (5.61), then

$$Fe_{0.947}O + H_2 = 0.947\ Fe + H_2O \tag{5.66}$$

$$\lg K_p = -\frac{940}{T} + 0.52. \tag{5.67}$$

The characteristic of (5.59) is that it contains trace amounts of reducing agent in the equilibrium of medium, which is almost a non-reversible reaction. Equation (5.60) is an endothermic reaction. When the temperature increases, the equilibrium will move to the right direction. The content of CO and H_2 in mixture of equilibrium will decrease. Equation (5.61a) is an endothermic reaction, while (5.61b) is an exothermic reaction.

The reduction reaction of magnetite to iron is as follows:

$$Fe_3O_4 + 4H_2 = 3Fe + 4H_2O - 145.8\,\text{MJ}, \tag{5.68a}$$

$$Fe_3O_4 + 4CO = 3Fe + 4CO_2 + 19.99\,\text{MJ}. \tag{5.68b}$$

Equation (5.68a) is an endothermic reaction, and its equilibrium constant is as follows:

$$\lg K_p = 4 \lg \frac{p_{H_20}}{p_{H_2}} = -\frac{5500}{T} + 4.89. \tag{5.69}$$

The equilibrium constant of reduction reaction for $1/4\ Fe_3O_4 + H_2 = 3/4Fe + H_2O$ is shown in Table 5.7.

Reduction process by H_2 is an endothermic reaction. Increasing the temperature is beneficial for equilibrium and reaction rate for the formation of α-Fe, but it also accelerates the recrystallization of α-Fe, thereby decreasing the activity of the catalyst. Small amounts of water vapor in the gas phase can oxidize α-Fe into FeO or Fe_3O_4 again. It is generally believed that the effect of reduction pressure on activity is insignificant, but increasing the gas velocity and reducing the concentration of water vapor is beneficial to the catalytic activity.

For pure Fe_3O_4, at 444°C, when $K_p = [H_2]/[H_2O] = 5$, Fe and Fe_3O_4 coexist. However, it is known from the experiment that at 444°C, $[H_2]/[H_2O] \approx 2{,}000$, there are still measurable oxygen remained on the iron surface. It is confirmed from poisoning experiments on ammonia synthesis catalyst that a very low concentration of water vapor in synthesis gas causes the oxygen to be retained on the iron and reduces the catalytic activity.

Figure 5.11 gives Fe–O–H_2 (CO) equilibrium conditions, each line indicating the relationship of the change of components and temperatures for Eqs. (5.60), (5.61) and (5.68). In Fig. 5.11, there is no equilibrium line corresponding to (5.59) because it is close to Y-coordinates. Figure 5.11 gives the necessary gas composition for iron oxides being reduced completely.

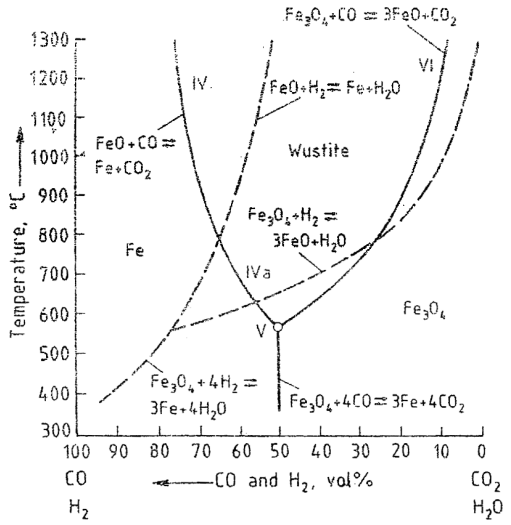


Fig. 5.11 Equilibrium diagram of Fe–O–H_2 and Fe–O–CO

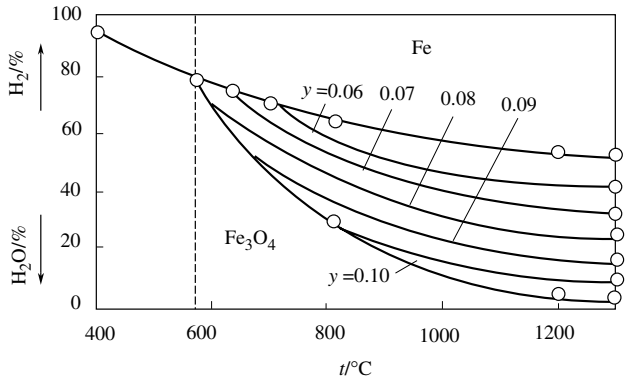


Fig. 5.12 Equilibrium diagram of Fe–O–H_2 system considering the non-stoichiometry of wüstite ($Fe_{1-y}O$)

Considering that the reductant of gas has to be superfluous, Eqs. (5.61a) and (5.68a) can be written as:

$$FeO + qH_2 \rightarrow Fe + (q-1)H_2 + H_2O \tag{5.70}$$

$$Fe_3O_4 + pH_2 \rightarrow 3Fe + (p-4)H_2 + 4H_2O \tag{5.71}$$

It is seen from Fig. 5.11 that Fe_3O_4 can be reduced to FeO by the gas. This reaction occurs at low temperatures and the beginning of the process, for instance, in the upper part of the catalyst bed.

The above data are in an ideal system, in which many of factors are not taken into account under the actual conditions (generated solid solution, etc.), and it will change the above data. The curve shape of the wüstite reduction by H_2 will change with the oxygen content i.e., the defect concentration y of iron in $Fe_{1-y}O$ (Fig. 5.12).

Iron oxide is a complex mixture and solid solution in the real catalyst. Wüstite can form solid solution with MnO, MgO, CaO etc. At 1100°C, wüstite can dissolve 28% CaO. Lattice constant (0.4327 nm–0.4329 nm) of wüstite in catalysts is larger than that of pure wüstite phases. This is because *ca.* 5% to 6% (molar fraction) of CaO is dissolved in wüstite.[19] Fe_3O_4 and cubic spinel (for example, Mn_3O_4, Co_3O_4, $FeAl_2O_4$ etc.) can generate solid solution. At 1350°C, about 5% chromium oxide can be dissolved in wüstite, and generates $FeCr_2O_4$, and then generates a series of solid solution with magnetite. Iron oxide also can form solid solution (iron silicate, olivine, and other) with SiO_2.

These compounds and solid solutions formed with iron oxide make the reduction of catalysts more complex and difficult. As a result, the activity of iron oxide in the compounds under normal circumstances is declined. Therefore, it is necessary to increase H_2 content in gas mixture and increase the reduction temperature.

Small amounts of iron silicate are difficult to be reduced in catalysts, but some studies[20] show that some parts of the most hard-to-be reduced in catalyst have the highest activity.

5.5 Reduction Reaction Kinetics of Iron Oxides

5.5.1 *Reduction mechanism of oxides*

Generally, the reduction of oxides is a complex and multi-stage process including the phenomenon with multiple independent. Each process has its unique law. Because the law is complex, the overall image is a complex, often extremely difficult to be explained clearly.

Under normal status, two fundamental questions for any reduction process need to be solved.

(1) In which medium chemical reaction can occur to capture oxygen from the oxide, which relates to the process procedures?

(2) Which step is the rate-determining step during the whole reduction process?

Typically, the interaction between oxygen and metal oxide happens in gas, in the boundary of metal and low valence and high valence oxides. Sometimes, the basic position of the interaction will change, which makes analysis of the reaction more difficult. So people assume that position of reaction capturing oxygen from metal oxide is unchanged, and the basic theory about the reduction of metal oxide is from this basic assumption.

A mechanism about reduction of oxide is the thermal-decomposition theory.

$$\begin{aligned} \mathrm{MeO} &= \mathrm{Me} + 1/2\mathrm{O_2} \\ \mathrm{B} + 1/2\mathrm{O_2} &= \mathrm{BO} \\ \hline \mathrm{MeO} + \mathrm{B} &= \mathrm{Me} + \mathrm{BO} \end{aligned}$$

The process is composed of two stages: The decomposition of metal oxides (MeO), as well as oxidation of reductant by oxygen expelled from oxide. Advantages of this model are that it is simple and convenient for calculation. It continues to be widely used when calculating the heat consumption and heat balance of the reduction process.

For iron catalyst of ammonia synthesis with Fe_3O_4 as precursor, from a mechanistic point of view complex, the simple overall reduction reaction is that it is a gas–solid interface reaction.

$$Fe_3O_4 + 4H_2 \rightarrow 4H_2O + 3Fe$$

The product iron is much denser than magnetite. The metal forms a layer around the core of oxide after the initial reduction and rapidly blocks the gas exchange from the outer gas–solid interface with the bulk. For this reason the mechanism cannot be based upon the removal of oxide ions from the lattice but it requires the iron to move to a reaction interface at the gas–solid boundary.

The mechanism is considered to involve diffusion of ions and electrons and to contain two types of sites. One type allows the oxidation of oxide ions and another type generates diffusion of iron ions and their reduction. The overall processes are:

$$4O^{2-} + 4H_2 \rightarrow 4H_2O + 8 \text{ electrons} \tag{5.72}$$

$$Fe_3O_4 + Fe^{2+} + 2 \text{ electrons} \rightarrow 4FeO \tag{5.73}$$

$$4FeO \rightarrow 4Fe^{2+} + 4O^{2-} \tag{5.74}$$

$$4Fe^{2+} + 8 \text{ electrons} \rightarrow 4Fe \tag{5.75}$$

$$Fe_3O_4 + Fe + 4H_2 \rightarrow 4H_2O + 4Fe \tag{5.76}$$

In the present context, two conclusions are important from this mechanism derived for metallurgical samples of magnetite/wüstite synthetic mixtures.[21]

(3) Elemental iron is essential to reduce magnetite with hydrogen gas at low temperatures. This elemental iron is produced from thermal decomposition of the wüstite admixture in the precursor. Stability and bulk distribution of the wüstite determine the abundance of reaction interface in the polycrystalline solid. To a large extent, the grain structure and porosity of the final catalyst are predetermined by the disposition of these reaction centers representing the nuclei of the iron metal crystallites.

(4) The reaction involves movement of all iron ions and allows a complete bulk restructuring of the solid at low temperatures. The topochemistry of the reduction process determines the texture of the resulting ion. The grain structure of the precursor oxide which is essential for a finite reactivity of the bulk oxide mixture is one of the factors controlling the reduction kinetics.

In wüstite structure, a large number of defects are iron ions, which allow the diffusion of iron into the lattice, and it is beneficial for the transfer of electrons. This is the structural reason that why $Fe_{1-x}O$-based catalyst is easy to be reduced.

Obviously, this mechanism cannot explain the reduction of pure Fe_3O_4. However, the traditional fused iron catalyst always contains a small amount of FeO. When FeO content increases significantly enough as an independent phase, many FeO will prevent the reaction of (5.73) going to the right direction, and the reaction will first follow the reactions (5.74) and (5.75). Then the elemental iron being generated from reaction (5.75) will promote reaction (5.73). The experimental results from the author show that when the catalyst is composed by the two different phases, such as FeO and Fe_3O_4, FeO is reduced to α-Fe first, and then the reduction of Fe_3O_4 phase starts by hydrogen, and both the phases are directly reduced into α-Fe. This

process occurs stage-by-stage according to the phase, and belongs to a competitive reduction mechanism.

The following conclusion is obtained according to the experimental data: The role of oxide decomposition is minor in the reduction process. Because as we all know, the partial pressure of decomposition which can be used to measure affinity of the oxide is very low, this can be neglected. The lower the pressure of decomposition, the bigger the affinity of the oxide is. At 700°C, the logarithm of the pressure of FeO decomposition is -20.8,[22] and the majority of oxides also have this nature, except for some high valence metal oxides. For example, decomposition reaction of $3Fe_2O_3 = 2Fe_3O_4 + 1/2O_2$ at 1383°C, of $6Mn_2O_3 = 4Mn_3O_4 + O_2$ at 940°C, of $4MnO_2 = 2Mn_2O_3 + O_2$ even at 460°C, the partial pressure of the oxygen equals atmospheric pressure. Of course, these oxides are scarce.

It should be noted that the decomposition is not necessary in accordance with $MeO = Me + 1/2\ O_2$. For example, decomposition may go in a manner of generating atomic oxygen:

$$MeO = Me + [O]$$

Some people think that the majority of cases are often that atomic oxygen is involved in decomposition reaction.[23]

Another mechanism of oxide reduction is based on the adsorption-autocatalytic theory. This theory can be expressed by the following procedures.[24]

$$\begin{aligned} MeO + B &= MeO{\cdot}B_{ads} \\ MeO{\cdot}B_{ads} &= Me{\cdot}BO_{ads} \\ Me{\cdot}BO_{ads} &= Me + BO \\ \hline MeO + B &= Me + BO \end{aligned}$$

Reduction reaction follows three stages: The adsorption of the reducing gas; the chemical reaction on the oxide surface and desorption of the gas products.

It is considered in adsorption-autocatalytic theory that the interaction happens at the interface of gas–solid. In some cases, it is found that of the auto-catalytic phenomenon happens at the early stages of reduction. The value of this theory indicates the necessity of direct contact of the reductant with metal oxides. It is possible to evaluate the mechanism and kinetics of reduction by use of law of physical chemistry, physics and surface chemistry. The great effect of product (H_2O) on the rate of reaction confirms the important role of adsorption. Because H_2O is a very active adsorbent, it can occupy the most active areas of oxide, and thus greatly reduce the rate and degree of reduction.

However, a large number of experimental data, especially the use of the latest research methods reveal the limitation of the theory of auto-catalysis. As is well-known, the adsorption capacity of substance decreases with temperature. In order to obtain reliable results, the experiments commonly are carried out at low temperatures, but this is not true under the actual conditions of catalytic processes.

In addition, there are a lot of studies on the mechanism of reduction. К·К·Школин provided the evidence to prove the importance of process of transmission of products of gas as well as the relations of catalyst structures and these processes.

At present, the study on catalyst reduction mechanism is focused on diversification of process. The role of solid-phase process i.e., the reaction and diffusion in the

solids should be emphasized. Unfortunately, this role has not been given sufficient attention. The following discussion will reveal that the solid-phase reaction processes are almost controlled under all conditions (start from the reduction degree of 50%–60%).

The proposal about the reduction of single particle catalysts by gas reductant is mature, but the theory and experimental work to clarify the of reduction process of catalyst bed by gas reductant are few. The following section will clarify the reduction of the single-particle catalysts by gas.

5.5.2 *Reduction of single particle catalyst*

The character of reduction process for single-particle catalyst is in its various stages which have certain orders. The reductant gas flows from the interspaces between the catalyst particles and large pores in the particles, and forms a border gas flow at around the particles and the surface of macro-pore.

The mass transfer between the gas and oxide and the transfer of reactants (reducing agent and product) have to pass this boundary layer. Then, in order to contact with particle surface for the gas reductant, the gas has to diffuse through micropores in particle, and through layer of solid products formed by reduction to reach internal part of particles.

The gas product derived from reduction should be expelled from the reaction region along the same path. Here, the reducing agent contacts with iron oxide, namely, it is adsorbed on the surface of the solid and starts surface reactions. The reduction reaction includes seizure of oxygen from oxides, the formation and growth of crystal nuclei of the product. The continuous growth of product layer is maintained by solid state reaction and the diffusion in solid state.

It will be seen from this that the reduction of oxide is the sum of all the processes, in which each process is its equilibrium and has own characteristics, where the deviation from these equilibriums in various stages is the driving force. For example, the driving force for diffusion is the difference of reactant concentration (or pressure) at the beginning and end of the process.

Generally, the reduction of single particle catalyst is composed of the following stages:

① Gas reductant transports to catalyst particle (i.e., external-diffusion).
② Reductant diffuses through the pore to surface.
③ Reductant is adsorbed on oxide surface.
④ Diffusion of gas and ions in solid.
⑤ Chemical reaction captures oxygen from oxide.
⑥ Formation of metal crystallite nucleus.
⑦ Desorption of the products of gas.
⑧ Expel of the reduced products from pore of particle.

Any of the above stages can limit the reduction rate, in which, stages ①, ②, ③, ⑦ and ⑧ are basically the same with the process of gas–solid catalytic reaction as mentioned at Sec. 2.5 in Chapter 2. It is different that the reactants are only gases in gas–solid catalytic reaction but that they are gases and solids in gas–solid noncatalytic reaction. So for the latter case, diffusion, adsorption and chemical reaction

not only involves gases but also solids. Here, stages ④, ⑤ and ⑥ in gas–solid non-catalytic reaction are discussed briefly[24]:

(1) Various processes in solid state. The reduction process of solid catalysts is different from the other reaction processes of complex phases, and the character is the formation of reaction product layer at the beginning stage of the process. The continuation of the process is related to the characteristics of reaction product layer at some extent. When the formation of porous product layer is achieved, reducing agent gas can spread to the internal of particles. For the formation of dense layer of product, reduction process cannot occur without solid state chemical reaction and diffusion.

Fe–FeO, FeO–Fe_3O_4 is in a state of direct contact with each other during the reduction of magnetite while the outer layer of wüstite interacts with the reductant gas. For example,

$$FeO + H_2 = Fe + H_2O.$$

In order to continue the reaction, the diffusion must be carried out in reduction products, and the diffusion is only carried out at marginal layers (outer layer) of the metal products or low-valence oxide can influence the overall reduction rates. The diffusion in the inner layer does not have a direct impact on the reduction rate. The driving force of diffusion is the concentration gradient of the iron among each border of the different phases. The iron activity can be established on both sides of oxides. Therefore, the reduction rate is related with internal layer thickness of oxide. The opposite side is the thickness of the outer layer of products, which increases with the degree of reduction.

Diffusion of crystal compounds mainly depends on the movement of defect in lattice, e.g., relying on the migration of defects between the crunodes or electrons. Therefore, there are similar defects in the lattice of active component.

In wüstite, most of defects are iron ions, which make the diffusion of iron in oxide lattice possible. Diffusion flow of iron can be expressed by Eq. (5.77)[25]

$$J_{\mathrm{Fe}} = D_V \frac{3}{V_{\mathrm{FeO}}} 4y, \tag{5.77}$$

where D_V is the diffusion coefficient of the defect of iron ion, V_{FeO} is the molar volume of FeO, $4y$ is the defect concentration difference at diffusion way.

The relationship between the self-diffusion coefficient D_{def} of iron and the diffusion coefficient D_V of defect in wüstite is as follows:

$$yD_V = (1 - y)D_{\mathrm{def}} \tag{5.78}$$

The defect diffusion coefficient has basically nothing to do with the concentration of defects. D_V can be obtained *via* the following methods:

$$D_V = D_V^0 \exp \frac{-127800}{RT},\ D_V^0 = 4.5 \times 10^{-2} cm^2/s. \tag{5.79}$$

Let ξ = thickness of layers, thus

$$J = \frac{1}{\xi V_{\mathrm{FeO}}}(1 + |z|)(D_{\mathrm{def}}^* + D_0^*)(1 - c/c'), \tag{5.80}$$

where J is the substance flow in wüstite, $/z/$ is the absolute value of defect charge, D_0^* is the self diffusion coefficient of oxygen, c, c' is the concentration of defects at the two phase boundary, and $c' > c$.

If $z = 2$, $c' > c$, $D^*_{\text{def}} > D^*_0$, then

$$J \approx \frac{3}{\xi V_{\text{FeO}}} D^*_{\text{def}} \tag{5.81}$$

If the growth rate of the thickness of the product layer is proportional to the diffusion rate passing the layer and inversely proportional to thickness of the layer, then:

$$\frac{d\xi}{d\tau} = kD\frac{\Delta c}{\xi}, \tag{5.82}$$

where Δc is the concentration difference of the diffusing component, k is the constant.

By integration Eq. (5.82) in the range of 0–τ, obtains

$$\xi = (2kD\Delta c\tau)^{1/2} \tag{5.83}$$

According to Fick's law,
$$J = F\left(\frac{D\Delta c}{2k\tau}\right)^{1/2}, \tag{5.84}$$

where F is the area of diffusion.

When the differences of concentration for each diffusion components is unchanged, at the boundary of layer the increase of thickness of the upper layer (i.e., reduction degrees) is proportional to $\tau^{1/2}$, and the decrease of diffusion rate through the layer (i.e., called reduction rate) is also proportional to $\tau^{1/2}$.

During the actual reduction process, the concentration gradient and range of diffusion keeps changing, and the above relationships change together as well.

There is no consensus about what kind of ions will diffuse. Most experts tend to think that the diffusion of iron ions and oxygen is relatively inactive in the magnetite and wüstite.[25]

The unreduced reactants undergo the solid state reaction in addition to diffusion.

$$Fe_3O_4 + Fe = 4FeO \text{ and } 4Fe_2O_3 + Fe = 3Fe_3O_4$$

Reduction process cannot happen without solid state reaction. Experimental results[2] indicate that the volume of solid oxide that can be penetrated is approximately 10% of the total mass during the whole reduction process. The heat-sintering phenomenon of metal iron was not observed. Under any reduction conditions, the controlling process should be various in solid-phase reaction at the second stage. A great deal of practical information accumulated in the past can serve as proof to support this view. Appearance of the non-stoichiometric magnetite at low temperatures and the disappearance of magnetite during reduction of hematite at high temperatures are additional proofs for the solid process of the product which is the controlling step in the reduction process.

The effect of the non-stoichiometric of pure wüstite (piece with about same density) on reduction is given in Fig. 5.13.[26] It shows that the degree of reduction (and reducing rate) with the defect ratio i.e., the diffusion in solid, has a proportional correlation. These curves have a good parabolic shape, which further confirms the solid-phase process is the controlling step.

(2) The reaction on the boundary of phases. The reducing agent and iron oxide must directly contact with each other during the reduction process, so the highest reduction rate is limited by the number of gas molecules colliding with the

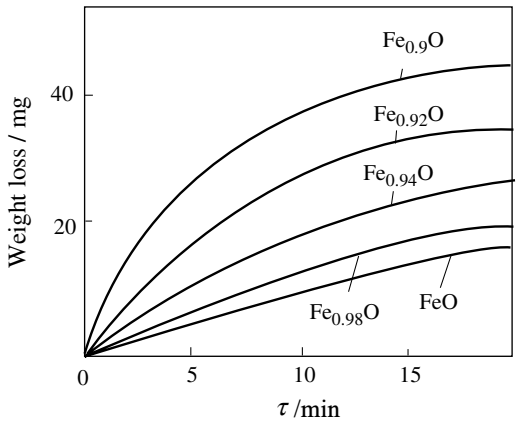


Fig. 5.13 Influence of non-stoichiometry to reduction degree

solid surface. For example, the collision number of hydrogen is $Zi = 6.4 \times 10^{23}$ times/(cm^2·s) at 500°C and 98 kPa. This collision number is about four orders of magnitude higher than the actually measured reduction rate. The molecule adsorbed or collided with iron oxides can initiate chemical reactions.

If the reduction process is controlled by chemical reaction, the reaction area goes through the deep particle linearly.

If the original radius of oxide sphere is r_0, and the original radius of the unreduced part is r_i, then

$$-\frac{dr_i}{d\tau} = \frac{k}{d_0}, \tag{5.85}$$

where, d_0 is the original oxygen content in particle and k is the constant
By integral:

$$r_i = r_0 - \frac{k}{d_0}\tau. \tag{5.86}$$

Degree of reduction $x_B = 1 - r_i^3/r_0^3$, may come to the following equation,

$$d_0 r_0[1 - (1 - x_B)^{1/3}] = k\tau. \tag{5.87}$$

Just like solid state reaction, if the reaction at the interface is the controlling step, then the particle size is located at the denominator of the rate constant with first power equation. Therefore, value of $[1 - (1 - R)^{1/3}]$ which is controlled by chemical reaction increases linearly with time.

In the case of a very dense and non-pore catalyst, the regions of the particle between being reduced and without being reduced have a clear reaction boundary (Fig. 5.14). However, when particles have high porosity, gas reductant can diffuse into the deep part of the particle freely, and then the reduction process is controlled by chemical reaction. This time the particle can be reduced fully, and the application condition of Eq. (5.87) of r is the radius of catalyst particle, and reduction speed is not related to the particle radius.

(3) Crystal nucleus formation. When oxygen is captured from the oxide in the surface of catalyst; the Me–O ratio will have regional changes. The metal formed by reduction is dissociative at the initial stage, and separated out in single crystal

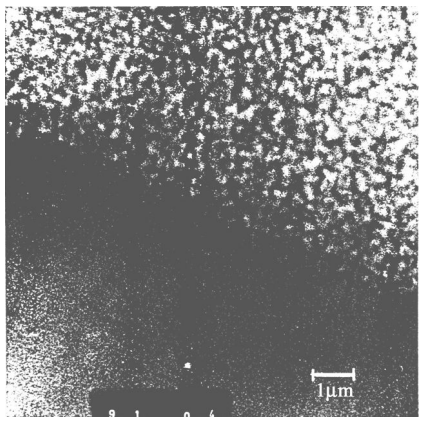


Fig. 5.14 Boundary between reduced and unreduced SEM image[27]

nucleus. The number and distribution of crystal nuclei is related with the surface structure of oxides. For the growth of crystal nuclei, the metal must be delivered to the crystal nuclei from the location of capturing oxygen. Transmission of the metal to the crystal nuclei depends on the diffusion of metal ions and electrons in the lattice and along the surface of oxide. The speed of capturing oxygen and diffusion of metal determines the necessary supersaturating of metal for formation of the next batch of crystal nuclei in the region between initially formed crystal nuclei, as well as whether or not a corresponding increase of the crystal nuclei density is followed. The density and shape of crystal nuclei as well as the development type of nuclei t restrict the crystal nuclei converting to the dense layer of a new phase, and this new phase separates the basic oxide from the gas or restricts the crystal nuclei to convert into a spongy. Gas transit through the porous of the spongy infiltrates the original material directly. The porous metal is often observed when reduced to metal.

Iron oxide supersaturated by iron is a prerequisite for the formation of metal phase and it will affect the reduction kinetics, because in the composition of FeO oxides, the activity of the iron and oxygen can be of the following relationship with each other:

$$\alpha_{\mathrm{Fe}}^{m}\alpha_{O}^{n} = \text{Constant} \tag{5.88}$$

Therefore, enhancing the activity of metal will reduce the activity of oxygen in oxide phase, which will take effect on the reaction rate at borders of the phase.

Many researchers verified that the strong effect of water vapor in gas phases cannot be ruled out during the reduction of magnetite at low temperatures, which can also be interpreted as the impact of the oxygen activity on nucleation and growth of metal. It has been identified that the critical value of α-Fe activity is not more than 1.015. In this case, if the activity of oxygen in gas phase is not near equilibrium, the supersaturation of the metal over phase boundary does not affect the reaction kinetics. It is believed that the critical supersaturation which is necessary for the formation of nuclei should be decreased when temperature increases. Therefore, the effect of nucleation on reduction rate is also reduced with increasing temperature.

(4) The reduction process and controlling steps. The steps that control the process include three stages,

① Gas diffusion through pores.
② Chemical reaction on phase boundary.
③ Processes in solid phase.

As mentioned, during reduction reaction at the second stage of the process, all solid state reaction processes are controlling steps. Determination of the controlling step for the first stage of reduction is a complex subject.

The degree of involvement of inner surface is related with the ratio of the diffusion rate of the gas passing through the pore in particles to the reaction rate on the surface of pore. If the diffusion rate is higher than the reaction rate of reductant with the solid oxide, then H_2 concentration in pore is the same as that on surface of particles, and the entire inner surface completely participates in the process. This process is called as the kinetically controlled process. When the gas diffusion rate in pore is the opposite proportional with the chemical reaction rates, the amount of reducing agent provided by the diffusion to inner surface is less than that is able to take advantage on the surface of pore, in which case, H_2 concentration drops to equilibrium value, and most of surface area is not involved in reduction. Such a system is called as the internal diffusion system.

Thiele[28] proved that the utilization (φ) of the inner surface is related with the parameter μ for the first order reaction. The equation of the surface reactions in the porous catalysts was proposed for the process with unchanged volume of materials. The equation was applied to gasification process of coal and the reduction of porous catalysts. Here, the reduction product layer appearing on the surface should be considered. It must also consider the effect of a variety of solid state processes on controlling all the processes. However, Thiele number does not take the impact into account for solid state process.

$$\mu = \sqrt{\frac{2kT}{273Dr}}, \tag{5.89}$$

where k is the rate constant of surface reaction, D is the gas diffusion coeffient, r is the pores radius, T is the temperature, (K).

Thus the utilization (φ) of the inner surface for the spherical catalysts with radius R:

$$\varphi = \frac{3}{\mu R}\left[c\mathrm{th}(\mu R) - \frac{1}{\mu R}\right] \tag{5.90}$$

And flake catalysts with thickness of 2L

$$\varphi = \frac{\mathrm{th}(\mu L)}{\mu L} \tag{5.91}$$

The utilization of inner surface φ is essentially the ratio of actual rate to the maximum possible reaction rate value of gas in the pore. The utilization ratio shows that the utilization of the inner surface is several times lower than the outer surface of particles.

Parameter φ is calculated according to pore distribution only along the direction of radius of sphere particle. Because the ratio of the cross-section area of pore and the outer surface area of particles is a constant for the same catalyst, the assumption is

that cross-section area of pore is proportional to square radius of sphere. This shows that the pores have a cone shape, and its conical top is located at sphere center; or the number of pores is proportional to the surface of sphere. This assumption has no foundation to actual catalyst. Therefore, the actual error is not known yet when Thiele equation is used.

The calculation results show that, when the value of μR reduces, φ approaches to one. If $\mu R < 0.2$, $\varphi > 0.993$. When the value of μR rises, φ is close to $16/(3\pi\mu R)$.

If $\varphi = 1$ ($\mu R < 0.2$), the discussed system is a dynamically controlled reduction. In this system, the process rate is proportional to the inner surface area, and has nothing to do with pore size, diffusion coefficient and the particle size of catalyst. When $\mu R > 15$ then this is an inner diffusion controlled process. In this case, the overall rate of process is related with particle size of catalyst, pore radius and the gas diffusion coefficient. When $0.2 < \mu R < 15$, it is a transitional area.

The main disadvantage of these indicators is that the pores of catalyst particle have different sizes, but the data used in Eq. (5.89) is the average pore size. As a result, the utilization of the pores in the same particles may be different, and the reduction systems are various for the catalysts with complex pores. With introduction of parameter S:

$$S = \sqrt{\frac{k\alpha}{D\beta}}R, \tag{5.92}$$

where k is the chemical reaction rate constant, D is the diffusion coefficient and gas coefficient passed the pores, α is the specific surface area of pore, β is the specific volume of pore.

When S value ($S < 0.1$) is small, the process is a kinetically controlled system, that is, reduction rate is controlled by chemical reaction rate. When S value is large ($S > 40$), the process is a diffusion controlled system. The intermediate value of S corresponds to a transition region. Reduction at low temperatures is the kinetically controlled system. Reduction at high temperatures is the diffusion controlled system.

Because S value is very rough, the total volume of pore cannot be used to characterize the resistance of gas diffusion because the diffusion mechanism is not the same in the pores with different diameters. In addition, and α and β in the Eq. (5.92) is linked through the following equation,

$$\alpha = \frac{2\beta}{r}, \tag{5.93}$$

where r is the average pore radius.

The average pore radius should be used for S parameter, rather than calculating the volume and surface area of pore respectively.

Of course, indicator of S also has the above mentioned shortcomings in the evaluation of μR quasi number. In addition, the two parameters cannot be used to express the system that the various processes in solid phase are controlled step. So generally speaking, these indicators can only be used to express the initial stage of the reduction process.

Kinetic region of the reduction process and the reduction rate (r) is related with reduction degree (x_B):

$$r = (1 - x_B)^{1/3}. \tag{5.94}$$

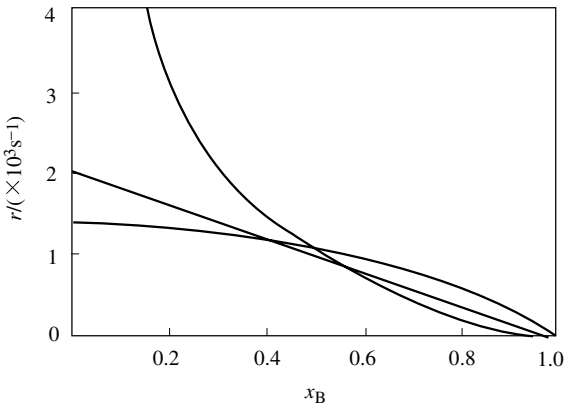


Fig. 5.15 Relationship between rate(r) and degree (x_B) of reduction

In the diffusion controlled region in the pore, the relationship of r and x_B is as the following equation:

$$r = \frac{(1 - x_B)^{1/3}}{1 - (1 - x_B)^{1/3}}. \tag{5.95}$$

In the actual process, the reduction transfers from one system to another with the increasing of the reduction degree, and the change of the total rate corresponds to a combination of these equations, and it can be simplified as a first order relationship

$$r = 1 - x_B. \tag{5.96}$$

These relations are shown in Fig. 5.15.

5.5.3 *The relation between activity and physical properties with the reduction degree*

(1) Relationship of reduction process and catalytic activity. Prior to reduction, fused iron catalyst is a dense solid and without catalytic activity. The activity of the fused iron catalyst is not only related with the chemical components and preparation method, but also dependent upon the reduction process because all physical properties such as the surface area, porous structure, pore size and distribution, specific volume of pore, especially, size and formation of α-Fe crystallite etc. are produced during the reduction process. Different reduction processes produce different physical properties, and the surface area and porous structure are also different. The high performance catalysts can only be obtained when the reduction process are carefully controlled. Therefore, the reduction of the catalysts is the last step of the catalysts preparation, and also a key step.

(2) Reduction degree with the physical properties of catalysts. The particle volume does not change during reduction, while the pore structure of the iron catalyst is created *via* removal of oxygen. According to the shrinking core model (SCM) with particle size unchanged, pore volume and surface area increase linearly with the degree of reduction, but the surface area increases slower than the increase in pore volume as shown in Figs. 5.16 and 5.17.[20]

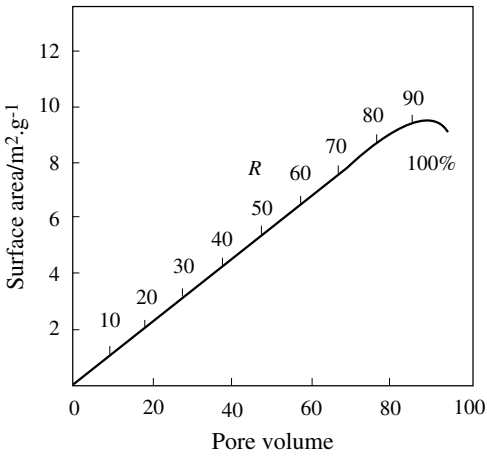


Fig. 5.16 Changes of surface area and pore volume in reduction process

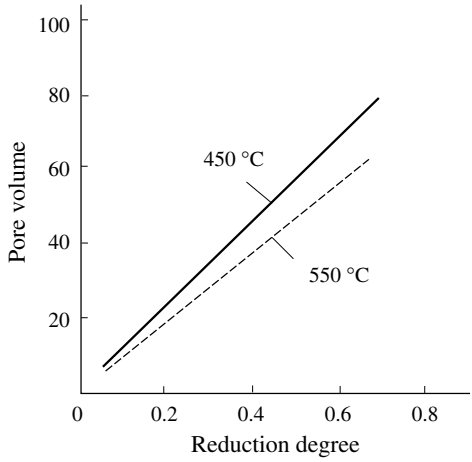


Fig. 5.17 Changes of pore volume along with reduction degree at reduction process

Assuming that the initial and final densities of the catalysts are known, the calculation of the pore volume is possible at any degree of reduction. If one gram of unreduced catalyst is made up of Fe_3O_4 or $Fe_{1-x}O$ and inert substance, the oxides are transformed into metallic iron during reduction. So pore volume is:

$$V = V_0 - V_x,$$

where V_0 is the initial volume per gram of catalyst, V_x is the real volume after reduced f of fraction per gram.

If the volume contribution of each component can be added, then

$$V_x = \sum_i V_i = \sum_i \frac{m_i}{\rho_i},$$

where V_i, m_i, ρ_i are the volume, mass and absolute density of the component i in the unreduced catalyst respectively. If the volume of the inert part which cannot

be reduced is V_b, the initial and final volumes are V_0 and V_F, and then the pore volume of fused iron catalyst can be estimated.

$$V_x = (V_F - V_b)f + (V_0 - V_b)(1 - f) + V_b = V_0 + (V_F - V_b)f \tag{5.97}$$

Because $V = V_0 - V_x$, inputting equation (5-97), then

$$V = (V_0 - V_F)f = (V_0 - V_F)[1 - (1 - x_B)^{1/3}] \tag{5.98}$$

V_0 and V_F can be calculated from the densities of unreduced and completely reduced catalysts.

Anderson *et al.* studied the reduction of Fe_3O_4–K_2O–MgO catalysts at 450°C.[26] He gave the curve of the changes of the surface area with the degree of reduction, which shows that when the degree of reduction is less than 90%, the surface area of catalyst increases linearly with the degree of reduction; at levels more than 90%, the slope of the curve decreases; when it is close to 100%, the slope is negative. CO chemisorption increases with degree of reduction, and its slope is relatively small, which is due to the degree of sintering of porous iron increases (see Fig. 5.18).

According to the model based on rigid cylindrical hole, degree of reduction changes from 20% to 95%, while average pore diameter d_{av} changes from 33 nm to 34.8 nm, but for 100% reduction, d_{av}increases to 37.1 nm. At low reduction degrees, the surface area and pore volume are relatively small, and d_{av} can be regarded as the true value of the maximum value.

Then d_{av} can be calculated by the following equation.

$$d_{av} = \frac{4V}{S}, \tag{5.99}$$

where V and S are the volume and surface area of pore, respectively.

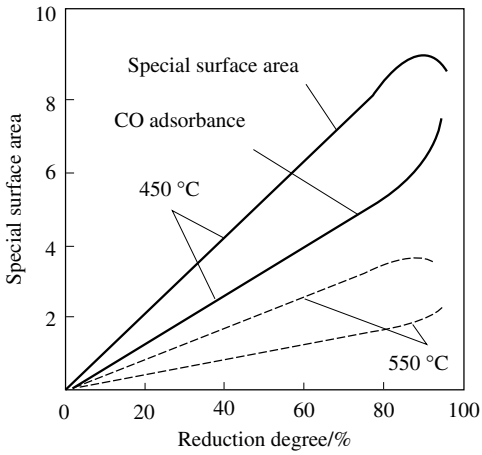


Fig. 5.18 Changes of special surface area along with reduction degree during reduction

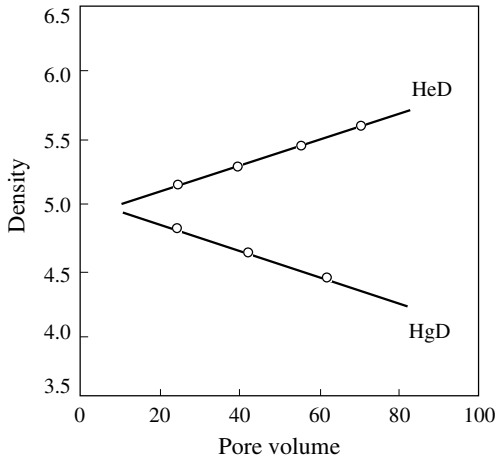


Fig. 5.19 Change of density with pore volume during reduction

HeD - density of helium displace; HgD - density of mercury displace

When the reduction temperature is increased from 450°C to 650°C, the pore volume and mercury displacement volume are constant, but the surface area decreases from $10.1\,m^2{\cdot}g^{-1}$ to $1.6\,m^2{\cdot}g^{-1}$, and the average pore diameter increases from 36.6 nm to 242 nm. The pore volume is obtained from the difference of mercury displacement volume and He displacement volume (Fig. 5.19).

5.6 Factors of Influence on Reduction Rate

Factors that influence reduction rate include gas composition, temperature, pressure, space velocity, particle size and composition of catalysts. Except composition of catalysts all other factors are adjustable in reduction process.[29–31]

5.6.1 *Influence of temperature*

Reduction of fused iron catalyst is a reversible and endothermic reaction. It can be known from thermodynamics that increasing temperature benefits for the generation of α-Fe and complete reduction of the catalyst. At the same time, the reduction time can be shortened. The reduction of fused iron catalyst is a gas–solid non-catalytic chemical reaction. As a single-phase reaction, the Arrhenius equation can be used to describe the relationship between reaction rate constant and temperature.

$$k = k_0 \exp\left(-\frac{E}{RT}\right), \tag{5.100}$$

where k is the rate constant, T is the temperature, k_0 is the pre-exponential factor, E is the activation energy.

The gas has to diffuse through the pore of product layer to the unreduced core part and generate reaction when reduction progresses to a certain extent. The

diffusion rate and temperature is related with the diffusion mechanism. The impact of temperature on diffusion rate has been discussed in Sec. 2.5 in Chapter 2.

Reduction temperature is the decisive condition for reduction quality and controlling the process. Very high temperature will cause α-Fe crystallite sintering, resulting in reducing of active sites on the catalyst surface. If the reduction temperature is too low, the catalyst cannot be reduced completely, the rate is decreased and the time is extended, which will affect the production time in factory and also increases the opportunities of repeated redox of catalyst. Therefore, there should be an optimum reduction temperature. Different types of catalysts have their own reduction temperatures, including the initial temperature of water production, a large number of water productions and the maximum reduction temperature.

5.6.2 *Influence of pressure*

As the number of gas molecules does not change before and after reduction, so the pressure does not affect the movement of reduction equilibrium. However, because the reduction process is not in equilibrium, the effect of pressure on the oxide reduction process is very complicated, which is related to reduction conditions and reductant. If hydrogen is used as a reductant, then, to a large extent, the effect of pressure on the reduction process is related with the relevance of which stage are the controlling steps.

A variety of processes for external diffusion (diffusion of gas at the border and the large pores) belong to the law of free diffusion. Therefore, the rate has nothing to do with pressure. However, increasing the total gas pressure will reduce the diffusion coefficient of water vapor, resulting in the increase of partial pressure of water vapor and residence time in micro-pore of catalyst, which may lead to the repeated redox of α-Fe crystallite, decreasing the activity of the catalyst. Therefore, the choice of pressure depends on the other synergetic conditions.[32]

The relationship between the chemical reaction rate and the partial pressure of reductant can be expressed by the following equation:

$$v = \frac{kp}{1 + kp}, \tag{5.101}$$

or by an approximate expression as

$$\nu \propto kp^n, \tag{5.102}$$

where k and n are constants, $n < 1$.

In the kinetic region, by increasing the total pressure and the corresponding hydrogen pressure, the rate of reduction reaction will be increased. Therefore, in order to avoid the sintering of α-Fe crystallite, the reduction should be carried out at a low temperature by increasing the total pressure or partial pressure of hydrogen so that maintaining reduction rate. However, the increase of pressure will also accelerate the formation of ammonia, thus consuming a large amount of hydrogen and hindering the reduction. Reduction rate increases with pressure before it tends to a certain maximum value.

Pressure changes have a strong impact on diffusion. It is because increasing the pressure will accelerate the gas diffusion in pores (pore size and molecular free path is comparable), so only in a catalyst with small pores the reduction can be accelerated.

The most pores of catalyst can be penetrated by the reducing agent. Increasing diffusion rate will increase the concentration of reducing agent and reduce the concentration of reduction products on catalyst surface. Therefore, when the pressure is increased, the reduction process should be able to speed up to some degree, which is equivalent to the impact degree of increasing concentration gradient in the layer of reduction products on the reduction rate.

For the catalyst with tiny pores — when the molecular free path length is shortened — as the pressure increases, more surface area will be affected by reducing agent and therefore results on the impact of the pressure should be relatively obvious.

No matter whether the system is kinetically or diffusion controlled, its role is gradually reduced as the pressure increases. For example, under certain pressures in the intrinsic diffusion region, further enhancing the pressure will have no effect on the reduction speed when the average molecular free path is smaller than the average size of the pore which have most small sizes.

5.6.3 *Influence of space velocity*

The reduction of fused iron catalyst commences from the external surface of particles, and then expands inward. The reduction rate can be increased obviously by increasing the space velocity of reducing gas. The higher gas space velocity, the more favorable the reduction is, i.e., the lower the concentration of water vapor in gas, the faster the diffusion rate, the easier for the water molecules in the pore of catalyst to escape. As a result, the poisoning effect of water vapor is decreased to minimum. In addition, it is also conducive for the reduction reaction to move to the right and to raise the rate of reduction. However, when the space velocity continues to increase, the extent of increasing reduction rate will be minor. When it reaches the "critical value," the space velocity of reductant gas on reduction rate has almost no impact. At the same time, in industrial production, increasing the space velocity is limited by the furnace heat supply and the temperature.

It was considered that only when the reduction progress was controlled by external diffusion, increasing the gas space velocity could strengthen the reduction. However, as described above, this is not consistent with the actual situation.

If the reduction rate can be expressed as (5.103)

$$v = wS_{\text{eff}}k(H_2 - \overline{H}_2) = wS_{\text{eff}}k(\overline{H_2O} - H_2O), \tag{5.103}$$

where v is the reduction rate, $\text{cm}^3\ \text{H}_2\text{O}\cdot\text{s}^{-1}$; w is the catalyst mass, g; k is the rate constant, $\text{cm}\cdot\text{s}^{-1}$; S_{eff} (or S) is the sum of outer surface and the permitted inner surface area for the reaction, $\text{cm}^2\cdot\text{g}^{-1}$; H_2, $H_2O, \overline{H_2}, \overline{H_2O}$ is the instant and the equilibrium content of hydrogen and water vapor in mixture gases.

With the progress of the reduction, the surface and surface properties of the catalyst changes (because changing the type of oxide), that is, the product value of S_{eff} and k changes. With the same reason, the equilibrium concentration of gas is also not fixed. Therefore Eq. (5.103) can be used to evaluate the impact of gas composition at any fixed reduction degree on the rate of reduction. According to Eq. (5.103), even when the consumption of the mixture gases is of any amount, increasing concentration of H_2O in gas mixture ($\text{H}_2 + \text{H}_2\text{O}$) results in that the reduction rate will reduce linearly.

The experimental results show that the first batch of water produced during reduction has a strong block effect. Because the adsorption capacity of H_2O is higher than that of H_2, H_2O occupies the activated site on the surface, reducing the rate of reduction.

In the actual reduction conditions at plant, there is no need to consider the adsorption characteristics of all gases so that the kinetic equation complexity can be limited to describe the increase of concentration of products (H_2O) on the block effect of reduction which is enough from thermodynamic constraints.

Rayment T. made a meaningful test[33] that the powder catalyst was reduced with sky-high space velocity at 450°C and atmospheric pressure, so that the concentration of water vapor was reduced to the level of difficult to measure by conventional methods. It is found from X-ray diffraction result that the catalyst after reduction mainly is not α-Fe, but amorphous iron with very high activity. Naturally, this method cannot be applied in industry.

Therefore, the space velocity of the gas is the key factor for controlling the concentration of reduction product H_2O and avoiding the repeated process of reduction of H_2 – oxidation of H_2O, to ensure the size of the iron crystallites. Generally, the higher the space velocity, the higher activity of the catalyst is. Therefore, the space velocity should be as high as possible during the reduction process, so that water vapor can be removed from the catalyst bed as efficiently as possible. The reduction starts from the external part of the particles and gradually moves to the inside part. For porous catalysts, the reduction process starts at the external surface and mouth of the pores and gradually develops to inside part of the pore. Hence, high space velocity is beneficial to take the water vapor produced in the internal surface of the pore and prevent the reversible poisoning from the reduced catalysts and pore mouth part.

5.6.4 *Influence of gas composition*

The best catalyst is derived by slow reduction by pure H_2, but in fact most of the reductions are done by using hydrogen–nitrogen mixture or syngas containing certain inert gas and product H_2O. However, high rates of reduction are maintained with syngas, which is beneficial for generating a considerable amount of ammonia on catalyst being reduced partially. Meanwhile, it produces reaction heat which allows the use of higher space velocity, so that it can reduce the concentration of water vapor, and prevent iron crystals from growing up. As a result, the hydrogen content is limited in a certain range during the reduction process for iron catalyst of synthesis ammonia.

The gas composition has an effect on the rate of reduction when the gas space velocity is fixed. Literature gives the following relationships. Increasing the content of inert gas in the mixture will significantly reduce the reduction rate, which is caused by lower concentration of reducing agent as well as the difficulty of diffusion for the reducing agent contacting to the catalyst surface.

Figure 5.20 gives the effect of the content of H_2 on the reduction rate for ZA-5 catalyst. It can be seen from Fig. 5.20 that an increase in hydrogen content results in the increase of reduction rate. Hydrogen content to reduction reaction of the average order is 1.5 for ZA-5 catalyst.

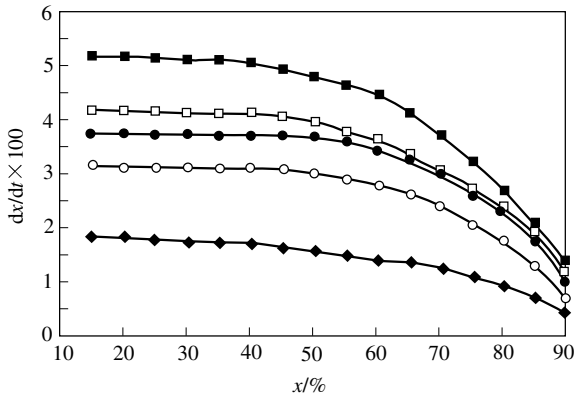


Fig. 5.20 Influence of H_2 content to the reduction rate of ZA-5 catalyst (pellet size: 0.054 mm–0.074 mm; weight: 10 mg; normal pressure, flow of H_2: 175 ml·min − 1; temperature: 500°C, content of H_2 from top to below, 100, 87.55, 83, 75, 50)

Changes in gas composition and other conditions have different impact on reduction rate of catalysts with different structures. When H_2 content is increased, the exchange intensity of the diffusion in pores is increased. When a molecule moves, every component in the mixed gas independently diffuses in the speed of inverse square root proportion to the molecular weight. Therefore, under the same conditions, diffusion of H_2 molecules in gas mixture (H_2 and H_2O) in the pores is faster than the diffusion of gaseous H_2O in the opposite direction. As the result, the absolute pressure in pore rises continuously until the partial pressure gradient of H_2 and H_2O reaches the value of ($\sqrt{M_{H_2O}/M_{H_2}} = 300\%$). The diffusion equations for the two gas flows (H_2 and H_2O) can be established at this time, while the diffusion gradient in the pores is determined by the slowest step i.e., the diffusion of product H_2O.

H_2, CO or synthesis gas is usually used for the reduction of iron catalyst for the Fischer–Tropsch synthesis. However, a substantial amount of research results show that whether at low temperatures or at high temperatures, H_2 as reducing agent is more suitable than the CO for the reduction of iron oxide.

5.6.5 *Influence of oxide precursor*

The reduction performance of catalyst is closely related with the composition of its precursor in hydrogen flow. As mentioned earlier, this is due to the different reduction mechanisms for catalysts with different precursors. All precursors of iron oxide such as Fe_3O_4, $Fe_{1-x}O$ and their mixture are possible for fused iron catalysts, while the sequence of the reduction rate as well as the reduction temperature is $Fe_{1-x}O > Fe_3O_4 >$ mixture. Apparently, the catalysts with non-stoichiometric $Fe_{1-x}O$ with wüstite structure as precursors have the fastest reduction rate and the lowest reduction temperature. As mentioned before, the defects of iron ions in lattice of $Fe_{1-x}O$ has serious impact on its reduction properties. It can be seen from Fig. 5.13 that the reduction process is faster and more complete when the amount of the defects is larger in wüstite.

Table 5.10 Reduction parameters of iron oxides

Oxides	Start temp./°C	Terminal temp./°C	Temp. of max. reduction rate/°C	Reduction rate/($\times 10^2$ mg· min^{-1})	Reduction degree/%
Fe_3O_4	348.0	619.0	526.0	6.20	95.51
$FeO{\cdot}Fe_3O_4$	356.5	636.9	456.2/577.3	5.96	93.00
$Fe_{1-x}O$	352.1	524.6	480.6	8.29	96.63

Note: Heating rate: 3°C· min^{-1}, H_2 flow rate: 175 ml· min^{-1}, instrument: Shimazi TGA-41.

The author's research results show that when the catalyst precursor is composed by two different phases, such as FeO and Fe_3O_4, two peaks appear on the DTG curve obtained from reduction by H_2, which correspond to the reduction of $Fe_{1-x}O$ and Fe_3O_4, respectively (Table 5.10). It indicates that the reduction process is followed by the reduction of phase by phase in turn, and belongs to the competitive mechanism. The easily reduced FeO is first reduced to α-Fe, and then the reduction of Fe_3O_4 starts. The result of phased reduction is that the reduction rate of the catalyst is decreased, while the reduction temperature is increased, and also the activity of catalyst after reduction is decreased.

The activity of ammonia synthesis catalyst is closely related to the performance of reduction. The easier the reduction, the higher is the catalytic activity. The reason for decrease of activity of catalysts in two-phase region is not only due to the non-uniform distribution of precursor oxides and promoters, but also as a result that the reduction is followed by phase in turn. In case the reduction is followed by phase in turn, α-Fe is generated by reduction of phase (FeO) in the first stage, which is easily oxidized by the water vapor produced at the second stage (Fe_3O_4). This repeated redox makes α-Fe crystallites grow up, resulting in decrease of the activity.

5.6.6 *Influence of promoters to reduction rate*

The reduction rate of iron catalyst is related with the type and content of promoters. Many researchers[34,35] studied the inhibitory effect of promoter content on reductions, indicating that structural promoters, such as Al_2O_3 etc. have strong inhibitory effect on the reduction of Fe_3O_4. MgO, TiO_2, SiO_2 etc. also inhibit the reduction rate. Electronic promoters such as K_2O etc. can help to speed up the reduction rate of the catalyst. In addition, addition of CuO, NiO promotes the reduction of iron oxide, but these oxides will reduce ammonia synthesis activity. Therefore, it is commonly accepted that the promoters which can reduce the reduction rate can increase the activity of ammonia synthesis, and it also can improve the thermal stability and anti-poisoning ability.

The solid solution formed with iron oxides impacts the reduction rate, for example, addition of 1%–10% CaO increases the reducibility, with the product of the reduction of CaO and α-Fe sponge. CaO and magnetite form $Ca_xFe_{3-x}O_4$, which affects both the thermodynamics and kinetics together, and $Ca_2Fe_2O_5$ has the lowest rate of reduction (Fig. 5.21).[36]

Addition of MgO in wüstite decreases the reduction rate. The impact of addition MgO to magnetite is complex. Low content of oxide additives decreases reduction

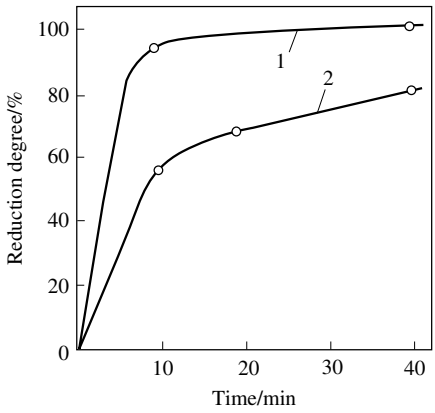


Fig. 5.21 Influence of CaO to reduction of magnetite $1 - Fe_3O_4; 2 - Ca_xFe_{3-x}O_4$ ($x = 0.05 - 0.25$)

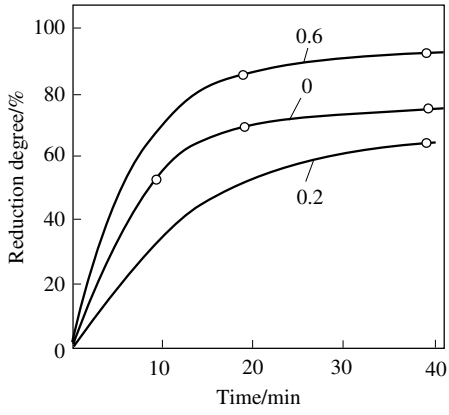


Fig. 5.22 Influence of MgO to reduction of $Mg_xFe_{3-x}O_4$ (The numbers on curve are the value of x)

rate, and more additives causes a slight increase of reduction rate. The mechanism involved is not clear up to now (Fig. 5.22).

5.7 Reduction in Industrial Equipments

Reduction process is a key step to obtain the active phase of fused iron catalyst. Reduction process directly relates to the application and the economic benefit of plant in the next few years or even longer than a decade, and that is why some plants work well while the other are not so ideal although with the same catalyst.

In industrial installations, although the reduction mechanism of catalyst in catalyst-bed is very similar with the single-particle catalyst as mentioned above, their reduction processes are quite different. The character of the reduction process for single particle is that the reduction is carried out in stages one by one, while the

reduction stages in catalyst bed is intersecting with each other during the whole process. At the same time, the theories and experiments of reduction in the catalyst bed in industrial equipments are lacking.

5.7.1 *Reduction rate of catalyst in industrial reactor*

For industrial installations, the goals and requirements for catalyst reduction are:1. to ensure that all the catalysts are thoroughly reduced, where "thoroughly" means entire catalyst in the reactor from the top to the bottom and each particle of catalyst from outside to inside are completely reduced; 2. to ensure that the catalytic activity of the reduced catalyst is not decreased. The former is for "quantity," and the latter is for the "quality," and both are indispensable.

In industrial reactor, the reduction rate of the catalyst is expressed and controlled by the generation speed of water or concentration of the water vapor. The relationship between the concentration of water vapor and the reduction rate are as follow.

$$w = W - \frac{16}{18} w_{H_2O} \tag{5.104}$$

$$-\frac{dw}{d\tau} = \frac{16}{18}\frac{dw_{H_2O}}{d\tau} \tag{5.105}$$

$$r_{H_2O} = \frac{\mathrm{dw_{H_2O}}}{\mathrm{d}\tau} = \mathrm{V_{in}}\theta = \mathrm{S_V V_K}\theta \tag{5.106}$$

Average concentration of water vapor:

$$\overline{\theta} = \frac{w_{H_2O}}{\tau V_{in}} = \frac{w_{H_2O}}{\tau S_v V_K}, \tag{5.107}$$

where W is the original mass of catalysts before reduction, kg; w is the mass of catalysts after reduction, kg; w_{H_2O} is the formed water, kg; r_{H_2O} is the reduction rate, kg - $H_2O{\cdot}h^{-1}$; τ is the reduction time, h; S_V is the space velocity, h^{-1}; V_K is the catalysts volume, m^3; V_{in} is the inlet gas flow, $m^3{\cdot}h^{-1}$; θ is the concentration of water vapor, $g{\cdot}m^{-3}$; $\overline{\theta}$ is the average concentration of water vapor in the effective reduction time, $g{\cdot}m^{-3}$.

It is seen from the Eq. (5.107) that the effective reducing time is not directly related to the size of reactor. The average water vapor concentration is inversely proportional to space velocity, reduction time and catalysts volume and proportional to water being formed.

Therefore, in industrial installations, the reduction rate and quality of catalysts is ensured by the strict controlling of the concentration of water vapor. Generally, the vapor concentrations are limited in $\leq (0.7 - 1.0)\,\mathrm{g/m^3}$ for small and medium-scale ammonia plants, and $\leq 3.0\,\mathrm{g/m^3}$ for large-scale ammonia plants.

After determining the standard of water vapor concentration, the required reduction time of whole catalyst can be estimated by Eq. (5.107). However, it should be noted that τ, calculated according to Eq. (5.107), is the real effective reduction time. It is the actual water generation time, and does not include the time of warming and decreasing temperature for reactor or the abnormal break time.

The theoretic water yield of catalyst in (5.107), $\mathrm{w_{H_2O}}$, can be obtained from actual oxygen loss on the TG curves under reduction conditions, or calculated by

chemical analysis data of the catalyst. Supposing that the total iron content is T, and W is the total mass of catalyst, and $w_{\mathrm{H_2O}}$ is total water, $R = \mathrm{Fe}^{2+}/\mathrm{Fe}^{3+}$, then

$$w_{H_2O} = WT\left(\frac{M_{H_2O}}{M_{Fe}}\right)\left(\frac{1.5+R}{1+R}\right), \tag{5.108}$$

where M_{H_2O} is the molecular weight of $\mathrm{H_2O}$, M_{Fe} is the atomic weight of iron.

[Example]

(1) Conventional $\mathrm{Fe_3O_4}$ based catalyst: $W = 153.625\,\mathrm{t}$, $R = 0.55$, $T = 68.50\%$;
(2) Novel type $\mathrm{Fe_{1-x}O}$ based catalyst: $W = 153.625\,\mathrm{t}$, $R = 6.82$, $T = 71.85\%$.

Calculate the theoretical formation of water quantity of w_{H20}.

[Calculate]

(1) For $\mathrm{Fe_3O_4}$ based catalyst, by Eq. (5.108),

$$w_{H_2O} = 153625 \times 0.6850\left(\frac{18}{55.85}\right)\left(\frac{1.5+0.55}{1+0.55}\right) = 44863.$$

(2) For $\mathrm{Fe_{1-x}O}$ based catalyst, by Eq. (5.108),

$$w_{H_2O} = 153625 \times 0.7185\left(\frac{18}{55.85}\right)\left(\frac{1.5+6.82}{1+6.82}\right) = 37815.$$

The results indicate that W_{H_2O} of novel $\mathrm{Fe_{1-x}O}$ catalyst is 18.7% less than the conventional $\mathrm{Fe_3O_4}$ catalyst.

If the average water vapor concentration is limited $\leq 2\ \mathrm{g{\cdot}m^{-3}}$, the gas flow is $300 \times 10^3\mathrm{m^3{\cdot}h^{-1}}$ in the inlet of reactor, and then the least required reduction time:

For $\mathrm{Fe_3O_4}$ based catalysts,

$$\tau \geq \frac{w_{H_2O}}{\overline{\theta}V_{\mathrm{in}}} = \frac{44863 \times 10^3}{2 \times 30 \times 10^4} = 75(\mathrm{h}).$$

For $\mathrm{Fe_{1-x}O}$ based catalysts,

$$\tau \geq \frac{w_{H_2O}}{\overline{\theta}V_{\mathrm{in}}} = \frac{37815 \times 10^3}{2 \times 30 \times 10^4} = 63(\mathrm{h}).$$

The result shows that the effective reduction time τ of the $\mathrm{Fe_{1-x}O}$-based catalysts is about 19% shorter than that of the traditional $\mathrm{Fe_3O_4}$-based catalysts.

5.7.2 *Characteristic of reduction processes in catalyst bed*

5.7.2.1 *Characteristic of reduction processes by pure H_2 in catalyst bed*

When reduction is changed from a single pellet to catalyst bed, the process conditions change correspondingly. Although there are a variety of contact routes between the reducing agent and the catalyst bed, the most frequently used route is feeding the gas from the top or bottom part of the reactor. In this situation, according to the ratio of the flow rate of gas and the reduction rate, there may be three kinds of reduction systems.[37]

(1) When the gas flow rate is low, the reduction takes place in the region of unreduced bed at the inlet of gas, and the concentration of the reduction agent changes from initial value to the equilibrium concentration at certain temperatures.
(2) When the amount of reducing agent is excessive, the reduction process happens in the whole bed, and the composition of the outlet gas is close to the inlet.
(3) The third situation is that the amount of gas in the unreduced part of the reaction layer is more than that the sub-layer of the reaction layer. Therefore, the reduction will happen in a certain part of the bed. Usually, this part is called "reaction region." In this region, the concentration of reducing gas changes from initial value of the inlet to the equilibrium concentration in the outlet. The size of the reaction region is determined by the amount of the gas in inlet, and the ratio between the reduction rate and the surface area of the particles in unit cubage.

Study on effect of temperature on the reduction dynamics in catalyst bed shows that the influence of the temperature on the thermodynamic and kinetic parameters of the reduction process must be considered. When wüstite is reduced, the characteristic of equilibrium of H_2 is the change in reverse direction, and the rate constant increases. With temperature increasing, the reduction ability of H_2 increases, and total amount of oxygen captured from oxides will be determined by temperature.

Using a cylinder filled with the massive catalyst as model (Fig. 5.23) and feeding reducing gas from the top, we tried to describe the reduction dynamics of reaction layer. According to the concentration of reducing agent, the single-order reversible reduction reaction in first stage was carried out between the reducing agent and oxides. In each unit bed, the reduction carries through at a certain rate.

$$\frac{d\alpha}{d\tau} = k(N'_p - N') = k(N - N_p) = k\Delta N, \tag{5.109}$$

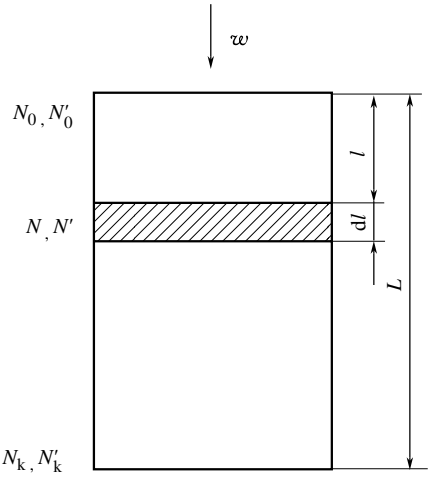


Fig. 5.23 Reduction schematic diagram in catalyst bed

N_0, N_k are the concentration of H_2; N'_0, N'_k are the concentration of H_2O at inlet and outlet, respectively

where $d\alpha$ is the amount of H_2O produced in unit volume in dL and dτ, k is the rate constant, N'_p, N' is the equilibrium concentration of H_2O and concentration of H_2O in gas flow, N_p, N is the equilibrium concentration of H_2 and concentration of H_2 in gas flow.

The $d\alpha$ value is related to the increase dN' of concentration in $d\tau$ time:

$$d\alpha = V_{\text{gas}} dN', \tag{5.110}$$

where V_{gas} is the gas volume in per unit bed.

As the volume does not change during the reaction, therefore, the time τ and the distance L has a proportional relationship with each other (more strictly, the temperature is the same along the height of the cylindrical reactor):

$$\frac{d\tau}{d\tau_1} = \frac{dl}{L} = dx, \tag{5.111}$$

where τ is the resident time in the reactor with height is L, x is the dimensionless coordinates in tenor moving gas (time or distance).

$$d\tau = \tau_1 dx, \frac{d\alpha}{d\tau} = \frac{V_{\text{gas}} dN'}{\tau_1 dx} \tag{5.112}$$

For $dV_{\text{gas}}/d\tau_l = w$ is the volume rate of gas flow, then (5.109) turns to

$$\frac{dN'}{dx} = \frac{k}{w}(N'_p - N') = \frac{k}{w}(N - N_p) = \frac{k}{w}\Delta N \tag{5.113}$$

The k of the first order reaction has the same dimension with w (time^{-1}), therefore, for this case

$$\frac{k}{w} = u. \tag{5.114}$$

where, u is a dimensionless quasi number of layered reductions in the bed; its value shows the type of process.

When u value is small (for example, the catalyst is hard to be reduced, or at low temperatures or at high gas rates), then the process is close to the so-called "dynamic" type, which means that the reduction is happens in the whole bed at the same time when there is very little reaction products remaining in gas.

When u value is large (for example, consumption of gas is very small), then the process is close to "flow control" type: The gas composition in the most reaction layer is close to equilibrium, in the limit (u $\to \infty$) the reduction reaction is restricted to section zone of bed, and it moves continuously from the top to bottom.

At the upper and lower parts of the beds, along the gas flow moving direction, the average temperature of the catalyst bed and gases decreases rapidly, while the middle part decreases slowly. Therefore, if we discuss the change of N' along the bed height direction when the temperature is changed or fixed, the thermal effect (exothermic or endothermic) of the reaction should also be considered.

(1) If the temperature and equilibrium concentration N'_p does not change along the height of the bed, then by integrating (5.113), we obtain:

$$N' = N_p[1 - \exp(-ux)]. \tag{5.115}$$

The actual concentration values (N') is asymptotically close to the equilibrium concentration (Fig. 5.24).

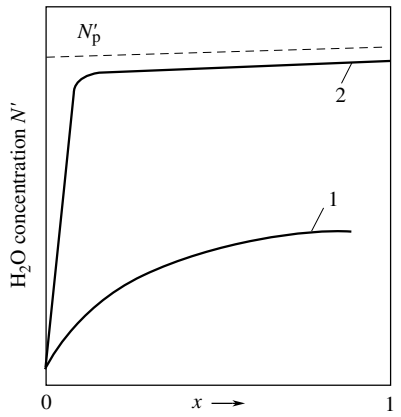


Fig. 5.24 Changes of H_2O concentration along with catalyst bed depth under isothermal condition

1-u value small; 2-u value large

The location and final value of N' curve is related to u. When u value is small, mixture gas of N' and N'_p could not be equilibrium at the height of whole bed and outlet position. Therefore, all catalysts along the height of whole bed can be reduced. When u is large, the gas composition would rapidly reach equilibrium. Thus, when reduction has happened in limited volume of bed, it will accelerate the accumulation of H_2O products.

(2) Non-isothermal condition of endothermic reaction (e.g., FeO catalyst reduced by H_2) Equilibrium concentration of H_2O (N'_p) decreases when temperature decreases. Suppose N'_p transforms according to linear principle.

$$N'_p = a - \varphi x. \tag{5.116}$$

From (5.116) and (5.113), we obtain:

$$N'_p = -\left(a + \frac{\varphi}{u}\right)\exp(-ux) - \varphi x + a + \frac{\varphi}{u}. \tag{5.117}$$

The curves 1 and 2 in Fig. 5.25 have the nature of extremum curves. The equation for the asymptote line is:

$$N_{\text{asy}} = -\varphi x + a + \frac{\varphi}{u} \tag{5.118}$$

Asymptote lines are parallel to the equilibrium lines and are located above the latter. Curves 1 and 2 are crossed with the equilibrium lines at the points of $x \approx a/(au+\varphi)$. Thus, wüstite can be reduced by hydrogen only in the catalyst bed where actual content of H_2O is lower than the equilibrium concentration; the height of this section is related to the process type and it decreases with u.

Equation (5.113) indicates the factors affecting the rate of the reaction in beds. The further the gas composition from the equilibrium, the faster the process goes. Therefore, when the gas is used for reducing the catalyst bed, the gas should include a minimum concentration of H_2O.

The lower the number u (the higher the gas speed w), the less H_2O is generated. However, too high gas speed will decrease the economic benefits of the process.

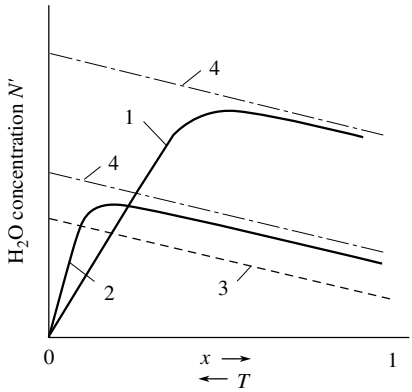


Fig. 5.25 Changes of H_2O concentration under nonisothermal condition and endothermic process

1-u value small; 2-u value large; 3-equilibrium line; 4-asymptote

5.7.2.2 *Characteristic of reduction processes by syngas in catalyst bed*

The above discussion was only for the reduction of the iron oxide catalyst in pure hydrogen. In industrial devices, usually the mixture gas of $H_2 + N_2$ is used as reducing reagent. Therefore, the actual reduction process is also accompanied by the formation of ammonia, and the process will become more complex.

The characteristic of this process is that several processes are parallel or cross-carried out i.e., the reduction process for the each catalyst particle proceeds from surface to core step-by-step and the reduction process of whole catalyst in reactor (bed) proceeds from the top (outside) down (internal) step by step, and also reaction process of H_2 with N_2 forms ammonia on reduced catalysts. Therefore, temperature (t) of catalyst bed, the reduction degree (R) of catalyst and water vapor concentration (φ) are changing. Trends of different types of reactors at different reduction stages are shown in Fig. 5.26.

Figure 5.26 (a) is the initial stage of the reduction. At this stage, the reduction starts just at the outside of particles at the inlet and very little ammonia is formed. The bed temperature is from high to low, generating water vapor flow through the unreduced catalysts and influences on the reduction quality is most insignificant. Therefore, the long stage of this process is favorable. However, once reduction reaction begins, ammonia synthesis reaction happens with generation of heat; and the bed temperature increases, as well as the reduction will soon enter the Fig. 5.26 (b) state. Unless the hotspot temperature (the highest temperature in the whole bed) is over the designed temperature (which is not allowed), the temperature of inlet part of the bed will stop rising [see (b), (c), (d) in Fig. 5.26]. Therefore, the catalyst at inlet parts is the most difficult to be reduced completely. To solve this problem, the fundamental approach is to avoid or inhibit the formation of ammonia synthesis. The ideal situation is to use pure hydrogen as reduction gas. Other options include such as preparation of prereduced catalyst as mentioned in Sec. 4.5 at Chapter 4. Practically, it commonly adopts conditions of as high as possible content of hydrogen

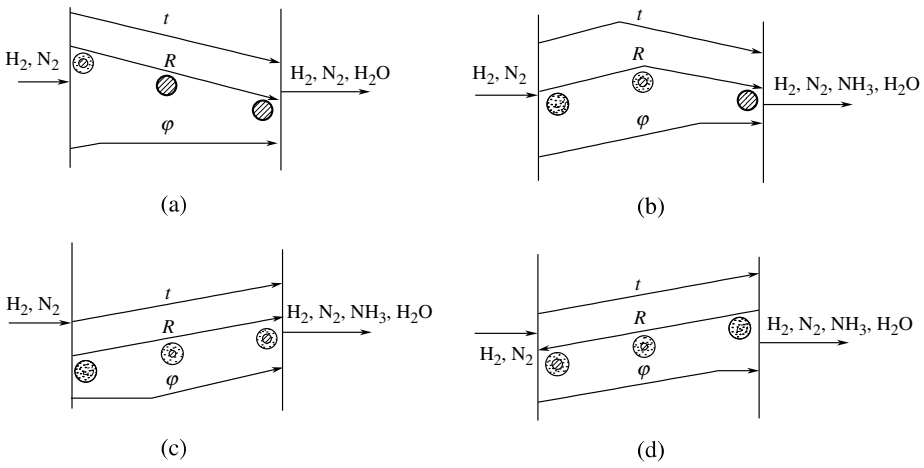


Fig. 5.26 Schematic diagram of catalyst reduction process

t-Reduction temperature; R-Reduction rate; $\varphi - H_2O$ concentration; (a): early stage reduction in adiabatic bed; (b): middle stage reduction in adiabatic bed or in continuously heat exchange bed; (c). final stage reduction in adiabatic bed; (d): Simultaneous ammonia synthesis and catalyst reduction process

in syngas, space velocity of syngas, or provides enough heat from furnace to raise the inlet temperature of the feeding gas.

In Fig. 5.26 (b) state, the hotspot temperature locates at the inside in bed (adiabatic bed), and gradually moves towards the outlet. The water vapor concentration increases gradually and flows through most of the unreduced catalyst. This stage is the main stage of the process and it continues until the end of the process [Fig. 5.26(c)]. Therefore, whether it is the axial or radial adiabatic bed of catalyst, it does not need to worry about the bottom or the outlet part catalyst whether or not is reduced completely i.e., generally they can totally be reduced because of high temperatures.

Figure 5.26 (b) shows another state of process of reduction in a catalyst bed with continuous heat exchange. Because there is a heat exchange process between hot gas flow in bed and cold gas flow in tube, the hotspot temperature reaches a certain location in the bed (usually in the middle or upper in bed), it will not further move down because of the balance of heat. Therefore, the temperature at the bottom of the bed does not increase so that it may not meet the needed temperature to reduce the catalyst completely. Therefore, for the catalyst bed of internal heat exchanger, the catalyst at the bottom and outlet section is difficult to be reduced completely, which are shortcomings of such reactor. For this, some reactor designers, such as the ZG-type reactor designed and produced by Machinery Factory at Zhejiang University of Industry, and add a section of adiabatic bed at the bottom of the bed with continuous heat exchange so that the temperature at the bottom can be increased to a certain extent solving the problem.

Figure 5.26 (d) shows a special situation of the catalyst bed, where the whole catalyst is not totally reduced in given time and conditions of reduction (rather than production) according to the schedule program. In this status, it should be sequentially reduced during production and according to conditions of production.

At this time, the temperature at outlet of the catalyst bed is higher than that of inlet so that the reduction of catalyst is forwarded from outlet to the inlet, or the reduction rate at outlet is higher than that of inlet. Therefore, the reduction of the catalyst at outlet would be completed earlier than that of inlet, namely, the pulsive direction of the reduction is opposite to the water vapor flow direction. As a result, the reduced catalyst at the outlet will be serious poisoned by the water vapor. So it is negative to reduce the catalyst during production in the production conditions. The reduction time cannot be shortened optionally and the production cannot prematurely begin before the catalysts is not reduced completely and every inch. It is not proper to consider that the catalyst could always be totally reduced during the long production run.

For the large particle of catalysts used in industry, it is worth noting for the following characteristics.

(1) For the retard of the diffusion in pore, the initial temperature of reduction and formation of water is low for the small particles and the stage of abundant water production will appear quickly. For example, the temperature of water appearance of catalyst size of 2.5 mm is 60°C lower than that of 12 mm. In addition, the temperature of abundant water stage is 50°C lower, and the temperature of totally reduction is 20°C–30°C lower, respectively. The activity of catalyst of large particles is low than that of small particles after reduction due to the former is reduced at higher water vapor concentration in pore and forms α-Fe on surface of particle, poisoned by the water vapor that was produced in pore and flow from interior to exterior. Figure 5.27 is the impact of the particle size on activity coefficient of catalysts after reduction.[38]

(2) The water vapor formed during reduction diffuses from the interior to exterior of particle, and then flows through α-Fe produced by reduction. This process is one-way and inevitable. It will repeatedly oxidize and reduce the α-Fe to cause the growth of crystallite of α-Fe, and the activity of the catalyst is decreased as well. Therefore, the water vapor concentration should be strictly controlled during the whole reduction process, generally lower than 0.7 g/m^3–1.0 g/m^3.

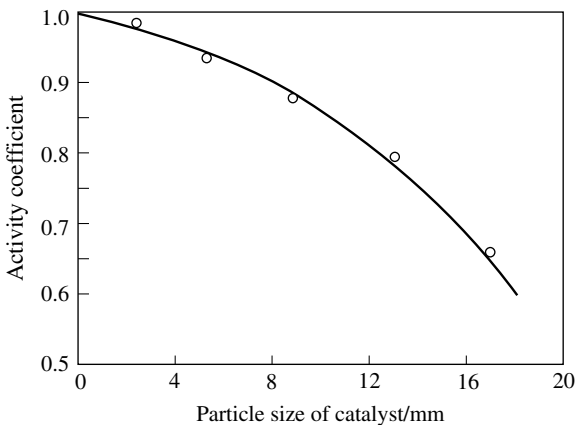


Fig. 5.27 Influence of particle size on activity coefficient of catalysts after reduction

Based on the above analysis, for insuring the reduction quality of ammonia synthesis catalyst in industrial equipments, the key factors are the control of water vapor concentration and the full reduction of the catalyst at bed entrance. Therefore, the following principles should be followed.

(1) To strictly control the concentration of water vapors. High space velocity should be used (10,000 h^{-1} above) and the reduction rate should be low. In order to reduce the vapor pressure, total pressure of system should be reduced to such as 4 MPa–6 MPa. If the reactor is multi-bed, the reduction should be carried out by stages in turn from first bed to last bed. This will reduce the water concentration in the abundant water period, and alleviate the poison effect of water vapor generated by up-bed on next bed catalyst. In order to control the water vapor concentration, reduction temperature ramp rate must be strictly controlled. Sometimes the temperature should be stable for decades of hours. At the same time, the following principles should strictly be abided by: The pressure and temperature should not be increased at the same time. After increasing the temperature or pressure each time, it should be kept for certain time and observe carefully the change of the temperature and the water vapor concentration. Only after the temperature is stable or water vapor concentration does not change, could the next round of pressure or temperature rising be operated. The rate of pressure change should not be too fast, and especially rate of pressure decrease should be less than 0.2 MPa/h. When the upper catalyst undergoes strong reaction of ammonia synthesis and releases a lot of heat, the circulation amount of syngas should be increased. When entering main reduction period of lower catalyst, in order to increase the space velocity, the pressure can be raised, but not more than 8 MPa. At the initial stage of reaction, it is necessary for large amounts of heat and for compensation heat loss during heat exchange. At this time, the load of the heater (or furnace) should be fully used to ensure the heat requirements.

(2) To ensure the fully reduction of the entrance part of the catalyst bed. To ensure the first bed, especially the upper of second bed to achieve the thorough reduction, at the initial stage of each bed, it is necessary to increase the content of H_2 in syngas to the fullest extent possible which is not lower than 78%–80% to inhibit ammonia synthesis reaction and reduce the reaction heat, to prevent the hotspot temperature from moving down prematurely. At the same time, the load of the heater (or furnace) should be fully used, which can increase the inlet gas temperature. Late in the reduction, as iron oxide content becomes less and less, it is more and more difficult to be reduced, especially for the part of solid solution, for example, $FeAl_2O_4$, $CaFe_2O_4$, $BaFe_2O_6$ all are difficult to be reduced. Unfortunately, the most difficult part for reduction commonly has the highest activity after reduction, but the reduction of them needs to keep certain times after achieving the final or highest temperature.

In order to evaluate reduction plan of the whole catalyst, the theoretical amounts of water should be calculated according to Eq. (5.108), and actual water production should reach about 95% of theoretical value during reduction.

The fresh catalyst after reduction has very high activity. A period of operation with light loading can avoid catalyst aging at early stage, and extend its life.

5.7.3 *The choice of reduction condition in industrial reactor*

In industrial devices, although the reduction rate should be considered because it relates to the time of non-production of enterprises, more importantly, it is the key factor to ensure the quality of catalyst, that is, to ensure that all the catalyst are reduced thoroughly and the activity of reduced catalyst is not lost, because it is not involved in the present several hours or tens hours of non-production time, but the economic interest and production time of the whole catalyst of reactor for the next several years or even more than 10 years.

For industrial devices, the most important part is not the rate, but the quality of reduction. The first consideration for the choice of reduction conditions is to ensure the quality, not the rate. The key factor for the reduction quality is temperature and water vapor concentration. Both of them will directly affect the α-Fe crystallite size, surface area size and activity level of the catalyst. The reduction rate is not indicated by the reduction time, but by the level of water vapor concentration, and this is the only criterion to control the rate of reduction.

Therefore, for the choice of reduction conditions of catalyst in industrial devices, it is necessary to consider thermodynamics and the dynamics as well as the technology and the equipments which can provide suitable conditions. It is necessary to consider reducing speed and time as well as to ensure the reduction quality and activity of the catalyst. And all these cannot ignore the requirements of performance of catalysts.

Table 5.11 is the characteristic parameters of the reduction for three types of catalysts most widely used in industry. It is seen from Table 5.11 that the reduction temperature of ZA-5 is 75°C and 108.5°C lower than ICI74-1 and A110-2, and the rate is 1.68 times and 3.73 times faster than ICI74-1 and A110-2, respectively. Compared with the conventional catalyst, ZA-5 catalyst has faster reduction speed, lower reduction temperature, and more thorough reduction, and it is a new type of catalyst which can be easily reduced.

Thus, the reduction of ZA-5 or A301 type $Fe_{1-x}O$-based catalysts which have extremely easy reduction properties are restricted by conditions of present process

Table 5.11 Reduction parameters of ZA-5, ICI74-1 and A110-2 catalysts[a]

Catalysts[b]	Initial temp./°C	Final temp. /°C	Temp. with the fastest rate/°C	Reduction degree R/%	Time with 85% reduction degree/min	Reduction rate/ relative	Weight of H_2O/ ($kg \cdot t^{-1}$)
ZA-5	342.0	501.2	471.3	97.89	41	1	246.3
ICI74-1	352.9	576.1	515.2	97.88	69	1.68	285.0
A110	348.0	619.7	524.8	95.48	153	3.73	289.7

[a]Instrument of Shimazhi TGA-40; size of 0.054 ~ 0.074 mm; mass of 10 mg; pressure of 101.3 kPa; H_2 flow rate of 175 $ml \cdot min^{-1}$; heating rate of 3 $\cdot min^{-1}$.

[b]ZA-5(A301) is $Fe_{1-x}O$-based catalyst; ICI74-1(A201, A202 etc) is cobalt-containing Fe_3O_4-based catalyst; A110 series catalyst (A110-1, A110-2 etc) is Fe_3O_4-based catalyst.

and equipment that are designed according to performance of conventional Fe_3O_4-based catalysts. For example, for the magnetite-based catalyst, when the concentration of water vapor is $2\,g/m^3$ at the most of space velocities in the present process and equipment, while for $Fe_{1-x}O$-based catalysts, the concentration of water vapor can reach $7.46\,g/m^3$ under the same conditions, which is not allowed absolutely. Therefore, in industrial devices, the reduction rate of $Fe_{1-x}O$-based catalysts cannot be speeded up as the magnetite-based catalyst, while inversely, and its rate should be restrained. The simplest and most effective way is to lower the reduction temperature. For the reduction of ZA-5 catalyst, it is necessary to shorten reduction time using its easy reduction property and to ensure the reasonable concentration of water vapor to thoroughly reduce and get high-activity catalyst. Considering the characters such as it is easy to be reduced at low temperatures and its induction period is short, and the effect of space velocity on the reduction rate and the activity is significant and not for pressure etc, the choice of reduction conditions of ZA-5 catalyst should consider the following principles.[39]

(1) Low-temperature reduction method. The temperature range is 400°C–430°C at main stage of reduction, and the final reduction temperature does not exceed 480°C, but holding for 8 h.
(2) Raising temperature alternately method. The method of raising temperature is as follows. Steps of raising temperature slowly–constant temperature– are undertaken alternately in order to prevent rising rate of temperature from exorbitant. It is because both the reduction rate is very fast to cause too high concentration of water vapor and the reaction rate for formation ammonia on the reduced catalyst is very fast to cause too fast temperature rising due to the heat of reaction.
(3) Space velocity as high as possible and low pressure. High space velocity will reduce vapor pressure and speed up the reduction rate, which is favorable to the reduction. However, the high space velocity will be restricted by the capacity of the heater and cause the increase of temperature to be difficult. The partial pressure of hydrogen and the reduction rate increases with increasing of total pressure, but the circulation volume of syngas will also increase to avoid high concentration of water vapor. However, with increasing of total pressure, the partial pressure of water vapor also increases. The diffusion of the water vapor adsorption in the microporous becomes difficult, which will increase the redox degree of catalyst.
(4) Strict control of concentration of water vapor may allow "former high-later low." At the initial stage of reaction, for the water vapor flowing through the unreduced catalysts, the effect of the water vapor on the redox of α-Fe is minor, and hence water vapor concentration may be high. But at the main and evening stage of reaction, most catalysts are reduced, the water vapor will flow through most reduced part of catalysts, and the effect of the water vapor on the redox of α-Fe is very great. Therefore, water vapor concentration must be controlled as low as possible.
(5) The use of reaction heat "earlier restraining -later using." The heat should be restrained at early stage to ensure complete reduction of top bed catalyst, while at the main and evening stage it should ensure thorough reduction of bottom catalyst. At initial stage of reduction, the heat is mainly supplied by the heater,

Table 5.12 Reduction conditions of A110 series catalysts

Operation steps	Time/h	Catalyst bed temperature/°C	Raising temperature rate /(°C·h^{-1})	Pressure /MPa	H_2 content /%	NH_3 refrigerated temp. /°C	H_2O concentration/ (g·m^{-3})
Raising Temp. stage	10	R.t ~ 330	30–40	3–4	≥70	0–5	≤0.7
Initial stage	8	330–400	5–10	3–4	≥75	−5–10	≤0.7
Main stage	65–70	400–440	2–3	4–7	≥80	–10 lower	≤0.7
		440–470	1–2	7 ~ 10		−10	≤0.7
Final stage	6–8	470–495	≤5 or stable	10–12	≥75	−5–10	≤0.05
Low-charge	24	470 ± 5	—				

while during the main reduction stage, the capacity of heater should be raised to full capacity as soon as possible to increase recycling syngas amount and reduce the concentration of water vapor.

(6) Content of hydrogen in syngas should be as high as possible because the catalyst reduced by pure hydrogen has the highest activity. At the same time it can suppress the reaction of ammonia synthesis, avoid hotspot temperature of bed moving down prematurely. However, too high hydrogen content will reduce the ammonia synthesis reaction and release less heat, and it cannot fulfill the deficiencies of the heat supplied by the heater.

(7) The temperature after ammonia cooler should ensure that the concentration of water vapor at inlet of reactor is $\leq 0.05\,\mathrm{g \cdot m^{-3}}$.

Table 5.12 is the reduction conditions of the A110 catalyst. Although its specific conditions may be different from ZA-5, the principle of selection is similar.

5.7.4 *The reduction program in the industrial converter*

The reduction program in an industrial converter, besides the above-mentioned common basic principles, should be considered synthetically according to the structure of reactor, catalyst type and their properties, processes and equipments of synthesis loop and their actual operation conditions. But the basic principle is consistent with the requirements of a catalyst. Therefore, the reduction of different catalysts has different methods and procedures. The scheme of reduction should be designed according to the scheme supplied by R & D researcher and manufacturer of the catalyst, and combined with the actual conditions of the plant.[40]

Let us take the reduction program of ZA-5 catalyst at Topsøe S-200-type converter with capacity of 1,000 t/d as example. The converter is a radial-flow reactor divided into two catalyst-bed and the indirect heat exchange between the beds. The structural parameters of the catalyst bed is as follows: The inner diameter of first bed is 1.170 m, outer diameter of 2.866 m, height of 3.400 m, filled with 18.8 m^3

Table 5.13 Schedule of reduction for ZA-5 in Topsøe S-200 radial-flow Converter

Stages	Highest temperature in bed/°C		Rate of temperature/ °C/h		P/ MPa	Vapor concen./ g/m^3(STP)		Times/h		Gas flow $\times 10^4$ m^3/h	H_2/ % at inlet
	Bed 1	Bed 2	Bed 1	Bed 2		Inlet	Outlet	Stage	Total		
1	RT ∼ 200	RT ∼ 100	RT ∼ 100	RT ∼ 50	4–5	<0.1		6	6	7–10	∼75
2	200–380	120–200	15–20	8–10	4–5	<0.1	<1.5	4	10	10–15	75–80
3	380–430	200–320	4–6	10–15	4–5	<0.1	<3.0	10	20	20–25	75–80
4	430–460	320–400	3–5	5–10	5–6	<0.1	<3.0	4	24	25–30	∼80
5	460	400–430	0–1	0–1	5–6	<0.1	<3.0	36	60	>35	∼80
6	460	430–460	0–1	0–1	6–7	<0.1	<3.0	24	84	>35	∼80
7	460	460–475	0–1	0–1	7–8	<0.1	<1.0	12	96	>35	65–70
Light load	470 ± 5	440 ± 5			9–10	<0.01	<0.01	>48			Normal

of prereduction ZA-5H catalyst with the size of 1.5 mm–3.0 mm ,and the actual loading is 47.68 t; the inner diameter of second bed is 0.650 m, outer diameter of 2.866 m, height of 7.400 m, loading volume of 46.5 m^3 ZA-5 catalyst with the size of 1.5 mm–3.0 mm, and the actual loading catalyst is 139.6 t. Therefore, the total catalyst loading volume is 65.3 m^3, and weight is 187.28 t. The flow direction of gas is from outside to inside. As the reduction temperatures of prereduced and the oxidation catalyst are different, in order to avoid the water from first bed causing the repeated redox of the catalyst in second bed, the reduction is carried out bed by bed, that is, the temperature of the second bed is controlled at temperatures lower than 300°C–320°C during the main reduction stage of catalyst in first bed. When the reduction of the catalyst in first bed completes, then the catalyst in second bed starts to be reduced.

According to the characteristic performances of ZA-5 catalyst, the reduction process should introduce the following conditions: High space velocity, high content of H_2, low temperature, low water vapor concentration, and the appropriate pressure. Recommended reducing program is shown in Table 5.13.

During operation, the concentration of water vapor always is a major indicator to control and regulate the conditions and process of reduction. Every technical staff and operator must be very clear, and know how to handle the relationship between concentration of water vapor and temperature, space velocity (Gas flow volume in inlet of reactor). Reduction processes follow the temperature-raising reduction curve set in advance. In addition, reduction process can be divided into heating stage, early reducing stage, main reducing stage, end stage, as well as the light-load stage. For detailed reference, please refer to the service manual provided by manufacturer of the catalyst.

References

1. Liu HZ, Hu ZN, Li XN. *Larger Nitrogenous Fertilizer*, **29**(2): 140–144, 2006.
2. Ю С Юсфин. Теория Металлизации Железорудного Сырья. Hou XL translated. Beijing: Metallurgical Industry Press, 1991, 27.
3. Froment GF, Bischoff KB. *Chemical Reactor Analysis and Design*. Zou RJ, *et al.* translated. Beijing: Chemical Industry Press, 1985, 261.

4. Chemistry of Department of Xiamen University, Nanjing Catalyst Co. Ltd. *Ammonia Synthesis Catalysts*. Beijing: Chemical Industry Press, 1980, 25.
5. Zhejiang University, East Chemical Engineering College, Chen GT. *Chemical Reaction Engineering*, Beijing: Chemical Industry Press, 1981, 196.
6. Levenspiel O. *The Chemical Reactor Omnibook*, Zhen YY, Zao YF translated. Beijing: Hydrocarbon Processing Press, 1988, 251.
7. Levenspiel O. *The Chemical Reactor Omnibook*, Zhen YY, Zao YF translated. Beijing: Hydrocarbon Processing Press, 1988, 301.
8. Liu HZ, Hu ZN, Li XN. *Petrochemisty*, **23**(1): 16–21, 1994.
9. Liu HZ, Li XN. *Ind. Eng. Chem. Res.* **36**: 335–341, 1997.
10. Ерофеев Б В. ДАН СССР СССР. **52**(6): 515518, 1946.
11. Christian JW. *The Theory of Transformations in Metals and Alloys*, New York: Pergamon Press, 1965.
12. Taplin JH. *J. Amer. Ceram. Soc.* **57**(3): 140, 1974.
13. Гегузин Я Е, Физика. спекания М. Наука. 360 с. с ил
14. Li YM. *Principle of Industrial Catalysis*. Tianjin: Tianjin University Press, 160, 1992.
15. Ю. С Юсфин Теория Металлизации Железорудного Сыръя. Hou XL translated. Beijing: Metallurgical Industry Press, 69–74, 1991.
16. Кингери У Д, Введение керамику Стройиздат. 1967.
17. Liu HZ, Li XN. *Chin. J. Chem. Ind. Eng.* **48**(3): 354–362, 1997.
18. Доменное, производство. Справочник т II М. Металлургия. 646, 1963. с. с ил
19. Li XN, Liu HZ, Xu YS. *Chin. J. Catal.* **20**(1): 76–80, 1999.
20. Department of Chemistry of Xiamen University, Nanjing Catalyst Company. *Ammonia Synthesis Catalysts*, Beijing: Chemical Industry Press, 1980.
21. Schütze J, Mahdi W. *Topics in Catalysis,* 1(3 & 4): 195, 1994.
22. Гольэштейн Н Л. Теория металлургичеких процессов, Свердловск, Изд УПИ, 1977, 108 с. с ил.
23. Куликов И С, Ростовцев С Т, Григорьев Э Н. Физикохимические основы прочессов восстановления окислов М. Наука. 1978.
24. Ю Юсфин. Теория Металлизации Железорудного Сыръя. Hou X L translated. Beijing: Metallurgical Industry Press, 74, 1991.
25. Богданби Л, Энгель Г Ю. Восстановление железных руд. М. Металлургия. 1971, 159 с. с. Ил.
26. Ю С Юсфин. Теория Металлизации Железорудного Сыръя. Hou X L translated. Beijing: Metallurgical Industry Press, 119, 1991.
27. Nielsen A, Topsøe H, Sosrensen O, Krag F, Candia R, Clausen BS, Mosrup S, Scand. *J. Metall.* **6**: 6, 1977.
28. Thiele E. *Ind. Eng. Chem.*, **31**(7): 1916–1921, 1939.
29. Lei L. *Middling Nitrogenous Fertilizer,* **12**: 19–22, 2004.
30. Chen ZY. *Design Technique for Smallness Nitrogenous Fertilizer,* **20**(1): 55–58, 1999.
31. Luo XS, He XH, Xu HS. *Design Technique for Smallness Nitrogenous Fertilizer*. **24**(4): 20–26, 2003.
32. Zheng XL, Yang JY, Yin SP. *Design for Nitrogenous Fertilizer*, **33**(6): 16–18, 1995.
33. Rayment T, Schlogl R, Thomas JM, *et al. Nature*. **315**(6017): 311, 1985.
34. Shen J (chief-editor), Zhu SY, Feng XT (vice-editor), Fertilizer Engineering Series Editorial Board. *Synthesis Ammonia*. Beijing: Chemical Industry Press, 2001.
35. Zuxi Y, Dehui X, *J. Chem. Ind. Eng.* (4): 192, 1965.
36. Мусиенко К А, Ростовцев С Т, Изв АН СССР, Металы, 1976, 6: 3 ∼ 10

37. Ю С Юсфин. Теория Металлизации Железорудного Сырья. Hou X L translated. Beijing: Metallurgical Industry Press, 139, 1991.
38. Yu ZH, Zhu BC, Shen DC, *et al. Process Analysis for Large Ammonia Plant*, Beijing: Chinese Petrochemical Industry Press, 1993.
39. Zhang SJ, Sun TJ. *Smallness Nitrogenous Fertilizer*, 9: 1–4, 1998.
40. Xu HS, Luo XJ, Cai JF. *Nitrogenous Fertilizer Industry*, **24**(1): 39–42, 1995.

Chapter 6

Ruthenium Based Ammonia Synthesis Catalysts

Introduction

The atomic number of Ruthenium (Ru) is 44 and relative atomic weight is 101.07. Ruthenium is a member of family VIII of the periodic table, which has seven stable isotopes. Ruthenium coexists with platinum in the earth's crust and usually it is derived from platinum ore. Ruthenium is white, hard, fragile and its Brinell hardness is 220. Its relative density is 12.41(20°C), with melting point of 2,310°C and boiling point of 3,900°C. Ruthenium cannot be contaminated at room temperature, but can be oxidized when exposed in air at 800°C. It cannot be dissolved in acid and *aqua regia*, but it can be eroded by some oxidants and molten alkaline. The physicochemical properties of ruthenium are as follows: Thermal conductivity ($1.17\,\mathrm{W}\cdot\mathrm{cm}^{-1}$ (25°C)), electrical resistivity ($7.1\,\mu\Omega\cdot\mathrm{cm}^{-1}$ (0°C)), electronegativity (2.2), magnetic moment (−0.68), spin (−5/2), electronic radius ($1.325\times10^{-10}\,\mathrm{m}$), covalent radius ($1.24\times10^{-9}\,\mathrm{m}$), crystal ionic radius ($+3(0.77\times10^{-9}\,\mathrm{m})$, $+4(0.63\times10^{-9}\,\mathrm{m})$, $+8(0.54\times10^{-9}\,\mathrm{m})$), melting enthalpy $\Delta\mathrm{H_m}=26.00\,\mathrm{kJ}\cdot\mathrm{mol}^{-1}$, vapor enthalpy $\Delta\mathrm{H_v}=592.04\,\mathrm{kJ}\cdot\mathrm{mol}^{-1}$.

Ruthenium is mainly used as the wear-resistant of platinum and palladium in jewel, electrical connector alloy, hydrogenation catalyst, medicine apparatus, anticorrosion alloy, electroplating films, nitrogen fixed reagent and solar cell. Ruthenium oxide is used as coating on the titanium anode plate in the production of nitrogen using electrolysis.

Ruthenium and iron are in the same family in the periodic table and the electronic configuration of iron is $3\mathrm{d}^6 4\mathrm{s}^2$, while Ru is $4\mathrm{d}^7 5\mathrm{s}^1$. The number of *d* electrons in hypo-outer shell of ruthenium is more than those of iron and the shielding effect of electron caused by inner electron is greater due to its long distance from nucleus. In other words, the bondage of the nucleus on *d*-electrons of ruthenium is weaker than that of iron.[1] Blyhoder supposed that in the interaction of carbon monoxide and metal, the five σ molecular orbitals of carbon monoxide provide part of electrons to unfilled *d*-orbital and the *d*-orbital back-donation electron to the $2\pi^*$ anti-bond orbital and results in the weakening of the C≡O bond. It has been confirmed by infrared spectrum (IR). Nitrogen and carbon monoxide molecules have equal electrons, so ruthenium should have the same influence on the N≡N bond.[2–4] The process of ammonia formed from hydrogen and nitrogen on ruthenium catalyst includes the adsorption of reactants on ruthenium surface; the formation of ammonia on surface and desorption of ammonia. The adsorption of nitrogen on ruthenium surface is considered as the rate determining step in the ammonia synthesis reaction.

At the same time, any substance which can promote the above three steps is a good promoter for ruthenium catalysts.

6.1 Chemical Compositions of Ruthenium Catalysts

The ruthenium based catalyst for ammonia synthesis commonly is composed of active components (Ru), promoters and supports, usually prepared by impregnation method.

6.1.1 *Ruthenium precursor compound*

The chemical valences of ruthenium range from +1 to +8 and the common valences are +2, +3 and +4. The main ruthenium compounds are as follows:

(1) **Ruthenium oxides.** Ruthenium tetroxide (RuO_4), the relative molecular weight is 165.07, in which the mass fraction of ruthenium and oxygen are 61.38% and 38.62%, respectively. Ruthenium tetroxide is a yellow crystal, which has high toxicity and sublimates at room temperature. The density, melting, boiling point of RuO_4 is 3.29, 25.4°C and 100°C, respectively. The solubility of RuO_4 in water is about 2% at 20°C and RuO_4 dissolves in CCl_4. RuO_4, as a strong oxidant, can severely react with an alcohol and filter paper. It might cause fire risk when it contacts with organic compounds. Therefore, it should be operated only under airtight conditions. Usually, RuO_4 is prepared by heating the mixture of acidic solution of ruthenium compounds with strong oxidant together, for instance, the mixture with mass ratio of Ru:K_2MnO_7:KOH = 1:2:20. RuO_4 mainly is used as the oxidant (the solvent is CCl_4).

Ruthenium dioxide (RuO_2) is a yellow square crystal. The relative molecular weight is 133.07 and the density is 6.97. It does not dissolve in water, but dissolves in molten alkali.

(2) **Ruthenium trichloride hydrates.** Ruthenium trichloride hydrate is also named as ruthenium trichloride with the molecular formula of $RuCl_3 \cdot xH_2O$ and the relative molecular weight of 207.43. Anhydrous ruthenium trichloride is a carmine solid and easily deliquescences in water and alcohol and its half-lethiferous dose (mouse, vein) is 360 mg/kg (anhydrous). $RuCl_3$ is often used as catalysts in oxidation reaction. $RuCl_3$ is usually prepared by dissolving ruthenium tetraoxide in hydrochloric acid, then distilling and evaporating until drying. The content of ruthenium is about 37.5%–40%, while chlorine is no less than 39% in chemical pure $RuCl_3 \cdot xH_2O$, and contains the impurities such as Na, Fe, Ca, Mg and water-insoluble matters.

(3) **Ruthenium salts**. Potassium ruthenate (K_2RuO_4) is a black crystal with green luster and the relative molecular weight is 243.26. K_2RuO_4 dissolves in water easily and forms an orange solution. It is unstable in both neutral and acid solution, which can form potassium perruthieniumate and ruthenium dioxide. It can be reduced by organic compounds. K_2RuO_4 is prepared by melting ruthenium, potassium hydroxide and potassium nitrate together.

(4) **Ruthenium carbonyl.** Ruthenium carbonyl ($Ru_3(CO)_{12}$) is bright bisque crystal with a relative molecular weight of 639.21. The wavelength of CO $\gamma_{(co)}$ in infrared spectra is 2062(vs), 2030(s) and 2004 cm^{-1}, respectively. Ruthenium carbonyl is prepared by the following methods: (i) 2g of $RuCl_3 \cdot 3H_2O$ is dissolved into 50 ml of methanol solution. The solution is put into 250 ml of a pressure pan. 2g of Zn particle is added and CO gas is introduced at 0.5 MPa–1.0 MPa and 650°C for 30 h, (ii) cool, deflate and filtrate the mixture, (iii) the solid is extracted with benzene, and the solution is concentrated, and then 1.5 g product of $Ru_3(CO)_{12}$ could be obtained with the yield of 75%.

$Ru_3(CO)_5$ is a colorless solution, with the relative molecular weight of 241.12, melting point of −22°C. It does not dissolve in water, but dissolves in benzene and 95% ethanol solution.

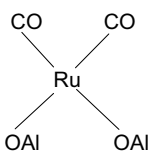
The above mentioned four kinds of ruthenium compounds can be divided into two groups: One is chlorine-containing and another is chlorine-free. Both of them can be used as the precursor of ruthenium in catalysts.

$RuCl_3 \cdot 3H_2O$ is the most common ruthenium compound containing chlorine with stable properties. It easily dissolves in water and is cheaper than other ruthenium compounds. In the past, the ruthenium catalysts were prepared by impregnation with $RuCl_3$ as the precursor and water as solvent. However, the chlorine of remnant after reduction can poison the ruthenium catalysts when a metal oxide is adopted as a support.[5] The poison effect of chlorine is not so obvious for ruthenium catalysts with activated carbon as support.[6,7]

$Ru_3(CO)_{12}$ is widely studied as precursor of chlorine-free ruthenium compound. A lot of studies have been conducted on $Ru_3(CO)_{12}$ due to its high activity caused by low valence states of Ru in $Ru_3(CO)_{12}$, high diserpsion on support and absence of chlorine which can poison the ruthenium catalyst.

Aika *et al.*[7] prepared a series of Ru/Al_2O_3 catalysts with the same content of Ruthenium [2% (mass fraction)] supported on Al_2O_3 without the addition of the promoters, with $RuCl_3$, K_2RuO_4, $Ru(acac)_3$, $Ru(NO)(NO_3)_3$ and $Ru_3(CO)_{12}$ as the precursors of ruthenium, respectively (Table 6.1). The activity and amount of hydrogen chemisorption were measured under the same reaction conditions as shown in Table 6.1.

It is seen from Table 6.1 that the activities of the Ru/Al_2O_3 catalysts prepared with chlorine-free precursors is much higher than those using $RuCl_3$. The dispersions of ruthenium are different by using different precursors. The order of dispersion is as follows: $Ru_3(CO)_{12} > Ru(NO)(NO_3)_3 > Ru(acac)_3 > RuCl_3 > K_2RuO_4$. As reported, the especially high dispersion of $Ru_3(CO)_{12}/Al_2O_3$ is caused by the reaction between $Ru_3(CO)_{12}$ and hydroxyl on Al_2O_3 surfaces and formation of following monoatomic layer anchor-type complex:



P Moggi *et al.*[8] considered that $Ru_3(CO)_{12}$ is the ideal precursor of the ruthenium catalytsts. Indeed, the precursor of the industrialized ruthenium catalyst is $Ru_3(CO)_{12}$.

Table 6.1 Characters of Ru/Al_2O_3 catalyst prepared with different precursors of Ru[a]

Samples	1	2	3	4	5
Ru precursor	$RuCl_3$	$Ru(acac)_3$	K_2RuO_4	$Ru(NO)(NO_3)_3$	$Ru_3(CO)_{12}$
Solvent	Acetone	Tetrahydrofuran	Water	3N–HNO_3	Tetrahydrofuran
Ru(mass fraction)/%	1.9	2.0	2.0	2.0	2.1
Activity[b]	8(32)[c]	20	33	53	62
[H(a)]/Ru[d]	0.23	0.28	0.03	0.35	0.43
TOF $\times 10^4$	0.5	1.3	18.5	2.2	2.2
Crystal size/nm	5.7	4.7	44	3.8	3.1
BET/$(m^2 \cdot g^{-1})$	202	184	190	194	184

[a]All the catalysts are reduced by hydrogen at 600°C for 4 h.
[b]The ammonia of the outlet of reactor at the conditions of 400°C, 101 KPa, H_2:$N_2 = 3$:1, μmol/(g · h).
[c]Washing with 300 ml 0.1% dilute ammonia solution to remove the Cl^{-1} after reduction.
[d]H(a) represents the amount of H atoms adsorbed, [H(a)]/Ru represents average H atoms adsorbed on each ruthenium atom.

6.1.2 *Supports of ruthenium catalysts*

Support is one of the important factors affecting the performance of catalyst, which include its type, composition, pore structure, surface properties and mechanical strength etc. The supports used include activated carbon, nanocarbon tube, carbon molecular sieves and carbon fiber,[9−18] oxide,[5,19−31] zeolite molecular sieve, alkali metal exchanged X- and Y-type molecular sieve,[32−38] carbon covered alumina (CCA),[29,39,40] and boron nitride[41] etc.

6.1.2.1 *Activated carbons*

As one of the supports, activated carbons have been widely used in many fields such as chemical industry, petroleum, light industry, foods, environmental protection, national defense and so on. The performances of activated carbon are closely related with its pore structures and its chemical properties of surface. Activated carbons have high specific surface area, abundance of pore structures, easily modulated surface functional groups, special electronic properties and specific physical chemical properties (such as acid- and base-resistant). As the supports of supported-type metal catalysts, activated carbons can make the noble metals and the promoter highly dispersed which can save the amount of noble metals and avoid the sintering of metal particles. Moreover, the surface area, pore structure and surface functional groups of activated carbon can be modified by physical and chemical methods[42−44] and the supported noble metals can be easily recycled by combustion of carbon supports. Therefore, it is a suitable support for ruthenium catalyst.[19,20,22,29,39−41,45] During the recent several decades, the catalysts supported on activated carbons have been widely used in many catalytic reactions which include halogenations, oxidation–reduction, manufacture, polymerization and isomerization of resin monomer and other various reactions.[46] The ruthenium based ammonia synthesis catalyst with potassium as the promoter and activated carbon as support was prepared by Ozika and Aika in 1972.[5,9,16,18,21−24,30,31,39,40,47] The performances of ruthenium catalysts supported on activated carbons are

greatly different with different types, physical structures and chemical properties of activated carbons.[48]

(1) **Structure of carbon material.** Unique characteristics of carbon materials, carbon clusters and carbon molecules are related with the electronic configuration of carbon atoms.[49–56] The latter is determined by hybridization of atomic orbits of carbon. The atomic number of carbon is six, which has six electrons. Elementary carbon is a molecule with many atoms. According to Pauli's principle and quantum mechanics theoretical calculation, the electronic configuration of carbon atom is $1\,s^2$, $2\,s^2$, $2\,p_x^1$ and $2\,p_y^1$ at the ground state. Two strong bonding electrons in 1s orbit are called core electrons. The electron cloud of 1 s and 2 s orbits show spherical symmetry and the orbit is no orientation. However, the electron cloud 2 p orbit is stretched-out spindly, spreading along with the three directions of *xyz*. Therefore, the *p*-electron has orientation in three-dimensional space.

Among elementary carbon substance, except that the graphite has certain amounts of natural storage and diamond has little, carbene, fullerene and all kinds of practical carbon materials are almost made.

It is well known that diamond and graphite with huge different characters are allotrope of carbon. The fullerenes molecules with C_{60} as representative and the carbon nano-tubes are the new discoveries in the recent 10 years. Carbon can form not only atomic crystals such as diamond and graphite, but also molecular crystals of carbine or C_{60}. The special character and variety of carbon materials are major reasons of their wide application. The allotropes of carbon can be classified into five types by different C–C bonding modes: Three-dimensional diamond crystal, two-dimensional graphite layer, one-dimensional linear carbine, zero-dimensional fullerene molecule and transitional state carbon with uncertain stable structures. Amorphous carbon is the most important transitional carbon. As one of the three-dimensional materials with short range order, amorphous carbon is composed with more or less different hybridized carbon atoms with arbitrary arrangement, mainly with the sp^2 and sp^3 hybridized carbon atoms. All kinds of carbon materials used daily can be almost attributed to the category of the amorphous carbons, such as diamond-like carbon (DLC), glassy carbon, activated carbon and all kinds of carbon black, soot, coke etc. Another group includes fullerenes, onion carbon, nanocarbontube (huge linear fullerens), supposed C_{120} torus, fullereneynes and relative diamond–graphite doped structures.

The phase diagram of carbon proposed by Bundy in 1989 is as shown in Fig. 6.1.[57] It can be seen from Fig. 6.1 that as a typical representation, diamond is a stable phase at high pressures and graphite is a stable phase at low pressures and carbene is a stable phase at high temperatures, which are corresponding to sp^3, sp^2 and sp hybridized carbon, respectively. The triple phase point of graphite–liquid–gas is about 10^7 Pa and 4,200 K, thereinto that of graphite–diamond–liquid is about 11 GPa and 4,000 K. However, only the thermodynamically stable phases are shown in the phase diagram. In fact, the recent study on the fullerenes has clearly shown that these phases, which are stable only in kinetics, even thermodynamic unstable, can stably exist under the common conditions. The formation heat of carbon of C_{60} is 42.51 kJ/g, C_{70} with stability of 40.38 kJ/g, relatively, while the values of graphite and diamond are zero and 1.67 kJ/g, respectively. The crystal fullerene is still a very stable molecule in kinetics even at high temperatures.[58]

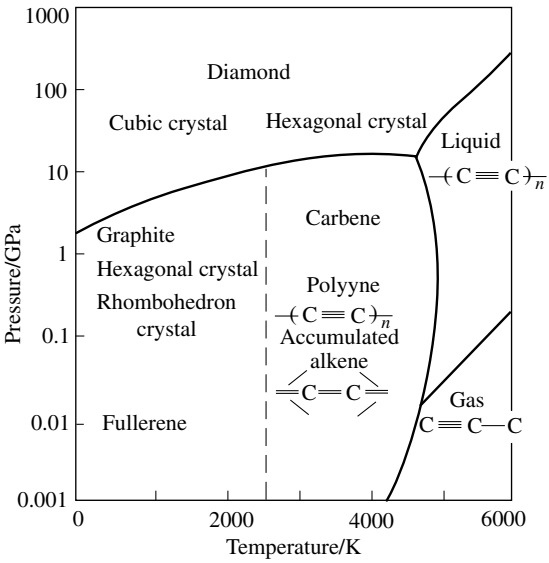
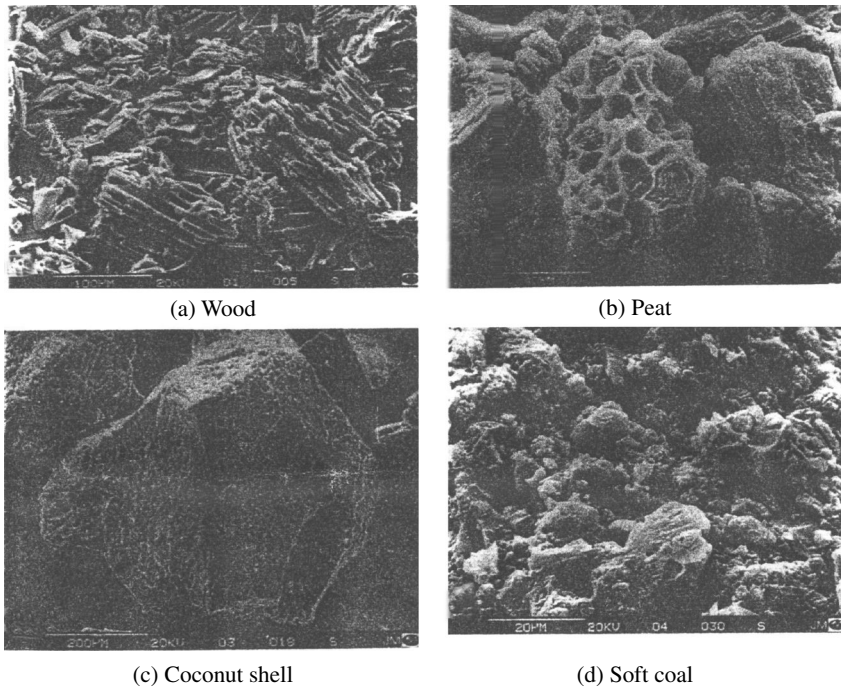


Fig. 6.1 P–T phase diagram with logarithmic pressure axis. Dubbed in are P–T paths a graphite specimen would take during fast energy insertion with various constraints on bulk expansion. 0 AV means heating at constant volume

(2) **Variety and preparation methods of activated carbon.** The structures, physical and chemical properties of activated carbons, prepared by different raw materials and different activated methods, are different. Activated carbons can be prepared by carbonization and activation treatment of all kinds of carbonaceous materials. But most of activated carbons are not produced specially as the support of catalyst. Figure 6.2 shows the surface morphologies of activated carbons prepared by different raw materials.[59] It is seen from Fig. 6.2, that the inherent structures are different from each other, although four kinds of carbons have more micropores and high specific surface area. The activated carbons produced from wood (Fig. 6.2(a)) have exoteric structures with many macroporouses of 5–10 μm and extended mesopores and microporous based on them. These pores have a needle shape, therefore, they form exoteric dense structures. The activated carbons, prepared with the raw materials of peat (Fig. 6.2(b)), have the exoteric structures and fewer amounts of macroporouses, rich in Si content on the surface. The activated carbons produced from coconut shell (Fig. 6.2(c)) are significantly different from those produced from the wood charcoal or the peat. They have more dense structure and fibrous shape. The activated carbons in Fig. 6.2(d), produced by soft coals, are much denser and without any open structures.

The effect of the raw materials of activated carbon on the activity of catalysts is shown in Table 6.2.[60,61] It can be seen from Table 6.2, that the effect of the raw materials of activated carbons on the properties of catalyst is very great. Therefore, we should be cautious in choosing the raw material of activated carbon as the support of ruthenium catalyst.



(a) Wood (b) Peat

(c) Coconut shell (d) Soft coal

Fig. 6.2 SEM image of activated carbon prepared by different raw materials

(a: wood, b: peat, c: coconut shell, d: soft coal)

Table 6.2 Effect of the raw materials of activated carbon on activity of catalysts

Raw material	BET/$(m^2 \cdot g^{-1})$	$V_{pore}/(ml \cdot g^{-1})$	Ammonia concentration of outlet (mol)/%
Soft coal	900	0.48	0.90
Coconut shell	1,050	0.54	8.57
Wood	938	0.50	7.31
Nut shell	1,000	0.60	10.90

Conditions of activity test: temperature of 450°C, pressure of 7 MPa, space velocity of 20,000 h^{-1} and N_2: $H_2 = 1{:}3$.

The physical and chemical properties of activated carbon are also related with the activation methods during the preparation process. Activation is classified into physical[62] and chemical methods.[63] The steps of carbonization and activation in physical method are separated. The raw materials should be carbonized, then selectively oxidized using oxygen-contained gases such as steam, CO_2 (flue gas), or oxygen (air) etc. as the activators at 600°C–800°C, so the raw carbon is activated during partial oxidation and cauterization. The chemical method is that the mixture of $ZnCl_2$, H_3PO_4 etc. with raw materials is heated in the carbonization furnace, and

meanwhile it is carbonized and activated. $ZnCl_2$ activation is the major chemical method of producing activated carbons. The raw materials are mainly sawdust. The activated carbons produced by this method contain large amounts of transitional pores.

Due to the different raw materials and processes of activation, the surfaces of activated carbon might have different impurities such as Na, K, Si, Al, Zn, P, N, Fe, Ca, Cl and S etc. When activated carbon is used as the support of catalyst, these impurities have direct influences on its hardness, surface area, redox property and acidity and basicity. Even some impurities themselves are the poisons of catalyst. And they will seriously affect the activity of catalyst. Probably these impurities can accelerate side reactions and change the sinter-resistant of supported metals and so on.[59] In order to solve this problem, steps of washing by water or acid are introduced during production of activated carbon, which can reduce the content of these impurities and remove partly or totally the surface impurities of activated carbon.[44,48,60]

(3) **Physical structures of activated carbon**. One of major roles of activated carbons as a support of catalyst is to increase the dispersion and stability of active components, to provide more active sites, which has close relationship with its pore structure and surface area. The amorphous structures of activated carbons determine their developed micropores. There are some interspaces formed during activation process through eliminating the carbons of carbon compounds and non-organic component filling in the pore between microcrystal and parts of carbons in the microcrystal structure. These micropores have some shapes, such as plane slit, cylindrical, V-shape, cone, inkpot and distortions of those shapes etc.[63] The adsorption abilities of activated carbon are closely related with the micropores structure and their distribution. The distribution of macropores, medium pore and micropores in activated carbon are listed in Table 6.3.[64]

Kowalczy *et al.*[19] investigated five kinds of ruthenium catalysts supported on activated carbons treated under ultra high vacuum at the temperature range of 2,000 K–2,200 K and made the correlations between the pore structures and the distribution of active components. The experimental results show that the surface areas and the pore volumes are different (Table 6.4) in different activated carbons. The dispersions of ruthenium are closely related with the pore structures of activated carbons. The fuller development of pore structures in activated carbon, the higher the dispersion of ruthenium is (Table 6.5).

Therefore, the pore distributions of the activated carbons not only determine the surface area, in which active components are deposited and then influence on the dispersion of the active components, but also determine whether the reactants can reach to the location where the active components are deposited. In general,

Table 6.3 Distribution of the pore size in activated carbon

Type	Pore size(r)/nm	Pore volume/ $(ml \cdot g^{-1})$	Surface area/$(m^2 \cdot g^{-1})$	Ratio of total surface area
Micropore	r < 1.5–1.6	0.15–0.50	Hundreds–1,000	>90%
Mesopore	1.5–1.6 < r < 100–200	0.05–0.20	20–70	*ca.* 5%
Macropore	r > 100–200	0.20–0.80	0.5–2.0	—

Table 6.4 Pore Structures of activated carbons and the chemical components of Ru–Ba/AC catalysts

Activated carbon	$S_{BET}/(m^2 \cdot g^{-1})$	$S_{Hg}/(m^2 \cdot g^{-1})$	$V_{Hg}/(ml \cdot g^{-1})$	Ru/%	Ba/Ru mole ratio
A	66	60	0.61	9.1	0.44
B	104	69	0.65	9.1	0.44
C	164	106	0.90	9.1	0.44
D	180	107.5	0.89	9.1	0.72
E	326	110	0.88	9.1	0.81

Table 6.5 Characterization of Ru/AC catalysts

Sample	XRD, d/nm	H_2 (0°C) FE	d/nm	O_2 (0°C) FE	d/nm	O_2 (−78°C) FE	CO (0°C) FE
Ru/A	7.5	0.110	12.2	0.162	8.3	0.169	0.205
Ru/B	6.0	0.140	9.6	0.216	5.9	—	—
Ru/C	4.8	0.164	8.2	0.318	3.6	—	—
Ru/D	3.5	0.168	8.0	0.325	3.5	0.298	0.347
Ru/E	Not detected	0.177	7.6	0.453	2.4	0.407	0.434

Note: FE is the exposure fraction of Ru atoms.

if the reactant approaching to the active sites of catalysts is more easi, the catalysts have relatively high activity in porous materials.

Different active components and the catalytic reactions have different requirements on the pore structures of activated carbon. Therefore, it should balance the proportion of the macroporous, mesopores and microporous by the concrete conditions in order to optimize the performances of catalyst.[20]

(4) **Surface chemical properties of activated carbon.** Surface chemical properties of activated carbon have prodigious influences on the conductivity, corrosion resistance, acidity and basicity, redox property, hydrophilicity and hydrophobicity of activated carbon.[59,65,66] The surface chemical groups of activated carbon mainly include oxygen-containing and nitrogen-containing functional groups.[67] The oxygen-containing functional groups of activated carbon detected successfully are shown in Fig. 6.3.[65]

The oxidation, acidity and basicity of activated carbon are closely related with surface oxygen-containing functional groups. The groups (a)–(e) of Fig. 6.3 show some acidity. The acidic surface groups have cation exchange ability and the surface groups with low contents of oxygen display both alkaline and anion exchange property. The existence of the oxygen-containing functional groups makes the hydrophobicity of activated carbon form some local hydrophilicity areas. The hydrophilicity and hydrophobicity of activated carbon have important influence on the preparation of catalyst. When the activated carbons acts as the support of metal catalysts, these oxygen-containing functional groups may benefit to produce highly dispersed metal microcrystal and stabilize them and then improve the sinter-resistant of catalysts.[68] The amount of oxygen-containing groups can be eliminated or increased by the modifying treatment. Furthermore, the distribution of these groups is more reasonable, which can benefit to prepare optimum catalyst.

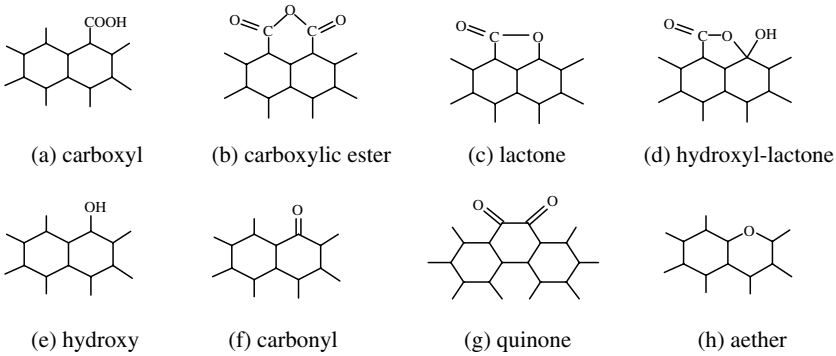


Fig. 6.3 Oxygen-containing functional groups on the surface of activated carbon

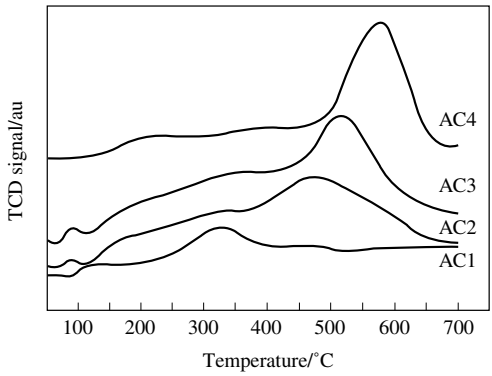


Fig. 6.4 H_2-TPR spectra of activated carbon after treated by HNO_3

(AC1-soft coal, AC2-coconut shell, AC3-wood, AC4-nut shell)

The studies have shown that the surface areas and pore size distribution are the major reasons to affect the adsorption ability of activated carbon during the gas adsorption rather than the surface properties. While the surface properties have a significant influence on the adsorption ability of activated carbons in liquid phase or activated carbon as the support.

The influences of the surface oxygen-containing groups on the catalytic activity of activated carbons supported ruthenium catalysts are shown in Figs. 6.4 and 6.5.[60] It is seen that the amount of surface oxygen-containing groups are obviously different among four activated carbons and the catalytic activity is closely related to the amount of the acidic groups. The more acidic groups, the higher the catalytic activity is.

Besides, there are a certain amount of nitrogen-containing functional groups on the activated carbon surface. These nitrogen-containing functional groups are mainly dependent on the preparation methods of activated carbon, which can be introduced by two methods: (i) reaction of activated carbon with the nitrogen containing reagents, such as ammonia; (ii) preparation by nitrogen-containing raw materials. Several kinds of nitrogen-containing functional groups on the surface of activated carbon are shown in Fig. 6.6.[69]

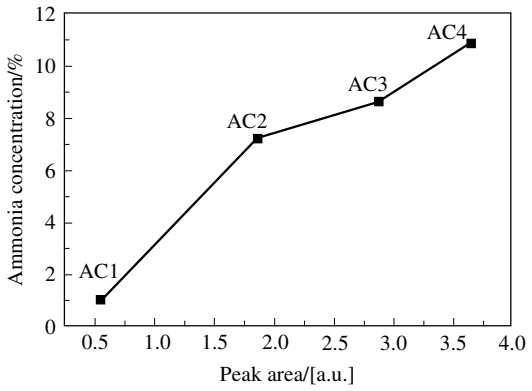
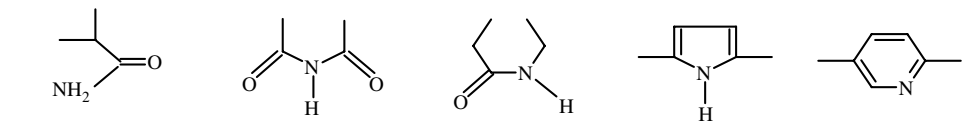


Fig. 6.5 Relationship between the amount of the acidic groups on surface of the activated carbons treated by HNO_3 and the catalytic activity

(AC-soft coal, AC2-coconut shell, AC3-wood, AC4-nut shell)



(a) acyl-amidocyanogen (b) imide (c) lactam (d) pyrryl (e) pyridyl

Fig. 6.6 Nitrogen-containing functional groups on the activated carbon surface

In summary, the determination of surface functional groups on the activated carbons and the catalytic properties are rather complicated. It is one of the key and difficult points for studying the catalysts supported on the activated carbons.[70−76] The influences of surface chemical property of activated carbons on ruthenium catalysts are very complicated and uncertain, which should be further investigated.

6.1.2.2 *Oxides*

When activated carbon is used as support, the support degradation by Ru-catalyzed methanation under ammonia synthesis conditions can occur, so it affects the life of catalysts. Therefore, many researchers have tried to use metal oxides to replace the activated carbons as the supports for ruthenium catalysts. Supported catalysts with high dispersion and high activity can be obtained when noble metals in precursor forms are supported on hardly reduced metal oxide. The oxides which are commonly used as ruthenium catalyst support include oxides of alkaline earth metals,[5,19−23] lanthanide,[24] and alumina.[2,3]

Aika *et al.*[2−4,24−29] have systematically investigated the activity of ruthenium catalysts supported on different metal oxides. A series of catalysts with 2% Ru (mass fraction) and without promoter were prepared by the same method with the $Ru_3(CO)_{12}$ or $RuCl_3$ as the precursors of ruthenium; MgO, CaO, Al_2O_3, Nb_2O_5 and TiO_2 etc. as the supports, respectively and compared their activities under the same conditions. It is found that without promoters, the catalytic activities are

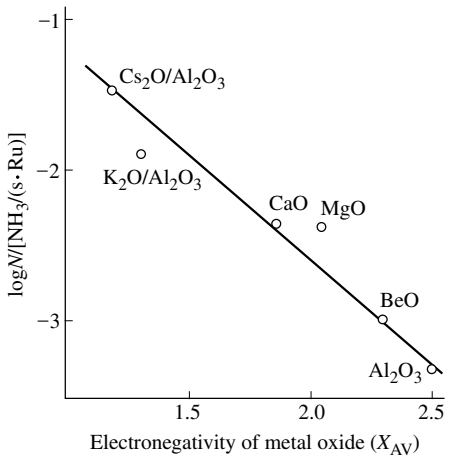


Fig. 6.7 Relationship between the ammonia conversion on Ru/M catalysts (667 K) and electronegativity of the metal oxide (M)

related with electronegativity of the oxides which function as supports, and the order of activity is $MgO > CaO > Al_2O_3 > Nb_2O_5 > TiO_2$,[30] wherein magnesium oxide is the most effective support. The relation of the electronegativity of supports and the reaction rate of the ammonia synthesis is shown in Fig. 6.7.[77]

The researchers of Ruhr University developed a ruthenium catalyst supported on the magnesium oxide with barium as promoter. Compared with the current iron catalyst, this catalyst has higher activity and longer life. It was reported that the activity of this Ba–Ru/MgO catalyst is 3–4 times higher than that of Fe-based or Ru-based catalysts and is more than two times higher than Pd–Ru catalysts. Furthermore, under the certain operation conditions, the output of ammonia can be further increased by changing the ratio of Ba and Ru. High activity of this catalyst can maintain more than 1,000 hours at high temperatures and high pressures. 97% Ru and 94% Ba in the catalysts can be recycled by a three step separation process, which can realize the purpose of the recycling.[78]

Ruhler *et al.* considered that Ba–Ru/MgO catalysts have high activities and stabilities. The researchers in Topsφe Company, Denmark developed series of ruthenium based ammonia synthesis catalysts support on different supports, with electronic and structural promoters. In these studies, the ruthenium catalysts supported on the Mg–Al spinel and high surface area graphite show promising activity (see Table 6.6). However, the stability has some problems under industrial conditions.[79]

In ammonia synthesis reaction, the dissociative adsorption of dinitrogen is the rate determining step. The electron donor type promoter, such as alkali metals, which can provide electrons to the Ru, is more propitious to activate the N≡N bond in N_2 molecule and thus enhance the dissociative adsorption of dinitrogen and increase the reaction rate of ammonia synthesis. The acidity and basicity of supports have important influence on the activity of the ruthenium catalysts without promoter. Acidic supports can easily accept electrons and decrease the activity of catalysts. Basic supports can easily provide electrons and enhance the dissociative

Table 6.6 Reaction rate in unit of volume and weight (T = 400°C)

Catalysts	Ru loading (mass fraction)/%	Packed density/ ($g \cdot cm^{-3}$)	Reaction rate		Reaction conditions	
			($g_{NH3} \cdot cm^{-3} \cdot h^{-1}$)	($g_{NH3} \cdot g_{Ru}^{-1} \cdot h^{-1}$)	p/bar	x_{NH3}/%
Ba-13.5Ru/ Mg–Al spinel	13.5	0.84	0.91	8.05	63	8.5
			0.94	8.30	90	11.5
Ba-4.9Ru/ $MgO–Al_2O_3$	4.9	0.73	0.05	1.3	63	8.5
			0.05	1.3	90	11.5
Ba-10Ru/MgO	10.0	0.75	2.54	33.9	63	8.5
			2.61	34.8	90	11.5
Ba-9.1Ru/C	9.1	0.39	1.29	36.2	63	8.5
		0.34	1.17	38.0	90	10
Ba–Cs-9.1Ru/C	9.1	0.34	2.33	75.3	90	10
Fused iron	—	2.50	0.37	—	63	8.5
Fused iron	—	2.50	0.50	—	90	10

adsorption of dinitrogen and the activity of ammonia synthesis. The interaction mechanism between the promoter, support and Ru was shown in Fig. 6.8.[80]

Rare earth metal oxides are not the ideal supports as expected, due to their weak basicity (biggish electronegativity). However, the study of Aika shown that rare earth oxides as the support are more effective, than as the promoter of ruthenium catalyst,[26,29] which might decrease the inhibition of H_2 adsorption on ammonia synthesis reaction. For example, with the $Ru_3(CO)_{12}$ as the precursors, with the CeO_2, Sm_2O_3, La_2O_3 as the supports, the catalysts of 0.5% (mass fraction) Ru/La_2O_3, 1.0% Ru/CeO_2, 0.4% Ru/Sm_2O_3 were prepared respectively and compared with 1.0% Ru/MgO catalyst, the results are shown in Fig. 6.9. Although the contents of Ru in 0.5% Ru/La_2O_3 and 0.4% Ru/Sm_2O_3 catalyst are low, the catalytic activities of ammonia synthesis are very high, but they are not stable. The activity decreases after several hours of reaction. The activity is recovered to initial activity after reduced by H_2 at 650°C for 1 h, which lose activity rapidly once again. However, the activity of 1.0% Ru/CeO_2 catalyst can keep longtime. Rare earth oxide is one kind of better support of Ru-based ammonia synthesis catalysts due to its relative large density, which can occupy few spaces in converter. At present, the studies of rare earth oxide as the support of ruthenium catalysts have been reported less. It is necessary to further investigate the mixed rare earth oxides due to their low cost.

The activity of supported ruthenium catalysts with potassium as promoter and with various substances such as activated carbon, γ-Al_2O_3, NaX molecular sieve, silicon dioxide, CeO_2, Sm_2O_3, Y_2O_3 and C_{60} as supports was investigated.[81] It was found that ruthenium catalysts supported on rare earth oxides have better activity than those on other supports. At normal pressure and 400°C, except for the catalyst supported on C_{60}, the order of the activities of the other supports is $Sm_2O_3 > CeO_2 > Y_2O_3 > \gamma$-$Al_2O_3 >$ NaX > AC > silicon dioxide. The catalysts supported on the rare earth oxide have high activity due to the formation of Ce^0 or the low valence ions as CeO_2 during the reduction process at high temperatures. Those

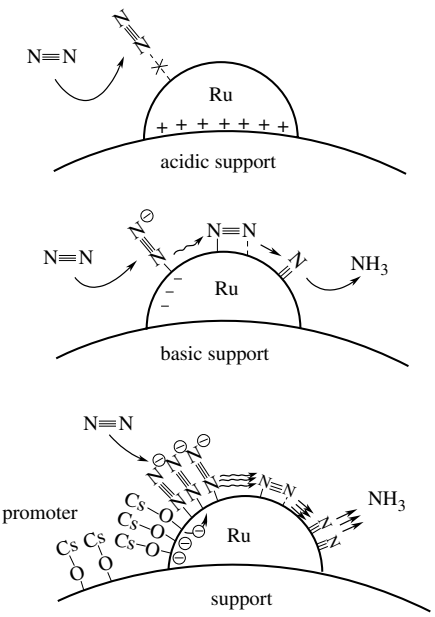


Fig. 6.8 A model of interaction among metal Ru, promoter and supports[81]

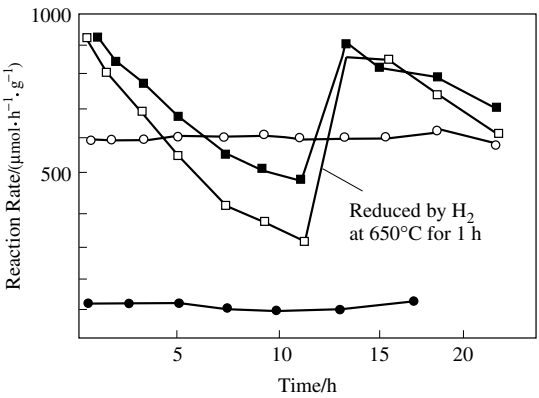


Fig. 6.9 Change of ammonia synthesis rate with the times on Ru catalyst. • 1.0 wt% Ru/MgO; ○ 1.0 wt% Ru/CeO_2; □ 0.5 wt% Ru/La_2O_3; ■ 0.4 wt % Ru/Sm_2O_3

zero or low valence ions can easily donate electrons to ruthenium and increase the catalytic activity.

Oxides, as supports of ruthenium catalysts, have high mechanical strength, good stability and highly basic sites, which can provide electrons in order to activation of N_2 and enhance the catalytic activity of synthetic ammonia. However, the low dispersion of ruthenium is a common problem. Therefore, it is a common topic on how to increase the dispersion of ruthenium.

6.1.2.3 *Molecular sieve*

As the support of metal catalysts, zeolite has some advantages as follows: (i) the grain size of the active components can be regulated through the pore size of zeolite; (ii) its surface acidity and basicity can be regulated by ion exchange. It is commonly considered that the activity of ruthenium catalyst is closely related with the acidity and basicity of the supports. Becue and Cisneros[32–34] investigated the activity of ruthenium catalysts supported on X and Y zeolite exchanged by alkali metal. It was found that the TOF for ammonia synthesis reaction of Ru–K/X catalysts are lower than that of nonzeolite, but the specific surface area of Ru metal is larger than others. At the same time, the TOF order of X zeolite exchanged by alkali metal is Cs < Na < K. The effect of promoters is obviously different with alumina and magnesium oxides as supports. They also found that the activity of the ruthenium catalyst supported on faujasite with alkali metal as promoters is higher than that of iron catalysts at normal pressure and 350°C–450°C. For example, the ammonia concentration in the outlet of reactor on Ru–K/X is $4.9 \times 10^{-5}\,\mathrm{mol_{NH3}} \cdot \mathrm{s^{-1}}\,\mathrm{Ru^{-1}}$ at 407°C, but the concentration is $1.2 \times 10^{-5}\,\mathrm{mol_{NH3}} \cdot \mathrm{s^{-1}} \cdot \mathrm{Fe^{-1}}$ on Fe catalyst. The activity of ruthenium catalyst supported on zeolite depends on the cation type and Si/Al ratio of the faujasite zeolite and the metal particle size.

Fishel *et al.*[35] investigated the ruthenium catalyst supported on alkaline zeolite. At atmospheric pressure, the TOF of ammonia synthesis reaction of Ru–K/X catalyst was increased markedly with the increasing particle size of ruthenium, which indicates that ammonia synthesis on the system is a structural sensitive reaction. The TOF of catalysts supported on zeolite exchanged with both alkaline metal and alkaline earth metal, the activity of zeolite exchanged with alkaline earth metal is higher than that of alkaline metal, especially higher than that of Ru/MgO catalyst. Becue and Davis *et al.* investigated the effect of promoters with different cations on Ru/X catalysts. It was found that superfluous barium ions can enhance the activity of Ru–Ba/X catalyst about one order of magnitudes. However, the superfluous potassium ions do not obviously influence on the activity. It is possible that the superfluous potassium ions block the micropores of zeolite.

For ruthenium catalysts supported on X zeolite, Becue *et al.*[32] also investigated the effect of cation on the promotional role and reaction kinetics of ammonia symtheis. The conclusions are drawn as follows: (i) Alkaline earth metal is better than of alkali metal; (ii) Alkaline earth metal might reduce the inhibition of H_2 adsorption; (iii) At pressure of 2.0 MPa, the kinetic order of N_2, H_2 is one and negative on the ammonia synthesis, while the influence of NH_3 is small. Schlögl *et al.*[36–38] also investigated the preparation, activated process and catalytic activity of ruthenium catalyst supported on A and Y zeolite.

6.1.2.4 *Other supports*

(1) Ruthenium atomic clusters. Izumi and Aika[27,28,47] investigated ruthenium atomic cluster as the supports. It was found that the reaction rate of the ruthenium catalysts supported on atomic cluster $[Ru_6N]$ prepared by $[Ru_6N(CO)_{16}]$ is much faster than those on the atomic cluster $[Ru_6]$ prepared by $[Ru_6(CO)_{18}]^{2-}$, and is also

faster than those on ruthenium cluster (N–Ru–Ru) prepared from $[Ru_6N(CO)_{16}]^-$. In addition, the ammonia synthesis activity of ruthenium catalysts supported on $[Ru_6N]$ prepared from the $[Ru_6N(CO)_{16}]^-$ and MgO, K^+–MgO, or Cs^+–MgO is higher than the one prepared by $[Ru_6C(CO)_6Me]^-$ or $[Ru_6(CO)_{18}]^{2-}$.

(2) **Nitrides.** Boron nitride, known as white graphite, is one of potential support materials of ruthenium catalysts for ammonia synthesis. It almost has similar structure with graphite (except the little difference of lamination on the monolayer). It is differed from graphite that boron nitride is very stable under all the hydrogenation reaction conditions. At the same time, to the opposite of graphite, boron nitride is an insulator due to its well known electrical resistance at high temperatures. Ba–Ru/BN catalysts promoted by barium with boron nitride (BN) as support have high activity and stability,[82] e.g., the catalysts (5.6 wt% Ba and 6.7 wt% Ru supported on the 81 m^2/g of supports) are stable during heat resistant test for 5,000 h under the conditions of 100 bar, 550°C and the ratio of H_2/N_2 is 3:1. It illustrates that electronic promoters (such as potassium, barium and cesium) affect the catalysts through the direct contact between promoters and metals rather than through the support, which are consistent with the electron microscopy results. Figure 6.10 shows the relationship between the reaction rate of Ba–Ru/BN catalyst and the pressure. Figure 6.11 shows the TEM images of Ba–Ru/BN catalyst after reaction at 550°C for 1,000 h. From the Figs. 6.10 and 6.11, the grain size of ruthenium are about 2 nm–2.5 nm, which are almost distributed on the steps of BN support planes. The similar structure of the ruthenium grain can also be observed on the ruthenium catalysts supported on activated carbon.[83]

Ba–Ru/BN and Ba–Ru/AC catalysts have the same reaction kinetics. When compared with the melting iron catalysts, the influence of ammonia concentration on Ba–Ru/BN catalysts is relatively small. In given reaction conditions (temperature, pressure, H_2/N_2 rate and concentration of ammonia etc.), the optimum activity of Ru/BN can be obtained by selecting the appropriate surface area of boron nitride, the content of Ru and promoter, size and density of grain. Moreover, the useful

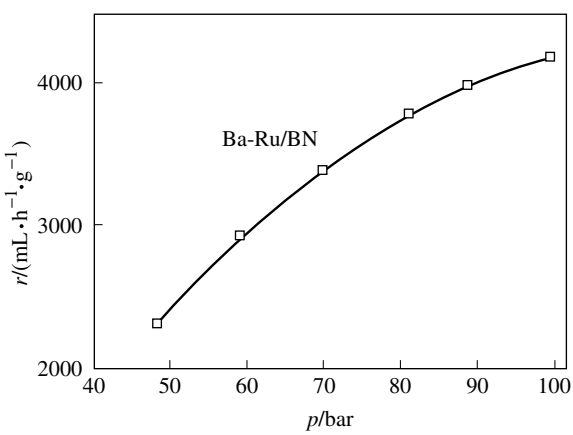


Fig. 6.10 Relation of reaction rate and pressure on Ba-Ru/BN catalyst (400°C, $H_2/N_2 = 3$. inlet ammonia concentration of 4.5%, outlet of 12.0%)

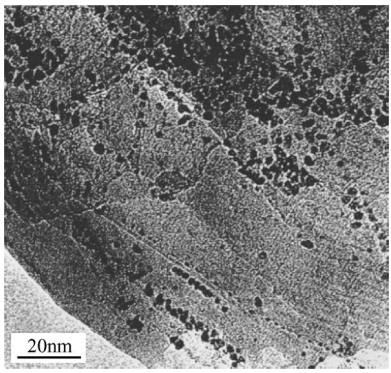


Fig. 6.11 TEM image of Ba–Ru/BN catalyst after reaction at 550°C for 1,000 h

Ba, Ru and B in Ba–Ru/BN can be recyled by the same treatment methods with Ba–Ru/MgO catalysts.[78]

(3) **Carbon nanotubes.** Carbon nanotubes have the nature of metallic or semiconductor due to its curvature like graphite layer and fiber structure. In addition, the geometric structure of carbon nanotube is beneficial to the formation of ammonia and desorption of products. The active components and promoter can be distributed on them very well due to the large surface, which is beneficial to the activation of N_2 and H_2 and the electron transfers. Therefore, some researchers[84,85] have investigated the ruthenium catalysts supported on the carbon nanotubes. Due to its high price, it now only has the theoretical value, probably without any industrialization prospect.

(4) **Molybdenum carbide and molybdenum nitride.** R Kojima *et al.*[86] in Japan investigated the activity and reaction rate of ammonia synthesis on γ-Mo_2N, two kinds of carbides (α-MoC_{1-x} and β-Mo_2C) and the effect of the addition of the second component (Cobalt and Cesium). The experimental results show that the order of the activity of the three catalyst for ammonia synthesis is: β-$Mo_2C >$ α-$MoC_{1-x} > \gamma$-Mo_2N. The α-MoC_{1-x} is not stable under the reaction conditions of the ammonia synthesis. The reaction rate and the activity are slightly increased after the addition of 2% cesium or 5% cobalt. The activity of the β-Mo_2C is comparable with that of the iron catalysts with double promoters. However, the reaction rate and the activity decrease slightly after the addition of 5% Cobalt. The β-Mo_2C catalyst can be obtained after heating MoO_3 at 973 K for 2 h and carbonized by $CH_4 + H_2$.

6.1.3 *The promoter of ruthenium catalyst*

It is generally considered that the structural factor of ruthenium catalysts is not as important as those of iron-based catalysts, while the electronic factor is the most important one. The catalytic activity of Ru/AC catalyst without promoter is very low. The promoters which can donate electron can remarkably increase the activity of catalyst.[87] The promoters of ruthenium catalysts mainly include alkali metals, alkaline earth metals, rare earth metal oxides and actinide metal compounds.

Table 6.7 Influence of promoter on ammonia synthesis rate on 2% Ru/AC catalyst

Promoter elements	Precursor of promoter	M/Ru (molar ratio)	Activity ($\mu\,mol \cdot h^{-1} \cdot g^{-1}$)	Particle size of Ru (nm)
No	—	0	0	—
K	KNO_3	10	65	—
Rb	$RbNO_3$	10	100	3.7
Cs	$CsNO_3$	10	80	6.2
Mg	$Mg(NO_3)_2$	10	24	—
Ca	$Ca(NO_3)_2$	10	32	—
Sr	$Sr(NO_3)_2$	10	55	—
Ba	$Ba(NO_3)_2$	10	83	4.0

Note: 1. Precursor of Ru is $RuCl_3 \cdot 3H_2O$, AC is not treated by acid.
2. The temperature of the reduction and reaction is 673K, $N_2 + 3H_2 = 80\,kPa$.

For ammonia synthesis reaction, the dissociative adsorption of dinitrogen on the surface of ruthenium is the rate determining step. Alkali metal such as potassium can donate and transfer electrons to metal ruthenium, and can weaken the bond of dinitrogen, in turn to speed up the dissociative adsorption of dinitrogen, and therefore enhance the reaction rate of ammonia synthesis.[9,87] Table 6.7 shows the influence of alkali metals and alkaline earth metal oxides, which can donate electrons, on the activity of Ru/AC catalysts.[7] From Table 6.7, the sequence of influence of promoters on the reaction rate of ammonia synthesis is Rb > Ba > Cs > K > Sr > Ca > Mg > No on 2% Ru/AC catalyst. The influences of the promoters are dependent on its ability of donating electrons and increase sharply with the decreasing electronegativity of the promoters. Especially, with barium as promoter, it can not only enhance the activity of catalyst, but also improve the dispersion of Ru, prevent the sintering of Ru crystallite, inhibit the methanation reaction of activated carbon and enhance the thermal stability of the catalyst. But, potassium only enhances the activity of the catalyst, but cannot prevent the sintering of Ru crystallite and the methanation of activated carbon.[19,20]

The ruthenium catalyst without promoter almost is inactive, and the outlet ammonia concentration of 4% Ru/C catalyst is only 0.13% under the conditions of 430°C, 10.0 MPa and 10,000 h^{-1}.[14] For single promoter of Ru/C catalyst with the alkali metal, alkaline earth metal nitrate acts as the precursors of promoter respectively, the alkali metal and alkaline earth metal nitrate can increase the activity of the ruthenium catalyst in different extent. The order of the influence, alkali metal nitrates are $CsNO_3 > RbNO_3 > KNO_3 > NaNO_3$ and that of alkali earth metal nitrate is $Ba(NO_3)_2 > Sr(NO_3)_2 > Mg(NO_3)_2 > Ca(NO_3)_2$. In the selected eight kinds of promoters, $Ba(NO_3)_2$ and $CsNO_3$ are the most effective and the outlet ammonia concentration are 13.38% and 9.89% at 430°C, 10.0 MPa and 10,000 h^{-1}, respectively.

The effect of promoter is related with support. For Ru–M/Al_2O_3 catalysts, alkali metal can enhance not only the TOF of the catalyst, but also the dispersion of Ru. And the hydroxide of alkali metal can prevent the poison of H_2O or CO.[25] For the Ru/Al_2O_3 catalyst promoted by alkali metal of Cs, Rb and K, the effect of promoter increases with the decreasing of the electronegativity or the increasing

of the alkaline, the order is Cs > Rb > K. Moreover, the effects of alkali metals are larger than that of alkaline earth metals. For Ru–M/AC catalysts, the change law of the effect of promoter is the same with that of the alkali (or electronegativity) of their hydroxide or oxide for same kind of compounds. However, for different kinds of compounds, the effect of alkaline earth metal is superior to that of alkali metal on the whole, which might be caused by these differences between alkaline earth metal and alkali metal such as the interaction between promoters, ruthenium and carbon support, donation of electrons, trickle-flow and valence and so on during the process of reduction and activation of catalyst. At the same time, it is found that the effect of $Ca(NO_3)_2$ is not as good as $Mg(NO_3)_2$ which is inconsistent with the change law of the alkaline or the electronegativity of CaO and MgO. It is probably that part of $Ca(NO_3)_2$ transformed into $CaCO_3$ and influenced the uniform distribution of the promoter in catalyst during the process of the preparation of the catalyst.

For Ru–M/MgO catalysts which were prepared by impregnation method with the MgO as support, the nitrates as the precursors of promoters, alkali metals and alkaline earth metals are the good promoters and the latters are better than the formers (Fig. 6.12).[26]

It can be seen from Fig. 6.12 that the activity of Ru–M/MgO catalysts with alkali metal as promoter is low. The main purpose of the addition of the alkali metal is to increase the basicity of the supports. But the role is not obviously due to the strong alkaline of MgO itself. The alkaline earth metals (especially Ba) can increase the specific surface areas of catalyst, on the other hand, Ba and Mg is in the same group in periodic table, so may be have the synergistic effect on each other, which can enhance the activities of the catalysts.

According to electronegativity, the rare earth metal oxides would be bad promoters. But Aika *et al.*[3,30] found that the rare earth metal oxide is ideal promoter for the Ru/Al_2O_3 catalyst with $Ru_3(CO)_{12}$ as the precursor. It is because that rear earth oxides are reduced to form low valence states oxide and covered on the surface of ruthenium. This low valence oxide is a good electronic donor on the ruthenium surfaces. In addition, the rare earth oxide can reduce the inhibition of hydrogen adsorption, which is beneficial to the adsorption of N_2. For the ruthenium catalysts

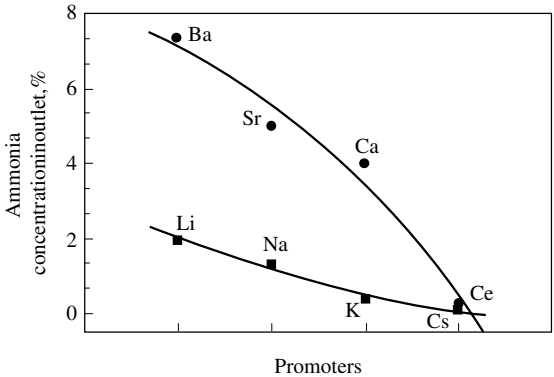


Fig. 6.12 Effect of promoters (M) on activity of Ru–M/MgO catalyst at 7 MPa, 475°C and 20,000 h^{-1}

supported on MgO, the rare earth oxide also has certain promotional effect, but which is not as good as the alkali metals and alkaline earth metals. Sm_2O_3 has some effect on enhancing the activity of the catalyst with activated carbon as the supports.[88]

The interaction among ruthenium, promoter (MO) and support plays a key role on the activity of catalyst. Aika[7] considered that there are some reactions among them as follows:

$$\text{Ru} + \text{MO} \rightarrow \text{Ru–OM} \tag{6.1}$$

$$\text{Support} + \text{MO} \rightarrow \text{support–OM} \tag{6.2}$$

$$\text{Ru} + \text{support} \rightarrow \text{Ru–support} \tag{6.3}$$

When activated carbon is used as support, they will accept electrons of ruthenium according to the Eq. (6.3). Therefore, it needs many promoters to neutralize Eq. (6.3) by reaction of Eq. (6.2) and finally the activity is increased by reaction of Eq. (6.1).

One of the common methods of enhancing catalytic activity is using two-metal catalysts. For example, Yunusov S. M. *et al.*[89] investigated the influences of Cobalt and Iridium on the activity of the Ru–K/AC catalysts. The results showed that the addition of Co and Ir greatly decreases reaction rate of ammonia synthesis. It might be because of lack of the synergistic effect between Ru, Co and Ir. Therefore, it should further investigate whether there is ruthenium based bimetal catalyst with higher activity.

6.1.4 *Mechanism on the role of support and promoter*

There is no consistent understanding on the role of mechanism of alkali metals and alkaline earth metals on ruthenium catalysts and their state under the operating conditions. The current studies[90] show that the dynamics of the ammonia synthesis reaction are different using the alkali metals and alkaline earth metals as the promoters, respectively. Therefore, using combination of promoters is more favorable to increase the catalytic activity.

The easily reduced noble metals usually are supported on metal oxides which cannot be reduced. The noble metal oxides are first reduced to form metal particles and the surfaces of these small grains have different crystal faces and different properties. The size of metal particles are also influenced by the chemical–physical property of supports, enrichment and agglomeration of metals, the reduction temperature and the formation process of metals grain. There is electronic interaction between the support, promoters and metal particles, and so can affect the activity.

6.1.4.1 *Hydrogenolysis of precursor of promoter*

For the ruthenium catalysts with nitrate as the precursor of promoters, nitrate needs to be reduced by hydrogen, then transform into effective components during the reduction and activation of the catalysts. The existence of ruthenium and the properties of support have great effect on the hydrogenolysis reaction of nitrates. Metal ruthenium can reduce the decomposition temperatures of nitrates significantly.[25] The optimum hydrogenolysis temperature of promoter on different

supports is different.[15] The hydrogenolysis reactions of potassium nitrate are possibly as follows[25]:

$$KNO_3 + 4H_2 \rightarrow 1/2K_2O + NH_3 + 5/2H_2O. \tag{6.4}$$

$$KNO_3 + 4H_2 \rightarrow KOH + NH_3 + 2H_2O. \tag{6.5}$$

$$KNO_3 + 9/2H_2 \rightarrow K + NH_3 + 3H_2O. \tag{6.6}$$

Reaction (6.6), with $\Delta_r G^{\Theta} = -309\,kJ/mol$, maybe happen in thermodynamics especially at the hydrogen atmosphere system. But reaction (6.4) can happen easily. Therefore potassium after hydrogenolysis has possibly three kinds of states, but generally is in K_2O or KOH.

The hydrogenolysis reaction of $CsNO_3$ can happen only in the presence of metal ruthenium. $CsNO_3$ with ruthenium powder together can decompose completely at 200°C. The decomposition ratio of reaction (6.7) can only reach 55% even at 400°C. DTA spectra shows that there are undecomposed $CsNO_3$ at 152°–370°.[25,91]

$$CsNO_3 + 4H_2 \rightarrow 0.5Cs_2O + NH_3 + 2.5H_2O. \tag{6.7}$$

TGA analysis indicates that Cs_2O partly transforms into Cs_2O_2 and Cs and finally changes to CsOH.[92]

$$CsNO_3 + 4H_2 \rightarrow CsOH + NH_3 + 2H_2O. \tag{6.8}$$

$$2Cs_2O \rightarrow Cs_2O_2 + 2Cs. \tag{6.9}$$

$$Cs_2O_2 + H_2 \rightarrow 2CsOH. \tag{6.10}$$

$$Cs + OH(a) \rightarrow CsOH. \tag{6.11}$$

Therefore, it is generally considered that cesium exists in the state of CsOH in the ruthenium catalysts. Catalytic activity of Ru–Cs^+/MgO (Cesium is in the forms of Cs_2O or CsOH) is very high, which is only inferior to Ru–K catalysts. This promoter is very stable even in the presence of steam. The activity can be adjusted by the addition of nitrate and depends on the surface area of catalyst.

Hydrogenolysis reaction of nitrate of alkaline earth metal and rare earth metal are as follows:

$$Ba(NO_3)_2 + 8H_2 \rightarrow BaO + 2NH_3 + 5H_2O. \tag{6.12}$$

$$2M(NO_3)_3 + 24H_2 \rightarrow M_2O_3 + 6NH_3 + 15H_2O \ (M = La, Ce, Sm). \tag{6.13}$$

These promoters generally exist in the state of oxide, distributed on the surface of ruthenium or around support by results of reaction.

The hydrogenolysis temperature of nitrates has influence on particle size of ruthenium.[93] The ruthenium particle sizes of Ru–M (M=K, Cs, Ba)/TC with different nitrate as promoter, measured after the hydrogenolysis reaction at temperatures in range of 430°C–550°C are shown in Fig. 6.13. The results show that promoters covered on the surface of ruthenium or interface between ruthenium and support. Therefore, the particle size of ruthenium in catalysts with single promoter is obviously bigger than the one (Ru/C) without promoter.

The sensitivity of different promoters on hydrogenolysis temperature is different. For example $CsNO_3$ and KNO_3 are suitable for the hydrogenolysis temperature below 475°C, while high temperature reduction will cause ruthenium particle sintering and growth. Due to the protection of promoter, ruthenium particles would

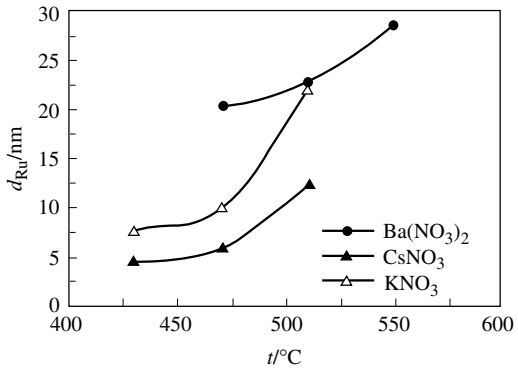


Fig. 6.13 Effect of hydrogenolysis temperature on the average Ru particle size in Ru catalyst with different promoters

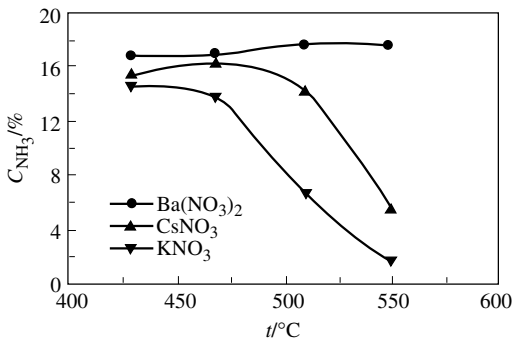


Fig. 6.14 Effect of hydrogenolysis temperature on activity of Ru catalyst with different promoters

not sinter and increase after hydrogenolysis of catalyst with barium promoter at temperatures higher than 500°C. The possible reasons are that the heat resistance of alkaline earth metal is much stronger than that of alkali metal hydroxide,[20] and at the same time, the mobility of barium oxide is low and its melting point is much higher (1,918°C). Therefore, ruthenium particles can be protected at high temperatures. Of course, the extremely high hydrogenolysis temperature can also cause the ruthenium particle sintering or induce methanation reaction of activated carbon.

The hydrogenolysis temperature of ruthenium catalysts with different promoters has big difference. Hydrogenolysis temperature has great influence on the activity of ruthenium catalysts[93] (Fig. 6.14). After hydrogenolysis, the activity of ruthenium catalysts using alkali metal nitrate as precursor of promoter is related with metal dispersion. The catalysts can reach ideal activity when hydrogenolysis of $CsNO_3$ and KNO_3 is carried out at the low temperatures (430°C–470°C). The influence of hydrogenolysis temperature on the activity was very little at this temperature range. The catalytic activity will sharply decrease when the temperature of hydrogenolysis exceeds 500°C. The ruthenium catalysts with alkaline earth metal nitrate as the

promoter require higher hydrogenolysis temperatures. The optimum activation temperature of $Ba(NO_3)_2$ is 510°C and it still keeps high activity even at 550°C. The diversity of the best hydrogenolysis temperatures of various promoters is closely related with its state. It is generally considered that alkali metal nitrates exist in the form of hydroxide, but barium nitrate is in the form of BaO/BaOH after hydrogenolysis at high temperature.[94] The ruthenium particle can enhance the hydrogenolysis of barium nitrate, and high temperature is beneficial to form BaO and can enhance the activity due to the stronger electron donation ability of BaO than Ba $(OH)_2$ (the electronegativity of BaO and $Ba(OH)_2$ are 1.77 and 2.17, respectively). This phenomenon can be explained by the formation of oxygen vacancies. The Ruthenium catalysts with cesium nitrate as promoter have high activity after hydrogenolysis even at low temperatures due to the stability order of hydrogenolysis products with $CsOH > Cs > Cs_2O$.

6.1.4.2 *Electronic contribution of active site*

Potassium is considered to be electron donor for the iron catalysts. For ruthenium catalysts, electronic effect of support and promoter is very important. According to the eletronegativity, the electronic effect of support and promoter are summarized and shown in Fig. 6.15 and Table 6.8.[95]

TOF of ammonia synthesis reaction and isotopic equilibrium rate of nitrogen molecule follow the order shown in Table 6.8. We can roughly estimate the performance of promoters from chemical property of element itself. The activity of ruthenium catalysts supported on Al_2O_3 is very low, while almost no activity is observed on activated carbon due to the acidicity of Al_2O_3 and absorption of electrons by activated carbon.

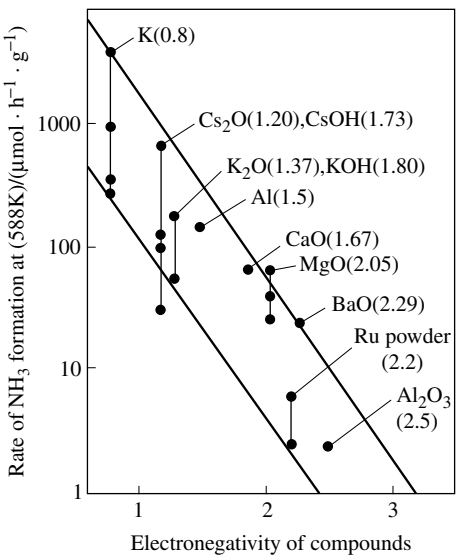


Fig. 6.15 Rate of formation at 588K and $N_2 + H_2 = 80$ kPa on Ru (2 wt% or 5 wt%) catalysts with various supports and promoters as a function of average electronegativity of compounds[26]

Table 6.8 Role of promoter and support of ruthenium catalyst ($N_2 + 3H_2 = 80\,kPa$) and isotopic equilibrium ($N_2 = 20\,kPa$)[26]

Major promoter	Catalyst	Ru dispersion/%	Ammonia rate (588 K)		N_2 equilibrium (588 K)	
			TOF $\times 10^4$	mmol · h^{-1} g^{-1a}	TOF $\times 10^4$	mmol · h^{-1} g^{-1b}
Metal K	4.7% Ru–K/AC	10.3	205	3.3	—	—
	5% Ru–K/AC	12.7	—	—	24	0.51
	5% Ru–K/BeO	8.6	204	2.9	175	2.5
	4.6% Ru–K/MgO	2.9	197	0.87	147	0.66
	2.0% Ru–K/Al_2O_3	5.0	100	0.34	—	—
	0.5% Ru–K/Al_2O_3	22.1	—	—	24	0.094
	4.2% Ru–K/CaO	2.5	75	0.26	139	0.49
	Ru powder-K	0.30	29	0.31	—	—
	Ru powder-K	0.25	—	—	6.9	0.061
	Raney Ru-K	3.1	17.5	1.76	—	—
Cs+(Cs_2O)[a]	1.96% Ru-Cs^+/MgO	8.5	19	0.083	—	—
	1.96% Ru–Cs^+/MgO	4.1	11	0.022	—	—
	1.96 Ru–Cs^+/MgO	35	27	0.47	—	—
	2% Ru–Cs^+/Al_2O_3	20	7	0.073	—	—
K+(K_2O)	2% Ru–K^+/Al_2O_3	21	3.8	0.046	—	—
	2% Ru–K^+/Al_2O_3	34	7.5	0.146	—	—
	2% Ru–K^+/Al_2O_3	18	4.2	0.052	—	—
CaO	4.2% Ru/CaO	2.5	18.7	0.066	—	—
MgO	4.6% Ru/MgO	2.9	14.3	0.063	—	—
	1.96% Ru/MgO	8.4	7.2	0.041	—	—
	1.96% Ru/MgO	12.5	3.0	0.026	—	—
Al and/ or Al^{3+}	Raney Ru	3.1	1.40	0.144	—	—
—	Ru powder	0.30	0.54	0.006	—	—
	Ru powder	0.25	—	—	0.020	0.0002
	Ru powder	0.18	0.41	0.0025	—	—
BeO	5% Ru/BeO	8.6	1.63	0.023	—	—
Al_2O_3	2% Ru/Al_2O_3	5.0	0.67	0.0023	—	—
	0.5% Ru/Al_2O_3	22.1	—	—	0.12	0.0005
AC	4.7% Ru/AC	10.3	Neg	Neg	—	—

[a] Cs^+ is CsOH or Cs_2O.

[b] Activity in the mass of unprocessed catalyst ($RuCl_3 \cdot 3H_2O$ + support + promoter) as the base of calculating, except the mass of metal K can be neglected in the Ru–K/support catalyst.

Alkali metals are good promoters. Figure 6.16 shows the influence of type and amount of alkali metal on the catalyst activity. Ru/AC catalyst without any promoter shows no activity, moreover, with the addition of alkali metal the activity increases. The highest activity is 4 mmol alkali metal per gram catalyst, where the outlet of ammonia concentration is 3.30, 1.28 and 0.12 $mmol \cdot h^{-1} \cdot g^{-1}$ when alkali metal is Cs, K and Na, respectively, which is consistent with the electronegativity of alkali metal or electron donating ability of element. XPS shows that electron transfers from promoter to ruthenium surface.[26]

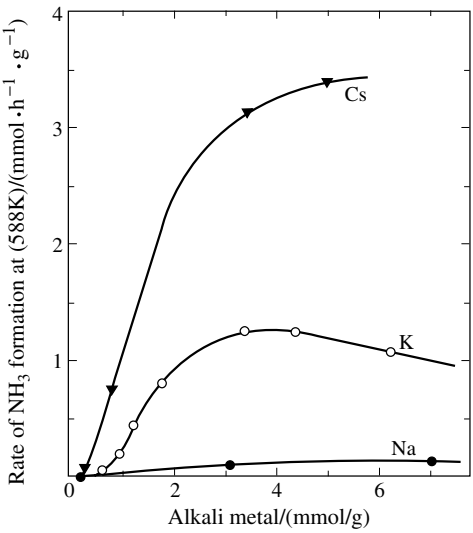


Fig. 6.16 Effects of alkali metal on the rate of ammonia formation at $N_2 + H_2$ = 80 kPa on 2.5% Ru-AC (1.0 g) at 588 K[95]

According to the promotion role of K on ammonia synthesis and nitrogen isotopic equilibrium over Ru/AC and pure ruthenium catalysts, it is found that with adding K at 673 K, the activity increases by 500 times on ruthenium catalyst, while the activity only increases by 25 times on Fe catalyst due to the inhibition of hydrogen. The inhibition of hydrogen is caused by the competitive adsorption of hydrogen which can inhibit the adsorption of nitrogen.[92,96]

A similar result has been reported. It is known that transition metal chlorides enter into graphite layer lattice[97] and lose activity for catalyst system including graphite because of chlorine atom is bringed in transition metal during the reduction process of these compounds. Although transition metal can be activated by potassium in the ammonia synthesis,[98] these conclusions are obtained from the study of the addition of potassium in electron donor receptor such as graphite or phthalocyanine.[99]

The detailed mechanism of the electronic contribution of promoter is not very clear because the addition of promoter does not change the activation energy. Several supposed mechanisms have been put forward: (i) to stabilize molecular adsorbed nitrogen (i.e., reaction intermediate species N(a)); (ii) to generate the active center by electronic promoter. Figure 6.17 shows the scheme of the first mechanism. It gives a model of the alkali promoter effect on the activation of N_2 on ruthenium surface.[9,100]

The promoting role of alkali metal has basically a consensus: Electrons transfer from alkali metal (K, Cs) to active component (ruthenium) surface, leading to the decreasing barrier of N_2 dissociative absorption[101–104] or the reducing stability of NH_x species,[105–109] then increasing the N_2 absorption active sites on ruthenium surface. And here alkali metal can also neutralize electronegative substance

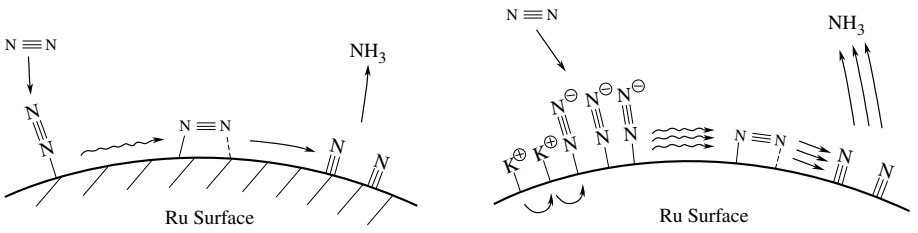


Fig. 6.17 A model of alkali promoter on activation of N_2 over Ru surface

from supports and ruthenium precursor[18] and accordingly increase the catalytic activity.

The effect of alkali metal salt as promoter can be fully shown after it is well reduced under the conditions of ammonia synthesis. The study by Forni *et al.*[111] showed that cesium can prevent metal sintering and increase the dispersion of active components. When activated carbon is used as support, Kowalczyk Z *et al.*[40] considered that the promoting role mainly occur in contact points between ruthenium and cesium adsorbed on activated carbon surface because parts of cesium salt are reduced to metal cesium. As alkali metals are unstable in ruthenium catalysts, (Cs + O) groups also exist, which mainly are distributed on the surface of ruthenium particles. The promotional effect of Cs + O groups is relatively lower when activated carbon is the support, while they play a major role when MgO is used as support, although with a lower extent than that in Cs–Ru/AC.[112]

The effect of alkaline earth metal as promoter still has disputation. Some researchers considered[90,111] that barium as a structural promoter can modify the ruthenium surface and is beneficial to form high active B5 sites. Others considered[110,112,113] that barium is an electronic promoter. Although there is disputation on promoting mechanism of barium, generally, barium atom is uniformly distributed on the surface of ruthenium atom in the form of (Ba + O) under the condition of ammonia synthesis.[90,94,111] Kowalczyk *et al.*[40] proposed the existence forms of cesium and (Ba + O) on the ruthenium surface as Fig. 6.18.

The chemisorption quantity of oxygen on Cs–Ru/C and Cs–Ba–Ru/C containing cesium is larger than that on Ru/C and Ba–Ru/C, which indicates that the cesium

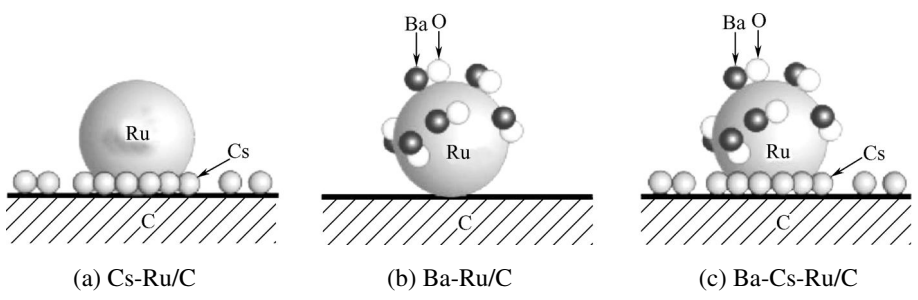


Fig. 6.18 A distributing model of promoters on the M (Cs and Ba)–Ru/AC catalyst at the condition of ammonia synthesis

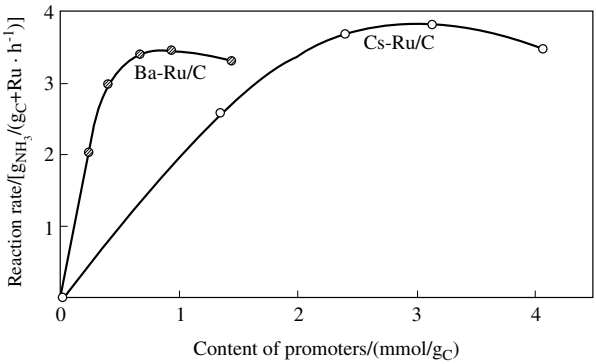


Fig. 6.19 Reaction rate of ammonia formation on Ba-Ru 9.1/C and Cs-Ru 9.1/C catalysts at p = 90bar, t = 400°C, H_2: N_2 = 3:1, xNH3 = 10%

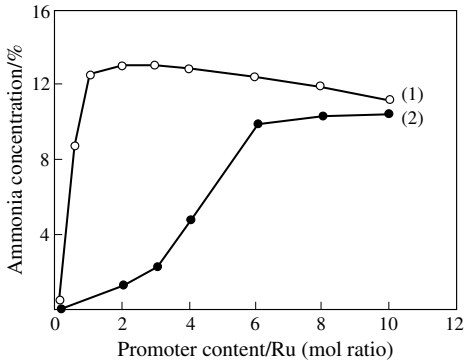


Fig. 6.20 Effect of promoters content on activity on 4% Ru PC catalysts

(430°C, 10.0 MPa, 10,000 h^{-1})(1) 4 wt% Ru 2Ba/C; (2) 4 wt% Ru 2Cs/C

nitrate is highly reduced to approximate zero valences under the condition of ammonia synthesis. It is implied that barium [(Ba + O) adlayer] located on the surface of ruthenium, play the role in structure or electronic promoters, but cesium (Cs^0) located on the surface of activated carbon, play the role in increasing contact point between cesium atom adsorbed on the activated carbon and ruthenium atom[114] (Fig. 6.19).

The loading amount of promoter has great relationship with the nature of promoter such as melting point and fluidity. For example, the influence of promoters ($CsNO_3$ and $Ba(NO_3)_2$) on the activity of ruthenium catalyst was shown in Fig. 6.20. Figure 6.21 shows the influence of Cs and Ba promoter on the pore distribution for 4% Ru/C catalyst. The study shows[115] that the 4% (mass ratio) Ru2Cs/C catalysts with $CsNO_3$ as promoter show high activity only with Cs/Ru > 4 (molar ratio). The activity increases obviously with increasing the Cs/Ru molar ratio. The activity still slightly increases even in the range of Cs/Ru = 6–10. The 4% (mass ratio) Ru2Ba/C shows higher activity with Ba/Ru > 1 (molar ratio). The activity increases with the increase of Ba/Ru molar ratio in the range of Cs/Ru = 1–3.

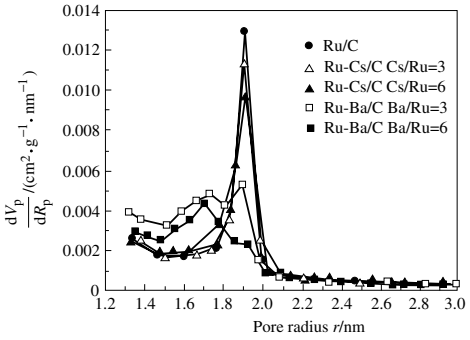


Fig. 6.21 Effect of promoters of Ba, Cs on distribution of pore size on 4% Ru/C catalysts

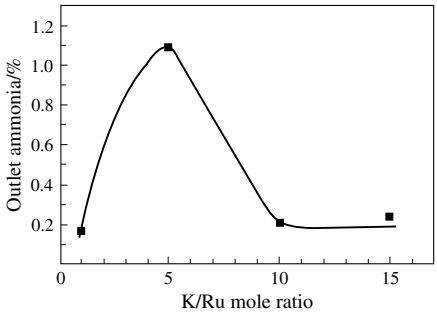


Fig. 6.22 Effect of K content on activity on Ru–K/MgO catalysts (Testing conditions: 475°C, 7.0 MPa, 20,000 h^{-1})

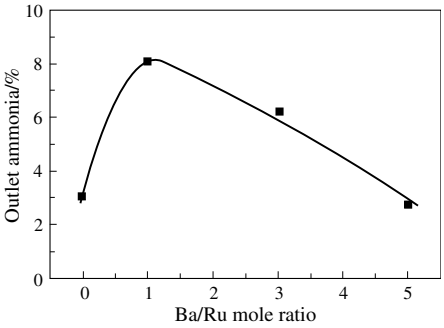


Fig. 6.23 Effect of Ba content on activity on Ru–Ba/MgO catalysts (Testing conditions: 475°C, 7.0 MPa, 20,000 h^{-1})

While the catalytic activity decreases with continuing increasing of Ba/Ru molar ratio.

There are optimum content proportion between promoter and ruthenium. Figures 6.22 and 6.23 show the effect of the content of potassium and barium independently as single promoter on the activity of the ruthenium catalysts. It can

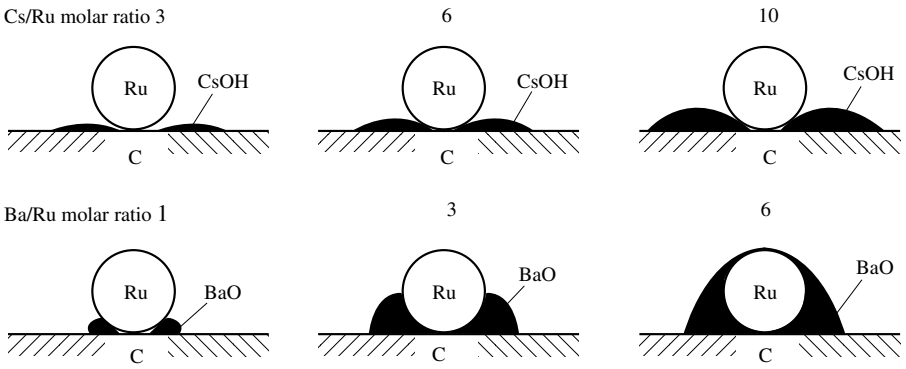


Fig. 6.24 Distribution pattern of Cs and Ba on the Ru/C catalyst surface[115]

be seen from these figures that when potassium is adopted as single promoter the best molar ratio of K/Ru is 5:1 and when Ba is used as single promoter, Ba/Ru is 1:1.

As promoters, the loading amount of alkali metal is more than that of alkaline earth metal. Rare earth metal is similar with alkaline earth metal.[3] The relationship between the distribution of cesium and barium on the Ru/AC surface and content are shown in Fig. 6.24.[116]

It is seen from Fig. 6.24 that the alkali metal hydroxide can be easily absorbed by carbon support due to its low melting point and its large fluidity. Therefore, only with enough quantity, the alkali metal can be accreted on the interface between ruthenium and carbon support and then plays the promotional roles effectively. As alkaline earth metal oxides have high melting point and poor fluidity, small amounts of them can be accreted on the interface between ruthenium and carbon support, which can produce effective active sites. The excessive promoters might cover the active sites of catalyst surface, which can influence the effective contact between active sites of ruthenium surface and reactant gases and therefore decrease the catalytic activity.

In addition, the role of promoter is also related with support. For Ru/AC catalyst, barium and alkali metal are equally effective promoters, while barium and cesium compounds are equivalent promoters. For Ru/MgO catalyst, promotional effect of barium nitrate is much poorer than that of alkali metal nitrate. For Ru/Al_2O_3 catalyst, rare earth metals and alkali metal compounds are equally effective promoters. But in the Ru/MgO catalyst, promotional effect of rare earth compounds is not obvious.

The effect of the types of alkali metal and alkaline earth metal salts on the activity for Ru–M (promoter)/AC with 4% of Ru is shown in Fig. 6.25. When the anions of metal salts are all NO_3^{-1}, the effect of promoters follows the descending order as $Ba(NO_3)_2 > KNO_3 > Sr(NO_3)_2$. When potassium as promoter and anion is SO_4^{-2}, CO_3^{-2}, NO_3^{-1} and OH^{-1}, respectively, except for K_2SO_4 significantly reduces the activity due to the introduction of the sulfur, the influence of the rest anions on activity have little difference wherein nitrate salts are a few better. Obviously, sulfur is also a serious poison for ruthenium catalyst (Fig. 6.26).

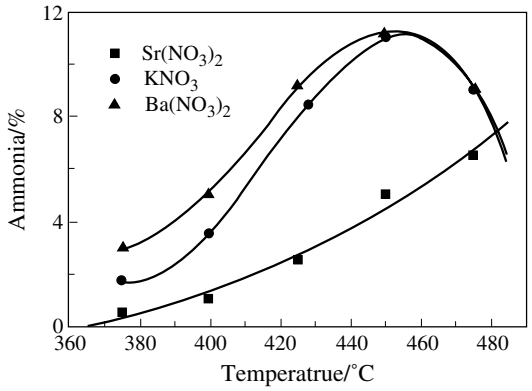


Fig. 6.25 Effect of promoters on activity of Ru–M/AC catalysts (7 MPa, 20,000 h^{-1}, N_2:H_2 = 1:3)

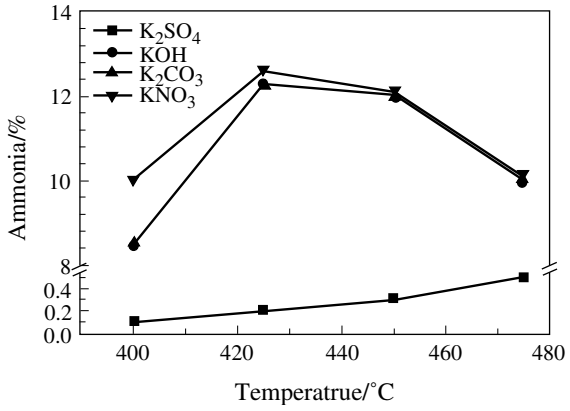


Fig. 6.26 Effect of anions in metal salt on activity of Ru-M/AC catalysts (7 MPa, 20,000 h^{-1}, N_2:H_2 = 1:3)

6.2 Preparation of Ruthenium Catalyst

6.2.1 *Outline*

The preparation methods of ruthenium catalyst include impregnation, melting, precipitation and sublimation. In initial stage of ruthenium catalyst development, coprecipitation method was usually used. But the catalyst prepared by this method has high content of ruthenium and high cost. Melting method has the same disadvantages, so they are seldom used. Impregnation is the most commonly used method to prepare supported metal catalyst, which only needs very low content of metal.

Impregnation is the key and unique step in the impregnation method. It is widely used to prepare catalyst. Usually support is put into solution containing active substance (or with promoter) to impregnate and then remove the remaining solution when impregnation reaches equilibrium, then followed by processing of washing, drying, calcining, activation and so on.

Commonly used porous supports are as follows: Alumina, silica oxide, activated carbon, molecular sieve, alumina silicate, diatomite, pumice, asbestos, pottery clay, magnesium oxide, activated clay and so on. The shape and size of supports can be chosen according to the requirement of catalysts.

Active substances should have large solubility, stability and can decompose into stable active compounds following calcining. Impregnating solution generally is made from nitrate, chloride, acetate, ammonium salt or molten salt such as molten nitrate.

The basic principles of impregnation are as follows: When pores of solid contact with active component-containing liquid, the liquid permeates into capillary due to the roles of the capillary pressure produced by surface tension; the active components in the liquid adsorb on the wall of the capillary or surface of support. In order to increase the amount of the active component adsorbed on support or depth in capillary, sometimes the gas in the pores of support is eliminated by vacuum before impregnation and increasing the temperature (reduce the viscosity) of solution and speed agitation.

Although impregnation method is operated easily, it can often falls across some complex problems. For example, when the catalysts after impregnation of active component are dried, the concentration of the active component in inner surface is lower than the surface because the active materials move to surface even if the support surface is not covered wholly.

Whether the distribution of active substance on transects of supports particle is uniform or not is an important issue. For some reactions, it is not necessary that the active materials are uniformly distributed on all inner surfaces, only on the surface and near surface layer of supports particle. The distribution of active component on supports particle has various types, as shown in Fig. 6.27.

Competitive adsorption is a method to prepare catalysts with various distribution types for active component on the supports transect. According to this method, it needs to add the second components called as competitive sorbent except for active components. Both active component and competitive sorbent is

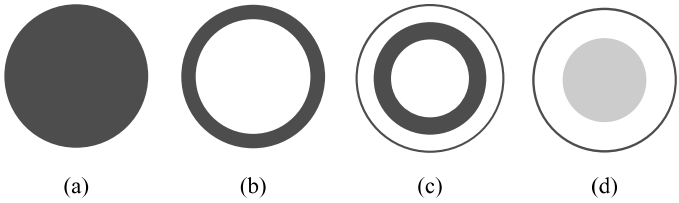


Fig. 6.27 Schematic diagram of distribution type of active component in support

(a) Uniform distribution, (b) Eggshell structure, (c) Egg-white structure, (d) Egg-yolk structure

adsorbed by supports during impregnation. Therefore, two sorbents undergo competitive adsorption with different speed and depth due to the different probability. The distribution types and depths of active component in the supports can be controlled by choosing various competitive sorbents and modifying impregnation process and conditions. For example, the thick eggshell distribution (Fig. 6.27(b)) can be obtained by using lactic acid, hydrochloride and mono-chloroacetic acid as competing sorbent. At the same time, the impregnative depth of active component can be controlled by using different amounts and concentrations of competitive adsorptions.

The impregnation method can be divided into superfluous-, isovolume-, times without number-, depositional-, fluidized spraying- and steam impregnation etc.[117]

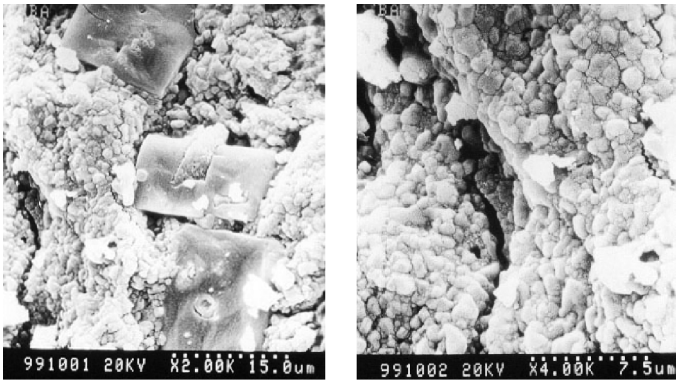
The SEM of Ru-based ammonia synthesis catalyst prepared by isovolume-impregnation is shown in Fig. 6.28. It can be seen from Fig. 6.28 that the active components are dispersed on support in three ways: (i) certain sized active component is dispersed on support unevenly (Fig. 6.28 (a)). (ii) Active component of atom-like state is dispersed on support in cluster (three-dimensional) or raft like (two-dimensional) (Fig. 6.28(b)). (iii) Active component is distributed on the support like accumulated snow (Fig. 6.28(c)), which is an amorphous phase amorphous phase by XRD analysis. Among them, sample 3 has the highest activity in which active component is accumulated like snow on the support after reduced with H_2 at 200°C for 2 h. The sample 1 and 2 are not reduced in H_2 and are just dealt with in vacuum or dried at low temperatures. Their activities are lower, which are only 1/5 to 2/5 of sample 3. It can be seen that the reduction of catalyst with H_2 is necessary during the preparation process.

Impregnation method has the following advantages: First, it could use the support with given shape and size so that we can omit the step of catalyst shaping and currently there are various support supplied in market; second, it could choose suitable support which can provide the necessary physical structure of catalyst such as surface, pore, thermal conductivity and so on; Thirdly, supported components mostly are distributed on the surface of support and its pore and high utilization effect, little dosage, low cost, which is very important for the noble metals catalyst such as ruthenium, platinum, palladium, iridium, rhodium etc. Therefore, impregnation is a simple and economical method so that it is widely used to prepare supported catalyst especially, the low content supported noble metal catalyst. The disadvantage is that the exhaust gas of decomposition during calcining may pollute the environment.

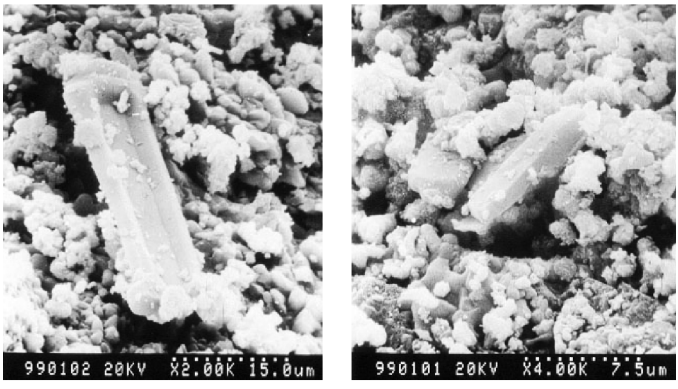
6.2.2 *Pretreatment of supports*

As the support of catalyst, the pretreatment of activated carbon is necessary. The main purpose of pretreatment is to improve the physical structure and chemical properties of the surface in order to meet the requirements of the catalytic supports. The method of pretreatment includes high temperature (graphitization), acid-alkali, gases and microwave treatment and so on.

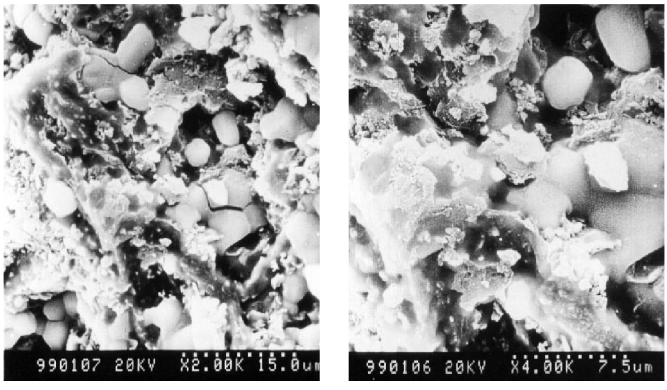
Under ammonia synthesis conditions, Ruthenium is an active catalyst for the activated carbons methanation, which leads to the losing of supports and the



(a) 1# catalyst



(b) 2# catalyst



(c) 3# catalyst

Fig. 6.28 SEM images of Ru-based ammonia synthesis catalyst

sintering of the active component.[111] Therefore, the pretreatment of the activated carbons has special important function. The inhibition of the methanation of activated carbons is one of the research focuses of activated carbons supported ruthenium catalysts.

6.2.2.1 *Graphitization of activated carbons*

The carbon containing graphite which is called as graphitized activated carbons was developed successfully by British Petroleum Company (BP) in 1974.[118] This carbon has good dispersion and stability because the supported metal atoms can be distributed in the reticular tissue of graphite. The graphitized activated carbons have more excellent character than the activated carbons because that graphite has more strong ability of transmitting electron and more stable structure.[119] BP and Kellogg realized the industrial application of ruthenium catalyst supported on graphited activated carbon in 1990.[119] The fundamental steps to prepare carbon containing graphite by BP are as follows[119]: (i) Original heat treatment in the inert atmosphere at 900°C–3,300°C, (ii) Oxidation at 300°C–1,200°C, (iii) Further heat treatment in the inert atmosphere at 900°C–3,000°C (should not exceed the temperature of original heat treatment). And the inert atmosphere can use nitrogen when the temperature is below 1,000°C, and argon and helium over 1,000°C. Oxidation medium is air at 300°C–450°C, and steam or CO_2 at 800°C–1,000°C. When heating in inert atmosphere, part of carbon transformed into graphite. The activated carbons treated by this way can increase the activity of ruthenium catalysts (Table 6.9).

The activated carbons treated by graphitizing have some characters as following: The specific surface area of main face is larger than or equal to $100\,m^2/g$, the ratio of the BET surface area to the surface area of main face is small than or equal to 5:1, the ratio of specific surface area of main face to edge is larger than or equal to 5:1, the pH value is in the range of 5–9, the amount of oxygen adsorption is small than or equal to 0.5%, the content of ash is smaller than or equal to 0.1%. BP Company prepared catalysts for ammonia synthesis by using their graphitized carbons as supports, alkali and alkaline earth metal nitrate as promoters, and all kinds of ruthenium compounds as precursors. The activities of these catalysts are 10–20 times more than that of traditional fused iron catalysts.

Generally, the processes of the heat treatment at high temperature (graphitization) include two steps of graphitization and activation of graphitized activated carbon. The purpose of the first step is to make part of activated carbon graphitization in high temperature and the second one is to recover the pore structure of activated carbon at oxidizing atmosphere.

Figure 6.29 shows the XRD spectra of the activated carbons after heat treating in different temperature. The diffraction peaks of activated carbons (AC) are very wide, and there are two smooth wide peaks at the range of 20°–30°, 40°–48° of 2θ from Fig. 6.29. The two peaks correspond the diffraction peaks of (002) face and (100) face in graphite structures, respectively. This is caused by the irregular

Table 6.9 Effect of graphitization of activated carbons on the activity of Ru/AC catalyst

Treatment of activated carbon	BET/$(m^2 \cdot g^{-1})$	Yield of ammonia/%
Without	1,300	1.6
At 1,500°C	700	3.2
At 2,600°C	220	5.1

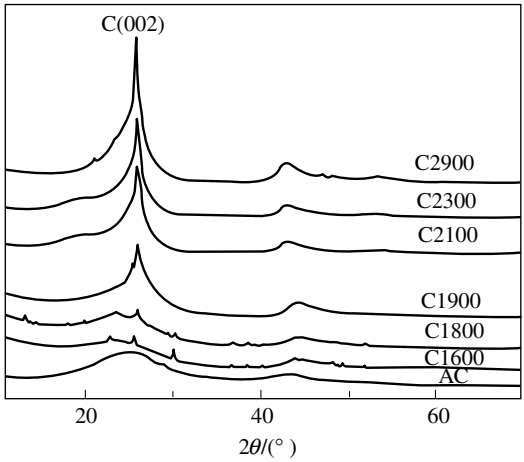


Fig. 6.29 XRD spectra of activated carbon after thermal treatment

arrangement of microscopic graphite crystal in activated carbons. Activated carbons belonged to microcrystalline carbon morphology and its characteristic peaks cannot be detected by XRD, shows amorphous structure. The distance between lattice inner layers is about 0.35 nm–0.37 nm little larger than 0.335 nm of graphite and generally, the thickness of crystallite is 1 nm–1.5 nm which is about the thickness of 4–5 layers mushy face. Therefore, it has the character of micro crystallization.[42,120] This kind of microcrystalline carbon as catalytic supports has some unique characters, such as high specific surface area and microporous structure. Heat treated activated carbons (C1600–C2900) show sharp characteristic peaks C (002) of graphite in different degree. And the C (002) peaks enhance gradually, the impure diffraction peaks decrease gradually with the increasing temperature of heat treatment. Therefore, the impure species in activated carbons can be eliminated and can form part of graphitized structure at the condition of high temperature. The high the temperature, the high the degree of graphitization is. Relatively more pure activated carbons with different graphitized degree can be obtained after the vacuum treatment at 1,600°C–2,900°C. However, the too high temperature also damages badly the structure of activated carbons. It is difficult to recover the pore structures, even the oxidation treatment subsequently, the activities of the supported ruthenium catalyst will be decreased.[121]

At the same time, heat treatment can also enhance the surface alkali and conductivity of activated carbons. The alkaline of the graphitized carbon is not caused from the alkaline groups on surface but from formation of the layered structure of graphite and the effect of the conjugated big π-bond delocalized electrons. Therefore, heat treatment can enhance the stability of activated carbons obviously, including the stability on water and carbon oxides, avoiding methanation under the ammonia synthesis reaction condition of high temperature and high pressure. These structural modification and character change are beneficial to the preparation of ruthenium catalysts and enhances the whole performance of ruthenium catalysts. Both of the chemical composition and physical structure of activated carbons have different

Table 6.10 Chemical compositions of activated carbon after heat treatment

Temperature of heat treatment	Chemical composotions of activated carbon/wt%					
	C	H	N	S	O	Ash
Without	91.79	1.43	0.81	0.19	2.42	3.36
At 1,600°C	93.52	1.25	0.58	0.16	1.75	2.74
At 1,800°C	95.98	0.98	0.33	0.03	0.58	2.10
At 1,900°C	97.04	0.57	0.24	0.02	0.38	1.75
At 2,100°C	97.85	0.23	0.04	0.01	0.26	1.61
At 2,300°C	98.55	0.11	0.03	0.01	0.05	1.25
At 2,900°C	99.42	0.07	0.02	0.01	0.03	0.45

Table 6.11 Physical structure of activated carbons after heat treatment

Temperature of heat treatment	BET/$(m^2 \cdot g^{-1})$	$V_{total}(P/P_0 = 0.99)/(cm^3 \cdot g^{-1})$	$V_{meso}/(cm^3 \cdot g^{-1})$
Without	1,023.2	0.5514	0.1814
At 1,600°C	628.4	0.3826	0.0809
At 1,800°C	543.6	0.2580	0.0684
At 1,900°C	354.6	0.1905	0.0654
At 2,100°C	142.8	0.0875	0.0424
At 2,300°C	28.2	0.0257	0.0200
At 2,900°C	1.5	0.0039	0.0030

degree change after graphitized treatment at high temperature (see Tables 6.10 and 6.11).

It is seen from Table 6.10 that heat treatment has large effect on the chemical composition of activated carbons. The content of carbon is about 91.79% and content of non-carbon is about 8% in original activated carbons. By increasing the temperature of the heat treatment, the content of carbon element is increased and the content of impurities is decreased. The total content of impurities except carbon is 0.58% when the temperature is 2,900°C, wherein, the content of ash is 0.45%. In the high-temperature graphitizing process of the activated carbons, on the one hand, the chemical bonds among the surface atoms (include heteroatom) are continuously recombined and arranged, so that the bonds break and the heteroatom are removed gradually. On the other hand, the crystallization degree of the activated carbons are increased and the pore structures and distribution of the raw materials as well as the surface electrical properties are improved. Therefore, activated carbons with special surface characters and pore structures can be obtained through controlling the graphitized degree.[119]

The effect of the surface structures of activated carbon on catalytic properties is large. Therefore, for the activated carbons as the support of ammonia catalysts, there are more rigorous and special demands, especially the surface area, mesoporous structure and surface groups. It can be seen from Table 6.11 that the specific surface area, whole pore volume and mesoporous volume of activated carbons are decreased apace and the pore structures are destroyed after heat treatment.

Table 6.12 Effect of oxidation on physical structure of activated carbons after heat treatment[a]

Temperature of heat treatment	BET/($m^2 \cdot g^{-1}$)	V_{total}/($cm^3 \cdot g^{-1}$)	V_{meso}/($cm^3 \cdot g^{-1}$)
Without	1023.2	0.5514	0.1814
At 1,600°C	992.6	0.4512	0.0940
At 1,800°C	891.8	0.4109	0.0712
At 1,900°C	811.8	0.3889	0.0665
At 2,100°C	511.5	0.2585	0.0575
At 2,300°C	147.2	0.0910	0.0471

[a]The conditions of oxidation are atmospheric pressure, 10% O_2 + 90% N_2, flow of 200 ml/min and temperature of 450°C for 16 h.

Therefore, the graphitized activated carbons acting as the catalytic supports are inadvisable. In order to recover the surface area and pore structure of activated carbons, it should be treated *via* oxidation and so on.

The activation is a key process to prepare graphitized activated carbons, which includes the process of complicate chemical reactions between activator and the carbon materials. The main role of activation is further extension of the original pores, formation of new pores as well as coalition and connection between pores based on the pores of graphitized carbon. Therefore, the graphitized carbon products with larger specific surface area and more reasonable distribution of aperture would be obtained by activation.

The common activators include oxidative gas, hydroxide of alkali and alkaline earth metal, inorganic salts and some acids. The physical structures of activated carbon treated with 10% O_2 + 90% N_2 are shown in Table 6.12.

It is seen from comparison of Table 6.12 and Table 6.11 that the surface area and pore volume are recovered in great degree after activation by oxygen–nitrogen gas mixtures. During the progress of graphitization, parts of pore structures in the activated carbons collapsed. After activation, the pore volume increased obviously because parts of micropore enlarged by removing of the stemming at the inner orifice of activated carbons. The high the temperature of graphitization, the more obvious the graphitized degree, the more serious the damage of activated carbon structure and the more difficult the recovery is. It is very difficult to expand pore size on highly graphitized activated carbon due to the highly stable of graphite. A rule can be seen from comparing Table 6.11 and Table 6.12 that the specific surface area of the activated carbons (OC1600) after heat treatment at 1,600°C is recovered from 628.4 m^2/g to 992.6 m^2/g, account for 97.01% of original carbons, the (OC1900) is 811.8 m^2/g, occupied 79.29% of original carbons when the temperature is 1,900°C and is low than 50% of original carbon when the temperature is over 2,100°C.

The effect of temperature and time by oxidation on the recovery of the surface structures and activities of catalyst with the graphitized activated carbons as support are shown in Table 6.13. Both of the surface areas and pore volume are recovered in largest degree when the temperature of activation is 450°C. When the temperature is too low the reaming ability of gas is not strong enough and therefore the reaming effect is unsatisfactory, while too high temperature will get

Table 6.13 Effect of time and temperature of oxidation on the activated carbons and catalytic activity

Sample[a]	Time/h	Temperature/°C	BET/ $(m^2 \cdot g^{-1})$	V_{total}/ $(cm^3 \cdot g^{-1})$	V_{meso}/ $(cm^3 \cdot g^{-1})$	NH_3(vol)/%[b]
OC1900	16	400	591.3	0.2941	0.0626	11.28
OC1900	16	450	811.8	0.3889	0.0665	16.24
OC1900	16	500	756.3	0.3589	0.0635	12.98
OC1900	12	450	680.9	0.3007	0.0476	9.65
OC1900	20	450	796.3	0.3029	0.0546	11.85
OC1900[c]	16	450	929.5	0.5405	0.1006	19.18

[a]The activated carbons were treated with oxidation at 450°C after heat treatment at 1,900°C.
[b]Testing condition: p = 10 MPa, T = 400°C, GHSV = 10,000 h^{-1}.
[c]Treated with HNO_3 after treatment with oxidation and heat treatment.

contrary result because of the amount of burnt carbon. Too long or too short time, the expanding pore treatment cannot achieve the optimal effect. On the range of test, the surface area and pore volume can be recovered in maximum degree in 10% O_2 + 90% N_2, when the temperature is 450°C for 16 h as shown in Table 6.13.

Another important purpose of graphitization of activated carbon is in order to prevent its methanation during ammonia synthesis conditions. This will be discussed in detail in Sec. 6.3.4.

6.2.2.2 *Acid treatment*

Some studies have shown that the surface oxygenic functional groups on activated carbons are the active adsorption sites for some metal ions.[75,76,122] From Table 6.13, the graphitized carbons with high purity and high stability can be obtained after high temperature graphitization and removing impurity and surface groups. The surface areas and pore structures of graphitized carbons are a certain extent recovered after activation at oxygenous atmosphere. Therefore, it has the fundamental requirements as supports of ammonia synthesis catalysts. However, the activities of the catalysts are not high because the surface oxygen-containing groups have been damaged badly during the graphitization and activation. The impregnation of active components and promoter are very difficult due to the influence of the surface polarity on the activated carbons. In order to prepare high active catalysts it is necessary that changing the surface polarity, recovering or enhancing the quantity of the useful surface groups of the activated carbons and changing the wetting property of supports which are beneficial to the adsorption and the enhancement of dispersion of active components. For example, under the conditions of 10 MPa, 400°C, and 10,000 h^{-1}, the ammonia concentration in outlet of reactor reached 19.18% for the sample with graphite carbons as the supports of OC1900 with the modified by HNO_3 in Table 6.13. Therefore, it is necessary to further modify the surface of activated carbons by HNO_3 treatment.

Therefore, further acid treatment is necessary on both original activated carbons and these after high temperature graphitized and oxidation treatment can introduce the surface oxygenous functional groups.[123,124]

Table 6.14 Effect of acid treatment on character of activated carbons

Samples	$V_{micro}/(ml \cdot g^{-1})$	$S_{meso}/(m^2 \cdot g^{-1})$	$O_{tatal}/\%$	Ash/%
A_1	0.372	126	6.46	2.80
A_5	0.575	173	15.51	3.81
A_{11}	0.393	146	13.37	1.92

Note: A_1 is the original activated carbons, A_5 is the product of A_1 treated in 5% O_2–N_2 at 425°C for 20 h, A_{11} is the product of A_1 treated in 5 M HNO_3 for 6 h at its boiling point.

The oxidation of activated carbons can be divided into two types: Gas–phase oxidation and liquid phase oxidation. The gas–phase oxidation is to heat activated carbons[125] at the oxygen-contained inert gas and the most common oxidant is HNO_3 in the liquid phase oxidation,[75,126–131] the other oxidants include HCl, HClO, HF,[74] H_2O_2,[132] and O_3^{133} and so on. The liquid phase oxidation can introduce oxygen-containing functional groups and can remove the ash in activated carbons. The effect of the different oxidation treatment on the activated carbons performances are listed in Table 6.14.[132]

The treatment by nitric acid on activated carbon (AC) belongs to the surface oxidation technique. It is a kind of the common methods of chemical modification of activated carbon because it can both regulate the pore structures and change the chemical property of activated carbon. At present, surface oxidation is the main method to increase the surface oxygenous functional groups and adjust the surface polarity of activated carbon. Activated carbons belong to non polarity adsorption materials. According to the similarity attraction principle, it has strong adsorption ability for hydrocarbon and organic vapor, generally. If the contents of the main oxygen-containing functional groups on surface are enhanced, it can widen the application range under the condition of adjusting the surface polarity. The studies by Abdel-Nasser[134] and Authors[135,136] have shown that the contents of all kinds of oxygen-containing functional groups and the hydrophilicity on surface is increased significantly after treated by HNO_3.

He-TPD-MS of activated carbons treated by different methods are shown in Fig. 6.30. The types and contents of the surface groups have large changes after

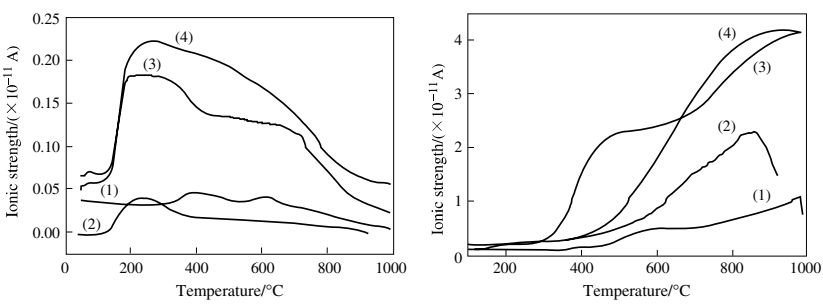


Fig. 6.30 The He-TPD-MS spectra of the activated carbons

(1) after graphitization treatment at 1,900 for C1900, (2) without treatment, (3) after by gas oxidation for C1900, (4) After treated by HNO_3 for C1900.

Table 6.15 Surface structures of activated carbons and the dispersion of active metal

Supports	A_{BET}/ $(m^2 \cdot g^{-1})$	S_{meso}/ $(m^2 \cdot g^{-1})$	V_{total}/ $(ml \cdot g^{-1})$	V_{micro}/ $(ml \cdot g^{-1})$	Ru dispersion/ %	Ru particle size/nm
AC1	760.53	177.42	0.4613	0.2903	22.51	5.26
AC2	771.22	181.58	0.4762	0.3001	23.16	5.01
AC3	987.73	384.16	0.6801	0.5468	34.67	4.13

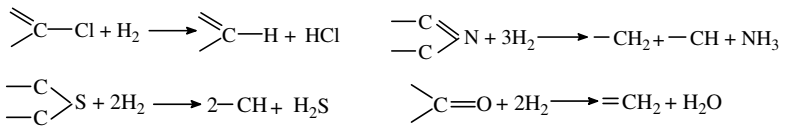
Note: AC1 is original activated carbons, AC2 is AC1 after treated in 5 M nitric acid for 12 h; AC3 is AC1 treated in 5% O_2–N_2 at 425°C for 12 h. The catalyst is reduced by H_2 at 400°C for 4 h.

treating by graphitization, oxidation and acid treatment, respectively. The amount of either CO or CO_2 liberation is very low after graphitization. It indicates that the graphitized treatment can eliminate the impurity and the surface active groups (include carboxyl, anhydride, phenol carbonyl, quinonyl, lactone and aether *et al.*). After gas oxidation and acid treatment, the amount of CO and CO_2 released from graphitized activated carbon is increased, indicating that the surface oxygen-containing groups are greatly increased. Therefore, the hydrophilicity and polarity of activated carbon surface is increased.

The relationship between surface structures of the activated carbons and the dispersion of active metal is shown in Table 6.15. It can be seen from Table 6.15 that after oxidation treatment, especially the gas phase oxidation, the pore structures of activated carbons are improved, and the dispersions of Ru are enhanced.[127]

6.2.2.3 *The treatment in H_2 or inert atmosphere*

Some surface groups can be eliminated and the surface alkaline can be enhanced when activated carbon is treated at high temperatures in the H_2 or inert atmosphere.[12,137,138] Aika *et al.*[17] have studied the effect of H_2 treatment on the character of activated carbons. They



considered that the following reactions will happen during the process of H_2 treatment at 950°C. It is seen from Table 6.16 that this method can efficiently remove the surface acidic impurities such as Cl, N, S and O etc, while the surface area and the pore structures of the activated carbons do not change obviously.

With the elimination of the impurities which can accept electrons, the activity of catalyst is increased obviously. The activities of catalysts using different types of untreated activated carbons as supports are low and the activity differences are very large. However, after treatment by H_2 at high temperatures, they all show the same high activity.

Table 6.16 Element analysis of activated carbons and effect of treatment with H_2 (wt%)

Source	Treat conditions	S_{BET}/ $(m^2 \cdot g^{-1})$	H	C	N	Halogens	$S(SO_4^{2-})$	Else
#76	Untreated	934	1.11	88.77	0.21	3.58	0.57	5.76
	950°C 4 h	934	0.34	94.47	—	n.d.	0.13	5.06
	950°C 12 h	1078	0.17	95.49	0.16	n.d.	n.d.	4.18
#80	Untreated	1084	1.17	92.42	—	2.84	0.46	3.11
	950°C 48 h	914	1.08	93.29	—	n.d.	n.d.	5.63
#75	Untreated	1007	1.00	92.51	—	n.d.	n.d.	6.49
	950°C 48 h	978	0.69	96.67	—	n.d.	n.d.	2.64

Note: n.d. indicate not been detected.

Table 6.17 Effect of microwave on the characters of activated carbons

Sample	Time of microwave treatment/min	Content of ash (%)	$S_{BET}(m^2 \cdot g^{-1})$	$V_T(ml \cdot g^{-1})$	$V_M(ml \cdot g^{-1})$
C	Original activated carbon	6.86	825.6	0.50	0.43
CW2	2	2.60	838.3	0.49	0.45
CW5	5	1.15	823.2	0.48	0.43
CW10	10	0.99	789.6	0.42	0.37
CW30	30	0.97	705.8	0.39	0.34

Note: V_T is total pore volume and V_M is the volume of the mesopore.

6.2.2.4 *Microwave treatment*

The time (1 ns–1 ps) of one vibration period of the microwave alternating electric field is consistent with the relaxation time of turning medium dipole to polarization or interfacial polarization. Therefore, the microwave heating can turn its electromagnetic energy into heat energy. The microwave treatment for activated carbons can achieve the high temperature from inner to outer in short time and remove the impurities on the surface, but does not change the surface structures of activated carbons obviously.[139] Therefore, microwave is introduced into the treatment of activated carbons.[140] The effect of microwave treatment on the characters of activated carbons is listed in Table 6.17.

The study has shown that under the protection of the nitrogen, activated carbons treated by microwave for five minutes, can increase the catalytic activity without obvious change in the surface area and the pore volume. Therefore, microwave treatment can avoid sintering of metal particles in special range of temperatures and it is possible to enhance the performance of catalysts.

A lot of studies have shown that different treatment methods have different effect on the characters of activated carbons and finally on the performance of catalysts. The surface of activated carbon as supports should have different performances for different active components and different catalytic reactions. Therefore, the activated carbon as supports, proper treatment based on given catalytic reaction can

improve the performance of the catalysts. This is one of the unique advantages of the activated carbons as the supports of catalysts.

6.2.3 *Impregnation*

6.2.3.1 *Impregnation methods*

Like the other noble metal catalysts, ruthenium catalysts are prepared with impregnation method, commonly. Practical operating methods include solution-superfluous, equal-volume, multi-time and impregnation-precipitation and so on.

The practical operation step of impregnation is simple. For example, the dried support is put into a vessel which has the solution containing the active component with definite pH value in agitated or static state. Here, the air in the pores of supports is expulsed depending on the capillary pressure of the solution. Generally, the air in the pores of supports should be vacuumed in advance. The redundant solution can be removed by methods of filtration and followed by drying, calcining and so on. The redundant solution can be reused without any treatment or with simple treatment. The volume of the solution is more than that of supports can absorb for solution-superfluous method and is equal to that for isovolume method. However, it should be noted that the volume of solution which can be absorbed is a function of property of impregnated compounds and the viscosity of the solution. It should be determined by premeasurement.

In order to prepare the catalysts with high concentration of active component or the multi-component catalysts, impregnation, drying and calcining are performed many times repeatedly. This is called multiple impregnation method for catalysts with high concentration of single active component or fractional impregnation method for catalysts with multi-component. There are two reasons to use the multiple impregnations: First, due to the low solubility of the impregnated compounds, the small loading in one impregnation, therefore, many times impregnation is necessary, repeatedly. Second, in order to avoid the competitive adsorption of the components, it should be impregnated in turn. After each impregnation, the drying and calcining are needed, so make them transform into insoluble substance. This can prevent the compounds impregnated on the supports being redissolved into the solution and can increase the uptake of active species. The multiple impregnations are a complex process, with low efficiency and high cost. Unless the special circumstances of the necessity, it should be avoided as possible.

In order to increase loading amount of active component, it should be considered that the competitive adsorption takes place between the two kinds of ions in the precursor compounds, which sometimes is used as special material called as competitive sorbent. For instance, the addition of some acetic acid into the solution can change the distribution of platinum on the supports when the platinum reforming catalysts are prepared. The catalytic activity has a maximum value when the amount of acetic acid reached a certain ratio.

In order to obtain the uniform distribution of active component on the inner surface of the supports and impregnation depth, the air in the supports should be removed in vacuum condition before impregnation or the impregnate temperature should be increased.

Table 6.18 Effect of preparation methods on the catalytic activity

Sample	Preparation process	Concentration of ammonia % 400°C	425°C
Z183	Impregnate $Ba(NO_3)_2$, drying, impregnate $RuCl_3$, drying and reduced, and impregnate the KNO_3	19.78	19.46
Z184	Impregnate $Ba(NO_3)_2$, drying, Reduced $Ba(NO_3)_2$, impregnated $RuCl_3$, the others are same to these of the Z183	16.79	19.10
Z185	Twice impregnated $RuCl_3$, and reduced after each impregnation, the others are same to these of the Z183	20.49	19.88
Z186	Twice impregnated KNO_3, and reduced after the first impregnation, the others are same to these of the Z183	20.90	19.57

Note: The condition of the activity test is H_2: $N_2 = 3$, 10 MPa, 10,000 h^{-1}.

The impregnation time of the support is determined by the structure of it, solution concentration and temperature and so on. The time may be a few minutes, hours, even several dozens hours.

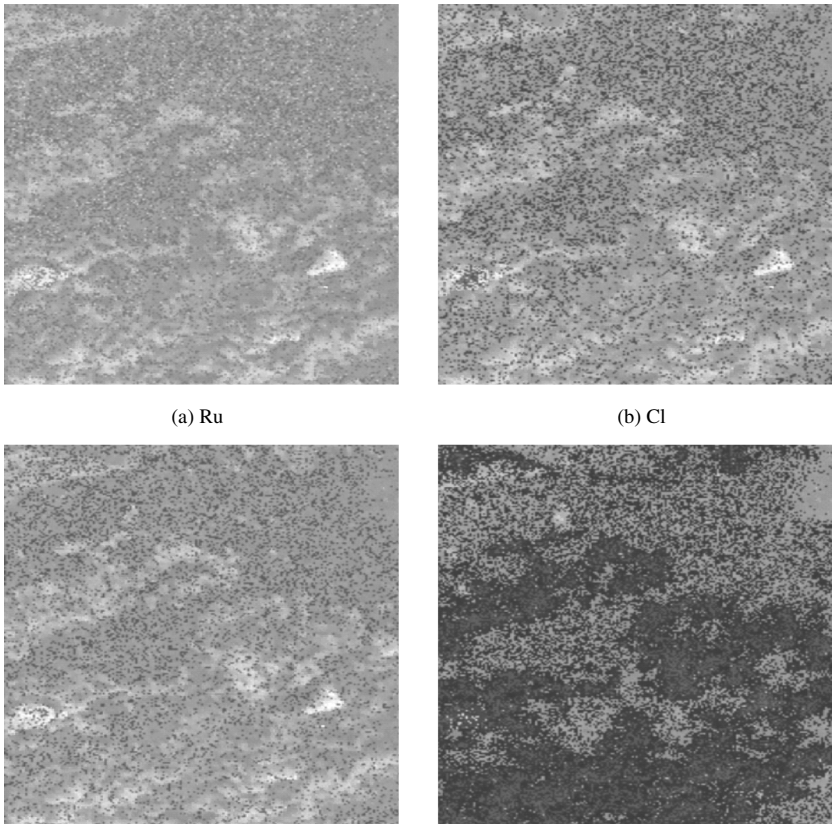
Fractional impregnation is commonly used for the preparation of the Ru–Ba–K/AC catalyst. Generally after the $RuCl_3$ solutions are impregnated, drying and calcining are necessary and subsequently the barium nitrate and potassium nitrate are impregnated in turn according to the above steps repeatedly.

The effect of different preparation methods on the catalytic activity is shown in Table 6.18.

It can increase the catalytic activity, either promoters or the active components are impregnated in multi-times because it can increase the effect of impregnation. Especially the impregnation of KNO_3 is very important. The multi-times impregnation can increase the catalytic activity at low temperatures. But the method of Z184 decreases the catalytic activity. It is possible that the first reduction of the $Ba(NO_3)_2$ is disadvantageous to the loading of the active components. The distributions of the components of Z186 measured by energy spectrum are shown in Fig. 6.31.[141] It can be seen from Fig. 6.31 that the active component of Ru and promoter of Ba are distributed very uniformly, but promoter of K is accumulated because there is more KNO_3 deposited on the supports after twice impregnation. Alkali metals are serving as electronic promoters for ruthenium catalysts. Due to their low melting point and high mobility, they can be easily adsorbed on the supports. Only when enough alkali metal is added, they can adsorb on the interface between ruthenium particles and carbon supports, which will help to play promotional effect.[142] There is chlorine (Cl) in the samples from Fig. 6.31, which indicates that the reduction of $RuCl_3$ and elimination of chlorine ions are not yet complete.

6.2.3.2 *The influencing factors during impregnation*

(1) **The influence of loading order.** For the multicomponent catalysts prepared by stepwise impregnation, the impregnation order of whether the active component or the promoter is introduced first has some effect on the dispersion of the active metal and the catalytic activity. For example, Ba–K–Ru/AC catalysts, BP have considered that the catalytic activity is independent on the loading order of the



(a) Ru (b) Cl

(c) Ba (d) K

Fig. 6.31 Distribution of the components in catalyst

components in which the promoters can be loaded before or after loading of active component (Ru). But Alberta research committee has considered that the loading order of the components have great effect on the catalytic activity when they used both alkali metal hydroxide and barium nitrate as the promoters. The barium should be first loaded and then is the ruthenium and the last is the potassium one.[143] The author *et al.*[144] has found that the loading order of the components has great effect on the dispersion of the active metal and the catalytic activity (Table 6.19). It can be seen from the Table 6.19 that the catalytic activities of the samples 95 and 96 in which promoters are first loaded, are obviously higher than those of the samples 97 and 98 in which the ruthenium is first loaded. The reason is probably that the ruthenium can be covered by the promoters, when the ruthenium and then the promoters are loaded. Furthermore, the parts of ruthenium directly contact with the activated carbons and the activated carbons can absorb some electrons from the ruthenium which makes the ruthenium part unable to play the catalytic role, so that to decrease the catalytic activities. And it is seen from Fig. 6.32 that there is much more KCl on the surface of the sample 96 and the chlorine is the serious poisons of the catalysts. Obviously, the dissolution again and again in the subsequently loading process affects seriously the dispersive property and

Table 6.19 Effect of loading order on the performances of Ba–K–Ru/AC catalysts

Catalyst No	Loading order	CO uptake/ ($cm^3 \cdot g^{-1}$)	Ru dispersion/%	Ru surface area/($m^2 \cdot g^{-1}$)	Ru grain size/nm	Activity (v/v)%	
						425°C	400°C
1	Ba→Ru→K	1.57	17.7	64.7	7.60	17.26	14.20
2	K→Ru→Ba	1.63	18.3	67.0	7.34	15.32	10.78
3	Ru→Ba→K	1.47	16.5	60.4	8.14	13.41	8.07
4	Ru→K→Ba	1.52	17.2	62.7	7.85	13.74	8.06

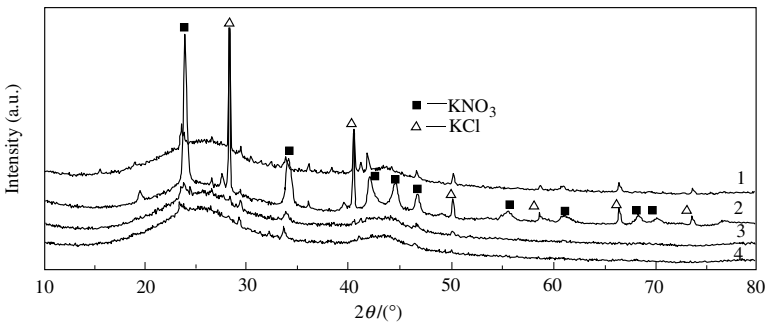


Fig. 6.32 XRD spectra of catalysts prepared by different impreagnating order

the crystallization is more complete due to the good solubility of the potassium. But the state of potassium in the other samples almost is amorphous phase and is well dispersed. It is noteworthy that large amounts of KCl are generated due to the ionic exchange in the process of the impregnation of $RuCl_3$ after loading of potassium. The chlorine ion in the KCl is hardly eliminated subsequently in the reduction and activation process of catalyst due to the stability of KCl. The chlorine can attract the electrons from ruthenium, decrease the electron density of the ruthenium, and is disadvantageous to the adsorption of nitrogen, and affect the activity for ammonia synthesis. Therefore, barium should be the first loaded component, then ruthenium and the last is potassium. Loading of barium is in order to prepare good surface for loading of active component of ruthenium. The strong alkali potassium is loaded last so that it is beneficial to increase the catalytic activity.

(2) **The effect of solvent.** For these catalysts prepared by the impregnation methods, the solvent has direct influence on the loaded effect and loaded amount of active components of $RuCl_3$. The water, acetone, ethanol and tetrahydrofuran (THF) etc. can be used as the solvents of the $RuCl_3$ solution. Table 6.20 shows the effect of four kinds of solvents on the dispersion, surface area and particle size of ruthenium.[141] It is seen from Table 6.20 that different solvents have great effect on the loading effect of the active components. The dispersion of ruthenium is the highest when H_2O is used as solvent, while with THF as solvent, the dispersion of ruthenium is the lowest and the catalytic activity is the worst. However, a lot of researchers considered that the effect of the acetones is better than that of the H_2O, which is related probably with the surface characters of the activated carbons, especially the hydrophilicity. The surface of the ordinary activated carbons is hydrophobicity,

Table 6.20 Effect of solvents on loaded effect of ruthenium

Solvent	Uptake of CO/ ($cm^3 \cdot g^{-1}$)	Dispersion of Ru/%	Surface area of Ru/($m^2 \cdot g^{-1}$)	Grain size of Ru/nm
H_2O	4.55	51.0	187.2	2.65
Acetone	2.70	30.40	111.04	4.43
Ethanol	4.03	45.48	166.14	2.96
THF	2.61	29.39	107.36	4.58

which should become hydrophilicity or remain as hydrophobicity after treating by different methods. For the hydrophobic activated carbons the dispersion of ruthenium will certainly be affected by using $RuCl_3$ aqueous solution. If the surfaces of activated carbons are changed into hydrophilicity, when acetone is used as solvent of $RuCl_3$ solution, the $RuCl_3$ can easily be precipitated in the acetone solution, form larger particles and is deposited on the surface. After reduction, the ruthenium particles on the surface of catalyst are very large which lead to low dispersion of ruthenium and activity. Therefore, the selection of the solvents is determined on the hydrophilicity or the hydrophobicity of the support and the solution.

(3) **The effect of the impregnation time of $RuCl_3$.** When the impregnation solutions contact with the supports with pores, the solutions can infiltrate into the center of the supports until the pores are filled due to capillary phenomenon. The infiltration takes only several minutes, which is not equal to the impregnating time. The infiltration of the solution into the pore center does not mean that the solution has been evenly distributed. If there is adsorption between the solution and the support, to achieve uniform distribution of solution on the support surface, solution must reach adsorption equilibrium inside pore, which requires more time than that of infiltration. The studies show that the impregnation time is ranges from several hours to days. Activated carbons as supports have large surface area, rich pores and complicated surface properties. During the impregnation, Ru^{3+} ions need the process of the diffusion and adsorption on the activated carbons surface. It needs enough time in order to realize the uniform distribution of ruthenium. At short impregnation time, ruthenium is mainly distributed at the orifice and edge of pore due to the inadequate diffusion of $RuCl_3$. At long impregnation time, $RuCl_3$ can uniformly distribute because of its diffusion from the orifice to the inner pores of the activated carbons.

We[145] studied the effect of the impregnation time on the activity and the structure of Ru/AC catalyst (seen in Figs. 6.33 and 6.34). Under the experimental conditions, the catalytic activity increased gradually with the increasing time of impregnation. When the impregnation time is more than 18 h, the differences are small in activity. Therefore, it is enough to select the 18 h of impregnation time during the preparation of catalysts.

It is seen from Fig. 6.34, based on the results by scanning electron microscopy that part of ruthenium particles show aggregated status, large size and distributed unevenly when impregnation time is 3 h and 6 h, respectively. It can be seen from Fig. 6.34(c) that when impregnation time is 18 h, ruthenium is evenly distributed over surface of activated carbon and the pore orifice of support which is very clearly eyeable without obvious blocked objects.

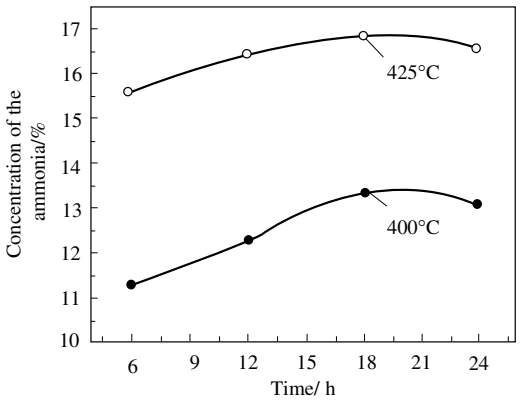
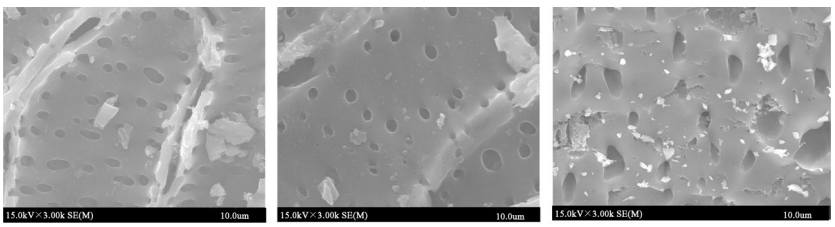


Fig. 6.33 Effect of impregnation time on the activity of Ru/AC catalyst. Reaction conditions: N_2:H_2 = 1:3, 10 MPa, 10,000 h^{-1}



(a) 3h (b) 6h (c) 18h

Fig. 6.34 SEM profile of the Ru/AC catalyst with different impregnation time

(4) **The effect of pH of $RuCl_3$ solution.** According to the theory of isoelectric point, the surface charge of supports and ionic charge are dependent on the interaction between supports and precursors of components. There is the pH value of the isoelectric points which is denoted as pH_{IEP}. The charge on the support surface is zero with the $pH = pH_{IEP}$ value. When the $pH > pH_{IEP}$, the support will adsorb the cations in the solution and $pH < pH_{IEP}$ the anion in the solution. The pH value in isoelectric point of the activated carbons after treating with acid and hydrogen is about eight. Therefore, according to point of view of the isoelectric point, in order to make the activated carbons adsorb Ru^{3+}, the pH value of the impregnating solution should be the higher than eight during the progress of the impregnation. In fact, during the impregnation, $RuCl_3$ is easily hydrolyzed with water as solvent and the hydrolyzed degree is different with different pH values. The pH value of $RuCl_3 \cdot 3H_2O$ aqueous solution is regulated by the mixture of nitric acid and ammonia and the effect of pH value of this solution on the catalytic activity is investigated as shown in Table 6.21. When activated carbons as supports, the pH of $RuCl_3 \cdot 3H_2O$ aqueous solution have very large effect on the properties of the catalysts and the best pH value is 0.40–1.05. When the pH of the impregnation solution is low, ruthenium in aqueous solution is Ru^{3+} in state. According to isoelectric point theory, the $pH \ll pH_{IEP}$ is disadvantageous to the adsorption of Ru^{3+} on activated carbon surface. The $RuCl_3$ aggregates on the activated carbons surface and makes the grain size of the Ru change largely after reduction. When

Table 6.21 Effect of pH of $RuCl_3$ solution on the impregnating effect

Catalyst	pH of solution	Activity[a] (v/v)/% 425°C	Activity[a] (v/v)/% 400°C	Particle size of Ru[b]/nm
1	−0.45	15.02	11.24	8.94
2	0.40	17.54	15.09	3.46
3	1.05	17.36	14.44	2.94
4	2.50	13.56	9.12	7.92

[a]Testing conditions: p = 10 MPa, $H_2/N_2 = 3$, GHSV = 10,000 h^{-1};
[b]CO pulse chemisorption.

pH value is higher than 1.05, with increase of pH values, although it is favorable on adsorption of the Ru^{3+} according to isoelectric point theory, the hydrolyzation exacerbates, the grain size of the Ru becomes larger and easily accumulates. This kind of effect can be confirmed from the particle size of Ru.

6.2.4 *Reduction of $RuCl_3 \cdot xH_2O$ and elimination of chlorine ions*

6.2.4.1 *The effect of chlorines on catalytic performances*

(1) The source and the existing mode of chlorines. There are many sources of chlorines. It can be introduced into catalysts by the precursor compounds of the active components, supports and the impurity contained in reagents. Among them, the precursor of $RuCl_3$ is the main source. The content of chlorine (Cl) is not less than 39% in $RuCl_3 \cdot xH_2O$ and there are also remained chlorines on catalyst even after it is reduced.[5,10] Besides, there are some complexes of H, N, S and halogen (Cl) on the surface of activated carbon.[146] At the same time, during preparation, the non-polarity chlorocarbon can be produced on activated carbon when it contacts with chlorinated gases or liquid or each other, which is difficult to be eliminated even under the conditions of reduction. Moreover, promoters, solvents and some other chemical mediums also contain some amounts of chlorines due to the different purity as shown in Table 6.22. For the relative content of chloride, the content of Cl in promoters and solvents is very small, but the effect on the ammonia synthesis reaction is not negligible.

(2) The existing states of chlorines in catalyst. Ruthenium particles have very high surface energy.[16] Therefore, after being reduced, the chlorine would remain on the ruthenium surface, and there are weak bond between chlorine and ruthenium ions of catalyst without promoters. $RuCl_3$ can be easily reduced from the view of the

Table 6.22 Content of chlorines in KNO_3 and $Ba(NO_3)_2$ (mass fraction of Cl/%)

Reagents	Guide pure	Analytical pure	Chemical pure	Industrial first grade	Agricultural grade
KNO_3	0.0005	0.001	0.002	0.02	0.03
$Ba(NO_3)_2$	0.0002	0.005	0.001	—	—

thermodynamics. Pure $RuCl_3$ may be completely reduced at the temperature of 175°C, producing elementary ruthenium and HCl.[147] The latter can be adsorbed once again by the former and support. The existing ways of the chlorine in catalysts are different for different supports and the strong or weak of negative role caused by it are also different. Shiffett *et al.*[148] have studied the effect of chlorine on Ru/SiO_2 and Ru/Al_2O_3 catalysts, in which chlorine is introduced into catalyst as the anions of precursor or the component of the supports (e.g., impregnate supports with hydrochloric acid). The results show that the chlorine remained in the Ru/SiO_2 has no effect on the catalytic performances, while the effect of the chlorine remained in Ru/Al_2O_3 on the catalytic performances is determined by the existing states of chlorine. If chlorines existed in the component of support, the apparent activation energy increases, and the activity of the catalyst decreases. If the chlorine existed as the form of the anion of precursor, the apparent activation energy decreases and the activities of the catalyst almost do not change. The remnant chlorine in the Ru/SiO_2 catalyst is mainly located on ruthenium particle, but the chlorine in Ru/Al_2O_3 is located on ruthenium particle and support.[149,150] Narita *et al.*[151] have studied the remnant status of chlorine and the effect of the chlorine on the adsorption of H_2 and CO in the Ru/Al_2O_3 catalyst after reduction by H_2. The result shows that the value of the $(CO + Cl)/Ru$ is not greatly decreased with the increasing reduction temperature. This shows that most parts of the chlorine remained on the supports, not on the surface of ruthenium particles. This result was also confirmed by another study. Murata and Aika[5] studied the effect of H_2 treatment temperature on elimination of chlorine on Ru/MgO by XPS and the results show that the chlorine can both bind with ruthenium surface and interact with MgO. The chlorines are not immobilized in catalysts. Ru/MgO catalysts prepared by using $RuCl_3$ as the precursor, chlorine can adsorb on the surface of ruthenium if it is reduced at low temperatures (<500°C), however, at high temperature (>500°C), most of chlorine migrate to the support and exist in the form of $MgCl_2$.

(3) The effect of chlorines on the performances of catalyst. How to increase the activity at low temperatures is one of the most important issues for ruthenium catalyst. The study has shown that the existence of chlorines has great effect on the activity at low temperatures as Table 6.23 shows. It is seen from Table 6.23 that when the content of chlorines is 4.57%, the activity of catalyst is very low. Therefore, the effect of the chlorines on activity of catalyst is larger at low temperatures than that at high temperatures. For example, the content of chlorines decreases from 4.57% to 0.10%, the catalytic activity increases from 6.82% to 20.23% which is enhanced by 13.41% at 375°C, while from 13.74% to 22.81% at 400°C which is enhanced by only 9.07%. It is shown that the less the remnant chlorines in the catalyst, the higher the activity of the catalyst at low temperatures. Therefore, although the content of chlorines is very small after reduced by H_2, it has great effect on activity of the catalyst at low temperatures. The clarification of the toxic effect of chlorine will be beneficial to further increase the activity of catalyst at low temperatures.

The investigation of hydrogen adsorption of the activated carbon supported $RuCl_3$ and carhonyl ruthenium (chlorine-free) indicates that the adsorption amount of the hydrogen of the sample containing chlorine is much larger than that of the chlorine-free sample (Table 6.24).

Table 6.23 Effect of Cl^{-1} content in catalyst on the catalytic activity

Dechlorine method	Cl (mass fraction)/%	Activity/%[a] 400°C	375°C
Untreated	4.57	13.74	6.82
Reduction by H_2	0.29	22.08	17.38
Reduction by hydrazine hydrate	0.22	21.89	17.83
Ammonia-precipitation washing	0.10	22.81	20.23

[a]Testing conditions: p = 10 MPa, $H_2/N_2 = 3$, GHSV = 10,000 h^{-1}

Table 6.24 Uptake of hydrogen for 4%Ru/AC catalyst with different precursor

Precursor	$RuCl_3$	$Ru_3(CO)_{12}$
H_2 uptake/(ml/g)	1.9271	0.4617

It is seen from Table 6.24 that the existence of Cl^- promotes the adsorption of hydrogen, which is consistent with the result of Lu.[152] There is competitive adsorption of hydrogen and nitrogen on the surface of the ruthenium catalyst. The strong adsorption of hydrogen is the common characteristics of the ruthenium-based ammonia synthesis catalyst. The existence of the chlorines will further strengthen the adsorption of hydrogen on the surface of catalyst. The strong adsorbed hydrogen occupies active sites and inhibits the activation of nitrogen. The dissociative adsorption of nitrogen is the rate controlling step of the ammonia synthesis reaction. Therefore, the chlorines have effect on the reaction rate of ammonia synthesis.

6.2.4.2 *The elimination of chlorines in catalyst*

(1) **H_2 reduction method.** The elimination of chlorines in catalyst is an important role and step during the preparation of ruthenium catalyst.[153] In order to eliminate the Cl in activated carbon supported ruthenium catalyst prepared using $RuCl_3$ as the precursors, it is necessary that $RuCl_3$ is reduced to elementary ruthenium and to eliminate chlorine.

The reduction reaction of $RuCl_3$ with H_2 is:

$$2RuCl_3 + 3H_2 = 2Ru + 6HCl. \tag{6.14}$$

The reaction enthalpy and Gibbs free energy at different temperatures of the above reaction are listed in Table 6.25.[153] It is seen from Table 6.25 that ΔH^{Θ} is less than 0, which illustrates that the reduction of $RuCl_3$ is an exothermic reaction and the equilibrium constant decreases with temperature. Therefore, low temperature is beneficial for the reaction equilibrium moving forward. However, the equilibrium constant is very high even at temperatures as high as 1,000 K.

This indicates that the reaction of (6.14) easily happens in thermodynamics. For both thermodynamics and kinetics, temperature has two opposite roles on the reaction of $RuCl_3$ reduction. Therefore, there is an optimum temperature for the reduction.

Table 6.25 Enthalpy, Gibbs free energy and equilibrium constant of reaction (6.14)

T/K	$\Delta H^{\ominus}$/ ($kJ \cdot mol^{-1}$)	$\Delta G^{\ominus}$/ ($kJ \cdot mol^{-1}$)	Equilibrium constant ($K^{\ominus}$)	Equilibrium pressure of HCl (p_{HCl}/Pa)
298	−47.60	−205.87	1.22×10^{36}	1.03×10^{11}
400	−57.18	−258.43	5.61×10^{33}	$1.33 \times 10^{10.5}$
600	−75.33	−355.09	8.19×10^{30}	1.42×10^{10}
800	−93.00	−445.60	1.41×10^{29}	$1.06 \times 10^{9.8}$
1,000	−108.52	−531.97	6.11×10^{27}	$1.35 \times 10^{9.5}$

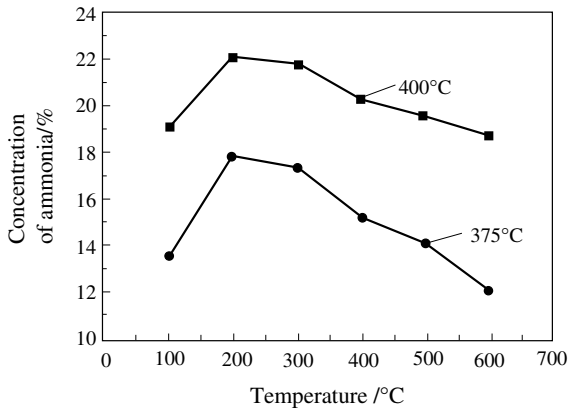


Fig. 6.35 Effect of reduction temperature on the catalytic activity. Reduction condition: For 12 h, 1080 $^{-1}$; activity test conditios: N_2: H_2=1:3, 10 MPa, 10,000 h^{-1}

The experimental results show that pure $RuCl_3$ begins to be reduced at 175°C[25] and finishes at about 200°C. But due to the interactions between $RuCl_3$ and supports, the reduction temperatures will be different when we use the different supports. The reduction temperatures of the $RuCl_3$ supported on activated carbons are different with each other in literature,[18,39,45,154,155] within the temperatures range of 200°C–650°C and the required time is from 2 h to 48 h. The effect of the reduction temperature of $RuCl_3$ on the catalytic activity is shown in Fig. 6.35.

It is seen from Fig. 6.35 that the catalyst reduced at 200°C has the highest activity. It cannot be reduced completely when the temperature is lower than 200°C. The change of temperature is not the significant effect on the catalyst activity when the temperature is in the range of 200°C–300°C. The activity is obviously decreased when the temperature is over 300°C.[61,141,156] This illuminated the dechlorination effect, the best when the temperature is about 200°C.

The efficiency of H_2 reduction method depends on the removal of the retained chlorines because HCl produced during the reduction process of the catalyst can be adsorbed once again so that the chlorines cannot be completely removed, even though the reduction reaction is complete.

Zeng *et al.* have studied the effect of the temperature and time of dechlorination on the catalytic activity (Fig. 6.36). It was found that the dechlorination effect is not complete (only 96% chloride ions were removed) when the catalysts were reduced by H_2 at low temperatures such as 350°C and 400°C. But there is

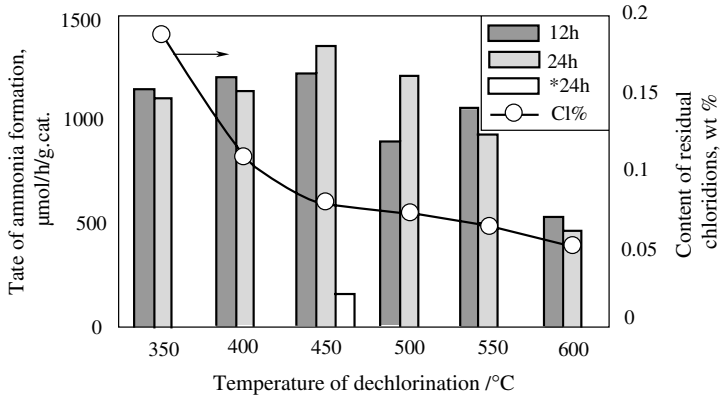


Fig. 6.36 Influence of the dechlorination temperatures on the reaction rate and the amount of residual chloridion of 1 $Ba(NO_3)_2$−5 Ru/AC catalyst (550°C). The dechlorination temperature: 350°C-600°C, time: 12-24 h, the reaction condition: 315°C, 1 atm, $N_2 + 3H_2$(60 ml/min)

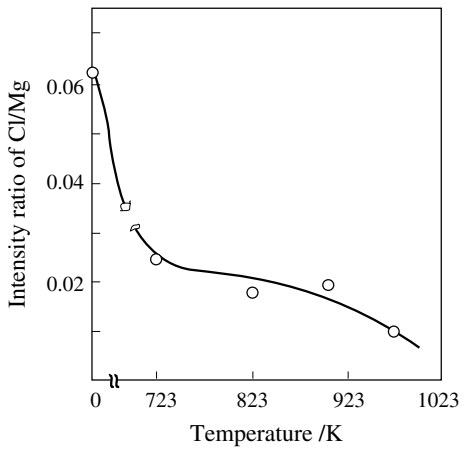


Fig. 6.37 XPS of the treatment temperature of H_2 on the intensity ration of Cl/Mg

no side reaction of the methanation of the supports at that time. Therefore, the dechlorination time has not obviously influenced on the catalytic activity. When the temperature of dechlorination is higher than 475°C, the methanation reaction of the supports occurs and the sintering of ruthenium particles is speeded due to the increasing temperature. It is considered that there is contradiction between the methanation reaction and the effect of the dechlorination with the increasing temperature. It can obtain the high catalytic activity, avoid the serious effect from the methanation reaction of the supports and realize the restructure of the ruthenium particle at the moderate dechlorination temperature of 450°C. Therefore, for the $RuCl_3$/AC catalyst, the dechlorination temperature of 450°C and the treatment time of 24 h are more ideal. The study of Murata and Aika has shown that the higher the temperature, the smaller the remnant chlorines (expressed by the value of Cl/Mg) is during the reducing process of Ru/MgO (Fig. 6.37).

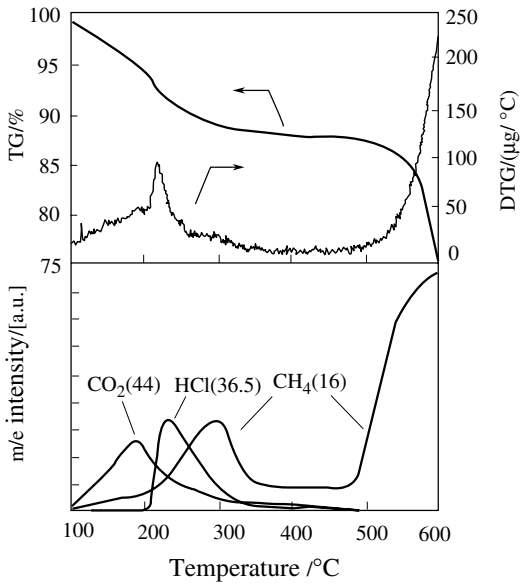


Fig. 6.38 TG-MS figure of dechlorination process of $5RuCl_3/AC$

The reduction conditions of the activated carbon supported by $RuCl_3$ are different. However, for the Ru-based catalysts with activated carbon as supports, the reduction temperature should not be too high because the methanation reaction would occur at high temperatures.

The dechlorination process of $5\,RuCl_3/AC$ was characterized using the TG, DTG and MS by Zeng *et al.* as shown in Fig. 6.38. In Fig. 6.38, the peak at 180°C is corresponding to the adsorbed CO_2 (44) peak and CO_2 may come from the carbonate impurities in the raw $RuCl_3$. The removal of chlorine in $RuCl_3/AC$ begins from 220°C and almost completes at 350°C: $RuCl_3/AC + 3/2H_2 = Ru/AC + 3HCl$ (g). However, the signal of HCl can be observed until 600°C. Interestingly, there are two peaks of CH_4 during the treatment process of H_2. It is possible that the reaction happened at 290°C is the methanation of the impure carbonates ($CO_3^{2-} + 5H_2 = CH_4 + 3H_2O$) and the reaction happened at 475°C is the gasification of the activated carbons ($C + 2H_2 = CH_4$).

The choice of reduction temperature is related with produced particle size of ruthenium. High temperature would lead to the sintering of the ruthenium particles, which increase rapidly with the temperature. For example, the ruthenium particle size is 2.1 nm–3.3 nm when reduction temperatures are 300°C–450°C and 3.3 nm–10.1 nm when reduction temperature are 500°C–650°C.[157]

Xu Jiao-Xing *et al.* have investigated the effect of the dechlorination temperature on the metal dispersion and the catalytic activity for ruthenium-based catalyst (Table 6.26). For Ru/AC catalyst, when the temperature is lower than 400°C, ruthenium particles are stable and the chlorines can be removed effectively. But the dechlorination at the higher temperatures will result in the sintering of the ruthenium particles. They considered that the dechlorination at 400°C–450°C would be more suitable for the catalyst with activated carbons as supports. The key of H_2

Table 6.26 Effect of dechlorination temperature on the dispersion of Ru in Ru/AC catalyst

T/°C	CO uptake/ (μmol · g^{-1})	Dispersion of Ru/%	$S_{Ru\ surface\ area}$/ ($m^2 \cdot g^{-1}$)	d_{Ru}/ nm
300	229.33	45.51	166.25	2.91
350	230.71	41.84	152.82	3.17
400	218.71	39.66	144.88	3.34
450	211.61	37.30	136.27	3.55
500	186.47	32.31	118.03	4.10

reduction method depends on the removal of the remnant chlorines because HCl produced during the reduction process can be adsorbed by supports once again and the chlorines cannot be removed completely, even though the reduction reaction is very completely, especially for the status with metal oxide as supports.

For the H_2 reducing dechlorination of the catalysts with different support, the temperature and time are the mainly factors on the effect of the dechlorination.

For Ru/MgO catalyst, the study of Murata *et al.*[2] shows that chlorines cannot be removed completely through only reduction by H_2. Even though the temperature reaches 700°C, there are still 20% Cl remained mostly in the form of $MgCl_2$. They considered that following reactions occurs at 700 K–900 K.

$$2RuCl_3 + 3H_2 = 2Ru + 6HCl. \tag{6.15}$$

$$2HCl + MgO = MgCl_2 + H_2O. \tag{6.16}$$

$$2RuCl_3 + 3MgO = Ru_2O_3 + MgCl_2. \tag{6.17}$$

$$Ru_2O_3 + 3H_2 = 2Ru + 3H_2O. \tag{6.18}$$

The remaining $MgCl_2$ (boiling point is 1,685 K, melting point is 987 K) on the catalyst surface are not the volatile substances, but they will transfer to the surface of ruthenium and cover part of ruthenium surface at temperatures in range of 700 K–900 K (Fig. 6.39).

During the reduction process of Ru/Al_2O_3 catalyst with H_2, Narita *et al.*[151] found that there are volume of chlorines enwrapped in the Al_2O_3 supports which cannot be removed even at temperature of 900 K. Zeng *et al.*[45] studied the dechlorination on the 5% Ru/AC catalyst at the different temperature. There is still 0.08% and 0.05% Cl remained on the catalyst after dechlorination reduction even at 450°C and 600°C for 24 h. Liang[158] using $AgNO_3$ solution to detect the Ru/AC catalyst after reduction by H_2 at 400°C, found the white AgCl generated rapidly on the sample surface, this proved the above suppose.

(2) **Liquid phase reduction method.** Liquid-reduction method uses hydrazine hydrate as reductant. Hydrazine hydrate is a kind of alkaline, corrosion and poisonous liquid which is miscible with water and has the good stability. It is mainly used in medicine and vesicant and reductant and antioxidant because of its strong reductivity. $RuCl_3$ can be reduced completely by hydrazine hydrate in thermodynamics.

Liquid-reduction process carries out through a certain concentration of hydrazine hydrate solution to reduce $RuCl_3$ into elementary ruthenium and remove Cl^- by

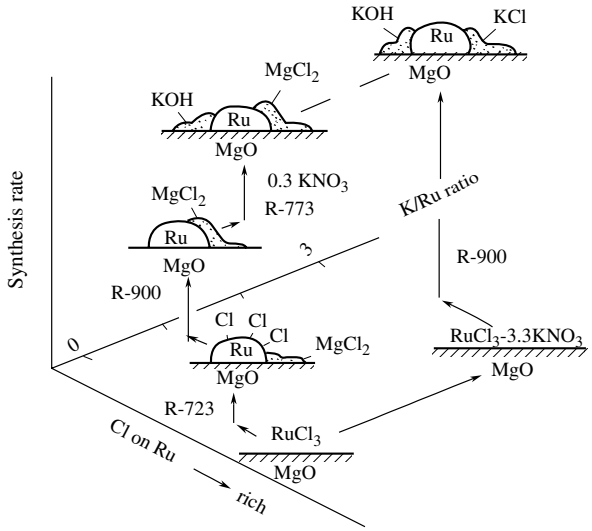


Fig. 6.39 Schematic diagram of dechloridions on the Ru/MgO by H_2 treatment and KNO_3

washing the solution. The steps are as follows[159]: (i) The sample after impregnation of $RuCl_3$ and KOH is reduced using 3% hydrazine hydrate solution at 90°C for 15 min and then the sample and the solution are separated. (ii) Use the deionized water to wash the sample until the Cl^- cannot be detected by 2% $AgNO_3$ solution in the washed water. (iii) The washed sample is dried and dewatered with infrared lamp at 50°C–80°C. (iv) $Ba(NO_3)_2$ is loaded as the promoter. The mass fraction of elementary ruthenium in finished catalysts is 4%, the molar ratio of the components is n(Ru): n(Ba): n(K) = 1: 0.55: 1.6.[160] For reduction of catalysts with activated carbons as the supports, with the $RuCl_3$ as the precursors, compared reduction effect with hydrazine hydrate solution, hydrazine hydrate vapor and H_2 as reducing agents respectively, it is fount that the reducing effect of the hydrazine hydrate solution is better than that of H_2, but the effect of the hydrazine hydrate vapor is the poorest.

The effect of reducing agent on catalytic activity is listed in Table 6.27. In Table 6.27, with the reduction temperature in the range of 300°C–500°C, sample 3 is reduced by hydrogen using the THF solution of $Ru_3(CO)_{12}$ as the impregnation solution. It is seen from Table 6.27 that the activity of sample 1 is similar to sample 2 and 3.

Table 6.27 Effect of reducing agents to activities of catalyst for ammonia synthesis

Catalysts	Precursors/supports	Reducing agent	Activity/%NH_3
1	$RuCl_3$/AC	Hydrazine hydrate	21.89
2	$RuCl_3$/AC	H_2	22.08
3	$Ru_3(CO)_{12}$/AC	H_2	21.68

Note: Activity testing conditions are 10.0 MPa, 10.000 h^{-1}, $H_2/N_2 = 3$ and 400°C.

Table 6.28 Content of element in catalyst reduced by different reducing agents (wt%)

Catalyst	Reduction methods	C	O	Cl	K	Ru	Ba
0	Unreduced	55.27	14.92	4.57	14.67	5.98	4.60
1	Hydrazine hydrate	56.57	19.20	0.22	15.52	4.10	4.39
2	H_2	55.60	18.15	0.27	16.43	5.17	4.38

The semi-quantitative analysis results for the chemical components of sample 1 and sample 2 with the EDS method are shown in Table 6.28. It is seen that the dechlorination effect of hydrazine hydrate solution is preferable than that by hydrogen, but the loss of the metal ruthenium is very significant which reaches more 30%. Both dechlorination effect and loss of metal ruthenium is possibly counteracted each other because the activity of sample 1 and sample 2 is equivalent. The dechlorination effect of the hydrazine hydrate solution maybe related to the following factors. (i) During the immersion cleaning of sample 1 with hot alkaline, it deepens the hydrolysis degree of the $RuCl_3$, transferring most chlorines to the water phase which benefits to enhance the efficiency of the subsequent dechlorination by water washing.

(ii) There are two different reactions during the progress of the reduction with the excess hydrazine hydrate in the hot alkaline solution i.e., the reduction reaction of $RuCl_3$ and the decomposition reaction of the hydrazine over ruthenium. The ammonia formed *via* the decomposition reaction is solved in the water to form ammonia-water solution, which benefit to clean the chlorines on the catalyst. As a result, it also leads to the loss of the metal ruthenium.

For the catalysts which are prepared with Al_2O_3 as the supports, $RuCl_3$ as the precursor and with barium nitrate as the promoter, after loaded with ruthenium, first it is washed by hot alkaline, and subsequently reduced by hydrazine hydrate, and Cl^- is removed by washing with water. It is found that there is almost no Cl^- remained in the catalysts (the residual amount is smaller than 0.0005%), and the residual amount is obviously lower than that of by reduction with hydrogen (the residual amount is 0.07%).[160]

(3) **Washing method.** The chlorines in catalyst can be effectively removed by washing method. Washing solution may be deionized water or alkaline solution.[7,151,161,162] Muria *et al.*[161] used ammonia washing technology to remove the chlorines residued on Ru/SiO_2, but they did not provide the experimental details. Wu *et al.*[162] confirmed the above conclusion by using NMR and chemisorption. The chlorines in the catalyst are removed effectively when catalyst of Ru/SiO_2 is washed by hot deionized water and the content of chlorines decreased with increasing of washing times (shown in Table 6.29).

It is found that the solution after washing, is acidic solution and contains chlorines which illuminated that the hydrolysis reaction of $RuCl_3$ occurs during the washing. Therefore, the washing process for the catalysts with $RuCl_3$ as precursor can be considered as a hydrolysis process:

$$RuCl_x + xH_2O \rightarrow Ru_{(s)}(OH)_x + xHCl. \quad (6.19)$$

Table 6.29 XRF and NMR results of 4% Ru/SiO_2 catalyst

Times of washing with hot water[a]	Cl^{-1} (mass fraction)/%[b]	30 Torr H_2		Irreversible H	
		Conversion/ ppm	Width/ kHz	Conversion/ ppm	Width/ kHz
0	0.33	−43	11.1	−42	16.0
1	0.12	−53	6.8	−52	9.2
5	0.01	−61	6.0	−58	8.1
6	0.00	−62	5.8	−59	7.8

[a]About 20 ml distilled water is used per gram catalyst per time.
[b]The data are gained by XRF.
Note: 1 ppm = 1 μl/l.

Table 6.30 Effect of washing by ammonia solution and deionized water on activity of 2% Ru–Rb^+/AC catalyst

Treatment	Rb/Ru ratio[a]	Activity[b]/(μmol · h^{-1} · g^{-1})	Ru particle size/nm
Without	10	100	3.7
Without	20	209	—
Without	25	170	3.7
H_2O	10	80	—
NH_4OH	10	161	—
NH_4OH	20	184	—

[a]Precursor of Ru is $RuCl_3 \cdot 3H_2O$, Rb is $RbNO_3$, the activated carbons are treated by 12 mol · L^{-1} HNO_3 solution.
[b]Reducing temperature is 673 K, the reaction temperature is 673 K, $N_2 + H_2$ = 80 kPa.

It is seen that the chlorines in $RuCl_x$ are replaced by OH^-, and enter into the washed solution in the forms of HCl. The dechlorination of washing methods has the similar principle. Because the hydrolysis is an endothermic reaction, so the increase of the washing temperature is beneficial to the removal of the chlorines.

Aika *et al.*[7] found that the ammonia washing process can increase the activity of the catalysts with low content of promoters. It can be seen from Table 6.30 that water washing has no effect on the activity of catalyst and the activity of the catalyst washed by ammonia is increased under the same condition of Rb/Ru (10), but the activity almost does not change when Rb/Ru = 20 (or 25). It is considered that the promoter is sufficient to neutralize the chlorines in the catalyst and provide electrons to active component when the content of the promoter is high enough.

For the Ru–Ba/AC catalyst prepared by $RuCl_3$ acetone solution and aqueous solution, washing process affects the adsorption capacity of H_2 and CO and the grain size of ruthenium.[158] The samples washed by ammonia have obviously larger adsorption capacity compared with the untreated samples. This shows that the ammonia washing can remove the residual chlorines.

Zhang Shu-Juan[163] considered that the Ru/Al_2O_3 washed by deionized water can remove part of chlorines and the activity of the catalyst is increased for Ru–Ba/Al_2O_3 catalyst. When Ru/Al_2O_3 first was washed by dilute ammonia

solution and then by deionized water, the chlorines combining with ammonia are further removed. Therefore, the activity of the catalyst is obviously increased. The authors[164] found that the catalytic activity is not high when the catalyst is washed by ammonia for Ru/MgO catalyst. Wu *et al.*[165] has proved the washing is more effective than the reduction for removing the Cl^- in the catalyst.

There are two problems for dechlorination relating to washing by deionized water. The first one is the ruthenium ions in the pore will be dissolved again, which leads to the loss of noble metal ruthenium as active components. The other one is that washing time is too long and the efficiency of the dechlorination is not ideal.

(4) **Precipitation-washing method.** The actual operation processes of the dechlorination method with reduction by H_2 or hydrazine hydrate and washing is one of six steps during preparation of catalyst which include impregnation, washing, drying, reducing, washing and drying.[159] The processes are quite complicated which have two times of washing and two times of drying. Although parts of $RuCl_3$ will produce $Ru(OH)_3$ precipitation due to the hydrolysis during washing, the most of $RuCl_3$ turning into elementary ruthenium is in the step of reducing by H_2 or hydrazine hydrate. There are three problems in this method. The first is the growth and aggregation of the metal ruthenium particles because of heating in the process of the reduction. The effect is more obviously with the increasing temperature. The dechlorination is not complete if the temperature is too low. The second one is the strong corrosiveness of the HCl emitted when H_2 or hydrazine hydrate are used as reducing agents. HCl will have some serious effect on the pipeline equipments. The last one is that hydrazine hydrate is a virulent liquid with corrosive.

Authors proposed a precipitation-washing method combined impregnation with precipitation together which undergoes loading of $RuCl_3$ and elimination of the Cl^- and immobilization of the Ru simultaneity. First, $RuCl_3$ is loaded on activated carbons as support and then converts the metallic chlorides ($RuCl_3$) into hydroxide ($Ru(OH)_3$) and deposited on the pore and surface of the supports using $NH_3 \cdot H_2O$ or other alkaline solution. And then $Ru(OH)_3$ is washed with deionized water which enables Cl^- to be eliminated completely. In this way, not only the active components of noble metals under these conditions are not easily loosed, but also the particle size is small. It can completely avoid the step of reduction by H_2 or hydrazine hydrate, avoid the defects of the growth and aggregation of the ruthenium particle which caused by the heating during H_2-reduction process and avoid using energy-consumed H_2 and virulent hydrazine hydrate. At the same time, the side product of NH_4Cl formed in precipitation is a useful chemical and fertilizer. The experimental studies show that it is completely feasible. The catalytic activity is greatly increased; the operation safety is also greatly improved. The precipitation-washing processes are different from the former method of impregnation — washing–drying–reducing–washing–drying. In the precipitation-washing processes, both the step of the reducing of $RuCl_3$ with H_2 or hydrazine hydrate and the step of the washing and the drying are substituted by the precipitation process so that the process becomes quite simple. Therefore, it is beneficial to the industrial scale-up.[166]

Table 6.31 Concentration of Ru^{3+} ions in solution with different pH during precipitation

pH of solution	$[OH^-]/(mol \cdot L^{-1})$	$[Ru^{3+}]/(mol \cdot L^{-1})$
2	10^{-12}	1
3	10^{-11}	10^{-3}
4	10^{-10}	10^{-6}
5	10^{-9}	10^{-9}
6	10^{-8}	10^{-12}
7	10^{-7}	10^{-15}
8	10^{-6}	10^{-18}
9	10^{-5}	10^{-21}
10	10^{-4}	10^{-24}
11	10^{-3}	10^{-27}

According to the principle of precipitation,

$$RuCl_3 + 3OH^- = Ru(OH)_3 + 3Cl^-. \tag{6.20}$$

$$K_{SP}\ (Ru(OH)_3) = [Ru^{3+}] \times [OH^-]^3 = 1 \times 10^{-36} (25°C). \tag{6.21}$$

It can be seen from Eq. (6.20) that the Ru^{3+} ions in $RuCl_3$ react with OH^- forming hydroxides, $Rus(OH)_3$ which are precipitated on the support surfaces. The chlorines in $RuCl_3$ are replaced by OH^- and enter into the washing solution as Cl^-.[162] The operation of this method is simple and the disadvantage of the demand of the heat source and hydrogen source in the H_2-reduction can be avoided completely.

From the point of view of chemistry, this kind of substances occur precipitation when its concentration in solution is larger than the solubility and the solubility product (K_{SP}).[167] When the ion concentration of the system reaches the solubility product, the concentration of the OH^- and Ru^{3+} can be calculated according to the pH of the system. According to Eq. (6.21), the calculated concentration of the OH^- (i.e., pH value) and the lowest concentration of the Ru^{3+} which can generate $Ru(OH)_3$ precipitation are shown in Table 6.31. It is commonly considered that if the concentration of the Ru^{3+} is lower than $10^{-6}\,mol \cdot L^{-1}$, it has been completely precipitated. It is seen from Table 6.31 that when the pH is four, the concentration of Ru^{3+} ion in the solution has reached that of the completely precipitated. In fact, the pH of $NH_3 \cdot H_2O$ solution is higher than 11, the concentration of the Ru^{3+} ions is below $10^{-27}\,mol \cdot L^{-1}$. So the Ru^{3+} ions can be completely precipitated even in the acid environment and must be completely precipitated in the alkali environment. Therefore, it is a feasible method of precipitation which can load Ru^{3+} and remove the Cl simultaneity.

Precipitation and dissolve are two reverse processes. The solutes in precipitate system must have certain supersaturation, as the driving force generates the precipitations. In precipitate process, molecules and ions first form clusters due to the collision motion and adhere to each other by van der waals force. After repeating the effective collision, gradually aggregates into the germules, and the germules develop into the crystal nucleus. Subsequently, the solutes are continuously deposited on the crystal nucleus and the grains continuously growth. The aggregate rate of the crystal nucleus is defined as the speed of the aggregate into crystal nucleus of ions.

The rate of the formation crystal from ions in a certain crystal lattice orientation is directional rate. The aggregate speed is determined mainly by the precipitation conditions and the supersaturation of the solute. The bigger the supersaturation, the more quick the aggregate speed is. When the aggregate speed is larger than the directional speed, the ions will form minimal amorphous precipitation because it is too late to directional alignment on the crystal lattice. The directional speed is determined by the nature of precipitated substances. When the supersaturation of the solution is very big, the aggregation rate will be very quick, and the molecules are unable to arrange in orderly, and the amorphous particles are formed. Therefore, it is necessary to select the appropriate conditions of depositions and washing in order to ensure the Ru^{3+} can completely precipitated and the Cl^- can be removed completely.

(i) **Precipitator.** It is obviously seen from Table 6.31 that the alkaline solutions (such as KOH, Na_2CO_3, $NaHCO_3$, $NH_3 \cdot H_2O$, urea etc.) maybe used as the precipitators of $RuCl_3$.[168] The effect of different precipitators on the dispersion of ruthenium is listed in Table 6.32. Among the selected precipitators, the catalyst prepared by $NH_3 \cdot H_2O$ as precipitator has the highest dispersion and surface area and the smallest particle size of ruthenium. Therefore, the precipitated effect of the ammonia is relatively superior. It is probably that the dissociation speed of ammonia is consistent with the precipitation of the ruthenium ions under the similar conditions, which results in the precipitation of ruthenium more uniformly and completely.

The effect of precipitator or reducing agent on the catalytic activity is shown in Table 6.33. The change of dispersion of ruthenium has the similar tendency with the catalytic activity. It is seen from Table 6.33 that precipitator has large effect on the catalytic activity. The effect of all kinds of precipitators on the activity (at 375°C) has the order as follows: $NH_3 \cdot H_2O > KOH > H_2 >$ urea $> NaHCO_3 > Na_2CO_3 >$ deionized water. The activity of the catalyst precipitated in $NH_3 \cdot H_2O$ solution is the highest at 400°C and 375°C. From the experimental results, it is feasible to replace H_2-reduction with precipitation and washing by alkaline solution such as $NH_3 \cdot H_2O$. As long as the appropriate precipitated conditions (precipitator and pH) are selected, the catalytic activity can be increased consumedly.

Table 6.32 Effect of precipitators on dispersion of ruthenium

Precipitator[a]	CO uptake/ $(cm^3 \cdot g^{-1})$	Ru dispersion/%	Ru surface area/$(m^2 \cdot g^{-1})$	Ru particle size/nm
$NH_3 \cdot H_2O$	2.4	27.3	99.8	4.93
KOH	2.10	23.7	86.4	5.69
$NaHCO_3$	1.95	22.5	80.5	6.24
Na_2CO_3	0.95	10.7	39.2	12.5
Urea[$CO(NH_2)_2$]	0.55	6.20	22.7	21.7
Deionized water	0.47	5.28	19.3	25.5

[a]Temperature of the precipitation: At 25°C for ammonia solution and at 65°C for others.

Table 6.33 Effect of precipitator or reducing agent on catalytic activity

Precipitator or reducing agent	pH value	Catalytic activity (10 MPa, 10,000 h^{-1})	
		400°C	375°C
$NH_3 \cdot H_2O$	11.8	22.67	18.60
Na_2CO_3	12	19.10	11.40
$NaHCO_3$	8	20.04	11.91
KOH	12	21.42	15.55
KOH	13	21.67	15.82
KOH	14	20.53	15.96
KBH_4	High-concentration	17.15	8.45
KBH_4	Low-concentration	16.30	8.01
Urea	—	20.76	15.14
H_2	Reduction at 200°C for 3 h	20.85	14.67

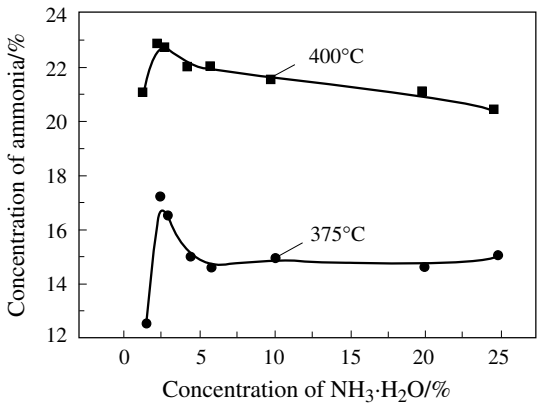


Fig. 6.40 Influence of $NH_3 \cdot H_2O$ concentration on the activity of catalyst

It is further found during the experiment that the chlorines in the system with ammonia ($NH_3 \cdot H_2O$) as the precipitator can be easily removed in the subsequently washing process. This part will be described in the subsequent study of the washing conditions in detail. Although H_2 reduction at low temperatures has small effect on the distribution of ruthenium, the effect of the dechlorination is rather poor.

Ammonia ($NH_3 \cdot H_2O$) is cheap and easy to get and its effect on the dechlorination is the best. Therefore, ammonia ($NH_3 \cdot H_2O$) is selected as the precipitator and the effect of precipitation conditions on the catalytic activity is studied.

(ii) **The concentration of precipitator.** The effect of the concentration of the ammonia ($NH_3 \cdot H_2O$) on the catalytic activity is great as shown in Fig. 6.40. In the process of preparation of the catalysts, the dilute solution of the ammonia ($NH_3 \cdot H_2O$) (the volume concentration is about 2%–3%) is most suitable. When the concentration of the ammonia ($NH_3 \cdot H_2O$) is too high, the precipitation speed is too quick and the precipitation will be uneven. At the same time, volume of formed

Table 6.34 Effect of washing temperature on Cl^{-1} content and activity of catalyst

Washing temperature/°C	Content of Cl^{-1} and Ru/wt%		Catalytic activity (10 MPa, 10,000 h^{-1})/% NH_3	
	Ru	Cl	400°C	375°C
Without washing	5.98	4.57	—	—
30	4.01	0.35	20.77	15.38
50	5.32	0.26	21.83	17.22
70	5.90	0.16	22.74	19.23
90	5.88	0.10	22.81	20.23

flocculent $Ru(OH)_3$ will quickly encapsulate the Cl^- surrounding ruthenium, which leads to the subsequent washing of Cl^- with deionized water slightly difficult.

The experiment results show that the Ru^{3+} almost was completely precipitated when the time is longer than 5 h. In the preparation process of the catalyst, in order to guarantee the complete precipitation, the precipitated time commonly is 10 h.

(iii) **Effect of washing process.** The flow rate of the washing agent (deionized water) will affect the catalytic activity when the catalyst is washed with the continuous flow. The smaller the flow rate of water, the larger quantities of the removed Cl^- and the better the catalytic activity are, but the longer the washing time results in the more amounts of the consumption of the washing solution and this is disadvantageous to the industrialization.

The washing temperature has large effect of the catalytic activity. The higher the temperature, the smaller the residual chlorine in catalyst, and the more obviously the effect of chlorine, the smaller the loss of the Ru is. When the washing temperature reaches 80°C, it will make the catalyst reach the ideal performance.

Cl^- in the catalysts washed at different temperatures after precipitated by ammonia ($NH_3 \cdot H_2O$) has been detected (Table 6.34). The results have shown that the catalytic activity increases with the washing temperature. The catalytic activity is the same with the effect of the dechlorination because with the increasing washing temperature, the remained chlorines decrease.

The amount of washing solution (deionized water) is related to the washing temperature and the time. With the same washing time, the lower the temperature, the more the time of the washing, the more amount of the washing solution consumption is. For example, when washing 10 times at 30°C, and 9 times at 40°C, only two times at 90°C, it can completely remove the Cl^- in the catalyst according to the observation with the silver nitrate ($AgNO_3$) solution to detect the Cl^{-1} ions in solution after washing. It is found that there is no white AgCl precipitation formed. This illuminated that increasing the temperature can remove the Cl^- more quickly and more completely. Therefore, the best washing conditions is 80°C, with about 90 ml washing solutions every time, and three times of washing, and then the effect will be satisfactory.

In summary, the precipitation-washing processes can be considered as the new method of preparing the efficient Ru based ammonia synthesis catalyst. It not only significantly increases the catalytic activity, but also simplifies operation, decreases the complexity of the catalyst preparation technology, and reduces the

costs of the catalyst with 2%–3% ammonia ($NH_3 \cdot H_2O$) as precipitator, and with the precipitated method instead of the steps of H_2 and hydrazine hydrate reducing in the prepared process of the catalyst.

6.2.4.3 *Discussion on mechanism of chlorine poison on Ru catalyst*

Chlorine is a serious poison for common metal catalysts including ruthenium-based and iron-based ammonia synthesis catalyst. Therefore, chlorine must be eliminated and its content is limited in the lowest by all means. The exploration of the poisoning effect of chlorine will be beneficial to further increase the activity of the catalyst.

In the first explanation, since chlorine (Cl) has strong electronegativity, so it can strongly attract the electrons of ruthenium and other promoters which can provide electrons. Consequently, the electron cloud density of ruthenium atom is reduced and the dissociation of N≡N is inhibited. Bond[169] has pointed out that residual Cl^- in the highly dispersed catalysts can lead to the charge density of ruthenium supported on Al_2O_3 decrease and should be studied earnestly. Blanchard and Charcosset[170] considered that the existence of Cl^- is the evidence which Ru^{3+} cannot completely reduced to elementary Ru^0. Bossi *et al.*[171] have the similar result that the tendency of the Cl^- residued on the Ru/Al_2O_3 is much larger than that on the Ru/SiO_2, even by the reduction treatment under the same conditions. The existence of Cl^- is responsible for the fact that the Ru^{3+} cannot be completely reduced to elementary ruthenium. Shiflett[148] considered that the existence of the Cl^- made the electronic density of ruthenium on the catalysts decreased, and inhibited the reaction rate, increased the apparent activation energy, also increased the inhibition effect of NH_3 on the reaction rate.[172] SiO_2 cannot adsorb the chlorines, but the Al_2O_3 will include volume of chlorines in its structures.[151] The residual Cl^- changes the surrounding environment of ruthenium, and therefore the adsorption of H_2 is decreased, and the adsorption of N_2 also is decreased, which make the ammonia synthesis rate decreased. Xin *et al.*[173] investigated the adsorption of CO on the Ru/Al_2O_3 with different Cl^- contents by *in situ* infrared spectroscopy, found that when $RuCl_3/Al_2O_3$ reduced with hydrogen at 300°C, Ru^{3+} was reduced, and meanwhile part of Cl^- transferred to Al_2O_3 surrounding ruthenium and forming strong L-acid center with Al_2O_3, and further forming electron-deficient ruthenium center by the interaction with ruthenium. After vacuumed at 400°C, except for small numbers of Cl^- is desorbed in HCl form, part of Cl^- forms $[Ru^{\delta+}\ Cl^{x-}]$ complex by the interaction with electron-deficient center of $Ru^{\delta+}$, resulting in the obviously decreasing amount of the adsorption of CO.

The second explanation considered that the existence of chlorines can promote the adsorption of H_2 (one chlorine can form about six adsorption sites for hydrogen), thus inhibits the activation of N_2. For example, Lu[152] studied and compared the conditions of H_2 active adsorption on two samples of Ru/Al_2O_3 catalysts with $RuCl_3$ and $Ru_3(CO)_{12}$ as the precursors, respectively. The results have shown that H_2 chemisorption on the sample with $RuCl_3$ as the precursor is very active, but is not so obviously on the sample without chlorination. This proved that the existence of the Cl^- can accelerate the adsorption of H_2. It was proposed in the succeeding reports[174] that due to the electronegativity, the chlorines are adsorbed on the surface sites of the high valence state and prevent the near surface site of low valence state

providing electrons to H_2. Finally, they considered that a chlorine can generate six H_2 adsorption sites.

Our experimental results tend to agree with the second mechanism. Cl^- strengthens the H_2 adsorption on the surface of catalyst, and makes the adsorption sites of N_2 decrease, and the dissociation adsorption of the N_2 is inhibited. The results about the catalytic activities for Ru–Ba–K/AC catalysts with $RuCl_3$ as the precursor show that the effect of strong hydrogen chemisorption on catalytic activity is very large. The H_2 adsorption capacity of $RuCl_3$ as the precursor is larger than that of ruthenium carbonyl as the precursor. The existence of chlorines benefits to the adsorption of H_2, leading to the activation of N_2 being inhibited, so the reaction rate of ammonia synthesis is decreased. But our experimental observations confirmed that the effect of the residual chlorines on the activity of Ru catalyst at low temperatures (375°C) is larger than that at high temperatures (above 400°C). Therefore, the first poisoning mechanism seems more reasonable to explain the reason that the effect of residual chlorine on activity at the low temperatures is more evident. The further studies on these issues are needed.

6.2.5 *Drying*

Drying is a step necessary for the preparation of catalysts with impregnation method.

Drying is the dehydration process of solid materials, which is generally conducted in air at 60°C–200°C. When materials contact with air at a certain temperature and humidity, the water will be excluded in order to reach certain content of water. If the conditions of air do not change, the content of water in the materials will not change and the value is called the equilibrium water content of the materials. The amount of water that can be removed in the drying process is more than the equilibrium water content in the materials. The excessive water is called free water. Therefore, drying process commonly has no influence on the chemical structure.

In the drying process of the catalyst prepared with impregnation, the sediments of active component in capillary can cause transferred phenomenon which leads to its non-uniform distribution. It is because that heat transfers from the outside to inner side of particles. The outside always first reaches the evaporation temperature of liquid. The vapor pressure on the concave meniscus of capillary is lower than that of the plane. Therefore, the solvent in the outer surface of catalyst or in the capillary pores is always first evaporated. The concentration of solution increases with the evaporation of solvent. When the concentration exceeds the saturation, the solutes will begin to precipitate from the solution. In order to keep the same liquid level in capillary, the solution containing the active components constantly moves to the outer surface from inner of capillary pores. With the solvent evaporating constantly, the solutes precipitate constantly. This makes the content of the active components on the outer surface higher than that of inner. Therefore, in order to reduce the transfer of the solutes, the rapid drying is commonly used and the repetitious impregnation steps with dilute solution also can be used to improve these conditions.

The factors influencing the drying rate mainly include the properties and shape of wet materials such as physical structure, chemical composition, shape and size, layer thickness of wet material, and the combination type of water, and the initial

and the final water content, the temperature and flow rate of drying medium, and contact with wet materials, which is related to the structure of drier.

The drying process during preparation processes of Ru–Ba–K/AC catalysts requires four times, i.e., after pretreatment of activated carbon with liquid, impregnation of active component and all promoters. The author[141] investigated the times, temperature and modes of drying after the impregnation for ruthenium catalysts as shown in the Figs. 6.41–6.44, respectively.

(1) **Drying temperature and time.** Activated carbon, as the support of Ru catalysts, has large surface area and the developed pore structures, strong adsorption ability for water vapor and other gases. The sufficient degassing and drying treatments are needed before catalyst preparation. It is seen from Fig. 6.41 that the drying of activated carbon needs about at least 6 h–8 h at the range of 110°C–200°C. However, if the temperature is too high, the activated carbon will easily react with the oxygen in air. The activated carbon will be burnt off and the pore structures of the activated carbon are destroyed. Figures 6.42–6.44 show the dehydration-drying curve at different temperatures during catalysts preparation. Under experimental conditions, the drying of catalysts needs at least about 8 h–14 h at the range of

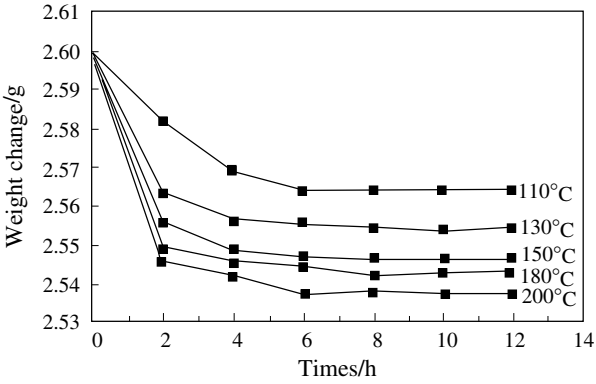


Fig. 6.41 Weight change of AC during drying at different temperature

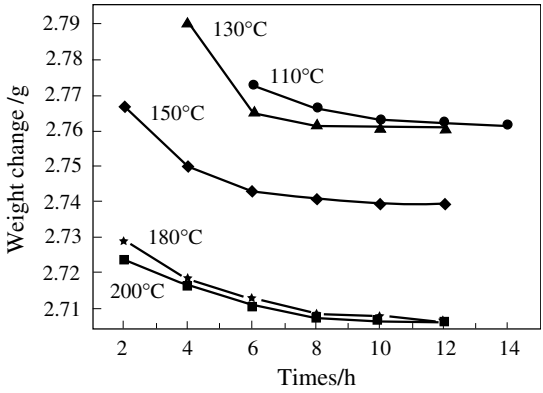


Fig. 6.42 Weight change of Ba/AC during drying at different temperature

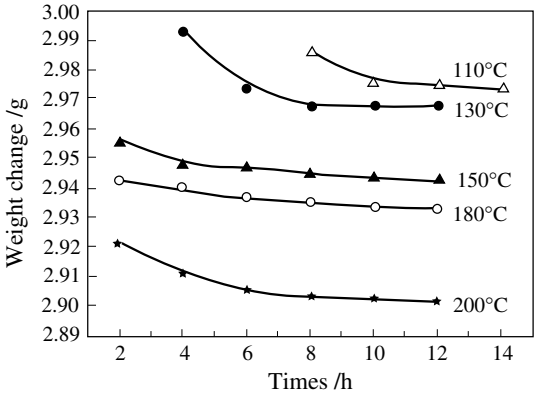


Fig. 6.43 Weight change of Ba–Ru/AC during drying at different temperature

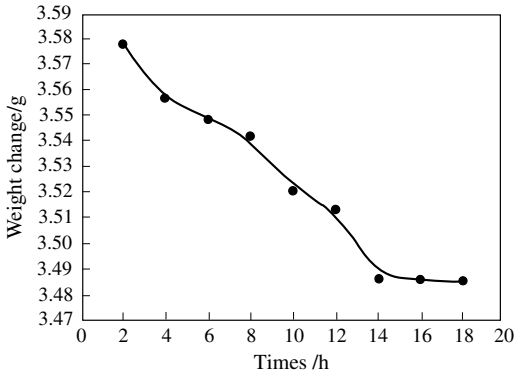


Fig. 6.44 Change of weight with time during drying at 110°C for Ba–Ru–K/AC

110°C–200°C. For example, for Ba–Ru–K/AC catalyst, the mass of catalyst reaches steady stage after drying at 110°C for 14 h (Fig. 6.44).

The dehydrating ratio is gradually increased with temperature. This means that the higher the drying temperature, the more completely the water in catalyst pores will be removed. But the dehydrating ratio has a certain value at a given temperature and this value is just the equilibrium water content of the materials at this temperature. The higher the drying temperature, the lower the equilibrium water content and the higher the dehydrating ratio is.

In order to select the suitable drying rate and temperature, it is necessary to understand the drying mechanism of porous materials. The drying process can be divided into three stages: (i) Early stage of the drying. The stress on the surface layer in porous materials is formed due to the compression of the surface. (ii) Intermediate stage of the drying. There is temporary equilibrium between the inner tensile stress and the outer compressive stress. (iii) Final stage of the drying. Contrary to the early stage of the drying, the outer surface is compressed by tensile stress. Commonly, there are many microporous in the inner surface of porous materials. The internal water is more than that of the surface layer, which forms the water content gradient

between the external layer and the inner layer. Therefore, the pressure of the water vapor in inner surface is larger than that of outer surface. Due to the pressure difference, the water in the state of liquid or steam moves from inside to outside along with the microporous and macroporous of inner surface.

Beside the water content gradient, the temperature gradient can also cause the water movement. The water content gradient is high in inside surface and low in outside, which compels water movement from inside to outside. But the temperature gradient, which is low inside and high outside, compels water movement from outside to inside. Therefore, there is an area which the water moves slowly at not far from the surface of porous materials. The drying process of porous materials is not in proportion. The water content gradient of the porous substances is an important intrinsic factor to determine the drying rate. And the external cause to determine the drying rate mainly is the temperature and the circulation velocity of the medium.

The ideal condition of the drying is that the moving speed of the water in the porous to the outer should be equal to the evaporation rate of the water on the surface to the medium. This can gradually reduce the difference between the moisture content in the surface layer of porous substance and the equilibrium moisture content. Therefore, it can avoid the crack of the surface due to the quick drying.

Generally, the drying temperature is about 60°C–120°C after impregnation of active component, and the drying of the promoters is basically controlled at 100°C–120°C. Our study[136] had shown that the best drying temperature of barium promoter and the active components of ruthenium is 150°C and 110°C, respectively. When the drying temperature is too low, the drying of the catalysts is not complete. When the temperature is too high, it leads to the growth of ruthenium particles and low dispersion, the change of pore structure. The drying temperature after loading of potassium almost has no influence on the activity. It is possible due to that the potassium nitrate is loaded last without subsequent preparation steps.

(2) **Drying methods.** For the catalysts prepared with impregnation method, the active components sediment in the pore of activated carbons will migrate during the drying process, which makes the active components to undergo redistribution on the surface of the activated carbons and influence its dispersion. Therefore, the suitable drying methods should be selected according to the characters of the materials. The results obtained by different drying methods for Ru/AC catalyst are shown in Table 6.36.

Table 6.36 Influence of drying methods on the activity and the dispersion of Ru for Ru/AC catalyst

	Activity at $H_2/N_2 = 3$, 10 MPa, 10,000 h^{-1}/%NH_3			
Drying methods	425°C	400°C	375°C	Ru dispersion (%)
Oven (110°C)	17.01	13.22	8.56	42.79
Rotary evaporator (110°C)	17.07	13.58	9.62	47.54
Vacuum (110°C)	17.14	13.92	10.35	49.75
Infrared	17.66	14.85	10.92	50.48

From Table 6.36, the activity of the catalyst dried by common oven is the lowest, while it is the highest by infrared. The uniform distribution of the ruthenium is influenced by the uneven heating in common oven. When using the rotary evaporator, the drying process is more uniform because the catalyst is rotated and tumbled continuously during the drying process. The vacuum drying is beneficial to prevent the oxidization and the growth of the ruthenium particle. Therefore, it is more beneficial to improve the dispersion of the active component than the common drying. The heat transfer mode of the infrared drying is radiation which can directly heat the inner of the materials because of its strong penetrating power. From the analysis of the difference of the heat transfer mode, the migration degree of the active component is smaller than that of other three drying modes and then the ruthenium dispersion is high and the catalytic activity is good. Therefore, the performance of the same catalyst may be different due to different drying methods.

6.3 Performance Characteristic of Ruthenium Catalysts

The main characteristics of ruthenium catalyst are high activity, high outlet ammonia concentration, wide applicable ratio range of H_2/N_2 at low temperatures and low pressures. Though ruthenium catalysts have high activity, they are very expensive, which is not comparable with fused iron catalysts. It has been more than 10 years since the ruthenium catalysts were successfully developed in 1992. Only 10 ammonia plants have used Ru-based catalysts. A lot of further studies are necessary in order to apply Ru-based catalysts widely.

6.3.1 *Structural sensitivity*

We have discussed the structural sensitivity in Chapter 2 and pointed out that ammonia synthesis over iron-based catalysts is a standard example of a structure sensitive heterogeneous catalytic reaction. This was the first evidence corresponding to the variation of the turnover frequency (TOF) with metal particle size. TOF is higher for large iron particles than for small ones in a Fe/MgO catalyst.[175] Later, measurements of the dissociation rate of N_2 over different iron surface on single crystals provided the support of the structural sensitivity. The Fe (111) surface is superior to the Fe (100) and the Fe (110) surfaces in both reactions of dissociation of N_2 and formation of ammonia. The results from the surface science[176,177] and the small iron particles considered that the most active site for ammonia synthesis over iron is an ensemble of Fe atoms including a C7 atom, i.e., a surface atom with seven nearest neighbors. The experimental findings on the Fe (111) surface have been supported by Density Functional Theory (DFT) calculations.

From recent single crystal studies, DFT calculations, and studies of supported catalysts, it was found that ammonia synthesis reaction over ruthenium is an even more structure-sensitive reaction than over iron-based catalysts.[178−180] In order to understand the structural sensitivity, Jacobsen *et al.*[181] studied the activity of the Ru catalysts with different supports. The surface area and the average radius of pore of four kinds of catalysts supported on $MgAl_2O_4$, AC, α-Si_3N_4 are shown in Table 6.37. Figure 6.45 shows the catalytic activities of the four catalysts tested in a 3:1 mixture of H_2 and N_2 at 50 bars and 400°C. From Fig. 6.45, the activity of Ru

Table 6.37 Surface area and pore radius for different catalysts

Catalyst	Ru/wt%	Surface area/$(m^2 \cdot g^{-1})$	Average pore radius/nm
$Ru/MgAl_2O_4$	6.8	209	5.8
Ru/AC(1)	9.9	123	4.4
Ru/AC(2)	5.4	123	4.4
Ru/Si_3N_4	7.6	12.5	31.7

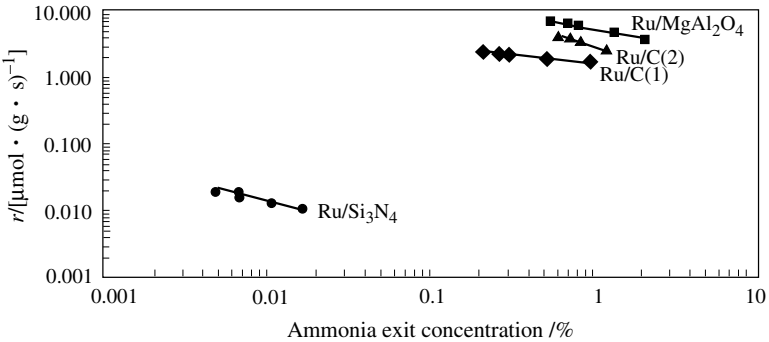


Fig. 6.45 Catalytic activity of supported ruthenium catalysts measured at 400°C and 50 bar in a 3:1 mixture of H_2/N_2.

Table 6.38 Average ruthenium crystal sizes/dispersions before testing determined by TEM and H_2 chemisorption and activation energies obtained at constant flow

	Dispersion before testing/%		$E_{a;CF}$		Dispersion before testing/%		$E_{a;CF}$
Catalysts	H_2	TEM	(kJ/mol)	Catalysts	H_2	TEM	(kJ/mol)
$Ru/MgAl_2O_4$	29	68	60	Ru/AC(2)	20	37	112
Ru/AC(1)	17	19	112	Ru/Si_3N_4	20	7	131

catalyst supported on $MgAl_2O_4$ is higher than that on activated carbon. They are both better than that on Si_3N_4. Apparent activation energies for the four catalysts are given in Table 6.38.

The dispersion of ruthenium, measured with chemisorption of H_2 and Transmission Electron Microscopy (TEM), are given in Table 6.38. It is seen from Table 6.38 that the dispersions obtained by these two methods are not in agreement. The chemisorption of H_2 considered only the strongly bound hydrogen and by assuming a surface stoichiometry of $H/Ru = 1$. The calculation of TEM was assuming spherical ruthenium crystals without contact to the support. Kowalczyk *et al.*[20] considered that the dispersions obtained from chemisorption of H_2 on Ru/carbon catalysts are not reliable. Therefore, a careful study of the TEM was conducted to obtain accurate estimates of the particle sizes and these numbers will also be used in the following discussion.

It is seen from Fig. 6.45 and Table 6.38 that the activity difference between Ru/AC and $Ru/MgAl_2O_4$ catalysts can be explained by the difference in the number

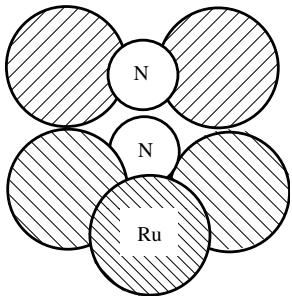


Fig. 6.46 Structure of reaction active center B_5

of active sites calculated from the metal concentrations and the TEM dispersions but not from the hydrogen chemisorption data. Also, the two catalyst systems show quite different activation energies. The activity of Ru/Si_3N_4 catalyst is much lower than expected based on either the TEM or H_2 dispersions. The present results show that there is no direct correlation between the activity of ruthenium supported on different supports and the dispersion. In microkinetic analysis it has shown that an excellent fit to the activity data can be obtained by taking the structural sensitivity of a $Ru/MgAl_2O_4$ catalyst into account.

Single crystal studies and DFT calculations have indicated that the most active sites for N_2 dissociation and ammonia synthesis are ensembles of five Ru atoms fulfilling two requirements: (i) they have to expose a three-fold hollow site and a bridge site close together and (ii) part of the atoms have to be low-coordinated surface atoms such as edge atoms on small crystals. Such reaction active center is shown in Fig. 6.46 that the B5 structure which formed by two top-layer Ru atoms and three low-layer Ru atoms. By fulfilling these requirements it is secured that the two nitrogen atoms of a dinitrogen molecule are not simultaneously bonded to the same Ru surface atom during dissociation.

There are some relationships between the B5-structure and the Ru particle size. The study shown that Ru particle has good catalytic activity at the range of 2 nm–4 nm and that range of Ru particle is easier to form the reaction center of B5 structure. In the terminology of Van Hardeveld and Van Montfoort these active sites are B5 sites involving edge atoms.[20,181,182] In their analysis of marble models of Ni face–face centered cubic crystals with a basic cubo-octahedral morphology, they found that B5 sites were only present on crystals with a size larger than *ca.* 1.5 nm. The maximum probability for B5 sites was found for particles of 1.8 nm–2.5 nm and for particles larger than that, the probability for B5 sites monotonically decreased. In Fig. 6.47, Jacobsen *et al.*[181] have similarly counted the relative number of B5-type sites, which are part of edges on small Ru crystals with only hcp (001) and (100) surfaces exposed. From Fig. 6.47, if crystal is too small, there is basically no B5 active site. After the active site numbers reaches maximum under the crystal size between 1.5 nm–2.0 nm, they may decrease with the growth of crystal grain, which is mainly caused by the rapid decline of edge atoms.

From the TEM (Fig. 6.48) of Ru catalysts on different supports, it can be seen that large Ru particles are in hexagonal shape. There are wide distributions of crystal size on $Ru/MgAl_2O_4$ and Ru/C, without specific crystal orientation. While it seems that the ruthenium crystal on Ru/Si_3N_4 has been depicted by supports.

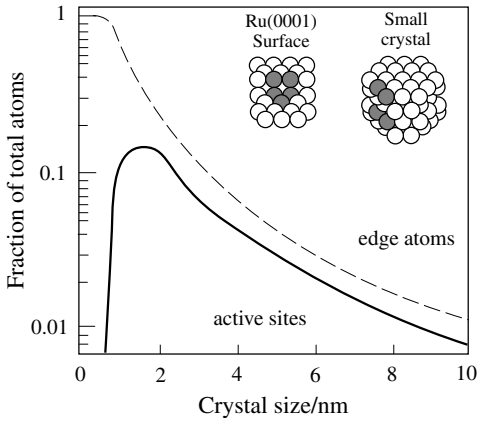
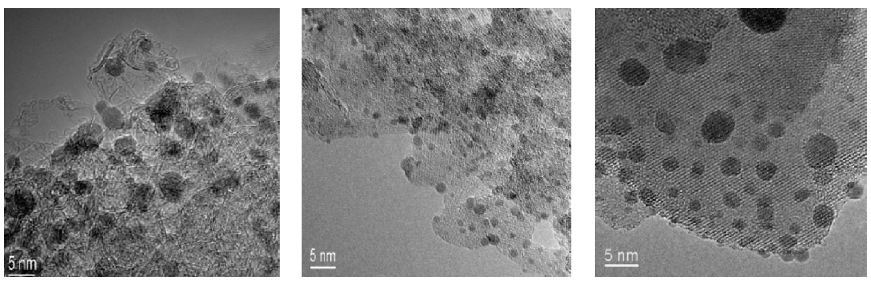


Fig. 6.47 Fraction of edge atoms and active sites on small Ru crystals relative to the total number of atoms as a function of crystal size.

The numbers are obtained from crystal models (see insert) exposing only (001) and (100) hcp surface planes. The active sites are present at the (100) surface. They consist of five Ru atoms exposing a three-fold hollow hcp site and a bridge site close together (a B5-type site) where part of the atoms are edge atoms. This criterium is based on the structure of the active step site on the Ru (0001) surface also shown.



(a) $Ru/MgA1_2O_4$ (b) Ru/C (c) Ru/Si_3N_4

Fig. 6.48 TEM image of ruthenium catalyst with different supports

It is parallel between the crystal edge and the lattice planes of support and most of the grain size is large. The big activity difference between $Ru/MgAl_2O_4$ and Ru/Si_3N_4 are probably caused by the different structures.

It is also found from Fig. 6.49 that ammonia synthesis activities of $Ru/MgAl_2O_4$ slowly increases in the initial stage of the reaction until they are stabilized. While the temperature programmed reduction (TPR) experiment of $Ru/MgAl_2O_4$ [at 1Bar (1Bar = 101.325 kPa, sic passim), in the argon with 1% hydrogen, the temperature range of room temperature to 600°C] shows that the reduction completes at 450°C. This will eliminate the possibility that the catalyst did not reduce completely.

From ruthenium particles size analysis before and after the catalyst test by TEM, the smallest size of Ru particles disappeares in the spent catalysts and the number of the large particles increases. Therefore the number of medium size particles may

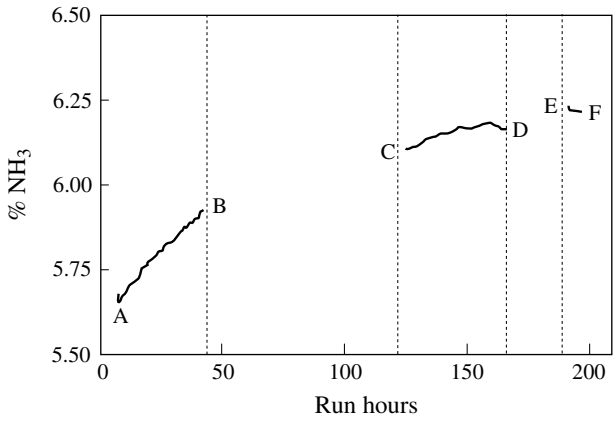


Fig. 6.49 Catalytic activity at 475°C and 50 bar in 3:1 H_2/N_2 of $Ru/MgAl_2O_4$ as a function of time on stream and pretreatment conditions

(A) Reduction at 450°C; (B, C) 500°C in synthesis gas; (D, E) 550°C in synthesis gas; (F) end of run

Table 6.39 Chemical composition of Ru/C catalysts with different promoters

Catalyst symbol	Ru content in (Ru+C) (wt%)	Ba content (mmol/gC)	Cs content (mmol/gC)	Catalyst symbol	Ru content in (Ru+C) (wt%)	Ba content (mmol/gC)	Cs content (mmol/gC)
Ba–Ru 1/C	1	1.0	—	Cs–Ru 20/C	20	—	3.3
Ba–Ru 3/C	3	1.0	—	Cs–Ru 32/C	32	—	3.6
Ba–Ru 5/C	5	1.0	—	Ba–Cs–Ru 1/C	1	0.9	3.4
Ba–Ru 9.1/C	9.1	1.0	—	Ba–Cs–Ru 3/C	3	0.8	3.2
Ba–Ru 20/C	20	1.2	—	Ba–Cs–Ru 3/C(H_2)	3	0.8	3.3
Ba–Ru 32/C	32	1.3	—	Ba–Cs–Ru 5/C	5	0.9	3.5
Cs–Ru 1/C	1	—	3.5	Ba–Cs–Ru 9.1/C	9.1	0.9	3.4
Cs–Ru 3/C	3	—	3.3	Ba–Cs–Ru 20/C	20	0.9	3.5
Cs–Ru 5/C	5	—	3.2	Ba–Cs–Ru 32/C	32	1.0	3.8
Cs–Ru 9.1/C	9.1	—	3.3				

be more than those of the catalyst before investigation. Combined with Fig. 6.47, it is not difficult to explain the activity with the phenomenon of slow increase.

Pilecka *et al.*[183] have carried out special study on the relationship between particle size and catalytic activity. The change of Ru particle size is realized through the change of load. The supports are all graphitized activated carbon. The catalysts with loading of ruthenium ranging from 1% to 3% with or without promoters were prepared. The former is mainly used for dynamics research and the latter is used for characterization. The components of Ru/C catalyst with promoters are shown in Table 6.39.

The ruthenium dispersion was measured with the chemsorption of O_2 and CO (Table 6.40); and the diameter of ruthenium particles can be calculated from the experimental data of O_2 chemsorption (Fig. 6.50). The dispersion is calculated by the chemsorption of O_2 and CO with the stoichiometric as O: Ru = 1:1 and CO: Ru = 0.6: 1.

Table 6.40 Chemisorbed characteristics of Ru/C catalysts without promoter

Catalyst	O_2 chemsorption		CO chemsorption	
	O_2 uptake (μmol/g(C+Ru))	FE^a_{O2}	CO uptake (μmol/g(C+Ru))	FE^a_{O2}
Ru 1/C	48.5	0.89	54.3	0.92
Ru 3/C	142	0.87	159	0.89
Ru 3/C(H_2)	140	0.86	154	0.87
Ru 5/C	206	0.76	234	0.79
Ru 9.1/C	332	0.67	376	0.695
Ru 20/C	541	0.50	648	0.55
Ru 32/C	496	0.285	608	0.32

[a]FE (fraction exposed) is defined as the number of surface Ru atoms referred to the total number of Ru atoms in the catalyst.

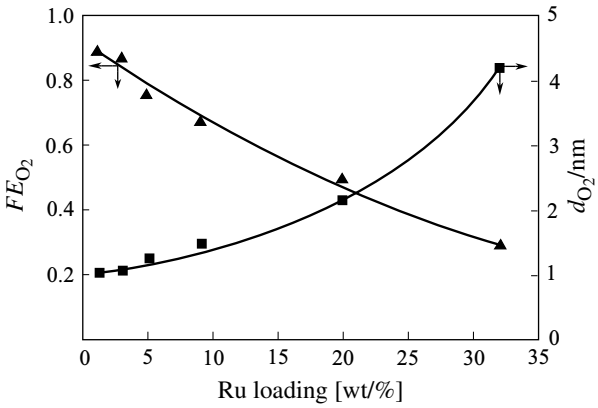


Fig. 6.50 Dispersion of ruthenium (FE_{O2}, d_{O2}) *vs* the metal loading in Ru/C

Generally, the chemsorption data of O_2 and CO is basically consistent. The gap between each other is less than 15%. Figure 6.50 shows that with the increasing of loading amount, the dispersion decreases monotonically, while the average particle size increases, but with little extent.

Ammonia synthesis reaction rate about three kinds of catalysts with different loading amount of ruthenium and promoters were studied. Based on O_2 chemisorption data, the relationship between the turnover of frequency (TOF) and the ruthenium particle size is shown in Fig. 6.51. A monotonic increase in TOF_{O2} *vs* d_{O2} is characteristic for each system. Extrapolation of the results to small crystallite diameters suggests (Fig. 6.51) that extra fine particles smaller than 0.7 nm 0.8 nm (critical size) might be totally inactive. Analogous trends in the surface activities were found (not shown) when the amount of adsorbed CO were used instead of O_2 uptake for the particle diameter and TOF calculation.

This is consistent with the results of calculation by Jacobsen, when the particle is small ($d < 1.5$ nm–2.0 nm), the relative amount of B_5 type active site shows the same trend with TOF. While the contradiction appears when the particle size is

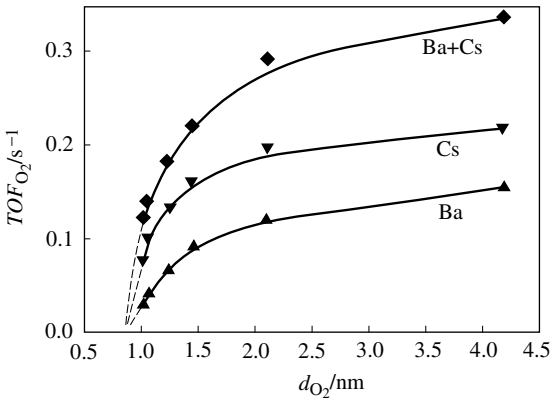


Fig. 6.51 Surface reaction rate

(TOF_O) vs Ru particle size (d_{O2}); $p = 63$ bar, $T = 400°C$, 8.5% NH3

larger ($d > 2.0$ nm), the active sites decrease but the TOF increases slowly with increasing of particle size.

According to the comprehensive consideration of Poltorak and Boronin,[184] the TOF increases with the increasing of particles, because the atoms on the crystal face is more active than that on the edge. According to the single-crystal research,[179] Dahl *et al.* states that the dinitrogen adsorption is mainly controlled by the terraces of ruthenium crystal and the atoms on the terraces almost have no activity. But the limitations of hypothesis of calculation on the number of B5 type active sites should be considered. The calculation by Jacobsen assumed that all the metal particles have formed perfect crystals, no matter how the crystal size changes, the crystal shape remains unchanged. While recent study on Ru/graphite system[185] show that when metal surface concentration is low (2%), the particle (∼2 nm) is spherical in shape; and when metal surface concentration is high (>10%), flake particles may form. The latter has better activity on nitrogen dissociation. Therefore, the particles on the catalyst without promoter is large (3 nm–4 nm). The crystal shape with high dispersion has more B5 type active sites. So, the ruthenium particles size with maximum B_5 type active site should have larger d value which may be larger than 4 nm. In addition, the investigation of catalytic activity is carried out on catalyst with promoter and then the surface reaction rate will increase. This is also one of the reasons for the phenomenon in Fig. 6.52 (the relationship between the relative number of B_5 active site, transformation of frequency and particle size).

It is seen from the above analysis that there is close relationship between the activity of supported ruthenium catalyst and the particle size and shape, which is an obvious structural sensitive catalyst.

It is also seen from Fig. 6.52 that crystallites about 1.5 nm–2.0 nm in diameter expose the highest reaction rates, regardless of the kind of promotion. The latter observation is important in practice. Ruthenium is an expensive metal, and its high productivity, related to its mass, is a key criterion of the catalysts usefulness. It is a

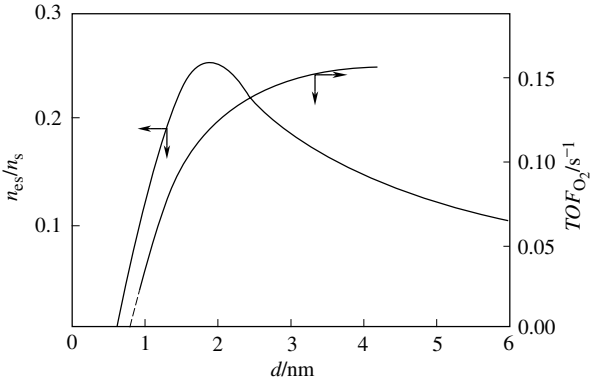


Fig. 6.52 Number of B5-type sites (*n*B5) referred to the total number of surface atoms (*n*S) and TOF of NH_3 synthesis for Ba–Ru/C *vs* particle diameter; trace *n*B5/*n*S was determined using the data presented in Ref. 176

question of art or technology rather than of science, however, how to manufacture catalysts with optimal ruthenium dispersion and required loading. From a scientific point of view, the relationship between particle size and surface activity, expressed in terms of turnover frequencies, seems to be more essential.

One of the key points of Ru/C catalyst is the structure sensitivity for ammonia synthesis reaction. It is determined that the cost of final products can be controlled by the suitable ruthenium loading amount. Rossetti *et al.*[186,187] found that the dispersion of ruthenium linearly decreases with the increasing of loading within 1%–5%. Based on the influence of ruthenium loading on catalytic activity and thermal stability, the appropriate ruthenium load is 3.5%. The highest activity can be obtained when the ruthenium dispersion is 10%–15%. Instead, the higher dispersion will reduce the performance of the catalyst (Fig. 6.53). The researchers from Alberta[188] of Canada considered that the ruthenium loading of Ba–Ru–K/AC catalyst should not be higher than 4% based on the performance-price ratio.

However, we considered that ruthenium loading amount has close relationship with the nature of support, the catalytic activity and the reaction conditions, especially the reaction temperature. Due to the high catalytic activity of ruthenium catalysts, under the space velocity at present industrial reactor (space velocity is 60,000 h^{-1} in Fig. 6.53, which is not applicable to industry), the ammonia concentration of the outlet of reactor has already close to equilibrium at above 425°C. In that case, the catalytic activity cannot be further increased by increasing the ruthenium loading amount. The influence of the reaction temperature on the ruthenium loading amount and catalytic activity of Ba–Ru–K/AC catalysts is shown in Fig. 6.54. It can be seen that the ruthenium loading amount has a large influence on catalytic activity at low temperatures, and small influence at high temperatures, e.g., the catalytic activity is almost the same at 425°C. Our result[144] further shows (Fig. 6.55) that when the ruthenium loading amount increases from 2% to 8%, the catalytic activity of Ba–Ru–K/AC catalysts is increased obviously

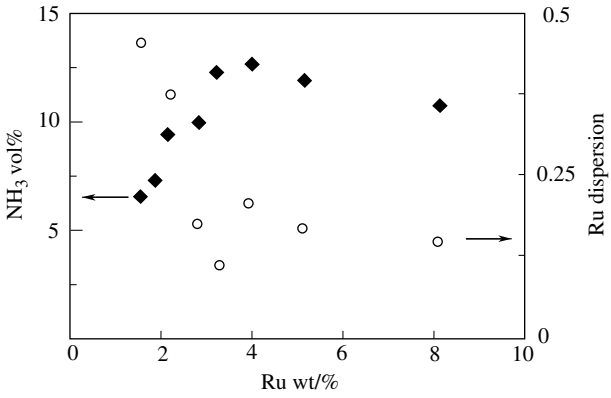


Fig. 6.53 Catalytic activity (♦) and ruthenium dispersion (○) (100 bar, 430°C, $H_2/N_2 = 1.5$, GHSV = 60,000 h^{-1})

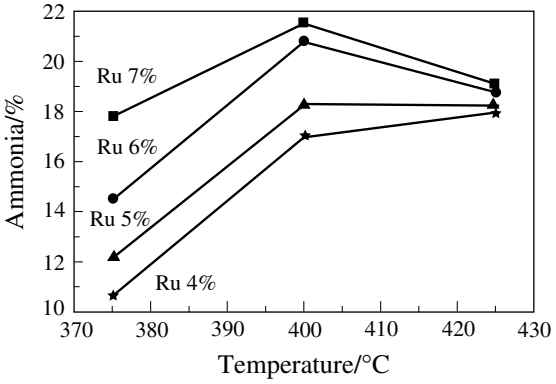


Fig. 6.54 Influence of temperature on catalytic activity on Ba–Ru–K/AC (N_2: $H_2 = 1$: 3, 10 MPa, 10,000 h^{-1})

in the conditions of 10 MPa, 400°C and 10,000 h^{-1} because the ammonia equilibrium concentration is 25.5% in 10 MPa, 400°C. Even if ruthenium loading amount reaches 8%, its outlet ammonia concentration is still far from the ammonia equilibrium concentration. But the catalytic activity decreases when the ruthenium loading amount is higher than 8%. It is because that the particle size increases, and the active sites reduce, and limit of the ammonia equilibrium concentration synchronously, in addition to the fact that beside with the increasing of ruthenium loading amount the dispersion decreases. The study of Fu W J *et al.*[157] confirmed that the particle size of ruthenium may increase from 6.72 nm–9.57 nm on Ru/C catalysts when the ruthenium loading increases from 8% to 10%.

In industrial application, the performance-price ratio of catalyst is a factor which must be considered. As precious metal, the amount of ruthenium must be reduced and kept at high activity at the same time. When the dispersion of active components has not reached saturation, increasing the amount of ruthenium may

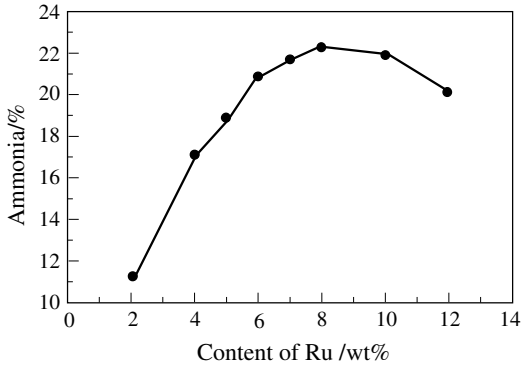


Fig. 6.55 Influence of Ru loading number on catalytic activity on Ba–Ru–K/AC (N_2: H_2 = 1: 3, 10 MPa, 400°C, 10,000 h^{-1})

increase the active sites, and increase the catalytic activity; when it reaches the saturated state, the increasing of loadings will make ruthenium particles assembled on the support.[188] Therefore, the ruthenium content should commonly not be higher than 4%.

The price of ruthenium catalyst is extremely costly. This is the main obstacle for its wide application in industry. In order to reduce the cost and achieve full use of the high activity characteristics, these problems can be solved by the following ways:

(i) To reduce the ruthenium content in the catalyst.
(ii) To recycle the ruthenium in the waste catalyst after use.
(iii) To combine Ru catalyst with iron catalyst to reduce the loading amount of ruthenium catalyst.
(iv) To reform the ammonia synthesis process to reduce the investment of construction and operating cost. The ammonia synthesis process must be reformed to adapt it because of the expensive cost, high activity and strong H_2 inhibition of the ruthenium catalyst.

6.3.2 *The activity of ruthenium catalyst*

High activity is the most significant feature of ruthenium catalyst. The ammonia concentration or ammonia net value in outlet of converter can be significantly increased in industry.

In order to investigate the catalytic activity of Ru catalysts, and compare with iron catalyst, we[189] choose the representative iron catalyst A301 with wüstite as precursor as the reference sample. A301 has the highest activity among all of the iron-based catalysts for ammonia synthesis and now it has been widely used in ammonia synthesis industry. In order to get the reliable and comparable data of the evaluation of catalytic activity, the experiment was conducted under the same conditions and four samples were filled in four reactor contained in one shell. The results were shown in Table 6.41 and Figs. 6.56–6.58.

Table 6.41 Outlet ammonia concentration at different temperature and pressure on Ba–Ru–K/AC catalysts/% ($H_2/N_2 = 3$, 10,000 h^{-1})

	Pressure/MPa		
Temperature/°C	10	15	20
425	20.44	25.91	32.08
400	23.20	28.14	33.28
375	21.37	26.88	31.15

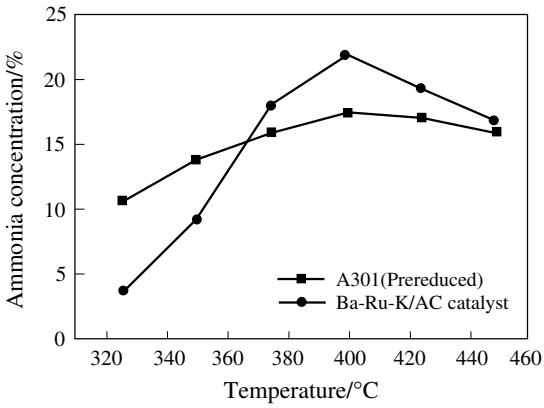


Fig. 6.56 Comparison of activity between Ba–Ru–K/AC and A301 iron catalyst ($p = 10$ MPa, $S_v = 10{,}000\ h^{-1}$, $H_2/N_2 = 3$)

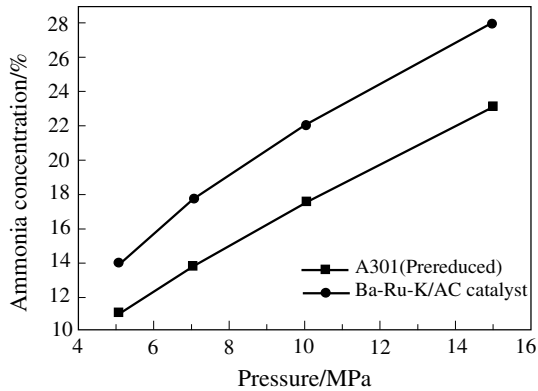


Fig. 6.57 Comparison of activity between Ba–Ru–K/AC and A301 iron catalyst at different pressures ($S_v = 10{,}000\ h^{-1}$, $t = 400°C$, $H_2/N_2 = 3$)

(1) The relationship between activity and temperature. It can be seen that the catalytic activity is the highest at temperature of 400°C for Ba–Ru–K/AC catalyst and the outlet ammonia concentration reaches 23.2% at $H_2/N_2 = 3$, 10 MPa, 10,000 h^{-1}. It is higher than A301 (17.5%) by 5.7 percentages, increases by 32.6% under the same conditions. Besides, from Fig. 6.56, we also found that Ba–Ru–K/AC

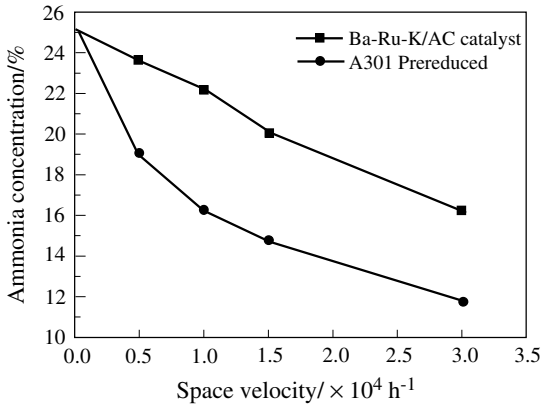


Fig. 6.58 Comparison of activity between Ba-Ru-K/AC and A301 catalyst under different space velocities ($P = 10$ MPa, $t = 400°$C, $H_2/N_2 = 3$)

catalyst is more sensitive to temperature than A301 especially at low temperatures (<375°C). The catalytic activity of Ru catalyst declines rapidly with the decrease of temperature. The activity is lower than A301 iron catalyst at temperatures below 370°C, and it lowers by 7% than iron catalyst at 325°C. It is obvious that the activity of Ru catalyst is strongly inhibited by the adsorption H_2 at low temperatures, which have been reported in many references.

Compared with Ba–Ru–K/AC catalyst, the inhibition of H_2 adsorption on the iron catalyst is weaker. Therefore, the activity of iron catalyst does not decrease sharply as Ba–Ru–K/AC catalyst at low temperatures.

(2) The relationship between catalytic activity and reaction pressure. Figure 6.57 shows the catalytic activity of Ba–Ru–K/AC and A301 catalyst at different pressures. The activity of the two catalysts increases with the increasing of pressure within 5 MPa–15 MPa. For the same catalytic activity, the pressure of Ba–Ru–K/AC catalyst is lower than A301 catalyst by 3 MPa–5 MPa. Therefore, Ba–Ru–K/AC catalyst is particularly suitable for ammonia synthesis processes with low pressures. For example, the activity of Ba–Ru–K/AC catalyst can reach 20% under 7 MPa, 10,000 h^{-1}, $H_2/N_2 = 1$, 400°C. Therefore, it is suitable for low pressure operation. As the company of Kellogg reported[190] that hot-wall converter can be adopted (need no internal part of converter) at low pressures. Thus it can reduce the requirements of the reactor and wall and there are savings in compression equipment and synthesis loop piping and equipments when KAAP synloop operating pressure is 8.96 MPa (91.4 kgf/cm^2). With these savings, the synthesis loop costs less and more than offsets the added catalyst cost.

Due to the high activity (ammonia neat value) used at above 15 MPa and the heat transfer problem of converter needs to be solved. One of the ways is to use multibeds, intercooled, radial-flow ammonia converter and to use ruthenium catalyst combined with iron catalyst. If the ruthenium catalyst was put after iron catalyst in converter, it can not only solve the heat transfer problem, but also reduce the quantity of the ruthenium catalyst. Therefore, the ruthenium catalyst can be applied in the present ammonia synthesis process. After further renovation of the process, the effect of save energy can be obtained.

(3) The relationship between catalytic activity and space velocity. Figure 6.58 shows the activity of Ba–Ru–K/AC and A301 catalyst under different space velocities. The effect of space velocity on Ba–Ru–K/AC catalyst is smaller than that on the A301. From Fig. 6.58, outlet ammonia concentration is about 19% with ruthenium catalyst at the space velocity of 18,000 h^{-1}. But in order to reach the same outlet ammonia concentration, A301 needs space velocity of 5,000 h^{-1} and the space velocity of the former is about 3.6 times higher than the latter. This show that the reaction rate (r_v) calculated from the unit volume (V_c) of catalyst is about 3.6 times of A301 iron catalyst. Design of industrial converter is based on the volume of it. Therefore, for the same capacity converter, the loading volume of catalysts should about 2.6 times less than A301 iron catalyst.

It is reported that KAAP-type Ru catalyst supported on graphitized carbon developed by BP is the best reported ruthenium catalyst. With the combination of this catalyst and iron catalyst, the designed outlet ammonia concentration is 20% and the actual concentration is 21.17% at 8.96 MPa (91.4 kgf/cm^2).

It is reported that catalytic activity of ruthenium catalyst is 10–20 times higher than that of iron catalyst by many sources including BP and Kellogg companies. For example, Kowalczyk *et al.*[40] considered that the reaction rate on Ba–Cs–Ru 9.1/C is 25 times faster and on Ba–Cs–Ru 23.1/C is 50 times faster than that on iron catalyst (KMI) (Table 6.42).

But this proposal is not so strict scientifically due to the lack of clear definition of "activity." The catalytic activity of ammonia synthesis catalyst can be expressed by outlet ammonia concentration of converter, conversion ratio of ammonia, reaction rate and rate constant of kinetics and turnover frequency of ammonia (TOF).

First, the outlet concentration of ammonia from reactor cannot be increased by 10–20 times due to the limitation of the ammonia equilibrium concentration under the same reaction conditions and at normal pressures and low temperatures, it does not have much practical significance.

The reaction rate in mass,

$$r_m = \frac{S_V V_C}{22.41 W_C} \cdot \frac{\varphi_{NH_3} - \varphi^0_{NH_3}}{(1 + \varphi_{NH_3})} = \frac{S_V}{22.41 \rho_C} \cdot \frac{\Delta\varphi_{NH_3}}{(1 + \varphi_{NH_3})}. \tag{6.23}$$

The reaction rate in volume,

$$r_V = \frac{S_V}{22.41} \cdot \frac{\Delta\varphi_{NH_3}}{(1 + \varphi_{NH_3})}. \tag{6.24}$$

Table 6.42 Ammonia synthesis rates of Ru/C catalysts with optimization of single or double promoter (p = 90 bar, T = 400°C, H_2: N_2 = 3: 1, x = 10%)

Catalyst	Cs content/ ($mmol \cdot g_C^{-1}$)	Ba content/ ($mmol \cdot g_C^{-1}$)	Reaction rate / ($g_{NH3} \cdot g_{C+Ru}^{-1} \cdot h^{-1}$)
Ba–Ru 9.1/C	0	0.95	3.45
Cs–Ru 9.1/C	3.15	0	3.78
Ba–Cs–Ru 9.1/C	2.75	1.0	6.85
Ba–Cs–Ru 23.1/C	2.80	1.05	12.5
Fe*(KMI)	—	—	0.23[a]

[a]Reaction rate in $g_{NH3} \cdot g^{-1} \cdot h^1$, from A Jedynak *et al.*, Catal. Lett., 2002, 81:213.

The TOF of ammonia,

$$TOF_{CO} = \frac{M}{3600}\left(\frac{r_m}{f_m D_m}\right). \tag{6.25}$$

The rate constant k_1 or k_2 in Temkin–Pyzhev kinetics equation,

$$r = k_1 f_{N_2} f_{H_2}^{1.5} f_{NH_3}^{-1} - k_2 f_{NH_3} f_{H_2}^{-1.5}. \tag{6.26}$$

From Eq. (6.23), we know that the packed density (ρ) of iron catalyst is about 3.3 times as that of the ruthenium catalyst. Even at the same outlet ammonia concentration (φ_{NH3}) the reaction rate (r_m) calculated from the mass of the catalyst (W_C) is higher by about 3.3 times than that of iron catalyst. As mentioned above, when the outlet ammonia concentration is the same, the space velocity of the former is about 3.6 times of the latter, so the reaction rate is increased about 11.9 times by Eq. (6.23), of which about 3.3 times are caused by the different of packed densities and about 3.6 times are gained by the increasing space velocity. But the increase of space velocity will be limited by power consumption and ammonia net value.

The design of industrial converter is commonly calculated by volume of catalysts. From (6.24), with the same ammonia concentration, the reaction rate of volume is increased by 3.6 times because space velocity is increased by about 3.6 times. But φ_{NH3} must meet the requirements of industrial ammonia net value because with increase of space velocity, the outlet concentration or net value of ammonia decreases.

From Eqs. (6.23) and (6.24), we know that no matter the reaction rate in mass or volume, both are proportional with space velocity. Therefore, when compared the reaction rate of different catalysts, the reaction conditions should be the same.

Under the same conditions, the comparison of reaction rate and TOF on ruthenium catalyst and iron catalyst is shown in Table 6.43. It can be seen form Table 6.43 that under the same conditions, the volume reaction rate (r_V) of ruthenium catalyst is higher by about 20%–26%, and the mass reaction rate (r_m) is higher by about four times than iron catalyst and the TOF is higher by about 2.8 times. They are basically consistent with the magnitudes of catalyst density. The latter observation is important in science, i.e., the activity (TOF) of ruthenium catalyst is about 2.8 times higher than that of iron catalyst in scientific signification.

Table 6.43 Comparison between Ruthenium-based and iron-based catalyst[a]

Catalyst	ρ/ ($g \cdot ml^{-1}$)	p/ MPa	t/°C	S_v/h^{-1}	φ_{NH3}/%	r_V/(mmol · $ml^{-1} \cdot h^{-1}$)	r_m/(mmol · $g^{-1} \cdot h^{-1}$)	TOF[b]/ s^{-1}
Ru–K–Ba/AC	0.75	7	400	10,000	16.98	64.77	86.36	0.173
		10	400	5,000	24.43	43.81	58.41	0.117
		10	400	30,000	15.06	174.81	233.08	0.467
ZA-5(Fe)	2.45	7	400	10,000	13.02	51.41	20.98	0.059
		10	400	5,000	19.23	36.53	14.91	0.042
		10	400	30,000	11.74	140.65	57.41	0.177

[a]Syngas: $H_2/N_2 = 3$, $CH_4 + Ar = 0$, $\varphi^0_{NH3} = 0$.
[b]For Ru–K–Ba/AC catalyst: Ru content $f_m = 4\%$, dispersion $D_m = 35\%$; and for ZA-5 (Fe) catalyst: Fe content $f_m = 91.5\%$, dispersion $D_m = 0.55\%$.[191]

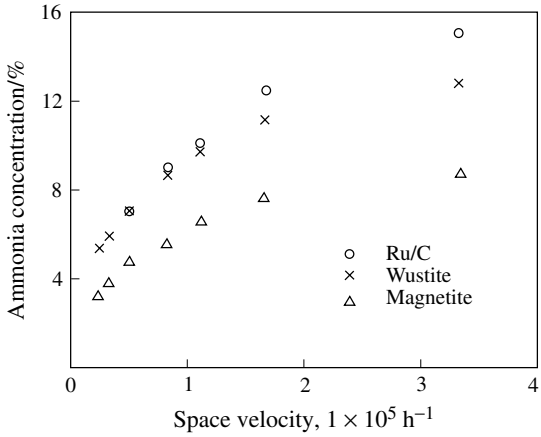


Fig. 6.59 Conversion curves of wüstite-, magnetite- and Ru/C-based catalysts (100 bar, 430°C, H_2/N_2 is three for the two Fe catalysts, but 1.5 for Ru/C)

Pernicone *et al.*[192] compared the activities of catalysts with wüstite as precursor of A301, magnetite as precursor (KMI in Table 6.42) of iron catalyst and the best Ru/C catalyst as shown in Fig. 6.59. It can be seen that wüstite catalyst and Ru/C catalyst are practically equal, except for the very high conversion, where the lower sensitivity of Ru to ammonia plays a decisive role. However, it should be stressed that, to give the highest activity, the Ru/C catalyst requires a H_2/N_2 feeding ratio of 1.0–1.5. Moreover, support degradation by Ru-catalyzed methanation under ammonia synthesis conditions, sometimes accompanied by additional adverse effects due to water traces, can occur, if the carbon support is not properly designed. So, catalyst A301 appears to be competitive with Ru/AC and the related choice should be made on the basis of the specific plant characteristics and working conditions.

Jacobsen *et al.*[193] considered that ruthenium, osmium and iron are the best catalysts among pure metals for ammonia synthesis. However, ruthenium and osmium have no commercial attraction compared with the third-best iron catalyst because they are very expensive.

From the point of view of industry, for ammonia plant with capacity of 2,000 t/d, by comparing characteristics between the traditional fused iron catalyst and the catalyst in which first bed using fused iron catalyst and the rests using ruthenium catalyst, it indicates: The H_2/N_2 ratio in the inlet of converter is different, even though the H_2/N_2 ratio of iron catalyst is 3.0, while it is less than two when ruthenium catalyst is used. When using high active ruthenium catalyst, it requires a smaller volume of catalyst in the converter, but there is no superiority of energy saving. A possible optimal solution, resulting from ammonia plant simulation, consists of loading catalyst A301 in the first two or three beds and the Ru/C catalyst in the final one, while keeping the stoichiometric feeding composition used with Fe catalysts.

There are much more serious problems of the catalyst with graphitized activated carbon as support at high hydrogen partial pressure due to the support degradation by Ru-catalyzed methanation under ammonia synthesis conditions. Despite so many

advantages, the high price makes ruthenium catalyst require a long cycle repay, so that it cannot compete with the iron catalyst.

Aiming at the industrial application of ruthenium catalyst, it is necessary that the essential improvement should rely on the ammonia synthesis process including new structural converter, new separation technology and further improving of former processes or by the establishment of new reaction mechanism on new catalyst.

6.3.3 *The strong inhibition of H_2*

6.3.3.1 *The phenomenon of strong H_2 inhibition*

On iron catalyst, the classical ammonia synthesis reaction kinetics equation of Temkin–Pyzhev is expressed as (with fugacity express when $\alpha = 0.5$):

$$r = k_1 f_{N_2} f_{H_2}^{1.5} f_{NH_3}^{-1} - k_2 f_{NH_3} f_{H_2}^{-1.5}. \tag{6.26}$$

Ammonia synthesis reaction order is 1.5 for H_2 and increases with the increasing of H_2 partial pressure; while it is negative one for NH_3 and decreases with the increasing of ammonia partial pressure. Therefore, the character of ammonia synthesis reaction on iron catalyst is the inhibition of NH_3.

The effect of H_2/N_2 on the activity of Ru–K–Ba/AC catalyst is shown in Fig. 6.60. This effect is very large in which the outlet ammonia concentration is decreased about 31% when H_2/N_2 is increased from 0.5 to 3.0. And the lower the temperature, the higher the pressure and the larger the degree of decrease is.

It is commonly considered that the dissociative adsorption of N_2 is the rate determining step on ruthenium catalyst as iron catalyst. The experimental results for Ru catalysts show that no complete satisfactory interpretation of kinetic

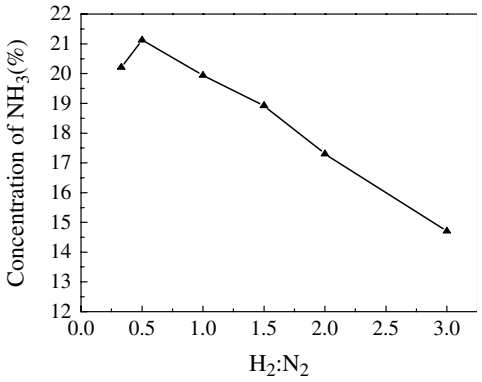


Fig. 6.60 Effect of H_2:N_2 on activity of Ru–K–Ba/AC catalyst (10.0 MPa, 375 °C, 10,000 h^{-1})

data could be obtained by using either the pure Langmuir–Hinshelwood–Hougen–Watson (LHHW) model, with explicit adsorption terms and restrictive hypotheses on the rate determining step or the Temkin equation, which was developed for a specific, different catalytic system. Moreover, changing the parameters of the Temkin equation by modulation of α of parameter was not sufficient to account for a catalytic behavior substantially different from that of the Fe-based catalyst. Pernicone[194] introduced terms accounting to the competitive adsorption properties of the Ru-based catalyst, by modifying the classical Temkin equation. A general form of the proposed model is the following:

$$r_{NH_3} = k_f \frac{f_{N_2}^n \left(\frac{(f_{H_2})^{3n}}{(f_{NH_3})^{2n}}\right)^{\alpha} - \frac{1}{(K_a)^{2n}} \left(\frac{(f_{NH_3})^{2n}}{(f_{H_2})^{3n}}\right)^{1-\alpha}}{1 + K_{N_2} \frac{1}{(K_a)^{2nw_2}} \frac{(f_{NH_3})^{2nw_2}}{(f_{H_2})^{3nw_1}} + K_{H_2}(f_{H_2})^{3nw_1} + K_{NH_3}(f_{NH_3})^{2nw_2}}. \tag{6.27}$$

In which, the adsorption term related to N_2 shows a negligible influence. The two kinds of parameters need to be confirmed i.e., four model parameters of n, α, w_1 and w_2,and three kinetic and thermodynamic parameters of k_f, K_{H2} and K_{NH3}. The optimized parameters is obtained as follows: $n = 1.0$, $\alpha = 0.15$, $w_1 = 0.5$ and $w_2 = 1.4$ according to our experimental data obtained at the conditions of H_2/N_2 in range of 1.0–3.0, temperature range of 350°–450°C, space velocity range of 6,000–1,80,000 h^{-1} and pressure of 10 MPa for Ba–Ru–K/AC catalyst. The proposed model of Modified Temkin Equation is obtained as following equation[195]:

$$\frac{dy_{NH_3}}{d\tau} = k_f (1 + y_{NH_3})^2 \frac{f_{N_2} \left(\frac{f_{H_2}^{0.45}}{f_{NH_3}^{0.3}}\right) - \frac{1}{K_a^2} \left(\frac{f_{NH_3}^{1.7}}{f_{H_2}^{2.55}}\right)}{1 + K_{H_2} f_{H_2}^{1.5} + K_{NH_3} f_{NH_3}^{2.8}}. \tag{6.28}$$

Hence, only three parameters, k_f, K_{H2} and K_{NH3}, need to be optimized. Data fitting shows a good agreement for every test run, giving an error mostly lower than 5%. The consistency of the optimized parameters was checked again through the Arrhenius or Van't Hoff equations, which allows to obtain reliable kinetic and thermodynamic parameters (Table 6.44), with excellent correlation coefficients. The values of $NH_{H2,ads}$ derived from this model confirm H_2 inhibition. The NH_3 adsorption term gives a significant contribution (Table 6.44).

Due to the equilibrium ammonia concentration changes with H_2/N_2 according to thermodynamics of ammonia synthesis reaction. Therefore, outlet ammonia concentration cannot directly reflect the influence of H_2/N_2 on catalytic activity. Hence, the catalytic efficiency is defined as the ratio of outlet ammonia concentration to equilibrium ammonia concentration at the same conditions. The effect of H_2/N_2 on catalytic efficiency for Ba–Ru–K/AC catalyst is shown in Table 6.45. It can be

Table 6.44 Kinetic and thermodynamic parameters of Ba–Ru–K/AC catalyst (Modified Temkin Equation)[a]

Ea	A	CC[b]	$\Delta H_{H_2,ads}$	$\Delta S_{H_2,ads}$	CC	$\Delta H_{NH3,ads}$	$\Delta S_{NH3,ads}$	CC
90.2	2.84×10^9	0.9991	−76.2	−125.9	0.9938	−43.4	−71.3	0.9971

[a]A Ea and ΔH_{ads} are expressed as kJ/mol, and ΔS_{ads} is expressed as J/(mol · K).
[b]Correlation coefficient.

Table 6.45 Effect of H_2/N_2 on catalytic efficiency for Ba–Ru–K/AC catalyst/%

H_2/N_2 ratio	3		2.5		2.0		1.5		1.0	
Temperature/°C	400	350	400	350	400	350	400	350	400	350
Pressure/MPa										
5	99.3	52.1	100	57.5	100	65.2	99.3	76.7	100	92.9
7	98.4	41.1	98.9	45.5	99.4	51.9	99.4	63.5	100	80.7
10	89.0	32.5	92.0	35.8	95.8	40.7	98.6	49.7	99.4	66.5
13	77.6	27.5	81.4	30.3	86.6	34.7	94.1	42.2	99.0	57.5
15	70.9	25.3	74.5	27.8	80.5	31.7	89.2	38.8	98.7	53.2

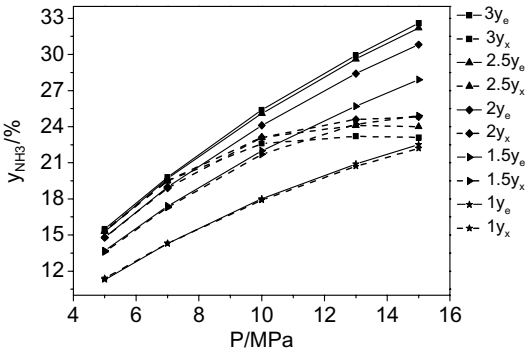


Fig. 6.61 Relationship of equilibrium (Solid) and predictive (Dash) of ammonia concentration at 400°C, 10,000 h^{-1}. ay_e-equilibrium concentration, ay_x-predictive concentration, a-H_2/N_2 value.

seen that the catalysts efficiency is increased with decrease of H_2/N_2 under the same pressure and temperature, for example, when H_2/N_2 is decreased from 3.0 to 1.0, the catalysts efficiency is increased from 32.5% to 66.5% at 10 MPa and 350°C and increased by 105%. And further, the lower the temperature, the higher the pressure, the larger the degree of increase is. This result is consistent with that of Fig. 6.60.

It is noteworthy that when pressure is higher than 10 MPa, except for $H_2/N_2 = 1$, where the outlet ammonia concentration decreases gradually with increase of pressure at 400°C (see Fig. 6.61), and especially at 350°C (see Fig. 6.62). That is, the outlet ammonia concentration is not increased with increase of pressure at low temperatures for activated carbon supported ruthenium. This phenomenon is inconsistent with the kinetics and thermodynamics of ammonia synthesis reaction and kinetics on iron catalysts. It is possibly due to existence of serious hydrogen inhibiting effect on the Ru catalyst. This inhibiting effect is more evident with increasing of pressure and the lower the temperature, the larger this inhibiting effect is.

Therefore, difference from iron catalyst, the adsorption of H_2 has a strong inhibition of the adsorption of N_2 on Ru catalyst, whereas it is not evident with the inhibition of product NH_3,[21,196–200] which is the nature character of Ru catalyst for ammonia synthesis reaction. Therefore, when $H_2/N_2 = 3$, the activity of Ru catalyst is higher than that of iron catalyst at high temperatures, while it is lower

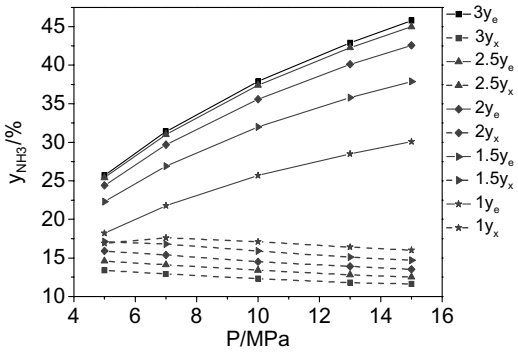


Fig. 6.62 Relationship of equilibrium (Solid) and predictive (Dash) of ammonia concentration at 350°C, 10,000 h^{-1}. ay_e-equilibrium concentration, ay_x-predictive concentration, a-H_2/N_2 value

at low temperatures (see Fig. 6.56). It is contrary at low H_2/N_2 ratio. So Ru catalyst is suitable for low H_2/N_2. The insignificant inhibition of NH_3 is an advantage of Ru catalyst. Therefore, Ru catalyst can be loaded after the iron catalyst, such as KAAP technology. The inhibition of H_2 is still a problem needing to be solved on Ru catalyst.

6.3.3.2 *The possible reasons of hydrogen inhibition*

(1) The strong adsorption of H_2 on Ru catalysts. There are a lot of assumptions on the reasons to induce inhibition of hydrogen, one of the most representative is competitive adsorption model proposed by Kadowaki *et al.*[30]

Assuming H_2 and N_2 occupy the same adsorption site with each other, based on Langmuir equation, when the adsorption processes reach the equilibrium, the coverage of N(a) and H(a) is a function of pressure.

$$N_2 + 2 \text{ sites} = 2N(a). \tag{6.29}$$

$$H_2 + 2 \text{ sites} = 2H(a). \tag{6.30}$$

The dissociation adsorption rate (r_a) and the desorption rate (r_d) of dinitrogen molecule are,

$$r_a = k_a P_{N2}(1 - \theta_N - \theta_H)^2, \tag{6.31}$$

$$r_d = k_d \theta_N^2, \tag{6.32}$$

k_a and k_d are the adsorption and desorption rate constants, respectively. On equilibrated state, $r_a = r_d$, obtains,

$$r_a = r_d = \frac{k_a P_{N_2}}{(1 + \sqrt{K_N P_{N_2}} + \sqrt{K_H P_{H_2}})^2}. \tag{6.33}$$

If without H_2, that is, there is only adsorption and desorption of N_2, Eq. (6.34) changes,

$$r_a = r_d = \frac{k_a P_{N_2}}{(1 + \sqrt{K_N P_{N_2}})^2}. \tag{6.34}$$

When the isotopic equilibration reaction rate of dinitrogen ($^{15}N_2+^{14}N_2 = 2^{14}N^{15}N$) is used instead of the adsorption and desorption rate on adsorption in equilibration, k_a,K_N and K_H can be obtained based on the experimental data. And activation energy of E_a (14.3 kcal/mol), adsorption heat of dinitrogen of Q_N (4.2 kcal/mol) and adsorption heat of H_2 of Q_H (9.9 kcal/mol) can be obtained *via* calculation. Adsorption heat of hydrogen is larger than the adsorption heat of dinitrogen, which indicates the adsorption of hydrogen is faster than nitrogen.

Dissociative adsorption of dinitrogen molecule ($N_2 + 2^* \rightarrow 2N^*$) is generally regarded as the rate determining step of ammonia synthesis reaction. The isotopic equilibration of nitrogen also needs dissociation of dinitrogen molecule:

$$^{14}N_2 + {}^{15}N_2 = 2^{15}N^{14}N. \tag{6.35}$$

Therefore, if the catalyst has activity for N_2 isotopic equilibrium, it has certain activity for the ammonia synthesis reaction. But the reaction rates of them are different because catalyst surface is only covered with nitrogen on the isotopic equilibration, while the part of the surface is covered with hydrogen during ammonia synthesis reaction.

Kadowaki Y *et al.*[30] detected the rate of ammonia synthesis and isotopic equilibration of nitrogen on the Ru catalysts without or with Sm_2O_3 and obtained the relationship between temperature and rate as shown in Fig. 6.63.

It can be seen from Fig. 6.63 that the rate of isotopic equilibration reaction is higher than the ammonia synthesis reaction without Sm_2O_3. At the same time, with the addition of Sm_2O_3, the rate of isotopic equilibration reaction declines a lot, while the rates of ammonia synthesis reaction are all higher. This indicates that the effect of hydrogen is very evident at this time, which is a problem that cannot be ignored on Ru catalyst.

For Raney Ru and Raney Ru–$CsNO_3$, Hikita *et al.*[92] studied the relationship between the rate of isotopic equilibration reaction of nitrogen with the pressure of hydrogen and compared its rate on equilibration and ammonia synthesis reaction, pointed out that the nitrogen dissociative adsorption on Ru catalyst are significantly

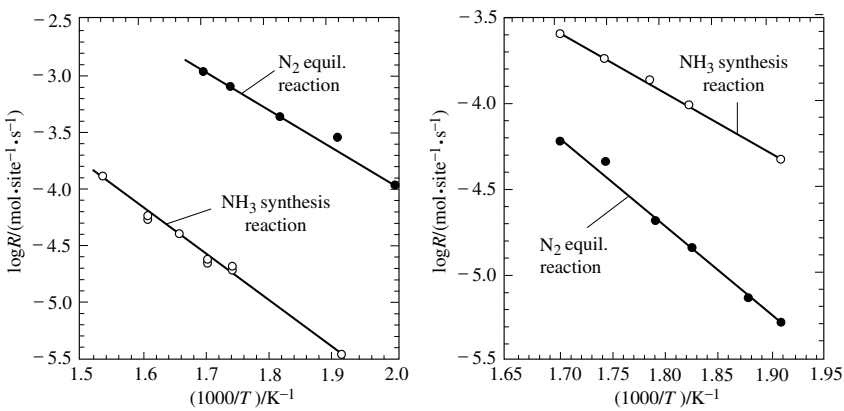


Fig. 6.63 Relationship of rate and temperature on ammonia synthesis reaction ($N_2 + 3H_2 = 600$ Torr) and isotopic equilibration reaction ($^{14}N_2 + {}^{15}N_2 = 150$ Torr)

restrained by hydrogen. This phenomenon should be related to two aspects, namely, the surface state and the type of promoters. It is a very important problem that the effect of hydrogen for ammonia synthesis reaction on Ru catalyst under industrial conditions. If we could control the inhibition of hydrogen on Ru catalyst, it will be a better catalyst for ammonia synthesis reaction because the rate of its isotopic equilibration reaction of nitrogen is higher than other catalysts.

It is seen that because there are the competitive adsorption of H_2 and N_2 on the surface of ruthenium catalyst and the adsorption heat of H_2 is larger than N_2, so the strong adsorption of H_2 occupies the active site of the catalyst surface, and is likely to generate hydrogen bridged compounds of sub-layer, especially on the system in which alkali metal hydroxide is used as promoter. Many of the activity sites on ruthenium catalyst are firmly occupied by H_2, which hindered the determining reaction step of N_2 dissociative adsorption and the reaction rate of ammonia formation is decreased.

From H_2-TPD spectrum of Ba–Ru–K/AC catalyst (Fig. 6.64 (II)), three desorption peaks are identified, which indicate that there are three kinds of adsorption active sites for H_2 on catalyst surface.[61] The first peak, at about 150°C, is more symmetrical, which is a typical secondary desorption; the second peak, at about 400°C, is very small, and compared with other two peaks, it basically can be ignored; the third peak, at above 500°C, is corresponding to the hydrogen of strong adsorption and spillover on the surface of the catalyst.

In order to verify the above mentioned reactive species of hydrogen, the catalyst with preadsorpbed hydrogen was first pulsed with N_2 several times at 425°C, then H_2-TPD spectrum was detected once again as shown in Fig. 6.64 (I). It can be seen from comparison of (I) and (II) in Fig. 6.64 that desorption peak at about 150°C significantly reduces, if with enough pulses, it could completely disappear. While the desorption peak at about 400°C and above 500°C basically does not change, which mean that the adsorbed hydrogen species at high temperatures basically are not reactive. There are mainly three kinds of viewpoints about these types

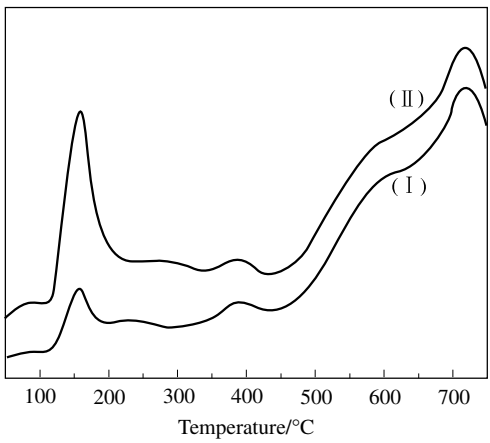


Fig. 6.64 Activity of reaction of adsored hydrogen with nitrogen on Ba–Ru–K/AC catalyst. (I) H_2-TPD spectrum after pulse N_2; (II) H_2-TPD spectrum before pulse N_2

Table 6.46 N_2-TPD and H_2-TPD of different catalysts (10°C/min)

	N_2 — TPD Low temperature desorption peak		H_2 — TPD Low temperature desorption peak		H_2 — TPD High temperature desorption peak	
Catalyst	T_m/°C	E_d/(kJ · mol^{-1})	T_m/°C	E_d/(kJ · mol^{-1})	T_m/°C	E_d/(kJ · mol^{-1})
Ru/AC	420.0	180.0	331	47.60	545	366.45
Ba–Ru/AC	412.5	160.0	330	48.22	560	242.86
K–Ru/AC	358.0	147.1	117	20.21	720	368.65
Ba–Ru–K/AC	360.0	140.4	147	26.24	725	151.09
Iron (A301)	529.5	167.9	120	32.70	325	34.70

Note: T_m is temperature of desorption peak; E_d is activated energy of desorption.

of high-temperature hydrogen adsorption: Spillover's hydrogen, strongly adsorbed hydrogen, and hydrogen formed metal hydride which is located in the metal subsurfaces or lattice defects. From view of points of inhibition of H_2 on ammonia synthesis reaction, there must contain strongly adsorbed hydrogen species in those high-temperature adsorption hydrogen. From Fig. 6.64, the adsorbed hydrogen peak at high temperatures is very large, which indicates a considerable part of adsorbed hydrogen is spillover's hydrogen.

Table 6.46 shows the peak temperature of desorption and desorption activation energy measured by N_2-TPD and H_2-TPD on ruthenium-based and iron-based catalysts. It can be seen that desorption activation energy of weak adsorption hydrogen at low temperature on the Ba–Ru–K/AC catalyst with potassium, especially K–Ru/AC catalysts is lower than that on iron catalyst and shows that the adsorption of H_2 on Ru catalyst with potassium is much easier than iron catalyst. Contrarily on Ru/AC and Ba–Ru/AC catalyst without potassium are all higher than iron catalyst. This also implies that potassium will promote the adsorption of hydrogen, while barium inhibits it. But when compared with the two high temperature desorption peaks, it can be found that the temperature and activation energy of desorption of H_2 on Ru catalyst with or without potassium are much higher than iron catalyst. The desorption activation energy of the former is basically about 10-fold higher than the latter. Therefore, the strongly adsorbed hydrogen on Ru catalyst is much higher and more stable than on iron catalyst under reaction conditions.

The desorption temperature and desorption activation energy of hydrogen are far lower than that of nitrogen on iron catalyst. Therefore, for iron catalyst, H_2 adsorption has little inhibition effect on the reaction, while the temperature and activation energy of desorption of hydrogen at high temperatures are all higher than that of nitrogen on Ru catalyst. These strongly adsorbed hydrogen species occupy the part of active sites, and therefore have an obvious inhibition effect on N_2 adsorption.

(2) The change of the surface status of catalysts. Researchers considered that the possible reasons causing hydrogen inhibition can come from to two facts, i.e., the non-structural changes and the reversible structural changes as shown in Table 6.47. Kubota [23] and Izumi Y *et al.*[201] identified the absorbed nitrogen and hydrogen atoms by FTIR at room temperature, respectively. They found that on Ru/MgO or Ru–CsOH/MgO, the adsorption process of nitrogen is hindered by hydrogen atoms

Table 6.47 Hydrogen effect on ruthenium-based ammonia synthesis catalyst

Reasons	
1. Non-structural changes (reversible)	2. Reversible structural changes
(i) Competitive adsorption of H_2 and N_2.	(i) Formation of hydride on sub-layer of Ru.
(ii) Induced-effect of adsorption of H_2.	(ii) Formation of reversible surface hydroxides on promoters and supports.
(iii) Changes of major adsorption species (such as from N to NH).	(iii) Formation of hydrogen bridge on interface interface of Ru and support.

and also mentioned the interaction of short-range and long-range between N_2(a) and H(a).

Some researchers found that many structural changes are caused by hydrogen effect. Hydrogen atom can combine with the surface in secondary layer of ruthenium,[202] which causes the relaxation of ruthenium atoms on the surface, thereby changes the activation character of nitrogen. On Pt/SO_4^{2-}-ZrO_2, spillover's hydrogen can change into the protons and many electrons on the surface.[203] While for Ru/support system, the spillover's hydrogen will also change the character of support. If there is very small amount of Pt particle on Al_2O_3, hydrogen will locate on the interface of Pt and oxide.[204] If this status happens in Ru-support system, the character of ruthenium may also be changed. These changes of the structure are all reversible for much long time at least.

From all the above-mentioned explanations for hydrogen inhibition phenomenon, no matter what kind of reasons, they are related to both the strong adsorbed hydrogen or through the role of hydrogen thereby to reduce the adsorption of nitrogen. It indicates that we should estimate the strong of hydrogen inhibition from the adsorption status of hydrogen and nitrogen.

Although the phenomenon of strong chemisorption of hydrogen causes a strong inhibition on the dissociative adsorption of nitrogen, it has attracted serious attention.[96,205,206] there is no unanimous view of the mechanism of hydrogen inhibition. Niwa *et al.*[207] found that the addition of rare earth compounds can effectively inhibit the strong adsorption of hydrogen. Siporin *et al.*[208] considered that the stronger the alkaline of support, the larger the adsorption enthalpy (large coverage) of hydrogen and the more negative the reaction order of hydrogen. The change of reaction orders may be caused by different geometries of hydrogen bonding with different supports. Each catalyst has at least two active sites and the alkaline promoter can generate a highly active site on catalyst. Through study of the decomposition of ammonia on ruthenium catalyst, it is found that desorption of nitrogen is the rate determining step of this reaction.[209] Desorption rate of nitrogen is related to the concentration of the surface hydrogen because of the nitrogen desorption is inhibited by the coadsorbed surface hydrogen. Here, there is spillover phenomenon of surface hydrogen and barium as promoter plays the role in hindering spillover of hydrogen. Therefore, author[210] considers that the strong adsorption of hydrogen may be related to the acid-alkali coverage of the surface on catalyst based on the following experimental results. Ruthenium catalyst supported on activated carbon (or MgO) usually uses alkali metal or alkaline earth metal oxides as promoters. The surface is wholly covered with alkaline, so the inhibition of hydrogen strong chemsorption is the most serious; the alkaline is stronger than acidic on the surface of iron catalyst

with Fe_3O_4 as precursor, and also exist hydrogen strong chemisorption phenomenon; on the surface of iron catalyst with wüstite as precursor, alkaline is weaker than acidic and mutual coordination, so there is no hydrogen strong chemisorption phenomenon. This fact indicates that the stronger the alkaline on the catalyst surface, the stronger the hydrogen strong chemsorption and there is a synergy between the acidity and alkalescency. Hereby, if we can introduce a suitable acidic promoter in ruthenium catalyst, this might play an inhibition role of hydrogen strong chemisorption, but this hypothesis still requires further experimental confirmation.

6.3.3.3 *Measures to reduce hydrogen inhibition*

(1) Promoter effect. Potassium (K) and barium (Ba) are good promoters for Ru/AC, while barium can increase not only the catalytic activity, but also the dispersion of ruthenium, as well as prevent the sintering of Ru crystallite, reduce the methanation reaction of activated carbon, improve the thermal stability of the catalyst. The role of electronic promoter about K is more evident, but it can only increase the catalytic activity, and it cannot prevent the sintering of Ru crystallite and the methanation of activated carbon.

But from above discussion on the kinetic parameters of different Ru-based ammonia synthesis catalysts, we have known that, on the catalyst with K, Cs and other alkali metals as promoters, the reaction orders of hydrogen are all negative and the rate of ammonia synthesis reaction decreases with the increasing of hydrogen pressure. The H_2-TPD results of Ru catalysts with K and Ba as promoters are shown in Fig. 6.65 and Table 6.46.[61] From Fig. 6.65, the adsorptions amount of H_2 on K–Ru/AC(c) and K–Ba–Ru/AC (d) are larger than that of on Ru/AC (a) and Ba–Ru/AC (b). The addition of K can significantly increase the strong adsorption of H_2 at high temperatures and Ba decreases the adsorption amount. This can be seen from the comparison of Ba–Ru/AC (b) with K–Ba–Ru/AC (d).

Urabe K *et al.*[96] considered that when ammonia exists on Ru–K/AC, part of K will transform to the amino or imide compounds. In the presence of hydrogen, part of K will transform to the hydrides which decreases the ability of supplying

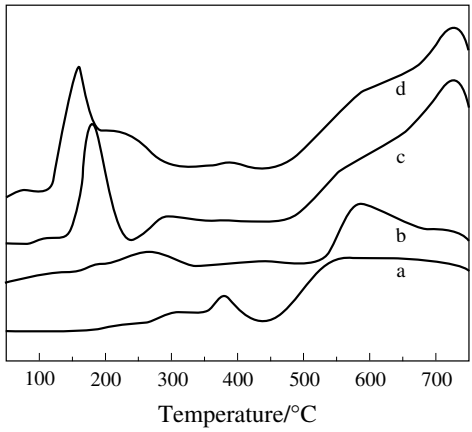


Fig. 6.65 H_2-TPD of different catalysts. a–Ru/AC; b–Ba–Ru/AC; c–K–Ru/AC; d–Ba–Ru–K/AC

electron of K. After the addition of hydrogen, the obvious decrease of the adsorption constant of nitrogen is probably caused by this change.

It can be seen that to weaken the strength and quantity of strongly adsorbed hydrogen on the catalyst promoted by K is very important for avoiding hydrogen inhibition. Therefore, it is possible that the metal oxides with weak alkaline or acidic as promoters can decrease the hydrogen inhibition and increase the reaction order of hydrogen. Apparently, barium is an effective promoter. The rare earth metals can decrease the hydrogen inhibition, which probably due to their weaker alkaline than that of the alkali metal and their strong ability supplied electron.

The study of Murata *et al.*[3] shows that, as the promoters of chlorine-free Ru/Al_2O_3 catalyst, $La(NO_3)_3$, $Ce(NO_3)_3$ and $Sm(NO_3)_3$ have much stronger promoting role than that of $CsNO_3$. The small amounts of $La(NO_3)_3$ (La/Ru = 1) can also achieve the same activity with large amount of $CsNO_3$(Cs/Ru = 10) for the 2% Ru/Al_2O_3 catalyst. For ammonia synthesis reaction at 101 kPa, the apparent activation energy (11–15 kcal/mol) with lanthanum as promoter is lower than that of Cs-promoted (24 kcal/mol). It can be known from XPS results that ruthenium is in metallic state in Ru/Al_2O_3 (462.1 eV) and Ru–M_2O_3/Al_2O_3 (M = La, Ce, Sm) (462.2 eV–462.6 eV) catalysts. The final state of $CsNO_3$ is CsOH in Ru/Al_2O_3; while for the lanthanide promoter are all their oxides in the catalyst. $La(OH)_3$ is very unstable and decomposes to La_2O_3 at 588 K and La_2O_3, while Ce_2O_3 and Sm_2O_3 have very high melting point (which are 2588, 1965 and (2573 ± 50) K, respectively), therefore they have good stability.

From experiments of hydrogen adsorption at room temperature, Aika *et al.* found that when the molar ratio of Sm/Ru was 10, the adsorption amount of hydrogen will reduce to 1/3 of the origin, which indicates that there is a very strong interaction between ruthenium and lanthanide oxides. The chemisorption amount of hydrogen is not reduced obviously following the addition of CsOH on ruthenium surface. For example, when Sm/Ru = 10.0, the H/Ru ratio will decrease to 0.18, while Cs/Ru = 10.1, the H/Ru ratio is 0.45.

For ammonia synthesis reaction (ASR) ($N_2 + 3H_2 = 2NH_3$, 80 kPa) and isotopic equilibration reaction (IER) of nitrogen ($^{14}N_2 + {}^{15}N_2 = 2{}^{14}N{}^{15}N$, 20 KPa) on Ru/Al_2O_3 catalyst at about 588 K (Table 6.48), Kadowaki *et al.*[30] compared with following three catalysts, found that the rate of ASR is faster than IER on Ru–Sm_2O_3/Al_2O_3 catalyst and the former rate is slower than the latter on Ru/Al_2O_3 and Ru–$CsOH/Al_2O_3$ catalyst. IER is seriously affected by the hydrogen poisoning on the Ru/Al_2O_3 and Ru–$CsOH/Al_2O_3$ catalyst. There also

Table 6.48 Rates of ASR and IER of dinitrogen on three ruthenium-based catalysts

	Ammonia synthesis reaction[a]		Isotope equilibrium reaction of dinitrogen[b]	
Catalysts	E_a/ (kcal/mol)	TOF/ (site^{-1} s^{-1} × 10^4)	E_a/ (kcal/mol)	TOF/ (site^{-1} s^{-1} × 10^4)
Ru/Al_2O_3	15.1	0.27	14.8	6.29
Ru-$CsOH/Al_2O_3$	27.7	1.89	15.9	9.57
Ru-Sm_2O_3/Al_2O_3	16.5	1.34	23.5	6.60

[a] $N_2 + 3H_2 = 2NH_3$ at 80 kPa and 588 K.
[b] $^{14}N_2 + {}^{15}N_2 = 2{}^{14}N\ {}^{15}N$ at 20 kPa and 588 K.

is this situation for other catalysts, such as Raney Ruthenium, Ru–K/AC and Ru–K/Al_2O_3 catalysts. The activity of nitrogen is hindered on these catalysts due to the fact that the adsorption of hydrogen is stronger than that of nitrogen. While on Ru–Sm_2O_3/Al_2O_3 catalyst, this inhibition caused by hydrogen can be neglected. The promotional effect of Sm_2O_3 is to eliminate the inhibition of hydrogen which consequently speeds up the nitrogen adsorption. So we can use Sm_2O_3 to change the physical properties of ruthenium surface. Because of lanthanum oxide cannot provide enough electrons, so cannot speed up the rate of IER of nitrogen.

Many studies have reported the strong metal-support interaction (SMSI) between metal oxides and transition metals.[211] It is possibly the similar status that the interaction between surface atoms may lead to the weakening of hydrogen adsorption on Ru–Sm_2O_3. Lanthanide oxides are regarded as not only the structural but also effective electronic promoter. Even though they have + 3 valences, the ionic radius is larger, so they are able to generate O_2^- or O_2^{2-} coordinated with O_2. Under experimental conditions, ruthenium may obtain electrons through the reaction with CeO_2 as shown in the following equation,

$$Ce^{4+}(O^{2-})_{2-x}(e^-)_{2x} + Ru = Ce^{4+}(O^{2-})_{2-x} + Ru(e^-)_{2x}. \tag{6.36}$$

(2) Double metal of Ru–M catalysts with bimetallic active centers. The existence of strongly adsorbed hydrogen is one of the main reasons of hydrogen inhibition. There is both strong and weak hydrogen absorption on most transition-metals.[212] Hall[213] has studied the influence of the hydrogen adsorption (pre-adsorption of hydrogen) in the ethylene hydrogenation reaction on Cu–Ni powder catalysts. The catalyst was treated in hydrogen flow at reaction temperature (200°C) or in helium flow, followed by the introduction of the reaction gas. It was found that the pretreatment of hydrogen hindered the reaction for pure Ni, while it can promote the reaction for the alloy. The promoted degree is the highest when the alloy contains 10%–20% Ni. The reaction rate difference of transition-metal and Cu–Ni alloy caused by the hydrogen or helium treatment at different temperatures has also been obtained.[214] It was found that Fe and Co are less active as same as Ni after treated in hydrogen. Therefore, it can be inferred that *d*-metals will be poisoned, while activities of *sp*-metal are promoted by hydrogen. The adsorption properties of the transition metals and their nearby metals are considered with their *d* electrons. The *d* orbit can totally contain 10 electrons. In fact, not each *d* orbit is filled and there are some unpaired electrons or the vacancy. The influence of *d* electron to the metallic bonds is called the "*d*−characteristic." The stronger of the *d*-characteristic, the *d* electrons are more tended to bind with metal and more difficult to participate in binding to the adsorbed atoms.

The *d*-characteristic (50%) of ruthenium is the strongest among the transition metals, and that of Ni, Co are about 40%. Therefore, the hydrogen poison of ruthenium is more obvious and more serious than that of Ni and Co. The *d*-characteristic of metal is reduced by alloyed catalyst in above ethylene hydrogenation, therefore the hydrogen inhibition is eliminated. In the alloy composed by Cu(x) and Ni (1−x), the vacancy of *d* orbit is 0.6−x when $x < 0.6$ and 0 when $x > 0.6$, respectively. According to the valence principle of Pauling, Hall has calculated the *d*-characteristic of Cu-Ni alloy as shown in Table 6.49.

Table 6.49 Relationship between Cu content in Cu-Ni alloy and *d*-characteristics

Cu content/%	*d*-characteristic	Cu content/%	*d*-characteristic
0	0.400	60	0.382
10	0.399	70	0.376
20	0.395	80	0.370
30	0.392	90	0.363
40	0.389	100	0.357
50	0.386		

Therefore, it can try that the formation of the Ru–M alloy may change the *d*-characteristic of Ru. As a result, it changes the quantity and the strength of the strongly adsorbed hydrogen on the Ru catalyst. The formation of the solid solution is needed before alloy formation. The two kinds of metal which can form the solid solution should have the same lattice type and their atomic diameters are close to each other. Ruthenium metal crystal lattice belongs to hexagonal close-packed (hcp) structure, but most of transition metals and their nearby metals are the face-centered cubic (fcc) or body-centered cubic (bcc) crystal lattice. Only the Os and Co are the same to Ru, and Co lattice will undergo transformation from the hcp to fcc at (417 ± 7)°C. But the d characteristic value of Os is close to that of Ru and their alloy is insignificance. Therefore, Ru–Co alloy can be chosen theoretically, but the hcp structure of the Co must be controlled and fixed. For example, double-metal Ru–Co catalyst supported on magnesia-alumina spinel, magnesium-alumina composite oxides and MgO prepared with the impregnation have good activity for ammonia synthesis.[215] The activity of the catalyst with 2% Ru and Co is equivalent to that of the catalyst with 4% Ru and Co, in which ruthenium is decreased by 50%. Therefore, this kind of catalysts with Ru–M can reduce the cost of the Ru catalyst.

(3) Change of H_2/N_2 ratio. The change of H_2/N_2 ratio is the most simple and the most direct method to weaken the hydrogen inhibition in industry. For iron catalysts, the results studied by author show that the optimum H_2/N_2 ratio with the maximum rate of ammonia synthesis reaction is related to the reaction conditions which can expressed by catalyst efficiency, $K = \varphi_{NH3}/\varphi^*_{NH3}$, as above mentioned i.e., the degree of outlet ammonia concentration (φ_{NH3}) reaching the equilibrium ammonia concentration (φ^*_{NH3}). According to the experimental results, we[216] obtained the quantitative relationship between the optimum $(H_2/N_2)_m$ and catalyst efficiency: $(H_2/N_2)_m = 1.5047 + 1.487K$. It indicates that $(H_2/N_2)_m$ is proportional to catalyst efficiency. The effect of strong inhibition of H_2 (in H_2/N_2) on the activity of ruthenium catalysts is very large and related to temperature. The effect of H_2/N_2 on catalytic activity at 400°C, 375°C and 350°C are shown in Figs. 6.66–6.68.

It can be seen from these figures that the change of activity of A301 iron catalyst is very little with H_2/N_2 ratio, while it is obvious on Ru catalyst. At 400°C, the activity of Ru catalyst increases with the decreasing of H_2/N_2 ratio when it is higher than 1.5 and decrease when H_2/N_2 ratio is lower than 1.5 (Fig. 6.66). Here, the activity is above 22% on ruthenium catalyst and the equilibrium ammonia concentration is about 25% at $H_2/N_2 = 3$. At the same time, equilibrium ammonia concentration also decreases with the decrease of H_2/N_2 ratio. Therefore, the effect of change of H_2/N_2 ratio is not too obvious. For iron catalysts, the activity does not change with the decrease of H_2/N_2 ratio until H_2/N_2 ratio is lower than 0.67 at 400°C.

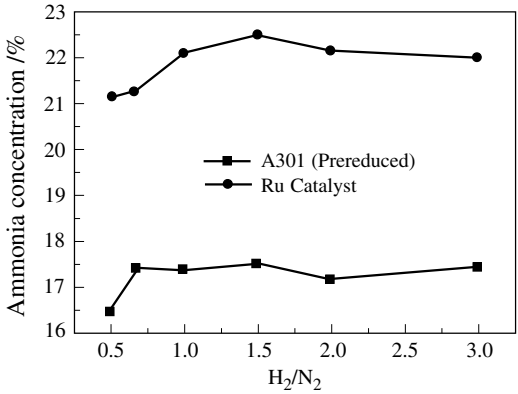


Fig. 6.66 Effect of H_2/N_2 on activities for Ru- and A301 iron catalysts (1) ($P = 10$ MPa, $t = 400°C$, $S_v = 10{,}000\ h^{-1}$)

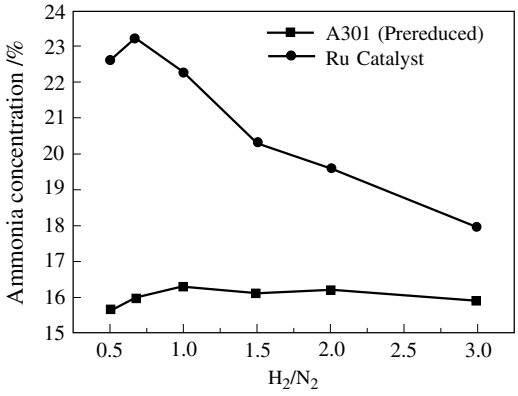


Fig. 6.67 Effect of H_2/N_2 on activities for Ru- and A301 iron catalysts (2) ($P = 10$ MPa, $t = 375°C$, $S_v = 10{,}000\ h^{-1}$)

As it was anticipated, the activity of ruthenium significantly increases with the decrease of H_2/N_2 ratio at 375°C (Fig. 6.67). The activity is above 18%, 22.25% and 23.18% for H_2/N_2 = 3, 1 and 0.67, respectively. The relative activities are increased by 24% and 29% for H_2/N_2 = 1 and 0.67, respectively, which is higher than that at 400°C. Therefore, the temperature of the highest activity on ruthenium catalyst is 375°C, the optimum H_2/N_2 ratio is 0.67. It is lower by about 50°C–75°C than that of the best iron catalyst (about 425°C–450°C) and the outlet ammonia concentration exceeds over 24%, which is higher by over 30% than the best iron catalyst.

At 350°C (Fig. 6.68), the activity of ruthenium catalyst increases from 9.33% to 15% when the H_2/N_2 ratio is 3 and 0.5, indicating that the relative activity increases by 60%. Fishel *et al.*[217] has also investigated the effect of H_2/N_2 ratio on the turnover frequency of ammonia (TOF). Similar results are shown in Fig. 6.69. The TOF increases in linearity with decrease of H_2 molar fraction and increase of N_2 molar fraction at 350°C.

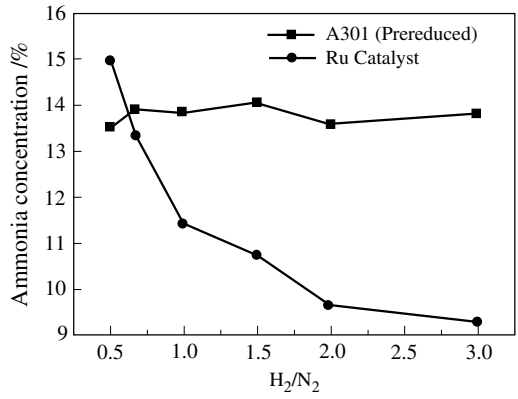


Fig. 6.68 Effect of H_2/N_2 on activities for Ru- and A301 iron catalysts (3) ($P = 10$ MPa, $t = 350°C$, $S_v = 10{,}000\ h^{-1}$)

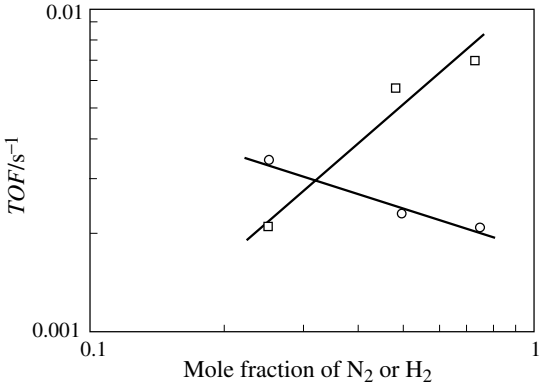


Fig. 6.69 Relation between TOF of ammonia synthesis reaction rate and mole fraction of N_2(□) and H_2(○) (623 K) (mole fraction of H_2 is 0.25 when change N_2 and mole fraction of N_2 is 0.25 when change H_2)

It can be seen that the hydrogen inhibition is closely related to the temperature for ruthenium catalysts. The lower the temperatures, the more serious the inhibition of hydrogen, the larger the effect of H_2/N_2 ratio is. This is related with catalysts efficiency. The lower the temperatures, the lower the catalysts efficiency and the larger the effect of H_2/N_2 ratio on the activity of high active catalysts is.

For high active ruthenium catalyst, the effect of change H_2/N_2 ratio on the activity is very little as the outlet ammonia concentration is very close to equilibrium at high temperatures and pressures. However, at low temperatures and low pressures, the catalytic activity increases with decrease of H_2/N_2 ratio due to reducing hydrogen inhibition. Low H_2/N_2 ratio not only decreases the operation cost and saves energy but also increases product yield.

The results show that decreasing the H_2/N_2 ratio or H_2 molar fraction in syngas is a direct and effective way to weaken hydrogen inhibition. Therefore the synthesis ammonia process must be reformed to suffice the demand of low H_2/N_2 ratio. But it

will make the process complex and increase investment costs. This is difficult in practice because the feeding gas composition and expended H_2/N_2 during formation of ammonia must be three. Therefore, before we can find the promoters which can inhibit the adsorption of hydrogen effectively, highly active ruthenium catalyst has not been completely used because of strong hydrogen inhibition at the conditions of industrial high-pressure, although the activity of ruthenium catalyst is much higher than the iron catalyst at atmospheric pressure.[30,207,218,219]

6.3.4 *Methanation reaction of activated carbon*

6.3.4.1 *The stability of ruthenium catalyst*

The stability of catalyst is one of the basic requirements in industry. Stability can be divided into chemical stability and physical stability. The former includes the stability of catalyst components and resists poison ability and the latter includes heat stability and mechanical strength. The heat stability of metal catalysts requires that the crystallite of active component does not sinter or grow up and crystal lattice cannot be destroyed or lattice defects cannot decrease, e.g., it cannot produce thermal sintering at the industrial operation temperature. Usually it is easy to sinter over their semi-melting temperature for the metal catalyst. Because the semi-melting temperature of metal ruthenium (the melting point is 2,583 K) is 356.5 K higher than the one of metal iron (the melting point is 1,870 K), the times-online (life times) of iron catalyst has preponderated over 18 years for in converter continuously using, while the operation temperature of ruthenium catalyst is at least 50°C lower than the one of iron catalyst. Therefore, heat-stability is not the major factor to determine the life times of ruthenium catalyst.

The experimental results shows that the activity was not changed after heating at 475°C for 20 hours for ruthenium catalyst. But if the temperature was increased to 500°C as same as that of iron catalyst, the activity would be significantly decreased up to above 20% for ruthenium catalysts. It is the reason that the activated carbon is lost due to methanation reaction. The operation situation of the first graphitized activated carbon supported ruthenium based ammonia synthesis catalyst put into application in 1992 was shown that the catalyst life of ruthenium based catalyst is determined by the loss of carbon support. Although the semi-temperature of metal ruthenium is 357 K higher than that of iron and might be used at higher temperatures, the ammonia concentration is close to equilibrium at 450°C. Therefore, it is not necessary that the reaction temperature is needed to increase to above 450°C in industry, and it is necessary and feasible to avoid the high temperatures above 500°C.

The chemical stability requires that the chemical compositions of catalyst are stable and can resist the poisoning effect of the harmful impurities (poison) on the catalyst at the reactive conditions. But for ruthenium catalyst with activated carbon as support, elementary ruthenium itself is an effective catalyst for carbon hydrogenation forming methane; and the support will be lost continuously with the methanation reaction. In other words, chemical compositions of ruthenium catalyst are unstable under the reaction conditions. This is a determining factor of affecting catalyst life and limiting its industrial application.

Therefore, one key subject for activated carbon supported ruthenium catalyst study is to solve the loss of activated carbon due to methanation and many scientists have done a lot of studies.[12−15,17,39,110,121,220] The current solutions way includes: (i) Graphitization of activated carbon and using promoter can inhibit the methanation; (ii) Seek for new support that can replace the activated carbon such as metal oxide.

6.3.4.2 *The effect of graphitization on methanation*

Kowalczyk *et al.*[13] suggested that the activated carbon was treated in pure argon flow at 1,300°C for one hour (AC1300) or in pure argon flow at 1,900°C (AC1900) for 2 h, then washed by water and dried at 120°C for 5 h. The surface properties of the activated carbon after treatment were measured with N_2 adsorption and high-pressure mercury method respectively as shown in Table 6.50.

It can be seen from Table 6.50 that the total micro-pores volume (V_{ODR}) changes slightly at 1,300°C, while the V_{ODR} changes from 0.33 to 0.036 $cm^3 \cdot g^{-1}$ at 1,900°C, and forms a kind of surface structure called as turbulent structure. Therefore, the micro-porous surface area (S_{DR}) is decreased from 890 $m^2 \cdot g^{-1}$ to 62 $m^2 \cdot g^{-1}$.

The average pore size (r_{DR}) is increased from 0.74 nm to 1.16 nm. The M–Ru/AC catalyst promoted by Ba or K was prepared by the activated carbon treated at 1,900°C, the conversion of activated carbon transform to methane in the H_2 flow (0.5 $ml \cdot s^{-1}$) for 24 h is shown in Table 6.51.

It can be seen from Table 6.51 that Ba promoter significantly inhibits the methanation of the activated carbon, the conversion drops from 21.8% to 3.2%, while K promoter is beneficial of the methanation and the conversion increases from 21.8% to 35.6%. The possible reason is that BaO partly covers ruthenium particles so that prevents the CH_x shifting towards ruthenium particles.

Forni L *et al.*[14] selected two kinds of activated carbons and one is pure activated carbon (G) which was made by coconut shell and treated respectively in the inert gas flow at 1,900°C or 2,000°C for 2 h. The sample treated at 1,900°C was calcined at 425°C in air flow for 12 h, then at 900°C in H_2 for 3 h. These samples are

Table 6.50 Effect of treatment with high-temperature on the surface properties of activated carbons

Surface properties	Original AC	AC1300	AC1900
$V_{ODR}/(cm^3 \cdot g^{-1})$	0.33	0.31	0.036
$S_{DR}/(m^2 \cdot g^{-1})$	890	540	62
$r_{DR}/(nm)$	0.74	1.15	1.16

Table 6.51 Conversion of activated carbon transform to methane

	Conversion of carbon/%		
Samples	743 K	793 K	Sum
Ru/AC	1.7	20.1	21.8
K–Ru/AC	2.6	33.0	35.6
Ba–Ru/AC	0.6	2.6	3.2

Table 6.52 Effect of treatment with high-temperature on the surface structures of activated carbon and catalytic activity of catalysts

Support	Ru/%	K/%	Ba/%	Cs/%	ρ/ $(g \cdot ml^{-1})$	Activity/ % mol	BET/ $(m^2 \cdot g^{-1})$	V_{total}/ $(cm^3 \cdot g^{-1})$
G	11.9	6.1	6.6	7.2	0.74	12.4	1188	0.49
G1900	11.8	6.5	6.6	7.1	0.87	15.0	187	0.11
G1900/OR	13.0	6.1	7.4	7.3	0.77	8.8	870	0.44
G1900/OR	17.6			22.1	0.78	14.3		
G1900/OR	17.6	21.1			0.75	5.8		
G1900/OR	17.2		2.4		0.68	12.1		
G2000	12.5	6.3	7.2	7.7	0.70	3.8	105	0.08
E	13.0	6.0	6.7	7.0	0.67	8.9	1253	0.75
E1500	12.3	6.2	6.2	6.9	0.74	14.7	964	0.72
E1500OR	13.0	5.9	6.5	6.8	0.72	15.2	1472	0.99
E2000	11.9	11.4	11.2	11.5	0.80	1.0	575	0.43
E2700	11.0	5.6	5.2	6.2	0.82	0.8	6	

Note: 1. G = activated carbon with granular (coconut shell), E = activated carbon strip (peach wood); 1,500, 1,900, 2,000, 2,700 is temperature (°C) of treatment in inert gas, respectively; O = oxidation in air, R = reduction in H_2 after oxidation in air.
2. The chemical composition based on the mass of catalysts.
3. ρ = packed density of catalyst bed.
4. Activity testing conditions: p = 100 bar, T = 430°C, GHSV = 30,000 h^{-1}

noted as G1900, G2000 and G1900OR, respectively. Another sample was as received activated carbon (containing 9% ash) (E) which was made of peach sawdust, and treated for 2 h in the inert gas at 1,500°C, 2,000°C and 2,700°C, respectively. The sample treated at 1,500°C was further treated as same as G1900OR and noted as E1500, E2000, E2700 and E1500OR, respectively. A series of catalysts with potassium ruthenium (K_2RuO_4) as precursor and K, Cs, Ba as promoter were prepared by impregnation method. The activity and the surface properties are shown in Table 6.52.

It can be seen from Table 6.52 that the surface area and pore volume decreased consumedly after treatment at high temperatures, and it can be partially restored by calcination in air, but it was difficult to restore after treatment at temperature above 1,500°C. The catalytic activity can be increased significantly for the impure E samples after treating at high temperatures, which shows that the purity of activated carbon has a great influence on the catalytic activity. It was a limit to increase activity by calcinations in air. The experimental results of methanation shows that the high temperature treatment increases the initial temperature of methanation from about 500°C to above 600°C, and therefore the higher the treatment temperature, the better the effect. However, there was no apparent effect of calcination treatment in air on inhibition methanation. This activated carbon is graphitized partly and increased the inhibition of methanation at high temperatures. The partial graphitization of activated carbon may enhance the basicity of surface and the capacity of the electron conduction. Strong basicity is resultant from enhancement of π bond between activated carbon layers, but not from the alkaline group, which is conductive to electron and inhibit methanation of carbon.[121]

Aika *et al.*[17] found that activated carbon treated by H_2 at 800°C–915°C for 90 h would start methanation at above 475°C. However, if methanation was controlled

at certain degree, methanation of support surface could increase surface area and porous volume and therefore improve the fine structure of activated carbon surface, which is favorable for the dispersion and generation of particles of ruthenium. Certainly, if methanation is out of control, catalyst activity will decrease due to aggregating of ruthenium particles. Therefore, it is necessary to control both the negative, positive effect of temperature by H_2 treatment. The best results are that the optimum temperature is 450°C for $RuCl_3$ reduction for 24 hours and 550°C for $Ba(NO_3)_2$ to decompose for three hours. The considered catalytic behavior is resulted from residual Cl^{-1} ions, ruthenium particle size, promoters and so on. Therefore, it was extremely important to effectively control the degree of methanation and reduction process during the preparation.

Non-carbon components in commercial activated carbons are removed effectively with treatment of microwave under the protection of N_2. In a certain temperature range, sintering of metal particles is prevented and methanation is difficult and therefore the thermal stability of catalysts is improved.[140,221]

It is reported that Pernicone *et al.* have conclusively resolved the problem of methanation by using high surface area graphite ($300\,m^2/g$–$400\,m^2/g$) without any pretreatment.[222]

6.3.4.3 *Influence of physical and chemical property of activated carbon on methanation*

(1) The effect of type and purity of activated carbon on methanation. Initial methanation temperature is related to element composition of six activated carbon made by different carbon materials, such as coconut shell (AC1), wood sawdust (AC2), peach shell (AC3), apricot shells (AC4), coal (AC5) and graphite (C6) as shown in Table 6.53.[223,224]

From Table 6.53, element compositions of activated carbon made by different carbon materials are significantly different. The purity (carbon content) of graphite with chemical pure is the highest, its ability of anti-methanation is the strongest among all shown carbon materials, and its initial temperature of methanation is above 600°C. It is due to the ordered crystal structure and low unsaturation of carbon atoms bond of graphite, which indicates that the structure of activated carbon, especially the existence of the edge carbon atoms with unsaturated bond is the main reason of its methanation.

Table 6.53 Effect of types of activated carbon on the initial temperature of methanation

Activated carbons	Composition of elements after treating by H_2 at 600°C–700°C for 6 h/wt%						Initial temperature of methanation/°C
	C	O	Si	S	P	Ash	
AC1	91.44	7.52	0.34	—[a]	0.33	0.37	493
AC2	85.97	12.77	0.31	—[a]	1.08	0.13	478
AC3	88.26	11.58	—[a]	—[a]	—[a]	0.16	480
AC4	86.24	12.19	0.21	0.39	—[a]	0.97	470
AC5	84.44	8.98	1.79	1.08	—[a]	3.71	523
C6	100	—[a]	—[a]	—[a]	—[a]	0	>600

[a]Not detected.

Four kinds of activated carbons derived from fruit shell, wood etc. were treated by H_2 at 600°C–700°C for six hours. The purity of activated carbon of coconut shell among them is the highest and reaching 91.44%.

Its ability of anti-methanation is stronger and initial temperature of methanation is 493°C. Therefore, purity of activated carbon derived from xyloid materials has the direct influence on methanation, the higher the purity, the stronger the ability of anti-methanation is. The possible reasons are that the unsaturated bond degree of the edge carbon atom is decreased with increasing of the purity. The activated carbon with low purity has many miscellaneous atoms, which have the influence on the combination between the carbon atoms or the strength of the C–C bond, making it easily fractured and leading to methanation. With activated carbon treated by H_2 at 600°C–800°C, its purity is increased. Although the graphitization degree is not increased, the ability of anti-methanation is improved, which indicates that impurity in activated carbon changes the inter-related strength between carbon atoms and makes activated carbon easy for methanation. Breaking of C–C bond may be the rate determining step.

Although the purity of activated carbon based on coal is the lowest, including the highest content of S, Si and other impurities, its ability of anti-methanation is not as good as graphite and better than that of activated carbon derived from xyloid materials, which is probably related to the special crystal structure of activated carbon derived from coal.

The purity of crude activated carbon derived from coconut shell is 90.86% and initial methanation temperature is 478°C. Its purity is increased to 91.44% after treatment by H_2 at 600°C–700°C for 6 h, and the initial temperature of methanation is increased to 493°C, which indicated that increasing purity is favorable to inhibit methanation of activated carbon.

(2) The effect of crystal structure of activated carbon on methanation. As mentioned above, the initial methanation temperature of activated carbon derived from coal is more than 500°C and above 600°C for graphite. Although low purity of activated carbon derived from coal, they have strong resist-methanation ability, which indicates the effect of micro-crystal structure on methanation is very significant. The main reason of methanation of activated carbon is the unsaturated dangling bonds of edge carbon atoms, which is confirmed from the crystal structure of carbon materials (Fig. 6.70).[223]

It is seen from Fig. 6.70 that the structures of activated carbon derived from different carbon materials are different. The activated carbon derived from coal has an obvious characteristic peak of graphite. From the crystal structure analysis of graphite, we can see that there is a hexagonal comby plane layer (A–B–A in Fig. 6.71) lattice structure formed *via* bonding the sp^2 hybrid orbit with three σ bond of neighboring atoms. There is still one $2p$ electron in the $2p$ orbit in per carbon atom. These p orbits parallel each other and perpendicular to sp^2 hybrid orbital plane, and therefore form a big π bond. Thus these π electrons can move on throughout the whole carbon plane, which is similar to metallic bond. The interaction between carbon layers with horizontal structure *via* intermolecular force (van der Waals force) forms graphite crystal (Fig. 6.71).

Due to the extremely high bond saturated degree of graphite surface, there cannot occur obviously methanation reaction below 600°C. The methanation degree of activated carbon derived from coal is low and the initial methanation temperature

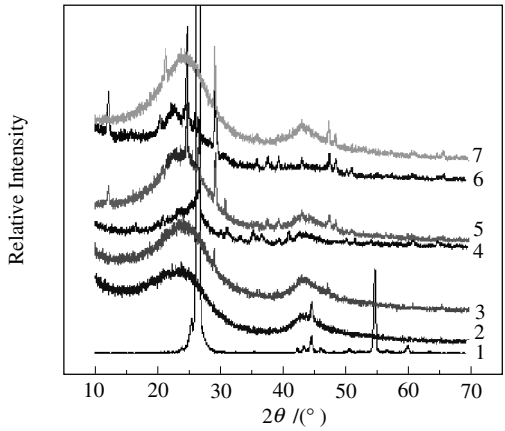


Fig. 6.70 XRD spectra of carbon materials (some spiculate peaks caused by ash in activated carbon).

1-graphite, 2-Coconut shell without pretreat, 3-Coconut shell with pretreat by H_2, 4-Soft coal, 5-apricot shell, 6-Wood, 7-peach shell

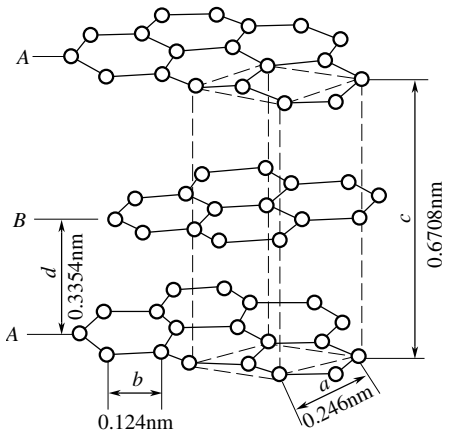


Fig. 6.71 Crystal structure of graphite

is high because the graphitization degree is higher than other four activated carbons.

(3) The effect of surface structure of activated carbon on methanation. As mentioned above, activated carbon was treated at high temperatures (especially above 1,900°C) and then its surface structure was restored in the O_2 flow, which greatly purified activated carbon and graphitized part of activated carbon. And with the higher temperature, the degree of graphitization is greater and the capacity of anti-methanation becomes stronger. Therefore, the activated carbon is not easily methanated,[12,14,121] but the specific surface area and pore volume are greatly reduced. Although specific surface area can be partly restored with the oxidation treatment, but the higher the temperature of treatment, the more difficult the surface area and pore volume are to be restored. It is notable that the surface area of

Table 6.54 Effect of physical structure of catalysts on the methanation

Sample	Micropore volume/ $cm^3 \cdot g^{-1}$	Mesopore volume/ $cm^3 \cdot g^{-1}$	Total volume/ $cm^3 \cdot g^{-1}$	Micropore areas/ $m^2 \cdot g^{-1}$	Mesopore areas/ $m^2 \cdot g^{-1}$	Total areas/ $m^2 \cdot g^{-1}$	Initial methanation temperature/°C
AC	0.255	0.240	0.492	528	265	793	493
Ru/AC	0.231	0.181	0.412	473	202	674	485
Ba–Ru/AC	0.134	0.145	0.250	274	167	380	538
Ba–Ru–K/AC	0.104	0.052	0.186	213	81	356	490

the activated carbon without the treatment at high temperatures is 2–4 times larger than that with high-temperature and then oxidation treatment, but the dispersion of ruthenium is equivalently close, which indicated that the dispersion of ruthenium is not closely related to the surface area of support. But the dispersion of ruthenium is closely related to the distribution of the pore size of the activated carbon treated at high temperatures. We considered that the fine structure of support is important for the dispersion of ruthenium due to most of the ruthenium particles distributed in the pore regions. After supported ruthenium and promoters, the surface microstructure of activated carbon derived from coconut shell (AC1) and the initial methanation temperature has some changes (Table 6.54). It can be seen from Table 6.54 there are the following four of phenomenon[223]:

(i) The volume and surface areas of mesopore of activated carbon decrease significantly after loading ruthenium which indicates that ruthenium is mainly located in around mesopore.
(ii) The surface area and volume of micropore, total surface area of activated carbon decrease by 40% after loading ruthenium and then barium, which indicates barium ions can mainly enter into the micropores.
(iii) The volume and surface areas of the mesopore decrease nearly to 1/3 and 1/2, respectively when loading potassium after ruthenium and barium, which indicates potassium fills most of the mesopore.
(iv) Barium promoter can effectively suppress methanation of support making its initial methanation temperature increase from 485°C to 538°C. It is possible that since barium mainly enters into and blocks in micropore, in particular, the micropore derived from mesopore, while the micropore includes more unsaturated carbon bond which lead to the methanation. As the electronic promoter, most of K which is distributed on the mesomicropore surface is not only beneficial to the ammonia synthesis reaction but also to the methanation of activated carbon. So the initial methanation temperature decreases from 538°C to 490°C for these catalysts impregnated with potassium after barium.

6.3.4.4 *The effect of compositions of catalyst on the methanation*

(1) Effect of ruthenium content. Rossetti[187] studied the the methane concentration at the methanation reaction for ruthenium contents being 1.9% and 8.9% Ru/AC (Fig. 6.72). The supports are graphitized activated carbon with BET $> 250\,m^2/g$, total pore volume of $0.4\,cm^3/g$, micropore volume of $0.07\,cm^3/g$. The ruthenium

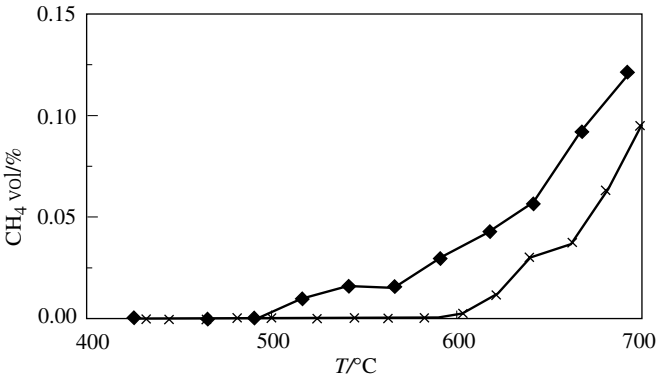


Fig. 6.72 Concentration of methane in experiment of methanation over Ru 1.9%(♦) Ru 8.9% (×)/AC catalysts (Ru precursor is K_2RuO_4)

precursor is K_2RuO_4. The promoter is K, Cs and Ba and the mole ratio of Ba/Ru = 0.6, Cs/Ru = 1 and K/Ru = 3.5.

It is found that the outlet methane concentrations are very low (beyond the instrument detection limit) for the above catalysts that can be detected when the micro-CH_4 at above 500°C. The initial temperature of methanation is higher over 8.9% Ru/AC than that over 1.9% Ru/AC. But initial methanation temperature of the latter has exceeded the operation temperature in industry, which shows that the above catalyst has high stability for methanation. Therefore, methanation is mainly determined on the nature of support, for example the degree of graphitization. The ruthenium content has nearly no influenced on methanation.[14,110]

(2) The inhibition effect of promoters on the methanation. It is commonly believed that for fused iron catalyst, Al_2O_3 increases iron surface area (structural effect), while K_2O donates electrons to iron atom, and increases electron density and enhances the activity of ammonia synthesis reaction (electronic effect). For the supported ruthenium catalysts, the effect of promoters on performances becomes more complex due to the existence of support. Although there are a lot of studies on the role of promoter for ammonia synthesis reaction, the chemical state, the distribution and the mechanism are still unclear. The role of promoters include covering chemisorption's site, donating electron to active metal, direct interacting with the adsorption intermediate and electrostatic field and so on.[26,158,226–230] For supported ruthenium catalysts, the role of promoter has a close relationship with its eletronegativity, and the smaller the eletronegativity, the better the catalytic effect is. So the alkali metal, alkaline earth metal oxides are commonly used as promoter because of their small electronegativity. But there is lack of deeply study on the inhibition of promoters on methanation. To understand the inhibition effect of alkali metal, alkaline earth metals, rare earth elements, transition metal on the methanation is beneficial to design effective promoters which can not only influence the activity but also inhibit methanation.

Table 6.55 shows the inhibition effect of alkali metal, alkaline earth metals as promoters on the methanation of activated carbon.[223,231] It can be seen that the alkali-earth metals have a good inhibition effect. There is a relationship between the effect and the relative atomic mass of alkaline-earth metal, i.e., the effect of inhibiting

Table 6.55 Inhibition effect of alkali metal, alkaline earth metals on methanation

Promoters	Without	K	Mg	Ca	Sr	Ba
Initial temperature of methanation/°C	493	475	506	507	516	538

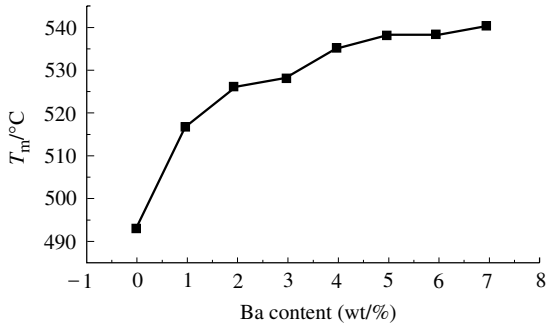


Fig. 6.73 Effect of Ba content on initial temperature of methanation

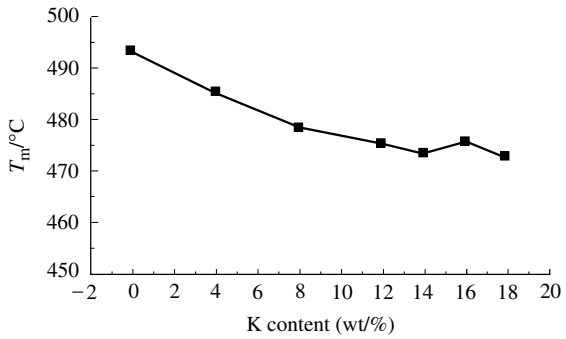


Fig. 6.74 Effect of K content on initial temperature of methanation

methanation is enhanced with increase of relative atomic mass. For example, the initial methanation temperature is increased from 506°C of Mg to 538°C of Ba. It is possible that the promoter plays a certain modified effect on the activated carbon topography and hindered CH_3^* species transfer toward ruthenium surface making it more difficult for the formation of CH_4. Therefore, the promoters increase the initial methanation temperature, reduce the degree of methanation and realize the purpose of inhibition of methanation. The effect of alkali metal K was contrary with alkaline-earth metals.

It decreases the initial methanation temperature from 493°C to 475°C. It can be seen from Fig. 6.73 that the initial methanation temperature is increased with the increasing content of Ba. The role gradually weakens after the Ba content reaches 4%. Therefore, the optimum content of Ba is about 4%. It can be seen from Fig. 6.74

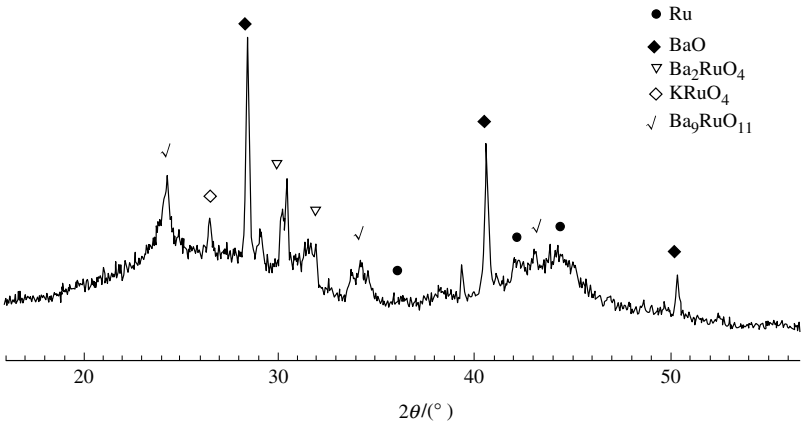


Fig. 6.75 XRD spectra of Ba–Ru–K/AC catalysts

that the initial methanation temperature decreases with the increasing of content of K. The initial temperature is kept at 473°C basically, when K content is higher than 10%. Therefore, if the operation temperature in industry for ruthenium catalyst is below 450°C, then it is feasible to add K in ruthenium catalyst.

The difference of inhibition of Ba and K on methanation may be related to their electronic properties. Electronegativity of compounds can be qualitatively used to evaluate their ability of electron gain and loss. Cs and K in $CsNO_3$–$RuCl_3$/Al_2O_3 and KNO_3–Ru/AC system might exist in the state of CsOH and KOH, respectively, and Ba as the state of oxides as alkaline earth metal hydroxides are easily decomposed into oxides. Their order of eletronagativity is K (0.8) < Cs_2O (1.20) < K_2O (1.37) < CaO (1.67) < CsOH (1.73) < KOH (1.80) < MgO (2.05) < BaO (2.29). The content of K is very high in ruthenium catalyst. The leading role of electronic promoter benefits to promote the methanation. Therefore, the inhibition effect of alkali earth metal on methanation is basically consistent with their electronagativity, and the smaller the electronagativity, the stronger the inhibition.

But it can be seen from Fig. 6.75 that the state of Ba is mainly as BaO, and still Ba_2RuO_4 and Ba_9RuO_{11}. The state of K is as $KRuO_4$ rather than KOH or K_2O in Ba–Ru–K/AC.[223] Therefore, the state K and Ba in catalyst is very complicated and little $KRuO_4$, Ba_2RuO_4 and Ba_9RuO_{11} etc. have not yet been completely reduced during activation.

(2) Rare earth oxide. The inhibition effect of lanthanide oxides on methanation should be obviously due to their high melting points and the low mobility. It can be seen from Table 6.56 that lanthanum (La), cerium (Ce) and samarium (Sm) have good ability to inhibit methanation, thereinto Sm is the best, whose initial methanation temperature reaches 534°C. The optimum mole ratio of La/Ru is about 0.5–1.0 (Fig. 6.76) and Sm/Ru = 1 (Fig. 6.77), and the role of increasing content is very small.

There is a close relationship between the inhibition role of Sm and the dispersion of ruthenium. From Table 6.57, with increased Sm content, not only the dispersion

Table 6.56 Inhibition effect of rear-earth oxide on methanation

Rare-earth oxide (M:Ru molar ratio = 1:1)	Without	La	Ce	Sm
Initial methanation temperature/°C	493	509	529	534

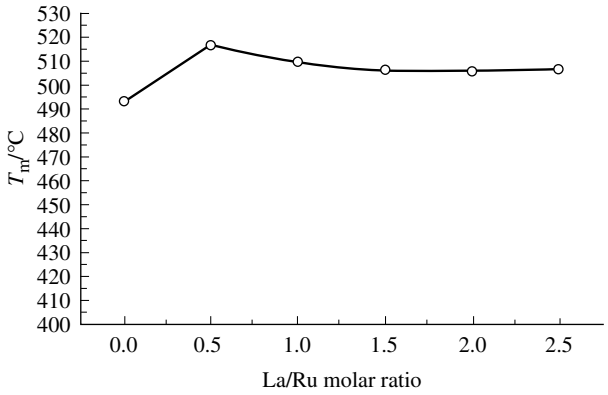


Fig. 6.76 Effect of La content on initial temperature of methanation

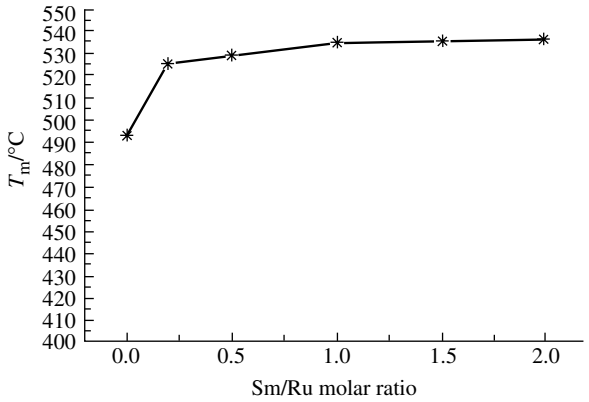


Fig. 6.77 Effect of Sm content on initial temperature of methanation

Table 6.57 Inhibition effect of Sm on methanation and the dispersion of Ru for Sm–Ba–Ru–K/AC1 catalyst

S_m/Ru molar ratio	0	0.5	1.0	1.5	2.0
Initial methanation temperature/°C	488	510	515	517	517
Ru Dispersion/%	15.2	21.5	20.0	20.0	19.8

Note: Ba/Ru molar ratio 1.

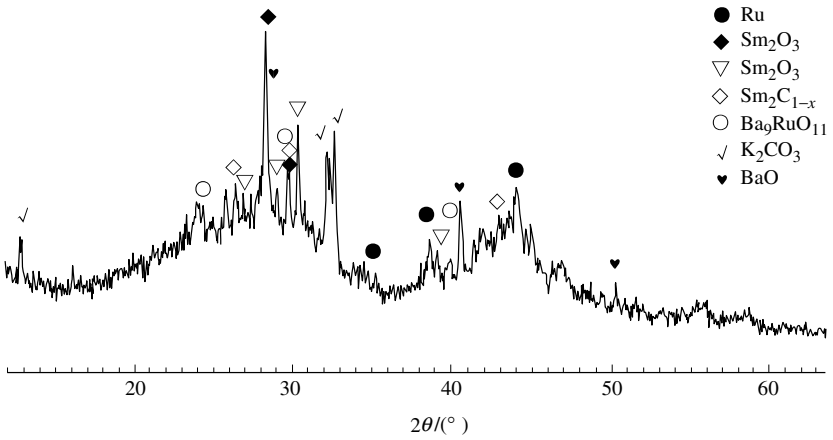


Fig. 6.78 XRD spectra of Sm–Ba–K–Ru/AC catalyst

of ruthenium increases (from 15% to 20%) but also the initial methanation temperature increases (from 488°C to 517°C). It is possible that the role of Sm is to modify the surface of activated carbon and weaken the H_2 adsorption, which not only inhibit the methanation but also provide part of active sites for N_2 dissociation. The effect of increasing content is very small and at the same time leading to the decrease of the activity of ammonia synthesis.

There are two kinds of Sm_2O_3(α, β-type) from XRD spectra of Sm–Ba–Ru–K/AC (Fig. 6.78). Probably two kinds of Sm species with different structures are formed after the reduction of catalyst. The leading role of Sm is the geometrical modification due to the bond changes combined between Sm and O. In addition, small amounts of Sm_2C_{1-x} species can be observed from Fig. 6.78. If there is some carbide species formed between Sm and the unsaturated bond in edge carbons, and then it is probably an evidence for the inhibition role of the Sm on methanation.

Figures 6.79 and 6.80 are *in situ* H_2–TPR–FTIR spectra of Ba–Ru–K/AC and Sm–Ba–Ru–K/AC catalyst. The FTIR spectra at different temperatures were directly taken from Nicolet *in situ* infrared spectrometer during reduction by H_2.

It is reported in the literature[232–234] that the M–H stretching vibration frequency on supported transition metal catalysts are 2,250 cm^{-1}–1,400 cm^{-1}. Therefore, 2,142 cm^{-1} could be attributed to atop-adsorption of hydrogen and 1,497 $cm^{-1}$and 1,303 cm^{-1} is bridge-adsorption mode of hydrogen, respectively. And 3016, 1398, and 878 cm^{-1} peaks belong to the symmetric stretching vibration, bending vibration of $–CH_3$ and rocking vibration of $–CH_2$, respectively.

It can be seen from FTIR spectra that, with temperature rising, all peaks of spectra are red-shifted, and their intensity are also increased, which indicates that the degree of the methanation of activated carbon increases with temperature gradually. In Fig. 6.80, the corresponding peak intensity of methane (3,016, 1,398 and 878 cm^{-1}) is significantly decreased at the existence of Sm. At the same time, it could also be observed that various peak intensity of hydrogen adsorption is significantly weakened because of the existence of Sm, resulting in the inhibition of

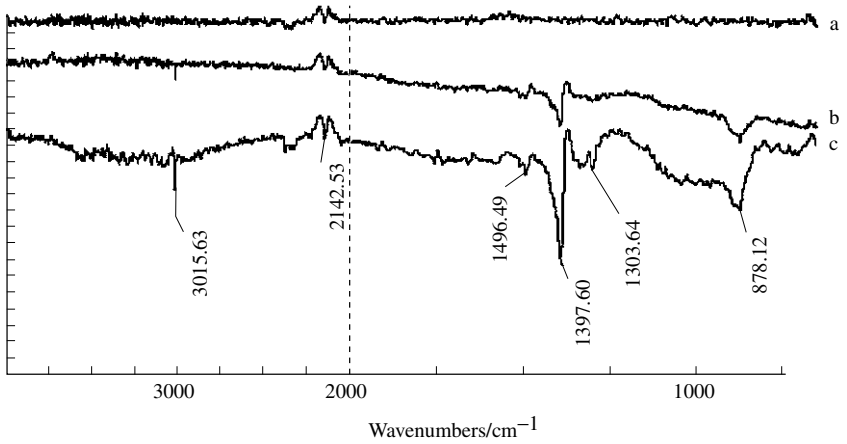


Fig. 6.79 *in situ* **FTIR spectra of Sm–Ba–K–Ru/AC catalyst a-20°C; b-260°C; c-450°C; d-500°C**

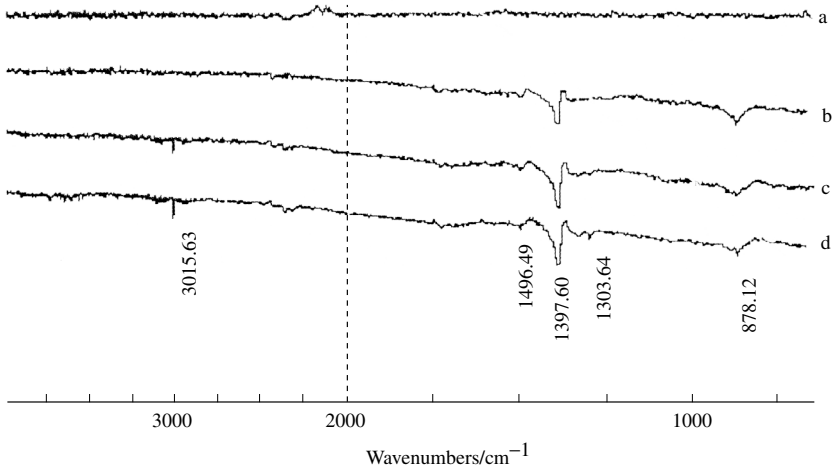


Fig. 6.80 *in situ* **H_2-TPR-FTIR spectra of Ba–K–Ru/AC catalyst a-20°C; b-260°C; c-450°C**

hydrogen adsorption, which not only is helpful to increase the catalytic activity, but also enhances the inhibition of methanation of activated carbon.

TPR results indicates that the methanation reaction cannot happen at temperatures below 400°C, and the degree of the methanation reaction is increased significantly at temperatures above 450°C. It indicates that the reaction of breaking bond C–CH_3 requires the higher activation energy (at 70–120 kJ · mol^{-1}), which results in reaction being particularly sensitive to the temperature at high temperatures.

(3) Transition metal. Transition metal oxides with high melting points have certain influence on methanation reaction (Table 6.58). From Table 6.58, Fe, Co, Ni, Mn, Zr, Mo, W and Al have the inhibition role on methanation except Ni,

Table 6.58 Effect of transition-metal on methanation reaction

Transition-metals (M: Ru molar ratio = 1:1)	Without	Fe	Co	Ni	Mn	Zr	Mo	W	Al	Ru
Initial temperature of methanation/°C	493	498	525	472	541	501	517	515	512	493

thereinto Mn, Co, Mo and W are the better metals. The low inhibitory capacity of Ni, Fe could be resulted from its strong adsorption of hydrogen.

6.3.4.5 *Thermodynamics and mechanism of methanation reaction of carbon*

Formation of methane from carbon and hydrogen is a reversible exothermic reaction:

$$C + 2H_2 \leftrightarrow CH_4. \tag{6.37}$$

The standard reaction heat is $\Delta_r H_m^\theta = -74.85\,\mathrm{kJ \cdot mol^{-1}}$. Therefore, low temperature and high pressure is beneficial to the forward reaction.

Through thermodynamic calculation, the standard Gibbs free energy of the reaction is,

$$\begin{aligned}\Delta_r G_m^\theta = &-60196.76 - 233.54T + 48.07T\ln T - 18.535\times 10^{-3}T^2 \\ &- 2.935\times 10^5 \frac{1}{T},\end{aligned} \tag{6.38}$$

$$\begin{aligned}\Delta_r G_m &= \Delta_r G_m^\theta + RT\ln\left(P_{CH_4}\frac{P^\theta}{P_{H_2}^2}\right) \\ &= \Delta_r G_m^\theta + RT\ln\left(y_{CH_4}\frac{P^\theta}{y_{H_2}^2 P}\right),\end{aligned} \tag{6.39}$$

At the standard pressure P^θ, with $T \leq 927.7\,\mathrm{K}$ and $\Delta_r G_m^\theta \leq 0$, the methanation reaction can occur at the pressure of P^θ and temperatures below 927.7 K (654.6 °C).

The carbon atoms are bonded with covalence among each other through three kinds of hybrid orbits (sp, sp^2, sp^3) in activated carbon molecules. The activated carbons have complex structures because the ratios of hybrid orbits are different in different samples. The unit structure for mediation of hybrid carbon may distribute randomly and the structure and amount are determined by the raw material, manufacture technique and conditions. Thus, the steric configuration of activated carbon is amorphous constructed by the short-range order three-dimensional structures, each of which results from the more or less randomly-arranged hybrid carbon atoms. Thereinto carbon atoms are mainly sp^2 and sp^3 hybrids.[225]

The edge carbon atoms have low bond saturation and rich dangling bond-electrons in the amorphous carbon, and therefore, the dangling bond in edge carbon atoms can be saturated by covalent with hydrogen atoms, which lead to the formation of methane. According to the experimental results, we suggest that the possible

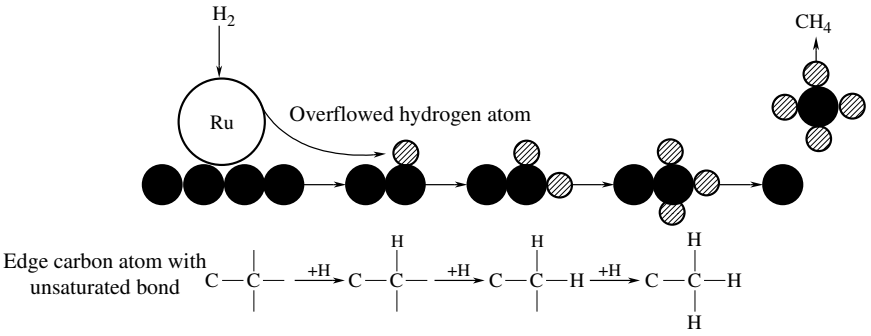


Fig. 6.81 Scheme of mechanism of methanation reaction for activated carbon

Table 6.59 Effect of H_2 content on initial methanation temperature

H_2/Ar(V/V)	1:0	3:1	1:1
Initial methanation temperature/°C	489	491	492

methanation mechanism is as follows:

$$H_2(g) + 2*(Ru) \leftrightarrow 2H_{ad}. \tag{6.40}$$

$$C{-}C + H_{ad} \leftrightarrow C{-}CH$$

(Unsaturated carbon covalent bonging with hydrogen). (6.41)

$$C{-}H + H_{ad} \leftrightarrow C{-}CH_2. \tag{6.42}$$

$$C{-}CH_2 + H_{ad} \leftrightarrow C{-}CH_3. \tag{6.43}$$

$$C{-}CH_3 + H_{ad} \leftrightarrow CH_{4ad}(C{-}CH_3 \text{ hydrogenation}, \sigma \text{ bond broken}). \tag{6.44}$$

$$CH_{4ad} \leftrightarrow CH_4(g) + *. \tag{6.45}$$

The scheme of formation of methane from carbon and hydrogen is shown in Fig. 6.81.

The activation energy is $33\,kJ \cdot mol^{-1}$ for forward and $105\,kJ \cdot mol^{-1}$ for reverse reaction of the dissociation of H_2 on the Fe (110) surface.[235] The activation energy of H_2 dissociation is very low, which is a fast step of these processes. It can be seen from Table 6.59 that the effect of hydrogen content on the initial methanation temperature is insignificant, which indicates that the effect of diffusion rate of H_2 on surface of activated carbon for methanation is very small. The results where little methane escapes at temperatures above 550°C based on the H_2–TPD–MS indicates that there has existence of CH_x in adsorption process of H_2.

The Eqs. (6.41), (6.42) and (6.43) are all the hydrogenation processes of the edge carbon atom with unsaturated bond in activated carbon. Edge carbon atoms have unsaturated dangling bond, which is easily covalently bonded with spillover hydrogen atom.

The C–C bond in C–CH_3 is bonded with σ-bond and the bond energy is $345.6\,kJ \cdot mol^{-1}$.[236] So the activation energy is 103.7 $kJ \cdot mol^{-1}$ in the 30% of the

Table 6.60 Activation energy of methanation and rate of ammonia synthesis

Number	Catalysts	Initial temperature of methanation/°C	Activation energy for methanation/ (kJ/mol)	Ammonia synthesis rate/ ($mmol \cdot g^{-1} \cdot h^{-1}$)	
				400°C	425°C
1	Al–Ru/AC	512	86.3	—	—
2	Fe–Ru/AC	498	76.1	—	—
3	Co–Ru/AC	525	97.4	—	—
4	Ni–Ru/AC	472	68.7	—	—
5	Mn–Ru/AC	541	120.1	—	—
6	Zr–Ru/AC	501	80.8	—	—
7	Mo–Ru/AC	517	90.1	—	—
8	W–Ru/AC	515	88.2	—	—
9	Ru–Ru/AC	493	72.8	—	—
10	Ce–Ba–Ru–K/AC	519	94.3	74.9	93.3
11	Mg–Ba–Ru–K/AC	508	85.1	78.4	96.6
12	Ba–Ru–K/AC	490	80.1	71.1	93.8
13	Sr–Ba–Ru–K/AC	518	93.9	75.6	97.9
14	Sm–Ba–Ru–K/AC	515	87.1	80.2	99.4

Note: 1. Molar ratio of M to Ru are 1 for samples of 1–9, of Ce, Mg and Sr to Ru are 0.2, Ru 4% (mass fraction), K 16% (mass fraction), Ba 4% (mass fraction); 2. Activity testing conditions: $p = 10\,MPa$, $H_2/N_2 = 3$, space velocity of $10{,}000\,h^{-1}$.

bond energy, which is much higher than the dissociation activation energy of H_2. Therefore, the σ-bond needs to be broken during the formation of CH_4 from the hydrogenation of C–CH_3. Large activation energy is needed in this step, which probably is the rate determining step for methanation of activated carbon.

Table 6.60 shows the reaction activation energy calculated by the methane peak height data of methanation and the activity of ammonia synthesis at different temperatures.

From Table 6.60, it suggests that the activation energy is inversely proportional to the initial temperature of methanation. The higher the activation energy, the higher the initial temperature of methanation is which is consistent with the general kinetic character. It shows that Sm, Sr, Ce, Mg and Ba can not only inhibit the methanation reaction but also increase the activity of ammonia synthesis reaction.

One of the important reasons of activated carbon supported ruthenium catalyst, which has not been widely applied, is the loss of activated carbon as support due to methanation.[12] Therefore, it has theoretical and practical significance to study the reaction mechanism of activated carbon methanation and inhibition of methanation for ruthenium catalysts.

Based on the above analysis, the main method of inhibition of activated carbon methanation is to reduce the edge carbon atoms which have unsaturated bond. The measures are listed as the following:

(1) The pretreatment of activated carbon at high temperatures or graphitizing. At high temperatures, the weak π bond between the plane layers of carbon atoms can be strengthened; microcrystal further grows up, which increases the order of carbon atoms. Therefore, the unsaturation degree of edge carbon bond

is reduced. Especially at high temperatures, the edge carbon atoms eventually form an ideal atom type of graphite crystal.

(2) The addition of effective promoter. It can weaken the strong adsorption of hydrogen and form stable compounds with the edge atoms by the dangling bond, which block the interaction of carbon with hydrogen producing methanation.

(3) Increase of the purity of the activated carbon. It can enhance the covalent bond strength between carbon atoms.

References

1. Lin WZ, Liu HZ. *Modern Chem. Ind.* **7**: 12–17, 1994.
2. Murata S, Aika K. *J. Catal.* **136**: 110–117, 1992.
3. Murata S, Aika K. *J. Catal.* **136**: 118–125, 1992.
4. Aika K, Takano T, Murata S. *J. Catal.* **136**: 126–140, 1992.
5. Murata S, Aika K. *Appl. Catal. A: General.*, **82**: 1–12, 1992.
6. Moggi P, Lbanesi GA, Predieri G, *et al. Appl. Catal. A: General.* **123**: 145–159, 1995.
7. Aika K, Kamahara T, Murata S. *Bull Chem. Soc. JPN.* **63**(4): 1221–1225, 1996.
8. Moggi P. *Appl. Catal.* **53**: L1–L4, 1989.
9. Aika K, Hori H, Ozaki A. *J. Catal.* **27**(3): 424–431, 1972.
10. Ozaki A, Aika K, Horri H, *et al. Preparation of Catalyst VI*, Amsterdam: Elsevier, 217, 1995.
11. Elofson RM, Gadallah FF. USP 4142993. 1979.
12. Kowalczyk Z, Sentek J, Jodzis S, *et al. Carbon.* **34**(3): 403–409, 1996.
13. Kowalczyk Z, Sectek J, Jodzis S, *et al. Catal. Lett.* **45**(1&2): 65–72, 1997.
14. Forni L, Molinari D, Rossrtti I, *et al. Appl. Catal. A:General.* 185: 269–275, 1999.
15. Zhong Z, Aika K. *J. Catal.* **173**(2): 535–539, 1998.
16. Zhong Z, Aika K. *Inorg. Chim. Acta.* **280**: 183–188, 1998.
17. Zhong Z, Aika K. *Chem. Commun.* **13**: 1223–1224, 1997.
18. Liang CH, Wei ZB, Xin Q, *et al. Appl. Catal A: General,* **208**: 193–201, 2001.
19. Kowalczyk Z, Jodzis S, Rarog W, *et al. Appl. Catal A: General*, **184**(1): 95–102, 1999.
20. Kowalczyk Z, Jodzis S, Rarog W. *Appl. Catal A: General*, **173**: 153–160, 1998.
21. Aika K, Kumasaka M, Oma T. *Appl. Catal.* **28**: 57–68, 1986.
22. Aika K, Kubota J, Kadowaki Y. *Appl. Surf Sci.* **121&122**: 488–491, 1997.
23. Kubota J, Aika K. *J. Phys. Chem.* **98**: 11293–11300, 1994.
24. Nawa Y, Aika K. *J. Catal.* **162**(1): 138–142, 1996.
25. Aika K, Shimazaki K, Hattori Y. *J. Catal.* **92**(2): 296–304, 1985.
26. Aika K, Ohya A, Ozaki A. *J. Catal.* **92**(2): 305–311, 1985.
27. Izumi Y, Aika K. *J. Phys. Chem.* **99**: 10346–10353, 1995.
28. Izumi Y, Aika K. *Chem. Lett.* **2**: 137–138, 1995.
29. Aika K, Niwa Y. *Sci. Tech. Catal.* **49**: 327, 1998.
30. Kadowaki Y, Aika K. *J. Catal.* **161**(1): 178–185, 1996.
31. Miyazaki A, Balint I, Aika K, *et al. J. Catal.* **204**(2): 364–371, 2001.
32. Becue T, Davis RJ, Graces JM. *J. Catal.* **179**: 129–137, 1998.
33. Cisneros MD, Lunsford JH. *J. Catal.* **141**: 191, 1993.
34. Oukaci R, Sayari A, Goodwin J. *J. Catal.* **106**: 318–322, 1987.
35. Fishel CT, Davis RJ, Garces JM. *J. Catal.* **163**: 148, 1996.
36. Wellenbuscher J, Rosowski F, Klengler U, *et al. Stud. Surf Sci.* **84**: 941, 1994.
37. Wellenbuscher J, Muhler M, Mahdi W, Schlogl R, *et al. Catal. Lett.*, **25**: 61, 1994.
38. Guntow U, Rosowski F, Muhler M, *et al. Preparation of Catalyst VI.* Amstedam: Elsevier, 217, 1995.

39. Kowalczyk Z, Jodzis S, Sentek J. *Appl. Catal. A: General.* **138**(1): 83–91, 1996.
40. Kowalczyk Z, Krukowski M, Raróg-Pilecka W, *et al. Appl. Catal. A: General.* **248**: 67–73, 2003.
41. Kadowaki Y, Murata S, Aika K. In: Guczi L, *et al* (eds.) Proc 10th Int Congr Catal, 1993, 2055.
42. Gao SY, Chen WY. *Association of Carbon Material, Fundamental and Application of Activated Carbon.* Chinese Forestry Press, 1984.
43. Wang ZY, Zhang SQ, Wang XG. *Journal of Hebei Mining and Civil Engineering Institute.* **3**: 10, 1996.
44. Shim JW, Park SJ, Ryu SK. *Carbon*, **39**: 1635, 2001.
45. Zeng HS, Aiha K. *Appl. Catal. A: General.* **219**: 235–247, 2001.
46. Roisson P, Brunelle JP, Nortier P. In Stiles AB (ed.) 11, 1987.
47. Izumi Y, Iwata Y, Aika K. *J. Phys. Chem.* **100**: 9421, 1996.
48. Gurrath M, Kuretzky T, Boehm HP. *Carbon*, **38**: 1241, 2000.
49. Kudryavtsev YP, *et al. Chemistry and Physical of Carbon*, Vol. 25, New York: Dekker, 1996.
50. Yoshio YD, Michio I, Tofu Inatsune (in Japanese), *Carbon*, **178**: 122, 1997.
51. Heimann RB, Evsvukov SE, Koga Y. *Carbon.* **35**: 1654–1658, 1997.
52. Whittaker AG, Wolten GM. *Science*, **17854**(4056): 54, 1972.
53. Kroto HW, *Nature*, **318**: 162, 1985.
54. Lijima S, *Nature*, **354**: 56, 1991.
55. Ugarte D. *Nature.* **358**: 707, 1992.
56. Jacobsen RL, Monthilux M. *Nature.* **385**: 211, 1997.
57. Bundy FD, *Physical,* **A156**: 69, 1997.
58. Diederich F, *Nature*, **369**: 199, 1994.
59. Cameron DS, Cooper SJ, Dodgson IL. *Catal. Today*, **7**: 113, 1990.
60. Han WF, Huo C, Liu HZ. *Journal of Chemical Engineering of Chinese Universities.* **5**(16): 565, 2002.
61. Wenfeng H. *Ruthenium Catalyst for Ammonia Synthesis,* Dissertation, Hanzou, Zhejiang University of Technology, 2002.
62. Wu MB. *Carbon Techniques* (in Chinese). **4**: 19, 1999.
63. Editorial Committee of Chemical Industry Encyclopedia. *Chemical Industry Encyclopedia*, Part X V, Beijing: Chemical Industry Press, 1994, 15.
64. Xu GB, *New Carbon Materials* (in Chinese), **2**: 13, 1999.
65. Qiu JS, Wang YB, Deng YZ. *Carbon Techniques* (in Chinese). **4**: 11, 1996.
66. Fanning PE, Vannice MA. *Carbon.* **31**(5): 721, 1993.
67. Biniak S, Szymanski G, Siedlewski J. Carbon. **35**(12): 1799, 1997.
68. Auer E, Freund A, Pietsch J. *Appl. Catal. A: General.* **173**: 259, 1998.
69. Fan YZ, Wang BZ. *Coal Conversion* (in Chinese). **23**(4): 26, 2003.
70. Haydar S, Moreno Castilla C, Ferro Garcia MA. *Carbon*, **38**: 1297, 2000.
71. Puente G, Menendez JA. *Solid State Ionics.* **112**: 103, 1998.
72. Dickinson AJ, Carrette LPL, Collins JA, *et al. ElectroChimica Acta.* **47**: 3733, 2002.
73. Moreno Castilla C, Carrasco Marin F, Mueden A. *Carbon.* **35**(10&11): 1619, 1997.
74. Wang SH, Lu GQ (Max).*Carbon.* **36**(3): 283, 1998.
75. Li YH, Lee CW, Gullett BK. *Fuel.* **82**: 451, 2003.
76. Lopez RMV, Stoeckli F, Moreno CC. *Carbon.* **37**: 1215, 1999.
77. Ozaki A. *Acc. Chem. Res.* **14**: 16–21, 1981.
78. He GW. *Chem. Week* **163**(14): 33, 2001.
79. Szmigiel D, Rarog PW, Miskiewicz E, *et al. Appl. Catal.* **273**: 105–112, 2004.
80. Aika K, Tamaru K, In: Nielsen A (ed.) *Ammonia Catalysis and Manufacture.* Chapter 3, Heidelberg: Springer, 104–143, 1995.
81. Wang LH, Lin YJ, Jiang J, *et al. J. Xiamen Univ.* (in Chinese) **38**(1): 148, 1999.

82. Claus JH Jacobsen, *J. Catal.* **200**(1): 1, 2001.
83. Thomas WH, Jakob BW, Poul LH, *et al. Science* **294**: 5546, 2001.
84. Chen HB, Lin JD, Cai Y. *Appl. Surf Sci.* **180**: 328, 2001.
85. Liang C, Li Z, Qiu J, *et al. J. Catal.* **211**: 278, 2002.
86. Kojima RI, Aika KI. *Appl. Catal. A: General.* **219**: 141–147, 2001.
87. Aika K, Ozaki A. *J. Catal.* **35**(1): 61, 1974.
88. Ji DH. *Role of Rare-Earth Element in Ammonia Synthesis Catalyst,* Dissertation,. Hangzhou: Zhejiang University of Technology.
89. Yunusov SM, Kalyuzhnaya ES, Moroz BL, *et al. J. Mol. Catal. A: Chem.* **165**: 141, 2001.
90. Rarog W, Kowalczyk Z, Sentek J, *et al. Catal. Lett.* **68**: 163, 2000.
91. Aika K, Ohya A, Ozaki A, Inoue Y, Yasumori I. *J. Catal.* **92**: 304–311, 1985.
92. Hikita T, Kadowaki Y, Aika K. *J. Phys. Chem.* **95**: 9396–9402, 1991.
93. Xu JX, Zheng XL, Liu GZ, *et al. Journal of Fuzhou University* (*Natural Science Edition*), **32**(2): 228–231, 2004.
94. Zeng HS, Inazu K, Aika K. *J. Catal.* **211**: 33–41, 2002.
95. Aika, K. Hori, H. Ozaki A. *J. Catal.* **27**(3): 424–431, 1972.
96. Urabe K, Aika K, Ozaki A. *J. Catal.* **42**: 197, 1976.
97. Croft RC. *Austr. J. Chem.* **9**: 184, 1956.
98. Volpin ME, Novikov YN, Postnikov VA, *et al. Z. Anorg. Allg. Chem.* **428**: 231, 1977.
99. Sudo M, Ichikawa M, Soma M, *et al. J. Phys. Chem.* **73**: 1174, 1969.
100. Ozaki A, Aika K, Hori H. *Bull. Chem. Soc. Jpn.* **44**: 3216, 1971.
101. Ertl G, Lee SB, Weiss M. *Surf Sci.* **114**: 527, 1982.
102. Ertl G. In: Jennings JR (ed.) *Catalytic Ammonia Synthesis: Fundamentals and Practice*. New York: Plenum Press, 1991, Chapter 3.
103. Mortensen JJ, Hammer B, Norskov JK. *Phys. Rev. Lett.* **80**: 4333, 1998.
104. Norskov JK, Holloway S, Lang ND. *Surf Sci.* **114**: 65, 1984.
105. Strongin DR, Somorjai GA. *J. Catal.* **109**: 51, 1988.
106. Strongin DR, Somorjai GA, In: Jennings JR (ed.) *Catalytic Ammonia Synthesis: Fundamentals and Practice*. New York: Plenum Press, 1991. Chapter 4.
107. Stolze P, Norskov JK. *Topics Catal.* **1**: 253, 1994.
108. Fastrup B. *Topics Catal.* **1**: 273, 1994.
109. Dahl S, Logadottir A, C Jacobsen JH, *et al*, *Appl. Catal. A: General.* **222**: 19, 2001.
110. Rossetti I, Pernicone N, Forni L. *Appl. Catal. A: General.* **208**: 271–278, 2001.
111. Szmigiel D, Bielawa H, Kurtz M, *et al. J. Catal.* **205**: 205, 2002.
112. Hansen TW, Wagner JB, Hansen PL, *et al. Science.* **294**: 1508, 2001.
113. Hansen TW, Hansen PL, Dahl S, *et al. Catal. Lett.* **84**: 7, 2002.
114. Kowalczyk Z, Krukowski M, Raróg-Pilecka W, Szmigiel D, Zielinski J, *Applied Catalysis A: General,* **248**: 67–73, 2003.
115. Zheng XL, Fu WJ, Zhang SJ. *Journal of Fuel Chemistry and Technology.* **31**(1): 86, 2003.
116. Aika K, Kawahara T. *Bull. Chem. Soc. Jpn.* **63**(12): 12212–12251, 1990.
117. Wang SD, Sun JQ. *An Introduction to Catalyst Engineering*, Beijing: Chemical Industry Press, 2001.
118. Mccarroll JJ, Clark JTK, Tennison SR. British Patent 1468441. 1977.
119. Benner GS, Le B. USP 4568532. 1984.
120. Ozaki A. *Catalyst Handbook* (Chinese translations), Beijing: Chemical Industry Press, 150, 1990.
121. Zheng XL, Zhang SJ, Xu JX. *Carbon*, **40**: 2597, 2002.
122. Rodriguez RF. *Carbon.* **36**(3): 159, 1998.
123. Lyubchik SB, Benoit R, Beguin F. *Carbon.* **40**: 1287, 2002.
124. Phabendra BK, Sandle NK. *Carbon.* **37**: 1323, 1999.

125. Yos HO, Robert GJ. *Carbon*, **31**(1): 109, 1993.
126. Joong SN, James AS. *Carbon*, **28**(5): 675, 1990.
127. Zheng XL, Zhang SJ, Wei KM, *Journal of Fuel Chemistry and Technology*, **29**(supplement): 99101, 2001.
128. Roman-Martinez MC, Cazokla Amokos D, inares Solano LA. *Carbon,* **31**(6): 895, 1993.
129. Erhan AAK, Madalena M, Freitas A. *Carbon*, **39**: 175, 2001.
130. Aksoylu AE, Freitas MMA, Figueiredo JL. *Appl. Catal. A: General*. **192**: 29, 2000.
131. de la Puente G, Gil A, Pis JJ. *Langmuir*, **15**: 5800, 1999.
132. Figueiredo JL, Pereiva MFR. *Carbon*, **37**: 1379, 1999.
133. Valdes H, Sanchez polo Rivera Utrilla MT. *Langmuir*, **18**: 2111, 2002.
134. Abdel NA, El HY. *Carbon*, **41**(4): 713–722, 2003.
135. Han WF, Zhao B, Huo C, *et al. Chinese Journal of Catalysis*, **25**(3): 194, 2004.
136. Han WF, Liu HZ, Zhao B. *Chinese Journal of Chemical Industry and Engineering*, **56**(7): 1225–1229, 2005.
137. Menendez JA, Jonathan P, Boxia, *Langmuir,* **12**: 4404, 1996.
138. Menendez JA, Jonathan P, Boxia, *Langmuir*, **13**: 3414, 1997.
139. Menendez TA, Menendez EM, Iglesias MJ. *Carbon*, **37**: 1115, 1999.
140. Zheng XL, Fu WJ, Yu YB, *et al. Chinese Journal of Catalysis*, **23**: 562, 2002.
141. Zhao B. Investigation into Activated Carbon of Structure and Surface Property and Ammonia Synthesis Catalyst with Ru Supported by It, Dissertation, Hangzhou: Zhejiang University of Technology. 2004.
142. Zheng XL, Fu WJ, Yu YB, *et al. Journal of Fuel Chemistry and Technology*, **31**, 1: 86, 2003.
143. Xing L. *Fertilizer Industry Collection of Translation*, (1): 13–21, 1990.
144. Wang XN, Zhu H, Xia WQ, *et al. Chinese Journal of Catalysis*, **21**(3): 276, 2000.
145. Han WF, Liu HZ, Zhao B, *et al. Chinese Journal of Chemical Industry and Engineering*, **56**(7): 1225–1229, 2005.
146. Zhu HF. *Preparation and Application of Catalysts Support*, Beijing: Petroleum Industry Press, 499, 2002.
147. Harber F, Van Ordt G. *Anorg. Z. Chem.* **43**(3): 111–113, 1905.
148. Shiflett WK, Dumesic JA. *Ind. Eng. Chem. Fund.* **20**: 246–250, 1981.
149. Mieth JA, Schwarz JA. *J. Catal.* **118**(1): 203–217, 1989.
150. Don JA, Pijpers AP, Fscholter JJ. *J. Catal.* **80**(2): 296–306, 1983.
151. Narita T, Miura H, Ohira M, *et al. Appl. Catal. A: General.* **32**: 185–190, 1987.
152. Lu K, Tatarchuk J. *J. Catal.* **106**(1): 166–175, 1987.
153. Yingjiao L, Yingchan C. *Thermodynamics Handbook of Inorganic Compound*, Beijing: Science Press, 171, 1993.
154. Chen HB, Lin JD, Cai Y, *et al. Appl. Surf Sci.* **180**: 328–335, 2001.
155. McClaine BC, Davis RJ. *J. Catal.* **211**(2): 379–386, 2002.
156. Gao DM. Investigation into Surface Property of Ru Catalyst Supported with Activated Carbon for Ammonia Synthesis, Dissertation, Hangzhou: Zhejiang University of Technology. 2005.
157. Fu WJ, Zheng XL, Xu JX, *et al. Journal of Fuzhou University* (Natural Science Edition). **31**(3): 340–343, 2003.
158. Liang CH, Ammonia Synthesis on Ru–Mn^{+}/C Catalysts: Effect of Promoters and Carbon Supports, Dissertation, Dalian Institute of Chemical Physics, Chinese Academy of Sciences, 2000.
159. Wang R, Wei KM, Lin JX, *et al. Chinese Journal of Catalysis*, **24**(12): 929–932, 2003.
160. Wang R, Wei KM, Lin JX, *et al. Industrial Catalysis*, **13**(4): 31–35, 2005.
161. Muria H, Hondou H, Sugiyama K, *et al. Intl. Congr. Catal. Ottawa* **3**: 1307–1313, 1988.

162. Xi W, Bernard CG, Terry SK. *J. Catal.* **135**: 68–80, 1992.
163. Zhang SJ, Preparation and Performance of New Ammonia Synthesis Catalyst, Dissertation, Fuzhou University.
164. Li Y, The study of ruthenium ammonia synthesis catalysts supported on Oxide, Dissertation, Hangzhou: Zhejiang University of Technology, 2002.
165. Wu S, Zheng XF, Chen JX, *et al. Symposium of the 12th National Catalysis Conference, Beijing.* 284 –286, 2004.
166. Han WF, Liu HZ, China Patent 200610050348.7, 2006.
167. Shen Z, Wang GT, *Colloid and Surface Chemistry*, Beijing: Chemical Industry Press, 7–19, 1997.
168. Cai HF (void). Dissertation, Hangzhou: Zhejiang University of Technology. 2006.
169. Bond GC. *Metal support and Metal additive Effect in Catalysis.* Amsterdam: Elsevier, 1982.
170. Tournayan L, Blanchard G, Charcosset H. *Stud. Surf Sci. Catal.*: 353–360, 1982.
171. Bossi A, Cattalani A, Garbassi F, *et al. J. Therm. Anal.* **26**: 81–86, 1983.
172. Dalla Betta PA. *J. Phys. Chem.* **79**: 2519–2525, 1975.
173. Xin Q, Zhang H, Yang JL, *et al. Chinese Journal of Catalysis*, **5**(2): 107–113, 1984.
174. Lu K, Tatarchuk J. *J. Catal.* **106**(1): 176–187, 1987.
175. Dumesic JA, Topse H, Khammouma S, *et al. J. Catal.* **37**: 503, 1975.
176. Spencer ND, Schoonmaker RC, Somorjai GA. *J. Catal.* **74**: 129, 1982.
177. Strongin DR, Carrazza J, Bare SR, *et al. J. Catal.* **103**: 213, 1987.
178. Dahl S, Logadottir A, Egeberg RC, *et al. Phys. Rev. Lett.* **83**: 1814, 1999.
179. Dahl S, Trnqvist E, Chorkendorff I. *J. Catal.* **192**: 381, 2000.
180. Dahl S, Sehested J, Jacobsen CJH, *et al. J. Catal.* **192**: 391, 2000.
181. Jacobsen CJH, Dahl S, Hansen PL, *et al. J. Mol. Catal. A: Chem.* **163**: 19, 2000.
182. Van Hardeveld R, Van Montfoort A. *Surf Sci.* **4**: 396, 1966.
183. Pilecka WR, Miskiewicz E, Szmigiel D, *et al. J. Catal.* **231**: 11–19, 2005.
184. Poltorak OM, Boronin VS. *J. Phys. Chem.* **40**: 1436, 1966.
185. Song Z, Cai TH, Hanson JC, *et al. J. Am. Chem. Soc.* **126**: 8576, 2004.
186. Rossetti I, Pernicone N, Forni L. *Appl. Catal. A: General.* **248**: 97–103, 2003.
187. Rossetti I, Forni L. *Appl. Catal. A: General.* **282**: 315–320, 2005.
188. Elofson RM, Gadallah FF. USP 4142993. 1979.
189. Zhao B, Liang HD, Han WF, *et al. Chemistry*, **11**: 853–856, 2006.
190. Rich S. *Nitrogen & Methanol*, **238**: 37–43, 1999.
191. Liu HZ, Li XN, Ling MC, *et al. J. Chem. Ind. and Eng.* **51**(4): 462–467, 2000.
192. Pernicone N, Ferrero F, Rossetti I, *et al. Appl. Catal. A: General*, **251**: 121–129, 2003.
193. Jacobsen CJH, Dahl S, Clausen BS, *et al. J. Am. Chem. Soc.* **123**: 8404–8405, 2001.
194. Rossetti I, Pernicone N, Ferrero F, Forni L. *Ind. Eng. Chem. Res.* **45**, 4150–4155, 2006.
195. Zhang K, Tang HT, Huo C, Li Y, Pan CG, Liu HZ. *Industial Catalysis.* **16**(12): 60–64, 2008.
196. Rambeau G, Amariglio H, *J. Catal.* **72**: 1–11, 1981.
197. Kiperman S. *Fizkhim Zhur*, **21**: 1435, 1947.
198. Holzman PR, Shiflett WK, Dumeste JA. *J. Catal.* **62**: 167, 1980.
199. Momkawa Y, Ozaki A. *J. Catal.* **23**: 97, 1971.
200. Baris H, Glinski M, Kijenski J, *et al. Appl. Catal.*, **28**: 295, 1986.
201. Izumi Y, Hoshikawa M, Aika K. *Bull. Chem. Soc. Jpn.* **67**: 3191, 1994.
202. Yates JT, Peden CHF, Houston JE, *et al. Surf Sci.* **160**: 37, 1985.
203. Ebitani K, Konno H, Tanaka T, *et al. J. Catal.* **135**: 60, 1992.
204. Martens JHA, Prins R, Koningsberger DC. *Catal. Lett.* **2**: 211, 1989.
205. Rambeau G, Amariglio H. *J. Catal.* **72**: 1, 1981.
206. Siporin SE, Davis RJ. *J. Catal.* **225**: 359, 2004.

207. Niwa Y, Aika K. *Chem. Lett.* **25**(1): 3, 1996.
208. Siporin SE, Davis RJ. *J. Catal.* **222**: 315, 2004.
209. Li ZL. Ammonia Synthesis on Ru Supported on Carbon Nanotubes and TAP Study of Ammonia Decomposition, Dissertation, Dalian Institute of Chemical Physics, Chinese Academy of Sciences, 2004.
210. Liu HZ, Li XN. *Chinese Journal of Catalysis*, **26**(1): 79–86, 2005.
211. Tauster ST. *Acc. Chem. Res.* **20**: 389, 1987.
212. Ozaki A, Tamaru K, *et al. Handbook of Catalyst*, Chemical Industry Press, 1982.
213. Hall WK, Emmett PH. *J. Phys. Chem.* **63**: 1102, 1959.
214. Hall WK, Hassell JA. *J. Phys. Chem.* **67**: 636, 1963.
215. Yang ZW, Guo WM, *et al. Chin. J. Catal.* **27**(5): 378–380, 2006.
216. Liu HZ, Li XN, Hu ZN, *et al. J. Chem. Eng. of China Univ.* **16**(1): 42–47, 2002.
217. Fishel CT, Davis RJ, Garces JM. *J. Catal.* **163**: 148–157, 1996.
218. Ozaki A, Aika K, In: Anderson JR, Boudart M (eds.) *Catal. Sci. Tech.* Berlin: Springer-Verlag, 1981.
219. Ogata Y, Aika K, Onishi T. *J. Catal.* **32**(2): 469–477, 1988.
220. Zeng HS, Hihara T, Aika K. *J. Catal.* **76**: 193, 2001.
221. Jiang WJ, Jiang X, Jin Y, *et al. Chem. Ind. Forest Products*, **24**(1): 21, 2004.
222. Forni L and Pernicone. N. U. S. Pat. No.7, 115, 339, 2006.
223. Zhu YF, The study of reaction and inhibition mechanism of activated carbon methanation on ruthenium catalysts, Dissertation, Hangzhou: Zhejiang University of Technology. 2005.
224. Zhu YF, Li XN, Ji DC, *et al*, *Chemistry*, **65**(12): 845–848, 2002.
225. Wang MZ, Yang QH, Cheng HM. *Carbon Techniques.* (1): 23, 2001.
226. Bird AJ. In: Stiles AB (ed.) *Catalyst Supports and Supported Catalysts.* Boston: Butterworths, 107, 1987.
227. Hoost TE, Goodwin JG. *J. Catal.* **130**: 283–292, 1991.
228. Uner DO, Pruski M, Gerstein BC, *et al. J. Catal.* **146**: 530–536, 1994.
229. Ohya A, Urabe K, Aika K, *et al. J. Catal.* **58**: 313–319, 1979.
230. Lang ND, Halloway S, Norskov JK. *Surf Sci.* 150: 24–38, 1985.
231. Zhu YF, Li XN, Ji DC, *et al. Chin. J. Chem. Eng.* **12**(3): 1–10, 2004.
232. Lao DW, Lin JD, Wang XY, *et al.* Symposium of the 11th National Catalysis Conference. HangZhou, 189, 2002.
233. Cai Y, Lin JD, Liao DW. Symposium of the 11th National Catalysis Conference. 311–312, 2000.
234. Zhang HB, Zhou ZH, Dong X, *et al. J. Light Scattering*, **13**(4): 21–215, 2002.
235. Hei MJ, Chen HB, Liao DW. *et al. J. Xiamen University* (Natural Science). **36**(6): 879–883, 1997.
236. Gu QC, Lou SC, Dai QP, *et al. Chemical Instruments.* Nan Jing: Jiangsu Science and Technology Press. 1979.

Chapter 7

Performance Evaluation and Characterization of Catalysts

The ultimate task of design and development for industrial catalysts is to invent or update the catalysts that can be applied in special reactions and realize industrial scale manufacture. Most of work involved is carried out in the medium-scale units in the lab. The main work in laboratory is to design chemical compositions of catalyst and to study preparation methods for catalyst. Meanwhile, the evaluation, testing and characterization of the different catalysts should be carried out for comparison and design. The work on design of catalyst is more difficult than that on preparation of catalyst and requires high technology.

It is hard to find out the most appropriate equipment/method and performance index to measure and assess the quality of catalysts, which is difficult in unified definition and standardization of methods. So far, some methods for evaluating the activities of a few catalysts such as those for catalytic ammonia synthesis and catalytic cracking have been standardized. The evaluation methods are different due to the varieties of catalysts and the experiences of researchers. Sometimes, the technical details of evaluation methods are a part of patent, such as formula and preparation process is confidential. Even then, some basic conceptions and methods for the evaluation and testing of catalysts are still worthy being introduced, which is the main focus of this chapter.

In general, three main indexes to measure the quality and efficiency of an industrial catalyst are activity (conversion), selectivity and stability. Other performances including mechanical strength, anti-deactivation, geometric physical properties, macro- and micro-physical structure and economic aspect, should also be examined comprehensively, as shown in Table 7.1.

With modern scientific and technological progresses, a lot of new evaluation methods and equipments have been developed. In the recent decades, the advancements on the evaluation and testing methods are much faster than those on the manufacture processes during development of industrial catalysts. It is really difficult to illustrate without pretermission all the methods, which are, in reality, still developing and increasing.[2−4] Table 7.2 lists the major experimental techniques employed in research on heterogeneous catalysis. The comprehensive application of these means and techniques as well as modern equipments has a profound influence on shortening the cycle for development of catalysts and saving the human and material resources as well as understanding the nature of catalytic phenomenon, and so on.

A catalyst developed successfully should provide three kinds of information of catalysts: The chemical composition and structure, the texture organization and mechanical property, and catalytic activity, which are different but connect to each

Table 7.1 Performance requirements and physical and chemical properties of industrial catalysts

Performance requirements	Physical and chemical properties
1. Activity 2. Selectivity 3. Stability (mechanical strength; heat-resistant; anti-toxic), tolerance of pollution 4. Physical and chemical property: shape, particle size, particle distribution, density, heat capacity, heat conduction, forming property, mechanical strength, abrasion, pulverization, calcined performance, moisture absorption, flow performance, and so on. 5. Preparation method: equipment, conditions, manufacturing easy and difficult, activation conditions, store and keeping conditions, and so on. 6. Use method: the type of reaction equipment, loading performance, reaction and operation conditions, safe and corrosion-resistant, conditions of activation and regeneration, recovery method 7. Innocuity 8. Cheap	1. Chemistry: active species, promoters, supports, additives, and so on 2. Electronic state: binding state, valence state 3. Crystallized state: crystal type, grain size, defect structure 4. Surface state: surface area, effective surface area of active component and so on 5. Pore structure: pore volume, pore diameter, pore size distribution 6. Adsorption properties: performances of adsorption and desorption, adsorption heat, wetting heat 7. Density, specific heat capacity, thermal conductivity 8. Acidity: species, intensity, intensity distribution 9. Electric and magnetic properties 10. Shape 11. Mechanical strength, abrasion, pulverization

other. This chapter will briefly introduce the major experimental methods involved for the evaluation, testing and characterization of catalysts. The evaluation is to investigate and quantitatively describe properties of a catalyst; the test is commonly to pay more attention to testing its physical property (macroscopic and microcosmic); whereas the characterization is often to focus, from a catalyst synthesis, on the internal relations and regularity between physical, chemical and physicochemical properties of catalysts, especially on the internal relations and regularities between activity, selectivity, stability and physical and chemical property of catalyst.

7.1 Performance Evaluation of Catalysts

The performance of catalyst generally refers to selectivity (no selectivity for ammonia synthetic catalyst) and stability including chemical stability (deactivation) and physical stability (heat-resistance, mechanical strength).

7.1.1 *Basic concepts*

7.1.1.1 *Activity*

According to the definition and functions of catalyst, the catalytic activity is a kind of measurement, which is used to measure the accelerated degree of chemical reation

Table 7.2 Main experimental technologies of the research on heterogeneous catalyst

Abbreviation symbol	Name	Remark
XRD	X-ray Diffraction	Techniques for determination of catalysts properties
AAS	Atomic Absorpted Spectroscopy	
AEM	Analytical Electron Microscopy	
AES	Auger Electron Spectroscopy	
AS	Atom Scatting	
EPMA	Electron Probe Microanalysis	
EXAFS	Extended X-ray Adsorption Fine Structure	
FEM	Field Emission Microscopy	
FIM	Field Ion Microscopy	
IMP	Ion Micro Probe or Ion Probe Microanalysis	
ISS	Ion Scattering Spectrometry	
RED	Radial Electron Distribution	
SEM	Scanning Electron Microscopy	
SEXAFS	Surface-sensitive EXAFS	
SIMS	Secondary Ion Mass Spectroscopy	
TEM	Transmission Electron Microscopy	
PAS	Photoacoustic Spectroscopy	
Physisorp	BET	
Merc	Mercury Poresimetry	
UV-vis	Ultraviolet-visible Spectroscopy	
XRF	X-ray Fluorescence Spectroscopy	
Möss	Mössbauer Spectroscopy	
CA	Chemical Analysis	
ICP	Inductively Coupled Plasma Spectroscopy	
XPS	X-ray Photoelectron Spectroscopy	Technologies for identification of adsorption species
UPS	Uv-Photoelectron Spectroscopy	
HREELS	High-Resolution Electron Energy Loss Spectroscopy	
Magn	Magnetic Susceptibility Measurements	
LEED	Low Energy Electron Diffraction	
IR & Ram	Infrared Spectroscopy and Raman Spectroscopy	
NMR	Nuclear Magnetic Resonance	
ESR	Electron Paramagnetic Resonance	
DTA	Differential Thermal Analysis	Technologies for determination of kinetic and thermodynamic properties
TG	Thermogravimetric Methods	
TPD	Temperature-Programmed Desorption	
TPSR	Temperature-Programmed Surface Reduction	
Isotopics	Isotope tracer	
Microcalorimetry	Micro-calorimetry	
Chemisorp	Chemical adsorption	
Kinetics	Chemical kinetics	

rate by catalyst. Strictly speaking, the catalytic activity should be the difference between catalytic reaction rate and non-catalytic reaction rate. The non-catalytic reaction rate is generally small and can be negligible, so the catalytic activity is just catalytic reaction rate. Turnover frequency (TOF) or conversion rate also can be used to express catalytic activity.

Activity is the most important property of catalyst, and there are many ways to evaluate catalytic activity. We can adopt different measurement methods of activity according to the different purposes in the development of new catalyst, the improvement of present catalyst, the production control and measurement of kinetic parameters for catalysts and theories of catalysis foundation, and due to the difference with different reactions and required conditions (such as strong exothermic and endothermic reaction, high and low temperature, high and low pressure).

The measurement methods of the catalytic activity can be divided into two series: flow method and static method. The reaction system of flow method is open and the feeding is continuous or semicontinuous; whereas the reaction system of static method is close and the feeding is discontinuous. In semicontinuous method used for some gas-liquid-solid three-phase reactions, the feeding gases are always in and out continuously, but feeding liquid and solid catalysts are always relatively closed. The flow methods used fixed-bed reactor can be divided into general flow method, flow-cycle method (no gradient reactor) and catalytic chromatography and so on. Evaluation method of catalyst is in nature a kind of simulation for industrial catalytic reaction. Therefore, the general flow method is the most widely used because most of industrial catalytic reactions are continuous flow systems. Flow cycle method, catalytic chromatography and static method mainly are used to study reaction mechanism and reaction kinetics.

(1) **Reaction rate.** According to the recommendation of International Union of Pure and Applied Chemistry (IUPAC) in 1981, the definition of reaction rate is:

$$\dot{\xi} = \frac{d\xi}{dt}, \tag{7.1}$$

where t is the reaction time; and $\dot{\xi}$ is the degree of reaction, unit is mol·s^{-1}, defined as:

$$\dot{\xi} = \frac{n_i - n_i^0}{\upsilon_i}, \tag{7.2}$$

where n_i, n_i^0 are the quantity of substance i at $t = t$ and $t = 0$, respectively, mol; v_i is the stoichiometric coefficient of component i.

We should introduce definition of specific rate, as shown in (7.3), (7.4) and (7.5), because the reaction rate relates to the volume, mass or surface area of catalyst.

$$\text{Reaction rate in unit volume} = \frac{1}{V}\frac{d\xi}{dt}, \text{ unit is mol·cm}^{-3}\text{·s}^{-1}. \tag{7.3}$$

$$\text{Reaction rate in unit mass} = \frac{1}{m}\frac{d\xi}{dt}, \text{ unit is mol·g}^{-1}\text{·s}^{-1}. \tag{7.4}$$

$$\text{Reaction rate in unit specific surface area} = \frac{1}{S}\frac{d\xi}{dt}, \text{unit is mol·cm}^{-2}\text{·s}^{-1}. \tag{7.5}$$

Here, V, m, and S are the volume, mass and surface area of catalyst, respectively.

In industrial production, the production capacity of catalyst is based on the unit volume of catalyst or reactor, and the quantities are always huge, so the reaction rate should be represented by volume rate. In some cases, it is convenient to represent the catalytic activity using specific rate. For the comparison of the natural catalytic property of solids the area rate should be used, because the heterogeneous catalytic reaction only occurs on the surface of solid.

(2) **Turnover frequency (TOF).** The area rate is the most logical in the three expressions, because catalytic reaction happens only on the surface of catalyst. However, the concentration (density) of active sites on the same surface area of catalysts may be different, so it may be more close to the nature of rate to characterize reaction rate according to the number of active sites. Borrowing the concept of turnover-number in zymochemistry we introduce the concept of Turnover Frequency (TOF) in catalysis.

TOF is also called conversion rate, which refers to the times generated reaction on per active site in unit time under the conditions of the given temperature, pressure, reactant composition and velocity (flow) as well as reaction degree. But there are still some problems when using turnover frequency. We cannot directly measure or calculate the number of active sites for a lot of catalysts, including metal catalysts, and can only measure or calculate atom numbers exposed on the surface of them. So TOF is just an average value of catalytic activity. Because only part of the atoms exposed on the surface of catalysts are active, so the average value of TOF is lower than that of their true activity. Furthermore, TOF is not a rate constant, so it still has some relationship with reaction conditions. When reporting on TOF value, it is necessary to give the reaction conditions.

(3) **Conversion.** For the expression of activity, another visual index is conversion. The properties of catalysts are often measured by this parameter for industrial purposes. The definition of conversion is:

$$\chi_A = \frac{\text{Amount of transformed reactant “}A\text{”}}{\text{Amount of starting reactant “}A\text{”}} \times 100\%. \tag{7.6}$$

Using this parameter, it is necessary to give clear indication of the contact time between reactants and catalysts, or no concept of the definition of rate. Therefore, some following related parameters are introduced in industrial practice.

(i) *Space velocity.* In flow system, the flow rate of materials (volume of unit time) divided by the volume of catalysts to get space velocity in volume, unit is h^{-1}

$$S_V = \frac{F}{V} \tag{7.7}$$

Sometimes S_v is expressed by Gas Hourly Space Velocity (GHSV).

The reciprocal of space velocity expresses the average contacting time between the reactant and the catalysts, and it is also called dummy contacting time, expressed by τ.

$$\tau = \frac{V}{3600F}, \tag{7.8}$$

where F is the volumetric flow rate of materials, $m^3 \cdot h^{-1}$; V is the volume of catalysts, m^3; τ is the dummy contacting time, s.

(ii) *Space time yield.* Space time yield (STY) is the amount of products produced per hour per cubic meter of catalyst, the unit is $kmol \cdot m^{-3} \cdot h^{-1}$. The value of STY also relates to operating conditions.

7.1.1.2 *Selectivity*

$$S = \frac{\text{Amount of targeted products}}{\text{Amount of converted key reactant}} \times 100\%. \tag{7.9}$$

In many cases, selectivity is much more important than activity. It is often dependent on the price of raw materials and the separation of products is difficult or easy when making choice between activity and selectivity.

If the amount of substance has changed in the reaction, S should be corrected by adding a coefficient. The two parameters that are commonly used and have some relationship with selectivity are as following:

(1) Yield

$$R = \frac{\text{Total amount of a certain class of product}}{\text{Amount of this class in starting reactant}} \times 100\%. \tag{7.10}$$

(2) Yield per pass

$$Y = \frac{\text{Amount of objective products}}{\text{Amount of starting reactant "A"}} \times 100\%. \tag{7.11}$$

Yield per pass is also called gained rate, which has following relationship with selectivity and conversion:

$$Y = X \cdot S \tag{7.12}$$

7.1.1.3 *Stability*

Stability of catalyst is commonly expressed by life time. It means the time maintained certain activity (Life time per pass) or accumulative time after regeneration (Total life time) under the application conditions. It also can be expressed by the total number of reaction conversion achieved on each active site.

According to the definition of catalyst, an ideal catalyst can be used forever. However, in reality due to chemical and physical reasons, the activity and selectivity of catalyst will gradually decrease with the running time, until it is lower than a certain value which will be considered to be inactive.

Stability of catalysts contains heat-resistant stability for high temperature and heat, mechanical stability for the effect of friction, impact and gravity as well as antitoxic stability for the effect of poison.

(1) **Heat-Resistant stability.** A good catalyst can maintain its activity at a certain level for a long time at reaction temperature. It is normal to come across high temperature in catalytic reaction. For example, the ammoxidation could be processed at 900°C on the platinum net catalyst, while the reforming reaction of hydrocarbons should be at 1,300°C on the Ni catalyst.

However, most of catalysts have their functionable temperatures during operation, which result from the fact that high temperature is easy to cause the microcrystalline in active components of catalysts to grow, destruction or losing defects of crystal lattice. Metal catalyst is easy to sinter above its semi-melting temperature. When the metal in catalyst has low melting-point, it should be added with some oxide with high melting point which is difficult to be reduced playing the role in protective isolation, preventing catalysts from sintering. Another way to improve the heat-resistant stability is to adopt the heat-resistant support.

A long time stability test and the so-called "accelerated aging" test method are usually adopted for thermal stability test of catalyst.[5,6] The former is to run for a long time at service temperature or slightly higher than that, and to express its thermal stability by the times which stable of activity. The latter is to run at the temperature of 1.2 to 1.5 times higher than the service temperature, and to express its stability by the reducing degree of activity.

The "accelerated aging" test is adopted for most of the solid catalyst used in heterogeneous catalytic reaction. For example, the test conditions of heat-resistant stability for China's A110 series, A2 series and A3 series iron catalyst are at 5 MPa, 30,000 h^{-1} and 500°C hold for 20 h, the loss of the ammonia concentration of the reactor outlet is not higher than 0.5%,[5] while literature[6] was to evaluate the stability by the reducing degree of activity at 600°C hold for 16 h.

(2) **Mechanical stability.** High mechanical stability of the catalyst can resist the friction and impact between particle and particle, particle and liquid, particle and container's wall, and cannot break and apparent pulverization during transportation, loading and self-weight or change of the reaction conditions, which is characterized by compressive strength and the degree of abrasion, see Chapter 8 for details.

(3) **Antitoxic stability.** The phenomenon that causes decrease of the activity, selectivity or life time of catalysts due to the poisoning effect of harmful impurities (poisons) is called catalyst poisoning. Generally, the poisons are sulfides such as H_2S, COS, SO_2, CS_2, RSH, R_1SR_2, thiophene, R_1SSR_2, RSO_3H, H_2SO_4, etc, the compounds containing P, As, halides, heavy metal compounds, metal organic compounds as well as oxygenous compounds including O_2, CO_2, and H_2O. For metal catalysts, the former will cause permanent poisoning, while the latter will cause temporary poisoning.

The phenomena of catalyst poisoning can be roughly explained by the following. The active center was adsorbed by poisons or further changed to more stable surface compounds. As a result, the active sites was inactivated or taken up forever.

There are several methods to investigate the antitoxic stability of catalysts.

(i) Add some poisons in the feeding gas to poison the catalyst, then resume catalyst tests using the pure feeding gas and check the extent to which the activity and selectivity is recovered. Reversible poisoning performance commonly

adopts this method, e.g., for the antitoxic performance of oxygenous compounds (O_2, CO_2, H_2O).

(ii) Poisons are inchmeal introduced to feeding gas till to the activity and selectivity of catalyst are maintained at a certain level, and to investigate the maximum content of the poison that catalyst can endure. Permanent or irreversible poisoning of sulfides commonly adopts this method.

(iii) The catalysts after poisoning are regenerated to investigate the resuming degree of activity and selectivity.

In addition to above three influence factors, one of the main reasons for deactivation of catalyst results from carbon deposition and coking, which are caused by impurities derived from macromolecular compounds containing carbon covering on the surface of active sites or blocking pore of catalyst.

7.1.2 *Performance evaluation of catalysts*

Although the aims for the performance evaluation and dynamic test of catalyst are different, both tests have almost the same experiment equipments, settings and processes. The slight difference is the operating conditions. The evaluation of catalyst is to measure the performance (activity, selectivity and stability) of catalysts and compare differences of different catalysts or the differences between performance and quality standard under the exactly same operating conditions (temperature, pressure, space velocity, material ratio and so on), while the dynamic test is to measure the quantitative relationship between the performance and operating conditions for a determined catalyst (which is the optimal catalyst selected) at different operating conditions. In other words, during the performance evaluation test, the catalyst (not the testing conditions) is changed; in contrast, in the dynamic test, the conditions (instead of catalysts) are varied. Therefore, first of all, we want to introduce the basic equipments, settings, process and methods for the performance evaluation and dynamic test of catalyst.

7.1.2.1 *The reactor for performance evaluation and dynamic test of catalyst*

All catalytic reactions should be implemented in the reactor, and evaluation and dynamic test of catalysts also should be carried out in the bench scale reactor. The bench scale reactor is the simulation and micromation of large-scale industrial reactor. Because lab reactor is research not production, it needs higher and more severe requirements than industrial reactor when observing and measuring catalytic reaction, and it has to have much more careful considerations on design, operation and control. However, in practice, researchers only consider the variety of special demands to design reactors.

In a common industrial heterogeneous catalytic reactor, the data need to include chemical reactions and physical transfer (heat transfer, mass transfer) in varying degrees. It is very difficult to evaluate whether the performance of catalyst is good or not, or to find the way to improve the performance of catalyst according to these combined data. Therefore, it is necessary to dismiss them from the coupling of chemical reactions and physical transfer *via* appropriate research tools and conditions, to

get the correct intrinsically dynamic parameters of catalytic reaction and physical parameters of transmission. Here, the key is to separate the process of chemical and physical, that is, the decoupling.

In the various lab reactors, some are suitable to get the dynamics data, some are not. This is according to the following three requirements. Firstly, the most important reaction condition is its isothermal characteristic because the effect of temperature on reaction rate is exponential, especially to complicated reaction. For a few simple reactions, the exact temperature distribution sometimes can be used as supplementary information on the dynamics, but that is a special case of the individual; secondly, the tangibility and uniformity of the settle-time; thirdly, whether the sampling and analysis of products is easy or not. The above three points decide the quality of the reactor, which also further decide the precision of dynamic model.

The lab reactor is the core of catalyst evaluation and dynamic test equipments. Various methods and special reactors have been developed.[7]

(1) **Integral reactor.** Integral reactor is a kind of micro-tube fixed bed reactor, which is commonly used in lab. This kind of reactor is packed with enough catalysts (about several to tens of millilitres) to reach a high conversion level. Because the compositions of streams between the inlet and outlet of the reactor are highly different, it is not appropriate just using an average value in mathematics to represent the whole composition of the reactor. The reaction rate always varies greatly in inlet and outlet of the reactor, and has great gradient of temperature and concentration along the bed of catalysts. The data of reaction rate obtained from the reactor can only represent the integral results of conversion *vs.* time-space as shown in Fig. 7.1.

Integral reactor has the following advantages: It is very similar with industrial reactor; it is convenient to get the visual results of the evaluation data for some reactions; due to high conversion, the accuracy requirements on analysis are not particularly high. Because of the large thermal effect, it is hard to maintain the temperature uniform and constant in whole bed, especially for some strong exothermic

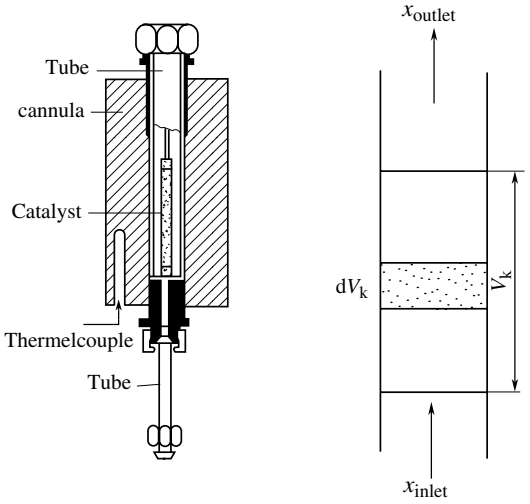


Fig. 7.1 Sketch map of integral reactor

reactions. The larger the difference of the thermal conductivity of catalysts, the greater is the temperature gradient in bed. Therefore, the comparability of reaction rate data is poor.

In the study of dynamics, the integral reactor can be divided into two types — isothermal and adiabatic reactor. Because isothermal integral reactor is simple and cheap as well as the lower demand on the accuracy on analysis, it is always the preferred option. In order to overcome its difficulties to maintain the temperature uniform, there are several actions. The first one is to reduce the diameter to obtain uniform radial temperature as much as possible. When the inner diameter of reactor is 4–6 times bigger than the particle size of catalyst, the effect of reducing the diameter of tube on the distribution of temperature still is the main factor. The second is to use various mediums with high thermal conductivity, to provide heating indirectly through the whole piece of metal or sand bath, which is commonly used presently. The third is to dilute the catalyst bed with inert materials.

The adiabatic integral reactor has the characteristics of uniform diameter, filling with homogeneous catalyst, and good insulation. The feeds preheated to a certain temperature inflood into the reactor, and measure axially the reaction heat and the corresponding temperature distribution of kinetic law. However, the data acquisition and mathematic explanation are difficult for the reactors.

(2) **Differential reactor.** The structure shape of differential reactor is similar to integral reactor, but the bed of catalyst is much shorter and thin, and the volume of catalyst is much less, and the conversion is much lower than that of integral reactor. If the conversion level through the bed is very low, the composition differences between the inlet and outlet of bed are so few that it could use their average value to represent the whole composition of bed. When the value is high enough to use a certain analytic method to determine the concentration of the inlet and outlet of bed, i.e. the $\Delta c/\Delta t$ is approximatively to dc/dt, and which is the same with reaction rate r, it can use this kind of reactor to get the differential data of r to temperature and partial pressure. In general, the single-pass conversion is below 5%, and some reactors are allowed to 10%. The volume of catalyst is from tens to hundreds of milligrams for the differential tube reactor.

The advantages of differential reactor are low conversion, neglectable thermal effect, little gradients of concentration and temperature, measuring the reaction rate corresponding with given temperature directly from experiments.

The disadvantages of differential reactor are low conversion, requiring accurate and sensitive analysis methods, high-precision analysis instruments otherwise it will be very difficult to ensure data accuracy and repeatability, which often restrict the choice for the differential reactor.

The integral reactor, because of its relative simplicity, has a higher conversion, facilitates the analysis, and can directly compare catalytic activity. It is therefore suitable for measuring the activity of a large number of industrial catalysts, especially for fast and convenient control analysis on site. However, the differential and integral reactors cannot completely avoid the gradient of gas flow velocity, temperature and the concentration in the catalyst bed, resulting in declining the reliability of the experimental data.

(3) **Non-gradient reactor.** Non-gradient reactors have many different names and types, and can be roughly divided into external circulation, internal circulation and continuous stirred kettle -style by the gas flowing mode. However, it is necessary to achieve the flow phase with constant temperature and ideal mixing, and the elimination of mass transfer resistance between phases in reactor. At the same time, on the premise of elimination of the gradient of temperature and concentration, it should be the same that the reaction rate equation is obtained from the circulation flow system or the ideal hybrid system.

The advantage of non-gradient reactor is that it isable to get the reaction rate data directly and accurately, which is valuable for performance evaluation of the catalysts or its dynamics research. In a sense, non-gradient reactor combines the advantages of differential and integral reactor, and avoids their shortcomings. In addition, the flow phase in this reactor is almost ideally mixed, so it is unnecessary to limit the ratio between size of catalyst and diameter of reactor strictly as the tube reactor. As a result, it can be filled with original size of the industrial catalyst, or even installed only one grain of catalyst to be able to measure the apparent activity under the industrial reaction conditions studying the macroscopical kinetics, which will further obtain the utilization coefficient of inner surface of catalyst, and provide a reliable basis for industrial development of catalysts and mathematical simulation and magnification for industrial reactor.

The characteristic of external circulation of non-gradient reactor, also known as plug-shaped reactor or flow cycle device, recycles gas after reaction through the loop in outside of reactors to carry out cycle. Generally, circulation pump is used to drive gas circulation as shown in Fig. 7.2.

In the external circulation reactor system, it introduces small amounts of fresh feed F_0 continuously, and at the same time, small amounts of gas after reaction is expelled from the outlet of the reactor allowing the system to maintain constant pressure. If the volume of circulation is F_R, the mole fraction of the B-component in F_0 is y_0, y_{in} is the mole fraction of B into the catalytic bed $(F_0 + F_R)$, and y_F is for the outlet, the material balance equation (7.13) can be obtained:

$$x = y_F - y_{in} = \frac{y_F - y_0}{1 + (F_R/F_0)}. \tag{7.13}$$

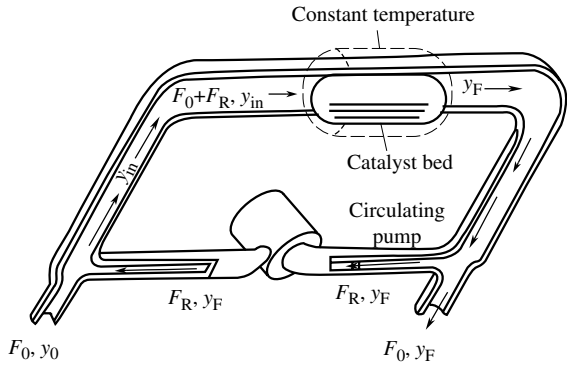


Fig. 7.2 External-recycling non-gradient reactor system

If the mass of catalyst in reactor is W, the reaction rate is r, the reaction rate with a change of dx at the reaction coordinate, then $rdW = Fdx$. When $F_R \gg F_0$ and $y_{in} \to y_F$ as well as $y_F - y_{in} \to 0$, so,

$$r = \frac{dx}{dW(F_0 + F_R)} \approx \frac{y_F - y_0}{(1 + F_R/F_0)W/(F_0 + F_R)} = \frac{y_F - y_0}{W/F_0}. \tag{7.14}$$

F_R/F_0 is defined as the ratio of cycle, and its value is about 20 to 40, higher than one. This is equivalent to make the micro-margin value of y_F–y_{in} enlarge into a larger margin value of y_F–y_0 which is easy to make an accurate mensuration.

Because the conversion through the bed is very low and the change of temperature is very small, while the amount of gases through the bed with a large speed is quite large, the influence of outside diffusion can be eliminated. This is the reason that the external circulation reactor can achieve non-gradient temperature and concentration.

Although external circulation reactor avoids the trouble in accurate mensuration, it makes trouble in manufacture of circulating pumps. It has a high requirement on the pumps: non-stained reaction mixture; small stranded dead space volume; large circulation volume (generally more than 4 L/min). To fully meet these three requirements, there will be some difficulties in equipments manufacture or defects of performance of the reactor. Pump body usually cannot operate at high temperatures, and the materials of reactor outlet should be cooled.

Non-gradient internal circulation reactor achieves high-speed circulation by the impeller of stirrer to promote gas flow in the reactor to obtain an ideal mixing in the reactor and to avoid the gradients of temperature and the concentration. Mixers are generally driven by magnetic to make dynamic seal become static seal, which is now more applicable. The performance of above main reactor is shown in Table 7.3.

Table 7.3 Performance comparison of several lab reactors

Reactor	Temperature uniform and definite degree	Contact time uniform and definite degree	Easy and difficult of sampling and analysis	Easy and difficult of mathematic explanation	Making and cost
Internal circulation reactor	Excellent	Excellent	Excellent	Excellent	Difficult, expensive
External circulation reactor	Excellent	Excellent	Excellent	Excellent	Moderate
Rotating basket reactor	Excellent	Good	Excellent	Good	Difficult, expensive
Differential tube-reactor	Good	Good	Uptight	Good	Easy, cheap
Adiabatic reactor	Good	Moderate	Excellent	Uptight	Moderate
Integral reactor	Uptight	Moderate	Excellent	Uptight	Easy, cheap

7.1.2.2 *Experimental device*

Catalytic reactor is the heart of catalytic activity evaluation device, which is considered as the center to organize the experimental process. The reactor is controlled by external conditions, such as the supply of raw materials, analysis and the measurement, preheating or (and) the pressurized device and so on. After reaction, it needs the means of separation, measurement and analysis to provide necessary flow and concentration data of reaction mixture to determine and to calculate the activity, and selectivity of catalysts. At present, the most commonly used device in the evaluation of catalysts is tubular reactor. Here, the high-pressure experimental device of ammonia synthesis catalyst is taken as an example.

First, the flow and the concentration of ammonia in the outlet of reactor should be measured for the performance evaluation and kinetics test of ammonia synthesis catalyst. As a result, the experiment needs to be carried out under the conditions of high-pressure, high temperature and high purity of synthesis gas. It is commonly realized by introducing the high-pressure synthesis gas into the laboratory from ammonia plant directly, then purifying them by a series of high-pressure vessel and entering into the reactor at last.[5] In general, universities and research institutes are far from the ammonia plant and do not have such conditions. To establish such a device usually needs high technologies and expenses, which restricts the universities and research institutes to carry out research on ammonia synthesis catalyst. Some labs decomposed ammonia to prepare syngas, which is pressurized by special reciprocating compressors with seven steps at least (the pressure up to 50 MPa), and then eliminated oil etc and purified the gases *via* a series of vessels with high pressure. However, this device is too complicated and expensive. To solve this problem, the author and his group adopted the film compressor in 1975, instead of the reciprocating compressor to compress the gas to high pressure as well as to keep the degree of purification of gas. In this route, it can use molecular sieve as purificant at atmospheric instead of high-pressure purification. In 1990, the experimental device was approved as the State Standard.[5] The test device process is shown in Fig. 7.3, and built up by the following parts.

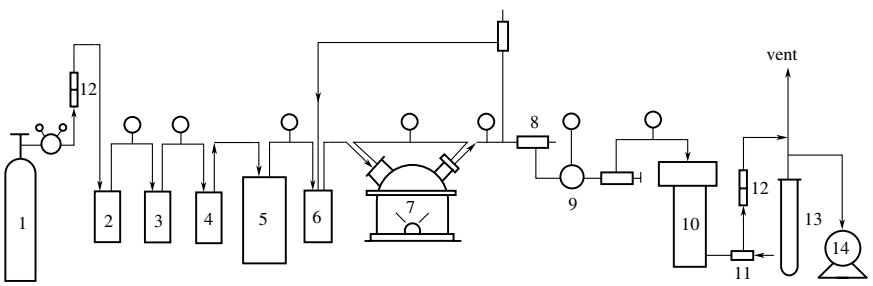


Fig. 7.3 Flowsheet of high-pressure test for performance evaluation of ammonia synthesis catalyst

1-liquid ammonia cylinder; 2, 4, 6-buffer tank; 3-ammonia decomposing furnace; 5-molecular sieve purifier series; 7-compressor; 8-control-valve; 9-manostat; 10-reactor; 11-adjustr-valve; 12-rotameter; 13-absorption bottle; 14-wet flow meter (⚲ are pressure gauge in Figure).

(1) **Preparation and purification of syngas.** Synthetic gas is obtained from decomposing of ammonia. Ammonia gas from liquid ammonia cylinder 1 enters into ammonia decomposition furnace 3 which is filled with large particles of ammonia synthesis catalyst. Thus ammonia is decomposed to the mixture of $H_2 : N_2 = 3 : 1$ at 650°C–700°C and at atmospheric pressure, with the decomposition ratio of 99.5%–99.7%. Remaining ammonia and small amounts of H_2O, CO_2, CO, O_2 and organic impurities in liquid ammonia are eliminated by series purifiers including the 5A molecular sieve, palladium molecular sieve and 13x molecular sieve. Purified synthetic gas (inlet of reactor) is composed of H_2 of 75% and N_2 of 25% (in volume), the steam and residual ammonia $\leq 10\,\mathrm{ml \cdot m^{-3}}$ (dew-point temperature ≤ -60°C).

(2) **Compressing of syngas.** Purified gas goes into the compressor 7 to be compressed to high-pressure. The compressor 7 is a kind of film-type compressor with the maximum pressure of 20 MPa and the flow of $5\,\mathrm{m^3 \cdot h^{-1}}$. Syngas purified at atmospheric pressure flows into the septum of the compressor, and does not contact with moving parts of the compressor, and thus will not be contaminated by lubricating oil etc. Syngas not only can be compressed to high pressures, but also can maintain the degree of purification. Therefore, we can use atmospheric molecular sieve purification instead of high-pressure purification.

(3) **Reactor.** The multi-reactor 10 is a self-preheated fixed-bed reactor with four-reactor contained in one shell, which is designed by authors, as shown in Fig. 7.4.[8] The trait of the reactor is able to self-preheat and can measure four different samples under the same conditions. The reactor is made of stainless steel, with the outer diameter of 100 mm and the height of 400 mm, in which the inner diameter of each reactor (slot) is 6–12 mm. The syngas enters into the cylinder from inlet 7, after preheating in central tube and being automatically divided into the four sections for four reactors (slots), respectively. The catalysts are loaded in the isothermal area of reactor. Each catalyst bed of the reactor has the thermocouple to measure

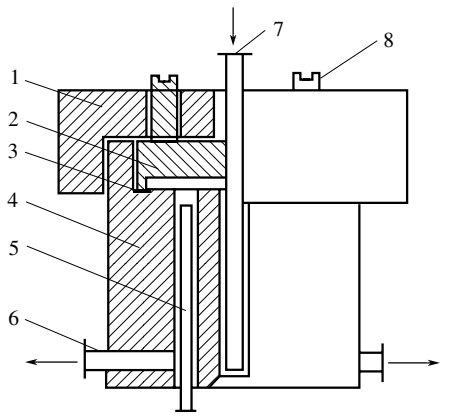


Fig. 7.4 Self-preheated fixed-bed reactor with four reactor contained in one cylinder

1-large lid; 2-impacted lid; 3-gasket; 4-cylinder; 5-thermocouple casing; 6-outlet; 7-inlet; 8-bolt

its temperature. The outside of the reactors is the heating furnace, and there is a copper ring between the heating furnace and the cylinder, enhancing the heat transfer and reducing the axial temperature difference of the cylinder (reactor) as well as increasing the length of isothermal area.

(4) **System of measurement and analysis.** The gases containing ammonia from the outlet of each reactor enter into absorption bottle 13 with the standard solution of sulfuric acid, in which all ammonia is absorbed. The volume of unabsorbed gases of N_2 and H_2 is measured by the wet flow meter. The rotor flow meter 12 in Fig. 7.3 only plays the role as the indicator, not for measurement.

(5) **Control system.** The pressure of the system is controlled by the open degree of loop-valve 8 and is stabilized by manostat 9. The flows of each reactor are controlled by the adjustive valve 11 in according to instructions of rotameter 12. The temperature of catalyst bed of each reactor is controlled and measured by the temperature-programmed and thermostatic controller.

This device can complete a series of experimental studies and measurement, including the evaluation of the activity, selectivity and stability of catalysts, the study on reduction performance, heat-resistant experiment and antivirus experimental, the study on reaction conditions such as H_2/N_2, content of inert gases etc, and the study on reaction kinetics and mechanism, and so on.

So far, a lot of studies on evaluation and dynamics of a variety of catalysts have been done. A number of companies have developed new and different models of equipment, such as the reaction systems for the development of catalysts. Basically, these systems have the same principles with the device mentioned above, although they are of multi-device support, full-function, high degree of automation, which reflect the specific application of the modern technology instruments in the field of chemistry and chemical engineering. There are reports on combined application of the evaluation equipments and the physical–chemical measurement technology and instruments, micro-chromatographic technique combined with thermal balance, DTA, X-ray diffraction, infrared adsorption spectrum and so on, which become a new hotspot of development of new testing methods of catalysts.

7.1.2.3 *Evaluation of catalytic activity*

(1) **Pre-experiment.** When using flow method to determine the catalytic activity or study the catalytic reaction kinetics, it should first consider the flow situation and diffusing effect of the gases in reactor in order to obtain the correct value of activity and the kinetic data. In other words, only on the premise of ruling out internal and external diffusing effect, can we conduct the evaluation of intrinsic activity and study on catalytic intrinsic kinetics. Otherwise, the different evaluation data are not comparable. The aim of pre-experiment is to reduce or eliminate the effect of the gradients of temperature and the concentration and the influence of inside and outside diffusion of catalyst beds before activity testing. The key is to determine some experimental parameters: the most appropriate particle size and volume of the catalyst and flow rate of gases. Chapter 2 discussed how to eliminate the effect of inside and outside diffusion. In this chapter, we just focus on the relationship between the temperature difference and the choice of the diameter of reactor, the particle size and the height of bed of catalyst.

Now the principles and methods about applying flow method to determine the catalytic activity have been proposed. Using these principles and methods can reduce the impact of macro-factors on activity measurement and the study on dynamics to a minimum. Here, in order to eliminate the wall effect of gases flow and local over-heating of beds, the ratio of diameter (d_r) of reactor and particle size (d_g) of catalyst should be $6 < d_r/d_g < 12$. The wall effect can be neglected when $d_r/d_g > 12$. However, as someone points out, even when $d_r/d_g > 30$, the flow speed of the liquid close to the wall is 10% to 20% higher than that of the bed axis direction, which is obviously related to effect of reaction heat.

On the other hand, reactions with a greater reaction heat have more difficulties in heat dissipation of bed when $d_r/d_g > 12$, because the temperature differences between cross-section center and the radial of catalyst bed are decided by the following equation.[9]

$$\Delta t_0 = \frac{\xi Q d_r^2}{16\lambda^*}, \tag{7.15}$$

where ζ is the reaction rate, $\mathrm{mol \cdot cm^{-3} \cdot h^{-1}}$; Q is the heat effect of reaction, $\mathrm{kJ \cdot mol^{-1}}$; d_r is the diameter of reactor, cm; λ^* is the effective conductivity factor of catalyst bed, $\mathrm{kJ \cdot (cm \cdot h \cdot {}^\circ C)^{-1}}$.

It can be seen from equation (7.15) that the temperature difference is proportional to reaction rate, heat effect and the square of diameter of the reactor, and is inversely proportional to the effective conductivity factor. The temperature difference increases with a decrease in the particle diameter of catalysts because the effective conductivity factor λ^* reduces with the decrease in the size of catalyst particles. When decreasing the particle diameter of catalyst in order to eliminate the effect of inside diffusion on reaction, it also enhances the factor of temperature difference. Therefore, it need to weigh the pros and cons of these factors in order to determine the most appropriate particle size of catalyst and the diameter of reactor.

There should be an appropriate proportion of the diameter of reactor, height of beds and the particle size of catalyst. According to the practical experience, it generally requires that the cross-section along the reactor can be placed side by side with 6 to 12 particles of catalyst. The ratio of height of bed to diameter of reactor (H/d_r) is greater than 2.5–3, and the ratio of height of bed to the particle size of catalyst (H/d_g) is higher than 50–100.

(2) **Activity determination and calculation.** The activity of ammonia synthesis catalyst is commonly expressed by the ammonia concentration of the outlet of reactor, and measured by neutralization method of sulfuric acid solution. The experiment is carried out in the fixed-bed reactor as shown in Fig. 7.4, which can measure four samples in one experiment. The inner diameter of reactors is 12 mm, with size of catalysts being 1.0–1.4 mm and volume being 2 ml. After reduction in the syngas, the outlet concentration of ammonia (NH_3 %) is measured at given temperature, pressure and space velocity. System of determining the outlet concentration of ammonia of reactor and the space velocity is shown in Fig. 7.5.

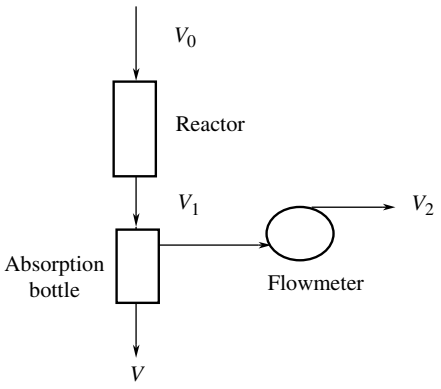


Fig. 7.5 System of determining the outlet concentration of ammonia and the space velocity of reactor

Calculation of ammonia concentration (φ) at reactor outlet

$$\varphi = \frac{N_{1/2H_2SO_4} \times V_{1/2H_2SO4} \times 22.08}{N_{1/2H_2SO_4} \times V_{1/2H_2SO_4} \times 22.08 + V_2 \times K} = \left(1 + \frac{K \times V_2}{22.08 \times N_{1/2H_2SO_4} \times V_{1/2H_2SO_4}}\right)^{-1}, \tag{7.16}$$

where $N_{1/2\mathrm{H_2SO_4}}$ is the number of substance of 1/2 $\mathrm{H_2SO_4}$, $\mathrm{mol \cdot ml^{-1}}$; $V_{1/2\mathrm{H_2SO_4}}$ is the volume of sulfuric acid solution, ml; 22.08 is the standard volume of ammonia gas, $\mathrm{l \cdot mol^{-1}}$; V_2 is the residual gas volume measured by wet-flow meter at the measurement conditions, liter; K is the conversion coefficient that gas volume under the measurement conditions conversing to gas volume at standard state.

$$K = \frac{P_0 - P_{H_2O}}{760(1 + t/273)}, \tag{7.17}$$

where p_0 is the atmospheric pressure, mmHg (1 mmHg = 133.322 Pa, the same below); p_{H_2O} is the saturated vapor partial pressure, mmHg; t is the temperature of wet flow meter, °C.

① Space velocity. When determining the outlet concentration of ammonia of reactor, it is necessary to measure the space velocity of the catalyst bed, as the reaction rate or outlet concentration of ammonia has close relationship with the space velocity. The method of measurement is to measure the absorption time and the volume of residual gas at the same time.

If the inlet flow rate of ($\mathrm{N_2 + 3H_2}$) without ammonia is V_0, the flow rate of formed ammonia is V, the residual gases after absorbed by sulfuric acid is V_2K, according to mass balance for $\mathrm{N_2 + H_2}$ gases in the system we get:

$$V_0 - 2V = V_2 \times K. \tag{7.18}$$

Then,

$$V = (V_0 - V_2 \times K)/2. \tag{7.19}$$

Because of $\varphi = \mathrm{V}/(\mathrm{V}_0 - \mathrm{V})$, substituted into the above equation,

$$\varphi = \frac{\frac{V_0 - V_2 \times K}{2}}{V_0 - \frac{V_0 - V_2 \times K}{2}} = \frac{V_0 - V_2 \times K}{V_0 + V_2 \times K}. \tag{7.20}$$

That is,

$$V_0 = \frac{1+\varphi}{1-\varphi} \times V_2 \times K. \tag{7.21}$$

According to the definition of space velocity,

$$S_V = \frac{V_0}{V_c t} \tag{7.22}$$

Then,

$$S_v = 3.6 \times 10^6 \times \frac{\frac{1+\varphi}{1-\varphi} \times V_2 \times K}{V_C \times t} = 3.6 \times 10^6 \times \left(\frac{V_2 K}{V_C t}\right)\left(\frac{1+\varphi}{1-\varphi}\right), \tag{7.23}$$

where S_V is the space velocity without ammonia, h^{-1}; t is the absorbing time, s; V_c is the volume of catalyst, cm^3.

The above equation obtains the space velocity based on the inlet gases of ($3\mathrm{H}_2 + \mathrm{N}_2$), also called space velocity without ammonia. Based on the volume (V_1) of gas ($\mathrm{H}_2 + \mathrm{N}_2 + \mathrm{NH}_3$) in reactor outlet, we calculate the space velocity (S'_V), that is,

$$S'_V = \frac{V_1}{V_c t}. \tag{7.24}$$

Because of $\mathrm{V}_0 = \mathrm{V}_1(1+\varphi)$, the equation (7.21) is substituted, thereby,

$$S'_V = 3.6 \times 10^6 \times \left(\frac{V_2 K}{V_C t}\right)\left(\frac{1}{1-\varphi}\right). \tag{7.25}$$

As ammonia synthesis is a kind of volume reducing reaction, the flow rate of outlet gas V_1 of the reactor changes with the reaction degree and the catalytic activity. Therefore, during evaluation, especially when comparing activities of different catalysts, it is appropriate to use the space velocity with ammonia free as equations (7.22) or (7.23) rather than space velocity with ammonia as equations (7.24) or (7.25).

② Reaction rate. After obtaining the concentration of ammonia and space velocity, the reaction rate can be calculated by following equations.

Reaction rate in mass:

$$r_m = \frac{S_V V_C}{22.41 W_C} \cdot \frac{\varphi - \varphi^0}{(1+\varphi)} = \frac{S_V}{22.41 \rho_C} \cdot \frac{\Delta\varphi}{(1+\varphi)}. \tag{7.26}$$

Reaction rate in volume:

$$r_V = \frac{S_V}{22.41} \cdot \frac{\Delta\varphi}{(1+\varphi)}. \tag{7.27}$$

Reaction rate in specific surface area:

$$r_S = \frac{S_V V_C}{22.41 S} \cdot \frac{\Delta\varphi}{(1+\varphi)}, \tag{7.28}$$

where r_m is the mass reaction rate, $\text{mmol} \cdot \text{g}^{-1} \cdot \text{h}^{-1}$; r_v is the volume reaction rate, $\text{mmol} \cdot \text{cm}^{-3} \cdot \text{h}^{-1}$; r_s is the surface reaction rate, $\text{mmol} \cdot \text{m}^{-2} \cdot \text{h}^{-1}$; W_C is the mass of reduced catalyst, g; Vc is the volume of reduced catalyst, cm^3; $\rho_C = \frac{W_C}{V_C}$ is the packed density of reduced catalyst, $\text{g} \cdot \text{cm}^{-3}$; S is the Specific surface area of reduced catalyst, $\text{m}^2 \cdot \text{g}^{-1}$; φ^0, φ are the ammonia concentration of the inlet and outlet of reactor, % (mol); $\Delta\varphi = \varphi - \varphi^0$ is the net value of ammonia, %.

③ Synthetic ratio of ammonia (α):

$$\alpha = \frac{2\Delta\varphi}{(1-\varphi^0)(1+\varphi)}. \tag{7.29}$$

④ Yield of ammonia in time and volume ($\text{g} \cdot \text{cm}^{-3} \cdot \text{h}^{-1}$):

$$y = \frac{17.03}{22.41} S_V \cdot \frac{\Delta\varphi}{(1+\varphi)}. \tag{7.30}$$

⑤ Turnover frequency of ammonia (TOF):

$$TOF = \frac{r_m}{3600N} = \frac{55.85}{3600}\left(\frac{r_m}{w_m D}\right), \tag{7.31}$$

where N is the number of active sites; w_m is the metal weight fraction in the reduced catalyst; and D is the surface exposure fraction of active metal atoms.

It can be seen from the above calculation that irrespective of the reaction rate, the synthetic ratio (conversion) of ammonia, space-time yield or the TOF of ammonia has a relationship with the outlet concentration of ammonia. Therefore, commonly it can directly use the outlet concentration of ammonia to characterize the activity of ammonia catalysts. It is worth noting that it should be necessary to indicate the reaction conditions, including pressure, temperature, space velocity, H_2/N_2 ratio, content of inert gas, particle size and volume of catalyst, and inlet concentration of ammonia etc.

7.2 Measurement of Physical Properties of Catalysts

Ammonia synthesis catalyst is a porous solid material containing atoms, ions or molecules (a general designation as particle) as all chemical substances. According to the principles of crystallography, these particles are arranged according to certain rules, in which the repeated and smallest structural unit is called cell. Then numerous cells make up of primary particle or crystal particles (the size of which is about 1–2 nm to 100 nm) and a number of primary particles can form the secondary particles. The secondary particles can pile up into particle aggregation of pellets with different shapes such as ball, bar, particle, powder and so on, as shown in Fig. 7.6. The effect and aggregation condition between each particles in pellet as well as the geometric shape of pellet, are decided by the preparation and forming condition. The size of pellet is generally 1–6 mm and more according to the varying demands.

In Fig. 7.6, (a), (b), (c) belong to the micro-structure of catalyst, while (d) and (e) belong to the macro structure. Among them, the size of (c) is nm-class size, also known as the submicroscopic structure.

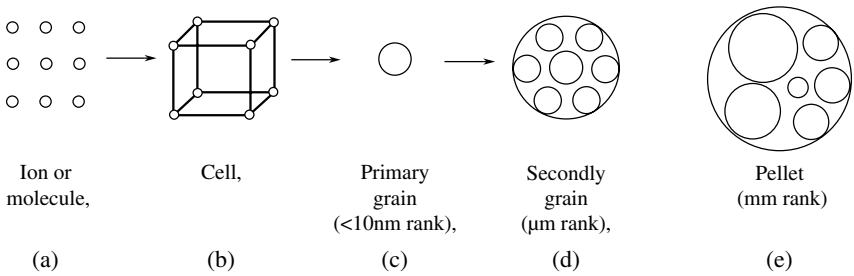


Fig. 7.6 Schematic diagram catalyst particles formation

The macro-scale physical character of catalysts refers to the characteristics of volume, shape and size distribution as well as related mechanical strength formed by the size, shape and void structure of particles and pellets. Industrial catalyst should have good macro-scale physical character, including surface area, pore volume, pore size and distribution, packing density, favorable particle size and shape and good mechanical strength. These properties not only influence the behavior of mass transfer, heat transfer and hydrodynamics (three transferes), but also directly influence the process of catalytic reaction kinetics. Therefore, macro-scale physical behaviours of catalysts is very important in the research of industrial catalyst.

7.2.1 *Particle size and density*

7.2.1.1 *Particle size and particle shape factor (φ_s)*

The particle size also called as granularity is the smallest basic unit that cannot be divided under the operating conditions in reactor. Therefore, its meaning and size differ with the reactor's requirements; on the one hand, it can be the particle size (secondary crystal particles), while on the other hand, it can also be the congeries of particle such as pellet size. In general, the granularity of industrial catalyst is almost the congeries of particle such as pellet size. However, irrespective of whether it is the particle or pellet, both define the real shape and size of catalyst in reactor, as well as the basic units of measurement and calculation for some physical behaviors (such as packing density, particle density, voidage of bed and shape factor, etc.). Therefore, in this book, the real size (particle and congeries) of catalyst in reactor are collectively called particles.

Granularity of single-particle is represented by particle size, also called particle diameter. The metal and compound particles that supported the catalysts generally are crystal particles or secondary particles, and their sizes are among the range of the normal definition of granularity. The size of spherical particle is just its diameter, and non-spherical and irregular particle size can be represented by "equivalent spherical diameter" that is usually measured by various measurement techniques. In addition, the irregular non-spherical particle size of the formed granulosity can be represented by "a considerable diameter", that is , the considerable diameter of irregular non-spherical particle size can be represented by the diameter of isopyknic sphere. If the volume of particle size is V_p, the particle's considerable diameter is

d_p, that is,

$$d_P = \left(\frac{6V_P}{\pi}\right)^{\frac{1}{3}}. \tag{7.32}$$

Then, using S_S to represent the surface area of isopyknic sphere, we get:

$$S_S = \pi d_P^2. \tag{7.33}$$

The surface area S_P of non-spherical particle is definitely higher than the surface area S_S of isopyknic sphere. Therefore, by introducing a dimensionless factor of φ_S called shape coefficient of particles, its value is expressed as:

$$\varphi_s = \frac{S_S}{S_P} = \frac{d_S}{d_P}. \tag{7.34}$$

For the spherical particle, $\varphi_S = 1$; and for the non-spherical particle, $\varphi_S < 1$. Shape coefficient presents the extent of difference between particle and sphere, sometimes also called as spherical coefficient. The Eqs. (7.33) and (7.34) are suitable to particles whose inner spaces are non-hollow, but not to ring-columnar hollow particles.

Shape factor is a basic parameter of catalyst particle, which is the basis of calculating pressure drop and thermal conductivity of catalyst beds. The φ_S of the regular particle can be directly calculated by the volume and surface area of particles; the φ_S of the irregular particle cannot be obtained directly. In general, it can be confirmed by measuring the pressure drop of beds of particles e.g. for irregular fused iron catalyst for ammonia synthesis.

When Reynolds number R_{em} is less than 10, the flow is in a form of laminar flow. By using Ergun equation,[14] the pressure drop of catalyst bed can be calculated as:

$$\Delta P = 150\frac{\mu u}{d_s^2}\frac{(1-\varepsilon)^2}{\varepsilon^3}L. \tag{7.35}$$

When $R_{\mathrm{em}} > 1{,}000$, the flow is in a form of turbulence state, and then the Ergun equation can be deduced as:

$$\Delta P = 1.75\frac{\rho_f u^2}{d_s}\frac{1-\varepsilon}{\varepsilon^3}L. \tag{7.36}$$

If the value of d_t/d_S is not large enough, it is necessary to consider the effect of wall on the pressure drop of catalyst bed. If the value of d_t/d is in the range of 7–91, the following correlation equation can be used.

$$\left(\frac{\Delta P\rho_f}{G^2}\right)\left(\frac{d_S}{L}\right)\left(\frac{\varepsilon^3}{1-\varepsilon}\right)\left(\frac{1}{M}\right) = \frac{150u\,(1-\varepsilon)\,M}{Gd_S} + 1.75, \tag{7.37}$$

where $M = 1 + \frac{2}{3}\left(\frac{d_S}{d_t}\right)\left(\frac{1}{1-\varepsilon}\right)$.

The surface equivalent diameter of particle d'_S can be calculated by measuring the pressure drop Δp and porosity ε of beds according to the Eq. (7.37), and then to calculate φ_S using the value of d_p according to the Eq. (7.34).

Bingchen Zhu *et al.*[15] obtained the surface equivalent diameter $d'_S = 1.92\,\mathrm{mm}$, and the shape coefficient is 0.487 for ammonia synthesis catalyst A301 with size of 3.3–4.7 mm.

7.2.1.2 *Density of catalyst*

Catalyst and catalyst support have different pore structures and chemical compositions, crystal structures, preparation and treatment methods. Therefore, some physical properties, such as density, porosity as well as surface area, pore volume and pore size distribution are necessary to be determined for research and application of catalyst.

The density of catalyst is defined by the mass of unit volume catalyst, volume is expressed by V, and mass is m. Then the density ρ is

$$\rho = \frac{m}{V}. \tag{7.38}$$

Usually, W (weight) is used rather than m (mass).

The real catalyst is a porous substance when it is heaped up in a vessel (reactor). Its volume includes solid skeleton volume (V_{sk}), inner pore volume (V_{po}) and the interstitial volume (V_{sp}) between particles. Therefore, the total stacking volume of catalyst (V_c) is

$$V_{\mathrm{c}} = V_{\mathrm{p}} + V_{\mathrm{sp}} = V_{\mathrm{sk}} + V_{\mathrm{po}} + V_{\mathrm{sp}}. \tag{7.39}$$

Different volumes substituted into the Eq. (7.38) result in densities with different meanings. The measurement of various densities is actually to measure volumes with different meanings.

(1) **Packing density (ρ_c).** It is expressed by the mass of unit volume of catalyst in the reactor, that is,

$$\rho_c = \frac{m}{V_C} = \frac{m}{V_{SK} + V_{PO} + V_{SP}}. \tag{7.40}$$

Packing density is usually measured by methods of vibration[16] and mechanical percussion.[17] ρ_c is determined under the condition of vigorous vibration, or sometimes even in a certain velocity of air flow, otherwise it only can be called as apparent bulk density.[18] At the same time, it should be noted that ρ_c is related with particle size, and it decreases with particle size. Table 7.4 shows the relationship between ρ_c and particle size.

(2) **Pellet density (ρ_p).** Pellet density is the ratio of the mass to geometric volume of single particle. In fact, it is hard to measure the geometric volume of a single particle accurately. In general, it should first accurately measure the interstitial volume (V_{sp}) between particles loaded in a certain packing volume V_c of catalyst, and then ρ_p is obtained according to the following equation:

$$\rho_p = \frac{m}{V_p} = \frac{m}{V_{sk} + V_{po}} = \frac{m}{V_c - V_{sp}}. \tag{7.41}$$

Table 7.4 Relationship between the compacted packing density and the particle size of catalyst ZA-5

Particle size/mm	1.0–1.4	2.2–3.3	3.3–4.7	4.7–6.7	6.7–9.4	9.4–13
ρ_{c} (oxidation state)/$(\mathrm{g \cdot cm^{-3}})$	3.0–3.05	3.21	3.27	3.31	3.33	3.37

The usual method to measure the gap volume between particles is Mercury-Displacement Method, which is because mercury can fill the free space between particles and does not enter into the pores of particles. The density measured by this method is also called as false density of particle.

(3) **Skeletal density (ρ_s).** Skeletal density is the mass of solid skeletal per unit volume catalyst, and is also called as true density (ρ_t).

Molecular diameter of helium is less than 0.2 nm, and it is almost not adsorbed by any sample. Hence, it is an ideal gas to measure the total volume including the volume of pores in particles and stacking gaps between particles. The testing equipments are conventional static gas adsorption devices. It detects the pressure difference of helium gas during the test, and then to V_{SK} of the sample is calculated by gas law, getting the value of skeletal density as shown in Eq. (7.42).[19]

$$\rho_s(\rho_t) = \frac{m}{V_{sk}} = \frac{m}{V_C - (V_{po} + V_{sp})}. \tag{7.42}$$

(4) **Apparent density (ρ_a).** Skeletal density is measured by the medium of benzene, isopropanol etc, (not helium gas) and is not considered as true density but rather apparent density. Because their molecular diameters are bigger than helium and absolutely cannot enter into the inner pores of catalyst (especially of microporous), the obtained skeletal volume is just an approximate value.

The measurement methods for apparent density include water, benzene and isopropanol etc, where the required equipment of the former are only a pycnometer and a precision balance, which are able to be followed by the general laboratories; the method of isopropanol is recommended by the American Petroleum Institute to be applied in the measurement of apparent density for catalytic cracking catalyst. This method is described as the following: A glass tube filled with isopropyl alcohol, the grinding mouth of which connects with a wade pycnometer, which is 10 ml of volume, with capillary plug and grinding lid of inner diameter of 1–2 mm and a 15 mm length. Before testing, it is necessary to check under measurement temperature using water and isopropanol.

(5) **Theoretical density.** The density calculated by volume and mass of the ideal crystal particle with regular arrangement of atoms is theoretical density of solid material. Usually XRD is used to measure phase and its crystal lattice constant for calculation. It is also known as the cell density or X-ray density. For example, the crystal structure changes of molten iron catalyst before and after reduction could be shown as Fig. 7.7.

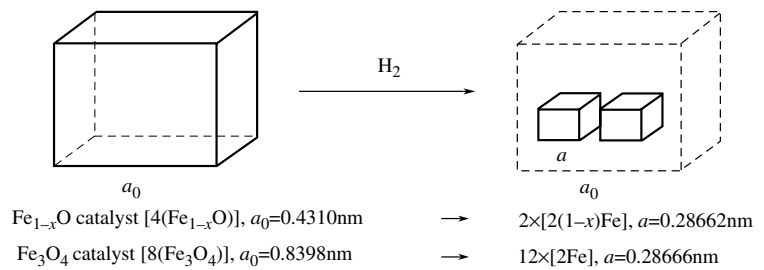


Fig. 7.7 Schematic diagram of the crystal structure changes of molten iron catalyst pre- and post-reduction

$Fe_{1-x}O$ has the halite-type of face centered cubic crystal lattice base on O^{2-} ions close packing, where the unit cell consists of four molecules of $Fe_{1-x}O$, and its side length of unit cell is a_0 (i.e., crystal lattice constant), and then the theoretical density (ρ_t^0) of $Fe_{1-x}O$ (that is the true density of $Fe_{1-x}O$) is:

$$\rho_t^0 = \frac{4[(1-x)M_{Fe} + M_O]}{N_A a_0^3}, \tag{7.43}$$

where M_{Fe}, M_O are relative atomic mass of iron and oxygen; x is the concentration of defects in crystal lattice; a_0 is the crystal lattice constant or cell constant; N_A is the Avogadro constant.

After reduction, the original cell volume of $Fe_{1-x}O$ basically keeps constant (a_0 unchanged), except only losing four oxygen atoms and forming a porous structure. Therefore, it still can use a_0 to calculate the theoretical pellet density for reduced catalyst (ρ_p^R),

$$\rho_p^R = \frac{4(1-x)M_{Fe}}{N_A a_0^3}. \tag{7.44}$$

After reduction, the theoretical true density of body centered cubic crystal cell with side length of "a" which is constituted by $2(1-x)$ of α-Fe atoms is expressed as Eq. (7.45).

$$\rho_t^R = \frac{2(1-x)M_{Fe}}{N_A a^3}. \tag{7.45}$$

When $x = 0$, i.e. the theoretical density (ρ_{Fe}) of pure iron ($a = 0.2866\,\text{nm}$), we get:

$$\rho_{Fe} = \frac{2M_{Fe}}{N_A a^3} = \frac{2 \times 55.85}{6.023 \times 10^{23} \times (0.2866 \times 10^{-7})^3} = 7.874.$$

However, the catalyst is not a pure $Fe_{1-x}O$ or elementary iron. In the oxidation state of catalyst, the $Fe_{1-x}O$ phase only accounts for $(1 - \Sigma b_i^0)$, in which Σb_i^0 is the total content of promoters. The promoter can be considered as an inert substance, whose mass and volume should remain unchanged before and after reduction. If the volume contribution of each component in catalyst is cumulative, and the average density of promoters is $\Sigma(b_i^0 \rho_t^i)$, then the theoretical density of oxidation state catalyst is:

$$\rho_t^{0'} = \left(1 - \sum b_i^0\right) \rho_t^0 + \sum (b_i^0 \rho_t^i), \tag{7.46}$$

where b_i^0, ρ_t^i are the mass fractions and densities of promoter i.

In the same way, the mass fraction of iron is $(1 - \Sigma b_i^R)$, that of promoters is Σb_i^R in total mass of catalyst after the reduction. The theoretical pellet density and true density of catalyst after the reduction are:

$$\rho_p^{R'} = \left(1 - \sum b_i^R\right) \rho_p^R + \sum (b_i^R \rho_p^i) \tag{7.47}$$

$$\rho_t^{R'} = \left(1 - \sum b_i^R\right) \rho_t^R + \sum (b_i^R \rho_t^i) \tag{7.48}$$

The experimental and theoretical results of compacted packing density (ρ_c), pellet density (ρ_p) and true density (ρ_t) of A301 and A110-2 catalysts are shown as in Table 7.5.

Table 7.5 Experimental and calculated results of ρ_c, ρ_p and ρ_t of A301 and A110-2 catalysts/($g \cdot cm^{-3}$)

Catalyst	ρ_c^a	ρ_p		ρ_t	
		Theoretical	Experimental	Theoretical	Experimental
A301	3.00–3.05	—	5.53	5.56	5.62
A301R[b]	2.34–2.38	4.30	4.32	6.846	6.85
A110-2	2.8–2.9	—	—	5.10	—
A110-2R	2.1–2.2	3.66	3.60	7.203	7.40

[a] ρ_c is related with the size of particle. In this experimental, the particle size is in 1.0–1.4 mm.
[b] R represented the catalyst after reduction.

Table 7.5 shows that the theoretical values and experimental values is fairly consistent. According to the values of ρ_p before and after reduction, it can calculate the amount (Δm) of removed oxygen during reduction by hydrogen,

$$\Delta m = 1 - \frac{\rho_{P,A301}}{\rho_{P,A301R}} = 1 - \frac{4.32}{5.53} = 0.219.$$

The above value is consistent with the result of thermogravimetry,[20] and shows that ρ_c, ρ_p data are accurate and reliable. The ρ_c, ρ_p value for A301 catalyst are larger than that of Fe_3O_4 based A110-2 catalyst, but smaller for ρ_t value, because the former has crystal lattice defects.

At present, there are many kinds of instruments that can be used for measuring the true density and the apparent density according to the gas volume replacement principle. These instruments commonly have the advantages of single structure, convenient operation and accurate result. The 1,320 type of automatic densimeter of Micromeritic Company can set an example for them. The density range that measured by automatic densimeter is 0–19.99 $g \cdot cm^{-3}$, the precision of measurement volume is $\pm 0.02\,cm^3$ for $9\,cm^3$ of samples. The largest factor of influence on precision is drying status of sample.

7.2.1.3 *Voidage of catalyst bed (ε)*

The voidage of the catalyst bed is closely related to pressure drop, which is an important engineering parameter. Voidage of the catalyst bed is the ratio of the void volume (V_{sp}) between particles to total stacking volume (V_c) of per unit mass catalyst, represented by (ε)

$$\varepsilon = \frac{V_{sp}}{V_c}. \tag{7.49}$$

ε changes with the particle size, shape and the extent of accumulation of catalyst, which has no direct relationship with pore structure of catalysts. Therefore, voidage can be calculated by the compacted packing density (ρ_c) and pellet density (ρ_p).[21]

$$\varepsilon = \left(\frac{1}{\rho_c} - \frac{1}{\rho_p}\right)\rho_c = 1 - \frac{\rho_c}{\rho_p}, \tag{7.50}$$

where ρ_c is related to the particle size, while ρ_p is not. Table 7.6 shows the voidages of different sizes of A301 catalysts.

Table 7.6 Voidage (ε) of different size of A301 catalyst

	Particle size/mm					
Catalyst	1.0–1.4	2.2–3.3	3.3–4.7	4.7–6.7	6.7–9.4	9.4–13.0
Unreduced catalyst	45.30	41.95	40.86	40.14	39.78	39.06
Reduced catalyst	45.37	41.90	40.97	40.00	39.81	39.12

Note: All data from author's experiment.

It is seen from Table 7.6 that the voidage is the same for catalysts before and after reduction. This indicates that the geometric volume of catalysts before and after reduction is nearly unchanged. The voidage decreases slightly with particle sizes of catalysts. The pressure drop Δp of catalyst bed is proportional to $[(1-\varepsilon)\varepsilon^{-3}]$, and is inversely proportional to particle size [Eq. (7.36)], although the increase in particle size will cause the decrease of ε leading to the increase of Δp, which cannot offset the influence of decrease of Δp due to increase of particle size. Therefore, it is useful to use larger particles to decrease the pressure drop Δp of catalyst bed.

7.2.2 *Surface area and pore structure*

The specific surface area and pore structure are the most basic macroscopic physical properties of solid catalysts. Pore and surface are the reactive rooms of heterogeneous catalytic reactions, and the amount of surface area directly influences the level of catalytic activity. If the surface properties of catalyst are uniform, then their activity is directly proportional to their surface area. Catalytic reactions are generally influenced by the diffusion under industrial conditions, and the activity, selectivity and lifetime and almost all properties of catalyst are related to these two macroscopic physical properties. Although the activity for most catalysts is not proportional to their surface area, the surface area is still a visual physical quantity to evaluate catalyst performance, and sometimes acts as a control index of preparation.

Therefore, it is not difficult to understand that the characteristic of pore structure and the measurement of surface area have penetrated into the nano-particles as well as molecular channels and holes cage, and its research work also has entered into a new development stage.

So far, for ordinary industrial catalysts, the main determination methods for pore structure and surface area are still dominated by the vapor physical adsorption technology and pressed mercury method.

7.2.2.1 *Specific surface area*

The determination of the structural parameters of solid such as surface area, pore volume, pore size and their distribution is based on the gaseous adsorption phenomena and theory on solid surface. The key is the determination of gaseous adsorption quantity. In the early 20th century, Langmuir first systematically investigated the adsorption phenomena, and proposed the famous Langmuir model of monolayer adsorption in 1918. The Langmuir adsorption theory is a principal mainstay for surface catalytic kinetics in heterogeneous catalysis, and others can be considered as its revision and supplement. For example, the BET equation, namely multilayer

adsorption model, is a significant modification of Langmuir model of monolayer adsorption, which was put forward by Brunauer, Emmett and Teller in 1938 and thus named after them. The BET adsorption theory has successfully interpreted various kinds of adsorption isotherms. A new method was developed (based on this theory) for the determination of surface area of catalyst, which makes the studies on catalyst enter into a new stage.

$$\frac{p}{V(p_0 - p)} = \frac{1}{V_m C} + \frac{(C-1)}{V_m C} \times \frac{p}{p_0}, \tag{7.51}$$

where V is the adsorption quantity; V_m is the monolayer saturation adsorption quantity; p_0 is the saturated vapor pressure of adsorbate at adsorption temperature; and C is a constant.

After V and the corresponding p values measured by a series of experiments, then plot $\frac{p}{V(p_0-p)}$ *vs.* $\frac{p}{p_0}$ obtains a straight line. From the slope of $m = (C-1)/(V_{\mathrm{m}}C)$ and intercept of $b = 1/V_{\mathrm{m}}C$ in a straight line, we get V_m as:

$$V_m = \frac{1}{m+b}. \tag{7.52}$$

If A_{m} is the section area occupied by each of the adsorbate molecule, then

$$S = A_m V_m \frac{N_A}{22414}, \tag{7.53}$$

where N_A is the Avogadro's constant.

For example, the section area occupied by N_2 molecules at -195.8°C of the boiling point of liquid nitrogen is $A_m = 0.162\,\mathrm{nm}^2$.

Then, $S = 4.36\,V_m$ (m^2).

If A_m is not under liquid nitrogen conditions, its value is often calculated by comparing with the adsorption of nitrogen. Therefore, the determination of surface area to a certain extent is half-experiential. The absolute error of experiment depends on the error of A_m value, which is about 10%. Table 7.7 gives the common values A_m of the adsorbate.

There are three methods for the common determination of the amount of gaseous adsorption, that is, the capacity method, the weight method and the gas chromatography. At present, the measurement and calculation of the specific surface area of catalyst has been instrumentally standardized. It must be particularly noted that the determination of the surface area is the base on the physical adsorption nature of the adsorbate, so any chemical sorption phenomenon must be avoided when using these apparatuses in the determination. So low temperatures and inert adsorbates

Table 7.7 A_m values of adsorbate[7]

Adsorbate	Adsorption temperature/K	Saturated vapor pressure p_0/Torr	$A_{\mathrm{m}}/\mathrm{nm}^2$
N_2	77.4	760	0.162
Kr	77.4	2.592	0.195
Ar	77.4	250	0.146
C_6H_6	293.2	74.1	0.40
CO_2	195.2	160	0.195
CH_3OH	293.2	96.0	0.25
n-C_4H_{10}			0.566

must be adopted in the experiment. Another restriction based on the experimental experience, is the general range of p/p_0 in Eq. (7.53) is between 0.05 and 0.35.

7.2.2.2 *Pore volume*

It is seen from the foregoing discussion of density that pore volume (V_g) of per gram of catalysts is V_{po}. Since $V_{po} = V_p - V_{sk}$, and V_p and V_{sk} are the reciprocal of the density of particle and true one, respectively. So the pore volume equals to

$$V_g = \frac{1}{\rho_p} - \frac{1}{\rho_t}. \tag{7.54}$$

Since the pore volume is correlative with pore size, it can be divided into the total pore volume, mesopore volume and micropore volume by the pore size. They can be directly measured by the detector of apparatus, and the Eq. (7.54) gives the total pore volume.

7.2.2.3 *Porosity*

Porosity is the ratio of the pore volume to the total volume for per gram of catalyst, which is expressed by θ,

$$\theta = \frac{V_{po}}{V_p} = \frac{V_p - V_{sk}}{V_p} = \frac{\rho_t - \rho_p}{\rho_t}. \tag{7.55}$$

When Eq. (7.54) is introduced into Eq. (7.55), Eq. (7.56) is obtained,

$$\theta = \frac{(1/\rho_p - 1/\rho_t)}{1/\rho_p} = V_g \rho_p. \tag{7.56}$$

Therefore, the porosity can be calculated by the particle density and pore volume or the density of true and particle.

The porosity of catalyst is correlative with the geometric accumulative ways between the particles in pellet. If the particles accumulate in the ideal way of crystal structure, the changes of the porosity with particles size are given by Graton–Fraser model (Table 7.8).

The theoretic pore volume and porosity of iron catalyst can be also measured and calculated by XRD. It can see from Fig. 7.7, the cube with side-length of a_0 before reduction is occupied by two α-Fe cubic unit cells with side-length of a after reduction, and thus the rest space is pore, so

$$V_g = (a_0^3 - 2a^3)\frac{Fe\% \cdot N_A}{4[55.85(1-x)]}. \tag{7.57}$$

$$\theta = \frac{a_0^3 - 2a^3}{a_0^3}. \tag{7.58}$$

Table 7.8 Porosity of Graton–Fraser model

Accumulation mode	Unit face angle	Unit volume	Contact point numbers	Porosity θ/%
Cubic packing	90°, 90°, 90°	1	6	47.64
Rhombic packing	90°, 90°, 60°	$\sqrt{3}/2$	8	39.54
Square — cuniform packing	60°, 60°, 116°34′	3/4	10	30.19
Rhombus packing	60°, 60°, 90°	$1/\sqrt{2}$	12	25.95

Table 7.9 Pore volume (V_g) and porosity (θ) of catalyst A301 and A110-2

	$V_g/(\mathrm{cm}^3 \cdot \mathrm{g}^{-1})$		$\theta/\%$	
Reducted catalyst	Theoretical	Experimental	Theoretical	Experimental
A301R	0.0865	0.0855	41.30	36.93
A110-2R	0.1273	0.1089	52.27	46.42

The above data is from author's lab.

When the data of Fig. 7.7 is introduced into it, and if $x = 0.05$, we obtain:

$$V_{g,A301} = [(0.4313)^3 - 2(0.28662)^3]\frac{0.92 \times 6.023 \times 10^{23}}{4 \times 55.85(1 - 0.05)} \times 10^{-21} = 0.0865$$

$$\theta_{A301} = \frac{(0.4313)^3 - 2(0.28662)^3}{(0.4313)^3} = 0.4130$$

The experimental and theoretical pore volume (V_g) and porosity (θ) of the catalyst A301 and A110-2 are shown in Table 7.9. The results show that the theoretical values of the pore volume and porosity are slightly larger than that of the experimental values because the theoretical values ignore the volume of promoters in catalyst.

It can be seen from the above calculation that the pore volume and porosity of catalysts are formed during reduction. Hence, the reduction process of catalyst plays an important role in the formation of porous structure. Thus it is necessary to have efficient reduction process of catalyst in industrial application.

7.2.2.4 *Average pore size*

On the assumption that all the pores have columniform pores with similar diameter, and their surface areas are much larger than outer surface area of particles, then the determined surface area equals the sum of the surface area of all pores.

$$S = n \cdot 2\pi \cdot r \cdot L, \tag{7.59}$$

where n is the number of pore; r is the radius of pore; L is the length of pore; S is the total surface area of pore.

The volume of the pore is:

$$V_{\mathrm{g}} = n \cdot \pi \cdot r^2 \cdot L. \tag{7.60}$$

By division of the two equations, an average radius of pore is obtained as:

$$\tilde{r} = \frac{2V_g}{S}. \tag{7.61}$$

Since the pores in real catalyst are very complex, there are two obvious differences with the above hypothesis for the calculation of average radius.

(1) The actual shape of the pore is different. There is not only the columniform pore, but other kinds of pores too; they may be straight or twist like a maze. The shape of the pore will affect the gas diffusion and hydrodynamics. The macroscopical nature of solid catalysts is usually characterized with twist-factor or maze-factor.

(2) The actual pores have different sizes and distribution. Sometimes catalysts with near average pore often have obviously different activities because they have different pore distributions. As a result, another important parameter of solid catalysts is the data of pore distribution.

7.2.2.5 *Twist-factor*

Twist-factor or maze-factor is an important parameter of solid catalyst. It has an important impact on the apparent rate of gas-solid catalyzed reactions, the productivity of reactor and efficiency of the catalyst. The determination of twist-factor has dynamic method and steady method. Steady method has some advantages such as simple equipment, easy operation, repeatability. However, it cannot reflect the effect of "dead pore." The shapes of catalyst are therefore limited to columniform or ring cylindrical with single pore.[22] In order to determine the twist-factor of the catalyst with irregular shapes, and reflect the effect of "dead pore" on diffusion, the dynamic method has gradually developed. The most common practice is carried out on a gas chromatography, by determination of the pulse response curve of adsorption, desorption, and diffusion for obtaining the necessary parameters which really reflect a variety of transmission characteristics in the catalyst. At present, the widely used chromatography is a single-particle string reactor method (SPSRM). Scott *et al.*[23] considered that, under certain conditions, the large particles of solid catalyst have the similar mass transfer processes with the small spherical particles. So the twist-factors of industrial catalysts with different shapes can be determined by SPSRM.

SPSRM is carried out in the following ways: Take the catalyst as a beading-strand into a bed until the total number of the catalyst particles is 50 or more, and the ratio of the diameter of packed bed to that of particle is of 1.1:1 to 1.4:1, then pulse inject tracer where the column is a single-particle line reactor under the operating conditions of chromatography. Use the analysis of the pulse response curve to obtain the value of the first order original matrix and the second-order central matrix. Through the valuation of parameters we can get a variety of parameters including effective diffusion coefficient (D_{effA}), and then determine the twist-factor (δ) of catalyst according the Eq. (7.62).[24,25]

$$D_{eff\,A} = \frac{\theta}{\delta} D_{EA}. \tag{7.62}$$

In the Eq. (7.65), D_{EA} is referred as the integrated diffusion coefficient when considering the impact of pore-size distribution on diffusion.

Bingchen Zhu *et al.*[26] used the dynamic method and determined the twist-factor of ammonia synthesis catalyst A301 in SPSRM. The twist-factor of catalyst A301 obtained is 3.28.

7.2.2.6 *Distribution of pore size*

The inner surface area of solid catalysts is mainly distributed in the pores and channels of crystal-particles, and furthermore the diffusion and mass transfer during reaction process is directly dependent on the pore structure. Hence, the pore size and pore volume are sometimes more important than the surface area of the pore as structural information.

The pore size of the catalyst relates to the mass transfer process of catalytic reaction. When reactions proceed in an inner diffusion area, the mass transfer rate is relatively slow, and the pore size relates to the surface utilization ratio of the catalyst in the reaction. If the target product is an unstable intermediate, the pore size will affect the selectivity of reaction. Therefore, for a given reaction condition and composition of the catalyst, a catalyst should have the uniform pore size distribution in order to develop of a good catalyst.

The analysis of the pore distribution needs to measure adsorption isotherms. In addition, it is mainly based on gas-liquid equilibrium theory in thermodynamics to study the characteristics of adsorption isotherm, and use the different pore models to calculate the distribution of pore. In the experimental methods for the pore structure determination, steam physical adsorption and pressed mercury ways are the two key technologies. These technologies correlate with the rationalization and continual development in theory and in a variety of simulation technologies of physical adsorption, while ensuring that the experimental equipment are easy-to-automate, small and bear good facilitation.

(1) Capillary cohesion phenomenon — Kelvin equation. The theory of capillary cohesion and Kelvin equation are the theoretical basis of physical vapor adsorption. When the steam of adsorbate contacts with porous solid surface, it will form liquid film of the adsorbate on the surface adsorption field. The films in the pore bend variously with the pore diameter, while the films in the outer surface of particles are relatively flat. The film thickness of liquid of adsorption increases with increase in vapor pressure. When it reaches a certain moment, the gravity between the curved liquid surfaces sufficiently liquidify the vapor from gaseous automatically, and completely fill the pores. This phenomenon is known as capillary cohesion.

It can see from the above-mentioned discussion that capillary cohesion is closely related to the curved liquid surface. The pressure boundary causes capillary cohesion — the critical vapor pressure relates to the curvature radius of liquid surface. Kelvin equation has been derived from thermodynamics, where the curvature radius (r_k) of the meniscus of hemispherical (concave) liquid and the equilibrium vapor pressure (p) has the following relationships:

$$ln\frac{P}{P_0} = -\frac{2\sigma V_M \cos\theta}{r_K RT}, \tag{7.63}$$

where p_0 is usually the saturated vapor pressure on large flat surface; σ is the surface tension of liquid adsorbate, $\times 10^{-5}\,\mathrm{N}\cdot\mathrm{cm}^{-1}$; V_M is the molar volume of liquid adsorbate, $\mathrm{mL}\cdot\mathrm{mol}^{-1}$; θ is the contact angle of curved surface with the solid walls, usually θ equals to zero when liquid wetting solid surface (the following has the same assumptions).

It can be seen from Eq. (7.63) that $p/p_0 \leq 1$, and the smaller is the r_k, the smaller is p/p_0. This means that for very small pore, capillary cohesion can occur when the steam pressure is lower than the saturated vapor pressure p_0 at the adsorption temperature. Furthermore, r_k means the critical pore diameter, and that is in the equilibrium vapor pressure p. When the pore radius of solid is smaller than or equal to the given value of r_k in Eq. (7.63), capillary cohesion takes place; while when the pore radius of solid is larger than the given value r_k in Eq. (7.63) cohesion would not happen, only casing the multi-layer film on the pore wall. Therefore, if

it ignores the existing volume of liquid before the capillary cohesion taking place, the difference of adsorption quantity of porous solid at two different vapor pressures (calculate by volume liquid) is the pore volume between the two corresponding pore radius of r_k.

For the pore in which the capillary cohesion has not yet taken place, they are not "empty," but the liquid film with a thickness of t on wall. Consequently, the pore radius r_p and the pore nuclear radius r_k of the cylindrical pore have the following relation:

$$r_k = r_p - t = -\frac{2\sigma V_M}{RTln(p/p_s)} \tag{7.64}$$

The thickness t of adsorption layer is usually calculated according to the Halsey equation, for nitrogen adsorption:

$$t = 0.354\left[\frac{-5}{ln(p/p_s)}\right]^{1/3}. \tag{7.65}$$

By Eq. (7.64) and (7.65), we are able to obtain the critical pore radius r_p when capillary cohesion occurs at a certain equilibrium pressure p. At this point, the capillary cohesion takes place in the pore where the radius is smaller than or equal to r_p for the porous materials.

(2) Calculation of pore distribution. Usually the pore distribution of porous material is represented by the ratios of the various pore volumes with a variety of pore sizes to the total pore volume. According to the definition of IUPAC (1972), the pore size can be divided into macropore with radius more than 50 nm, mediumpore (also known as mesoporous) with radius of 2–50 nm and micropore with radius of less than 2 nm.

Pore distribution in general is calculated according to the desorption isotherm, which is a desorption process with equilibrium steam pressure descending and adsorption volume reducing. The relationship between the total adsorption quantity and pore radius is shown in Fig. 7.8. The relationship between the differential values of adsorption quantity *vs.* pore radius is the so-called pore distribution curve, as shown in Fig. 7.9.

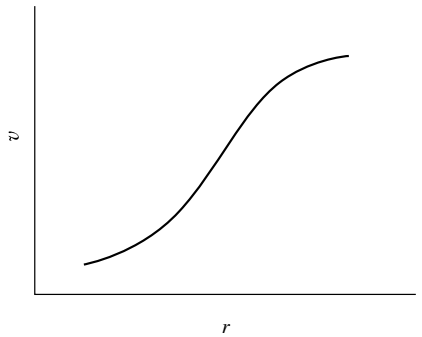


Fig. 7.8 Relationship between the total adsorption quantity and pore radius

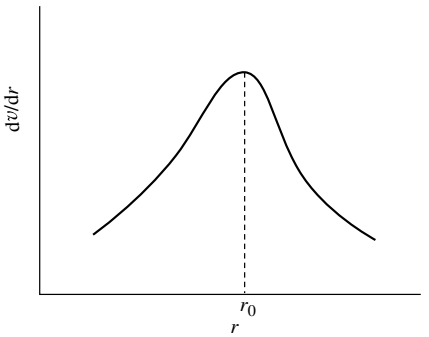


Fig. 7.9 Pore size distribution curve

The radius r_0 corresponding to the maximum value of curve in Fig. 7.9 is known as the most probable pore radius. It means that the proportion of the pore whose radius r_0 is the highest in the porous catalyst. In order to obtain the curve of pore size distribution, it needs to detect the contribution of a variety pore on the adsorption quantity, and then use the following ways to calculate the relationship of pore size distribution according to the scope of pore size of a variety of materials.

Calculation of pore size distribution by capillary cohesion method. Capillary cohesion method for the calculation of pore size distribution including the classical BJH method[27] based on Kelvin equation for the analysis of pore size distribution; DH method[28] and its improved "modificatory non-Model" (ML method[29]) for the calculation of medium pore size distribution; MP method[30]; DR equation[31]; HK equation[32]; CA equation[33]; density functional theory method[34] for the calculation of micropore size distribution, and so on, have been introduced in many monographs.[1–4] As for the adsorption experimental technology, the instrumental automation of static capacity way has been achieved and the dynamic way has become common method. In particular, the apparatus of the static capacity way is small, and equipped with a variety of computer simulation softwares, and thus becomes a universal and standardized analytical instrument.

Capillary cohesion method is generally applicable to the calculation of the pore size distribution of medium pore substance.

"Pressed Mercury" method. When some liquids and solids are non-humid, surface tension will prevent the liquid entering into the small pore of solid. Using external force to overcome the surface tension can force the liquid to enter into the pore. As the surface tension relates to the pore size, the pore size can be related with external forces. The "pressed mercury" method is based on this principle.

When the outside force and the surface tension come to balance, the following relationships exist.

$$p\pi r^2 = -2\pi r\sigma\cos\phi \tag{7.66}$$

$$r = \frac{-2\sigma\cos\phi}{p}, \tag{7.67}$$

where p is the plus pressure, $\mathrm{N}\cdot\mathrm{cm}^{-2}$; σ is the linear-surface tension, $\mathrm{N}\cdot\mathrm{cm}^{-1}$; r is the pore radius, cm; Φ is the contact angle.

Because most of the solids and mercury are not humid, mercury is used as a medium, which is called as "pressed mercury" method. When mercury is used as a medium, $\sigma = 4.8\times10^{-3}\,\mathrm{N}\cdot\mathrm{cm}^{-1}$, $\Phi = 140°$. By the appropriate translation, then,

$$r = \frac{73500}{P}. \tag{7.68}$$

If $p = 7350\,\mathrm{N}\cdot\mathrm{cm}^{-2}$, then $r = 10\,\mathrm{nm}$. This shows that this method is applicable to the determination of pore size distribution for large pore and medium pore of more than 4 nm.

7.2.2.7 *Lag-ring and pore structural model*[35]

For a catalyst, adsorption isotherm should be unique. During measurement, the actual porous catalyst will give an isotherm in the adsorption process, while giving

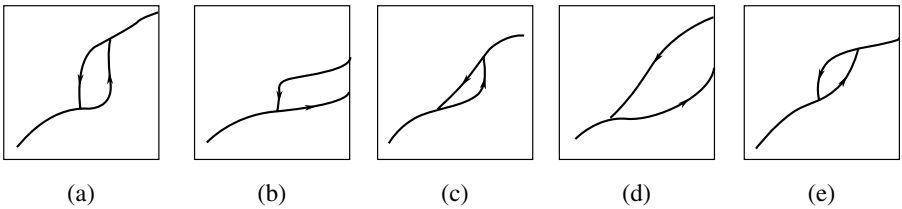


Fig. 7.10 Five kinds of adsorbed loops

another isotherm in the desorption process, which overlaps with the adsorption isotherm at the beginning and at the end, and a ringy curve is formed at the middle part, as shown in Fig. 7.10. This phenomenon is called as hysteresis, and the non-overlapping part is known as lag-ring.

The pore structures of various solid are very anfractuous and multifarious, and their lag rings are different from each other. Der Booer considered that it would not exceed the five kinds of a, b, c, d, e as shown in Fig. 7.10. In the study of pore structure of catalytic materials, the analysis of these five lag rings can help to provide useful information for the understanding of the pore structural characteristics and for the reasonable choice of the pore structural models.

(1) **Type A.** Adsorption and desorption branch separate in the medium zone of p/p_0, and are very steep. This type reflects the pore structures such as the tube-like pores opening at both ends, the little wide tubular pores, tubular pores with both ends narrow and centre wide, wide mouth inkstand-shaped pores with $r_n < r_w < 2r_n$ and narrow mouth inkstand-shaped pores (Fig. 7.11). Groovy-shaped pores also show the A–type lag ring.

(2) **Type B.** Adsorption branch zooms in the point of the saturated vapor pressure, while desorption branch precipitately drops in the middle p/p_0. A pore with parallel wall slit-like openings is a typical type B lag ring. Those with special wide-body and

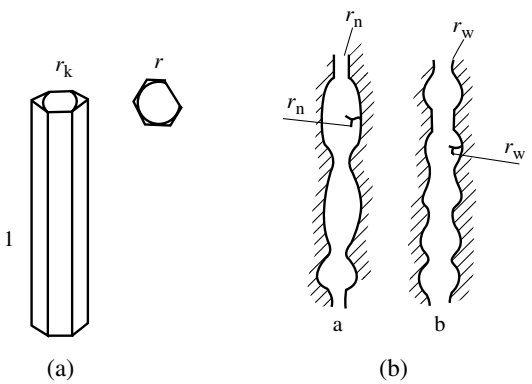


Fig. 7.11 Typical pore model reflected by a-type back line r_n — Narrow-pore radius; r_w — Wide-pore radius

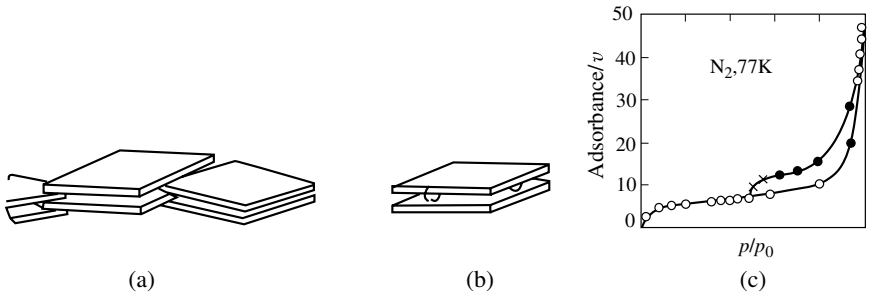


Fig. 7.12 Typical pore model reflected by B-type back line (a) Cubicles separated by accumulation model; (b) Cubicles separated by small particles; (c) Typical isothermal loop of montmorillonite

narrow neck also belong to this type. Catalytic materials of layered clay mineral such as montmorillonite are present as typical B lag ring (Fig. 7.12).

(3) **Type C.** Adsorption branch zooms in the middle p/p_0 zone, while desorption branch grows slowly. It is a typical lag ring formed from uneven distributed pores. Cone-shaped or double cone-shaped capillary pores, and wedge pores are closed at sides and opening at both ends belong to this type. The C-ring is very rare.

(4) **Type D.** Adsorption branch is very steep in the point of the saturated vapor pressure, and desorption branch declines slowly. This corresponds to uneven pore structure which is characterized as four open areas, with a volatile narrow neck and special wide-body. Tip-cut pore opening at both ends also belongs to this ring features. D-ring is rarely encountered in practice.

(5) **Type E.** Absorption branch ascends slowly before achieving a stable state with p/p_0 approaching saturated vapor pressure, while desorption branch moves very slowly to the middle of p/p_0 zone, and then displays a sharp decline. For the pores with the characteristics of A-type lag ring, in which the parts are uneven in pore size result in the adsorption branch of this type, and the others equal in pore size result in the desorption branch. The adsorption isothermal lag ring of TiO_2 also shows characteristics of the E-ring.

The five kinds of lag rings reflect the typical pore structural information. The real catalytic materials are rarely similar, mostly as superposition-like of various lag rings, which reflects the complexity of the pore structure. This analysis should be used to identify the main types of pore structure.

The physical structural parameters have been systematically measured for a new ZA-5 $Fe_{1-x}O$-based catalyst as show in Table 7.10.

7.3 Nature and Structure of Surface

7.3.1 *Introduction*

Gas-solid catalytic reaction process on porous catalyst, from reactants to products, in general will experience seven steps including outside-diffusion, inside-diffusion, adsorption, surface-reaction, desorption, inside diffusion and outside

Table 7.10 Basic physical and chemical parameters for ZA-5 type catalyst

Entry	Parameters	Entry	Parameters
Chemical composition	$Fe_{1-x}O$	Pore volume (cm^3/g)	0.0855
Phase	Wüstite	Porosity (%)	36.93
Magnetism	Non-ferromagnetic	Average pore radius (nm)	12.29
Packed density (kg/L)	2.45 (size 2.2–3.3 mm)	Most probable distribution (nm)	5–20
Particle density (kg/L)	4.32	Voidage (%)	40 (size 3–13 mm)
True density (kg/L)	6.85	Twist-factor	3.28
Specific surface area (m^2/g)	13.92	Shape factor	0.487
Surface area of Fe (m^2/g)	3.955	α-Fe particle size (nm)	25.3
Base surface area (m^2/g)	4.596	α-Fe lattice constant (nm)	0.2866
Acid surface area (m^2/g)	5.366		

diffusion. Selecting the right reactor and operating conditions can fasten the rate of inside and outside diffusion. At this moment, the control step of catalytic process only correlates with the surface process. Thus there is a very close relationship between the adsorption and heterogeneous catalysis, which is the key step of catalytic process.

Physical adsorption is one of the important ways for the precise characterization of the surface structure of the catalyst.[36,37] In the chemisorption, the interactive force between adsorption molecule and the solid surface is of the chemical affinity, which makes the chemical bond form between the adsorbed molecule and the solid surface. In general, they form covalent bond or coordinated bond containing enough parts of ion-bond on the metal surface, and obviously ionic bond on the surface of semiconductor oxide as well as some compounds, so chemisorption has significant selectivity. By the use of the selectivity of chemisorption, the surface area of metal components and the number of active sites in the multi-component catalyst and supported catalyst can be measured. Thus a lot of useful information can be achieved.

Chemisorption of CO has widely been used in the measurement of surface area for Fe, Pt, Pd, Ni, Co and other metals. Combined with the infrared spectrum, the change of stretching vibratory frequency of adsorbed CO can be used to determine the electricity-loaded state of supported metal in high dispersion.

The selective chemisorption of H_2 and O_2 for the determination of supported metal surface area, combined with the determination of specific activity, gives to the concept "structural sensitive reaction" and "structural-non sensitive reaction" in the field of heterogeneous catalysis. Within a certain range (1–5 nm), changes in the size of metal particle may influence its surface structure. Experience has shown that the specific activity of some reactions changes with the surface structure of the metal. Such a reaction is called as structural sensitive reaction. Reaction in which specific activity does not change with the surface structure is called as structural non-sensitive reaction. Research results have shown that the non-structural sensitive reactions may become sensitive when the metal particles further become smaller in the highly dispersive state.

The method using selective chemisorption to determine the surface area of the active component is that a kind of stylet-molecule is adsorbed on the surface atoms of the active component, which can fully react with the atoms of active component and form a single chemisorption layer. The scattering state or surface area of the active component can be determined and calculated by the quantity of chemisorption. This method is often applied in the case of metal used as active component. At an early stage, H_2 was often used as adsorbate to measure the surface area for the highly dispered metal such as Pt, Pd, Os, Fe etc. at about 200°C. Later, H_2 was used to titrate to atoms of Pt, Ni, etc. on the surface under low temperatures and low pressures. It is clear that, for the measurement of different metals, one needs to choose the right stylet-molecule as adsorbate and conditions.

At present, due to the development of ultra-high vacuum technology and application in chemisorption with related tools, such as infrared spectroscopy, electron spectroscopy, low- and high-energy electron diffraction, auger spectroscopy and nuclear magnetic resonance, secondary ion mass spectrometry, field emission etc. In particular, combining a variety of modern physical-chemical ways with the conventional techniques, the investigation of the surface structure and molecular adsorption-state of chemisorption layer in the molecular level makes the understanding of the surface chemical of catalytic process progress markedly both in breadth and depth. In this section, we only introduce the general methods for the study of catalysts and catalytic processes from the viewpoint of chemisorption.

7.3.1.1 *Intensity and quantity of chemisorption*

From the perspective of chemisorption to catalyst research, it must first measure the intensity, adsorption capacity as well as adsorption state of chemisorption, and then understand the physical meaning of these parameters *via* investigation of the nature and the structure of the surface of catalysts.

(1) **Measurement of adsorption heat.** Quantitative measurement of adsorption heat can be used not only to distinguish physisorption from chemisorption, but also to estimate the type of chemical bonds and the adsorption intensity. The measurement of adsorption heat in different coverages can determine whether the surface is uniform.

Integral adsorption heat is the average value of adsorption heat of adsorbate on the surface covered by the adsorbate in equilibrium. It reflects the average value of heat produced by adsorption process in a long period of time.

The changes in differential adsorption heat with the surface coverage reflect the surface distribution of energy-state of adsorptive site and the intensity of adsorbate molecule bonding with the surface. The changes in adsorption heat of NH_3 with the surface coverage characterize the changes of the surface acid intensity for acid catalyst.

Finally, it should be pointed out that finding the relationship between adsorption heat and catalytic activity is difficult in the development process of catalyst due to various constraints. First, it is difficult to determine the adsorption heat, which is generally much more complex than the evaluation of catalytic activity. Second, since adsorption heat changes with the surface coverage, it is difficult to

determine at which coverage the adsorption heat is appropriate for measurement. Due to the absence of necessary experimental data, although it has been known that the initial adsorption heat has little to do with the catalytic activity, in the examples of hydrogenation of ethylene and ammonia synthesis, we have to adopt the initial adsorption heat for correlation. This shows that the study of the catalyst and catalytic reaction according to the adsorption heat has a certain limitation.

(2) **Adsorption capacity.** Adsorption capacity is defined as gaseous quantity adsorbed by unit weight of catalyst, and is often recorded as V_{STP}. It can determine the relationship between adsorption capacity and pressure (Isotherms) at fixed temperature or fixed pressure (Isobar), but usually isotherms are used, that is, the equilibrium relation between pressure and the adsorption capacity (isothermal equation).

Langmuir monolayer adsorption model can also be used to deal with chemisorption process due to its simplicity. However, in the Langmuir adsorption model, the hypothesis of the uniformity of solid surface is different from the actual surface. So it needs necessary amendments. In the chemisorption, it often occurs with the competitive and dissociative adsorption, and their adsorption isotherm equations can be obtained by Langmuir adsorption model, respectively.

Competitive adsorption isotherm equation is defined as:

$$\theta_i = \frac{K_i P_i}{1 + \sum_{i=1} K_i P_i}. \tag{7.69}$$

Dissociative adsorption isotherm equation is defined as:

$$\theta = \frac{\sqrt{KP}}{1 + \sqrt{KP}}, \tag{7.70}$$

where $\theta = V_{STP}/V_m$, V_{STP} means adsorption capacity, and V_m means monolayer saturation adsorption capacity.

Adsorption capacity on solid surface is a basic data, and accurate measurement of adsorption capacity is the basic skill for the study of adsorption. The methods used for the measurement of adsorption capacity include the capacity method, the weight method and the chromatography. The capacity method is often used in the research of chemisorption for most gases, that is, a certain amount of gas is introduced into an adsorption container with a certain volume in a static device, then according to the changes of gas pressure to detect the adsorption capacity on the surface of the solid adsorbent. Such a device is generally composed by the vacuum pump system, adsorbate container, measurement systems for pressure and volume.

7.3.1.2 *Adsorbed state of gas on surface of catalysts*

When relating the surface nature and surface structure of catalyst according to the adsorption capacity of solid surface, it is indispensable to understand the relationship between the probe-molecule and the metal elements on surface, including adsorption species and stoichiometry of the probe-molecule, both of which are closely related.

Chemisorption species generally refer to the chemical state, electronic structure and geometrical configuration of atoms or molecules which are chemisorbed on the

solid surface. The determination of chemisorption state and surface intermediate are of great significance for disclosing the catalysis and catalytic reaction mechanism. Hence, study on the chemisorption state has become an important subject for the research of catalysis. Infrared spectroscopy is a main tool for study of chemisorption state. The developments of modern experimental methods such as tempreture-programed desorption and electron-energy spectroscopy etc., and provides a new powerful tool for its study.

The common probe-molecules for chemisorption include H_2, N_2, NH_3, CO and O_2 etc. The chemisorption state of H_2, N_2, NH_3 has been introduced in Chapter 2. Here, we only introduce the chemisorption state of O_2 and CO.

(1) Chemisorption state of carbon monoxide. The adsorption of carbon monoxide on the surface of solid catalyst has been studied extensively. As early as in 1950s, Esschens *et al.* have concluded that there are two states of the CO chemisorption by infrared spectrum: One is linear structure, which is a single metal atom adsorptive site, that is, the carbon atom is adsorbed by a metal atom, with the wave number being at about 2,050 cm^{-1}; the other state is the bridge-like structure, which is double-metal atoms adsorptive site, that is, carbon atom is adsorbed by two adjacent metal atoms, with the wave number being at about 1,905 cm^{-1}.

The stretching vibration frequency of free CO molecule corresponds to 2,143 cm^{-1}. It decreases after chemisorption. Studies of Aüger spectrum and ESDA spectrum also show that when the CO was adsorbed on Pt (100) crystal surface, the negative surface potential was detected, which means that some metal electron transfer to the CO molecule.

Both the linear and bridge states can be generated on the surface at the same time. Their proportions are affected by the surface coverage: initial adsorption mainly is in bridge state, and then the linear state gradually increases along with the increase in coverage. In addition, it is also related with the support. For example, the linear structure on Al_2O_3 supported metal catalyst is more than SiO_2 supported metal catalyst. These two adsorption states have different activities for different reactions.

Murtterties *et al.*[38] have brought forward a so-called side-on adsorption state, in order to distinguish from the original two adsorption patterns as end-on adsorbed states. They believe the side-on adsorption state is a CO adsorbed flatly on metal atom of the surface. A research from Fudan University considered that the adsorption peak in 1969 cm^{-1} relates to the strong interaction between support and metal, the adsorbed CO can call as an iso-bridge adsorbed state.

(2) Adsorbed state of oxygen. Research on the adsorbed state of oxygen plays an important role in the reactive mechanism study of catalytic oxidation of hydrocarbon molecules and ammonia oxidation. In general, the adsorptive states of oxygen in the transition metal oxides and metal catalysts are the negative ion type, such as $O^{\bar{*}}$, $O_2^{\bar{*}}$, O_2^{2-} and O^{2-} etc. Of course, there are also molecular O_2, as well as unstable O_3^- etc.

The adsorptive state of radical $O^{\bar{*}}$ is very reactive. It is extremely easy to react with H_2, CO, C_2H_4, even if the temperature is very low on vanadium, molybdenum, tungsten and other metal oxides. For example, CO_2^- can be detected when it reacts with CO and CH_2–CH_2O^- by reacting with ethene. As $O^{\bar{*}}$ have great reactivity, it is generally agreed that the deep oxidation of hydrocarbons is mainly caused by it.

The adsorbed state of radical ion $O_2^{\bar{*}}$ is more stable than that of $O^{\bar{*}}$. It will be generated on the surface of zinc, tin, vanadium, titanium oxide, as well as decationed Y-zeolite etc.

Ion O_3^- can be produced by the following reaction: $O^- + O_2 \rightarrow O_3^-$. However, ion O_3^- is very unstable, and it is believed that it is only an activated intermediate-state in oxidative reactions.

A variety of adsorbed states of oxygen can be transformed according to the following equation.

$$O_2(g) \xrightarrow{e} [O_2^{\bar{*}}] \xrightarrow{e} 2[O^{\bar{*}}] \xrightarrow{2e} 2[O^{2-}] \text{ (The oxygen in crystal lattice)}$$

The chemisorptive state of oxygen significantly exceeds the single-layer saturated adsorption quantity for many metals. This shows that the absorbed oxygen can penetrate into the bulk-phase of catalyst. With isotopic tracer experiments, it can be proved that the lattice oxygen in metal oxide is also involved in the reactions.

The main research tool for the adsorbed state of negative oxygen ions is electron paramagnetic resonance (EPR).

7.3.1.3 *Chemisorption stoichiometry*

Chemisorption stoichiometry is defined as the ratio between the total number of surface metal atoms and the total number of chemisorbed molecules. The physical meaning of stoichiometry refers to a gas molecule's reactions with several (n) metal atoms. The value depends on the nature of the gas as well as the measured metal. The methods traditionally used by the catalytic community for measuring the number of total surface metal atoms per catalyst gram ($N_{Me,S}$) are based on chemisorption. In practice, the number of probe molecules that disappear from the gaseous phase in contact with the catalyst under the chosen experimental conditions (temperature and pressure) can be experimentally measured. Unfortunately nobody knows what the real fate is for the disappeared probe molecules although ultra high vacuum (UHV) adsorption studies on monocrystals can give some information on the geometrical aspects of the interaction with the metal surface. However, this can hardly be extrapolated to industrial catalysts. In practice, for the calculation of $N_{Me,S}$ from the experimental data (the chemisorbed STP gas volume per catalyst gram Vg) the following assumptions are made:

(i) The degree of coverage is one (very harsh assumption, the actual case could be much lower).
(ii) The chemisorption stoichiometry (ratio between metal atom and chemisorbed molecule, or atom in the case of dissociation) is arbitrarily taken as one in most cases, probably for the sake of simplicity.
(iii) All the disappeared probe molecules only interact with surface metal atoms (unfortunately spillover and subsurface chemisorption cannot always be neglected).

Therefore, it is especially noteworthy that calculation of the surface structure and nature by the chemisorption data of probe molecules, such as the total number of surface metal atoms, may produce prodigious errors, sometimes as high as 100%, which of course are transferred to related properties such as

Table 7.11 Experimental results of chemisorbed stoichiometry for some gases[39]

Adsorbate	Experimental conditions	Chemisorption stoichiometry
H_2	Static, 273 K	$H/Ru_s = 1$[40,41]
O_2	Pulse, 273 K	$O/Ru_s = 1.1$[41,42]
O_2	Pulse, 195 K	$O/Ru_s = 0.75$[40,43]
CO	Pulse, 273 K	$CO/Ru_s = 0.60$[42]

Table 7.12 Stoichiometric reference value of the gas adsorbed in a variety of metals[7]

		Operating conditions		
Metal	Gas	Temperature/°C	Pressure/torr	Chemisorbed stoichiometry
Cu	CO	20	10	1–2
Ag	O_2	200	10	2
Co	H_2	20	10	2
Ni	H_2	20	10	2
Ni	C_2H_4	0	100	2
Rh	CO	20	10	1–2
Pd	CO	20	10	>2
Pt	H_2	20	10	2
Pt	H_2	250	100	2
Pt	O_2	25	100	1–2

turnover frequency (TOF). However in some cases, since (i) + (ii) and (iii) give opposite errors, a fortuitous compensation may occur. In other words, a wrong choice of the probe molecule, giving the problems mentioned in (iii), may give an advantage.

Table 7.11 is the experimental results of stoichiometric number of chemisorption for some gases. Table 7.12 is the stoichiometric reference values of the gases adsorbed in a variety of metals.

In the following section, we take fused iron catalyst for ammonia synthesis as an example to introduce the idiographic applications of chemisorption in the study of catalyst.

7.3.2 *Physical and chemical adsorption experiment on iron catalyst*

The first use of chemisorption in the study of heterogeneous catalysis was introduced by Emmett[44] during the study of iron-based catalyst for ammonia synthesis which used the chemical adsorption of CO and CO_2 to measure the surface area of active Fe iron and promoters of K_2O and Al_2O_3. He obtained the following instructive revelation: Although content of promoters is very little, they cover most of the surface of the catalyst, which shows that the promoters tend to occupy the surface phase. Since then, many researchers[45−47] have used chemisorption to study the effects of various components in the traditional iron catalyst, as well as the relationship between the mutative trends of various component and changes in activity

in ammonia plant. Streltsov[48] also studied the effect of the content of FeO on the surface area of Fe_3O_4-based catalyst, which shows that the surface area of iron and the alkaline surface area are reduced by 3/5 and 3/4, respectively with the content of FeO increasing from 21% to 64%.

The authors[49] studied the relationship between the surface active site and its activity of ammonia synthesis using N_2 low-temperature physical adsorption combined with chemisorption of CO and CO_2.

The experimental samples used were fused iron catalyst, which contain promoters such as Al_2O_3, K_2O, CaO, SiO_2 and used the different iron oxides as precursors. First, samples were reduced for 96 h in pure hydrogen (99.9999%) at atmospheric pressure. The H_2 flow rate was $270\,ml \cdot min^{-1}$. Temperature-program steps were as follows: 450°C for 72 h, 475°C for 12 h and 500°C for 12 h with temperature ramp for all stages of $10\,ml \cdot min^{-1}$.

The physical adsorption of N_2 at low temperature and the chemisorption of CO, CO_2 were carried out on Coulter Omnisorp 100CX apparatus. Figure 7.13 is a typical physical adsorption isotherm for N_2.

The experimental steps of chemisorptions of CO and CO_2 are as follows: after a low-temperature physical adsorption of N_2, the sample, under the protection of N_2, was quickly transferred to the sample-pool for chemical adsorption, and was vacuumed up to 10^{-6} Torr. Then the system was pueged again with helium gas for 1 h and vacuumed up to 10^{-6} Torr followed by switching gas to CO (CO_2) to fill the system. After that, sample-pool was placed in liquid nitrogen (for CO) or dry-ice-alcohol solution (195.2 K) (for CO_2) for the measurement of the physical-chemical adsorption (total chemisorption) isotherms (upper-line). Then the physically adsorbed gas was removed, and once again the physical adsorption isotherm was determined (nether-line). The difference of the both monolayer adsorption capacity was regarded as chemical absorption capacity (Vg).[50] Figures 7.14 and 7.15 are typical chemical adsorption isotherm of CO_2 and CO, respectively.

After obtaining adsorption capacity and other data by chemical-physical adsorption experiments, the surface structure parameters of catalyst based on the related theories and experiences can be calculated.

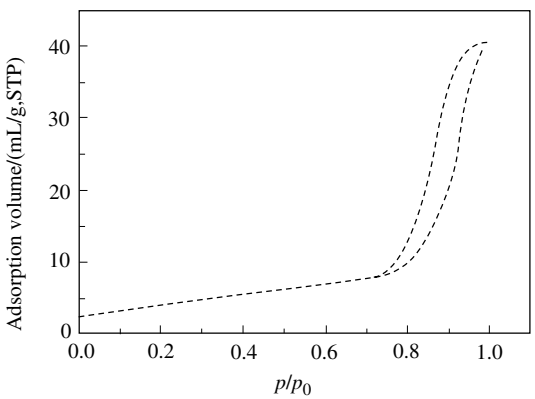


Fig. 7.13 Typical physical adsorption-desorption isotherms of N_2 (77.4 K) on iron-based catalyst

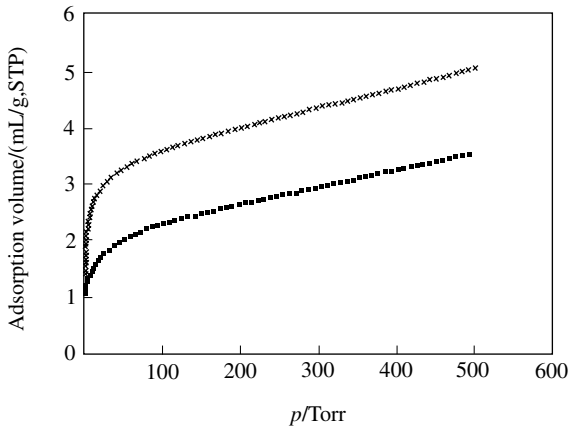


Fig. 7.14 Typical chemical adsorption isotherms of CO (77.4 K) on iron-based catalyst

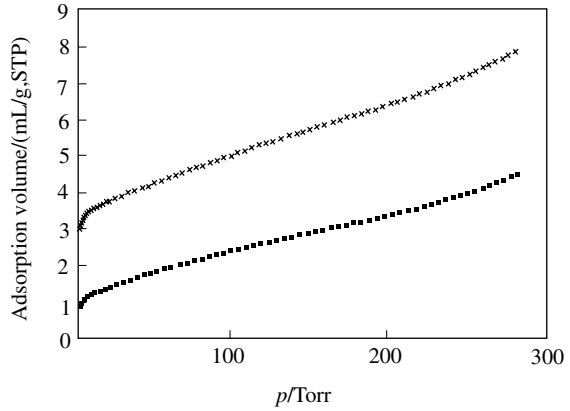


Fig. 7.15 Typical chemical adsorption isotherms of CO_2 (195.2 K) on iron-based catalyst

7.3.3 *Measuring the number of total surface metal atoms by chemisorption*

From the experimental value of chemical absorption capacity (V_g), the number of total surface metal atoms (N_S) can be calculated for the catalyst by the following equation:

$$N_S = \frac{V_g}{V_M} \times N_A \times n = 2.7 \times 10^{19} \cdot n \cdot V_g, \tag{7.71}$$

where V_g is the volume of chemisorption of gas, $\mathrm{cm}^3 \cdot \mathrm{g}_{\mathrm{cat}}^{-1}$; V_M is the molar volume of gas, $\mathrm{cm}^3 \cdot \mathrm{mol}^{-1}$; n is the average chemisorbed stoichiometry; and N_A is the Avogadro's number.

7.3.4 *Measuring surface area and acid-base of various component by chemisorption*

In the research and industrial practice of heterogeneous catalyst, measurement of the surface area of every component in multi-component catalyst is often required, but this problem is not easily solved. However, by the use of chemisorption method, measurement of the surface area of the metal components in a multi-component catalyst as well as supported catalyst can get a lot of useful information.

According to the number of total surface metal atoms on catalyst as shown in equation (7.71), the surface area S_m of active component can be calculated:

$$S_m = \frac{N_S}{C_m}, \tag{7.72}$$

where C_m is the atomic density of surface metal atom, atoms $\cdot$ m^{-2}. Common surface atom densities of metal are shown in Table 7.13.

In the iron catalyst, the surface area of the active phase α-Fe was measured by selective CO chemisorption at the temperature of liquid nitrogen (77.4 K). If the chemisorption stoichiometry of CO adsorbed for iron is one, and the surface atom density of iron ($C_{m,Fe}$) is 1.5406×10^{19}, thus the surface area (S_{Fe}) of α-Fe is:

$$S_{Fe} = \frac{V_{CO} N_A n}{22414 C_{m,Fe}}, \tag{7.73}$$

The basic surface areas of base metals and alkaline earth metal oxides represented by K_2O were measured by selective CO_2 chemisorption at the temperature of dry ice and alcohol (195.2 K). If the chemisorption stoichiometry of CO_2 adsorbed in K_2O is two, and the surface atom density of K ($C_{m,K}$) is 1.4136×10^{19}, thus the basic surface area S_K is:

$$S_K = \frac{V_{CO_2} N_A n}{22414 C_{m,K}}. \tag{7.74}$$

Alkali metals and alkaline earth metal oxides are commonly used as electron-type promoters in iron-melted catalyst. Experimental samples contain K_2O, CaO, and other basic oxides. Therefore, the surface area measured by the selective chemisorption of CO_2 at 195.2 K should be the total surface area of alkaline oxides in catalyst.

Table 7.13 Surface area and density of surface atom of some metals[51]

Metal	Relative atomic weight	Density ($g \cdot cm^{-3}$)	Surface area with 100% of dispersion/ ($m^2 \cdot g^{-1}$)	Density of surface atom on metal/ ($\times 10^{19}$ atom $\cdot$ m^{-2})
Pt	195.08	21.45	235	1.3138
Pd	106.42	12.0	432	1.3101
Rh	102.91	12.5	445	1.3152
Ir	192.22	22.4	239	1.3110
Ru	101.07	8.6	453	1.3155
Os	190.2	22.48	242	1.3085
Fe	55.85	7.86	700	1.5406
Co	58.93	8.89	654	1.5625
Ni	58.59	8.99	667	1.5386
K	39.09	0.87	1090	1.4136

Al_2O_3, SiO_2 (impurities), and other acidic or amphoteric oxides are the main structural promoters of iron-based catalyst. In the total surface area of catalyst after reduction, in addition to the surface area of basic oxides and metal iron, it should also include the surface occupied by acidic or amphoteric oxides. Subtracting the surface area of metal iron and basic oxides from the total surface area of catalyst results in the surface area of acidic and amphoteric oxides, also known as acid surface area (S_A), that is,

$$S_A = S_T - S_{Fe} - S_K, \tag{7.75}$$

where S_T is the total surface area of catalyst (BET).

The results from authors show that the total surface area is 13–14 $m^2\,g^{-1}$ after reduction for the $Fe_{1-x}O$-based catalyst, in which, the surface area of active iron is about 3.5–4.0 $m^2\,g^{-1}$, accounting for 27% to 32% of total surface area; alkaline surface area is of 3.7–6.5 $m^2\,g^{-1}$, and its surface coverage degree is of 33% to 35%; acid surface area is of 4.8–5.4 $m^2\,g^{-1}$, and acid coverage is of 37.6%–38.6%. It is shown that most of the surface is covered by a small amount of promoters. It is interesting to note in particular that, *via* the research on ammonia-synthesis catalyst using different iron oxides (Fe_3O_4, $Fe_{1-x}O$, and their mixtures) as precursors, we found that the surface of the fused iron catalyst existed in cooperation of acid center and alkali center, that is, the activity of fused iron catalyst has a close relationship with its surface S_A/S_K. The surface of $Fe_{1-x}O$-based catalyst has the best synergy between base and acid, and thus has the highest activity. The acid-base synergy on the surface of catalyst relates to the nature and composition of iron oxide precursor, while has no direct relationship with the absolute content of acidic and alkaline oxides.[52]

From the practical point of view, the selective chemisorption has been widely applied in the study of acidity of solid catalysts, whose surface acidity of the solid catalyst is usually measured by the adsorption of basic nitric compounds. Ammonia, pyridine, quinoline, trimethylamine, etc. are used for the measurement of solid surface acidity. Due to the adsorption isotherms relating to the distribution of adsorption heat on the uneven surface, the number of adsorption sites distributed according to the intensity of acid can be roughly estimated by the changes of adsorption isotherms of basic materials.

Using infrared spectroscopy to study the chemisorption of pyridine on the surface of solid acid can identify the proton acid and Lewis acid on the surface. It is based on the 1,540 cm^{-1} characteristic absorption band from the product of pyridine with proton acid in IR. Pyridine reacts with Lewis acid to form coordinated complex, which shows 1,455 cm^{-1} absorption band in IR. This method is often used in the qualitative identification of type of acid sites.

When the steams of alkaline compounds are used to measure the acidity of solid surface, the key problem encountered is that the selectivity of the alkaline molecules adsorbed on acidic-site is not always ideal. For example, when using NH_3 as a molecular probe, it is not only adsorbed on the acid-site, but also in other cations, so as to interfere with measurement results, which should be paid special attention in the study of cation exchange of molecular sieves.

Although the selective chemisorption provides data such as metal surface area and dispersion which cannot be obtained by other physical methods, and has been an important means for the research on supported metal catalysts, it is still very

difficult to obtain precise results. Selective chemisorption suffers some limitations in the measurement of active surface. First, although we can choose the conditions of single chemisorption as far as possible, we could not avoid the physical adsorption at low temperatures, leading to the occurrence of spillover phenomenon or other side reactions at high temperatures during chemisorption experiments. As the metal surface only accounts for a small portion of the total surface, if a small amount of hydrogen spillovers into the support from the metal surface, it will produce a significant error. In addition, the uncertainty of chemisorption stoichiometry also causes considerable error in the measurement results. Chemisorption stoichiometry is usually calculated from the single-layer chemisorption capacity of massive metal and BET surface area. It is also assumed that Chemisorption would be consistent with the high degree of decentralization state. In fact, this assumption is unreliable. For example, due to the different patterns of catalysts, the chemisorption stoichiometry of oxygen and surface Ni changes from 1–4. Taking the chemisorption stoichiometry as 1 and 4, the calculated surface area or dispersion has four times of difference. As a result, the application of this method deserves our close attention.

7.3.5 *Measurement of exposed fraction of surface metal atoms*

The ratio of the number of surface metal atoms to the total number of metal atoms in catalysts is defined as the exposed fraction of surface metal atoms, and also called as dispersion of metal (D). The methods traditionally used by the catalytic community for measuring the exposed fraction of surface metal atoms are based on chemisorption.

$$D = \frac{N_S}{(w_m/M)N_A} = \frac{nV_gM}{22.414w_m}, \tag{7.76}$$

where M is the relative atomic mass of metal and w_m is the mass fraction of the metal in catalyst.

The results of study on low-temperature N_2 adsorption, CO and CO_2 chemisorption show that for the ammonia synthesis catalyst with different iron oxides as precursors, with the total iron content ranging from 91% to 92% of reduced catalyst, only 0.54% to 0.73% of the iron atoms are exposed on the surface, and more than 99% of the iron atom are still confined in the inner of the catalyst or covered by promoters.[53] Only those iron atoms exposed on the surface will possibly have activity on ammonia synthesis reaction, so most of irons in fused iron catalyst do not work (equivalent to a support for electronic transmission). If more iron atoms are exposed to the surface of the catalyst, it is possible to further enhance the activity of fused iron catalyst.

The exposed fraction of potassium atoms is calculated to be 68.49%–94.33% by CO_2 chemisorption according to the content of K_2O and the chemisorption stoichiometry of two. Because the amount of adsorbed CO_2 includes that from K_2O, and from CaO and other basic oxides, and the chemisorption stoichiometry of CO_2 may deviate from two. As a result, using CO_2 chemisorption quantity to calculate the exposed fraction of potassium atom is not very accurate, but most of the basic oxides being exposed on the surface of catalyst are, as the sparks fly upward.

7.3.6 *Measurement of metal particle nanosize on the surface of catalyst*

Physical techniques and chemisorption method can be used to measure the metal particle nanosize on the surface of catalyst.

For physical techniques, transmission electron microscopy (TEM) seems to be the optimal technique for measuring the size of nanoparticles, as it allows us to look at them directly. However, its use is problematic. For example, the analysis is carried out on a microscopic amount of catalyst, and is hardly representative of the whole sample. Many observations must be made on each of several independently loaded samples in order to get reliable data, with the considerable expenditure of time that entails. Moreover, small or flat nanoparticles may be lost due to the insufficient contrast. However, a careful use of TEM is very valuable in some cases.

X-Ray Diffraction (XRD) techniques are more practical, but they also have some specific limitations. Briefly, when the metal nanoparticles are relatively large, approaching or exceeding 10 nm, each of them may consist of several nanodomains, so that the size measured by X-ray line broadening will be smaller than the real one. In such cases, HRTEM (High Resolution Transmission Electron Microscopy) analysis and SAXS (Small Angle X-ray Scattering) can be used to ensure the metal particle size is a very important property of supported metal catalysts. However, several other properties are equally or more important, such as the lattice disorder or work function. The regulation of such properties can be obtained by tuning a range of variables, some of which are interconnected, thus making it very difficult to change one at a time.

The choice of the support plays a crucial role, of course. I do not refer to the first-step choice (among carbon, alumina, silica and so on), as it is usually straightforward for a catalyst specialist, but to the very numerous commercial or home-made samples of each type of support.

For example, it is a general rule that, when the surface area of the support is high, small metal nanoparticles are usually obtained. However it is not easy to change the support surface area without affecting other properties, such as the chemical nature of the support surface. Something can be done for oxide supports, in that their surface area can be decreased by suitable, not too drastic, thermal treatments, provided that surface hydroxylation does not change too much. For active carbons this approach is precluded, as the decrease of surface area is connected with graphitization, which definitely alters the physicochemical properties of the material.

The chemical species present on the support surface interact, more or less, with the metal nanoparticles deposited thereon. This phenomenon is currently called as "metal-support interaction" (MSI) and is usually stronger when the metal particles are smaller. It regulates the mobility of metal atoms and clusters on the support surface. In practice, when a strong metal-support interaction (SMSI) occurs, smaller (and more resistant to sintering) metal nanoparticles are usually obtained.

For the support usually employed in industrial catalysis, the intensity of MSI decreases from alumina to silica to activated carbon. However the surface properties of activated carbons can be widely changed by proper oxidizing and reducing

treatments, thus allowing us to tune the metal particle nanosize and the resistance to sintering correct size measurement. On the other hand, when the metal particles are smaller than about 2 nm, they do not contribute to the diffraction "visible" lines, thus giving an overestimated particle nanosize. However, in most cases it is possible to determine, using a suitably tailored Rietveld analysis,[54] the content of undetectable metal nanoparticles, to which a reasonable average size can be assigned, for example on the basis of ASAXS data.[55] In this way, a surface average size of the whole population of metal particles can be calculated. Incidentally, it can be remarked that the widely used Scherrer equation, apart from the abovementioned problems, gives a volume average particle size, completely useless in catalysis (the difference from the correct surface average can be dramatic in the frequent cases of wide particle size distribution). In conclusion, XRD techniques, when used by qualified specialists, allow us to get reliable values of metal particle nanosize in the large majority of metal-support couples, while the use of TEM is being restricted to few cases.

For catalytic purposes, once the correct surface average metal particle nanosize d_{av} is known, it is convenient to calculate the number of total surface metal atoms per catalyst gram (N_S), given by the equation:

$$N_s = \frac{kC_m w_m}{\rho_m d_{av}}, \tag{7.77}$$

where k is a constant depending on metal particle shape and on the extent of contact with the support surface (usually $k = 5$)[56], C_m is the surface density of metal atoms, w_m is the metal weight fraction in the catalyst and ρ_m is the metal true density. In this way an easier connection with chemisorption data can be reached.

By the chemisorption data (V_g), the metal nanoparticle size of the catalyst surface can be calculated. First, from the experimental value of V_g, one can calculate the total number (N_S) of metal atoms on the surface as shown in Eq. (7.71), and assume that all disappeared probe molecules only interact with metal atoms on the surface (flooding and the chemisorption under surface had to be ignored).

Combining Eq. (7.71) and Eq. (7.77), we obtain

$$n = \frac{kC_m w_m}{2.7 \times 10^{19} V_g \rho_m d_{av}}, \tag{7.78}$$

which allows us to calculate the average chemisorption stoichiometric n from the experimental values of V_g (chemisorption) and d_{av} (XRD), while the other factors in (7.68) are known constants for any supported metals (in the most favorable case) or for any metal-support couple. Now N_S can be correctly determined from chemisorption measurements with equation (7.71). Of course the problems mentioned remain where all the disappeared probe molecules interact only with surface metal atoms (unfortunately spillover and subsurface chemisorption cannot always be neglected), but can be minimized through a careful choice of the probe molecule and of the experimental conditions. Spillover is mainly given by hydrogen, therefore, should not be chosen as a probe molecule. Subsurface chemisorption is mainly given by oxygen, but in most cases a careful choice of the chemisorption temperature allows us to avoid this problem.

The average nanoparticles size (d_{av}) of metal is obtained as:

$$d_{av} = \frac{kC_m w_m}{2.7 \times 10^{12} n \rho_m V_g}. \tag{7.79}$$

It should be noted that value V_g strongly depends on the experimental techniques used in measurement. The time-consuming, error-causing ways should be avoided (such as the surface titration method), and instead a much simpler way i.e. pulse technology could be used. When the measurement of chemisorption is carried out by the pulse technology at room temperature, the nature of the support does not relate to the fraction of the metal. Because it provides a more precise measurement for turnover frequency, this approach has opened up a new prospect for fundamental research.

7.3.7 *Turnover frequency and active site*

In more fundamental studies, the reaction rate should not refer to the mass of catalyst or metal, but to the active site. As the total number of the active sites is not known, it is common practice, as recently discussed by the author *et al.*[57] to substitute it with the total number of surface metal atoms, which can be correctly calculated by Eq. (7.71). The reaction rate expressed as the number of reacting molecules transformed per surface metal atom per second is often called as turnover frequency (TOF) and is expressed as sec^{-1}. TOF is currently used to draw fundamental conclusions about the intrinsic activity of metals and the mechanism of the reaction. Unfortunately, many TOF values have been so frequently affected by large errors in d_{av}, at least for supported metal catalysts, that they require a substantial revision. It is rather obvious that the number of active sites will always be lower than that of surface metal atoms, because either the latter one is not energetically equal in the reaction conditions or the active sites consist of nanoensembles of metal atoms (this point should be taken into account for any comparison with homogeneous or enzymatic catalysis). Hence, it is convenient to introduce the concept of real turnover frequency, given by the $\text{TOF}_\text{R} = \text{TOF}/\text{f}_\text{AS}$, where f_{AS} is the fraction of surface atoms working as active sites.

When f_{AS} does not depend on d_{av} the reaction is called "structure-insensitive" and the reaction rate is inversely proportional to d_{av}. In fact the reaction rate r_m (Eq. (7.26)), expressed as moles of reactant transformed per catalyst gram per second, is related to TOF_R by the equation:

$$r_m = \frac{kC_m w_m f_{AS} TOF_R}{N_A \rho_m d_{av}} \quad \text{or} \quad TOF_R = \frac{N_A \rho_m d_{av} r_m}{kC_m w_m f_{AS}}. \tag{7.80}$$

Therefore, when the reaction rate is plotted versus reciprocal d_{av}, for structural insensitive reactions a straight line is obtained, from whose slope the product $f_{AS} \times \text{TOF}_\text{R}$ can be calculated. Unfortunately there is presently no way to separate the two factors.

Accordingly, a wide range of experiments about the metal particle nanoradius depending on the reaction rate for evaluating the performance of the catalyst and the active site will bring some impetus. Needless to say, such experimentation absolutely

depends on the availability of accurate and reliable methods for the measurement of metal particle nanosize, as discussed in this section.

7.3.8 *Chemisorption: measure the rate and activation energy of adsorption*

The measurement of rates and activation energy of chemisorption is very important for catalytic mechanism and its applied research. It is clear that when the adsorption is the reaction determining step of catalytic reaction, the rate of adsorption process will determine the rate of the reaction and activity of catalysts. Therefore, activation energy and heat of adsorption can reflect the nature of the active site and distinguish the type of active site under certain conditions.

There are two major chemisorption patterns. One is non-activated chemisorption, which can happen at low temperatures. The adsorption rate is very fast, and does not require any activation energy. For example, H_2 can be quickly adsorbed in Ni, Pt and Pd at 77 K. Another pattern is activated chemisorption, which is referred as activated adsorption, which requires a higher temperature. It is characterized by the activation energy need, just as the real chemical reaction.

Studies on the adsorption kinetics have shown that the adsorption activation energy also increases with the increase of the surface coverage. As a result, the concept of adsorption activation energy as adsorption heat is referred to the given surface coverage, which is represented by the Eq. (7.81)

$$E_a = RT^2 \left(\frac{\partial lnk}{\partial T} \right)_\theta , \tag{7.81}$$

where E_a is the activation energy; k is the rate constant; and θ is the surface coverage.

The rate constant k can be calculated by the relationship between the amount and the time of adsorption, which have many types of expression. On the uniform surface, it can use Langmuir rate equation:

$$\frac{d\theta}{dt} = K_a p(1-\theta)e^{-E_a/RT} - K_d \theta e^{-E_d/RT}, \tag{7.82}$$

where $\frac{d\theta}{dt}$ is the adsorption rate; t is the time; T is the temperature; E_a, E_d are the activation energy of adsorption and desorption; K_a, K_d are the equilibrium constant of adsorption and desorption.

On the uneven surface, we usually use Elovich's rate equation:

$$\frac{dA}{dt} = a \cdot e^{-bA}, \tag{7.83}$$

where A — adsorption amount; a, b — constant.

The integral of the above equation is:

$$A = \left(\frac{2.3}{b} \right) \left[\lg ab + \lg \left(t + \frac{1}{ab} \right) \right]. \tag{7.84}$$

If the adsorption rate represented by Arrhenius equation, we get:

$$\frac{dA}{dt} = k_0 \cdot e^{-E_a/RT}. \tag{7.85}$$

To measure the adsorption rate $\left(\frac{dA}{dt}\right)_1$ and $\left(\frac{dA}{dt}\right)_2$ where both achieve the same adsorption capacity of A at temperature T_1 and T_2 respectively, then the adsorption activation energy E_a can be obtained as:

$$E_a = \frac{2.3RT_1T_2}{T_2 - T_1} \lg \frac{T_1}{T_2}. \tag{7.86}$$

It is clear that such a calculation is based on the assumption that the mechanism of adsorption will not change in the whole temperature range.

There exist a relation between the adsorption activation energy E_a, desorption activation energy E_d and adsorption heat Q_0, that is, $E_d - E_a = Q_0$. Therefore, study on the process of desorption also provides some message for the process of adsorption, that is, the TPD technology can be used to study desorption rate and obtain desorption activation energy.

7.4 Temperature Programmed Analysis Technology (TPAT)

The process of heterogeneous catalysis is extremely complex on the surface of catalyst, in which the catalyst and reaction molecule are the key players. In order to clarify a catalytic process, the first thing is to understand the properties, structure of catalyst, and the mechanism of the interaction between catalyst and reaction molecules. Molecules taking place in the catalytic reaction on the surface need to go through a lot of steps, in which the main two steps are adsorption and surface reaction. Therefore, it is necessary to deeply study the adsorption properties of catalyst (the structure of adsorption center, the state of energy distribution, the adsorption state of molecule on the adsorption center etc) and catalytic properties (the nature and structure of the active site of catalyst, and the reaction course of the molecule on its surface etc.) in order to clarify inbeing of catalysis and the mechanism of the interaction between catalyst and reaction molecule during catalytic reaction process. The best way to study these properties is to obtain the information in process of a catalytic reaction. However, it is difficult to fully achieve this purpose. *In situ* infrared spectroscopy (including Raman spectroscopy), dynamic analysis technology can be used effectively to study such process under working or close to the working conditions. In this section, a widespread application of Temperature Programmed Analytical Technology (TPAT) is introduced. For other dynamic analysis and *in situ* infrared spectroscopy technologies (including Raman spectroscopy), we refer the readers to other literatures.[58]

The following important information of desorption and reaction behaviors of the molecule on surface of catalysts can be obtained by TPAT:

① The type, density and energy distribution of surface adsorption center, and the bond energy and bond state of the adsorption molecules and the adsorption enters.
② The type, density and energy distribution of active center of catalyst, dynamic behavior and reaction mechanism of reaction molecules.
③ The interactions between active components and support, between active components and active components, between active components and promoters, between promoters and support.

④ Varieties of catalytic effect – concerted reaction effect, spillover effect, alloying effect, promoter effect and support effect.
⑤ Deactivation and regeneration of catalysts.

TPAT technologies include temperature programmed desorption (TPD), temperature programmed reduction (TPR), temperature programmed oxidation (TPO), temperature programmed sulfide (TPS), temperature programmed surface reaction (TPSR) and so on. TPD is the most extensively studied, widely applied and the most mature method. Hence, TPD will be focused in the following section.

7.4.1 *Temperature programmed desorption (TPD)*

The following phenomena may occur during the process of TPD: Molecules desorption from the surface, re-adsorption into the surface from gaseous; molecules diffusion from the surface to the subsurface, and diffusion from the subsurface to the surface; and molecules diffusion in the inner of pore.

The nature of adsorption site of catalyst surface has a direct impact on the molecular adsorption-desorption behaviors, and the interactions between the adsorbed molecules will also have some impact on the TPD performance.

(1) TPD of uniform surface. On an ideal uniform surface, the dynamics of the molecule desorption from the surface can be used as Eq. (7.88),

$$-\frac{d\theta}{dt} = k_d\theta^n - k_a(1-\theta)^n C_G \tag{7.87}$$

$$k_d = \nu \exp\left(-\frac{E_d}{RT}\right), \tag{7.88}$$

where θ is the surface coverage; k_a is the adsorption rate constant; k_d is the desorption rate constant; C_G is the concentration of gas; E_d is the desorption activation energy; v is the pre-exponential factor; n is the desorption series; T is the temperature, K; R is the molar gas constant; t is the time.

Equation (7.87) ignores the diffusion of molecule from the surface to the subsurface layer and molecule interaction.

Under desorption conditions with constant heating rate, we get:

$$T = T_0 + \beta t \quad \text{or} \quad dt = \frac{dT}{\beta}, \tag{7.89}$$

where β — heating rate, $\mathrm{K}\cdot\mathrm{min}^{-1}$.

Equation (7.87) is expressed as

$$\beta\frac{d\theta}{dT} = k_a(1-\theta)^n C_G - k_d\theta^n. \tag{7.90}$$

Further practical equation of TPD is obtained on basis of Eq. (7.91) by Amenomiya[59]:

$$\left(\frac{\beta V_S V_M(1-\theta m)^{n+1}}{F_C \nu n \theta_m^{n-1}}\right)\left(\frac{\Delta H_a}{RT_m^2}\right) = \exp\left(-\frac{\Delta H_a}{RT_m}\right), \tag{7.91}$$

where $\nu = k\exp\frac{\Delta S}{R}$ (hereinto ΔS indicates the adsorption entropy).

By taking logarithm on both sides,

$$2\lg T_m - \lg\beta = \left(\frac{\Delta H_a}{2.303R}\right)\left(\frac{1}{T_m}\right) + \lg\left(\frac{V_S V_M \Delta H_a (1-\theta_m)^{n+1}}{F_C R\nu n\theta_m^{n+1}}\right), \tag{7.92}$$

where T_m is the peak temperature in TPD spectrum; $-\Delta H_a$ is the adsorption enthalpy ($-\Delta \mathrm{H_a} = \mathrm{Q_a}$, i.e. adsorption heat); V_S is the volume of absorbent; V_M is the single layer saturated absorbent volume; F_C is the flow speed of support gas.

If there is no re-adsorption during desorption, TPD equation can be expressed as:

$$\frac{E_d}{RT_m^2} = \left(n\nu\frac{\theta_m^{n-1}}{\beta}\right)\exp\left(-\frac{E_d}{RT_m}\right). \tag{7.93}$$

By taking logarithm on both sides, we get:

$$2\lg T_m - \lg\beta = \left(\frac{E_d}{2.303R}\right)\left(\frac{1}{T_m}\right) + \lg\left(\frac{E_d}{\nu R n\theta_m^{n-1}}\right). \tag{7.94}$$

When $n = 1$,

$$2\lg T_m - \lg\beta = \left(\frac{E_d}{2.303R}\right)\left(\frac{1}{T_m}\right) + \lg\left(\frac{E_d}{\nu R}\right). \tag{7.95}$$

Equation (7.94) can be applied under the following conditions: Homogeneous surface, i.e. all adsorption sites are the same; no interaction between adsorbed molecules; without re-adsorption during desorption; and without new diffusion process after desorption. Equation (7.95) can be only applied to the first order desorption process.

How to eliminate the phenomena of re-adsorption? It can be seen from Eq. (7.91), if TPD process is accompanied by the readsorption, then T_m is related to F_c. If F_c increases, F_c and T_m have no correction from each other, that is, Eqs. (7.93) and (7.94) are obtained. Here, TPD turn into a simple process of desorption. Therefore, it can be determined by changing F_c based on whether the process of re-adsorption takes place or not, and can eliminate the occurrence of the phenomena of re-adsorption.

How to decide n to be 1 or 2? The results simulated according to desorption kinetics equation show that,[60] the desorption kinetics is primary ($n = 1$) when TPD pattern shows a dissymmetry, while the desorption kinetics is the secondary ($n = 2$) when TPD pattern shows a symmetrical. As a result, the value of n can be determined by the graphics.

How to measure the adsorption enthalpy? Experiments show that, parameter β will affect the peak temperature.[61] Corresponding T_m value can be obtained by changing β. Then according to the equation (7.92), plotting $2\mathrm{lg}T_\mathrm{m} - \mathrm{lg}_\beta$ *vs.* $1/T_\mathrm{m}$, the adsorption enthalpy ΔH_a is obtained from the slope of the straight line.

How to determine desorption kinetic parameters? By changing β. If re-adsorption does not occur and $n = 1$, according to equation (7.94), plotting $21\mathrm{g}T_m - \mathrm{lg}_\beta$ *vs.* $1/T_m$, then desorption activation energy E_d is obtained from the slope of the straight line. The value of pre-exponential factor v can be obtained by E_d and intercept of the straight line.

Because $\theta = V/V_M$ when re-adsorption does no occur, equation (7.87) may be rewritten as

$$\frac{1}{V_M}\left(\frac{dV}{dT}\right) = \nu\left(\frac{V}{V_M}\right)^n \exp\left(-\frac{E_d}{RT_m}\right). \tag{7.96}$$

Several group TPD spectrums can be measured with different T_m by changing β; its peak height h is direct proportion to desorption rate dV/dT. Plotting lgh vs. $1/T_m$, the slope of the straight line is E_d.

If $n = 1$, Eq. (7.96) becomes:

$$\frac{dV}{dT} = V\nu\exp\left(-\frac{E_d}{RT_m}\right). \tag{7.97}$$

If desorption rate $r_d = \frac{dV}{dT}$, then

$$\frac{r_d}{V} = \nu\exp\left(-\frac{E_d}{RT_m}\right). \tag{7.98}$$

When V is direct proportion to peak area A of TPD, then

$$\frac{h}{A} = \nu\exp\left(-\frac{E_d}{RT_m}\right). \tag{7.99}$$

Plotting $\lg(\frac{h}{A})$ *vs.* $\frac{1}{T_m}$, the activation energy of desorption E_d is obtained from the slope of the straight line. The value of v can be obtained by the intercept of the straight line.

(1) Graphics analysis.[62] At the top of peak h_m of TPD at temperature T_m, the slope of curve on the right side of T_m is for different peak height h_i and at the corresponding temperatures T_i and peak areas A_i (Fig. 7.16); plotting lg ($\mathrm{h_i/A_i}$) vs. $\mathrm{1/T_i}$, E_d and ν can be obtained.

Other solution of TPD curves can be found in literature.[62–64]

(2) TPD of non-uniform surface. In many cases, the energy distribution on the surface of a catalyst is non-uniform; or there are different adsorption sites or active sites. It is of great importance for the nature of the catalyst surface. TPD has played a major role in this area. During the process of TPD, if there are two or more peaks

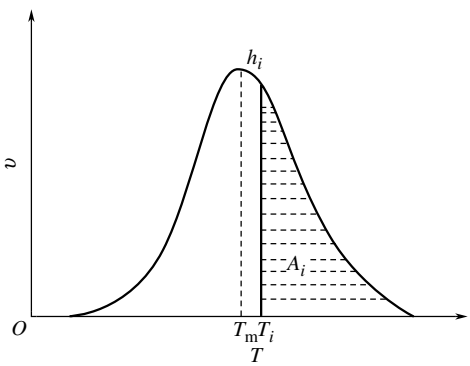


Fig. 7.16 TPD graphics analysis

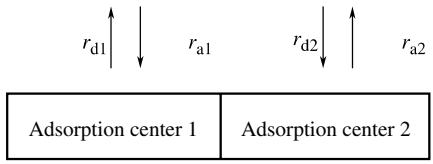


Fig. 7.17 Multi-center adsorption model

(separating peak or overlapping peak), generally speaking, this is a signal of non-uniform surface. There are exceptions, for example, the existence of transverse role between adsorption molecules or the forward-reverse direction diffusion of adsorbed molecules between the surface and sub-surface or the distribution of double pore size, which result in multi-peaks. As a result, TPD theory on non-uniform surface becomes very complicated.

The treatment with TPD process is relatively simple if peaks are caused by the different nature of the surfaces. If different TPD peaks are separated from each other, and each peak can be observed as a TPD peak with the same energy, then the TPD peaks can be dealt with uniform surface. As to the overlapping peaks, the first thing is to judge whether they are caused by a variety of adsorption sites or other reasons, and then find a theoretical model to solve this problem.

Multi-site adsorption model.[61] Upon the assumption that there are two sites with different natures, in the course of TPD, and they only take place adsorption and desorption, it can be imagined that following adsorption-desorption process can occur on the surface (Fig. 7.17). The adsorption rate equation for each adsorption site is:

$$\begin{aligned} r_{d1} &= k_{d1}\theta_1^n \\ r_{a1} &= k_a(1-\theta_1)^n C_G \\ r_{d2} &= k_{d2}\theta_2^n \\ r_{a2} &= k_a(1-\theta_2)^n C_G \end{aligned}$$

Desorption rate equation for each desorption site is:

$$\frac{d\theta_1}{dt} = k_a(1-\theta_1)^n C_G - k_{d1}\theta_1^n \tag{7.100}$$

$$\frac{d\theta_2}{dt} = k_a(1-\theta_2)^n C_G - k_{d2}\theta_2^n. \tag{7.101}$$

According to the material equilibrium, the molecule concentration in gaseous is:

$$C_G = -\frac{N_S}{F_C}\left(X_1\frac{d\theta_1}{dt} + X_2\frac{d\theta_2}{dt}\right), \tag{7.102}$$

where, N_s is the total number of adsorption center and X_1, X_2 are possessive fractions of center 1 and center 2 respectively.

From Eqs. (7.101) and (7.102) we can obtain the net desorption rate r'_d as:

$$r'_d = -\left(X_1\frac{d\theta_1}{dt} + X_2\frac{d\theta_2}{dt}\right). \tag{7.103}$$

During adsorption, the center (Center 2) of the stronger bond-energy is firstly occupied; during desorption, on the contrary, center (Center 1) of the weaker bond-energy is first desorbed. The boundary conditions of TPD course is $t = 0$, $T = T_0$, if $\theta_T^0 < \mathrm{X}_2$, namely $\theta_2^0 = \frac{\theta_T^0}{X_2}$ and $\theta_1^0 = 0$; if $\theta_T^0 > X_2$, namely $\theta_2^0 = 1$ and $\theta_1^0 = \frac{\theta_T^0 - X_2}{X_1}$.

It can be seen from Eqs. (7.100)–(7.103) that the law of multi-center TPD is not described through simulation TPD law in each site independently, especially when the energy difference between the two sites is not significant. If the energies of two sites are very different; in other words, then the TPD peak is separated from each other. At this time, when desorption occurs on one site with the temperature increasing, another site with high energy does not desorb. As a result, desorption process of two sites may be treated by the method of TPD on uniform surface, respectively.

According to the Eq. (7.103), by appropriately setting up some parameters,[61] two-site TPD curve can be simulated.[65,66]

(3) Flash desorption. Burning flash desorption method is putting a pure metal wire or film into a certain low-pressure gas (in general lower than 1.33×10^{-5} Pa). At this time, here, even if non-activated chemisorption, it takes several minutes to complete the monolayer adsorption. In principle, the absorption rate can be measured. After the adsorption is completed, the wire (film) is heated, and then the adsorbed gas is desorbed from the surface. Desorption rate and the probability of collisions on surface can be calculated by the change of pressure. If using an instant heating and rising temperature, different adsorbed species with different bond energy according to the bond energy by order from small to large is desorbed, and the desorption rate is determined by mass spectrometry. The relationship between desorption rate or pressure of p and T can be obtained. In this spectrum, each type of chemisorption shows a characteristic peak. For example, the maximum desorption rate of H_2 is at 85°C on Ni (111), 60°C on Ni (110) and 90°C on Ni (100) crystal surface.

If the heating rate is constant, desorption rate can be expressed as:

$$-\beta\left(\frac{dm}{dT}\right) = -\left(\frac{dm}{dt}\right) = \nu m^n \exp\left(\frac{E_d}{RT}\right), \tag{7.104}$$

where m is the number of absorbed atom;

From Eq. (7.104), it is clear that the desorption rate is very slow at low temperatures and at high temperatures. The desorption rate is also very slow due to the absorbed atomic number is small. So, at the middle of a particular temperature, and desorption rate shows a maximum value. Therefore, according to the rate equation, the characteristic desorption activation energy can be obtained for each of adsorbed species.

Thermal desorption spectra for CO on W (100) crystal surface with different coverages is shown as Fig. 7.18.[67] α-adsorbed type of CO is most easily desorbed, and the apparent activation energy is about 62.76 kJ/mol. Desorption at high temperatures include three states of β_1, β_2 and β_3 and their desorption activation energies are about 376.56 kJ/mol. Other methods show that α-adsorption is a linear absorption on W, while β-adsorption is very strong, as a result of C≡O bond becoming very weak.

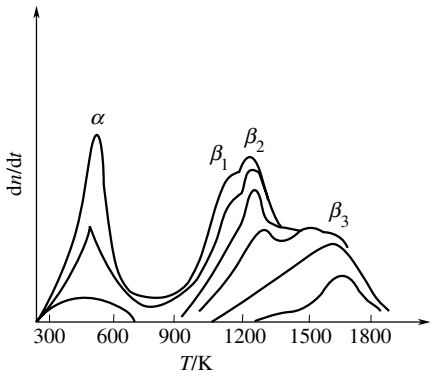


Fig. 7.18 Thermal desorption spectra of CO on W (100) with different coverage

Research on chemisorption on single-crystal surface by flash desorption technology provided a lot of important information. For example, H_2 on different crystal surface of Ni showed different characteristics desorption temperatures. On the different crystal surfaces of W metal, there are two chemisorbed states of H_2 of β and γ types. γ is considered to be adsorbed hydrogen molecule, and β is adsorbed hydrogen atom on different sites. These results are beneficial for the understanding of the different crystal surfaces with different catalytic activities.

TPD technique is a very effective way to study the metal catalyst.[68,69] In this method, we can derive series of important information such as the nature of the active center of metal catalyst, the dispersion of metal, alloying, metal-support interaction, the effect of structure and the effect of electronic ligand etc. TPD technique is widely used in the study the surface nature on metal catalyst (single crystal, polycrystalline and supported metal catalysts). The author used H_2-TPD and N_2-TPD to study the fused iron catalyst, and found that there are three adsorption states including non-activated, activated and strong chemisorption in the Fe_3O_4 based catalyst. The strong chemisorption does not have the activity for synthesis of ammonia. However, in $Fe_{1-x}O$-based catalysts there are only two adsorption states i.e., non-activated and activated.[70] N_2 desorption activation energy is consistent with ammonia synthesis reaction activation energy with dissociative adsorption of dinitrogen as the rate-determining step.[71] Someone used TPD combined with low-energy electron diffraction to study the change of energy of surface on Ni single crystal after cementite.[72] It was observed that there are three different adsorption centers of H_2 on the surface of Pt-black, corresponding to the $T_{m1} = -20°C$, $T_{m2} = 90°C$, $T_{m3} = 300°C$;[73] subsequently also found the other two adsorption center corresponding to the $T_{m4} = 400°C$, $T_{m5} = 500°C$.[74] In addition to Pt, other metals such as Ru, Ni, Co, Rh, Ir, Pd etc, showed a variety of adsorption centers,[74] and there are complex energy distributions on the metal surface. However, there are two areas on the whole. One is the high-energy area ($E_d > 83.68\,kJ \cdot mol^{-1}$) corresponding to low coverage, and H_2 adsorption in this region occurrs dissociative adsorption (that is, the desorption series (n) is 2). Another one is the low energy zone ($E_d < 83.68\,kJ \cdot mol^{-1}$) when the coverage is higher than 0.3, and in this area desorption series equals to one.

TPD technique can be used to study the surface nature of alloy catalyst effectively. The technique can also help in securing interaction information between metal components, and also information regarding the size of a metal particle and composition of the surface.

7.4.2 *Temperature programmed reduction (TPR)*

TPR technique is the reduction process under the conditions of a constant temperature rising rate. If the sample is reduced with the increasing of temperature, the concentration of hydrogen in the gas changes with temperature. The change of the concentration of hydrogen with temperature is recorded, and the curve of TPR is obtained.

A pure metal oxide has a specific reduction temperature which can be used to express as a qualitative indicator of the oxide. When two kinds of oxides are mixed, then they cannot produce chemical reactions with each other. Each metal oxide keeps its specific reduction temperature which can be expressed by T_m. On the other hand, if the two oxides create a solid-state chemical reaction before reduction, the characteristic reduction temperature of each oxide will be changed.

A variety of metal catalysts are commonly used with their oxides as precursors. The oxide may undergo chemical reaction with support, and reactions may take place between the components in multi-component metal catalysts during preparation process. Thus, TPR peaks of each oxide will be different from its pure oxides. In other words, the interaction between metal components and support or between metal components can be studied by TPR method for metal catalysts. The sensitivity is so high that it can detect the reduction reaction with consumption of only 10^{-8} mol H_2.

7.4.2.1 *TPR dynamic equation*

On the assumption that the reduction reaction is:

$$G + S \rightarrow P, \tag{7.105}$$

where G is the hydrogen gas; S is the solid oxide; and P is the product.

The variety of concentration of hydrogen gas is expressed as:

$$\Delta C_G = C_{G1} - C_{G2}, \tag{7.106}$$

where C_{G1}, C_{G2} refer to the concentration of hydrogen gas in the inlet and outlet.

Reaction rate is expressed as:

$$r = \frac{dC_G}{dt} = \frac{-ds}{dt} = k_r C_G^P S^q, \tag{7.107}$$

where S is the quantity of un-reacted solid.

According to Arrhenius equation,

$$k_r = \nu \exp\left(\frac{-E_r}{RT}\right), \tag{7.108}$$

where E_r is the activation energy of reduction reaction.

On the assumption that gases are "piston" flows without diffusion of the axial and radial, consumption volume of H_2 is expressed for ΔV at the unit dz zone of reactor:

$$\Delta V = f\frac{dx}{dz}, \tag{7.109}$$

where f is the feeding rate of H_2 at inlet; and dx is the conversion at dz.

In the low conversion rate, the composition of the gaseous phase is invariable in the whole reactor, so the reaction rate is:

$$r = fx, \tag{7.110}$$

where $f = F_c C_G, F_c$ is flow rate of mixture gas, and:

$$x = \frac{\Delta C_G}{C_G}. \tag{7.111}$$

So

$$f = F_C \Delta C_G. \tag{7.112}$$

Because the rising temperature rate is linear of $T = T_0 + \beta t$,

$$dt = \frac{dT}{\beta}. \tag{7.113}$$

From Eqs. (7.101), (1.108), (7.113), and if $p = q = 1$, we obtain:

$$r = \beta\left(\frac{-dc_G}{dT}\right) = \beta\left(\frac{-dS}{dT}\right) = \nu C_G S \exp\left(-\frac{E_r}{RT}\right). \tag{7.114}$$

Differential coefficient of equation (7.115) for T is:

$$\frac{dr}{dT} = \nu \exp\left(-\frac{E_r}{RT}\right)\left(C_G S\frac{E_r}{RT^2} + S\frac{dC_G}{dT} + C_G\frac{dS}{dT}\right). \tag{7.115}$$

When the reduction rate achieves maximum rate, we express it as:

$$\frac{dr}{dT} = 0, \tag{7.116}$$

and

$$\frac{dC_G}{dT} = 0 \tag{7.117}$$

From Eqs. (7.115), (7.116) and (7.117), we can obtain:

$$S_m\frac{E_r}{RT_m^2} + \frac{dS}{dT} = 0. \tag{7.118}$$

From Eqs. (7.114) and (7.118), we can obtain:

$$\frac{E_r}{RT^2} = \frac{\nu C_{Gm}\exp[-E_r/(RT_m)]}{\beta}. \tag{7.119}$$

Equation (7.119) is the rate equation of TPR. By taking logarithm on both sides, we get:

$$2\ln T_m - \ln\beta + \ln C_{Gm} = \frac{E_r}{RT_m} + \ln\left(\frac{E_r}{\nu R}\right), \tag{7.120}$$

where C_{Gm} is the concentration of H_2 at the reduction rate of maximum.

Plots $(2\ln T_m - \ln\beta)$ *vs.* $1/T_m$, the activation energy E_r can be obtained from the slop of the straight line. If C_{Gm} is regarded as the similar average concentration of H_2, the Pre-exponential factor can be obtained by the line intercept and E_r.

7.4.2.2 *Impact factors of TPR dynamic equation*

If the reaction of H_2 with solid is *via* one step and primary order, at temperature of T[75] the reduction rate can be expressed as:

$$\frac{d\alpha}{dT} = \frac{\nu \exp[-E_r/(RT)](1-\alpha)}{(\beta/C_0) + P\nu \exp[-E_r/(RT)](1-\alpha)}, \tag{7.121}$$

and

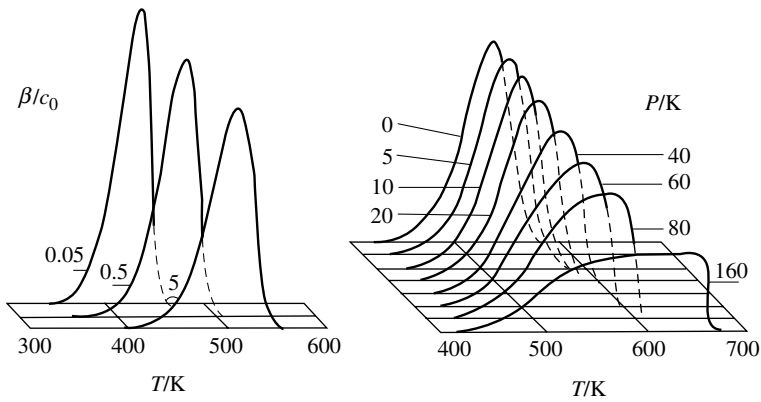
$$P = \frac{\beta S_0}{F_C C_0}, \tag{7.122}$$

where α is the the reduction degree of solid ($\alpha = S/S_0$); S_0 is the primary quantity of solid; C_0 is the the concentration of H_2 the inlet of reactor; β is the heating rate; F_C is the flow of mixture gas.

By this token, TPR curve is affected by β/C_0 and P. According to Eq. (7.121), fixing P and changing β/C_0, and fixing β/C_0 and changing P, TPR curves shown in Fig. 7.19 are obtained.

It is seen from Fig. 7.19 that, T_m is moved to high temperatures with increasing of β/c_0; here, the form of TPR curves do not change; when P is changed to significantly change the TPR curve, i.e., when $P \geq 600\,\mathrm{K}$, TPR curve is obviously distorted, and a platform peak occurs. When $\frac{d\alpha}{dt} = \frac{1}{P}$, H_2 is consumed wholly (*viz.*, $c = 0$), and TPR peak temperature has nothing to do with this platform. By the theoretical calculation, when consumption of H_2 is less than 2/3 in the process of reduction, the normal TPR curve can be guaranteed.

For a dynamic equation of reduction with two-step, similar as the one-step TPR process, it is also affected by P and β/c_0. With β/c_0 increasing, the separation of the reduction peaks becomes worse; and becomes better when P drops; but when P is large, the two peaks are overlapped into a peak. When β, F_c and c_0 are unchanged and the quantity of solid is increased, the two reduction peaks will overlap into a peak.



(a) P = 5K, β/c_0 effect (b) β/c_0=20 , P effect

Fig. 7.19 TPR simulation curve of one-step reduction process ($\mathbf{E = 100\,kJ \cdot mol^{-1}}$; $\mathbf{v = 6.0 \times 10^9\,min^{-1}}$)

7.4.2.3 *Measurement dispersion of metal catalyst by TPR*

TPR can be used to study processes of reduction reaction where the reactant is mainly oxide. In the process of reduction, the metal ions change from high valence to low, until elementary metal. The most commonly used reducing agent is H_2 and CO for reduction of catalysts. For the two-metal catalyst, the formation of alloy (or metal clusters) is critical. The content of metal component is generally very low in two metal-supported catalysts such as only several in a thousand. In this case, XRD cannot determine whether the clusters of metal or alloy are formed, and it is also difficult to affirm the results for XPS because of the sensitivity restriction. TPR has high sensitivity, and can accurately disclose. Therefore, the study of TPR technology not only obtains the results of reduction temperature, reduction degree and reduction reaction rate etc, but also determines the metal dispersion in metal catalyst. For example, the authors[76] have measured the dispersion of the copper in Cu — $ZnO/Al_2O_3/ZrO_2$ catalyst for methanol synthesis by TPR. Under the conditions of heating the sample from room temperature up to 493 K with the heating rate for 5K/min and keeping at that temperature for 2 h in the atmosphere of H_2, the catalyst (CuO) was reduced by H_2, and its consumption quantity of H_2 was recorded as curve *A* as shown in Fig. 7.20. Subsequently, the system was purged by pure Helium gas for 0.5 h, and the sample was cooled to 143 K in Helium atmosphere.[77] The mixed gas O_2–N_2 with O_2 of 10% was pulsed to make Cu exposured on surface was re-oxidized into CuO at 143 K. The pulse conditions were determined through trial and error in order to avoid oxidizing the inner layer of metal Cu. Finally, again H_2–TPR experiment was carried out under the same conditions, and the second consumption quantity of H_2 shown as curve *B* in Fig. 7.20 was recorded. The consumption quantity of hydrogen was determined by gas chromatography during the TPR reduction process. The dispersion of copper was calculated according to the consumption quantity of hydrogen obtained twice from H_2-TPR. From curve A in Fig. 7.20, the consumption amount of hydrogen is 101.512 ml/g_{cat} for fresh catalyst, curve B is 24.918 mL/g_{cat} for catalyst after the

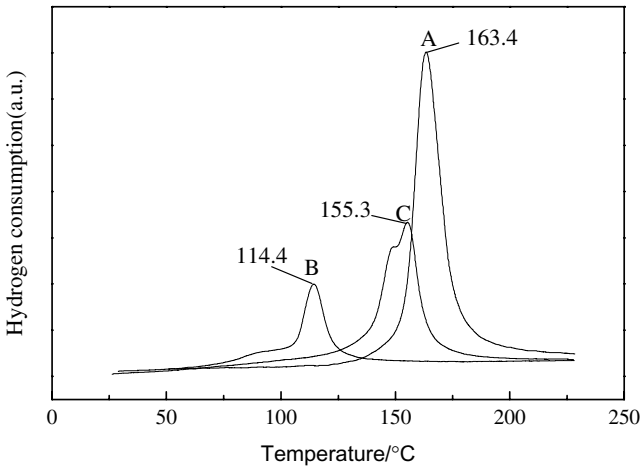


Fig. 7.20 H_2-TPR profiles of copper catalyst for methanol synthesis A: un-reduced catalyst; B: reduced catalyst; C: after 556 h reaction catalyst

oxidation and passivation at low temperature. Hereby, the dispersion of copper in the catalyst is 24.6%.

7.4.3 *Temperature programmed oxidation (TPO)*

The activity of catalyst will gradually decline during application, and one of the reasons is the aggradation of carbon on catalyst surface. TPO technology[78] is an effective way to study the formation mechanism of carbon deposition. For example, TPO is used to study Pt/Al_2O_3 catalyst for the mechanism of carbon deposition. TPO shows two peaks after the carbon deposition on surface of Pt/Al_2O_3, that is, $T_{o1} \approx 440°C$, $T_{o2} \approx 530°C$. After the catalyst was deposited with carbon, it was partially oxidized (that is, the oxidation of deposition carbon of the first peak at 440°C), where the adsorption amount of H_2 almost equals the fresh catalyst, and the activity of the catalyst is almost recovered. This proves that the carbon deposition takes place on surface of Pt metal, from which it can be inferred that the oxidation peak at high temperatures corresponds to the oxidation of carbon deposited on support.

7.4.4 *Temperature programmed sulfuration (TPS)*

The content of sulfur in oil products must be controlled at very low level (mass fraction of about 10×10^{-6}) for environmental protection and the follow-up process (such as the reforming process). In petroleum industry, in order to meet this requirement, hydrodesulfurization (HDS) process is mainly adopted with Mo [Mo–Co(Ni)]/Al_2O_3 as catalyst. The catalyst must be sulfurized to obtain activity for HDS. The nature of active phase on HDS catalyst has been a hot topic of research. The methods from the complex apparatus, such as EXAFS, XPS, and FTIR to the conventional XRD, TPR, and TPS[79] have been effectively adopted.

It is very important to study sulfuring process for HDS catalyst. TPS technologies are one of the most effective methods. The change of H_2S concentration recorded during sulfuring use H_2S–H_2 as sulfuring gas and with constant temperature heating rate to get TPS curve (the change of H_2S concentration with temperature). Research results show that MoO_3 sulfurized at low temperatures (T_s = 400–500 K) is the main active phase of the HDS catalyst, and MoO_3 sulfurized at high temperatures (T_s = 500–600 K) is the bulk phase, and its activity is very low.[79]

7.4.5 *Temperature programmed surface reaction (TPSR)*

The chemical reactions occurring on the surface of solid in the process of heating, such as decomposition reaction, reactions between surface and absorbed species and between absorbed species (for example, dehydrogenation, hydrogenolysis, aromatization etc), are the research objects of TPSR. The nature of the active site and the mechanism of surface reaction can be revealed.

TPSR method can be used to study the kinetics and mechanism of surface reaction. The reactants pre-adsorption on the surface takes place reaction during heating process, and the location and the peak shape of the TPSR peak (T_r) can be determined by the kinetic parameters.[80] Reaction on the surface is much more complex than the desorption process. TPSR kinetic equation can be obtained as

the same to TPD dynamic equation if a uniform surface and simple reaction with one order are assumed.

$$\frac{\beta E_r}{RT_r^2} = k_{0r} \exp\left(-\frac{E_r}{RT_r}\right). \tag{7.123}$$

Changing T_r can obtain the different values. Plotting $(2\lg T\mathrm{r} - \lg\beta)$ *vs.* $1/T_\mathrm{r}$, the activation energy E_r and the frequency factor k_{0r} can be obtained from the slope and intercept of straight line.

When TPSR was used to study the mechanism of dehydrogenation reaction of n-hexane on Pt/Al_2O_3 catalyst, the results showed that the reaction for n-hexane dehydrogenation cyclizating formation benzene may have different courses.[80]

7.5 Application of Thermal Analysis Technology in Catalyst Research

Thermal analysis is an experimental technology to study the changes of characters and states of substances as a function of temperature during the process of heating or cooling. As it is a method based on dynamic state, comparing with the static analysis, it shows more advantages such as fast, simple and continuous etc. Therefore it is a powerful tool of material research and is used widely in various fields.

Because the thermal analysis can track the changes of heat, mass and state in the process of preparation and reaction of catalyst, it achieves many applications, not only in the analysis of raw materials, but also in the analysis of process of preparation and usage of catalysts to provide valuable information.[1–4] The Thermal analysis has about 20 kinds of different technologies (Fig. 7.21), wherein thermogravimetric analysis (TG), derivatography analysis (DTA) and differential scanning calorimetry (DSC) etc are most widely used in catalyst study.

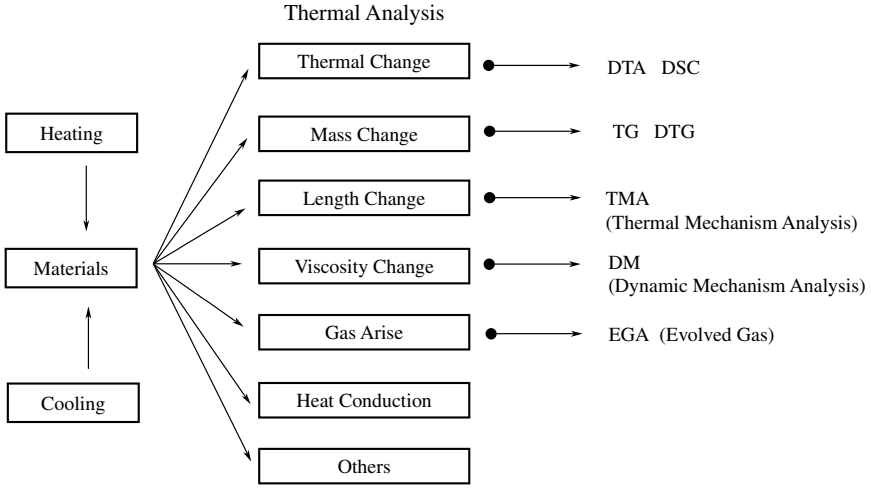


Fig. 7.21 Thermal analysis technologies

7.5.1 *Derivatography analysis (DTA) and its application*

The basic principle of derivatography analysis is measuring the temperature difference (ΔT) between sample and reference compound under the same heating and cooling conditions. In order to compare them easily, the thermal property of the reference compound is known which is rather stable in the process of heating and cooling. Two ends of thermocouple are inserted into sample and reference compound, respectively. During the process of heating and cooling in certain programs, if the sample undergoes change of heat at a specific temperature, its temperature will be different from the reference compound, and gives the signal of temperature difference, i.e. $\Delta T \neq 0$. If it is exothermic reaction, ΔT is positive and forms an exothermic peak, or by contrast, ΔT is negative and forms an endothermic peak. Typical DTA curve of ΔT changing as a function of temperature is shown in Fig. 7.22.

The selection of best preparation conditions of catalyst is very important to obtain an excellent performance of the catalyst. The process of calcination and activation is the key step to determine the structure of catalysts during preparation. Differential thermal analysis techniques can determine the specific conditions for various steps, such as the beginning and the end of the decomposition temperature and, suitable for calcining temperature etc.

DSC-MS (Mass Spectrometry) technology can be used in the preliminary selection of compositions of catalysts. For example, selection of automobile exhaust purification catalyst was studied by DuPont 900 thermal analyzer. The feed gas was C_3H_6 of 0.025%, CO of 1.0%, O_2 of 1.25%, water of 10% balanced by nitrogen. A series of CuO/Cr_2O_3 catalysts were measured by DSC in 20°C/min heating rate. It was found from DSC curve that there was an exothermic peak from a carbon monoxide shift into carbon dioxide. MS analysis showed that the height of the exothermic peak is direct proportion to amount of carbon dioxide generated, and therefore the results of preliminary selection for CuO/Cr_2O_3 catalysts can be obtained according to the height of the exothermic peak.

In organic chemistry reaction, the catalyst is often inactive due to carbon deposition on its surface. The regeneration of the catalysts often adopts the method of burning carbon. At this time, the choice of the temperature and duration of burning carbon is very important. It is not difficult to determine the appropriate conditions for burning carbon according to the exothermic peak of DTA curve.

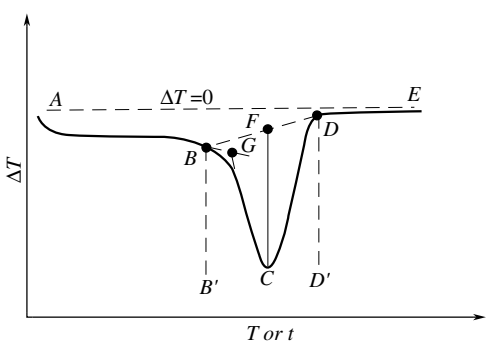


Fig. 7.22 Typical DTA curve

Using similar methods, when studying the thermal effects on the catalyst, such as water loss, released CO_2, NH_3, nitrogenous oxides etc, as well as thermal changes during the reduction by hydrogen gas and CO, can help to identify the appropriate conditions for these special reactions (decomposition, reduction, oxidation etc).

7.5.2 *Thermogravimetric analysis (TGA) and its application*

Thermogravimetry is mainly composed of thermal balance and heater. The principle of thermal balance and general balance is the same, except that the former can continuously weigh material and give relationship between change of weight with temperature in the case of heating, that is, the TG curve and the DTG curve of weight loss rate from differential TG curve. Computer-controlled heat balance has high sensitivity, and it can show changes in the weight of 0.001 mg. Therefore, it may be used to study the reactivity of compound such as oxides in the case of heating and different gases, and the heat stability usually in the air or inert atmosphere. TG technology can also be used to study the chemical valence changes of oxides to speculate on the change of the molecular formula from the perspective of the weight of compounds. The author used thermal balance technology in an atmosphere of hydrogen to study the chemical valence changes of iron in fused iron catalysts to determine the valence and composition of the active phase as well as the behavior of weight loss for different iron ferrite and oxides, to study the effect of additives on reduction properties. For example, the TG and DTG curve of A110-2, ZA-5 iron catalyst during reduction at hydrogen are shown in Fig. 7.23. It can be seen from Fig. 7.23 that there is a small flat peak in the left DTG curve of A110-2, which is the reduction peak of the FeO contained in Fe_3O_4-based catalyst, followed by a large peak which is the reduction peak of the Fe_3O_4 and the main component in Fe_3O_4-based catalyst. It indicates that A110-2 catalyst is composed of small amounts of FeO and large amonts of Fe_3O_4, while ZA-5 catalyst with $Fe_{1-x}O$ as precursor is composed of pure wüstite. According to the calculation of the oxygen losing weight on the TG curve, the A110-2 catalyst contains 11% FeO and 89% Fe_3O_4. The reduction temperature ranges of catalysts are determined by the started and ended temperatures of the weight loss. Reduction conditions should

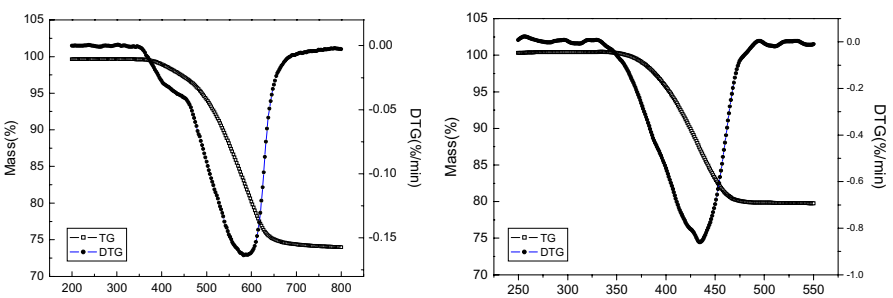


Fig. 7.23 TG-DTG curves of reduction for A110-2 and ZA-5 catalyst

Table 7.14 Relationships of reduction degrees with temperature for A110-2, ZA-5 catalyst

	Reduction degrees			Reduction degrees	
Temperature/°C	A110-2	ZA-5	Temperature/°C	A110-2	ZA-5
320	0.65	3.43	460	16.15	84.43
350	1.79	5.05	480	23.76	99.66
390	4.11	10.68	500	34.04	100
410	6.47	18.23	520	47.52	100
430	9.41	35.66	560	82.71	100
450	12.91	63.99	620	90.48	100

consider two aspects, first, the active component should be reduced completely as far as possible, and another one is to avoid the sintering of metal particles, both of them closely are related to the reduction temperature. Therefore, relationships of reduction degrees with temperature for A110-2, ZA-5 catalyst were studied by TG technology as shown in Table 7.14. The reduction degree is defined as the ratio of the actual loss amount of oxygen obtained from TG curves to oxygen content of the catalyst in theory. It is seen from the Table 7.14, the reduction temperature of ZA-5 is lower more 100°C than that of A110-2, that is, ZA-5 has been fully reduced at 480°C, while the reduction degree of A110-2 is only about 24%, and is not yet fully reduced until 620°C. This may be related to the fact that Fe_3O_4 may form a small number of compounds which such as $FeAl_2O_4$, $KFe_{11}O_{17}$ or solid solutions with promoters such as Al_2O_3, K_2O, CaO, etc., and such solid solution is more difficult to be reduced.

At present, thermogravimetric analysis has developed into a commonly used technology for the study of catalysts. With the extensive research, the method itself has improved continually. When the heat balance and reaction unit are linked together, it forms a so-called "ambi-thermogravimetric analysis technology," which can be used to track the weight change of the catalyst during the reaction process. Therefore, it can be used to study the reaction process in which the weight of catalyst may be changed with the extent of catalytic reaction, such as oxidation, reduction, activation, passivation, aggradation of coke, burning coke, poisoning and regeneration process etc. of catalysts. Among them, especially the aggradation and burning of coke is most widely used in the study, which has become a conventional means for the evaluation of the performance of the carbon deposition (Fig. 7.24).

7.6 Characterization of the Microstructure and Properties of Catalysts

The chemical constitution and structural factors of solid catalyst such as phase composition, surface distribution, crystal texture, crystallite dimensions, specific surface, pore structure and etc., are the dominant factors of the catalytic properties. The progresses in the modern physical methods and equipments have paved the way for the study of catalysts.

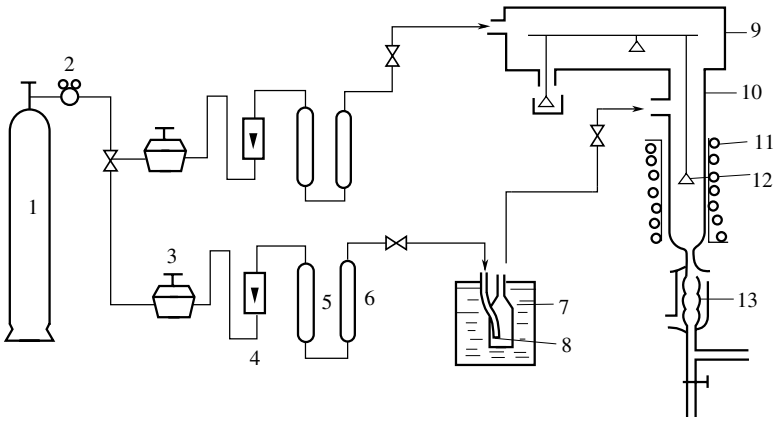


Fig. 7.24 TG study carbon deposition reaction process diagram[1]
1-Gas cylinder; 2-Reductor; 3-Steady flow valve; 4-Flow meter; 5-Dryer; 6-Deoxidant; 7-Water bath; 8-Carburetor; 9-Balance-box; 10-Quartz tube; 11-Furnace; 12-Basket; 13-Condenser.

This section mainly introduces the X-ray diffraction technique (XRD) applied in the catalysis research. Several other commonly used modern physic methods are simply introduced with their basic principles.

7.6.1 *Application of XRD in the study of catalysis*

The aim of XRD in the catalyst is to study the characters of structure of crystals, and reveal the relationship between the characters of structure and the catalytic reaction. It is necessary for researchers to possess the basic knowledge of crystallogphy.

Crystal is a matter constituted by atoms (ions, molecules or atom clusters) ranked periodically in three-dimensional space, otherwise it is called amorphous matter. In fact, there is no strict limit between crystal and amorphous one, because the difference between amorphous and crystal can be considered as the repetitive times of periodicity—from less to more causing quantitative change to qualitative change in the process, but once the formation the crystal with internal structure ranked in rules, it displays a series of different characteristics unlike that of amorphous matters. Solid crystals possess regular polyhedral shape, symmetry of a crystal shape, with the anisotropy for electricity, heat, light, and constant melting point and so on.

When atoms, molecular radicals stack into a solid, the performance of the crystal is closely related to the stacking types (structure), and the relationship between them is one of research topic in material science, especially in the exploration of new materials. For this purpose, researchers have investigated and developed variety of instruments and methods for structure analysis. Most of the solid material stacked by atomic and molecular groups in the three-dimensional space has characteristics of short-range or long-range order, and this can result in the unique structure of the corresponding diffraction pattern under the monochromatic X-ray or neutron (interaction between X-ray and extranuelear electron and between neutron and nucleus) radiation. Since Laue discovered diffraction phenomenon in

1912, XRD and neutron diffraction have been the most effective tool in exploring the rank of atomic, molecular group in three-dimensional space on solid material. XRD becomes an indispensable tool in the research of structure of solid material because of its intact theory. In particular, with the use of modern high-performance computer, it is even more surprising with its effectiveness and speed in material research.

It is well known that XRD image usually is a reflection of structural characteristics of matters. Researchers generally use powder diffraction pattern to understand the structure of materials. Currently, the XRD is widely used in laboratories for the identification of material phase, the nature of which is a structural analysis. XRD was first used to establish the diffraction image of all materials, or alternatively, the image can be compared with the standard substance. The principle is identical with single crystal diffraction, but the latter is specifically designed to explore the crystal structure of the new materials. By contrast, multi-crystal XRD is much more widely used than the single crystal diffraction in the study of materials.

X-ray structure analysis is the most powerful tool to reveal the structure of atoms in crystal. The application of XRD can obtain many useful structural information of catalyst. The kind of matter, state, crystal type, lattice parameters and size of crystallite on catalysts can be measured according to the diffraction of the direction in space, intensity and width, and sometime the average surface area and pore size and distribution of particle size can also be measured accessorily.

According to multi-crystal XRD theory, the diffraction intensity y_{ci} of a point in any X-ray diffraction image, can be expressed by the equation:[81]

$$y_{ci} = s \sum_k L_k |F_k|^2 \phi(2\theta_i - 2\theta_k) P_k A S_r E + y_{bi}, \tag{7.124}$$

where S is the scale factor; k is the Miller index hkl of Prague reflection; L_K is the comprehensive factor of Lorentz polarization and multiplicity; ϕ is the peek type functions decided by characteristics of sample and diffraction geometric; P_K is the preferred orientation function; A is the absorption factor; S_r is the absorption correction factor caused by sample surface roughness; E is the extinction factor; y_{bi} is the background of intensity of point i; F_K is the structural factor of Bragg reflect of K.

According to Eq. (7.124), many structural information can be extracted from the diffraction image, such as:[82]

① Location and types of atoms in crystal cell, also called stack type.
② Size and type of crystal cell (parameters of crystallogphy).
③ Structural information of matters.
④ Characteristics of micro-structure, particle size and lattice distortion.
⑤ Phase abundance in multiphase system.
⑥ Information of short-range in order of amorphous composition.

7.6.1.1 *Quantitative analysis of phase composition*

A substance with different chemical compositions and structures is called different phases. Chemical composition difference can be resulted from phase. With the

same chemical composition and different inner structure, it is also called as different phases. For example, α-Fe_2O_3, β-Fe_2O_3 and γ-Fe_2O_3 are the three different phases whose chemical compositions are the same, but their inner structures and performances are different.

Since the 1980s, with wide applications of the highly automated X-ray spectrometer, scientists have used X-ray spectrometry to perform quantitative analysis of phase. This analysis principle is based on the relationship between phase content and diffraction intensity, and the method is simple and fast. Its accuracy can also meet the requirements if its component is not too complex. There are more than 20 quantitative methods such as internal standards, external standards, nil standards, adiabatic methods and theoretical calculations etc. Generally speaking, the more mature internal standard method requires a lot of time to draw the standard curve, and the curve can only apply to one matter, so this method has certain restrictions in quantitative analysis. In 1974, F. H. Chung proposed a "skeleton washing method", also called as K-value method, which greatly simplified the X-ray quantitative analysis method, and has been widely used in various research fields.

Standard K value method is essentially the internal standard method, but with a difference that K value method does not require drawing the standard curve and it is very suitable of a large number of samples for analysis. When determining the content of one phase (a) in mixture contained N phases, it can be added a new known standard phase (s) to the sample which is not present in the sample, making a complex sample containing $N + 1$ phases. If the intensity of strongest diffraction line of phase (a) is I_a, the intensity of the standard material (s) is I_s, based on quantitative analysis of the basic equation,[83] we can obtain:

$$\frac{I_a}{I_s} = \frac{K_a}{K_s} \times \frac{V_a}{V_s} = \frac{K_a}{K_s} \times \frac{(W/\rho)_a}{(W/\rho)_s} = \frac{K_a \rho_s}{K_s \rho_a} \times \frac{W_a}{W_s} \tag{7.125}$$

$$W_a = W w_a, \quad W_s = W w_s \tag{7.126}$$

$$\frac{I_a}{I_s} = \frac{K_a}{K_s} \times \frac{\rho_s}{\rho_a} \times \frac{w_a}{w_s} = K_s^a \times \frac{w_a}{w_s}, \tag{7.127}$$

where I_a, I_s are the intensity of strongest X-ray diffraction for phase a and s; K_a, K_s are the diffraction constant of phase a and s; W is the total mass of sample; w_a, w_s are the relative mass content of phase a and s; K_s^a is the intensity of reference value of phase a and s.

K_s^a is unrelated to the content of standard material and the diffraction conditions. The existence of the other phases only act as the role of thinner, or the absorption, but the impact of absorbing can be eliminated by using the ratio of two-phase diffraction intensity. Thus K_s^a only relates with the crystal structure and the selected anode target. When selecting the same radiation, K_s^a only relates with phase (a) and phase (s), and therefore, K_s^a is a characteristic constant of phase (a) and phase (s).

When K_s^a and w_s are known, as long as I_a/I_s is measured, w_a can be obtained by Eq. (7.127). If the sum of mass fraction of added standard material and various phase in the sample equals to one, the sum of the mass fraction of various phase in the sample equals to $(1 - w_s)$, and therefore mass fraction of various phase in the sample can be obtained by equation of $w'_a = w_a/(1 - w_s)$.

If mass ratio of phase (a) and phase (s) is constant in the preparation of the binary mixture, for example, if $w_a/w_s = 1$, then $I_a/I_s = K_s^a$, here I_a/I_s is also the K_s^a value needed. In addition, powder diffraction card index records hundreds of K_s^a values of commonly used substances known as the reference intensity value that equals to the intensity ratio of two phases' strongest line in diffraction pattern made by some matter and synthetic corundum ($\alpha-Al_2O_3$) by 1:1 mixture. Because $\alpha-Al_2O_3$ has the advantages such as easy access to high-purity, good chemical stability, low price and no preferred orientation effect, it was selected as the standard matter. When measuring the relative content of sample of two phases, it can make use of reference intensity values to process quantitative analysis, because they have the following relationships:

$$\frac{I_1}{I_2} = \frac{K_s^1}{K_s^2} \times \frac{w_1}{w_2}, \quad \text{i.e.} \quad \frac{w_1}{w_2} = \frac{I_1/K_s^1}{I_2/K_s^2}. \tag{7.128}$$

It is well known that with the known K_s^1 and K_s^2, and measured I_1/I_2 from the diffraction pattern, the mass ratio of the two phases can be obtained. Selection of reference intensity values to perform quantitative analysis can solve the actual work of the difficulty in accessing to pure material, and it is not limited to the analysis of binary mixture.

Authors[84] use K-value method to investigate the disproportionation reaction of FeO. According to Greenwood,[85] when wüstite generates the disproportionation reaction, it first makes iron-rich wüstite close to stoichiometry $Fe_{1-y}O$ and Fe_3O_4 at temperatures above 227°C:

$$Fe_{1-x}O = [(4x-1)/(4y-1)]Fe_{1-y}O + [(y-x)/(4y-1)]Fe_3O_4 \tag{7.129}$$

Then, wüstite iron-rich $Fe_{1-y}O$ further disproportionates to generate Fe and Fe_3O_4:

$$Fe_{1-y}O = [(1-4y)/4]Fe + 1/4Fe_3O_4. \tag{7.130}$$

The first step of the reaction is very fast, while element iron is generated during the second step.

Figure 7.25 is the XRD of MnO doped $Fe_{1-x}O$ sample ($x = 0.059$) before and after the sample is treated for 60 h under vacuum and at 400°C. It can be found that only the single-phase of $Fe_{1-x}O$ exists in the sample before treatment and there are three-phase of Fe_3O_4, Fe, $Fe_{1-y}O$ existing together after treatment, and this shows

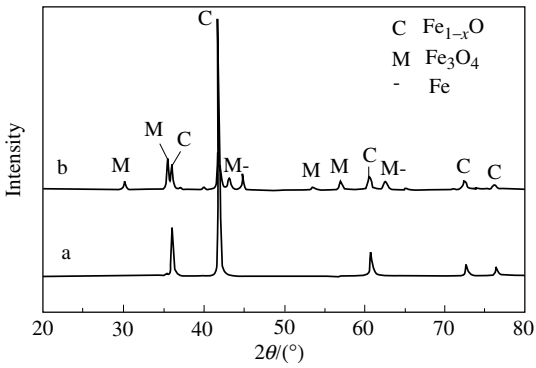


Fig. 7.25 XRD of $Fe_{1-x}O$ sample before (a) and after (b) the heat treatment

that sample undergoes disproportionation reaction during the heat treatment process. The strongest diffraction peaks of Fe_3O_4, $Fe_{1-y}O$, Fe are shown in Fig. 7.25 with peak value of $2\theta = 35.4°$, $41.9°$, $44.67°$ respectively, and the diffraction intensity of which are expressed by integral area (S).

According to Eq. (7.128), the mass ratio of three phases is:

$$w_{Fe_{1-y}O} : w_{Fe_3O_4} : w_{Fe} = \frac{S_{Fe_{1-y}O}}{K_s^{Fe_{1-y}O}} : \frac{S_{Fe_3O_4}}{K_s^{Fe_3O_4}} : \frac{S_{Fe}}{K_s^{Fe}}. \tag{7.131}$$

Then the molar ratio of each phase can be thus obtained:

$$x_{Fe_{1-y}O} : x_{Fe_3O_4} : x_{Fe} = \frac{w_{Fe_{1-y}O}}{71.85} : \frac{w_{Fe_3O_4}}{231.55} : \frac{w_{Fe}}{55.85}. \tag{7.132}$$

Then the disproportionation ratio of the Wüstite can be calculated with equation below:

$$N\% = \frac{3x_{Fe_3O_4} + x_{Fe}}{(1-y)x_{Fe_{1-y}O} + 3x_{Fe_3O_4 + x_{Fe}}} \times 100. \tag{7.133}$$

Before disproportionation defect concentration x in $Fe_{1-x}O$ of sample could be calculated by the measured ratio of Fe^{2+}/Fe^{3+}, but y in $Fe_{1-y}O$ in the sample after the disproportion is difficult to be measured because the first step of the reaction is very fast. Thereby, the Wüstite iron-rich $Fe_{1-y}O$ after first step of disproportionation is close to stoichiometry resulting in the assumption of $y \approx 0$ in the calculation.

Looking up from powder diffraction card index, the reference intensity of the three matters is $K_s^{FeO} = 4.8$, $K_s^{Fe_3O_4} = 4.9$, $K_s^{Fe} = 10.8$ respectively and the strongest diffraction peak area (that is, the intensity of diffraction), of each phase after disproportionation, and the disproportionation ratio of $Fe_{1-x}O$ can be calculated, as shown in Table 7.15.

Assuming wüstite disproportionation process is in accordance with equation (7.131), then the molar ratio (calculated) of elementary iron and Fe_3O_4 after disproportionation can be calculated based on the defect concentration $x = 0.059$ before disproportionation. The ratio between the two (experimental) can also be calculated by K value method from the result of XRD after disproportionation, as shown in Table 7.15.

Table 7.15 Disproportionation ratio of $Fe_{1-x}O$ doped MnO

Strongest diffraction peak area/wt%				n(Fe)/n(Fe_3O_4)	
$Fe_{1-y}O$	Fe	Fe_3O_4	Disproportionation ratio/%	Calculated	Experimental data
515(60.59)	96(11.29)	239(28.12)	34.63	0.7622	0.7553

It can be seen from Table 7.15 that the experimental value is smaller than the calculated one, and the result of which may be due to the incompleteness of the second step of reaction, i.e. incomplete disproportionation of iron-rich wüstite.

7.6.1.2 *Determination of lattice constant*

The smallest unit that can be repeated in crystal is called as cell. Cell constant of a pure crystal material under normal conditions is a fixed value that means the parallelepiped side length is a certain value. But when there are other substances co-existed, solid solution is produced, and isomorphously substituted, and defect exists. The lattice constant may change, which may affect the catalytic activity and selectivity.

Lattice constant can be calculated by the diffraction direction of X-ray diffraction; here, the accuracy can reach 0.1%.

Lattice parameter of solid powder sample is not only affected by its element constitution, but also the outside conditions such as temperature, and pressure. At the same time, the change of crystal lattice parameter of series samples is often very small, which can only be found in a more precise determination. The key issue is to accurately measure the 2θ value of diffraction line, and calculate the lattice parameter by 2θ value. In order to reduce systematic errors in experiments, one should strictly control the temperature and facture of flat plate sample, and use single-color, step-scan method of data collection. At the same time, when measuring the crystal lattice parameter of the cubic crystal system of Fe_3O_4, systematic errors can be eliminated by extrapolation, Cohen least square methods.

When calculating the lattice parameter, the diffraction peak data $K_{\alpha 1}$ and $K_{\alpha 2}$ of the sample should be separated first, and then peak values can be calculated by parabola function fitting method.[86] As the accuracy of the determination of lattice parameters is determined by the precision of the angle measured, so in order to enhance the accuracy when reading value of angles and to avoid errors caused by human factors, as shown in Fig. 7.26, in the vicinity of peak $2\theta_M$, 10 to 15 data of diffraction intensity are collected, with parabola equation fitting near the peak intensity distribution curve by the least square method to obtain the best 2θ peak value. With known lattice parameters of the silica powder and sample together, the test results are obtained under the same condition to establish curve correction.

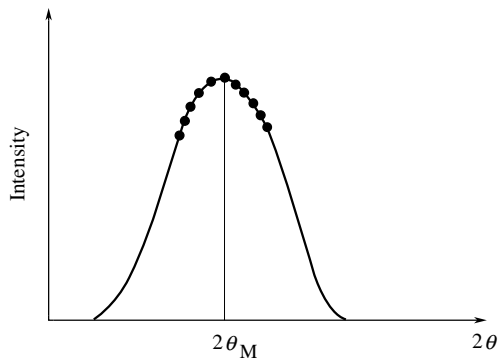


Fig. 7.26 Diffraction peaks $2\theta_M$ by parabola fitting method

Finally, through the 2θ value of the *hkl* diffraction peaks obtained from the above-mentioned treatment, the lattice parameter can be obtained by Cohen least squares methods.

In research of materials in series, even without the 2θ correction, the order of lattice parameters of each sample will not reverse.

7.6.1.3 *Determination of average nanoparticle size by line width method*

Most of the solid catalyst is the porous solid composed of tiny particles. Surface area provided by active substance per unit mass is related to the nanoparticle size, and hence the determination of nanoparticle size is of great practical significance for the preparation and application of supported Ru, Pt, Pd, etc. precious metal catalyst particularly.

Due to the difference in the type, preparation method of material, and operating conditions, the nanoparticle size distribution of catalyst can vary in a great range such as from one nanometer (nm) to tens of nm, or even to hundreds of nm, and that of active metal catalyst is in the range of 1–10 nm.

A particle of less than 200 nm can widen the diffraction peak, and the finer the nanoparticle, the wider the peak is, and therefore the method is also called as the line width method. This method can be calculated by using the following equation:

$$d_{av} = \frac{0.89\lambda}{B\cos\theta}, \tag{7.134}$$

where λ is the wavelength, nm; θ is the diffraction angle; B is the half-peak width (the width in half height of maximum diffraction peak), rad; d_{av} is the average nanoparticle size, nm.

The smaller the average nanoparticle size of metal, the greater is the dispersion of metal. Nanoparticle size is one of the factors that affect catalyst activity. When metal is highly decentralized, it provides more active surface, so it often has higher catalytic activity. During the application of catalysts, sintering and cohesion of metal particle can result in the decrease of activity. For a long time, people have taken great efforts to explore the issue of how to get high dispersion and avoid metal particle growing up. The average nanoparticle size can reflect the active metal dispersion, and provide useful information for judgment.

The wider the diffraction peak (the finer particle), the higher is the activity of iron catalyst in ammonia synthesis. Generally, the nanoparticle size of iron catalyst is about 20–30 nm.

7.6.1.4 *Extended X-ray absorption fine structure (EXAFS) analysis*

Some X-ray beams will be absorbed when drilling through a material where the absorption coefficient varies along with the energy of X-photon. When the photon energy is large enough to excite the inner electron of atom, there will be an absorption break. Precise determination of absorption coefficient near the edge of the absorption can be used to calculate the coordination state of absorbed atoms around. This method can measure crystal, and also amorphous material. Due to

the far enough apart of different atomic absorption edge, their EXAFS spectrum will not overlap from each other. In principle, the coordination structure of every atom in sample can be measured in one experiment. EXAFS method requires high-intensity X-ray sources, generally with high-intensity X-ray spectrum with broad frequency produced by synchrotron radiation. For common requirement, rotating target X-ray sources can be satisfied.

Many information of surface structure of catalyst can be obtained by surface EXAFS method. It can be seen from the following examples that this information of the structure is often related to a more sophisticated molecular or atomic scale features.

For example, when studying the osmium, iridium, platinum metal clusters dispersed on silica and alumina by EXAFS, comparing the EXAFS results of the metal clusters after reduction and the corresponding metal dollops, the following conclusions can be drawn: The bond length between the nearest neighboring atoms in clusters is 0.002 nm which is shorter than that in metal piece; the nearest neighbor atomic coordination number of atoms in metals cluster is 7 to 10, while the corresponding metal piece is 12, and such a low coordination number indicates that metal is highly dispersed on the catalyst; heat disturbance of atoms in metal cluster is 1–1.4 times larger than that in metal piece, reflecting the metal cluster has more surface atoms.

EXAFS method is also applied in the study of metal structure of bimetallic catalyst composed of Ru (Os) — Copper — silica support. Analysis of the metal coordination number proved that the structure characteristics of the bimetallic catalyst are Ru (Os) cluster was covered by Cu, the structure of which are associated with its chemisorption and catalytic properties.

7.6.1.5 *Multicrystalline structure determination*

Exact XRD is able to measure the structure of multicrystalline, and provide additional information of some catalyst because it has a ladder scanning devices and high-power X-ray tubes. The structure parameters of the coordinates location and possessive ratio of atoms, and bond length and bond angle can be calculated according to the diffraction pattern, integral intensity measured by advanced X-ray instrument and conceive structure model by least squares amendment. In the study of catalyst, the most prominent achievements are the study on the structure of the molecular sieve. As the molecules of the reactants in the catalytic reaction take place within the channel of the molecular sieve crystals, and thus the arrangement of the molecules in crystal, the shape of the channel and the location of the active center are the decisive factors of activity of molecular sieve catalysts. The Exact XRD method can determine atomic location in skeleton, the location as well as possessive ratio of cation outside in skeleton of molecular sieve, and calculate pore shape and size of molecular sieves. In the past 30 years, the structures of the all the molecular sieves have been measured and described, and the possible structures of the molecular sieves are predicted based on the principles of geometry crystallography. Scholars also carefully studied the affect of the different preparation techniques and treatments conditions on the location of the cations, pore shape, and the results from these change of structural stability, activity and selectivity. For example, some scholars determined the changes of the location of the cation

in rare earth Y-zeolite at different calcination conditions, and found that the rare earth ion is mainly exchanged to go into large cages and it is much more difficult to go into small cages during exchange. However, after calcinations, the rare earth ions can enter into small cages and replace the sodium ion from small cages to large cages. This explains the necessity of processes with the twice exchanges and once calcination in theory.

Some scholars determined the structural parameters of 5A molecular sieve before and after treatment with steam at 380°C, and found cation Ca^{2+} (Na^{+}) in outside the skeleton was moved into the α-cage by 0.02 nm along the diagonal direction of crystal after water vapor heat treatment. The effective spherical volume of the pore is 0.691 nm^3 and 0.641 nm^3, and effective diameter of octahedron ring is 0.434 nm and 0.382 nm in molecular sieve before and after treatment calculated according to the coordinates and atomic radius of oxygen atoms. These data indicate that the effective volumn of α-cage and pore size of octahedral ring of CaA zeolite is reduced by steam treatment at high-temperature, and affected its properties of absorption and diffusion, which explains why the 5A molecular sieve is not water-resistant in structure.

7.6.1.6 *Structure analysis by Rietveld fitting*

In multicrystal diffraction, the diffraction of many small crystals in the three-dimensional space are compressed into one-dimensional, and lose the independence of all diffraction *hkl*, where the overlapping of the symmetry or the unsymmetry of diffraction peak obscures the profile of distribution curve of *hkl* diffraction intensity. So the abundant structural information contained in the powder diffraction pattern cannot be extracted, so for a long time the powder diffraction could only be used as the identification of phases.

In 1967, Rietveld[88] proposed least squares fitting structure amending for all-powder diffraction pattern in the powder neutron diffraction analysis of the structure using computer. In 1974, Malmros[89] and Young[90] introduced it into X-ray powder diffraction analysis of the structure, and with the widespread use of computers, the method has been developed rapidly and used widely.

The outline of Rietveld analysis of the structure is to compare the digital intensity y_{i} of a powder diffraction pattern obtained by experiment to intensity y_{ci} of calculation by a model, and the difference between the two models leads to the excursion amendatory value of structure parameters by the least squares method, and by adding it to the corresponding model structure parameters, the difference between y_{i} and y_{ci} achieves the minimum value.

$$S_y = \sum_i w_i (y_i - y_{ci})^2. \tag{7.135}$$

The use of the least squares method first need to establish a normal equation, including the differential of all the calculation intensity of y_{ci} to each adjustable parameter, and then solve the corresponding formal matrix inversion. The element of the formal matrix M_{jk} can be calculated by the following equation:

$$M_{jk} = -\sum_i 2w_i \left[(y_i - y_{ci}) \frac{\partial^2 y_{ci}}{\partial x_j \partial x_k} - \left(\frac{\partial y_{ci}}{\partial x_j} \right) \left(\frac{\partial y_{ci}}{\partial x_k} \right) \right], \tag{7.136}$$

where x_{j} and x_{k} are a set of adjustable parameters.

Table 7.16 Crystallography parameters of Fe_3O_4[61]

Type	Atom	Wyck	x	y	z
Fe_1	Fe	8a	0	0	0
Fe_2	Fe	16d	5/8	5/8	5/8
O	O	32e	3/8	3/8	3/8

Rietveld structural analysis of multicrystalline X-ray is based on the intensity value and position of diffraction *hkl*. Small changes in the structure are reflected in the intensity, so it demands precise experiment and cannot use general conventional method.

When Rietveld analysis is used to amend the structure of chromium-doped iron oxide samples, the structural parameters of pure γ-Fe_2O_3 is used as initial parameters. γ-Fe_2O_3 has a spinel structure of Fe_3O_4 with iron ions defect, and Fe_3O_4 has the space group Fd-3m, lattice constants $\alpha = 0.8333\,\text{nm}$, $Z = 8$. The parameters of atomic coordinates are listed in Table 7.16.

In the crystal cell, there are 32 oxygen atoms located in the 43m, half of Fe^{3+} in the interspace of tetrahedron with 8a43m and the other half Fe^{3+} and 8 of Fe^{2+} in the interspace of octahedron with 16d3m. Software of Rietveld analysis is Rietica.[91] In determining the parameters of oxygen, electron-cloud density determination is used after taking off the contribution of metal atoms on scattering.

Among structural analysis, in the quantitative analysis or diffraction peak-type analysis, the data of diffraction intensity are collected by ladder scanning. For example, using Rigaku D/max-3B multicrystal X-ray diffractometer, CuKα radiation, power of $40\,\text{kV} \times 30\,\text{mA}$, K_β radiation is removed by graphite monochromator, where the band width is 0.02° (2θ), with a stay time on each ladder of 10–30 s. Cell parameters of samples are obtained by the least square method, using standard silicon powder with SRM640 ($\alpha = 0.54309\,\text{nm}$) as internal standard. The 311, 440, 444, 800 diffractions are selected as diffraction lines. Internal standard for the determination of the relative abundance of amorphous phase in sample is α-Fe_2O_3 annealed at 900°C for 5 h, and the mass ratio between the sample and α-Fe_2O_3 is 1:1. The results are used in determination of the content of amorphous phase and analysis of Fe_3O_4 metastable structure as follows.

(1) Determination of the content of amorphous phase by Rietveld analysis[61]

Quantitative analysis of phase in the multi-phase system has always been a problem. Although the XRD is the most studied technique in the past as quantitative analysis of phase, but because multicrystalline XRD has problems of bulk effect of different X-ray absorption factors, the peak-overlap and changes in the intensity of diffraction *hkl* is caused by difference of fine structure which cannot be solved by traditional method. Thus, the results are always unsatisfied and considered to be unreliable. Rietveld analysis has completely solved the problem. The basic equation is:

$$W_p = \frac{S_p(ZMV)_P}{\sum S_i(ZMV)_i}, \tag{7.137}$$

where W_P is the relative mass content of p-phase in n-phase mixture; S is the Rietveld scale factor; Z is the number of molecule in cell; M is the molecular weight in cell; V is the cell volume.

If an internal standard with mass fraction of W_S is added to the powder mixture, then the absolute mass fraction of p-component in the mixture are:

$$W_P = \frac{W_n S_P (ZMV)_P}{S_n (ZMV)_n}. \tag{7.138}$$

When the total mass fraction of each phase is not equal to one, the mass fraction of amorphous phase in the sample can be estimated.

Rietveld multi-phase quantitative analysis is also called as model method, and can solve X-ray quantitative problem in the multi-phase system. This method has the following advantages: It is free of internal standards; it is free of the standard sample; there is no need to separate peaks; and finally, it overcomes the effect of the structure. With the scale factors of S_α and S_γ of reference sample α-Fe_2O_3 and experimental sample γ-Fe_2O_3 obtained by multi-phase Rietveld analysis, the relative abundance of amorphous phase in sample can be calculated by the following equation.[92]

$$W_{\gamma\alpha} = 1 - \frac{W_\alpha [S_\gamma (ZMV)_\gamma]}{W_S [S_\alpha (ZMV)_\alpha]}, \tag{7.139}$$

where $W_{\gamma\alpha}$ is the relative abundance of amorphous phase; W_α is the relative mass fraction of α-Fe_2O_3 in the mixture of the sample and reference sample; W_S is the relative mass fraction of sample in the mixture of the sample and reference sample.

(2) Rietveld analysis of metastable structure of Fe_3O_4

① Metastable structure of $Fe_3O_4 \cdot Fe_3O_4$ reduced from α-Fe_2O_3 and γ-Fe_2O_3 is different in structure, due to the transition process of their phase being different during reducing process. The process of α-Fe_2O_3 into Fe_3O_4 involves the significant restructure of the crystal structure, and the sub-lattice of oxygen ions transfer from the *hcp* into *fcc* and sub-lattice of iron ions from a single octahedral coordination into tetrahedral coordination and octahedral coordination, both of which are moved substantially. Such a transfer of phase belongs to the restructure of phase-change, in addition, to the need of high-energy, and stable Fe_3O_4 crystals can be obtained. γ-Fe_2O_3 is a metastable structure of trivalent iron ions, and has a similar *fcc* dense accumulation of sub-lattice of oxygen ions with Fe_3O_4, but the number and distribution of iron atom in octahedral coordination have some differences, the process of change of γ-Fe_2O_3 into Fe_3O_4 causes the iron atoms to diffuse into the octahedral location and reduce the vacancy. This process belongs to the partial regular-replacement of transfer phase. This phase-change is easy to occur and needs less activation energy, so the metastable structure of the precursor has been easily inherited during the process of reduction, and the Fe_3O_4 obtained has larger parameters of oxygen, smaller of lattice parameters, and has the remnant vacancy in B site. Low-intensity spectrum of B site in Mössbauer spectrum belongs to the transition state, or the intermediate phase during the γ-Fe_2O_3 change to normal Fe_3O_4. The metastable structure of γ-Fe_2O_3 has been inherited. Under industrial conditions, as long as the temperature does not exceed 400°C, such a structure state could exist for a long time, but high temperatures such as 600°C will change it into the normal stable structure.[61]

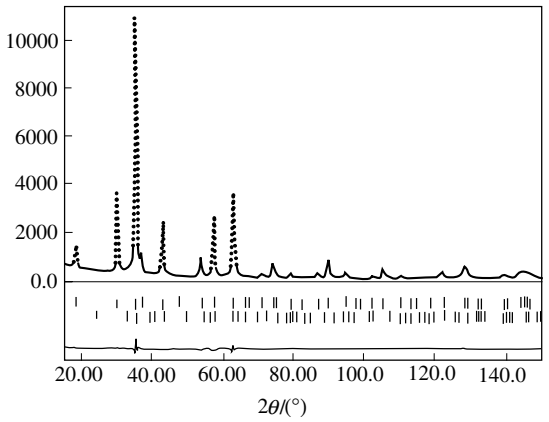


Fig. 7.27 Rietveld fitting curve of Fe_3O_4 reduced from γ-Fe_2O_3 (Dot line for the observation curve, solid line for the calculated curve, below curves is the difference value, a short vertical strokes are positions of Bragg reflections)

Table 7.17 Rietveld analysis results for Fe_3O_4[61]

Sample parameters		Fe_3O_4 derived from γ-Fe_2O_3	Fe_3O_4 derived from α-Fe_2O_3	Fe_3O_4 obtained after heating at 600°C for 5 h
Oxygen parameters (u)		0.3806	0.3780	0.3779
Bond length/nm	d_{A-O}	0.1897	0.1860	0.1858
	d_{B-O}	0.2050	0.2073	0.2073
	Fe Fe (8a)	2.78	3.11	3.13
Average electron valence of Fe (16d)		2.68	2.52	2.52
Lattice parameters (a)/nm		0.8388	0.8391	0.8389
Correction factor	R_{wp}	4.50	5.03	4.06
	R_p	3.22	3.82	4.05
	S	1.81	2.01	1.61

Figure 7.27 is the Rietveld structure amendatory fitting curve of Fe_3O_4 reduced from γ-Fe_2O_3.[61] As seen from fitting curve, the experimental observation and the calculation are very similar.

Table 7.17 is the structural parameter of different samples after Rietveld structure amendment. The parameters of oxygen (u) indicates the distortion degree of sub-lattice of oxygen ions in spinel structure, the product (ua) with lattice parameter (a) equals to the distance from the cation plane in sub-lattice of tetrahedral (001) to anion sub-lattice plane in the nearest neighbor (001). In ideally close accumulation of face-centered cubic crystal, oxygen parameters are $3/8 = 0.375$. Electron valence of iron atom in tetrahedral and octahedral can be calculated by valence-bond formula,[93] i.e. $S = (R/R_0)^{-N}$, where the R_0 is the unit bond length, and N is a constant ($R_0 = 0.201$ nm, $N = 5.3$ for Fe^{3+}), while R is the bond length between iron atoms and coordinate oxygen atoms, and S is the intensity of the bond at the bond length of R, and S_0 is the ideal intensity of the bond at the bond length of R_0.

It can be seen from Table 7.17 that Fe_3O_4 reduced from the different crystal structures of Fe_2O_3 has different parameters of oxygen. Oxygen parameters in Fe_3O_4 reduced from γ-Fe_2O_3 is larger than that reduced from α-Fe_2O_3, but after high temperature treatment, oxygen parameters are the same with that from α-Fe_2O_3. Oxygen parameters of Fe_3O_4 reduced from α-Fe_2O_3 are the same with that reported from normal Fe_3O_4 with value of 0.3780 (1).[94] This shows that the crystal structures of Fe_2O_3 affected the extent of the close accumulation of the sub-lattice of oxygen ions in obtained Fe_3O_4.

It also can be seen from Table 7.17 that the electron valence of iron atom with different coordination by bond-valence calculation method is different. Electron valence of iron atom in Fe_3O_4 reduced from α-Fe_2O_3 is very close to the theoretical value 2.5 and 3.0 of Fe_3O_4; however, the electron valence of iron atom in Fe_3O_4 reduced from γ-Fe_2O_3 deviates from normal values, although the values change into the normal electron valence in Fe_3O_4 after heat treatment at 600°C.

Microstructure distortion of Fe_3O_4. To determine lattice distortion, first a widened curve of apparatus is measured by using a good crystal without intrinsic widening. Usually samples need pretreatment, so as to achieve a certain size and to eliminate stress. For example, GR-class KCl powder after 500°C annealing for 48 h can be used as sample without intrinsic widening. The diffraction peaks of KCl are collected in the range of 2θ between 30°–150° and with improved Rachinger $K_{\alpha1}$ and $K_{\alpha2}$ double-line peel off method,[95] the $K_{\alpha2}$ of the diffraction *hkl* is peeled off and obtain integral width (β) and half height width (2ω) values of each *hkl* diffraction. Figure 7.28 is the change curve of the β and 2ω with 2θ of apparatus.

The diffraction intensity of 400, 511, 440 diffraction of samples is collected by step-scanning under the same experimental conditions as the determination of correction curve of instrument. The β and 2ω are obtained after $K_{\alpha1}$, $K_{\alpha2}$ are separated. Table 7.18 indicates the Gaussian and Cauchy component β value corresponding with 400, 511, 440 diffraction of sample. From the wide correction curve of instrument, β, 2ω and Voigt function factor Φ-value of 400, 511, 440 diffraction of sample at 2θ angle can be read.[96] here, the Φ-value lies in the range of the

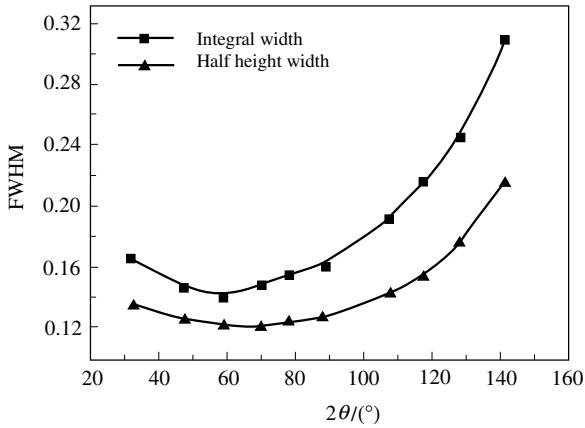


Fig. 7.28 Relationship between integral width, half height width and 2θ of apparatus

Table 7.18 Gaussian and Cauchy component integral width of 400, 511, 440 diffraction of sample[61]

Diffraction	$2\omega(^\circ)$	$\beta(^\circ)$	Φ	$\beta_C^g(^\circ)$	$\beta_G^g(^\circ)$
400	0.124	0.145	0.8552	0.114	0.0451
511	0.120	0.144	0.8333	0.106	0.0588
440	0.121	0.146	0.8288	0.105	0.0588

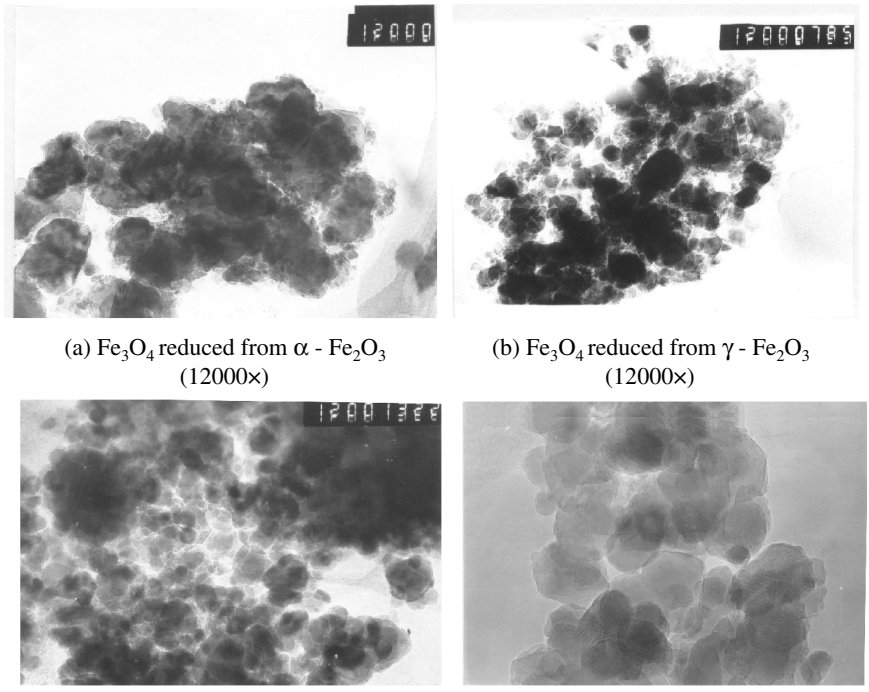
Table 7.19 Experimental values and results of analysis of Voigt function[61]

Parameters		Samples				
		γ-Fe_2O_3	Fe_3O_4 reduced from γ-Fe_2O_3	Fe_3O_4 reduced from α-Fe_2O_3	Fe_3O_4 on industrial use for 10 months	Fe_3O_4 after high temperature treatment
400 Diffraction	$2\theta/(^\circ)$	50.81	50.51	50.52	50.58	50.42
	$2\omega/(^\circ)$	0.514	0.464	0.375	0.455	0.234
	$\beta/(^\circ)$	0.653	0.607	0.514	0.594	0.325
	$e \times 10^3$	3.54	2.94	1.93	2.90	0.77
	D/nm	36.7	34.4	34.5	35.6	56.7
511 Diffraction	$2\theta/(^\circ)$	67.71	67.32	67.33	67.52	67.26
	$2\omega/(^\circ)$	0.578	0.517	0.402	0.518	0.248
	$\beta/(^\circ)$	0.759	0.667	0.553	0.681	0.348
	$e \times 10^3$	2.62	2.45	1.49	2.34	0.63
	D/nm	29.5	37.1	35.2	33.1	57.5
440 Diffraction	$2\theta/(^\circ)$	74.65	74.21	74.24	74.53	74.17
	$2\omega/(^\circ)$	0.643	0.544	0.398	0.556	0.257
	$\beta/(^\circ)$	0.867	0.702	0.549	0.744	0.367
	$e \times 10^3$	2.39	2.28	1.28	2.10	0.51
	D/nm	24.0	36.7	37.0	29.3	53.5

approximate function of the single peak Voigt function analysis. β_G^g and β_C^g are calculated values of Gaussian and Cauchy component integral width.

Table 7.19 shows the 2ω, β, distortion value (e) and crystallite size (D) of the diffraction peaks (400, 511, 440) of samples by Voigt function with single-peak analysis. It can be seen from the Table 7.19 that the γ-Fe_2O_3 prepared by Fe^{3+} (Cr^{3+})/Fe^{2+} mixing ion method has 0.25% to 0.35% lattice distortion. The distortion value of Fe_3O_4 after reduction despite in use in the plant for 10 months only results in a slighter decrease than that of the precursor of γ-Fe_2O_3. However, the Fe_3O_4 obtained from the reduction of α-Fe_2O_3, the method of the reduction and the preparation are the same with γ-Fe_2O_3, the lattice distortion of the former is obviously smaller but the two have no significant difference in particle size. High-temperature treatment significantly increases crystal size, and reduces lattice distortion.

Figure 7.29 is the transmission electron microscopy images of the above samples. Figure 7.30 is the distribution of the secondary crystallite size. It can be seen from



(a) Fe_3O_4 reduced from α - Fe_2O_3 (12000×)

(b) Fe_3O_4 reduced from γ - Fe_2O_3 (12000×)

(c) Fe_3O_4 online at industry for 10 months (12000×)

(d) Fe_3O_4 reduced from γ - Fe_2O_3 (36000×)

Fig. 7.29 Transmission electron microscopy images[61]

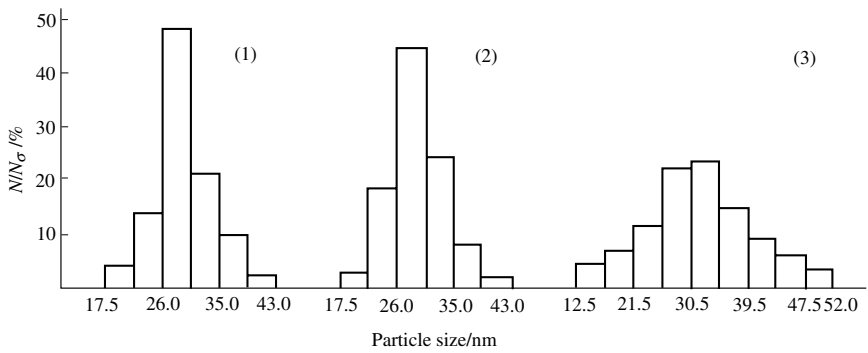


Fig. 7.30 Secondary crystallite size distribution of Fe_3O_4, (1) a, (2) b, (3) c

Figures 7.29 and 7.30 that the crystallite size is almost the same, and the crystallite size distribution of the sample reduced from α-Fe_2O_3 is more non-uniform than that reduced from γ-Fe_2O_3, and the range of which is about 12.5–52.0 nm. The average size of them is approximate to the results obtained from X-ray analysis about 35.0 nm.

Fe_3O_4 reduced from γ-Fe_2O_3 has greater lattice distortion than that reduced from α-Fe_2O_3, and this is related to the different crystal structures of γ-Fe_2O_3

and α-Fe_2O_3. Both γ-Fe_2O_3 and Fe_3O_4 are the spinel structure with oxygen ions *fcc* stacked. γ-Fe_2O_3 has the deficiency of iron in its octahedron compared with Fe_3O_4, and during the reduction, partial cation transfers to the octahedron, and the fcc dense accumulation structure of oxygen ions has not changed, thus the original lattice structure is retained and the distortion of the original structure is maintained. In α-Fe_2O_3 crystal structure, oxygen ions are accumulated in *hcp*, and during reduction, the stack of oxygen ions changes from *hcp* to *fcc*, is a restructure-type phase transition. Thus in the phase transition process, the original crystal body collapses into rough-and-tumble, and the produced ions have to assemble again. Here, the structure of the Fe_3O_4 by this reform is more complete and less distorted, and the crystallite size also is more non-uniform. After high temperature treatment, the catalyst is sintered, and the metastable microstructure is destroyed, resulting in growth of the crystallite, and the distortion reduces. As a result, the difference in micro-structure of Fe_3O_4 generated from different crystal phase of Fe_2O_3 is due to the different phase-change mechanism.

Different phase-change mechanism of α-Fe_2O_3 and γ-Fe_2O_3 into Fe_3O_4 is clearly reflected in the submicroscopic structures. TEM analysis shows that the γ-Fe_2O_3 and Fe_3O_4 are similar in the shape, size and distribution of crystallites, but the crystallite size distribution is narrower than that of Fe_3O_4 with α-Fe_2O_3 as precursor.

7.6.2 *Application of XRD in the research of ammonia synthesis catalysts*

The research of XRD in the ammonia synthesis catalyst is to measure the phase of its precursor. With the maturity of XRD technique, it is used to study the microstructure and the relationships between the structure and its activity. As known to all, the activity of active α-Fe in ammonia synthesis catalyst is quite different from that of the conventional iron. This issue has been raised a long time ago, but it did not have very effective methods to characterize, and thus could not find the answers directly. The significance of structural and electronic promoters was highlighted. But still there is no explanation of the structural identity of "ammonia iron." The turn-over number (TON) of the active site was determined using high-temperature chemisorption of nitrogen on a variety of iron species and was found to be independent on the catalysts nature.[97] The value of the TON points to the presence of C7 sites on (111) or higher indexed surface planes of iron.[12] This is in full agreement with the results from single crystal measurements[98] and indicates that it is not a principally different chemical property discriminating "ammonia iron" from normal iron but rather a different abundance of active sites. We conclude that this should be reflected in a different microstructure and thus look for average structural differences by X-ray diffraction.

The concept of paracrystallinity introduced by Hosemann *et al.* in 1966[99,100] was used earlier to describe the phenomenon of "ammonia iron." They developed the theory of paracrystallinity from XRD data which seemed to explain the special properties of the activated iron catalyst. A three-dimensional, endotactic incorporation of hercynite ($FeA1_2O_4$) motives into the α-iron lattice was thought to create substitutional point defects in the crystal lattice leading to a modified bulk and surface structure of the activated catalyst material. The interplanar spacings change

and a strain field exists in the vicinity of those defects. Paracrystallinity was defined as the normalized standard deviation of a crystallographic interplanar distance, and it is measured by the width of XRD lines.[101−103]

The explanation of endotactic heterostructures in molecular dispersion for the X-ray anomalies of "ammonia iron" was proved by H. Topsoe[104] by Mössbauer spectroscopy. The Mössbauer data imply the presence of small amounts of non-metal iron components which are present, however, as large particles of structural promoter oxides. They are located in grain boundaries and at the outer surface of the catalyst. This location also explains the SIMS data on Fe–Al–O fragments which were intended to support the hypothesis of endotactic heterostructures.[105] The EXAFS data[106,107] provide clear evidence for the identical average local coordination of iron in "ammonia iron" and normal iron.

In 1999, Lendzion-Bielunz *et al.*[108] established a set of methods for the quantitative distribution of various crystals phase of promoters in ammonia synthesis precursor using XRD and ICP methods. According to this method in the precursor, 64% of calcium exist in-between particles, 21% of the calcium is distributed in Fe_3O_4, and the remaining 15% calcium is spread over $Fe_{1-x}O$ phase; only 9% of aluminum is distributed between particles while remaining is in the magnetite crystals as solid solution. The distribution of 91% of potassium is not directly related to iron oxide.

XRD technique has very broad application in the ammonia synthesis catalyst research, and as an improvement of the technique, it has expanded the scope and depth of its application. Now, we will discuss the major applications and major findings of microstructure analysis on XRD in the study of ammonia synthesis catalyst.

7.6.2.1 *Structure of precursor and active phase of Fe_3O_4-based ammonia catalyst*

Bernhard Herzog[109] studied the precursor, the composition and the structure of the active phase for Fe_3O_4-based ammonia synthesis catalyst, and further studied the phase composition and characteristics of microstructure of its precursor, in particular, the disappearance of precursor and the generation of active phase during the whole reduction process with *in situ* XRD experiment; at the same time, the toxicity of the catalyst was also explored.

A well-resolved XRFD pattern displays all components constituting a technical catalyst for ammonia synthesis. In Fig. 7.31, the main reflections can be assigned to magnetite (Fe_3O_4) and wüstite (FeO). Additional faint reflections are observed arising from calcium ferrite ($CaFe_3O_5$), potassium hydrogen carbonate ($KHCO_3$) and α-iron. The prehistory of this catalyst precursor is reflected in the coexistence of magnetite, wüstite, and α-iron within a single sample. This combination of phases is unique for this catalyst precursor as within one solid metastable phase both with respect to their oxygen fugacity and the phase equilibrium at ambient conditions do coexist.

While some of the aluminum and the silicon components are not detectable by phase analysis with XRD because of their X-ray amorphous microstructure, the presence of them is indicated by distinct textural changes of the reflection intensities of the magnetite precursor (Table 7.20). The fine structure of some reflections,

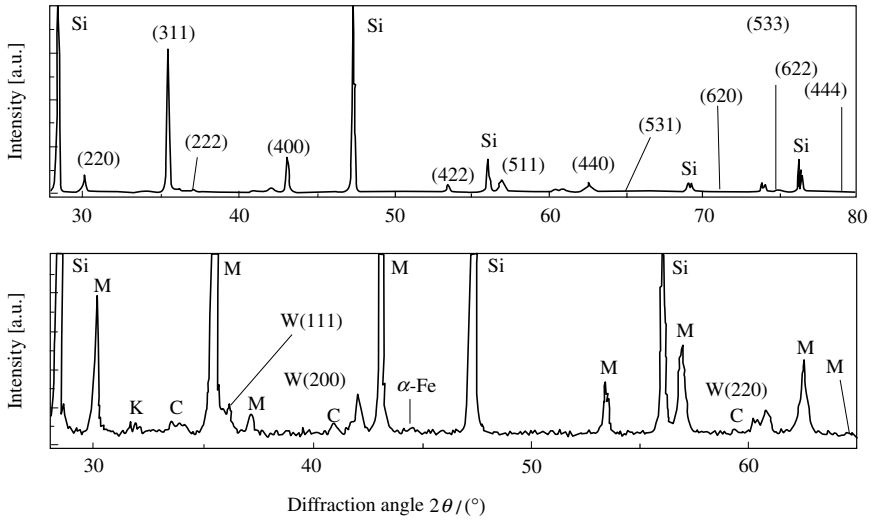


Fig. 7.31 Phase analysis of a technical catalyst precursor for ammonia synthesis[109] K = $KHCO_3$, C = $CaFe_3O_5$, M = magnetite (Magnetite reflections are indexed in the upper diagram)

Table 7.20 Comparison of the reflection intensities (%) of pure magnetite and catalyst precursor

Miller index	Pure magnetite	Magnetite precursor	Miller index	Pure magnetite	Magnetite precursor
(220)	30	12	(511)	30	9
(311)	100	100	(440)	40	7
(222)	8	3	(533)	10	9
(400)	20	25	(622)	4	3
(422)	10	6			

together with deviation in the lattice constants of magnetite, point to the presence of a solid solution with hercynite ($FeAl_2O_4$).

The importance of Fe_3O_4-based catalyst with a small amount of $Fe_{1-x}O$ phase in the process of reduction has long been focused by experts and scholars worldwide. Because many commercial iron catalysts contain 5% to 11% (mass) of wüstite, a small regional wüstite spread between the large particles of the magnetite whose main role of which is to connect. A. Pattek-Janczyk[110−112], through analysis of the fine structure of the wüstite in Fe_3O_4-based catalysts found that there exist two different super-structures of wüstite, that is, non-stoichiometric structure of the $Fe_{1-x}O$ (N) and close to the stoichiometry of the FeO (S). The results from high-resolution XRD detection and analysis of the fitting of diffraction peak, as well as related XRD quantitative calculation show that there is a good correlation of the relative content of two superstructures of wüstite and the cooling rate during catalyst preparation. Rapidly cooling only results almost N structure, S structure is very small, with the slowdown in the cooling rate, N structure gradually reduced and S structure increased, when reaching the slowest rate of cooling, the

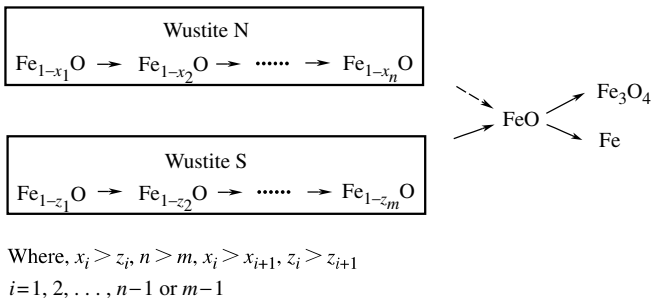

Wustite N
$Fe_{1-x_1}O \rightarrow Fe_{1-x_2}O \rightarrow \cdots\cdots \rightarrow Fe_{1-x_n}O$
Wustite S
$Fe_{1-z_1}O \rightarrow Fe_{1-z_2}O \rightarrow \cdots\cdots \rightarrow Fe_{1-z_m}O$
FeO
Fe_3O_4
Fe
Where, $x_i > z_i$, $n > m$, $x_i > x_{i+1}$, $z_i > z_{i+1}$
$i = 1, 2, \ldots, n-1$ or $m-1$

Fig. 7.32 Transformation of different structure of wüstite during cooling process[100]

content of both are almost equal. It can be considered that in the process of catalyst solidation, S structure is transformed from the N structure gradually. The transformation of N wüstite to S is also found in the early stages of the process of activating the catalyst. In the early stages of low temperature (473 K, 523 K and 573 K), with the length of time, S wüstite increased and N wüstite decreased, and the lattice parameters are slightly increased, that is N gradually transformed into S. Therefore, Pattek-Janczyk drew the phase transformation sequence of wüstite in the process of activation in iron catalyst: N wüstite first transformed into S wüstite, S wüstite and part of N wüstite then changed into a FeO phase, finally FeO transformed into magnetite and metal iron and its transformation processes as shown in Fig. 7.32. This theory was further confirmed by mössbauer spectrum.

Studying the reduction process of magnetite catalyst by *in situ* XRD, Bernhar Herzog[109] found that the early formed active phase iron was from the reduction of a small number of wüstite in magnetite precursor. The first step of reduction is thermal decomposition of wüstite into isotropic α-Fe crystal nuclei, which is the reaction center of the reduction of magnetite, and became the collective core of free iron ion from magnetite. It is crucial that initial iron core as reaction center promoted the reduction of magnetite at low temperature.

Figure 7.33 is XRD profile of catalysts with different Fe^{2+}/Fe^{3+} (R) values.[87] According to the calculation by XRD fine patterns with scale-free quantitative analysis, the content of Fe_3O_4 and FeO in all samples (when $Fe^{2+}/Fe^{3+} < 0.5$, other micro-phases do not participate in the calculation), is shown in Table 7.21. It is worth noting that a small number of wüstite ($Fe_{1-x}O$) still exists in the sample of $Fe^{2+}/Fe^{3+} < 0.5$, which is impossible theoretically. The reason may be related to a minor disproportionation reaction happening during the preparation process. However, compared with/without promoter, wüstite formation is few when with promoter, thus promoter can inhibit the disproportionation reaction.[113]

According to the results obtained by the authors[52] when $Fe^{2+}/Fe^{3+} > 3.15$, Fe_3O_4 no longer exists, and Fe^{3+} cannot form magnetite phase independently, but non-stoichiometricly dissolves in wüstite-phase, and forms wüstite as $Fe_{1-x}O$ with much lattice defects. In Fig. 7.33, when $Fe^{2+}/Fe^{3+} > 3.47$, there are only traces of Fe_3O_4 which means that most of the Fe^{3+} has been dissolved in the lattice of wüstite, and the existence of promoter can promote the generation of wüstite with lattice defects.

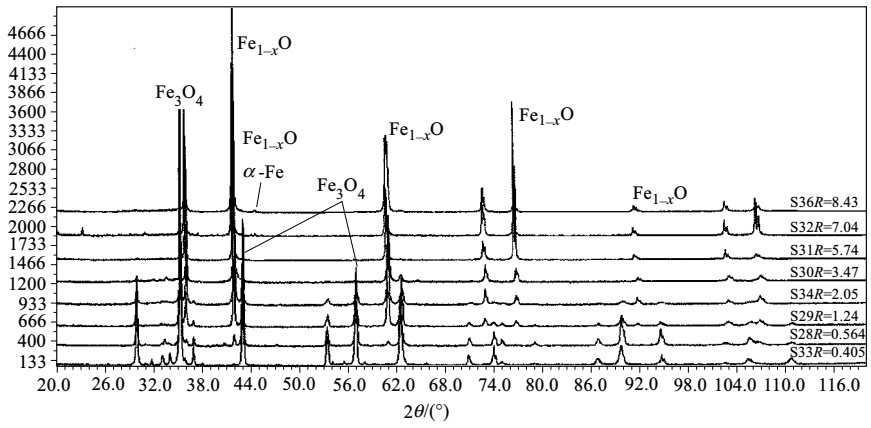


Fig. 7.33 XRD of catalysts with different Fe^{2+}/Fe^{3+} (R)

Table 7.21 Content of Fe_3O_4 and FeO in the catalysts in Fig. 7.33

	Fe_3O_4		FeO	
Fe^{2+}/Fe^{3+}	Mass fraction/%	Molar fraction/%	Mass fraction/%	Molar fraction/%
0.405	99.04	96.98	0.96	3.02
0.564	93.75	82.20	6.25	17.100
1.24	56.45	28.77	43.54	71.23
2.05	41.98	18.26	58.02	81.74
3.47	5.53	1.77	94.47	98.23
5.74	2.59	0.82	97.61	99.18
7.04		0	100	100
8.43			100	

In situ XRPD data is shown in Fig. 7.34, where the first change in the phase inventory with beginning activation is the loss of the FeO phase being converted into iron nuclei. This elemental iron is produced from thermal decomposition of the wüstite phase within the precursor as can be seen by inspection of the diffraction pattern. The metastable wüstite can disproportionate at any temperature between room temperature and 840 K:

$$4FeO \rightarrow Fe + Fe_3O_4. \tag{7.140}$$

The apparent isotropic particle size of the iron particles was estimated from the full width at half maximum (FWHM) using the Scherrer equation to be *ca.* 80 nm as shown in Fig. 7.35. Whether the iron nuclei are formed by thermal decomposition of wüstite or by reduction of magnetite can be decided from the observation that "ammonia iron" exhibits a strong texture. Microscopic studies showed the iron particles to be textured in the [111] direction. Unfortunately, the Fe (111) line is not detectable for symmetry reasons. But the texture is characterized by smaller $(hOO)/(hkO)$ ratios than calculated from the structure factors of isotropic α-iron. The fact that the (200):(110) ratio of the initially formed detectable iron particles is identical with the theoretical value of 0.2 unambiguously indicates the formation of

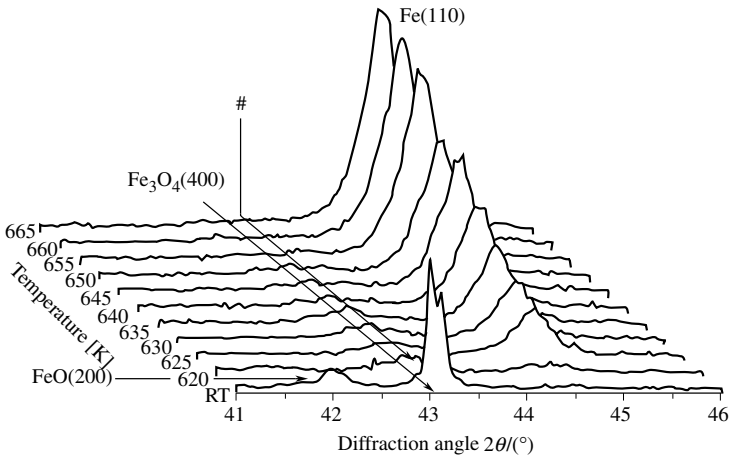


Fig. 7.34 Development of "ammonia iron" from the magnetite precursor. Nuclei of isotropic a-iron form in the beginning of the activation process (see also Figs. 7.35 and 36). Diffuse reflections of a non-stoichiometric wüstite phase (#) superimpose the Fe_3O_4 (400)

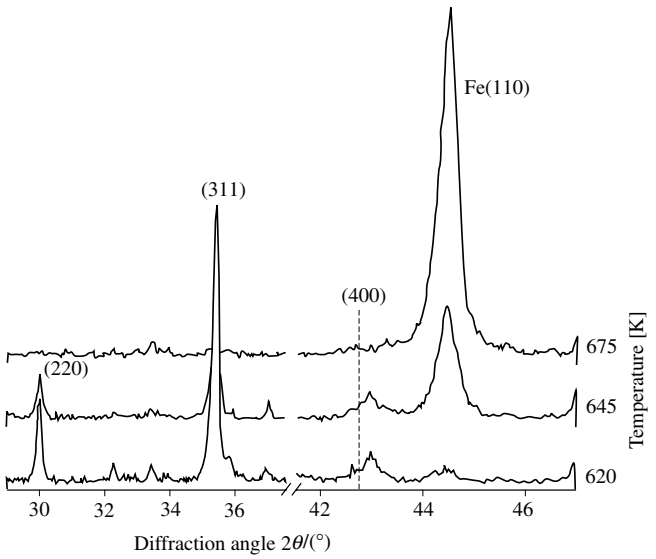


Fig. 7.35 Although the (400) reflection (indicated by the dashed line) has almost disappeared, the phase magnetite is still predominant as seen from other reflections. We note the strong difference in line shape between educt and product[86]

isotropic iron formed form decomposed wüstite. This elemental iron is essential to initiate the reduction of magnetite with hydrogen at low temperatures. Iron nuclei require reaction centers since reduction of magnetite does not follow the simple overall reaction:

$$Fe_3O_4 + 4H_2 \rightarrow 3Fe + 4H_2O. \tag{7.141}$$

The mechanism of activation rather proceeds *via* two types of reactions involving the diffusion of ions and electrons:

Type 1 is:

$$4O^{2-} + 4H_2 \rightarrow 4H_2O + 8e^-. \tag{7.142}$$

Type 2 is:

$$Fe_3O_4 + Fe^{2+} + 2e^- \rightarrow 4FeO \tag{7.143}$$

$$4FeO \rightarrow 4Fe^{2+} + 4O^{2-} \tag{7.144}$$

$$4Fe^{2+} + 8e^- \rightarrow 4Fe \tag{7.145}$$

$$Fe_3O_4 + Fe + 4H_2 \rightarrow 4Fe + 4H_2O \tag{7.146}$$

In this mechanism the iron nuclei are centers to which iron ions diffuse driven by a local gradient of the electrochemical potential. Otherwise the reaction would stop after the initial reduction, when the magnetite core of a grain is covered by a dense iron layer. This mechanism of reduction causes a restructuring of the magnetite crystals and the loss of the topochemistry of the magnetite grains provided that the reaction is slow enough to permit the migration of cations according to the concentration gradients. The fact that highly dispersed wüstite is present in the magnetite matrix permits the simultaneous formation of many iron nuclei and hence the occurrence of a network of concentration gradients of iron ions which is not determined by the grain structure of the magnetite. Consequently, the resulting iron particles are of smaller size and may be of different shape than the magnetite precursors. This is illustrated by Figs. 7.34 and 7.35. The line profile of the iron formed is different from that of the magnetite precursor. In addition, the intensity of the magnetite reflections disappears highly anisotropically with increasing abundance of the crystalline iron. The magnetite crystals do not shrink isotropically in size but change their shape as the migration of iron along certain directions is faster than along other directions. The reflection intensity ratio of (440)/(511) in the magnetite changes from 0.78 at room temperature to 0.37 at 650 K. This texture effect is interpreted to be the result of hercynite-rich magnetite portions which form disperse aluminum oxides in the last step of reduction (an observation which corresponds to measurements done by the group of Hosemann *et al.* and Borghard[103]); and these portions are the same which form the difficult-to-reduce ternary oxides detected with bulk and surface sensitive techniques such as Mössbauer spectroscopy,[104] XRD,[103] SIMS,[114] and photoemission.[115] At the marked position (#) in the diffraction pattern in Fig. 7.33, a broad weak reflection occurs under the magnetite (400) peak. It disappears gradually with the conversion of magnetite to iron and does not follow in its intensity evolution the changes observed with the magnetite reflection. This allows conclude that the reflection belongs to an intermediate phase during activation. In Refs. (115 and 116) this intermediate reflection was also observed and attributed to a second wüstite phase with different composition than the initial phase. R. Schlog[115] thinks it was a second wüstite phase with a different composition than the initial phase. Then the reflection would be the wüstite (200) peak which occurs, however, significantly displaced relative to its expected position. On the other hand, in a recent Mössbauer study it was found that a stabilized form of wüstite was present as reaction intermediate as long as magnetite could be observed.

Figure 7.35 illustrates the absence of any Ostwald ripening during the activation procedure as the line width of the first detected iron particles stays the same until all precursor material is converted to iron. It is noted that activation at more severe conditions (faster heating rate, less water in the exit gas) will lead to progressively smaller particles down to about 30 nm in apparent size with, however, the same absence of any growth of the crystals during activation. Only when all diffracted intensity from the precursor phase had disappeared (at 670 K), the production of ammonia was detectable in the mass spectrum at 15 amu. This clearly indicates that the catalytic activity in "ammonia iron" does not scale with the bulk iron content, but develops only at the very end of the activation process. The observation is in line with the evolution of the BET surface area[37] and the formation of the metallic surface[115] at reduction degrees above 90%. Either a transformation of the initially formed iron into the active state or surface poisoning of the iron by the still present water from other reaction fronts in the gas phase can explain this finding.

The *in situ* XRD results of Fe_3O_4-based ammonia synthesis catalyst are shown in Fig. 7.36.[109] It summarizes the evolution of diffracted intensities of three main iron reflections with increasing temperature. First of all, from Fig. 7.36 it can be seen clearly that the growth of the reflections of α-iron is asymmetric, at the end of the reduction the intensity ratio of the first three iron reflections (110), (200) and

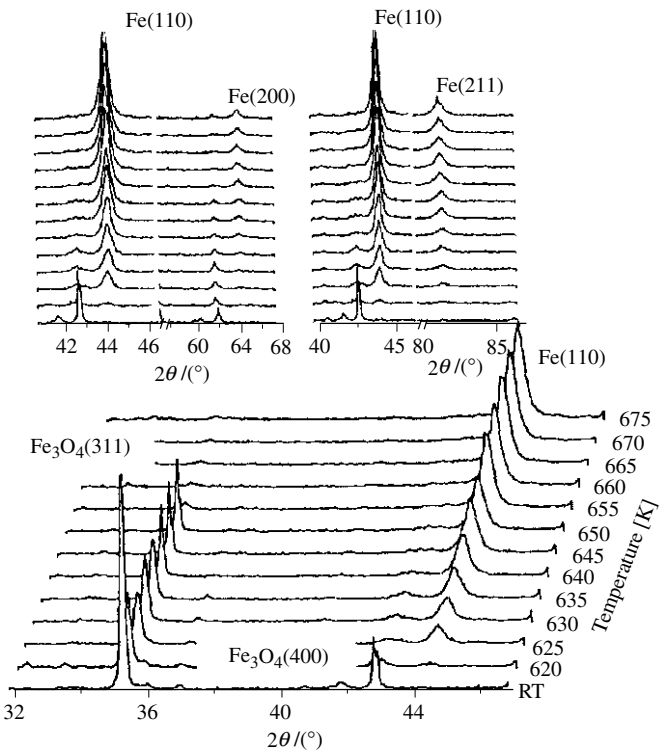


Fig. 7.36 Course of reduction of the magnetite precursor and formation of the anisotropic "ammonia iron." The upper diagrams prove the anisotropic formation of the α-iron[109]

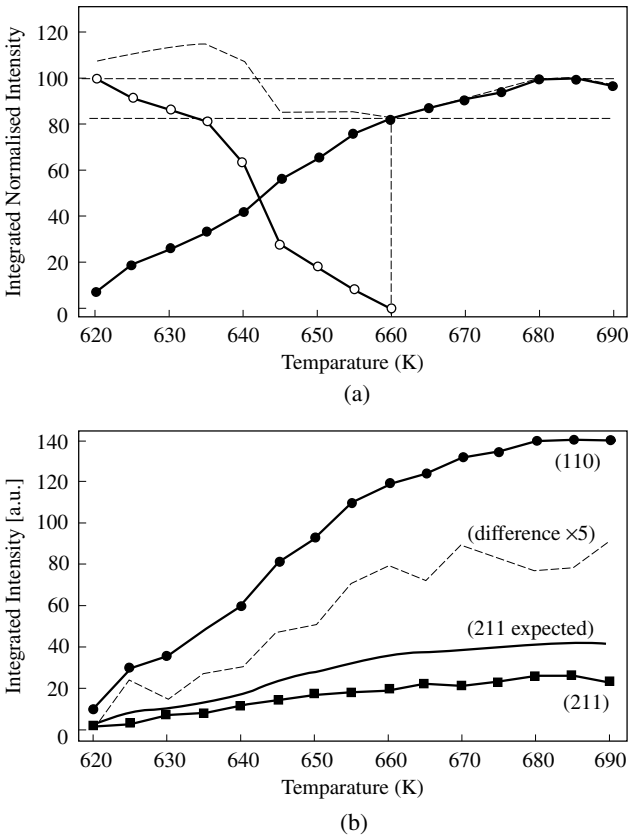


Fig. 7.37 Variation of integrated intensities with reaction temperature. In (a) the total intensity of the magnetite pattern (decreasing) and of the iron pattern (increasing) are composed. The straight lines indicate the discrepancy of the sum of the total diffracted intensity from the expected constant value. In (b) the evolutions of the iron (110) and (211) intensities are composed. The expectation value for the (211) reflection is calculated from the suitable scanned structure factor normalised to the (110) intensity[109]

(220) is 100:10:16, while the ratio should be 100:20:30 for isotropic c∼-iron. The value of the (200)/(110) ratio is changed from 0.2 to 0.08 which is an indication of a significant anisotropy of the activated iron particles. The non-simultaneous evolution of the iron diffracted intensity in different orientations with temperature is an obvious sign of the non-isotropic nature of the activated catalyst.

A numerical analysis of the integrated intensity changes displayed in Fig. 7.36 is given in Fig. 7.37. Figure 7.37(a) reveals that the formation of the active phase is not terminated with the disappearance of the diffracted intensity from the precursor. 17% of the iron diffracted intensity develops only after all intensity from magnetite has disappeared. The final portions of magnetite are enriched in alumina and its exsolution causes a structurally damaged magnetite matrix to remain the final reservoir of educt which is invisible to the X-ray beam.

The presence of iron-bearing material which is invisible to the X-rays is further indicated by the change of the sum of the oxide and iron diffracted intensity. At

low temperatures the generation of iron from an amorphous source (metastable dispersed wüstite) is observed whereas the various processes acting on the magnetite crystals lead to a significant formation of X-ray invisible material which recrystallises at the very end of the reduction process.

Figure 7.37 (b) shows the anisotropy growth of Fe (211) reflection. The anisotropy of the elemental iron can be seen from the deviations of the measured intensities of the Fe (211) reflection from the theoretical intensity calculated from the intensity of the Fe (110) base reflection. A similar difference was also observed for the Fe (200) reflection. These observations which were made with several batches of catalyst show that the crystallites of the catalyst are not isotropic and that an average deviation from e.g. iron octahedra which are the normal structure of low-temperature iron develops during activation. The small number of reflections observed and the absence of the (111) peak preclude any meaningful prediction of the main dominating crystal termination plane. It may well be that several non-equilibrium orientations do coexist with the sum of all anisotropies being observed in the data of Fig. 7.37. The detection of this integral anisotropy is a strong hint towards the texture of the iron being a major difference between normal (isotropic) iron and "ammonia iron".

It is very important to study the microstructure of active phase iron in ammonia synthesis catalyst, because it is closely related with its activity. According to the data taken from *in situ* XRD test at 650K, in the 2θ region of the Fe (110) reflection the diffraction profile function is best defined by a Lorentzian^2 (L^2) function, as it was verified by analysing the (220) reflection of the Si standard illustrated in Fig. 7.38.

From Fig. 7.39(a) it appears, however, that the L^2 function does not fit the (110) profile of the "ammonia iron," even when the $K\alpha_1$ $K\alpha_2$ splitting is involved. The deviation of the asymmetric wings in the profile of the difference pattern ($R = 10.33\%$). In Fig. 7.39(b) it is illustrated that a minimum of three pairs of lines were

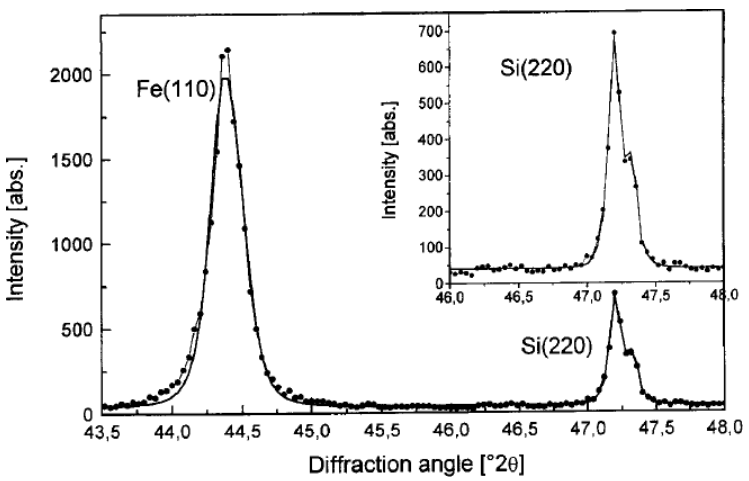
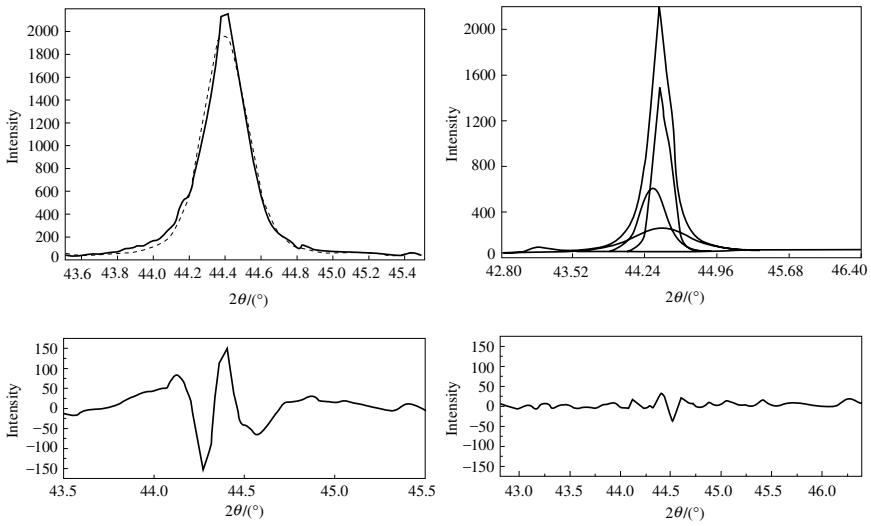


Fig. 7.38 Comparison of measured (line + symbol) and fitted profiles (straight line) of the Fe (110) and Si (220)[109] lines. The data were taken at 650 K in synthesis gas atmosphere



(a) A single line fit using a Lorentzian^2 function (straight line:measured profile,dashed line:fitted profile)

(b) The fitted result by introducing two additional lines by visual inspection in a Lorentzian^2 function

Fig. 7.39 A well-resolved XRD pattern of fitted active phase iron (110) reflection[109]

required to reasonably fit the measured profile ($R = 3.68\%$). The character of a global minimum of this model was checked by testing variations of constraints and starting parameters which all resulted in the same solution.

The observed Fe (110) profile is a convolution (see Fig. 7.39(b)) of the normal bulk (110) reflection ($d = 204\,\text{pm}$, FWHM $= 0.13°2\theta$) and one diffuse reflection at the same position ($d = 204\,\text{pm}$, intensity 10% (110), FWHM $= 0.64°2\theta$) with a third contribution at a higher d value ($d = 204.3\,\text{pm}$, FWHM $= 0.25°2\theta$). The diffuse reflection at the Fe (110) position arises from defective elemental iron giving rise to a wide distribution of interplanar distances and/or small particles of *ca.* 15 nm diameter, while the main reflection results from bulk iron with a narrow distribution of d spacing and a larger particle size of about 70 nm. The fact that two well-resolved contributions to the total diffracted intensity of alpha-iron exist is not adequately described by one average peak profile, and is proof for a structural inhomogeneity of the iron. Regions of good crystallinity must coexist with parts of much more disordered iron.

The reflection at a larger d spacing is attributed to a species of iron with intercalated nitrogen atoms which enlarge the lattice constant. The assignment was verified by changing the synthesis gas atmosphere at isothermal conditions. Figure 7.40 summarizes the results which reveal the merit of *in situ* observations on the relationship between structural inhomogeneity and the chemical environment. In Fig. 7.40, the grey blocks show the synthesis gas feed, vertical coordinate represents the integral intensity of the diffraction peak, as the relative content. Diffraction data were taken for 15 h at each data point of Fig. 7.40 in either H_2 or synthesis gas atmosphere. The overall diffracted intensity remains independent of the atmosphere, but the relative intensities of the contributions change depending on the presence of nitrogen. The contribution from the defective part of metallic iron remains almost unaffected

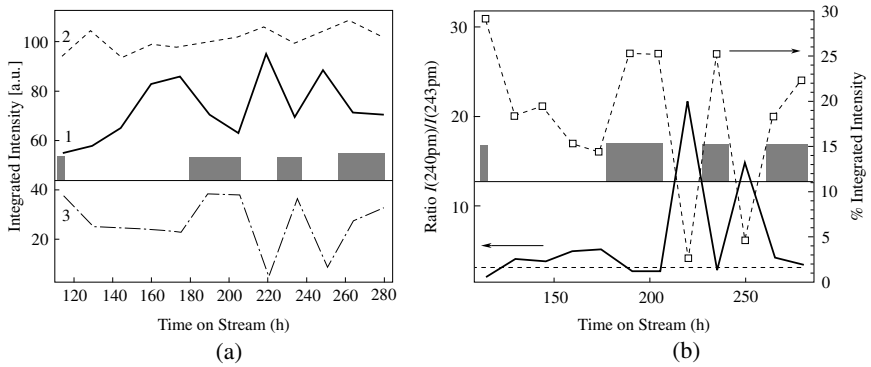


Fig. 7.40 Different contributions to the Fe (110) line profile during an isothermal treatment (at 650 K). Data were taken each 15 h in He (50 ml/min). Measurements were done under the addition of Ar or nitrogen (grey blocks). Contribution 1 denotes the main intensity at 240 pm with the narrow linewidth, contribution 2 the peak at 240 pm with the wide profile, contribution 3 the peak at 243 pm. In the lower panel the ratio of the 240 to 243 pm intensities and the relative contribution of the total (110) intensity are compared with each other and the gas phase composition[109]

(trace 2 in Fig. 7.40); trace 1 represents the contribution of normal iron; trace 3 represents the contribution of iron with intercalated nitrogen atoms, and the iron with intercalated nitrogen and normal iron present a complementary relationship. Composition 3 increased remarkably in content under synthesis gas. Figure 7.39(b) shows the nitride and 0.204 nm peak, which are the functions of the ratio of total iron and time, separately. The dashed line is the ratio of nitride and total iron, while the solid line is the ratio of the peak 0.204 nm and total iron. In addition to the above results, it can also be seen that the formation of the nitride phase occurs rapidly on the time scale of this experiment. The effects caused by nitrogen removal take more time, as the bulk-dissolved nitrogen is only slowly consumed by ammonia synthesis. The experiments show that the presence of a nitride such as described in earlier investigations[117] is the normal state of the iron catalyst not only as surface nitride but as a phase detectable by XRD.

According to the complex composition of the active phase iron, it can be obtained that the reaction kinetics cannot be described by a core-and-shell model which would leave the grain structure of the precursor oxide unchanged in the resulting iron metal. Also, a modification, the crackling core-and-shell model does not describe the defined and very pronounced change in texture from the oxide to the metal. We observe a restructuring process controlled by the iron ion transport. These findings explain the correct representation of the catalyst synthesis by model experiments (done by D R Strongin[118]) with alumina-promoted single crystals of (100) and (110) orientations which were activated by an oxidation-reduction cycle into (110) iron.

It should be noted that the above analysis is preliminary; more complex methods such as Fourier transform analysis of the peak shape will be more effective. The detection of a distribution of d spacings over a considerable extent (from about 0.2066 to 0.2010 nm) has further implications on the mechanism of nitrogen dissociation. A recent publication gave evidence that regions of high strain and defect density have a strong influence on the activation of molecular nitrogen.[119]

7.6.2.2 *Grain-growth kinetics and microstructure evolution of nanocrystalline iron*

Active phase is the source of the catalytic activity which value has a direct relationship with the microstructure of active phase. Ammonia synthesis reaction is the most sensitive to structure. The results from single crystal measurements by field-ion microscopy (FIM)[120,121] shows that the opened iron (111) and (211) surface is the most active, and the wrapped (110) surface almost has no activity. The results by determining the effect of different crystal surfaces of α-iron on the activity of formation ammonia from N_2 and H_2 under 2.0 MPa shows the relative activity of Fe (111), Fe (100) and Fe (110) is 418:25:1. The activity of reflection of Fe (111) is 418 times higher than that of Fe (110); the difference is amazing.

The result above is obtained under strictly controlled conditions in laboratory, but the single surface of α-iron and fully exposed α-iron (111) surface are hard to get during the preparation and reduction of catalysts. Even more important, because of the existence of promoter, 50% or more surface of α-iron is covered by K_2O or KOH and the structure of active phase changes because of the addition of the promoter, and even the active site distribution or active order on the crystal plane of α-Fe are greatly changed. As a result, the impact of microstructure changes on the mechanism of activity is worth exploring.

H. Natter[122,123] studied the grain-growth kinetics and evolution of the microstructure of nanocrystalline iron. Pulsed electrodeposition (PED) is used to prepare nanocrystalline iron with an average grain size of 19 nm and thermal stability up to 550 K. At $663\,K \leq T \leq 783\,K$ the kinetics of grain growth, with respect to size and size distribution, is studied *in situ* by means of real-time synchrotron XRD. The Bragg peak line shapes of the large number of diffractograms are analyzed using a Warren/Averbach procedure improved with respect to reliability and efficiency. They observe two regimes of grain growth: at less elevated temperatures grain growth is smooth and moderate up to limiting size values between 50 and 100 nm, depending on temperature. The initially rather narrow width of the size distribution increases slightly, and the activation energy of grain growth, about 100 kJ/mol, corresponds to the literature value for grain boundary self-diffusion in nanocrystalline Fe. At higher temperatures the grains grow first rapidly and then slowly up to limiting values between 200 and 400 nm, depending on temperature. The size distribution becomes rather broad and the activation energy for grain growth, about $175\,kJ \cdot mol^{-1}$, corresponds to the literature value for grain boundary self-diffusion in coarse-grained polycrystalline Fe. It does not find evidence for a change of the type of distribution which indicates normal grain growth.

Thus, the distribution of particle size, micro-stressand other parameters are obtained, (Table 7.22 and Fig. 7.41), where μ is middle particle size, D_{area} is average particle size by area weighted, D_{vol} is average particle size by volume weighted. Natter did crystal growth experiments at each fixed temperature simultaneously, the extension of growth time is 150 min, nearly 20 XRD diffraction patterns were collected (Fig. 7.42, along (110) reflection). It can be seen that the diffraction peak width is rapidly narrowed in the initial stage from Fig. 7.42. The results of the evolution of crystal growth micro-stress and D_{vol} with time at different temperatures analyzed by peak shapes is as shown in Figs. 7.43 and 7.44.

Table 7.22 Results of evaluation of grain-size distributions for nano-Fe in initial state and in final states at the end of the different isothermal real-time experiments

T/K	D_{area}/nm	D_{vol}/nm	μ/nm	σ	Micro-stress/%
Initial state	16	19	9.8	1.54	0.684
663	37	46	22.0	1.58	0.303
683	70	92	36.6	1.67	0.201
703	76	103	36.0	1.73	0.179
739	104	150	42.6	1.82	0.103
753	145	234	44.5	1.99	0.076
783	215	395	47.2	2.18	0.023

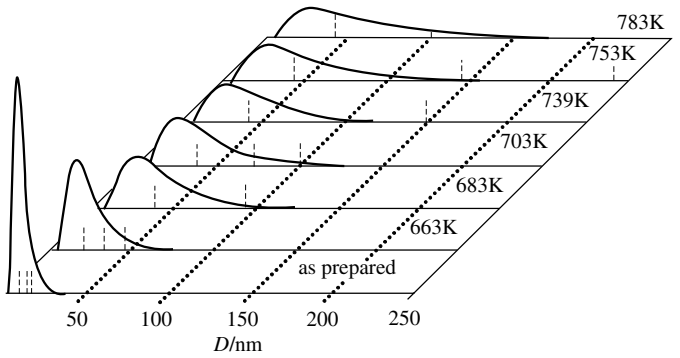


Fig. 7.41 Initial and final grain-size distributions of the different isothermal grain growths experiments on nano-Fe; the dashed/dotted/solid marks indicate the $\mu/D_{area}/D_{vol}$ values, respectively

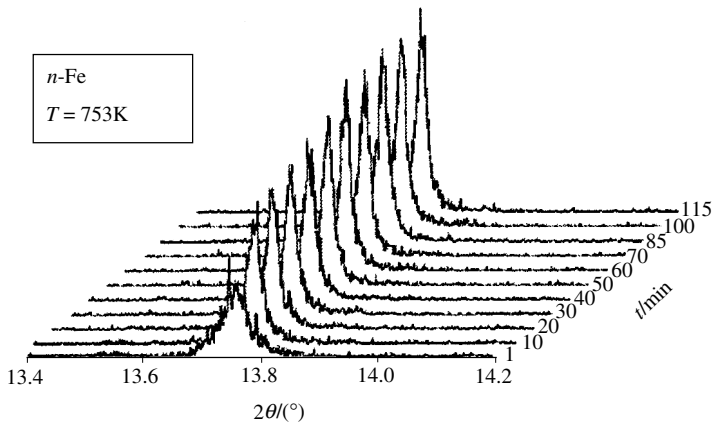


Fig. 7.42 Set of diffractograms of nano-Fe recorded at 753 K; only the selected angular range is displayed, which comprises the (110) Bragg peak

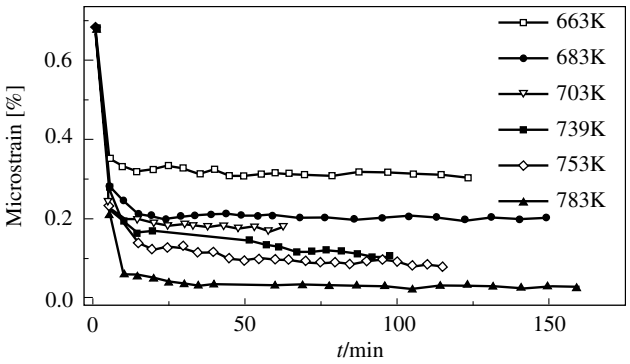


Fig. 7.43 Temperature and time evolution of the microstrain of nano-Fe

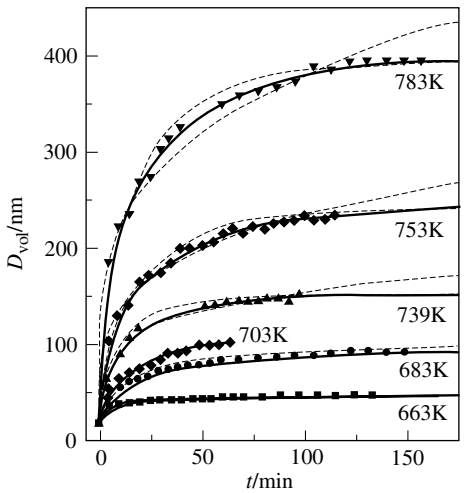


Fig. 7.44 Temperature and time evolution of the volume-weighted average crystallite diameters of nano-Fe; the lines represent fits with different kinetic grain-growth models. Dashed lines represent fits with the generalized parabolic grain-growth model; solid lines represent fits with the grain-growth model with impediment; dashed-dotted lines represent fits with size-dependent impediment

As can be seen from Fig. 7.43, the average value of micro-stress decrease when temperature increasing after 10 min rapid decrease of stress, it basically unchanged later. The rate of increase of particle size distribution at low temperatures is small from wide to narrow, representing the self-spread movement on the edge of nanocrystalline Fe particle is relatively slow, and the crystal growth activation energy is about $100\,\mathrm{kJ \cdot mol^{-1}}$.

At high-temperature, initial growth of particle is rapid, the particle size distribution has become very wide, the crystal growth activation energy increases to $175\,\mathrm{kJ \cdot mol^{-1}}$, which mean nano-iron crystal strengthens its self-spread ability at the edge of coarse particles.

7.6.3 *Application of other modern physical methods in catalyst characterization*

(1) TEM, SEM analysis. High-Resolution Transmission Electron Microscopy (HRTEM) is one of the effective techniques to study the sub-microscopic structure of solid materials. They can observe nano-scale structure of microcrystalline and its defects, the pore structure of zeolite, as well as layered materials. All these information can be hardly provided by other equipments.

HRTEM is a common way to observe the surface morphology, crystal state, as well as changes in the particle size during the study of catalyst, as shown in Fig. 7.45, which is the TEM image of 5Ru/HTAC catalyst after dechlorination for 24 hours,[124] and its corresponding data are listed in Table 7.23. It can be seen from Fig. 7.45 and Table 7.23 that in dechlorination as the temperature increasing, due to sintering, microcrystallines of Ru grow up clearly, and the dispersion and exposure fraction of Ru reduce.

(2) Electron Probe Microanalysis (EPMA). Electron beam from electron gun is accelerated before it focuses on the point of surface of a sample catalyst. The electron in the inner shell of atom is hit out and outer shell of electron fills in shoot characteristic X ray representing the nature of the element. The qualitative analysis of elements can be carried out by which energy (or wavelength) and intensity is related to content or concentration of element with high resolving power. The use of this technology, the electron beam in addition to point analysis, also along the line or surface scan, can obtain the distribution of the electron along lines and surface,

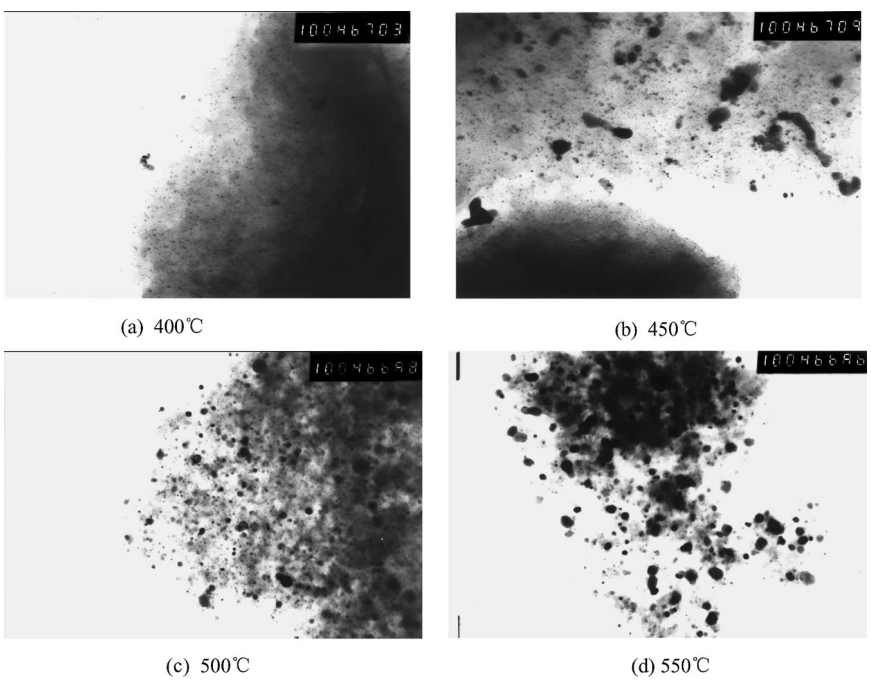


Fig. 7.45 TEM image of 5Ru/HTAC catalyst after dechlorination for 24 hours (a) 400°C; (b) 450°C; (c) 500°C; (d) 550°C

Table 7.23 Particle size, dispersion of Ru and TOF for 5Ru/AC catalysts

Temperature of dechlorination[a]/°C	Particle size of Ru[b]/nm	Ru dispersion[c]/%	Ru exposed area[d]/m^2/g	TOF[e] $\times 10^3/s^{-1}$
400	3.74	35	5.46	2.14
450	4.88	27	4.18	3.31
500	6.08	22	3.36	3.66
550	9.55	14	2.14	4.38

[a]Dechlorination time is 24 h; [b]from the TEM; [c]ruthenium particles are assumed as spherical, concentration of atoms on the surface is $1.63 \times 10^{19}\,m^{-2}$, density $12.45\,g\,cm^{-3}$; [d]data from dechlorination of $1Ba(NO_3)_2$ — 5 Ru/HTAC catalyst; [e]data calculated according to NH_3 % and $Ru_{surface}$ on $1Ba(NO_3)_2$ — 5 Ru/HTAC catalyst after dechlorination.

and the depth of its bombardment is about 200 nm. The elements in periodic table except the first few of elements can be analyzed in this way by commercially equipment. Besides, the distribution of heavy metals from the surface to depth extended in catalysts can be determined with desquamating method, observing the existence and distribution of toxins or promoters in catalysts, such as the distribution of active phase along cross section in supported catalyst.

(3) X-ray photoelectron spectroscopy (XPS). X-ray photoelectron spectroscopy is the opposite to electron microprobe. If the samples have been bombarded by monochromatic X-ray from X-ray gun, the electrons of the outer layer from different electronic layer are transformed into photoelectrons, and the intensity of electron in the top few atomic layers is relatively high, and then drops with the depth of less than 4 nm. The energy spectrum can be got between the energy and the intensity of the electron. Because each element has its characteristic peak (the related atomic ordinal number), the qualitative and half quantitative analysis can be carried out. If combining with ion sputtering technology, it can be also used for further analysis of the composition at different depth, and all elements except hydrogen can be measured. XPS has become a very important tool in research of catalysts, providing the composition on surface, valence, binding energy etc., which are significantly important in researching the nature of catalytic active center and poisoning mechanism. For example, the bond energy (B · E) and composition of element on surface for ZA-5 catalyst after reduction are shown in Table 7.24.

As the catalyst after reduction is extremely active, part of it has been oxidized when transferring to the sample room during experiment, Fe_{2p} occurs displacement and its content is lower that real one. It is worth noting that the more elements of chlorine (Cl) were found on the surface of the catalyst.

(4) Auger electronic spectroscopy (AES). When the ionizing atom at an excited state as a result of electron-beam bombardment comes back to the initial one,

Table 7.24 Bond energy (B · E) and content of element on surface for ZA-5 reduced catalyst

Item	Fe_{2p}	Ca_{2p}	K_{2p}	Cl_{2p}	Al_{2s}	Si_{2p}
B.E/eV	710.85	347.10	293.05	198.40	119.75	101.50
Content/wt%	85.644	0.437	1.247	0.077	0.138	0.561

it will produce X-ray fluorescence or Auger electrons, and can get Auger electronic spectroscopy. Similarly, except hydrogen, Helium, each element has its own AES characteristic peak and its inherent energy spectrum. AES also has become a unique identification sign. Since the energy of Auger electron is related to the atoms, molecules and their states in catalysts; therefore, it can be used to carry out the physical and chemical analysis of samples, particularly suitable for the studying of the surface properties of catalysts, such as identification of loss status of palladium in automobile exhaust catalysts and catalyst poisoning.

Electron spectroscopy of the adsorbed species has been developed. Both AES and XPS can give information about the electronic state of atoms in the outermost layer of a solid surface, thus permitting the study of adsorbed species.[125] When dinitrogen is adsorbed at 83 K on Mo or 373 K on Fe, at which temperatures molecular adsorption is expected, a single peak is observed at around 385 eV. While, when it is adsorbed on Mo at 273 K or on Fe at 673 K, three peaks are observed. Since Mo_2N gives three similar peaks, the absorbed species obtained at high temperatures are assigned to atomic nitrogen.[126]

Similar AES of N_2 absorbed on W (110) at 100 K was observed. The amount of absorbed nitrogen can be monitored by the peak height of the AES. Nitrogen molecules adsorbed on W, Ni, Fe at 100 K or lower temperatures have two peaks in XPS at around 400 eV and 406 eV, which are interpreted in different ways: ① the peak in 406.6 eV is a molecular adsorption of N_2 (a), and the peak in 397.6 eV is an atomic adsorption of N (a) on W because the former disappeared while the latter remained at 300 K[127]; ② two types of N_2 (a) one is an end group,[128] another one is a bridge type[129]; ③ two nitrogen atoms of an end group dinitrogen, as W–N≡N.[130]

It is more unanimous that the atomically adsorbed N (a) of nitrogen gives the peak of around 400 eV, e.g. 397.2 eV and 398.0 eV on W at 300 K,[127] 397.2 eV for N (a) on iron at 290 K[129] and 397.5 eV for N (a) on promoted iron at 673 K.[131] Surface science reviews have been published.[132]

(5) Mössbauer Spectroscopy (Mössb). In γ-ray irradiation, when the atomic nucleus is excited from the ground state to the excited state and then come back to the ground state, it will release γ-rays with high energy, which, through its path, will happen resonance and is absorbed by neighboring atomic nuclear. If these atoms are located on certain crystal lattice, because of the shackles by the lattice, this kind of absorption will not cause energy loss by recoil of atom. Mössbauer first found this resonance-absorption of the γ-ray without recoil, and further it was developed into a tool to study the microstructure of matters, such as the structure of active species, the function of promoter, particle size and adsorption state on surface in catalysts. It has been used to study the valence of metal, the interaction of active component with the support for heterogeneous catalysts, and so on. Example, these characteristics of A301 and A110-2 catalysts was studied by Mössbauer as shown in Table 3.22 in Chapter 3.[133]

(6) Magnetic Analysis and Electron Paramagnetic Resonance (EPR) Spectroscopy. Some metals and metal oxide catalysts have unique nature of magnetism because of their structure or d-orbit features. In general, these matters can be divided into paramagnetic, anti-magnetic and ferromagnetic according to whether they have unpaired electron pair and permanent magnetic moment. In the magnetic field, the

relationship between the magnetization extent (M) of matters and the intensity (H) of magnetic field can be expressed as:

$$M = \eta H, \tag{7.152}$$

where η is the magnetic susceptibility, $\eta < 0$ for anti-magnetic and $\eta > 0$ for paramagnetic or ferromagnetic.

To determine magnetization extent and magnetic susceptibility redound is the key to the understanding of the electronic structure of the catalysts or the adsorption state of reactants on the catalyst.

The unpaired electron in low-energe level for paramagnetic matter can absorb energy in the magnetic field and then can transit to high-energy level. It is called electron paramagnetic resonance (EPR) spectroscopy which is the method to record and investigate these adsorption spectra. The substances with different structure produce different spectral splitting factor (g factor). According to above information, the nature and structure of the active center of catalyst, the acid centers on surface and reaction intermediates can be understood.

(7) Fourier Transform Infrared spectroscopy (FTIR). Each molecule has its own vibration frequency which is accompanied by secondary oscillation, and can absorb and emit infrared radiation wave, which is so closely related with the frequency and intensity of vibration, as well as molecular weight, geometric shape, chemical bond, functional group in molecules. As a result, this infrared absorption spectrum is gradually becoming a useful technique to the study of surface chemistry, adsorption species of solid surface. It is widely used to study the solid acid, adsorption state and surface compounds, and further understanding of the catalytic reaction mechanism in catalysis field. Whether reflection or transmission spectrum is used, both of them have been explored extensively, in particular the use of specially designed absorption pool and sampling technology. At present, it can be used *in situ*, that is under conditions at a specific temperature, pressure during the reaction.

On the iron catalyst, the adsorbed state of nitrogen was studied by various instrumental and spectroscopic technologies. These adsorbed species observed at room temperature may be desorbed at high temperatures, but they may be short-lived intermediates in ammonia synthesis. Generally N_2 must be dissociated before the reaction with hydrogen. Hence, N (a), the main adsorbed species, is more important than N_2(a) in the reaction mechanism.[134] FTIR gives important information, for example, how N_2 is activated by surface and turned to the dissociated form of N(a). Although Ni used to be known as inactive metal in the chemisorption of N_2, an IR-active adsorbed dinitrogen was found on Ni/SiO_2 which disappeared on evacuation at 303 K. The adsorbed state was confirmed to be molecular as evidenced by the isotope shift (2,195, 2,160 and 2,123 cm^{-1} for $^{28}N_2{}^{29}N_2$ and $^{30}N_2$, respectively) and was assigned to Ni-N≡N^+. It was later found that the IR-active species is formed only when the size of the nickel particles on silica is in the range of 1.5 to 7.0 nm. The effect of particle size was interpreted as the concentration of "B5" sites (inverted square pyramid) was highest when the particle diameter ranged from 1.5 to 7.0 nm. Later on other metals similar IR-active species were found. Tesee bands were also shown to be diatomic by the isotopic balance and the first order kinetics of desorption. The high extinction coefficient associated with the adsorption bands, comparable to the value of chemisorbed CO, has given evidence for an end-on type of coordination rather than side-on type.[134]

The weak absorption was been formerly interpreted as an interaction with the electronic field on the metal surface,[135] but later findings disclosed a chemical nature of adsorption as suggested by: (1) a very high initial heat of adsorption ($50\,kJ\,mol^{-1}$) on Ni; (2) the fact that the larger change of wave number in IR band frequency; ③ the impact of hydrogen which makes a shift toward higher wave numbers.[136−138] The deviation from gaseous N_2 ($2{,}331\,cm^{-1}$) is a kind of measure of M–N bond strength in the case of metal surface. Such cases are seen on ZnO, zeolite, TiO_2, and ZrO_2.

Despite iron is well known as a dinitrogen-activated metal, analogous IR-active species observed on iron are formed by treatment with ammonia or N_2-H_2 mixture at high temperature. The adsorption strength, shown as the deviation of the wave number from that of gaseous N_2, is influenced by the co-adsorbed hydrogen on Co/Al_2O_3,[139] by the oxidized site of Rh on Al_2O_3, or by the diluent element in Pt on SiO_2.

A very stable and IR-active dinitrogen species which can be converted to ammonia by hydrogen treatment has been found on Ru–K/Al_2O_3 at $2020\,cm^{-1}$ by N_2 treatment above at 473 K.[140] $^{15}N_2$ gives rise to an isotopic shift to $1{,}997\,cm^{-1}$. Since IR absorption at $2{,}020\,cm^{-1}$ was also observed when ammonia was decomposed on Al_2O_3–K (without Ru) at 623 K, it was tentatively assigned to a new K–N_2 surface compounds. Therefore, it does not seem to be the intermediate but rather a side product on the surface. The spectra which might be due to the intermediate complex were observed on active Ru catalysts. The isotope balance confirms these species are end-on adsorbed species (Ru–N≡N). The wave numbers (cm^{-1}) are 1,910 for Ru–CsOH/MgO, 2268 for Ru/MgO, 2214 for Ru/Al_2O_3, 2240 for Ru/SiO_2. The deviations from the gas N_2 molecule are 421, 163, 117 and $111\,cm^{-1}$, respectively. This number is a measure of N_2 activation, N≡N bond looseness, and the extent of electron donation by the Ru atom which is interacting with the support or the promoter. Interestingly, the ammonia synthesis activity is ranged in this order. Although the life time of these species might be very short at the synthesis reaction conditions, the species might be a precursor of the disassociated state.

So far, no matter the determining technology of catalyst structure is improved from classic methods or developed and applied from new physical technology, the aim is to determine the structural characteristics of catalysts faster and more accurately and thus associate these structural characteristics with the performances of the catalyst, in an attempt to understand the nature of catalysis. Now a variety of methods have made many achievements, but either theoretical base or experimental technology need futher improvement, particularly to make them effectively functional under reaction conditions (*in situ*) is still a key issue. It is more important to reasonably combine these methods to take comprehensive test, and combined with the study of catalytic kinetics and surface chemisorption. The details are discussed in Sec. 2.1.3 of Chapter 2.

References

1. Wang SD, Sun JQ. *Introduction to Catalyst Engineering*, Beijing: Chemical Industry Press, 2001.

2. Yin YG. *Research Methods on Multiphase Catalysts*, Beijing: Chemical Industry Press, 1988.
3. Xin Q. *Research Methods on Solid Catalysts*, Beijing: Science Press, 2004.
4. Liu XR, *et al. Analysis and Characterization of Industrial Catalysts*, Beijing: China Petrochemical Press, 1990.
5. ZB G 74002 90.
6. Pernicone N, Ferrero F, Rossetti I, *et al. Appl. Catal. A: General*, **251**: 121–129, 2003.
7. Ying Y, editor in chief. *Research Method for Heterogeneous Catalysts*. Beijing: Chemical Industry Press, 1988, p. 333.
8. Zhejiang College of Chemical Engineering. In: Institute of Botany. Chinese Academy of Science, Chemical Modeling of Biological Nitrogen Fixation (unpublished communication), 1976.
9. Wang WX, *Industrial Catalysis*, Beijing: Chemical Industry Press, 1978.
10. Kobozev NJ, *Acta Physicochim* (USSR), **9**: 805, 1938.
11. Huang KH. In: Seigama T, Tanabe K (eds.) *Proc. 7th Intern. Congr. Catalysis*, Tokyo, Kodansha, Tok. 1981.
12. Spencer ND, Schoonmaker RC, Somorjai GA. *J. Catal.* **74**: 129–135, 1982.
13. Lu J. *Science Bulletin*, **20**(12): 540–543, 1975.
14. Ergun S. *Fluid Flow Through Packed Columns. Chem. Eng. Progr.* **48**: 89–94, 1952.
15. Li T, Gan L, Xu MS, *et al. Chemical Reaction Engineering and Technology.* **15**(4): 390–394, 1999.
16. ASTM D 4180 82.
17. ASTM D 4164 82.
18. UOP 254 65; UOP 294 66; UOP 563 82; UOP 778 81. *Laboratory Test Method for Petroleum and Its Products Universal Oil Products*, Des Plaines, IL, USA, 1984.
19. Kokes RJ. *Anal. Chem.* **32**: 446, 1960.
20. Liu HZ, Li XN. *J. Chem. Ind. Eng.* **48**(3): 354–362, 1997.
21. Xiang DH, Liu HY. *Practical Handbook on Fertilizer Catalysts*, Beijing: Chemical Industry Press, 1992.
22. Zhu BC. *Inorganic Chemical Reaction Engineering*, Beijing: Chemical Industry Press, 1981, 146–147.
23. Scott DS, Lee W, Papa. *J. Chem. Eng. Sci.* **29**: 2155–2176, 1974.
24. Kucera E. *J. Chromatogr.* **19**: 237–248, 1965.
25. Zhu Y, Li SS, Gao C, *et al. Computers and Applied Chemistry*, **15**(4): 237–242, 1998.
26. Li T, Zhu Y, Li SS, *et al. J. East China Univ. Sci. Tech.* **26**(3): 256–259, 2000.
27. Sing KSW. *Adv. Colloid. Interface Sci.* **77**: 3, 1998.
28. Wang NN, Zheng G, Cai XS. *China Powder Science and Technology*, **2**: 41, 1996.
29. Brunauer S, Mikhail RS, Boder E. *J. Colloid Interface Sci.* **24**: 451, 1967.
30. Hagymassy JJr, Brunauer S, Mikhail RSh. *J. Colloid Interface Sci.* **29**: 485, 1967.
31. Spitzer Z, Biba V, Kadlec O. *Carbon*, **14**: 151, 1976.
32. Horvath G, Kawazoe K. *J. Chem. Eng. Japan*, **16**: 470, 1983.
33. Dobruskin VK. *Langmiur*, **14**: 3847, 1988.
34. Tarazona P. *Phys. Rev.* **31**: 2672, 1985.
35. Liu XY, *et al.* (eds.) *Characterization of Industrial Catalyst*, Beijing: China Petrochemical Press, 1990, pp. 58–60.
36. Muller J. *Rev. Pure Appl. Chem.* **19**: 151, 1969.
37. Schütze J, Mahai W. *Topics in Catalysis*, **1**: 195–214, 1994.
38. Muetterties EL, Stein J. *Chem. Rev.* **79**: 479, 1979.
39. Kowalczyk Z, Jodzis S, Rarog W, *et al. Appl. Catal. A: General*, **184**: 95–102, 1999.
40. Della Betta RA. *J. Catal.* **34**: 57, 1974.
41. Taylor KC. *J. Catal.* **38**: 229, 1975.
42. Buyanova NE, Karnaukhov AP, Koroleva N, *et al. Kinet. Katal.* **13**: 1533, 1972.

43. Masthan SK, Chary KVR, Rao PK. *J. Catal.* **124**: 289, 1994.
44. Emmett PH, Brunauer S. *J. Am. Chem. Soc.* **59**: 1553–1564, 1937.
45. Nielsen A, Bohlbor H. *J. Am. Chem. Soc.* **74**: 963–966, 1952.
46. Emmett PH, Takezawa N. *J. Res. Inst. Catal. Hokkaido Univ.* **26**(1): 37–52, 1978.
47. Nielsen A. *Catal. Rev. Sci. Eng.* **23**(1&2): 17–51, 1981.
48. Streltsov OA, Dvornik OS, Lytkin VP. *Chem. Chem. Eng.* **20**(11): 1662–1666, 1977.
49. Liu HZ, Li XN. *Science in China* (Series B), **38**(5): 529–537, 1995.
50. Coulter Omnisorp 100/360 Series Operations Manual, 1992.
51. Altamira Instruments, Inc. AMI-1 Review Software Version 5.0 Operations Manual.
52. Liu HZ. *Chin. J. Catal.* **22**(3): 304–316, 2001.
53. Liu HZ, Li XN. *Chin. J. Catal.* **26**(1): 79–86, 2005.
54. Fagherazzi G, Canton P, Riello P, *et al. Langmuir*, **16**: 4539, 2000.
55. Benedetti A, Polizzi S, Riello P, *et al. J. Catal.* **171**: 345, 1997.
56. Pernicone N. *Cattech.* **7**(6): 196–204, 2003.
57. Liu HZ, Li XN, Shzyki S, *et al. J. Chem. Ind. Eng.* **51**(4): 462–467, 2000.
58. Arai M, Fukushima M, Nishiyama Y. *Appl. Surf Sci.* **99**: 145–150, 1996.
59. Amennomiya Y, Cvetanovic RJ. *Advances in Catalyts*, New York: Academic Press, 1967, 103–149.
60. Wang JX, Xie YF. *Chin. J. Catal.* **1**(3): 229–240, 1980.
61. Leary KJ, Michaels JN, Stacy AM. *AIChE J.* **34**(2): 263–271, 1988.
62. Yang SR. *Chin. J. Catal.* **4**(1): 57–65, 1983.
63. Yang SR. *Chin. J. Catal.* **6**(2): 179–182, 1985.
64. Duan X, Wang Q. *Chin. J. Catal.* **7**(2): 169–172, 1986.
65. Sun YH, Zhou LX, Chen S, *et al. Acta Petrolei Sinica* (Petroleum Processing Section), **6**(3): 25–31, 1990.
66. Tokoro Y, Ucijima T, Yoneda Y. *J. Catal.* **56**: 110–118, 1979.
67. Viawanath Y, Schmidt LD. *J. Chem. Phys.* **59**: 4184, 1973.
68. Falconer JL, Schwarz JA. *Catal. Rev. Sci. Eng.* **25**(2): 141–227, 1983.
69. Hurst NM, Gentrey SJ, Jonnes A, *et al. Catal. Rev. Sci. Eng.* **24**(2): 233–309, 1982.
70. Liu HZ, Liu CB, Li XN, *et al. Ind. Eng. Chem. Res.* **42**(7): 1347–1349, 2003.
71. Guan S, Liu HZ. *Ind. Eng. Chem. Res.* **39**(8): 2891–2895, 2000.
72. Madix R. *J. Catal. Rev.-Sci. Eng.* **15**(2): 293–329, 1977.
73. Tsuchiya S, Amenomiya Y, Cvetanovic RJ. *19th Canadian Chem Eng Cong, 3rd Symposium on Catalysis*, **1**: 49, 1969.
74. Popova NM, Babenkova LV. *React. Kinet. Catal. Lett.* **11**(2): 187–192, 1979.
75. Malet P, Caballere A. *Chem. Soc. Farad. Trans. I.* **84**(7): 2369–2375, 1988.
76. Wu ZG. Copper-based methanol synthesis catalyst to enlarge the pilot prepared by acid — base alternately deposition, Dissertation,. Hangzhou: Zhejiang University of Technology, 2007.
77. Pernicone N, Fantinel T, Baldan C, *et al. Appl. Catal. A: General*, **240**: 199–206, 2003.
78. Lin LW, Zhang T, Zang JL, *et al. Appl. Catal.* **67**: 11–23, 1990.
79. Amoldy T, van den Heukant JAM, de Bok GD, *et al. J. Catal.* **92**: 35–55, 1985.
80. Розанов ВВ, Скляров АВ, Кин и Кат, **19**: 1533, 1978.
81. Young RA. *The Rietveld Method*, Oxford: Oxford University Press. 1995, Version 5.
82. Chen LS. Iron compounds Preparation, Characterization and CO, CO_2 reactivity: Dissertation. Hangzhou: Zhejiang University. 2002.
83. Zhou SQ. *Principle, Methods and Applications of X-ray Diffraction Analysis*, Chongqing: Chongqing University Press, 1991, 3.
84. Li XF. Element doping Wustite micro-structure, structural stability and macroscopic properties: Dissertation. Hangzhou: Zhejiang University of Technology, 2006.

85. Greenwood NN, Howe A. *J. Chem. Soc. Dalto Trans.* **1**: 116–121, 1972.
86. Pei GW, *et al. X-ray Diffraction of Single Crystal, Polycrystalline and Amorphous Materials*. Jinan: Shandong University Press, 1989.
87. Zheng YF. Applied research of XRD microstructure analysis in melt iron ammonia synthesis catalyst and nano-materials: Dissertation. Hangzhou: Zhejiang University, 2007.
88. Rietveld HM. *Acta Crystallogr.* **22**: 151–152, 1967.
89. Malmros G, Thomas OJ. *J. Appl. Crystallogr.* **10**: 7–11, 1977.
90. Young RA, Mackie PE, Dreele RB V. *J. Appl. Crystallogr.* **10**: 2629, 1977.
91. Howard CJ, Hunter BA. A computer program for Rietveld analysis of X-ray and neutron powder diffraction patterns, Lucas Heights Research Lab, Australia, 1997.
92. Hill RJ, Howard CJ. *J. Appl. Cryst.* **20**: 467, 1987.
93. Brown ID. *Acta Crystallogr.* **B32**: 1957, 1976.
94. Romeijn FC. *Philips. Res. Rep.* **8**: 304, 1953.
95. Rachinger WAJ. *Sci. Instrument*, **25**: 254, 1948.
96. Keijser Th H De, Langford JI, Mittemeijer EJ, *et al. J. Appl. Cryst.* **15**: 308, 1982.
97. Topsoe H, Topsoe M, Bohlbro H, Dumesic JA. *Proceedings 7th International Conference on Catalysis*, Tokyo, 1981, p. 247.
98. Stoltze P, Norskov J. *Phys. Rev. Lett.* **55**: 2502, 1985.
99. Hosemann R, Preisinger A, Vogel W. *Ber Bunsenges Phys. Chem.* **70**(8): 796–802, 1966.
100. Hosemann R, Bagchi SN. *Direct Analysis of Diffraction by Matter*, Amsterdam: North Holland Publishing Company, 1962.
101. Fischer A. Ph.D. Thesis. FU Berlin. 1979.
102. Fischer A, Hosemann R, Vogel W, Kouteck J, Ralek M. *International Congress on Catalysis*, Tokyo, Preprint A 22. 1980.
103. Borghard WS, Boudart M. *J. Catal.* **80**(1): 194–206, 1983.
104. Topsoe H, Dumesic JA, Boudart M. *J. Catal.* **28**(3): 477–488, 1973.
105. Ludwiczek H, Preisinger A, Fischer A, *et al. J. Catal.* **51**(3): 326–337, 1978.
106. Niemann W, Clausen BS, Topsoe H. *Bunsen ges Phys. Chem.* **91**(11): 1292–1296, 1987.
107. Schlögl R. In: Jennings JR (ed.) *Catalytic Ammonia Synthesis Fundamentals and Practice*, New York: Plenum Press, 1991, 41.
108. Lendzion B Z, Arabczyk W. *Appl. Catal. A: General*, **207**(1&2): 37–41, 2001.
109. Herzog B, *et al. Appl. Catal. A: General*, **141**(1&2): 71–104, 1996.
110. Pattek-Janczyk A, *et al. Solid State Ionics*, **117**(1&2): 95–103 , 1999.
111. Pattek-Janczyk A, Miczko B. *Solid State Ionics*, **58**(3&4): 249–259, 1992.
112. Pattek-Janczyk A. *Appl. Catal. A: General*, **124**(2): 267–280, 1995.
113. Li XN, Liu HZ. *Chin. J. Catal.* **20**(1): 76–80, 1999.
114. Ludwiczek H, Preisinger A, Fischer A, Hosemann R, Sch ∼ Snfeld A, Vogel W. *J. Catal.* **80**: 194, 1978.
115. Schlögl R. In: Jennings JR (ed.) *Catalytic Ammonia Synthesis Fundamentals and Practice*, New York: Plenum Press, 1991.
116. Rayment T, Schlögl R, Thomas JM, Ertl G. *Nature*, **315**: 311, 1985.
117. Ertl G, Huber M, Thiele N. *Z. Naturforsch.* **34a**: 30, 1979.
118. Strongin DR, Bare SR, Somorjai GA. *J. Catal.* **103**(2): 289–301, 1987.
119. Homann K, Kuhlenbeck H, Freund HJ. *Surf Sci.* **327**(3): 216–224, 1995.
120. Somorjai GA, Materer N. *Topics in Catalysis*, **1**(3&4): 215–221, 1994.
121. Somorjai GA, Materer N. *Topics in Catalysis*, **1**(3&4): 228, 1994.
122. Natter H, Schmelzer M, Loffler MS, *et al. Materials Science Forum*: 683–688, 2000.
123. Natter H, Schmelzer M, Loffler MS, *et al. J. Phys. Chem. B*, **104**(11): 2467–2476, 2000.

124. Aika KI, Tamaru K. In: Nielsen A (ed.) *Ammonia Catalysis and Manufacture*. Chapter 3, Springer, Heidelberg, 1995, 139–143.
125. Mahnig M, Schmidt LD. *Z. Phys. Chem.* (NF). **80**: 71, 1972.
126. Madey T, Yates JT Jr, Erickson NE. *Surf Sci.* **43**: 526, 1974.
127. Brundle CR. *J. Vac. Sci. Tech.* **13**: 301, 1976.
128. Kishi K, Roberts MW. *Surf Sci.* **62**: 252, 1977.
129. Fuggle Jc, Menzel D. *Vak. Tech.* **27**: 130, 1978.
130. Ertl G, Thiele N. *Appl. Surf Sci.* **3**: 99, 1979.
131. Kunimori K, Kawai T, Kondow T, *et al. Surf Sci.* **54**: 525, 1976.
132. Liu HZ, Ning WS, Fu GP, *et al. J. Chem. Ind. Eng.* **50**(5): 671–677, 1999.
133. Egerton TA, Sheppard N. *J. Chem. Soc. Farad. Trans.* **170**: 1357, 1974.
134. Hardeveld RV, Montfoort AV. *Surf Sci.* **4**: 396, 1966.
135. Eischens RP, Jacknow J. In: Sachtler WHM, *et al* (ed.) *Proc. 3rd Intern. Congr. Catal.* Amsterdam: North Holland Publisher, 1965, 627.
136. Hardeveld RV, Montfoort AV. *Surf Sci.* **17**: 90, 1969.
137. Borodko YG, Lyutov VS. *Kinet. Katal.* **12**: 238, 1971.
138. Kinoshita K, Kido K, Domen K, *et al. J. Chem. Soc. Farad. Trans.* **182**: 2269, 1986.
139. Oh-kita M, Aika K, Urabe K, *et al. J. Catal.* **44**: 460, 1976.
140. Oh-kita M, Aika K, Urabe K, Ozaki A. *J. Chem. Soc. Chem. Commun.* 147, 1975.

This page intentionally left blank

Chapter 8

Performance and Application of Catalysts

The iron catalysts for ammonia synthesis have been discussed for over a century, and the topic continues to be researched and improvised all over the world owing to their tremendous economic benefits and potential energy-saving characteristic. If the catalytic activity is only increased by 1% NH_3 (one percent), ammonia productivity can be enhanced by 7% to 10% in modern plants. As China annually produces 53 million tons of ammonia, an increase of 1% catalytic activity will increase ammonia production by about 5 million tons. This is equivalent to the productivity of ten ammonia plants with a capacity of 1,000 t/d, resulting in a great saving. However, the catalysts have steadily improved in the last century so much so that it is extremely difficult to increase their activity further even by 0.5% to 1%. It took 40 years from 1950s to 1990s in China to raise the activity of A106 catalyst to A202 catalyst by 2%–3%. The performance of the catalyst is influenced significantly by the conditions under which it is used in the ammonia production process and with proper operation and maintenance. The catalyst works economically only with the correct selection of process conditions, strict management and appropriate operations.

The ammonia synthesis reaction is affected by many factors. The fundamental basis of choosing process conditions is the thermodynamics and kinetics of the ammonia synthesis reaction, and the activity of the catalyst. In selecting the optimum conditions, it is necessary to consider many factors including thermodynamics, reaction kinetics, yields, and energy consumption. Both the process and the equipment need to be considered, all of which must be subjected to the constraints of the catalyst.[1]

It is well known that the yields (space-time yields) of ammonia can be calculated by (8.1) according to the mass balance of ammonia for reactor.

$$y = \frac{17.03}{22.414} V_{in} \frac{\varphi - \varphi_0}{(1+\varphi)} = 0.7600 S_V V_K \frac{\Delta\varphi}{(1+\varphi)} \tag{8.1}$$

$$y' = 0.7600 S_V \frac{\Delta\varphi}{(1+\varphi)}, \tag{8.2}$$

where y is the yield of ammonia, $kg{\cdot}h^{-1}$; y′ is the space time yield of ammonia, $kg{\cdot}h^{-1}{\cdot}m^{-3}$ (catalyst); V_{in} is the gas flow rate in inlet of converter, $m^3{\cdot}h^{-1}$; S_V is the space velocity, h^{-1}; V_K is the volume of catalyst, m^3; φ_0, φ is the ammonia concentrations in inlet and outlet of converter, %; $\Delta\varphi$ is the net value of ammonia concentrations, %, i.e. $\Delta\varphi = \varphi - \varphi_0$; 17.03 is the molar mass of ammonia; 22.414 is the molar volume of gas, $Liter{\cdot}mol^{-1}$.

Equation (8.2) is the reaction rate based on unit volume of catalyst. The reaction rate based on the mass of catalyst can be calculated as follows:

$$r = \frac{S_V V_K}{22.414 W_r} \cdot \frac{\varphi - \varphi_0}{(1+\varphi)}, \tag{8.3}$$

where r is the reaction rate, $\text{mol}\cdot\text{g}^{-1}\cdot\text{h}^{-1}$; W_r is the mass of reduced catalyst, g.

The above equations show that the production of ammonia depends on the inlet gas flow rate, the concentration of ammonia at the outlet and the net values of ammonia at the inlet and outlet of the converter. The production increases with increasing V_{in} and φ and φ_0 from (8.1). The concentration (φ) of ammonia at the outlet is related to the pressure (p), temperature (T), space velocity (S_v), H_2/N_2 ratio, content of inert gases (φ_i), type (M), volume (V_k), particle size (d_p) and reduction (R) of catalyst, gas purity (N), and the concentration of ammonia at the reactor inlet (φ_0). These factors can be expressed by the function below.

$$\varphi = f(p, t, S_V, H_2/N_2, \varphi_i, M, V_K, d_p, R, N, \varphi_0) \tag{8.4}$$

This chapter discusses how these factors affect the ammonia concentration at the reactor outlet, as well as how to choose the optimum operating conditions.[2–5] The effect of reduction (R) had been discussed in detail in Chapter 5.

8.1 Activity of catalysts

8.1.1 *Reaction pressure*

Ammonia synthesis is a volume-reduced reaction. In view of the thermodynamics and kinetics of the reaction, the reaction rate can be enhanced by raising the reaction pressure. Therefore, the reaction pressure should be chosen according to the catalytic activity. Figure 8.1 illustrates the relationship between activity and pressure. Figure 8.2 shows the effect of pressure on the activity of A301 catalyst.[3]

From Figs. 8.1 and 8.2, it is seen that the relationship between the activity (ammonia concentration of outlet) and reaction pressure is linear: the higher the pressure, the higher would be the concentration of outlet ammonia. It should be noted that in industrial applications the effective adopted catalyst with higher catalytic activity can be reached by either increasing the concentration of outlet ammonia under the same pressure, or decreasing the pressure with the same outlet ammonia concentration but it is not possible to give satisfaction to both conditions concurrently. Either one of these factors can increase ammonia production and reduce energy consumption. It should be noted that there is a certain relationship between temperature and pressure. Our research results show that the effect of a 25 degree Kelvin temperature is equivalent to 5 MPa of pressure, i.e., a drop of 25 K of temperature at the same pressure is equivalent to reduce 5 MPa of pressure at the same temperature. However, energy-saving is higher and more economical by reducing pressure than by reducing temperature.

It is seen from Fig. 8.2 that the outlet ammonia concentration on A301 catalyst at 15 MPa, 400°C and $0.6 \times 10^4\,\text{h}^{-1}$ achieved 26%, indicating A301 (ZA-5) is an excellent catalyst at low-temperature and low-pressure for ammonia synthesis.

The general aim of optimizing the process is to realize ammonia synthesis at lower pressures. This objective is achieved within the realm of feasible

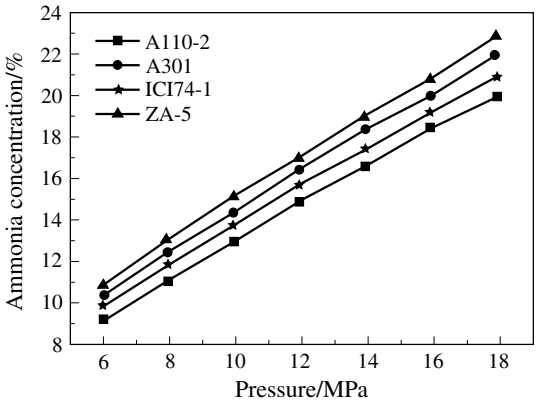


Fig. 8.1 Relationship between the activity of ZA-5, A301, ICI74-1, A110-2 and pressure ($t = 425°C$, $S_v = 20000\,h^{-1}$, $H_2/N_2 = 3.0$)

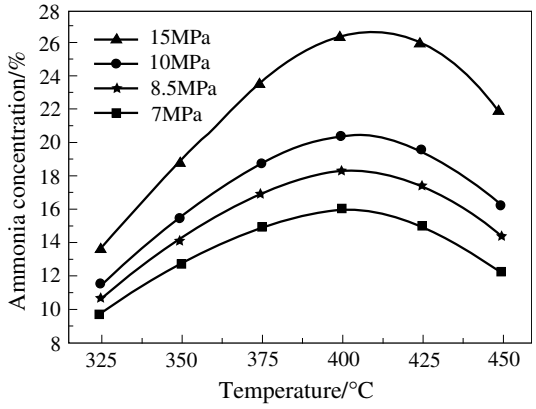


Fig. 8.2 Effect of temperature on the outlet ammonia concentration on A301 catalyst at different pressure ($S_V = 0.6 \times 10^4\,h^{-1}$, $H_2/N_2 = 3.0$)

thermodynamics, kinetics (catalyst), compression techniques, and related issues of chemical reaction engineering. Thermodynamics, being the basis for the possibility of a reaction, plays a guiding role in chemical reactions. Table 8.1 shows the equilibrium concentration of ammonia at different pressures and temperatures for H_2:N_2 = 3:1. The data in the table shows that it is possible to operate at lower than 10 MPa or even 3 MPa; but a lower temperature, such as lower than 350°C is needed. In other words, the loss in the equilibrium of ammonia concentration resulting from decreasing pressures can be compensated by reducing the temperature. The key is to develop good catalysts with a high activity at low temperature. With the development of catalyst technology, in particular the successful development of new $Fe_{1-x}O$-based catalysts and Ru-based catalysts, ammonia synthesis at a lower pressure is no longer a dream.

On the other hand, the author believes that from the view of dynamics, the ammonia synthesis pressure is determined by the volume of catalyst (contact time); i.e., the loss in the equilibrium of ammonia concentration caused by decreasing

Table 8.1 Equilibrium concentration of ammonia/% ($H_2/N_2 = 3{:}1$, $CH_4 + Ar\ (He) = 0$)

	Pressure/MPa								
Temperature/°C	3	5	7	10	12	15	20	25	30
300	30.20	39.39	45.81	52.80	56.39				
325	23.30	31.74	37.96	44.97	48.68	53.30	59.36		
350	17.72	25.13	30.87	37.61	41.24	45.93	52.17	57.16	
375	13.37	19.63	24.73	30.95	34.43	38.95	45.15	50.24	54.54
400	10.07	15.23	19.61	25.15	28.34	32.57	38.54	43.54	47.86
425	7.60	11.78	15.45	20.26	23.10	26.94	32.50	37.28	41.48
450	5.78	9.12	12.15	16.23	18.70	22.11	27.15	31.59	35.57
475	4.43	7.10	9.57	12.98	15.09	18.05	22.53	26.56	30.24
500	3.43	5.56	7.56	10.39	12.17	14.71	18.62	22.21	25.54

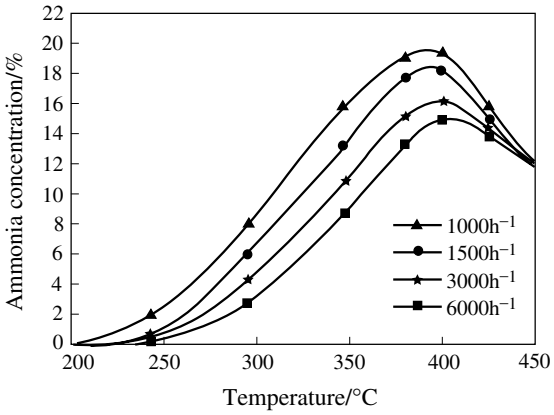


Fig. 8.3 Effect of space velocity on activity of ZA-5 catalysts at 7.0 MPa and $H_2/N_2 = 3.0$

pressures also can be compensated by increasing the volume of catalyst. Precisely,, it depends on the thermodynamic equilibrium temperature of reaction. Figure 8.3 shows the activity of ZA-5 catalyst at a low space velocity, which illustrates that the ZA-5 has activity starting at 200°C. The ammonia concentration at the reactor outlet reaches beyond 18% at 7.0 MPa, 375–400°C and 1000–1500 h^{-1}. Therefore, increasing the volume of catalyst can reduce space velocity, increase the ammonia concentration at the outlet and realize the aim of reducing pressure. For example, there are now converters in which the volume of catalyst have been increased from about 60 m^3 to about 120–140 m^3, with a simultaneous reduced pressure from 15 MPa to 10 MPa and below. Gradually reducing reaction pressure is a trend in the ammonia synthesis industry.

However, in China the pressure of small to medium ammonia plants still exceed 30 MPa; and the energy consumption of ammonia production is about 50% higher than the average international level. Such a situation is not consonant with the trend of development in the ammonia synthesis industry. Ironically, it is China that has already developed high activity catalysts that operate at low temperature and

Table 8.2 Activities of A301 catalyst at low temperature and low pressure/%

Pressure/MPa	Space velocity/h^{-1}	Temperature/°C		
		425	400	375
3	3000	7.59	8.81	8.87
3	5000	7.52	8.52	8.25
5	5000	11.67	13.08	12.65

Table 8.3 Activities of ZA-5, A301, ICI74-1 and A110-2 catalyst

Catalysts	Outlet concentration of ammonia (15.0 MPa and $3 \times 10^4\ h^{-1}$)/NH_3%								
	500°C	475°C	450°C	425°C	400°C	375°C	350°C	325°C	300°C
ZA-5	15.09	17.36	19.15	18.51	16.68	13.75	10.13	5.92	1.20
A301	14.90	17.10	18.12	17.36	15.20	12.75	8.99	4.89	0.80
ICI74-1	14.83	16.87	17.70	16.45	14.65	12.02	8.27	4.30	0.74
A110-2	14.51	16.30	16.90	15.47	13.20	10.13	6.61	2.95	0.15

low pressure, e.g. A301 (Table 8.2) and ZA-5 catalysts. The best catalysts are used in the worst process. Therefore, the author and colleagues[6] proposed that small and medium ammonia plants in China should reduce their reaction pressure from 30 MPa to 10 MPa, thereby reducing the energy consumption. In fact, the A301 and ZA-5 catalysts completely possess the appropriate optimum reaction conditions and are able to meet the synthesis requirements.

8.1.2 *Reaction temperature*

Increase of reaction temperature on one hand accelerates the reaction speed; but on the other hand, decreases the equilibrium ammonia concentration. The change of temperature affects the total rate of ammonia synthesis positively and negatively. Therefore there is an optimum reaction temperature at which the reaction velocity is the fastest and the synthesis efficiency is the highest.

8.1.2.1 *Active temperature of catalyst*

The ammonia synthesis reaction temperature depends on the active temperature of catalyst; hence the process operator should know the active temperature of catalyst. Tables 8.3 and 8.4, and Fig. 8.4 show the relationships between the activity and temperature of ZA-5, A301, ICI74-1 and A110-2 catalysts.

Table 8.3 showed that the activity of ammonia synthesis catalyst was increased to a large extent. For example, the activities of ZA-5 catalyst reach 19.15%, 18.51%, 16.68%, 13.75%, 10.13%, 5.92% and 1.20% at 450°C, 425°C, 400°C, 375°C, 350°C, 325°C and 300°C (equivalent to 30.78% at 30.0 MPa, $3 \times 10^4\ h^{-1}$ and 450°C, breakthroughs 30%) at the conditions of 15.0 MPa, $3 \times 10^4\ h^{-1}$, respectively. Compared with A110-2, the ammonia concentrations are 2.25%, 3.04%, 3.48%, 3.62%, 3.52%, 2.97% and 1.05% higher, and the relative activities increase by 13.31%, 19.65%, 26.36%, 35.74%, 53.25%, 100.7% and 700%, respectively.

Table 8.4 Activities of ZA-5 and A110-1 industrial catalysts

Catalysts	NH_3% (400°C)
ZA-5	15.20
A110-1	11.61

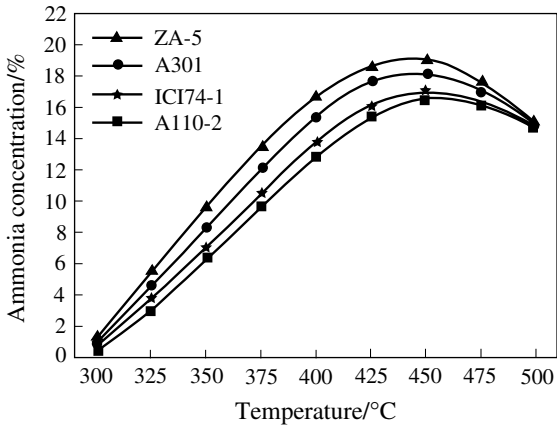


Fig. 8.4 Relationships between activity and temperature of ZA-5, A301, ICI74-1 and A110-2

Table 8.4 gives the activity of ZA-5 and A110-1, which are both produced and tested by Nanjing Chemical Industrial Group Co., Ltd. Table 8.4 indicates that the ammonia concentration at the outlet of a reactor using the ZA-5 is 3.59% higher than that of A110-1, which corresponds to an increase of 30.92% in catalytic activity.

Under the conditions listed in Table 8.3, the activity is close to the equilibrium ammonia concentration above 475°C, so the differences of activity between different catalysts become small. However, at lower temperatures, especially at 350–450°C, the activity of ZA-5 is dramatically higher compared with that of A110-2. During the design of the reactor and practical operations, the temperature of the catalyst bed should be set within the optimum range of temperatures of the catalyst.

According to Table 8.3, to maintain the same ammonia concentration at the outlet, the active temperatures of different catalysts are shown in Table 8.5. The table shows that when achieving the same ammonia concentration at the outlet (16.68%), the active temperature of ZA-5 is 30°C or 40°C lower than that of ICI74-1 and A110-2 respectively. The activity of ZA-5 at 400°C is equivalent to that of the A110-2 at 440°C and ICI74-1 at 430°C respectively. In other words, if the reaction temperature of ZA-5 catalyst is reduced by say 40°C, it would still achieve the same ammonia concentration at the outlet as A110-2 could at 440°C. We call this effect the "temperature effect". The initial hotspot temperature (the highest temperature point in beds) of ZA-5 catalyst bed is 430–450°C, and the operational temperature range is 300–500°C. Therefore, ZA-5 is an excellent catalyst that could be used at a low temperature and within a wide temperature range.

Table 8.5 Active temperature of ZA-5, A301, ICI74-1 and A110-2 catalysts/°C

NH_3 %	18.5	16.7	13.8
ZA-5	425	400	375
A301	450	415	388
ICI74-1	—	430	400
A110-2	—	440	405

8.1.2.2 *The optimum reaction temperature*

Ammonia synthesis is a reversible and exothermic reaction without any side reaction. With the rising of temperature the reaction rate constant increases while the equilibrium constant decreases. For a given reactant composition, the reaction rate is affected by two contradictory factors; thus there exists an optimum reaction temperature.

$$\begin{aligned} r_A &= k_1 f_1(y) - k_2 f_2(y) \\ &= k_1 f_1(y) \left[1 - \frac{k_2 f_2(y)}{k_1 f_1(y)}\right] = k_1 f_1(y) \left[1 - \frac{f_2(y)}{K_y f_1(y)}\right] \end{aligned} \tag{8.5}$$

In a lower temperature range, the equilibrium constant K_y is larger, and the temperature has a marked effect on the reaction rate constant k_1. However, as the temperature is gradually increased, the reversible exothermic reaction equilibrium constant K_y is decreased. The value in the square brackets in equation (8.5) is reduced, with the effect of temperature on reaction rate decreased too. When the temperature reaches a certain point, the effect of temperature on reaction rate becomes zero. Under continuously rising temperature, the impact of temperature on the equilibrium constant reverses, the reaction rate reduced when the temperature increases. That is, for a given composition of reactants, at a low temperature range $(\frac{\partial r_A}{\partial T})_y > 0$. When the temperature reaches a certain value with $(\frac{\partial r_A}{\partial T})_y = 0$, the reaction rate reaches a maximum, which is the optimum temperature under this certain composition. After that, $(\frac{\partial r_A}{\partial T})_y < 0$ with the temperature continues increasing.

When the reaction is controlled by process dynamics, the optimum temperature curve of the reversible exothermic reaction (without any side reaction) can be obtained according to the kinetic equation using the common method that for finding the extremum.

$$r_A = k_1 f_1(y) - k_2 f_2(y) = k_{10} e^{-\frac{E1}{RgT}} f_1(y) - k_{20} e^{-\frac{E2}{RgT}} f_2(y), \tag{8.6}$$

where E_1, E_2 are the activation energies of the forward and reverse reactions respectively, $\mathrm{kJ \cdot mol^{-1}}$; and k_{10}, k_{20} are the frequency factors of positive and reverse reactions respectively.

When the composition of the reactants is fixed, differentiating r_A with respect to T, T_m being the optimum temperature, leads to the following equation:

$$f_1(y) k_{10} \left(\frac{E_1}{R_g T_m^2}\right) \exp\left(-\frac{E_1}{R_g T_m}\right) - f_2(y) k_{20} \left(\frac{E_2}{R_g T_m^2}\right) \exp\left(-\frac{E_2}{R_g T_m}\right) = 0$$

i.e

$$\frac{E_1}{E_2} \exp\left(\frac{E_2 - E_1}{R_g T_m}\right) = \frac{f_2(y) k_{20}}{f_1(y) k_{10}}.$$

In addition, when the reaction reaches equilibrium, $r_A = 0$, the equilibrium temperature is T_e, then,

$$f_1(y)k_{10}\exp\left(-\frac{E_1}{R_gT_e}\right) - f_2(y)k_{20}\exp\left(-\frac{E_2}{R_gT_e}\right) = 0$$

Combining the above two equations

$$\frac{E_1}{E_2}\exp\left(\frac{E_2 - E_1}{R_gT_m}\right) = \exp\left(\frac{E_2 - E_1}{R_gT_e}\right)$$

After simplification,

$$\frac{E_2 - E_1}{R_g}\left(\frac{1}{T_m} - \frac{1}{T_e}\right) = \ln\left(\frac{E_2}{E_1}\right)$$

The optimum reaction temperature $\mathrm{T_m}$ can then be obtained:

$$T_m = \frac{T_e}{1 + \frac{R_gT_e}{E_2 - E_1}\ln\frac{E_2}{E_1}} \tag{8.7}$$

where $E_2 - E_1 = (-\Delta \mathrm{H_R})$ is the heat of reaction, $\mathrm{kJ{\cdot}mol^{-1}}$, $(-\Delta \mathrm{H_R}) = 49.110 + 0.01163 \times \mathrm{t_r}$, at 15 MPa, t_r being the reaction temperature in °C. According to (8.7), the relation between the optimum temperature and the equilibrium temperature can be calculated for a given catalyst under a certain gas composition. In order to obtain the optimum temperature curve, we need the equilibrium curve for the relationship between the equilibrium temperature and the composition of reactants. Figure 8.5 shows the optimum temperature curve of ammonia synthesis reaction.

Equation (8.7) indicates that the optimum reaction temperature T_m is related to equilibrium temperature T_e and performance of catalyst i.e., activation energy of E_1, E_2 for forward and reverse reactions. The optimum temperature is indirectly affected by both the pressure and contents of inert gas in the reactants because the equilibrium temperature is affected by both.

Large size catalysts in a reactor have a great influence on diffusion in the pore. Under such conditions, the values of optimum reaction temperature should be modified, as the values will be smaller than the ones calculated by the above equation.[7]

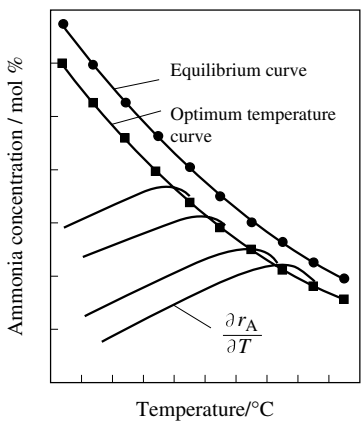


Fig. 8.5 Optimum temperature curve of ammonia synthesis reaction

Table 8.6 Optimum reaction temperatures of A301 and A110-2 catalysts

Temperature (T_r)/°C	A301 (15 MPa, 30000 h^{-1})			A301 (7.0 MPa, 6000 h^{-1})			A110-2 (15 MPa, 30000 h^{-1})		
	E_2 = 164.25 kJ·mol^{-1}			E_2 = 162.565 kJ·mol^{-1}			E_2 = 173.85 kJ·mol^{-1}		
	φ_{NH_3}	T_e/°C	T_m/°C	φ_{NH_3}	T_e/°C	T_m/°C	φ_{NH_3}	T_e/°C	T_m/°C
475	16.97	481.6	437.0	—	—	—	16.09	489.1	447.7
450	18.12	472.3	429.0	12.20	440.3	400.2	16.45	486.0	445.1
425	17.59	476.5	432.9	14.58	418.6	381.0	15.34	495.9	454.1
400	15.20	497.2	451.3	15.22	413.4	376.5	12.80	521.7	477.3
375	11.80	533.5	483.6	14.21	421.7	384.0	9.63	563.4	514.5
350	8.07	590.2	533.5	11.34	449.2	408.6	6.38	627.4	571.2

Note: T_r, T_e and T_m are the temperatures of activity testing, equilibrium temperature and optimum reaction temperature, respectively. Activity data in the Table are from author's laboratory.

The optimum temperatures of A301 and A110-2 catalysts are shown in Table 8.6. The activation energies are calculated according to the data in Table 8.3, the intrinsic kinetics of reaction and the heat of reaction.

It can be seen from the table that the optimum temperature of A301 catalyst is 437–484°C at 15 MPa and 376–410°C at 7 MPa, which is 10–31°C lower than that of A110-2 (448–515°C) at 15 MPa.

8.1.2.3 *Realization of the optimum reaction temperature curve*

Since reversible exothermic reactions have an optimum temperature, if the whole process is conducted along the optimum temperature curves, the reaction rate will be highest, and the loading of catalyst is minimized for a given production rate. Therefore, selecting the distribution of temperature in the catalyst bed in accordance with the optimum temperature is a basic requirement for reactor design and a means of evaluating reactor quality.[7,8] However, it is hard to fully realize the requirement in a practical reactor, because the reaction speed is very high initially and restricted by external conditions, which render it either impossible or unnecessary to achieve the optimum temperature. The ammonia concentration increases as the reaction continues. When the ammonia concentration approaches the equilibrium value, it is difficult to achieve the optimum reactive temperature. Therefore, it is necessary to depend upon the configuration of the reactor and the reaction conditions to reach this requirement as much as possible.

In order to conduct the reactions along the optimum reactive temperature curve, the heat of reaction must be removed from the catalyst bed, and to reduce the reaction temperature (to recover the extracted heat).

Regardless of the configuration of ammonia converters and their diameters, there are only two modes of heat extraction from the catalyst bed: *in situ* heat-exchange or external heat-exchange. The former is called fixed bed with continuous heat exchange: the reactor has only one bed housing all the catalysts, and is called a "cold-type reactor" (Fig. 8.6). The latter is called an adiabatic fixed bed reactor: the reactor consists of two or more beds of catalyst, with heat exchange between the beds (Fig. 8.7).

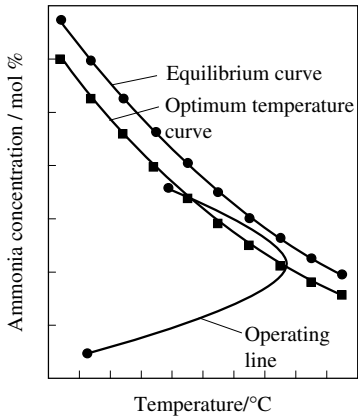


Fig. 8.6 Optimum operating line of temperature at the continuous heat-exchange reactor

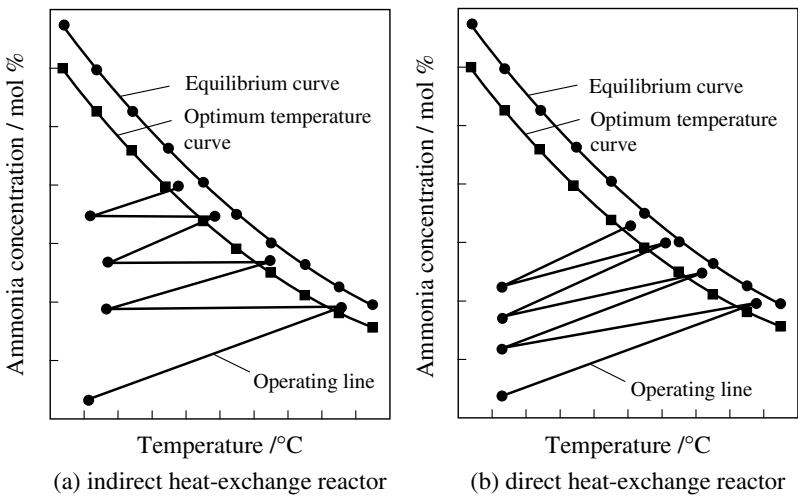


Fig. 8.7 Optimum operating line of temperature of the adiabatic fixed-bed reactor

In the continuous heat-exchange catalytic reactor, the reaction processes are conducted along with the heat-exchange processes. It is called a cooled-type reactor with many cooling pipes set parallel to the axes of reactor in the catalyst bed providing surfaces to exchange heat between the reactive gas and the 'coolant'. If the catalyst is located inside the pipes, and boiling water is used as coolant outside the pipes, with steam as a by-product, the reactor is called the "external cooled bed". In order to enhance loading of catalysts in the high pressure reactor vessel, in an "internal cooled bed" reactor, the coolant flows inside the pipes. This is called a "cold pipe converter", an example is the single-pipe retracing-flow converter of Zhejiang University of Technology. To enhance the circulation of boiling water coolant, the "external cooled bed" loads the catalyst inside the pipes and the boiling water flows

outside the pipes, making the reactor a shell-and-tube configuration. The "External cooled bed" is frequently used for synthesis of basic organic chemicals, such as methanol. On the catalyst bed in a continuous heat-exchange reactor, especially in the bottom part of the catalyst bed, there is always an adiabatic layer. Reactive gas enters the bed of catalyst at a relatively low temperature (but higher than the initial active temperature of catalyst), and carries out the adiabatic reaction, producing the heat of reaction increasing the bed temperature reaching to around the optimum temperature curve. Then in the cooling section, in order to reach the optimum temperature curve, the heat is removed by the cooling medium. Although the initial temperature of adiabatic reaction is far away from the optimum reaction temperature curve, (as the initial reaction is also far away from the equilibrium reaction), the reaction rate is much higher than that later, and the volume of catalyst required is not too much. This not only reduces the heat-exchange area for preheating the reactant gas but also makes it easy to control the temperature of catalyst bed, so that the temperature will not exceed the heat-resistant temperature of the catalyst. During the course of ammonia synthesis, when the content of ammonia in the reaction mixture is very low, but the corresponding optimum temperature is very high, the heat-resistant temperature of the catalyst is always exceeded. Under such circumstances, there is no point in reacting along with the optimum temperature curve. The temperature in the lower part of a continuous heat-exchange bed is always too low, and especially the catalyst at the bottom of the reactor cannot be completely reduced during the reduction process.

In adiabatic multi-bed reactors, the reaction and heat transfer process are separated, with adiabatic reaction in the beds, and heat transfer between beds. The so-called multi-bed refers to repeated adiabatic reaction alternating with heat exchange in turn, so that the whole process is as close as possible to the optimum temperature curve (Fig. 8.7). According to the different methods of heat exchange between beds, adiabatic multi-bed reactors can be divided into direct heat exchange between beds (cold-quench), indirect heat exchanger between beds, and combination of the two. The heat exchange between the beds for the indirect heat exchange reactor is achieved in a space-wall heat exchanger, such as the Topsøe S-200 type for the ammonia synthesis converter of the Fotherby-Montecatini company.

Heat exchange in multi-bed direct heat exchange reactor is by directly adding a cold gas to the reaction gas to lower the reaction temperature; this is the so-called "cold-quench". If the quenching gas is the feed gas, it is called "feedgas quench", such as the Topsøe S-100 type ammonia converter, and ICI cold-quencher ammonia synthesis converter. If the quenching gas is not the feed gas, it is called "non-feedgas quench", such as the steam cold-quench carbon monoxide shift reactor.

Figures 8.6 and 8.7 respectively show the operating temperature profile in a continuous heat-exchange reactor and in an adiabatic fixed-bed reactor. The operating line in Fig. 8.6 is based on the heat balance, $t_2 = t_0 + (14{-}15)\Delta_y \times 100\%$, where t_0 is the entrance temperature, t_2 is the outlet temperature, Δ_y is the net value of ammonia.

The reaction rate of the whole process in some reversible exothermic reactions, such as the carbon monoxide shift reaction, can be considerable. The heat needed to be extracted from unit volume of catalyst at the beginning and the ending stages of the reaction may vary by 10 times or more. These reactions require multi-stage heat exchange reactors. Other reactions, such as the ammonia synthesis

reaction, are restricted by equilibrium, and with their reaction rates at beginning and the ending stage more or less the same. The heat needed to be extracted from unit volume of catalyst at the beginning and the ending stage of the reaction is more or less the same. For these reactions, the continuous heat-exchange reactor with an adiabatic layer can meet the process requirements. Most large converters with a capacity of 1000 tons per day, adopt the multi-adiabatic type-fixed bed reactor.

From Figures 8.6 and 8.7, we can see that among the three types of reactors, the transfer of heat (temperature) and mass (the concentration of ammonia) change dramatically in multi-bed direct heat exchange reactors. In the multi-bed indirect heat exchange reactors, only heat transfer (temperature) has a significant change; but in a continuous heat exchange reactor, both changes in heat and mass are gentle. From the point of irreversibility in thermodynamics, the sequence is: direct-heat exchange > indirect heat exchange > continuous heat exchange, i.e., the irreversibility of the continuous heat exchange reactor is the minimum in thermodynamics. However, because of the great resistance of gas flowing in this type of reactor, along with the so-called "cooled type effect," it is generally used in small or medium-sized converters. The reactor with direct heat exchange between the beds has not been recommended now. Large-scale converters usually adopt inter-stage indirect heat exchange.

8.1.2.4 *Control of temperature of catalyst beds*

The reaction temperatures of the catalyst bed are determined by the active temperature of catalysts. For the selection of the reaction temperature, not only the optimum reaction temperature but also the requirements of catalyst performance should be considered. In an industrial process, the temperature of catalyst beds should be especially controlled in the range of active temperature of catalysts. The inlet temperature of the catalyst bed should not be less than the initial active temperature of the catalyst. The highest bed temperature must not exceed the heat-resistance temperature of the catalyst. The characteristics of the operating temperatures of iron catalysts are shown in Table 8.7.

In a multi-bed adiabatic reactor, the first bed of catalyst bears about 70% production task of the whole converter, thus the protection of the catalyst in the first bed is very important. The inlet gases of the reactor must not contain water vapor, liquid ammonia, and trace amounts of $CO + CO_2$ or other poisons. Above all, the temperature in catalyst bed must not exceed the heat-resistant temperature of the catalyst. This is because high temperature can quicken up catalyst-aging, decrease catalytic activity and the net yield of ammonia due to decrease of equilibrium ammonia concentration.

Table 8.7 Operating temperatures of series ammonia synthesis catalysts of China

Type	Activity starting temperature/°C	Heat-resistant temperature/°C	Type	Activity starting temperature/°C	Heat-resistant temperature/°C
A110	370	500	A301	325	500
A201	360	500	ZA-5	300	500

Table 8.8 Relationships of the temperature of inlet and outlet, and net yield of ammonia and adiabatic temperature rise at first catalyst bed for the Topsøe S-200 type radial-flow converter using ZA-5 catalyst

Case	Bed radial position[a]/m Catalyst volume/m^3	1.433 (Inlet) 0.00	1.221 6.01	1.009 11.06	0.797 15.15	0.585 (Outlet) 18.28	Adiabatic temperature rise of bed/°C	Net ammonia of bed/%
1	Temperature/°C	290	334	370	401	425	135	—
	Ammonia/%	1.78	4.40	6.70	8.70	10.30	—	8.52
2	Temperature/°C	300	352	394	429	451	151	
	Ammonia/%	1.78	4.90	7.60	9.90	11.40		9.62
3	Temperature/°C	310	371	419	453	467	157	—
	Ammonia/%	1.78	5.50	8.60	10.90	11.90	—	10.12
4	Temperature/°C	320	390	444	470	476	156	
	Ammonia/%	1.78	6.10	9.50	11.30	11.70		9.92
5	Temperature/°C	330	411	464	479	481	151	—
	Ammonia/%	1.78	6.70	10.20	11.30	11.40	—	9.62
6	Temperature/°C	340	431	478	485	485	145	
	Ammonia/%	1.78	7.40	10.50	11.00	11.00		9.22
7	Temperature/°C	350	451	487	490	490	140	—
	Ammonia/%	1.78	8.10	10.50	10.6	10.60	—	8.82
8	Temperature/°C	375	491	501	501	501	126	—
	Ammonia/%	1.78	9.00	9.70	9.70	9.70	—	7.92

[a]diameter of reactor in the first bed is Φ 2866 mm, internal diameter is Φ 1170 mm, gas flow is from outside to inside.

In an adiabatic fixed bed, the temperature at the outlet of the bed is determined by the temperature at the inlet, and hence the inlet temperature of first catalyst bed is particularly important. For example, based on computer simulation calculations, the relationships between the temperature at the inlet and outlet and net yield of ammonia and adiabatic temperature rise in first catalyst bed for the Topsøe S-200 type converter using ZA-5 catalyst are shown in Table 8.8. The change in bed temperature with the temperature of inlet in the first bed is shown in Fig. 8.8.

It can be seen from Table 8.8 and Fig. 8.8 that:

(1) In Case 8 (inlet temperature of 375°C, outlet temperature of 501°C), the ammonia synthesis reaction is completed at about 20 cm after the inlet (1.433–1.221 m), and the net yield of ammonia is only 7.92%. Despite most of catalyst (about 67% vol.) is not needed or is non-working, it has to withstand baking at high temperature. Cases 6, 7 and 8 are all undesirable.
(2) On the contrary, in Case 3 (inlet temperature of 310°C, outlet temperature of 467°C), although the outlet temperature is only 467°C, the net yield of ammonia reaches 10.12%, so the net yield of ammonia is increased and the catalyst is protected. Cases 3 and 4 are the best operating conditions.
(3) Comparing Case 2 with Case 5, the outlet temperature are 451°C and 481°C respectively, but the net yield of ammonia is as same as 9.62%. Because the temperature of 451°C is sufficient, there is no need to increase it to 481°C. This means that the first-bed outlet temperature should be low rather than high.

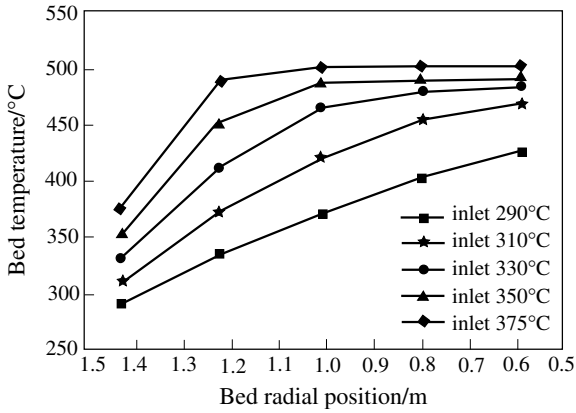


Fig. 8.8 Relation between the bed temperature and the temperature of inlet for first bed in radial-flow reactor (Gas flow direction from left to right)

For the inlet temperatures of the second and subsequent bed, because their outlet temperature will not be higher than the heat-resistant temperature of catalyst (due to small temperature rises), it is best to set the inlet temperatures of the second and subsequent beds such that the temperature difference between the inlet and outlet of the beds is maximum or the net yields (production) of ammonia highest.

8.1.3 *Space velocity*

Space velocity directly affects the production capacity of an ammonia synthesis system. In an industrial process, it increases generally space velocity to increase productions. The relationship between activity and space velocity is shown in Fig. 8.9. Increasing space velocity will reduce the synthesis efficiency of ammonia, the concentrations of ammonia in the recycle gas and the outlet temperature of converter, and increase the pressure drop of the synthesis loop. These will increase the energy consumption required for cooling the recycle gas and separation of product ammonia; the power consumption of the recycle compressor and ammonia compressor. Thus, there is an economic optimum value of space velocity. In an industrial process, the space velocity is normally chosen according to the pressure of the system, the structure of reactor and energy cost. It is common for the space velocity of a low-pressure loop set at 5000–10000 h^{-1}, a middle-pressure loop at 15000–30000 h^{-1}, and a high-pressure loop at as high as 60000 h^{-1}.

Large-scale ammonia plants that use turbo-compressor tend to use low space velocity according to the characteristics of the turbine recycle-compressor, the combination of safe, reliable and economic operation of the synthesis system. The relationships between space velocity and outlet concentration of ammonia and production are shown in Fig. 8.10.

Figure 8.9 shows that the activity of A301 catalysts is much higher than A110-2 and ICI74-1 under various space velocities. If A301 catalyst is used in existing converters (designed based on the performance of magnetite catalysts such as A110-2, KM etc) and at the same space velocity and other operating conditions, it will lead to increasing bed temperature because of higher conversions. However, since

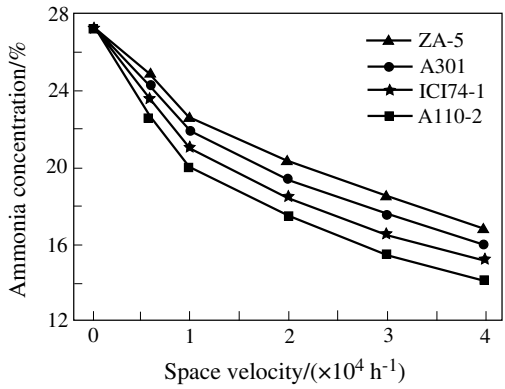


Fig. 8.9 Relationship between activity and space velocity of ZA-5, A301, ICI74-1 and A110-2 catalyst (P = 15 MPa, t = 425°C)

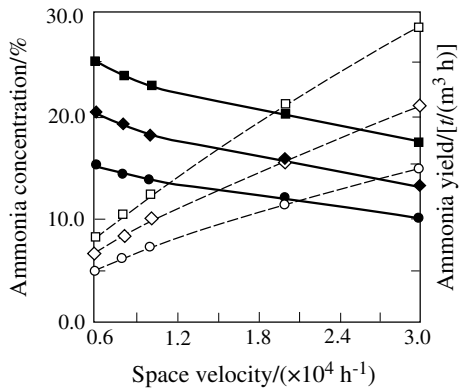


Fig. 8.10 Relationship between space velocity and concentration and production of ammonia for A301 catalysts Solid line: the ammonia concentration of outlet (unit: $\times 10^{-1}$%); dotted line: the production of ammonia (unit: t/m^3·h) ($\varphi_{NH_3,inlet} = 3.0$, t = 425°C, Ar + CH$_4$% = 0, H$_2$/N$_2$ = 3.0)

the operating temperature (hotspot) of the A301 catalyst is lower than that of the A110-2 (see Table 8.5), necessitating an increase amount of circulating gas (space velocity), so as to decrease the bed temperature. As a result, using the A301 catalyst can increase production. For example, if the ammonia concentration at the outlet of the converter is to reach 18% at 15.0 MPa and 425°C, the space velocity should be lower than $1.75 \times 10^4\,h^{-1}$ when using A110-2 catalyst; but when the A301 catalyst is used, the space velocity can be up to $2.8 \times 10^4\,h^{-1}$. The latter is 60% higher than the former; that means the space-time yield is increased 60%, thereby dramatically increasing the production capacity of the reactor. In such cases, if the amount of circulating gas cannot be increased (for certain plants), and the bed temperature is required to be controlled at that allowed by the A301 catalyst, the following conditions may be used: ① Open the cold-auxiliary valve or increase amount of cold-quench gas, or lower the temperature of the gas into the converter; ② increase

the amount of inert gas; ③ reduce the operating pressure or (hotspot) temperature, ④ increase the temperature for cooling the ammonia.

Adopting a highly activity catalyst (such as the A301, etc.) and increasing the space velocity can increase the production of ammonia within the constraint of allowable pressure drop of the converter. It can be seen from Fig. 8.10 that from the view of production, the higher the space velocity, the greater increase of the yield can be. The energy consumption of the production of ammonia is also very important. Dybkjaer Ib[9] has shown that the power consumption in a synthesis loop depends mainly on the volume of catalyst, that is increasing the volume and (or) the activity of catalysts will improve energy efficiency. Increasing the volume of catalyst leads to reduce space velocity. The result of increasing the volume of catalysts, reducing the space velocity and (or) increasing the activity (adopting high activity catalysts) will lead to an increase in the concentration of ammonia at the converter outlet. Increasing the concentration of ammonia at the reactor outlet reduces the amount of circulating gas, thus leading to reduced power consumption of the ammonia compressor and recycling compressor, and increased recovery efficiency of heat of reaction. As a result, from the perspective of energy-saving, low space velocity is beneficial. In current practice, high space velocity is not recommended, and large-scale ammonia plants usually use low space velocity.

8.1.4 *Gas compositions*

The parameters of gas compositions at the inlet of converter include the H_2/N_2 ratio, the content of inert gas and of ammonia in the circulating gas.

8.1.4.1 *H_2/N_2 ratio*

According to the thermodynamics of ammonia synthesis, the optimum H_2/N_2 ratio should be three. From Temkin reaction kinetics equation, H_2/N_2 ratio is related to the outlet of ammonia concentration. That is, the optimum H_2/N_2 ratio should increase from 1.5 to 3 when the ammonia concentration of outlet increases from 0 to 100% (equilibrium concentration of ammonia). As far as the reaction velocity is concerned, there is a maximum instantaneous reaction speed and an optimum H_2/N_2 ratio at different ammonia concentrations; but the optimum is difficult to achieve in practice. As a result, the optimum H_2/N_2 ratio should be set taking activity of catalysts, bed pressure, temperature, space velocity of reaction, amount of inert gas and other factors into consideration. That is to say, the optimum H_2/N_2 ratio is related to these factors, but is finally decided according to the process operability. Experimental results indicate [7,10–12] that when the H_2/N_2 ratio of circulating gas is 2.5:1, the outlet ammonia concentration is highest. This is probably because active adsorption of nitrogen is the rate-determining step for the ammonia synthesis reaction. Even under high pressure, the optimal ratio of hydrogen and nitrogen clearly deviates from that indicated by reaction stoichiometry. This conclusion has already been confirmed in practice. Some researchers, basing on calculations, argued that the best ratio of hydrogen and nitrogen is 2.15 [13]; others considered that the best ratio is about 2.0[14]. It is generally believed that when the reaction pressure is 9.81–98.07 MPa (100–1000 $kgf \cdot cm^{-2}$), the ratio of hydrogen and nitrogen for the best equilibrium ammonia concentration is about 3:1. Zhang M Z[15], in their discussion

of the effect of H_2/N_2 based on the Temkin-Pyzhev kinetic equation, argued that there is a best H_2/N_2 ratio governed by the dynamics of the synthesis process and that this best H_2/N_2 ratio varies under different conditions. However, they neglected the influence of thermodynamics. Based on our experimental results, we show below the effect of H_2/N_2 on the basis of kinetics and thermodynamics of the ammonia synthesis reaction, and suggest a quantitative relation between the best H_2/N_2 and the efficiency of the catalyst.

Figures 8.11–8.13 shows the effect of H_2/N_2 ratio on the activity of ZA-5 catalysts. It is seen from the results that H_2/N_2 ratio has a certain effect on the catalytic activity. For given space, velocity and pressure the optimum H_2/N_2 ratio changes with the reaction temperature.

Under the conditions of 15 MPa and 10000 h^{-1}, the optimum H_2/N_2 ratio is 2.55 to 3.0 at 450°C, 2.23–2.55 at 400°C, 1.76–2.22 at 350°C.

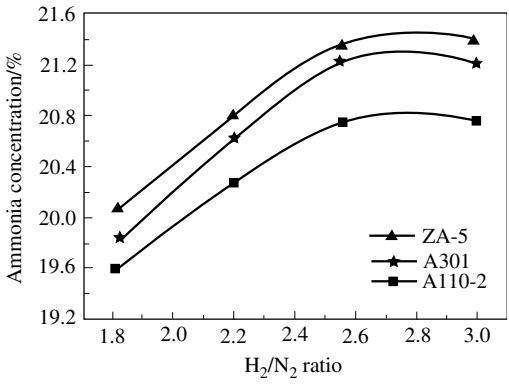
Under the conditions of 10 MPa and 8000 h^{-1}, the optimum H_2/N_2 ratio is 2.59 to 3.0 at 450°C, 2.19–2.61 at 400°C, 1.84–2.23 at 350°C.

Under the conditions of 7.0 MPa and 6000 h^{-1}, the optimum H_2/N_2 ratio is 2.51 to 3.0 at 450°C, 2.15–2.61 at 400°C, 1.76–2.20 at 350°C. At 350°C, when H_2/N_2 ratio is decreased from 3.0 to 2.20, the ammonia concentration is increased by 0.52 percent.

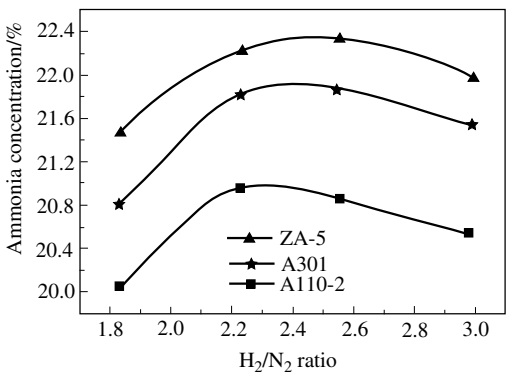
Therefore, the best H_2/N_2 ratios are related to the temperature, pressure, space velocity, inert gases and the activity (outlet concentration of ammonia) of catalysts.

In a practical reactor, the temperature of catalyst bed is changing; and in a multi-bed reactor, there are different temperatures in different beds. Which bed temperature and which temperature in any one bed should be used for choosing the best H_2/N_2 ratio? The author believes that the production of ammonia is related to the outlet concentration of ammonia of the reactor, and that this outlet concentration of ammonia is determined by the reaction condition of the final bed of catalysts. For example, for a two-bed reactor, if the temperature of reaction gas exiting the second bed is 400°C, the H_2/N_2 ratio between 2.2 to 2.6 is more appropriate for a ZA-5 catalyst. According to the chemical equilibrium of the ammonia synthesis reaction, the H_2/N_2 ratio is three when reaching the highest equilibrium concentration of ammonia (regardless of the effect of H_2/N_2 ratio on the equilibrium constant and the gas fugacity). When the reaction does not reach chemical equilibrium, the effect of H_2/N_2 ratio on the reaction rate is different. According to the Temkin–Pyzhev kinetic equation, at the initial stage of reaction, the H_2/N_2 ratio is 1.5 when the reaction rate reaches the maximum. As the reaction proceeds, if the reaction rate is maintained at the maximum, the H_2/N_2 ratio should gradually increase from the original 1.5 to 3.0 until the reaction reaches chemical equilibrium. Since the consumption of N_2 and H_2 in the synthesis gas for ammonia synthesis is based on ratio of 3:1, the reaction path proposed above is not realistic.

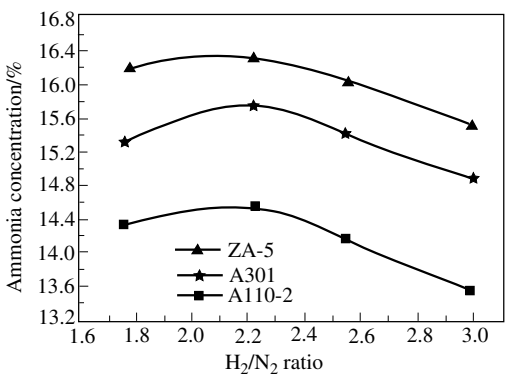
For a given reactor configuration, under certain conditions, there is bound to be the best H_2/N_2 ratio that leads to the fastest reaction rate and the highest concentration and production of ammonia. It is clear that the best H_2/N_2 ratio relates to the degree of reaction and the degree of reaction relates to how close the outlet concentration of ammonia is to the equilibrium ammonia concentration (approach degree of equilibrium). Here we can define K as a catalyst efficiency which characterizes the degree the catalyst enables the outlet concentration of ammonia



(a) 450 °C



(b) 400 °C



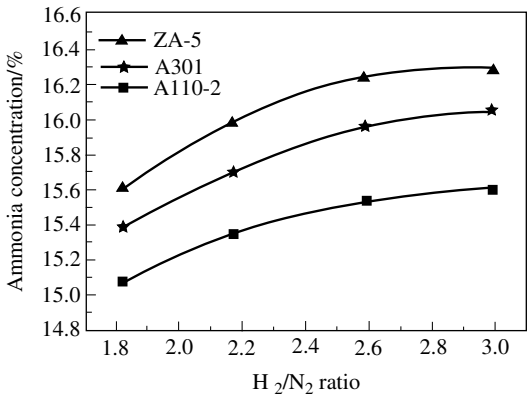
(c) 350 °C

Fig. 8.11 Effects of H_2/N_2 ratio on catalyst activity at 15 MPa ($S_V = 10000\,h^{-1}$)

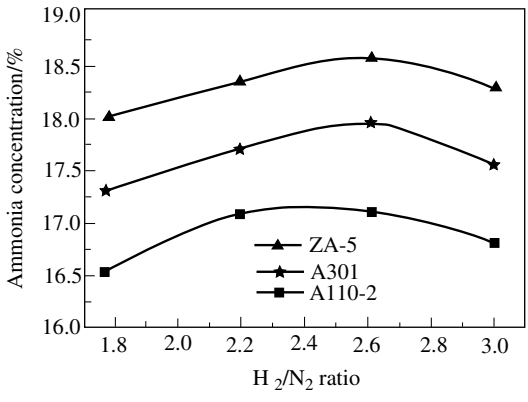
to approach the equilibrium concentration.

$$K = \varphi_{NH_3}/\varphi^*_{NH_3}, \tag{8.8}$$

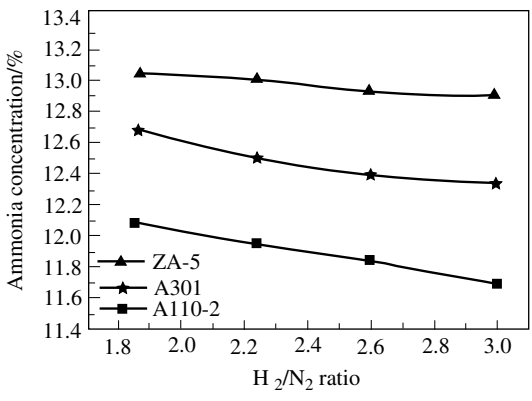
where φ_{NH_3} is the actual ammonia concentration at outlet of the reactor; $\varphi^*_{NH_3}$ is the equilibrium ammonia concentration under the same conditions with the φ_{NH3}.



(a) 450 °C

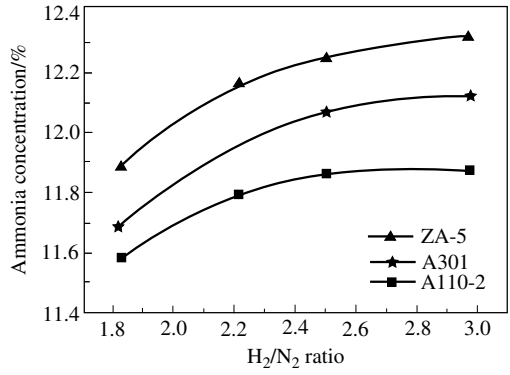


(b) 400 °C

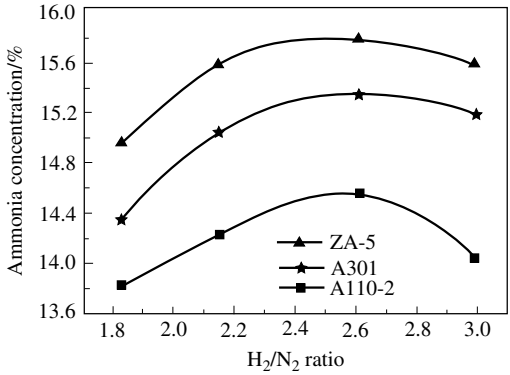


(c) 350 °C

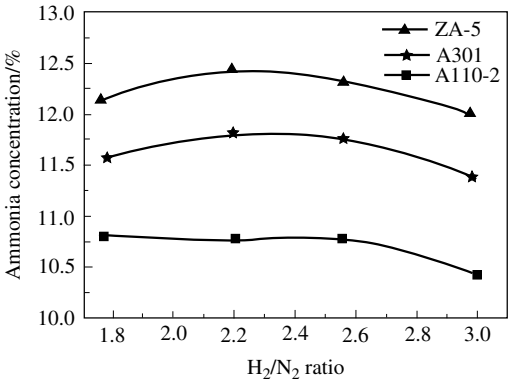
Fig. 8.12 Effects of H_2/N_2 ratio on catalyst activity at 10 MPa ($S_V = 8000\ h^{-1}$)



(a) 450 °C



(b) 400 °C



(c) 350 °C

Fig. 8.13 Effects of H_2/N_2 on activity at 7 MPa ($S_V = 6000\ h^{-1}$)

According to the theoretical results mentioned above, at the initial reaction stage, $\varphi_{NH_3} = 0$, so $K = 0$, the best ratio H_2/N_2 is 1.5 with the reaction reaching the maximum rate. When the reaction reaches equilibrium situation (for example, space velocity near zero), $K = 1(\varphi_{NH_3} = \varphi^*_{NH_3})$, the best H_2/N_2 ratio is 3.0. When

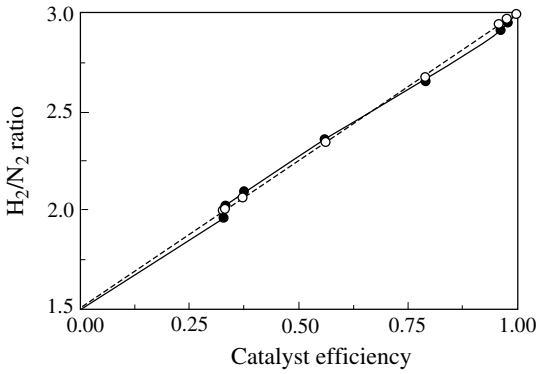


Fig. 8.14 Relationship between the optimum H_2/N_2 ratio and catalyst efficiency Dotted line: calculation value of equation (8.9); Solid line: the experimental data

the reaction is in progress, φ_{NH_3} increases from 0 to $\varphi^*_{NH_3}$, K increased from 0 to 1, the H_2/N_2 ratio should be increased from 1.5 to 3.0, and the equation (8.9) should come into existence:

$$\left(\frac{H_2}{N_2}\right)_m = 1.5\left(1 + \frac{\varphi_{\mathrm{NH_3}}}{\varphi^*_{\mathrm{NH_3}}}\right) = 1.5(1+K). \tag{8.9}$$

That is, there should be a dotted line as shown in Fig. 8.14.

According to equation (8.3), the highest concentration of ammonia and maximum reaction rate are shown in Figs. 8.11–8.13 when S_{V}, V_{cat} and W_{cat} are the same. The ratio of the maximum concentration of ammonia in the curves to the corresponding equilibrium concentration of ammonia under the same conditions is the catalyst efficiency K. The H_2/N_2 ratio with the maximum concentration of ammonia as a function of K is plotted as a solid line in Fig. 8.14. By the least square method (relative coefficient = 0.9957), we obtain

$$\left(\frac{H_2}{N_2}\right)_m = 1.5047 + 1.487K \approx 1.5(1+K) \tag{8.10}$$

Taking the experimental error into account, equation (8.10) is consistent with (8.9), which shows that the above theory in equation (8.9) to be correct.

Thus it can be seen that under certain working conditions, $(H_2/N_2)_m$ for the maximum reaction rate is directly proportional to the efficiency of catalysts; and any factor which lowers the catalyst efficiency (activity) will lower the best H_2/N_2. The various factors that affect the best H_2/N_2 ratio are shown in Table 8.9.

Therefore, the best operating H_2/N_2 ratio should be determined based on the efficiency of the catalyst for a given reactor configuration and operating conditions (including the activity of different catalysts), so that the reaction rate is the fastest, and the outlet concentration of ammonia the highest. Under the conditions of low temperature (low pressure), because the reaction temperature is lower, the equilibrium concentration of ammonia ($\varphi^*_{\mathrm{NH_3}}$) is higher and the outlet concentration of ammonia ($\varphi_{\mathrm{NH_3}}$) is lower, thus reducing the value of K leads to a reduction of the best H_2/N_2. That means a lower H_2/N_2 should be used. This is why the UDE-ICI-AMV low pressure (10 MPa) synthesis process uses a H_2/N_2 ratio of about 2.25.[16]

Table 8.9 Effects of process parameters on optimum $(H_2/N_2)_m$

Factors	Factor changing	$\varphi^*_{NH_3}$	φ_{NH_3}	$K = \varphi_{NH_3}/\varphi^*_{NH_3}$	$(H_2/N_2)_m$
Catalyst efficiency	R(D)	Unchanged	R(D)	R(D)	R(D)
Temperature	D(R)	R(D)	$t \le t_m$: D(R) $t \ge t_m$: R(D)	D(R) With the change of K	D(R) With the change of K
Space velocity	D(R)	Unchanged	R(D)	R(D)	R(D)
Pressure	D(R)	D(R)	D(R)	With the change of K	With the change of K
Inert gases	R(D)	D(R)	D(R)	With the change of K	With the change of K

Note: R-represents a rise; D-represents a reduction; t_m-represents the temperature with highest catalytic activity.

Table 8.10 Equilibrium concentration of ammonia $[H_2/N_2 = 2{:}1, CH_4 + Ar\ (He) = 0]$/%

	Pressure/MPa								
Temperature/°C	3	5	7	10	12	15	20	25	30
300	28.63	37.01	42.75	48.82	51.88	55.53			
325	22.22	30.06	35.75	42.03	45.30	49.29	54.38		
350	16.97	23.94	29.28	35.45	38.76	42.91	48.36	52.60	56.03
375	12.84	18.79	23.58	29.37	32.57	36.69	42.26	46.73	50.43
400	9.69	14.62	18.77	23.99	26.97	30.89	36.36	40.87	44.70
425	7.33	11.33	14.84	19.40	22.08	25.69	30.86	35.25	39.06
450	5.58	8.79	11.69	15.59	17.94	21.16	25.91	30.05	33.72
475	4.28	6.85	9.22	12.49	14.51	17.33	21.58	25.38	28.82
500	3.32	5.37	7.30	10.02	11.73	14.15	17.88	21.29	24.45

Here, it should be noted that when the H_2/N_2 in the circulating gas is reduced, the equilibrium ammonia concentration is also reduced. Table 8.10 to Table 8.12 gives the equilibrium ammonia concentration at different pressures, temperatures and H_2/N_2 ratios.

8.1.4.2 *Content of inert gas*

The content of inert gas (Methane, Argon, Helium etc.) in the feed gas depends on the methods of gasification and purification for the feed gas. The copper-ammonia solution washing process is employed to purify the synthesis gas, which is produced by coal as the raw materials, the content of inert gas in the synthesis gas is generally from 0.5% to 1%, more than 1% with the methanation purification process; and only a few $ml \cdot m^{-3}$ with the methanol and liquid nitrogen wash purification process.

Because the hydrogen and nitrogen gas continuously react and hence consumed in the circulation loop, the content of inert gas continues to accumulate. High concentration of inert gas does not favor reaction equilibrium and kinetics.

Table 8.11 Equilibrium concentration of ammonia [$H_2/N_2 = 1.5{:}1$, $CH_4 + Ar$ (He) = 0]/%

	Pressure/MPa								
Temperature/°C	3	5	7	10	12	15	20	25	30
300	25.97	33.21	38.04	43.05	45.52	48.43	51.96		
325	20.31	27.22	32.13	37.45	40.17	43.44	47.53	50.55	
400	8.98	13.48	17.24	21.90	24.54	27.97	32.69	36.51	39.70
425	6.81	10.49	13.69	17.81	20.21	23.42	27.96	31.75	35.00
450	5.19	8.16	10.82	14.37	16.50	19.40	23.62	27.26	30.46
475	3.99	6.37	8.56	11.56	13.40	15.96	19.79	23.17	26.21
500	3.10	5.00	6.79	9.30	10.86	13.08	16.47	19.54	22.36

Table 8.12 Equilibrium concentration of ammonia [$H_2/N_2 = 1{:}1$, $CH_4 + Ar$ (He) = 0]/%

	Pressure/MPa								
Temperature/°C	3	5	7	10	12	15	20	25	30
300	21.08	26.60	30.19	33.83	35.59	37.64	40.09	41.83	43.13
325	16.67	22.06	25.79	29.76	31.74	34.11	37.00	39.11	40.72
350	12.92	17.88	21.54	25.62	27.73	30.31	33.57	36.00	37.91
375	9.89	14.24	17.64	21.62	23.76	26.43	29.92	32.62	34.77
400	7.53	11.21	14.24	17.94	20.01	22.66	26.24	29.08	31.42
425	5.73	8.77	11.38	14.70	16.62	19.14	22.65	25.54	27.97
450	4.38	6.85	9.05	11.95	13.66	15.98	19.31	22.14	24.57
475	3.37	5.36	7.19	9.66	11.16	13.24	16.30	18.97	21.33
500	2.62	4.22	5.72	7.80	9.09	10.91	13.65	16.12	18.34

Although the existence of inert gas has without poison on the iron catalyst, from the perspective of chemical equilibrium, increasing the content of inert gas (φ_i) is equivalent to the reducing the effective pressure (p_e). The relationship for operating pressure (p_0), effective pressure (p_e) and content of inert gas (φ_i) is as follows:

$$p_e = p_0(1 - \varphi_i)^2, \tag{8.11}$$

Here, p_0 and the corresponding equilibrium concentration of ammonia (φ_0) to reduce to the p_e and the corresponding equilibrium concentration of ammonia (φ_e) reduces the driving force in reaction.

The effect of the content of inert gas on the activity of ZA-5 catalysts under different conditions is shown in Table 8.13, Figs. 8.15 and 8.16.

It can be seen from Table 8.13 that increase in the inert gas significantly reduces the catalytic activity. For example, under the conditions of 15 MPa, 440°C and 10,000 h^{-1}, the ammonia concentration at the outlet of A301 catalyst drops from 21.6% to 16.29% when the content of inert gas increases from 0 to 15%, and the respective catalytic activity is reduced by 26%. Increasing the content of inert gas by 1% leads to a reduction of the ammonia concentration at the outlet (net ammonia) by 0.2 to 0.35 percent on average. This behavior is similar to that shown in our earlier results:

$$\varphi_{NH_3} = \varphi^0_{NH_3} - 0.23\varphi_i \tag{8.12}$$

Table 8.13 Effect of inert gas (Ar) on the activity of A301 catalysts

			φ_{NH_3}/%					
P/MPa	S_v/h^{-1}	Ar/%	350°C	375°C	400°C	425°C	450°C	475°C
15	10000	0.00	—	18.90	22.13(410°C)	—	21.60(440°C)	18.24
		10.22	—	16.20	18.97	—	17.90	14.65
		14.72	—	14.47	17.23	—	16.29	13.13
10	8000	0.00	13.23	15.80	18.11	18.20	16.22	—
		5.69	12.29	14.70	16.84	16.69	14.77	—
		10.11	11.25	13.64	15.29	15.39	13.85	—
7	6000	0.00	11.40	14.03	15.00	14.48	12.28	—
		5.87	10.63	12.87	13.85	13.22	11.35	—
		10.46	9.85	11.71	12.70	12.32	10.56	—

where $\varphi^0_{NH_3}$ is the outlet concentration of ammonia at the same temperature when $\varphi_i = 0$.

The net value of ammonia decreases with increasing the content of inert gas, while the venting quantity of circulating gas also decreases, leading to a decline of unit gas consumption. As a result, the content of inert gas in the gas recycle is determined by process economics. The activity of catalyst and production of ammonia improves with a lower content of inert gas. The appropriate content of inert gas to use can be selected according to the price of raw materials, power consumption and the capability of the equipment, etc. In general, the content of inert gas should be kept to within 16%–20% for a medium pressure synthesis loop, and 8%–12% for a low pressure synthesis loop.[7, 17] Evaluating the optimal content of inert gas to use by computer calculations has been reported.[14] It can be seen from Table 8.13 that higher than 10% of inert gas is not desirable especially for a low pressure loop process.

Usually, it is needed to vent the inert gas. The amount of inert gas needed to be vented is determined by a material balance of the inert gases (CH_4 and A_r) in the system:

For CH_4:

$$V_f y_{CH_4,f} = V_v y_{CH_4,v} + S_{CH_4} \tag{8.13}$$

For Ar:

$$V_f y_{Ar,f} = V_v y_{Ar,v} + S_{Ar} \tag{8.14}$$

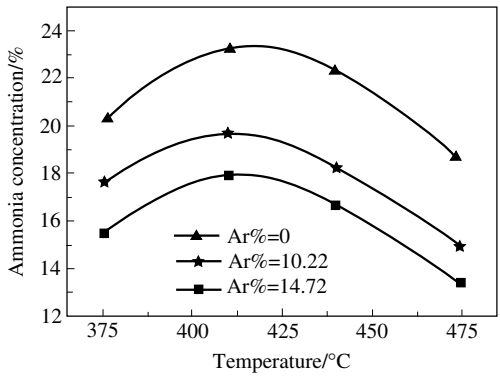
Here, V_f, V_v is the amount of fresh syngas and vented gas (including leakage) per ton of ammonia, respectively, $m^3 \cdot t^{-1}_{NH_3}$;

$y_{CH_4,f}$, $y_{Ar,f}$, $y_{CH_4,v}$, $y_{Ar,v}$ are the contents of CH_4 and Ar in fresh syngas and vented gas, respectively;

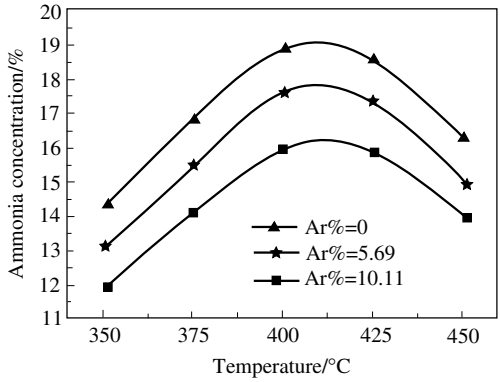
S_{CH_4}, S_{Ar} are the amounts of CH_4 and Ar dissolved (including carry secretly) in liquid ammonia, $m^3 \cdot t^{-1}_{NH_3}$).

It should be noted that Ar in the recycle loop ($y_{Ar,p}/y_{Ar,i}$) accumulates more than CH_4 because the solubility of Ar in liquid ammonia is lower than that of CH_4.

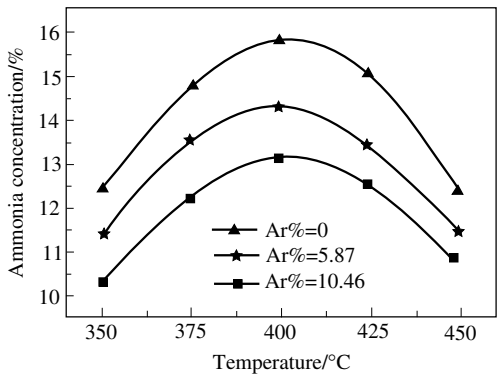
Ordinarily, the vent gas contains about 80% of usable hydrogen and nitrogen and certain amount of ammonia. To use this hydrogen as a fuel would be wasteful. For this reason, the hydrogen and ammonia in the vent gas should be recovered.



(a) p=15MPa, S_v=10000h^{-1}



(b) p=10MPa, S_v=8000h^{-1}



(c) p=7MPa, S_v=6000h^{-1}

Fig. 8.15 Effect of contents of inert gas (Ar) on the activity of ZA-5 catalyst

8.1.4.3 *Content of ammonia in the inlet gas and temperature of ammonia refrigeration*

The content of ammonia in the inlet gas to the converter may be called the initial content of ammonia. Under certain conditions, the higher the ammonia content

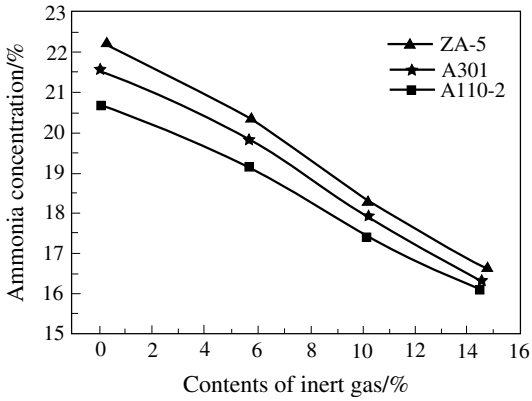


Fig. 8.16 Effect of contents of inert gas (Ar) on activity of ZA-5, A301 and A110-2 catalysts ($p = 15$ MPa, $t = 440°C$, $S_V = 10000\ h^{-1}$)

in the inlet gas, the smaller is the net production of ammonia, and the lower is the efficiency of the synthesis. The content of ammonia in the inlet gas depends on the efficiency of the separation system. Generally, when considering the recycle compressor and the energy consumption for refrigeration, the inlet gas should have a lower content of ammonia.

In a practical industrial process, it is well accepted that the condensing temperature should be controlled to adjust the ammonia content in the recycle gas. Commonly the content of ammonia in the inlet gas is 3%–4% for a low-pressure process, 2.0%–3.0% for a medium-pressure process, and 3.0%–3.8% for a high-pressure process. If the absorption by water is used for the separation of, the content of ammonia in the inlet gas can be reduced to below 0.5%.[5]

The condensing temperature of ammonia not only affects the content of ammonia in the converter inlet, but also affects the stability of the temperature in the catalyst bed. With the fluctuation of 1°C in the condensing temperature of ammonia, the temperature of catalyst bed will fluctuate by 3–5°C. Hence, the condensation temperature of ammonia is a matter of concern in practical operations.

8.2 Particle Size of Catalysts

The particle size of catalyst is an important parameter for an industrial catalyst. It not only significantly affects the pressure drop of the reaction gas through the catalyst bed, but also affects the diffusion rate, and thus the macro reaction rate. Reducing the size of catalyst can increase the utilization ratio of the inner surface of catalyst and decrease the influence of intraparticle diffusion, improve the macro reaction rate, and reduce the needed amount of catalyst. Reducing the amount of catalyst can reduce the height of catalyst bed and pressure drop. However, if the particle size of catalysts is reduced, the resistance of unit bed of catalyst to gas flow increases and power consumption for gas transmission also increases. Thus the particle size of catalyst has contradictory effects on a reactor.

Table 8.14 Relation between particle size and outlet ammonia concentration for A110-1 catalysts

Particle size/mm	2.5		4.8		8.4		12	
Temperature/°C	382	454	380	451	381	451	379	454
Outlet ammonia concentration/%	12.6	17.3	10.3	15.8	10.3	15.8	9.4	14.5

Table 8.15 Relationship between particle size and the reaction rate for ICI35-4 catalysts

Particle size/mm	0.6–1.2	3–4.5	6–9
Rate/kmol $N_2 \cdot h^{-1} \cdot m^{-3}$ (catalyst)	300	112	61

8.2.1 *Effect of particle size on catalytic activity and reaction rate of catalyst*

Large particles of catalyst are limited by the diffusion. Additionally, the outer surface of the particles is poisoned by water produced within the catalyst pores during reduction; hence the intrinsic activity of large catalyst particles is significantly lower than that of small particles. The extent of decline in activity with the increase of particles size varies with the type of catalyst for ammonia synthesis (Tables 8.14 and 8.15).[2,18]

In ammonia production, the space velocity is often $(0.6-2) \times 10^4\,h^{-1}$. In axial flow converters, the velocity of gas flow can be up to several $m \cdot s^{-1}$; the effect of external diffusion should be absent, but the effect of intraparticle diffusion cannot be ignored. The gas flow area in a radial flow converter is very large, the gas velocity is very low, and thus both effects of external and intraparticle diffusion cannot be ignored. Among the many factors that influence diffusion, the particle size of catalyst is the most significant and can be easily adjusted.

The author has studied the effect of particle size on the outlet ammonia concentration reaction rate and utilization ratio of the pore surface on the A301 catalyst at 7 MPa, 10 MPa and 15 MPa respectively.[19] Tables 8.16, 8.17 and 8.18 show the results.

(1) Figure 8.17 shows that with increasing particle size, the ammonia concentration at the outlet decreased. For example, when the particle size increases from 0.6–0.9 mm to 4.0–6.7 mm, the ammonia concentration at the outlet at 15.0 MPa and 400°C decreases from 23.42% to 19.43%, representing a 17.0% reduction in ammonia concentration. At a low pressure of 7.0 MPa, the net value of ammonia is not so high, and the percentage of decrease in ammonia concentration is especially considerable. Taking the bed resistance and other factors into consideration, low pressure ammonia synthesis loop should as far as possible use smaller catalyst particles.

(2) Effect of particle size on reaction rate. The bulk density of catalysts varies with particle size. Although the volume of catalysts is the same, the weights are different as can be seen in Tables 8.16–8.18. The ammonia concentration at the

Table 8.16 Relationship between particle size and outlet ammonia concentration, reaction rate, the utilization ratio of the inner surface of A301 (7.0 MPa, 6000 h^{-1})[a]

	Particle size/mm								
	0.6–0.9			1.6–2.5			2.5–3.0		
Temperature[b]/°C	φ_0^c	r_0^d	η_0^e	φ_1^c	r_1^d	η_1^e	φ_2^c	r_2^d	η_2^e
325	9.74	10.29	1	9.56	9.75	0.948	9.26	9.19	0.893
350	12.65	13.02	1	12.30	12.23	0.939	11.86	11.49	0.882
375	14.94	15.07	1	14.67	14.29	0.948	14.37	13.62	0.904
400	15.86	15.88	1	15.70	15.16	0.955	15.45	14.50	0.913
425	14.88	15.02	1	14.77	14.37	0.957	14.50	13.73	0.914
450	12.97	13.32	1	12.70	12.59	0.945	12.50	12.04	0.904

	Particle size/mm					
	3.0–4.0			4.0–6.7		
Temperature[b]/°C	φ_3^c	r_3^d	η_3^e	φ_4^c	r_4^d	η_4^e
325	8.90	8.78	0.853	8.27	8.05	0.782
350	11.30	10.90	0.837	10.74	10.22	0.785
375	13.85	13.06	0.866	12.98	12.11	0.804
400	15.00	14.07	0.886	14.20	13.11	0.826
425	14.25	13.39	0.891	13.80	12.78	0.851
450	12.30	11.76	0.883	12.02	11.31	0.849

[a]Composition of inlet gas: H_2 75%, N_2 25 %, CH_4+ Ar = 0; loading capacity of catalyst: V_k = 20 ml; [b]Catalyst bed temperature of outlet; [c]Ammonia concentration of outlet, %; [d]Reaction rate, mmol·g^{-1}·h^{-1}; [e]Utilization ratio of the pore surface: $\eta_i = r_i/r_0$.

reactor outlet does not accurately reflect the effect of particles size on reaction rate. The reaction rate must be calculated by equation (8.3) based on unit mass of catalyst in order to truly reflect the effect of particle size. The change of reaction rate for different particle size of catalysts with temperature is similar to the change of outlet ammonia concentration with temperature. The reaction rate decreases dramatically with increasing particles size, as can be seen clearly from Fig. 8.18. The reduction in reaction rate with increasing particle size is more considerable than the decrease in outlet ammonia concentration. For example, when the particle size increases from 0.6–0.9 mm to 4.0–6.7 mm, the reaction rate (r) (15 MPa, 400°C) decreases from 36.68 (r_0) mmol·g^{-1}·h^{-1} to 28.58 (r_4) mmol·g^{-1}·h^{-1}, a reduction of 8.1 mmol·g^{-1}·h^{-1}, which is equivalent to a 22.08% drop in reaction rate. In practice, it is more reasonable to compare the reaction rate based on the volume of catalyst ('volume rate') because the volume of catalyst in the reactor is fixed. In a low pressure (7.0 MPa) process, using a catalyst particle size of 1.6–3.0 mm, the highest 'volume rate' (400°C, according to that calculated by the activity of the size of 2.5–3.0 mm) is about 35 mol·m^{-3}·h^{-1} (or 0.60 t·m^{-3}·h^{-1}). If the concentration of ammonia and content of inert gas at the reactor inlet are zero, it would need 70 m^3 of catalysts for a plant of 1000 t/d capacity.

8.2.2 *Effect of particle size on the utilization ratio of inner surface of catalyst*

Experiments show that when the catalyst particle size is less than 0.6–0.9 mm, the intraparticle diffusion has been basically eliminated, and the rate could be regarded

Table 8.17 Relationship between particle size and outlet ammonia concentration, reaction rate, the utilization ratio of the inner surface of A301 (10.0 MPa, 8000 h^{-1})[a]

	Particle size/mm								
	0.6–0.9			1.6–2.5			2.5–3.0		
Temperature[b]/°C	φ_0^c	r_0^d	η_0^e	φ_1^c	r_1^d	η_1^e	φ_2^c	r_2^d	η_2^e
325	10.56	14.77	1	10.06	13.61	0.921	9.61	12.67	0.858
350	14.66	19.77	1	14.05	18.35	0.928	13.43	17.11	0.865
375	17.32	22.83	1	16.79	21.41	0.938	16.30	20.25	0.887
400	19.11	24.81	1	18.67	23.43	0.944	18.06	22.11	0.891
425	18.38	24.01	1	18.06	22.78	0.949	17.88	21.92	0.913
450	16.36	21.74	1	16.26	20.83	0.958	16.06	19.98	0.919

	Particle size/mm					
	3.0–4.0			4.0–6.7		
Temperature[b]/°C	φ_3^c	r_3^d	η_3^e	φ_4^c	r_4^d	η_4^e
325	9.20	12.06	0.817	8.81	11.37	0.770
350	12.95	16.42	0.831	12.46	15.56	0.787
375	15.53	19.25	0.843	14.96	18.28	0.801
400	17.68	21.51	0.867	17.04	20.46	0.825
425	17.39	21.21	0.883	16.99	20.41	0.850
450	15.80	19.54	0.899	15.52	18.87	0.868

Note: The same as Table 8.16.

as the intrinsic reaction rate.[20,21] As a result, η in the fourth row of Tables 8.16–8.18 which is the ratio of reaction rate of different particle sizes to the intrinsic reaction rate of 0.6–0.9 mm catalyst particles, may be used a measure of the utilization ratio of the catalyst' inner surface.

It is seen from Fig. 8.18 that some of the curves of the change of reaction rate with particle size at different temperatures intersect. This indicates that when the reaction temperature varies, the effect of particle size on reaction rate will also vary. This phenomenon shows that the pore surface utilization ratio does not just vary with the size of particles, but also with the reaction temperature and the so-called catalyst efficiency as defined in equation (8.8). The pore surface utilization ratio (ISUR) for different sizes of particles at different temperatures is shown in Fig. 8.19. It can clearly be seen from Fig. 8.19 that particle size has the greatest effect on η. The ISUR (η) is significantly lowered with increasing particle size. For example, when the reaction temperature (350°C) and other factors are the same, with the size increased from 0.6–0.9 mm to 4.0–6.7 mm, η is decreased from 1 to 0.785 and 0.740 at 7.0 MPa and 15.0 MPa respectively.

The effect of reaction temperature on ISUR (η) is shown in Fig. 8.20. The ISUR (η) decreases with the lowering of temperature. The greater the particle size, the greater is the reduction in reaction rate when pressure and other conditions are the same. However, the rate increases with temperature once the temperature is less than 350°C. This appears to be inconsistent with the common reference that the ISUR (η) is high at low temperatures. In fact, η is related not only with the catalyst particle size and temperature, but also with the approach of gas composition to the equilibrium composition ('equilibrium approach'). That is η is related to the equilibrium approach expressed as the catalyst efficiency K in equation (8.8).

Table 8.18 Relationship between particle size and outlet ammonia concentration, reaction rate, the utilization ratio of the inner surface of A301 (15.0 MPa, 10000 h^{-1})[a]

	Particle size/mm								
	0.6–0.9			1.6–2.5			2.5–3.0		
Temperature[b]/°C	φ_0^c	r_0^d	η_0^e	φ_1^c	r_1^d	η_1^e	φ_2^c	r_2^d	η_2^e
325	11.92	20.59	1	11.43	19.10	0.927	10.90	17.76	0.863
350	17.81	29.22	1	17.20	27.37	0.935	16.31	25.33	0.867
375	21.59	34.32	1	20.97	32.27	0.940	19.96	30.06	0.876
400	23.42	36.68	1	22.79	34.55	0.942	22.05	32.64	0.890
425	22.35	35.31	1	21.90	33.44	0.947	21.50	31.97	0.905
450	21.25	33.72	1	21.14	32.49	0.963	20.90	31.23	0.926

	Particle size/mm					
	3.0–4.0			4.0–6.7		
Temperature[b]/°C	φ_3^c	r_3^d	η_3^e	φ_4^c	r_4^d	η_4^e
325	10.30	16.71	0.812	9.81	15.69	0.762
350	15.12	23.51	0.805	14.03	21.62	0.740
375	18.69	28.48	0.821	17.26	25.86	0.753
400	20.79	30.81	0.840	19.43	28.58	0.779
425	20.72	30.72	0.870	19.89	29.10	0.820
450	20.28	30.18	0.895	19.61	28.80	0.854

Note: The same as Table 8.16.

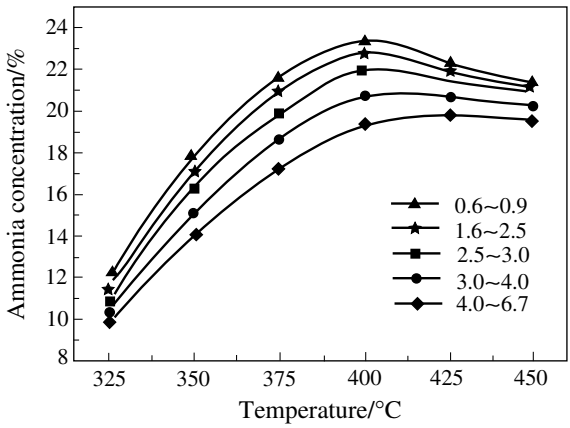


Fig. 8.17 Effect of particle size on activity of A301 ($p = 15$ MPa, $S_V = 10000\ h^{-1}$, $V_k = 20$ ml, $H_2/N_2 = 3$)

Table 8.19 gives the relationship between the catalyst efficiency and reaction temperature with particle size of (2.5–3.0) mm for the A301 catalyst at different pressures and space velocities.

It can be seen from Table 8.19 and Fig. 8.20 that when the particle size, space velocity and pressure are the same, increasing the temperature increases the catalyst efficiency, the reaction gas approaches equilibrium (for example, the catalyst efficiency is about 100% closing to equilibrium at 7 MPa, 6000 h^{-1} and

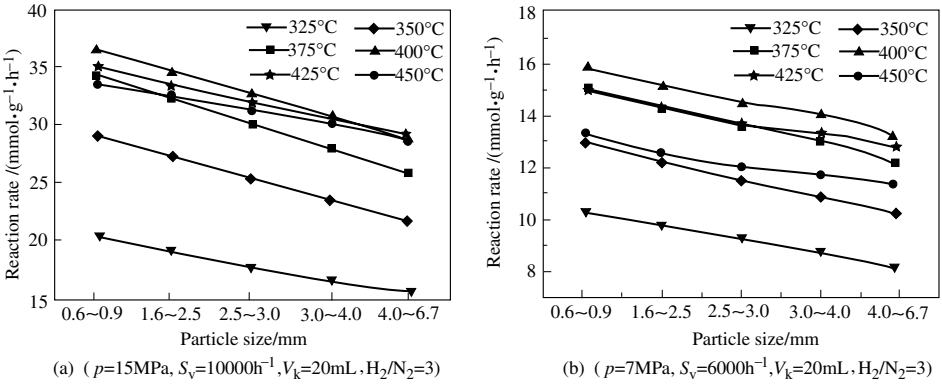


Fig. 8.18 Effects of particle size on reaction rate of A301

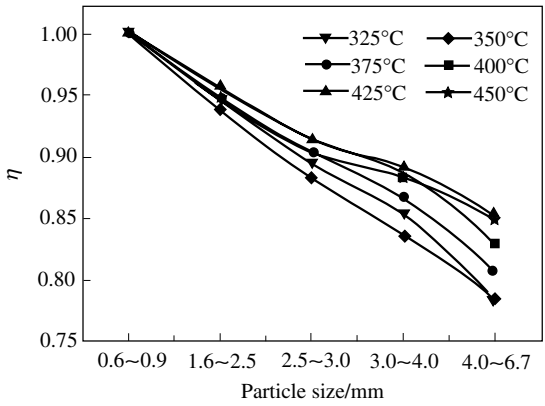


Fig. 8.19 Effect of particle size on the inner surface utilization ratio of A301 catalysts ($\mathbf{P = 7\,MPa,\ S_V = 6000\,h^{-1},\ V_k = 20\,ml,\ H_2/N_2 = 30}$)

Table 8.19 Relationship between catalyst efficiency and reaction temperature (particle size: 2.5–3.0 mm)

Pressure/MPa	Space velocity/h^{-1}	Catalyst efficiency K/%					
		325°C	350°C	375°C	400°C	425°C	450°C
7.0	6000	24.2	38.1	57.6	78.1	92.9	100
10.0	8000	21.3	35.5	52.3	71.2	87.5	98.0
15.0	10000	20.4	35.3	50.9	67.2	79.1	93.7

450°C), decreasing the reaction rate so that η is increased. However, when the reaction temperature is less than 350°C, η tends to increase, especially for large size catalysts. This is because when the temperature is less than 350°C, although the equilibrium concentration of ammonia increases, the catalytic activity decreases more significantly, resulting in a decrease of reaction rate, thus η rises with decreasing temperature. At the same time, it can be seen from Table 8.19 that with an

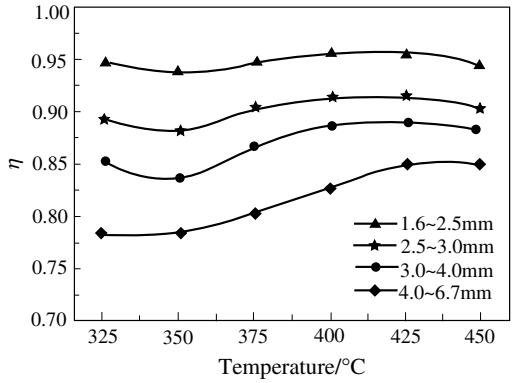


Fig. 8.20 Effect of temperature on the inner surface utilization ratio of A301 catalysts ($P = 7$ MPa, $S_V = 6000\ h^{-1}$, $V_k = 20$ ml, $H_2/N_2 = 3$)

Table 8.20 Relationship between catalyst efficiency and particle size (400°C)

Pressure/MPa	Space velocity/h^{-1}	Catalyst efficiency K/%				
		0.6–0.9 mm	1.6–2.5 mm	2.5–3.0 mm	3.0–4.0 mm	4.0–6.7 mm
7.0	6000	80.1	79.3	78.1	75.8	71.8
10.0	8000	75.4	73.6	71.2	69.7	67.2
15.0	10000	71.4	69.4	67.2	63.3	59.2

increase in the space velocity, the catalyst efficiency is reduced and η declines. This is the effect of space velocity on η. Similarly, the effect of particle size on η can be explained from its effect on the catalyst efficiency. Table 8.20 gives the relationship between catalyst efficiency and particle size at 400°C and different pressures and space velocities for the A301 catalyst. With increasing particle size, the catalyst efficiency is reduced, and η declines.

The discussion above shows that the effect of particle size on the catalytic activity is related to the reaction temperature. The lower the temperature, the greater the effect is. As a result, in loading the catalyst into a converter, the small catalyst particles should be loaded at the low-temperature positions of the catalyst bed (for example, inlet of bed and the last beds), and the large particles at the high temperature positions (for example, outlet or hotspot section of bed and the first bed).

For the A301 catalyst, when the reaction temperature is higher than 350°C, the catalyst efficiency plays the main role, that is, as the temperature increases, η increases. When the temperature is lower than 350°C, the reaction temperature plays the main role, η increases with decreasing temperature.

8.2.3 *Effect of particle size on the pressure drop of catalyst bed*

For a fixed-bed reactor, the size and shape of the catalyst not only relate to η but also to the bed pressure drop; and to a certain extent, the production capacity of the process, thereby also relate to the energy consumption.

The pressure drop of fluid in a fixed-bed reactor can be determined using the following equation:

$$\Delta P = f_m \frac{\rho_f u^2}{d_s} \left(\frac{1-\varepsilon}{\varepsilon^3} \right) L, \tag{8.15}$$

where u is the average flow rate of liquid calculated in cross-sectional area of bed, m·s $^{-1}$; ρ_f is the liquid density, kg·m^{-3}; d_s is the equivalent diameter of particle in geometric surface area, m; ε is the voidage of bed; L is the height of bed, m; f_m is the corrected friction factor, as determined using the following equation.

$$f_m = 1.75 + \frac{150}{\mathrm{Re}_m}. \tag{8.16}$$

The corrected Reynolds number

$$\mathrm{Re}_m = \frac{d_S \rho_f u}{\mu(1-\varepsilon)} = \frac{d_S G}{\mu(1-\varepsilon)}. \tag{8.17}$$

When $\mathrm{Re}_m < 10$, in the viscous flow region, $f_m = \frac{150}{\mathrm{Re}_m}$, so

$$\Delta P = 150 \frac{\mu u}{d_S^2} \frac{(1-\varepsilon)^2}{\varepsilon^3} L.$$

When $\mathrm{Re}_m > 1000$, in the turbulence region, $f_m = 1.75$. So,

$$\Delta P = 1.75 \frac{\rho_f u^2}{d_S} \frac{(1-\varepsilon)}{\varepsilon^3} L$$

Table 8.21 shows the pressure drop from experimental measurements for the A301 catalyst bed.

The factors that affect the pressure drop in fixed-beds are:

(1) Flow and physical properties of fluids; e.g. viscosity (μ), density (ρ) and mass flux (G) of fluids.

(2) Height of bed (L). When the fluid flow is turbulent, Δp is proportional to $G^2 L$; for a given bed volume, Δp is proportional to the $(\frac{W}{A})^2 L$, i.e., Δp is proportional to the L^3. When the fluid is in viscous flow, Δp is proportional to the GL, for a given bed volume, Δp is proportional to the L^2. Thus, it can be seen that decreasing the bed height and increasing the cross-sectional area of beds can reduce the pressure drop. For high-pressure vessels, the ratio of height to diameter cannot be too small. However, the fluid flow may be changed from an axial to radial direction, which

Table 8.21 Pressure drop of catalyst bed (A301, $t = 20°C$)

Fluid flow/(L·min^{-1})	ΔP/Pa	Fluid flow/(L·min^{-1})	ΔP/Pa
0.40	18.8	1.20	64.1
0.60	30.5	1.60	87.8
0.80	39.7	2.00	112.8
1.00	53.6	2.40	136.9

Note: When loading catalyst particles into Φ 48 mm × 3.5 mm galvanized pipes, and a rubber hammer is used for packing the particles, so that the bed is tightly filled. The distance of two pressure points is the 1600 mm. There is a steady flow zone between the height of 650 mm and 500 mm at top of the upstream pressure point and the bottom of the downstream pressure point (From literature[22]).

Table 8.22 Bed Voidage (ε) for A301 catalysts/%

Particle size/mm	Unreduced	Reduced	Particle size/mm	Unreduced	Reduced
1.0–1.4	45.30	45.37	4.7–6.7	40.14	40.00
2.2–3.3	41.95	41.90	6.7–9.4	39.78	39.81
3.3–4.7	40.86	40.97	9.4–13	39.06	39.12

can greatly reduce the path of fluid flow in the bed, increase the cross-sectional area of fluid flow and reduce the velocity of gas flow, so that the pressure drop is significantly reduced.

(3) Bed voidage. When the fluid flow is turbulent, Δp is proportional to the $\frac{1-\varepsilon}{\varepsilon^3}$. When the fluid flow is in the viscous region, Δp is proportional to the $\frac{(1-\varepsilon)^2}{\varepsilon^3}$. Increasing the bed voidage will decrease the bed resistance. The bed voidage is related to the shape of particles, distribution of particle size, and the method of loading the particles.

Table 8.22 shows the bed voidage for catalyst A301 with different particle sizes. The data in the table are calculated according to compacted packing density (ρ_b) of bed and particle density (ρ_p) by the following equation.

$$\varepsilon = \left(\frac{1}{\rho_b} - \frac{1}{\rho_P}\right) \Big/ \rho_b = 1 - \frac{\rho_b}{\rho_p} \tag{8.18}$$

Table 8.22 shows that the bed voidage of industrial fused iron catalyst is about 40%, reducing slightly with increasing particle size. The bed voidage for A301 catalyst is $\varepsilon = 0.466$ obtained by experiments used particles[22] with the size of 3.3–4.7 mm with undefined shape, which is slightly larger than that in Table 8.22.

The pressure drop Δp of a catalyst bed is directly proportional to $\frac{1-\varepsilon}{\varepsilon^3}$, and inversely proportional to the size or the square of size of particle. Although particle size increases, as a result of reduced bed voidage, thus increasing Δp, the reduction of Δp due to increased particle size cannot be offset. As a result, using large size of catalysts will help to reduce the bed pressure drop.

If a bed is mixed with two catalysts of different particle size, the bed voidage will be greatly affected. It can be seen from Table 8.23 that the more uneven the particles size are (i.e. small particles with smaller radius); then such small particles will fill among large particles, reducing the bed voidage, thus increasing the bed pressure drop. Manufacturers of ammonia synthesis catalyst should as far as possible supply products of uniform size. The catalyst particles should be sieved prior to loading them into the converter. Particles with sizes that are too small should be removed to avoid increasing the pressure drop. Broken catalyst particles during continuous use will reduce the bed voidage and increase the pressure drop.

(4) Particle size. When the flow is turbulent, Δp is proportional to the d_p^{-1}; for viscous flow, Δp is proportional to d_p^{-2}. The pressure drop of a bed is reduced with increase of particle size. When the flow direction of gases in the bed is changed from axial flow to radial flow, the pressure drop of the bed is reduced considerably, which allows the use of small size of catalyst particles, creating favorable conditions for enhanced catalytic activity and increased production.

Table 8.24 shows the effects of size and shape of catalyst particle on activity and pressure drop.[23] It can be seen that the bed pressure drop is relatively small

Table 8.23 Voidage packed with particles of two different sizes/%

Fill method	Contact number	Voidage of kind of a particle	Two kinds of particle size			
			Voidage of big ball (radius R)	Small ball		Voidage of mixture ($R:r = 1:1$)
				Radius (r)	Voidage	
Array cube	6	47.64	47.67	0.732R	39.2	27.10
Ordered monoclinic	8	39.55	39.54	0.5276R	14.69	30.67
Ordered tetrahedral	12	25.95	25.95	0.255R	2.27	19.01
Ordered octahedral	12	25.95	25.95	0.414R	7.10	19.01

Table 8.24 Effects of particle size on activity and pressure drop of the catalyst bed

Particle size/mm	Relative activity	Relative pressure drop
6–12	1.00	1.00
6–9	1.02	1.14
3–9	1.09	1.80
3–6	1.11	2.14
2–4	1.19	3.35
1–3	1.26	6.04
1–1.5	1.28	8.22

when large size of particles are used. Large particles are limited by diffusion, and the outer layer of the catalyst is poisoned by the vapor produced from inner core of the catalyst during reduction, so the catalyst's intrinsic activity is significantly lower than that of small catalyst particles. For different types of ammonia synthesis catalyst, the extent of the decline in catalytic activity varies with the increase of particle size. Under the same allowable pressure drop, one should choose the small catalyst particles. For example, when the catalyst particle size is decreased from 6–12 mm to 1.5–3 mm, the respective catalytic activity can be increased by 26%, and the production capacity can be increased by 10%–20% for unit volume of reactor.

At the same time, small particle size catalysts can also reduce the dosage of catalyst loading to a certain extent. Table 8.25 shows that when the catalyst particle size is reduced from 6–10 mm to 1.5–3 mm, the apparent catalyst volume can be reduced by 18% to 20%.

(5) Particle shape factor. The particle shape factor is a dimensionless parameter. For non-hollow particles, the shape factor is defined as the ratio of the external surface area S_S of a spherical particle with the same particle volume to the actual surface area S_P of the particle. This is equivalent to the ratio of the particle diameter d_S to the diameter d_P of a spherical particle with the same volume, that is, $\phi_S = S_S/S_P = d_S/d_P$, where $d_S = 6V_P/S_P$. The shape factor indicates how much a particle differs from a spherical one. For spherical particles, $\phi_S = 1$; for non-spherical particles, ϕ_S is less than 1. The particle shape factor can be calculated from the volume and external surface area. The volume and external surface area for particles with

Table 8.25 Relations between particle size and diminishable volume of catalyst

Catalyst size/mm	Apparent equivalent diameter/mm	Diminishable volume catalyst/%
6–10	7.5	0
4.5–8	5.5–6.5	4.8–7.4
3–6	4.5–4.7	10–11.5
1.5–3	2.0–2.2	18–20
1–1.5	1.2–1.3	21–22.3

regular shape can be calculated directly; and the shape factor can be calculated according to its definition.

In turbulent fluid flow, Δp is proportional to the ϕ_s^{-1}; in viscous flow, Δp is proportional to the ϕ_s^{-2}. Therefore, increasing the catalyst particle shape factor can reduce the pressure drop.

Ammonia synthesis catalysts generally have irregular shape. The preparation method for irregular shape particles is simple, hence the production yield is higher, and the cost of production is lower. However, the resulting shape factor will also be lower. Usually the corners of the particles are ground to improve the shape factor. Generally, the shape factor of irregular shape ammonia synthesis catalyst is about 0.33. Particles such as the A301 and ZA-5 catalysts have high mechanical strength. After grinding, the shape factor $\phi_S = 0.487$ for 3.3–4.7 mm A301 catalyst.[24]

Because spherical shape catalysts have a higher shape factor, up to about 0.9, they can significantly reduce bed pressure drop. Figure 8.21 shows the comparison of bed pressure drop for irregular shape catalysts with spherical shape catalysts.[25] For the same size of particles, spherical catalyst can reduce pressure drop and power consumption.

It can be seen from the discussion above that the selection of radial flow converter, using small size catalyst particles or spherical particles is one of the main strategy for saving energy. At present, large-scale ammonia synthesis converters that are in use are almost all radial flow beds with small catalyst particles. Most small and medium-scale converters still use axial flow catalyst beds and large catalyst particles, which is one reason why such ammonia plants have high energy consumption. This is one area of improvement for this type of ammonia plant.

8.2.4 *Choice of catalyst particle size for industrial applications*

Since the size of catalyst particles has adverse effects on catalytic activity and bed pressure drop, there is a reasonably economic catalyst particle size for use. Therefore, there is a need in choosing the optimum size of catalyst particle to arrive at the lowest total cost (the cost of the catalyst and the cost of consumption of energy) and the highest productivity. The general principle is to select particle size as small as possible given an allowable pressure drop.

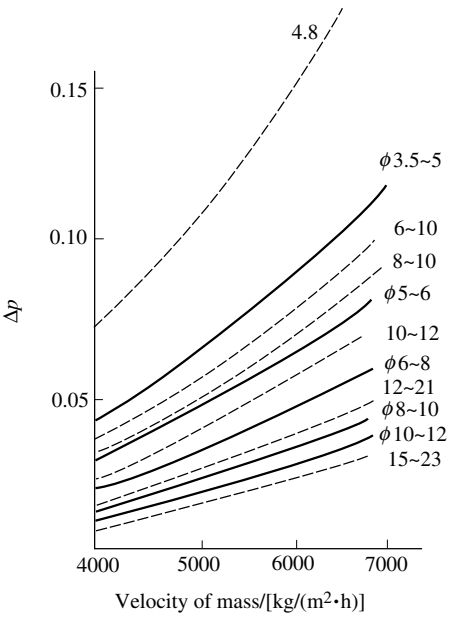


Fig. 8.21 Contrast the pressure drop of catalyst bed of spherical and irregular shape (-Spherical; . . . Irregular shape)

Table 8.24 shows that with an increasing catalyst particle size, both the catalytic activity and pressure drop of catalyst bed are lowered. However, the benefits of decreasing the pressure drop are outweighed by the drawback of reduced catalytic activity. If the activity of catalysts is reduced, along with the yield of product, then not only sales revenue is reduced, but also energy consumption is increased. In general, the activity increases by 5% to 10% when a new type of ammonia synthesis catalyst (except the A301 and ZA-5 catalysts) is developed. Table 8.24 shows that this gain will be offset if the particle size increases from 2–4 mm to 3–6 mm or 6–9 mm.

The optimum particle size depends on the gas flow and the specific bed characteristics in question. As the size of catalyst particles affects the reactor bed diameter, the particle size of catalysts should be chosen based on the type and diameter of reactor, height of beds and specific plant conditions.

Axial-flow ammonia converters should use a larger particle size of catalysts. For the multi-bed axial-flow converter with direct heat-exchange between beds (cold-quench) having a diameter of 1600–3200 mm and a production capacity of $1000\,t{\cdot}d^{-1}$ or more, and the height of catalyst bed 10–12 m, choose large particles with a diameter of 6.7–9.4 mm and 9.4–13 mm to minimize the pressure drop. For an axial-converter with a diameter of 800–1300 mm, height of catalyst bed 7–8 m, use 4.7–6.7 mm or 9.4 mm particles to keep the low pressure drop. For an axial-converter with a diameter of 500–600 mm, the height of catalyst bed is only about 5 m, 2.2–3.3 mm, 3.3–4.7 mm, and smaller particles may be used to increase the ammonia production.

For the radial-flow ammonia converter, one generally can use small size catalyst particles, such as 1.5–3 mm, that have relatively high activity. As the cross-sectional area for gas flow is larger and the flow velocity lower, the path of gas flow is short. Even if small size catalysts are used, the pressure drop is small. However, the effect of external diffusion is significant.

For a multi-bed converter, the catalyst in the different beds should be of different sizes. The choice of particle size should be based on the reaction behavior of the catalyst in the different beds, the composition of synthesis gas and the pressure drop of the beds. In general, the effect of diffusion decreases with increasing concentration of ammonia and decreasing temperature. As a result, in the first half period of the synthesis process, the reaction rate is very high, the effect of diffusion is the main limitation, and the bed should be filled with small particles of catalyst. The second half of the bed should be filled with larger particles of catalyst. At the inlet of this part of the converter, which is a low temperature zone with more poisons affecting the catalyst, mass transfer limitation is not significant even enough the concentration of ammonia is low here, the catalyst particles should not be too small.

8.3 Poison and Life of Catalyst

Unfortunately, all catalysts will deactivate under the same reaction conditions, but at different rates of deactivation. Catalyst designers need to continue to find ways that could render the catalyst being used most economically for a longer life. Deactivation can be divided into two types: reversible and irreversible. Both types of deactivation are not desirable. Even for the former case, the deactivated catalyst has to be taken out of the production line for reduction.

Like living things, a catalyst goes through a life-death process, thus deactivation is inescapable. A good environment is needed to keep a catalyst active. Even in the worst environment, attempts are needed to overcome the adverse effects of the environment on the catalyst as far as possible. The catalyst will deteriorate and die without such efforts to maintain its activity.

In a good environment, certain living things may be exempted from getting sick. However, a catalyst cannot always be in a good environment. Adverse environments are inevitable. The most obvious example is the catalyst in an automobile catalytic converter, where the catalyst has to perform several reactions in a hostile environment in order to extend the life of a practical catalyst, and the catalyst has to be able to withstand the adverse environmental conditions. For a catalyst that has a high activity but is sensitive to environmental conditions, it will easily deactivate when subjected to small environment changes. Therefore, catalyst designers often make the catalyst more robust to resist harsh environments at the expense of a small loss in catalytic activity. Even so, catalyst users still need to use the catalysts correctly.

It can be seen that the key for correct use of a catalyst rests with knowing how to use the catalyst more efficiently and attaining a longer catalyst life. The first requirement is to investigate the reason why deactivation happens.

There are seven reasons that would cause the loss of catalytic activity.[26] Most of the time, two or more of these cases can happen at the same time, thus accelerating the deactivation process.

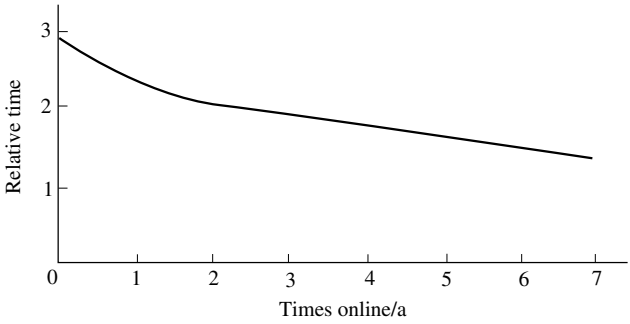


Fig. 8.22 Typical deactivation curve of ammonia synthesis catalysts[25]

① Sintering (semi-sintered)	non-reversible
② Change of chemical composition	non-reversible
③ Formation of new compounds	non-reversible
④ Formation of temporary compounds	reversible
⑤ Adsorption	reversible
⑥ Conglutinating of reactants and/or other substances	non-reversible
⑦ Cracking or desquamating	non-reversible

Generally ammonia synthesis catalysts have a long life time of 5 to 15 years. A typical deactivation curve with time is shown in Fig. 8.22. The main reasons of deactivation are due to thermal sintering and poisoning.

8.3.1 *Thermal sintering and changes of chemical composition of catalyst*

If the catalyst is subjected to a high temperature or heated for a long time, its surface structure will stabilize, and the surface area or the lattice defects will be reduced. This phenomenon is known as sintering or a semi-sintered condition. Sintering is a physical change which can cause the catalytic activity to decline, and the activity cannot be recovered by physical methods.

Sometimes chemical changes can also occur during heating, resulting in a new component from chemical reactions between the active components or between the active components and other impurities contained in the catalyst. The chemical changes can also reduce the catalyst's activity, and like sintering the activity cannot be recovered by physical methods.

The above two phenomena, which take place under high temperatures, change the catalyst's intrinsic properties. These changes are observed in gas-phase reactions but not in liquid-phase reactions.

Active components of various catalysts and their support are solids with very high surface area and each catalyst has a different porosity. The catalyst surface area always tends to minimize driven by the thermodynamic principle of decreasing surface free energy. It is not possible for catalysts to sinter instantaneously due to the limitation of the nature of a solid, the dynamics of physical arrangement and solid rearrangement. Although the chemical properties of solids and the surrounding environment affect the sintering rate, in general temperature is the factor that

Table 8.26 Physical and chemical properties of the catalyst metal for ammonia synthesis

Catalyst metal	Fe	Ru
Typical operating temperature/K	623–773	598–723
Melting point temperature T_m/K	1809	2583
Tamman temperature $a_v(=0.5\,T_m)$/K	905	1292
Huttig temperature $a_s(=0.3\,T_m)$/K	543	775

plays a dominant role. As a result, at a low enough temperature, a solid can maintain its original structure for a very long time. When the temperature rises due to the heat of reaction, surface diffusion becomes important. Initially the unstable surface becomes smooth followed by the formation of round or flat particles. When settled catalyst particles come into contact with each other, or when they break through particle surfaces, or when they pass through voids, the particles may grow in size.

When the temperature continues to rise, volume diffusion becomes an important factor; changes in the overall structure of the catalyst become more apparent, at a very high temperature, evaporation of solids could be very significant; but such a phenomenon seldom occurs in practice. The most commonly used index for describing sintering based on experimental observations was proposed by Tamman.[27] He noted that the temperature at the commencement of sintering a_v (Tamman temperature) is about half the value of the solid's melting point $T_m(K)$; that is, $a_v \approx 0.5\,T_m$. Once the catalyst is subjected to a temperature higher than the Tamman temperature, sintering of the metal crystallite in the catalysts will become noticeable. The typical operating temperature of ammonia catalyst is 350–500°C, which is lower than the Tamman temperature of iron (Table 8.26), thus the iron catalyst has a relatively long life and stable activity. Ruthenium catalysts are even more stable because of their higher Tamman temperature. In a practical production process, the temperature of catalyst beds often fluctuates, as a result of the exothermic of the ammonia synthesis reaction, and changes of the process operating conditions. It is inevitable that there are differences of temperature between different beds of a converter or in the different locations of the beds. The superheat in local may occur, which may cause the α-Fe crystallite in the catalyst to grow, leading to the loss of surface area and deactivation.

Huttig and other researchers have made some improvements[29] to identify the onset of sintering. They found that initial sintering was caused by surface diffusion. When the surface temperature reached a_s, sintering begin, with $a_s \approx 0.3T_m$.

The relationship can be a very useful guide to study and estimate the effect and the extent of sintering. For example, the sintering temperature of silver catalyst should be around 350°C ($a_v = 480$°C, $a_s = 320$°C), whereas aluminum oxide ($a_v = 600$°C, $a_s = 400$°C) and silicon oxide ($a_v = 855$°C, $a_s = 570$°C) could still be stable up to 500°C. In fact, a common feature for all catalyst supports is that they do not easily sinter when the temperature does not exceed the operating temperature of the catalysts. If the melting point of a composite solid is not known, it can be deduced reasonably well from the crystal lattice energy or from the

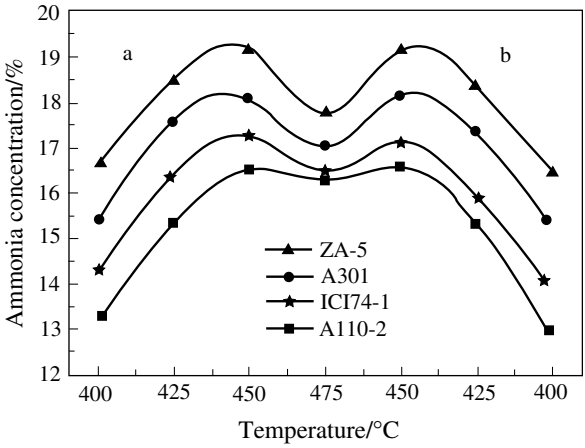


Fig. 8.23 Comparison of the heat-resistant properties for ZA-5, A301, ICI74-1 and A110-2. Heat treating conditions: 500°C for 20 hours; Activity testing conditions: 15 MPa, 30000 h^{-1}. a-before heat-resistant, b-after heat-resistant

ionizing potential, which have the same tendency of change as that of the melting point.

Catalyst designers need to adequately address the issue of prevention of sintering. Sintering caused by phase transfer is a major problem for the catalyst support. The nature of the catalyst and its support as well as the surrounding environment has a significant influence on sintering. However, the relative importance of these various factors depends on the sintering mechanism. The mechanism of sintering should first be identified before appropriate measures can be taken to prevent the catalyst from sintering.[30−32]

The rate of sintering increases with increasing grain size, increasing degree of dispersion and the amount of doped metal. Although a catalyst has very high activity when the grains of the particles are super-small, the rate of sintering decreases with increasing grain size.[33] Hence the grain size on the catalyst support is limited by these two opposing factors. Grain growth can be prevented by dispersing it very uniformly on a support with a high surface area.

The sintering rate of catalysts may be expressed by their heat-resistant properties. Figure 8.23 shows a comparison of the heat-resistant properties of ZA-5, A301, ICI74-1 and A110-2 catalysts. It can be seen from the figure that the activity is almost unchanged for all catalysts after heating at 500°C for 20 h (according to the Chinese Standard Method). The data indicates that these catalysts have a good heat-resistant performance, and ZA-5 is better than A301, ICI74-1 and A110-2.

The decrease of activity is more significant for the upper layer of catalyst in an axial converter. Table 8.27 illustrates the changes in the property of catalysts after they have been used for 13 months.[34] The table shows that the composition of the promoters did not change much after usage, whereas the activity decreased and the porosity, the average pore size increased remarkably for the upper and middle layers

Table 8.27 Property change of catalysts before and after of use

Sample		Promoter contents/%				
		Al_2O_3	CaO	SiO_2	K_2O	SO_3
Before use		3.82	3.55	0.90	1.20	trace
After use	Top of bed	3.92	3.55	0.93	1.28	0.08
	Middle of bed	3.92	3.55	0.98	1.29	0.01
	Bottom of bed	3.92	3.55	0.98	1.29	0.01

Sample		Surface area/ $(m^2 \cdot g^{-1})$	Ammonia contents/%	Rate constant/ $(Mpa^{0.5}\ h^{-1})$	Total porosity/%	Average pore size/$(\times 10^{-9} m)$
Before use		13.0	13.1	609.6	32.5	10.7
After use	Top of bed	9.2	0.1	0.025	37.4	16.6
	Middle of bed	10.0	4.6	79.16	35.8	15.0
	Bottom of bed	13.0	5.9	110.3	35.4	10.7

[a]Activity testing conditions: $P = 30.40\,MPa$, space velocity: $30000\,h^{-1}$, $t = 400°C$.

of catalysts after being used. The result shows that the catalytic activity decreased as a result of grain growth in the upper and middle layers of catalyst.

8.3.2 *Poisons and the phenomenon of poisoning of catalyst*

Poisoning is another main reason that causes the deactivation of catalysts. In this case, the support of catalyst usually does not play an important role.

The phenomenon of catalyst poisoning arises from the preferential adsorption of substances on the catalyst's active site, or the formation of a strong chemical bond or a new compound. These changes will affect the performance of the catalyst, and will not free the catalyst to participate in the adsorption or reaction of the reactants. The catalyst's activity will decline, or even more seriously, completely lose its activity. Because the poison can selectively adhere to different active sites, poisoning may also cause a decline in the catalyst's selectivity.[35,36]

Different catalytic systems have different causes of poisoning. Even for the same system, the reasons of deactivation caused by the same poison may not be the same under different reaction conditions. The causes of poisoning give rise to the appearance of specific poisons. A specific poison will cause the active sites of a specific catalyst to exhibit poisoned behavior under specific process conditions. This means that even a very small content of poison may lead to marked deactivation. If the catalyst is continuously in a toxic environment, the effect of poisoning is cumulated.[37]

8.3.2.1 *Types of catalyst poisoning*

The phenomenon of catalyst poisoning may be divided into three types according to the different effect: reversible poisoning, irreversible poisoning and selective poisoning.

Because poisoning is due to the interaction between a poison and the active component in a catalyst, this interaction may be strong or weak. According to the strength or weakness of this interaction, poisoning may be divided into two kinds. One is that the interaction is so weak that the poison on the active site can be

removed by appropriate means to recover the catalytic activity. In this case, the nature of the catalyst is not affected, and is called reversible or temporary poisoning. Another is that the interaction is so strong that the activity of the catalyst cannot be recovered by normal means. This is called irreversible or permanent poisoning.[35,36,38]

For example, oxygen and water vapor are poisons to ammonia synthesis catalysts. Because these poisons can be removed by reduction by H_2 or by treatment using a fresh synthesis gas without poisons, this is reversible poisoning. However, poisoning caused by sulfide, chlorine, phosphorus and heavy metal is very difficult to be removed; so the poisoning is irreversible.[39]

Although a poisoned catalyst becomes inactive to some particular reaction, it can be active for other reactions. This is known as the selective poisoning. In a series-reaction, if the poisoned catalyst is only deactivating to the last reaction in the series, then the process can stay in the intermediate stage, the yield of the intermediate product could be expected to be high. For certain catalysts, the introduction of a small amount of poison can therefore selectively enhance the catalytic activity and stability.[35,40,41]

8.3.2.2 *Poisons of catalyst*

Catalyst poisons include metal and non-metal compounds.

For the non-metal compounds, the elements that are harmful to the catalyst are mostly main group *A* elements in the period table, that is, the VA group (N, P, As, Sb), the VIA group (O, S, Se, Te), the VIIA group (F, Cl, Br, I). Among these elements, phosphorus, arsenic, sulfur, halogens are the common poisons.

Compounds containing these elements sometimes are toxic but sometimes are promoters, depending on the type of catalyst. It is the character of non-metal compounds. For instance, water is harmful to solid acid catalysts, but is a promoter for hydrogenation reactions on ruthenium catalyst. Hydrogen sulfide can poison a nickel catalyst, but a sulfate does not. If hydrogen sulfide is oxidized to form a shield-type structure, it is a non-toxic substance.

Compounds which are toxic to catalysts have unshared electronic pairs. After oxidation, the electronic pairs are transformed into fully shared electron octets, which is a non-toxic substance. It is worth noting that in non-toxic substances, inorganic salts have the shielded structure.

Most toxic substances are negative ions. The ammonia is a positive ion, and it will change to be non-toxic after contact with water or acid. Therefore should note the poisoning effect of ammonia and organic amines.

In examining metallic compounds that serve as supports for Pt and Pd catalysts, the metals and metallic compounds as catalyst support are only limited to a few elements. This is because some metals, such as lead, mercury, cadmium, bismuth, tin, zinc, copper and iron have a toxic effect on the catalyst, whereas light metals and alkaline earth metal compounds are without toxic for catalyst, and they can in some cases enhance the selectivity and activity of the catalysts.

Metals may be classified according to their electronic configuration in outer shell orbit as shown in Table 8.28.[42] In this table, the poisoning phenomenon is tested with the decomposition reaction of hydrogen peroxide using Pt catalyst.

Table 8.28 Toxicity of metal ions (Mexted)[42]

Metal ion					Outer orbit of the electronic arrangement								Toxicity on Pt
Li^+	Be^{2+}				no *d*-layer								poison-free
Na^+	Mg^2	Al^{3+}			no *d* layer of inner								poison-free
K^+	Ca^{2+}												
Rb^+	Sr^{2+}		Zr^{4+}		3d	◯	◯	◯	◯	◯	4s	◯	poison-free
Cs^+	Ba^{2+}	La^{3+}			4d	◯	◯	◯	◯	◯	5s	◯	poison-free
		Ca^{3+}			5d	◯	◯	◯	◯	◯	6s	◯	poison-free
			Th^{4+}		6d	◯	◯	◯	◯	◯	7s	◯	poison-free
	Cr^{2+}				3d	⊙	⊙	⊙	⊙	◯	4s	◯	poison-free
		Cr^{3+}			3d	⊙	⊙	⊙	◯	◯	4s	◯	poison-free
Cu^+	Zn^{2+}				3d	⊙	⊙	⊙	⊙	⊙	4s	◯	poison
Cu^{2+}					3d	⊙	⊙	⊙	⊙	⊙	4s	◯	poison
Ag^+	Cd^{2+}	In^{3+}			4d	⊙	⊙	⊙	⊙	⊙	5s	◯	poison
					4d	⊙	⊙	⊙	⊙	⊙	5s	◯	poison
Au^+	Hg^{2+}		Sn^{2+}		5d	⊙	⊙	⊙	⊙	⊙	6s	◯	poison
	Hg^+				5d	⊙	⊙	⊙	⊙	⊙	6s	◯	poison
		Tl^+	Pb^{2+}	Ei^{2+}	5d	⊙	⊙	⊙	⊙	⊙	6s	◯	poison
Mn^{2+}					3d	⊙	⊙	⊙	⊙	⊙	4s	◯	poison
Fe^{2+}					3d	⊙	⊙	⊙	⊙	⊙	4s	◯	poison
Co^{2+}					3d	⊙	⊙	⊙	⊙	⊙	4s	◯	poison
Ni^{2+}					3d	⊙	⊙	⊙	⊙	⊙	4s	◯	poison

According to the Table, the metals with toxic are those with the *d*-orbits all occupied or occupied by one electron each orbit. Contrarily, if the *d* orbit is completely empty, the metal is non-toxic. The atomic weight of the non-toxic metals may be small, also have large such as zirconium, barium, cerium, and thorium. For the iron catalyst, except in the four rows (Cu^+ etc.), potassium, aluminum, magnesium, calcium, barium, zirconium, lanthanum are widely used as promoters. Consequently, Table 8.28 provides a useful guideline for the selection of catalyst supports and promoters, the preparation of catalysts with more than two components, the identification of catalyst poisons, and the selection of materials for reactor construction.

It is seen from Table 8.28 that the toxicity of metals is either strong or weak. The metals which have strong toxicities are mercury, cadmium, lead. Among them, mercury has the strongest toxicity.

8.3.2.3 *Factors affecting toxicity*

According to reports in the literature,[38] the degree of toxicity of a poison molecule is related to two factors. One is coverage-factor (s), which refers to the number of atoms or groups of active sites on the catalyst covered by the atoms or molecules of adsorbed poison. The other is life-factor (t) of adsorption, which refers to the average residence time of the molecules of poison on the catalyst surface.

Thus the effective toxicity of poison can be expressed as a function of these two factors:

$$\text{Effective toxicity} = f(s, t)$$

The factor (s) relates to the nature and structure of the toxic elements, and the effective volume of the moving at space for the poison; the life-factor (t) of adsorption depends largely on the nature of the toxic elements and their molecular structure. As the life-adsorption of poison is much longer than that of the reactant molecule, so even a very low concentration of poison still can inhibit the adsorption of the reactant molecule and lead to the catalyst losing its activity as the poison accumulates on the catalyst's surface.

There are three toxic effects of poisons.[40]

(1) The concentration effect of poisons. There exists a range of concentration of poison that can make the catalyst inactive. This range varies with different catalysts, the chemical reactions involved and the reaction conditions. For instance, a 0.63% of sulfur adsorbed on an industrial ammonia synthesis iron catalyst will completely deactivate the catalyst. A typical curve of the activity associated with the concentration of poison on an iron catalyst is shown in Fig. 8.24. Even if the concentration of poisons is very low, the activity of catalyst decreases linearly with the increase of the content of poisons.

(2) The temperature effect of poisons. The influence of poison on the catalyst can be different with the change of reaction conditions. For example, there are three temperature ranges for the poisoning of metal catalyst by sulfide (see the following text about the effect of reaction conditions on catalyst poisoning).

(3) The geometrical effect of poisons. This poisoning effect relates to the molecular size and geometrical structure of the poison. Similarly, take sulfides as an example, their poisoning effect on nickel or platinum hydrogenation catalysts have the following trends:

① Toxicity increases with increasing molecular weight, e.g., hydrogen sulfide < carbon disulfide < thiophene < cysteine;

② Toxicity increases with the increasing carbon chain in sulfur compounds;

③ Toxicity of the sulfides, which have a sulfur atom at each end of the chain, is less than that of only one sulfur atom at one end of the chain.

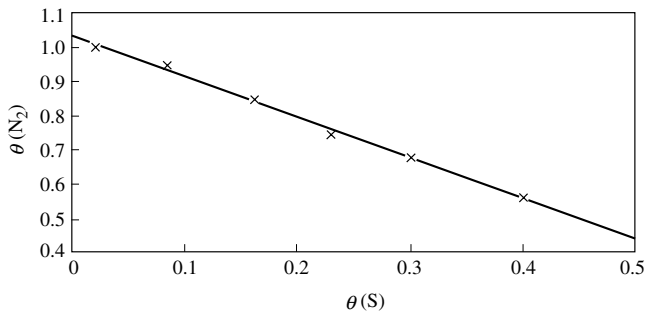


Fig. 8.24 The competitive adsorption between sulfur and nitrogen atoms on Fe (111) face

The above rules can be explained by the coverage area of the poison molecules. Usually, the maximum randomized coverage surface area of the poison molecules is about the same as the circumferential area of a circle with a radius equal to the length of the carbon chain. The coverage areas increase with the increasing of molecular weight and chain length, so does the toxicity. If each of the two ends of the molecular chain of the poison has a sulfur atom, the two ends of the poison molecules will simultaneously adsorb on the surface of the catalyst, limiting the freedom of movement of the carbon chain, reducing the coverage area, therefore reducing the effect of the poison.

The effects of poison are closely related to the reaction conditions.[43,44] It is generally agreed that, the higher the pressure the more severe is the poisoning, because the actual concentration of poison increases with increasing pressure. For reversible poisoning, the poisoning effect is not so obvious when the temperature is high. Take the industrial ammonia catalyst for example, when the syngas contains $400 \times 10^{-6}\,m^3$ of CO the yield is 50% lower than that with pure synthesis gas of at 450°C, whereas the yield is only 14% lower at 525°C. In addition, the higher the concentration of poison and the longer the residence time of poison in the system, the more significant the poisoning effect. At the same time, the higher the activity of catalyst, the more sensitive it is to the poison.

Although the degree of poisoning is lower at high temperature, the trend to permanent deactivation increases. For example, when the catalyst is operated at the pressure of 30 MPa and 450°C with $100 \times 10^{-6}\,m^3$ of CO in the inlet syngas, after six days of operation the concentration of ammonia decreases by 25% at the outlet. The activity of the poisoned catalyst could be fully restored after treatment with pure syngas for one day. However, when the catalyst containing $50 \times 10^{-6}\,m^3$ of O_2 works at 30 MPa and 500°C, the activity cannot be restored by treatment with pure syngas and the concentration of ammonia at the outlet is decreased by 4%. It is generally believed that the permanent deactivation of a catalyst by oxygen as a poison is due to the continuous oxidation-reduction of the active component in the catalyst, which may lead to the conglomeration of the iron crystallites. Since this growth of iron crystallite is irreversible, the loss of activity is permanent.

As a result, increasing the temperature, pressure and concentration of poison, as well as a protracted contact time of catalysts with a poison, will aggravate and continue the redox process, heightening the tendency of permanent poisoning.

For irreversible poisoning, the role of poison on active components of catalysts may be different at different temperatures. Take sulfide as an example, there are three temperature ranges of different behavior for metal catalysts. When the temperature is below 100°C, the free electron pair in the valence electron shell of sulfur is the cause for toxicity. This free electron pair forms a coordinate bond with the *d*-electron in a transition metal catalyst and the catalyst is poisoned. The poisoning of hydrogen sulfide on platinum belongs to this type. However, sulfuric acid without free electron pair is not toxic to the hydrogenation reaction at low temperatures. When the temperature is higher than 100°C, for instance, at 200–300°C, whatever the structure of the sulfide, they all have toxicity. This is because the sulfides with various structures can react with the metals at higher temperatures. When the temperature is higher than 800°C, the role of poisoning becomes irreversible because the chemical bonds between atoms of sulfur and the active components of the catalyst are not stable at such high temperatures. At the temperatures used in industrial ammonia synthesis processes, sulfide is one of the most deadly poisons.

8.3.2.4 *Poisons and the poisoning phenomena for ammonia synthesis catalysts*

In the process of ammonia synthesis, the common toxic compounds that lead to poisoning and loss of catalytic activity are oxygen and oxygenous compounds (CO, CO_2, H_2O), and non-metallic compounds such as sulfur, phosphorus, arsenic and chlorine, etc. Toxic metals may be present in the catalysts themselves, while metallic compounds are rarely present in the reaction gas. Oxygen and oxygenous compounds are reversible poisons which cause temporary poisoning; but sulfur, phosphorus, arsenic, chlorine and their compounds are irreversible poisons which cause permanent poisoning.

(1) Oxygen and oxygenous compounds. Oxygen and oxygen compounds, such as H_2O, CO and CO_2, are the most commonly encountered poisons for ammonia catalysts. Their presence will accelerate the growth of iron crystallites, leading to loss of surface area of catalysts. Generally speaking, the poisoning effect of 1 mol of O_2 or CO_2 is equal to 2 mol of CO or H_2O.[45] The poisoning effect of oxygen and oxygenous compounds is reversible, as seen in Fig. 8.25.[28] For the synthesis of ammonia, $CO + CO_2 \leq 10\,mg/m^3$ is present in the feed for large-scale plants, and $CO + CO_2 \leq 20 \sim 25\,mg/m^3$ for small and medium-scale plants.[43] The presence of any excessive amount of oxygenous compounds is usually abnormal operations in upstream of the synthesis process.

① Oxygen: Table 8.29 shows that active α-Fe in catalysts is easy oxidized and the oxide can be reduced to iron again by the hydrogen in the synthesis gas. This will cause oxidation and reduction repeatedly, resulting in the conglomeration of iron crystallites. The catalytic activity is decreased gradually because of irreversible grain-growth. Figure 8.26 shows that the isobar line of converge of oxygen on the catalyst in three different concentrations of oxygen (A, B, C).[28]

② Water vapor: The poisoning effect of water vapor on the ammonia synthesis catalyst is similar to that of O_2. The effect of water vapor on the activity of the catalyst relates to the concentration of water vapor, the temperature and pressure as follows.[43]

$$\xi_p \approx A \cdot \frac{T^6}{\sqrt{H_2O} \cdot P^{0.15}}, \tag{8.19}$$

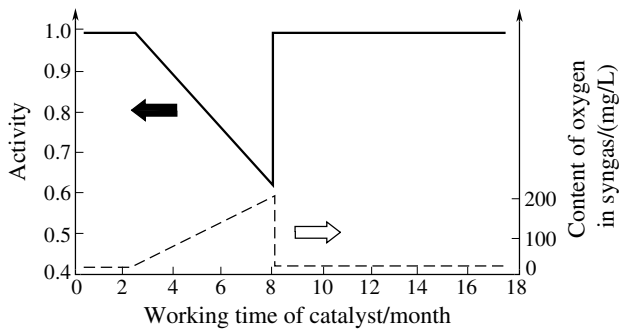


Fig. 8.25 Reversible poison of ammonia synthesis catalyst[28]

Table 8.29 Apparent activation energy of A110 catalyst at different contents of water vapor

Pressure/MPa	Contents of water vapor/(mg·L^{-1})	Apparent activation energy/(kJ·mol^{-1})	Temperature range/°C
7.3	<3	157.4	360–490
7.3	14	181.2	400–490
7.3	15	231.1	380–415
7.3	30	203.0	400–490
14.6	<5	163.3	400–490
14.6	10	171.7	400–490
14.6	30	211.4	400–490

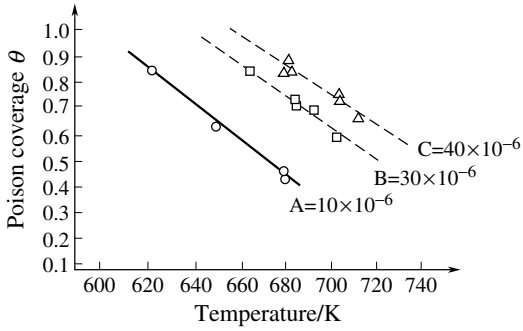


Fig. 8.26 Linear isobar of converge of oxygen on ammonia synthesis catalyst[28]

where ξ_p is the poisoning factor; T is the temperature, K; p is the pressure, MPa; A is the proportion coefficient of different catalysts.

Figure 8.27 shows the poisoning (ξ_p)-temperature (t) plot for the A110 catalyst. The poisoning effect of a trace content of water vapor on the A110 catalyst is shown in Table 8.29.

The active α-Fe in an ammonia synthesis catalyst is easily poisoned by water. Research shows that the effect of water vapor on the catalytic activity is still reversible when the water vapor content is as high as 27 mol% or more; but the activity cannot be restored when the content of water vapor reaches 42 mol%.

If the content of water vapor is too high, the water-soluble potassium in the catalyst will dissolve, leading to mal-distribution of potassium, and the loss of activity cannot be restored.

The content of water vapor in the ammonia converter is related to the temperature of the ammonia refrigeration system, especially in the reduction step of catalysts. When the temperature in the ammonia refrigeration system is higher, the content of water vapor at the converter inlet may reach several hundred mg·m^{-3}, exerting a great effect on the catalytic activity. Therefore, during the catalyst reduction stage, the content of water vapor is the main index for control and must be strictly controlled.

In the early papers on fused iron catalysts,[44] the reversible poisoning of oxygen and oxygen-containing on catalyst was studied. Emmet[46] found that the amount of

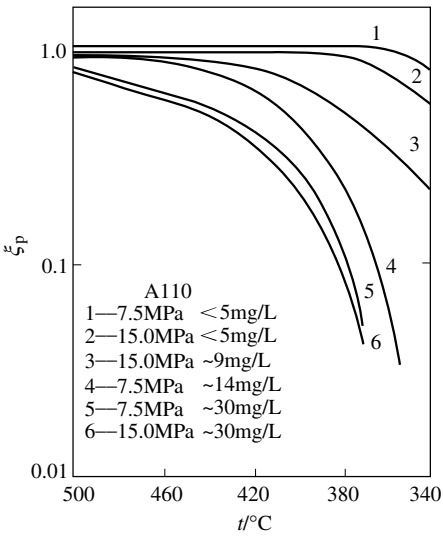


Fig. 8.27 Plot of $\xi_p - t$ poisoning curve of A110 at 7.5 and 15.0 MPa[43]

oxygen adsorbed on the catalysts is proportional to the ratio of $\sqrt{P_{H_2O}}/\sqrt{P_{H_2}}$, and the amount of oxygen adsorbed on the catalyst with promoters is more than that on the catalyst without promoters. A dynamic equation which takes into account the effect of oxygen or water vapor on the reaction rate has been proposed.

$$r = k_1 p_N \left(\frac{p_{H_2}^{2.5}}{p_{NH_3} p_{H_2O}} \right) - k_2 \left(\frac{p_{NH_3}}{p_{H_2}^{0.5} p_{H_2O}} \right)$$

Assuming the following reaction occurs in the overall process:

$$2N_{ads} + 2H_2O + H_2 = 2O_{ads} + 2NH_3$$

The dynamic equation of the effect of water vapor on the reaction rate is as follows:

$$r = \frac{k_1 p_{N_2} - k_2 \frac{p_{NH_3}^2}{p_{H_2}^3}}{\left(\frac{p_{NH_3}^2}{p_{H_2}^3} + C \frac{p_{H_2O}}{p_{H_2}} \right)^{\alpha}}$$

③ Carbon monoxide: The amount of carbon monoxide on the catalyst that will initiate poisoning is lower than that of water vapor (Fig. 8.28). The activity of A110 catalysts begins to decline significantly when the content of carbon monoxide reaches $10^{-6}\,m^3$at 370°C. With increasing temperatures, the initial content of poison for threshold poisoning increases. The CO poisoning factor ξ_p for ammonia synthesis catalyst is related to the content of CO and temperature, as seen in Table 8.30 and equation (8.20).[47]

$$\xi_P = A \frac{T^{10}}{V_{CO}^{0.57}}, \tag{8.20}$$

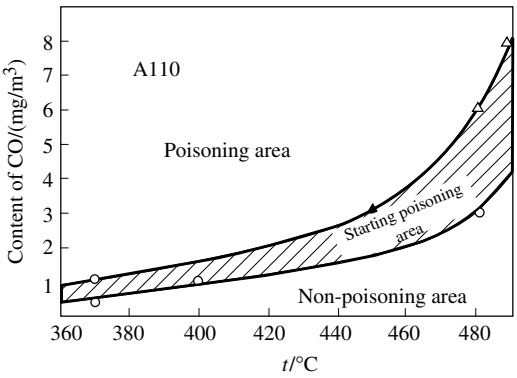


Fig. 8.28 Temperature range of starting poisoning

Table 8.30 Toxic coefficients (ξ_p/y_{CO}) of CO

	$CO < 6\,g{\cdot}m^{-3}$	$CO = 6–30\,g{\cdot}m^{-3}$
Temperature/°C	Toxic coefficient/($g{\cdot}m^{-3}$)	Toxic coefficient/($g{\cdot}m^{-3}$)
370	0.125	
400	0.092	
425	0.050	All about 0.013
450	0.033	
480	0.013	

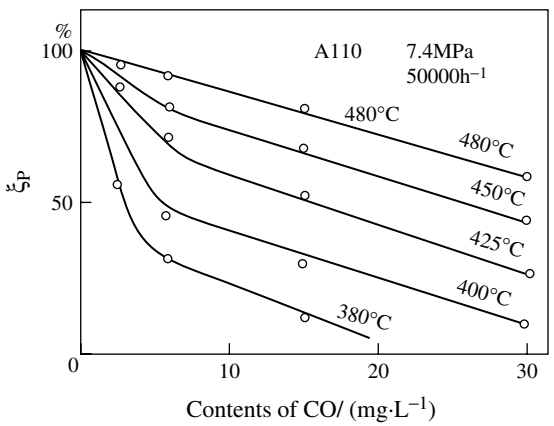


Fig. 8.29 Isotherm of CO poisoning

where ξ_p is the poisoning factor; T is the temperature, K; V_{CO} is the concentration of carbon monoxide, $g{\cdot}m^{-3}$; A is the proportion factors of different catalysts.

In Fig 8.29, the turning point on the poisoning isotherms (i.e. commencement of poisoning) is about $6\,mg{\cdot}m^{-3}$ and the corresponding values of the toxicity factor

ξ_p/y_{CO} are listed in Table 8.30. It can be seen from equation (8.20) that the toxicity factor is inversely proportional to the content of CO with the power of 0.57, and is proportional to the temperature with the 10th power. Compared with water vapor (8.19), the effect of temperature on the toxicity factor is more pronounced. It can be concluded from the above that poisoning by carbon monoxide is more serious than that by water vapor for ammonia synthesis catalysts.

The reason is that the hydrogenation of carbon monoxide is not fast enough due to strong chemisorption of carbon monoxide on the active iron and poisoning the active sites. It causes more serious poisoning than that by water vapor.

From the point of view of electronic structure, toxic elements in the molecules O_2, H_2O, CO_2 do not possess lone electron pair or unsaturated bonds; so these three poisons cause the poisoning of iron catalyst entirely due to their reversible chemical reaction with the active component α-Fe in the catalyst. However, as CO contains an unsaturated bond, it can provide electrons and combine with the d-orbit of the active iron atoms to form the bond of $Fe + x{\cdot}CO \rightarrow Fe\ (CO)_x$, thereby causing poisoning of the active site in the iron catalyst. From the point of view of dynamics, it is difficult to form Fe $(CO)_x$ under high temperature conditions and the low content of CO used with the ammonia synthesis catalyst. Generally speaking, the basic mechanism of CO poisoning is the same as other oxygenous catalysts.[48]

Figure 8.30 shows the serious poisoning and detoxification curves of ZA-5 and A110-2 catalysts for a carbon monoxide concentration of $500 \times 10^{-6}\,m^3$.[48] It can be seen that after the appearance of the poison, the decrease of activity for the ZA-5 is slower than that of the A110-2 during the poisoning stage (AB step). This indicates that the ZA-5 is less sensitive to the poison than the A110-2. This means that in industrial operations, subsequent to the intrusion of poisons, the bed temperature drop in converter for the ZA-5 is slower than that of the A110-2. The concentration

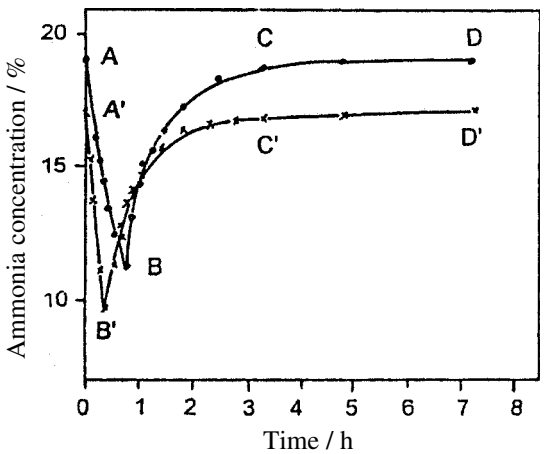


Fig. 8.30 Poisoning-detoxification curves of ZA-5 and A110-2 (• – ZA-5; × – A110-2) Measurement conditions: 15 MPa; 450°C; 30000 h^{-1}; Concentration of poison (CO): $500 \times 10^{-6}\,m^3$

of ammonia at B point is higher than that at B′ point; the residual activity of ZA-5 is higher than that of A110-2 after poisoning. At the restoration (detoxification) stage (BC step), the activity of ZA-5 is increased faster than that of the A110-2. Finally, at point D, the catalytic activity is basically restored to the original value. This result shows that the ZA-5 catalyst has a better anti-poisoning behavior than that of A110-2.

④ Carbon dioxide: The poisoning mechanism and effect of CO_2 is equivalent to two times of CO. In addition, CO_2 will react with K_2O in catalyst, and CO_2 will also react with NH_3 and form ammonium carbonates or ammonium salts such as ammonium bicarbonate. As a result, the pipeline and equipment is jammed.

(2) Compounds of sulfur, chlorine, phosphorus and arsenic. The compounds of sulfur, chlorine, arsenic and phosphorus will cause permanent poisoning of catalysts. The sulfides in the synthesis gas are commonly larger than the compounds of phosphorus, chlorine and arsenic, and the toxic effect of sulfides to catalysts is more serious than that of phosphorus, chlorine and arsenic. The following discussion will focus on the poisoning effect of sulfur and its relation to the life of catalyst.

The compounds H_2S, CS_2, COS, etc, enter the synthesis ammonia system easier, and CS_2, COS will form H_2S in an atmosphere of hydrogen.

First, it should be noted that sulfur enters the system, but does not leave the synthesis loop. Because, after the synthesis gas is introduced into the synthesis loop, although the single-pass conversion is not high, the synthesis gas will be consumed completely after recycling several times (except a small amount of inert gas), so the sulfur introduced with the synthesis gas will also remain outright in the converter. For this reason, sulfur should not be allowed to enter into the converter.

Second, the toxic effect of sulfur is permanent and cannot be reversed. Toxic sulfides include inorganic and organic sulfur. Inorganic sulfur is mainly hydrogen sulfide, organic sulfur include COS, CS_2, RSH, C_4H_6S (Thiofuran). Previous studies showed that when the sulfide comes into contact with the active component of the catalyst, chemisorptions follows two paths:

① Direct adsorption, such as

$$Fe + H_2S \leftrightarrow Fe \ldots SH_2$$

$$Fe + S\langle^{C=C}_{C=C} \leftrightarrow FeS \ldots S\langle^{C=C}_{C=C}$$

② Adsorption after hydrogenation, such as

$$CS + 4H_2 \leftrightarrow CH_4 + 2H_2S$$

$$COS + 4H_2 \leftrightarrow CH_4 + H_2O + H_2S$$

$$H_2S + Fe \leftrightarrow Fe \ldots SH_2$$

It can be seen that, with both organic and inorganic sulfur, the irreversible poisoning of the catalyst occurs after the sulfide is reduced to H_2S and adsorbed on the surface of the fused iron catalyst.

It can be seen from the results of XRD analysis that during the process of poisoning (Fig. 8.31) the hydrogen sulfide will react with the active center of α-Fe and form stable FeS, resulting in the active center of α-Fe losing its activity.

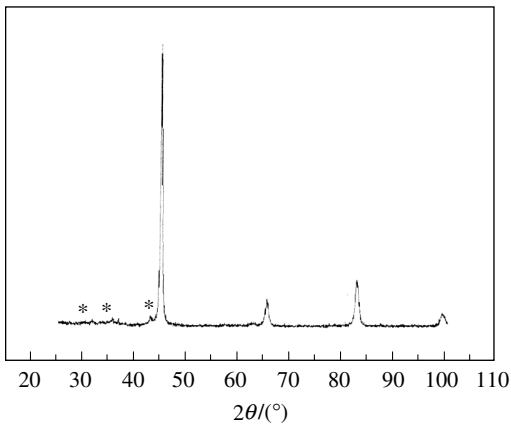


Fig. 8.31 XRD pattern of catalyst after poisoning (sulfur) (*-FeS)

The poisoning effect of sulfide compounds (including phosphorus) on catalyst may be as follows: ① Some of the surface of catalysts will lose the ability to chemisorbs nitrogen after the catalyst is covered by sulfur or chemisorbed with hydrogen sulfide; ② The work of electronic effusion increases after sulfur has adsorbed on the catalyst surface, so increasing the difficulty for the chemisorption of nitrogen on the uncovered surface of the catalyst; ③ Sulfur, similar to oxygen, will speed up the re-crystallization of the catalyst. Temperature also has a great effect on hydrogen sulfide poisoning. If the catalyst contains a calcium oxide, calcium sulfide may form on the catalyst surface and increase the stability of the sulfide.[7] The sulfur within an ammonia synthesis catalyst will congregate on the surface of catalyst during use.

During the preparation of an ammonia synthesis catalyst, sulfur may be introduced via the catalyst material itself or other raw materials. The sulfur often congregates on the catalyst surface during its use, thus affecting the catalytic activity. Reports in the literature show that when there is 0.02% or 0.03% (mole fraction) of sulfur in the bulk catalyst, the catalytic activity is reduced by 15% or 30% respectively. Figure 8.32 shows the relationship between the sulfur content in the catalyst bulk and relative activity.[49] It can be seen from the figure that even very small contents of sulfur in the catalyst bulk will lead to a sharp decline in the catalytic activity. When the sulfur content reaches 0.2%, the catalyst is almost inactive. As a result, a trace content of sulfur introduced during the preparation of catalyst has great effect on the catalytic activity. The sulfur content within the catalyst should therefore be less than 0.01%.

XRD spectra show that the sulfur mostly congregates on the catalyst surface, and reacts with the active iron atoms to form sulfide(s) of iron, FeS and FeS_2 at high sulfur content, and mainly FeS at low sulfur content.

In Chapter 3 it has been pointed out that the contents of Fe in reduced catalyst are as high as 91% to 92%; but the active α-Fe exposed on the surface is just only 0.5%–0.7%. For example, with 10 tons of oxide catalyst in the reactor, only 39–55 kg of active α-Fe exposed on the catalyst surface participates in the catalytic reaction. According to the poisoning reaction of H_2S, with 23.7–33.5 kg of H_2S (or 26.5–37.4 kg

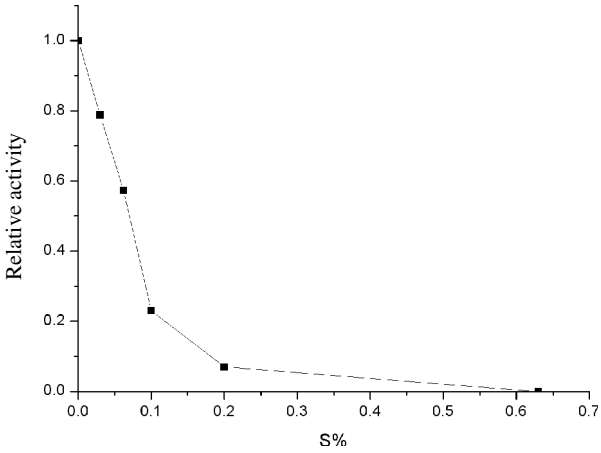


Fig. 8.32 Effect of sulfur contents of catalyst on the catalytic activity

of CS_2) passing through the catalyst, the catalyst will be completely inactivated. In other words, even if the sulfur content in the fresh syngas only is $0.1\,g{\cdot}m^{-3}$, the content of sulfur (CS_2) introduced into an ammonia plant of 40,000 tons·year^{-1} capacity, can be up to 11.2 kg per year (the sulfur content on the catalyst surface is up to 0.14%). Two years of operation would be enough to completely deactivate the catalyst. The simple calculation above shows that sulfur cannot be allowed to enter the synthesis loop.

In plants with a methanation process, before coming into the ammonia synthesis converter, the fresh syngas first passes through the Ni methanation catalyst. Ni catalyst is sensitive to sulfur in the same way as Fe catalyst. The Ni catalyst becomes a "scapegoat" to protect the Fe catalyst. Therefore, the life of a Fe catalyst in these plants could be as long as 10 to 15 years.

In plants without a methanation process, such as small and medium-scale plants, there is no Ni catalyst serving as a protection for the Fe catalyst, the latter is under the threat of sulfur. As a result, sulfur is the main reason for the deactivation of catalyst in these plants. Table 8.31 shows the measurements of organic sulfur for several plants. The sulfur content in the fresh syngas is 0.29–0.88 $g{\cdot}m^{-3}$ (standard). The shortest life of the catalysts is only 41 days, the longest only 264 days (Table 8.32), which are fully expected. The average sulfur content found in the waste catalysts

Table 8.31 Contents of organic sulfur in ammonia synthesis processes/$g{\cdot}m^{-3}$

Plants	Semi-water gas	Shift gas	Carbonation gas	Water-washed gas	Fresh syngas	Inlet of converter
A	210	26.7	24.5	0.461	0.461	—
B	207	17.0	4.40	0.882	0.882	0.098
C	210	14.0	3.0	0.35	0.35	0.04
D	232–311	0.006–8.56	—	0.005–0.54	0.005–0.29	—

Table 8.32 Contents of accumulated sulfur in the waste ammonia catalysts after used in ammonia plants/wt%

Status and location of the catalyst		A plant (used 131 days)	A plant (used 104 days)	B plant (used 264 days)	C plant (used 41 days)
Fresh catalysts		0.0092, 0.0012	0.003	0.0052	0.0022
Waste catalyst	Top of bed	0.39	0.503	0.42	0.58
	Middle of bed	0.43	0.413	0.351	0.11
	Bottom of bed	0.33	0.008	0.0923	0.029
	Average	0.284	0.308	0.287	0.24

Table 8.33 Contents of accumulated sulfur in the waste ammonia catalysts after used in some ammonia plants/wt%

Status and place of catalyst		A plant (used 95 days)	B plant (used 305 days)	C plant (used 370 days)	D plant (used 730 days)	E plant (used 630 days
Fresh catalysts		—	0.04	—	0.04 (surface)	—
Waste catalyst	Top of bed	0.82	0.36	0.153	0.71[a]	0.16[a]
	Middle of bed	0.60	0.172	0.108	0.34[b]	0.04[b]
	Bottom of bed	0.80	0.182	0.053	—	—
	Average	0.74	0.238	0.105	—	—

By X-ray fluorescence analysis: [a]the surface of the waste catalyst particles at the top of the bed; [b]the inner of the waste catalyst particles at the top of the bed.

discharged from these plants is 0.24%–0.31%, 0.39%–0.58% in the top part of the bed; which is enough proof that the catalyst has been completely deactivated, and sulfur is the main reason of catalyst deactivation.

For example, the life of catalyst in some plants is less than a year, the shortest period being less than 100 days (as plant A in Table 8.33), it is often suspected that the catalyst itself is not good or has poor anti-poisoning property. In reality, any metal catalyst, including the Fe catalyst that all can not resist to sulfur poisoning. Metal catalysts can not have anti-sulfur poisoning ability. In order to prove this view, the sulfur content is measured in waste catalysts discharged from these plants, as shown in Table 8.33, to identify the cause of short life.

It is seen from the Table 8.33 that the catalyst of plant A had a much shorter life, which is caused by poisoning of sulfur. The catalyst of plant D was used for more than two years, and the decrease of activity was due to the accumulation of sulfur. The catalyst of plant E was forced to be replaced because of leakage in process equipment. The table shows that poisoning of sulfur on catalyst generally occurs in the upper part of the catalyst bed.

It may be seen from this that the life of a catalyst under normal conditions is determined mainly by the sulfur content in the syngas. The reason of catalyst deactivation is chiefly due to the cumulative effect of chronic poisoning by sulfur.

The loss of catalytic activity will continue, as the effect of chronic poisoning accumulates up to a point, the catalyst will completely deactivate. The rate of accumulation of the effect of chronic poisoning will determine the life of the catalyst. The life of catalysts can be predicted provided by the following method of calculation according to the sulfur content in the fresh syngas: that is catalyst life (years) $\leq (W_{\text{cat}}/y_{\text{NH}_3} \times C_{\text{CS2}}) \times 10^3$, where W_{cat} is the weight of the loaded catalyst, y_{NH_3} is the annual throughput of ammonia, C_{CS2} is the sulfur content in the fresh syngas, $\text{mg}\cdot\text{m}^{-3}$ (standard). With the aid of desulfurization and refining equipment, the most effective way for controlling the sulfur content of sulfur coming into the ammonia converter is to control the sulfur content of coal.

With the progress of the desulfurization technology, the service life of iron catalysts for ammonia synthesis is continually extended, as much as 20 years.

(3) Chlorine and chlorine compounds. Chlorine and chlorine compounds can react with K_2O promoters to form volatile potassium chloride at high-temperature, leading to the loss of the potassium and reduction of the catalyst's activity. In addition, chlorine compounds have low melting points and are slightly volatile, causing the growth of iron crystallites and damage to the structure of the catalyst. The toxicity of chlorine on the catalyst is far greater than that of oxygen-containing compounds (about 100 times).[47] Chlorine in an ammonia synthesis catalyst body is also one of the sources of chlorine poisoning. The chlorine content should be controlled to below $5 \times 10^{-6}\,\text{g}\cdot\text{m}^{-3}$.

(4) Lubricating oil. Partial cracking of lubricating oil will form carbonaceous materials depositing on the surface of the ammonia synthesis catalyst denying the reacting gas access to the catalyst, rendering the catalyst inactive. The sulfur in lubricating oil can also cause catalyst poisoning. Under normal circumstances, H_2S will not enter the synthesis loop directly from the feed gas, because the purification processes of raw gas (such as methanation and copper-ammonium solution washing) can completely remove H_2S. However, valve leakages and misuse of bypass valve of the compressor, and sulfur poisoning of ammonia synthesis catalyst can occur from time to time. Potential catalyst poisoning due to the trace content of sulfur in the lubricating oil contain in a few of sulfur is sometimes overlooked.

The above issues related to the inactivation of catalysts are significant not only in industrial practice but also in academic studies, especially with partial melting and poisoning, which has appeared in many academic reports and papers.[26,28,38,40,44,49]

In principle, the adsorption of oxygen-containing compounds on catalyst is reversible. As long as the concentration of poison in the raw material is reduced, the poison on catalyst will be desorbed and the catalytic activity restored. However, in industry, because the rate of desorption of these poisons from the catalyst pores is very slow, this reduction process is often slow. As the heat of adsorption of the poison is high, appropriate increase of the operating temperature is an effective measure during reduction under a reduction atmosphere. Figures 8.33[28] and 8.34 show the reduction-time curve for the Fe catalyst/O poison system, revealing the time for the recovery of an adsorbed oxygen monolayer on the catalyst. The shortest reduction time shown in the figure does not take into account the effect of diffusion. After the catalyst bed is treated with hydrogen (for a space velocity of $1000\,\text{h}^{-1}$) at constant temperature, the oxygen is removed from the iron at a reasonable rate under typical plant operating temperatures.

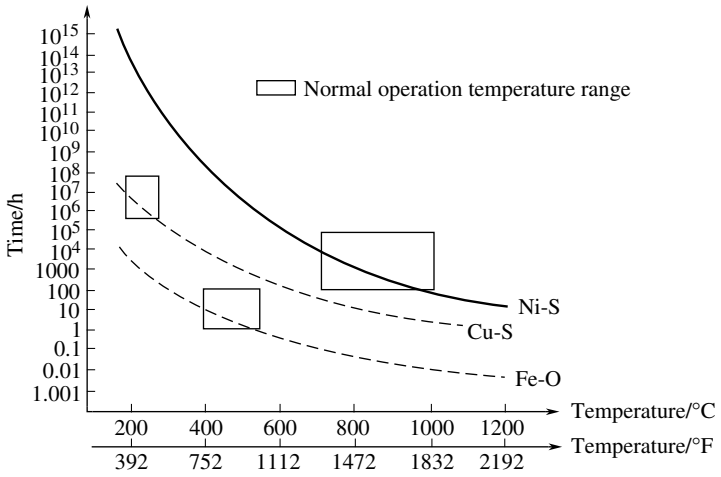


Fig. 8.33 Calculated values of oxygen desorption time (Required time of coverage reduced from 1 to 0.5)

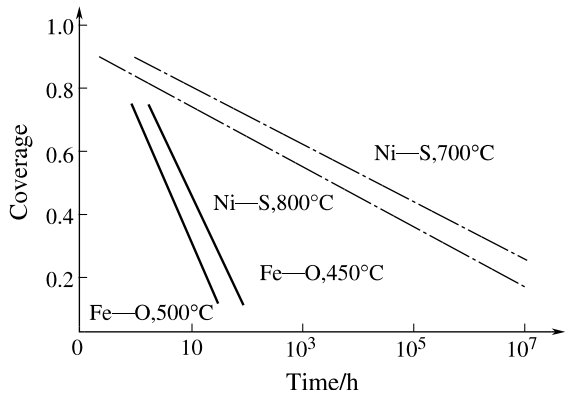


Fig. 8.34 Desorption and renewable with non-toxic raw gas

The half-time for the removal of a monolayer of adsorbed oxygen is about ten hours.[28]

8.4 Mechanical Strength of Catalysts

The mechanical strength of a solid catalyst is very important for normal operation in an industrial process. Breach and pulverization of catalyst particles during industrial production are common occurrences. Poor mechanical strength of catalysts often lead to poor gas flow and rise in bed pressure drop, forcing the plant to stop production. The development and production of catalysts with good mechanical strength is a basic requirement for industrial catalysts.[50]

Usually, a solid catalyst will be subjected to many forms of mechanical stress during manufacturing and using. These include collision and attrition during transportation, impact and collision during loading, internal stress generated by phase changes during activation and reduction, heat stress caused by cycling in temperature change, friction and pressure drop generated by fluid flow as well as gravitational pull caused by the weight of the catalyst and so on. As a result, steady operation can be guaranteed only when the catalyst has sufficient mechanical strength.

8.4.1 *Theoretical research on the mechanical strength for the solid catalyst*

The strength of a catalyst has a close relationship with its material characteristics and microstructure. Knudson[51,52] proposed that the crush strength (σ) of a catalyst is a function of the diameter (d) of the particle and its porosity (θ):

$$\sigma = Kd^a \exp(-b\theta), \tag{8.21}$$

where K, a, b are constants determined by the material type, destruction mechanism and the measurement condition respectively.

The equation shows that other than the chemical composition of the catalyst, the pore structure, preparation method and molding conditions are the major determining factors on catalyst strength. Kono *et al.*[53] proposed that the strength of a catalyst is determined by the number of contact points and strength of each contact point between the particles. Increasing the particle porosity reduces the number of contact points and thereby decreases the particle's strength. Kono's empirical equation is as follows:

$$\sigma = \frac{nF(1-\theta)}{\pi d^2}, \tag{8.22}$$

where n is the number of contact points between the particles; F is the bonding force between contact points.

Others used the principles of soil mechanics to study the size effect of the crush strength of a single particle, and proposed that the behavior should follow Huit's equation.[54]

$$\frac{L}{d_P^2} = C, \tag{8.23}$$

where L is the external load when the particles are broken; d_P is the particle diameter; C is the a constant; its value depends on the property of the vessel where breakage occurs and the characteristics of the broken particle.

Kapur *et al.*[55] suggested another empirical equation for spherical particles:

$$L = P_0 M^P, \tag{8.24}$$

where P_0 is a constant of the stress experienced; M is the mass of the spherical particle; P is Modulus, its value about 0.6.

When based on particle diameter, the equation can also be written as:

$$\frac{L}{d_P^{1.8}} = C. \tag{8.25}$$

At present, the theory of abrasion is not yet mature, and only a few research reports on brittle material have appeared. The abrasive resistance of brittle material depends on the relative hardness and density of the particle material and that of the material coming into contact with the particle. The abrasion of a brittle material is caused by the slip movement of two surfaces and the surface between two particles, and also the fracture and cracking of the surface due to the impact of particles. Therefore, the degree of abrasion is related to the smoothness of the surfaces in contact and the particle size. The smoother the surfaces and the less sliding movement of particles, the higher are the intensity of abrasion.[56] In addition, the hardness of the brittle material increases with reducing particle size, and the abrasive resistance increases with enhanced hardness.[57]

8.4.2 *The basis of catalyst solid mechanics*

A large number of test results indicate that supported metal catalysts and metal-oxides have properties similar to that of brittle materials.[58,59] That is to say, basically plastic deformation does not occur before the materials fracture under external stress, and the fracture is instantaneous without any obvious forewarning. Solid catalysts are highly porous with crystal boundaries and a lot of defects, such as dislocation or discontinuities arising from the presence of promoters. They are similar to cracks, as defined in fracture mechanics, where fracture stresses are focused, eventually leading to breakup of the catalyst particles.[60,61]

The well-known Griffith's theory constitutes the principle of fracture mechanics. In fracture mechanics, the fracture of a brittle material is caused by the increase of tension-stress at the edges of micro-cracks (disfigurements) in the material.[62] The breaking strength of a catalyst follows the Griffith equation.

$$\sigma_c = \sqrt{\frac{2Er}{\pi c}}, \tag{8.26}$$

where E is the modulus of elasticity, r is the surface energy and c is the crack size.

Increasing the modulus of elasticity and surface energy or reducing the size of cracks in the material can improve the strength of a solid catalyst. In addition, the size, shape and random orientation of micro-cracks (disfigurements) result in the data of catalyst strength exhibiting a high degree of scatter.[61] For example, the difference between the maximum and minimum lateral pressures on a single particle of certain high temperature shift catalysts is larger than the average lateral pressure.[63] Research results show that the scattered nature of the fracture strength of a brittle material can be described by the Weibull distribution.[58,60,61,64]

In 1951, Weibull proposed the "weakest link model",[64] and gave corresponding distribution functions on the basis of the model. The model is formulated using a chain link under symmetrical tension-stress as shown in Fig. 8.35. The chain has n links, and the whole chain would disconnect if any one link is broken under the action of the σ stress. The broken strength of each link follows a uniform distribution. The critical defect or crack is the smallest crack or flaw with the least stress. In a brittle material, the critical defect or crack for a given stress distribution is the weakest link. A brittle material can be regarded as a material with n defects or cracks which are independent of each other, with the cracks under a uniform distribution of damage stress. Under the effect of an external force, the invalidation of the material

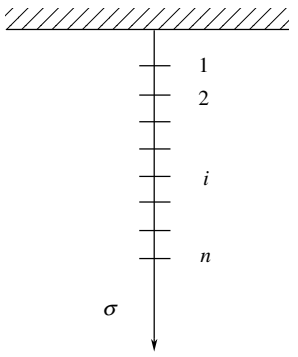


Fig. 8.35 The weakest link model

depends on the critical defects or cracks, and is not necessarily dependent on the cracks or defects (the largest defects or cracks) with the smallest damage stress, and not always dependent on cracks or defects in the area with the highest stress. This is because the seriousness of the defect is not only related to the attributes of the defect itself (size of the defect), but also to its location, shape, orientation (compared with the externally imposed load). The weakest link model also suggests that only the invalidation of a sample is caused by the tension-stress, and not determined by pressure or shear stress.

Two necessary conditions are required by the Weibull statistical distribution: ① all samples should have the same size and distribution of tensile stress; ② all samples contain a unified and uniform distribution of defects. The derivation of Weibull's distribution is as follows.

Assuming that the number of cracks is proportional to the size of the space under consideration, the cracks in this space are randomly distributed, and the tensile stress is uniform, and combining with the weakest link assumption, the probability of structural fracture may be expressed as:

$$\begin{cases} F(\sigma) = 1 - \exp\left[-V\left(\dfrac{\sigma - \sigma_u}{\sigma_0}\right)^m\right] & \sigma \geq \sigma_u \qquad (8.27) \\ F(\sigma) = 0 & \sigma < \sigma_u. \qquad (8.28) \end{cases}$$

Here, σ is the utmost fractured stress; σ_0 is the standard factor; σ_u is the critical stress, no fracture occurred under this stress; m is the Weibull modulus; V is the volume of the space with the highest stress.

Taking $\sigma_u = 0, V(\frac{1}{\sigma_0})^m = \beta_0$, the above equation is simplified to the two-parameter Weibull distribution:

$$F(\sigma) = 1 - \exp[-\beta_0 \sigma^m] \quad \sigma \geq 0. \qquad (8.29)$$

Here, $F(\sigma)$ is the disabled probability of sample; σ is the largest tensile stress of the disabled sample; β_0 is the size factor; m is Weibull modulus.

In the formula above, it is worth noting that the statistical approach based on the highest tensile stress in the sample is only a mathematical one. It does not mean that the sample always begins to fail at the place with the highest tensile stress.

For samples with different shapes or are bearing different loads, there is a different relation between the highest tensile stress σ induced in the sample and the external load F. The location of σ and its distribution also varies.

For a sphere with its center under pressure, the disabled strength is[65]:

$$\sigma = 2.8\frac{F}{\pi d^2}. \tag{8.30}$$

For a sphere with surface disabled[65,66]:

$$\sigma = 1.6\frac{F}{\pi d^2}. \tag{8.31}$$

For a cylinder under radial stress[67]:

$$\sigma = \frac{2F}{\pi dl}. \tag{8.32}$$

Here σ is the largest tensile stress of sample; F is the external load; d is the diameter of sample particle; and l is the length of sample particle.

For the determination of the strength of single catalyst particles, the relationship between σ and external force F is still not clear. As an approximation, σ can be considered proportional to F in the measurement of single-particle strength for a variety of catalysts in common use.[61] That is,

$$\sigma = \Phi F, \tag{8.33}$$

where Φ should be a factor related to the shape, geometric size and the load-bearing of the sample, reflecting the relationship between the external load and the highest tensile stress.

Inserting equation (8.33) into equation (8.29), we get:

$$F(F) = 1 - \exp[-\beta F^m], \tag{8.34}$$

where $F(F)$ is the disabled probability of sample; F is the external load; β is the size factor; m is the Weibull modulus, reflecting the scattered nature of the distribution of strength, the smaller the m value, the more scattered the distribution of strength.

Equation (8.34) is the often used form of Weibull's distribution with two parameters characterizing the strength of the catalyst. Using this distribution, when taking into account the average strength of the catalyst, the Weibull modulus represents a measure of the uniformity of catalyst strength. If the average strength of two kinds of catalysts is similar, the probability of damage to the catalyst with the higher Weibull modulus is small.[68]

On the basis of the Weibull statistical distribution for the "Single-Particle Crush Strength (SPCS)" of catalysts, one can extend the application to the measurement of the "Whole-Stack Crush Strength (WSCS)" of catalysts. In the measurement of the WSCS, the catalyst particles are randomly deposited in a cylindrical container. The axial external load (pressure P) is applied to a piston, transferring the load from one particle to another through the contact points between the particles. In this case, a single particle in the container is primarily subjected to three forces, i.e., the gravity of particles themselves, the external force P and the frictional resistance of the vessel walls. However, the bulk of the catalyst bed is usually not high, so the effect of gravity can be ignored. Moreover, when the diameter D of the container is much larger than the diameter d_P of the catalyst particles, the effect of vessel wall can also be ignored.[69]

Bagster *et al.*[70,71] proposed an ideal three-dimensional stack model for a sphere with a constant diameter (Fig. 8.36). In this model, the spheres rest on each other

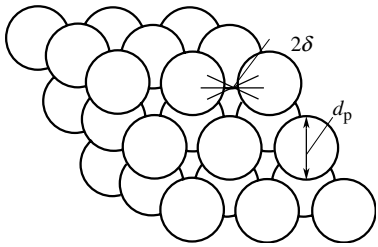


Fig. 8.36 Ideal three-dimensional bulk model of the ball

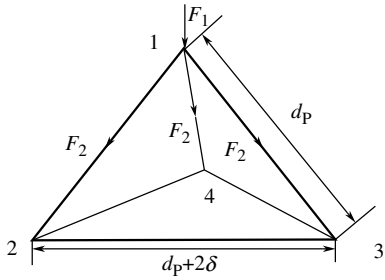


Fig. 8.37 Delivery system of force in tetrahedron

tetrahedron. There is no contact between any two adjacent spheres on the same layer and the space between two surfaces is 2δ. Therefore, every sphere in the interior makes contact with only six other spheres. (three in the upper layer and three the lower), i.e., the coordination number is six. Figure 8.37 shows the mode of transfer of forces in a tetrahedron of the model. Each interior sphere is subject to the same six contact forces F_2, with the value expressed as:

$$F_2 = \frac{F_1}{\sqrt{6}}\left(1 - \frac{2\delta^2}{d_P^2} - \frac{2\delta}{d_P}\right)^{1/2}. \tag{8.35}$$

Li *et al.*[66] assumed that the stack of spherical catalyst particles in a packed bed agreed with the above tetrahedron stack model, and ignored the gravity and wall effects. In the measurement of WSCS, each sphere on the top of layer is subject to a downward pressure F_1 under the effect of the pressure P.

$$F_1 = \frac{\sqrt{3}}{2} P d_P^2 \left[1 + \frac{2\delta}{d_P}\right]^2. \tag{8.36}$$

Li *et al.*[63] assumed that the crush strength of the spherical catalyst agrees with the two–parameter Weibull distribution under six contact forces F_2;

$$F(\sigma) = 1 - \exp[-B_0\sigma^M]. \tag{8.37}$$

The internal tensile stress σ of the spherical particles may be considered to be proportional to F_2, that is,

$$\sigma = \Phi F_2, \tag{8.38}$$

where Φ is a constant associated with the diameter of the spherical particles.

Inserting equations (8.35), (8.36) and (8.38) into (8.37), we get:

$$F(P) = 1 - \exp[-BP^M], \tag{8.39}$$

$$B = B_0 \left[\frac{\sqrt{2}}{4} \phi d_P^2 f \left(\frac{\delta}{d_P} \right) \right]^M, \tag{8.40}$$

$$f\left(\frac{\delta}{d_P}\right) = \left(1 + \frac{2\delta}{d_P}\right) \left(1 - \frac{2\delta^2}{d_P^2} - \frac{2\delta}{d_P}\right)^{1/2}. \tag{8.41}$$

From equation (8.39), one can obtain the relationship between the stack "fine powder ratio" (the relative amount of broken) and the external load, yielding a simplified overall model for the "stack crush strength" of the catalyst.[63]

$$\frac{dm}{m} = 1 - \exp[-BP^M], \tag{8.42}$$

where B and M are the parameters; and P is the external axial-load; dm/m is the "fine powder ratio" (equivalent to the disabled probability of $F(P)$), that is the mass ratio of broken spherical particles to the whole spherical particles.

Equation (8.42) shows that the relation between the fine powder ratio and external force P can be expressed by the Weibull equation. The broken curve (the relationship curve between the fine powder ratio and external force) is a Weibull curve. This is closely related to the agreement between SPCS and the Weibull distribution. Experimental results in the literature[63] show that the parameter M of the WSCS has a value very close to the Weibull modulus in the SPCS data. Both relationships are reflections of the distribution of defects in the material. In the measurement of WSCS, the disabled probability of $[F(P)]$ is the fine powder ratio (dm/m).

In many aspects, the catalyst bed in a practical fixed-bed reactor is similar to the catalyst bed in the cylindrical container of the WSCS test. For example, the catalyst particles in a fixed-bed reactor and the small stack WSCS bed have the same stacking law; the pressure on the catalyst particle of a practical reactor is mainly the gravity itself and the pressure drop generated by fluid flow, all of which are axial, similar to the pressure of the piston of the small stack bed. The test process in WSCS may be considered as the most simplified simulation of a practical reactor. This model is a good representation of the law of invalidation of spherical catalysts in the WSCS measurements.

If the fine powder ratio obtained after particles are subjected to an external force is regarded as an index of strength disabled, the WSCS model may also be extended to describing the disabled behavior of non-spherical particles in a catalyst bed.[72] Taking the logarithm of equation (8.42) twice, we have:

$$\ln \ln \left(\frac{1}{1 - dm/m} \right) = M \ln P + \ln B, \tag{8.43}$$

The data of P and dm/m can be obtained directly from the WSCS measurements. The values of M and B for all samples can be obtained through linear regression of equation (8.43). Experiments showed that[72] the data obtained by substituting the disabled probability of $F(P)$ with the fine powder ratio still satisfies the linearity of change. Because broken catalyst particles are more easily broken further than whole catalyst particles, the M value obtained from the slope of the linear curve is always slightly larger than the M value obtained from the fine powder ratio. By introducing the fine powder ratio, the WSCS model can extend its application to the non-spherical catalyst particles. Through this relation, if the dm/m is defined as the fine powder ratio, and regarded as the index of disabled strength , the WSCS model of spherical particles can be used to evaluate the relative strength and the disabled behavior of non-spherical particles catalyst (such as the flakes, the cylindrical — and the clover — type etc).[72] As the fine powder ratio can be readily measured, the adjusted model has great practical value in experiments.

8.4.3 *The measurement of mechanical strength for solid catalyst*

As mentioned above in the beginning of Section 8.4, solid catalysts are subjected to many different mechanical stresses from the stage of manufacturing to usage. As it is not possible to design a single test to take into account all these factors, different tests should be taken to measure the catalyst particle's capability in bearing mechanical stress, abrasion and collision.

In 1974, a scientific method of measurement for the mechanical strength of catalyst particles and the issues of its standardization were discussed[73] in the first conference on the standardization for measurement methods in the U.S. Thereafter, some of the measurement methods for mechanical strength of catalysts were developed as standards[74−81] in many countries. At present, the characterization of mechanical strength of catalysts can be mainly divided into two kinds.

The first is the strength of anti-fracture. This experimental method is divided into: single particle crush strength (SPCS), the whole stack crush strength (WSCS) and the drop-shatter test.

(1) Single particle crush strength (SPCS). SPCS measures the particle strength by using a single catalyst pellet. The value of the average external load applied before a certain number of particles with uniform size fail is regarded as the measurement of the particle strength. With regard to the number of particles to be used, the standards of ASTMD 4179-2001 and ASTMD 6175-1998 stipulated 50 to 200,[74,75] HG/T2782-1996 in China 30 to 100.[76] Depending on the method of loading, the SPCS method can be divided into: positive pressure, lateral pressure, "blades" and "three-point bending" crush strength. As for the representation of the value of particle strength, the positive and lateral pressure on spherical and tableting column s are directly expressed by the value of the external load according to ASTMD4179-2001, the positive pressure on cylindrical tablets by ratio of the external load to the cross-sectional area of particles according to standards in China; the lateral pressure on extrusive pellet by the ratio of the external load to the length of the particle according to ASTMD6175-1998.

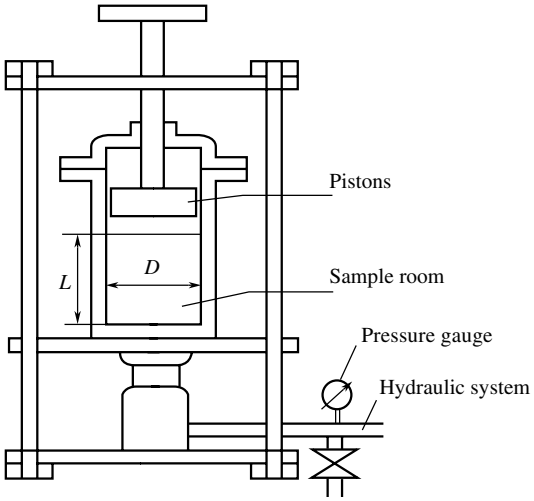


Fig. 8.38 Equipment for testing the whole stack crushes strength of catalysts

(2) The whole stack crushed strength (WSCS). The mechanical strength of catalysts is closely related to its geometric shape. Industrial catalysts have many geometric shapes due to the requirement of the catalytic reaction process and the reactor configuration design. For some particle shapes, it is very difficult to measure their mechanical strength using the SPCS method. SPCS also does not directly reflect the complete conditions of catalyst fracture in a fixed-bed. WSCS is closer to the practical conditions of the catalyst in a fixed-bed.[82,83] In the WSCS method, a certain number of catalyst pellets are placed into a cylinder, with pressure applied to the top of the cylinder. The fine powder ratio generated under a prescribed external pressure is regarded as the measurement of strength (Fig. 8.38). There are two test methods that use the same basic principles; they differ in that one method measures the amount of fine powder under a fixed load; while the other method breaks the catalysts under an increasing load, and draws the curve of the amount of fine powder amount generated under different loads.

(3) The drop-shatter test. The impact caused during the process of catalyst loading is much larger than that during the process of catalyst transport, so the strength of the catalyst (especially tablets) can be expressed by the drop-shatter test.

The nature of the area for dropping the catalyst must be prescribed. The ideal condition is that the area has the same hardness as that of the catalyst; it can be harder than that of the catalyst and not softer. For tablets, the minimum drop height for particle fracture is related to the diameter/height ratio and the tablet's utmost tensile strength (UTS). A rough approximation of the relationship is as follows:

The drop height for particle fracture $(m) = 0.075 \times d/L \times (\text{UTS})$, UTS is expressed in $\text{kg}\cdot\text{cm}^{-2}$.

It can be seen from the above equation, the strength of tablets that are thin but long is poorer than that of tablets that are thick but short. The value of the d/L is usually one, and the design value of minimum drop height for the tablet is 3 m or the UTS is $40\,\text{kg}\cdot\text{cm}^{-2}$.

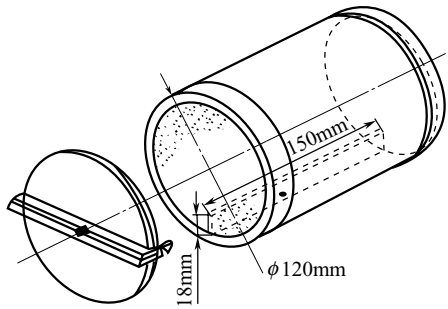


Fig. 8.39 Cylinder for abrasion experiment

The strength of a spherical catalyst for ammonia synthesis can be expressed by the minimum drop height, with a design value above 10 m.

The second is the abrasion strength. There are many methods to measure the abrasion strength of a catalyst, but only two of which are commonly used. One is the rotating abrasion method, and the other gas-flow abrasion method. According to the abrasion conditions of catalysts during use, the first method is generally applied to measure the strength of the catalyst used in a fixed bed, and the second method is often applied to measure the strength of the catalyst used in a fluidized bed. Regardless of which method is used, the method must ensure that the failure of strength is caused by abrasion, rather than fracture.

The rotating abrasion method is the typical method to measure the abrasion of catalysts used in fixed beds. The method has been repeatedly adopted by ASTM in America and as national standards in China.[77−79] The basic approach of the method is that the catalyst is loaded in a rotating drum with an internal baffle (Fig. 8.39), the drum rotates at a definite rate, and the catalyst is abraded when rolling up and down during rotation. After a prescribed time, the sample is taken out and sieved. The catalyst strength can be expressed by the amount of fine powder generated per unit time from unit mass of the catalyst, and this is called the "abrasion ratio". For the gas-flow abrasion method such as the ASTMD5757-1995,[80] the underlying theory is that the catalyst is flowing within a high rate of gas flow, and a fine powder is generated by friction between the particles. The "abrasion ratio" is the amount of fine powder generated per unit mass of catalyst per unit time, and is regarded as an evaluation index of the abrasion performance of catalysts.

The SPCS cannot be used to measure the abrasion of irregular-shaped fused iron catalysts. The abrasion of these catalysts should be characterized by the WSCS method. Figure 8.40 shows the relationship between the external load and the fine powder ratio for irregular-shaped $Fe_{1-x}O$-based fused iron catalyst measured by WSCS. The figure shows the results fitted according to equation (8.43) and the data of Fig. 8.40. The fitting parameters are shown in Table 8.34.[84] In the experiments, there are two different particle sizes of fine powder (<0.42 mm and <0.85 mm) used for the calculation of the fine powder ratio (dm/m).

It can be seen from Fig. 8.41 that two batches of WSCS' data are all in the form of a straight line for the irregular-shaped fused iron catalyst, the correlation coefficients R^2 are very close to one, which indicates that equation (8.42) fits the experimental data well. Thus, the WSCS model can describe the relationship of

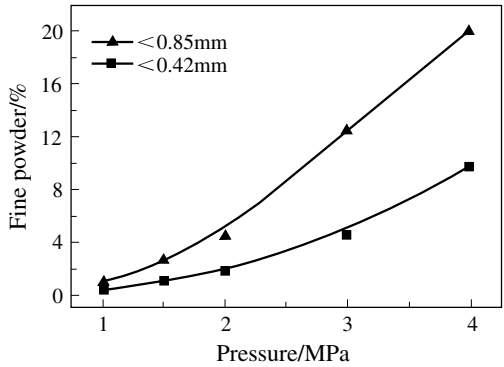


Fig. 8.40 Relation between fine powder ratio and loadings of irregular-shaped fused iron catalyst measured by WSCS

Table 8.34 Parameters of WSCS fitted by equation (8.43)

Particle size of fine powder < 0.42 mm			Particle size of fine powder < 0.85 mm		
M	B	R^2	M	B	R^2
2.30	0.00389	0.996	2.26	0.0102	0.997

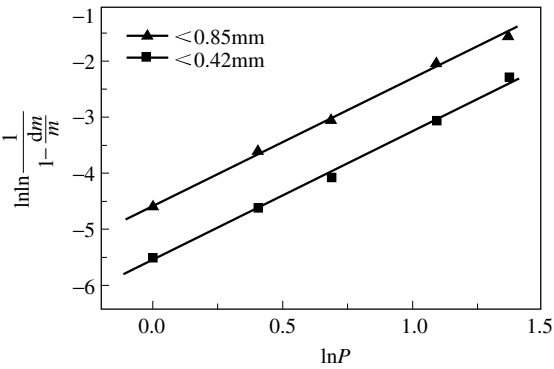


Fig. 8.41 Results fitted according to equation (8.43) and Fig. 8.40 for irregular-shaped fused iron catalyst

fine powder ratio and external pressure in a stack bed of irregular-shaped fused iron catalyst.

Furthermore, it can be seen from Table 8.34 that the values of the M parameter obtained from the WSCS measurement of the same sample using either large or small size sieved particles are very close to each other. In fact, the parameter M reflects the distribution of defects in the catalyst material; and the value of M is determined by the characteristics of the catalyst itself, independent of the sieve size.[72] As long as the selection of sieves is appropriate for fine powders, the method will be a convenient method to use in the experimental measurements.

However, the WSCS model can only be used for a certain range of fine powder ratio. When the external load exceeds a certain limit, the measured fine powder ratio will depart from the model.[85] The main reason for this is that when the pressure is high enough, a large number of fine powders appear and fill the interstices between the particles in the stack bed. The contact force between the particles is reduced, increasing the coordination number between particles, thus the actual probability of particles crushing in the bed is reduced. In addition, the diameter of the sample particles should be much smaller than the internal diameter of the container, in order to reduce the effect of the container wall on the spatial distribution of the particles. As a result, the WSCS model is applicable only when the external load meets a threshold value in equation (8.42). Different catalysts will have different threshold values of external load.

8.4.4 *Effect of chemical composition of catalysts on its mechanical strength*

(1) The effect of Fe^{2+}/Fe^{3+} on the abrasion strength of unreduced catalysts. The effect of Fe^{2+}/Fe^{3+} on the abrasion strength of unreduced catalysts is shown in Table 8.35.[84] It shows that under the same abrasive conditions, the abrasion ratio of the unreduced catalyst is lower with increasing Fe^{2+}/Fe^{3+}, or the content of FeO. The higher Fe^{2+}/Fe^{3+} is, the lower is the abrasion ratio and the higher is the mechanical strength of the catalyst. It can be seen that the mechanical strength of samples 6, 7 and 8 FeO-based catalysts is obviously better than that of samples 1 and 2 Fe_3O_4-based catalysts. The overall trend of the stack crush strength is basically the same as the abrasion intensity.

The effect of Fe^{2+}/Fe^{3+} on the abrasion ratio of reduced catalysts and the stack crush strength is shown in Table 8.36 and Fig. 8.42.

The effect of Fe^{2+}/Fe^{3+} on the abrasion strength of pre-reduced catalysts is very small. Irrespective of the value or quantum of the Fe^{2+}/Fe^{3+} before reduction, they will all become α-Fe after reduction, and form an oxide film through passivation.

Table 8.35 Effect of Fe^{2+}/Fe^{3+} on the abrasion ratio of unreduced catalysts

Sample No.	Fe^{2+}/Fe^{3+}	Phase composition (By XRD)		Abrasion ratio/wt%
		Main phase	Minor phase	
1	0.52	Fe_3O_4	—	3.82
2	0.66	Fe_3O_4	FeO	4.00
3	1.35	FeO	Fe_3O_4	3.60
4	2.15	FeO	Fe_3O_4	3.53
5	3.57	FeO	—	3.25
6	5.84	FeO	—	2.73
7	7.14	FeO	—	2.67
8	8.53	FeO	—	2.68
9	11.45	FeO	Fe	2.32
10	13.40	FeO	Fe	1.89

Note: The particle size of catalyst is 2.2–3.3 mm; the abrasion ratio is measured in accordance with the standards of HG/T2782-1996.

Table 8.36 Effect of Fe^{2+}/Fe^{3+} on the abrasion ratio of reduced catalyst

Fe^{2+}/Fe^{3+} before reduction	0.52	2.15	5.84	8.53	11.45
Abrasion ratio after reduction/wt%	4.86	5.02	4.81	4.73	4.56

Note: The abrasion ratio is measured by China' standard of HG/T2782-1996.

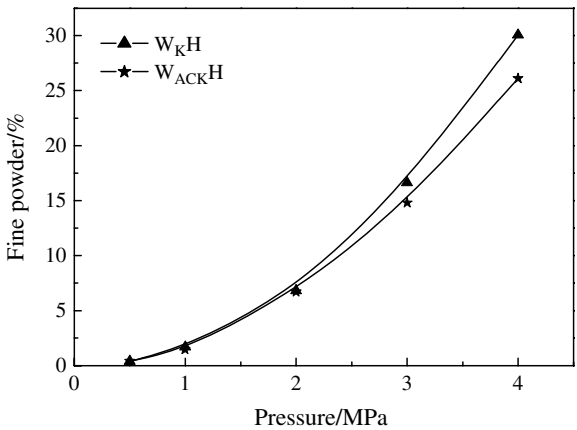


Fig. 8.42 Stack crush strength of WKH and WACKH (K, A, C, stand for K_2O, Al_2O_3 and CaO respectively, H stand for the pre-reduced type)

The abrasion strength of pre-reduced catalysts is determined by the thickness of this oxide film.

(2) The abrasion strength of the pre-reduction catalyst is related to the degree of passivation the degree of passivation is defined as the ratio of the amount of oxygen (oxide film) in the pre-reduced catalyst to that in the iron oxides in the oxidized state catalyst.

Suppose the chemical composition of the oxide film generated during passivation is the same as that of iron oxide before the reduction, the degree of passivation may be represented as:

$$Passivation\ \ degree = \frac{b(1-a)}{(1-b)a} \times 100\% \tag{8.44}$$

where a is the fraction of lost weight of oxidation state catalyst (content of oxygen); and b is the fraction of lost weight of the pre-reduced catalyst (content of oxygen).

The values of a and b can be obtained from thermo-gravimetric analysis (TG). When the degree of passivation reaches 31%, the abrasion strength is the lowest (the abrasion rate reaches 6.96% of the maximum value). Industrial catalysts require the abrasion strength to be below 4%, so the degree of passivation of a pre-reduced catalyst must be below 20%. Obviously, the abrasion rate of pre-reduced catalyst is closely related to the thickness of the oxide film, so the control of the oxide film thickness and the degree of passivation are the key parameters in the preparation of high-strength pre-reduced catalysts.

However, in industrial practice, the pre-reduced catalyst will be reduced again, so the oxide film will disappear. The above abrasion rate, which primarily reflects

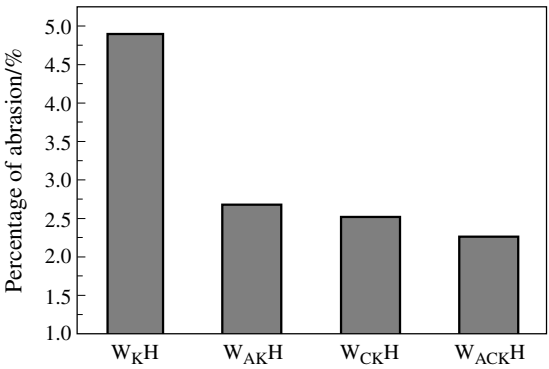


Fig. 8.43 Influence of promoter on the abrasion strength of the pre-reduced $Fe_{1-x}O$-based catalysts

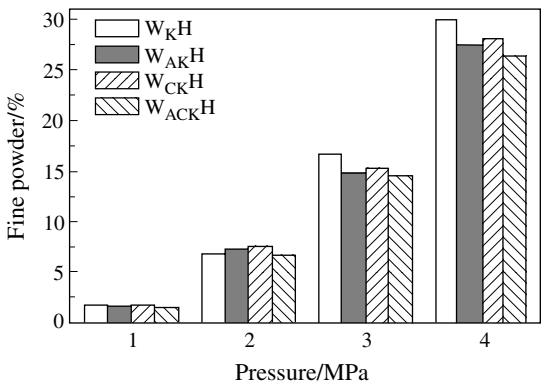


Fig. 8.44 Influence of promoter on bulk crush strength of the pre-reduced $Fe_{1-x}O$-based catalysts

the thickness of the oxide film and its ability to combine with metals does not truly represent the abrasion strength of a reduced state catalyst in an industrial reactor. Moreover, due to the sensitivity of a reduced state catalyst to oxygen, it is difficult to measure the catalyst's abrasion rate directly. Therefore, the stack crush strength can better reflect the mechanical strength of pre-reduced catalysts.

(3) The effect of promoters on the mechanical strength of pre-reduced catalysts. Figures 8.43 and 8.44 show the effect of promoters on the abrasion strength and stack crush strength of pre-reduced $Fe_{1-x}O$ based catalysts. K_2O has little influence on the abrasion strength, but Al_2O_3 and CaO can notably improve the abrasion strength and the stack crush strength of pre-reduced $Fe_{1-x}O$ based catalysts.

8.4.5 *The requirement of mechanical strength of catalysts in industry*

The mechanical strength of catalysts will inevitably decrease during usage, and hence the mechanical strength of catalysts in-use is more important than that of fresh catalysts. It is essential to know the minimum value of mechanical strength of

catalysts allowable in industrial equipment. This value not only provides an index of the mechanical strength that the catalyst should have, but also the criterion for determining the threshold catalyst strength below which the catalyst needs to be changed.

There are two different forces that exert on the catalyst in a fixed-bed reactor: One is the gravity of the catalyst itself and the pressure drop due to fluid flow, both of which are axial. The WSCS of the catalyst reflects the mechanical strength needed to withstand this force. The other force is due to the friction and collision caused by the rubbing and impact between gas flow and the catalyst surface in either a fixed-bed or fluidized-bed reactor. In an abrasion experiment, the friction between catalyst particles themselves or between particles and the wall of the rotating drum, and the impact stress on the particles as they fall from the top of the drum reflect the mechanical strength required to withstand the impact force and friction. The values of the mechanical strength measured by the above two experimental methods are indispensable catalyst design information. Under certain conditions, the gravitational force of the particles and the bed pressure drop of bed do not change; but they would increase with the abrasion of the catalyst. However, the friction and impact between the gas flow and the catalyst surface are present throughout the time of reactor operation. Therefore, attention must be given to the abrasion strength of the catalyst.

The minimum required mechanical strength of a catalyst varies with different industrial reactors. This minimum required that mechanical strength can be calculated through the analysis of forces acting on the catalyst that is in operation, as shown in Fig. 8.45. Clearly, the catalyst at the bottom of the reactor bears the highest stress.

Assuming that the total stress at the bottom of catalyst bed is W,

$$W = hF\rho_b + (P_1 - P_2)F \times 10^4 \tag{8.45}$$

$$w = \frac{W}{F} = h\rho_b \times 10^{-4} + (P_1 - P_2), \tag{8.46}$$

where W is the total stress on the catalyst at the bottom of the bed, kgf (1 kgf = 9.80665 N); w is the stress on the catalyst at unit sectional area of the

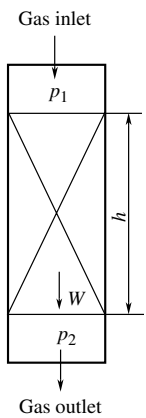


Fig. 8.45 Force on catalyst in fixed-bed reactor

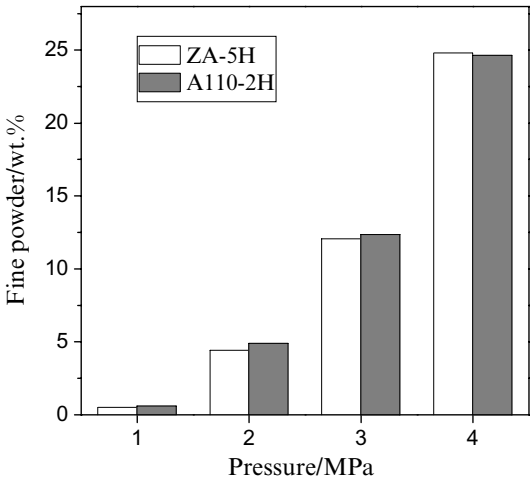


Fig. 8.46 Stack crush strength of ZA-5H and A110-2H

bottom of the bed, kgf·cm^{-2}; h is the height of catalyst bed, m; F is the cross-sectional area of bed, m^2; ρ_b is the bulk density of catalyst, kgf·m^{-3}; p_1 is the pressure at the inlet of bed, kgf·cm^{-2}; p_2 is the pressure at the outlet of bed, kgf·cm^{-2}.

For example, if $h = 9.558$ m, $p_1 - p_2 = 7.8$ kg·cm^{-2}, $\rho_b = 3200$ kg·m^{-3} (ZA-5), D_1 (outside diameter of bed) = 0.771 m, D_2 (inner diameter of bed) = 0.273 m, then using equation (8.46), $w = 10.86$ kg·cm^{-2} for an axial flow converter. In a radial flow converter, the bed pressure drop is small, far below that in an axial flow converter. It is commonly accepted that when the stack crush strength (crushed rate) of the catalyst is less than 0.5%, the catalyst will meet the requirements for industrial applications. It can be seen from Fig. 8.46 that the crush rate of ZA-5H is less than 0.5% at 1 MPa. The stack crush strength of ZA-5H can therefore meet the requirements for industrial applications.

Spherical catalysts are usually characterized by the single-particle crush strength. Assuming that the horizontal projection area of a catalyst is F_1 (m^2/pellet), the number of catalyst pellets on unit cross-sectional area of the bed bottom is given by:

$$n = F/F_1\mathrm{n} = \mathrm{F/F_1} \tag{8.47}$$

Inserting equation (8.47) into (8.45), the force acting on each catalyst is:

$$f = hF_i\rho_b + (P_1 - P_2)F_1 \times 10^4, \tag{8.48}$$

where f is the force acting on each catalyst pellet, kgf/pellet.

For a 0.565 cm spherical catalyst, the horizontal projection area $F_1 = \pi(0.565)^2/4$. Taking the above parameters of the axial flow converter, $f = 2.72$ kgf/pellet can be calculated by equation (8.48). However, in reality, the force acting on the catalyst particles is between points of contact and the bed area; the value of f calculated using the horizontal projection area is therefore smaller, and should be only used as a reference. Table 8.37 shows the single crush strength of several spherical catalysts.

Table 8.37 Strength of various spherical catalysts/(N/grain)

	Catalyst type		
Particle size/mm	A110-5Q	A202Q	HA310Q
2–3	≥100	≥80	≥120
3–4	≥120	≥100	≥200
4–5	≥200	≥150	≥300
5–7	≥250	≥200	≥400

Table 8.38 Abrasion strength of pre-reduced catalyst measured by STM standards

	Abrasion ratio (mass)/%		
Catalyst	Standard of HG/T	Standard of ASTM	Particle size/mm
ZA-5H	1.36	3.30	1.5–3.0
A110-1H		3.70	1.5–3.0
ICI74-1H		6.90	4.6–6.7

A standard value for the minimum abrasion strength (that is, the abrasion rate) of the fused iron ammonia synthesis catalyst has been proposed to be less than 4.0% under the standard experimental conditions of ASTM. It can be seen from Table 8.38 that the abrasion rate of ZA-5H is 3.30%, which is better than that of the A110-1H and ICI74-1H.

Regardless of the catalyst in the oxidation state or pre-reduction state, the abrasion strength or crush strength of the ZA-5 is slightly better than that of the ICI74-1 and A110-1. This is because the porosity of ZA-5H is less than that of ICI74-1H and A110-2H. It can be seen from equation (8.21) that the crush strength of a catalyst is a function of the diameter of the particle and its porosity. For a pre-reduction state catalyst, whichever the catalyst framework is, the major factors that affect the abrasion strength of the catalyst are the porosity, the surface smoothness, the thickness of the oxide film on the surface, and the bonding between the oxide film and catalyst framework. The latter two factors are determined by the process of passivation; and the surface smoothness is closely related to the shape factor of the catalyst. The shape factor of the ZA-5 type catalyst can be up to 0.594 before the milling treatment of the particle edges. After milling of the edges, the value of the shape factor may far exceed 0.6, which is much higher than that of other fused iron catalysts with a shape factor of only 0.33.[87] The high shape factor of the ZA-5 catalyst enhances the smoothness of the surface and the abrasion strength of the catalyst.

8.5 Usage and Maintenance of Ammonia Synthesis Catalysts

8.5.1 *Selection of the type of catalyst to use*

There are more than 500 sets of ammonia synthesis installations in China, and the production capacity of a single converter varies from tens of tons to a thousand tons

per day. The converter configuration includes axial, radial and radial-axial. There are three kinds of heat removal methods: continuous heat exchange by cold-pipe in bed, the indirect heat exchangers between beds and direct heat exchange with a cold gas between beds. Because of variations in the size and configuration of converters, the requirements on the catalysts to be used are different. Generally, the selection of an ammonia synthesis catalyst includes the type (activity) and the particle size. The size selection has been discussed in Section 8.2.4.

At present, the two major types of ammonia synthesis catalyst are the fused iron catalyst and the ruthenium catalyst, but the fused iron catalyst is still the primary catalyst in use. A fused iron catalyst may be classified in several ways: according to the operating temperature as medium-temperature and low-temperature; according to the state before use as pre-reduction and oxidized state; or according to shape as irregular shape and regular shape. The ruthenium catalyst is a low temperature catalyst, but is not widely used because of its high price.

8.5.1.1 *Type of catalysts for ammonia synthesis*

There are various-type catalysts for ammonia synthesis in the world. They may be divided into three series of A1, A2 and A3 according to the precursor of iron oxide and the chemical composition as shown in Table 8.39. The activity of catalysts follows the order A3 > A2 > A1. Typical physical parameters and catalytic properties of catalyst are shown in Table 8.40.

(1) A1 series catalyst for ammonia synthesis. A1 series of catalyst is the conventional fused iron catalyst with Fe_3O_4 as the precursor. There are A103, A106, A109 and A110 series of products in China. The A110 series includes A110-1, A110-2, A110-3, A110-4, A110-5Q, A110-6, etc, but A103, A106, A109, A110-3, A110-6 are already discussed. A110-1, A110-2 are the pre-reduced state products, A110-5Q is a spherical catalyst.

The A110 series catalyst, especially A110-1, A110-2, is the most widely used catalyst. It has good activity at medium-temperature, is easy to be reduced, has good thermal stability and resistance to toxicity and is similar to Denmark's KM-II series catalyst. The A110 series products can be used in three-pipe and single pipe parallel flow axial converters, as well as various types and sizes of the radial, axis — radial and other converters.

The KM-type series catalysts of Topsøe in Denmark are the main traditional fused iron catalyst for ammonia synthesis, capturing 50% of the international market. The KM-I type is a mid-temperature catalyst, which has a good activity, heat resistance and high anti-toxicity against oxides. The KM-II is a low-temperature catalyst, which has higher activity at low temperatures, but its heat-resistance and anti-toxicity are poorer than that of KM-I. KM-VII has good heat-resistance and anti-toxicity; it can also be used for pre-convertor gas purification. The AS-4 and AS-4F catalysts in Norway occupy about 10% of the international market. Others are the British ICI35-10, the US UCIC73-1, the German BASF-S6-10 and the Russian CA. The C73-1 is a mid-temperature catalyst, and C73-2 is a low temperature catalyst. In addition, Montedison EN type of Italy is also a low-temperature catalyst, but their FN type is a mid-temperature catalyst. It should be noted that the BASF ammonia catalyst of Germany has merged with the British ICI, but the catalyst type remains unchanged as a sign of distinction.

Table 8.39 Main types of ammonia synthesis catalysts in the world

Class	Country	Type	Precursor	Promoters/%					Note
				K_2O	Al_2O_3	CaO	MgO	SiO_2	
A1 Series	China	A110-1	Fe_3O_4	0.5–0.7	2.4–2.8	1.9–2.3		≤0.45	BaO of 0.2–0.4
		A110-2	Fe_3O_4	0.6–0.8	2.2–2.6	1.4–1.8		≤0.4	0
		A110-4	Fe_3O_4	0.6–1.0	2.1–2.5	1.4–1.8		≤0.45	0
		A110-5Q	Fe_3O_4	0.8–1.3	2.0–2.6	0.7–1.5		≤0.4	—
		A203	Fe_3O_4	0.34	1.49	1.50		≤0.4	CeO_2 of 0.53
	USA	C73-1-01	Fe_3O_4	0.5–0.8	2–3	0.7–1.2		<0.4	
		C73-2-01	Fe_3O_4	0.7–0.9	3–4	1.0–1.3		<0.4	
		C73-NH-RS	Fe_3O_4	1.1–1.3	1.0–1.7	0.03–0.1			
		G-82	Fe_3O_4	0.8	2.5	2.0			
	UK	ICI 35-4	Fe_3O_4	0.8	2.5	2.0	0.3	0.4	
		ICI 35-8	Fe_3O_4	1.0	3.2	2.5	0.4	0.5	
	German	BASFS6-10	Fe_3O_4	0.54	2.9	2.8	0.32	0.35	
		S6-10red	Fe_3O_4	0.70	3.7	3.6	0.43	0.45	
	France	GPS7	Fe_3O_4	0.47	2.68	2.55	0.36	0.57	
		GPS9	Fe_3O_4						
	Italy	EN	Fe_3O_4	0.78	2.28	0.94			
		FN	Fe_3O_4						
		FNMS	Fe_3O_4						
	Denmark	KM-I	Fe_3O_4	0.66	2.85	3.27	0.28	0.78	
		KM-IR	Fe_3O_4	0.90	3.90	4.48	0.38	1.07	
		KM-IRC	Fe_3O_4	0.90	3.90	4.48	0.38	1.07	

(*Continued*)

Table 8.39 (*Continued*)

Class	Country	Type	Precursor	Promoters/%					
				K_2O	Al_2O_3	CaO	MgO	SiO_2	Note
		KMII	Fe_3O_4	0.60	3.17	2.05	0.84	0.62	
		KMIIR	Fe_3O_4	0.80	4.22	2.73	1.12	0.82	
		KMVII	Fe_3O_4	0.26	4.32	3.40	4.11	0.88	
	Austria	LN-11	Fe_3O_4	0.58	3.16	3.54	0.56	0.50	
	Switzerland	Cl6.3.5	Fe_3O_4	0.8–2.0	2.5–3.5	2.0–3.5	0.1–0.4	0.2–0.5	CeO_2 of 0.5–2.5
	Norway	AS-4	Fe_3O_4						
		AS-4F	Fe_3O_4						
	Russia	CA-1	Fe_3O_4	0.7–1	3–4	2–3	<0.7	<0.7	
		CA-1П	Fe_3O_4	0.5	3.42	1.95	0.6	0.21	
		CA-1B	Fe_3O_4	0.87	2.85	1.90	0.9	0.35	
		CA-1BП	Fe_3O_4	0.87	2.85	1.90	0.9	0.35	
		CA-2	Fe_3O_4						V_2O_5
		CA-2B	Fe_3O_4						
A2 series	UK	ICI 74-1	Fe_3O_4-CoO	0.8	2.5	1.9	0.2	0.5	CoO of 5.2
	USA	C73-3-02	Fe_3O_4-CoO	0.6	2.4	1.4			CoO of 5
	China	A201	Fe_3O_4-CoO	0.45–0.7	1.9–2.6	1.0–1.8		≤0.4	CoO of 1.0–1.2
		A202	Fe_3O_4-CoO	√	√	√		≤0.4	CoO of 0.6–1.0
A3 series	China	A301	$Fe_{1-x}O$	√	√	√		≤0.4	0
		ZA-5	$Fe_{1-x}O$	√	√	√		≤ 0.4	0

Note: Data of A110-1, A110-4, A110-5Q, A201 from Ref. 43; Data of A110-2, A301 and ZA-5 from author's Laboratory; others from Ref. 89.

Table 8.40 Physical parameters and catalytic properties of ammonia synthesis catalyst

Indexs	A110-1	A110-2	A301	ZA-5
Particle size/mm	1.5–20	1.5–20	1.5–20	1.5–20
Magnetic (oxidation state)	Ferromagnetism	Ferromagnetism	Non-ferromagnetic	Non-ferromagnetic
Bulk density/($g \cdot cm^{-3}$)	2.7–2.9	2.7–2.9	3.0–3.2	3.0–3.21
Particle density[a]/($g \cdot cm^{-3}$)	3.5–3.6	3.6	4.32	4.33
Framework density[a]/($g \cdot cm^{-3}$)	6.5–6.7	7.4	6.85	6.86
Porosity[a]/%	46	46.42	36.93	37.00
Pore volume[a]/($cm^3 \cdot g^{-1}$)	0.129	0.1089	0.0855	0.086
Total surface area[a]/($m^2 \cdot g^{-1}$)	13	13.31	13.34	13.92
Surface area of iron[a]/($m^2 \cdot g^{-1}$)	—	4.092	3.747	3.955
Coverage degree of iron[a]/%	—	30.75	28.10	28.41
Surface area of alkali[a]/($m^2 \cdot g^{-1}$)	5.2	4.868	4.535	4.596
Converge of alkali[a]/%	40	36.58	34.00	33.02
Main pore radius distribution[a]/nm	10–40	4–25	4–30	4–30
Average pore radius/nm	12.8	16.36	12.85	12.85
α-Fe particle size[a]/nm	28	25.2	25.3	25.3
α-Fe lattice parameters[a]/nm	0.28650	0.28666	0.28662	0.28661
Initial reduced temperature/°C	300–320	300–320	300–320	300–320
Final reduced temperature/°C	~500	~500	~475	~475
Temperature use range/°C	370–510	370–510	325–500	325–500
Outlet concentration of NH_3)/%[b]	≥13.5(425°C)	≥13.5(425°C)	≥14.5(400°C)	≥15(400°C)
Outlet concentration of NH_3) after heat-resistance/%[c]	≥13.5(425°C)	≥13.5(425°C)	≥14.5(400°C)	≥15(400°C)

[a]Activated catalyst. [b]test conditions: Particle size is 1–1.4 mm, space velocity is 30000 h^{-1}, pressure is 15 MPa, H_2 75%, N_2 25%. [c]after heat-resistance at 500°C for 20 h
Note: The data of A110-1 from Ref. 43, the data of A110-2, A301 and ZA-5 from author's laboratory.

(2) A2 series catalysts containing cobalt The A2 series catalyst, including A201, A202, AC, NCA, HA, ICI74-1 and C73-3, is a conventional Fe_3O_4 based catalyst containing cobalt. All these catalysts have been used in the ammonia synthesis plants. The activity of the A2 series catalyst at low-temperature is better than that of A1 series, but its mechanical strength and thermal stability are poorer than that of the A1 series.

The A2 series of catalyst has been used in ICI-LCA and ICI-AMV processes. The AMV is the process used in the Zhongyuan Fertilizer Plant. The ammonia

concentration at the outlet of the ICI74-1 has increased from 8% to 11%[88] at (10–44) MPa and 470°C, with clear energy-saving benefits.

(3) A3 series of low-temperature and pressure catalyst for ammonia synthesis the A3 series catalyst such as A301 and ZA-5 is completely different from A1, A2, as it is a new series of $Fe_{1-x}O$-based catalysts. It is a new generation of low-temperature and low-pressure catalyst which was first invented in China. The invention is a great breakthrough in the field of ammonia synthesis catalyst research. The catalyst has especially high activity, is particularly easy to be reduced, and has high mechanical strength and high activity in exceptionally low temperatures. This catalyst has leading performances internationally in the ammonia synthesis catalyst market, and has been widely used.

China has the most production of ammonia synthesis catalysts, with the average sales of about 5000 tons per year. The main manufacturer is Süd-Chemie AG, Catalysts (Nanjing) Co. Ltd (Munich, Germany); Shangyu Catalyst Co., Ltd; Zhejiang University of Technology Catalyst Plant and Shandong Linju Chemical Group Co. Ltd etc.

8.5.1.2 *Pre-reduced catalysts*

Pre-reduced catalysts mainly include A110-1H, ZA-5H and A103H, KMIR, KMIRC, KMIIR, C73-NH-RS, S6-10, ICI35-8, AS-4F, CA-1B, CAIB II and CA-2B, and so on. Pre-reduced catalysts are commonly used, having sales that occupy close to half of the total world production with a gradually increasing upward trend. Some ammonia synthesis plants only use pre-reduced catalysts in the first bed of the converter, but other plants use the pre-reduced catalyst in the entire converter. The effect of pre-reduced catalysts on energy consumption is significant. A pre-reduction catalyst is commonly loaded in the first bed or the upper part of a bed. This is because only about 15% of the oxygen need to be reduced, compare with the oxidized catalyst, hence the catalyst can be quickly reduced and go online to produce NH_3. The heat generated by the reaction is supplemented by the heat supplied by an external furnace, so that the lower part of the oxidized catalyst can be reduced more rapidly.

A pre-reduced catalyst can be easily reduced again. Not only the amount of oxygen which needs to be removed is only about 15% to 30% of that of the oxidized catalyst, but also the bond between iron atoms and oxygen atoms is loose in the oxide film after passivation. As a result, this thin layer of iron oxide film is easier to be reduced, and the reduction temperature of the a pre-reduced catalyst is 20–25°C lower than that of the oxidized catalyst.

When filling a bed with a pre-reduction catalyst, attention should be given to ensure the security of the operators, enabling them to evacuate quickly and provide a large volume of an inert gas (N_2) in an emergency.

8.5.1.3 *Spherical catalysts for ammonia synthesis*

There are many types of spherical catalysts for ammonia synthesis in China, e.g., the A110-5Q, HA310Q and so on. Spherical catalyst particles have a regular shape, a smooth surface and can freely roll; thus the distribution of gas flow can be improved

and the pressure drop reduced. They can be used in small and medium-scale axial converters, where the problem of pressure drop is more serious.[90,91]

8.5.2 *Proper use of catalysts*

The performance of a catalyst for ammonia synthesis is related to its quality, the reduced conditions, its proper use and maintenance. Scientifically sound management and use of a catalyst will not only slow down the decline in catalytic activity, but also render its operation economically.

A catalyst just after reduction should not bear a prematurely increased the load of production; the operation temperature should not be too high or fluctuates too often. The inlet temperature and hot spots in the catalyst bed should be controlled well, and the amount of poisons in the synthesis gas kept low to prevent poisoning. Stabilizing the proportion of H_2/N_2 ratio should be controlled within a small range, so as not to cause the bed temperature to fluctuate.

(1) The control of inlet temperature. The inlet temperature significantly affects the changes of the temperature distribution in the entire catalyst bed, directly influences the adiabatic temperature rise, and also impacts the hot spots in the catalyst bed. In order to maintain the low-temperature activity of an ammonia synthesis catalyst, the inlet temperature should be kept relatively stable over a reasonable period. In industrial practice, the inlet temperature of the ammonia synthesis catalyst is maintained higher than the temperature for high activity. For example, the inlet temperature for an A110-2 catalyst is controlled at (370 ± 10)°C (adiabatic bed) or (400 ± 20)°C (multi-stage heat exchange beds). For A301, ZA5 catalysts, and other low-pressure, low-temperature catalyst beds, the inlet bed temperature is controlled at (320 ± 20)°C (adiabatic bed) or (370 ± 20)°C (multi-stage heat exchange beds).

(2) The control of hot spot temperature. The hot spot temperature is the highest temperature in a catalyst bed. For the adiabatic reactor, the hot temperature is the outlet temperature of the catalyst bed, *viz.* the first catalyst bed. For the multi-stage heat exchange beds reactor, the location of the hot temperature is in the middle of the catalyst bed, which changes and shifts gradually with load, space velocity and the cumulative operation time. When the load and space velocity are basically unchanged, the location of the hot spot and its moving rate along the direction of gas flow are indications of the age of the catalyst.

The hot spot temperature of the catalyst used in different period(s) is shown in Table 8.41. Under the condition of steady production capacity and stable catalytic activity, the hot spot temperature should be maintained as low as possible. This will not only benefit in maintaining the low-temperature activity of the catalyst, but also enhances the equilibrium of the ammonia synthesis reaction. Especially for the A301, ZA-5 and other low-temperature and low-pressure catalysts, because the temperature for high activity is low, the hot spot temperature should be strictly controlled and should not exceed the designed limit. When operators who were used to using the medium-temperature catalyst change to the new low-temperature catalyst, they are not accustomed to operate the process at low temperatures. They might raise the hot spot temperature intentionally or unintentionally, which would reduce the catalyst utilization efficiency and shorten the catalyst life. This issue has been discussed in Section 8.1.2.4.

Table 8.41 Hotspot temperature of a series of catalysts in different stages of use/°C

Type	Converter-type (heat transfer way)	In the initial stage	In the middle stage	In the end stage
A110	Continuous bed (cold-tube type)	460–470	480–490	490–510
	Adiabatic bed	480–490	490–500	500–510
A201	Continuous bed (cold-tube type)	460–470	475–485	485–500
	Adiabatic bed	480–490	490–500	500–510
A301(ZA-5)	Continuous bed (cold-tube type)	430–450	450–465	475–500
	Adiabatic bed	465–475	470–480	490–500

(3) Poison. When the oxygen containing poisons become excessive, causing temporary poisoning of the ammonia synthesis catalyst, production load should be reduced, and the hotspot temperature increased slightly by 5–10°C. When the oxygen containing poison is severely excessive, fresh synthesis gas supply should be cut off and opens the venting valve for the fresh syngas. At the same time, the flow of recycle gas should be reduced, and closed auxiliary valve for the fresh syngas until the converter is stopped run and the fresh synthesis gas conforms to process requirements.

8.5.3 *The transport and storage of catalysts*

Ammonia synthesis catalysts are usually transported in sealed metal barrel. In order to prevent the catalyst from broken loose and the barrel leaks because of a loose cap, rolling of the metal barrel should be avoided during transportation. When in storage, moisture and contaminants should be kept out. The best storage period should not exceed six months. If the ammonia synthesis catalyst is exposed to air for a long time, it will absorb moisture and precipitate potassium turning into a white material. It is better not to use an ammonia synthesis catalyst that has been affected by damp.

References

1. Yu ZH, Zhu BC, Shen DC, *et al. Technology Process Analysis for Large Ammonia Plant*, Beijing: Chinese Petrochemical Industry Press, 1993.
2. Shen J, editor in chief; Zhu SY, Feng X, vice-editor. Editorial Board of Fertilizer Engineering Series, *Ammonia*, Beijing: Chemical Industry Press, 2001.
3. Liu HZazhang, Hu Z, *et al. Chemical Reaction Engineering and Technology*, **17**(1): 28–34, 2001.
4. Liu HZ, Li X, Hu Z, *et al. Journal of Chemical Engineering of Chinese Universities*, **16**(1): 42–47 , 2002.
5. Chen G, editor in chief; Chen JY, Shi J, Zu Y, Associate editor in chief, Board of Encyclopedias of Chemical Industry, *Encyclopedias of Chemical Industry*, Volume VI, Beijing: Chemical Industry Press, 1994.
6. Dai XH, Liu HZ. *Journal of Chemical Fertilizer Industry*, **33**(3): 12–16, 2006.

7. Jiang S, *et al. Ammonia Engineering*. Volume III, Beijing: Petroleum Chemical Industry Press, 1977, 131–138.
8. Zhu BC. *Chemical Reaction Engineering*, Second Edition, Beijing: Chemical Industry Press, 1998.
9. Dybkjaer Ib, Gam EA. CEER, **16**(9): 29–35, 1984.
10. Murthg CLN. *Fertilizer News*, **33**(5): 53–58, 1988.
11. Taglor HS, *et al. J. Am. Chem. Sci.* **57**: 660, 1935.
12. Emmett PH, *et al. J. Am. Chem. Sci.* **55**: 1738, 1933.
13. Yao **B**. *Chem. Eng. Proc.* **2**(3): 54, 1986.
14. Robert CR, *et al. Ind. Eng. Chem. Process Design & Development*, **19**(4): 580, 1980.
15. Zhang MZ, Chen JS, Chen Y. *Nitrogenous Fertilizer Design*, **2**: 2–9, 1984.
16. Li W. *Large Nitrogenous Fertilizer*, **3**: 169–173, 1993.
17. The 4th Design Institute of the Ministry of Chemical Industry. *Ammonia Converter*, Beijing: Petroleum Industry Press, 1977.
18. Martyn VT. *Catalyst Handbook* 2nd (ed.) London: Wolfe Publishing Ltd, 1989.
19. Liu HZ, Li X, Hu Z, *et al. Journal of Chemical Industry and Engineering* (China), **52**(11): 1030–1034, 2001.
20. Chen G. *Chemical Reaction Engineering*, Beijing: Chemical Industry Press, 1981, 166–185.
21. Zhu BC. *Chemical Reaction Engineering*, Second Edition, Beijing: Chemical Industry Press, 1998, 111–118.
22. Li T, Lin G, Xu MS, *et al. Chemical Reaction Engineering and Technology*, **15**(4): 390–394, 1999.
23. Zardi U, Antonini A. *Nitrogen*, **122**: 33–40 , 1979.
24. Li T, Lin G, Xu MS, Fan D, Zu B. *Chem. Eng. Proc.* **15**(4): 390–394, 1999.
25. Chen G, editor in chief; Chen JY, Shi J, Zu Y, Associate editor in chief, Board of Encyclopedias of Chemical Industry. *Encyclopedias of Chemical Industry*, Volume VI, Beijing: Chemical Industry Press, 1994, 890.
26. [Japan] Longyuu Yamnaka. Availably practical Application of Catalysts, Translated by Ruzhong Zou, Dao Wang, Qinyin Zhen, Beijing: Chemical Industry Press, 1988.
27. Tamman G, Mansuri QA, *Zanorg. allg. Chem.* **126**: 119, 1923.
28. Zhou JP translation. Ammonia Plant and Corresponding Facilities for the Safety Proceeding of the 37th American Chemical Engineers Conference on Ammonia Plant Safety, Zibo in Shandong: *Large Nitrogenous Fertilizer*, 1993.
29. Huttig GF. *Disc Farad. Soc.* **8**: 215, 1950.
30. Mullins WW. *Trans. Met. Soc.* AIME, **218**: 354, 1960.
31. Presland AEB, Price GL, Trimm DL, *Progr. Surf Sci.* **3**: 63, London: Pergamon, 1972.
32. Dowden DAI.*Chem. E. Symp. Sci.* **27**: 18, 1968.
33. Coble RL, Burke JE. In: *Progress in Ceramic Science*. Vol. 3 Pergamon: London, 1963.
34. АСимупинН, ЯМелъниковЕ. Спраъочния азотника. Том 1. Москва: Химия: 1967.
35. Calvin H, Bartholomew. *Appl. Catal. A: General*, **212**: 17–60, 2001.
36. Forzatti P, *et al. Catal. Today*, **52**(2&3): 165–181, 1999.
37. Wang R, Zhang Z. *Coal Mine Automation*, **3**: 4–6, 2001.
38. Li C, *et al. Deactivation of Catalyst*. Beijing: Chemical Industry Press, 1989.
39. [Japan] Longyuu Yamnaka. Availably practical Application of Catalysts, Translated by Ruzhong Zou, Dao Wang, Qinyin Zhen, Beijing: Chemical Industry Press, 1988.
40. Sun J. *Deactivation and Regeneration of Catalyst forIindustrial* [M], Beijing: Chemical Industry Press, 2006.
41. Hughes R. *Catalyst Deactivation* [M]. Beijing: Science Press, 1990.
42. Martyn VT. *Catalyst HandBook*. 2nd ed. London: Wolfe Publishing Ltd, 1989.

43. Xiang D, Liu HY. *Fertilizer Catalyst Practical Manual* [M], Beijing: Chemical Industry Press, 1992.
44. Samahuofu AA, *et al. Activity Changing of Catalyst Used In the Course*. Beijing: Chemical Industry Press, 1981.
45. [Japan] Longyuu Yamnaka. Availably practical Application of Catalysts, Translated by Ruzhong Zou, Dao Wang, Qinyin Zhen, Beijing: Chemical Industry Press, 1988, p. 56.
46. Emmett PH, *et al.* ibid. **52**: 2682, 1930.
47. Ningbao H, *J. Chem. Ind. Eng.*, (2): 125, 1981.
48. Liu HZ, Li X, Hu Z, *et al. Journal of Chemical Industry and Engineering* (China). **45**(4): 385–392, 1994.
49. Huang WH. Study On Anti-poisoning of FeO-based ammonia synthesis catalyst [MS Dissertation], Hangzhou: Zhejiang University of Technology, 2006.
50. Chen HB, Zhang HB, Tsai KR, *et al. Proc. 9th ICC.Canada*. **II**: 537–544, 1988.
51. Knudson FP. *J. ACS*. **42**: 376, 1959.
52. Liu X. *Industrial Catalyst Analysis and Test Characterization*, Beijing: Hydrocarbon Processing Press, 1990, 34.
53. Zhao Y, Luo A, Yu K, *et al. Oil Refining and Petrochemical Technology*, **26**(3): 26–29, 1995.
54. Le Page JF, Miquel J. *Determining Mechanical Properties of Industrial Catalysts*: Correlations with Their Morphological and Physical Chemical Properties. Amsterdam Oxford, New York: 1976. Elsevier Scientific Publishing Company, 1976, 39.
55. Kapur, PC, Fuerstenau DW. *J. Am. Cer. Soc.i,* **50**(1): 14–18, 1967.
56. Jin Z, Bao Y. *Characterization of Mechanical Properties for Brittle Materials and Ceramics*, Beijing: China Railway Press, 145–151, 1996.
57. Sun M. *Mechanical Performances of Metals*. Harbin: Harbin University of Technology Press, 2003, 222–242.
58. Wei H. *Chemical Fertilizer & Catalysis*, **2**: 1, 1985.
59. Li Y, Zhang L, Li Z, *Journal of Tianjin University*, **3**: 9–17, 1989.
60. Li YD, Li XM, Chang L, *et al. Catalysis Today*, **51**(1): 73–84, 1999.
61. Li YD, Wu DF, Zhang JP, *et al. Powder Technology*, **113**(1&2): 176–184 2000.
62. Griffith AA. *Phil. Trans. Roy. Soc. Lond. A*, **221**: 163, 1920.
63. Li Y, Wu D, Liu C, *et al. Ind. Eng. Chem. Res.*, **38**(5): 1911–1916, 1999.
64. Weibull WJ. *Appl. Mech.* **18**(3): 293–297, 1951.
65. Shipway PH, Hutchings IM. *Philos. Mag. A*, **67**: 1389, 1993.
66. Shipway PH, Hutchings IM. *Philos. Mag. A*, **67**: 1045, 1993.
67. Wright PJF. *Mag. Conc. Res.*, **7**:87, 1955.
68. Fu G, Jin Z. *Bulletin of the Chinese Ceramic Society*, **5**(2): 28–33, 1986.
69. Shahinpoor M. *Powder Technology*, **25**: 163, 1980.
70. Bagster DF, Li E. *Powder Technology*, **76**: 213, 1993.
71. Li E, Bagster DF. *Powder Technology*, **74**: 271, 1993.
72. Li YD, Wu D, Zhang J, *et al. Ind. Eng. Chem. Res.*, **39**(3): 838–842, 2000.
73. Weller SW. *Standardization of Catalyst Test Methods*. AIChE Symposium Series 143, New York: AIChE, 1974, 70.
74. ASTM D-32, D4179 — 2001.
75. ASTM D-32, D6175 — 1998.
76. HG/T 2782 — 1996.
77. GB 10505.2 — 89.
78. HG/T 2976 — 1999.
79. ASTM D-32, D4058 — 1996.
80. ASTM D-32, D5757 — 1995.
81. Li X, Liu HZ, Chen SY. *Chinese Journal of Catalysis*, **19**(3): 201–205, 1998.

82. Richardson JT. *Principles of Catalyst Development*. New York: Plenum Press, 1989, 143.
83. Liu X. *Petrochemical Technology*, **28**(12): 850–857, 1999.
84. Lin J. Study On Anti-poisoning of FeO-based ammonia synthesis catalyst: MS dissertation, Hangzhou: Zhejiang University of Technology, 2005.
85. Wu D. *Study on Solid catalyst Mechanical Strength: MS Dissertation*, Tianjin: Tianjin University, 2002.
86. Wang W, Zhang Y, Hu P, *et al. Journal of Chemical Fertilizer Industry*, **24**(3): 16–17, 1997.
87. Zhu J, Li T, Fan R, *et al. Journal of East China University of Science and Technology*, **27**(6): 697–700, 2001.
88. Zhao X. *M-sized Nitrogenous Fertilizer Progress*, (3): 1–27, 1994.
89. Nitrogen. **193**(9&10): 19, 1991.
90. Wu P. *Industrial Catalysis*, **4**: 46–49, 1999.
91. Mu S, Li L. *Journal of Chemical Fertilizer Industry*, **30**(2): 26–30, 2002.

This page intentionally left blank

Chapter 9

Effect of Catalyst Performance on the Economic Benefits of Catalytic Process

Solid catalysts are used in almost 80% of all the production process of basic chemicals. Although catalyst cost has an influence on the product price, it usually accounts for a small part. The cost of catalyst is about 0.001%–1% of the whole product cost in basic chemicals production, which is somewhat larger only for special chemicals such as medicaments.

However, the performance such as activity, selectivity and life period etc of catalysts will influence on the whole production cost of the chemicals. The selection and preparation of catalysts must be closely integrated with the chemical production process in regard to the influence of the performance of catalysts on the process parameters and to the appraisement of the economic benefits of catalysts.[1–3]

The production process of ammonia synthesis is an extremely complex system engineering process which can be divided into three parts according to their functions: gas production, purification and synthesis; the three parts interact with one another. For a well-designed ammonia plant, it is necessary to appraise the relative size of unit equipment designed respectively in the points of investment and consumption of public engineering, so as to get the largest annual profit in operation by all the results selected. Many factors must be considered to get a reliable and economic design of ammonia plant. Although the discussion is limited to the synthetic loop here, more attention must be paid to the designs and operation cost of gas-production and purification equipment, because they are closely related to the operation of synthetic loop, and then affect the total cost.

It goes without saying that the basic task of the ammonia plant is to produce ammonia, which is the purpose of building plant. Because ammonia synthesis is a green chemical reaction with 100% of atom utilization and no by-product, the quality of product is not the criterion for appraising synthetic technology, and, usually, since the freeze-separating process is adopted, the quality of product can be up to the quality standards i.e. the content of ammonia in product is greater than 99.8% as long as the standards of purification is up to. It is also not the output of ammonia because the output is determined by the scale and margin capacity of the design and the supplied amount of fresh syngas. The criterion appraising the synthesis technology is mainly the energy consumption and the degree of reliability. The comprehensive criterion of whole system of synthesis equipment is the energy consumption per ton of ammonia. If supplementary purified syngas at a given pressure and composition can be obtained, then the energy consumption per ton of ammonia in synthesis loop is related to the following factors.[3]

(1) The pressure level of the syngas. It cannot judge only the pressure level whether it is good or not. It is focused not only on the sub-system of the synthesis loop but also the large system of whole plant.
(2) The performances of the converter. It includes the net value of ammonia, the pressure difference between inlet and outlet of the converter, the rate of utilizing the high-pressure space, distribution of temperature, the degree of the difficulty in reduction, the complex degree of the structure, operation flexibility and so on.
(3) The way of separating ammonia. It includes freeze separation and the series of separating, solvent separation and solvent selection.
(4) Amount of degassing gas per ton of ammonia as well as the reclaim way of effective components.
(5) The reclaim way of the waste heat.
(6) The activity and life period of catalyst.

These technical factors and the criteria interact. For example, degassing amount per ton of ammonia is related to the pressure level, the content of the inert gas in fresh syngas and the net value of ammonia (concentration difference of ammonia in outlet and inlet of reactor). The freezing separation series of ammonia are related to the pressure level and the net value of ammonia. The reclaim way of the waste heat is related to the energy equilibrium of whole plant and the net value of ammonia. They are all related close to the performance of catalyst because of the operating conditions of whole plant which is determined according to performance of catalysts. Therefore, the performance of catalysts has a great influence on the economic benefits of whole catalytic process.

9.1 Synthesis Processes and Catalysts

It is known from analysis of the thermodynamics that the process of synthesis ammonia from H_2 and N_2 is limited by the thermodynamic equilibrium, so the outlet content of ammonia obtained is below about 15% under general industrial conditions. In order to increase the utilization ratio of H_2 and N_2, the un-reacted H_2 and N_2 should be recycled. Therefore, the product of ammonia should be separated from the mixed gas, and then the un-reacted H_2 and N_2 are circulated by circle-compressor for next reaction. The synthesis of ammonia, separation of ammonia and the recycle of unreacted H_2 and N_2 make up the recycle process flow for the ammonia synthesis.

The process flow of synthesis ammonia has changed a lot in one century, but so far the basic steps are the same including the final purifying of the syngas, the synthesis of ammonia, the utilization of reaction heat, separation of ammonia, recompression of the recycle gas, the discharge of the inert gas, the callback, use of H_2 and so on.

Reducing the energy consumption is always the hankering aim of the technical progress in ammonia synthesis industry, the key and core of which is the ammonia synthesis catalyst. It can be seen from Table 9.1 that the energy consumption per ton of ammonia and synthesis pressure decreases with the progress of ammonia synthesis catalyst. So the progress of technology and process of synthesis ammonia is dependent on the technical level of catalyst to some extent. It also can be seen from

Table 9.1 Relation between catalysts and synthesis process and energy consumption

Catalysts	Process	Synthesis pressure/MPa	Energy consumption/($GJ \cdot t^{-1}$)
Classical iron	Small- and medium-scale plant	30.4	54
Classical iron	Kellogg	15	42
Iron–cobalt	ICI–AMV	12	30
Ruthenium	KAAP	9.1	27

Table 9.1 that whenever a new type of catalyst was developed successfully, a new relative process of synthesis ammonia would also be developed. For example, the AMV process was developed corresponding to the 74-1 Fe-Co catalyst developed by the Imperial Chemical Industries (ICI) Corporation, which made the operating pressure and energy consumption decline to 10–12 MPa and 30 $GJ{\cdot}t^{-1}$, respectively. After the Ru/AC catalyst was developed successfully, the BP and Kellogg Corporation developed the Ru/AC catalyst along with the Kellogg Ammonia Advance Process (KAAP), which made the operating pressure and the energy consumption decrease further to below 10 MPa and 27 $GJ{\cdot}t^{-1}$, respectively. The successful development of the Fe1-xO-base catalyst will establish a technical foundation for synthesis of ammonia at low pressure. These technique reforms have obviously reduced the energy consumption of synthesis ammonia.

In order to decrease energy consumption, the tendency of the technical progress in ammonia industry is to develop and use new types of high activity and energy-saving catalyst at low pressure and low temperature, where the scale of single-series equipment will grow larger. The process of synthesis has been uninterruptedly improving and developing in the last 100 years. In 1960s, the design concept of "almightiness" was put forward, which brought a single-series of large equipment with capacity of 300 kt/year. A whole process system could be considered as a system utilizing energy synthetically. This system included three basic units — the synthesis of ammonia, the separation of ammonia and the cycle of unreacted gas. The process flow is different because of the different (a) source of the material gases, (b) recovering and utilization of reaction heat and the discharge gases.

9.1.1 *Process with classical molten iron catalysts*

9.1.1.1 *Kellogg process*

The Kellogg Corporation has made outstanding contribution to the development of the synthesis ammonia technology, and its technology level was superior to others during 1960s to early 1970s. At present, about 50% of the large ammonia plants in the world are designed by it. The process flow of Kellogg is shown in Fig. 9.1. In addition to adopting the centrifugal compressor and the preheating of boiler feed water by recovering the reaction heat, the process also uses the multistage ammonia cooler, multistage flash evaporation and discharges the vent gas in front of the compressor, then places the unit to recover H_2 from the vent gas, thereby setting the condensation process after the compressor for reducing the energy consumption and increasing degree of purification. For example, the technology for removing CO_2

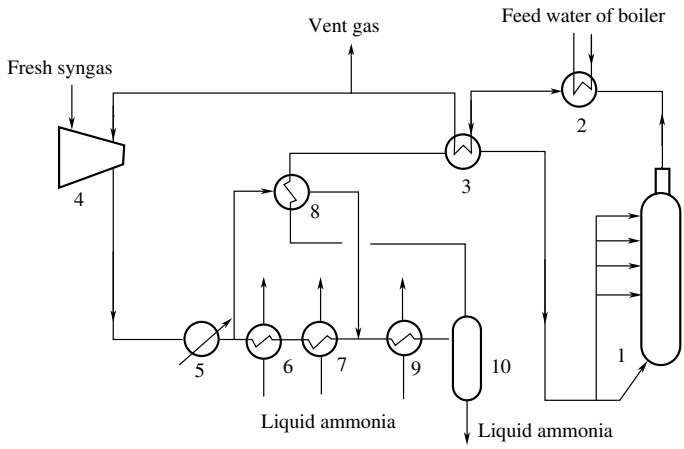


Fig. 9.1 Kellogg process flow of the synthesis loop

1-Converter; 2-Heat recovery boiler; 3-Gas-gas heat exchanger; 4-Compressor; 5-Water cooler; 6,7,9-Ammonia cooler; 8-Cold exchanger; 10-separator

Table 9.2 Technical parameters of the various processes

Process type	Small and medium plant	Kellogg	Topsøe	Braun	ICI–AMV
Pressure/MPa	31.4	14	26	15	10
Net value of ammonia/%	8–10	10	10–12.5	17	13
Out temperature of converter/°C	300	280	325	420	414
Resistance of reactor/MPa	1.1	0.63	0.39	0.7	0.25
Particle size of catalyst/mm	3–9	6–9	3–6, 1.5–3	6–10	1.5–3
Temperature of refrigeration/°C	5–10	−23	0	1–2	−10
Space velocity/h^{-1}	30,000	10,000	12,000	7,600	8,000

and H_2O from the fresh syngas by molecular sieve by which the fresh syngas can come directly into the converter can save energy by $0.67 \times 10^6\,kJ \cdot t^{-1}$. The main technical parameters are shown in Table 9.2.

A major feature of this process is using the horizontal converter and small-particle catalyst, so that the gas flows the path shortly, its linear speed is small, the pressure drop decreases in the catalyst bed, and consequently the recycle-compress power can be saved; the catalytic activity can be improved by 12%–25%. Thus the catalyst volume and the equipment size decreases, the net value of the ammonia increases, the amount of the recycle gas declines; there is homogeneous distribution of the gas-flow so that gets the higher synthetic ratio, and the energy consumption is significantly reduced.

9.1.1.2 *Topsøe process*

The pressure (26.38 MPa) of synthesis loop for the Topsøe process is higher than other processes, and it uses the two-stage ammonia cooler and separates in front in

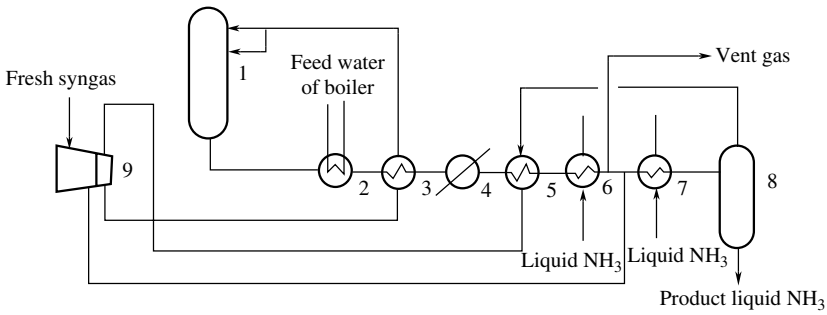


Fig. 9.2 Process flow of Topsøe ammonia synthesis

1-Converter; 2-Waste heat boiler; 3-Gas-gas heat exchanger; 4-Water cooler; 5-Cold exchanger; 6,7-cooler; 8-Separator; 9-Syngas compressor.

the compressor as is shown in Fig. 9.2. The converter is a new type of radial-flow reactor. Compared with the Kellogg process, the feature of the Topsøe process is that the recycle section is placed in front of the converter, so that the pressure of converter is in the highest point in the recycle loop, and the recycle compress is placed after the separation of ammonia, so that the amount of the recycle-gas and the power of recycle-compressing is decreased. The main technical parameters of the process are shown in Table 9.2.

In order to meet the need to process with lesser energy consumption, the Topsøe corporation designed a synthesis loop (S-250 series), which included two converters, three beds and two waste heat boilers in order to by-produce high pressure steam as much as possible as shown in Fig. 9.3. The Topsøe S-250 series is composed of a radial-flow S-200 converter (1) with two beds and a radial-flow S-50 converter, and (2) with one bed. The outlet of every converter has the waste heat boiler to

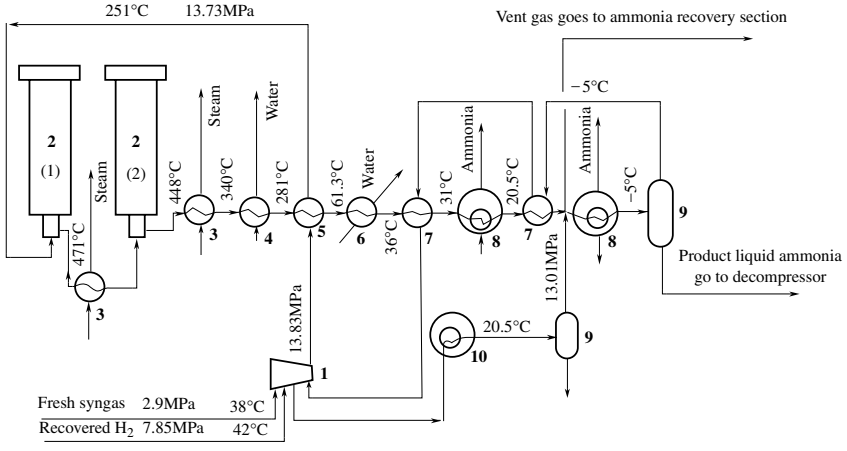


Fig. 9.3 Process flow of Topsøe S-250 synthesis loop

1-Syngas compressor, 2-Converter, 3-Waste heat boiler, 4-Pre-heater of feed water of boiler, 5-Interchanger, 6-Water cooler, 7-Cool exchanger, 8-Ammonia-cooler, 9-Separator, 10-Ammonia-cooler for fresh syngas.

by-produce high pressure steam (12 MPa). The outlet gas of converter after being cooled to 281°C by the preheater of feed water of boiler, comes into the preheater in front-converter to go to preheat the cycle gas from the outlet of the cycle-compressor to 251°C to come back into the converter. Then the outlet gas of converter is further cooled to −5°C; later, *via* a water-cooler, two ammonia-coolers and the liquid ammonia are separated from it.

There are three catalyst beds to reaction in the S-250 series so that the net value can be increased further and more high-pressure steam can be produced, and thereby the consumption energy is decreased.

The S-250 series can be applied to all kinds of pressure ranges, and the pressure drop is 0.2 MPa and 0.1 MPa in S-200 and S-50 converter respectively. The net value of ammonia can reach 16.5% at 14.0 MPa.

9.1.1.3 *Braun process*

The Braun process adopts the deep cooling purification process, three converters and the pressure of 15 MPa. The prominent feature of the Braun process is the deep cooling purification which is its proprietary technique. The syngas is refined and purified finally by deep cooling to remove the superfluous N_2 and without the trace of water and CO_2. The fresh syngas of high quality is a major advantage for all deep cooling purification processes, which benefits the synthesis system greatly, raises the capacity of the synthesis system efficiently and reduces the energy consumption. When the loop pressure is 15 MPa, the concentration of ammonia in the gas at the outlet of the third converter can be up to 21% and about 4% at the inlet of the first converter respectively. The process flow is shown in Fig. 9.4, and the main technical parameters are shown in Table 9.2.

The equipment of deep cooling brings a series of convenience for operation sequences before and after the purification and excellent comprehensive effects on the whole plant. For example, due to the deep cooling purification, the requirements for the secondary steam reformer are decreased remarkably, and there are no strict requirements for the ratio of H_2 to N_2 and the content of CH_4. The outlet temperature of the secondary steam reformer can be lower than the conventional operation

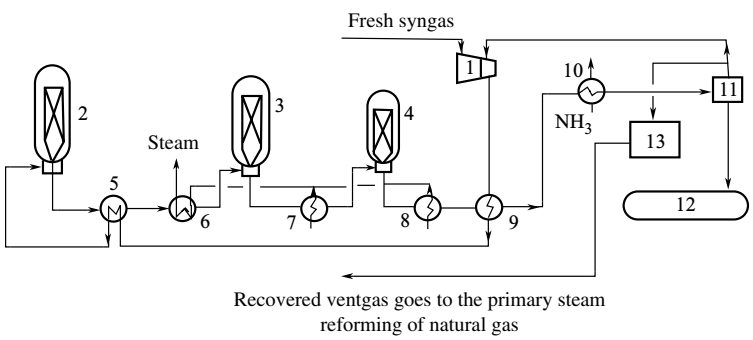


Fig. 9.4 Process flow of Braun synthesis loop

1-Synthesis gas compressor; 2–4-Converter; 5,9-Heat exchangers; 6–8-Waste heat boilers; 10-Ammonia cooler; 11-Separator; 12-Liquid ammonia tank; 13-Set of recovery ammonia from vent gas.

by 100°C, the content of CH_4 at the outlet can be up to 1.3%, the quantity of air in the secondary steam reformer can be 1.5 times of the conventional operation, so that the outlet temperature in the primary steam reformer falls to 700°C, and finally, the content of CH_4 can be up to about 25%, meaning that the CH_4 conversion is less than 50%. This would decrease the heat load of primary steam reformer, coupled with using the waste gas at 525°C expelled from the gas turbine as burning air, therefore, the fuel consumption of the primary steam reformer is decreased significantly, the life period of tube-furnace and the catalyst is prolonged, and the investment of the equipment is declined. At the same time, the equipment of deep cooling purification becomes the adjuster of all fluctuations, and the operating flexibility becomes larger. Therefore, accidents of stopping can be decreased greatly and the operation rate can be increased. Some data indicates that while the operation rate increases by 4%, the profit increases by 14%. Long period of operation is an effective measure of energy-saving for plants.

9.1.2 *ICI–AMV process with Fe-Co catalyst*

The ICI–AMV process was developed by the ICI Company for its 74-1 Fe-Co catalyst, where the process was designed by ICI and the engineering was designed by Uhde Company, Germany. The core of the synthesis loop at low-pressure is the radial-flow converter with three beds of catalysts using 74-1 catalyst of small-particle and indirect interchanger, and in series an inverted U-shaped waste heat boiler.[8−10] The process flow is shown in Fig. 9.5. The main technical parameters are shown in Table 9.2.

AMV adopted a part of the advanced technology of Kellogg and Brown processes. The characteristics are as follows:

(1) Volume of catalyst was increased by 122 m^3 and the operation pressure was declined to 10–12 MPa due to using small particles of 74-1 Fe-Co catalysts.

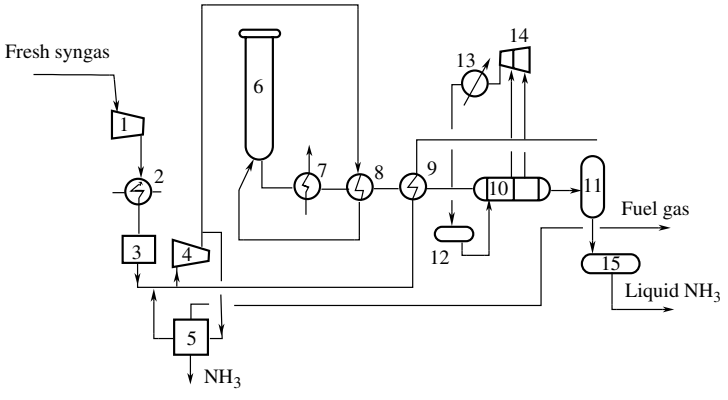


Fig. 9.5 Process flow of ICI-AMV synthesis loop

1-Syngas compressor; 2,8,9-Heat exchanger; 3-Desiccators; 4-Circular gas compressor; 5-Freezing-recycling set of hydrogen; 6-Converter; 7-Waste heat boiler; 10-Ammonia cooler; 11-Separator; 12-Storage of ammonia; 13-Water cooler; 14-Ammonia compressor; 15-Storage.

(2) The ratio of H_2 to N_2 in the synthesis loop is 2.4. The superfluous H_2 is reclaimed by deep-cooling device and redundant N_2 is eliminated. Therefore, similar to the Braun process, the superfluous air can be injected in the secondary steam reformer, so that the operating pressure of the primary steam reformer is 2.5–3.5 MPa, the operating temperature is 705–788°C, the outlet temperature of secondary steam reformer is 871–954°C, and the outlet content of CH_4 is about 1%. The deep-cooling purification process is different from Braun process, where the fresh syngas does not enter deep-cooling system directly, but a part of gas extracted from the recycle gas enters to it and adjusts the ratio of the H_2 to N_2 of the recycle gas.

To enhance the output of high pressure steam produced by the waste heat boiler, the Uhde Company also proposed a synthesis loop with two converters and two waste heat boilers (Fig. 9.6) which were applied in the process with residual oil as raw materials and the cryogenic purification. The loop pressure is 16 MPa, the first converter has two beds, inter-cooled, radial-flow, and the outlet temperature of syngas is 473°C. The outlet gas goes through the waste heat boiler to by-produce high pressure steam then enters the second converter.

The second converter is a radial-flow with single-bed of catalyst, and the outlet gas temperature is 442°C. The gas goes through the second waste heat boiler, the interchanger, the water cooler and the cool exchanger, then enters the ammonia condenser where the condensing temperature is 0°C. Under cold area environment, the ammonia compressor is not necessary to obtain 40% liquid ammonia and 60% gaseous ammonia. The net value of ammonia could reach 19.3%, the total pressure drop of the first and the second converters is 0.35 MPa, 1.54 tons of high pressure steam per ton ammonia (10.2 MPa) is by-produced (the water temperature supplied to the boiler is 210°C), the volume of catalyst is 76 m^3 for the process flow with two converters and two waste heat boilers.

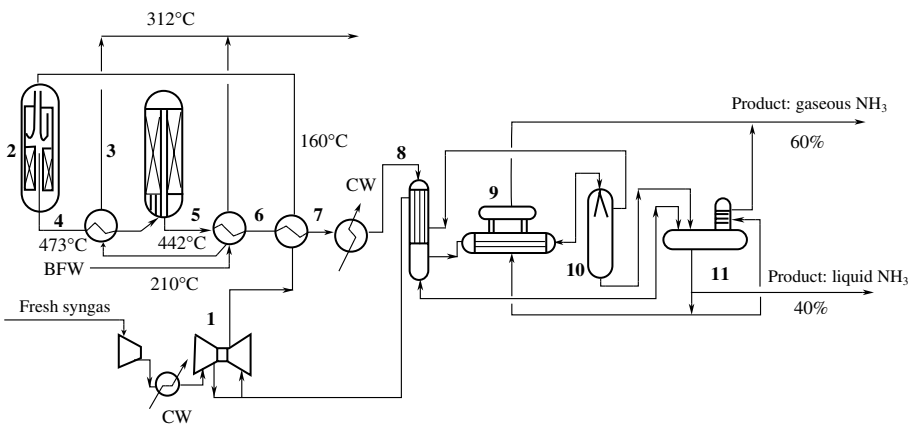


Fig. 9.6 Process flow of Uhde synthesis loop with two converters and two waste heat boilers

1-Syngas compressor, 2,3-Converter, 4,5-Waste heat boiler, 6-Interchanger, 7-Water cooler, 8-Cool exchanger, 9-NH_3 cooler, 10-NH_3 separator, 11-NH_3 tank.

9.1.3 *Synthetic process flow with Ru catalysts*

The characteristics of Ru catalyst are high activity (concentration), intense inhibition of hydrogen, insensitivity to ammonia, high catalyst cost and so on. In view of engineering applications, first, its high activity can be used to operate in low temperature and low pressure where there is the possibility to realize synthetic process of non-circulation; second, it is suitable to be applied to the process at low ratio of H_2 to N_2 because of its intense inhibition of hydrogen; third, it is suitable to be co-used with Fe catalyst since it is insensitive to ammonia and simultaneously this also reduces the amount of Ru catalyst used. Therefore, many kinds of new synthesis processes flow have been proposed.

9.1.3.1 *The synthesis process with low ratio of H_2 to N_2*

The effect of strong inhibition of H_2 (in H_2/N_2) on the activity of ruthenium catalyst has been discussed in Section 6.3.3, Chapter 6. The suitable ratio of H_2/N_2 measured at 400°C, 375°C and 350°C at 10 MPa is 1.5, 1.0 and 0.67, respectively.

Figure 9.7 shows that Kellogg proposed the principle process diagram of synthesis loop by changing the radio of H_2 to N_2. Fresh syngas containing 65% H_2, 32.5% N_2, 1.9% CH_4, 0.4% Ar and 0.2% H_2O is sent into the syngas compressor and is compressed to 7.5 MPa, after separating the condensate liquid, then it is mixed with recycle gas for which the molar ratio of H_2 to N_2 is 0.8:1. Thus, the gas mixture obtained consists of 45% H_2, 45% N_2, 2.5% NH_3, 6.2% CH_4 and 1.3% Ar. The gas is compressed to 8.0 MPa by the circulator compressor, and is heated to 355°C in the interchanger. It is then sent into the converter 10 where it produces 7.2% ammonia. The gas, whose temperature at the reactor outlet is 430°C, is cooled to 335°C in the cooler 11 by the boiler feed water, then enters the catalyst beds of reactor 9, produces 11% ammonia. The gas, whose outlet temperature is 410°C, is cooled to 350°C in the cooler 12 and then enters the third bed of catalyst in the reactor 8, where the concentration of ammonia in the gas reaches 13.5%, and the outlet temperature 385°C. The gas consisting of 33.8% H_2, 44% N_2, 13.5%,

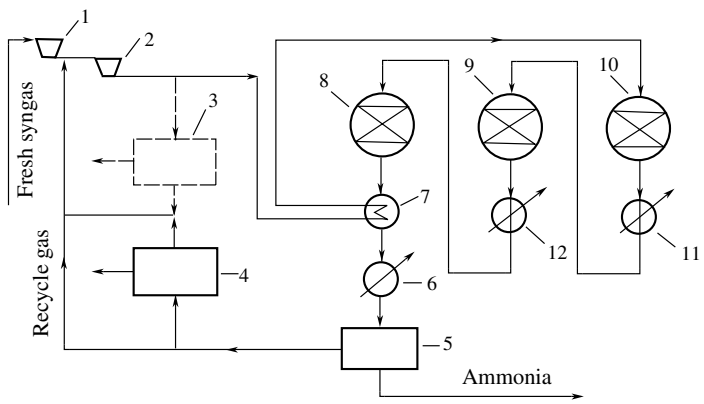


Fig. 9.7 Principle process flow of Kellogg synthesis loop with Ru catalysts
1-Syngas compressor; 2-Circulat compressor; 3,4-Separating-hydrogen devices; 5-Separator; 6,11,12-Cooler; 7-Cool-exchanger; 8,9,10-Converter.

6.8% CH_4 and 1.5% Ar after reaction is cooled to 40°C in the interchanger 7, and is then continuously cooled to −33°C in the cooler 6. The condensed ammonia is separated from the separator no. 5, and the residual gas is recycled to the inlet of compressor 2. The vent gas (7% H_2) is sent to the H_2 separator 4, where H_2-rich gas (85% H_2) is obtained and mixed with recycle gas.

The N_2–H_2 ratio is stoichiometric at all points in the traditional synthesis loop. But, at low N_2–H_2 ratio loop, N_2–H_2 mixture with the mole ratio of H_2 to N_2 at inlet is 2:(1–0.671) (1:1 will be better) is sent into a converter. During the reaction process, it keeps stoichiometric ratio, but because the raw material with H_2/N_2 of 1:1 is sent into the converter, more H_2 is consumed than N_2, so H_2 is needed to be complementary to the system in order to maintain the proportion needed. For example, someone suggested that H_2 could be injected to every point of the system respectively.[11]

The experiment means that the fresh syngas whose molar ratio of H_2 to N_2 is (1.7–2.5):1 is mixed with the recycle gas current, and the molar ratio of H_2 to N_2 increases to (0.5–1.7):1 by separating H_2 from vent gas. The mole ratio of H_2 to N_2 of the syngas entering the converter is (0.8–1.8):1. In this situation, the space velocity ratio of the recycle gas to the fresh gas is (2.2–3.7):1.

9.1.3.2 *Synthetic process flow without circulation*

In the traditional industrial process, the concentration of ammonia in the N_2–H_2 mixture from converter outlet is 10%–18%. Therefore, it is necessary to recycle the N_2–H_2 mixture, which needs the auxiliary facility, consumes energy, thus causing high initial investment and operation cost.

The British Petroleum Company thought that Ru catalyst is most suitable for the bypass-type flow in which if the conversion of processed N_2–H_2 mixture is not below 75%, there is no need to circulate N_2–H_2 mixture unreacted. Therefore, we need a N_2–H_2 reaction area comprising many continuous working procedures to separate ammonia in the middle.

The process conditions are as follows: The temperature is 250–500°C, the pressure is 6.0–20.0 MPa, and the ratio of N_2 to H_2 is 2:1–0.25:1 (best is 1:1). There are the following merits for the process:

(1) Compared to the traditional flow, converter in the by-pass type flow can use the high content of inert gas and CH_4 as feed gas.
(2) In the synthesis condition that the ratio of H_2 to N_2 is 1:1 and hydrocarbons are reformed in the oxygen in the air, the cheaper raw materials including natural gas, liquid fuel and coal can be used. The principle process flow diagram of the synthesis loop with non-circulation by N_2–H_2 mixture is shown in Fig. 9.8.

The process uses two or more converters in series and Ru catalyst consisting of 7% Ru, 14% K and rest of carbon carrier containing graphite.

The N_2–H_2 mixed feed gas heated by interchanger 3 is sent to the first converter, where the partial ammonia is synthesized on Ru catalyst, then the N_2–H_2 mixture through the interchanger 3 and the cool-condenser 2 is sent into the separator 1 to separate the liquid ammonia. After unreacted N_2–H_2 mixture is heated by the interchanger 5, it is sent into the second converter.

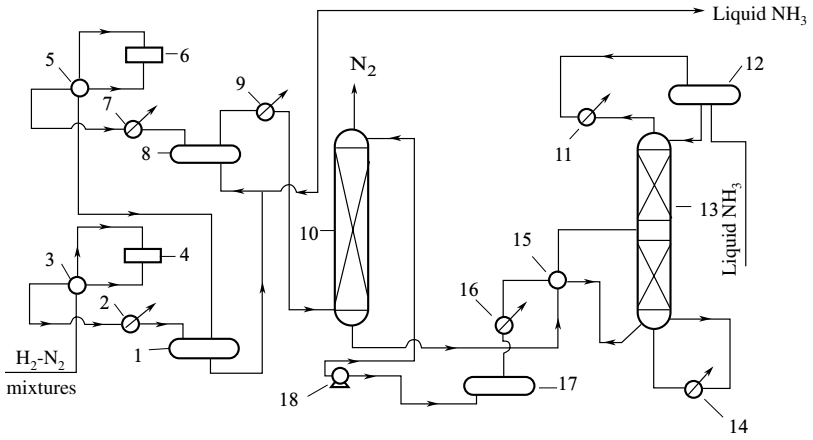


Fig. 9.8 Principle process flow of the synthesis loop without circulation of N_2–H_2 mixture

1,8-Separator; 2-Cool condenser; 3,5,15-Heat exchanger; 4–1st converter; 6-second converter; 7,9,16-Cooler; 10-Absorption column; 11-Condenser; 12-Tank; 13-Stripper; 14-Water heater; 17-Tank; 18-Pump.

The product is cooled by the interchanger 5 and cooler 7 and is then sent into the separator 8. The liquid ammonia which is separated from the separator 1 and 8, respectively is incorporated and is then sent to the user. Unreacted N_2–H_2 mixture derived from the separator 8 is cooled in the cooler 9 and is then sent into the absorption column 10 where it contacts the aqueous solution of ammonia, thereby, the concentrated solution of ammonia obtained is discharged from the bottom of absorption column 10, is then heated by the interchanger 15, and sent into the stripper 13. Unreacted gas consisting of more than 75% N_2 and trace impurities are discharged from top of absorption column. This gas may be used as fuel for turbine and so on.

In the non-circulation process flow, it is necessary to recover H_2 from vent gas besides recovering in the unreacted gas in vent gas. In the traditional process, the amount of vent gas in synthetic loop is 10%–20% which is used as fuel of first steam reforming, so that large quantity of H_2 is lost. There are some methods to draw H_2 from vent gas and to use vent gas:

(1) H_2 is drawn from vent gas by means of adsorption, cooling or membrane separation and is returned to the synthesis system.
(2) In order to increase the output of ammonia or reduce consumption of fuel as raw materials, the N_2 and H_2 in vent gas are further synthesized to ammonia using an auxiliary converter. It is not economic at the same temperature and pressure as main synthesis system on Fe catalyst because the content of inert gas in vent gas is very high, and if it continues rising, then the pressure can increase the energy consumption.

In 1981, British Petroleum Company suggested a supplemental synthesis process on Ru catalyst without rising of the pressure. It consumes only a little energy to recycle. According to this method, the main converter uses the traditional Fe

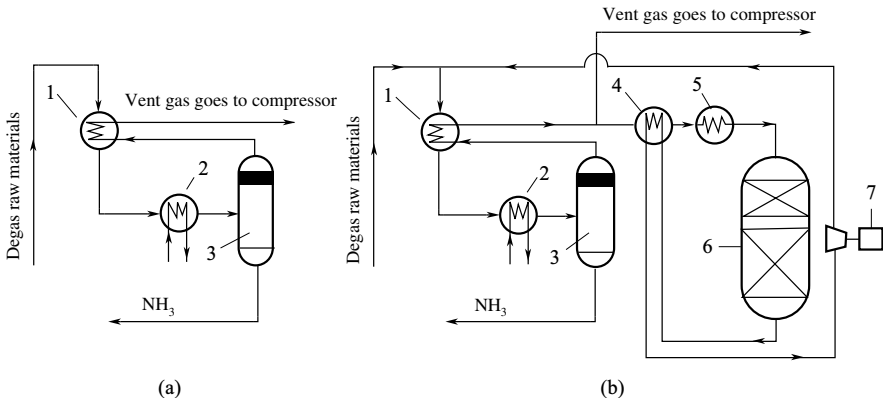


Fig. 9.9 Principle process flow of separating ammonia from the vent gases (a) conventional process; (b) improved process

1,4-Heat exchanger; 2,5-Cooler; 3-Separator; 6-Auxiliary converter; 7-Blower.

catalyst or Ru catalyst, the pressure is 12–25 MPa; the auxiliary converter uses Ru catalyst, the pressure is equal to or even lower than that of the main converter.

In the auxiliary converter, it may be realized for vent gas to synthesize ammonia in both bypass type flow and cycle type flow. However it is found that content of the inert gas may be higher level in the cycle type flow. In order to prevent the accumulation of the inert gas, it is suggested to remove vent gas.

The difference between the improved process and the traditional process is shown in Fig. 9.9. The ammonia is condensed in the separator 3, residual vent gas is heated in the interchanger 1 and is divided into two parts, one of them is sent into the tube furnace to burn, and another is heated by interchanger 4 and the cooler 5, and is then sent into the auxiliary converter 6 to react on Ru catalyst. After the reaction, the gas is cooled by interchanger 4, and is then sent by the blower 7 to mix with vent gas from main converter, where the ammonia is separated by the separator 3.

9.1.3.3 *Process flow of using Fe catalyst combined with Ru catalyst*

In order to reduce the effects of inert gas and increase output, three or four beds of catalysts are used under the industrial condition of traditional process, which will make the pressure drop and increase in energy consumption. Kellogg Company considered [14] that the energy consumption can be reduced greatly if Ru catalyst is co-used with Fe catalyst. There are three ways to co-use Fe and Ru catalyst:

(1) Adding auxiliary converter with Ru catalyst after the converter with Fe catalyst

In the condition that the ratio of H_2/N_2 is less than stoichiometric ratio, Ru catalyst has very high activity and is insensitive to ammonia. So, synthetic ammonia reaction can use the syngas with excessive NH_3 on Ru catalyst and decrease the quantity of circulation gas, i.e., it is possible that the reaction is first carried out on Fe catalyst in the condition of stoichiometic ratio of H_2/N_2 and then is carried out in supplement on Ru catalyst in the condition that the mole ratio of H_2/N_2 is (2.2–2.8):1 and with excessive N_2. The round structure of auxiliary converter, with

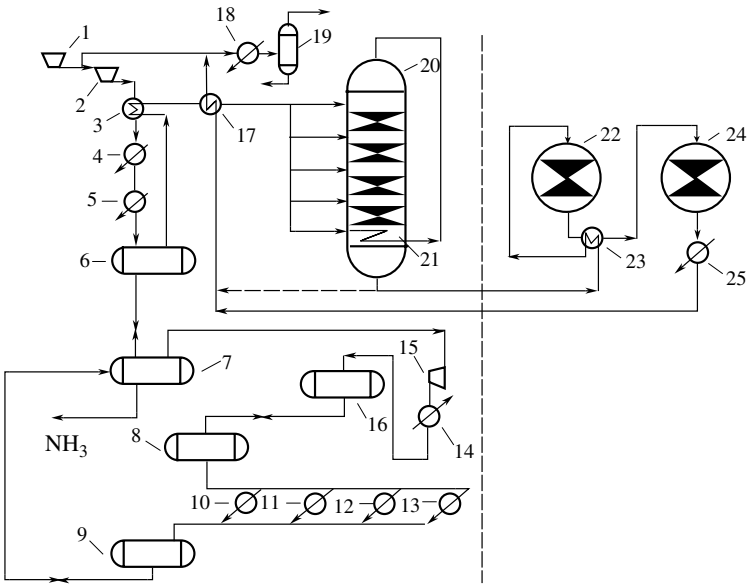


Fig. 9.10 Principle process flow diagram of using Fe catalyst combine with Ru catalyst

1-Fresh syngas compressor; 2-Circulate compressor; 3,17,21,23-Heat exchanger; 4,5,10–14,18,25-Cooler; 6–9,16,19-Segregator; 15-Ammonia compressor; 20-Main converter; 22,24-Auxiliary converter.

"hot" wall and single bed catalyst, is simple. If a high conversion is expected, two converters loaded with Ru catalyst can be used. If the process is carried on at low pressure of 10.0 MPa and 16.0 MPa, concentration of ammonia can reach 13% and 18% (vol.) after auxiliary converter. The principle process flow using Fe and Ru catalyst is shown in Fig. 9.10.

The fresh gas containing stoichiometric H_2 ($H_2/N_2 = 3{:}1$) and 1.3% of Ar and CH_4 is compressed to 14.0 MPa by the compressor 1, and mixed with recycle gas containing 12% NH_3 and inert gas. The obtained mixed gas is compressed to 14.8 MPa by the compressor 2, and then cooled to $-23°C$ by the interchanger 3, the cooler 4 and 5, and the liquid ammonia is obtained by the separator 6. The mixture of H_2 and N_2 discharged from the separator 6, which contains a little ammonia and inert gas, is heated by interchanger 3 and 17, and is then sent in the reactor 20 with Fe catalyst.

In Fig. 9.10, the main flow of N_2–H_2 mixture is heated to reaction temperature by interchanger 21 in the converter 20. The outlet gas of converter 20 is cooled by the interchanger 23, and is sent through auxiliary converter 22 operating at 14 MPa, interchanger 23, the second auxiliary converter 24, cooler 25 and interchanger 17 in turn, and finally returns to the ingress of compressor 2.

Because the ammonia synthesis reaction is carried out at the condition that the ratio of H_2/N_2 is 3:1, no fresh syngas is injected in the process. At the outlet of converter 22 and 24, the ratio of H_2/N_2 decreases to 2.6 and 2.4, with temperature at 349°C and 382°C, respectively. A part of the recycle gas is drawn from the interchanger 17 as vent gas in order to adjust the content of inert gas (13.6%) in

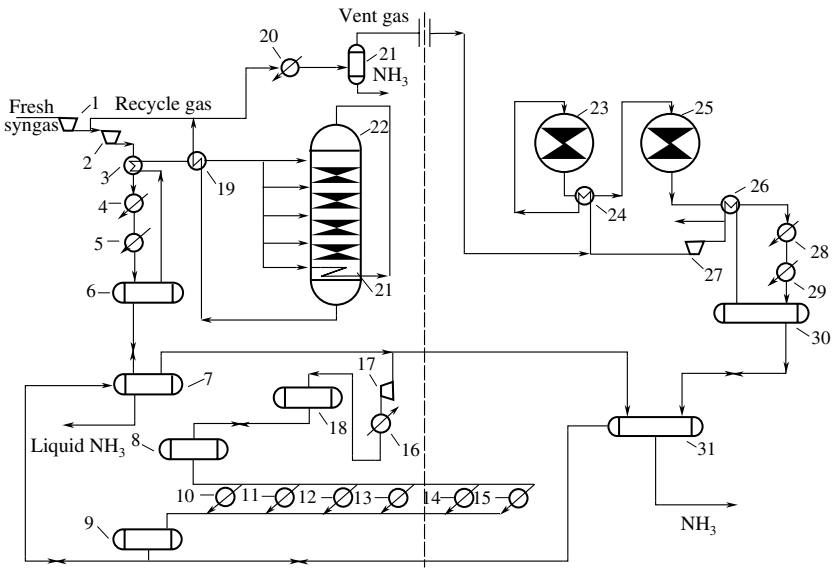


Fig. 9.11 Principle process flow of the supplemental synthesis by the vent gas
1-Fresh gas compressor; 2-Circulator; 3,19,24,26-Interchangers; 4,5,9,11–16,20,28,29-Coolers; 6–8,10,18,21,30,31-Segregators; 22-Main converter; 23,25-Auxiliary converters; 17,27-Compressors.

the synthesis system. After the ammonia in the vent gas cooled by cooler 18, it is discharged from the separator 19. The concentration of ammonia is increased from 10% at the outlet of converter 20 to 18% at the outlet of converter 24. In this process, the flow rate of gas is slower, and it decreases from 25 kmol·h^{-1} to 14.9 kmol·h^{-1} at the outlet of converter 20, so less gas is compressed by compressor 2.

(2) The method of supplemental synthesis by the vent gas from converter using Fe catalyst

The principle process flow of the supplemental synthesis by the vent gas from main converter of Fe catalyst is shown in Fig. 9.11. This process flow is basically similar to that of Fig. 9.10.

The difference between the two process flows is that the reactant gas entering the auxiliary converters of 23 and 25 with Ru catalyst is the vent gas from the main converter 22 with Fe catalyst, but not the outlet gas from the main converter or the circular gas. Actually, in Fig. 9.10, the reaction takes place on Fe catalyst only once, and again for quadratic on Ru catalyst; in Fig. 9.11, the main reaction takes place on Fe catalyst, and supplemental synthesis is carried out on Ru catalyst. In comparison with the traditional process, the ratio of H_2 to N_2 in the converter 22 decreases to 2.9:1, the flow of the vent gas increases to 6.3%, and the content of inert gas reaches 5.6%. In this method, the amount of the vent gas can be reduced because the content of the inert gas in the vent gas is higher, the compression cost can be decreased, and the yield can be increased. Besides, the load of hydrocarbon reformation in the primary is alleviated because the hydrogen of vent gas is used.

(3) KAAP process of coupling using Ru and Fe catalysts in a single converter

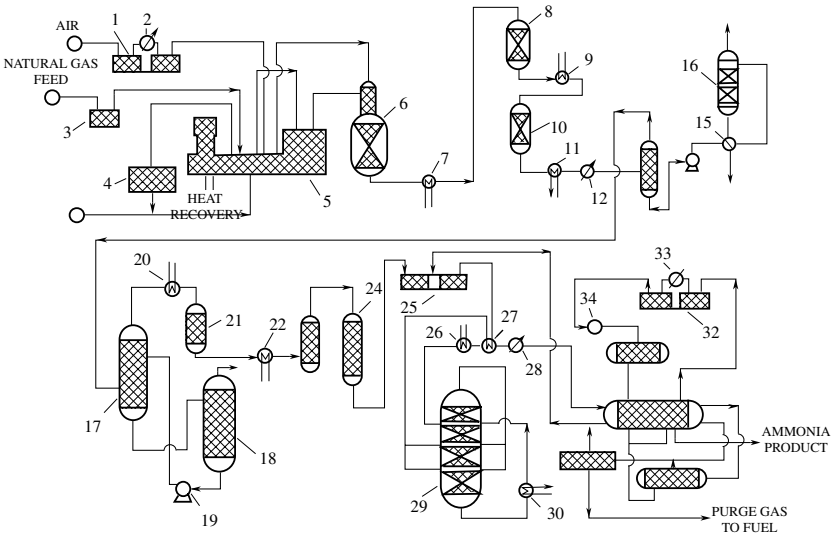


Fig. 9.12 Flow-sheet for KBR advanced ammonia process

1-Air compressor; 2,12,28,33,34-Cooling; 3-Feed gas compressor; 4-Waste heat boiler; 5-Primary reformer; 6-Secondary reformer; 7,9,11,15,20,22,26,27,30-Heat recovery; 8-HTS; 10-LTS; 16-Condensate stripper; 17-CO2 absorber; 18-CO2 stripper; 21-Methanator; 24-Dryer; 25-Synthesis gas compressor; 29-KAAP ammonia converter; 32-Refrigeration compressor.

If the auxiliary and main converters in Fig. 9.10 are united into one converter, and Fe and Ru catalysts are loaded in the upper and lower beds respectively, it is more practical to reform the existing synthesis device and the effect between them is not different. After 10 years of collaboration, BP and Kellogg Company finally determined to adopt first the single-converter process, and the first Kellogg Ammonia Advance Process (KAAP) flow based on Ru catalyst was developed successfully in October 1990. In 1998, two new grassroots ammonia plants using KBR Advanced Ammonia Process (KAAP) technology were started up in Point Lisas, Trinidad. These plants represent the first of a new generation of Kellogg Brown & Root ammonia plants. This is the first time the KBR Advanced Ammonia Process (KAAP) and KAAP catalyst have been used in a grassroot ammonia plant. Not only were these the first grassroot plants to use KAAP technology, but they also had the largest nameplate capacity ($1850\,t \cdot d^{-1}$) of any ammonia plant built to date. The flow-sheet is shown in Fig. 9.12.[15–16] The operating pressure of KAAP synloop is $91.4\,kg \cdot cm^{-1}$ (about 9.0 MPa). It was chosen because that pressure matched well with a single-case syngas compressor while KAAP remains very active even at this lowest pressure. At the same time, at a pressure of $91.4\,kg \cdot cm^{-1}$, there are savings in the compression equipment and synthesis loop piping and equipment. With these savings, the synthesis loop costs less and more than offsets the added catalyst cost.

The characteristics of this device are single-series and large, and its core is a KAAP converter. This converter has the flowing characteristics: (1) Hot-wall design was adopted first; (2) This converter is a radial-flow, four bed and inter-cooled, the first four bed inter-cooled ammonia converter contained in one shell; (3) The first bed contains an iron catalyst, which accounts for about half the total catalyst

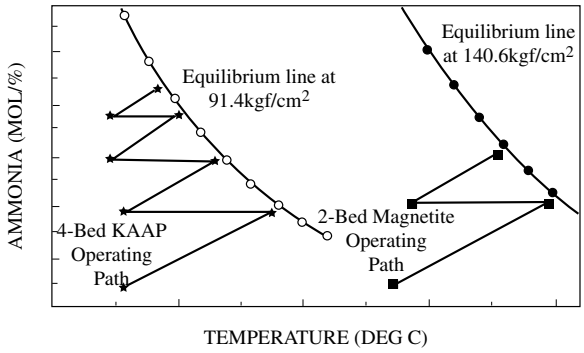


Fig. 9.13 Compare of KAAP and traditional converters

volume. The remaining three beds contain KAAP catalyst. Figure 9.13 shows the comparison of the operation lines between KAAP and traditional converters. It can be seen from Fig. 9.13 that the outlet concentration (reach to 21.7%) if much higher than that of converter with conventional two beds of Fe catalyst operated at the pressure of 140.6 $kgf \cdot cm^{-2}$ when the KAAP converter with four beds is operated at the pressure of 91.4 $kgf \cdot cm^{-2}$.

Using Ru catalyst can increase the productivity of the device and decrease the energy consumption by 1.2 $GJ \cdot t^{-1}$. The life period, poison and anti-poisoning of Ru catalyst is the same as Fe catalyst, and its life period is dependent on the loss of the carrier of activated carbon.[16]

9.1.4 *Pressure of reaction and isopiestic process*

9.1.4.1 *Pressure of reaction*

The biggest controversy about a modern large ammonia plant focuses on the choice of synthesis loop pressure. After careful study on the technological process, Ib Dybkjaer[17] considered that energy consumption is mainly dependent on the catalyst volume. Exactly speaking, it is dependent on the temperature which makes the reaction system build the thermodynamics equilibrium. This means that increasing catalyst volume and/or catalytic activity can improve the energy efficiency. If the activity of catalyst with the same volume is increased as much as four times, the energy consumption about 0.8 $GJ \cdot t^{-1}$ can be saved, and the efficiency of saving energy increases with decrease of the equilibrium temperature of catalyst bed.

The research[18] indicated that the total power of fresh syngas, recycle gas and ammonia compressor is the minimum when the synthesis pressure is selected at 15 MPa (absolutely). But the practical selection of the loop pressure is closely related to plant scale and type of compressors. For example, an early research compared low pressure (15 MPa) to high pressure (20–22.5 MPa and 33 MPa) systematically from three aspects such as the cost of main equipment (including heating furnaces, interchangers, converters and their tanks, ammonia compressors and related heat exchangers and tanks; compressors and their inter-stage devices, pipeline and tube fittings and so on); the total trigger power of three compressor sets (syngas, circulating gas and ammonia compressor) and the cost of catalyst. The result indicated that for the plant with productivity of 600 net $t \cdot d^{-1}$ (1 net ton = 907.2 kg) and

1000 net $t \cdot d^{-1}$, it is proper and favorable in economy to choose the loop pressure of 15 MPa. In fact, the most of modern ammonia plants with capacity of 1000 t/d choose the pressure below 15 MPa.

Synthesis pressure is related to the type of compressor. The type of compressor used in ammonia plant is dependent on its productivity and pressure level. If the capacity of plant is close to or less than $400\,t \cdot d^{-1}$, then the reciprocating compressor can entirely meet the requirements. If the pressure level needs high than 15.0 MPa should use reciprocating compressor. The centrifugal compressor is used in all modern large-scale ammonia plants with a capacity of $1000\,t \cdot d^{-1}$ or more. Several kinds of centrifugal compressor used in modern ammonia plan are shown in Table 9.3.

The effect of synthesis loop pressure on the relative investment of the compressor factory and running power of the compressors for the plant is shown in Fig. 9.14. It can be seen from Fig. 9.14 that in the above range of synthesis pressure, the power change is small (about 6%). The influence of synthesis loop pressure on investment is obvious. Pressure rising makes the investment of compress section increase by 20% or more.

It should be pointed out that the condensing temperature of ammonia at the outlet of converter changes with the synthesis pressure, which makes the investment of

Table 9.3 Some centrifugal compressors used in modern ammonia plant

Type	Pressure range/MPa	Typical power/kW for $1000\,t \cdot d^{-1}$ of ammonia
Natural gas compressor	0.68–4.1	1,100
Air compressor	Atmosphere pressure ~4.1	6,300
Syngas and recycle gas compressor	2.7–15.1	13,000
Ammonia compressor	0–1.8	7,800

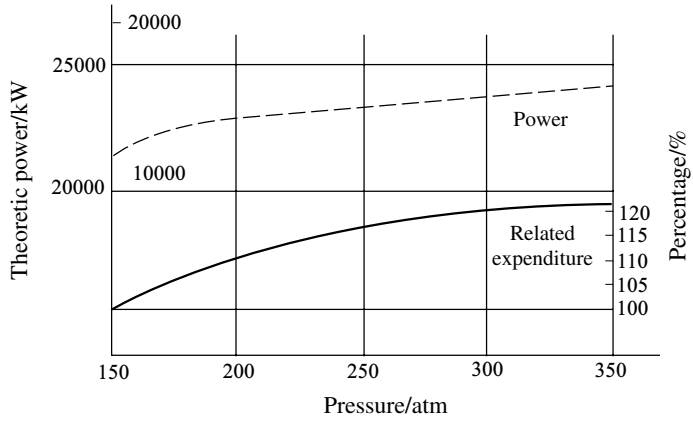


Fig. 9.14 Relationship of power and investment to synthesis pressure

[Power is the sum of syngas compressing, syngas recycle and refrigerating. The condensing temperature of syngas is same in all circs. The inhaling pressure of gas in syngas compressor is 23.8 atm].

compressor close in different pressure. For example, increasing the condensing temperature in higher pressure declines the refrigerator power. The tendency shown in Fig. 9.14 will still be maintained, because the efficiency is lower and the investment of equipment is higher at higher pressure.

9.1.4.2 *Process of synthesis at isotonic pressure*

Among the processes where the syngas is produced from residual oil or pulverized coal (coal–water slurry) at 8.5 MPa, the following procedures can be adopted for the synthesis loop.

(1) The isotonic-pressure process. The gas is produced at 8.5 MPa, following desulphurization, steam shift, de-carbonization, reinforcing N_2, and then enter the converter at 7.5 MPa.
(2) The micro-pressurized process. The gas is produced at 8.5 MPa, following desulphurization, steam shift, de-carbonization, reinforcing N_2, and is then micro-pressurized to 9.0–10.0 MPa (by the circulation compressor with micro-pressurizing section) and enter converter.
(3) The raising-pressure process. The gas is produced at 5.0 MPa, following purification and reinforcing N_2, then the pressure is increased to 15–22 MPa and enter converter. This process flow is present in most large-scale ammonia plants.

The advantage of the synthesis process at 7.5 MPa is to omit a syngas compressor consuming a lot of energy; for the micro-pressurized process at 9.0–10.0 MPa, though it needs to pressurize syngas, the compression ratio is very small and not much energy is consumed; the advantage of raising pressure process at 15–22 MPa is lower cycle energy consumption of unreacted syngas which is convenient for separation of ammonia because of the higher pressure.[19]

One of the keys to achieve the synthesis process at 7.5 MPa is to use ammonia synthesis catalyst used in low temperature and low pressure. A301 and ZA-5 catalysts with wüstite as precursors have very high activity at low temperature and low pressure, which establish a good foundation for developing ammonia synthetic process at low pressure and created favorable conditions.[20] Tables 9.4–9.7 have shown the operating data of A301 loaded in the bypass device in a plant which was measured in the actual industrial conditions.[21]

(1) The isotonic-pressure process at 7.5 MPa. Table 9.4 shows the outlet concentration ($\varphi_{,\text{out}}/\%$) of and net value ($\Delta\varphi/\%$) of ammonia for A301 catalyst at 7.0 MPa and 7.5 MPa, and 6000 h^{-1} respectively.

It is known from Table 9.4 that the outlet concentration and the net value of ammonia on A301 catalyst is up to 14.35% and 10.75% when the pressure is 7.0 MPa, the space velocity is 6000 h^{-1}, the ratio of H_2/N_2 is 2.6, inert gas (mainly He) is less than 2%, the concentration of ammonia in the inlet gas is 3.6% and the size of the catalyst particle is 1.6–3.0 mm. Under the same condition, the outlet concentration of ammonia is 13.54% (425°C) and the net value of ammonia is 10% when the space velocity is 8000 h^{-1}. In the lower space velocity, the outlet concentration of ammonia is higher. For example, when the space velocity is 3000 h^{-1}, the concentration of ammonia is 16.55% and the net value of ammonia is 13%. In 7.5 MPa, the net value of ammonia is up to 11.2%.

Table 9.4 Activity of A301 catalyst in the bypass device at 7.0 MPa and 7.5 MPa

No	Temperature of catalyst bed/°C[a]					S_v/h^{-1}	P/MPa	$\varphi^b_{,out}$/%	$\varphi^b_{,in}$/%	$\Delta\varphi$/%
	1	2	3	4	5					
1	450	453	455	456	455	5,998	7.0	12.38	/	/
2	425	430	432	432	431	6,025	7.0	14.35	3.66	10.69
3	400	405	406	405	403	6,045	7.0	14.35	3.61	10.74
4	375	380	380	379	378	6,053	7.0	12.93	3.60	9.33
5	350	353	353	351	350	6,050	7.0	10.72	3.69	7.03
6	425	430	432	432	430	6,047	7.5	14.65	3.62	11.03
7	400	404	406	406	404	6,034	7.5	14.80	3.60	11.20

[a]The thermocouples 1, 2, 3, 4, 5 were placed in the bed inlet by 0%, 50%, 75%, 98% and 108% respectively.
[b]Average value for 8 h.
Note: The particle size of the catalyst is 1.6–3.0 mm, volume 20 cm^3, the composition of the inlet gas were $H_2/N_2 = 2.4$–2.65, $(CH_4 + Ar + He) < 1.67\%$, $NH_3 = 3.5\%$–3.7%.

Table 9.5 Volume of catalyst needed at isotonic process of 7.0 MPa–7.5 MPa (1000 t/d)

No	P/MPa	T/°C	Inert gas/%	φ_{in}/%	$\Delta\varphi$/%	S_{in}/ ($\times10^{-4}m^3\cdot h^{-1}$)	S_v/h^{-1}	$V_{cat.}/m^3$
1	7.0	425	<2	3.57	9.97	61.56	8,000	76.95
2	7.0	425	<2	3.66	10.69	57.82	6,000	96.37
3	7.0	400	<2	3.62	11.98	52.16	4,000	130.40
4	7.0	400	<2	3.62	12.93	48.51	3,000	161.72
5	7.5	400	<2	3.60	11.20	55.41	6,000	92.35

According to the estimation from some relative experts, it is economic when the net value of ammonia is more than 8.4% in low-pressure ammonia synthesis. When the A301 catalyst is in the conditions of 7.0 MPa and space velocity of 4000–8000 h^{-1}, and the net value of ammonia is 10%–12%, it can meet the needs of economy to net value. Table 9.5 shows the amount of inlet syngas (S_{in}) and catalyst volume (V_{cat}) needed at isotonic pressure ammonia plant with capacity of 1000 t/d at 7.0–7.5 MPa.

In the isotonic-pressure process, the outlet concentration and the net value on A301 decline because the equilibrium ammonia concentration decreases at low pressure. In order to achieve the purpose of 1,000 $t\cdot d^{-1}$, it is necessary to increase the amount of inlet gas of converter, i.e. to increase the catalyst volume or/and space velocity. It is known from Table 9.5 that the syngas flow into the converter is dependent upon the demand on net value. The amount of inlet gas of converter will decrease with the increase of the net value. Therefore, increasing the net value of ammonia can decrease the amount of recycling syngas, and then reduce the power consumed in the circulating compression and in the frozen-separation. However, the net value of ammonia is related to the space velocity and increases with declining of the space velocity.

The catalyst volume increases though the amount of circulating gas reduces. For example, at 7.0 MPa, space velocity decreases from 6000 h^{-1} to 4000 h^{-1}, the net

value of ammonia increases by about 1.3%, the amount of circulating gas reduces from $57.8 \times 10^4\,m^3 \cdot h^{-1}$ to $52.2 \times 10^4\,m^3 \cdot h^{-1}$, and the catalyst volume increases to $130.4\,m^3$. The increase in the catalyst volume leads to an increase of investment in converter and the catalyst cost. Thus, it is necessary to evaluate its technology and economy between the net value of ammonia and space velocity, and between the amount of circulating gas and the catalyst volume, in order to determine the optimum value. It is known from Table 9.5, if A301 catalyst is used for isotonic pressure process, the appropriate operating conditions is that space velocity is $6{,}000\,h^{-1}$–$8{,}000\,h^{-1}$, catalyst volume is $80\,m^3$–$100\,m^3$. As a result, for isotonic-pressure process, the following processes and the technical parameters should be used.[22]

The gasification process of pulverized coal or coal–water slurry or residual oil should be at 8.5 MPa–9.0 MPa to ensure that the gas pressure into the synthesis loop is 7.0 MPa–7.5 MPa.

Cooling purification process, i.e. the purification process of washing by methanol and liquid nitrogen at low temperature ensures that the content of inert gas ($CH_4 + Ar + He$) in the recycling gas is less than 2%.

The condensing separation process, i.e., if the concentration of inlet ammonia of converter is less than 4% at 7.0 MPa, the condensing temperature should be lower than −20°C, which is approximately the same with the existing technologies such as the Kellogg, and compared with which the refrigerating power consumption would not increase; However, compared with Topsøe process (the condensing temperature is 0°C–10°C), the refrigerating power consumption will increase.

It is appropriate for converter to adopt small catalyst particles (1.5 mm–3.0 mm) and the radial-flow reactor with multi-bed indirect heat exchange, and to reduce the pressure drop as far as possible.

The highest reaction temperature should be below 450°C because at 7.0 MPa, 450°C, $H_2/N_2 = 3$, $CH_4 + Ar + He = 0\%$, the equilibrium ammonia concentration is 12.28%. Thus, the converter can be a hot-wall reactor and does not require special inner accessory.

H_2/N_2 is 2.4–2.6 in circulating gas and the optimization of H_2/N_2 should be 2.0–2.2.

The process mentioned is about the cooling purification process. For most of modern ammonia plants, it is more popular to use the thermal purification method. In the thermal purification process, the final purification is methanation, and the content of inert gas (CH_4+Ar) is usually higher. The increase of the inert gas content will reduce the concentration and the net value of the outlet ammonia. The research results[23] show that, while the inert gas content increases by 1%, the net value will reduce by about 0.3%–0.4%. In the condition No. 2 of Table 9.5, if the inert gas content increases to 6%, the net value will decrease from 10.69% to 9.49%. Then the amount of inlet gas of converter and the catalyst volume are $64.45 \times 10^4\,m^3 \cdot h^{-1}$ and $107.4\,m^3$, respectively. If the inlet concentration of ammonia of the converter is reduced to 2% (condensing temperature is about −30°C), the net value of ammonia will reach 11.15%, and the amount of inlet gas of converter and the catalyst volume are $54.85 \times 10^4\,m^3 \cdot h^{-1}$ and $91.4\,m^3$, respectively. It will be seen from this that, for the thermal purification process, it is necessary to limit the inert gas content below 6%–8% and to decrease the condensing temperature of ammonia to about −30°C.

Table 9.6 Activity of A301 catalyst in the bypass industrial device at 8.5 MPa and 10.0 MPa

No	Catalyst bed temperature/°C[a]					S_v/h^{-1}	p/MPa	$\varphi^b_{out}/\%$	$\varphi^b_{,in}/\%$	$\Delta\varphi/\%$
	1	2	3	4	5					
1	450	454	455	457	457	6,013	8.5	14.51	3.67	10.84
2	425	431	433	432	432	6,075	8.5	16.66	3.62	13.04
3	400	404	406	406	406	6,023	8.5	16.45	3.61	12.84
4	375	381	382	380	380	5,995	8.5	14.64	3.58	11.06
5	350	354	353	352	351	5,976	8.5	11.95	3.60	8.35
6	450	456	461	462	460	8,041	10.0	15.86	3.65	12.21
7	425	431	435	435	433	8,051	10.0	17.20	3.63	13.57
8	400	406	409	407	405	8,010	10.0	16.81	3.61	13.20
9	375	379	381	379	376	8,014	10.0	14.70	3.62	11.08

Note: The conditions are the same as Table 9.4.

Table 9.7 Volume of A301 catalyst at 8.5 MPa and 10.0 MPa for 1000 t/d

No	p/MPa	T/°C	Inert gas/%	$\varphi_{,in}/\%$	$\Delta\varphi^a/\%$	$S_{in}/(\times10^{-4}\,m^3{\cdot}h^{-1})$	S_v/h^{-1}	V_{cat}/m^3
1	8.5	425	<2	3.62	13.04	48.36	6000	80.60
2	8.5	425	<2	6.64	11.60	53.70	8000	67.13
3	10.0	425	<2	3.61	15.19	42.28	6000	70.46
4	10.0	425	<2	3.63	13.57	46.69	8000	58.36
5	10.0	425	<2	3.61	12.23	51.20	10000	51.20

(2) The micro-pressurized process at 9–10 MPa. In the dreg oil gasification process, syngas compressor is divided into two sections — the first (divided into two-stage) is the compression section in which the syngas pressure is increased from 7.25 MPa to 22.74 MPa, and the power is 9,454 kW; the second is the circulating section, the pressure rises from 21.3 MPa to 22.74 MPa, the power is 4,809 kW when gas flow is $5.2 \times 10^5\,m^3 \cdot h^{-1}$.

In the micro-pressurized process at 9–10 MPa, the first section can be omitted. The syngas pressure would be increased to 8.5–10 MPa only through the circulating section. It functions as both compressor and circulator. This is the so-called micro-pressurized process. Table 9.6 shows the outlet concentration and the net value of ammonia for A301 at 8.5 MPa and 10.0 MPa.

Table 9.6 shows that in the micro-pressurized process, the outlet concentration and net value of ammonia is 16.66% (425°C) and 13% at 8.5 MPa and $6000\,h^{-1/}$. It is 17.20% (425°C) and 13.57% at 10 MPa and $8{,}000\,h^{-1}$, respectively. Table 9.7 shows the amount of inlet syngas (S_{in}) and catalyst volume (V_{cat}) needed at micro-pressurized ammonia synthesis plant with capacity of $1000\,t \cdot d^{-1}$ at 8.5–10 MPa.

It is obvious that if A301 catalyst is used, it only needs to increase catalyst volume of converter or to decrease condensing temperature properly to reform synthetic technology of the gasification of dreg oil or pulverized coal at 8.5 MPa–9.0 MPa to the micro-pressurized process at 8.5 MPa or 10 MPa. For the thermal purification process, the inert gas content and condensing temperature should be adjusted appropriately.

Table 9.8 Comparison of power consumption between high-pressure and low-pressure process

Item	High(middle)-pressure process	Low(isotonic)-pressure process	Comparison
Capacity/kt/a	300	300	
Gasification pressure/MPa	8.53	8.53	
Synthesis pressure/MPa	22.0[a]	7.5[b]	
Power decrement of the synthesis loop/kW	6,702.99	2,393.5	Reduced 4,309.49 kW
Include: Syngas compressor/kW	5,819.09	0	Without syngas compressor at isotonic pressure process
Circulating compressor/kW	607.84	889.58	
Refrigerating compressor/kW	276.05	1504.0	
Capacity/kt/a	100	100	
Gasification pressure/MPa	0.1	0.1	
Synthesis pressure/MPa	30[c]	10[d]	
Total power consumption/kW	10,871.96	9,383.44	Reduced 1488.5 kW
Include: Syngas compressor/kW	10,374.13	8,344.6	
Circulating compressor/kW	362.78	697.36	
Refrigerating compressor/kW	135.05	341.4	

[a]The radial-flow converter with two beds of indirect heat exchange; [b]The radial-flow converter with three beds of indirect heat exchange, [c]The axial-flow converter with one bed continuously heat exchange by cool piping; [d]The axial and radial-flow converter with three beds and direct heat exchange between bed by cold gas.

Table 9.8 reveals the comparison of power consumption calculated by simulation between high (middle)-pressure and low (isotonic)-pressure. It can be known from Table 9.8 that, for a plant with capacity of $1{,}000\,t \cdot d^{-1}$, the synthesis pressure decreases from 22 MPa to 7.5 MPa, the power of the synthesis loop decreases by 4,309.49 kW, and energy consumption can be saved by $1.30\,GJ \cdot t^{-1}$; for the small and medium plant with capacity of $300\,t \cdot d^{-1}$, the synthesis pressure decreases from 30 MPa to 10 MPa, the power of the synthesis loop decreases by 1,488.5 kW, and energy consumption can be saved by $1.36\,GJ \cdot t^{-1}$.

For the purpose of saving energy and reducing consumption, adopting the low (isotonic)-pressure process is not enough to consider decreasing pressure and thereby saving power consumption. It is mentioned earlier that when the ratio of H_2/N_2 decreases from 3.0 to 1.8–2.2 at low temperature and low pressure, the outlet concentration of ammonia (net value of) increases by 0.4%–0.52% which is considerable in the synthetic process with low temperature and low pressure. However, the more important role of lower ratio of H_2/N_2 is to provide a guarantee for saving energy and reducing consumption in the steam reforming section. Because the production of synthesis ammonia is an integrity system, each unit process is interdependent and interacts independently. Any change of a unit process will affect the other parts. When lower ratio of H_2/N_2 is used in synthesis loop, two concerns are inevitable: First, the former section has to be injected with more N_2 (air); second, the latter section has to remove redundant N_2 and recover H_2. The former is required for the steam reforming section to save energy and reduce consumption because the steam

reforming section is the largest section of energy consumption in the whole plant. All raw materials and fuel are charged into the steam reforming system, where the loss of effective energy accounts for 60% in the whole plant.[21] There is much effort to realize energy-saving in this section. This is just one of the main measures where the energy consumption of per ton can be decreased to 28 GJ in the Uhde-ICI-AMV synthesis process at low pressure. Therefore, reducing the ratio of H_2/N_2 is preferred not only in order to increase net value of ammonia in the synthesis loop, even more so in order to supply more air for the steam reforming section to save energy and reduce consumption.

With industrial applications of the high activity catalyst ($Fe_{1-x}O$ catalyst and Ru catalyst), synthesis ammonia at isotonic pressure, which people have expected for long time, can be expected soon.

9.1.4.3 *The low-pressure renovation for the small-medium ammonia plant*

There are hundreds of the small-medium ammonia devices with capacity of 100–600 $t \cdot d^{-1}$ in China whose operation pressures exceed 30 MPa. Liu huazhang *et al.* put forward the low-pressure renovation, and reduced the pressure of synthesis loop from 30 MPa to 15 MPa in order to reduce the energy consumption.[24,25] For the newly built ammonia plant, it is suggested that the designed pressure should be reduced to 10–15 MPa; in the present plan where the operating pressure is 30 MPa, the pressure of synthesis loop should be reduced to 10–15 MPa. When the pressure is 10 MPa, adopting the appropriate technology (such as increasing the catalyst volume) can basically keep the previous net value of ammonia and circulating gas quantity, and the energy consumption of ammonia compressor and circulating compressor can be basically unchanged, but the power of the fresh syngas compressor can be reduced to a great degree, thereby achieving reduction in the energy consumption and operation cost. The simulation calculation of synthesis loop and the result of technological economy evaluation are showed in Tables 9.9 and 9.10.

Table 9.9 shows that the power of the fresh syngas compressor declines by 2,440 kW when the synthetic loop pressure is decreased from 30 MPa to 15 MPa. Although the power of ammonia compressor and circulating compressor increase slightly, the total power consumption is decreased by 2,258 kW, thereby saving the energy consumption by 2.06 $GJ \cdot t^{-1}$ only. Table 9.10 shows that at the pressure

Table 9.9 Calculation result of energy consumption of synthesis loop using ZA-5 catalyst (330 $t \cdot d^{-1}$)

Synthesis loop pressure	10 MPa	30 MPa
Power of the fresh syngas compressor/kW	7,970	10,410
Power of the circulating compressor/kW	295	240
Power of the refrigeration compressor/kW	311	184
By-product steam (1.3 MPa)/($t \cdot h^{-1}$)	9.09	9.66
Desalination water used in waste heat boiler/($t \cdot h^{-1}$)	9.09	9.66
Amount of vent gas/($m^3 \cdot h^{-1}$)	1,853	1,405
Catalyst volume/m^3	19.94	5.78

Table 9.10 Estimation of energy consumption of synthesis loop using ZA-5 catalyst (330 t/d)/(MJ/h)

Operating pressure/ MPa	Recovery energy from the waste heat boiler	Desalination water	Energy consumption of the circulating, refrigerating, and fresh gas compressor	Vent gas	Total energy consumption	Energy consumption/ ton ammonia
10	−34,299.8	129.3	101,534.1	−18,558.4	48,805.2	3,790.3
30	−36,376.2	137.6	128,273.7	−14,072.0	77,963.1	5,985.7

Note: The more the vent gas, the more cost of synthesis ammonia is; but vent gas is recovered for hydrogen or returns directly to the boiler as fuel, just in the view point of energy consumption, the energy of the vent gas is recovered, so it is negative.

of 10 MPa, the energy consumption of synthetic loop can be saved 29,158 MJ/h or 2.20 GJ · t^{-1} in comparing with 30 MPa.

9.2 Ammonia Converter and Catalysts

Ammonia converter is the key equipment of the ammonia plant. In the process, the synthesis reaction must be carried out, as much as possible, close to the optimum reaction temperature of catalyst to achieve bigger productivity and higher synthesis rate. It should also strive to reduce the pressure drop of the converter, so as to reduce the power consumption of the recycle gas. In the structure, it should strive to be simple and reliable to meet the demand of high-temperature and high-pressure. These are the basic principles for designing ammonia converter and one of the symbols for evaluating reactor quality.

In view of that, the optimum reaction temperature of ammonia synthesis decreases with the increase of the concentration of ammonia, which requires the temperature to be decreased continuously with the ongoing reaction. However, this conflicts with the heat release of the reaction. In order to solve this problem, it is necessary to measure cooling along with the reaction. According to the cooling methods in the industry, converters can be divided into cold-tube type, middle direct cold-quench type and middle indirect heat exchange type. Figures 9.15–9.17 represent the schematic diagrams of the cooling methods, respectively.

(1) Cold-tube type converter uses a cooling pipe built-in catalyst bed to eliminate the reaction heat and decline the reaction temperature. The cooling gas flows in inner side of the cooling pipe, preheats the gas before reaction and cools the catalyst in the outside of the pipe. Cold-tube type converter was developed much earlier. Because its pressure drop of catalyst bed is larger, now it is only used for small-medium converter. Figure 9.18 is the structure sketch diagram of single pipe baffling converter with an adiabatic layer in bottom of the bed, developed by Zhejiang University of Technology.[4]
(2) Cold-quench type converter uses the cold-state syngas before reaction to undergo quench-cool between beds so as to decrease the temperature of reaction gas. The merit of cold-quench type converter is its simple and reliable structure. But it is more difficult to get high net value because of the dilution

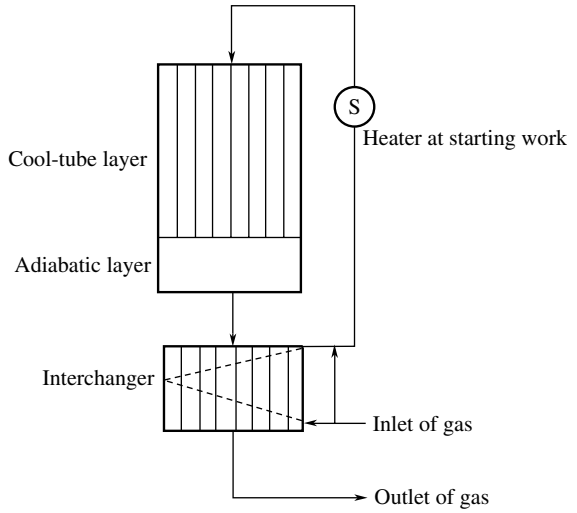


Fig. 9.15 Schematic diagram of the cold-tube type of converter with continuous heat exchange

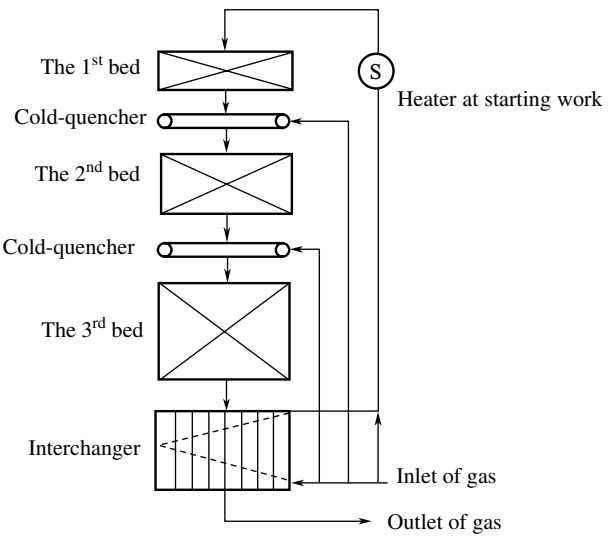


Fig. 9.16 Schematic diagram of the direct heat exchange type of converter

of ammonia content in the reaction gas by cold-quench gas, in which the uniform mixture of the cold-quench gas and syngas is the key of design structure. Figure 9.19 shows the structure sketch diagram of cold-quench type of horizontal converter.[4]

(3) The indirect heat exchange type of converter sets an intermediate interchanger between the adiabatic catalyst beds to preheat the unreacted syngas and decrease the reaction temperature of the beds. The indirect heat exchange

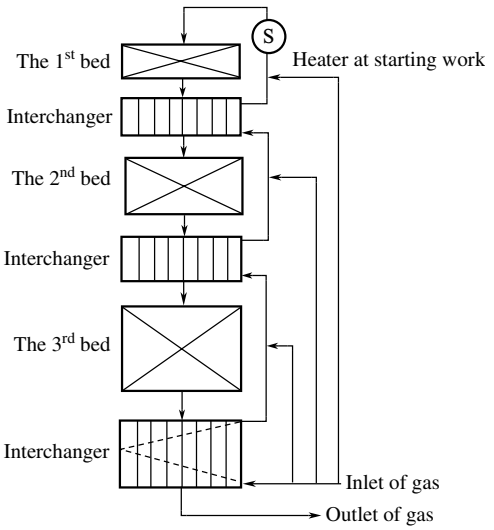


Fig. 9.17 Schematic diagram of the indirect heat exchange type of converter

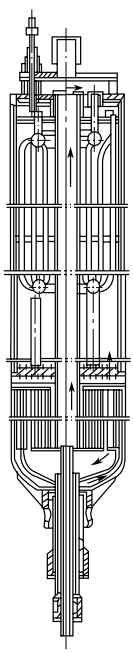


Fig. 9.18 Inner structure of single pipe-retracing converter

type-converter is used widely. Although its structure is a little complex, it has recently become trend, so it begins to be used in the small-medium converter. Figure 9.20 is the structure sketch diagram of the Topsøe S-200 converter.[4] Figure 9.21 is S-200 converter after renovation.

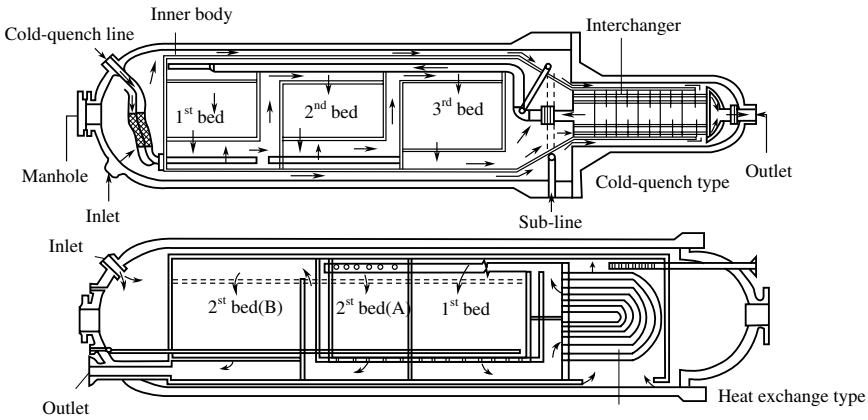


Fig. 9.19 Horizontal type of converter

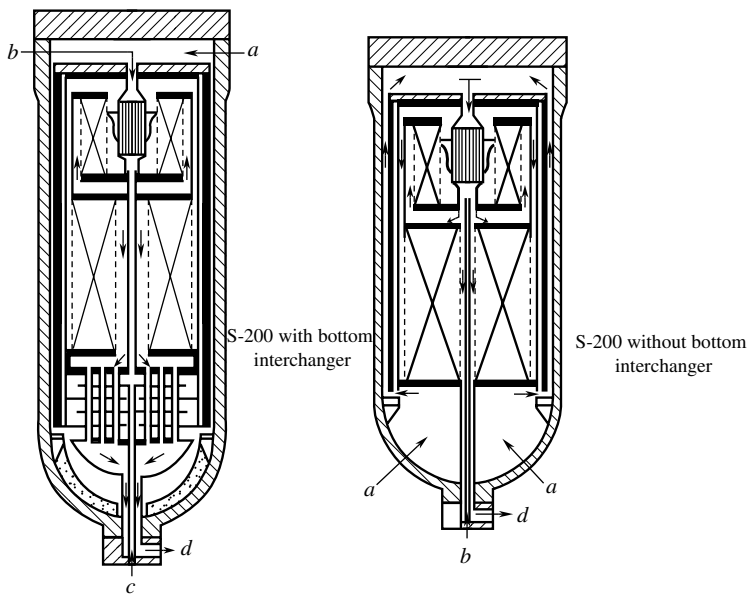


Fig. 9.20 Diagram of the Topsøe S-200 converter

a-Inlet of main gas; b-Inlet of cold gas; c-Cold sub-line; d-Outlet of gas.

In the converter, only one of the three cooling methods mentioned above can be used, also two of them can be combined for application. For example, the cold-quench type is used between the first and the second bed, and the indirect heat exchange type is used between the second and the third bed. Some interchangers between beds are placed outside the converter such as Brown converter (Fig. 9.22).[4]

It is worth noting that because the ammonia synthesis reaction on the Fe catalyst needs high temperature (400–550°C) and high pressure (over 10 MPa), the

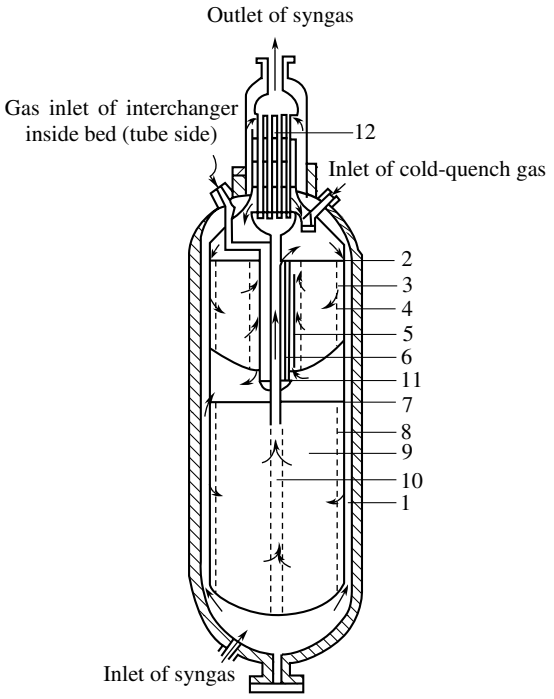


Fig. 9.21 S-200 converter after renovation

1-Inlet annular gap; 2-Top cap of the first bed; 3-Gas distributor of the first bed inlet; 4-the first bed catalyst; 5-Outlet annular gap of the first bed; 6-Interchanger in bed; 7-Top cap of the second bed; 8-Gas distributor of the second bed; 9-The second bed catalyst; 10-Outlet pipe of the second bed; 11-Outlet pipe; 12-Top interchanger.

existing reactor is designed using the principle of high pressure but not high temperature (the outside cylinder) and high temperature but not high pressure (the inside cylinder). The converter is a double-cylinder reactor with outside and inside cylinders. However, for Ru catalyst, the temperature and pressure of the reaction are decreased to 350–450°C and below 10 MPa respectively. The super large KAAP converter with capacity of $1850\,t \cdot d^{-1}$ designed by Kellogg company is a single-cylinder reactor and uses a hot-wall shell, the first cancel inside cylinder following for nearly one century. This can be called a revolutionary improvement.

9.3 Performance of Catalyst and Recovery of Reaction Heat

9.3.1 *The theoretic energy consumption of synthesis ammonia*[4]

Synthesis ammonia is a major energy-consumer. It is estimated that 3% of energy in the world is consumed in synthesis ammonia industry, and the proportion in China accounts for 5%.[26] Energy comprises the raw materials, fuel and power of

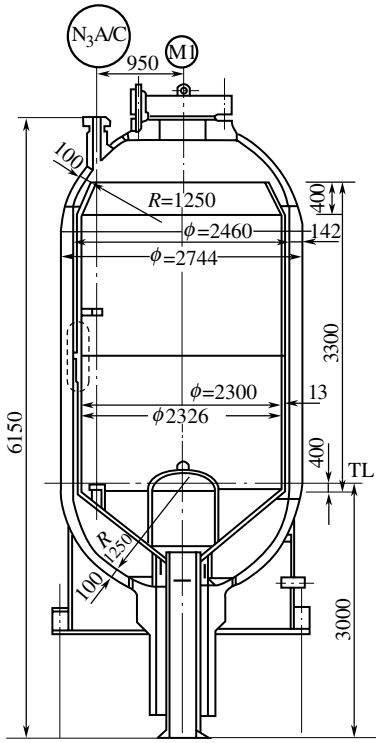


Fig. 9.22 Brown adiabatic converter

(The first converter)

synthesis ammonia. Therefore, energy consumption is the most important symbol of estimating technical level and economic benefit of synthesis ammonia industry.

In the actual production process, the theoretic energy consumption is impossible to achieve, but can be used as the comparison standard and struggling goal for the minimum energy consumption which is the value of the energy consumption when the process is reversible. Because only the exergy in the energy is the valuable resource, exergy is theoretically to obtain it without paying and to discard it without reducing the cost. Therefore the so-called energy consumption should be measured by exergy consumption and not by the heat value or the enthalpy value. This is essentially consistent with the energy consumption said in the industry; for example, the actual energy consumption of per ton product discussed later is calculated by converting the consumed energy by varieties of energy and work mediums into standard coal and standard heat value; the exergy value in fuel is desirable as the low calorific power.

Theoretic energy consumption can be divided into theoretic energy consumption of process and product. The theoretic energy consumption of process refers to the energy consumption by unit product made by raw materials (may or may not be the primary standard substance in environment), i.e. the ideal power of process. The product energy consumption refers to the energy consumption by unit product made from raw materials in environment state. The difference between them is

the primary standard and the state of the raw materials. When the raw materials are not in environment state, it is calculated in its exergy value as energy carrier. Usually, for calculating the theoretic energy consumption of both the process and the product, the temperature and pressure of raw materials and product must be pointed out, which generally refers to the ambient temperature and pressure T_0, p_0 (Table 9.11). For example, synthesis ammonia is produced by carbon, air and water as raw materials, $T_0 = 298.15\,\mathrm{K}$, $p_0 = 0.1013\,\mathrm{MPa}$ of the raw materials. The product is liquid ammonia in the saturation state at 298.15 K.

The theoretic energy consumption of the process and the product is now explained.

The total reaction equation of the production process of ammonia is:

$$0.885\mathrm{C} + 1.5\mathrm{H_2O} + 0.641(0.78\mathrm{N_2} + 0.21\mathrm{O_2} + 0.01\mathrm{Ar}) \rightarrow \mathrm{NH_3} + 0.885\mathrm{CO_2} + 0.0064\mathrm{Ar} \tag{9.1}$$

Using the data in Table 9.11, we calculate the enthalpy change (ΔH) and ideal power (IW) in the process:

$$\begin{aligned}\Delta H &= \mathrm{h}\nu^{\ominus}_{\mathrm{NH3}} - 0.885\,\mathrm{h}\nu^{\ominus}_{\mathrm{C}} = 3{,}62{,}154 - 3{,}48{,}486 = 13{,}668\,\mathrm{kJ/kmolNH_3} \\ &= 0.80\,\mathrm{GJ/tNH_3} \\ IW &= 0.885\mathrm{ex}^{\ominus}_{\mathrm{ch,c}} - \mathrm{ex}^{\ominus}_{\mathrm{ch,NH3}} - 0.0064\mathrm{ex}^{\ominus}_{\mathrm{ch,Ar}} = 3{,}45{,}817 - 3{,}42{,}434 - 73 \\ &= 3310\,\mathrm{kJ/kmol\text{-}NH_3} = 0.194\,\mathrm{GJ/tNH_3}.\end{aligned}$$

This calculation illuminates that because the exergy value supplied by raw materials is higher than that of product, where the ideal power of this process is positive. Producing one ton saturated liquid ammonia at 25°C, theoretically, does not consume power, but also delivers 0.194 GJ power.

Since product energy consumption is energy consumption of unit product made by the raw materials in environment state, the value is:

$$\begin{aligned}\mathrm{ex}^{\ominus}_{\mathrm{ch,NH3}} &= 0.885\,\mathrm{ex}^{\ominus}_{\mathrm{ch,c}} - IW - 0.0064\,\mathrm{ex}^{\ominus}_{\mathrm{ch,Ar}} = 342434\,\mathrm{kJ/kmolNH_3} \\ &= 20.11\,\mathrm{GJ/tNH_3}\end{aligned}$$

It is consistent with the calculation result by the datum $\mathrm{ex}^{\ominus}_{\mathrm{ch,Ar}}$ directly from Table 9.11.

It is observed that the theoretical energy consumption of the unit product is just the exergy value of it, which is independent of raw materials and methods used. However, the theoretical energy consumption of the process is related to the raw materials, and when raw materials used is different, the value may be quite different.

Table 9.12 lists the enthalpy change (the change of heat value in broad sense), the energy consumption of process and the energy consumption of product in producing ammonia by different raw materials. The data in Table 9.12 shows that the producing process of ammonia with other kinds of raw materials can theoretically be the process of making external power, except that the process of producing by water and air must consume power.

Table 9.11 Standard molar heat and standard molar exergy of some substances

State parameters and elements	Environment states	State parameters and elements	Environment states
Temperature	25°C	H	H_2O (l), pure
Pressure	0.1013 MPa	N	Air, $y_{N2} = 0.78$
Ar	Air, $y_{Ar} = 0.01$	O	Air, $y_{O2} = 0.21$
C	CO_2, (g), y = 1		

Name	Δh_f^{Θ}	Δg_f^{Θ}	s^{Θ}	$h\nu^{\Theta}$	$ex^{\Theta a,b}$
Ar	0	0	154.84	0	11,422
C(lead)	0	0	5.74	3,93,769	3,90,754
H_2	0	0	130.67	2,86,042	2,35,432
N_2	0	0	191.63	0	615
O_2	0	0	205.17	0	3,873
CH_4	−74,898	−50,828	186.35	8,90,955	8,10,795
C_2H_2	2,26,900	2,09,340	75.45	13,00,479	12,26,284
C_2H_4	52,318	68,169	219.68	14,11,940	13,20,546
C_2H_6	−84,724	−32,908	229.69	15,58,679	14,54,905
C_3H_6	20,427	62,651	267.62	20,59,860	19,41,218
C_3H_8	−103,916	−23,505	270.22	22,21,558	20,90,494
1–C_4H_8(g)	1,172	72,084	367.81	27,20,415	25,76,841
n–C_4H_{10}(g)	−1,24,817	−15,717	310.41	28,80,468	27,24,472
n–C_5H_{12}(g)	−1,46,538	−8,206	348.76	35,38,558	33,58,174
n–C_5H_{12}(l)	−1,73,166	−9,253	285.96	35,11,930	33,57,127
C_6H_6(l)	49,061	1,24,582	173.17	32,69,799	31,75,420
C_6H_{12}(l)	−1,56,335	26,754	204.40	39,22,529	37,83,887
C_7H_8(l)	11,250	1,14,224	217.50	39,11,798	37,91,248
CH_3OH(l)	−2,38,815	−1,66,635	127.57	7,27,038	6,96,922
C_2H_5OH(l)	−2,77,794	−1,74,841	160.77	13,67,869	13,14,906
C_6H_5OH(g)	−90,895	−26,209	312.08	31,29,842	30,26,582
C_6H_5OH(l)	−1,58,261	−46,139	152.99	30,62,477	30,06,633
HCOOH(l)	−4,09,469	−3,46,248	129.54	2,70,342	2,83,811
CH_3COOH(l)	−4,86,506	−3,91,717	160.06	8,73,115	8,64,532
CH_3CHO(g)	−1,66,300	−1,31,717	259.41	11,93,322	11,22,598
CO	−1,10,615	−1,37,252	197.68	2,83,153	2,55,437
CO_2	−3,93,768	−3,94,627	213.80	0	0
H_2O(g)	−2,42,625	−2,29,386	188.85	43,417	9,984
H_2O(l)	v2,86,042	−2,37,366	70.00	0	0
NH_3(g)	−45,971	−16,454	192.80	3,83,092	3,37,004
NH_3(l) at saturated pressure	−66,939	−11,024	104.28	3,62,145	3,42,434
$(NH_2)_2CO$ (urea)	−3,33,412	−1,97,274	104.71	6,32,441	6,66,899

[a] Δh_f: standard enthalphy of formation, kJ/kmol; Δg_f: standard free enthalphy of formation, kJ/kmol; s: absolute entropy, kJ/(kmol·K); hν: standard heat value, kJ/kmol; ex: standard exergy, kJ/kmol.

[b] Superscript Θ express that the compose condition is non-environment condition.

9.3.2 *The actual energy consumption of the ammonia production*

Regardless of what kinds of materials and methods are used, the production process of ammonia is irreversible. Therefore, the actual product energy consumption is

Table 9.12 Theoretical energy consumption of synthesis ammonia/(GJ/t)

Raw materials	Total reaction equation of producing ammonia process	$\Delta H = \Delta Hv$ (g)	$\Delta H = \Delta Hv$ (l)	Theoretical energy consumption of process[a] (g)	Theoretical energy consumption of process[a] (l)	Theoretical energy consumption of product (g)	Theoretical energy consumption of product (l)
H_2O, air	$1.5H_2O + 0.641(0.78N_2 + 0.21O_2 + 0.01Ar) \rightarrow NH_3 + 0.885O_2 + 0.0064Ar$	22.50	21.26	19.99	20.31	19.79	20.11
Coal, air, H_2O	$0.885C + 1.5H_2O + 0.641(0.78N_2 + 0.21O_2 + 0.01Ar) \rightarrow NH_3 + 0.885CO_2 + 0.0064Ar$	2.03	0.80	−0.51	−0.19	19.79	20.11
CH_4, H_2O, air	$0.442CH_4 + 0.615H_2O + 0.641(0.78N_2 + 0.21O_2 + 0.0064Ar) \rightarrow NH_3 + 0.442CO_2 + 0.0064Ar$	−0.63	−1.85	−1.26	−0.94	19.79	20.11
Light oil, H_2O, air	$0.063C_9H_2O + 0.868H_2O + 0.641(0.78N_2 + 0.21O_2 + 0.01Ar) \rightarrow NH_3 + 0.569CO_2 + 0.0064Ar$	−0.18	−1.41	−1.97	−1.65	19.79	20.11
Coal, H_2O, O_2, N_2	$1.5C + 0.75O_2 + 1.5H_2O + 0.5N_2 \rightarrow NH_3 + 1.5CO_2$	−12.19	−13.42	−14.82	−14.50	19.79	20.11
Heavy oil, H_2O, O_2, N_2	$0.811CH_{1.7} + 0.405O_2 + 0.811H_2O + 0.5N_2 \rightarrow NH_3 + 0.811CO_2$	−7.84	−9.07	−8.46	−8.12	19.79	20.11
CH_4, H_2O, O_2, N_2	$0.5CH_4 + 0.25O_2 + 0.5H_2O + 0.5N_2 \rightarrow NH_3 + 0.5CO_2$	−3.66	−4.89	−4.09	−3.77	19.79	20.11
H_2, N_2	$1.5H_2 + 0.5N_2 \rightarrow NH_3$	−2.70	−3.95	−0.95	−0.63	19.79	20.11

[a]The process theoretic energy consumption: "−" expresses making external power, "+" expresses consumed external power, contrary to symbol stipulation of ideal power.

Note: Raw materials at 25°C and 0.1013 MPa; product is the gas state ammonia (g), at 25°C and 0.1013 MPa, product is liquid ammonia (l) at 25°C in saturation state.

Table 9.13 Designed energy consumption of ammonia produced by various raw materials (in liquid ammonia per tons)

Raw material	Production method	Capacity/ $(t \cdot d^{-1})$	Energy consumption/ GJ	Ratio of designed to theoretic
Coal	Pressurized continuous gasification (Lurgi)	1,000	50.37	2.50
	Pressurized continuous gasification (Texco)	1,000	44.12	2.19
	Atmospheric pressure intermittent gasification (UGI) (the production value)	150	53.31	2.65
Natural gas	Steam reformation at 3.6 MPa	1,000	28.4	1.41
	Steam reformation at 3.01 MPa (the production value)	1,000	35.42	1.76
Light oil	Steam reformation at 3.30 MPa	900	41.8	2.08
Residual oil	Pressurized gasification at 8.53 MPa (Texco)	1,000	38.52	1.92

higher than the theoretical energy consumption of product, and the actual process energy consumption is also higher than the theoretical energy consumption of process. The process does not work outside, but consumes the external power (supplied by the exergy of consuming fuel or electric energy).

The so-called "actual energy consumption" refers to the calculation that results from the real energy consumption in the period of planning statistics in industry production, after deducting the energy supplied outside, is divided by the output in the same period. The actual energy consumption is different from the theoretical energy consumption, which is different with the kinds of raw materials, the production methods and the technical level of the process flow and equipments, the design of energy supplied and recovered, and the production scale as well as the management level. Table 9.13 shows the designed energy consumption of ammonia production by different raw materials. It is also the actual energy consumption, and its value is not affected by the external conditions such as the quality change of raw material, supply of water, electricity and steam, and management level.

Table 9.13 shows that the lowest designed energy consumption is the nature gas steam reformation process with a capacity of $1{,}000\,t \cdot d^{-1}$, where the energy consumption is $28.4\,GJ \cdot t^{-1}$, which is about 1.41 times of the theoretical energy consumption at 3.6 MPa, and $35.42\,GJ \cdot t^{-1}$ and about 1.76 times at 3.01 MPa, respectively. The energy consumption of other methods is higher than the theoretical energy consumption by about one time or more. This shows that the potential of energy-saving is still huge.

Average inferior calorific value of various energies and energy equivalent value of energy-consumed medium according to China's GB/T 2589–2008 are shown in the Table 9.14 (1 & 2). The equivalent heat value refers to the energy of the primary energy converted from the energy of the secondary energy and the energy-consumed medium.

Table 9.14 (1) Average coefficient of various energies folded as standard coal

Energy	Average inferior calorific value[a]	Coefficient folded as standard coal[a]
Raw coal	20,908 kJ/kg (5,000 kcal/kg)	0.7143 kgce/kg
Washing fine coal	26,344 kJ/kg (6,300 kcal/kg)	0.7143 kgce/kg
Other washing coal		
Washing middling coal	8,363 kJ/kg (2,000 kcal/kg)	0.7143 kgce/kg
Coal slime	8,363 kJ/kg–1,2545 kJ/kg (2,000 kcal/kg–3,000 kcal/kg)	0.2857 kgce/kg ~ 0.4286 kgce/kg
Coke	28,435 kJ/kg (6,800 kcal/kg)	0.9714 kgce/kg
Crude oil	41,816 kJ/kg (10,000 kcal/kg)	1.4286 kgce/kg
Fuel oil	41,816 kJ/kg (10,000 kcal/kg)	1.4286 kgce/kg
Gasoline	43,070 kJ/kg (10,300 kcal/kg)	1.4714 kgce/kg
Kerosene	43,070 kJ/kg (10,300 kcal/kg)	1.4714 kgce/kg
Diesel oil	42,652 kJ/kg (10,200 kcal/kg)	1.4571 kgce/kg
Coal tar	33,453 kJ/kg (8,000 kcal/kg)	1.1429 kgce/kg
Residual oil	41,816 kJ/kg (10,000 kcal/kg)	1.4286 kgce/kg
Liquefied petroleum gas	50,179 kJ/kg (12,000 kcal/kg)	1.7143 kgce/kg
Refinery dry gas	46,055 kJ/kg (11,000 kcal/kg)	1.5714 kgce/kg
Oil field nature gas	38,931 kJ/m^3 (93,100 kcal/m^3)	1.3300 kgce/m^3
Gas field nature gas	35,544 kJ/m^3 (8,500 kcal/m^3)	1.2143 kgce/m^3
Coal mines gas	14636 kJ/m^3–16726 kJ/m^3 (3,500 kcal/m^3–4,000 kcal/m^3)	0.5000 kgce/m^3 ~ 0.5714 kgce/m^3
Coke oven gas	16,726 kJ/m^3–1,7981 kJ/m^3 (4,000 kcal/m^3–4,300 kcal/m^3)	0.5714 kgce/m^3 ~ 0.6143 kgce/m^3
Blast furnace gas	3,763 kJ/m^3	0.1286 kgce/m^3
Other coal gas		
(a) Producer gas	5,227 kJ/kg (8,000 kcal/m^3)	0.1786 kgce/m^3
(b) Heavy oil catalytic cracking gas	19,235 kJ/kg (8,000 kcal/m^3)	0.6571 kgce/m^3
(c) Heavy oil thermal cracking gas	35,544 kJ/kg (8,000 kcal/m^3)	1.2143 kgce/m^3
(d) Coke production gas	16,308 kJ/kg (8,000 kcal/m^3)	0.5571 kgce/m^3
(e) Pressure-gasification gas	15,054 kJ/kg (8,000 kcal/m^3)	0.5143 kgce/m^3
(f) Water gas	10,454 kJ/kg (8,000 kcal/m^3)	0.3571 kgce/m^3
Crude benzene	41,816 kJ/kg (10,000 kcal/kg)	1.4286 kgce/kg
Heat power (calorific value)	—	0.03412 kgce/MJ
Electric power (calorific value)	3,600 kJ/(kW·h) (860 kcal/(kW·h))	0.1229 kgce/(kW·h)
Electric power (equivalent value)	Calculation by current thermal power generation consumed standard coal	
Steam (low pressure)	3,763 MJ/t (900 kcal/t)	0.1286 kgce/kg
Discharged gas from synthesis loop	10.0 (MJ/m^3)	0.3417 kgce/m^3

(1) The fuel, which inferior calorific value is equal to 29,307 kJ $\cdot$ kg^{-1}, is called standard coal and marked as 1 kgce.

It can be seen from Table 9.13 that the designed energy consumption of synthetic ammonia production is changed with the difference in the raw materials, gasification pressure and plant scale.

The following factors decide the actual energy consumption:

(1) The raw materials and process flow. In every raw material, the average energy consumption of using nature gas is lower than that of using coal and heavy oil.

Table 9.14 (2) Energy equivalent value of energy-consumed medium

Variety	Energy consumption of unit energy-consumed medium	Coefficient folded as standard coal
Fresh water	2.51 MJ/t (600 kcal/t)	0.0857 kgce/t
Soft water	14.23 MJ/t (3,400 kcal/t)	0.4857 kgce/t
Deoxygenated water	28.45 MJ/t (6,800 kcal/t)	0.9714 kgce/t
Compressed air	1.17 MJ/m^3 (280 kcal/m^3)	0.0400 kgce/m^3
Blast air	0.88 MJ/m^3 (210 kcal/m^3)	0.0300 kgce/m^3
Oxygen	11.72 MJ/m^3 (2,800 kcal/m^3)	0.4000 kgce/m^3
Nitrogen (by-product)	11.72 MJ/m^3 (2,800 kcal/m^3)	0.4000 kgce/m^3
Nitrogen (major product)	19.66 MJ/m^3 (4,700 kcal/m^3)	0.6714 kgce/m^3
Carbon dioxide	6.28 MJ/m^3 (1,500 kcal/m^3)	0.2143 kgce/m^3
Acetylene	243.67 MJ/m^3	8.3143 kgce/m^3
Calcium carbide	60.93 MJ/kg	2.0786 kgce/kg

In every process flow, the pressurized gasification is *prior* to the atmosphere gasification, and the pressurized steam shift is *prior* to the atmosphere one. The reason is that the compression work for the feed gas is saved.

(2) Energy system. The design of the energy supply and the recovery system is one of the main factors determining the energy consumption of production ammonia. For example, the modern ammonia plant has a lot of the characteristics favorable to increase the energy efficiency of whole plant.[1]

(3) Production management. Raw materials, process flow and designed energy system are the intrinsic factors affecting energy consumption, however, production management is an external factor.

As regards the energy conversion, the product of ammonia is considered as the result of conversion of different forms of energy at specific conditions. Therefore, the efficiency of energy conversion is the efficiency of the process. The efficiency of energy conversion can be expressed as:

$$\text{The efficiency of energy conversion}(\%) = \frac{\text{The exported or supplied energy}}{\text{The imported or consumed energy}} \times 100\% \tag{9.2}$$

At present, the efficiency of energy conversion of various raw materials for producing synthesis ammonia is only 40%–70%. It means that the potential of energy-saving in synthesis ammonia industry is very huge.

9.3.3 *Catalyst activities and the use of the reaction heat*

The reaction heat of the ammonia formation is large. For example, producing one kmol of ammonia at 450°C will give out 54.5 MJ of reaction heat which is equal to the heat of low-pressure saturated steam of 1.44 t/t. Actually, the reaction heat cannot be recovered fully because of the temperature difference losses among the heat-recovery equipments where only 50%–90% of reaction heat can usually be recovered.

There are two kinds of heat-recovery way according to its usages: Heating feed water of boiler and direct by-product steam. The selection of recovery way mainly depends on the balance of the heat-supply in the whole plant.

The by-product stream can be divided into two types, according to their sites, the built-in form inside the catalyst bed and built-out form outside the catalyst bed. The built-in form is not to be used now because of its complicated structures and the low volumetric coefficient of the converter. The built-out form of by-product steam can be subdivided into three sorts: Front-type, mid-type and back-type according to their sites in which the heat is recovered (shown in Fig. 9.23). In front-type boiler process, the reaction gas from the catalyst bed enters into waste heat boiler to recover the reaction heat, and then enters into the interchanger. It would produce high-pressure steam at 4 MPa–12.5 MPa. The mid-type waste heat boiler is located between the first and the second interchanger, the temperature of reaction gas is lower than that in front-type boiler, and can only produce steam at 0.9–1.6 MPa. The back-type boiler is applicable to outlet gas at low-temperature of the converter.

The recovery process of reaction heat is composed of converter, boiler or heater for feed water of boilers and interchangers (Preheater before converter) (Fig. 9.24).

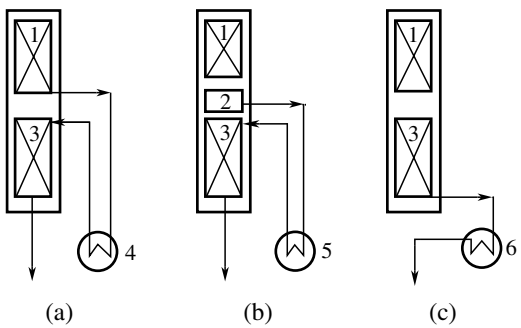


Fig. 9.23 Schematic diagram of various kinds of heat recovering process
1-Catalyst basket; 2-Second interchanger; 3-First interchanger; 4-Postpositive-boiler; 5-Mid-boiler; 6-Prepositive-boiler.

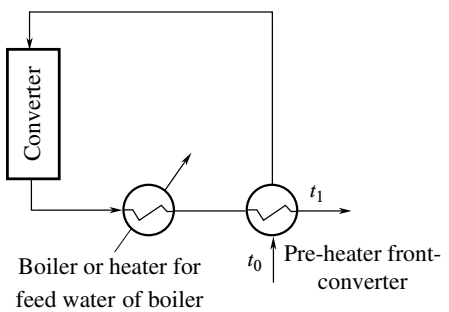


Fig. 9.24 Schematic diagram of recovering the reaction heat

By balance of heat on this system, the recovery ratio (η_h) of the reaction heat can be induced as follows:

$$\eta_h = 1 - \frac{\Delta t_1}{\Delta t_s} \tag{9.3}$$

Where Δt_1 is the sum of temperature difference loss at the cool side of the interchangers and the heat loss of the system (expressed in temperature difference), i.e. $\Delta t_1 = t_1 - t_0$.

Δt_s is the adiabatic temperature rising of ammonia synthesis reaction which is proportional to the net value ($\Delta\varphi_{NH3}$) of ammonia, i.e., $\Delta t_s = (14-15)\Delta\varphi_{NH3}\times 100$, put it in Eq. (9.3):

$$\eta_h = 1 - \frac{\Delta t_1}{(14 \sim 15)\Delta\varphi_{NH3} \times 100} \tag{9.3'}$$

It can be seen from Eq. (9.3′) that the main way of increasing the recovery rate of the reaction heat is to raise the net value of ammonia and decrease the temperature difference loss of the recovery system.

The main measures of raising the net value of ammonia are to adopt high activity catalyst, converter with high net value and operate in low space velocity.

The important measures to reduce the temperature difference loss are to improve the design of the interchanger, increase the heat-transfer coefficient and areas, prevent the leak between shell-side baffles and crust and to strengthen the heat preservation system.

The recovery of reaction heat at synthesis loop includes both the quantity and the quality of the heat. The former is determined by Eq. (9.3), i.e., the net value of ammonia and the temperature difference loss of the recovery system. For example, in Fig. 9.25, inlet temperature of converter is 141°C, the outlet temperature is 284°C, so the adiabatic temperature rise of the converter is 143°C, the temperature difference lost at the cool side of the preheater front-converter is 19°C, and the rest heat can be applied to the feed water of the boiler. The recovery ratio of the reaction heat reaches 86.7%.

The converter technology is up-to-date, and net value of ammonia for the new designed converter increases, usually to 12%–16%, and adiabatic temperature rises of the reaction to 174–232°C. When KAAP technology with Ru catalyst is adopted,

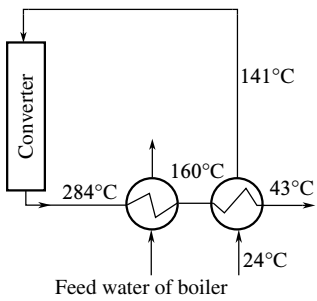


Fig. 9.25 Schematic diagram of the feed water system of boiler heated by the reaction heat

the adiabatic temperature rise of the converter would be as high as 286°C, and the recovery ratio of the reaction heat would be 93.0%.

The recoverable reaction heat from the synthesis loop was basically a constant in certain productivity. Because the circulating gas volume directly is with change of the loop pressure and the single-pass synthesis rate, the amount of the recovery heat would be little different. When the loop pressure rises, the amount of gas circulation decreases, so that the reaction heat can be used in higher temperature grade.

The quality of the recovery heat is related to the temperature or pressure of the steam. In ammonia synthesis loop, the reaction heat is forepart applied to heat the feed water of waste heat boiler. With the use of turbocompressor, the reaction heat is commonly used to get high pressure steam as power to drive it, and use in rundle as shown in Fig. 9.26.

Higher the temperature, higher would be the efficiency of the heat engine. Therefore, it needs to increase the temperature of the steam i.e., out temperature of converter. In order to produce 12.5 MPa of high-pressure steam, the temperature of its saturated steam is 323.1°C, hence the inlet syngas temperature of the waste heat boiler must reach much higher than 340°C. Here, there are three ways to reach this goal. First way is to adopt the front-type heat recovery process, such as Braun process flow with three converters and three boilers (Fig. 9.4) and the Topsøe S-250 synthesis loop (Fig. 9.3). Second way is to increase the inlet temperature of converter. In the above example, if inlet temperature of converter is increased from 141°C to 220°C, the outlet temperature would reach 363°C. Kellogg process flow of the synthesis loop (Fig. 9.1) adopts this way. For Uhde process with two converters

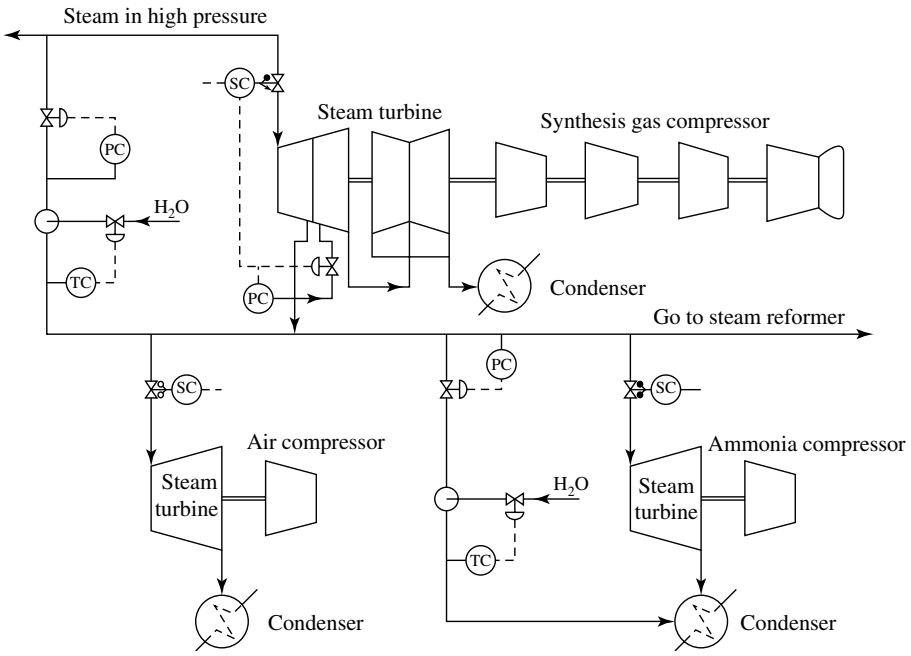


Fig. 9.26 Steam system of the plant with syngas compressor derived by draw-congealing steam turbines

and two waste heat boilers (Fig. 9.6), the outlet temperature of syngas is as high as 473°C. The Third way adopts the new catalyst with high activity to increase the net value of ammonia converter. As for the converter mentioned above, if we use ZA-5 catalyst and decrease space velocity, the net value of ammonia could be increased from 9.9% to about 18%, so the adiabatic temperature rise of the converter could be increased from 143°C to 261°C, and the outlet temperature would reach 402°C, as indicated in the process flow of ICI–AMV synthesis loop (Fig. 9.5). Among the three ways, only the third way could increase the recovery ratio of the reaction heat.

9.4 Influence of Performance of Catalyst on the Economic Benefits of Catalytic Process

To appraise the influence of catalyst on the economic benefit of catalytic process, only four items composing the production cost should be checked i.e., raw materials (including catalyst), direct pay, the fixed consumption of the cost of the production equipment (i.e. depreciation) and single servicing. The performance of catalyst can hardly have any influence on the miscellaneous expenditure (management and sale). When catalyst performance has dramatic influence on the expenses of capital construction, production cost often has a decisive criterion on preference catalyst. Although there are many ways to deal with production process, the production cost may be a small discrepant, so it is necessary to take investment recovery rate (i.e., the ratio of the annual profit to capital construction investment) as the best criterion. It is well known that it is not difficult to evaluate the production cost during the process design stage, and there may be some problems for such evaluation to control product prices and costs as well as calculate the recovery rate of capital construction investment. Therefore, other ambience factors should be considered when the optimum catalyst is selected.

The catalyst performance would hardly affect the direct pay, so other three items are considered for production cost.

9.4.1 *Catalyst-consumed cost*

Right selection of catalyst is one of the key for the synthesis plant to have a stable and high yield with low consumption. Generally, the basic requirements for a catalyst are: Excellent catalytic activity, high selectivity, good physical strength, endurance (including heat and toxicity resistance), low ventilation resistance, easy to reduce, no contamination to downstream devices and catalyst, easy to storage and transport, and low cost. Appraisement in total and in economics concurrently would provide a decisive criterion on choosing catalyst rightly. Table 9.15 shows the investment cost of three kinds of catalyst — A110 (Fe_3O_4 based), ICI74-1 (Fe_3O_4–CoO based) and ZA-5 ($Fe_{1-x}O$ based) (loading volume is 65.3 m^3). It can be seen from the Table 9.15 that the investment cost of the catalyst is ICI74-1 > ZA-5 > A110. When the catalyst is used for 10 years, the annual cost is 0.23–0.24 million Yuan. Compared with A110, the added value of annual catalyst cost of ICI74-1 and ZA-5 is (0.17 and 0.09) million Yuan respectively. The performances of ICI74-1and ZA-5, especially ZA-5 catalyst, is much better than A110. Therefore, the all-important

Table 9.15 Investment cost of the catalyst

Items	Catalyst type					
	A110		ICI74-1		ZA-5	
The first bed catalyst	Pre reduced	Un reduction	Pre reduced	Un reduction	Pre reduced	Un reduction
Bulk density/(kg/l)	2.3	2.88	2.3	2.88	2.45	3.0
Weight of catalyst/t	43.24	54.14	43.24	54.14	45.12	56.4
Unit price/(10^4 Yuan/t)	2.6	0.9	3.5	1.9	2.8	1.4
Amount of money/10^4 Yuan	112.42	48.73	151.34	102.87	128.96	78.96
The second bed catalyst	Unreduction		Unreduction		Unreduction	
Weight of catalyst/t	133.9		133.9		139.5	
Amount of money/10^4 Yuan	120.528		254.41		195.30	
Total cost of catalyst/10^4 Yuan	232.95	169.26	405.75	357.28	324.27	274.26
Added cost of catalyst (comparing with A110)/10^4 Yuan	—	—	172.80	188.02	91.32	105.00
Annual cost of catalyst(for ten years)/(10^4 Yuan/year)	23.295	16.926	40.575	35.728	32.427	27.426
Added annual cost of catalyst (comparing with A110)/10^4 Yuan	—	—	17.28	18.80	9.132	10.50
The cost of the catalyst for per ton of ammonia/(Yuan/t[a])	0.71	0.52	1.21	1.07	0.98	0.83

[a]Life of the catalyst is supposed to be 10 years, operate for 330 d/a, product of 1000 t/d, the production cost is 2000 Yuan/t.

Table 9.16 Proportion of catalyst's cost to the cost of ammonia/%

Parameters	Activated carbon	Zinc oxide	Primary reforming	Secondary reforming	High-Temp. shift	Low-Temp. shift	Methanezation	Synthesis	Total
Proportion/%	0.162	0.034	0.191	0.109	0.216	0.496	0.063	0.279	1.55
Equivalent of output/d	—	0.28	0.56	0.26	0.46	1.56	0.15	0.21	3.48

factor is the catalyst performance rather than its price because the price can be neglected if the performance is good.

It can be seen from Table 9.15 that the cost of catalyst in product cost of ammonia is 0.52–1.21 Yuan/t catalyst, and accounts for 0.26%–0.6% of total cost per ton ammonia. It is inappreciable of comparing with total production cost (2000 Yuan/t-ammonia). Table 9.16 further shows the data where the proportions of various catalyst cost accounts for the total cost of the ammonia. It indicates that the proportion of cost of all catalysts (including expense of operations such as catalyst reduction) accounts for less than 2% of the total cost of ammonia. Therefore, it is always right to choose the catalyst performance rather than its price. If the yield of ammonia declines or if the production is stopped because of its poor performance of the cheap catalyst, the economic loss will surpass the cost of replacing catalyst. For example, the cost of catalyst for ammonia is only equal to the production value of the produced at 0.21 day (Table 9.16). So it is necessary to spare no expense to select a good catalyst. Do not spoil the ship for halfpennyworth of tar.

It is worth noticing the cost of Ru catalyst and the calculation of the unit consumption because Ru catalyst belongs to noble metal catalyst. Appraising the cost of noble metal catalyst usually should be considered for only three items as listed (however, the list does not include the price of noble metal).

(1) The cost of catalyst should be composed of the price of carrier and promoter, the cost of preparation of the catalyst and loss of the noble metal while preparing the catalyst when the own price of the noble metal is excluded out of the price of the catalyst.
(2) The loss of the noble metal while using the catalyst;
(3) The cost of recovering the noble metal from the wasted catalyst, where the recovery company should return all the noble metal. Here, the technological loss is made up by its own devices and is included in the recovery price. The recovery cost increases with the decrease of the concentration of the noble metal. For example, the loss of recovering Pt and Pd from wasted catalyst is commonly about 1%.

The way of appraising the cost of noble metal catalyst mentioned above is also suitable for the Ru catalyst. However, the using period of the Ru catalyst is too long (more than 10 years) to carry into execution. Whereas, because the operation pressure of synthesis loop of KAAP process is $91.4\,\mathrm{kgf\cdot cm^{-2}}$, the investment of the

synthesis loop decreases by 20%, and the saved cost of the piping and devices in the synthesis loop is enough to counteract the addition in the catalyst cost.

9.4.2 *Economic factor of reduction for catalyst*

The reducing process of catalyst is a key step to preparing and using catalyst. It is a non-productive process with endothermic and consuming H_2 which impropriates production time. Therefore, it is related to the economic factors. The chemical reaction equation of reduction of Fe catalyst is:

For Fe_3O_4-based catalyst such as A110, A201and ICI 74-1 etc.:

$$Fe_3O_4 + 4H_2 = 3Fe + 4H_2O - 60.6\,kJ/mol\,Fe$$

Theoretical amount of the H_2 consumption is $364\,m^3$(STP) H_2/t; and the theoretical yield of water is 292.5 kg/t.

For $Fe_{1-x}O$-based catalyst such as 301, ZA-5 etc.:

$$Fe_{1-x}O + H_2 = (1 - x)Fe + H_2O - 37.3\,kJ/mol\,Fe$$

Theoretical amount of the H_2 consumption is $304\,m^3H_2 \cdot t^{-1}$; and the theoretical yield of water is $244.3\,kg \cdot t^{-1}$ (both less than Fe_3O_4-based catalyst by 19.7%).

Besides, the reduction temperature is lower and the reduction rate is faster for the $Fe_{1-x}O$-base catalyst than that for the Fe_3O_4-base catalyst, so the loss of heat during the reduction process and the reduction time would decrease. The economic factors during the reduction process for the plant with capacity of $1{,}000\,t \cdot d^{-1}$ and catalyst volume of $65\,m^3$ are listed in Table 9.17.

From Table 9.17, it can be seen that although the weight of A301 (ZA-5) catalyst is more about 10 times than that of A110 series due to its bulk density been larger than that of one, the water output, the H_2 consumption, the supplied heat by starting-work heating furnace as well as the effective reduction time decrease on the contrary. It is worth noticing that the effective reduction time is shortened by 11.5 hour than A110 series, which is calculated by the average steam concentration without the reduction speed. In fact, the reduction speed of the A301 (ZA-5) is three or more times faster than A110, and the reduction time is shorter than A110 by more 24–48 h. Therefore, full utilization of the performance of ZA-5 catalyst,

Table 9.17 Economic factors of catalyst reduction

Type of catalyst	Weight of catalyst[a]/t	Output number of H_2O/t	Consumption of H_2/m^3	Heat supplied		Effective reduction time/h[b]
				MJ	*kWh*	
A110 series (ICI74-1)	185.25	54.19	67,431	1,38,122	10,977	90.5
A301(ZA-5)	195	47.63	59,280	99,001	7,882	79
Related ratio/%	+5.3	−12.1	−12.1	−28.3	−28.3	−12.7

[a]Bulk density of catalyst: $2.85\,kg \cdot L^{-1}$ for A110 series (ICI74-1); $3.00\,kg \cdot L^{-1}$ for A301 (ZA-5);
[b]Effective reduction time does not contain rising or declining temperature and is calculated according to average space speed of $5000\,h^{-1}$ and average steam concentration of $2\,g/m^3$.

especially reduction time, can get significant economic benefits during the reduction stage of the start-up.

(1) Since ZA-5 catalyst can be reduced easily, not only the reduction temperature is low, but also the condition of reduction speed is restrained (limited by present process and equipments condition), the reduction time is shorter than that of A110-2 by 1–2 days, and can be further shortened if the process and equipment conditions are permitted. According to the estimation of the some plants, the average daily cost of reduction is more than one million Yuan. If 1.5 day can be shortened in reduction, the benefits of 1.5 millions Yuan can be obtained.

Meanwhile, the reduction time is shortened by one day i.e., the production time is increased by one day, so more ammonia can be produced (which would be wasted and vented to the atmosphere). If the output of ammonia should be 600 t/d for a plant with capacity of 1,000 $t \cdot d^{-1}$, additional 900 t can be produced in 1.5 days. It is equivalent to the output value of 1.8 millions Yuan according to 2,000 Yuan/t.

(2) The active temperature of ZA-5 catalyst is low and its activity at low-pressure is high, so when the temperature reaches 430–450°C, lot of ammonia would be produced, and the concentration of ammonia in the first and second ammonia separators can reach above 90%, which can directly enter the product tank (it is discharged into dilute ammonia pool because of its low concentration by A110-2). That is to say, the reduction process of the ZA-5 catalyst is also a process in which the reduction of catalyst and production of ammonia takes place concurrently that is beyond the sweep of the traditional catalysts. Therefore, ZA-5 catalyst can shorten the reduction time by 1–2 d, and also produce much ammonia during the reduction process, thereby its economic benefit is notable. If the synthesis during the reduction period is calculated by 50% of the 1.5 d, another 750 t would be produced, which is equivalent to the output value of 1.50 millions Yuan.

Besides, the cost of treatment with the diluted ammonia is reduced because the yield of water of $Fe_{1-x}O$-based catalyst is less than that of Fe_3O_4-based catalyst by 19.7%.

9.4.3 *The economic benefits using the pre-reduced catalyst*

About 15%–30% of the active α-Fe is poisoned by O_2 in order to form passivation film during preparation of prereduced catalyst (this part of α-Fe is the most active site on surface and takes part in the actual catalytic activity, whereas the inside of α-Fe which is not poisoned by O_2 does not work in real reaction). It is sure to lose a part of its activity when reduction is carried on again in the ammonia plant. That is to say that the activity of prereduced catalysts is lower than that of oxidation state catalysts after reduction is directed in the ammonia plant. However, when the prereduced catalyst is used in the plant, the indexes such as the net value and output of ammonia are dependent on the activity of the catalyst, and also on some other factors, which are hard to be expressed by exact amount. In point of view of economy, the use of prereduced catalyst shows some obvious economic benefits for the plant.

Table 9.18 is a simple statistic data which includes few types of converter with different structures like Topsøe, Kellogg and Casale etc.[28]

Compared with the catalyst in oxidation state, even if part of the prereduced catalyst is used, the heater with small capacity is also used during the initial working

Table 9.18 Economic benefits using the pre-reduced catalyst

No.	Loading situation of catalyst	Catalyst cost (relative)	Reduction time/d	Unvalued dilute ammonia solution
1	100% unreduced	100.0	6–7	Many
2	80% unreduced + 20% prereduced	127.6	4–6	Middle
3	50% unreduced + 50% prereduced	169.0	3–4	A few
4	100% prereduced	237.9	1–2	Rare

stages, because the reaction of ammonia formation will take place fast when the reaction heat would replenish the heat of heater. If more than 50% of the prereduced catalyst is used, there is nearly no problem to deal with the dilute ammonia solution which is very worried about the ammonia plant. Another obvious benefit is to shorten the reduction time, thus obviously economizing raw material, fuel and non-productive time including foregoing processes such as gasification and purification.

It is statistics that although the unit weight price of the prereduced catalyst is as much as 3–4 times of the catalyst in oxidation state, if the primary investment of the catalyst is increased, and if part or all prereduced catalyst is used, when compared with using catalyst in oxidation state, the net benefit is equivalent to the value of 1,000–4,000 t of ammonia for a plant with capacity of $1{,}000\,t \cdot d^{-1}$.

The required amount of catalyst is not proportional to the increase of yield of ammonia. In the past decades, the amount of catalyst required per ton of ammonia has been reducing. One reason is that the quality or purification of syngas is continuously improved. Another is that the heat stability and antitoxic property of catalysts is increased which prolong the usage life of the catalyst. At the same time, by reducing the pressure class in synthesis loop, the volume of catalyst used is increased significantly.

The calculation shows that the use of prereduction catalyst, whose price is as much as 3–4 times of unreduction catalyst, is favorable to the plant loaded with less catalyst and operated at middle- and high-pressure (26 MPa–30 MPa), but is unfavorable to the plant at low-pressure (10 MPa–13 MPa). However, when part (15% of the total) of the prereduced catalyst is used, it is favorable even if it is used in low-pressure; but it is much more favorable to use it in high-pressure. If the non-productive time of replacing catalyst is influenced by the reduction time or reduction conditions, the cost of production is also affected by the catalyst properties. The prereduction catalyst is expensive but the non-productive time is short; the unreduction catalyst is cheap but the efficiency of production is higher and period between two stops is longer, so it is economical usually in view of output obtained. The other factors influencing the economic balance will be described in Section 9.4.4 in detail.

9.4.4 *Effect of catalyst performance on the economic benefits of process*

The catalytic activity determines the unit productivity of the reactor, and the investment of capital to construct the reactor. Increase in the catalytic activity can decline

the reaction temperature for some exothermic reactions, and then enhance the equilibrium conversion. Therefore the investment in capital construction is saved and the energy needed in the recovery for raw materials in the production process is saved. Although the effect of catalytic activity on the economics of some process does not conform with the experts' expectation in the range of catalyst action, it has a decisive effect in one-direction reaction (for example the ammonia synthesis, oxidation of sulfur dioxide and carbon monoxide shift etc.). If the range of maximum productivity of whole production line varies by heightening catalytic activity, a lot of investment of capital construction can be saved.

In the organic synthesis, the consumption of raw materials accounts for 50%–80% of the production cost, so the selectivity of catalyst affecting the consumption of raw materials has a huge economic significance. For example, the cost of all equipment accounts for about 1% of the yield of ethylene oxide for production equipment of ethylene oxide with capacity of 50 kt. The increase in the catalytic selectivity sometimes can be represented in saving the investment of capital construction and the energy consumption of the separation process.

In many cases, using the higher active catalyst can lead to deep change in the production process in chemical industry. The equilibrium conversion rate of some reversible exothermic reactions is very low at definite temperature, but when the activity of catalyst is greatly increased, it is possible to decrease the reaction temperature, and reform the technology and bring a good influence on the economic benefits of the process. For example, the carbon monoxide steam shift reaction is a good example when Fe-Cr catalyst is replaced by higher active Cu catalyst. In the reactor with roughly same units productivity, if reaction temperature decreases by 100–120°C, the equilibrium constant can increase by 4–5 times. To get the same equilibrium concentration of CO, it is enough that the amount of steam is about 1/3 at low-temperature, hence, energy can be saved greatly. If the superfluous steam at low-temperature CO shift is equal to that at high-temperature, the equipment removing residual CO from H_2 can be saved, so that the investment of capital construction decreases. Obviously, it is the optimal solution to use comprehensively two kinds of catalysts and the intermediate process of absorbing CO_2, and to remove residual H_2S to meet the needs of Cu catalyst.

The economic benefit of synthesis ammonia production depends on energy consumption. Increase in productivity is influenced by many factors in which the reactor's volume plays an important role. The reactor's volume is limited by the possibility of mechanical manufacture. For example, high-pressure reactor is restricted by the allowed weight of forging. In addition, the size of the heat exchanger is limited by the number of tubes in the tube bundle. Usually the number of tube is not more than 10,000. The tube reactor, whose catalyst volume is more than 30 m^3, is rarely seen in the mechanical industry. Factors such as the size of reactors may pose difficulties in transporting from mechanical work to the construction site as well as the ability or the inability of the crane in capital construction and so on.

If more active catalysts are used i.e. the catalyst has more productivity, resulting in fewer numbers of parallel production lines, then there is a possibility of saving investment in capital construction.

It is necessary to consider the effect of catalytic activity on the reactor volume when a new device is designed. If the improvement of catalytic activity cannot lead to a fundamental change of the technology, the obtained economic benefits will be smaller. Investment of capital construction accounts for about 10% of the

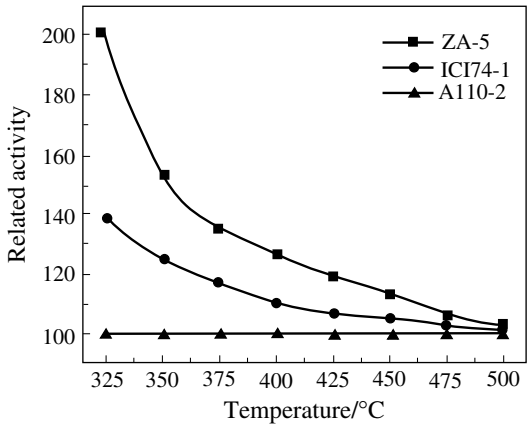


Fig. 9.27 Comparison of relative activities of ZA-5, ICI74-1 and A110-2 catalysts (15 MPa, 30,000 h^{-1}; syngas: 75% H_2 and 25% N_2)

production cost in which the reactor's investment is usually less than 10%. It can be seen that the influence of reducing the reactor weight on the production cost only is by several percent, sometimes by the tens of percent. Because in some cases the productivity is still limited by the reactors, the better economic benefits can be obtained by improving the activity of catalyst in existing industry equipment.

Specifically, the comprehensive economic benefits such as increased production, decreasing-pressure and decreasing-temperature, reducing consumption, energy saving etc. are obtained by using high activity catalyst in present industrial equipment. For example, outlet concentration of ammonia on ZA-5 catalyst has surpassed 30% in conditions of 450°C, 30.0 MPa and $3 \times 10^4 h^{-1}$. It is seen from Fig. 9.27 that compared with A110-2, it has been improved by 50%–100% at low temperature (325°C and 350°C). If the suitable reactor is designed and accompanied with new process, for such a high efficient catalyst, there will be a potential possibility of saving investment of capital construction. Even though it is used in the present industrial equipment, a good economic benefit as discussed would be obtained.

Table 9.19 shows the effect comparisons of A110, ICI74-1 and ZA-5 catalysts used in S-200 converter with capacity of 1,000 t/d. Table 9.19 gives two operation conditions: One is the existing set of conditions (including pressure, temperature, flow and composition of gas), while the other refers to the existing load i.e., the same output for three kinds of catalysts.

In the case of similar operating conditions, and compared with A110, the comprehensive economic benefits such as increased production, decreased temperature, reduced consumption and energy saving are obtained by using high activity catalyst ZA-5 or ICI74-1.

In the case of the same output, good energy saving benefit can be achieved as listed:

(1) The benefit of increased production. In case (A) in Table 9.19, it is known that when three kinds of catalysts are used at the same conditions of pressure, flow, temperature and composition of inlet gas of the converter, the purpose of increasing

Table 9.19 Comparison of effect using A110-2, ICI74-1, ZA-5 catalysts for converter with 1000 t/d

No.	Item	(A) Same conditions			(B) Same output		
1	Catalyst type in the 1st bed	A110H	ICI74-1H	ZA-5H	A110H	ICI74-1H	ZA-5H
2	Catalyst type in the 2nd bed	A110	ICI74-1	ZA-5	A110	ICI74-1	ZA-5
3	Inlet pressure/MPa	12.64	12.64	12.64	13.40	12.64	11.00
4	Inlet gas flow/(kmol/h)	22,300	22,300	22,300	22,300	22,300	22,300
5	Inlet gas composition/%: H_2	62.9	62.9	62.9	62.9	62.9	62.9
6	N_2	22.8	22.8	22.8	22.8	22.8	22.8
7	$CH_4 + Ar$	12.0	12.0	12.0	12.0	12.0	12.0
8	NH_3	2.3	2.3	2.3	2.3	2.3	2.3
9	Inlet/outlet temperature in 1st bed./°C	365/489	355/484	330/473	360/490	355/484	345/473
10	Inlet/outlet temperature in 2nd bed./°C	390/446	380/440	360/426	385/444	380/440	365/426
11	Outlet ammonia of converter/%	14.31	14.95	16.41	14.94	14.95	14.93
12	Temp. of inlet/outlet of converter/°C	140/313	140/322	140/344	140/322	140/322	140/322
13	Liquid ammonia output/(t/d)	956.3	1,001.6	1,102.9	1,001.1	1,001.6	1,000.25
14	Output increasing value (A110 as 100)	100	104.74	115.33	—	—	—
15	Gas consumption/(m^3/t)	2,779.34	2,778.52	2,776.70	2,778.40	2,778.53	2,778.57
16	Unit gas consumption/(m^3/t)	0	−0.82	−2.64	—	—	—
17	Syngas compressor power[a]/kW	25,239.9	26,426.5	29,080.4	26,773.5	26,426.5	25,597.3
18	Circulator power/kW	1,441.3	1,422.0	1,378.8	1,332.9	1,422.0	1,284.1
19	Ammonia compressor power/kW	1,095.5	1,069.2	1,010.5	1,006.1	1,069.2	1,224.5
20	Total compress power/kW	27,776.7	28,917.7	31,469.8	29,112.5	28,917.7	28,105.9
21	Power consumption/(kWh/t)	697.2	692.88	684.72	697.92	692.88	674.40
22	Power saved/(kWh/t)	0	−4.32	−12.48	0	−5.02	−23.52
23	Heat recovery (1 MPa)[b]/(GJ/t)	2.147	2.200	2.309	—	—	—
24	Extra heat recovery per ton/(GJ/t)	0	+0.053	+0.162	—	—	—
25	Synthesis efficiency[c]/%	23.46	24.70	27.59	23.15	24.70	28.94

[a]Power consumption is calculated by inspiratory pressure of compressor of 0.1 MPa.
[b]Heat recovery is calculated only for 1MPa steam produced by waste heat boiler.
[c]In accordance with Xiao Jianqing *et al.,* Large Nitrogen Fertilizer, 2002, 25(3): 192.
Note: The converter is a radial-flow converter with two beds and indirect intermediate interchanger, structural parameters of beds are as follows: Inner diameter 1.170 m, outer diameter 2.866 m, height 3.4 m, filled 18.8 m^3 of catalyst with size of 1.5–3.0 mm for the first bed; inner diameter 0.650 m, outer diameter 2.866 m, height 7.500 m, filled 46.5 m^3 of catalyst with size of 1.5–3.0 mm for the second bed; gas flow from outside to inside.

Table 9.20 Benefit of increasing output

No.	Item	Unit price (RMB)	Catalyst type[b]		
			A110	ICI74-1	ZA-5
1	Liquid ammonia output/($t \cdot d^{-1}$)		956.3	1,001.6	1,102.9
2	Increase of output per year (related to A110)/($t \cdot a^{-1}$[a])		—	+14,949	+48,378
3	Increase of production value per year/(10 thousand Yuan $\cdot a^{-1}$[a])	2,000 Yuan/t	—	+2,989.8	+9,675.6
4	Profit of unit gas consumption decrease/(10 thousand Yuan $\cdot a^{-1}$[a])	1.0 Yuan/m^3	—	+27.10	+87.12
5	Benefits of power-saving/ (10 thousand Yuan $\cdot a^{-1}$[a])	0.7 Yuan/kW.h	—	+99.95	+288.31
6	Benefit of heat recovery/ (10 thousand $\cdot a^{-1}$[a])	26 Yuan/GJ	—	+45.55	+153.49
7	Total/(10 thousand Yuan $\cdot a^{-1}$[a])		—	+3,162.4	+10,204.5

[a]According to the annual operation time as 330 days.
[b]Operating conditions are working conditions (A) in Table 9.19.
Note: The A110 as a basis for comparison, "−" means less benefit than A110, "+" means increasing benefit than A110.

output can be reached by using a highly effective catalyst. Increasing output can be calculated according to the data in Table 9.19, the results are shown in Table 9.20.

It is seen from Table 9.20 that under similar conditions, the output when using ZA-5 catalyst is increased by 15.33% or 146.6 $t \cdot d^{-1}$ than that of the A110. If the annual operation time is 330 days, about 48,378 t and 96.76 million Yuan per year is increased. At the same time, because output increases, the gas consumption reduces, heat recovery rate increases, power consumption declines and integrative economic benefits can be obtained.

It is worth noticing that the profits obtained by enterprise are closely related to the output of the product. The more the output of the product, the larger the profits obtained. Figure 9.28 shows profit and loss balance curve of the plant with a capacity of 1,000 $t \cdot d^{-1}$. In the Fig. 9.28, $B = PQ$ is sale income of products where P is the unit sale price and does not change with the sale quantity of products, and Q is the sale quantity amount of products. $C = C_f + C_v Q$ is the total production cost of the product, in which C_f is the fixed cost unchanged with the output, and includes depreciation, salary and administration cost, maintenance, interest, welfare and labor protection and all expenses unrelated to the amount of product, which the enterprises must spend even if it does not operate. C_v is the variable cost of unit product and changes with the output, which includes raw materials, fuel and power etc. For an ammonia plant with capacity of 1,000 $t \cdot d^{-1}$, if the product price is assumed to be 2,000 Yuan $\cdot t^{-1}$ in which the variable cost of raw materials, fuel and power etc. is 1,400 Yuan $\cdot t^{-1}$, and if C_f is taken to be 0.5 million Yuan $\cdot d^{-1}$, then the business sales earning change with output is represented as the line B, total cost of production is represented as the line C. The crossing point of line B and line C is the break-even point of the enterprise. Here, the value is 833 $t \cdot d^{-1}$, i.e., when the output is less than 833 $t \cdot d^{-1}$, the enterprise will earn losses. Only

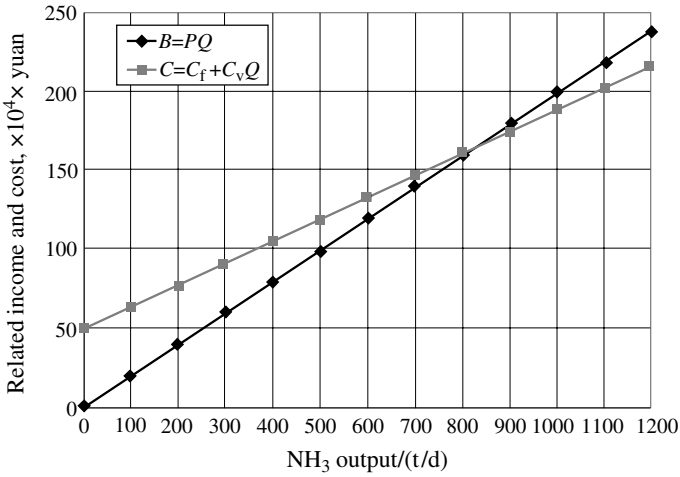


Fig. 9.28 Profit and loss balance curve of plant with capacity of 1,000 t/d
B-Enterprise sales; P-Unit product price; Q-Product sales; C-Total production cost of product; C_f-Fixed cost; C_v-Variable cost of unit product.

when the output is greater than $833\,t \cdot d^{-1}$, the enterprise would earn profits which is represented by the margin between B and C at the right of break-even point. For the enterprise in the condition above mentioned, when the output reaches the designed value of the $1000\,t \cdot d^{-1}$, its profits would reaches to 0.1 million Yuan $\cdot\, d^{-1}$.

In Fig. 9.28, it can be seen clearly that a more significant benefit can be obtained by increase of output. For example, using a new highly-effective catalyst would increase the output from $1{,}000\,t \cdot d^{-1}$ (the designed value) to $1{,}100\,t \cdot d^{-1}$, while the profit increases from the 0.1 million Yuan $\cdot\, d^{-1}$ to 0.16 million Yuan $\cdot\, d^{-1}$, i.e. the profit is 100 Yuan $\cdot\, t^{-1}$ when the output is designed value of $1{,}000\,t \cdot d^{-1}$, while the profit of the increased output is 600 Yuan $\cdot\, t^{-1}$, the later six times higher. Therefore, the increased production is the main way for the enterprise to earn profit, and the most effective measure to increase output is to use new high-effective catalyst.

(2) Benefit of energy saving (reduce pressure). According to the balance of mass and energy for ammonia converter:

$$y = 0.778 V_{\text{in}} \frac{\Delta\varphi}{1 + \varphi_{\text{out}}} \tag{9.4}$$

$$t_{\text{out}} = t_{\text{in}} + (14 - 15)\Delta\varphi \times 100 \tag{9.5}$$

When the load or output (y) and inlet gas flow (V_{in}) of the converter is the same, the outlet concentration (φ_{out}) and the net value ($\Delta\varphi$) of ammonia must be the same; if the temperature (t_{in}) and the composition of inlet gas is the same, then the temperature of outlet gas (t_{out}), volume of recycle gas and vent gas is the same, i.e., the heat recovery rate and the gas consumption of the converter is the same too (seen in Table 9.19). Therefore, in such conditions, the benefits of using the new highly-effective catalyst are embodied in the benefits of energy saving and pressure reducing which is shown in Table 9.21 which is an extension of Table 9.19.

Table 9.21 Benefits of energy saving (pressure reducing)

No.	Item	Catalysts[c]		
		A110-2	ICI74-1	ZA-5
1	Liquid ammonia output/(t/d)	1,001.1	1,001.6	1,000.25
2	Operation pressure at same output(p)/MPa	13.40	12.64	11.00
3	Power of syngas compressor (0.1→p)[a]/kW	26,773.5	26,426.5	25,597.3
4	Power of circulating compressor/kW	1,332.9	1,422.0	1,284.1
5	Power of ammonia compressor/kW	1,006.1	1,069.2	1,224.5
6	Overall driven power/kW	29,112.5	28,917.7	28,105.9
7	Power consumption per ton ammonia/(kW.h/t)	697.92	692.88	674.40
8	Power saving per ton ammonia/(kW.h/t)	—	−5.02	−23.52
9	Power saving per year/($10^4\times$ kW.h/year[b])	—	−165.66	−776.16
10	Benefit of power saving/($10^4\times$ yuan/year[b])	0	+116.15	+543.45

[a]According to the inspiratory pressure of compressor of 0.1 MPa.
[b]According to the annual operation time as 330 days and 0.7 Yuan/kW.h.
[c]Operating conditions are working condition (B) in Table 9.19.
Note: The A110 as a basis for comparison, "−" means less benefit than A110, "+" means increasing benefit than A110.

It can be seen from Table 9.21 that when the load or output (y) and inlet gas flow (V_{in}) of the converter is the same, the power consumption per ton ammonia of ZA-5 catalyst, in comparison with A110-2 and ICI74-1, is reduced by 23.52 kW·h and 18.48 kW·h respectively. It is comparatively saving energy of $0.28\,\text{GJ}\cdot\text{t}^{-1}$ and $0.22\,\text{GJ}\cdot\text{t}^{-1}$.

The catalytic activity will gradually decrease with the prolongation of catalyst service time. At this time, it can be known from Eq. (9.4) that in order to keep the liquid ammonia output, it should increase the reaction pressure, reduce the content of inert gas and inlet ammonia of the converter, to retain $\Delta\varphi/(1+\varphi_{\text{out}})$ in the equation unchanged; or the flow of recycle gas (V_{in}) must be increased which is the easiest way. The flow of recycle gas (V_{in}) is related to catalytic activity (outlet concentration of ammonia). Here the recycle ratio is related to catalytic activity (net value of ammonia). The so-called recycle ratio is the ratio of recycle gas to fresh syngas (Fig. 9.29).

Assume:

$R_{\text{before}} = V_{\text{in}}/V_{\text{fresh}}$ (add fresh syngas before circulator, $V_{\text{in}} = V_{\text{recycle}}$);
$R_{\text{after}} = V_{\text{recycle}}/V_{\text{fresh}}$ (add fresh syngas after circulator, $V_{\text{in}} = V_{\text{fresh}} + V_{\text{recycle}}$);

By

$V_{\text{fresh}} = 2V_{\text{NH3}} + V_{\text{vent}}$
$V_{\text{NH3}} = V_{\text{in}}\Delta\varphi_{\text{NH3}}/(1+\varphi_{\text{out,NH3}})$;
$V_{\text{vent}} = V_{\text{fresh}}\varphi^0_{\text{inert}}/\varphi_{\text{inert}}$;

So

$$R_{\text{befroe}} = \frac{1}{2}\left(\frac{\Delta\varphi_{\text{inert}}}{\varphi_{\text{inert}}}\right)\left(\frac{1+\varphi_{\text{out,NH3}}}{\Delta\varphi_{\text{NH3}}}\right) \tag{9.6}$$

$$R_{\text{after}} = R_{\text{before}} - 1, \tag{9.7}$$

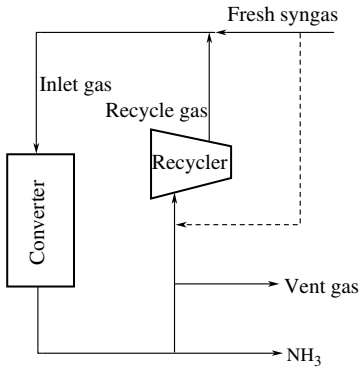


Fig. 9.29 Gas recycles of synthesis loop

where R_{before} and R_{after} are the ratios of recycle gas and fresh gas before/after circulator, respectively. $V_{\text{in}}, V_{\text{fresh}}, V_{\text{recycle}}, V_{\text{vent}}, V_{\text{NH3}}$ is the flow of inlet gas, fresh syngas, recycle gas, vent gas and ammonia gas, respectively, $\text{km}^3 \cdot \text{h}^{-1}$. $\varphi^0_{\text{inert}}, \varphi_{\text{inert}}$ is the content of inert gas in fresh gas and vent gas, respectively, %. $\varphi_{\text{out,NH3}}, \Delta\varphi_{\text{NH3}}$ is outlet content and net value of ammonia, respectively, %.

It will be seen from this that the recycle ratio of gas in synthesis system is dependent on the outlet concentration, net value of ammonia and the content of inert gas of the synthesis loop. Recycle gas flux (recycle ratio) increases with the decrease in net value and the increase in the inert gas content. Because $\frac{\Delta\varphi_{\text{inert}}}{\varphi_{\text{inert}}}$ value is close to 1, recycle ratio is basically inverse proportion to synthesis efficiency of $\alpha = 2\left(\frac{\Delta\varphi_{\text{NH3}}}{1+\varphi_{\text{NH3}}}\right)$ or net value of $\Delta\varphi_{\text{NH3}}$.

When the decrease of catalytic activity leads to the decrease of net value of ammonia, it is necessary to increase the flow of recycle gas (inlet gas of converter) in order to keep liquid ammonia output (see Eq. 9.4). However, the power consumption of circulating compressor or ammonia compressor is proportional to the volume of inhalational gas i.e. the flow of recycle gas. When other operating parameters of circulating compressor or ammonia compressor are not changed, the power consumption will increase $\Delta N/N_0$.

$$\frac{\Delta N}{N_0} \times 100\% = \frac{N - N_0}{N_0} \times 100\% = \frac{R - R_0}{R_0} \times 100\% \tag{9.8}$$

Here, the N_0, N is the power consumption of circulating compressor or ammonia compressor when recycle ratio is R_0 and R respectively, kW.

For example, when $\varphi^0_{\text{inert}} = 0.5\%$, $\varphi_{\text{inert}} = 10\%$, $\varphi^0_{\text{NH3}} = 2\%$ remains unchanged and φ_{NH3} declines from 14% to 13% ($\Delta\varphi_{\text{NH3}}$ decreases from 12% to 11%), R_{before} increases from 4.5 (R_0) to 4.88 (R) and $\Delta\text{N}/\text{N}_0 = 8.4\%$; R_{after} increases from 3.5(R_0) to 3.88 (R) and $\Delta N/N_0 = 10.9\%$, i.e. when the catalytic activity (net value) reduces by 1%, the power consumption of circulating compressor or ammonia compressor will increase by 8.4% or 10.9%. In the condition of Table 9.21 and catalyst A110, the power of circulating compressor should increase by 112 kW or 145 kW. The relative effect on the process flow of supplementing fresh syngas after circulating compressor is greater than that of before (but absolute value is small because N_0 is small).

Thus, it can be further understood that the power consumption of the circulating compressor or ammonia compressor can be saved by using the catalyst with high activity.

Among the three kinds of catalysts in Table 9.19, the price of ICI74-1 is the highest, of A1110 is the lowest and of ZA-5 is the moderate, but the comprehensive energy consumption of unit product for A110 series is the highest, so its daily running cost is the highest but ZA-5 is the lowest. Therefore the choice of cheap but low-activity catalyst is a serious mistake for decreasing the costs and increasing the profits of enterprise. In short, by selecting high-activity catalyst, we will obtain the benefits of energy saving and economy irrespective of the type of device used. Especially, it is suitable for a large installation in expansion from $1000\,t \cdot d^{-1}$ to $1500\,t \cdot d^{-1}$.

9.4.5 *Selectivity of catalyst*

The selectivity of catalyst is not involved in synthesis loop of ammonia. Therefore, the influence of catalyst selectivity upon the process of ammonia production mainly takes place in the working procedure such as steam reforming etc. In the catalytic conversion of organic compounds, some raw materials transform more or less to by-products. The yield of purpose product is influenced by the catalyst selectivity to a great degree. For example, the decisive factor of the economy of oxidation process is just the catalyst selectivity. As a result, for this kind of chemical process, the catalyst selectivity has great economic significance than its activity.

9.4.6 *Life period and service time of ammonia catalyst*

It is recognized that the loss caused by replacing the catalyst is enormous in a modern ammonia plant, and so does the ammonia processing device that requires continuous supply of ammonia.

The common service time of ammonia catalysts is shown in Table 9.22. The longest service time of single furnace (converter) in a large installation has reached 15 years. The service time of catalyst refers to the interval time in replacing the catalyst in the converter, which is influenced by many factors such as using conditions, level and conception of management (for example, some enterprises think that it is most worthwhile to utilize catalyst "adolescence" with its best activity and to replace it after "adolescence"), it cannot reflect the real life period of catalyst. For example, in small, medium and large converter, the excellence order of use conditions on catalyst is that: Large-scale > medium-scale > small-scale, but the order of production intensity is that: Large-scale < medium-scale < small-scale, so the service time of catalyst is that: Large-scale > medium- scale > small-scale. The using condition of small device is the worst but the production intensity is the biggest, so it is inevitable that the service time of the catalyst used in the small device is shortened. The catalyst which has experienced test in adverse conditions in small devices can be used in large devices directly. In addition, generally speaking, the design principles about the amount of catalysts are different in the synthesis loop between large plants and small one. For a small converter, it is designed to use shorter time (general 2–5 years) and the amount of catalyst is small because the

Table 9.22 Service time of synthesis catalyst

Types of devices (catalyst)	Average service time/year	Longest service time of single-loading/year
Large-scale plant (A110)	8–10	18
Medium-scale plant (A110)	3–4	—
Small-scale plant (A110)	2–3	7
Small-scale plant (A301, ZA-5)	3–4	7

Table 9.23 Catalyst consumption for unit output of ammonia/ ($g_{\text{-cat}}/t_{NH3}$)

Type of devices	Average level	Advanced level
Large-scale plant	88.8	54.8
Small and medium-scale plant (A110, A201)	111.0	—
Small and medium-scale plant (A301, ZA-5)	—	55.7

catalyst replacement of converter is easier and the production intensity is bigger. In a large plant, the service time of the catalyst is short, but the loss in stoppage due to replacements and reduction of the catalyst are very great. On the other hand, if the designed service time is longer, a longer period of service time will be allowed. However, a larger size of converter and much more first investment are needed.

It should be specially noted that the service time of catalyst is not equal to the life period of catalyst. The life period of catalyst is its own characteristic and does not change with the difference of using conditions. But the service time changes with the difference of the using conditions. So, if the catalyst is used in different plant or in different conditions in the same plant, its service time is different. At this time, we cannot say that its life period is different but can only affirm that its service time is different. The life period of the catalyst can generally be expressed as the output of ammonia produced per ton catalyst in its life period in the same condition, i.e., $g_{\text{-cat}}/t_{NH3}$-expended catalyst per ton ammonia (Table 9.23); it can also be expressed as the longest service time of the catalyst used in single furnace in its all industrial application.

The unit consumption of the catalyst as its cost can determine its ratio accounting for the production cost. The frequency of replacement and regeneration of catalyst will affect the service time of the equipment, and then affect the reclaiming of investment of capital construction and maintenance expenditure.

It is well known that the life period or service time of ammonia catalyst is the longest among eight catalysts in ammonia plant. It is seen from Table 9.23 that the unit consumption of novel $Fe_{1-x}O$-based A301 and ZA-5 catalysts used in small devices is only $55.7\,g_{\text{-cat}} \cdot t_{NH_3}{}^{-1}$, which has been at or below the advanced level of large device. Its life period of usage is the same as large devices. The longest service time of single furnace in small device for A301 and ZA-5 is more than seven years, which is enough to prove that novel $Fe_{1-x}O$-based catalyst has good thermal stability.

9.4.6.1 *Economic appraisement of the service time of the catalyst*

Literature[1] analyzed a plant of $1{,}000\,t \cdot d^{-1}$, the designed service time of catalyst was selected to be two or five years, and its analytical and comparative results on economic benefit are summarized in Fig. 9.30. Line AB shows the relationship between output and the service time of catalyst which is designed to be two years. If the capacities of syngas compressor and other equipments are abundant, the service time of the catalyst is designed to be two years, and the output is $1{,}040\,t \cdot d^{-1}$ because of its high-activity in the early stage of the operation. Similarly, the potential capacity of fresh catalyst is $1{,}070\,t \cdot d^{-1}$ when the service time is designed to be five years as shown in line CD. When the safety coefficient of the compressor as well as related equipments is 5%, the obtained results are shown in Table 9.24.

(1) When the nominal service time is designed to be two years, the productivity is $1{,}050\,t \cdot d^{-1}$ within 1.4 years after running, then the output declines because the catalytic activity decreases. When the period reaches 3.3 years, the output decreases to rated output of $1{,}000\,t \cdot d^{-1}$. This potential increase in production is shown as the shadow area I. As a result, when this design is adopted, if the safety coefficient of the compressor is 5% during the operation, the nominal service time of catalyst can prolong from two years designed to 3.3 years.
(2) When the nominal service time is designed to be five years, the productivity is $1{,}050\,t \cdot d^{-1}$ within four years after running, then the output declines because the catalytic activity decreases. When the period reaches 6.8 years, the output decreases to rated output of $1{,}000\,t \cdot d^{-1}$. This potential increase production is shown as the sum of shade area I and II. As a result, if this design is adopted, the nominal service time of catalyst can prolong from five years designed to 6.8 years.

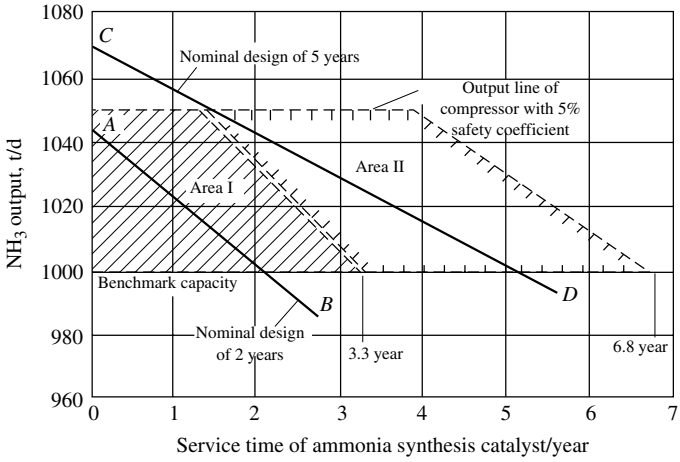


Fig. 9.30 Comparison of catalyst between two and five years of service time designed
Benchmark: (1) Capacity of 1,000 t/d; (2) Inert gas contents $_{at}$ inlet of converter 13.6%; (3) low-pressure synthesis loop.
Note: (1) Area I shows the output over 1,000 t/d for two-years service time of the catalyst when increased capacity of compressor is 5%. (2) Sum of area I and II show the increasing capacity of catalyst having five years service time, when increased capacity of compressor is 5%.

Table 9.24 List of economy (based on the life period of catalyst)

Parameters	Nominal service time designed	
	Two years[a]	Five years[a]
Cost of primary loading of catalyst/dollar	1,18,000	1,36,000
Times of catalyst replacement	1(after 3.3 years)	nothing
Cost of catalyst replacement (prereduce)/dollar	2,84,000	nothing
Total cost of catalyst/dollar	4,02,000	1,36,000
Cost saving of catalyst during 6.8 years[b]/(dollar/year)	39,000	(benefit for five years design)
Saving investment because of smaller converter/dollar	37,000	
Potential increment of ammonia output (during 6.8 years)/t	82,000	94,500
Output loss caused by catalyst reduction/t	1,500	nothing
Net increment of ammonia output/t	80,700	94,500
Margin of net output increment (benefit for five years design)/t	—	13,800
Potential profit increment (calculated by 15 dollars/t)/ dollar	207000	(benefit for 5 years design)

[a]Assuming that 5% safety factor of the compressor is used to increase output, the service time of catalyst can be prolonged to 3.3 years (for two years design) and 6.8 years (for five years design) respectively.

[b]6.8 years is taken as data benchmark for one cycle. During this period, the catalyst should be replaced one time for two years design and can be replaced in the time of the planning stop of the plant.

It is clear that the increment of potential profit augments when the service time of catalyst is prolonged, but it does not mean that the longer the service time of the catalyst is, the better the result is. The reason is that, as mentioned above, a more significant benefit will be obtained only by increasing output, and in particular, the service time of synthesis catalyst can reach over 15 years. Similarly, a plant with capacity of $1000\,t \cdot d^{-1}$ is taken as example, if the safety coefficient of the compressor as well as related equipments is 5%, the catalytic activity does not change during 7.5 years, the ammonia output is $1050\,t \cdot d^{-1}$ and then the output declines with the catalytic activity decrease. The output drops to 90% of rated value when it is used for 15 years, i.e. daily ammonia output is $900\,t \cdot d^{-1}$, the obtained results are shown in Table 9.25.

It is known from Table 9.25 that for the plant whose service time of the catalyst is 7.5 years, although the catalyst should be replaced once (but the replacement can be arranged during temporary stoppages at the plant, which does not occupy the production time), the cost of catalyst increases by one time, and part output will be lost during the catalyst reduction. However, in the view of running period of 15 years, potential profit increment of the enterprise with the service time of 7.5 years is much more than that of 15 years. It is the basis of the concept of "adolescence" and is most worthwhile for some plants to utilize catalyst's "adolescence" with its best activity and replace soon after "adolescence". As a result, it is not appropriate to say that the longer the service time of catalyst is, the better the result would be. Once it is found that the catalytic activity declines, the catalyst should be replaced generally in time.

Table 9.25 Real using time of catalyst and economy benefit

Parameters	Real using time	
	7.5 years[a]	15 years[a]
Cost of first loading of catalyst/dollar	3,88,253	3,88,253
Times of catalyst replacement	1(after 7.5 years)	nothing
Cost of catalyst replacement (same as 1st time)/dollar	3,88,253	nothing
Total cost of catalyst/dollar	7,76,507	3,88,253
Cost saving of catalyst during 15 years[b]/(dollar)	—	3,88,253
Potential increment of ammonia output (during 15 years)/t	2,47,500	61,875
Ammonia output loss caused by catalyst reduction/t	1,500	nothing
Net increment of ammonia output/t	2,46,000	61,875
Margin of net output increment)/t	1,84,125	—
Potential profit increment (calculated as 71 dollar/t)/dollar	1,30,72,875	(benefit for real using of 7.5 years)

[a]Assuming that 5% safety factor of the compressor is used to increase output (i.e., daily productivity is $1050\,t \cdot d^{-1}$), catalytic activity does not change during 7.5 years.
[b]15 years is taken as data benchmark for one cycle. During this period, the catalyst used for 7.5 years should be replaced one time and can be replaced in the period of the planning stop of the plant.

9.4.6.2 *Economic appraisement on replacement of catalyst*

Wenshan Wang *et al.* had discussed catalyst replacement.[29,30] Zuxi Yu *et al.* took a chilled converter with four beds used in some ammonia plants with capacity of $1{,}000\,t \cdot d^{-1}$ as an example, applied "REACTOR" program to calculate the effect of catalytic activity on productivity, forecast the time to replace the catalyst in normal condition of production as well as forecast the economic benefits of output increment probably obtained after the replacement.[31] Someone brought forward that the influence of the service time of catalyst on the economic benefits of the plant is appraised by the efficiency of converter (α), and α is token as a judgment of catalyst replacement.[32] The efficiency of converter α is defined as:

$$\alpha = \frac{2 \times 22.4\,W/M}{F - 22.4\,W/M} = \frac{2W}{kp(1 - y_i) - W} \tag{9.9}$$

where α is the efficiency of converter, %; W is the ammonia output, $t \cdot h^{-1}$; M is the molecular weight of ammonia; F is the flow of recycle gas, $km^3 \cdot h^{-1}$; $k = FM/(22.4\,p(1 - y_i))$; p is the synthesis pressure, MPal; y_i is the content of inert gas.

Synthesis efficiency of converter can truly reflect the situation of the activity of catalyst, and the comprehensive level of energy consumption of synthesis loop to a great degree. At the same time, the data can be an important criterion for the evaluation of the economic efficiency of enterprises. Synthesis efficiency is not only determined by the catalytic activity, but also influenced by loop pressure, temperature, ratio of H_2 to N_2, space velocity and other reaction conditions which are a comprehensive reflection of running situation of synthesis system. In the same

Table 9.26 Effect of converter efficiency dropping 1% on the three compressors

Compressor	Rotation speed/ ($\mathrm{r\cdot min^{-1}}$)	Design power/kW	Designed flow/ ($\mathrm{kg\cdot h^{-1}}$)	Outlet pressure/ MPa	Added power when converter efficiency drops by 1%/kW
101-J	6,490	9,765	50,842	3.487	190.4
103-J(recycle section)	10,413	4,679	3,66,043	15.243	46.79
105-J	6,620	9,765	27,096	1.89	97.65
Total	—	—	—	—	334.84

conditions, the efficiency of converter declines every time by 1%. There will be 1% recycle gas unreacted to participate in useless recycle, more parts of useless work are made by syngas compressor (103-J), ammonia compressor (105-J) and air compressor (101-J). According to estimates, when the efficiency of converter declines by 1%, the effects on the three compressors are shown in Table 9.26.

Because all 101-J, 103-J and 105-J use steam as power, the efficiency of converter falls by 1%, the power increment in three compressors requires incremental steam with middle pressure of $690\,\mathrm{kg\cdot h^{-1}}$ or the incremental energy of $144.84\,\mathrm{kW\cdot h^{-1}}$, leading to an annual incremental cost in energy consumption of 276,300 Yuan when the ability of steam supply of the synthesis system can support. If the synthesis system cannot support the increment of recycle gas, the incremental energy of $334.84\,\mathrm{kW\cdot h^{-1}}$ is consumed and annual incremental energy cost of 641,000 Yuan is paid. However, the annual average cost of whole catalyst in converter is only 2,00,000–3,00,000 Yuan. So, when the efficiency of converter declines close to the designed level, annual expenditure of energy consumption cost will be more than one million Yuan, and it will be uneconomic to run continually.

On the contrary, it can be seen from Table 9.19 that the efficiency of converter can be improved by using high activity catalyst. For example, in both the situations with similar conditions and with the same ammonia output, the efficiency of converter of ZA-5 catalysts increases by 4.13% and 5.79% than A110, respectively. According to the data of Table 9.26, the power of the three compressor units can decline by 1383–1938 kW, and its energy-saving effect is very significant.

As a result, the catalytic activity influences significantly the efficiency of the catalytic process. In the existing converters, the substitution of high activity catalyst to low activity catalyst can greatly increase the economy of production process.

In addition, using suitable geometry shape of catalyst, making full use of active surface and reducing the fluid resistance of beds are economically beneficial.

9.5 Benefits of Operating Rate and Management of Enterprise

In the profit and loss balance curve of enterprise (Fig. 9.28), the profit of enterprise is $\Delta B = PQ - (C_f + C_v Q) = (P - C_v)Q - C_f$ as mentioned. Assuming that the operating rate (utilization of capacity) is K, designed running time is 330 days and daily output is q, then

$$\begin{aligned} Q &= 330Kq \\ \Delta B &= 330(P - C_v)Kq - C_f. \end{aligned} \tag{9.10}$$

Obviously, the profit (ΔB) of enterprise is proportional to its operating rate (K). Some datum indicates that the profit of enterprise can increase by 14% when operating rate increases by 4%.

At the same time, running in long periods, i.e. improvement of operating rate is also the efficient way of energy-saving of plant. The actual energy consumption in ammonia synthesis production can be calculated as following equation:[4]

$$E_d = \frac{1}{(330Kq)} \left[\sum_{i=1}^{n} (e_i k_i) + \sum_{i=1}^{n} (e_{\text{iff}} k_i) \right] \tag{9.11}$$

Here E_d is the actual energy consumption, kg-standard coal/t-NH_3 or GJ/t-NH_3; e_i is the consumption in processes system of ammonia synthesis, kg; e_{iff} is the amount and loss of some energy and working medium consuming energy in auxiliary system of ammonia synthesis; k_i is the coefficient of standard coal converted by some energy or working medium consuming energy; n is the total of the energy or working medium consuming energy.

It can be seen from the Eq. (9.11) that when daily output q is unchanged, if operating rate is increased, the energy consumption will be declined. In order to reduce the energy consumption, long periods and full load of production are efficient ways of energy-saving, besides the factors such as technologies, processes, equipments and raw materials. This should be the first thinkable measure for digging the potential of energy-saving.

All is related to the management of enterprise, either the operating rate or the energy consumption. For example, the production of ammonia contains the ranges covered by production systems both technological process and auxiliary process. It can be traced back to complex systems such as pretreatment of raw materials and fuels before going to furnace, the pumping, treatment and transportation of raw water as well as electric energy, dynamical energy, the production of steam, O_2, N_2 and compressed air and so on. How to reduce the consumption of various materials, to ensure reliable and stable run of the equipments and to protect the activity of catalysts should be the core goals concerned by the supervisors of enterprise.

References

1. Slake AV, James GR. *Ammonia* (in four parts), Part III, Translated by inorganic chemical engineering section of Dalian Institute of Technology. Beijing: Chemical Industry Press, 1980.
2. Sheng JJ, *et al. Ammonia Synthetic Engineering*, 3rd, Beijing: Chemical Industry Press, 1977.
3. Zun HY, Bingchen Z, Caida S, *et al. The Process Analysis of Large Ammonia Plant*, Beijing: China Petrochemical Press, 1993.
4. Shen J, Zhu S and Feng X. The editorial board of Fertilizer industry series. *Synthetic Ammonia*, Beijing: Chemical Industry Press, 2001.
5. The editorial board of cyclopedia of fertilizer industry. *Cyclopedia of Fertilizer Industry*, Beijing: Chemical Industry Press, 1988. 182–183.
6. Li S, *et al. Lager Nitrogen Fertilizer*, (2): 126, 1986.
7. Chen J. *Chemical Engineering and Universal Machine*, (8): 44, 1974.
8. Zhou Y. *Chemical Fertilizer and Catalysis*, **3**: 7–28, 1992.
9. Li W. *Lager Nitrogen Fertilizer*, **3**: 169–173, 1993.

10. Li J. *Lager Nitrogen Fertilizer*, **6**: 460–472, 1992.
11. Xing L. *The Collection of Translation of Fertilizer Industry*, **1**: 13–21, 1990.
12. Xing L. *The Collection of Translation of Fertilizer Industry*, **2**: 31–37, 1990.
13. Niu J. *Lager Nitrogen Fertilizer*, **19**(5): 329–332, 1996.
14. Aika K. *The Trend and Expectation of Catalysis Technology* (in Japan), 14–23, 1997.
15. Strait R. *Nitrogen & Methanol*, **238**: 37–43, 1999.
16. Kellogg–Engelhard. Ammonia Technology Seminar Organized by the Ministry of Chemical Industry, Beijing, 1997.
17. Dybkjaer IB, Gam EA. *Chem. Econ. Eng. Rev.* **16**(9): 29–35, 1984.
18. Liu H, Li XN, Hu ZN, *et al. J. Chem. Ind. Eng.* (China), **52**(11): 1030–1034, 2001.
19. Liu H, Hu ZN, Li XN, *et al. Lager Nitrogen Fertilizer*, **24**(3): 162–166, 2001.
20. Liu H, Hu ZN, Li XN, *et al. J. Chem. Ind. Eng.* (China), **52**(12): 1063–1067, 2001.
21. Liu H, Li XN, Hu ZN, *et al. Chemical Reaction Engineering and Process*, **17**(1): 28–34, 2001.
22. Dai XH. Imitative calculation of low pressure reconstruct of small and medium synthesis plant and the research of the feasibility: Dissertation. Hangzhou: Zhejiang University of Technology, 2006.
23. Dai XH, Liu H. *Chemical Fertilizer Industry*, **33**(3): 12–16, 2006.
24. RCPE. Research Report of the Utilization Ratio Improvement of Chemical Fertilizer in China, Research Report of the Utilization Ratio Improvement of Chemical Fertilizer in China, 1998.
25. James GR.C E P, **80**: 6, 1984.
26. Xiang DH, Liu HY. *Fertilizer Catalyzed Practicality Manual*. Beijing: Chemical Industry Press, 1992.
27. Wang W. *Lager Nitrogen Fertilizer*, **5**: 7–13, 1983.
28. Chen W. *Lager Nitrogen Fertilizer*, **5**: 44–51, 1983.
29. Yu Z, *et al. Application Technique of Fertilizer Catalyst*, Beijing: Chemical Industry Press, 1988.
30. Xiao J, *et al. Lager Nitrogen Fertilizer*, **25**(3): 192, 2002.

This page intentionally left blank

Chapter 10

Innovation and Speculation

10.1 New Exploration of Ammonia Synthesis Catalyst

Recently, the ammonia synthesis was called as "the setting sun industry" and someone[1] also lamented the foreground obscuration of the chemistry of nitrogen fixation, in particular, in the research area of organometallic biochemical nitrogen fixation. However, ammonia is a fundamental building block for modern society and is essential for ammonia synthesis industry which drives the innovation and development of ammonia synthesis catalyst forward.

Nitrogen atoms are essential for the function of biological molecules and thus are important components of fertilizers and medicaments. Bonds to nitrogen also find non-biological uses in dyes, explosives, and resins. The synthesis of all these materials requires ammonia as an activated nitrogen building block. This situation is true for natural processes and the chemical industry. Knowledge of the various techniques for the preparation of ammonia is thus of fundamental importance in chemistry. The Haber–Bosch synthesis was the first heterogeneous catalytic system employed in the chemical industry and is in use until date. Understanding the mechanism and the translation of the knowledge into technical perfection has become a fundamental criterion for scientific development in catalysis research.

It would not be convincing to argue that a higher research effort in ammonia synthesis (which would certainly be desirable) would be justified by the necessity for developing totally different routes with higher degrees of efficiency than the modern Haber–Bosch processes, and would not be considered simply that the ammonia synthesis industry is built only for production of fertilizers, particularly when the following thermodynamic efficiency numbers are considered. Liquid ammonia at atmospheric pressure is needed as starting material, made from air, liquid water ($T = 300\,K$) and natural gas. The resulting ammonia theoretically contains $6.8\,Gcal.t^{-1}$ as chemical energy if the process is energetically isolated. Industrial processes achieve total degrees of efficiency of up to 70% for the processes described above (approximately $4.81\,Gcal.t^{-1}$ NH_3), whereas the biggest loss in efficiency is made in the methane reforming process ($1.18\,Gcal.t^{-1}$). Only a slight loss is made during the actual ammonia synthesis ($0.37\,Gcal.t^{-1}$). These efficiencies are achieved with commercially available iron catalysts and with modern ruthenium-based catalysts. Any further improvement in the catalysts would help to increase the thermodynamic efficiency and reduce the specific price of this basic compound through a reduction in the pressure during synthesis.[2]

Ammonia synthesis process without both side reaction and selectivity is one of the simplest green chemical reactions with an atomic utility ratio of 100%. In the chemical industry, catalytic ammonia synthesis processes is one of the most complicated chemical engineering processes. In theory, this reaction can occur at normal temperature and atmospheric pressure but is very difficult and therefore must occur at high-temperature and high-pressure in practice. It is more important that as well as being capable of producing activated nitrogen, the catalytic ammonia synthesis is also a key reaction for creating new life and a prototypical model reaction that helps to gain a fundamental understanding of catalysis in general and therefore of considerable scientific and cultural importance. It is mainly this reason that drives the research in ammonia synthesis forward, especially since evidence for a knowledge-based improvement of a catalyst would have a strong signaling effect on other fields of catalysis research.

Much research interests are fascinated toward the catalytic chemistry in ammonia synthesis. Many famous scientists related to physical chemistry and catalysis such as Nernst, Ostward, Emmett, Haber, Bosch, Mittasch, Ertl, Nielsen, Topsøe, Samorjai, Dumesic, Nørskov, Boudart, *et al.* had studied the catalytic ammonia synthesis. Among them, Haber, Bosch and Ertl won the Noble prizes in 1919, 1932 and 2007, respectively, because of their contributions in ammonia synthesis technology.[3,4]

Although much research importance has been toward the development in new catalyst, the melting-iron catalyst is still widely applied in the ammonia synthesis industry for about a century. This catalyst has high intrinsic activity, i.e., every active site possesses high activity, long-time stability and high density. In addition, another well-accepted advantage of meting-iron catalyst is its low price. Despite of these advantages, researchers are still engaged in looking for new catalysts, particularly in non-iron catalysts for ammonia synthesis.

10.1.1 *Revelation of theory and practice of fusing-iron catalyst*

The breaking of $N \equiv N$ bond is the rate determining step for synthesis of ammonia from H_2 and N_2 on iron catalyst, indicating that N_2 dissociated adsorption is the hardest step during formation of ammonia. Weakening or breaking $N \equiv N$ bond is one of important functions of the catalyst. This leads to dissociated adsorption species or the formation of surface nitride species. Therefore, the scientific research relevant to catalytic ammonia synthesis during the past one century was also a process that explored for the essential of N_2 dissociated adsorption and the mechanism of their reaction with H_2. On the other hand, the decomposition of ammonia is a simple reaction but also important model reaction in the field of surface science.[5] Table 10.1 shows the history and current development of catalyst related to ammonia synthesis during the past century.

During the early researching stages of melting-iron catalyst, the concept of multi-component mixed catalyst proposed by Mittasch, the BET equation and the selective chemisorption method for determining active site on catalyst proposed by Emmett *et al.*, proposed the iron catalyst as a prototypical model catalyst established on the basis of N_2 adsorption on iron catalyst. Brill has proved that Fe (111) face first adsorbs N_2, and found that the transformation of small distorted manifests

Table 10.1 History and current development of catalyst for ammonia synthesis

				Chemical compositions	
Developing stage	Date	Country	Catalyst type	Precursor	Promoter
Fe_3O_4-based	1913	Germany	BASF	Fe_3O_4	Al_2O_3, K_2O, CaO, ...
$Fe_{1-x}O$-based	1986	China	A301, ZA-5	$Fe_{1-x}O$	Al_2O_3, K_2O, CaO, ...
Ru-based	1972–1992	Japan/GB	KAAP	Ru/AC	Ba, K, **Cs**...

on (100) and (110) faces to (111) orientation when uncovering in gas momentarily.[6] Somorjai *et al.* confirmed these observations by kinetics study. They also measured the ammonia formation rates upon different crystal faces of iron single crystal.[7] On the basis of selective adsorption of N_2 on iron crystal face, Somorjai *et al.* also built a metal clusters catalytic theory and made an important hypothesis, that is, the crystal face that possesses the biggest coordinating group has the highest catalytic activity. Horiuti has pointed out a concept of stoichiometric number in order to determine whether the ammonia is formed from atomic nitrogen or hydrazine (molecular nitrogen).[8–10] Currently, most of researchers support atomic nitrogen routes,[11] and recognize the nitrogen dissociated adsorption as rate determining step. Temkin and Pyzhev also used this model to build a kinetic equation of ammonia synthesis reaction,[12] which is available such-and-such so that it is in use since 1939. These new techniques, methods, and theories of catalysis have initially been developed and applied in connection with studies of this system.

Ertl used modern surface energy spectrum technologies to characterize ammonia synthesis catalyst and provided experimental evidences for promoting the effect of alkaline.[13] Alkaline accelerates the nitrogen dissociated adsorption which is a rate determining step. The effect of Al_2O_3 on texture of metallic iron can be explained by the Hosemann's paracrystallinity concept.[14] Boudart's experimental results had confirmed it[15] and he also suggested the structure-sensitive concept.[16,17] These series of theories and researching results establish the fundaments for heterogeneous catalysis science and further drive the development of series of fundamental theories. The catalytic ammonia synthesis is a miniature during the foundation and development of heterogeneous catalysis science.[3,18]

This is a continuous process. In addition to questions about the elementary steps of the reaction and the importance of the real structure and subnitrides for the catalyst efficiency, as well as the wide-open question about new catalyst materials, there are also new challenges for new applications.[4] The ammonia synthesis industry still requires higher efficient catalyst.

The reaction and catalyst of ammonia formed from N_2 and H_2 on iron catalyst is an attractive problem in catalysis all along. Even after a century, the concept holds great potential in the reaction system, and can create more fortune for the human after improving the catalyst and process technology.

Since the last century, it has been commonly believed that the catalyst has the best activity when its chemical composition and crystal structure of the precursor are most similar to those of magnetite. The relationship between the activity and the ratio (Fe^{2+}/Fe^{3+}) is a volcano type curve, which seems to be an unquestioned

classical conclusion. For several decades, researchers developing new catalysts, while rigidly adhering to the conclusion, never changed the precursor composition (Fe_3O_4), but only the promoter components and their amounts. Thus almost all elements in the Periodic Table which might be used as promoter have been investigated widely. However, the activity of the catalyst increased only little. Liu[19] systemically studied the relationship between three types of iron oxides (Fe_3O_4, FeO, Fe_2O_3) and their mixtures and the catalytic activities. We found that $Fe_{1-x}O$-based catalyst with wüstite structure has highest activity in all iron oxides. It is clear that such a discovery has a strong impact on the consolidated scientific knowledge of ammonia catalysts and moreover opens the way to interesting industrial application. It is possible that an extensive and deeper investigation of the new catalyst will bring some revision in the present consolidated knowledge on ammonia synthesis.[20]

The modern industrial iron catalyst is a nanostructured metastable substance, which is formed during the surprisingly complex synthesis of the oxide precursor.[20,21] This differs significantly from pure iron especially in the mesoscopic area despite the similarities in the local structure. Its metastability is the reason for its sensitivity towards thermal overstress during activation and oxidation of the activated material and confirms the complex structure of this seemingly very simple ammonia iron.

Alternative preparation routes for the nanostructured system are possible.[22−24] One surprising example is that the different precursors can lead to marked change of nanostructure on metal surface. The new developed catalyst with wüstite structure has been proofed to have higher activity than the magnetite derived iron-based catalyst. It is known that the presence of special nanoclusters of Fe atoms, having specific geometrical requirements, is necessary to activate the dinitrogen molecule. The same active sites are probably present also on the ex-wüstite Fe surface, but are much more effective in performing the dissociation of dinitrogen. Though extensive structural and surface investigations are yet to be performed on the wüstite-based catalyst, it should be remarked that wüstite is much more possible than magnetite to dissolve Ca^{2+} ions within its structure. The best proof of such an intimate interaction is represented by the very unusual stabilization of the wüstite structure down to room temperature (wüstite can disproportionate to magnetite and iron below 575°C). After reduction, nanosize CaO particles should be on the surface of the ex-wüstite catalyst and contribute to activate dinitrogen — due to their basic nature — in addition to the well-known role of potassium. It is expected that a careful optimization of both size and distribution of such CaO nanoparticles can further increase the already existing considerable gap between wüstite and magnetite catalysts.

The ammonia synthesis catalyst is the most stable catalyst among all industrial catalysts. Its structure is almost unchanged during work for about 20 years in the porous and slashing reaction conditions at high-pressure and temperature. Many models have been proposed to explain such a stable active surface structure. Arabczyk *et al.*[25] suggested a double-layer model for fused iron ammonia synthesis catalyst. It is assumed that the iron surface is covered with a double layer due to wetting by promoter oxides. The first sublayer in the direct vicinity of the iron atoms is filled with oxygen atoms and the free adsorption sites are in this sublayer. The second sublayer located on the first one is filled with promoter atoms. The

number of oxygen atoms and free adsorption sites are determined by the nature of the promoter. Every atom of alkali metal needs one oxygen atom to be stable on the iron surface under ammonia synthesis conditions; one atom of alkali earth element needs two oxygen atoms; one atom of aluminum needs three. The number of the free adsorption sites is directly related to the number of oxygen atoms on the surface. The more oxygen atoms on the iron surface, the less free adsorption sites are available for dinitrogen adsorption. The surface area of the iron catalyst is also dependent on the number of oxygen atoms on the surface. Therefore, elements such as Ca and Al, which need a high concentration of oxygen on the surface, lead to the formation of the catalyst exhibiting the highest surface area. Thus, the surface structure is caused by the interaction between iron, promoters and oxygen atoms. The structure of the iron catalyst changes after the activation and nitridation of bulk phase. This change is very important to realize the function of catalyst.[26] Among the surface, the iron bulk, and the spacers located between the iron crystallites the thermodynamic equilibrium are maintained. On the basis of this model, an interpretation of some properties of the iron catalyst is presented.

A quantitative analysis has shown[24] that 1% of the geometric iron surface participates in the activation of nitrogen on an industrial catalyst. The remaining adsorption sites are filled from these centers by surface diffusion. Thus, the duality of plates and blocks has a functional equivalent as nitrogen activation and storage regions, which coincides quantitatively with theoretical and experimental findings.

For the still industrially important iron catalyst, a good picture of its structure and its activity as an accelerator for the dissociation of dinitrogen, which is the kinetically determining step, can be drawn. Results from pioneering experiments on iron crystals[27] at lower pressures were quantitatively corroborated by high-pressure experiments.[28] This apparent lack of a pressure gap allowed the theoretical description of the nitrogen activation and therefore the quantitative extrapolation of the kinetics from ultra-high vacuum (UHV) conditions to industrial conditions. Furthermore, studies on single crystals[27] showed that the lack of a pressure gap only occurred at low nitrogen coverage, whereas at high nitrogen coverage a considerable deviation from the theoretical adsorption behavior is caused by the formation of a subnitride surface phase.

Under industrial conditions the nitrogen coverage is low[29] (hence the theoretical description applies), but in the bulk phase the catalyst is nitrified, which causes a distorted crystal structure. Through suitable pretreatments, this structure has also been included in model experiment, however, it was not further characterized. After the required activation — a process now well understood — the industrial catalyst shows a distorted iron structure that has been demonstrated to be essential for its catalytic function. This distortion manifests itself as metastable plates in the (111) orientation, which are formed by the topotactic reduction of the magnetite precursor at extremely mild conditions, but also by stress states in the regularly orientated (100) regions of the ammonia iron. These stress states participate in the structure-sensitive activation of nitrogen, which is particularly efficient on the (111) faces, but also on different faces and on strain-induced step defects. These recent theoretical[30] and experimental[31] results require that the discussion about the role of the promoters (especially the potassium), which is normally considered as closed, is reopened.

Therefore, there is practically no other relevant reaction that leads to such a close interconnection among theory, model catalysis, and experiment as the high-pressure ammonia synthesis by Haber and Bosch.[16] This statement is valid not only for the iron system but also for the ruthenium system and, in foreseeable future, for the Co–Mo–N alloy system. The time frame for the acquirement of knowledge is truly remarkable. It took decades for the case of the iron system but just 10 years for the ruthenium system, and it will take only a few years for the case of the alloy system. This is despite the catalyst getting more complex both chemically and structurally. Analysis of the reasons leading to this story of success reveals the factors that include the persuasiveness of the pioneering experiments that persists even 30 years later, the enormous maturation of experimental and theoretical methods, and the increased precision of the world-wide research efforts.

As well as being of high industrial relevance, the catalytic ammonia synthesis is also a key reaction for creating new life and a prototypical model reaction[32] that helps to gain a fundamental understanding of catalysis in general and therefore of considerable scientific and cultural importance. It is mainly this reason that drives the research in ammonia synthesis forward, especially since evidence for a knowledge-based increase of a catalyst would have a strong signaling effect on other fields of catalysis research. Except for the self-development of ammonia synthesis catalyst, catalytic ammonia synthesis is still an ideal model reaction for research of heterogeneous catalysis.

10.1.2 *Exploration of non-iron and alloy catalysts*

Since 1970s, the scientists began to look for a new non-iron metallic catalyst to replace iron-based catalyst, and studied widely the element which has activity for activation of N_2 in Periodic Table,[33] because they did not expect to further increase the activity of conventional Fe_3O_4-based catalyst.

The catalytic activities of single metal catalysts including both the hard and easily reduced metals in ammonia synthesis reaction had systemically been studied by Haber *et al.* These early results showed that Os and Fe elements have higher activities for ammonia synthesis while Ru has the highest activity for NH_3 decomposition reaction under the reaction conditions reported by Haber. Ru is the most active metal among potassium-promoted transition metals supported on active carbon (588 K and 80 kPa). It is commonly considered that Fe, Ru and Os are most active elements for ammonia synthesis, ammonia decomposition and N_2 isotope equilibrium reactions, since they have moderate metal-N_2 binding energies. The radioactive element of Tc, a product derived from fission reaction of U element, is one of most active elements for ammonia synthesis catalysts. Ru-based catalyst was developed under these backgrounds.

Based on the research results of monometallic catalysts, scientists also studied on bimetallic catalysts for N_2 activation. They realized that the adsorption energy of N_2 determines the catalysts properties. Under specific reaction conditions, it can estimate adsorption energy of N_2 on catalyst. The catalytic efficiency of the elements for the synthesis and decomposition of ammonia was correlated with the chemisorption energy of nitrogen. An inverted parabolic function (volcano curve) was obtained by Ozaki *et al.*,[34] in which iron, ruthenium, and osmium mark the top of the volcano.

The idea of optimizing the performance of the elements on the curve *via* the formation of alloys of the elements which react either too slowly or too vigorously with nitrogen, was proposed. The formation of metal subnitrides and their effectiveness as inhibitors for the decomposition of ammonia was described about 30 years ago. Thus, the routes for development were set out a long time ago. Not surprisingly, an efficient non-ruthenium catalyst on the basis of cobalt–molybdenum nitride was recently presented, which can be regarded as the current climax of a systematically but empirically justified development.[35−39] The research relevant to alloy catalysts accumulates large number of knowledge and experience. Nørskov *et al.*[40] proposed a more scientific and effective theory, i.e., interpolation in the Periodic Table, for designing bimetallic catalysts based on Ozaki's volcano-curve. It is a rational catalyst development strategy that can be developed on the basis of simple, physically motivated concepts, and use the ammonia synthesis reaction to illustrate the approach, but the general principles should be broadly applicable. The starting point is the volcano-shaped relation between the ammonia synthesis activity of different catalysts and their nitrogen adsorption energy as shown in Fig. 10.1. This curve describes the activity trends of some transition metals at different ammonia partial pressures. The other unlabeled metals can be obtained by interpolation or extrapolation method according to their positions in the Periodic Table. The curve shows (in complete agreement with experimental evidence) that Ru and Os are the best catalysts among the pure metals.[39]

The volcano shape of the plot in Fig. 10.1 implies that there is an optimum for the nitrogen adsorption energy. This optimum reflects a compromise between two mutually opposing ways of achieving a high activity: A small activation barrier for N_2 dissociation and a surface with low coverage of adsorbed atomic nitrogen during ammonia synthesis. This requires a strong and a weak N-surface interaction,

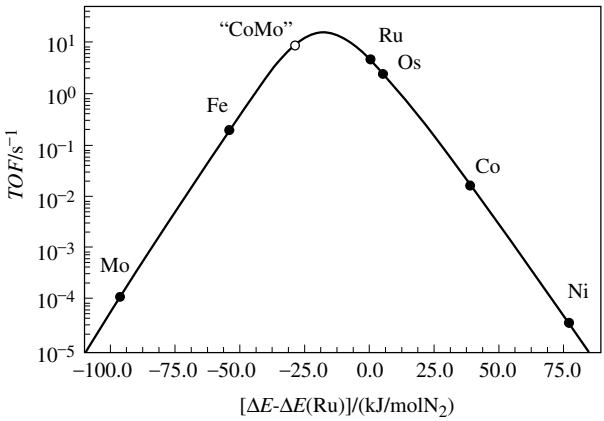


Fig. 10.1 Calculated turnover frequencies for ammonia synthesis as a function of the adsorption energy of nitrogen.

The synthesis conditions are 400°C, 50 bar, gas composition (H_2:N_2) 3:1 containing 5% NH_3. The numbers are obtained by combining a micro-kinetic model describing ammonia synthesis rates with the linear relation existing between the potential energy and the activation energy for N_2 dissociation. The known entropy barrier for N_2 dissociation and the effect of adding electropositive promoters such as K and Cs have been taken into account in the model.[40]

Table 10.2 Comparison of iron-based and Ru-based catalyst

Catalyst compositions	Source of precursor	Cost of catalysts	Operating conditions			Energy Consumption/ (GJ/t)
			Temperature/°C	Pressure/MPa	H_2/N_2	
Fe–K_2O–Al_2O_3–CaO	Abundant	Inexpensive	350–525 (broad)	10–30	2–3	∼28
Ru–K_2O –BaO/AC	Rare	Very costly	≤450 (narrow)	≤10	≤2	∼27

respectively. In conditions relevant to industrial processes, Nørskov reaches closest to the optimum by using Ru or Os as catalysts. However, these metals are very expensive and thus less commercially attractive compared to the third-best catalyst, Fe.[40] In addition, these catalysts do not exhibit obvious advantages for saving energy (Table 10.2). Although the Ru/C catalyst prepared by using Ru carbonyl as precursor and activated carbon containing graphite as support has high activity and has been industrialized, the graphite is unstable under the condition of ammonia synthesis thermodynamically. Moreover, Ru catalyzes the hydrogenation of carbon to form methane. Ba can inhibit the formation of methane, but it cannot totally avoid (methane's formation). This conclusion was drawn by Haber in the early 20th century. At that time (March, 1909), Haber found that Os exhibits good activity for ammonia synthesis. BASF Company purchased all of Os (total about 100 kg) from all over the world. However, Os (Ru) is rare in the earth and was finally replaced by the cheaper Fe catalyst.[41] Therefore, Ru-based catalyst only has theoretical meaning that is bigger than applied meaning. It is necessary to explore a more effective and cheaper catalyst than Ru-based catalyst for industry.

A rational approach could be to construct a surface (active sites) with the desired intermediate nitrogen interaction energy by combining two metals: One with too high adsorption energy and one with too low adsorption energy. As indicated in Fig. 10.1, a combination of Mo (which binds N too strongly) with Co (which binds N too weakly) should be close to optimum. The activities of Co–Mo–N catalysts are closer to top of volcano-shaped curve than Ru and Os. Figure 10.2 shows the measured TOF values for promoted Ru, Co_3Mo_3N and Fe catalysts. Co–Mo catalyst has higher activity than that of constituents, and even higher than those of Fe and Ru at low ammonia concentration.

Figure 10.3 shows transition-state energies for N_2 dissociation and nitrogen adsorption energies on Co, Mo and $Co_{0.5}Mo_{0.5}$ surface. The energy is shown as function of the relative number of Co neighbors in the active sites. For atomic N the most stable site is three-fold site with one Co and two Mo neighbors, corresponding to $(\mathrm{Co}/\ (\mathrm{Co}+\mathrm{Mo}) = 0.33)$. On the other hand, five metallic atoms are involved for transition state. They are two Co and three Mo atoms, giving a value of $(\mathrm{Co}/(\mathrm{Co}+\mathrm{Mo}) = 0.4)$. It appears that alloy's barrier and nitrogen binding energy is intermediate between above two values. The other sites have other Co concentrations and thus other adsorptions and barriers will coexist. In fact, the distribution of binding energy and barrier exist for a given distribution of sites on the surface of an alloy catalyst.

The results in Fig. 10.3 indicate that activation energies and bond energies are strongly correlated. Different active sites correspond to different points along

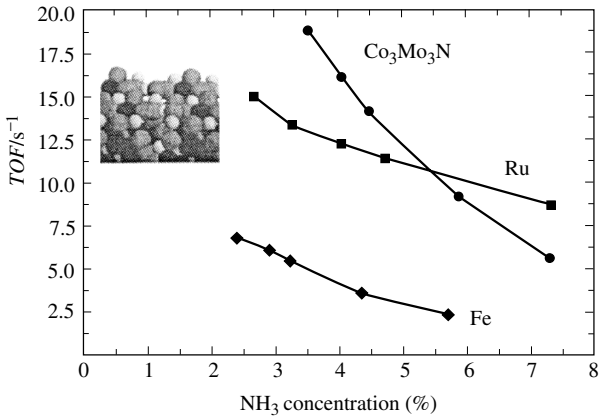


Fig. 10.2 Measured turnover frequencies for promoted Ru, Co_3Mo_3N, and Fe catalysts.
The number of active sites is calculated from the surface areas of the active components, assuming that 1% of the total surface sites ($\times 19\,m^{-2}$) are active for N_2 dissociation. Inset: Surface structure of Co_3Mo_3N showing the existence of mixed Co-Mo sites. Light gray: N; dark gray: Co; black: Mo[40]

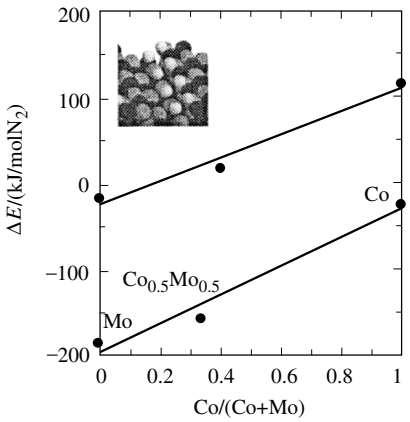


Fig. 10.3 Calculated transition-state energies for N_2 dissociation and nitrogen adsorption energies on Co, $Co_{0.5}Mo_{0.5}$, and Mo close-packed surfaces with a step.
The energies are relative to the situation where the N_2 molecule is far from the surface. The geometry of the surface site and the N_2 molecule at the transition state are shown in the insert (for $Co_{0.5}Mo_{0.5}$). Light gray: N; dark gray: Co; black: Mo[40]

volcano-shaped curve in Fig. 10.1. The points that are close to the maximum will have the highest contribution to measured rates.

We hypothesize this is a general phenomenon: To a first approximation, the interaction energy between an adsorbate and the surface at a mixed site is simply an interpolation between the interaction energies of the individual components. Consequently, other combinations of metals are also expected to have N adsorption energies close to the optimum and thus higher activity than their constituents. The

experimental results of Fe-Ru, Fe-Co alloys[42,43], and ternary nitrides like Ni_2Mo_3N and Co_3Mo_3N shown that to be in consistent with above hypothesis. If the interpolation method can be applied for other reactions, the alloy with bimetallic sites would have higher activity than constitutes when the catalyst activity is a non-linear function of the interaction energy, as for reactions with volcano-shape relationship.

Since the mixed-metal catalysts have interpolation properties, it is very important that both metals have similar numbers on the surface. This is not always the case. Generally, one metal will segregate to the surface because one component strongly binds to the adsorbate on the surface or the bimetallic alloy has its own property. This impact may be inhibited if there is a trend to be ordered in the alloy. As compared with the data listed in Fig. 10.2, the measured alloy catalyst is a ternary nitride with composition of Co_3Mo_3N. Figure 10.2 inserts the (111) face of $Co_3Mo_3^{44}$ indicating the existence of mixed Co-Mo surface sites in the structure of nitride. Microkinetic modeling and isothermal dinitrogen sorption analysis results show that the activation energy and nitrogen-binding energy of Cs/Co_3Mo_3N have intermediate value between those of Co and Mo. Furthermore, adsorption analysis confirms that most nitrogen elements in ternary nitrides do not participate in the reaction. Therefore, the nitrogen atoms in ternary nitride act as inducing agent to required ordering. The small content of nitrogen in the bulk is not believed to significantly affect other properties.[45]

Preparation of ammonia synthesis catalysts by combining metals with high and low nitrogen interaction energies to obtain the desired intermediate interaction strength is an example of a rational approach to catalyst design. Since the nitrogen binding energies on different metals vary monotonically with the position of the metal in the Periodic Table, the present approach is an example of catalyst design by interpolation in the Periodic Table.

R. Kojima *et al.*[46] systematically studied the performances of Co–Mo bimetallic nitrides for ammonia synthesis as shown in Table 10.3. It is seen from Table 10.3 that the Co_3Mo_3N have higher activity, especially, 2% Cs promoted Co_3Mo_3N-Cs2 catalyst has two-fold higher activity than conventional Fe-K_2O-Al_2O_3 catalyst.

Kojima *et al.*[47] also studied the impact of molybdenum nitride (γ-Mo_2N) and molybdenum carbides (α-MoC_{1-x}, β-Mo_2C) as well as the addition of second component (Co, Cs) on the activities and rates of ammonia synthesis. Their orders in ammonia synthesis activity were β-$Mo_2C > \alpha$-$MoC_{1-x} > \gamma$-Mo_2N. The α-MoC_{1-x} is unstable in the condition of ammonia synthesis. The addition of 2% of Cs and 5%

Table 10.3 Comparison of Fe-K_2O-Al_2O_3 and MoN catalysts (673 K, 0.1 MPa)

Catalyst	Reaction rates/ (μmol·h^{-1}·g^{-1})	Surface area/ (m^2·g^{-1})	Specific activity/ (μmol·h^{-1}·m^{-2})
Fe–K_2O–Al_2O_3	330	14	24
Co_3Mo_3N	652	21	31
Co_3Mo_3N–Cs2	986	16	62
Co_3Mo_3N–Cs10	586	10	59
Co_3Mo_3N–K30	364	8	46
Ni–Mo–N	275	20	14
Fe–Mo–N	143	7	20
Mo_2N	68	121	1

of Co could increase its activity and rate. The β-Mo_2C is as active as the iron-based catalyst with two promoters, however, its rates and specific activity decreased upon adding of 5% of Co. The β-Mo_2C catalyst is prepared by calcimining MoO_3 precursor at 973 K and held for 2 h with CH_4 and H_2 mixed flow.

The promoted Cs/Co_3Mo_3N catalyst has desired activity, while its surface area has not attained expected value. Even if the value were to be reached, it would be reasonable to suspect whether this kind of catalyst can compete with the conventional iron catalyst, because of the high prices of Co and Mo currently.

Experiments carried out by Ertl[48] and Somorjai[49] were designed to enhance the understanding of the ammonia synthesis and allow a quantitative theoretical description of this reaction. Two predictions for the future development of this subject resulted from this work. First of all a quantitative description of the volcano curve for the catalytic efficiency of the elements in the ammonia synthesis could be given, which was based on fundamental knowledge of the reaction path and the theory of the transition state. This description allowed a specific prediction of the catalytic efficiency of alloy systems with extreme properties on the volcano curve. The studies on the Co–Mo–N system, which were carried out almost simultaneously but with totally different motivation, led to similar results. They confirm in a remarkable way, how theory and chemical intuition are becoming equally useful with respect to the choice of research topics. Disregarding the "old empirical knowledge," one could speak of a remarkable example of "designing" a catalytic system, based on pure theoretical knowledge about the process of the target reaction. Despite these significant advances, this good catalytic behavior is only achieved at relative small synthesis rates; there are also significant stability problems. Much more research effort is needed here. Ru and Mo-based catalysts are outstanding among all non-iron catalysts. Ru-based catalyst has a long history of development and is industrialized.[50] The study on the supports of carbon and alkaline metal has reached a high level. These systems are divided as a new generation of ammonia synthesis catalyst, and their speculations are fundamental for researching of basic theory. The discovery of a highly effective Ru-free Co-Mo-N catalyst is recognized as a new summit for fundamental research. The interpolation method in the Periodic Table is one of the more effective and scientific methods for designing of alloy catalyst, and this theory can be widely applied. Therefore, the development of new alloy and non-iron catalysts will drive the research of heterogeneous catalytic science forward.

10.1.3 *Exploration of other non-iron catalyst for ammonia synthesis*

In the early research stages of ammonia synthesis catalyst, Mittasch *et al.* studied almost all metal elements and their bimetallic alloy in the Periodic Table. Several metals have no or less catalytic functions themselves. However, the addition of some promoter could increase their activities.[51] The addition of a secondary metal into Fe, Mo, W, Co, Ni, Pd, Pt, Os, Mn enhances their activities. The different ratio between two metals leads to a different activity. It can be concluded from these results that the addition of metals in VIII or VI groups favors enhancing of iron-based catalyst activity. For example,[52] Fe–Mo (1:1) catalyst has high activity. If the Mo content is less than 80%, the activity decreases after running for a long-time. These catalysts are prepared by calcinations of metal nitrates and ammonium molybdate

mixture in N_2–H_2 flowing. The adsorption content of N_2 on these catalysts increases with increasing of Mo content, however, the adsorbed N_2 molecules desorbed subsequently during the reaction resulting in lower activity. X-ray analysis indicates that the Mo-(Co-Ni-Fe) mixed crystals is formed accompanied with desorption of N_2. It seems that the active component is Mo for this system, and the catalytic functions of Fe or Mo were lost when accompanying the formation of mixed crystals. For other Mo-Metal alloys, Cu acts as a simple diluter only. Unlike Cr and W, Mn favors to activity.

The Researchers of Zhejiang College of Chemical Engineering[53] studied the properties of Fe–Cu, Fe–Mn, Fe–Mo, Mg–Ni and Fe–Co bimetallic catalysts at high pressure condition. The alloy effect of Fe–Co and Fe–Ni has been studied in detail.[54] Ni decreases activities of Fe-based catalyst.[55,56] The addition of Co on a conventional iron catalyst can enhance the promotion effect. These catalysts are prepared by combusting the Fe–Co alloy in oxygen followed with addition of promoters.[57] The experimental data showed that Fe–Co has high activity. The ammonia concentration is 26.25% in outlet of reactor, which is 1% higher than iron catalyst at condition of 30 MPa, 30,000 h^{-1} and 450°C. Fe–Co catalyst is prepared by fusion of Co_2O_3, Al_2O_3, KNO_3, $CaCO_3$ and magnetite. It could also be prepared by fusion of Fe–Co alloy containing 10%–17% of Co and suitable amount of promoters. The experimental data showed that the Fe–Co catalyst has the best activity when the Al_2O_3 content is less than 3%.[58] The curve described the relationship between Co content and specific rate; this has two summits, one locates at 15% of Co and another is around 50% of Co.[59] Co itself has low activity for ammonia synthesis; however, it could significantly increase activities of doubly promoted iron catalyst as a promoter. There are many research reports relevant to the promotion effect of transition metals in groups of iron or neighbored iron, recently. The mixed catalysts including Fe–W, Fe–Ni, Co–Ni, Os–Pt, Ru–Pt, Fe–Cu, Bi–Sn, An–Pt have been studied.[48]

Fe is a surface active material in Fe–W alloy. Fe–W catalyst is prepared by simultaneous agglomeration of W and Fe from a solution containing H_2WO_4 and Fe $(OH)_3$.[60] NH_4NO_3 is used as the agglomerating agent. The precipitate is dried at 80°C–90°C. The resulting amorphous solid is grinded into powder with size of 0.5 mm–1 mm and reduced in N_2–H_2 (1:3) flowing. The yield of ammonia and the activity of Fe–W alloy increase with increasing of W content until W reached 60%. The activity of Fe–W catalyst is higher than that of pure iron catalyst. It has been reported that deposition of one surface active material on another one with both surface activity and catalytic activity can increase previous one's catalytic activity because its surface area is enhanced.

Mo and W have higher affinities for nitrogen and fusing points than Fe. The addition of Mo and W into Fe catalyst leads to hard hydrogenation of chemisorbed nitrogen because nitrogen would adsorb on Mo and W with high bond energies. However, the existence of alkaline metal (potassium) would decrease N-Metal bond energy. When the contents of Mo and W are some ratios, the bond energy could approach an optimum value where chemisorption of N_2 and hydrogenation of chemisorbed N_2 could occur at comparable rates which would increase activity and heat-resisting properties. However, the preparation procedure is essential for catalyst property. The catalyst prepared by concurrent addition of calcium salt, tungsten oxide, molybdenum oxide and promoters with addition sequence from acidity to basic has best activity.[61]

Mn–Fe alloy catalysts with 32%–40% of Mn have high activities. The addition of 3%–7% of RuO_2 into Fe-based catalyst containing cobalt ferrite (25%–35% of Co), magnesium ferrite (20%–25% of Mg), K_2O (0.5%–2%) and iron oxide increases activities and heat-resistant properties of catalysts.[62]

Transition metals can be activated by alloys with positive charges. In contrast to activity of Ru as per area, Raney Ru catalyst prepared by Al–Ru alloy has higher activity than pure Ru catalyst. When added with metallic K, this catalyst has higher activity, and it also has activity even at 373 K.[63] Raney Ru is also very active by using $CsNO_3$ as promoter.[64,65]

Rare earth-transition metals intermetallic compounds such as $CeCo_3$, $CeCo_5$, $CeRu_2$, $CoFe_2$ have higher activities than doubly promoted Fe-based catalyst (condition: One BET unit, 5 MPa, 873 K), although actual activity is very low as their surface areas are small. Table 10.4 shows the reaction rates after recalculation at 5 MPa and 588 K. Intermetallic compounds of Ce with Fe, Co and Ru have higher activities. Pr–Co intermetallic compounds and $ErFe_3$ are also active. $CdFe_3$, $GdFe_{17}$, $ThFe_{17}$, $HoFe_2$, $TbMn_2$, $CeCu_5$, $LaCu_5$, Y_6Mn_2, Tb_6Mn_{23}, $CeNi_5$, $CeCo_5$, CeIn, $CoOs_2$, $CeRe_2$, $HoCo_2$, $DyCo_3$ have lower activities than those in Table 10.4. During the reaction, these intermetallic compounds decompose to highly dispersed transition metals and cerous nitrate.[66,67] The observed high specific activities reflect the rare earth elements that donate electron to active transition metals.[66] *In situ* XRD technique is used to characterize $CeRu_2$, $CeCo_2$ and $CeFe_2$. The results indicate that these intermetallic compounds convert to hydride of cerium (CeH_{2+x}) and transition metals under the reaction condition (50 bar, 450°C–550°C). These phases are considered active components for reactions, however, they are sensitive to oxygen containing compounds (CO, air, H_2O) and form inactive CeO_2/transition metals.

Table 10.4 Ammonia synthesis rates of rare earth metals intermetallic compounds (5 MPa and $S_V = 1,20,000\,h^{-1}$)

Catalyst[a]	Surface area/ (m^2/g)	Rates(588K)/ [m mol NH_3/(g·h)]	Activation energy/ (kcal/mol)
Fe–Al_2O_3–K_2O[b]	5.21	3.50	20.5
$CeFe_2$	0.45	0.41	13.2
Ce_2Fe_{17}	—	1.01	8.0
$TbFe_{17}$	—	0.04	23.0
$DyFe_3$	—	0.10	7.4
$HoFe_3$	—	0.02	18.6
$ErFe_3$	—	1.24	(4.3)
$ThFe_3$	0.60	0.36	10.6
$CeRu_2$	0.33	1.41	10.3
$Ce_{24}Co_{11}$	—	1.06	5.6
$CeCo_2$	0.61	1.45	9.2
$CeCo_3$	0.12	1.33	8.7
$CeCo_7$	0.11	0.30	13.6
$CeCo_5$	0.21	0.73	9.3
$PrCo_2$	0.38	0.13	14.4
$PrCo_3$	0.12	0.17	11.9
$PrCo_5$	0.20	0.51	11.9

[a]Catalyst weight = 3.3 g, volume = 1 cm^3; [b]catalyst 416 (Fe–0.97 % Al_2O_3–0.65 % K_2O).

The Ti–Fe alloy comprising Ti–Fe alloy and the surface phase of Fe, TiN and TiO_x is an active catalyst for ammonia synthesis. However, Ti–Ru is not good for ammonia synthesis because its surface is covered with TiN and TiO_2.[68] According to this, the alloy will not yield positive effect in increasing the activity of catalyst.

Moreover, researchers have widely studied the iron-based catalyst prepared by non-fusing method. For example, one K–C–Fe/Al_2O_3 catalyst was prepared by co-precipitation of $Al(NO_3)_3$ and $Fe(NO_3)_3$ followed by drying at 115°C for 24 h. Obtained powders were calcined at 450°C and holding for 4 h, and then reduced in mixed H_2–N_2 (3:1) at 475°C for 24 h to obtain Fe/Al_2O_3. The precursor of Fe–C/Al_2O_3 was prepared by the carburization of the Fe/Al_2O_3 by n-hexane at 475°C. This precursor was sprayed by metallic potassium for 3 h under 350°C and pressure of 6 Pa to obtain K–C–Fe/Al_2O_3 catalyst. The reduction, carburization and activation processes were carried out in the same flowing reactor. The activity of K–C–Fe/Al_2O_3 catalyst is three-fold higher than those of a commercial catalyst at condition of 450°C, atmospheric pressure and 5,000 h^{-1} (see Table 10.5).[69]

Morawski, Lendzion Bieluń, Kaklucki *et al.*[70] also reported a new preparation method for Fe/C/K catalyst: (1) the mixture of polymer (PAN), Fe $(NO_3)_3$ and KNO_3 was dissolved in DME solution; (2) precursor of Fe $(NO_3)_3$/PAN/KNO_3 was dried and crushed into pieces; (3) precursor of Fe $(NO_3)_3$/PAN/KNO_3 was carbonized; (4) *in situ* reduction before measuring of activity. Table 10.6 shows various properties (e.g. BET surface area, average pore size, size of α — Fe crystallite) and the activities measured at 673 K, atmospheric pressure and 1,000 h^{-1} of the catalysts with different chemical components. It is seen from in Table 10.6 that this preparation method increases surface area of catalysts.

Jacobsen, Blosen, Seichst J *et al.*[71] introduced a new catalyst for ammonia synthesis. This catalyst is a ternary compound consisting of metals in VIII and VIB

Table 10.5 Chemical composition and activities of K-C-Fe/Al_2O_3 ammonia synthesis catalysts

Catalyst	Chemical composition				Activity (vol.)/ % NH_3
	Fe	K	$A1_2O_3$	C①	
K–C–Fe(3)/$A1_2O_3$	11.09	48.20	38.46	2.25	0.18
K–C–Fe(7)/$A1_2O_3$	33.51	47.57	15.90	3.02	0.48
Commercial iron catalyst	—	—	—	—	0.18

Conditions: T = 350°C, S_V = 5, 000 $h^{-1}$and atmospheric pressure. ① The remnant.

Table 10.6 Surface area, average pore diameter, size of α — Fe and activity of Fe-C-K catalyst

Catalyst	Surface area/ (m^2/g)	Average pore diameter/ nm	α — Fe crystallite size/nm	Activity (volume fraction) % NH_3
E_1	34.9	1.67	69.6	0.069
E_2	24.44	1.57	19.1	0.073
E_3	22.9	1.54	14.5	0.098
Industrial catalyst	9.1	6.46	22	0.079

groups. Under the condition of ammonia synthesis, the formula of active catalyst was $M'_xM''_yN$, M' was metals in VIB group, M'' represented metal in VIII group, x, y were fractions between 1 and 10. The maximum yield of ammonia of Cs–Co–Mo catalyst reported in the patent is 680 $ml{\cdot}h^{-1}{\cdot}g^{-1}$ at conditions of 400°C, 10 MPa, where ammonia volume fraction in inlet gas is 4.5%, H_2/N_2 ratio is 3.

Liu *et al.* reported an ammonia synthesis catalyst prepared by using complex of tri-iron formic acid as precursor. The testing results showed that it had high activity.[72]

Zhu[73] at Zhejiang University studied on AB_5-type metallic hydride (e.g. $LaNi_5H_6$). He observed that AB_5-type catalyst shows high activity for ammonia synthesis at room temperature. The synthesis rate is 0.5 ml $NH_3{\cdot}g^{-1}{\cdot}h^{-1}$, corresponding to the activity of various supported and promoted Ru-based catalysts at 300°C. However, the surface area of AB_5 catalyst is lower by several orders of magnitude than those of Ru-based catalysts, which limited its application. Unlike conventional Fe-based and new Ru-based catalysts, AB_5-type catalyst could activate both H_2 and N_2 molecules, resulting in their high activity.

10.1.4 *Non-crystal catalyst*

Currently, ultra fine and non-crystal alloys are regarded as one of the new materials. Because of their great application potential and various unique properties such as excellent and unusual physical, chemical and mechanical properties as compared with metallic materials, the non-crystal materials attract much research interest. As one of new catalysts, non-crystal materials have lots of advantages. First, the chemical component of amorphous alloy can be adjusted in a wide range which is favorable to adjust their electrical properties. By continuously adjusting their electrical properties, it can get suitable active centers which are impossible for crystal phase. Second, it eliminates internal diffusion influence that inherently existed in conventional heterogeneous catalysts, because of their non-porous surfaces. The diffusion-limitation problem does not affect surface reaction at all. Third, amorphous materials have isotropy and do not have crystal interface, stacking fault and segregation. Therefore, their monophasic properties lead to uniform distribution of catalytic active centers in single form in a homogeneous chemical environment. Fourth, their surfaces are highly unsaturated and have high surface energies, reflecting that they are highly coordinated unsaturated sites with high concentration. Thus, the catalytic activity and selectivity of amorphous catalysts are better than corresponding crystal catalysts.

The research of non-crystal alloy has been mainly focused on transition metals like Ni-series metals. There are few researching reports relevant to another important transition metal: α-Fe-series. Currently, some references mentioned that Fe–P non-crystal alloy showed high activity for HDS and HDN reactions of crude oil. If a good catalyst can be developed for wide application in the petroleum industry, it would carry great economical value. It is also well known that Fe-based catalyst has been widely applied in the industry, but the problem of rigorous reaction condition has not been solved well. The application of new Fe-based non-crystal catalysts for ammonia synthesis is expected to solve this problem.

The current characterization instrument can only obtain some statistical information of non-crystal alloy, which limits the research and their development. It is

impossible to collect all structural information by experiments. Therefore, it should use computers to simulate the non-crystal structure. Some special properties like catalytic, magnetic, electrical and corrosion-resisting properties of non-crystal materials are closely relevant to material electrical structure. To explain and speculate the properties of non-crystal materials, the full understanding of material electrical structure by theoretical studying is required. For most metal and metallic alloys, much information can be acquired by calculation using theory of energy band. However, this theory is not suitable for non-crystal materials because of their structures of long-range disorder but short-range order. It is difficult to get effective and true electrical structures of non-crystal materials. Due to their metastable structure, it is also unpractical to create a precise model for non-crystal alloys in order to calculate quantum chemistry. As Messmer said, the pathway is still open for collecting useful information by using practical methods instead of discovering of general theories. This so-called practical method focuses on some local atomic environment in solid. It uses suitable model to simulate partial structure of non-crystal alloy and does quantum-chemistry calculation to obtain detailed information of some electrical structure. This method has been successfully used for chemical adsorption, atomic bonding, magnetic property and other knowledge related electron-effect. Fudan University and Anshan University of Technology have already carried out valuable work.

Figure 10.4 shows experimental equipment for preparation of $Fe_{90}Zr_{10}$ non-crystal alloy.[74] The non-crystal $Fe_{90}Zr_{10}$ ribbon is activated in syngas. The surface morphology, surface chemical states and surface element distribution on free and dull sides before and after activation of $Fe_{90}Zr_{10}$ alloy can be studied by using AES, XPS, SAM, SEM techniques and integrating *in situ* argon ions bombing. The results show that Zr element enriched on free-side of original ribbon, while Fe element mainly distributed on dull side initially. Iron oxide is Fe_3O_4 and Fe_2O_3 on free and dull sides, respectively. After activation, the concentration of Zr on free-side decreases and on dull side increases. Iron oxide is totally reduced on dull

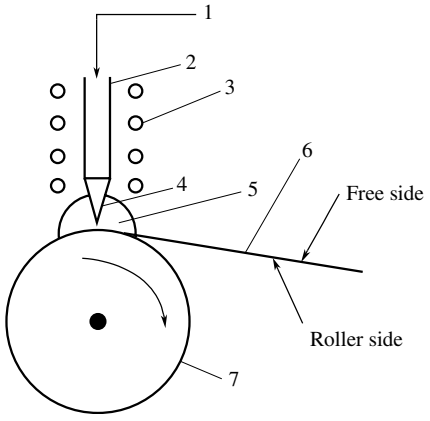


Fig. 10.4 Schematic diagram of preparation of non-crystal ribbon.
1 — Ar gas; 2 — Quartz crucible; 3 — High frequency heater; 4 — Alloy liquid; 5 — Ar protective area; 6 — Non-crystal ribbon; 7 — Copper roller

side. The ribbon bulk undergoes crystallization after activation and forms lots of honeycomb-shaped structure and ring-like cracks on surface.

10.2 New Catalytic Technique for Ammonia Synthesis

10.2.1 *Progress in ammonia synthesis at normal pressure and temperature*

Although the standard equilibrium constant for ammonia synthesis reaction at 298 K is 6.8×10^5, the reaction rate is not detectable. To increase the reaction rate and activate catalyst at optimal temperature, the industrial synthesis ammonia is carried out at 400°C–500°C. Because of the thermodynamic limitation, the standard equilibrium constant is 1×10^{-5} at this temperature which leads to low conversion. In order to enhance conversion, it is common to introduce high pressure and increase concentration of N_2 to move the equilibrium to right. However, the conversion of ammonia synthesis in one attempt is 10%–15% only.

Therefore, it is a new challenge to speculate ammonia synthesis at normal temperature and pressure. Fixed nitrogen is critical for life and development of human being. Therefore, scientists are engaged in pursuing the target of ammonia synthesis at normal temperature and pressure and have made many achievements.

It is a key problem of how to activate nitrogen molecules and how to supply energy in order to fix and come down from dissociative dinitrogen in air and to realize ammonia synthesis at normal temperature and pressure.

(1) Activation of nitrogen molecules. Nitrogen molecule is one of the most stable but the simplest molecules in the nature (CO_2, H_2O, CH_4, N_2 and O_2). N≡N ternary-bind is also one of the most stable chemical bonds (N≡N, C≡N, C≡C, C≡O) (Table 10.7).

The electron arrangement of nitrogen molecule is $(1s)^2(1s^*)^2(2s)^2(2s^*)^2(2p)^4(2p)^2$, and electron structure is $(1\sigma)^2(1\sigma^*)^2(2\sigma)^2(2\sigma^*)^2(1\pi)^2(3\sigma)^2$ where the bonding orbital $(1\sigma)^2$ and antibonding orbital $(1\sigma^*)^2$, and $(2\sigma)^2$ and $(2\sigma^*)^2$ can be almost offset, respectively. In fact, three pairs of electrons in $(1\pi)^4$ and $(3\sigma)^2$ form N≡N bond where one is σ-bond and two are π-bonds. The dissociation energy for N≡N bond is 962 kJ·mol^{-1} which requires extreme high energy to break this bond that is the highest among all diatomic molecules. At the same time, the highest occupied orbits $(1\pi)^2$ and $(3\sigma)^2$ in dinitrogen molecule have low energies, they are −15.59 eV and −16.73 eV, respectively. It is hard to capture one electron from dinitrogen molecule. On the other hand, the lowest empty orbit $(1\pi^*)$ has high energy

Table 10.7 Bonding energy/(kJ·mol^{-1})

Bond type	Bonding energy	Difference of bonding energy, Δ	Bond type	Bonding energy	Difference of bonding energy, Δ	Bond type	Bonding energy	Difference of bonding energy, Δ
C–C	335		C–N	301		N–N	155	
C=C	607	272	C=N	615	314	N=N	419	264
C≡C	829	222	C≡N	879	264	N≡N	962	523

(8.17 eV) and it is not easy to accept exotic electron. Therefore, N_2 molecule is both hard to accept or lose electron and has very high stabilities.[75] Activating nitrogen is essential for fixing nitrogen. The activation of nitrogen molecule becomes one of model molecule in the research field of chemistry and catalysis.

The activation of dinitrogen molecule is a process to break or weaken the N≡N bond. There are three methods to be used to activate nitrogen molecule: (1) Adsorbed activation of catalyst; (2) Electron donation activation by using dinitrogen complex; (3) Coordinated activation by biologic nitrogenase.

Chemical fixing nitrogen is a process that dinitrogen converse to compounds containing nitrogen element *via* chemical reaction. This reaction is a reversible reaction in the presence of catalysts with multi-components. The adsorbed activation of catalyst is that dissociative dinitrogen molecules in air are first adsorbed on the surface of suitable catalyst, and the subsequent transformation of physical adsorption to chemical adsorption weakens the N≡N bond. This is an activation method used by Haber–Bosch process for ammonia synthesis, and it is a research emphasizing its industrial application. The further effort direction for Haber–Bosch process is to exploit a new and highly efficient catalyst for ammonia synthesis at low-temperature. The catalyst working at low-temperature can markedly increase formation rate of ammonia at low-temperature, which can not only can avoid the negative effect of high-temperature on reaction equilibrium conversion, but also can decrease the consumption of energy.[76]

The chemical activation for dinitrogen molecule can be divided into three different approaches.

A. Reduction method:This method donates electron to dinitrogen by reducing agent. Metallic Li can react with dinitrogen to form Li_3N at normal temperature. Catalytic synthesis ammonia belongs to reduction method. It is a sole chemical method for nitrogen-fixing in industry.
B. Oxidation method: This method captures electron from dinitrogen by oxidizing agent. No oxidizing agent is strong enough to oxidize dinitrogen at conventional condition because the first ionization power of dinitrogen is very high. Even fluorine (F_2) which is the most active molecule does also not react with nitrogen.
C. Explode method: This uses non-natural conditions such as plasma and high-voltage discharge to excite the dinitrogen molecule from fundamental state to high energy state, and indeed makes its bond disconnect to convert to atoms or ions of nitrogen, and then reacts with other molecules. For example, the electric arc process developed in early 20th century and $CaCN_2$ method developed in 1898 belong to this method. In the former, O_2 directly reacts with N_2 to form NO at high-temperature (3,250°C) generated by electric arc. This NO can be oxidized to NO_2 by air which was absorbed by water to produce nitric acid in 1902. CaO reacts with carbon to form Ca_2C at high-temperature. The subsequent reaction between Ca_2C and N_2 forms $CaCN_2$. Before the First World War, the latter became the principal method for fixing nitrogen. However, these methods consumed electrical energies of 50 kW·h–80 kW·h and 16 kW·h–18 kW·h for fixing 1 kg of nitrogen, respectively. This huge consumption of energy limits their application in the industry. These two techniques had been forsaken after the discovery of catalytic ammonia synthesis technique.[77] Therefore, the catalytic ammonia synthesis technology holds incontestable status in the field of chemical fixing nitrogen.

The dinitrogen complex can donate electron to activate nitrogen. During this process, dinitrogen reacts with transition metals to form dinitrogen complex. The donation of electron from central atom to anti-bonding orbit in nitrogen weakens N≡N bond. Like CO and CN^-, dinitrogen is also an isoelectronic body. Although it has been speculated to form dinitrogen complex long time ago, the first dinitrogen complex, $[Ru(NH_3)_5(N_2)]^{2+}$, was successfully synthesized from hydrazine hydrate and $RuCl_3$ in aqueous solution until 1965 by Allen *et al.*, because N_2 is not only a weak electron-donator, but also has weak ability to accept electron from central atom.[78] Then, they directly synthesized such complex by using N_2 as precursor instead of hydrazine. The success in synthesis of $[Ru\ (NH_3)_5(N_2)]^{2+}$ leads to fast development of dinitrogen activation. More than 300 dinitrogen complexes have been successfully synthesized so far. The length of N≡N bond in dinitrogen complex has been extended from 109.8 pm in free state to 138 pm (N=N bond is 125 pm) or even to 150 pm (N–N bond is 147 pm) ($1\,pm = 10^{-12}\,m$).[79–81] In particular, Laplaza and Commins [82] at MIT found that the use of simple inorganic complex, $Mo(NRAr)_3$, could completely break and convert N≡N bond to complex with N^{3-} species at negative 30°C. This result has contributed to the study on the ammonia synthesis mechanism at normal temperature and pressure. However, how to transfer the ligand of N^{3-} into H^+ to form ammonia and how to regenerate the complex precursor became a new question.[79] Shilov (1971) and Manriquez (1974) synthesized ammonia and/or N_2H_4 by protonation of dinitrogen bridged bimetallic complex.[83] The cis — $[Mo\ (N_2)_2\ (PMe_2Ph)_4]$ and cis — $[W(N_2)_2\ (PMe_2Ph)_4]$ synthesized at normal temperature and under atmospheric pressure, was protonated with methanol solution of sulfuric acid at 20°C in THF solution, and then alkali was added and distillated to obtain ammonia in high yield.[83,84] This reaction could be expressed as following:

$$[M(N_2)_2(PR_3)_4] + H_2SO_4 \xrightarrow{MeOH} 2NH_3 + N_2 + \text{Other products} \tag{10.1}$$

This process is an indirect ammonia synthesis. There are three steps including formation of dinitrogen complex, protonation and eduction of ammonia. This method requires complete destruction of complex, otherwise, the N–N bond cannot be disbanded and an effective synthetic cycle for ammonia cannot be realized. The effective way to solve this problem is to supply extra electron by chemistry or electrochemistry in order to realize controllable break of N–N bond and a synthetic recycle from nitrogen to ammonia.[79,85]

The research results indicate that some unstable dinitrogen complex can transform to ammonia by hydrogenation, however, such cases are few and the yields are low because the activation extent of dinitrogen in complex may not be enough. On the other hand, stable dinitrogen complex cannot be reduced to ammonia.[86,87]

Biological nitrogen fixation is that the azotobacter in organism finishes the adsorption, activation and reaction of dinitrogen synchronously by its special structures in nitrogenase, and converts the nitrogen in air into nitrogenous compounds at normal temperature and pressure.

$$N_2 + 8H^+ + 8e^- + 16MgATP \xrightarrow{\text{Nitrogenase}} 2NH_3 + H_2 + 16MgADP + 16P \tag{10.2}$$

A nitrogenase is a redox enzyme with multi-functions which comprised of MoFe-protein and Fe-protein. The molecular weight of MoFe-protein is about 2,20,000 and it contains two molybdenum atoms, 24–33 iron atoms and 24–27 sulfur atoms. The molecular weight of iron-protein is about 60,000 and it contains four irons and four sulfur atoms. They are very complicated. One possible mechanism of nitrogen fixation is that the MoFe-protein may bind in coordination with one end of dinitrogen molecule. The electron from Fe-S part in the cluster of Fe-protein and the proton from the solution may supply to dinitrogen molecule.

The study on mechanism of nitrogen fixation of nitrogenase started in 1960 when the nitrogenase was first separated from extract of cell.[79] In 1977, Brill separated the Mo-Fe coenzyme with molecular weight of 2,000 from MoFe-protein, unfortunately, it had no activity of nitrogen fixation because the coenzyme might lose the synergistic effect during the transformation of electron and proton.[88] The structure of nitrogenase has been studied for a long time and several theoretic models were proposed.[89, 90] However, partial structure of nitrogenase had been clearly understood in 1992.[91] Biological nitrogen fixation has advantages of moderate operating condition and high conversion (near to 100%). Although people recognized that some biological organics have the ability to fix nitrogen in 1888, no satisfied practical results have been realized so far.[79]

(2) The state of energy. The nitrogen in ammonia comes from air, and hydrogen comes from water. Obviously, water is most ideal hydrogen resource, because it is clean and available in plenty. However, it has to consume energy to separate nitrogen from air and to get hydrogen from water, as well as to convert them into ammonia.

Chapters 1–9 discussed the Haber–Bosch process of nitrogen fixation on iron- or ruthenium-based catalysts which use mineral fuels such as coal, petroleum and natural gas as raw materials. The energies required by nitrogen fixation process are the chemical energies (heat energies) of these mineral fuels. Thus, Haber–Bosch process does not require extra energy theoretically and can provide work to external. For example, it can provide $0.194\,GJ/t_{NH_3}$ of external work during production process when using air, coal and water as raw materials and fuel. However, if it uses directly air and water as raw materials, the theoretical consumption-energy of the production process is $20.31\,GJ/t_{NH_3}$, i.e., 20.31 GJ of energy is required to produce one ton of liquid ammonia although their theoretical consumptions of energy for the product are same $20.11\,GJ/t_{NH_3}$ in two cases (Table 10.8).

In the Haber–Bosch process, the chemical (heat) energy of mineral fuel is the sole drive power for ammonia synthesis reaction. But, the process does not concern

Table 10.8 Comparison of theoretical consumption of energy for ammonia synthesis using different materials/(GJ/t_{NH_3})

Raw material	Total reaction equation	ΔH	Theoretical consumption of energy	
			Process	Product
Water, air	$1.5H_2O + 0.641(0.78N_2 + 0.21O_2 + 0.01Ar) \rightarrow NH_3 + 0.885O_2 + 0.0064Ar$	21.26	20.31	20.11
Coal, air, water	$0.885C + 1.5H_2O + 0.641(0.78N_2 + 0.21O_2 + 0.01Ar) \rightarrow NH_3 + 0.885CO_2 + 0.0064Ar$	0.80	−0.194	20.11

other types of energies like photo energy, electrical energy etc and the role of catalyst in transformation of different energies.

We used natural energy such as solar energy, wind energy and hydropower etc in our early lives. About 10,000–20,000 years ago, people acquired heat energy from substances because of the discovery of fire. The invention of cell started the era of electrical power 200 years ago. Subsequently, we moved to the age of nuclear power. All these energies are derived from transformation of chemical energy which materials possess. The transformation of chemical energy to heat energy by burning of fuels is one of the simplest and the oldest ways. In the modern practice of production, it has attracted much attention especially other types of energy transformation such as chemical energy to electrical energy, electrical energy and photo energy to chemical energy. The former is fuel cell and the latter is photo-hydrolysis or electro-hydrolysis of water.

The introduction of electrical, photo and radiation energies into ammonia synthesis process to assist activating dinitrogen or to change reaction pathway also attracts researching interest. If they can be introduced into the nitrogen fixation process, it can not only create some non-spontaneous reaction in thermodynamics on the basis of electrical energy so as to extend the research field of ammonia synthesis quomodo, but can also reduce and break the limitation of conversion of ammonia synthesis caused by thermodynamic equilibrium.

The next section introduces the fundamental theories and application of photocatalysis, electrical-catalysis and biological catalysis in the ammonia synthesis.

10.2.2 *Photocatalysis for ammonia synthesis*

10.2.2.1 *Photocatalytic reaction and photocatalyst*

In 1972, Fujishima and Honda found that water can be split by photo-electrocatalysis decomposition on n-type semiconductor of TiO_2 electrode. This is a milestone for heterogeneous photocatalysis.[93] Plenty of research has been carried in the last 20 years in the areas of physics, chemistry and chemical engineering in order to understand the mechanism of this process and increase the efficiency of TiO_2 photo-catalysis. Previous work was only relevant to the storage and development of new energy.[94,95] Currently, heterogeneous photocatalysis has been widely used in the field of environmental protection as in removal of organic pollutions from the gas and water phases.[96] Furthermore, photo-catalysis is also a natural phenomenon and has been studied widely in the fields of electrical-, photo-, catalytic- and biological chemistry. At the same time, the definitions of photo-catalysis vary with time and research objects have diversification too. The initial definition of photocatalytic reaction is that the catalytic reaction that arose by photo irradiation and the photocatalyst here is actually the photosensitizer. However, the current photocatalyst is not merely a photosensitizer-relevant material. Except for semiconductor catalyst used for photodecomposition of water, there are many other kinds of relevant catalysts, in particular, some homogeneous metal complexes can be used directly as homogeneous catalysts in photocatalysis reaction which discriminates to electrocatalysis. To summarize, the application areas and research objects of photocatalytic reactions and photocatalysts have been extended apparently. As a new technology, the photocatalysis is speculated to be well developed on the basis of the collection of new achievements from other technologies.

Until now, there are many references relevant to electron- and energy-transfer processes occurring in photocatalysis. Many books and reviews can be referred.[97,98] Here, we only emphasis on the unusual property of photocatalysis processes different from common catalysis processes whether heterogeneous system or homogeneous system.

There are various interactions between photos and materials. Photocatalysis reaction is one of them. The catalytic reaction and photochemical reaction can be described by following equations.

$$A \xrightarrow{K} B \tag{10.3}$$

$$A \xrightarrow{h\nu} B \tag{10.4}$$

In catalytic reaction (10.3), the catalyst (K) is defined as the materials that can enhance reaction rate but does not change equilibrium of reaction at definite temperature. From the thermodynamic point of view, the difference in free energy between the initial and final states of reaction (10.3) at constant temperature and pressure can be expressed as Eq. (10.5).

$$\Delta_r G^{\Theta} = -RT \ln \frac{[B]_e}{[A]_e} = -RT \ln K_e \tag{10.5}$$

In catalytic reactions, the heat energy is the sole power for reaction, and is limited to those reactions that have thermodynamical possibilities. Comparatively, in a photochemical reaction (10.4), the photo energy ($h\nu$) can be used directly in the elementary steps in chemical reactions to overcome the potential barrier which is provided by excitation of reactive particles (molecules or ions) or by irradiation of semiconductor acting as whole or partial reactive system. Photochemical reaction is a "threshold" or "quantum" reaction generally, indicating that photoenergy is absorbed by single quantum. At such status, quantum energy should be above one eigenvalue of potential barrier (threshold value). According to two determined rules in photochemistry, only the photo which is absorbed by materials can be used to excite photochemical reaction (Grottus–Draper rule i.e. first rule, 1818); and the photo absorbed for activating one molecule in the initial stage of photochemical reaction is defined as one photon (i.e. second rule, Stark 1908, Einstein, 1912). Therefore, the total yield of photon should be equal to 1.

If all adsorbed photoenergy is used for reaction, the change ($\Delta_r G^{\Theta}$) of free energy in photo-reaction (10.4) will increase. However, the $\Delta_r G^{\Theta}$ in reaction (10.4) will drop and appear as status of $\Delta_r G^{\Theta} = 0$ if the photoenergy adsorbed by the reaction system is transferred to heat energy and is released.

It may be seen that light-catalyzed reaction would be an amalgamation of reactions (10.3) and (10.4).

$$A \xrightarrow{K,h\nu} B \tag{10.6}$$

This suggests that the reaction (10.6) cannot occur in the presence of catalyst (K) or light (hv) separately. Only concurrent presence of light and catalyst leads to occurrence of reaction. Moreover, the catalyst K used in such a reaction should be consistent with the definition of catalyst, i.e. the catalyst cannot be present in the stoichiometric reaction. It goes without saying that the reaction (10.6) seem to include those reactions with the increase in $\Delta_r G^{\Theta}$ according to reactions (10.4). In

other words, some reactions which do not occur at mild conditions in thermodynamics can occur. It is evident that this is ambivalent to the definition of catalyst. However, the researchers prefer to express the photo-catalysis reaction as Eq. (10.6).

For better understanding the properties of photocatalyst, the catalyst used for photo decomposition of water is exemplified here.[99] During the photochemical decomposition reaction (10.4), water should absorb ultraviolet light with wavelengths smaller than 165 nm for exciting the electron to break the bond. Catalyst of TiO_2 powder, an n-typed semiconductor used for photolysis water, should absorb light with wavelength small than 400 nm to form a pair of cavity and electron. The formed electrons reduce water to hydrogen and the cavities oxidize water to oxygen. Therefore, water can be decomposed into hydrogen and oxygen by light with longer wavelength in the presence of TiO_2. The energy of light with wavelength of 165 nm is equal to about 7.5 eV, and that of the wavelength of 400 nm is equal to about 3 eV only. These results indicate that lower light energy can be used for photolysis in the presence of TiO_2. The catalyst of Ru $(bpy)_3^{2+}$ complex is widely studied for water photolysis. When its solution is irradiated by light, the excited state of Ru $(bpy)_3^{2+}$ which has maximum absorption at wavelength of 450 nm has strong ability to reduce H^+ ions to hydrogen, while $Ru(bpy)_3^{3+}$ complex formed by oxidation reaction can oxidize OH^- ions to oxygen. The light with wavelength of 450 nm is equal to the energy of electrolysis water (2.12 eV). Therefore, the light irradiation with similar energy to electrolysis (2.12 eV) can decompose water theoretically. In generally, semiconductor of TiO_2 and Ru $(bpy)_3^{2+}$ is called as photocatalyst. In the broader sense, the homogeneous photocatalytic system would include the metal complex, while in the narrow sense, it would be a heterogeneous system with only the semiconductor as the photocatalyst. Photocatalytic reaction is composed of several elementary steps. Natural photosynthesis is well-known among of them.[100]

$$CO_2 + H_2O \rightarrow (CH_2O) + O_2 \tag{10.7}$$

Green plants absorb sunlight and synthesize hydrocarbons and release O_2 simultaneously from CO_2 and H_2O. This is a complex catalytic process. The antenna chlorophyll molecule absorbs photoenergy. After the energy is delivered among the different antenna chlorophyll molecule, finally, it is delivered to reactive center where the photochemical reaction occurs. Photosynthesis combines the light with many enzyme reactions. Because this process can occur irrespective of the presence light, it can be divided into photoreaction and dark reaction. The former forms "active" species while the latter CO_2 is reduced by active species. In contrast to this process, the photolysis on TiO_2 catalyst seems simple, and it can also be divided into several elementary steps. For example, the reaction when the H^+ is reduced to H_2 can also occur in the presence of colloidal Pt where the present RuO_2 can oxidize HO^- to oxygen. In this way, it markedly decreases the overvoltage for generation of H_2 and O_2, and the reaction rates increase.[101] Here, Pt and RuO_2 are the catalysts for reduction of H^+ and oxidation of HO^-, respectively. In this sense, TiO_2 in the presence of light only acts as photosensitizer in a reaction system, but the TiO_2^+-colloidal Pt and TiO_2^+-RuO_2 are photocatalysts strictly. When compared to the catalytic system with photochemical reaction, the same reaction can take place with low photoenergy.

It can be seen from the above introduction that irrespective of the reduction reaction of CO_2 in nature or the redox reaction of water to produce H_2 and O_2,

they all take place by multi-electrons pathways. Here, there is a question: How to match the reduction-oxidation potential between the photosensitizer and catalysts? We need to find the intermediate and a process which can carry out all these multi-electron reactions; we will need to establish a catalytic system of positive reaction to overcome reverse reaction. The answers to this question requires a photosensitizer (PS) for photo redox reaction at suitable potential conditions, electrical intermediate (R) used for adjusting the electron transfer (ET) process and homogeneous or heterogeneous catalysts for enhancing the production of H_2 and O_2. Of course, the number of components in one photocatalytic system is dependent upon their independent functions. For catalysis, the photolysis process of water requires various different types of catalysts.

(1) Photocatalyst participates in photo irradiated electron-transfer reactions and joins the reaction cycle under some status.
(2) Electron-transfer catalyst promotes the movement of electron from PS to reaction center (transfer photochemical ET to heat ET) or transfer the electron among other components.
(3) Reaction catalyst directly participates in heterogeneous or homogeneous reactions to form targeting products (for example, H_2 and O_2 etc).

10.2.2.2 *Photocatalytic ammonia synthesis by water and dinitrogen*

It is reported that the chemists in U.S. synthesized ammonia from water and dinitrogen by using sunlight and a special catalyst of TiO_2 powder incorporated with iron oxide. This process can be carried out at near room temperature and atmospheric pressure.

IIeperuma *et al.* studied TiO_2 catalysts doped by Mg for photocatalytic ammonia synthesis.[102,103] Their results showed that the yield of ammonia depends on the amount of metal doping, pH value, temperature in doping and heating time. The optimum conditions are that the mass fraction of metal doped is between 2%–4%, the pH value is around 10 and heating at 500°C for 2 h. Later on, IIeperuma *et al.*[104] reported TiO_2 doped by metal Ce, V and their photocatalytic performances. It is found that doping Ce and V have higher yields than other doping metals. Tennakone *et al.* [105] also reported photocatalytic ammonia synthesis on $Sm_2O_3{\cdot}(H_2O)_n$, Eu_2O_3 $(H_2O)_n$ and Fe(O)OH.[106]

The study on photocatalytic synthesis ammonia is based on the plenary water as a source of hydrogen and solar energy as energy sources, and how it directly transforms dinitrogen in air to ammonia using the photocatalytic method. It is a good idea and has theoretical probability, however, the conversion of photocatalytic ammonia synthesis is far away from practical level for application. Thus, it cannot be industrialized now.

Recently, along with the progress of photochemistry by solar energy, Schrauzer *et al.*[107] first reported a photocatalytic method for reduction of nitrogen on TiO_2 powder. Fujiashima *et al.*[108] synthesized ammonia by TiO_2, ZnO and SiC powders in a N_2 saturated aqueous solution, but the yield of ammonia is low. Miyama *et al.*[109] increased the yield by TiO_2, ZnO and Sr-TiO_2, CdS, GaP semiconductor doped Pt and SiC. The synthetic rate of ammonia is $25\,\mu mol \cdot g^{-1}$ on GaP-Pt, but the efficiency of solar energy is still low. Fan *et al.* used α-Fe_2O_3-based photocatalyst with small of forbidden band gap ($E_g = 2.2\,eV$) in order to use solar

Table 10.9 WO_3-based photocatalysts and yield of ammonia

Photocatalyst (g)	Blank/pH	Sample/pH	Corrected/pH	Ammonia yield/(μg/g)
WO_3(0.3)	5.3	6.0	5.9	391
WO_3(0.28)–Pt(0.02)	5.3	6.0	5.9	390
WO_3(0.2)–TiO_2(0.1)	6.0	6.15	6.4	102
WO_3(0.2)–CdO(0.1)	6.2	6.2	5.3	95
WO_3(0.2)–Ta_2O_3(0.1)	5.2	5.7	5.9	249
WO_3(0.2)–α–Fe_2O_3(0.1)	5.3	6.5	6.5	1076
WO_3(0.2)–V_2O_5(0.1)	4.4	5.7	6.6	1190
WO_3(0.1)–spinal(0.2)	5.9	6.4	5.8	36
WO_3(0.25)–α, α'–bipyridine(0.025)–Pt(0.025)	5.9	6.6	5.9	465
WO_3(0.25)–RuO_2(0.025)–Pt(0.025)	6.0	6.3	5.5	176
WO_3(0.25)–α, α'–bipyridine(0.025)–RuO2(0.025)	6.1	6.5	5.5	142
WO_3(0.2)–CdO (0.08)–Pt (0.02)	6.2	6.2	5.2	57

Note: The pH value of distilled water is 5.20.

energy efficiently. Their experimental results indicate that the ammonia yield was $45\,\mu\text{mol}\cdot\text{g}^{-1}$ on α-Fe_2O_3-Nd_2O_3 catalyst in irradiation by artificial visible light. This value is 31-fold higher than that with the industrialized potential as suggested by Schrauzer. Li *et al.*[110] used WO_3-based catalysts ($E_g = 2.7\,\text{eV}$) which gain high ammonia yields (Table 10.9). WO_3/Fe_2O_3 and WO_3/V_2O_5 catalysts markedly increase yields of ammonia after irradiation by light. Their yields are 43- and 47.6-fold higher than that with industrialized potential as suggested by Schrauzer. For example, the yield of ammonia is $63\,\mu\text{mol}\cdot\text{g}^{-1}$ in water solution suspended WO_3-α-Fe_2O_3 catalyst after sunlight irradiation. This value is 43-foldr higher than that of Schrauzer's industrialization standard.

It is a struggling target for a long time to achieve the direct conversion of nitrogen in air to ammonia by using water as resources of hydrogen and solar energy as drive power. People are endeavoring to explore more efficient catalysts and to develop new methods for ammonia synthesis at normal temperature and pressure.

10.2.3 *Electrocatalytic ammonia synthesis at normal pressure*

10.2.3.1 *Electrocatalytic reaction and electrocatalyst*

The electrochemical reaction, also called as the electrode reaction, takes place in electrolyte. The electrode reaction will occur when two metals or semiconductors called electrodes are inserted into aqueous electrolytes solution etc. and voltage is added between electrodes. In a broad sense, the electrode which is capable of inducing electrode reaction can be defined as an electrocatalyst. However, it is well-known that the variation of electrode type often leads to significant change in rate and selectivity in many cases. In fact, only such an electrode can be defined as an electrocatalyst, and this reaction is an electrocatalytic reaction. The formation of

H_2 by hydrogen electrode reaction on cathode is a typical electrocatalytic reaction. In this electrode reaction, when using Pt or Pd as catalysts reaction, current can be observed near the equilibrium potential calculated by Nernst equation (reference electrode potential), however, when the Hg and Pb are used as electrodes the reaction current cannot be observed when the added voltage is lower than one Volt. It is seen that the Pt and Hg electrode have different impacts on reaction rate. Their ratio is more than 10^{11}. Therefore, Pt or Pd electrode has to be used in order to yield hydrogen from water electrolysis. The application of Hg or Pb electrode, however, inhibits the production of hydrogen. The addition of Hg in dry battery has the function of preventing the unnecessary releasing of hydrogen from oxidation of anode (Zn) to Zn^{2+}. There are some multi-electron transfer redox reactions in electrochemical reaction. These reactions often require via intermediate states. One typical example is hydrogen releasing reaction using adsorbed hydrogen atoms as intermediate compounds. Since these intermediate compounds have strong adsorption functions on the electrode surface, they often need to add other electrocatalysts or promoters or chemicals to modify the semiconductor surface besides the electrode as catalyst when using semiconductor as electrode especially in order to catalyze the reaction to enough degree.

The electrochemical reaction often takes places in a cell which is different from catalytic reaction. As mentioned above, all cells have two electrodes, one is cathode and the other is anode. Generally, the anode is an electrode in which oxidation reaction takes place and provides electron to external electrocircuit. The cathode is an electrode in which the reduction reaction takes place and receives electron from external electrocircuit. These definitions change in terms of different conditions. For example, in a cell, because the current in an external electrocircuit is transferred from cathode to anode during the discharging process, so the cathode noted as ⊕ is also called as positive pole, and the anode noted as Θ is also called as negative pole. When the cell is electricized to become an electrolytic cell, the reactions happen reversely on the electrodes since whole chemical reaction carries out backward. The original anode becomes a cathode of electrolytic cell and the cathode becomes to an anode of electrolytic cell. Here, the cathode of electrolytic cell connects the negative pole of external electrocircuit, and is called as negatively charged electrode. On the contrary, the anode of electrolytic cell is called as positively charged electrode (Fig. 10.5).

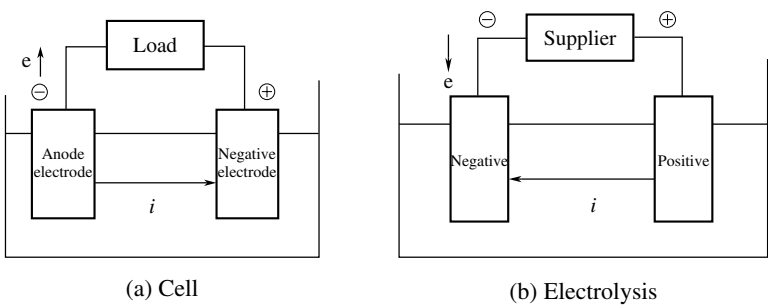


Fig. 10.5 Electrode in cell and electrolysis

Another difference between an electrochemical reaction and a catalytic reaction is that a so-called electrical double layer will form as the appearance of electrostatic potential gradient in the interface of electrolyte solution and electrode (conductor). Graham summarized in more detail the electrical double layer in 1947.[112] He considered that this electrostatic potential, i.e. the double layer potential, is different from the electrode potential. He also discussed and observed in detail the double layer potential of Hg-electrode-water solution system. He found that it could not observe such potential when electrode reaction occurred while the ideal polarization happened in a wide range of electrode potential if there was no electrode reaction. Hg is a liquid and it is thus easy to observe its surface tension and calculate the relationship between surface tension and double layer potential. Therefore, its structure is clearer. The structure of electrical double layer is composed of Helmholz layer and diffusion layer. The Helmohloz face is located between Helmholz layer and diffusion layer. The external of Helmohloz face is diffusion double layer. The model of Helmholz electrical double layer corresponds to simple parallel-plate capacitor. According to its equation, it can quantitatively describe the structure of diffusion double layer.[113,114]

In electrochemistry, electrode potential is an important parameter for the activity of electrode. The measurement of electrode potential is to determine the flowing electron between two electrodes. Oxidation reaction takes place on one electrode and reduction reaction takes place on the other electrode. The electrode reaction can be expressed as:

$$\mathrm{M}^{\mathrm{n}+} + \mathrm{n}\, e \leftrightarrow \mathrm{M}. \tag{10.8}$$

Its electrode potential can be calculated by Nernst equation:

$$E = E_0 + \frac{RT}{nF} \ln \frac{a[M^{n+}]}{a[M]}, \tag{10.9}$$

where, $a[x]$ is the activity of $[x]$. It is seen from Eq. (10.9) that the higher the concentration of oxidation state, the stronger would be the trends of reduction reaction and the larger the E value of electrode potential. Therefore, the value of E can be used to measure the trend of reduction reaction. This defined electrode potential is also called as reductive potential.

The calculation of electrode potential (E) from Eq. (10.9) requires a series of standard electrode potential (E_0) data. It is well accepted that the standard hydrogen potential is standard electrode potential in the world. Its electrode reaction is:

$$\frac{1}{2} H_2(p_{H_2}) \leftrightarrow H^+(a_{H^+}) + e. \tag{10.10}$$

When P_{H2} corresponds to the statue in which fugacity is equal to 101 kPa, the $\mathrm{a_{H2}}$ is 1 and the determinate temperature (generally 25°C), this half hydrogen electrode is called as standard hydrogen electrode and its electrode potential is prescribed as zero, i.e. $E^0_{H^+/H_2} = 0$.

Various standard electrode potentials can be calculated for a half-cell after the definition of standard electrode potential. Currently, most of standard electrode potentials can be obtained from the text.

The intrinsic difference between electrode reaction and catalytic reaction is that they have different electron transfer processes on themselves with reactive interfaces.

In a typical catalytic reaction, the electron transfer between reactant and catalyst is localized, thus, it cannot introduce the electron from external electrocircuit and cannot also export the electron from reaction system to form current during the reaction process. Moreover, the electron transfer cannot be controlled by external force for catalytic reaction. On the contrary, there is net electron transfer during the electrode reaction. The electrode, a heterogeneous catalyst, is a local site not only for reaction, but also for electron donation-acceptance. This means that electro catalysis possesses the bi-properties of chemical reaction and electron transfer simultaneously.

In contrast to typical gas-solid or solid-liquid heterogeneous catalytic reactions, the electro catalysis has following properties.[115]

(1) The electrode potential is an important parameter. The electrode potential over equilibrium potential (overvoltage) is a drive power resulting in reaction for determinate composition of reaction system (decreases free energy), and is also called as affinity. This is important for studying of reaction kinetics.
(2) It is easy to control rate and reaction conditions by using external circuit loop (e.g. constant voltage) to control overvoltage, so that vigorous electrolysis and redox reaction are realized.
(3) The current can be used as a quantity to measure reaction rate. Therefore, high precision and sensitivity will be attained (precision is three magnitude higher than that obtained by other methods). Furthermore, a fast step like transition state can also be determined more easily.
(4) The value of $-\Delta_r G^{\Theta}$ changes significantly. In common chemical reactions, the pressure and concentration vary in the range of several magnitudes, but energy changes in the range of several unit of RT. Therefore, the reaction orientation can be speculated according to its reaction type and reaction condition for most typical chemical reactions. Comparatively, the energy varies 10–20 units of RT by changing the electrode potential for electrode reaction so as to control the reaction orientation of reduction and oxidation and to lead to a change of reaction mechanism.
(5) From energy point of view, the chemical reaction involves the object corresponding to enthalpy change. And the electro catalysis involves the object corresponding to free energy change. It is well known that the change of free energy directly correlates to the change of electrode potential. Such values can be measured directly.
(6) For some electrocatalytic reaction (e.g. fuel cell), parts of energy accompanied with chemical reaction can be used as electric energy for external application. Moreover, by reverse reaction, electric energy can be converted to chemical energy and can be stored (secondary cell and electrolytic synthesis etc).
(7) The reaction mainly takes place in electrolytical solution, thus, the electrode is limited to conductive materials such as metals, semiconductors etc.
(8) The type of reaction, which is only related to the situation of ion appearance, is limited to the system of electrolytical solution including fusing salts at high temperature and solid electrolyte.

10.2.3.2 *The progress of electrochemical ammonia synthesis*

(1) The superiority and peculiarity of electrochemical ammonia synthesis. Ammonia synthesis reaction is an exothermic reaction accompanying volume reduction. In

order to enhance the conversion, there is a need to maintain high pressure but low temperature. However, low temperature often leads to low reaction rate. This is so-called thermodynamic limitation for ammonia synthesis. Introducing electric energy into the reaction may make the reaction conversion have no or little limit by thermodynamic equilibrium. The electric energy motivates the occurrence of non-spontaneous reaction and extends the researching fields of ammonia synthesis quomodo. For example, the conversion of hydrogen may be close to 100% at high temperature (570°C) and normal pressure by using electrochemical ammonia synthesis.[116] The use of electrochemical method can also realize ammonia synthesis at normal temperature and pressure.[117−121]

In the electrochemical ammonia synthesis, the nitrogen molecules are activated by adsorption on electrocatalysts modified on the surface of electrode first. The electrode subsequently supplies extra electrons to adsorbed nitrogen molecules, then activates them by supplying electrons required for reduction reaction. Simultaneously, the solid electrolyte and/or electrolyte solution provides H^+ needed for protonation.[116,119−121] Unlike adsorption activation on heterogeneous catalysts and donating-electron activation of nitrogen–complex compound in which the activation, reduction and protonation processes are dissevered from one another, electrochemical ammonia synthesis favors to building a nitrogen fixation condition such as synergy of activation and reduction resembling with that of nitrogenase. The activation degree of dinitrogen molecule can be controlled effectively by adjusting the electrode potential. Moreover, it can easily control the synthesis process by controlling the transfer rates of dinitrogen and proton which is very favorable to the study on the kinetic and mechanism.

The experimental results reported by Chatt *et al.* make it possible for dinitrogen to converse to ammonia at normal temperature and atmospheric pressure by reaction cycle. To form an effective cycle and prevent complex precursor from destruction, the coupling of protonation with electronificaiton is an attractive method. In 1985, Pichett and Talarmin[117,122] first realized a cycle process of ammonia synthesis by using electrochemical method. Trans-$[W(NNH_2)TsO(Ph_2PCH_2CH_2PPh_2)_2]^{2+}$(II) is produced by the reaction of trans-$[W(N_2)_2(Ph_2PCH_2CH_2PPh_2)_2]$(I) and p-$CH_3C_6H_4SO_3H{\cdot}H_2O$ ($TsOH{\cdot}H_2$) in THF solution, then electrolyzed at constant voltage (−2.6 V) by using Hg electrode in a solution of THF/$[NBu_4]BF_4$ ($0.2\,mol{\cdot}dm^{-3}$) saturated by dinitrogen. The research results show that reduction of 1 mol of II in this reaction cycle would consume 2 mol of electron and yield 0.22–0.24 mol of ammonia, 0.01–0.02 mol of N_2H_4 and 0.85–0.95 mol of (I). This process can be expressed by following equation, which forms a cycle as shown in Fig. 10.6.

$$8TsW^{IV}NNH_2^+ + 9N_2 + 16e^- \rightarrow 2NH_3 + 8W^0(N_2)_2 + 8TsO^- + 5H_2 \quad (10.11)$$

In electrolysis, II is not only an electric active species, but also provides protons required for the reaction. Pichett described the probability of ammonia synthesis in small-scale industrialization by this principle. In his method, the protonation was realized by adding $TsOH{\cdot}H_2O$. It did not form a real cycle and they did not report the reaction and material of positive electrode as well as the rates of ammonia formation.

In 1987, Tames *et al.* at Ben-Curion University (Israel) found that the reduction of Cp_2TiCl_2 at constant electric potential in the presence of N_2 and catechol led to

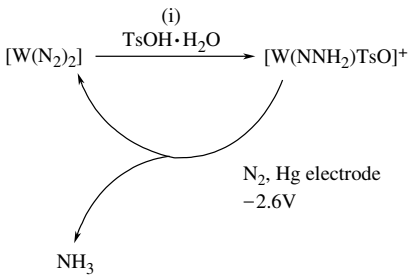


Fig. 10.6 Schematic diagram of electrochemical ammonia synthesis cycle

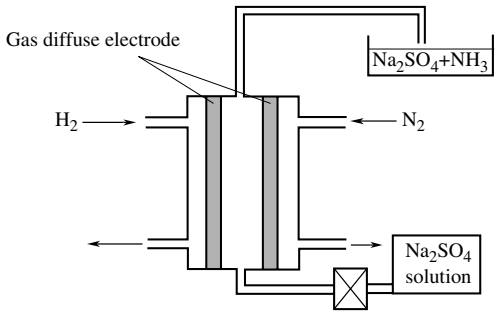


Fig. 10.7 Schematic diagram of electrochemical ammonia synthesis using gas diffusion electrode in aqueous solution

the formation of ammonia selectively in the yield low than 0.11% when they studied the electrochemical behavior of Cp_2TiCl_2 on glassy carbon and Pt electrodes in methanol/THF solution by cyclic volt-ampere method. The presence of CH_3ONa or Mg^{2+} could enhance the yield up to 0.65% or 1.45%, respectively.[118]

The above ammonia synthesis processes take place in nonaqueous solution. Their chemical environment is very different from that of biological nitrogen fixation. They are not true electrochemical ammonia synthesis because the electrochemical method is used for regeneration of precursor of complex only.

In 1989, Huruyanagai and Kichihaneshou at University of Yamanashi reported an electrochemical ammonia synthesis method at normal temperature and atmospheric pressure in aqueous solution.[119−121] The gas diffusion electrode supported Fe-Phthalocyanine catalyst was used and the experimental instrument was shown in Fig. 10.7.[119]

The gas diffusion electrode is composed of copper current collector, gas permeation layer containing of hydrophobic graphite and teflon (PTFE) and reaction layer including hydrophilic and hydrophobic graphite and PTFE. The anode supports 0.56 $mg \cdot cm^{-2}$ of Pt and cathode supports 0.2 $mg \cdot cm^{-2}$ of Fe-Phthalocyanine catalyst. The electrolyte solution is 1 $mol \cdot dm^{-3}$ of Na_2SO_4. The dihydrogen and dinitrogen is supplied by back side of electrode, i.e. gas permeation layer. When the electric potential of cathode is lower than −0.2 V (corresponding to standard hydrogen electrode potential), the ammonia starts to form on cathode. When the electrode potential was −0.6 V, the initial current efficiency was 1.64% and this value

decreased to ∼0.16% after reaction for 50 min. It is probably due to the destruction of cathode. They also studied the influence of 14 types of center metallic ions on current efficiency of electrochemical ammonia synthesis and the stability of gas diffusion electrode, and found that Sn- Phthalocyanine is the best catalyst.[124]

The main problem of this method is that the current efficiency is too low and decreases sharply during the reaction. The mechanism leading to above problems is not clear but may be related to the poisoning of the catalyst and insufficient activation of dinitrogen by metal-Phthalocyanine. Because water is a stronger complex than dinitrogen, when water molecule reaches the surface of metal-phthalocyanine after permeating the hydrophobic layer on electrode, it should bond strongly with center metallic ions to form complex structure so that the metal-phthalocyanine loses the ability of coordinating and activating dinitrogen.

Therefore, how to enhance the catalytic efficiency of catalyst in water solution and prevent catalyst from poison are important factors in increasing the current efficiency and stability of electrode in the electrochemical ammonia synthesis. The use of solid electrolyte is one of ways to solve these problems.[122]

In order to break the thermodynamic limitation, in 1998, Marnellos[122−126] at the University of Aristotelian studied electrochemical synthsis of ammonia by the reaction of nitrogen and H^+ at 570°C and in atmospheric pressure with a solid electrolyte cell in which the Pd was used as electrode and the $SrCe_{0.195}Yb_{0.105}O_3$ was used as high temperature proton conductor, and realized electrochemical synthesis of ammonia in high conversion at high temperature and in atmosphere pressure. The experimental instrument is showed in Fig. 10.8.

This instrument comprises an external quartz cylinder and a bottom-sealed internal cylinder made of $SrCe_{0.195}Yb_{0.105}O_3$ ceram (SCY) with good mechanical strength and high proton conductivity. 1.3 cm^2 of porous multi-crystallite Pd was deposited on the internal and external sides of the bottom in SCY ceramic internal tubing. It was used as electrode and the real surface area for catalysis on cathode was found to be 80 cm^{-2}. The bottom of this instrument was heated and kept at 570°C. The dinitrogen diluted by He (1.8% N_2) was induced into ceramic internal tubing and the H_2 was induced in the voids between the internal and external

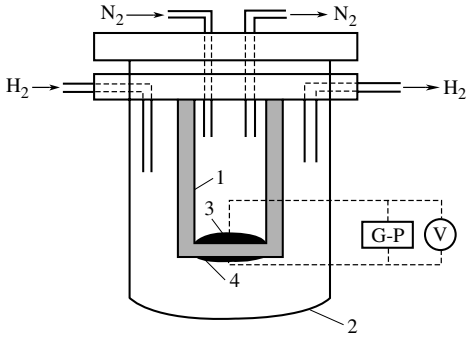


Fig. 10.8 Schematic diagram of electrochemical ammonia synthesis using SCY ceramic solid electrolyte

1 — SCY ceramic internal tubing; 2 — quartz external tubing; 3 — Pd cathode; 4 — Pd anode

tubing. The cell was constructed by:

$$H_2(g)(Pd)|SCY|(Pd)N_2 - He(g)$$

The oxidation reaction of H_2 took place on anode.

$$3H_2 \rightarrow 6H^+ + 6e^- \tag{10.12}$$

The formed hydrogen ions diffused to cathode through the SCY ceramic. The reduction reaction of nitrogen with hydrogen ions took place to form ammonia on cathode.

$$N_2 + 6H^+ + 6e^- \rightarrow 2NH_3 \tag{10.13}$$

The pressure of gas was 101.325 kPa. The ammonia synthesis rate was stable after passage of current for 2–6 min and this rate was at least three magnitudes higher than that of conventional catalytic reactor. The conversion of hydrogen was close to 100% which eliminated thermodynamic equilibrium limitation. The main problem of this method is that the conductivity of SCY ceramic is very poor at normal temperature. Even at 570°C, its conductivity is unsatisfied because the current density was smaller than 2 $mA{\cdot}cm^{-2}$ and could not be further increased. This limited the efficiency of ammonia synthesis and theoretical research. The use of solid electrolyte with high proton conductivity at low temperature to replace the SCY ceramic may be favorable to decreasing the synthesis temperature and increasing the current density and production efficiency.

(2) Electrolytic ammonia synthesis in a molten salt under atmospheric pressure. In 2005, Murakami *et al.*[127] proposed an electrolytic ammonia synthesis process from water and nitrogen gas in molten salt under atmospheric pressure and at lower temperature. In this process, water vapor and N^{3-} was electrolyzed *via* electrochemical reaction to form ammonia gas and O^{2-} ions in molten salt. Nitride ions were formed on metallic cathode and oxygen ions were removed from metallic anode during electrolysis. The electrolyte was alkaline metallic chloride containing N^{3-}. The principle is showed in Fig. 10.9.

$$3/2\,H_2O + N^{3-} \rightarrow NH_3 + 3/2O^{2-} \tag{10.14}$$

The nitrogen ions consumed in reaction (10.14) are formed by reduction of nitrogen gas on cathode:

$$1/2\,N_2 + 3e^- \rightarrow N^{3-} \tag{10.15}$$

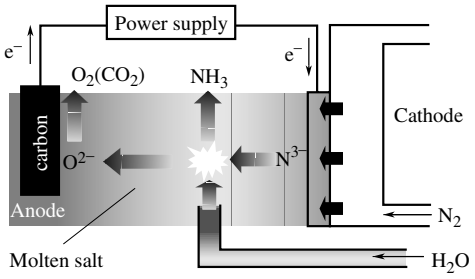


Fig. 10.9 Schematic drawing of the principle of electrolytic ammonia synthesis from water and nitrogen gas.[113]

The electrode potential of N^2/N^{3-} is 0.382 V [relative to Li^+/Li in LiCl–KCl solution (723 K)]. The nitrogen gas is electrochemically reduced to nitrogen ions almost quantitatively according to Eq. (10.15), and hence the nitrogen ions can be continuously supplied for 15 h.[128] The oxygen ions generated in reaction (10.14) form oxygen gas and releases from the inserted metallic anode:

$$3/2\,O^{2-} \rightarrow 3/4\,O_2 + 3\,e^- \tag{10.16}$$

The standard electrode potential of O_2/O^{2-} is 3.0 V [relative to Li^+/Li in LiCl-KCl solution (723 K)].[129] When kryptol is used as anode, CO_2 gas can be produced and released from anode.

$$3/2\,O^{2-} + 3/4\,C \rightarrow 3/4\,CO_2 + 3\,e^- \tag{10.17}$$

Reaction (10.18) shows the overall reaction of ammonia synthesis from water and nitrogen gas according to reaction (10.16) and (10.17). Here, the by-product is oxygen gas only.

$$3/2\,H_2O + 1/2\,N_2 \rightarrow NH_3 + 3/4\,O_2 \tag{10.18}$$

Figure 10.10 shows a schematic drawing of the experimental equipment. The reactants are LiCl, KCl and CsCl. All of them are dried in vacuum at 473 K for 24 h to remove residual water. The eutectic mixture (LiCl: KCl: CsCl = 57.5: 13.3: 29.2, molar fraction, 538 K) is used as an electrolyte and is melted in an alumina crucible under pure argon atmosphere. All experiments are conducted in a glove box filled with argon gas under atmospheric pressure at 573 K. The resource of nitrogen ion is Li_3N. The working electrode is glassy carbon rod (Φ4 mm × 50 mm). The counter electrode is a nitrogen gas electrode consisting of porous nickel. This porous nickel (Φ6 mm × 1.6 mm, surface area of 7500 $m^2 \cdot m^{-3}$) is attached to the bottom of an alumina tubing (inner diameter: 5.0 mm). The reference electrode is an Al–Li alloy in the ($\alpha + \beta$) coexisting phase state.[130] Potential of the reference electrode is calibrated with reference to that of the Li^+/Li electrode.[131]

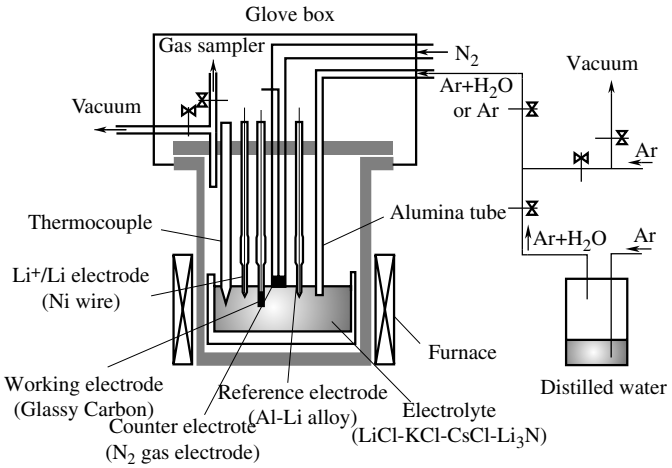


Fig. 10.10 Schematic drawing of the experimental equipment[113]

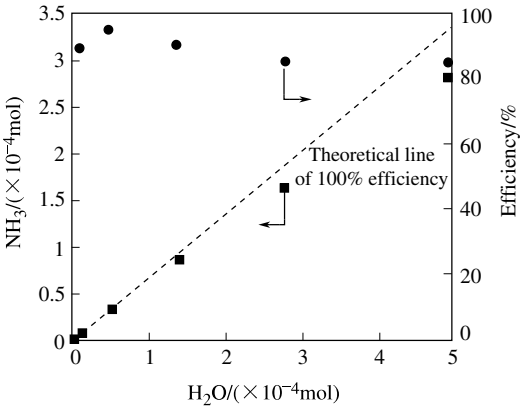


Fig. 10.11 Relationship between the amounts of the supplied water vapor and the output of ammonia.[113]

(■) Dotted line represents complete conversion of water vapor to ammonia according to the following reaction; $3/2H_2O+N^{3-}\cdot NH_3+3/2\ O^{2-}$; (●) Conversion

Water vapor used for molten salt is supplied by flowing argon gas which passes through a bath of distilled water. The amount of water vapor is determined by controlling the partial pressure of the supplied gas mixture (water vapor and argon gas).

The experimental results confirm that the amount of ammonia formed increases linearly with the content of supplied water vapor, indicating that the ammonia is formed by reaction of water vapor with nitrogen ion (Fig 10.11). The average ammonia synthesis rate is 0.72 $mol\cdot h^{-1}\cdot m^{-2}$. Although the current efficiency of ammonia is 23% only, it demonstrates the probability of ammonia synthesis by using water and nitrogen gas at atmospheric pressure.

(3) Electrochemical promotion effect on industrial fusing of iron catalyst at high-pressure ammonia synthesis. As reported by Marnellos, the surface of Pd electrode coated on high temperature proton conductor ($SrCe_{0.95}Yb_{0.05}O_3$) used in solid electrolyte cell is catalytic inert. Yiokari *et al.*[132] took the industrial iron catalyst coated on electrode surface to connect with the catalyst, proton conductor ($CaIn_{0.1}Zr_{0.9}O_3-R$) and the electrochemical supplied proton. The activity of the industrial catalyst is enhanced by 1,300% or even higher through interfacing the catalyst surface with proton conductor and supplying electron to catalyst surface from the differential potential between the catalyst and counter electrode.

Figure 10.12 is a pellet cell reactor operated at 5 MPa. The BASF S6-10RED catalyst is milled and mixed with iron powder. They are coated on one side of proton conductive plate and then calcined at 400°C. The average loading weight of catalyst is 12 mg for every disk before reduction. Counter electrodes (Ag) and reference electrodes (Ag) are deposited on both side of working electrode (catalyst), and then dried in air at 120°C (Fig. 10.12(a)). Special ceramics, Macor and holders are used to support pellets of catalyst. Each holder has eight openings in its circular configuration to expose the catalyst in gaseous reactant mixture. A screw is passed through a large hole in the middle of ceramic holders in order to connect the ceramic holder tightly and maintain a better contacting state between eight pellets and conducting gold electrode ring. This screw is also used to hold the three layers

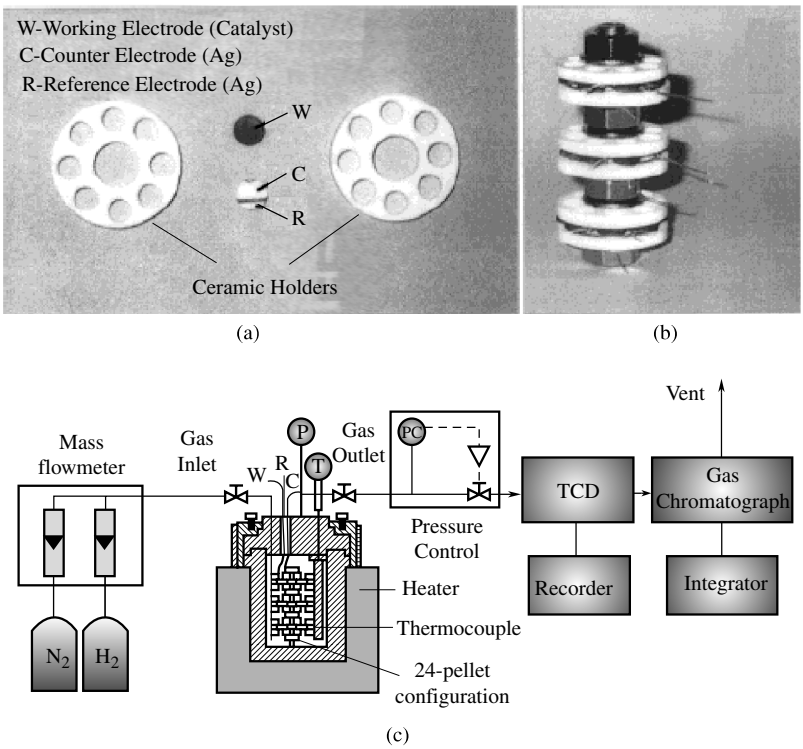


Fig. 10.12 Experimental equipment[117] (a) Machinable ceramic holders and two proton-conducting pellets showing the location of catalyst, counter and reference electrodes. (b) Twenty-four pellet unit. (c) High-pressure reactor, gas feed and analysis unit

of 24-pellet units together (Fig. 10.12(b)). The 24-pellet units are suspended in a 300 ml of reactor as shown in Fig. 10.12(c). All experimental data are collected in the instrument as shown in Fig. 10.12(c). The reaction conditions are 400°C, 5 MPa, with an inlet flow of 100 $cm^3 \cdot min^{-1}$. The gas feed is a high pure mixture of N_2 and H_2 and its flow rate is controlled by high-pressure mass flow meters and controllers. Three transducer glands that fitted in gold wires are equipped on the top of reactor and connect the positive and counter electrodes in parallel to make 24-pellet units of catalysts work. These three wires maintain the constant voltages and currents and supply proton for catalyst surface simultaneously. On-line GC is used to monitor the ammonia yields and reaction rates. The consumption rate (r) of the proton can be calculated by $r = 3r_{NH_3}$. The blank experiment result confirms that only the catalyst has effect on ammonia synthesis.

Figure 10.13(a) shows the ammonia synthesis rates (mol $H \cdot s^{-1}$) at constant voltage and inlet $p_{H2}/p_{N2} = 0.82$. Reaction rate increases from 6.9×10^{-8} mol $H \cdot s^{-1}$ to 1.35×10^{-7} mol $H \cdot s^{-1}$ as increasing of reaction time. $\rho = r/r_o$ is defined as enhancement coefficient in this figure and its value is 2. $\Lambda = \Delta r/(-I/F)$ is defined as inductive efficiency, reflecting the influence of electrochemical proton transfer to catalyst. This parameter is used to differentiate the inductive and non-inductive efficiency. The Λ is 0.6 in Fig. 10.13(a), indicating that 60% of proton transfers to

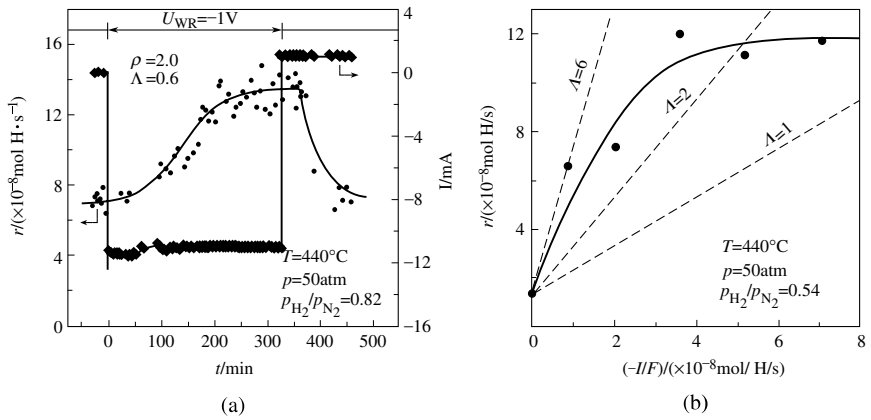


Fig. 10.13 Effect of applied potential and applied negative current on the rate of NH3 synthesis.[117] (a) Effect of applied potential (•) and on cell current (♦) on the rate of NH_3 synthesis; (b) Effect of applied negative current, i.e., H^+ supply to the catalyst at a rate –I/F, on the rate of ammonia synthesis at steady-state (Dashed lines are constant faradaic efficiency lines)

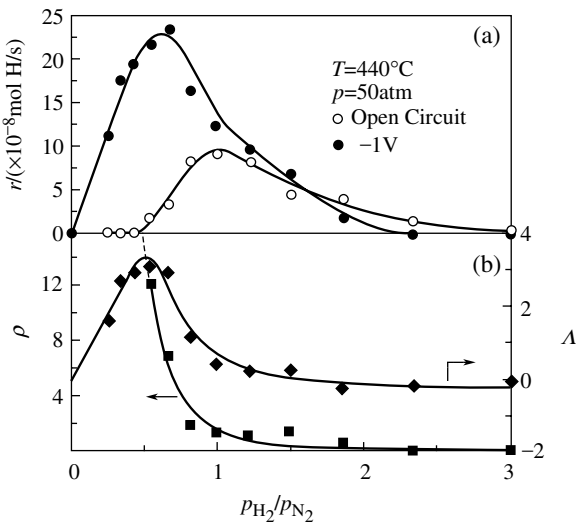


Fig. 10.14 Effect of inlet H_2/N_2 ratio on the rate of NH_3 synthesis[117] (a) Effect of inlet H_2/N_2 ratio on the rate of NH_3 synthesis under open-circuit (O) and for $U_{WR} = -1.0$ V (•); (b) Corresponding ρ(■) and Λ(♦) values

the catalyst surface and participates in ammonia synthesis reaction. Decreasing the inlet p_{H2}/p_{N2} ratio could increase non-inductive rate. As shown in Fig. 10.14(b), the inductive efficiency reaches to six at low current when the inlet gas p_{H2}/p_{N2} decreases to 0.54. This indicates that each proton transfers to catalyst surface and six protons participate in the formation of ammonia.

The nature of electrochemical effect mainly depends on gas composition. Fig. 10.14 exhibits the influences of inlet N_2/H_2 ratio on ammonia synthesis rates and corresponding Λ and ρ values under opened or closed-conditions. In an opened-circuit, the maximum reaction rate is 9.4×10^{-8} for a N_2/H_2 ratio of 1. The ammonia synthesis rate increases to 23.3×10^{-8} at negative voltage (-1 V), where N_2/H_2 ratio is 0.67 only. The increase in rate indicates an increase in H adsorbed on the catalyst surface and concomitant increase of H^+ supplied to the catalyst by negative voltage. As P_{H2}/P_{N2} is larger than 1.5, the ammonia synthesis is poisoned by supplied protons. The catalytic activity is lost when P_{H2}/P_{N2} is above 2.3, implying that catalyst surface is covered by H completely which inhibits the chemisorption of N_2. It is seen from this result that there is the competitive adsorption of N and H on catalyst surface. The inductive efficiency is negative in this region, i.e. the catalytic activity decreases along with proton transfers to catalyst surface.

In Fig. 10.14(b), a strong non-inductive behavior could be observed in the region of $0.33 < P_{H2}/P_{N2} < 0.67$ and $\Lambda = 0.3$. The maximum enhancement coefficient ρ could also be obtained in this region ($\rho = 13$ at $P_{H2}/P_{N2} = 0.54$, and even larger ρ value, approaching to infinite). Here, the ammonia synthesis rate is too low to be detected at the opened-circuit. In fact, the data shown in Fig. 10.14 (the conversion of hydrogen was 1%) are far from the thermodynamic equilibrium (the conversion of hydrogen is 8% and $k_\alpha = 7.76 \times 10^{-3}$ at 400°C).

Fig. 10.15 shows the influence of potential (U_{WR}) catalyst on ammonia synthesis rates. This reaction demonstrates a strong electrophilic effect, i.e. negative potential can promote reaction while positive potential can envenom reaction. The catalyst will deactivate after prolonged treatment at positive potential (3–4 h), suggesting the existence of hysteresis phenomena. The treatment of H_2 can restore the activity of catalysts.

The marked enhancement of catalytic activity with negative potential could be explained by taking into account two synergetic factors used for rationalization of

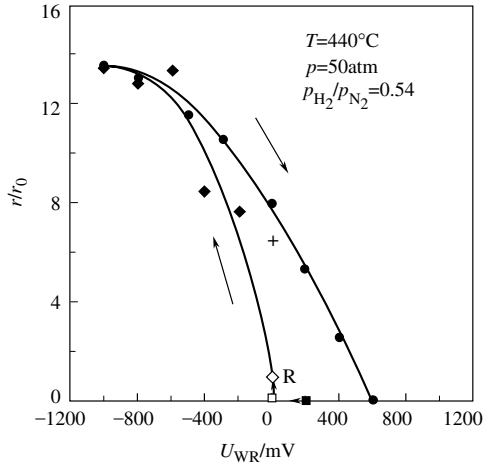


Fig. 10.15 Effect of catalyst potential on the rate of NH_3 synthesis in steady state[117] Arrows indicate the sequence of measurements; Open symbols correspond to open-circuit, $r_0 = 10^{-8}$ mol H/s

electrochemical promotion. First, the enhanced supply of proton onto catalyst surface, and, second the enhanced chemisorption binding energy and sticking coefficient of N_2 on catalyst surface which decreases the activation energy and work function. The maximum catalytic rate obtained by decreasing activation energy and work function exceeds the maximum value obtained under the opened-circuit. This result strongly confirmed the change of chemical binding energy (Fig. 10.14). The synergetic effect of electrochemical promotion and classic chemical promotion markedly enhanced the catalytic activity. At low p_{H2}/p_{N2}, the reaction rate increased by electrochemical method is 13-fold of conventional catalyst, and six-fold of transferring proton to catalyst surface, respectively. This is the maximum electrochemical reaction rate forecast according to Farady law. Yiokari *et al.* estimated that the reaction temperature can reduce 50°C and pressure can decrease 30% for industrial ammonia synthesis under the synergetic effect of electrochemical promoters and chemical catalyst.

(4) Speculation for the development of electrochemical ammonia synthesis. Electrochemical ammonia synthesis cannot offer cheaper ammonia than that obtained by Haber–Bosch process at current stage.[133] The use of expensive high-temperature proton semiconductor consisted of rare metals and the consumption of electrical energy may be economically impossible. However, the study on electrochemical ammonia synthesis probably realizes the direct ammonia synthesis from water and air which is a thermodynamic non-spontaneous reaction. It also markedly enhances the current efficiency and reaction conversion. Accordingly, the cost of ammonia synthesis is mainly focused on the consumption of electrical energy. The electrochemical ammonia synthesis is thereby to be applied probably in the backland with enough electrical energy or effective conversion of solar energy to electrical energy. In the future, the electrochemical ammonia synthesis will be a helpful choice if the cost of Haber–Bosch process has doubled and redoubled because the energy crisis leads to significant increase price of coal, petroleum oil and other raw materials for ammonia synthesis. Therefore, the electrochemical ammonia synthesis has great application potential.

The study of electrochemical ammonia synthesis should emphasize on the basis of water solution and solid electrolyte. Because water molecule is a stronger ligand than dinitrogen molecule, it must consider the poison effect of water molecules on catalyst used for activation of dinitrogen when designing the electrolysis cell. By optimizing electro-catalyst and improving the technique of the loading catalyst, high activity of catalyst and stability of electrode can be maintained. The use of high proton-conducting solid electrolyte at normal temperature (e.g. high proton conducting ion-exchange resin membrane with low water content) to replace water solution or conducting ceramic can decrease the operating temperature and increase current density. On the basis of above methods and further optimization design of cell structure, it is possible to markedly increase density and efficiency of current for ammonia synthesis. These should be the important orientations for study of electrochemical ammonia synthesis in the future. At the same time, it is believed that the electrochemical ammonia synthesis will play an important role in the study of ammonia synthesis methodology and biological nitrogen fixation mechanism after pronounced increase of current density and yield, because electrochemical ammonia synthesis has advantages of easy controlling and synergistic progress of adsorption, activation, reduction and protonation process.[134]

10.2.4 *Biocatalytic ammonia synthesis at normal temperature*

In the nature, the people find that there is one kind of nitrogen fixation animalcule having a special catalyst — nitrogenase in its body. It can reduce the nitrogen in the air to ammonia directly at normal temperature and atmospheric pressure. The amount of nitrogen reduced per unit time and per nitrogenase is thousands times higher than that on industrial iron-based catalyst. According to estimates, 90% of nitrogen fixed from air every year on the earth is by biological fixation, only 10% is by chemical fixation in industry. So it is seen that biological nitrogen fixation is higher than the chemical nitrogen fixation from both reaction condition and productivity. It becomes a reasonable expectation to develop a new and good catalyst by simulating the function of nitrogenase to synthesize ammonia at normal temperature and under atmospheric pressure.

The Chinese scientists researched biological nitrogenase as well as its chemical simulation since that later parts of 1970s and have reported some achievements.[135−140] However, the industrial catalyst activities are several magnitudes lower than the values required for ammonia synthesis at normal temperature and in atmospheric pressure.

It appears that the biological nitrogen fixation is mainly dependent on two proteins containing transition metals in cells i.e. nitrogenase system consisting of Mo-Fe protein and Fe protein, and electron-donator (biological reductants and corresponding enzymes), electron transfer (e.g. Fe-O protein, flavoenzyme or methyl violet) as well as ATP-Mg^{2+} etc.[135]

It is approximately agreed that nitrogen is complex activated on an active center of nitrogenase and accepts electron and H^+ from electron-donator.

$$N_2 + 6H^+ + 6e + H_2O \rightarrow 2NH_4OH \tag{10.19}$$

It relies on a complicate biological electron route for electron to transfer from electron-donator to N_2 (adsorption). The transfer orientation is electron-donator → Fe redox protein → Fe protein → Fe-Mo protein. It requires ATP-Mg^{2+} to activate electron in order to ensure the smoothness of the electrical route. ATP itself hydrolyzes to ADP during this process. H^+ may be transferred to active center by side-groups (−SH, imidazole, −OH) on proteins.

The electron-donators are pyruvic acid, butanedioic acid, H_2 etc., generated by its metabolism. Electrons and protons are produced via corresponding enzymes (natural catalyst). For example, pyruvic acid via dehydrogenated enzyme and H_2 via hydrogenated enzyme.

What is the real structure of active center for complex activation of nitrogen among the macromolecules of nitrogenase? It is very important to understand the mechanism of biological nitrogen fixation and explore the approach of chemical simulation. The current hypothesis and simulation are qualitative and do not consider the spatial structure of active center. Based on well-known reaction and theories of complex catalysis, the nitrogen fixation research group at Xiamen University proposed an active center model of 2Mo-1Fe-tri-nuclear which comprises one pair coupling of cubane-like structural Fe_2S, Mo_2O_2 eight-atom clusters structure. They used this model to explain the mechanisms of enzyme-enhanced reduction on various substrates.[137] Fujian Institute of Materials Structure reviewed the structural conditions for dual-dinitrogen complex activation and proposed the tuck net-shaped

four-nuclear atomic cluster model in which the active center of nitrogenase catalyzes fixing nitrogen.[138]

The study on chemical nitrogenase simulating nitrogenase began in 1964. The U.S., Great Britain, Soviet Union Bloc and Japan had engaged in researching this field. There are several basic methodologies for chemical simulation of biological nitrogen fixation.[141]

(1) Simulating the structure of nitrogenase. By using Fe and Mo complexes as catalysts, traces of ammonia can be formed with water as source of hydrogen in the presence of strong reductant. For example, in the system of Na_2MoO_4+ cysteine (or 1−S replaced glycerol), C_2H_4 can be formed from C_2H_2 in the presence of reductants, i.e. $NaBH_4$ or NaS_2O_4. When added with few $FeSO_4$, 3−5 μg of ammonia is yielded at 135 atm of N_2 (the ammonia is also formed in atmospheric pressure). Because the protein structure of nitrogenase contains Fe, Mo and –SH and fixes nitrogen in the presence of water, it has special significance to study the simulating system of nitrogenase by using water as medium.

(2) Nitrogenation used Fe-free and Mo-free metallic system. The system comprised main metallic compounds where the reductant can adsorb nitrogen irreversibly and then hydrolyze the nitride of transition metals to ammonia. The experiment carried out at University of Stanford is an example.

Tamalen *et al.* designed a method of electrolytic reduction. However, the formation of one mole of ammonia would consume one mole of metallic aluminum.

The researchers tried to use metallic nitride as an intermediate for ammonia synthesis in the early studying stages of nitrogenase (20th century). For example, Pechiney Financial Group built a factory at Arthas. The alumina was reduced in the presence of N_2 at 1,600°C to aluminum nitrideand which then was hydrolyzed to ammonia.

$$Al_2O_3 + 3\,C + N_2 \rightarrow 2\,AlN + 3\,CO \tag{10.20}$$

$$2\,AlN + 6\,H_2O \rightarrow 2\,NH_3 + 2\,Al(OH)_3 \tag{10.21}$$

However, this process was replaced by Haber–Bosch method because they did not find a suitable heat-resisted material at high temperature.

(3) Synthesis and reduction of stable transition metal complex containing N_2 to obtain ammonia. More than 150 of single-nuclear and more than 50 of binuclear dinitrogen complexes have been synthesized. All of them are stable dinitrogen complexes and cannot be reduced to ammonia. The unstable dinitrogen complexes can only be formed during ammonia synthesis process at moderate temperature, and they are unstable and could not be isolated.

People expect to form an ideal dinitrogen complex. Tri-bond in nitrogen molecule can completely be weakened and activated, but does not form stable compound. So it is possible to reduce dinitrogen to ammonia. People now engage in theoretical studies and synthesis of dinitrogen complex. Mr. Aoqing Tang, a famous chemist in China, summarized experimental data from about 150 of dinitrogen complexes, and proposed a chemical bond theory of dinitrogen complex based on quantum chemistry. He also concluded an optimal condition for the formation of single and bi-nuclear dinitrogen complex. These results provide theoretical understanding for synthesis of new dinitrogen complexes.[139]

The nitrogenase consists of MoFe protein ($\alpha_2\beta_2$ tetramer, molecular weight is about 3.8×10^{-19} g) and Fe protein (γ_2, dimer, molecular weight is about

1.08×10^{-19} g). It has been confirmed that MoFe protein contains N_2 and other out-substrates' complex active sites. Shah and Brill have successfully separated the FeMo-co from brown nitrogenase. This restrains the study of complex active site from MoFe protein to FeMo-co small molecules (molecular weight $< 1.66 \times 10^{-21}$ g). Kim and Ress studied the single crystal X-ray diffraction electron density pattern of MoFe protein in nitrogenase. They showed a K–R structural modal of M-clusters in MoFe protein (protein binding-FeMo-co). This model indicated that the M-cluster consists of cubane-like clusters (i.e. MoS_3Fe_3 and FeS_3Fe_3) with two gaps. These two M-clusters are bridged by three protein-free ligands (two S and one "Y" which light than S) and create a cage with diameter of 0.4 nm between them. The distances of bridged and non-bridged Fe are 0.27–0.28 nm and 0.38 nm, respectively.

According to intuitionistic structure of FeMo-co, the complex of N_2 in M-clusters can occur inside or outside cage. Huang *et al.*[142] used ethene as probe molecule to study the binding site of dinitrogen in nitrogenase. The results showed that ethene cannot compete with dinitrogen in nitrogenase. The binding sites of dinitrogen in nitrogenase may be 6Fe site $\mu_6(\eta^2, \varepsilon 4)$ in protein binded FeMo-co cage and 3Fe+1Mo site $\mu_4(\eta^3, \varepsilon_1)$ instead of 2Fe $\mu_2(\eta^2)$ in the mouth of cage. The complex method of dinitrogen on Fe-based ammonia synthesis catalyst may be $\mu_6(\eta^3, \varepsilon_3)$.

Based on the similarity between the Fe catalyst and M-cluster structure in MoFe-protein, Huang *et al.* proposed an active sites model with 6 Fe atomic clusters (Fig. 10.16). The A, B and C in Fig. 10.16 are the empty sites on single crystal of α — Fe. N_2 forms a complex of $\mu_6(\eta^3, \varepsilon_3)$ on 1, 2, 3, 4, 5, 6 Fe atomic sites. S_{234} is Fe (111) crystal face. Because the distances from Fe1 to S_{234} and body-centered C are 0.185 nm and 0.248 nm, respectively, and the bonds length of Fe–N is 0.187 nm and that of activated N–N is 0.12–0.13 nm, so the one end of perpendicular adsorbed N_2 on Fe (111) face almost locates on S_{234} face. The center of N_2 molecule basically locates on empty body-centered atom C position of α-Fe. The distances between Fe2, Fe3, Fe4 and center of N_2 molecule are all 0.248 nm which is favorable to form complex with three lateral groups and to exert its role of complex activation enough. Besides, one end of N_2 molecule may complex with Fe1, the other end may complex with Fe5 and Fe6 positions on the top of α-Fe by double end-group complex. This use remained orbits enough on catalyst surface to feedback the π^* of N_2 molecule. The different actions on each end of N_2 molecule lead to asymmetrical activation of N_2 molecule. This significantly weakens N≡N bond and enhances complex activation of N_2 molecule. According to the structure, the configuration of four opened Fe atoms leads to large space for N_2 molecule function and favors to complex of N_2 molecule

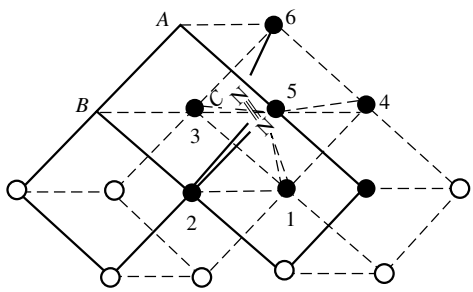


Fig. 10.16 Model of active center with 6Fe atom cluster on fusing iron catalyst[126]

and removal of product generated from reduction reaction. Except for the opened side, the distance between neighbored Fe atoms is 0.404 nm which is close to K–R model.

Rod *et al.*[143] studied the mechanism of ammonia synthesis on simulated nitrogenase. Their data showed that simulated nitrogenase of $MoFe_6S_9$ may synthesize ammonia at normal temperature and under atmospheric pressure. This reaction does not involve the breaking process of N–N bond, but form ammonia by reacting molecular nitrogen with hydrogen proton. It breaches thermodynamic limitation and makes it possible to form ammonia at normal temperature and under atmospheric pressure. Ru-based and electrochemical catalysts having similar reaction mechanisms lead to good activities at low temperature. However, some questions should be resolved to industrialize this reaction process. For example, the competition between formation of ammonia and reduction of hydrogen (reduction of proton state and atomic state hydrogen to dihydrogen) during the reaction is a big problem. The ammonia synthesis by simulated nitrogenase was very hot in 1970s and 1980s. However, lots of researchers gave up this research because it is far from industrialization.

The exploration for ammonia synthesis at moderate condition is not limited to above methodologies. Breakthrough of thermodynamic limitation is the basic idea of above researches. Although ammonia synthesis at normal temperature and under atmospheric pressure is an ideal target, it still requires long time to realize it because there is no report about industrialization until now.

10.2.5 *Ammonia synthesis at supercritical condition*

The reaction rates of current industrial ammonia synthesis catalysts, e.g. $Fe_{1-x}O$-based and Ru-based catalysts at high temperature (above 748 K) are close to equilibrated concentration of ammonia. The further increase of conversion is limited by chemical equilibrium. There are two ways to solve this problem. First, it is to decrease reaction temperature or to increase equilibrium ammonia concentration to enhance conversion. The developments of $Fe_{1-x}O$-based catalyst[144] and Ru-based catalyst[145] are just in order to maintain higher activities at low temperature. Second, other than the catalyst development, there is another method that can be used to break equilibrium limitation (it should be noted that the chemical equilibrium cannot be breached). This is so-called nitrogen hydrogenation technique of non-equilibrium limitation. The basic idea of this technique is that immediate removal of product of ammonia from reaction system ($N_2 + 3H_2 \Leftrightarrow 2NH_3$) can eliminate converse reaction. Accordingly, the reaction only carries out along the orientation of ammonia formation. The use of supercritical technique is likely to realize this idea, because hydrogen, nitrogen and ammonia have distinct physical properties. Under supercritical condition, the added medium has strong extraction effect on ammonia; but it is inert for reactants. The produced ammonia is extracted from catalyst surface to form agglomerations so that the produced ammonia is enveloped by supercritical medium molecules to prevent them from adsorption on the catalyst which decreases the ammonia concentration on catalyst surface. This favors to the reaction of ammonia formation and enhances the positive reaction rates. Accordingly, it breaches reaction equilibrium of $3/2H_2 + 1/2N_2 \Leftrightarrow NH_3$ macroscopically and changes the reversible reaction limited by equilibrium to irreversible reaction. The reaction conversion single pass increases and the recycle times of syngas decreases to achieve low consumption of energy.

We studied the supercritical ammonia synthesis in fix-bed reactor.[146] The impact of 15 different medium including saturated hydrocarbon (C_7–C_{13}) and supercritical conditions (e.g. catalyst, reaction temperature, space velocity and partial pressure of medium) on ammonia synthesis were investigated. Our experimental results indicate that the decompositions of the above-mentioned supercritical mediums take place under the reaction conditions of using fusing iron and activated carbon supported Ru as catalysts. The decomposed products decrease catalyst activities. The saturated hydrocarbons have minimum decomposition degree which leads to the lowest catalyst deactivation rate among all supercritical mediums. Therefore, saturated hydrocarbon is a better medium for supercritical ammonia synthesis. The decomposition of medium is the main reason leading to a decrease in catalyst activities. Besides, the addition of supercritical medium decreases the effective partial pressure of syngas. This is another reason for decreasing of catalyst activities. Therefore, the active temperature of catalyst is a key factor to supercritical ammonia synthesis. Supercritical reaction should carry through preferably at low temperature. Supercritical ammonia synthesis is still possible if the catalyst with low active temperature (below 300°C) can be developed successively and supercritical medium will not decompose.

George *et al.* [147] studied supercritical ammonia synthesis on four alkaline, silver, Sb sulfide catalysts including MAg_2SbS4, M_2AgSbS_4 (M: K, Rb), and characterized their structures.

10.3 New Application of Ammonia

Methane, ammonia, hydrogen and water can be converted to amino acid on graphitic catalyst which existed as universal dust by sunlight irradiation induced photocatalysis in the universe. According to one hypothesis, the formed amino acid dissolved in ocean at primitive times and then converted to peptide. After evolution, the life was born on earth (Fig. 10.17).

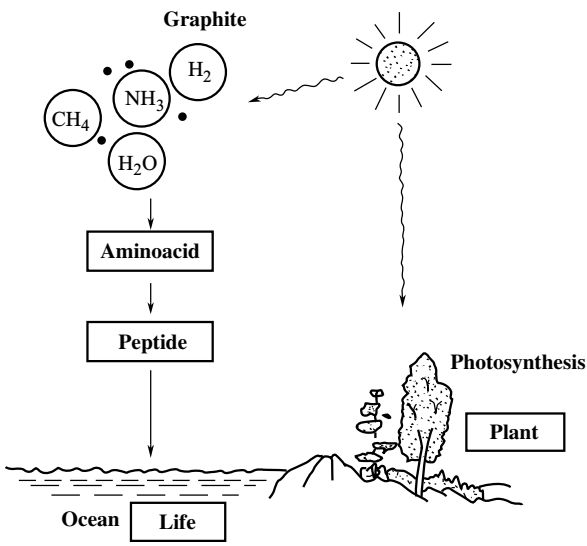


Fig. 10.17 Sun–ammonia, methane, water and hydrogen lead to the naissance of life

Table 10.10 Principal chemical elements in crops

No	Element	Percentage %	No	Element	Percentage %	No	Element	Percentage %
1	C	45.0	9	Mg	0.3	16	Cl	Trace
2	O	43.0	10	Mn	0.05	17	Co	Trace
3	H	6.5	11	Fe	0.02	18	Si	Trace
4	N	2.0	12	Zn	0.01	19	Se	Trace
5	K	1.5	13	B	0.005	20	V	Trace
6	Ca	0.6	14	Cu	0.001	21	Ni	Trace
7	P	0.5	15	Mo	0.0001	22	Na	Trace
8	S	0.5		Total	99.9861	23	I	Trace

In terms of research results, the plant comprises more than 16 kinds of chemical elements (see Table 10.10). Partial nitrogen is from air and converted by rhizobium and the rest of nitrogen is absorbed by plants from the solution in soil. Besides carbon, oxygen and hydrogen, nitrogen is another essential nutrition for plant. Nitrogen atom which is essential elements for bio-molecule and important component in drug, chemical fertilizer needs ammonia as activated nitrogen. Nitrogen cycle is one of important cycles to maintain life in the nature.[148] Catalytic ammonia synthesis is an important tache of nitrogen cycle in nature and more importantly complements activated nitrogen required for life (in particular for human beings). Moreover, it is a sole method to obtain activated nitrogen in industrial scale. Therefore, the story of the catalytic ammonia synthesis is never ending.

Initially, Haber found the most suitable Fe catalyst for industrialization after screening for about 5,000 catalysts. In order to reduce energy consumption and consummate the technology, further improvements of catalysts can only be speculated.

In this never-ending story, in addition to questions about the elementary steps of the reaction and the importance of the real structure and subnitrides for the catalyst efficiency, as well as the wide-open question about new catalyst materials, there are also new challenges for new applications of ammonia.[149]

10.3.1 *Ammonia synthesis device is a highly efficient device for energy transformation and hydrogen production*

The production procedure of ammonia synthesis is a complex systematic engineering. It can be divided into gas production, gas purification and ammonia synthesis unit in terms of their functions. The previous two units are the common processes in the gas turn liquid technique (GTL), i.e. the production of liquid fuels and chemical materials (DME, ME, F-T gasoline, F-T diesel) from coal and natural gas. The product, ammonia, generated from the third unit is also a high-octane fuel. Therefore, the industry of ammonia synthesis is an energy-source conversion industry (hydrogen production) practically. Besides chemical industry and nitrogenous fertilizer industry, it also has consanguineous relationship with the energy industry. During times of food shortage, the ammonia is mainly used for fertilizer.

Table 10.11 lists the raw materials for hydrogen production in ammonia synthesis, joint production process and use of ammonia. As an energy industry, it appears that the ammonia synthesis industry has following characteristics.

Table 10.11 Raw materials used for hydrogen production, joint production process and use of ammonia

Raw materials	Joint production process	Main use of ammonia
Coal	After ammonia synthesis (ammonia)	Fertilizer
Petroleum	Joint — urea	Explosive
Natural gas	Joint — alkaline	Medicaments (sulfanilamide)
Oven gas	Joint — carbon	Dye
Refining gas	Before ammonia synthesis (syngas)	Resin
Coal field gas	Joint — energies (liquid fuel,	Acrylonitrile
Oil field gas	Hydrogen)	Refrigeration agent
Industrial tail gas:	Joint — alcohol (methanol, DME)	Sodium cyanide
Tail gas for production of C_2H_2	Low- and high-carbon alcohol	Hydrazine
	Ethyl glycol, isobutanol	Amine
Tail gas for production of ethene	Liquid fuel (gasoline, diesel)	Hydrogen-storing
	Joint process of heat/	Fuel cell
Tail gas for production of Cl_2	electricity/cold	Reduction of nitrogen oxide
	Hydrogen production	Energy (solar energy)
Water (electrolysis)	Hydrogen production	storage and transportation
Biomass	Chemical products (alkene)	
	Ethanol, acetic acid, formaldehyde	
	Others (H_2O_2 etc.)	

Table 10.12 Comparison of investment and energy consumption of ammonia plant using different raw materials

Gasification method	Total energy consumption/ (GJ/t_{NH3})[a]	Investment cost/million U.S. dollar	Comparative ratio for investment
Steam reforming of natural gas	32.6	75.0	1.0
Steam reforming of naphtha	37.7	85.5	1.14–1.15
Partial oxidation of heavy oil	39.0	120.0	1.5–1.6
Coal gasification at 2.5 MPa	48.6		
Coal gasification at atmospheric pressure	58.6[b]	150.0	1.8–2.1
Electrolysis of water	117.3		

[a] include the supplied energy;
[b] Total energy consumption of BASF-type ammonia plant is 92GJ/t NH_3 in 1940.

(1) Wide raw materials for hydrogen production. In addition to coal, petroleum and natural gas, the co-called black gold, the industrial exhaust and, in particular, biomass can also be used as raw materials for hydrogen production.

(2) High efficiency of energy conversion. The different raw materials are converted to hydrogen (and nitrogen) by suitable processes. Table 10.12 shows the values of energy consumption for ammonia production by using different raw materials. Initial energy consumption of BASF industrial system was as high as $92\,GJ{\cdot}t^{-1}$. This value is about 2.8-fold higher than the advanced process in existence. However, the entropy value of ammonia is $18.4\,GJ{\cdot}t^{-1}$, and the theoretical energy consumption for ammonia is only about $21\,GJ{\cdot}t^{-1}$. Therefore, there is a great potential for energy saving. For example, Fig. 10.18 shows energy balance chart for a plant of ammonia synthesis (the ammonia production is 1,200 tons every day by

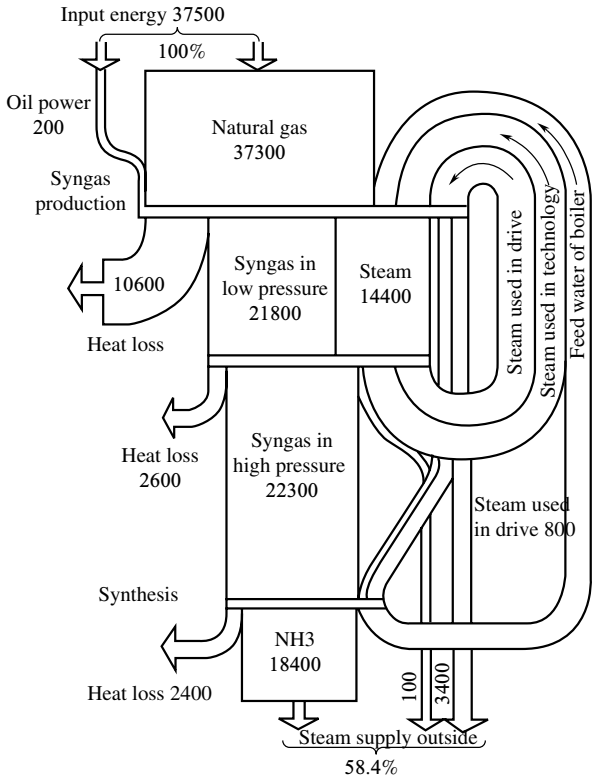


Fig. 10.18 Energy-flow diagram of ammonia synthesis device with capacity of 1200 t/d (All data is MJ/t NH_3)

natural gas vapor conversion method). Such ammonia plant utilizing energy synthetically is practically combines the ammonia production with power production in order to reduce energy loss. The data in Fig. 10.18 is the energy balance per ton of ammonia. When ammonia output is 50 ton per hour, the heat of vapor byproduct is 720,000 MJ which is about 38.4% of supplied energy, corresponding to a power unit with 60–70 MW which is attached to ammonia plant. 49% of supplied energy is converted into liquid ammonia. The total energy efficiency is 58.4% if considering the heat of outlet vapor. The total heat lose during processes is 41.6% in which loss in syngas production is 28.3%, loss in compression is 6.9% and loss in synthesis loop is 6.4%. Accordingly, about 70% of energy is lost in the syngas production process. How to reduce this part of energy consumption as much as possible is a significant potential for energy saving in the future. Thus, reduction energy consumption close to a theoretical value is the development trend as well as technology progress of ammonia synthesis industry.

Modern ammonia plants are designed based on "all round-energy" concept. The whole technological process is a system for comprehensive use of energy. Currently, liquid ammonia at atmospheric pressure is needed as starting material, made from air, liquid water ($T = 300\,K$), and natural gas. The resulting ammonia theoretically contains 28 GJ as chemical energy if the process is energetically isolated. Industrial



Fig. 10.19 Panorama of modern ammonia synthesis plant

processes achieve a total degree of efficiency of up to 70%, however, the total degree of efficiency of general heat power station is only 30% under similar conditions. The total degree of efficiency of ultrahigh pressure and sub-critical boiler power station is 40%–50% only. This is the reason why the total degree of efficiency of a plant still drops although the low efficient vapor-driving centrifugal compressor is used to replace for high efficient electromotion reciprocating compressor in ammonia synthesis plant. Fig. 10.19 shows a modern ammonia plant. All the large aggregates in the foreground are needed to generate hydrogen from methane and purify it, and the actual rector is in comparison very small and cannot be seen. The picture clearly illustrates where the development potential lies and when the optimization has reached a high maturity. This picture also demonstrates that the ammonia synthesis equipment is a high-efficient and mature energy conversion unit. According to above 30% of energy loss, much research interest has been attracted to develop a new technology.

(3) Flexibly jointed production to change the product. After production of syngas, it can be used to produce alcohol (methanol, DME, mixing alcohol with high and low carbon number), oils (gasoline, diesel and wax) and chemical products (alkene), hot/cold/electric joint production and town gas etc. After production of ammonia, there are many mature processes for production of urea, alkaline and carbon oxide. Therefore, the ammonia synthesis equipment can be flexibly changed to high efficient units of energy conversion. Fig. 10.20 shows a schematic diagram of ammonia synthesis equipment coupling with other chemical processes.

The materials on which persons or things rely for existence can be divided into two parts, i.e. natural bioplasm and artificial machining materials. For example, crop's products, animal, fruit, fish etc. (can be directly edible) and coal, natural gas, petroleum and biomass etc. (can be directly used as fuel) are natural bioplasm materials, while the other materials are artificially manufactured *via* modern chemical engineering process (e.g. chemical processing of coal, chemical processing of natural gas, biochemical processing, petrochemical processing, oil refining processing, chemical processing of energy etc.) from coal, petroleum natural gas and biomass as well as water and air. Therefore, the equipment for ammonia synthesis is

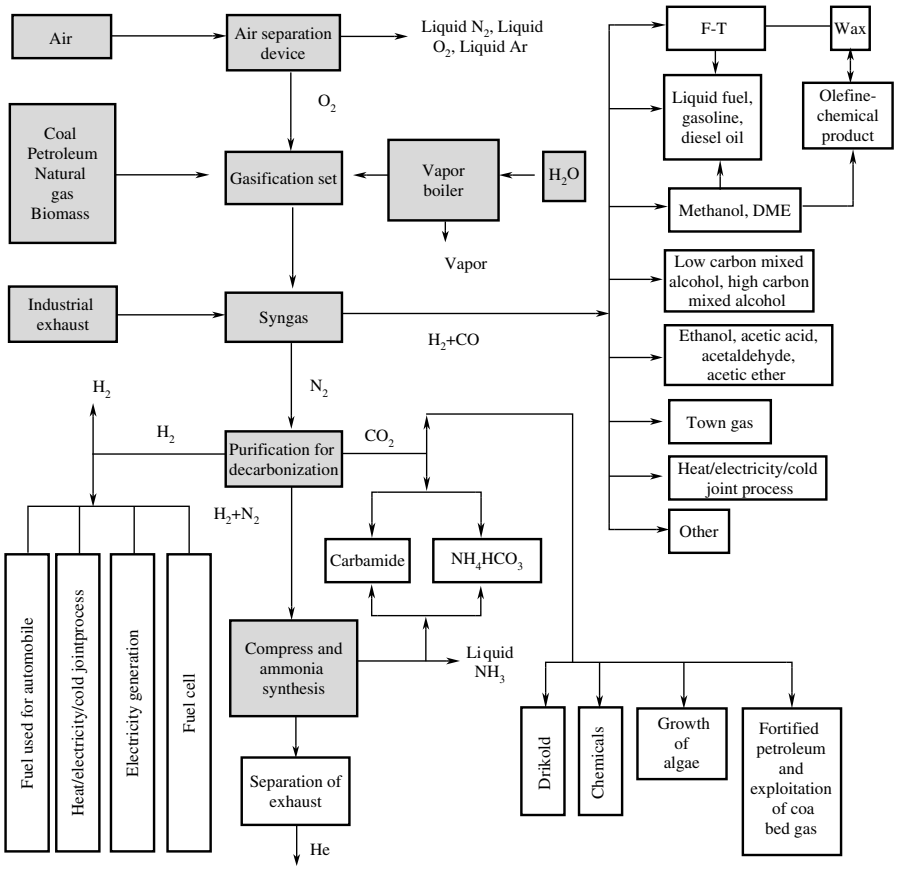


Fig. 10.20 Schematic diagram of change — jointed production and integrative using system derived from ammonia plant

fundamental equipment for above processes, except petrochemical process because ammonia synthesis also uses coal, natural gas, petroleum, water and air as raw materials. Ammonia synthesis process is only one of the fundamental processes for this fundamental equipment (Fig. 10.20). Except for the special equipment used in ammonia synthesis loop, the other equipment used during the process of ammonia synthesis can be utilized as fundamental equipment for above processes too. That is, the three units during ammonia synthesis processes in terms of their functions, except for ammonia synthesis unit, gas production unit and gas purification unit are same. Thus, the ammonia synthesis industry is never "the setting sun" industry but is a universal and fundamental chemical process used for manufacturing mass materials on which persons or things rely for existence from coal, natural gas, petroleum and biomass etc.

For example, the GTL technique develops quickly, and can be used during resource shortage of petroleum. This process can be used to produce liquid fuels (methanol, DME, gasoline and diesel by Fischer-Tropsch Synthesis, FTS) from coal and natural gas, which supplement and replace the petroleum. The GTL technique

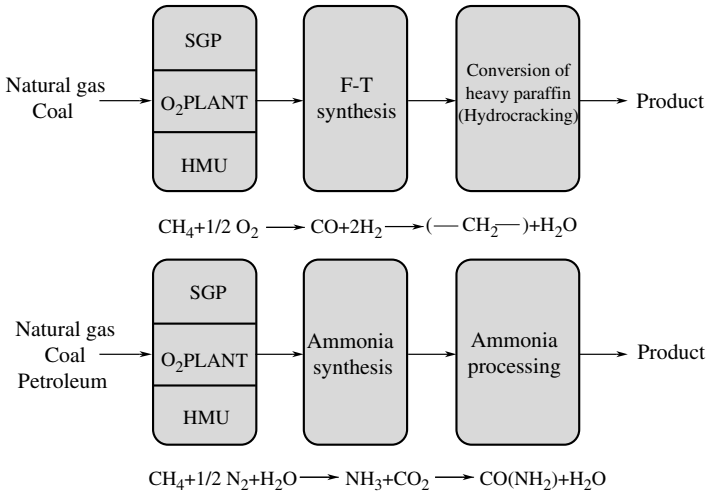


Fig. 10.21 Comparison of processes of ammonia synthesis and F-T synthesis (GTL, CTL, BTL)

has similar process and catalyst as for ammonia synthesis (Fig. 10.21). For example, the ammonia synthesis uses Fe and Ru as catalysts, the F-T synthesis also uses Fe, Co and Ru as catalysts. In particular, fusing iron catalyst is a good catalyst for both ammonia synthesis and F-T synthesis.

10.3.2 *New application of ammonia*

China has abundance of resource of solar energy. The irradiation amount is between $3.3 \times 10^3 \times \text{kJ}\cdot\text{m}^{-2}$ and $8.4 \times 10^6 \times \text{kJ}\cdot\text{m}^{-2}$ every year. The solar energy received by the land in China is close to 2.4×10^{12} ton of standard coal comparatively. If 8% of land in China is covered by crops with high energies and reaches average coverage degree of forests in the world, the produced energies are equal to 12.6×10^9 ton of standard coal when the efficiency of photosynthesis is 6.6%.

The waste biomasses generated by agriculture are close to 1.4×10^9 ton including 0.75×10^9 ton of straw and other wastes. It is possible to replace 0.3×10^9 ton of petroleum if the joint production of heat-electric and chemicals is realized.

The Development and Revolution Commission of China reported that China plans to use biofuel to replace 10 million tons of finished products of liquid fuel in 2020. The reproducible energy will provide energy corresponding to $(400\text{–}500) \times 10^6$ of standard coal every year.

In 2020, the power generation capacity supplied by reproducible energy will exceed $360 \times 10^6\,\text{kW}\cdot\text{h}^{-1}$ including $300 \times 10^6\,\text{kW}\cdot\text{h}^{-1}$ of hydropower generation capacity, 30 million $\text{kW}\cdot\text{h}^{-1}$ of synchronized wind turbine generation capacity, $1.5 \times 10^5\,\text{kW}\cdot\text{h}^{-1}$ of energy supplied from small wind turbine system, 30 million $\text{kW}\cdot\text{h}^{-1}$ of biomass power and 1.8 million $\text{kW}\cdot\text{h}^{-1}$ of solar energy power. At same time, the production capacity of fuel ethanol and bio-diesel will reach 12 million tons which can be used to replace about 10 million tons of finished product of oil.

At present, the annual production capacity of fuel ethanol from corn is 1.02 million ton and test production of fuel energy from sorghum is 5,000 tons in China, respectively. The annual production capacity of bio-diesel is about 20,000 tons by using waste oil, barbadosnut, Chinese pistache and coleseed etc. as raw materials.

Currently, China is trying to manufacture the ethanol-gasoline in Heilong Jiang, Jilin, Liaonin, Henan and Anhui provinces. It has attained good effect now and plans to extend to other areas.

It seems that the problem of foodstuff has been solved basically in China now. We are improving the environment by decreasing the cultivated land and increasing the coverage of forest and grassland. Where is the target of the nitrogenous fertilizer industry? Does it have future? The author's answer is positive. The nitrogenous fertilizer industry will continue to have contribution to both developments of agriculture and bioenergy in the 21st century.

The movement of the human society was basically dependent upon petroleum in 20th century. Petroleum provides fuel for motor vehicles and resource for chemical production. However, the king status of petroleum will be challenged soon. The crops may gradually replace petroleum to become the source of all substances from plastic to fuels. In all probability, the "black gold" will be replaced by "green gold" in the future. The development of bio-technique is a key for "green gold" to replace the "black gold."

The revolution has already begun. The plastic product strengthened by the fiber of kenaf was manufactured by Ford Company in U.S. Kenaf grows very fast (3.6 meter every year). Some companies also manufactured the architecture materials to replace the wood, stone and plastic by using this fiber and straw. Dow Chemicals and Cargil Incorporated reported that they could produce commercially viable plastic wholly from corn instead of petroleum.[150]

The "industrialized farmers" in U.S. can grow enough fuel and chemical raw materials in the next 25 years so that the U.S. will be almost independent of foreign petroleum. The experts also estimate that U.S. can produce 75 billion gallon of ethanol (1 gallon = 3.785 dm^3) every year if they decide to use 50 million acre of unused croplands. The current productivity of gasoline is 70 billion gallon every year by using imported petroleum in U.S. The U.S. has developed a technology to produce bio-diesel from soybean etc.

It can be anticipated that the world will grow enough plants for fuel and chemicals raw materials in the 21st century. The development of world economy will not depend on petroleum. The movement of the human society will use "green gold" to replace "black gold" gradually. Based on the development of industrial biotechnology to use biomass effectively, China can walk on a way toward green and ecological modernization.[151]

The bioenergy is derived from plants and crops (Fig. 10.22). Besides C, H and O, the growth of plants and crops require N, K and P which are supplied by chemical fertilizers. Therefore, the chemical fertilizer is one of main supporting system for biomass, in particular, bioenergy. For example, the nutrition required by oil plants and leguminous crops is three-fold higher than that used for crops. One-third depends on the chemical fertilizers. It is thereby confirmed that the nitrogenous fertilizer is not used in agriculture only. It is also an industrial product that has both functions for increasing production of agriculture and biomass resource in the 21st century. As one of main supports for increasing of crops and

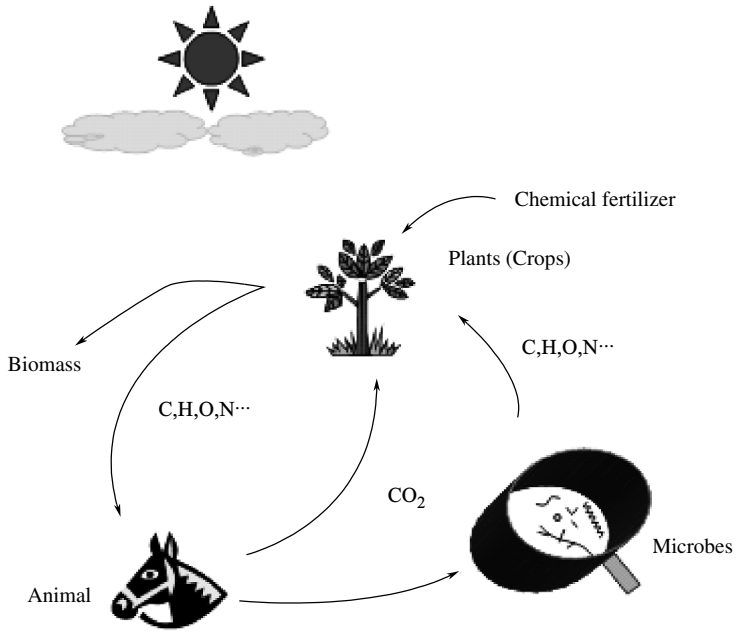


Fig. 10.22 Fertilizer is one of supporting systems for biomass resource

biomass resource, there will be a huge requirement for ammonia in the future. In order to develop biomass resource, it must call for producing advanced and highly efficient nitrogenous fertilizers, and supply and marketing system of farm produces.

In fact, the chemical fertilizer enhances the leaf area of plants and the content of chlorophyll that can improve the fixing ability of solar energy and convert it to bioenergy. As for corn, the production of one kilogram nutrient of chemical fertilizer needs 105×10^3 kJ of chemical energy. After adding the fertilizer into the cropland, it can obtain $630-840 \times 10^3$ kJ of bioenergy by the corps. These values are 6–8 times higher than that used for production of fertilizer. The energy consumption used for production of chemical fertilizer is 1% of the total energy consumption in 1980s in U.S., however, the increasing farm products due to the use of chemical fertilizer is 33% of total farm products.

During growth of plants, the amount of absorbed CO_2 and released O_2 increases with photosynthesis-raising of its chlorophyll due to increase of chemical fertilizer. It is roughly estimated that it would absorb excessive CO_2 of 26.9 kg and liberate excessive O_2 of 19.6 kg by every one kilogram of chemical fertilizer, which is by six times increasing than required O_2 and released CO_2 in order to produce one kilogram of chemical fertilizer, respectively. Substantively, this is a resultful way to repel the greenhouse effect caused by CO_2 mainly. This is also an important aspect to understand positively the effect of chemical fertilizer on biological environment.

The nitrogenous fertilizer is not used in agriculture only. It is an industrial product that has both functions for increasing production of agriculture and biomass

resource in the 21st century. As one of main supports for increasing of crops and biomass resource, there will be a huge requirement for ammonia in the future. In order to develop biomass resource, it must call for producing advanced and highly efficient nitrogenous fertilizer and supply and marketing system of farm produces. Xinjiang Construction Corps used liquid ammonia as fertilizer for more than ten years and therefore possess rich experience. The negative opinion of probability of development of biomass resource in China based on average cropland area per person is incorrect. Germany, that has similar average cropland area per person and Japan that has fewer average cropland area per person than China are studying the bioenergy actively, and their annual amount of bio-diesel production has reached 1.67 million ton and 0.4 million ton in 2005 respectively.[151]

Ammonia would be a convenient storage molecule for hydrogen for operation in fuel cells, because it is free of carbon and so less likely to poison the fuel cell, or create any harmful contribution to the ecobalance. Synthesis and decomposition of ammonia out of and to the elements are well controlled. If a practical and safe transfer of the industrial logistic[152] into an end-consumer field is to be obtained, then a powerful alternative for the generation of hydrogen could be at our disposal.

The ammonia is also a work medium for effective conversion, transportation and storage of solar energy (Fig. 10.23).

Solar energy is endless and can be used everywhere. It need not transport and exploit. Moreover, the use of solar energy will not pollute environment and break the ecological balance. The use of solar energy thereby attracts interest in the world now and becomes an important content for utilization of new energy and reproducible energy.

Among use and development of solar energy, the light-heat and photovoltaics are two technologies that have been widely used and have the potential to relieve the crisis in fossil energy currently. For example, there are 11 large commercial solar thermal electric plants with a total capacity of 365 MW in U.S after researching successfully in early of 1980s. Israel, Europe, Japan, Australia and

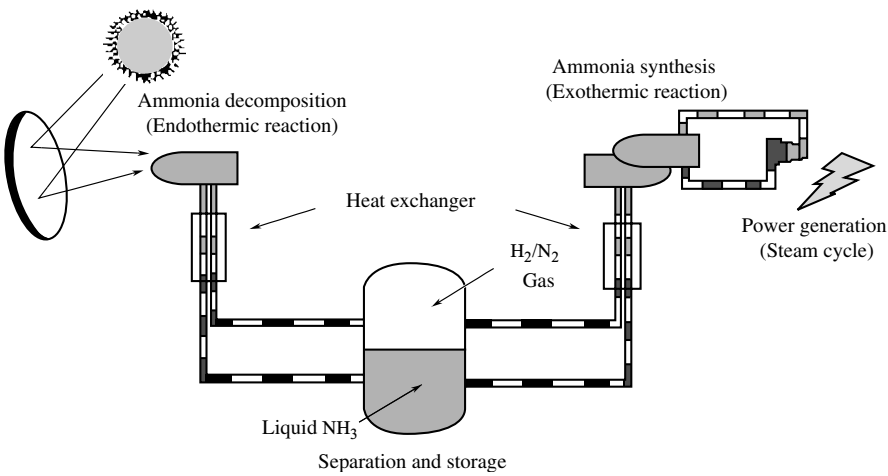


Fig. 10.23 Schematic diagram of conversion, transportation and storage of solar energy by using ammonia as medium

other countries have engaged in studying this technology actively. Solar thermal electricity generation plants with various solar energy concentrators including tower-, dish-, and trough-like shapes have been operated and successfully demonstrated the technology. They are now optimizing the systematic design and are pushing the commercialized progress of the pyroelectric technology of solar energy forward.[153–155]

There are two different storages of solar energy. One is the storage of apparent heat and latent heat based on physical change e.g. phase transformation. Another is the storage of reversible chemical reaction heat. Comparatively, the latter has following advantages; (1) high density of energy (2–10-fold higher than that of the former); (2) long storing time at normal temperature; (3) low cost relevant to transportation and energy. Therefore, it will make a breakthrough for application of solar energy if the chemical storage of solar energy can be effectively combined with solar thermal generator and refrigerating air-condition. The technology of solar thermal generator has not been applied in our country until now.[156] The study of solar thermochemical reactions involves catalytic reaction, product separation and heat-inhibited reaction. The reversible thermochemical storage based on catalytic reaction has great application potential and is being widely studied. The gas phase exists in both reactants and products in such reactions, and the temperatures of reaction equilibrium distribute widely. There is no reaction between products without catalyst. Products generated from catalytic endothermic reaction can be stored for long time. The reaction work medium is mainly focused on SO_3, CH_3OH and NH_3. Among the three work mediums, the use of ammonia as work medium has advantages of non-poison, environment-friendly, reaction complete and good industrial background (Synthesis and decomposition of ammonia out of and to the elements are well controlled, with easy optimization of reactor size and more numbers). The disadvantage of ammonia is that its reaction heat is slightly lower than the values of SO_3 and CH_3OH. This shortcoming can be effectively overcome by increasing of reaction pressure.[157–159]

Figure 10.23 shows schematic diagram of reversible reaction by using ammonia as the work medium. The solar energy is collected by concentrator and provides the energy for reaction. Ammonia molecules are decomposed to nitrogen and hydrogen on catalyst at high temperature in a left-sided reactor at high temperature. By heat exchange, these two gases with NH_3 together are stored in a separator at normal temperature. When heat is required, N_2 reacts with H_2 to form ammonia in a reactor listed in the right-side which releases out chemical heat. The released heat can be used to supply heat for refrigerating machine and electricity generation by heat exchange. Such system has high efficiency and is also a good continuity of supply heat. Thus, it has great application potential.

It is important to control the NO_x discharge globally. Ammonia can be used as reducing reagent for NO_x discharged by fixed equipments.

Human beings need food and food requires nitrogen element. The industrial requirement for nitrogen also increases continuously. Except in the industry of ammonia synthesis, the other industries requiring nitrogen are scientific topic only. Ammonia synthesis requires hydrogen which can be supplied from carbon-containing fuels. The ammonia synthesis industry's continued development, based on progress in science and technology, will determine how it would address the problems of shortages in energy supply or how it might safeguard the environment.

References

1. Leigh J. *Chem Br.* **37**: 23–24, 2001.
2. Schlögl R. *Angew Chem. Int. Ed.* **42**: 2004–2008, 2003.
3. Timm B. *Ammonia Synthesis and Heterogeneous Catalysts.* In: Dechema (ed.) *Proc. 8th Intern. Congr. Catal.* Weinheim: Verlag Chemie, 1984.
4. Roberts MW., *Catal Lett.* **67**(1): 1–70, 2000.
5. Ertl G. In: Anderson JR, Boudart M (eds.) *Catalysis, Science and Technology*, Vol. 4, Berlin: Springer Verlag, 1983, 209.
6. Brill R, Richter EL, R Ruch. *Angew Chem. Int. Ed.* **6**: 882, 1967.
7. Spencer ND, Schoonmaker RC, Somorjai GA. *J. Catal.* **74**(1): 129, 1982.
8. Horiuti J, Polanyl M. *Trans. Farad. Soc.* **30**: 1164, 1934.
9. Horiuti J, *J. Res. Inst. Catalysis. Hokkaido Univ.* **1**: 8, 1948.
10. Enomoto S, Horiuti J, Kobayaski H. *Hokkaido Univ.* **3**: 185, 1955.
11. Tanaka K. *Hokkaido Univ.* **13**: 119, 1965.
12. Temkin MI, Pyzhev V. *J. Phy. Chem.* (USSR), **13**: 851, 1939.
13. Ertl G, Lee SB, Weiss M. *Surf Sci.* **114**(2&3): 527, 1982.
14. Hosemann R, Preisinger A, Vogel W, *et al. Phys. Chem.* **70**: 796, 1966.
15. Borghard WS, Boudart M. *J. Catal.* **80**(1): 194, 1983.
16. Boudart M. *Advan. Catal. Relat. Subj.* **20**: 153, 1969.
17. Boudart M, Djéga — Mariadassou G. *Reaction Kinetics of Heterogeneous Catalysis*, Translated by Gao Z, Zheng SA, Li CR, *et al.* Shanghai: Fudan University Press, 1988, 141.
18. Liu HZ, *Chinese Journal of Catalysis*, **22**(3): 304–316, 2001.
19. Liu HZ, Li XN. *Science in China* (Series B). **38**(5): 529–537, 1995.
20. Pernicone N, Ferrero F, Rossetti I, *et al. Appl. Catal. A: General*, **251**(1): 121–129, 2003.
21. Liu HZ, Li XN. *Chinese Journal of Catalysis.* **26**(1): 79–86, 2005.
22. Guan S, Liu HZ. *Ind. Eng. Chem. Res.* **39**(8): 2891–2895, 2000.
23. Pernicone N. *Cattech.* **7**(6): 196–204, 2003.
24. Liu HZ, Li XN, Shzyki S, Ohnishi R and Ichikawa M. *J. CIESC.* **51**(4): 462–467, 2000.
25. Arabczyk W, Narkiewicz U, Moszynski D. *Langmuir*, **15**(18): 5785–5789, 1999.
26. Herzog B, Herein D, SchlJgl R. *Appl. Catal. A: General*, **141**(1&2): 71–104, 1996.
27. Ertl G. *J. Vac. Sci. Technol. A.* **1**: 1247–1253, 1983.
28. Alstrup I, Chorkendorff I, Ullmann S. *J. Catal.* **168**(2): 217–234, 1997.
29. Mortensen JJ, Hansen LB, Hammer B, *et al. J. Catal.* **182**(2): 479–488, 1999.
30. Lang ND, Holloway S, Norskov JK. *Surf Sci.* **150**: 24–38, 1985.
31. Jedynak A, Kowalczyk Z, Szmigiel D, *et al. J. Chem.* **75**(11): 1801–1805, 2001.
32. Boudart M. *Top Catal.* **13**(1& 2): 147–149, 2000.
33. Aika K, Tamaru K. *Ammonia, Catalysis and Manufacture.* Chapter 3, Berlin: Springer Verlag, 1995, 110.
34. Ozaki A, Aika K, Hori H. *Bull. Chem. Soc. Jpn.* **44**: 3216, 1971.
35. Kojima R, Aika K. *Appl. Catal. A: General*, **219**(1&2): 141–170, 2001.
36. Kojima R, Aika K. *Appl. Catal. A: General*, **219**: 157–170, 2001.
37. Kojima R, Aika K. *Appl. Catal. A: General*, **218**(1&2): 121–128, 2001.
38. Kojima R, Aika K. *Appl. Catal. A: General*, **215**(1&2): 149–160, 2001.
39. Kojima R, Aika K. *Chem. Lett.* **29**(5): 514–515, 2000.
40. Jacobsen CJH, Dahl S, Clausen BS, *et al. J. Am. Chem. Soc.* **123**(34): 8404–8405, 2001.
41. Timm B. *Ammonia Synthesis and Heterogeneous Catalysts* Vol. 1. In: Dechema (ed.) *Proc. 8th Intern. Congr. Catal.* Verlag Chemie, Weinheim, 1984, 7.

42. European Patent 174079. 1985.
43. German patent 493793. 1925.
44. Alconchel S. *J. Mater Chem.* **8**(8): 1901–1909, 1998.
45. Oyama ST. In: Oyama ST (ed.) *The Chemistry of Transition Metal Carbides and Nitrides*. Chapter 1, Blackie Academic, London: 1996.
46. Kojima R, Aika K. *Appl. Catal. A: General*, **215**(1&2): 149–160, 2001.
47. Kojima R, Aika K. *Appl. Catal. A: General*, **219**(1&2): 141–170, 2001.
48. Ertl G. *J. Vac. Sci. Technol. A*. **1**: 1247–1253, 1983.
49. Strongin DR, Carrazza J, Bare SR, *et al. J. Catal.* **103**(1): 213–215, 1987.
50. Bielawa H, Hinrichsen O, Birkner A, *et al. Angew Chem.* **113**: 1093–1096, 2001.
51. Liu HZ. *Technological Communications of Zhejiang College of Chemical Engineering*, **1**: 55–68, 1978.
52. Keunecke E. *Z. Elektrochem.* **36**: 690, 1930.
53. Research Group of Catalysis at Department of Chemical Engineering, Technological Communications of Zhejiang College of Chemical Engineering. **1**: 1–3, 1974.
54. Smith PJ, Taylor DW, Dowden DA, *et al. Appl. Catal.* **3**(4): 303, 1982.
55. Brill R, Osumi Y. *Bull. Chem. Soc. Jpn.* **39**: 1678, 1966.
56. Zabuga VY, Markova GP. *Katalizi Katalizatory*. Akad Nauk Ukr SSR, Resp Mezhved sb. 1965, 110 (CA64: 4312d).
57. Artyukh YN, Rusov MT, Boldyreva NA. *Kinet. Katal.* **8**: 1319, 1967.
58. Research Group of Catalysis at Department of Chemical Engineering, Technological Communications of Zhejiang College of Chemical Engineering. **1**: 9–13, 1973.
59. Artyukh YN, Rusov MT, Boldyreva NA. *Kinet. Katal.* **8**(6): 1319–1324, 1967.
60. Ichikawa M, Kondo T, Kawase K, *et al. J. Chem. Soc. Chem. Commun.* **3**: 176, 1972.
61. Блескин О И. Хим Пром, **10**: 29–31, 1986.
62. Komarov VS, Efros MD, Rabina PD, *et al.* SU 988327. 1983 (CA98: 114516b).
63. Urabe K, Yoshioka T, Ozaki A. *J. Catal.* **54**(1): 52, 1978.
64. Hikita T, Aika K, Onishi T. *Catal. Lett.* **4**(2): 157, 1990.
65. Hikita T, Kadowaki Y, Aika K. *J. Phys. Chem.* **95**(23): 9396, 1991.
66. Takeshita T, Wallace WE, Craig RS. *J. Catal.* **44**(2): 236, 1976.
67. Wallace WE, France J, Shamsi A. *Rare Earth Mod. Sci. Technol.* **3**: 561, 1982.
68. Kirch G, Schwab E, Wicke E, *et al.* In: Dechema (ed.) *Proc. 8th Intern. Congr. Catal.*, Weinheim: Verlag Chem., **4**: 209, 1984.
69. Agnieszka PJ, Barbara M, Antoni WM. *Appl. Catal. A: General*, **141**(1&2): 1–16, 1996.
70. Morawski AW, Lendzion BZ, Kaklucki K, *et al. Appl. Catal. A: General*, **156**(1): 19–27, 1997.
71. Jacobsen CJH, Blosen M, Seichst J, *et al.*, Preparation Method of Ammonia and Ammonia Synthesis Catalyst. CN 1266815A. 2000.
72. Liu ZQ. *Acta Scientiarum Naturalium Universitatis*, **1**: 76–78, 1998.
73. Zhu HY. *Journal of Alloys and Compounds*, **240**: 1–3, 1996.
74. Wang XK, Shen NF, Han SH, *et al. Journal of Chemistry*, **52**(6): 613–619, 1994.
75. Zhang XL. *Chemistry of Complex*, Beijing: Higher Education Press, 1991, 422.
76. Zhang SY. *Chemistry Letters* (Internet), **c01005,** 2001.
77. Shen J (Editor in Chief), Zhu SY, Fen XT (Associate Editor). Committee of Board of Fertilizer Technology. *Ammonia Synthesis*, Beijing: Chemical Engineering Press, 2001.
78. Allen AD, Senoff CW. *Chem. Commun.* **24**: 621–622, 1965.
79. Leigh GJ. *Science*, **268**: 827–828, 1995.
80. Hidai M, Mizobe Y. *Chem. Rev.* **95**: 1115–1133, 1995.
81. Shi, QZ, Gao YC, Tang ZX, *et al. Chemistry of University*, **12**(5): 1–5, 1997.
82. Laplaza CE, Commins CC. *Science*, **268**: 861–862, 1995.

83. Chatt J, Pearman AJ, Richards RL. *Nature*, **235**: 39–40, 1975.
84. Chatt J, Pearman AJ, Richards RL. *J. Chem. Soc. Dalton Trans.* 1852–1860, 1977.
85. Pickett CJ, Talarmin J. *Nature* **317**: 652–653, 1985.
86. Xiamling Z. *Coordination Chemistry*, Beijing: Higher Education Press, 1991, 422.
87. Pan DK, Zhao CD, Zheng ZX. *Structure of Materials*. Beijing: Higher Education Press, 377–383, 1982.
88. Beijing Normal University, *et al. Inorganic Chemistry*. Beijing: People Education Press, 581–583, 1981.
89. Lu JX. *Chemistry*, **33**: 417–434, 1979.
90. Chai QR, Lin ST, Wan HL. *Journal of Xiamen University* (Natural Science). **2**: 30–43, 1979.
91. Kim J, Rees DC. *Science*, **257**: 1677–1682, 1992.
92. Wu Y. *Chemistry in Catalysis*, Beijing: Science Press, 1324–1329, 1998.
93. Fujishima A, Honda K. *Nature*, **37**: 238, 1972.
94. Parmon VN, Zamaraev KI. In: Photo Catalysis Fundamentals and Application. Serpone N, Pelizzetti E (eds.) Wiley Interscience. New York, 1989, 565.
95. Pelizzetti E, Schiavello M (eds.) *Photochemical Conversion and Storage of Solar Energy*, Kluwer Academic Publishers, Dordrecht, 1991.
96. Ollis DF, AlEkabi H (eds.) *Photocatalytic Purfication and Treament of Water and Air*, Amsterdam: Elsevier, 1993.
97. Fox MA, Dulay MT. *Chem. Rev.* **93**: 341, 1993.
98. Kamat PV. *Chem. Rev.* **93**: 267, 1993.
99. Lehn JM. *Plannarg Lecture of the 8th International Congress in Catalysis*. Berlin, 1984, Part 1.
100. Moore WJ. *Physical Chemistry Langman*, London, 1976, 863.
101. Kalyansundaram K, Gratzel M, Pelizzetti E. *Coord. Chem. Rev.* **69**: 57 1986.
102. Ileperuma OA, Tennakone K, Dissanayake WDDP. *Appl. Catal.* **62**(1): 1–5, 1990.
103. Chen JJ, Huang CR, Gan SF. *Progress in Chemical Engineering*, **21**(6): 417–419, 2002.
104. Ileperuma OA, Thaminimulla CTK, Kiridena WCB. *Solar Energy Materials and Solar Cells*. **28**: 335–343.
105. Tennakone K, Ileperuma OA, Bandara JMS, *et al. Solar Energy Materials*, **22**: 319–325, 1991.
106. Tennakone K, Bandara JMS, Thaminimulla CTK, *et al. Langmuir*, **7**(10): 2166–2168, 1991.
107. Schrauzer GN, Guth TD. *J. Am. Chem. Soc.* **99**(22): 7189, 1977.
108. Fujushima A, *et al.* In: *The Autumnal Meeting of the Chemical Society of Japan*, Nagoya, 1978, 17.
109. Miyama H, Fujii N, Nagae Y. *Chem. Phys. Lett.* **74**(3): 523, 1980.
110. Li SF, Wen XZ, Chui CL, *et al. Chemistry Letters*, **3**: 13, 1983.
111. Wu Y. *Catalytic Chemistry*. Beijing: Science Press, 1291–1296, 1998.
112. Gilbert A, Baggott J. *Essentials of Molecular Photochemistry*. Boca, Raton: CRC Press, 1991.
113. Calvert JG, Pitts JN. *Photochemistry*, John Wiley & Sons Inc. 1966.
114. Fox MA, Chanon M (eds). Photo Induced Electron Transfer Part A. Conceptional Basis, Amsterdam: Elsevier, 1988.
115. Wu Y. *Catalytic Chemistry*. Beijing, Science Press, 1998.
116. Marnellos G, Stoukides M. *Science* **282**: 98–100, 1998.
117. Pickett CJ, Talarmin J. *Nature*, **317**: 652–653, 1985.
118. Tames YB, Shlomit A, Barry P. *J. Electroanal. Chem.* **230**(1&2): 143–153, 1987.
119. Huruyanagai, Kichihaneshou. *Denki Kagaku*. **57**(3): 261–262, 1989.
120. Furuya N, Hiroshi Y. *J. Electroanal. Chem.* **263**(1&2): 171–174, 1989.

121. Furuya N, Yoshiba H. *J. Electroanal. Chem.* **272**(1&2): 263–266, 1989.
122. Marnellos G, Stoukides M. *Science*, **282**: 98–100, 1998.
123. Leigh GJ. *Science*, **268**: 827–828, 1995.
124. Zhang XL. *Chemistry of Complex*, Beijing: Higher Education Press, 1991, 422.
125. Pan DK, Zhao CD, Zheng ZX. *Structure of Materials*, Beijing: Higher Education Press, 1982, 377–383.
126. Wang LH, Chen SZ, Liao DW, *et al. Progress in Chemical Engineering*, **11**(4): 376–384, 1999.
127. Murakami T, Nohira T, Goto T, *et al. Electrochimica Acta*, **50**(27): 5423–5426, 2005.
128. Goto T, Ito Y. *Electrochim Acta.* **43**(21&22): 3379–3384, 1998.
129. Masuko N, Hisamatsu T, *Molten Salts*, **7**: 520, 1964.
130. Amezawa K, Tomii Y, Ito Y. *J. Electrochem. Soc.* **141**(11): 3096, 1994.
131. Murakami T, Nohira T, Ogata YH, *et al. Electrochem. Solid State Lett.*, **8**(1): E1–E3, 2005.
132. Yiokari CG, Pitselis GE, Polydoros DG, *et al. J. Phys. Chem. A* **104**(46): 10600–10602, 2000.
133. Leigh GJ. *Science*, **268**: 827–828, 1995.
134. Zhang SY. *Chemistry* (Internet), **c01005**, 2001.
135. Translated by Research Group of Nitrogen fixation at Department of Chemistry at Jilin University, *Progress in Chemical Simulation of Biological Nitrogen Fixation*. Beijing: Science Press, 1973.
136. Translated by Research Group of Nitrogen fixation at Fujian Institute of Research on Structure of Material. CAS, and Research Group of Nitrogen fixation at Department of Chemical Engineering and Chemistry, *Progress in Chemical Simulation of Biological Nitrogen Fixation*. II. Beijing: Science Press, 1976.
137. Research Group of Nitrogen fixation at Department of Chemistry at Xiameng University. *Science in China*, **5**: 479, 1976.
138. Research Group of Catalysis at Fujian Institute of Research on Structure of Material. CAS. *Science Bulletin*, **12**: 540, 1975.
139. Research Group of Nitrogen fixation at Department of Chemistry at Jilin University. *Science in China*, **1**: 28, 1974.
140. Liu HZ. *Technological Communications of Zhejiang College of Chemical Engineering.* **1**: 55–68, 1978.
141. Research Group of Nitrogen fixation at Department of Chemistry at Jilin University. In: Translated by Research Group of Nitrogen fixation at Department of Chemistry at Jilin University. *Progress in Chemical Simulation of Biological Nitrogen Fixation*, Beijing: Science Press, 1973, 28–60.
142. Huang JW, Zhang FZ, Xu, LS, *et al. Chemical Journal of Chinese Universities*, **16**(6): 920–923, 1995.
143. Rod TH, Logadottir A Nørskov JK. *The Journal of Chemical Physics* **112**(12): 5343–5347, 2000.
144. Liu HZ, Li XN, Hu ZN. *Appl. Catal. A: General*, **142**(2): 209–222, 1996.
145. Wang XN, Zhu H, Xia WQ, *et al. Chinese Journal of Catalysis*, **21**(3): 276–278, 2000.
146. Liu HZ, Tang HD, Li XN. *Journal of Chemical Industry and Engineering*, **55**(12): 2067–2071, 2004.
147. George LS, William TP, Paul TW, *et al. J. Solid State Chem.* **123**: 277–284, 1996.
148. Shen J (Editor in Chief), Zhu SY, Fen XT (ed.). *Committee of Collection of Fertilize Technology, Ammonia Synthesis*, Beijing: Chemical Engineering Press, 2001, 1–3.
149. Schlogl R. *Angew Chem. Int. Ed.* **42**: 2004–2008, 2003.
150. Wu HY. *Design of Chemical Engineering*, **12**(4): 3–5, 2002.
151. Ming EZ, Zhang LX (Editor in Chief). *Development of Industrial Chain of Biodiesel-Refining Plant of Biodiesel*, Beijing: China Petrochemical Press, 2006.

152. Nielsen A. In: Nielsen A (ed.) *Ammonia, Catalysis and Manufacture*. Berlin: Springer, 1995. 330–345.
153. Sargent & Lundy LLC Consulting Group. Assessment of parabolic trough and power solar technology cost and performance forecasts, October 2003, National Renewable Energy Laboratory, US.
154. Mills D. *Solar Energy*, **76**(1): 19–31.
155. David M, Graham LM. *Solar Energy*, **68**(3): 263–283, 2000.
156. Luo YJ, *et al* (eds.) *Application of Solar Energy*, Beijing: Chemical Engineering Press, 2004.
157. Lovegrove K, Luzzi A, Soldiani I. *Solar Energy*, **76**(1): 331–337, 2004.
158. Soteris AK. *Progess in Energy and Combustion Science*. **30**(3): 231–295, 2004.
159. Lovegrove K, Luzzi A, Mccann M. *Solar Energy*, **66**: 103–105, 1999.

Index

A

A301 ammonia synthesis catalyst, 158
AB_5-type metallic hydride, 807
Abrasion ratio, 714, 716, 717, 721
Abrasion resistance, 46, 48
Abrasion strength, 343, 344, 714, 716–719, 721
Accelerated aging, 549
Accumulation of the inert gas, 744
Acid treatment, 462–464
Acid-alkali coverage, 514
Acid-base synergistic effect, 233
Acidic surface area, 232
Activated carbon, 8, 20, 32, 59, 62, 108, 111, 237, 257, 319, 427–435, 437, 440, 442, 444, 447, 450, 451, 455–466, 468–475, 477, 479, 481, 482, 489, 491, 493, 496, 506, 509, 514, 515, 521–529, 532–537, 589, 748, 800, 835
Activated carbon supported ruthenium catalysts, 59, 108, 457
Activated chemisorption, 592
Activated energy, 513
Activated energy of desorption, 513
Activation energy of methanation, 536
Activation of dinitrogen, 49, 50, 810, 823, 830
Activation treatment, 430
Active barrier, 133, 799
Active coefficient, 162, 163, 167, 168
Active site, 7, 50, 67–69, 75, 79, 81–83, 88, 93, 94, 96, 103, 118, 122, 124, 125, 127, 128, 131–133, 135, 136, 140–142, 144, 146, 151, 152, 162, 197, 210, 214, 229, 231, 236–238, 251, 253, 273, 274, 283–285, 287, 292, 294–304, 377, 404, 432, 433, 447, 449, 453, 474, 492, 494, 495, 497, 498, 500, 501, 512–514, 532, 547–550, 561, 578, 584, 591–593, 596, 604, 624, 636, 690, 692, 699, 775, 794, 796, 800, 801, 833
Active site density, 285, 297
Active site group theories, 68
Active site intensity, 238
Active site number, 285, 295, 297, 494
Active temperature of catalyst, 653, 659, 660, 835
Activity determination and calculation, 558
Activity of ruthenium catalyst, 59, 435, 439, 440, 446, 447, 451, 458, 499, 501, 504, 518, 519, 521, 741
Activity of wüstite-based catalyst, 39, 47
Activity pattern, 223, 224
Adiabatic bed, 168, 171, 416, 727, 728
Adiabatic reactors, 169
Adsorbed state of gas, 580
Adsorbed state of oxygen, 581
Adsorption, 8, 19, 20, 49, 51–53, 57, 59, 60, 68, 74–108, 110–112, 117–119, 122–124, 127, 129–131, 133, 134, 136, 138, 140, 145, 146, 148, 152, 153, 229, 232, 233, 235–237, 243, 244, 246, 247, 249, 251, 253–255, 257, 271, 273, 274, 276–279, 281, 282, 284, 289, 297, 304, 392, 393, 406, 420, 425, 432, 434, 436, 437, 439, 442, 443, 449, 455, 456, 458, 462, 463, 466, 469–474, 481, 487–489, 498, 503, 507–517, 521, 522, 528, 532–535, 537, 544, 545, 557, 565, 568, 569, 572–585, 587, 588, 592–599, 604, 641–643, 664, 687, 690, 692, 693, 700, 704, 743, 794–802, 804, 808, 810, 811, 818, 821, 829–831, 834
Adsorption activation energy, 77
Adsorption capacity, 8, 86, 392, 406, 481, 488, 579, 580, 584, 593

Adsorption enthalpy, 236, 514, 595
Adsorption equilibrium constant, 84
Adsorption heat, 52, 75, 77–79, 82, 84, 86, 87, 94, 95, 99, 101, 236, 244, 251, 253, 257, 273, 511, 512, 544, 579, 580, 587, 592, 593, 595
Adsorption isotherms, 83, 84, 140, 569, 573, 585, 587
Adsorption of N_2 on non-iron metals, 97
Adsorption property, 235, 508, 517, 544, 593
Adsorption species, 75, 90, 235–237, 545, 580, 642, 794
Adsorption states of nitrogen, 89, 98
Adsorption theory, 68, 83, 146, 568, 569
Adsorption-autocatalytic theory, 392
Affinity, 19, 20, 51, 57, 82, 83, 100, 113–115, 125, 126, 133–135, 138, 141, 142, 145, 146, 379, 392, 578, 820
Alkali metal, 57, 59, 101, 108, 231, 232, 236, 237, 247, 249, 276, 315, 428, 436, 439, 441–444, 446–450, 453, 467, 468, 512, 514–516, 528, 529, 586, 797
Alkali metal hydroxides, 236, 446, 453, 468, 512
Alkali promoter, 232, 285, 449, 450
Alkali surface area, 231
Alkaline earth metal, 315, 435, 439, 441–446, 450, 453, 458, 461, 514, 528–530, 586, 691
Alkaline zeolite, 439
Alloy effect, 57, 804
Alumina, 7, 13, 27, 212, 245, 246, 248, 251, 253, 254, 259, 260, 263, 264, 271, 274, 276, 279, 280, 312, 347, 348, 352, 428, 435, 439, 455, 518, 589, 616, 632, 635, 825, 832
α-Fe crystallite, 228, 229, 246, 247, 249, 270–272, 285, 286, 294–296, 302, 339, 340, 360, 400, 404, 408, 419
Ammonia combustion, 17
Ammonia converter, 61, 138, 503, 657, 659, 685, 686, 696, 704, 747, 756, 771, 781
Ammonia decomposition, 53, 55, 100, 106, 109–111, 149, 164, 169, 237, 556, 798
Ammonia equilibrium concentration, 500, 504
Ammonia process, 21, 60, 62, 520, 747, 764
Ammonia productivity, 17, 27, 649, 650, 652, 675, 685, 765, 766, 777, 784, 837, 838
Ammonia refrigeration, 673, 696
Ammonia synthesis rates, 78, 97, 100, 101, 106, 148, 162, 438, 442, 487, 504, 799, 805, 824, 826, 827, 829
Ammonia synthesis reaction, 49, 51, 53, 58, 60, 70, 71, 82, 91, 96, 102, 105, 111–113, 117, 118, 123, 147, 152, 158, 159, 165, 166, 173, 204, 223, 233, 236–239, 242, 243, 251–253, 279, 288, 337, 361, 415, 418, 421, 436, 437, 439, 442, 444, 447, 459, 472, 474, 492, 497, 499, 507–509, 511–513, 515, 516, 518, 520, 527, 528, 588, 599, 636, 649, 653, 656, 660, 661, 664, 665, 688, 727, 745, 759, 769, 795, 798, 799, 809, 812, 828
Ammonia synthesis reactor, 67, 103, 119, 163, 176
Amorphous alloy, 807
Amorphous phase, 379, 381, 456, 469, 618, 619
Analysis of reactor, 118
Annual production of ammonia, 30
Anti-methanation, 524–526
Antichlor, 20
Antitoxic stability, 548, 549
Apparent activation energy of diffusion, 385
Apparent density, 565, 567
Apparent reaction kinetics, 153
Application of catalysts, 272, 359, 615, 649
Application of thermal analysis technology, 605
Application of XRD in the study of catalysis, 609
Applied form of kinetic equation, 163
Arrhenius equation, 166, 403, 592, 600
Artificial neural network, 244
Ash layer-diffusion-controlled process, 369
Associative adsorption of dinitrogen, 130
ASTM standard method D4058-96, 46, 48
Atomic arrangement, 210, 213, 289
Atomic defect, 206, 209, 211, 382
Attrition, 342, 706
Auger electronic spectroscopy (AES), 640
Automobile catalytic converter, 686
Average nanoparticles size, 591
Average pore size, 265, 271, 399, 522, 571, 689, 806

Average reaction order of H_2, 376
Axial-flow ammonia converters, 685

B

B5 structure, 494
B5 type active site, 498
BASF, 23–26, 28, 35, 50, 722, 795, 800, 826, 837
Basic surface area, 232, 586
Basicity of the catalyst, 11, 60
Basis of catalyst solid mechanics, 707
Bed voidage, 682
Bench scale reactor, 550
Benefit of energy saving, 781
Benefit of increased production, 778
BET adsorption theory, 569
Bettie–Bridgeman state equation, 166
Bimetallic catalysts, 56, 798, 799, 804
Bimetallic complex, 811
Binding energy of defect cluster, 195
Biocatalytic ammonia synthesis, 831
Biochemical nitrogen fixation, 793
Biochemistry, 68
Bionic catalysis, 67
Body centered cubic, 152, 285–287, 566
Body defect, 211
Bond energy, 51–53, 57, 118, 244, 535, 536, 593, 598, 640, 804
Boron nitride, 428, 440
Bottom energy level, 70
BP network, 244
BP network with genetic Algorithm, 244
Braun process, 30, 31, 738, 740, 770
British petroleum, 31, 458, 742, 743
Bronsted relation, 134, 144, 145
Bronsted-type relation, 133
Bulk distribution, 224, 391
Bulk restructuring, 224, 391

C

C_7 site, 251, 253, 292, 293, 298
Ca^{2+} replacement, 269
Calcium carbide, 1, 767
Calcium carbonate, 312
Calcium cyanamide, 1
Calcium ferrocyanide, 311
Calculation of ammonia concentration, 559
Calculation of pore size distribution, 575
Capacity of ammonia synthesis catalysts, 30
Capacity of the electron conduction, 523
Capillary cohesion phenomenon, 573
Capillary phenomenon, 470
Carbon deposition, 11, 550, 604, 606, 608, 609
Carbon dioxide, 3, 258, 606, 700, 767
Carbon monoxide, 2, 3, 46, 150, 257, 258, 271, 425, 581, 606, 659, 697–699, 777
Carbon nanotube, 441
Carbonaceous materials, 430, 704
Carbonization, 430, 431, 750
Carl Bosch, 2, 23, 24
Catalyst cost, 503, 733, 741, 747, 752, 771, 773, 774, 776
Catalyst design, 241, 243–245, 719, 802
Catalyst efficiency, 31, 518, 665, 669, 670, 677–680, 795, 836
Catalyst poisoning, 16, 549, 641, 690, 693, 704
Catalytic hydrodesulphurization, 6
Catalytic reaction mechanisms, 67, 76, 104
Catalytic reactor, 550, 555, 658, 824
Cation assignment of spinel structure, 187
Cation defect, 36, 202, 211, 218, 365
Cerium intermetallic compound, 58
Cerium nitrate, 58, 312
Cesium, 254, 255, 440, 441, 445, 447, 450, 451, 453
Change of chemical composition, 687
Change void model, 372
Characteristic of reduction processes, 411, 415
Characteristic parameter of reduction, 227
Characterization, 1, 74, 76, 234, 296, 297, 433, 496, 543, 544, 578, 608, 639, 712, 807
Characterization of active sites, 296, 297
Characterization of catalysts, 74, 76
Characterization of Properties, 608
Characterization of the microstructure, 608
Chemical composition of natural magnetite, 314
Chemical essence of catalysis, 70
Chemical model, 69
Chemical reaction during catalyst preparation, 319
Chemical stability, 521, 544, 612
Chemical stoichiometric number, 67, 126
Chemical titration, 122
Chemical valence, 185, 267, 316, 426, 607
Chemisorption, 51, 52, 55, 57, 67, 74, 75, 77, 79, 80, 83, 87–89, 94, 98–100,

105–107, 111, 117, 122, 146, 148, 150–152, 229–232, 235–237, 244, 249, 257–259, 271, 279, 281, 284, 285, 293, 294, 297, 304, 402, 427, 450, 472, 480, 487, 488, 493, 494, 497, 514–516, 528, 578–592, 598, 599, 616, 624, 642, 643, 699–701, 794, 798, 804, 829, 830
Chemisorption for nitrogen, 52, 82
Chemisorption heat of N_2, 52
Chemisorption of CO, 229, 230, 258, 284, 285, 294, 487, 578, 583, 584
Chemisorption of pyridine, 587
Chemisorption on single-crystal surface, 599
Chemisorption state, 88, 99, 581
Chemisorption state of carbon monoxide, 581
Chemisorption stoichiometry, 285, 582, 586, 588
Chemisorption strength, 80
Chlorine, 11, 20, 73, 312, 315, 426, 427, 449, 467–469, 472–478, 480–483, 485–488, 516, 640, 691, 695, 700, 704
Chlorine compounds, 704
Chlorine-free ruthenium compound, 427
Choice of catalyst particle size, 684
Choice of reduction condition, 419, 420
Chromium-free shift catalysts, 13
Classification of defects, 209
Claus method, 17, 18
CO high-temperature shift catalysts, 11
CO low-temperature shift catalysts, 14
CO selective oxidation catalysts, 16
CO shift reaction, 9, 11, 12, 14
CO_2 dehydrogenation catalysts, 16
Co_3Mo_3N, 800–803
Co–Mo hydrogenation catalyst, 3, 6
Co-precipitation method, 12, 806
Coconut shell, 430, 431, 434, 522–527
Cold-quench, 659, 663, 685, 756, 757, 759
Cold-quench type converter, 756
Cold-tube type converter, 756
Collision theory, 83, 102
Comparison between Ruthenium-based and iron-based catalyst, 505
Comparison of power consumption, 754
Comparison of reduction properties, 377
Compensation effect, 144, 146, 214
Competitive, 47, 226, 236, 266, 300, 302, 392, 408, 449, 455, 456, 466, 474, 506, 508, 510, 512, 514, 580, 693, 829
Competitive adsorption, 236, 449, 455, 456, 466, 474, 508, 510, 512, 514, 576, 577, 580, 693, 829
Competitive adsorption isotherm, 580
Compound-type complex oxides, 202
Compounds of sulfur, 700
Compression of synthesis gas, 3
Concentration effect of poisons, 693
Concentration gradient, 154, 394, 395, 405, 630
Concentration of ammonia, 21, 22, 31, 41, 59, 150, 297, 337, 440, 504, 555, 558–561, 650–653, 660, 662, 664, 665, 669–672, 676, 686, 694, 700, 738, 741, 742, 745, 746, 750, 752, 754, 756, 775, 778, 782, 834
Concentration of defect, 45, 191, 383, 394, 566
Concentration of precipitator, 485
Concentration of water vapor, 339, 388, 405, 406, 410, 418, 420–422, 695
Condensing temperature of ammonia, 674, 749, 752
Conglutinating of reactants and/or other substances, 687
Conglutination of α-Fe crystals, 360
Consequence, 140, 187, 191, 201, 223, 231, 373
Content of ammonia, 106, 169, 659, 673, 674, 733, 734
Content of chlorine, 472, 473, 480
Content of hydrogen, 405, 421
Content of inert gas, 30, 33, 406, 557, 561, 650, 664, 670–672, 676, 742, 743, 745, 746, 752, 782, 783
Content of water vapor, 337, 339, 696
Continuous glomeration method, 351
Continuous heat exchange bed, 167
Continuous heat-exchange reactor, 658–660
Control of hot spot temperature, 727
Control of inlet temperature, 727
Control of temperature of catalyst bed, 660
Control system, 557
Conversion rate, 99, 366, 545, 547, 601, 777
Cooled-type reactor, 658
Coordinated activation, 810
Coordination chemistry, 68, 242
Coordination model, 81

Coordination number, 81, 142, 145, 151, 288, 616, 710, 716
Copper-ammonia solution washing process, 670
Copper-based catalyst, 17
Coprecipitation, 7, 454
Core-shell structures, 287
Corundum-type hexagonal structure, 201
Cost of recovering the noble metal, 773
Coverage of adsorbed nitrogen, 78, 100, 106
Coverage-factor, 692
Crack core model, 372
Cracking, 19, 20, 70, 343, 543, 565, 687, 704, 707, 766
Crackling core-and-shell model, 635
Critical parameters, 176
Crush strength, 349, 706, 709–712, 716–718, 720, 721
Crushing and sieving of molten materials, 319
Crushing strength, 46
Crystal cell, 185, 566, 610, 618
Crystal face, 68, 74, 76, 80, 81, 91, 96, 98, 99, 105, 119, 142, 147, 151, 152, 210, 214, 229, 237, 238, 251–253, 270, 271, 279, 280, 287–295, 302, 303, 335, 444, 498, 795, 833
Crystal growth process, 360, 361, 377
Crystal irregularity, 213
Crystal lattice types, 204
Crystal nucleus formation, 396
Crystal nucleus growing model, 377
Crystal phase, 12, 36, 38, 39, 193, 199, 202, 218, 273, 301, 311, 381, 624, 807
Crystal shape, 295, 296, 378, 498, 609
Crystal structure, 33, 36–39, 185–187, 189, 190, 193, 202, 204, 205, 211, 215, 216, 218–220, 222, 223, 248, 266, 267, 285, 287, 301, 302, 327, 332, 333, 335, 381, 524–526, 564, 565, 570, 610, 611, 619, 621, 623, 624, 795, 797, 808
Crystal structure of wüstite, 190
Crystal-lograpic orientation, 147
Crystallization degree, 460
Crystallization of kernel, 287
Cu–Ni alloy, 517
Cu-based catalyst, 15, 20
Cu-based de-arsenic agents, 20
Curie point, 188
Current efficiency, 822, 823, 826, 830
Cyanamide process, 1

D

d-electron character, 70, 517, 518
d-electrons of ruthenium, 425
De-arsenic agents, 20
De-chlorination, 16, 20, 475–478, 480–482, 485, 486, 639, 640
De-chlorination temperatures, 476
De-poison catalyst, 16, 19
Deactivation, 7, 12, 15, 16, 27, 28, 45, 46, 162, 163, 242, 254, 257, 362, 544, 550, 594, 686–688, 690, 694, 702, 703, 835
Dechlorination effect, 475, 480
Defect cluster, 192–195
Defect concentration, 36, 191, 196, 199, 201, 218, 219, 228, 269, 326, 359, 389, 394, 613
Defect structure, 192, 193, 205, 207–209, 269, 380, 544
Defective electron, 190
Degree of coverage, 582
Degree of methanation, 524, 529
Dehydrogenation catalyst, 16, 18
Dendrite segregation, 330, 331
Density of catalyst, 118, 523, 564, 566, 675, 720, 774
Design of promoter, 240, 242
Designed energy consumption, 765, 766
Desorption activation energy, 49, 87, 101, 235–238, 513, 593–595, 598, 599
Desorption kinetic parameters, 595
Desorption of adsorbed ammonia, 105
Desorption temperature, 91, 98, 105, 235, 237, 513, 599
Desquamating, 640, 687
Desulfurization technology, 704
Desulphurization of the feedstock, 6
Determination of average nanoparticle size, 615
Determination of lattice constant, 614
Development of catalysis theory, 68
Development of fused iron catalysts, 25, 36
Development trend, 30, 838
Diameter of isopyknic sphere, 562
Diamond-like carbon, 429
Differential reactor, 552
Diffusion coefficient, 153, 154, 156–160, 191, 331, 365, 369, 384–386, 394, 399, 404, 572
Diffusion coefficient of defect, 191
Diffusion coefficient of the cation, 365
Diffusion equation, 407

Diffusion of reactant molecules, 153
Diffusion process, 154, 156, 162, 343, 365, 595
Dinitrogen complex, 810, 811, 831, 832
Direct by-product steam, 768
Discharging and cooling of molten material, 318
Discovery of ruthenium based catalysts, 51
Discovery of wüstite based catalysts, 300
Dislocation, 190, 210, 211, 213, 214, 287, 707
Disordered state, 187, 188
Dispersion of metals, 284
Displacement of atoms, 384
Displacement of defect, 385
Disproportionation reaction, 47, 322, 326, 612, 613, 627
Dissociated adsorption, 88, 90, 98, 100–102, 105, 107, 111, 117, 123, 127, 129, 130, 794, 795
Dissociation coefficient, 90, 91
Dissociation energy for N≡N bond, 809
Dissociation of adsorbed dinitrogen, 105, 119
Dissociation probabilities of N_2, 251
Distinguish, 112, 119, 196, 279, 579, 581, 592
Distortion of lattice, 209
Distribution function, 133, 134, 140, 707
Distribution of pore size, 452, 572
Distribution of promoters, 49, 222, 223, 260, 265, 302, 317, 318, 332, 334, 335, 353
Donor-receptor, 449
Dosage of the catalyst, 5
Double cone-shaped capillary pores, 577
Double layer structure model, 247
Double logarithm calculations, 378
Drop-shatter test, 712, 713
Drying, 12, 19, 426, 455, 466, 467, 482, 488–492, 567, 806
Drying mechanism of porous materials, 490
Drying method, 491, 492
Dynamic research of catalyst, 75

E

Economic appraisement, 786, 788
Economic benefits using the pre-reduced catalyst, 775, 776
Economic catalysts, 3, 14
Economic factor of reduction, 774
Edge carbon atoms, 524, 525, 534–537
Edge dislocation, 210
Effect of chemical composition of catalysts, 716
  Mechanical strength, 12, 32, 33, 46, 48, 300, 339, 342, 345, 348, 349, 352, 428, 438, 521, 543, 544, 562, 684, 705, 706, 712, 713, 716, 718, 719, 725, 726, 823
  Methanation, 3, 6, 8, 12, 15–17, 47, 60, 257, 300, 435, 442, 446, 456, 457, 459, 462, 476, 477, 506, 515, 521–537, 670, 702, 704, 752
Effect of chlorine, 427, 472, 473, 486, 487
Effect of crystal structure of activated carbon, 525
Effect of Fe^{2+}/Fe^{3+}, 716, 717
Effect of gas composition, 159, 376
Effect of graphitization, 458, 522
Effect of H_2 content on initial methanation, 535
Effect of H_2/N_2 on the activity, 507
Effect of micro-crystal structure, 525
Effect of particle size, 94, 150, 151, 376, 642, 675–680
  Pressure drop, 13, 30, 33, 345, 346, 348, 349, 563, 567, 568, 662, 664, 674, 680–686, 705, 706, 711, 719, 720, 727, 736, 738, 740, 744, 752, 756
  Reaction rate, 10, 13, 25, 41, 45, 47, 55, 56, 58, 71, 73, 78, 80, 97, 100, 106–108, 110–114, 124, 126, 129, 132, 137–139, 145–147, 153–157, 160–164, 166–168, 170, 171, 189, 218, 238, 251, 253, 258, 273, 290, 296–299, 360, 362, 365, 366, 368, 370, 371, 373, 375, 377, 388, 397–399, 403, 404, 420, 436, 437, 439–442, 444, 451, 474, 476, 487, 488, 498, 504, 505, 511, 512, 517, 545–547, 551–554, 558–561, 591, 600, 601, 603, 650, 655, 657, 659, 660, 665, 669, 674–679, 686, 697, 802, 805, 809, 814, 815, 818, 820, 821, 827, 829, 830, 834
  Utilization ratio of the inner surface, 674, 676–678
Effect of pH of $RuCl_3$ solution, 471, 472
Effect of preparation methods, 467

Effect of promoters on the mechanical strength, 718
Effect of purity of activated carbon, 524
Effect of reaction temperature, 677
Effect of solvent, 469, 470
Effect of surface structure of activated carbon, 526
Effect of temperature on the reduction, 412
Effect of the content of inert gas, 671
Effect of the raw materials of activated carbon, 430, 431
Effect of washing process, 486
Effects of size and shape, 682
Efficiency of energy conversion, 767, 837
Efficiency of H_2 reduction method, 475
Effusion work of electron, 250
Eggshell distribution, 456
Electric arc furnace, 312, 315, 317–320
Electric arc method, 1
Electric conductivity, 311
Electric furnace technology, 311
Electric resistance furnace, 312, 315, 316
Electrical double layer, 819
Electrical energy, 813, 830
Electro catalysis, 67, 820
Electrocatalyst, 817, 818, 821
Electrocatalytic ammonia synthesis, 817
Electrocatalytic reaction, 817, 818, 820
Electrochemical ammonia synthesis, 820–823, 830
Electrochemical promotion effect, 826
Electrode potential, 818–822, 825
Electrode reaction, 817–820
Electrolytic ammonia synthesis, 824
Electron conductivity, 186, 191
Electron defect, 208, 213
Electron donor-acceptor (EDA), 32, 59
Electron paramagnetic resonance (EPR), 582, 641, 642
Electron probe microanalysis (EPMA), 258, 639
Electron spectroscopy of chemical analysis, 258, 265
Electron transfer process, 68, 819
Electronegativity, 213, 243, 267, 425, 436, 437, 442, 443, 447, 448, 487, 528, 530
Electronic configuration, 425, 429, 691
Electronic contribution of active site, 447
Electronic defect, 211
Electronic density of ruthenium, 487
Electronic donor, 443
Electronic promoter, 29, 239, 249, 255, 267, 341, 408, 440, 449–451, 467, 515, 517, 527, 530, 624
Electronic state of atoms, 641
Electronic theory, 68, 70
Energy consumption, 1, 2, 10, 17, 29–31, 48, 51, 61, 317, 349–351, 359, 649, 650, 652, 653, 662, 664, 674, 680, 684, 685, 726, 733–738, 743, 744, 748, 750, 754–756, 760–767, 777, 784, 788–790, 836–838, 843
Energy consumption of ammonia production, 652, 765
Energy consumption of synthesis loop, 755, 756
Energy equivalent value, 765, 767
Energy well, 77
Energy-consumed medium, 765, 767
Energy-saving technology, 2
Engelhard Industrial Corp, 18
Enrichment phenomena, 255
Ensemble, 56, 119, 125, 131–133, 144–146, 152, 274, 492, 494
Enthalpy change, 92, 363, 762, 820
Enthalpy of reaction, 133
Entropy change, 92, 363
Entropy of reaction, 134
Enzyme catalysis, 68, 69, 128
Equilibrium concentration of ammonia, 22, 31, 41, 651, 652, 664, 665, 669–671
Equilibrium constant, 6, 12, 16, 17, 21, 84, 98, 106, 112–114, 126, 133, 138, 139, 145, 149, 164–166, 387, 388, 474, 475, 592, 655, 665, 777, 809
Equilibrium deviation, 119, 120
Equilibrium diagram, 197, 389
Equilibrium isotherm, 149
Equilibrium state approximation, 105
Equilibrium temperature, 652, 656, 657, 748
Equivalent spherical diameter, 562
Etching degree, 262, 263
Etching method, 260, 262
Ethylene hydrogenation, 79, 122, 214, 517
Evaluation of catalyst activity, 75, 79
Evolution of the microstructure, 636
Existing states of chlorines, 472
Exothermal reaction, 117, 361
Experimental device, 26, 555
Expert system for catalyst design, 244
Expert system for the selection and optimization of catalysts, 244

Expert system of molecular design, 244
Exploration of non-iron and alloy catalysts, 798
Exploration of other non-iron catalyst, 803
Exponential law equations, 124
Exposed fraction of potassium atoms, 588
Exposure percentage, 284
Extended Hückel method, 291
Extended X-ray absorption fine structure (EXAFS) analysis, 615
External circuit loop, 820
External circulation reactor system, 553
External cooled bed, 658, 659
External diffusion, 102, 153–156, 161, 162, 404, 405, 675, 686
Extruder, 348

F

Face center cubic structure, 268
Face defect, 210
Factors affecting toxicity, 692
Factors of influence on reduction rate, 403
Farbenfabriken Bayer method, 311
Fast-cooling, 327, 335
Fe (100), 76, 151, 152, 278, 492, 636
Fe (111), 71, 76, 91–93, 104, 122, 123, 151, 152, 274, 289, 290, 294, 492, 628, 636, 693, 794, 833
Fe^{2+}/Fe^{3+} ratio, 39, 201, 215–219, 221, 222, 225, 249, 260, 301, 312, 319, 320, 352, 355, 356
$Fe_{1-x}O$ based catalyst, 30, 42
Fe_2O_3, 12, 13, 36, 37, 185–188, 192, 201–205, 217, 218, 220–223, 242, 267, 268, 311, 316, 319, 321, 323, 326, 343, 379, 382, 386, 387, 392, 611, 618–624, 808, 816, 817
Fe_3O_4, 5, 12, 13, 27, 32–40, 43–45, 48, 49, 88, 185–188, 196, 197, 199–205, 211, 215–218, 220–223, 225, 226, 228, 229, 231, 232, 234–238, 242, 245–249, 266–268, 270, 285, 294–297, 300, 301, 303, 304, 311, 312, 316, 317, 319–323, 325–327, 340, 343, 352, 355, 356, 359, 360, 363, 367, 377, 387–392, 394, 401, 402, 407, 408, 411, 419, 420, 515, 567, 584, 587, 599, 607, 608, 612–614, 618–628, 631, 716, 722–725, 771, 774, 775, 795, 796, 798, 808
Fe_3O_4 based catalysts containing cobalt, 32
Fe–Co catalyst, 29, 33, 36, 804
Fe–Cr catalyst, 11–14
Fe–O equilibrium phase diagram, 323
Fe-Mo catalyst, 831
Fe-Phthalocyanine catalyst, 822
$FeAl_2O_4$, 187, 204, 245, 246, 248, 279, 322, 327, 390, 418, 608
Femi energy level, 68
FeO, 34, 36, 37, 39, 48, 185, 186, 188, 190–192, 196, 200–206, 208, 216–221, 223, 225, 226, 228, 229, 231, 232, 237, 238, 242, 245, 247–249, 260, 264, 267–269, 297, 302, 315–317, 319–323, 325, 326, 332, 334, 335, 343, 355, 359, 367, 381, 385, 387–389, 391, 392, 394, 408, 414, 584, 607, 612, 625–628, 716, 796
Ferromagnetic, 185, 188, 641, 642
Fick's diffusion, 154
Fictitious equilibrium pressure, 149
Field-ion microscopy (FIM), 636
Fine desulfurizer, 8
Fine powder ratio, 711–716
Finger structure, 274
First ammonia plant, 2, 27
First ammonia synthesis catalyst, 21, 29
Fische–Tropsch synthesis reaction, 271
Fixed bed, 167, 169, 551, 657, 660, 661, 714
Fixed-bed reactor, 546, 556, 558, 658, 659, 680, 681, 711, 719
Flake structure, 274
Flash desorption, 237, 598, 599
Flash desorption method, 237, 598
Flow method, 546, 557, 558
Formation mechanism of carbon deposition, 604
Formation of α-Fe crystallite, 296, 360, 400
Formation of new compounds, 687
Formation of reduction product α-Fe, 377
Formation of temporary compound, 687
Four-bed intercooled ammonia converter, 61
Four-fold cluster, 195
Fourier transform analysis, 635
Fractional impregnation method, 466
Fractional-dimension structure, 242
Frenkel defect, 196, 209, 212, 382
Freundlich isotherm, 87
Fritz Haber, 2, 23
Front-exponent factor, 167

Frontal orbital, 71
Fugacity, 138, 163–166, 507, 625, 665, 819
Fugacity coefficient, 165, 166
Full width at half maximum (FWHM), 628
Fundamental hypothesis, 131
Fundamental understanding of catalysis, 124, 794, 798
Fused iron catalyst, 25, 29, 32–34, 36, 42, 47–49, 60, 62, 91, 105, 158, 202, 204, 214, 215, 219, 220, 222–225, 229, 231, 232, 237, 238, 240, 242, 243, 247, 248, 265, 266, 268, 270, 271, 276, 285, 297, 311–316, 319, 321, 323, 326–329, 331–334, 337, 355, 359, 361, 367, 372, 375, 380, 381, 384, 387, 391, 400, 402, 403, 405, 407, 409, 492, 506, 528, 563, 583, 584, 587, 588, 599, 607, 682, 696, 700, 714, 715, 721, 722
Fused slurry, 312, 314, 317

G

Gas composition, 82, 159, 169, 170, 173, 359, 376, 388, 403, 405–407, 413, 414, 521, 656, 664, 677, 779, 799, 829
Gas hourly space velocity, 547
Gas transfer, 375
Gas–phase oxidation, 463
Gas–solid interface reaction, 224, 391
Gas-film diffusion-controlled process, 362
Gas-flow abrasion method, 714
Gas-solid catalytic reaction, 153, 577
General laws of solid state reaction, 361
General relation, 125
Geometrical effect of poisons, 693
Gibbs free energy, 70, 82, 113, 125, 320, 474, 475, 534
Grain structure of the precursor, 225, 391, 635
Grain-growth kinetics, 636
Granularity of single-particle, 562
Granulator, 348, 349
Graphic method, 378
Graphics analysis, 596
Graphited activated carbon, 59, 458
Graphitization, 456, 458, 459, 461–464, 522, 523, 525, 526, 528, 589
Graphitization of activated carbons, 458
Graphitized activated carbon, 458, 461, 464, 496, 506, 521, 527
Griffith's theory, 707

H

H_2 reduction method, 475, 478
H_2 TPD, 235
H_2/N_2 ratio, 60, 118, 300, 506, 509, 510, 518–520, 561, 650, 664, 665, 668–670, 727, 807, 828
Haber–Bosch process, 27, 793, 810, 812, 830
Half-peak width, 615
He-TPD-MS, 463
Heat conductivity, 153, 175
Heat exchange, 3, 28, 167–170, 172, 173, 176, 416, 418, 421, 657, 659, 660, 722, 727, 752, 754, 756–759, 845
Heat recovery, 736, 747, 770, 779–781
Heat resistance, 58, 239, 446, 722
Heat transfer, 153, 168, 488, 492, 503, 550, 557, 562, 659, 660, 728
Heat-exchange reactor, 658–660
Heat-resistant, 16, 48, 171, 172, 215, 544, 548, 549, 557, 659, 660, 662, 689, 805
Heat-resistant property, 689, 805
Heat-resistant stability, 548, 549
Heat-resistant temperature, 171, 172, 215, 659, 660, 662, 689
Heat-sintering phenomenon, 395
Height of bed, 557, 558, 681, 685
Helmholz layer, 819
Hematite, 185, 188, 190, 202, 267, 382, 386, 395
Heterogeneous catalysis, 21, 28, 49, 67, 69, 76, 77, 79, 80, 82, 124, 147, 213, 214, 229, 244, 255, 296, 543, 568, 578, 583, 593, 795, 798
Heteromorphism, 185
Hexagonal close packed structure, 287
Hexagonal comby plane layer, 525
High resolution transmission electron microscopy, 284, 589
High surface area graphite, 436, 524
High-speed water impact method, 351
High-temperature evacuation, 82
Highly active mechanism, 303
Historical evolution, 1
Historical retrospect, 21
History and current development of catalyst related to ammonia synthesis, 794
Horiuti formulation, 114
Horiuti–Temkin relation, 115
Hosemann's paracrystallinity concept, 795

Hot spot-temperature, 361
Hot-wall converter, 503
Hougen–Watson equation, 128
HRTEM, 74, 284, 286, 287, 589, 639
Huit's equation, 706
Hump-type activity curve, 216, 229, 233, 237, 300
Hutting temperature, 243, 257
Hydrazine hydrate, 474, 478–480, 482, 487, 811
Hydrocarbon steam reforming catalysts, 8, 9
Hydrodesulfurization (HDS), 604
Hydrogen production, 14, 836, 837
Hydrogen–deuterium exchange reaction, 88
Hydrogen-arc plasma, 283
Hydrogenation, 3, 5–7, 16, 18, 28, 51, 57, 79, 93, 97, 100, 102, 103, 106, 107, 110, 117, 122, 138, 214, 244, 245, 425, 440, 517, 521, 535, 536, 580, 691, 693, 694, 699, 700, 800, 804, 811, 834
Hydrogenolysis, 6, 20, 93, 444–447, 604
Hydrogenolysis of precursor, 444
Hydrogenolysis temperature, 444–446
Hydrophilicity, 433, 463, 464, 469, 470
Hydrophobicity, 433, 469, 470
Hyperbolic tangent function, 160

I

ICI-AMV process, 725
Immersion solid solution, 382
Imperial Chemical Industries Ltd (ICI), 8
Impregnating solution, 455, 471
Impregnation, 7, 11, 13, 14, 16, 55, 348, 426, 427, 443, 454–456, 462, 466, 467, 469–471, 479, 482, 488, 489, 491, 518, 523
Impregnation time, 467, 470, 471
Impurity defect, 211, 213
Incident kinetic energy, 90, 91
Indirect heat exchange, 167, 169, 170, 176, 421, 659, 660, 752, 754, 756–759
Induction furnace, 315, 317, 318
Induction period, 45, 366, 377, 420
Industrial applications, 14, 50, 51, 257, 272, 300, 337, 344, 458, 500, 507, 521, 571, 650, 720, 755
Industrial catalytic process, 76, 258
Influence of loading order, 467
Influence of particle size, 376, 417
Influence of performances of catalyst, 771
Influence of promoters, 408, 442, 451
Influence of temperature, 200, 403, 500
Influencing factors during impregnating, 467
Infrared drying, 492
Infrared spectroscopy, 94, 95, 487, 545, 579, 581, 587, 593, 642
Inhibition effect of H_2 adsorption, 60
Inhibition effect of NH_3, 487
Inhibition effect of promoters, 528
Inhibition effect of Rare-earth oxide, 531
Inhibition of the methanation, 457
Initial content of ammonia, 673
Initial methanation temperature, 524, 525, 527–532, 535
Innovation and speculation, 793
Inorganic sulfur compounds, 6
Integral reactor, 551–554
Intensity and quantity of chemisorption, 579
Interaction energy between an adsorbate and the surface, 801
Interaction mechanism of solid–solid, 365
Interactions between active components and support, 593
Interface and boundary, 383
Intermetallic compound, 32, 58, 213, 805
Internal cooled bed, 658
Internal diffusion, 11, 153, 156–158, 160–162, 168, 345, 398, 807
Interpolation method, 803
Interspace of tetrahedron, 190, 192, 266, 268, 618
Interstitial nitrides, 51
Intrinsic defects, 190, 211
Intrinsic kinetic, 163, 167, 168, 375–377, 557, 657
Intrinsic or micro-kinetics, 153
Intrinsic rate constant, 162
Inverted parabolic function, 798
Investment of capital construction, 777, 778, 785
In situ measurement, 74, 258
Ion probe microanalysis, 258, 545
Ion scattering spectroscopy, 258
Ionic radius of metal ion, 243
Iron oxide, 8, 12, 13, 17, 34, 36, 37, 42, 49, 58, 185–188, 201, 202, 205, 214,

216–225, 228, 229, 231–239, 242, 243, 260, 265–268, 284, 297, 300–302, 304, 311, 321–323, 327, 328, 335, 354, 355, 359, 364, 373, 386–388, 390, 393, 395–397, 407, 408, 415, 418, 584, 587, 588, 618, 625, 717, 722, 726, 796, 805, 808, 816
Iron single-crystal surface, 292
Iron surface area, 229, 231, 250, 528
Irregularity of lattice, 213
Irreversible poisoning, 550, 690, 694, 700
Isopiestic process, 748
Isothermal characteristic, 551
Isothermal integral reactor, 552
Isothermal kinetic equation, 378
Isothermal reduction curves, 42, 43
Isotherms, 83–85, 140, 569, 573, 580, 584, 585, 587, 698
Isotherms of chemisorptions, 83
Isotope exchange of N_2, 101
Isotope jump technique, 131
Isotope tracer method, 115
Isotopic equilibration of nitrogen, 511
Isotopic equilibration reaction, 511, 512, 516
Iterative method, 166
IUPAC, 284, 546, 574

J

Jaw crusher, 319

K

KAAP process of coupling using Ru and Fe catalysts in a single converter, 746
KAAP-type Ru catalyst, 504
KBR advanced ammonia Process (KAAP), 62, 747
Kellogg advanced ammonia process, 60
Kellogg Brown & Root (KBR), 61
Kelvin equation, 573, 575
Kinetic equation for ammonia synthesis, 67
Kinetic model of solid state reaction, 367
Kinetic parameter, 73, 82, 83, 103–105, 108, 109, 119, 122, 176, 258, 366, 368, 412, 515, 546, 595, 604
Kinetics of overall reactions, 124
Kink, 80, 272, 273
KMR type catalyst, 337
Knudsen diffusion, 156–159
Kono's empirical equation, 706
Kulun titration, 196
K-value method, 611, 612

L

Lag-ring, 575, 576
Langmuir equation, 107, 510
Langmuir isotherm, 84
Langmuir kinetics, 82
Langmuir monolayer adsorption model, 580
Langmuir surface, 84, 124
Langmuir–Hinshelwood equation, 128
Langmuir–Hinshelword mechanism, 79
Lanthanide oxide, 516, 517, 530
Lattice constant, 39, 185–187, 191, 192, 196, 204, 205, 218, 219, 268–270, 385, 390, 565, 566, 578, 614, 618, 626, 634
Lattice defect, 49, 51, 189, 190, 196, 269, 301–304, 326, 334, 365, 382, 513, 521, 567, 627, 687
Lattice irregularity, 214
Lattice structure, 185, 190, 209, 210, 285, 287, 288, 381, 382, 525, 624
Lattice tensions-stress, 256
Ledge, 80, 81, 272
Lennard–Jones diagram, 77
Lewis acid, 587
Lewis base, 233
Life period, 733, 734, 739, 748, 784, 785, 787
Life-factor, 692, 693
Lifetime, 8, 11, 13, 16, 17, 19, 60, 92, 127, 568
Light-oil steam reforming, 9
Line defect, 210
Line width method, 615
Linear structure, 581
Liquid phase oxidation, 463
Liquid phase reduction method, 478
Liquid spurt impact dispersion, 350
"Localized" interaction, 68
Long-range segregation, 329
Loss of carbon support, 60, 521
Loss of the noble metal, 773
Low energy electron diffraction, 258, 292, 545
Low pressure ammonia synthesis process, 30
Low temperature shift, 6
Low-pressure renovation, 755
Low-temperature reduction method, 420
Lowest empty orbit, 809

Lubricating oil, 556, 704

M

Mössbauer spectroscopy, 36, 192, 258, 545, 625, 630, 641
Macro-kinetic equation, 161, 163
Macro-rate of ammonia synthesis, 105
Macro-scale physical character, 562
Macro-segregation, 327, 329–335
Macro-simulation-mathematics modeling, 139
Magnesium oxide, 122, 260, 312, 382, 436, 439, 455
Magnetic analysis, 641
Magnetic separation methods, 312
Magnetite, 26, 27, 31–33, 36, 37, 39, 41–43, 45, 46, 49, 50, 57, 60, 185, 187, 188, 198, 201, 202, 214–216, 218, 219, 221, 223, 224, 242, 245–249, 262, 264, 265, 267, 270, 271, 273–276, 282, 296, 301, 311, 312, 314–321, 323, 326, 334, 347, 350, 355, 356, 360, 363, 385, 386, 388, 390, 391, 394, 395, 397, 408, 409, 625–633, 662, 795–797, 804
Magnetite-based catalyst, 30, 41, 44, 46–48, 50, 249, 420
Main reaction, 93, 319, 746
Maintenance of ammonia synthesis catalysts, 721
Management of enterprise, 790
Mari, 126, 129–131
Mass transfer, 153, 161, 162, 360, 369, 393, 550, 553, 562, 572, 573, 686
Mathematic model, 167
Maxwell distribution law, 212
Measurement dispersion of metal catalyst, 603
Measurement of adsorption heat, 79, 579
Measurement of mechanical strength, 712
Measurement of physical properties, 561
Measurement of single-particle strength, 709
Measures to reduce hydrogen inhibition, 515
Mechanical impact dispersion, 350
Mechanical stability, 548, 549
Mechanical strength, 12, 32, 33, 46, 48, 300, 339, 342, 345, 348, 349, 352, 428, 438, 521, 543, 544, 562, 684, 705, 706, 712, 713, 716, 718, 719, 725, 726, 823
Mechanical stress, 706, 712
Mechanism of ammonia synthesis, 51, 67, 89, 111, 124, 834
Mechanism of CO poisoning, 699
Mechanism of nitrogen fixation of nitrogenase, 812
Mechanism of sintering, 689
Mechanisms of ammonia decomposition, 109
Mechanistic models, 79
Melting, 27, 39, 48, 57, 185, 186, 201, 202, 204, 212, 215, 222, 223, 239, 243, 245, 257, 262, 272, 311, 312, 314, 316–320, 323, 326, 327, 330, 332–335, 347, 349, 350, 353, 355, 359, 425–427, 440, 446, 451, 453, 454, 467, 478, 516, 521, 530, 533, 549, 609, 688, 689, 704
Melting point of promoter, 243
Melting temperature, 262, 316–318, 326, 327
Mercury-displacement method, 565
Mesh-like skeleton of crystal plane, 347
Metal cluster, 55, 67, 603, 616, 795
Metal inter-metallic compounds, 58
Metal ions radius, 267
Metal nitride, 25, 51, 52, 100, 111
Metal oxide, 13, 32, 56, 88, 95, 191, 202, 204, 205, 207–209, 231, 232, 237, 239, 249, 256, 285, 318, 359, 379, 390, 392, 427, 435–437, 441, 443, 444, 478, 516, 517, 522, 533, 581, 582, 600, 641
Metal particle nanosize, 282, 298–300, 589, 590, 592
Metal-support interaction, 150, 517, 589, 599
Metamorphic spinel structure, 187
Metastability, 282, 796
Metastable structure of Fe_3O_4, 619
Methanation, 3, 6, 8, 12, 15–17, 47, 60, 257, 300, 435, 442, 446, 456, 457, 459, 462, 476, 477, 506, 515, 521–537, 670, 702, 704, 752
Methanation catalyst, 15, 16
Methanation reaction of activated carbon, 521
Methane steam reforming, 9, 10
Methodology, 73, 830
Mg–Al spinel, 436, 437
Michaelis–Menten equation, 128
Micro-crack, 707
Micro-kinetic model, 82, 104, 799
Micro-pores volume, 522
Micro-porous surface area, 522

Micro-pressurized process, 750, 753
Micro-reaction kinetics, 117
Micro-segregation, 329–331
Microcrystalline carbon, 459
Microkinetic analysis, 123, 494
Micropore structure, 432
Microporous structure, 459
Microstructure distortion of Fe_3O_4, 621
Microstructure evolution of nanocrystalline, 636
Microstructure of active phase iron, 633
Microwave treatment, 456, 465
Middle direct cold-quench type, 756
Miller index, 80, 81, 96, 289, 610, 626
Minimum drop height, 713, 714
Minimum required mechanical strength, 719
Mixing efficiency, 316
Mobility of ions, 243
Model of defect structure, 192
Moderate coverage, 86, 87, 107, 136
Mohs hardness, 347
Molar ratio, 9, 202, 218, 323, 326, 451, 453, 479, 516, 531, 534, 536, 613, 741, 742
Molecular design, 241, 242, 244
Molecular diffusion, 156–160
Molecular ratio, 49, 219–222, 233
Molecular ratio of iron oxide, 49, 219
Molecular sieve, 16, 18, 19, 242, 339, 428, 437, 439, 455, 555, 556, 587, 616, 617, 736
Molecular sieve desiccant, 16, 18
Molecule design, 76
Molecule ratio of different iron oxide, 34
Molten method, 311
Molten salt, 455, 824, 826
Molybdenum carbide, 441, 802
Mono-molecular layer, 272
Monolayer adsorption theory, 83
Monophase of iron oxide, 34
Monophasical principle, 219
Most abundant reaction intermediate, 118, 119, 122, 125, 126, 129–131, 137, 145, 148
Most probable pore radius, 271, 575
Multi site adsorption, 597
Multi-bed adiabatic reactor, 660
Multi-bed reactor, 167, 169, 659, 665
Multi-component diffusion model, 158
Multi-stage heat exchange reactors, 659, 727
Multicrystalline structure determination, 616
Multilayer adsorption, 85, 86, 569
Multiple fine particle model, 372
Multiple impregnation method, 466
Multiple site, 146, 147

N

N_2 adsorption, 87, 88
N_2 production, 16, 17
N_2 TPD, 238, 513, 599
n-type semiconductor, 68, 213, 813
NaCl type structure, 190, 201
Nano material, 281
Nanoclusters of Fe atom, 50, 796
Nanometer effect, 281
Nanostructured metastable substances, 49
Naphtha steam reforming, 8
Natural magnetite, 26, 214, 312, 314, 315, 319, 320, 355
Nature and structure of surface, 577
Nature gas steam reformation process, 765
Negative temperature effect, 90
Net ammonia concentration, 33, 51
Net value of ammonia, 30, 33, 505, 561, 649, 659, 672, 675, 734, 736, 738, 740, 750–753, 755, 769, 771, 782, 783
New breakthrough of the technique, 33
New catalytic technique, 809
New exploration, 793
Nickel-based catalyst, 16, 17
Nitride, 24–26, 51–55, 89, 100–102, 111, 149, 151, 311, 339, 428, 440, 441, 635, 794, 799, 802, 824, 832
Nitrification, 339
Nitrogen adsorption state, 92, 94
Nitrogen binding energy, 800
Nitrogen fixation, 2, 29, 793, 811–813, 821, 822, 830–832
Nitrogen titration, 122
Nitrogen-containing functional group, 433–435
Nitrogenase, 117, 810–812, 821, 831–834
Nitrogenous fertilizer, 1, 2, 836, 842–844
Non-activated chemisorption, 592, 598
Non-catalytic gas–solid reaction, 360, 361, 367
Non-circulation process flow, 743
Non-crystal catalyst, 807
Non-feed gas quench, 659

Non-ferromagnetic, 185, 190, 578
Non-gradient reactor, 553
Non-iron metals, 97
Non-isothermal condition, 414
Non-productive time, 317, 318, 776
Non-reversible reaction, 388
Non-stoichiometric ferrous oxide, 223, 326
Non-stoichiometric reaction, 323, 363
Non-stoichiometry, 188–190, 256, 365, 396
Non-uniform distribution, 132, 144, 163, 222, 316, 318, 327, 345, 408, 488
Non-uniform surface, 83, 86, 87, 125, 131, 136, 137, 140, 144, 149, 596, 597
Number of d electrons in hypo-outer shell, 425
Number of total surface metal atoms, 582, 585, 586, 590

O

Occupy, 190, 193, 211, 213, 229, 236, 264, 266, 267, 278, 293, 294, 386, 392, 437, 510, 513, 583, 722, 726, 787
Octahedral interspace, 190, 201, 266, 268, 386
One-dimension quasi-homogeneous model, 167, 169
One-dimensional defect, 210
One-dimensional linear carbine, 429
One-step shaping method, 349
Operating rate, 789, 790
Optical microscope, 332
Optimum, 104, 141, 142, 146, 149, 169–173, 215, 239, 265, 337, 338, 404, 433, 440, 444, 447, 452, 474, 518, 519, 524, 529, 530, 649, 650, 653–660, 662, 664, 665, 669, 670, 684, 685, 752, 756, 771, 799–801, 804, 816
Optimum H_2/N_2 ratio, 518, 519, 664, 665
Optimum reaction conditions, 653
Optimum reaction temperature, 653, 655–657, 659, 660, 756
Optimum reaction temperature curve, 657, 659
Optimum value of space velocity, 662
Organic metallic chemistry, 68
Oscillation amplitude of atom, 382
Over-heating of bed, 558
Overall reaction rate, 107, 110, 129, 138
Oxidation combustion method, 18
Oxidation degree, 262, 316–318, 320
Oxidation of activated carbon, 463
Oxidation–reduction titration, 196
Oxides, 6, 7, 10–14, 16, 20, 32, 34, 36, 42, 49, 52, 55, 69, 75, 88, 95, 185, 186, 188, 191, 192, 198–202, 204, 205, 207–209, 214, 216–225, 228, 229, 231–239, 242, 243, 245, 247–250, 255–257, 260, 262, 265, 267, 271, 276, 277, 282, 285, 297, 301, 302, 311, 312, 316, 318, 321, 322, 326, 327, 354, 359, 363, 364, 373, 379, 380, 383, 385–388, 390, 392–394, 396, 397, 401, 408, 412, 426, 435–439, 441–444, 453, 459, 514, 516–518, 528, 530, 533, 581, 584, 586–588, 600, 607, 625, 630, 707, 717, 722, 796
Oxygen, 1–3, 10, 15, 19, 20, 39, 42, 45, 48, 57, 75, 79, 111, 142, 185–188, 190, 191, 193, 196, 202, 205, 208, 209, 218, 228, 234, 246, 247, 251, 253–255, 258, 266–268, 270, 271, 273, 276–280, 285, 289, 292, 311, 316, 318, 319, 321, 323, 324, 326, 339, 340, 343, 344, 355, 359, 365–367, 374, 379–381, 384–386, 388–390, 392–397, 400, 410, 412, 426, 431, 433, 447, 450, 458, 489, 566, 567, 581, 582, 588, 590, 607, 608, 617–621, 624, 625, 691, 694–697, 701, 704, 705, 717, 718, 726, 728, 742, 767, 796, 797, 804, 805, 815, 824, 825, 836
Oxygen-containing functional group, 433, 434, 463
Oxygenous compound, 59, 549, 550, 695

P

Packing density, 292, 562, 564, 566, 567, 682
Packing, storage and transportation, 319
Particle shape factor, 562, 683, 684
Particle size, 11, 38, 43, 94, 142, 147, 150–152, 158, 160, 161, 176, 282, 284, 315, 316, 319, 346, 350–352, 359, 360, 370–372, 375–377, 384, 396, 399, 400, 403, 417, 439, 442, 445, 446, 469, 472, 477, 481, 482, 484, 492–494, 496–500, 524, 544, 552, 557, 558, 561, 562, 564, 567, 568, 578, 589, 590, 610, 622, 628, 634, 636, 638–642, 650, 674–680, 682–686, 707, 714–716, 721, 722, 725, 736, 751
Particle size and density, 562
Passivation, 283, 319, 338–344, 604, 608, 716, 717, 721, 726, 775
Pebble-shaped grain, 352
Pellet density, 564, 566, 567

Percent of iron atom exposed on surface, 297
Performance characteristic, 492
Performance evaluation, 543, 544, 550, 553, 555
Performance of reduction, 408
Performances of the converter, 734
pH value of the isoelectric point, 471
Phase boundary, 362, 365, 372, 394, 397, 398
Phase diagram analysis, 323
Phase diagram of carbon, 429
Phase fraction, 220
Phase transformation, 323, 335, 627, 845
Phase-change, 372
Phase-change mechanism, 624
Phenomenological investigation, 75
Phenomenon of poisoning of catalyst, 690
Phenomenon of strong H_2 inhibition, 507
Photo-catalytic reaction, 813
Photocatalysis, 813, 814, 835
Photocatalytic ammonia synthesis, 816
Photoelectric catalysis, 67
Physical adsorption, 77, 87, 91, 92, 229, 568, 569, 573, 578, 584, 588, 810
Physical model, 69, 379
Physical stability, 521, 544
Physical structure, 11, 12, 229, 346, 429, 432, 456, 459–461, 488, 527, 543
Platinum filament, 110, 128
Platinum-based catalyst, 17
Plug-flow reactor, 118–120
Point defect, 209, 211, 213, 214, 272, 624
Point-time yields, 122
Poison, 11, 13, 15–17, 32, 46, 204, 344, 418, 427, 442, 453, 487, 517, 521, 549, 550, 671, 690–695, 697, 699, 704, 728, 748, 823, 830, 844
Poison and life of catalyst, 686
Poisoning effect of sulfide compound, 701
Poisoning phenomena, 695
Poisoning-resistant, 46, 48
Polarographic analysis, 196
Polycrystal, 99, 101, 110, 192, 210
Pore distribution, 271, 398, 432, 451, 572–574
Pore size, 19, 84, 265, 271, 359, 399, 400, 404, 432, 434, 439, 452, 461, 522, 527, 544, 562, 564, 568, 570–575, 577, 597, 610, 617, 689, 806
Pore structure, 38, 234, 235, 270, 271, 273, 275, 336, 367, 400, 428, 432, 433, 458–464, 489, 491, 544, 564, 567, 568, 572, 573, 576, 577, 608, 639, 706
Pore surface utilization ratio, 677
Pore volume, 38, 234, 235, 265, 270, 400–403, 432, 460–462, 465, 523, 526, 527, 544, 562, 564, 568, 570–572, 574, 578, 725
Pore with parallel wall, 576
Porosity, 38, 142, 158, 169, 224, 234, 235, 270, 277, 284, 345, 349, 375, 391, 396, 563, 564, 570, 571, 578, 687, 689, 690, 706, 721, 725
Porous skeleton, 270
Porous structure, 8, 11, 277, 281, 345, 359, 372, 400, 571
Porridge-like zone, 331
Possible reasons of hydrogen inhibition, 510
Possible reduction reaction of iron oxide, 387
Potassium aluminum ferrocyanide, 311
Potassium carbonate, 312
Potassium ferrocyanide, 311
Potassium nitrate, 312, 426, 445, 467, 491
Potassium oxygen layer, 277
Potassium ruthenic acid, 523
Potential energy, 72, 77, 383, 799
Potential of energy-saving, 765, 767, 790
Power, 2, 20, 30, 48, 76, 97, 108, 122, 124, 128, 145, 158, 362, 396, 505, 618, 662, 664, 672, 674, 684, 699, 736, 737, 748, 749, 751–756, 762, 765, 766, 770, 779, 780, 782–784, 789, 810, 812–814, 820, 838, 839, 841
Power consumption, 30, 48, 505, 662, 664, 672, 674, 684, 752, 754–756, 779, 780, 782–784
Pre-experiment, 557
Pre-exponential factor, 50, 102, 135, 214, 376, 377, 403, 594, 595, 601
Pre-reduced catalyst, 716–718, 721, 726, 775, 776
Precipitation, 16, 311, 323, 454, 482–486
Precipitation method, 16
Precipitation-washing method, 482
Precipitator, 484, 485, 487
Precursors of promoter, 442, 443
Preparation method, 57, 158, 232, 259, 359, 400, 430, 434, 454, 467, 543, 544, 615, 684, 706, 806
Preparation of $Fe_{1-x}O$ based catalyst, 39, 301

Preparation of fused iron catalysts, 311, 361
Preparation of ruthenium catalyst, 454, 459, 474
Pressed mercury method, 568
Pressing and sintering technology, 349
Pressure drop, 13, 30, 33, 345, 346, 348, 349, 563, 567, 568, 662, 664, 674, 680–686, 705, 706, 711, 719, 720, 727, 736, 738, 740, 744, 752, 756
Pressure level, 734, 749
Pretreatment, 150, 151, 256, 257, 456, 457, 489, 496, 517, 524, 536, 621, 790, 797
Primary particle, 561
Primary steam reforming catalyst, 3, 9
Principle of single-phase, 49
Probability of structural fracture, 708
Process flow of using Fe catalyst combined with Ru catalyst, 744
Product energy consumption, 761–763
Production capacity of catalyst, 547
Production cost, 2, 29, 39, 48, 733, 771–773, 777, 778, 780, 781, 785
Production management, 767
Production of synthesis gas, 2, 9
Programmed-temperature desorption, 88, 89, 118–120, 123
Progress of electrochemical ammonia synthesis, 820
Promoter effect, 515, 594
Promoters of fused iron catalyst, 238
  Al_2O_3, 7, 10, 11, 18, 27, 39, 58, 95, 96, 105, 204, 205, 229, 232, 245–249, 256, 259, 260, 262, 264, 267, 294, 311, 318, 322, 327, 328, 335, 354, 355, 359, 427, 435, 447, 478, 480, 487, 528, 530, 581, 583, 584, 608, 643, 718, 795, 800, 804, 805
  CaO, 10, 11, 16, 27, 39, 50, 192, 198–201, 205, 215, 217, 230, 231, 239, 240, 247–249, 260, 264, 267, 282, 285, 322, 327, 328, 354, 355, 359, 390, 408, 409, 435, 443, 584, 586, 588, 717, 796, 810
  K_2O, 12, 39, 58, 91, 215, 229–233, 239, 240, 248, 249, 251, 259, 260, 267, 268, 270, 279, 285, 294, 327, 328, 354, 355, 408, 445, 528, 530, 584, 586, 588, 608, 636, 700, 795, 805
  MgO, 8, 10, 11, 14, 16, 27, 95, 192, 198–200, 205, 231, 237, 239, 245, 247, 249, 250, 260, 264, 267, 311, 318, 322, 354, 359, 390, 408, 409, 435, 437, 440, 443, 450, 473, 514, 518
  TiO_2, 10, 95, 247, 256, 408, 435, 577, 813, 815, 816
Proper use of catalysts, 727
Property of elements, 447
Proportion and mixing of material, 311, 315
Protective catalyst, 3
Proton acid, 587
Protonation, 811, 821, 830
Pulsed electrodeposition (PED), 636
Pulverization, 544, 549, 705
Purification, 2, 3, 10, 14, 19, 311, 312, 356, 555, 556, 606, 670, 704, 722, 733, 735, 738–740, 750, 752, 753, 776, 836, 840
Purification of syngas, 556, 776

Q

Quantitative analysis, 196, 199, 282, 335, 480, 610–612, 618, 619, 627, 640, 797
Quantum chemistry, 68, 242, 808, 832
Quasi-chemical species, 213
Quasi-equilibrium, 115, 366
Quasi-steady approximation, 132
Quasi-steady state, 111, 132
Quench wall, 332
Quenching, 318, 332, 335, 659

R

Radial bed, 168
Radial-flow, 61, 421, 422, 503, 661, 662, 686, 737, 739, 740, 747, 752, 754, 779
Raising temperature alternately method, 420
Raney, 58, 97, 101, 111, 448, 511, 517, 805
Rapid cooling process, 334
Rapid flash vaporization, 214
Rapid solidification technique, 335
Rare earth metals, 453, 516, 805
Rate determining step, 51, 60, 75, 93, 97, 100, 101, 105–107, 110–118, 122, 125, 126, 128, 129, 131, 137, 140, 145, 148, 152, 153, 233, 237, 253, 425, 436, 442, 507, 508, 511, 514, 525, 536, 794, 795
Rate expression, 82, 83, 97, 103, 110, 112, 118, 124, 126, 128, 130, 148, 366
Rate of accumulation, 704

Rate of adsorption, 87, 133, 592
Rate of desorption of these poison, 704
Rate of sintering, 689
Rate of solidification, 327, 334
Ratio of two-phase diffraction intensity, 611
RDS, 105, 106, 113, 114
Re-crystallization of the catalyst, 701
Reaction activation energy, 70, 72, 77, 91, 214, 237, 238, 536
Reaction equilibrium constant, 655
Reaction mechanism, 8, 51, 67, 69, 72–76, 79, 83, 89, 90, 93, 94, 102–105, 107–109, 112, 117, 119, 122, 124–126, 129, 142, 147, 154, 240, 241, 243, 258, 273, 378, 507, 536, 546, 581, 593, 642, 820, 834
Reaction on the boundary of phases, 395
Reaction order, 102, 107–110, 124, 128, 162, 236, 237, 362, 363, 376, 379, 514–516
Reaction pathway, 71, 73, 75, 93, 198, 813
Reaction pressure, 30, 42, 503, 650, 652, 653, 664, 782, 845
Reaction rate, 10, 13, 25, 41, 45, 47, 55, 56, 58, 71, 73, 78, 80, 97, 100, 106–108, 110–114, 124, 126, 129, 132, 137–139, 145–147, 153–157, 160–164, 166–168, 170, 171, 189, 218, 238, 251, 253, 258, 273, 290, 296–299, 360, 362, 365, 366, 368, 370, 371, 373, 375, 377, 388, 397–399, 403, 404, 420, 436, 437, 439–442, 444, 451, 474, 476, 487, 488, 498, 504, 505, 511, 512, 517, 545–547, 551–554, 558–561, 591, 600, 601, 603, 650, 655, 657, 659, 660, 665, 669, 674–679, 686, 697, 802, 805, 809, 814, 815, 818, 820, 821, 827, 829, 830, 834
Reaction rate in volume, 504, 560
Reaction temperature, 9, 15, 90, 107, 111, 156, 157, 197, 363, 481, 499, 517, 521, 549, 632, 653–657, 659, 660, 665, 669, 677–680, 745, 752, 756, 757, 777, 830, 834, 835
Reaction-controlled process, 362
Reactor, 3, 7, 9, 10, 13, 15, 16, 18, 23, 25, 27, 30, 31, 41, 42, 47, 60, 61, 67, 102, 103, 117–120, 122, 124, 139, 162, 163, 167–173, 176, 177, 215, 257, 290, 294, 297, 318, 339, 344, 346–348, 360, 410, 411, 413, 415, 416, 418, 419, 421, 422, 428, 439, 462, 499, 501, 503, 546, 547, 549–562, 564, 572, 578, 601, 602, 649, 650, 652, 654, 656–665, 669, 674, 676, 680, 681, 683, 685, 692, 701, 711, 713, 719, 727, 736, 737, 741, 752, 756, 760, 776–778, 804, 824, 826, 827, 835, 845
Reactor for performance evaluation, 550
Reclaim way of the waste heat, 734
Recovery of reaction heat, 760, 769
Recovery of the surface structure, 461
Recovery process of reaction heat, 768
Recovery ratio of the reaction heat, 769–771
Recrystallization effect, 249
Recycling of waste catalyst, 354–356
Reduction degree, 42–44, 227, 265, 271, 374–376, 393, 395, 396, 399–402, 405, 408, 415, 419, 602, 603, 608, 631
Reduction equilibrium, 404
Reduction in industrial equipment, 409
Reduction mechanism of oxides, 390
Reduction of catalyst with industrial size, 377
Reduction of fused iron catalysts, 359, 361, 367, 375, 387
Reduction of $RuCl_3 \cdot xH_2O$, 472
Reduction of wüstite-based catalyst, 46
Reduction parameter, 408, 419
Reduction pressure, 388
Reduction process, 13, 15, 16, 45, 47, 48, 163, 224, 225, 270–272, 327, 339, 340, 344, 347, 359–361, 375, 379, 383, 386, 388, 390–396, 398–401, 403–409, 411, 412, 415–417, 422, 437, 449, 475, 478, 482, 524, 571, 600, 602, 603, 625, 627, 633, 659, 704, 774, 775
Reduction process of oxide, 379
Reduction program, 421
Reduction rate, 34, 39, 44–47, 226, 228, 245, 304, 352, 361, 372, 373, 375, 393–397, 399, 403–412, 417–420, 601, 602, 774
Reduction reaction kinetics, 390
Reduction reaction of $Fe_{1-x}O$, 42
Reduction temperature, 33, 39, 43, 45, 46, 226–228, 246, 271, 303, 337, 379, 380, 387, 390, 403, 404, 407, 408, 416, 418–420, 422, 444, 473, 475, 477, 479, 600, 603, 607, 608, 726, 774, 775
Reduction thermodynamics, 386
Refine catalysts, 16
Refrigerant, 1
Regeneration, 7, 256, 544, 548, 594, 606, 608, 785, 822

Relation of Polanyi and Semenov, 133
Relationship between catalyst efficiency and particle size, 680
Relationship between catalytic activity and space velocity, 504
Relationship between output and the service time of catalyst, 786
Relationship between the B5-structure and the Ru particle size, 494
Relationship of reduction process and catalytic activity, 400
Repeated redox reaction, 228
Replacement of catalyst, 15, 788
Requirement of mechanical strength, 718
Revelation of theory and practice, 794
Reversible poisoning, 406, 549, 690, 691, 694, 696
Reynolds number, 563, 681
Rhombohedral crystal lattice structure, 185
Riddling searching, 140
Rideal–Eley mechanism, 79
Rietveld analysis, 590, 617–620
Rietveld fitting, 617, 620
Rigid cylindrical hole, 402
Rock-salt type metal oxide, 204, 205
Role of electronic promoter, 515, 530
Role of support and promoter, 444
Rotating abrasion method, 714
Ru–M alloy, 518
Ru–M catalyst, 517
Ru-catalyzed methanation, 47, 300, 435, 506
Rubidium, 254, 255
Ruthenium based catalysts, 31, 51, 426, 521
Ruthenium carbonyl, 34, 427, 488
Ruthenium dioxide, 426
Ruthenium oxide, 257, 425, 426
Ruthenium precursor, 426, 450
Ruthenium salt, 426
Ruthenium tetroxide, 426
Ruthenium trichloride hydrates, 426

S

Sabatier's principle, 80
Scanning tunneling microscope, 258
Scherrer equation, 38, 302, 303, 590, 628
Schottky defect, 209, 212, 383
Screw dislocation, 210
Second ion mass spectroscopy, 258
Secondary desorption, 512
Secondary particle, 561, 562
Secondary steam reforming, 10, 11
Sediments of active component, 488
Segregation of promoter, 327
Selection of catalyst, 69, 125, 692, 771
Selective chemisorptions, 67, 150, 151, 229, 284
Selective oxidation of CO, 17
Selective poisoning, 690, 691
Selectivity of catalyst, 548, 550, 555, 777, 784
Self-diffusion coefficient, 191, 386, 394
Self-ignition, 341
Semi-melting temperature, 521, 549
Sensitivity of Ru to ammonia, 47, 506
Separation of ammonia, 3, 734, 735, 737, 750
Service time of catalyst, 784–788
Seven atomic cluster active center model, 291
Shape coefficient, 352, 563
Shape factor, 350, 562, 563, 578, 683, 684, 721
Shape of the catalyst, 680
Shaping technique of catalysts, 345
Sheet-like pore, 276
Shell-and-tube configuration, 659
Short-range segregation, 330
Shrinking core model, 362, 367, 372, 400
Side-on adsorption state, 581
Simulating design calculation, 176, 177
Single crystal iron, 91, 99, 102, 104, 118–120, 151
Single crystal surface, 52, 80, 81, 292
Single particle crush strength, 712
Single-component diffusion model, 158
Single-crystal structure, 285
Single-cylinder reactor, 760
Single-fold cluster, 195
Single-particle crush strength (SPCS), 709
Single-particle string reactor method, 572
Sintering, 10, 14, 16, 20, 33, 45, 142, 245, 246, 249, 256, 277, 311, 336, 345, 349, 350, 371, 375, 402, 404, 428, 442, 445, 446, 450, 457, 465, 476, 477, 515, 521, 524, 549, 589, 590, 608, 615, 639, 687–689
Sintering process, 311
Size effect, 282, 706
Skeletal density, 565
Skeleton washing method, 611
Slow-cooling, 327

Small crystal grain, 327
Small-medium ammonia plant, 755
Solid solution of iron, 202
Solid state chemistry, 281
Solid state reaction, 322, 361, 363, 364, 366, 367, 377, 393, 395, 396, 398
Solid state reaction kinetic, 377
Solid's melting point, 688
Solid–state topochemical reaction, 365
Solidification process, 312, 327, 329–335
Solubility of metal ion, 222
Sosoloid type complex oxide, 202
Space time yield (STY), 649
Space velocity, 30, 31, 33, 35, 39, 40, 42, 47, 58, 118, 155, 164, 215, 218, 297, 337, 339, 359, 361, 403, 405, 406, 410, 416, 418, 420, 422, 431, 499, 504, 505, 508, 536, 547, 550, 558–561, 649, 650, 652, 662–665, 668, 675, 678, 680, 690, 704, 725, 727, 742, 750–752, 769, 771, 788, 835
Specific surface area, 85, 164, 229, 231, 234, 247, 264, 282, 283, 297, 399, 428, 430, 439, 443, 458–461, 526, 560, 568, 569
Spherical catalyst, 33, 159, 160, 216, 332, 334, 349–354, 398, 684, 710, 711, 714, 720–722, 726
Spherical coefficient, 352, 353, 563
Spillover, 512–514, 535, 582, 588, 590, 594
Spinel type crystal structure, 204
Spinel-type cubic crystal, 185
Spraying balling method, 351
Spraying glomeration method, 351
Stability, 10, 11, 13, 17, 28, 32, 45, 67, 73, 103, 142, 185, 193, 202, 224, 229, 243, 247, 249, 260, 280, 288, 294, 345, 381, 382, 391, 408, 429, 432, 436, 438, 440, 442, 447, 449, 455, 458, 459, 462, 469, 478, 499, 515, 516, 521, 524, 528, 543, 544, 548–550, 557, 607, 612, 616, 636, 674, 691, 701, 722, 725, 776, 785, 794, 803, 823, 830
Stability of ruthenium catalyst, 521
Stability of the structure of electron shells, 381
Static method, 546
Steady-state equation, 118
Steady-state method, 828
Steam reforming, 3, 5, 8–11, 743, 754, 755, 784, 837
Steam reforming reactions, 9, 10
Sticking coefficient, 84, 91, 92, 98, 100, 101, 104, 118, 122, 123, 830
Stoichiometry of chemisorption, 284, 285
Storage molecule for hydrogen, 844
Stretching vibration frequency, 532, 581
Strong inhibition, 89, 108, 507, 509, 514, 518, 741
Strong inhibitory effect, 408
Strong metal-support interaction, 517, 589
Structural image, 266–268
Structural promoter, 12–14, 29, 204, 232, 245, 247–249, 255, 264, 265, 314, 359, 408, 436, 450, 587, 625
Structural property, 345
Structural sensitivity, 290, 492, 494
Structure analysis by Rietveld fitting, 617
Structure of activated iron catalyst, 270, 272
Structure of active center, 290, 831
Structure of active phase, 636
Structure of carbon material, 429
Structure of fused iron catalysts, 185
Structure of nitrogenase, 812, 832
Structure of precursor, 625
Structure of unreduced catalyst, 266
Structure sensitive catalytic reaction, 290
Sublayer hydrogen-bridged compound, 236
Sublimation heat, 243, 256
Sulfur recovery catalyst, 16–18
Sulfur tolerant shift catalyst, 13, 14
Sulfuring process for HDS catalyst, 604
Super activity, 214
Super high vacuum, 258
Super-Claus process, 18
Supercritical ammonia synthesis, 835
Support of ruthenium catalyst, 430, 437, 448
Surface abundant reaction intermediate, 117
Surface acidity, 11, 244, 439, 587
Surface active site, 81
Surface adsorption affinity of nanoparticle, 283
Surface area, 8, 12, 19, 38, 58, 74, 82, 85, 102, 105, 159, 161–164, 204, 214, 229–234, 239, 240, 245, 247, 249, 250, 253–255, 258, 262, 264, 265, 268, 271, 277–279, 282, 283, 285, 297, 327, 359, 377, 384, 398–403, 405, 412, 419, 428, 430, 432, 434, 436, 439, 440, 443, 445, 458–462, 464, 465, 469, 470, 484, 489, 492, 493, 522–524, 526–528, 544, 546,

547, 560–564, 568, 569, 571, 572, 578, 579, 583, 584, 586–589, 610, 615, 631, 681, 683, 687–690, 694, 695, 725, 797, 801–807, 823, 825
Surface chemical property, 435
Surface coverage, 52, 77–80, 82, 83, 122, 123, 141, 148, 231–233, 579, 581, 587, 592, 594
Surface diffusion, 156, 282, 688, 797
Surface effect, 282, 283
Surface element composition, 524
Surface energy, 141, 152, 254, 277, 281, 288, 289, 383, 384, 472, 707, 795
Surface equivalent diameter of particle, 563
Surface geometric structure, 287
Surface heterogenicity, 82
Surface molecular model, 69
Surface reaction mechanism, 102, 241
Surface reconstruction, 49, 96, 151, 152, 304
Surface science, 49, 68, 91, 92, 105, 118, 242, 492, 641, 794
Surface species, 59, 79, 103, 117, 118, 257, 258
Surface structure, 13, 74, 75, 81, 99, 142, 147, 151, 258, 272, 273, 278, 279, 281, 289, 290, 292, 301, 397, 460, 461, 464, 465, 522, 523, 526, 578–580, 582, 584, 616, 624, 687, 796, 797, 801
Surface tension, 243, 256, 282, 350, 351, 383, 455, 573, 575, 819
Surface texture, 229
Synergy effect between acid and base sites, 49
Synloop's operating pressure, 60, 503
Synthesis efficiency of ammonia, 662
Synthesis gas, 2, 3, 9, 11, 12, 14, 17, 30, 45, 61, 151, 246, 338, 388, 407, 496, 555, 633–635, 665, 670, 686, 691, 694, 695, 700, 727, 728, 738, 747
Synthesis loop, 3, 19, 60, 61, 421, 503, 662, 664, 672, 675, 700, 702, 704, 733, 734, 736–743, 747–750, 752, 754–756, 766, 769–771, 773, 774, 776, 783, 784, 786, 788, 838, 840
Synthesis pressure, 651, 734, 748, 749, 754, 788
Synthesis process, 2, 6, 10, 23, 24, 30, 501, 503, 507, 665, 669, 686, 695, 735, 741, 743, 750, 755, 794, 813, 821, 832, 840
Synthetic process flow, 741, 742
Synthetic process flow without circulation, 742
Synthetic ratio of ammonia, 561
System of measurement and analysis, 557

T

Tabletting method, 346
Tamman temperature, 257, 688
Technical characteristics of wüstite-based catalysts, 46
Technological measures to reduce macro-segregation, 333
Temkin equation, 107, 163, 508
Temkin isotherm, 86, 149
Temkin theory, 67, 106, 131, 133, 137, 140
Temkin–Pyzhev equation, 41, 106, 139, 163
Temkin–Pyzhev mechanism, 109, 111, 140
Temperature at the commencement of sintering, 688
Temperature difference, 153, 339, 557, 558, 606, 662, 767, 769
Temperature effect of poison, 693
Temperature programmed analysis technology (TPAT), 593
Temperature programmed desorption (TPD), 279, 594
Temperature programmed oxidation, 594, 604
Temperature programmed reduction, 495, 594, 600
Temperature programmed sulfuration, 604
Template, 279
Tension-stress, 707, 708
Terminal group adsorption, 96
Terrace, 80, 111, 272
Tetrahedral interspace, 190, 201, 266, 268, 386
Tetrahydrofuran, 428, 469
Textbook catalyst, 49, 224, 282, 300
Theoretic energy consumption, 760–762, 764
Theoretic water yield, 410
Theoretical amount of the H_2 consumption, 774
Theoretical amount of the H_2 consumption, 774
Theoretical density, 565, 566
Theoretical research on the mechanical strength, 706
Thermal analysis technology, 605

Thermal conductivity, 257, 425, 456, 544, 552, 563
Thermal decomposition model, 372
Thermal expansion coefficient, 212, 384
Thermal-decomposition theory, 390
Thermo-stability, 247
Thermochemical kinetic profile, 71, 72
Thermodynamics and mechanism of methanation, 534
Thermodynamics of ammonia synthesis, 122, 508, 509, 664
Thermogravimetric analysis (TGA), 340, 360, 375, 607
Thickness of the molten material layer, 334
Thiele modulus, 160
Thiele number, 398
Three-dimensional defect, 211
Three-dimensional diamond crystal, 429
Three-dimensional stack model, 709
Three-fold hollow site, 494
Three-phase arc, 318
Threshold catalyst strength, 719
Ti–Fe alloy, 59, 806
Tip-cut pore, 577
TLK model, 80, 82
TOF, 285, 296–298, 428, 439, 442, 447, 448, 492, 497–499, 504, 505, 516, 519, 520, 545, 547, 561, 583, 591, 640, 800
Topochemistry of the reduction process, 224, 391
Topsøe process, 30
Tortuosity factor, 158, 270
Total cost per ton ammonia, 773
Total reaction equation, 762, 764, 812
Total stacking volume, 564, 567
TPD of non-uniform surface, 596
TPR dynamic equation, 600, 602
Transfer coefficient, 133, 134, 769
Transformation of electron and proton, 812
Transient-response, 112
Transition metal, 58, 59, 283, 449, 517, 518, 528, 532, 533, 581, 694, 798, 799, 804, 805, 807, 811, 831, 832
Transition-state energies for N_2 dissociation, 800, 801
Transitional metal oxides, 207–209
Transmission electron microscopy, 246, 273, 284, 493, 545, 589, 622, 623, 639
Transport of catalyst, 728
Transportation stage by stage, 386
Treatment in H_2 or inert atmosphere, 464
Trial-and-error, 243
Tube-like pore, 576
Tubular reactor, 555
Turbo-compressor, 662
Turbulence state, 563
Turbulent structure, 522
Turnover frequency, 140, 141, 147, 296–298, 492, 504, 519, 545, 547, 561, 583, 591
Turnover frequency (TOF), 140, 296
Turnover number, 119, 122, 296
Turnover rate, 127, 132, 142, 144, 150–152
Twist-factor, 270, 571, 572, 578
Two step mechanism, 125, 140, 148
Two-dimensional defect, 210
Two-dimensional graphite layer, 429
Two-step mechanism, 125, 126, 137, 138
Two-step sequence method, 126, 128
Type of catalyst for ammonia synthesis, 675
Type, density and energy distribution of surface adsorption center, 593
Typical model reaction, 124, 794, 798

U

Uhde-ICI-AMV synthesis process, 755
Ultimate tensile strength, 349
Understratum structure, 289
Uniform conversion model, 372
Unsaturated bond degree of the edge carbon atom, 525
Unstable intermediate complexe, 71
Use of the reaction heat, 767
Utilization of inner surface, 398
Utilization ratio of the inner surface, 674, 676–678
Utmost tensile strength, 713

V

Vacuum drying, 492
Valence state, 427, 443, 487, 544
Virtual pressure, 149–151
Viscosity of mixture gas, 174
Void volume, 567
Voidage of catalyst bed, 567
Volatile potassium chloride, 704
Volcano-type activity curve, 214, 222

W

W-Type mechanism, 110, 111
Wüstite, 33, 34, 36, 37, 39, 42, 44–51, 152, 176, 177, 185, 189–194, 196–202, 211, 216, 218, 219, 221, 224, 228, 245, 249, 260–265, 268–270, 282, 300–304, 320, 322, 323, 326, 332, 352, 359, 363, 375, 377, 382, 383, 385, 388–391, 394, 395, 407, 408, 412, 414, 501, 506, 515, 578, 607, 612–614, 625–630, 633, 750, 796
Wüstite-based catalyst, 46–51, 152, 176, 359, 375, 796
Wall effect, 558, 710
Washing method, 480–482, 611
Waste catalyst, 354–356, 501, 702, 703
Waste heat, 18, 734, 737–740, 747, 755, 756, 768, 770, 771, 779
Water vapor, 228, 248, 271, 279, 280, 337, 339, 377, 388, 397, 404–406, 408, 410, 411, 415–422, 489, 491, 617, 660, 691, 695–697, 699, 824, 826
Weakest link model, 707, 708
Weibull curve, 711
Weibull distribution, 707, 708, 710, 711
Whole-stack crush strength (WSCS), 709
Work function, 70, 75, 292, 293, 589, 830

X

X-ray diffraction technique (XRD), 609
X-ray photoelectron spectroscopy (XPS), 258, 279, 640
Xyloid material, 525

Y

Yield, 3, 14, 17, 22, 25, 42, 122, 141, 145, 244, 317, 319, 350–352, 410, 427, 458, 520, 548, 561, 649, 660–664, 684, 685, 691, 694, 746, 771, 773–777, 784, 804, 806, 807, 811, 814, 816–818, 821, 822, 827, 830
Yield of ammonia, 17, 22, 458, 561, 649, 660, 661, 773, 776, 804, 807, 816, 817
Yield per pass, 548

Z

ZA-5 ammonia synthesis catalyst, 166
Zero-dimensional defect, 209
Zero-dimensional fullerene molecule, 429
Ziegler–Natta catalyst, 73
Zinc oxide desulfurizer, 3, 7, 8
$ZnCl_2$ activation, 432